*SF2A 2016*
*C. Reylé, J. Richard, L. Cambrésy, M. Deleuil, E. Pécontal, L. Tresse and I. Vauglin (eds)*

# Proceedings of the annual meeting of the French Society of Astronomy & Astrophysics Lyon, June 14-17, 2016


Credit: Caroline Vilatte

# Contents

**Table of contents** **i**

**Foreword** **vii**

**List of participants** **ix**

**SF2A — Plenary session (S00)** **1**

Identifying the non-linearities in the period-luminosity relations of Cepheids
*J. Dassa-Terrier* **3**

Modeling Small Exoplanets Interiors: a Numerical Scheme to Explore Possible Compositions
*B. Brugger, O. Mousis, and M. Deleuil* **11**

Sciences pour les Exoplanètes et les Systèmes Planétaires
*F. Roques, C. Balança, Y. Bénilan, J.M. Griessmeier, E. Marcq, T. Navarro, S. Renner, J. Schneider, and C. Schott* **17**

SITELLE's Data Release 1
*T. B. Martin, and L. Drissen* **23**

**Gravitational waves (S01)** **29**

Searching for gamma-ray counterpart of gravitational wave transients
*H. Sol* **31**

**High energy and cosmic phenomena (S02)** **37**

Multiwavelength study of the flaring activity of Sgr A* in 2014 February–April
*E. Mossoux, N. Grosso, H. Bushouse, A. Eckart, F. Yusef-Zadeh, R. L. Plambeck, F. Peissker, M. Valencia, D. Porquet, W. D. Cotton, et al.* **39**

Why curvature radiation in neutron-star magnetospheres should be treated in the framework of quantum electrodynamics
*G. Voisin, S. Bonazzola, and F. Mottez* **45**

Models of magnetized white dwarfs
*M. Oertel, D. Chatterjee, A.F. Fantina, N. Chamel, and J. Novak* **51**

Understanding Active Galactic Nuclei using near-infrared high angular resolution polarimetry I : MontAGN - STOKES comparison
*L. Grosset, F. Marin, D. Gratadour, R. Goosmann, D. Rouan, Y. Clénet, D. Pelat, and P. A. Rojas Lobos* **57**

From FERMI-LAT observations to the blind pulsar survey SPAN512 with the Nançay Radio Telescope
*F. Octau, G. Desvignes, I. Cognard, D. Champion, P. Lazarus, D. Smith, and G. Theureau* **61**

Consequences of rotating off-centred dipolar electromagnetic field in vacuum around Pulsars
*A. Kundu, and J. Pétri* **65**

Steady-state model of accretion columns in magnetic cataclysmic variables
*L. Van Box Som, É. Falize, J.-M. Bonnet-Bidaud, M. Mouchet, C. Busschaert, and A. Ciardi* **69**

Energy dependent variability and outburst evolution in black hole X-ray binaries
*H. Stiele, and A. K. H. Kong* **73**

GCT, the Gamma-ray Cherenkov Telescope for multi-TeV science with the Cherenkov Telescope Array
*H. Sol, J.-L. Dournaux, P. Laporte, and the GCT Team and CTA Consortium* **77**

Models of fast radio bursts at cosmological distances
*F. Mottez, C. Guépin, K. Kotera, G. Voisin, and P. Zarka* **83**

Modeling the reverberation of optical polarization in AGN
*P. A. Rojas Lobos, R. Goosmann, and F. Marin* **89**

Multiwavelength Study of *Fermi-LAT blazars Variability and Radiation Production Mechanisms*
*R. J. Britto, E. Bottacini, M. Böttcher, D. A. H. Buckley, S. Buson, B. Lott, J. P. Marais, P. J. Meintjes, et al.* **93**

Understanding Active Galactic Nuclei using near-infrared high angular resolution polarimetry II: Preliminary results
*F. Marin, L. Grosset, R. Goosmann, D. Gratadour, D. Rouan, Y. Clénet, D. Pelat, and P. A. Rojas Lobos* **103**

Hall-MHD simulations of the Kelvin-Helmholtz instability at the solar wind/magnetosphere interface
*M. H. J. Leroy, and R. Keppens* **107**

From Auger to AugerPrime: Understanding Ultrahigh-Energy Cosmic Rays
*F. Montanet, for the Pierre Auger Collaboration* **111**

Which mechanism for gamma-ray flares of the Crab nebula ?
*T. Akramov, and H. Baty* **115**

**Numerical simulations in astrophysics (S03)** **119**

Numerical relativity and spectral methods
*P. Grandclement* **121**

Hall magneto-hydrodynamics in protoplanetary discs
*W. Béthune, G. Lesur, and J. Ferreira* **129**

Perspectives in numerical astrophysics: Towards an exciting future in the exascale era
*V. Reverdy* **133**

The gaseous proto-cluster: better characterizing the initial conditions of stellar cluster formation?
*Y.-N. Lee, and P. Hennebelle* **139**

How baryonic feedback processes can affect dark matter halos: a stochastic model
*J. Freundlich, A. El-Zant, and F. Combes* **153**

Kinetic simulations of collisionless magnetic reconnection
*N. Aunai, J. Dargent, B. Lavraud, A. Ciardi, M. Drouin, and R. Smets* **157**

Chemistry and dynamics: a post-processing tool towards a real coupling
*V. Valdivia, B. Godard, P. Hennebelle, M. Gerin, and P. Lesaffre* **163**

Simulating the local Universe
*J. G. Sorce* **169**

## Stellar physics (S04) 177

Influence of plume-induced internal gravity waves on the rotation profile of low-mass stars
*C. Pinçon, K. Belkacem, and M. J. Goupil* **179**

Magnetic activity of seismic solar analogs
*D. Salabert, R. A. García, P. G. Beck, and the SSA team* **185**

The gaseous proto-cluster as a product of gravo-turbulent interaction: modified local environment for stellar cluster formation?
*Y.-N. Lee, and P. Hennebelle* **189**

The changing magnetic fields of intermediate-mass T Tauri stars
*F. Villebrun, E. Alecian, J. Bouvier, G. Hussain, and C. P. Folsom* **199**

Formation history of old open clusters constrained by detailed asteroseismology of red giant stars observed by *Kepler*
*E. Corsaro, Y.-N. Lee, R. A. García, P. Hennebelle, S. Mathur, P. G. Beck, S. Mathis, D. Stello, and J. Bouvier* **203**

PAIX the First Robotic Antarctica Polar Mission
*M. Chadid* **207**

HR8844: a new hot Am star?
*R. Monier, M. Gebran, and F. Royer* **209**

HD 30963: a new HgMn star
*R. Monier, M. Gebran, and F. Royer* **213**

Internal rotation of $\gamma$ Doradus stars
*R.-M. Ouazzani, S. J. A. J. Salmon, V. Antoci, T. R. Bedding, and S. J. Murphy* **217**

The PHOENIX Model Atmosphere Grid for Stars
*F. Allard* **223**

The photometric variability of $\zeta$ Ori Aa observed by BRITE* **
*B. Buysschaert, C. Neiner, and BEST* **229**

## Users meeting of the French telescopes - TBL/OHP193 (S05) 235

Telescope Bernard Lyot: operation, instrumentation, perspectives
*R. Cabanac, and TBL Team* **237**

Follow-up and characterization of the *TESS* exoplanets with SOPHIE, SPIRou, and *JWST*
*N. Crouzet, X. Bonfils, X. Delfosse, I. Boisse, G. Hébrard, T. Forveille, J.-F. Donati, F. Bouchy, C. Moutou, R. Doyon, et al.* **243**

Ground-based follow-up of the Gaia-RVS radial velocity standards
*C. Soubiran, G. Jasniewicz, C. Zurbach, F. Crifo, P. Sartoretti, D. Katz, O. Marchal, P. Panuzzo, and S. Udry* **249**

A new family of magnetic stars: the Am stars
*A. Blazère, C. Neiner, P. Petit, and F. Lignières* **253**

## WEAVE (S06) 257

WEAVE-QSO: A Massive Intergalactic Medium Survey for the William Herschel Telescope
*M. M. Pieri, S. Bonoli, J. Chaves-Montero, I. Pâris, M. Fumagalli, J. S. Bolton, M. Viel, P. Noterdaeme, J. Miralda-Escudé, N. G. Busca, et al.* **259**

WEAVE an overview and status update
*P. Bonifacio, G. Dalton, S. Trager, A. L. Aguerri, E. Carrasco, A. Vallenari, D. C. Abrams, K. Middleton, F. Sayède, and the WEAVE Instrument Consortium* **267**

The WEAVE-LOFAR Survey
*D. J. B. Smith, P. N. Best, K. J. Duncan, N. A. Hatch, M. J. Jarvis, H. J. A. Röttgering, C. J. Simpson, J. P. Stott, R. K. Cochrane, K. E. Coppin, et al.* **271**

The WEAVE disk dynamics survey
*B. Famaey, T. Antoja, M. Romero-Gomez, A. Siebert, C. Babusiaux, P. Di Matteo, F. Figueras, F. Fragkoudi, F. Garzon-Lopez, C. Gonzalez-Fernandez, et al.* **281**

Red-giant stars: Chemical clocks in the Milky Way
*N. Lagarde, A.C. Robin, C. Reylé, and G. Nasello* **287**

## National and international synergies in space meteorology (S07) 291

METEOSPACE, solar monitoring and space weather at Calern observatory
*T. Corbard, J.-M. Malherbe, D. Crussaire, F. Morand, F. Ruty, L. Biree, J. Aboudarham, N. Fuller, C. Renaud, and M. Meftah* **293**

Space-weather assets developed by the French space-physics community
*A. P. Rouillard, R. F. Pinto, A. S. Brun, C. Briand, S. Bourdarie, T. Dudok De Wit, T. Amari, P.-L. Blelly, E. Buchlin, A. Chambodut, et al.* **297**

## Cosmic rays and interstellar medium (S08) 307

Consequences of warm $H_2$ on the chemistry of diffuse molecular clouds: the case of CH
*V. Valdivia, B. Godard, P. Hennebelle, M. Gerin, and P. Lesaffre* **309**

H.E.S.S. and CTA, present and perspectives in ground-based gamma-ray astronomy
*H. Sol* **315**

## Exogenous inputs and origin of life (S09) 319

Complex organic molecules toward low-mass and high-mass star forming regions
*C. Favre, C. Ceccarelli, B. Lefloch, E. Bergin, M. Carvajal, N. Brouillet, D. Despois, J. Jørgensen, and I. Kleiner* **321**

## Services and databases in spectroscopy (S11) 327

Desirable evolutions of stellar spectroscopic services in the light of current studies of remote stellar populations.
*A. Lançon, P. Prugniel, M. Powalka, and I. Vauglin* **329**

Re-grouping stars based on the chemical tagging technique: A case study of M67 and IC4651
*S. Blanco-Cuaresma, and C. Soubiran* **333**

**SKA-LOFAR (S12)** **337**

The NOIRE Study
*B. Cecconi, A. Laurens, C. Briand, J. Girard, M. Bucher, D. Puy, B. Segret, M. Bentum, and the NOIRE team* **339**

Mapping the radio sky from 0.1 to 100 MHz with NOIRE
*B. Cecconi, A. Laurens, C. Briand, J. Girard, M. Bucher, D. Puy, B. Segret, M. Bentum, and the NOIRE team* **343**

Observations of Fast Radio Bursts and perspectives at low frequencies
*P. Zarka, and F. Mottez* **347**

Faraday tomography with LOFAR: new probe of the interstellar magnetic field
*M. I. R. Alves, V. Jelić, K. Ferrière, and F. Boulanger* **353**

Algorithmic aspects for the reconstruction of spatio-spectral data cubes in the perspective of the SKA
*D. Mary, A. Ferrari, C. Ferrari, J. Deguignet, and M. Vannier* **357**

Non-thermal emission and dynamical state of massive galaxy clusters from *CLASH* sample
*M. Pandey-Pommier, J. Richard, F. Combes, A. Edge, B. Guiderdoni, D. Narasimha, J. Bagchi, and J. Jacob* **367**

The low-frequency radio emission in blazar PKS2155-304
*M. Pandey-Pommier, S. Sirothia, P. Chadwick, J.-M. Martin, P. Colom, W. van Driel, F. Combes, P. Kharb, P.-J. Crespeau, J. Richard, et al.* **373**

AGN duty cycle and relic emission in the low frequency sky
*M. Pandey-Pommier, H. Intema, G. Heald, and on behalf of the MSSS team and the LOFAR collaboration* **379**

Radio mode feedback via BCGs in cool core clusters
*S.-L. Hamer, M. P. Pommier, A.-C. Edge, and F. Combes* **385**

**The Epoch of Reionisation (S13)** **391**

The intrinsic evolution of Ly$\alpha$ -emitting galaxies from z $\approx$ 3 to the epoch of reionization
*T. Garel* **393**

Stellar feedback during the reionization with EMMA
*N. Deparis, D. Aubert, and P. Ocvirk* **399**

21cm bispectrum as method to measure cosmic dawn and EoR
*H. Shimabukuro* **403**

Feedback regulated escape of ionising radiation from high redshift galaxies
*M. Trebitsch, and J. Blaizot* **407**

Photometric and Spectroscopic analysis of lensed re-ionising sources at the frontier of the Universe
*N. Laporte, R. Ellis, G. Roberts-Borsani, L. Infante, W. Zheng, F.E. Bauer, D. Bina, I. Chilingarian, S. Kim, R. Pelló, et al.* **411**

High-z galaxies & Reionization
*R. Pelló* **417**

Large scale opacity fluctuations in the Lyman alpha forest: Do QSOs dominate the UVB at z$\sim$5.5-6?
*J. Chardin, E. Puchwein, and M. G. Haehnelt* **423**

## The (sub) millimetric universe at high angular resolution: the ALMA and NOEMA revolution continues (S14) 427

A new insight of the northern filaments of Centaurus A
*Q. Salomé, P. Salomé, F. Combes, and S. Hamer* **429**

The axisymmetric envelopes of RS Cnc and EP Aqr
*T. Le Bertre, D. T. Hoai, P. T. Nhung, and J. M. Winters* **433**

NIKA2, a dual-band millimetre camera on the IRAM 30 m telescope to map the cold universe
*F.-X. Désert, R. Adam, P. Ade, P. André, H. Aussel, A. Beelen, A. Benoît, A. Bideaud, N. Billot, O. Bourrion, et al.* **439**

## Observation of the discs with the new generation instruments - ALMA, SPHERE...- (S15) 443

Evolution of solids in the Jovian subnebula: Implications for the formation of the Galilean satellites
*T. Ronnet, O. Mousis, and P. Vernazza* **445**

Growing porous grains: a solution to the radial-drift barrier
*A. J. L. Garcia, J.-F. Gonzalez, and F. C. Pignatale* **449**

Could the stellar magnetic field explain the vertical structures in the AU Mic debris disk?
*É. Sezestre, and J.-C. Augereau* **455**

Review of gas and dust in debris discs
*Q. Kral* **463**

Migration of accreting giant planets
*A. Crida, B. Bitsch, and A. Raibaldi* **473**

Spirals, gaps, cavities, gapities: What do planets do in discs?
*A. Crida* **477**

## Author Index 481

# Foreword

The annual meeting of the French Society of Astronomy and Astrophysics (*Société Française d'Astronomie et d'Astrophysique* - SF2A), nickenamed *Journées* or *Semaine de l'Astrophysique*, is an absolute must in the landscape of French Astronomy. The XXXVI$^{\mathrm{th}}$ session, hosted by the *Centre de Recherche Astrophysique de Lyon* from June 14 to 17 did not depart from the tradition.

These *Journées* were very well attended with about 286 registred professional astronomers and astrophysicists (and many unregistred colleagues!), who participated in plenary sessions organized by the SF2A and 14 workshops organized by the scientific committees of the *Programmes Nationaux* (PN) and *Actions Spécifiques* (AS) of INSU-CNRS, as well as the community.

The talks were exciting and well received. The discussions were very lively and often continued well into the coffee breaks. During the plenary sessions, scientific reviews focused on outstanding scientific results (such as the new messengers, i.e. gravitational waves and neutrinos). Our special guest, the German *Astronomische Gesselschaft* (AG) represented by Joachim Wambsgan$\beta$, emphasized the similarities between our two societies.

Other general talks led to topical discussions on the organization and the future of French astronomical research in the fast moving national and international environment. In particular, Denis Mourard (INSU) provided the community with a thorough overview of our observing infrastructures. François Menard convincingly promoted the *Unité Mixte Internationale* based in Chile. Michel Marcelin gave a review of the CoNRS section 17 activities during the last 4 years.

A large number of SF2A members attended the General Assembly where the annual activity and financial reports of our Society were presented by the president and treasurer of the SF2A Council, resp. H. Wozniak and A. Palacios. According to SF2A rules, half the board members have been changed. The new elected members are: Olivier Berné, Fabrice Herpin, Eric Lagadec, Ariane Lançon, François Lique, and Paola di Matteo.

Several new features were introduced in 2016. After the successful experiment last year, we opened the meeting to four workshops organized by the community, in reply to a call of opportunity (S03, S05, S06, and S10 workshops). A gender–lunch meetings was scheduled on Tuesday, whereas the AUDDAS (*Association Unissant les Doctorants en AStrophysique, http://auddas.fr/*) organized a successful experiment–happening event in the evening.

A key moment of these *Journées* was the prize ceremony (and buffet) in the splendid *Terrasses du Parc*. The laureates of the SF2A Young Researcher prizes were Laurène Jouve (IRAP) and Frédéric Bournaud (CEA). Corinne Charbonnel (Geneva) and Eric Emsellem (ESO) delivered vibrant speeches for the recipients. Sandrine Codis (IAP and now CITA) was presented with the Thesis prize by F. Bernardeau (IAP). We warmly thank the long–term sponsors of these prizes, EdP Sciences and the Exelis company for their continuing interest in our science and support to our Society. For the first time, DELL supported the two Young Researcher prizes. We want here to warmly thank M. Pascal Delivré, from the DELL company, for his enthousiatic support and presence in Lyon. We sincerely hope that this partnership can be renewed next year.

All along the *Journées* a number of social, outreach, and cultural events were organized. The SF2A Prize *Découvrir l'Univers* sponsored by EdP Sciences aimed at promoting astronomy among children and young students. Three classrooms were awarded the prize during a special ceremony held in the *Planétarium de Vaux-en-Velin* which offered a party and a planetarium session to the winners. On Tuesday, Cathy Quentin-Nataf

(LGL) gave a public conference in a packed auditorium of the *Musée des Confluences*, entitled "*Chroniques Martiennes*" (The Martian Chronicles).

Another exceptionnal event took place in the *Musée des Confluences*: the SF2A board decided, almost one year ago, to award the special (and rare) prize *Science et Société* to Alexandre Astier, a well-known French writer, director, editor, scriptwriter, humorist, actor and composer (no less), for his excellent comic show "L'Exoconférence" (The Exo-conference). This show demolishes many weird unphysical theories (on cosmogony and UFOs for instance). But this Exoconference is definitively an act of vulgarisation, done by a non-specialist but well adviced showman, that may improved the perception of science by a large public.

The venue of these *Journées* was made possible through a number of sponsoring organizations: the INSU-CNRS, the CNES, the Service d'Astrophysique du CEA/DSM/IRFU and the LabEx "Lyons Institute of Origins". PN and AS of INSU-CNRS have supported the organization of the workshops. We are extremely grateful to the Observatoire des Sciences de l'Univers de Lyon and the University of Lyon for assisting and hosting the *Journées*.

The success of the meeting hinged on the efforts of many people. The Local Organizing Committee was led by Johan Richard and consisted of the further members : Mylène François, Marie-Hélène Lassalle, Emmanuel Pécontal, Laurence Tresse (CRAL director), Isabelle Vauglin, Stéphanie Vigner, Caroline Vilatte. Their fool-proof enthusiasm for preparing this event was undoubtedly a great part of the success. Thanks also to the SF2A board, acting as Scientific Organizing Committee, for its active contribution, and to the editors of these proceedings.

In conclusion the success of these XXXVI$^{\mathrm{th}}$ *Journées*, which brought together colleagues from all branches of astrophysics, was overwhelming, so that we feel encouraged to think of the organization of the next conference, in Paris, in 2017. And the next one... and the next one...

Hervé Wozniak, President of the SF2A

# List of participants


**ABDELMOTALEB Eman** (e-mail: emanaly541@gmail.com )
**AKRAMOV Tohir** (e-mail: tohir.akramov@astro.unistra.fr )
**AL-MAOTAHNI Anas** (e-mail: maotahni@ph1.uni-koeln.de )
**ALECIAN Evelyne** (e-mail: evelyne.alecian@univ-grenoble-alpes.fr )
**ALEXANDROVA Olga** (e-mail: olga.alexandrova@obspm.fr )
**ALLARD France** (e-mail: fallard@ens-lyon.fr )
**ALLEN Mark** (e-mail: mark.allen@astro.unistra.fr )
**ALVES Marta** (e-mail: marta.alves@irap.omp.eu )
**AMRAM Philippe** (e-mail: philippe.amram@lam.fr )
**ARNAUD Nicolas** (e-mail: narnaud@lal.in2p3.fr )
**AUNAI Nicolas** (e-mail: nicolas.aunai@lpp.polytechnique.fr )
**BACHOLLE Simon** (e-mail: simon.bacholle@apc.in2p3.fr )
**BACON Roland** (e-mail: roland.bacon@univ-lyon1.fr )
**BALLET Jean** (e-mail: jballet@cea.fr )
**BARUTEAU Clément** (e-mail: clement.baruteau@irap.omp.eu )
**BAUDINO Jean-loup** (e-mail: jean-loup.baudino@cea.fr )
**BEHAR Etienne** (e-mail: etienne.behar@irf.se )
**BELLIER Pascale** (e-mail: pascale.bellier@laposte.net )
**BENISTY Myriam** (e-mail: myriam.benisty@univ-grenoble-alpes.fr )
**BERNARDEAU Francis** (e-mail: francis.bernardeau@iap.fr )
**BÉTHUNE William** (e-mail: william.bethune@univ-grenoble-alpes.fr )
**BÉZARD Bruno** (e-mail: bruno.bezard@obspm.fr )
**BIREE Lionel** (e-mail: lionelbiree@hotmail.fr )
**BLAIZOT Jeremy** (e-mail: jeremy.blaizot@univ-lyon1.fr )
**BLANCHET Luc** (e-mail: blanchet@iap.fr )
**BLANCO-CUARESMA Sergi** (e-mail: Sergi.Blanco@unige.ch )
**BLAZÈRE Aurore** (e-mail: aurore.blazere@obspm.fr )
**BLELLY Pierre-louis** (e-mail: pierre-louis.blelly@irap.omp.eu )
**BLONDIN Stéphane** (e-mail: stephane.blondin@lam.fr )
**BOCCALETTI Anthony** (e-mail: anthony.boccaletti@obspm.fr )
**BOISSIER Samuel** (e-mail: samuel.boissier@lam.fr )
**BONIFACIO Piercarlo** (e-mail: Piercarlo.Bonifacio@obspm.fr )
**BOONE Frederic** (e-mail: frederic.boone@irap.omp.eu )
**BORG Janet** (e-mail: borgjanet@gmail.com )
**BORGNIET Simon** (e-mail: simon.borgniet@univ-grenoble-alpes.fr )
**BOSMA Albert** (e-mail: bosma@lam.fr )
**BOUCHY Francois** (e-mail: francois.bouchy@lam.fr )
**BOURNAUD Frederic** (e-mail: frederic.bournaud@gmail.com )
**BRAINE Jonathan** (e-mail: jonathan.braine@u-bordeaux.fr )
**BRIAND Carine** (e-mail: carine.briand@obspm.fr )
**BRITTO Richard** (e-mail: dr.richard.britto@gmail.com )
**BROUSSINE Kirill** (e-mail: kirillbroussine@sfr.fr )
**BRUGGER Bastien** (e-mail: bastien.brugger@lam.fr )
**BRUN Allan Sacha** (e-mail: sacha.brun@cea.fr )
**BRUNETTO Rosario** (e-mail: rosario.brunetto@ias.u-psud.fr )

**BUAT Véronique** (e-mail: veronique.buat@lam.fr )
**BUCHERT Thomas** (e-mail: thomas.buchert@univ-lyon1.fr )
**BUCHLIN Eric** (e-mail: eric.buchlin@ias.u-psud.fr )
**BURGARELLA Denis** (e-mail: denis.burgarella@lam.fr )
**BUYSSCHAERT Bram** (e-mail: bram.buysschaert@obspm.fr )
**CABANAC Rémi** (e-mail: rcabanac@irap.omp.eu )
**CAMBRÉSY Laurent** (e-mail: laurent.cambresy@astro.unistra.fr )
**CASSE Fabien** (e-mail: fcasse@apc.univ-paris7.fr )
**CECCONI Baptiste** (e-mail: baptiste.cecconi@obspm.fr )
**CHABRIER Gilles** (e-mail: chabrier@ens-lyon.fr )
**CHADID Merieme** (e-mail: chadid@unice.fr )
**CHAPILLON Edwige** (e-mail: chapillon@iram.fr )
**CHARDIN Jonathan** (e-mail: jc@ast.cam.ac.uk )
**CHAUVEAU Joanne** (e-mail: joanne.chauveau@univ-lyon1.fr )
**CLARET Arnaud** (e-mail: arnaud.claret@cea.fr )
**CLÉMENT Benjamin** (e-mail: benjamin.clement@univ-lyon1.fr )
**CODIS Sandrine** (e-mail: codis@cita.utoronto.ca )
**COGNARD Ismaël** (e-mail: icognard@cnrs-orleans.fr )
**COïSSON Pierdavide** (e-mail: coisson@ipgp.fr )
**COLLIN-ZAHN Suzy** (e-mail: suzy.collin@obspm.fr )
**COMMERÇON Benoit** (e-mail: benoit.commercon@ens-lyon.fr )
**CORBARD Thierry** (e-mail: thierry.corbard@oca.eu )
**CORBEL Stéphane** (e-mail: CEA Saclay )
0 **CORSARO Enrico** (e-mail: enrico.corsaro@cea.fr )
**COTTALORDA Eric** (e-mail: cottalorda76@gmail.com )
**COURANT Alain** (e-mail: alain.courant@gmail.com )
**COURCOL Bastien** (e-mail: bastien.courcol@lam.fr )
**COURTIN Régis** (e-mail: regis.courtin@obspm.fr )
**CRIDA Aurélien** (e-mail: crida@oca.eu )
**CROUZET Nicolas** (e-mail: crouzet@dunlap.utoronto.ca )
**CUDEL Maxime** (e-mail: maxime.cudel@univ-grenoble-alpes.fr )
**DAIBOO Soobash** (e-mail: soobash.daiboo@obspm.fr )
**DAIGNE Frédéric** (e-mail: daigne@iap.fr )
**DANGER Grégoire** (e-mail: gregoire.danger@univ-amu.fr )
**DARTOIS Emmanuel** (e-mail: emmanuel.dartois@ias.u-psud.fr )
**DASGUPTA Aayush** (e-mail: aruni.dasgupta@gmail.com )
**DASSA-TERRIER Julien** (e-mail: julien.dassa-terrier@obspm.fr )
**DE BARROS Stephane** (e-mail: stephane.debarros@oabo.inaf.it )
**DELAHAYE Franck** (e-mail: franck.delahaye@obspm.fr )
**DELEUIL Magali** (e-mail: magali.deleuil@lam.fr )
**DELFOSSE Xavier** (e-mail: Xavier.Delfosse@univ-grenoble-alpes.fr )
**DEPARIS Nicolas** (e-mail: nicolas.deparis@astro.unistra.fr )
**DESCHARLES Christophe** (e-mail: descharles.christophe@yahoo.fr )
**DÉSERT François-Xavier** (e-mail: desert@univ-grenoble-alpes.fr )
**DESPREZ Guillaume** (e-mail: desprez.guillaume@gmail.com )
**DEVOST Daniel** (e-mail: devost@cfht.hawaii.edu )
**DI MATTEO Paola** (e-mail: paola.dimatteo@obspm.fr )
**DINTRANS Boris** (e-mail: boris.dintrans@irap.omp.eu )
**DOUGADOS Catherine** (e-mail: catherine.dougados@obs.ujf-grenoble.fr )
**DOUSPIS Marian** (e-mail: marian.douspis@ias.u-psud.fr )
**DRAKE Alyssa** (e-mail: alyssa-bryony.drake@univ.lyon1.fr )
**DUBUS Guillaume** (e-mail: guillaume.dubus@univ-grenoble-alpes.fr )
**DUTREY Anne** (e-mail: anne.dutrey@u-bordeaux.fr )
**DUMOULIN Jérémy** (e-mail: jerem.dumoulin@gmail.com )
**DUPUY Alexandra** (e-mail: dupuy@ipnl.in2p3.fr )

**DUVERNAY Fabrice** (e-mail: fabrice.duvernay@univ-amu.fr )
**DVORKIN Irina** (e-mail: dvorkin@iap.fr )
**EAMES Evan** (e-mail: evaneames7@gmail.com )
**EGAL Auriane** (e-mail: auriane.egal@obspm.fr )
**EGRET Daniel** (e-mail: daniel.egret@obspm.fr )
**EMERIAU-VIARD Constance** (e-mail: constance.emeriau@cea.fr )
**ERARD Stéphane** (e-mail: stephane.erard@obspm.fr )
**FALGARONE Edith** (e-mail: edith.falgarone@ens.fr )
**FALIZE Emeric** (e-mail: e.falize@cea.fr )
**FAMAEY Benoit** (e-mail: benoit.famaey@astro.unistra.fr )
**FAUROBERT Marianne** (e-mail: marianne.faurobert@unice.fr )
**FAVRE Cecile** (e-mail: cecile.favre@univ-grenoble-alpes.fr )
**FERNANDEZ TRINCADO Jose Gregorio** (e-mail: jfernandez@obs-besancon.fr )
**FRANÇOIS Mylène** (e-mail: mylene.francois@univ-lyon1.fr )
**FREUNDLICH Jonathan** (e-mail: jonathan.freundlich@obspm.fr )
**FROMANG Sébastien** (e-mail: sebastien.fromang@cea.fr )
**GALLET Florian** (e-mail: Florian.gallet@unige.ch )
**GARCIA Anthony** (e-mail: anthony.garcia@univ-lyon1.fr )
**GAREL Thibault** (e-mail: thibault.garel@univ-lyon1.fr )
**GÉNOT Vincent** (e-mail: vincent.genot@irap.omp.eu )
**GIRARD Julien** (e-mail: jgirard@ska.ac.za )
**GLORIAN Jean-michel** (e-mail: jean-michel.glorian@irap.omp.eu )
**GODARD Benjamin** (e-mail: benjamin.godard@obspm.fr )
**GOMEZ LOPEZ Jesús Alberto** (e-mail: jesus.gomez-lopez@lam.fr )
**GONZALEZ Jean-françois** (e-mail: Jean-Francois.Gonzalez@ens-lyon.fr )
**GOOSMANN René** (e-mail: rene.goosmann@astro.unistra.fr )
**GORCE Adélie** (e-mail: agorce@ias.u-psud.fr )
**GOUPIL Mariejo** (e-mail: mariejo.goupil@obspm.fr )
**GRANDCLEMENT Philippe** (e-mail: philippe.grandclement@obspm.fr )
**GROSSET Lucas** (e-mail: lucas.grosset@obspm.fr )
**GROULD Marion** (e-mail: marion.grould@obspm.fr )
**GUENNOU Chloé** (e-mail: gueth@iram.fr )
**GUETH Frédéric** (e-mail: c.guennou@gmail.com )
**GUIDERDONI Bruno** (e-mail: bruno.guiderdoni@univ-lyon1.fr )
**GUILLARD Pierre** (e-mail: guillard@iap.fr )
**GUSDORF Antoine** (e-mail: antoine.gusdorf@googlemail.com )
**HAMER Stephen** (e-mail: stephen.hamer@univ-lyon1.fr )
**HAYWOOD Misha** (e-mail: misha.haywood@obspm.fr )
**HEBRARD Guillaume** (e-mail: hebrard@iap.fr )
**HENRI Pierre** (e-mail: pierre.henri@cnrs-orleans.fr )
**HESTROFFER Daniel** (e-mail: hestro@imcce.fr )
**HILL Vanessa** (e-mail: Vanessa.Hill@oca.eu )
**IFFRIG Olivier** (e-mail: olivier.iffrig@cea.fr )
**INTEMA Huib** (e-mail: intema@strw.leidenuniv.nl )
**JOSSELIN Eric** (e-mail: eric.josselin@univ-montp2.fr )
**JOUVE Laurène** (e-mail: ljouve@irap.omp.eu )
**KAZERONI Rémi** (e-mail: remi.hosseini-kazeroni@cea.fr )
**KONOVALENKO Alexander** (e-mail: akonov@rian.kharkov.ua )
**KORSAGA Marie** (e-mail: marie.korsaga@lam.fr )
**KRAL Quentin** (e-mail: qkral@ast.cam.ac.uk )
**KUNDU Anu** (e-mail: anu.kundu@astro.unistra.fr )
**LAGARDE Nadège** (e-mail: nadege.lagarde@utinam.cnrs.fr )
**LAMY Philippe** (e-mail: philippe.lamy@lam.fr )
**LANÇON Ariane** (e-mail: ariane.lancon@astro.unistra.fr )
**LANGER Mathieu** (e-mail: mathieu.langer@ias.u-psud.fr )

**LAPORTE Nicolas** (e-mail: n.laporte@ucl.ac.uk )
**LASSALLE Marie-hélène** (e-mail: marie-helene.lassalle@univ-lyon1.fr )
**LAZAREFF Bernard** (e-mail: bernard.lazareff@laposte.net )
**LE BERTRE Thibaut** (e-mail: thibaut.lebertre@obspm.fr )
**LE BRUN Amandine** (e-mail: amandine.le-brun@cea.fr )
**LE FLOC'H Emeric** (e-mail: emeric.lefloch@cea.fr )
**LE GUILLOU Corentin** (e-mail: corentin.san@gmail.com )
**LE SERGEANT D'HENDECOURT Louis** (e-mail: ldh@ias.u-psud.fr )
**LE TIEC Alexandre** (e-mail: letiec@obspm.fr )
**LE VAN SUU Auguste** (e-mail: auguste.levansuu@osupytheas.fr )
**LEBRE Agnès** (e-mail: Agnes.Lebre@umontpellier.fr )
**LEBRETON Yveline** (e-mail: yveline.lebreton@obspm.fr )
**LECLERCQ Floriane** (e-mail: floriane.leclercq@univ-lyon1.fr )
**LEE Yueh-ning** (e-mail: yueh-ning.lee@cea.fr )
**LEMORTON Joël** (e-mail: Joel.Lemorton@onera.fr )
**LEROY Matthieu** (e-mail: matthieu.leroy@kuleuven.be )
**LESTRADE Jean-François** (e-mail: jean-francois.lestrade@obspm.fr )
**LEYRAT Cédric** (e-mail: cedric.leyrat@obspm.fr )
**LEWIS Joseph** (e-mail: j.s.w.lew@gmail.com )
**LILENSTEN Jean** (e-mail: jean.lilensten@univ-grenoble-alpes.fr )
**LOH Alan** (e-mail: alan.loh@cea.fr )
**MAHLER Guillaume** (e-mail: guillaume.mahler@univ-lyon1.fr )
**MALHAN Khyati** (e-mail: kmalhan07@gmail.com )
**MARCELIN Michel** (e-mail: michel.marcelin@lam.fr )
**MARCHAND Pierre** (e-mail: pierre.marchand@ens-lyon.fr )
**MARCHAUDON Aurélie** (e-mail: aurelie.marchaudon@irap.omp.eu )
**MARCOWITH Alexandre** (e-mail: Alexandre.Marcowith@univ-montp2.fr )
**MARET Sébastien** (e-mail: sebastien.maret@univ-grenoble-alpes.fr )
**MARIN Frédéric** (e-mail: frederic.marin@astro.unistra.fr )
**MARINO Raffaele** (e-mail: raffaele.marino@ens-lyon.fr )
**MARTEL Etienne** (e-mail: etienne.martel@ens-lyon.fr )
**MARTIN Thomas** (e-mail: thomas.martin.1@ulaval.ca )
**MARTINEZ Johany** (e-mail: Johany.martinez30@gmail.com )
**MARTINOD Marc-antoine** (e-mail: mamartinod@oca.eu )
**MARTINS Zita** (e-mail: z.martins@imperial.ac.uk )
**MARY David** (e-mail: David.MARY@unice.fr )
**MASSON Sophie** (e-mail: sophie.masson@obspm.fr )
**MATTER Alexis** (e-mail: Alexis.Matter@oca.eu )
**MEHEUT Heloise** (e-mail: heloise.meheut@oca.eu )
**MELIANI Zakaria** (e-mail: zakaria.meliani@obspm.fr )
**MENARD Francois** (e-mail: francois.menard@univ-grenoble-alpes.fr )
**MERTENS Florent** (e-mail: florent.mertens@gmail.com )
**METRIS Gilles** (e-mail: Gilles.Metris@oca.eu )
**MEUNIER Nadège** (e-mail: nadege.meunier@univ-grenoble-alpes.fr )
**MICHEL Thibault** (e-mail: thibault.michel@obspm.fr )
**MICHEL Alexandre** (e-mail: alexandre.michel@ens-lyon.fr )
**MICHEL-DANSAC Leo** (e-mail: leo.michel-dansac@univ-lyon1.fr )
**MIRABEL Felix** (e-mail: felix.mirabel@cea.fr )
**MONCEAU-BAROUX Rémi** (e-mail: remi.monceaubaroux@kuleuven.be )
**MONIER Richard** (e-mail: Richard.Monier@obspm.fr )
**MONTANET François** (e-mail: montanet@in2p3.fr )
**MONTMERLE Thierry** (e-mail: montmerle@iap.fr )
**MORAUX Estelle** (e-mail: estelle.moraux@univ-grenoble-alpes.fr )
**MORBIDELLI Alessandro** (e-mail: morby@oca.eu )
**MORENO Raphael** (e-mail: raphael.moreno@obspm.fr )

**MORIN Julien** (e-mail: julien.morin@umontpellier.fr )
**MOSSOUX Enmanuelle** (e-mail: enmanuelle.mossoux@hotmail.com )
**MOTTEZ Fabrice** (e-mail: fabrice.mottez@obspm.fr )
**NASELLO Guillaume** (e-mail: guillaume.nasello@obs-besancon.fr )
**NOVAK Jérôme** (e-mail: jerome.novak@obspm.fr )
**OCTAU Franck** (e-mail: franck.octau@cnrs-orleans.fr )
**OCVIRK Pierre** (e-mail: pierre.ocvirk@astro.unistra.fr )
**OERTEL Micaela** (e-mail: micaela.oertel@obspm.fr )
**OLIVARES Javier** (e-mail: Javier.Olivares@univ-grenoble-alpes.fr )
**OUAZZANI Rhita-Maria** (e-mail: rhita-maria.ouazzani@phys.au.dk )
**PADOVANI Marco** (e-mail: marco.padovani@umontpellier.fr )
**PALACIOS Ana** (e-mail: ana.palacios@umontpellier.fr )
**PARIAT Etienne** (e-mail: etienne.pariat@obspm.fr )
**PATRICIO Vera** (e-mail: vera.patricio@univ-lyon1.fr )
**PECONTAL Emmanuel** (e-mail: emmanuel.pecontal@univ-lyon1.fr )
**PELLO Roser** (e-mail: rpello@irap.omp.eu )
**PETIT Pascal** (e-mail: ppetit@irap.omp.eu )
**PETITEAU Antoine** (e-mail: petiteau@apc.univ-paris7.fr )
**PIEL Quentin** (e-mail: piel@lapp.in2p3.fr )
**PIENKINA Anastasiia** (e-mail: anastasia.penkina@obspm.fr )
**PIERI Matthew** (e-mail: matthew.pieri@lam.fr )
**PIETU Vincent** (e-mail: pietu@iram.fr )
**PIGNATALE Francesco** (e-mail: francesco.pignatale@univ-lyon1.fr )
**PINCON Charly** (e-mail: charly.pincon@obspm.fr )
**PINTO Rui** (e-mail: rui.pinto@irap.omp.eu )
**POMMIER Mamta** (e-mail: mamtapan@gmail.com )
**PRUGNIEL Philippe** (e-mail: philippe.prugniel@univ-lyon1.fr )
**PUY Denis** (e-mail: Denis.Puy@umontpellier.fr )
**RAYMOND Sean** (e-mail: rayray.sean@gmail.com )
**REVERDY Vincent** (e-mail: vince.rev@gmail.com )
**RÉVILLE Victor** (e-mail: victor.reville@cea.fr )
**REYLÉ Céline** (e-mail: celine@obs-besancon.fr )
**RICHARD Johan** (e-mail: johan.richard@univ-lyon1.fr )
**RIGOPOULOU Dimitra** (e-mail: dimitra.rigopoulou@physics.ox.ac.uk )
**RINCON Francois** (e-mail: francois.rincon@irap.omp.eu )
**ROBBINS Glenn** (e-mail: glenn.robbins@univ-lyon1.fr )
**ROBIN Annie** (e-mail: annie.robin@obs-besancon.fr )
**ROJAS LOBOS Patricia Andrea** (e-mail: andrea.rojas@astro.unistra.fr )
**RONNET Thomas** (e-mail: thomas.ronnet@lam.fr )
**ROQUES Françoise** (e-mail: francoise.roques@obspm.fr )
**ROSDAHL Joki** (e-mail: joki@strw.leidenuniv.nl )
**ROUILLARD Alexis** (e-mail: arouillard@irap.omp.eu )
**ROUSSEAU Batiste** (e-mail: batiste.rousseau@obspm.fr )
**ROYER Frédéric** (e-mail: frederic.royer@obspm.fr )
**SALABERT David** (e-mail: david.salabert@cea.fr )
**SALOME Quentin** (e-mail: quentin.salome@obspm.fr )
**SEMELIN Benoit** (e-mail: benoit.semelin@obspm.fr )
**SEZESTRE Elie** (e-mail: elie.sezestre@univ-grenoble-alpes.fr )
**SHIMABUKURO Hayato** (e-mail: hayato.shimabukuro@obspm.fr )
**SIMONS Doug** (e-mail: simons@cfht.hawaii.edu )
**SINGH Raj Laxmi** (e-mail: raj-laxmi.singh@obspm.fr )
**SLEZAK Eric** (e-mail: eric.slezak@oca.eu )
**SMITH Dan** (e-mail: daniel.j.b.smith@gmail.com )
**SOL Hélène** (e-mail: helene.sol@obspm.fr )
**SORCE Jenny** (e-mail: jsorce@aip.de )

**SOUBIRAN Caroline** (e-mail: caroline.soubiran@u-bordeaux.fr )
**SPIGA Aymeric** (e-mail: aymeric.spiga@upmc.fr )
**STEHLE Chantal** (e-mail: chantal.stehle@obspm.fr )
**STIELE Holger** (e-mail: hstiele@mx.nthu.edu.tw )
**SULIS Sophia** (e-mail: ssulis@oca.eu )
**SURACE Christian** (e-mail: lamcsurace@gmail.com )
**TASSE Cyril** (e-mail: cyril.tasse@obspm.fr )
**TESSORE Benjamin** (e-mail: ben.tessore@gmail.com )
**THORENS Louison** (e-mail: louison.thorens@ens-lyon.fr )
**TIRARD Stéphane** (e-mail: stephane.tirard@univ-nantes.fr )
**TREBITSCH Maxime** (e-mail: maxime.trebitsch@ens-lyon.org )
**TRESSE Laurence** (e-mail: laurence.tresse@univ-lyon1.fr )
**TUCKEY Philip** (e-mail: philip.tuckey@obspm.fr )
**TURC Lucile** (e-mail: lucile.turc@esa.int )
**TURCK-CHIEZE Sylvaine** (e-mail: cturck@cea.fr )
**TURON Catherine** (e-mail: catherine.turon@obspm.fr )
**VAKILI Farrokh** (e-mail: vakili@oca.eu )
**VALDIVIA Valeska** (e-mail: valeska.valdivia@cea.fr )
**VAN BOX SOM Lucile** (e-mail: lucile.vanboxsom@obspm.fr )
**VAN ELEWYCK Veronique** (e-mail: elewyck@apc.univ-paris7.fr )
**VAUGLIN Isabelle** (e-mail: isabelle.vauglin@univ-lyon1.fr )
**VERGANI Susanna** (e-mail: susanna.vergani@obspm.fr )
**VERICEL Arnaud** (e-mail: arnaud.vericel@gmail.com )
**VILATTE Caroline** (e-mail: caroline.vilatte@univ-lyon1.fr )
**VILLEBRUN Florent** (e-mail: florent.villebrun@univ-grenoble-alpes.fr )
**VINOGRADOFF Vassilissa** (e-mail: vassvino@yahoo.fr )
**VOISIN Guillaume** (e-mail: guillaume.voisin@obspm.fr )
**WOZNIAK Hervé** (e-mail: herve.wozniak@astro.unistra.fr )
**ZARKA Philippe** (e-mail: philippe.zarka@obspm.fr )
**ZUCCARELLO Francesco** (e-mail: francesco.zuccarello@obspm.fr )

# Session SF2A

# Plenary session

*SF2A 2016*
*C. Reylé, J. Richard, L. Cambrésy, M. Deleuil, E. Pécontal, L. Tresse and I. Vauglin (eds)*

# IDENTIFYING THE NON-LINEARITIES IN THE PERIOD-LUMINOSITY RELATIONS OF CEPHEIDS

J. Dassa-Terrier[1]

**Abstract.** The period-luminosity relation of Cepheids is essential to characterize the second step of the cosmological distance ladder. However, the possible non-linearity and breaking points around a period of 10 days have important consequences for their use. We review and challenge four different statistical methods on our simulations. We constrain the conditions in which these methods can be applied.

Keywords: stars: variables: Cepheids

## 1 Introduction

It is possible to segment the cosmological distance ladder into three main steps. First, the measurement of parallax in the Milky Way, initiated by both von Struve and Bessel in 1837 and 1838 respectively. Then, the period of pulsation of Cepheids in the Local Universe, done by Leavitt for the first time in Leavitt & Pickering (1912). Finally, the magnitude of type Ia supernovae in distant galaxies.

Our work is focused on the second step, the Period-Luminosity relation, also known as Leavitt Law (LL):

$$\langle M \rangle = a \log P + b, \tag{1.1}$$

where $\langle M \rangle$ is the mean absolute magnitude, $P$ the period, $a$ and $b$ the slope and zero point of the linear fit respectively. Cepheids being standard candles, the slope $a$ of the LL can be found by observing the magnitude and period of a group of Cepheids while the zero point $b$ must be found using galactic Cepheids with known distances.

The knowledge of the deduced absolute magnitude $M$ combined with the observed apparent magnitude $m$ allows to find the distance modulus:

$$\mu = \langle m \rangle - \langle M \rangle = 5 \log d - 5, \tag{1.2}$$

where $d$ is the distance to the star. Applied to Cepheids in M31, this method allows to estimate its distance at $d_{M31} = 752 \pm 27\ kpc$ (Riess et al. 2012). This permits us to know distances to type Ia supernovae in the nearby galaxies, hence, calibrate their light curves which peaks at a standard absolute magnitude, leading to the Hubble constant $H_0$ (Sandage et al. 2006).

However, recent studies, including Tammann et al. (2002), Ngeow & Kanbur (2009) and Kodric et al. (2015), strongly imply that the LL shows a non-linear behaviour in the Large Magellanic Cloud (LMC), Small Magellanic Cloud (SMC) and the M31 galaxy with the presence of a breaking point at $P \simeq 10\ days$. This break in slope was already suggested by Karkurin in 1937 but still lacks a consensus for its physical explanation. Several solutions were suggested for this empirical observation such as: the dependence of the LL on metallicity, or the interaction of stellar photosphere with the hydrogen ionization front (Kanbur & Ngeow 2006). An example of LL with breaking point is shown in figure 1.

This breaking point impacts the distance modulus calculation with non-negligible consequences. Kodric et al. (2015), who uses a model with breaking point, estimates $H_0$ to be 3.2% larger than the one found in Riess et al. (2012), who uses a linear model.

We explore four different statistical techniques: the F-test, the testimator, the BP from Bai & Perron (2003) and the bcp from Barry & Hartigan (1993), to estimate rigorously the statistical significance of this non-linearity in the LL.

[1] Observatoire de Paris, Paris, France

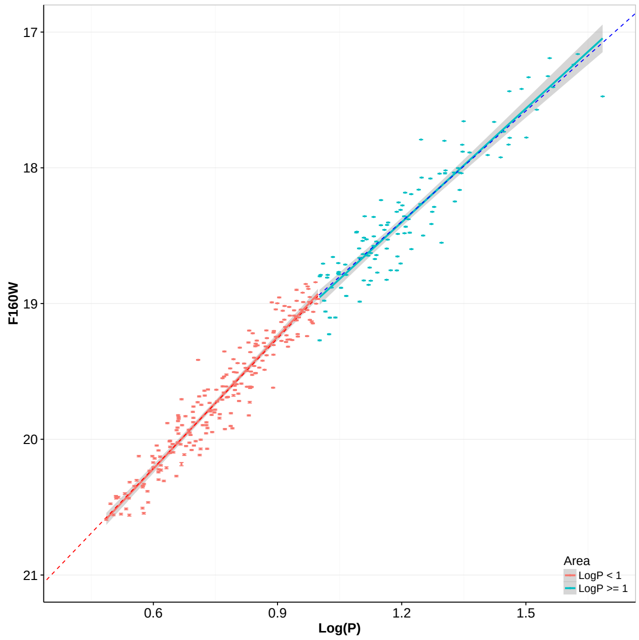


**Fig. 1.** The LL breaking point for 319 fundamental mode Cepheids in M31 as shown in Kodric et al. (2015).

## 2 Statistical methods

To test the ability of these methods to detect a breaking point in observations, we build simulations with similar ranges of period, magnitude and uncertainties as in the SMC, LMC and M31. These simulation can be fitted by two linear regressions with variable slopes and degrees of freedom.

### 2.1 F-test

Applied in Bhardwaj et al. (2016) and Kanbur & Ngeow (2004), the F-test is a ratio of the variance between the sample means and the variance within the samples. We choose two models:

$$M = a + b \log P, \tag{2.1}$$

and:

$$M = a_1 + b_1 \log P + \lambda(a_2 + b_2 \log P), \tag{2.2}$$

where $\lambda = 0$ if $P < 10$ days and $\lambda = 1$ if $P > 10$ days.

Our null hypothesis is the data being fit by a single linear regression. The F-test can be applied using the residues of the regressions as samples:

$$F = \frac{(RSS_1 - RSS_2)/[DF_1 - DF_2]}{RSS_2/DF_2}, \tag{2.3}$$

where $RSS_1$ and $RSS_2$ are the residual sums of squares in the 1-regression model and 2-regressions model respectively, $DF_1$ and $DF_2$ the degrees of freedom (DF) of the two models. $RSS_1$ and $RSS_2$ are found adaptating the general case: $RSS = \sum_{i=1}^{n}(y_i - f(x_i)^2$. We rely on the F-distribution for these DF to calculate the p-value associated with the value of F found.

The F-test needs to satisfy the following assumptions to be applied: homoscedasticity of the sample, normality of the residues and independent identically distributed observations. It is essential to check if these assumptions are met by the samples.

### 2.2 *Testimator*

The testimator (for test estimator) method is a variation on the estimator and was proposed by Bancroft (1944). In our case, the sample has to be divided in several independent subsets of increasing period. The slopes of the first two subsets will be compared with a t-test. If the null hypothesis, the two slopes are statistically identical, is accepted, then the two subsets are merged and its slope becomes the testimator. This new subset will be compared to the next adjacent subset under the same conditions and so on, until the null hypothesis is rejected (Bhardwaj et al. 2016; Kanbur et al. 2007).

In the case of a simple linear regression:

$$y = \beta_i x + a, \tag{2.4}$$

where $\beta_i$ is the slope of the subset $i$, you can test the hypothesis $\beta_1 = \beta_0$, where $\beta_0$ is the prior (here the slope for the first subset). If successful, the testimator $\beta_\omega$ can be calculated:

$$\beta_\omega = k\beta_1 + (1-k)\beta_0, \tag{2.5}$$

where $k$ is the ratio of the t-value found and the t-value which would be associated to a p-value of 0.05.

Kanbur et al. (2007) provides a detailed demonstration that the testimator is an unbiased estimator under the null hypothesis and that it has a smaller variance than the usual least-square estimator. It also has the interesting property of smoothing the impact of outliers. The main challenge of the testimator method is the choice of the size of the subsets. It also provides only an upper or lower limit to the value of the breaking point.

### 2.3 *breakpoints*

Bai & Perron (2003) describes the theoretical framework of the beakpoints (BP) algorithm in detail. Their dynamic programming algorithm segments the sample and look for its optimal partitioning, by minimizing the sum of squares in each segments. The implementation of this algorithm in the R package $STRUCCHANGE$ will find the optimal model based on the Bayesian Information Criterion (Erdman & Emerson 2007).

### 2.4 *bcp*

Barry & Hartigan (1993) gives a bayesian solution to the breakpoint identification problem. This method can be applied for observations independent under the normal assumption $N(\mu_i, \sigma^2)$ and it gives the probability $p_i$ for a breaking point at position $i$. The full theoretical framework of this method being extensive, we will only give a brief description here.

The sample is subdivided into blocks, for each block from position $i+1$ to $j$, a prior distribution $\mu_i j$ with normal assumption $N(\mu_0, \sigma^2/(j-i))$ is defined. At each position $i$, the probability for a break point at position $i+1$ is calculated from the ratio:

$$\frac{p_i}{1-p_i} = \frac{P(U_i = 1|X, U_j, j \neq i)}{P(U_i = 0|X, U_j, j \neq i)}, \tag{2.6}$$

where $U_i$ is an indicator of the presence or absence of change point at position $i+1$. If $U_i = 1$, a break point is identified at $i+1$.

This method was implemented in R in the package *bcp* by Erdman & Emerson (2007)

## 3 Simulations

In order to test these methods, we build simulations consisting of $N$ observations with x-axis values ranging from 0 to 1.7 and y-axis values calculated with the model from equation 2.2 to which we add a normal perturbation $\sigma$:

$$y = a_1 + b_1\ x + \lambda(a_2 + b_2\ x) + \sigma, \tag{3.1}$$

where $\lambda = 0$ if $x < \tau$ days and $\lambda = 1$ if $x > \tau$ days. $\tau$ is the breaking point we are choosing.

We know the methods to be impacted by the number of observations, the noise and the difference between $b_1$ and $b_2$. Two different sets of data are built. In the first set, $N$ will vary from 50 to 500 on a log scale, $\sigma$ will vary from 0.05 to 0.5 by steps of 0.05 and $\Delta$ will vary from 0 to 0.9 by steps of 0.1. This data will serve for the F-test, the Testimator and BP. In the second set, $N$ will vary from 50 to 235 on a log scale, $\sigma$ will vary from 0.05 to 1 and $\Delta$ will vary from 0 to 0.3. This data will serve for the bcp method.

Each combination will be used to produce 200 samples (first set) and 27 samples (second set).

## 4 Results

We apply the four methods described to our simulations. In figure 2, we display the p-value found by the F-test and observe for high $\Delta$, low $\sigma$ and high $N$ a clear trend toward low p-values. For no difference between the two slopes, we have no false identification, which confirms the F-test as a reliable tool for false positive checks.

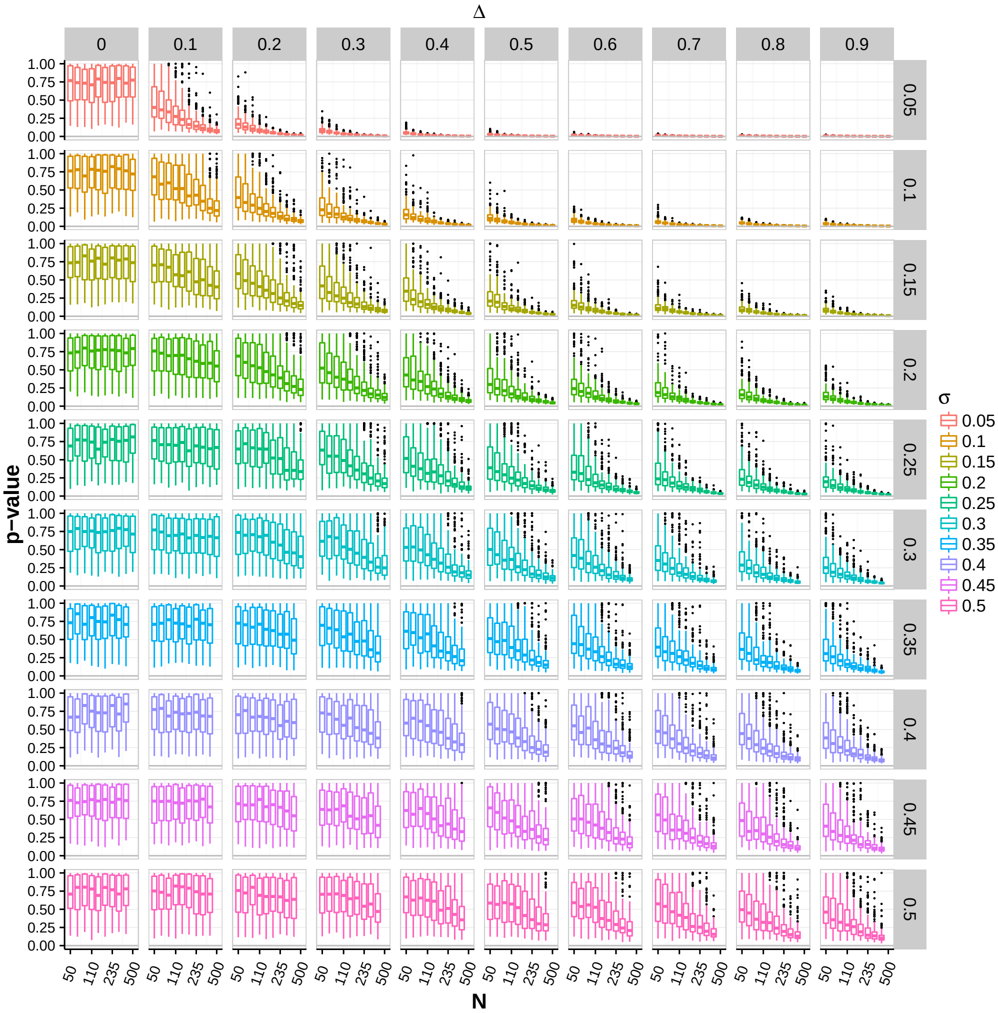


**Fig. 2.** Evolution of the p-value found by the F-test with the number $N$ of observations given for each combination of added noise $\sigma$ and slope difference $\Delta$. Outliers are shown in red.

In figure 3, we show the difference between the real breaking point $\tau$ and the breaking point found by Testimator. Though the trend is not as strong as in the F-test, it is important to note that the Testimator can only provide a lower limit to the value of the breaking point. We see for $\Delta = 0$ that the testimator will go through all the subsets without detecting any breakpoint in most of the samples.

The BP method is tested in figure 4. Again we show the difference between the predefined $\tau$ and the one found by the method. Promising results are found even for high values of $\sigma$ where the average value is close to 0. It is even more remarkable given the fact that, contrarily to the F-test, the BP algorithm does not receive any input else than the data itself.

The bcp method requires a few more steps. In the first place, a probability density function (PDF) is produced from each combination, such as in figure 5. Then the maximum value of the PDF is used to choose a breaking point and applied the Bayesian Information Criterion (BIC) and the Akaike Information Criterion (AIC) to the reduced and full regression model (see equations 2.1 and 2.2). We will note $AIC = AIC_r - AIC_f$ and $BIC = BIC_r - BIC_f$. This leads to figure 6 and figure 7, in which we show the difference between the BIC and the AIC found from the reduced and full model, respectively.

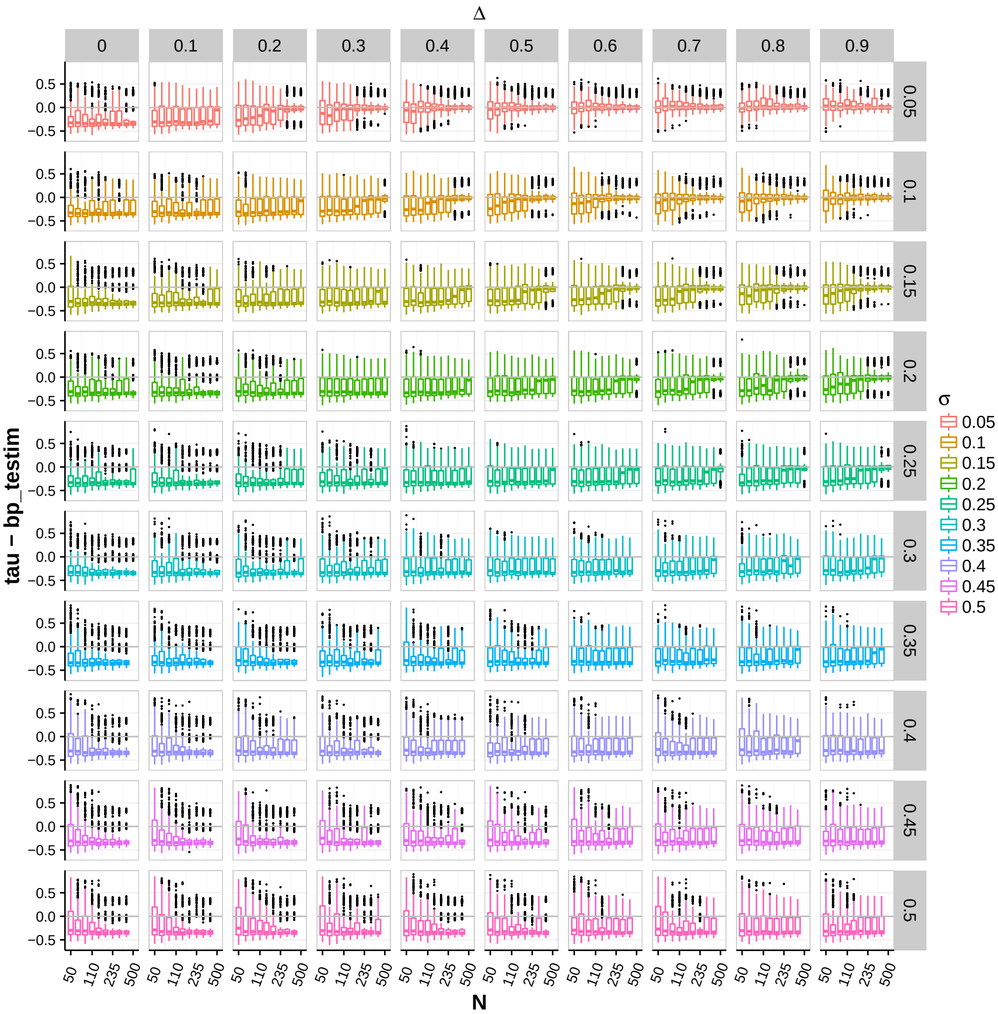


**Fig. 3.** Evolution of the breaking point value found by Testimator with the number $N$ of observations given for each combination of added noise $\sigma$ and slope difference $\Delta$.

Values of AIC and BIC tend to get higher following the same trend as the other methods.

## 5 Discussion and Conclusions

Breaking points can be identified by all four methods. A first estimation would suggest that, for samples of approximatively 200 or more observations, $\Delta$ is required to be twice as large as $\sigma$ in order to have an identification occurring.

The F-test never gave a false positive identification.

Testimator has not shown a very strong resolving power but is strongly dependant of the way the bins are chosen. Defining the optimum number of subsets according to $N$, $\sigma$ and $\Delta$ should be investigated in further works.

The BP algorithm has strong results but finds a non-negligible number of false positive for $\Delta = 0$. Hence, a verification with the F-test is advised, as it showed that the probability of a false positive with this method is extremely small.

The bcp method shows promising results and requires further investigation with a higher number of simulations and wider range of values for $N$, $\sigma$ and $\Delta$. We will also adapt our simulations in order to make them closer to real observations (particularly populations of Cepheids). More statistical methods will be challenged and be applied to real data after similar analysis are completed.

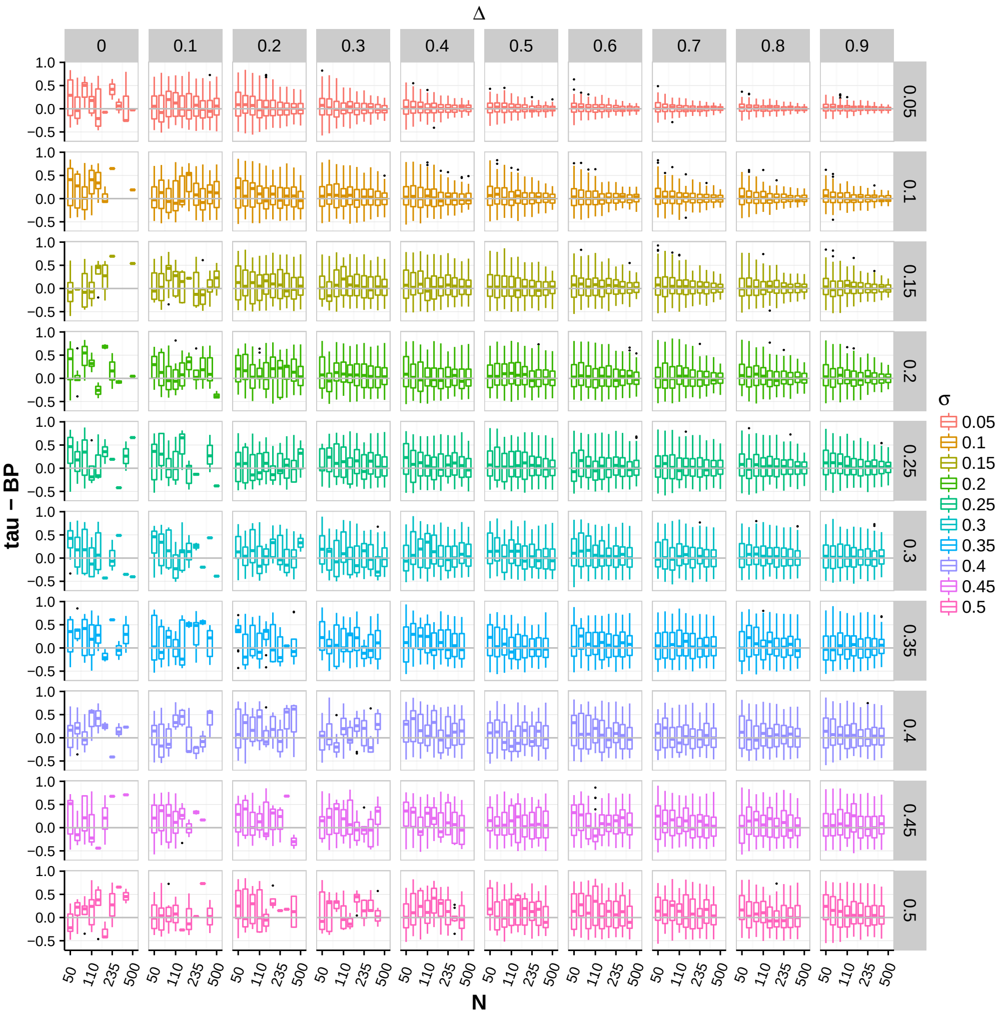


**Fig. 4.** Evolution of the breakpoint $\tau$ value found by BP with the number $N$ of observations given for each combination of added noise $\sigma$ and slope difference $\Delta$. BP returns no value if no breakpoint is identified.

We would like to thank David Valls-Gabaud, Anne-Laure Melchior and Gérard Grégoire.

## References

Bai, J. & Perron, P. 2003, Journal of Applied Econometrics, 18, 1

Bancroft, T. A. 1944, Ann. Math. Statist., 15, 190

Barry, D. & Hartigan, J. 1993, Journal of the American Statistical Association, 88, 309

Bhardwaj, A., Kanbur, S. M., Macri, L. M., et al. 2016, MNRAS, 457, 1644

Erdman, C. & Emerson, J. 2007, Journal of Statistical Software, 23, 1

Kanbur, S. M., Ngeow, C., Nanthakumar, A., & Stevens, R. 2007, pasp, 119, 512

Kanbur, S. M. & Ngeow, C.-C. 2004, MNRAS, 350, 962

Kanbur, S. M. & Ngeow, C.-C. 2006, MNRAS, 369, 705

Kodric, M., Riffeser, A., Seitz, S., et al. 2015, apj, 799, 144

Leavitt, H. S. & Pickering, E. C. 1912, Harvard College Observatory Circular, 173, 1

Ngeow, C. & Kanbur, S. M. 2009, in Astronomical Society of the Pacific Conference Series, Vol. 404, The Eighth Pacific Rim Conference on Stellar Astrophysics: A Tribute to Kam-Ching Leung, ed. B. Soonthornthum, S. Komonjinda, K. S. Cheng, & K. C. Leung, 262

Riess, A. G., Fliri, J., & Valls-Gabaud, D. 2012, apj, 745, 156

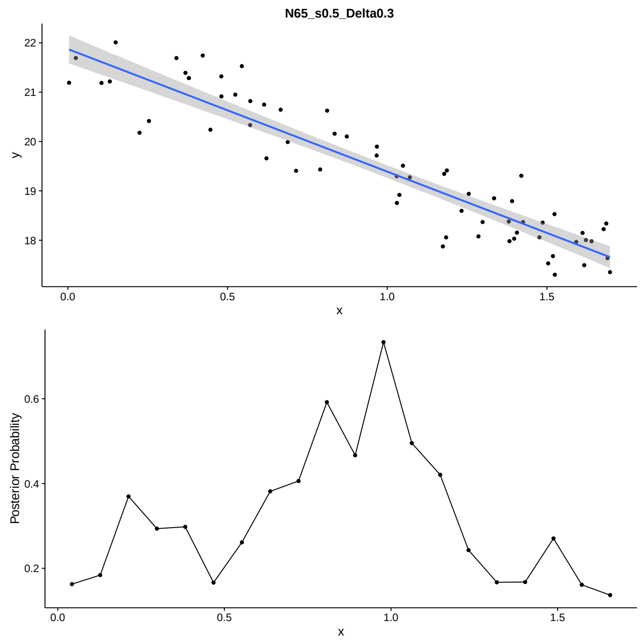


**Fig. 5.** Simulation for 65 observations with $\sigma = 0.3$ and $\Delta = 0.3$ (up) and associated PDF for a breaking point (down).

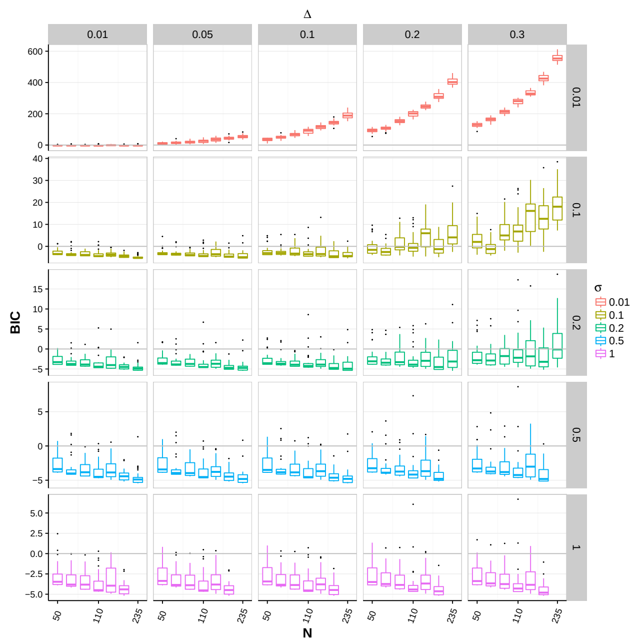


**Fig. 6.** Evolution of $BIC = BIC_r - BIC_f$ with the number $N$ of observations given for each combination of added noise $\sigma$ and slope difference $\Delta$.

Sandage, A., Tammann, G. A., Saha, A., et al. 2006, apj, 653, 843

Tammann, G. A., Reindl, B., Thim, F., Saha, A., & Sandage, A. 2002, in Astronomical Society of the Pacific Conference Series, Vol. 283, A New Era in Cosmology, ed. N. Metcalfe & T. Shanks, 258

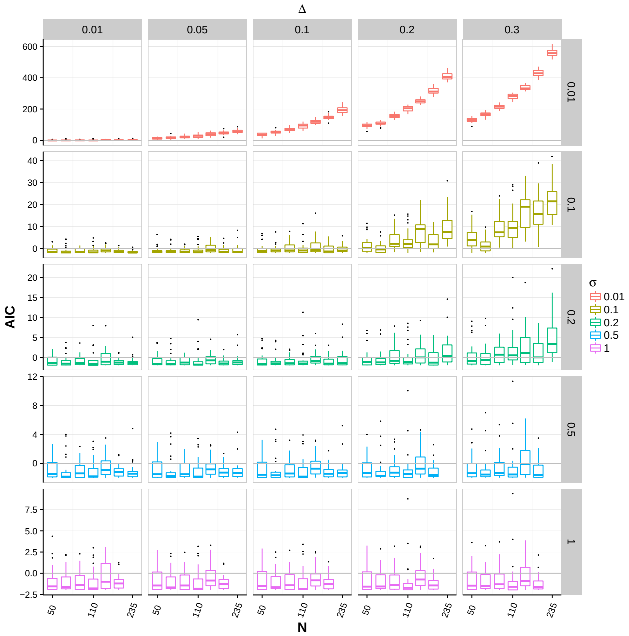


**Fig. 7.** Evolution of $AIC = AIC_r - AIC_f$ with the number $N$ of observations given for each combination of added noise $\sigma$ and slope difference $\Delta$.

*SF2A 2016*
*C. Reylé, J. Richard, L. Cambrésy, M. Deleuil, E. Pécontal, L. Tresse and I. Vauglin (eds)*

# MODELING SMALL EXOPLANETS INTERIORS: A NUMERICAL SCHEME TO EXPLORE POSSIBLE COMPOSITIONS

B. Brugger[1], O. Mousis[1] and M. Deleuil[1]

**Abstract.** Despite the huge number of discovered exoplanets, our knowledge of their compositions remains extremely limited. Modeling the interiors of such bodies is necessary to go further than the first approximation given by their mean density. Here we present a numerical model aiming at computing the internal structure of a given exoplanet from its measured mass and radius, and providing a range of compositions compatible with these data. Our model assumes the presence of a metal core surrounded by a silicate mantle and a water layer. Depending on their respective proportions, we can model various compositions, typically from terrestrial planets to ocean or Mercury-like planets. We apply this model to the case of CoRoT-7b, whose mass and radius values have recently been updated to 4.73 ± 0.95 $M_\oplus$ and 1.585 ± 0.064 $R_\oplus$, respectively. We show that these values are fully compatible with a solid composition, and find that CoRoT-7b may present a core mass fraction of 80% at maximum, or on the opposite, a maximum water mass fraction of 51%. If this latter composition is compatible with that of several icy moons in the solar system, a 80% core in mass is less conceivable and a lower limit can be placed from solar system formation conditions. These results confirm the Super-Earth status of CoRoT-7b, and show that an Earth-like composition may be obtained more easily compared to previous conclusions.

Keywords: Earth — planets and satellites: composition — planets and satellites: interiors — planets and satellites: individual (CoRoT-7b)

## 1 Introduction

The new exoplanet families now fill the gap existing between rocky and gaseous planets that compose the solar system. CoRoT-7b is considered as the first Super-Earth with known mass and radius. It was discovered by Léger et al. (2009), who detected a planet with a 1.68 ± 0.09 $R_\oplus$ radius orbiting the star CoRoT-7 with a period of $0.85359 \pm 5{\cdot}10^{-5}$ day. The mass of this planet was later obtained from HARPS radial velocity measurements, with a value of 4.8 ± 0.8 $M_\oplus$ (Queloz et al. 2009). Recently, Barros et al. (2014) and Haywood et al. (2014) performed new measurements of the radius and mass of CoRoT-7b, updating the values to 1.585 ± 0.064 $R_\oplus$ and 4.73 ± 0.95 $M_\oplus$, respectively. They also confirmed the semi-major axis of the planet's orbit at 0.0172 ± 0.00029 AU, corresponding to an equilibrium temperature of ∼1750 K (Barros et al. 2014).

Knowing the mass and radius of an exoplanet provides its mean density, which gives a hint on its possible composition (mainly to differentiate rocky from gaseous planets). However this value is just a first approximation, and our knowledge regarding the composition of exoplanets remains extremely limited. Here we want to go further by modeling the interiors of these bodies by presenting a numerical model that computes the internal structure of a given exoplanet from its measured mass and radius. We apply our model to the case of CoRoT-7b, which has never been studied with its updated physical parameters, in order to explore the possible interiors of the planet, assuming that it belongs to the class of dense solid planet (rocky with possible addition of water). We excluded from this study the cases where CoRoT-7b could harbor a thick atmosphere, unlike Earth.

## 2 Model and parameters

Based on the one-dimensional approach described by Sotin et al. (2007), our model is capable of computing the internal structure of a given planet, assuming that its mass and composition are known. Earth is taken

[1] Aix Marseille Univ, CNRS, LAM, Laboratoire d'Astrophysique de Marseille, Marseille, France (e-mail: `bastien.brugger@lam.fr`)

as a reference for several parameters and constants of the model, since it is the planet with the best known composition and internal structure. In our model, a planet can be made of up to five fully differentiated concentric layers (see Figure 1):

1. a metallic core made of pure iron and FeS iron alloy (Sotin et al. 2007);
2. the lower mantle, composed of a mixture of silicate rocks perovskite and magnesiowüstite;
3. the upper mantle, made from the same elements but in the form of olivine and enstatite;
4. a layer made of high-pressure water ices VII and X (Hemley et al. 1987);
5. a liquid water layer.

The mass of these layers – and thus their size – are variable, given as fractions of the total planet mass. This allows the model to simulate different planet compositions, from terrestrial (fully rocky) planets to ocean planets. Thus, we define two parameters of the model, the core mass fraction (CMF) and water mass fraction (WMF), forming a pair (CMF,WMF) to which the "composition" of a planet refers. The values of the CMF and WMF fix the locations of the core/lower mantle and upper mantle/water layer boundaries, respectively. The remaining boundaries (lower/upper mantle, water ice/liquid water) are directly computed from phase diagrams of the respective materials. The model also needs several compositional parameters, namely the fraction of alloy in the core and the relative distribution of the different types of silicate rocks in the mantle. Since we lack them in the case of CoRoT-7b, we use the Earth's values by default, as detailed in Figure 1.

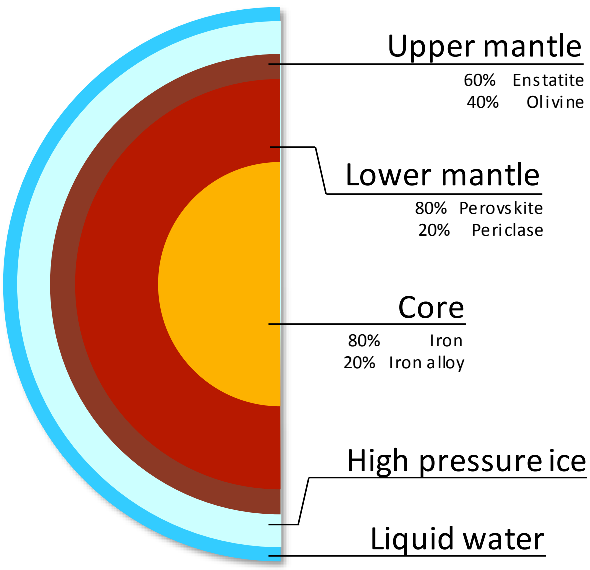


**Fig. 1.** Internal structure of an ocean planet, with five concentric layers: metallic core, silicate mantles (lower and upper), and water layers (solid and liquid). Our model is able to handle any combination based on these layers.

In our model, the interior of a planet is described by a one-dimensional spatial grid, ranging from the planet center until beyond its surface. For each point of this grid, the model computes the gravitational acceleration $g$, pressure $P$, temperature $T$, and density $\rho$, by solving the differential equations verified by these quantities:

$$\frac{dg}{dr} = 4\pi G\rho - \frac{2Gm}{r^3}, \tag{2.1}$$

$$\frac{dP}{dr} = -\rho g, \tag{2.2}$$

$$\frac{dT}{dr} = -g\frac{\gamma T}{\Phi}, \tag{2.3}$$

$$\frac{dm}{dr} = 4\pi r^2 \rho, \tag{2.4}$$

with $r$ the radius inside the planet, $m$ the mass at a given radius, $G$ the gravitational constant, and $\gamma$ and $\Phi$ the Grüneisen and seismic parameters, respectively (Sotin et al. 2007). These quantities govern the internal structure of a planet, therefore the model iterates on the solution of Equations 2.1–2.4, computing new positions of the layer boundaries at each iteration, until convergence is reached. This occurs when the simulation matches the asked planet mass, CMF, and WMF, and when the boundary conditions are verified: no central gravitational acceleration, surface temperature and pressure fixed to the given values. Since the model is not yet able to handle layers of gaseous materials (mostly hydrogen and helium), we do not consider in this work the possibility that CoRoT-7b possesses a thick atmosphere made of gas, as it is the case for Uranus or Neptune. However, in order to allow the existence of liquid water on the surface of the planet, we assume that CoRoT-7b's surface conditions (pressure and temperature) are similar to those of Earth (1 bar and 288 K, respectively). This assumes the presence of at least a thin Earth-like atmosphere, but does not have any influence on the computations of the planet radius (since the mass of such an atmosphere would be negligible relatively to the planet mass, as it is the case on Earth). The physical and orbital parameters of CoRoT-7b and its host star CoRoT-7, are summarized in Table 1.

**Table 1.** List of physical and orbital parameters of CoRoT-7b and its parent star CoRoT-7

| Parameter | Value | Reference |
|---|---|---|
| *Planet parameters* | | |
| Orbital period (day) | $0.853585 \pm 0.000024$ | Queloz et al. (2009) |
| Orbital distance (AU) | $0.0172 \pm 0.00029$ | Queloz et al. (2009) |
| Planet mass ($M_\oplus$) | $4.73 \pm 0.95$ | Haywood et al. (2014) |
| Planet radius ($R_\oplus$) | $1.585 \pm 0.064$ | Barros et al. (2014) |
| Equilibrium temperature (K) | $1756 \pm 27$ | Barros et al. (2014) |
| *Stellar parameters* | | |
| Effective temperature (K) | $5259 \pm 58$ | Barros et al. (2014) |
| Star mass ($M_\odot$) | $0.913 \pm 0.017$ | Barros et al. (2014) |
| Star radius ($R_\odot$) | $0.820 \pm 0.019$ | Barros et al. (2014) |

To accurately simulate the behaviors of all materials used in the different layers, and therefore compute the density profile inside the planet, the model uses equations of state (EOS) for each of these materials. These equations are fitted to laboratory experiments that study the behavior of a material's density (or equally its volume) under variations of pressure and temperature. Here we choose to follow the work of Sotin et al. (2007) and Valencia et al. (2007), who use the third-order Birch–Murnaghan (BM3) and Vinet EOS, respectively. The BM3 EOS is particularly fast for computations, but diverges for high pressure values (>1.5–3 Mbar; Seager et al. (2007), Valencia et al. (2009)). We opted to use it in the upper layers (water ice and liquid water). For denser materials, namely the metals and rocks of the core and mantles, we switch to the Vinet EOS, that has been shown to better extrapolate at very high pressures (Hama & Suito 1996).

## 3 Results

We first consider the possibility that CoRoT-7b presents the same composition as Earth, corresponding to (CMF,WMF) = (0.325,0). Using the central mass inferred for this planet by Haywood et al. (2014), namely $M_P = 4.73\ M_\oplus$, we compute its internal structure via the use of our model. As for Earth, the result is a planet composed of a metallic core surrounded by silicate mantles, but no significant water layer. The boundaries between these three layers are respectively located at 5018 km and 9384 km from the center, and the planet radius is 9704 km, i.e. $R_P = 1.523\ R_\oplus$. This value lays within the range measured by Barros et al. (2014), meaning that an Earth-like composition for CoRoT-7b is fully compatible with the measurements.

However, CoRoT-7b may present a composition different from that of the Earth, following the variations of the CMF and WMF. Thus, we repeated the aforementioned simulation for every composition allowed by the variations of the CMF and WMF of the planet. The parameter space formed by these variations is represented by a ternary diagram, displayed three times on Figure 2. Each point of the ternary diagram corresponds to a unique composition, i.e. to a unique value of the pair (CMF,WMF). A planet located in one corner is fully composed of the corresponding compound (core, mantle, or water), whereas planets located on one side of the diagram do not contain any of the compound indicated on the opposite corner (as it is the case for Earth and Mercury, whose WMF is considered zero). Since the planet mass is fixed for the entire ternary diagram, each point of the diagram yields a corresponding planet radius (via the use of the model of internal structure). Thus, the ternary diagram can be seen as a heatmap of the planet radius, and we can draw curves on which the value of the radius is the same (named isoradius curves). Since the mass of CoRoT-7b is known with an uncertainty, we choose to plot a ternary diagram for three different values of the planet mass, namely 3.78, 4.73, and 5.68 $M_\oplus$ (i.e. the minimum, central, and maximum values inferred for the mass of CoRoT-7b).

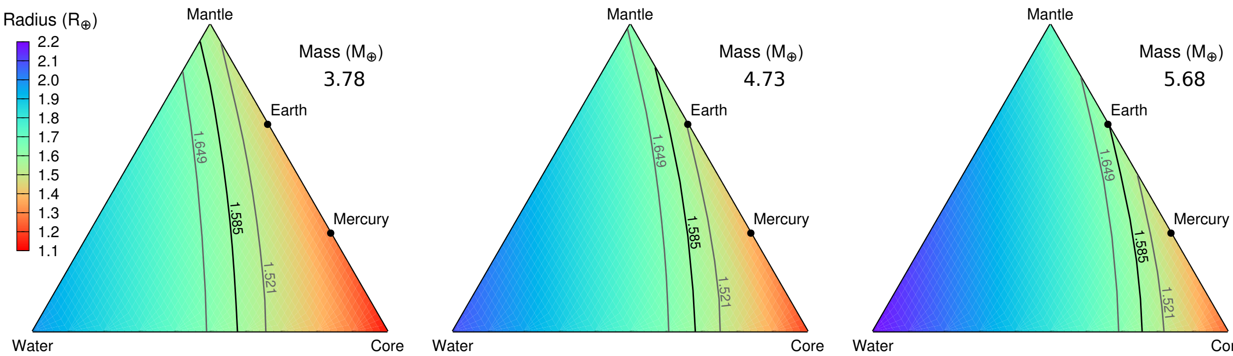


**Fig. 2.** Ternary diagrams displaying the investigated compositional parameters space: each point corresponds to a unique composition. From left to right, diagrams correspond to the minimal, central, and maximal masses inferred for CoRoT-7b. Each diagram shows a colored map of the planet radii obtained for the corresponding compositions. Also shown are isoradius curves denoting the minimal, central, and maximal radii measured for CoRoT-7b.

Since we know the radius of CoRoT-7b from Barros et al. (2014), we plot the isoradius curves corresponding to the minimum, central, and maximum values of its range of uncertainty, namely 1.585 $\pm$ 0.064 $R_\oplus$. As shown by Figure 2, these curves delimit an area on each of the three ternary diagrams. This is the domain of compositions that are allowed by the variations of the radius of CoRoT-7b within the measured range of uncertainty. It is interesting to follow the evolution of this area when the planet mass increases. For $M_P = 3.78$ $M_\oplus$, the domain of compositions allowed for CoRoT-7b lays in the center of the diagram, and we can deduce the limitations thus placed on the planet's CMF and WMF. The maximum CMF that can be reached with $M_P$ = 3.78 $M_\oplus$ is 66%, forming a 1.521 $R_\oplus$ planet. On the opposite, the WMF can go up to 51%, and in this case the planet's radius is 1.649 $R_\oplus$. Note that for this value of the planet mass, an Earth-like composition cannot be reached. This is not true when using a planet mass of 4.73 $M_\oplus$, where a planet with the composition of the Earth has a radius of 1.523 $R_\oplus$. In general, as we increase the mass of the planet, the domain of compositions allowed for CoRoT-7b shifts to the right of the ternary diagram. This expresses the need to increase the planet's mean density in order to keep the same planet radius, when increasing the planet mass. Thus, we see that for $M_P = 5.68$ $M_\oplus$, the maximum CMF becomes 80%, and the maximum WMF 30%. Also, we see that for this maximum value of the mass, an Earth-like composition yields a radius of 1.586 $R_\oplus$. In any of these cases, CoRoT-7b may never present a composition corresponding to that of Mercury (CMF,WMF) = (0.68,0), since the corresponding point on the ternary diagram lies always outside of the domain of compositions allowed for this planet.

## 4 Conclusions

Assuming that CoRoT-7b is solid, we investigated the compositions this planet could present, taking into account the limits placed by the measurements of the planet's mass and radius. Via the use of a model of internal structure, we find that CoRoT-7b may present a CMF up to 80% (in the case where $M_P = 5.68$ $M_\oplus$ and $R_P = 1.521$ $R_\oplus$), whereas the WMF of the planet reaches 51% for a 3.78 $M_\oplus$ planet with a radius of 1.649 $R_\oplus$. Interestingly, if the planet mass is set higher than the central measured value 4.73 $M_\oplus$, then the composition of the Earth ($\sim$33% CMF with no water) enters the domain of compositions allowed for CoRoT-7b. This confirms the Super-Earth status of the planet, that was suggested by the first measurements on the planet's radius.

Valencia et al. (2010) investigated the possible interiors and compositions of CoRoT-7b, using the first measurements on the mass and radius of the planet. They also restrained their simulations to the cases of dense rocky planets (with possible addition of water). Their main conclusion was that CoRoT-7b probably was depleted in iron compared to the Earth. Indeed, in their results, an Earth-like composition was possible only for $M_P = 5.68\ M_\oplus$ and $R_P = 1.521\ R_\oplus$ (otherwise the composition of the Earth was never in the domain of compositions allowed for the planet). Here, using the updated values of CoRoT-7b's mass and radius by Haywood et al. (2014) and Barros et al. (2014), we show that there is no need for an iron depletion since an Earth-like composition can be reached more easily.

The case of CoRoT-7b shows some limitations of the model of internal structure in its current form. For instance, we have considered that the surface conditions on this planet are similar to those on Earth, in order to allow the presence of liquid water at the surface. Considering the equilibrium temperature inferred for CoRoT-7b ($\sim$1750 K), it is probable that liquid water cannot exist at its surface. However, using a surface temperature of 1750 K would not be relevant either: because of its proximity to the parent star, CoRoT-7b is probably tidally locked in its orbit, always showing the same side to the star. To know what surface temperature has to be used, we would need a climatic model, that simulates the heat redistribution on the planet's surface.

We have used Earth values for the composition of CoRoT-7b as well. This assumes that the protoplanetary nebula that gave birth to CoRoT-7b was similar in composition to the protosolar nebula. The validity of this assumption could be constrained if we had measurements of the elemental abundances of the star CoRoT-7, that can be compared to the composition of the Sun.

This work has been carried out thanks to the support of the A*MIDEX project (n° ANR-11-IDEX-0001-02) funded by the "Investissements d'Avenir" French Government program, managed by the French National Research Agency (ANR). O.M. also acknowledges support from CNES.

## References

Barros, S. C. C., Almenara, J. M., Deleuil, M., et al. 2014, A&A, 569, A74

Hama, J. & Suito, K. 1996, Journal of Physics Condensed Matter, 8, 67

Haywood, R. D., Collier Cameron, A., Queloz, D., et al. 2014, MNRAS, 443, 2517

Hemley, R. J., Jephcoat, A. P., Mao, H. K., et al. 1987, Nature, 330, 737

Léger, A., Rouan, D., Schneider, J., et al. 2009, A&A, 506, 287

Queloz, D., Bouchy, F., Moutou, C., et al. 2009, A&A, 506, 303

Seager, S., Kuchner, M., Hier-Majumder, C. A., & Militzer, B. 2007, ApJ, 669, 1279

Sotin, C., Grasset, O., & Mocquet, A. 2007, Icarus, 191, 337

Valencia, D., Ikoma, M., Guillot, T., & Nettelmann, N. 2010, A&A, 516, A20

Valencia, D., O'Connell, R. J., & Sasselov, D. D. 2009, Ap&SS, 322, 135

Valencia, D., Sasselov, D. D., & O'Connell, R. J. 2007, ApJ, 665, 1413

*SF2A 2016*
*C. Reylé, J. Richard, L. Cambrésy, M. Deleuil, E. Pécontal, L. Tresse and I. Vauglin (eds)*

# SCIENCES POUR LES EXOPLANÈTES ET LES SYSTÈMES PLANÉTAIRES

F. Roques[1], C. Balança[2], Y. Bénilan[3], J.M. Griessmeier[4], E. Marcq [5], T. Navarro[6], S. Renner [7], J. Schneider[8] and C. Schott[1]

**Abstract.** The websites **Sciences pour les Exoplanètes et les Systèmes Planétaires** È (SESP) and **Exoplanètes** present planetary and exoplanetary sciences with courses, interactive tools, and a didactic catalogue connected to the Encyclopedia exoplanet.eu. These websites have been created in the context of the LabEx ESEP (Exploration Spatiale des Environnements Planétaires) and they are directed towards undergraduate level. They can be used as support for face-to-face courses and self-training. The websites will be translated and will be used to create e-learning degree courses.
SESP : `http://sesp.esep.pro/fr/index.html`
EXOPLANETES : `http://exoplanetes.esep.pro/`

Keywords: exoplanets, planetary systems, website, e-learning

## 1 Introduction

The aim of this project is to provide free access to high quality scientific information and multimedia tools developed for learning planetary and exoplanetary sciences. Both websites **SESP** and **Les exoplanètes** are created under Creative Common license (BY NC SA) : *You are free to - Share (copy and redistribute the material in any medium or format) - Adapt (remix, transform, and build upon the material).* A more precise description of the License is here : `https://creativecommons.org/share-your-work/licensing-types-examples/`. The courses are for undergraduate level (equivalent to L1 to L3 in the European LMD system) and the Exoplanètes website is for general public. They can be used for face-to-face or remote learning scientific degrees, or training courses aimed at high-school teachers, scientific mediators or journalists.

## 2 A digital book on (exo)planetary sciences

The digital book **Sciences pour les exoplanètes et les systèmes planétaires,** , presents the current knowledge about planetary systems through the sciences that support this knowledge: maths, physics, chemistry... The chapters are standalone modules written by researchers and professors who are specialists in the field. Each of them corresponds to roughly 10 hours of studentÕs work.

They share a common structure: - **Discover**: description of the astrophysical object, with none or few equations. - **Understand**: the sciences necessary for the study of the object. **Self-test**: self-assessment exercises, to check that the chapters are understood and known. - **Mini-project**: a data analysis project with scientific data about solar system planets or exoplanets.

The authors followed these guidelines to create the chapters listed below. The titles in bold are chapters accessible from Autumn 2016. Several interactive tools have been created for these modules (Fig. 1).

[1] LESIA, Paris Observatory, France
[2] LERMA, Paris Observatory, France
[3] LISA, Univ. Paris-Est, France
[4] LPC2E, Univ. Orléans, France
[5] LATMOS, Univ. Versailles, France
[6] LMD, IPSL, France
[7] IMCCE, Paris Observatory, France
[8] LUTH, Paris Observatory, France

| | |
|---|---|
| **Planètes et exoplanètes: Histoire et définitions** | **Formation et évolution des systèmes planétaires** |
| **Exoplanètes : Statistique et probabilités** | Les orbites planétaires |
| Dynamique des systèmes planétaires | **Surfaces planétaires** |
| Structure interne | Composition des atmosphères planétaires |
| **Structure thermique des atmosphères planétaires** | **Modèle de circulation générale des atmosphères** |
| **Dynamique atmosphérique** | **Petits corps du système solaire** |
| **Rayonnement électromagnétique : Flux et spectre** | **Polarisation** |
| **Flux U.V.** | Flux radio |
| **Plasmas planétaires: mesures in-situ** | Relations étoile-planètes |
| **Imagerie directe d'exoplanètes** | **Méthodes de détection d'exoplanètes par vitesse radiale et astrométrie** |
| Détection de transits d'exoplanètes | Exobiologie |
| **Habitabilité.** | |

## 3 An educational website on exoplanets

The website **Exoplanètes,** is based upon a catalogue of exoplanets which is a simplified mirror of the catalogue of the Encyclopedia `http://exoplanet.eu`. It is less complete than the research catalogue, however it is up to date with the latest discovered exoplanets. Whenever possible, the catalogue computes an equilibrium temperature (assuming a 0.3 albedo) and the planet density. In addition to the catalogue, the website contains visualization tools to work on the data, histogram and 4-parameter diagram (Fig. 2). Commented diagrams show how these statistical tools help to explore the properties of the exoplanetary systemsÕ properties and the outstanding issues. The site contains a table of exoplanet families, an exoplanet counter, 2D and 3D sky maps, along with small chapters answering questions about exoplanet definitions, discovery methods, habitabilityÉ A 3D simulator shows the structure of all the exoplanetary systems, compares it with the solar system and displays an estimation of the habitable zone, with all the precautions on the use of this term.

## 4 Future: E-learning projects

Further chapters are still in progress in the digital book. Projects are underway for diploma distance training on planetary sciences and exoplanets, taking advantage of the 10 years e-learning experience of the Paris Observatory. These training will be given at University of Versailles and at the Paris Observatory : `http://ufe.obspm.fr/Formations-en-ligne/ASTROPHYSIQUE-SUR-MESURE/Parcours.html`. Moreover, the exoplanets website will be translated into English, Brazilian, Italian, Spanich, Chinese.

## 5 The team

### 5.1 *The editorial comitee*

Françoise Roques (LESIA), Stefan Renner (IMCCE), Thomas Navarro (LMD), Jean-Mathias Griessmeier (LPC2E), Christian Balança (LERMA), Emmanuel Marcq (LATMOS), Yves Bénilan (LISA) et Jean Schneider (LUTH).

### 5.2 *The authors and reviewers*

Alain Doressoundiram (LESIA), Christian Balança (LERMA), Jean-Loup Baudino (LESIA), Yves Benilan (LISA), Benjamin Charnay (LESIA), Jean-Yves Chaufray (LATMOS), Valérie Ciarletti (LATMOS), Thierry Dudok de Wit (LPC2E), Stéphane Erard (LESIA), Sylvain Fouquet (GEPI), François Forget (LMD), Thierry Fouchet (LESIA), Nicolas Fray (LISA), Jean-Mathias Griessmeier (LPC2E), Anaelle Halle (LESIA), Nathan Hara (IMCCE), Jacques Laskar (IMCCE), Sébastien Lebonnois (LMD), Emmanuel Lellouch (LESIA), Alice Le Gall (LATMOS), Lucie Maquet (IMCCE), Emmanuel Marcq (LATMOS), Sophie Masson (LESIA), Stéphane Mazevet (LUTH), Ronan Modolo (LATMOS), Yael Nazé (U. Liege), Thomas Navarro (LMD), Filippo Pantellini (LESIA), Didier Pelat (LUTH), Arianna Piccialli (LESIA), François Raulin (MNHN), Françoise Roques

(LESIA), Loic Rossi (LATMOS), Patricia Schippers (LESIA), Jean Schneider (LUTH), Bruno Sicardy (LESIA), Philippe Thébault (LESIA) et Martin Turbet (LMD).

### *5.3 The technical team*

Project manager : Cédric Schott - Groupe Informatique du LESIA : Florence Henry, Emmanuel Grolleau, Julien Brulé - Graphics : Sylvain Cnudde - Software maintenance : Soufiane Ayadi, Damien Guillaume - Communication : Séverine Raimond.

## 6 Conclusions

These websites are free of use, in face-to-face or distance courses. Any experience feedback on the use of these resources are welcome.

The SESP project is supported by the LabEx ESEP. The authors are grateful to the University of Versailles Saint-Quentin-en-Yvelines, the University Paris-Est Créteil Val de Marne, the University of Orléans and the Paris Observatory for their participation. We also thank the UNT Unisciel for funding the project.

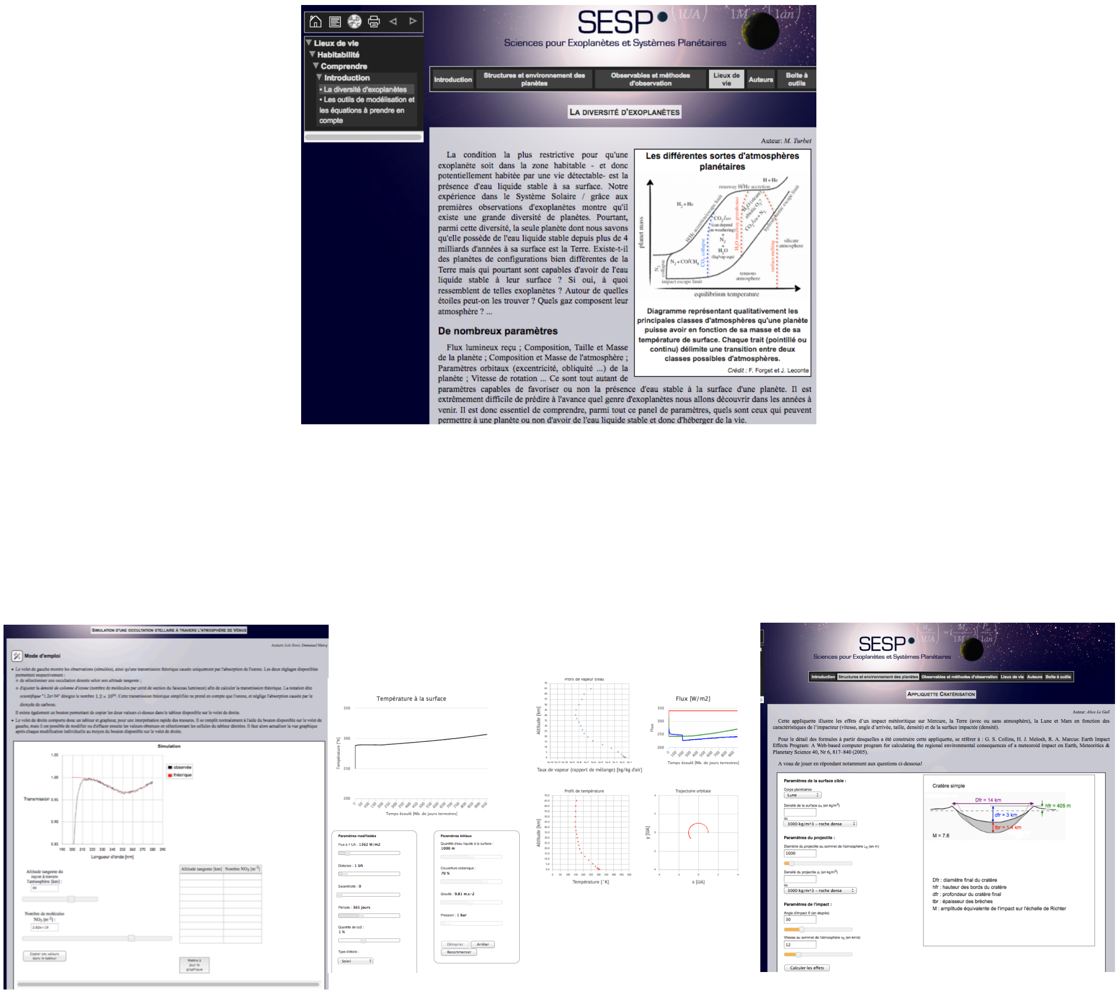


**Fig. 1.** One page of the digital book **Sciences pour les Exoplanètes et les Systèmes Planétaires** and exemples of applets : occultation by Venus - interactive GCM - crater formation.

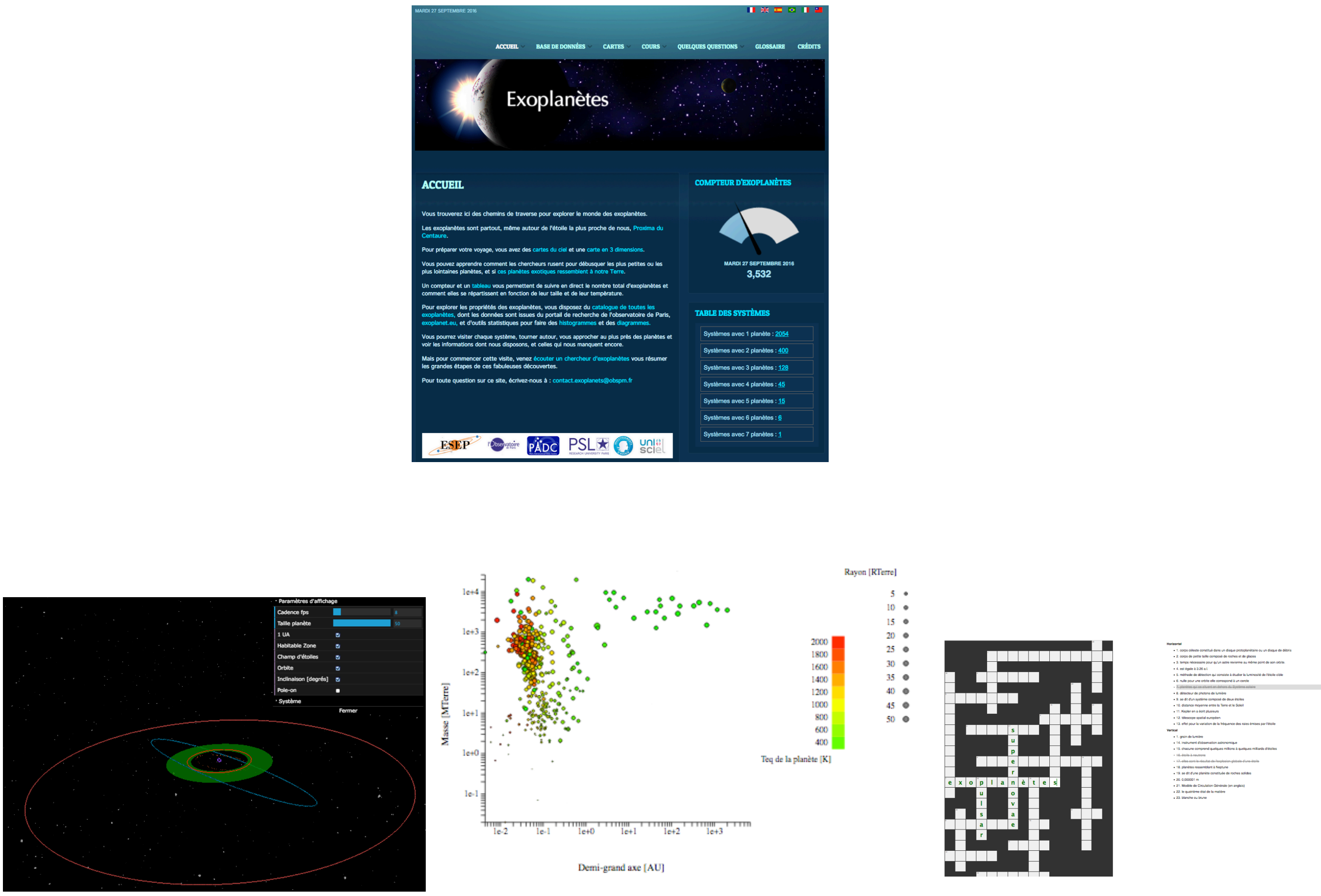


**Fig. 2.** Pages of the website **Exoplanètes**

# SITELLE'S DATA RELEASE 1

T. B. Martin[1] and L. Drissen[1]

**Abstract.** Installed at the Canada-France-Hawaii Telescope (CFHT) since August 2015, SITELLE is an Imaging Fourier Transform Spectrometer (IFTS) with an 11×11 field of view. After its prototype SpIOMM, installed at Mont Mégantic (Québec, Canada), it is the second IFTS in the world operating in the visible band (350–1000 nm). It delivers hyperspectral data cubes of 4 million spectra at R∼1500–5000 with a spatial sampling of 0.32" and a filling factor of 100 %. A suite of softwares has been designed to reduce (ORBS) and analyze (ORCS) the data. Based on commissioning data obtained in August 2015, a first stable version has been released in March 2016 which is capable of reducing all the data. In this paper the quality of the calibration is discussed.

Keywords: SITELLE, SpIOMM, Imaging Fourier transform spectrometry, ORBS, ORCS, Data calibration

## 1 Introduction

Installed at the Canada-France-Hawaii Telescope (CFHT) since August 2015, SITELLE is an Imaging Fourier Transform Spectrometer (IFTS) with an 11×11 field of view. After its prototype SpIOMM (Drissen et al. 2008; Bernier et al. 2008), installed at Mont Mégantic (Québec, Canada), it is the second IFTS in the world operating in the visible band (350–1000 nm). It delivers hyperspectral data cubes of 4 million spectra at R∼1500–5000 with a spatial sampling of 0.32" and a filling factor of 100 %. The input light, modulated by a Michelson interferometer, is collected by two 2k×2k CCD cameras. A raw data set is composed of multiple couples of interferometric frames, one for each camera, taken at different position of the moving mirror. A suite of softwares has been designed to reduce (ORBS, Martin et al. 2012; Martin 2015) and analyze (ORCS, Martin et al. 2015, 2016) the data. Before the instrument's first light, ORBS was exclusively used to reduce the data of the prototype SpIOMM. Based on commissioning data obtained in August 2015 (Baril et al. 2016, Drissen et al., in preparation) and Science Verification data obtained in January 2016, a first stable version has been released in March 2016 which is capable of reducing all the obtained data with a first order calibration which will be enhanced in the next data release (Martin et al., in preparation). The quality of the calibration is going to be discussed in the next sections.

## 2 Instrumental line shape

The ideal instrumental line shape (ILS) of a phase corrected Fourier transform spectrum is a sinc. Any error in the phase correction may eventually result in a deformation of the ILS (e.g. Bell 1972) that will therefore generate wavelength and flux errors. When phase correction is possible, the attained level of precision of the phase correction is better than 1 percent for the relative pixel-to-pixel flux error and for the relative channel-to-channel flux error. Furthermore, no asymmetry of the instrumental line shape has been detected and its general model is very well described by our theoretical model (Martin et al. 2016).

## 3 Flux calibration

Flux calibration is based on the measurement of a spectrum of a spectrophotometric standard star every year in each filter. The obtained spectrum is used to correct for the wavelength dependant transmission of the

[1] Université Laval, 2325, rue de l'université, Québec (Québec), G1V 0A6, Canada

instrument and the telescope. A set of images of a standard star is also obtained at least once for each scan to get an accurate measurement of the mean sky transmission in the filter band. We have checked the accuracy of the flux calibration against various references: independant punctual sources (HETDEX Field, M1-71) and the integrated spectrum of a galaxy covering the whole field of view in three different filters (NGC 628, see Figure 1). All the results are reported in Table 1). There is an obvious general bias around -5 % which comes from the rough estimate of the modulation efficiency. A better estimate of the modulation efficiency can be derived from the ratio of the total spectral energy present in the output spectra and the total energy deposited by the photons in the input interferograms. It will be corrected in the next release. A conservative estimate of the precision of the flux calibration, i.e. without taking the bias into account, is around 5 %. The pixel-to-pixel precision of the flux calibration has been checked by comparing the H$\alpha$ map of the planetary nebula M 57 obtained with SITELLE and the map obtained through the F656N filter of the Hubble Space Telescope (O'Dell et al. 2013). After a careful alignment and convolution of the HST map to respect SITELLE's pixel scale, an histogram of the flux ratio has been computed (see Figure 2). We can see that the error is smaller than 1.5% and the standard deviation of the ratios is smaller than 1.6%. Note that the object covers only a small part of the field of view (around 1×1 arcminute) so that general biases cannot be detected. A more careful testing with a larger object is required.

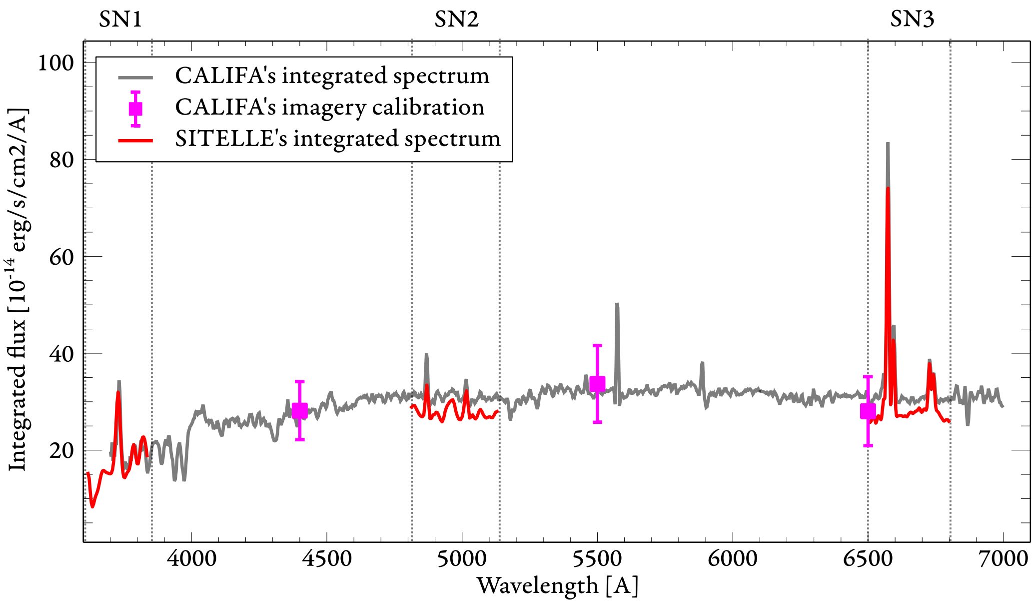


**Fig. 1.** Integrated spectrum of NGC 628 obtained with SITELLE in three filters (SN1, SN2 and SN3) superimposed on the integrated spectra obtained with PPaK (Sánchez et al. 2011; Kelz et al. 2006). SITELLE's spectra have been convoluted to respect PPaK's low resolution. A correction factor of 0.65 has been applied to consider PPaK's filling factor. The photometric calibration points used to calibrate PPAK spectrum are shown in purple along with their uncertainty. Part of the figure has been taken from Sánchez et al. (2011)

## 4 Wavelength calibration

A serious advantage of Fourier transform spectra when compared to any kind of dispersive technique is that the wavelength zero point is the only uncertainty. In other words there is no uncertainty on the relative wavelength calibration from one channel to the other. The observation of the light with an angle $\theta$ with respect to the axis of the interferometer translates in a position-dependant correction

$$\frac{\lambda_{\text{real}}}{\lambda_{\text{obs}}} = \cos(\theta)\ . \tag{4.1}$$

The zero point must therefore be calibrated for each spectrum of the cube. It is done via the observation of a laser source at Zenith. The deformation of the optical structure when the telescope moves from the Zenith position to the direction of the source is likely to produce an error in the relative wavelength calibration of up to

**Table 1.** Flux calibration check against various references. Three different filters have been checked: SN1 (362.6–385.6 nm), SN2 (482–513 nm) and SN3 (647.3–685.4 nm).

| Object | Description | Error |
|---|---|---|
| NGC3344 | Hα vs. SpIOMM | **-4%** ±2% |
| (Rousseau-Nepton et al.) | Hα + [NII]λ6584 vs. SpIOMM | **-4%** ±3% |
| M1-71 | Hα vs Wright (2005) | **-7%** ±3% |
| | [NII]λ6584 vs Wright (2005) | **-11%** ±3% |
| NGC628 | SN1 vs. CALIFA | **-6%** ±6% |
| | SN2 vs. CALIFA | **-7%** ±6% |
| | SN3 vs. CALIFA | **-9%** ±6% |
| HETDEX field | Lyα flux of ∼ 20 high redshift | **-5%**±7% |
| (Drissen et al.) | galaxies | |

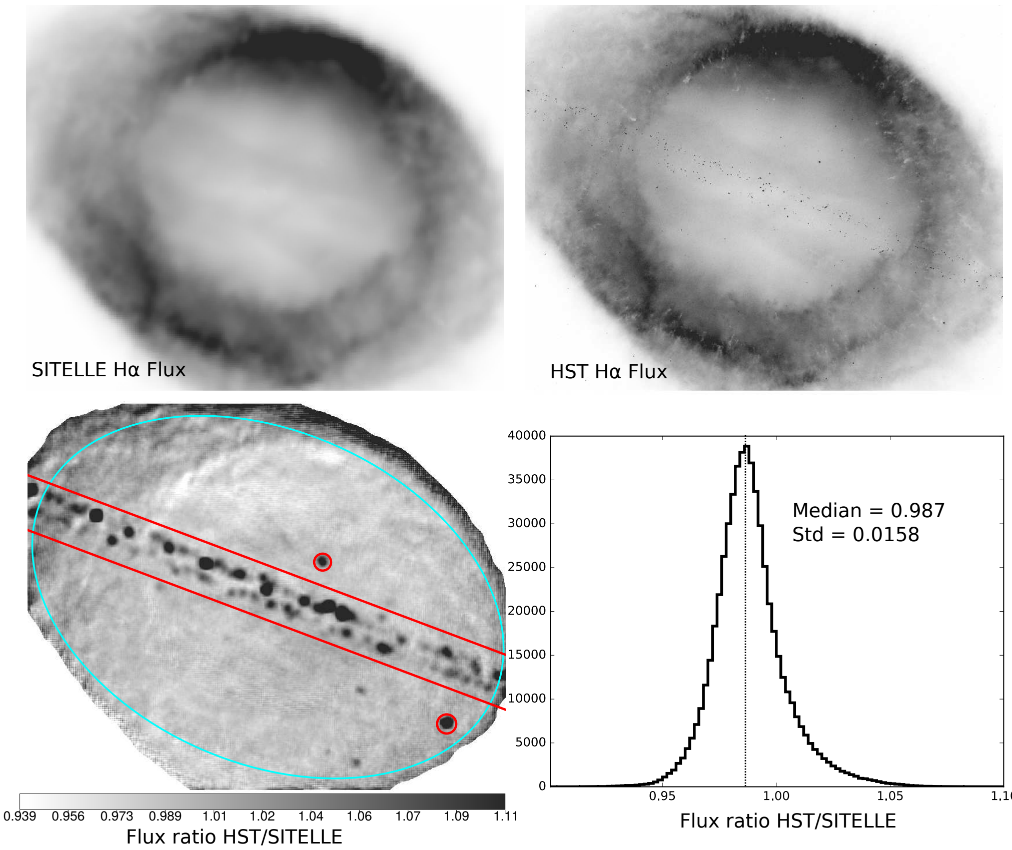


**Fig. 2.** Comparison of the Hα flux maps of the planetary nebula M 57 obtained with SITELLE (top-left) and the image obtained through the F656N filter with the Hubble Space Telescope (O'Dell et al. 2013, top-right). The bottom-left quadrant shows the pixel-to-pixel flux ratio and the bottom-right quadrant shows the histogram of the ratios. The HST map has been convoluted with a 8×8 kernel to fit the SITELLE's pixel scale. The regions shown in red have been excluded of the histogram because they are strong stars and reconstruction errors in the HST mosaic. The region included in the histogram is indicated as a blue ellipse.

15 km s$^{-1}$. The quality of the the calibration has been checked by comparing the velocity of 124 planetary nebulæ (PNe) detected with SITELLE in M 31, from a low resolution data cube obtained during the commissioning, with the velocity measured by Merrett et al. (2006). 86 of the 124 PNe show a compatible velocity within the uncertainties (see Figure 5). A much more precise checking has been obtained from the comparison of the velocity map of M 57 obtained with SITELLE versus the data obtained by O'Dell et al. (2007, 2013) with an Echelle spectrograph (Martin et al. 2016). Note that the original wavelength calibration of a cube (especially

in the SN3 red filter) can be improved to a precision of 0.3 km s$^{-1}$ (at R=5000) by fitting the Meinel OH bands which are generally present everywhere in the cube (see Figure 3 and Figure 4). This operation can be done with ORCS.

Another source of absolute calibration uncertainty is the lack of precision on the calibration laser wavelength. The error on the velocity measurement is

$$\Delta v = c \frac{\Delta \lambda_{\text{HeNe}}}{\lambda_{\text{HeNe}}} . \tag{4.2}$$

Therefore an error of 1 Å on the calibration laser wavelength translates into an error of 55 km s$^{-1}$. This bias is easy to correct since the measurement of the Meinel OH bands in a few cubes is enough to get a better estimation. For the data release 1 we have used the manufacturer value of 543.5 nm which is biased by 80±5 km s$^{-1}$.

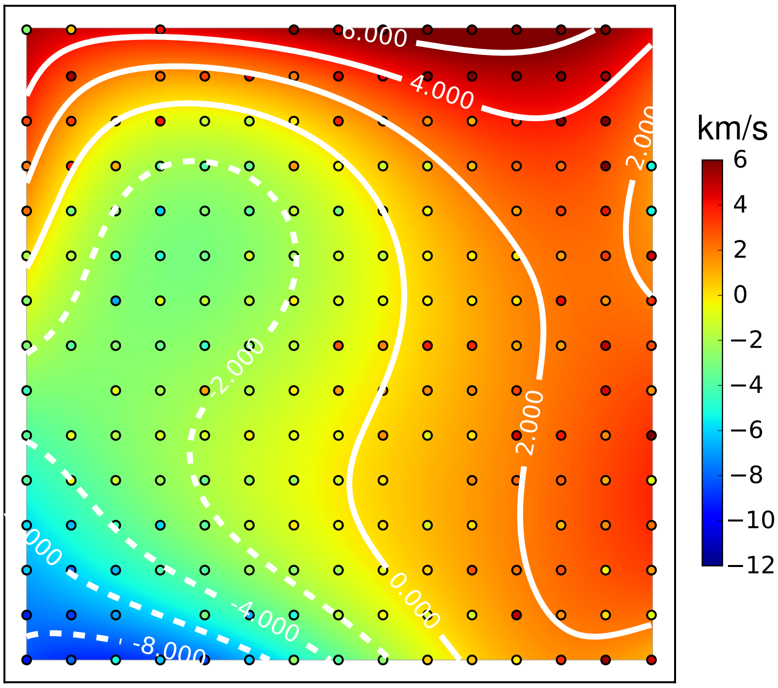


**Fig. 3.** Relative velocity map calculated from sky lines. Extracted from PG1216+069 in the SN3 filter at R=1900 (courtesy of Wei Hao Wang).

## 5 Astrometric calibration

Astrometric calibration is computed from the fit of the star-like sources detected in the field-of-view and the transformation of their celestial coordinates (Greisen & Calabretta 2002) found in the USNO-B1 catalog (Monet et al. 2003). The quality and the number of sources of the more recent Gaia data release 1 catalog has motivated its use for the next release instead of the old USNO catalog (Gaia Collaboration et al. 2016). The fitting engine fits all the stars at the same time which enhances the precision of the transformation parameters. The astrometric calibration is limited to 3 pixels (∼1") in an 11 arc-minutes circle around the center of the field by the optical distortions which are not taken into account in the present data release (see Figure 6).

## 6 Conclusions

We have discussed the calibration quality of SITELLE's first data release. We have shown that the absolute flux calibration was biased by -5% and that it was subject to a 5% variability from one observation to another. The general bias is likely to be corrected in the next release via a more precise estimation of the modulation efficiency. A ∼2 % pixel-to-pixel error is expected on the basis of a comparison with an Hubble images of M 57. The absolute wavelength calibration is also biased by 80±5 km s$^{-1}$ due to the lack of precision on the calibration laser wavelength. The pixel-to-pixel error on the calibration can be as large as 15 km s$^{-1}$ but it can be easily

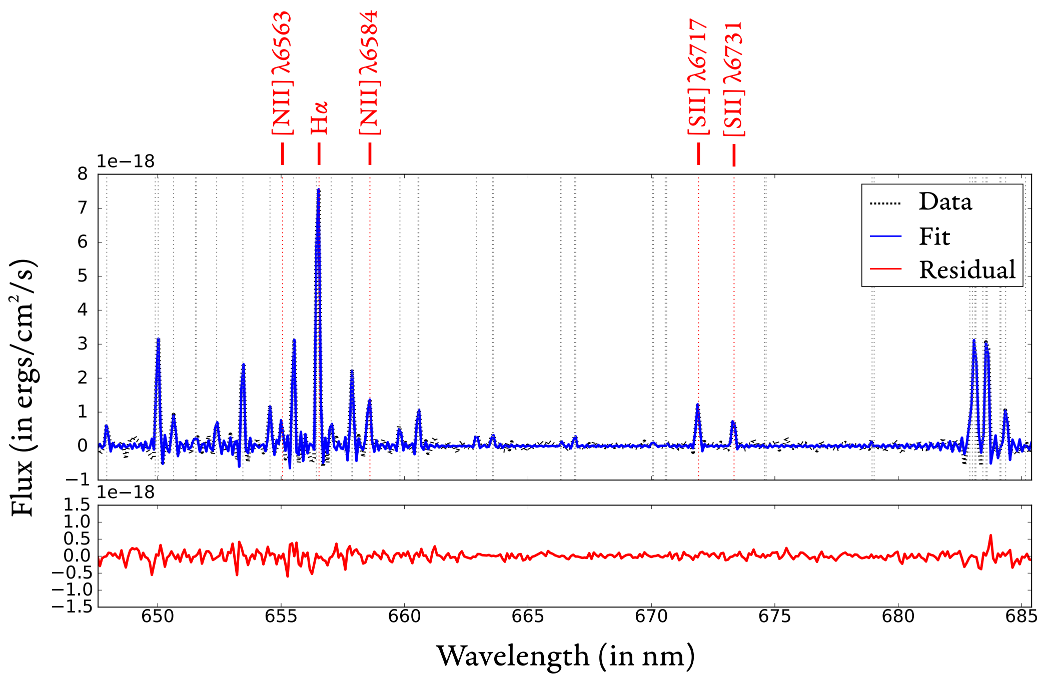


**Fig. 4.** Example of a fit of the Meinel OH bands of a sky spectrum in the field of IC 348. R = 4500 (courtesy of Gregory Herczeg). The fitted emission lines of the diffuse gas around the nebula are shown.

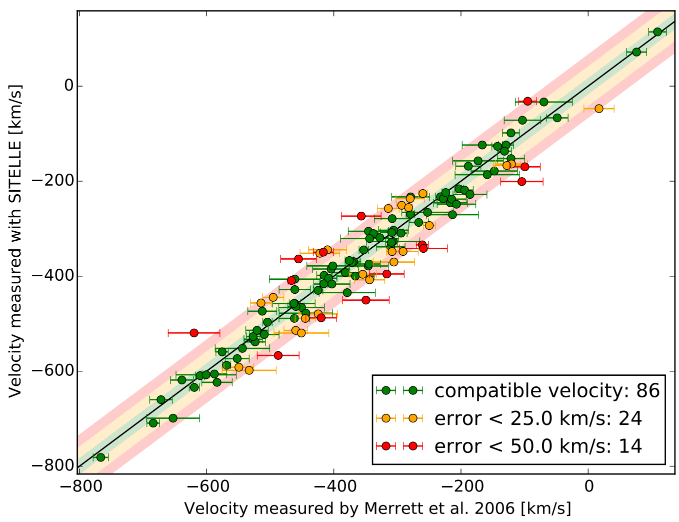


**Fig. 5.** Comparison of the measured velocity of 124 planetary nebulæ detected with SITELLE in M 31 with the measurement made by Merrett et al. (2006). The resolution of the cube is 400. The one-to-one line is indicated by a black line.

corrected by measuring the velocity of Meinel OH bands in the cube. This operation can be done with ORCS. The astrometric calibration is done via the comparison with the USNO-B1 catalog and is limited to ∼1" by the optical distortions which are not corrected in the present release. All the observed biases will be corrected in the next release. The precision on the pixel-to-pixel wavelength calibration will also be enhanced by the analysis of the internal phase of each cube that is directly related to the angle of the incident light and therefore to the velocity calibration (Martin et al., in preparation). The precision of the pixel-to-pixel flux calibration will also be enhanced by using a 3D phase correction and a better flatfield correction.

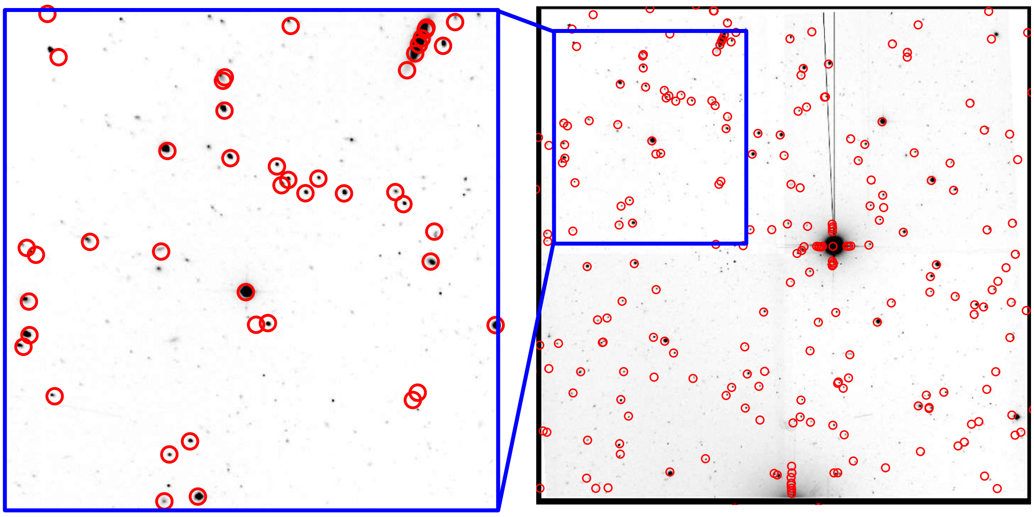

**Fig. 6.** Positions of the stars from the USNO-B1 catalog transformed with the computed World Coordinate System (WCS) of the field around the planetary nebula M1-71.

This paper is based on observations obtained with SITELLE, a joint project of Université Laval, ABB, Université de Montréal and the Canada-France-Hawaii Telescope (CFHT) which is operated by the National Research Council (NRC) of Canada, the Institut National des Science de l'Univers of the Centre National de la Recherche Scientifique (CNRS) of France, and the University of Hawaii. LD is grateful to the Natural Sciences and Engineering Research Council of Canada, the Fonds de Recherche du Québec, and the Canadian Foundation for Innovation for funding.

## References

Baril, M. R., Grandmont, F. J., Mandar, J., et al. 2016, in Proc. SPIE, ed. C. J. Evans, L. Simard, & H. Takami (International Society for Optics and Photonics), 990829

Bell, R. J. 1972, Introductory Fourier transform spectroscopy (London: Academic Press)

Bernier, A.-P., Charlebois, M., Drissen, L., & Grandmont, F. 2008, in Proc. SPIE, Vol. 7014, Ground-based and Airborne Instrumentation for Astronomy II, 70147J

Drissen, L., Bernier, A.-P., Charlebois, M., et al. 2008, in Proc. SPIE, Vol. 7014, Ground-based and Airborne Instrumentation for Astronomy II, 70147K

Gaia Collaboration, Prusti, T., de Bruijne, J. H. J., et al. 2016, A&A, 595, A1

Greisen, E. W. & Calabretta, M. R. 2002, A&A, 395, 1061

Kelz, A., Verheijen, M. A. W., Roth, M. M., et al. 2006, PASP, 118, 129

Martin, T. 2015, Phd thesis, Université Laval

Martin, T., Drissen, L., & Joncas, G. 2012, in Proc. SPIE, Vol. 8451, Software and Cyberinfrastructure for Astronomy II, 84513K

Martin, T., Drissen, L., & Joncas, G. 2015, in PASP Conference Series, Vol. 495, Astronomical Data Analysis Software an Systems XXIV (ADASS XXIV), ed. A. R. Taylor & E. Rosolowsky, 327

Martin, T. B., Prunet, S., & Drissen, L. 2016, MNRAS, 463, 4223

Merrett, H. R., Merrifield, M. R., Douglas, N. G., et al. 2006, MNRAS, 369, 120

Monet, D. G., Levine, S. E., Canzian, B., et al. 2003, AJ, 125, 984

O'Dell, C. R., Ferland, G. J., Henney, W. J., & Peimbert, M. 2013, AJ, 145, 92

O'Dell, C. R., Sabbadin, F., & Henney, W. J. 2007, AJ, 134, 1679

Sánchez, S. F., Rosales-Ortega, F. F., Kennicutt, R. C., et al. 2011, MNRAS, 410, 313

# Session SF2A

# Gravitational waves

*SF2A 2016*
*C. Reylé, J. Richard, L. Cambrésy, M. Deleuil, E. Pécontal, L. Tresse and I. Vauglin (eds)*

# SEARCHING FOR GAMMA-RAY COUNTERPART OF GRAVITATIONAL WAVE TRANSIENTS

H. Sol[1]

**Abstract.** With the recent direct detection of gravitational waves (GW), the search for electromagnetic counterpart of gravitational transients appears as a new challenge for astronomers. Information provided by electromagnetic data is complementary to the one deduced from the gravitational signal. Detecting the same event through the two messengers would be highly interesting to better identify the sources and refine their parameters. The scarcity of cosmic sources detected at very high energy (VHE) suggests that the gamma-ray domain could be useful to catch first electromagnetic signatures and reduce error boxes. Present IACT (Imaging Atmospheric Cherenkov Telescopes) like the High Energy Stereoscopic System (H.E.S.S.) operating in Namibia, the Major Atmospheric Gamma Imaging Cherenkov Telescopes (MAGIC) in the Canary Islands and the Very Energetic Radiation Imaging Telescope Array System (VERITAS) in the USA are already participating in the electromagnetic follow up of LIGO-Virgo gravitational wave event candidates. In the next decade the Cherenkov Telescope Array (CTA), operating with a larger field of view, a higher sensitivity in the VHE gamma-ray range between 20 GeV and 300 TeV, and a fast re-positionning, will be perfectly adapted to this observational program.

Keywords: very high energy astrophysics, gamma-ray astronomy, gravitational wave transients, electromagnetic counterparts

## 1 Introduction

Multimessenger gravitational wave astronomy aims to coordinate observations with a large variety of electromagnetic and non-photonic detectors to benefit from the synergy expected when combining different data of the same gravitational event. Joint observations can allow to better identify the source and determine independently its sky location and distance, to refine all parameters (even the ones deduced from the GW signal), and to confirm the GW detection and the nature of the event by providing complementary clues to implement a detailed modeling of the emitting source (Sathyaprakash, Schutz 2009). Information on the orientation of the source, on its cosmic environment, origin and evolution can also be deduced, with an interesting potential for discovering new types of sources and phenomena. There are various ways to achieve the goal of multimessenger GW astronomy. The most challenging one at the moment is to follow up GW transients by multimessenger instruments. This requires either all-sky surveys and monitoring, or a very efficient global alarm network to trigger quick observations of targets of opportunity, or else the possibility to predict the location and the time of GW events early enough to have the opportunity to plan multimessenger campaigns in advance. Another quite promizing approach is to look afterwards in recorded GW data for positive GW signal at the time of specific cosmic events like gamma-ray bursts (GRB) detected by electromagnetic instruments, which allows in addition to lower the GW detection threshold. Indeed refining the parameters used in the GW search, thanks to electromagnetic data obtained on the source, can change a GW event candidate into a confirmed GW detection. Given the benefit expected from such counterpart detection, the astronomical and astroparticle community has responded very positively to the call of the LIGO-Virgo collaboration in 2013. More than 70 Memorandum of Understanding have been signed, with more than 160 multiwavelength and multimessenger instruments ready to contribute to the search of GW transient counterparts, and among them several gamma-ray experiments particularly well suited for such stimulating project.

[1] LUTH, Observatoire de Paris, PSL Research University, CNRS, Place J. Janssen, 92 195, Meudon, France

## 2 Electromagnetic follow up of the first LIGO gravitational-wave events

GW150914, the first ever detected GW transient, was difficult to localize in sky position and in distance. The detection by only two GW instruments limited the accuracy and resulted in a large "error box" of about 600 squaredegrees (90% credible region). A distance of the order of 410 Mpc (z = 0.09) was estimated under some assumptions to solve the distance-inclinaison degeneracy. The "error volume" of about $10^7 Mpc^3$ then corresponds to about $10^5$ galaxies! Moreover, this first GW transient happened to be due to the coalescence of two black holes, an event believed to possibly occur without any strong emission of electromagnetic waves (Abbott et al. 2016a,b). Despite all these difficulties, multiwavelength and multimessenger follow up of GW150914 was reported by at least 25 teams (see Fig. 1 and Fig. 2).

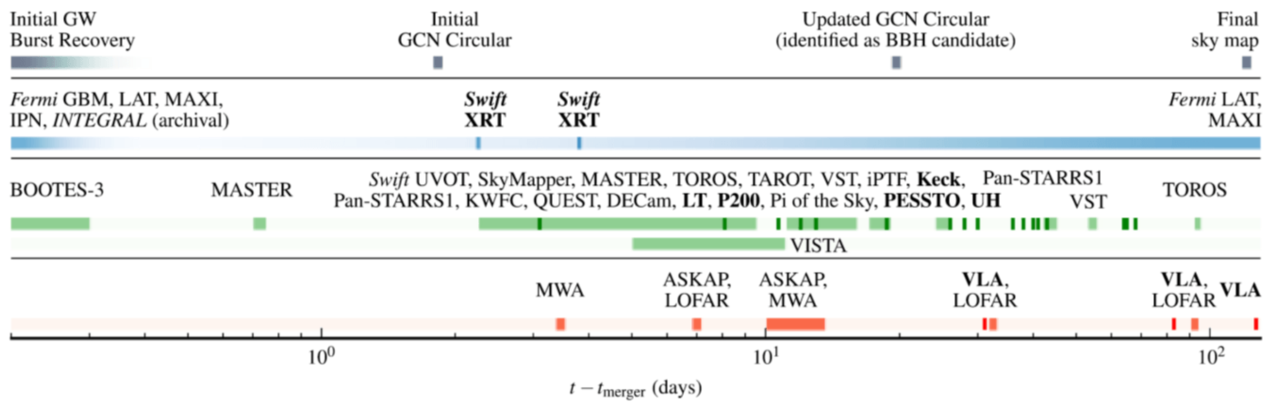


**Fig. 1.** Timeline of observations of GW150914 as a function of the observational delay following the GW trigger. From top to down: (I) GW observation and releases, (II) gamma-ray and x-ray, (III) optical and infrared, (IV) radio observations. From Abbott et al. (2016b).

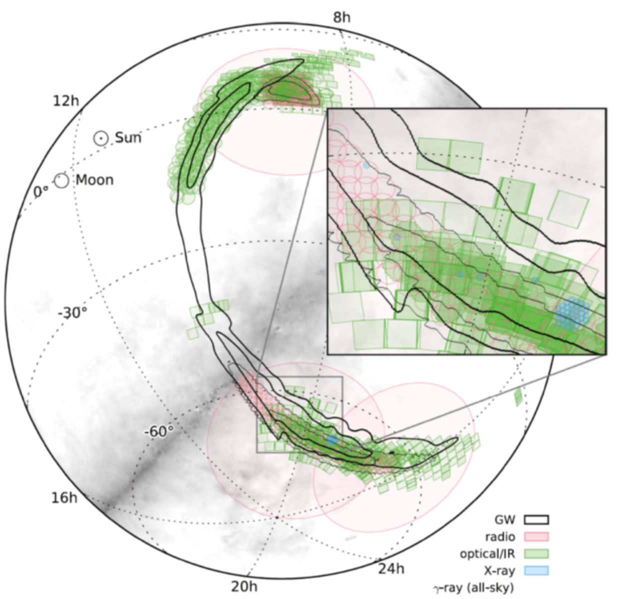


**Fig. 2.** Footprints on the sky of the observations listed in Fig. 1 (with same color code) overlaid on the 50% and 90% credible levels of different GW localization maps (black contours). All-sky surveys are not shown. Location of Sun, Moon and Galactic plane is given (Abbott et al. 2016b).

Work is still in progress but counterparts were extremely difficult to find. Many transients were detected in the region of interest but further investigation showed that they were not associated with the GW event. Only one possible counterpart was reported at the moment, namely a weak transient above 50 keV in the Fermi

Gamma-ray Burst Monitor data, recorded 0.4 seconds after the GW event and lasting 1 second, with a false alarm probability of 0.0022 (Connaughton et al. 2016). It is not yet clear whether this signal is a plausible counterpart or a chance coincidence. Indeed its characteristics suggest that it could be a weak GRB, consistent with the direction of GW150914. However it was not detected by other high energy instruments such as Fermi-LAT, INTEGRAL, AGILE, Swift or MAXI, which might be difficult to explain. Nevertheless further analysis of the Fermi-GBM data by Bagoly et al. (2016), with a new method to search for short-duration transients, finds a possible detection of counterpart of GW150914, and of LVT151012, a GW transient candidate reported by the LIGO-Virgo collaboration. If real, such association of short GRB with binary black holes mergers could be explained for instance by the scenario proposed by Perna et al. (2016) considering the evolution of a binary system with two low-metallicity massive stars, resulting in a "dead" accretion disk surrounding one of the black hole which can power the short GRB at the merger phase. More recent developments though did not find any candidate counterpart in the Fermi-LAT and GBM data (Racusin et al. 2016), neither for LVT151012, nor for GW151226, the second GW transient reported by the LIGO-Virgo collaboration (Abbott et al. 2016c). The search for electromagnetic counterparts remains completely open.

## 3 Ground-based gamma-ray astronomy and the Cherenkov Telescope Array project

During the last decade, the IACT experiments like H.E.S.S., MAGIC and VERITAS (see Fig. 3) showed the richness of our cosmos when seen in the TeV range, with the detection of various types of sources and especially compact ones with a number of pulsars and pulsar wind nebulae, supernova remnants, binary stellar systems, blazars, radio galaxies, and the galactic center. The sample of confirmed sources detected in the VHE range now include 178 objects. Present experiments are continuously gathering new results but their current sensitivity limits their possibilities of investigation.

CTA, the next generation main instrument of ground-based gamma-ray astronomy will benefit from improved performance, especially with an increase by a factor of ten of the sensitivity, a large spectral range, a large field of view of about 8 degrees, a better duty cycle and a fast re-positionning time down to 20 seconds (Acharya et al. 2013; Sol 2016a). CTA array will consist of several tens of Cherenkov telescopes of different types and sizes, with 23m, 12m and 4m telescopes in order to cover a wide domain in energy from 20 GeV up to 300 TeV (see Fig. 4). Two arrays are going to be implemented, one in La Palma, Canary Islands, and one in Chile near Paranal to have access to the whole sky. Lifetime should be 30 years.

Several prototypes of CTA telescopes and cameras have been implemented in the world especially in France, Germany, Italy, Poland, Switzerland and UK and are under construction in Spain and USA. Their first Cherenkov light has been obtained by the 4m prototype built and installed at the Observatoire de Paris in Meudon at the end of 2015 (Sol et al. 2016b). Production and deployment of the first telescopes on the two CTA sites are foreseen for 2017-2018.

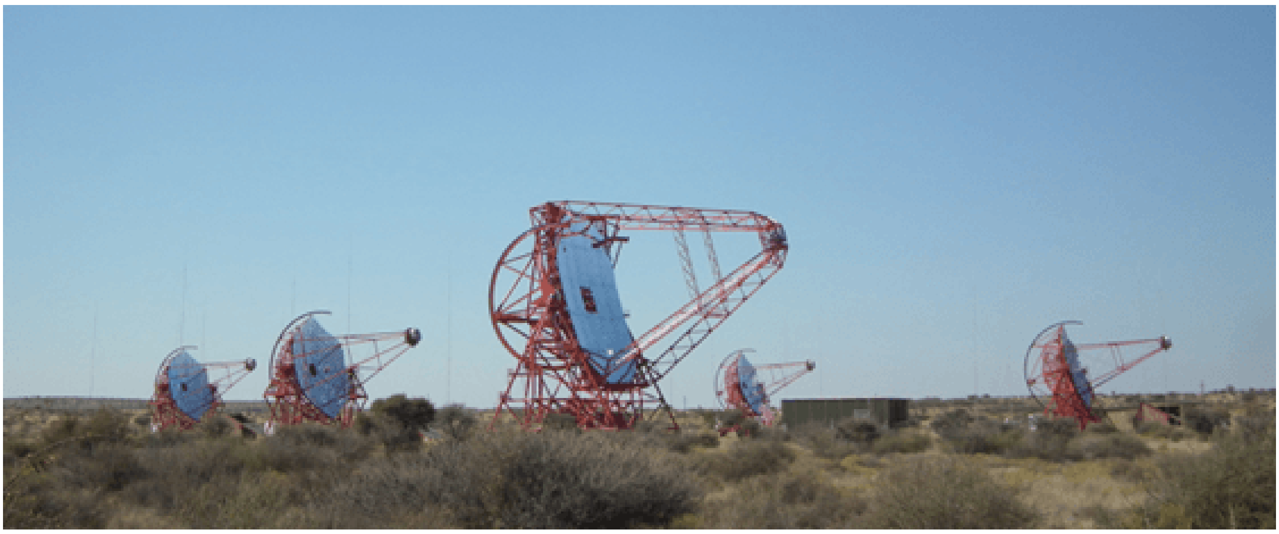

**Fig. 3.** The High Energy Stereoscopic System (H.E.S.S.) operating in Namibia.

**Fig. 4.** Artist's view of the future southern Cherenkov Telescope Array. Telescopes of different types and sizes allow to cover a very large domain in energy, from 20 GeV to 300 TeV.

At least a thousand of cosmic sources should be reachable with CTA. A special issue of Astroparticles Physics, volume 43, has been devoted to the CTA science case in 2013, with a large part dedicated to compact sources and various VHE phenomena potentially related to GW events. Especially some GRB should be detectable by CTA, with an expected detection rate of a few GRB per year (Meszaros 2013; Inoue et al. 2013). Indeed, thanks to its large detection area, CTA can resolve flares and variable emission on sub-minute time scales and appears as a very performant instrument to explore cosmic transients (see Fig. 5). The possibilities for searching GW transient counterparts are promizing. As shown by Bartos et al. (2014), CTA should be able to follow up GW event candidates over large sky areas. Despite several unknowns as regards to the electromagnetic properties of the relevant sources, it has the capability to detect some short GRB from compact binary merger events triggered by advanced LIGO-Virgo during its lifetime (see Fig. 6).

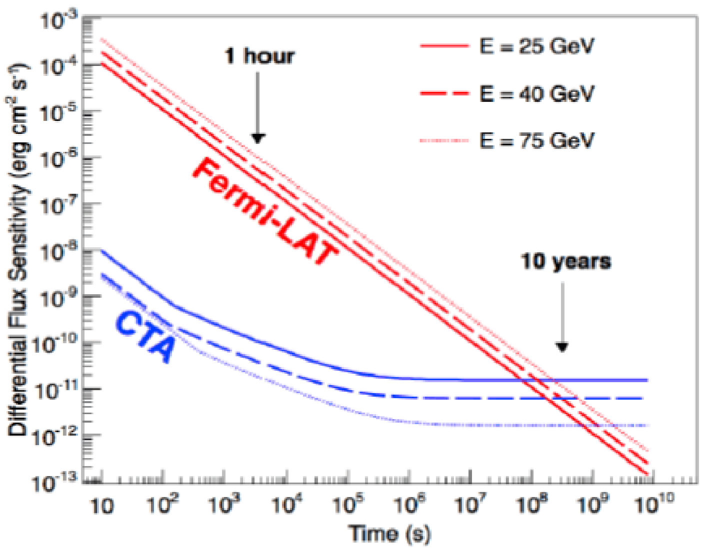


**Fig. 5. Left:** Differential flux sensitivity of Fermi-LAT and of CTA in the domain of overlap of their spectral range (namely from 20 GeV to 80 GeV) as a function of the time scale of interest. For time scales below 100 seconds CTA will improve the sensitivity by 4 orders of magnitude compared to the present Fermi-LAT performance (copyright@CTA).

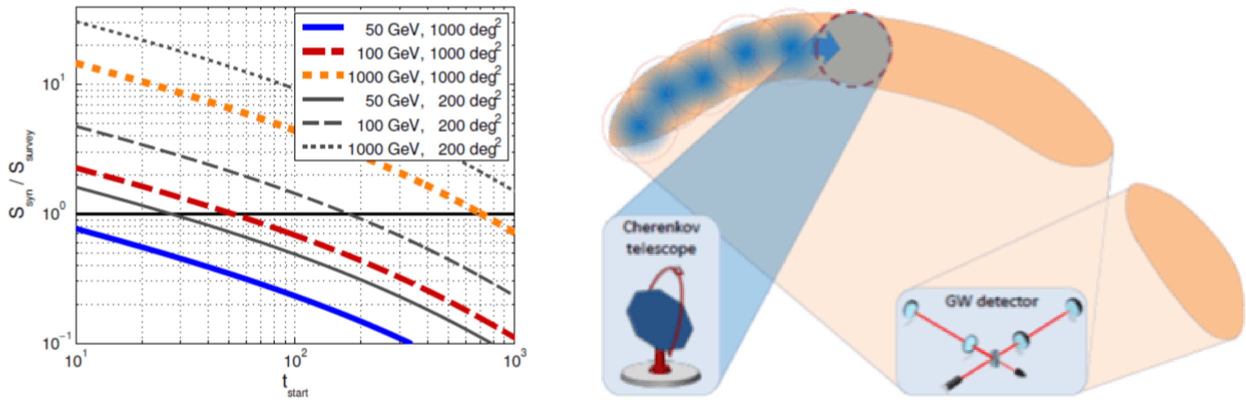


**Fig. 6. Left:** Detectability of a typical short gamma-ray burst with CTA as a function of the observationnal delay (in seconds) following the event. Results are shown for three different high-energy emission cutoff energies, and for two CTA survey operational modes. **Right:** Sketch of the sky areas of a GW event candidate and of the subsequent follow-up observation by a CTA telescope in survey mode. Actually several Cherenkov telescopes and GW detectors will be involved. From Bartos et al. (2014).

The nature of the GW event candidates and the detection rate per year of the different types of GW transients by LIGO-Virgo will be crucial to enable or disable the possible detection of counterparts. Current modeling of GRB offers many scenarios in which significant gamma-ray signal can be associated to GW transients. While the coalescence of isolated binary black holes could produce only faint or even no electromagnetic signal, gravitational collapses and mergers of binary systems with a neutron star or an accreting black hole are good candidates to be strong electromagnetic emitters at the time of the GW event, with the ejection of relativistic plasmas and jets and a wealth of possibilities to induce efficient and extreme particle acceleration by centrifugal forces, shocks, turbulence, or magnetic reconnection.

## 4 Conclusion and perspectives

Full operations of CTA are planned for 2022 and should last until 2050. CTA will open a window on the extreme, turbulent, transient and cataclysmic universe, mostly overlapping the realm of GW astronomy. The synergy between GW and VHE domains should be interesting. In this regard, strategies are being developped for global alarm networks between the large infrastructures of the coming decades in astrophysics and astroparticle physics (ALMA, AUGER, CTA, HAWC, Km3-IceCube, LHAASO, LIGO-Virgo, LOFAR, SKA and others), with the exchange of prompt alerts in a time delay limited to the record and analysis of the prime signal. The whole procedure raises many organizationnal questions that are currently under consideration.

## References

Abbott, B., et al, 2016a, Phys.Rev.Lett., 116, 061102
Abbott, B., et al, 2016b, ApJL, 826, L13
Abbott, B., et al, 2016c, Phys.Rev.Lett., 116, 241103
Acharya, B.S., et al, 2013, Astroparticle Physics, 43, 3
Bagoly, Z., et al, 2016, A&A, 593, L10
Bartos, I., et al, 2014, MNRAS, 443, 738
Connaughton, V., et al, 2016, ApJL, 826, L6
Inoue, S., et al, 2013, Astroparticle Physics, 43, 252
Meszaros, P., 2013, Astroparticle Physics, 43, 134
Perna, R., Lazzati, D., Giacomazzo, B., 2016, ApJL, 821, L18
Racusin, J.-L., 2016, submitted to ApJ (2016arXiv160604901R)
Sathyaprakash, B.S., Schutz, B.F., 2009, Living Rev. Relativity, 12, 2 ($http://www.livingreviews.org/lrr-2009-2$)
Sol, H., 2016a, these proceedings
Sol, H., Dournaux, J.-L., Laporte, P., et al, 2016b, these proceedings

# Session SF2A

# High energy and cosmic phenomena

# MULTIWAVELENGTH STUDY OF THE FLARING ACTIVITY OF SGR A* IN 2014 FEBRUARY–APRIL

E. Mossoux[1], N. Grosso[1], H. Bushouse[2], A. Eckart[3,4], F. Yusef-Zadeh[5], R. L. Plambeck[6], F. Peissker[3], M. Valencia[3], D. Porquet[1], W. D. Cotton[7] and D. A. Roberts[5]

**Abstract.** The supermassive black hole Sgr A* is located at the Milky Way center. We studied its flaring activity close to the DSO/G2 pericenter passage with XMM-Newton, HST/WFC3, VLT/SINFONI, CARMA and VLA to constrain the physical properties and origin of the flares. We detected two X-ray and three NIR flares on 2014 Mar. 10 and Apr. 2 with XMM-Newton and HST and two NIR flares on 2014 Apr. 3 and 4 with VLT. The 2014 Mar. 10 X-ray flare has a long rise and a rapid decay. Its NIR counterpart peaked 4320 s before the X-ray peak implying a variation in the X-ray-to-NIR flux ratio. This flare may be a single flare where change in the flux ratio is explained by the adiabatic compression of a plasmon or two close flares with simultaneous X-ray/NIR peaks. We observed an increase in the rising radio flux density on 2014 Mar. 10 with the VLA. It could be the delayed emission from a NIR/X-ray flare preceding our observation. The 2014 Apr. 2 X-ray flare occurred for HST in the Earth occultation of Sgr A*. We thus only observed the start of its NIR counterpart. After the occultation, we observed the decay phase of a bright NIR flare with no X-ray counterpart. On 2014 Apr. 3, two CARMA flares were observed. The first one may be the delayed emission of a VLT NIR flare. We thus observed a total of seven NIR flares whose three have an X-ray counterpart. We studied the physical parameters of the flaring region for each NIR flare but none of the possible radiative processes can be ruled out for the X-ray flares creation. Our X-ray flaring rate is consistent with those observed in the 2012 Chandra XVP campaign. No increase in the flaring activity was thus triggered close to the DSO/G2 pericenter passage. Moreover, higher X-ray flaring rates had already been observed with no increase in the quiescent level. There is thus no direct link between an X-ray flaring-rate increase and an accretion-rate change.

Keywords: Galaxy: center, X-rays: Sgr A*, radiation mechanisms: general

## 1 Introduction

Our Galaxy hosts Sgr A* the closest supermassive black hole at a distance of about 8 kpc (Genzel et al. 2010; Falcke & Markoff 2013). It has a mass $M_{\mathrm{BH}} = 4 \times 10^6\ M_\odot$ (Schödel et al. 2002; Ghez et al. 2008; Gillessen et al. 2009) and is usually in a non-flaring state, emitting predominately in radio to submillimeter wavelengths. Above this steady level, flares in near-infrared (NIR), X-rays and radio are observed. The NIR emission from Sgr A* is an overall flaring activity mostly with low amplitude, with several brighter flares up to 32 mJy (Witzel et al. 2012). The X-ray emission is composed by a non-flaring state plus a flaring activity characterized by a flaring rate of 1.1 $(1.0 - 1.3)$ flare per day with an intrinsic flare luminosity larger than $10^{34}$ erg s$^{-1}$ in the 2–8 keV energy band (Neilsen et al. 2013). When NIR and X-ray flares are detected simultaneously, their light curves have similar shapes with a delay shorter than 3 min between their maximum (e.g., Yusef-Zadeh et al. 2006; Dodds-Eden et al. 2009; Eckart et al. 2012). While NIR flares are known to be due to synchrotron emission

[1] Observatoire Astronomique de Strasbourg, Université de Strasbourg, CNRS, UMR 7550, 11 rue de l'Université, F-67000 Strasbourg, France.
[2] Nicolaus Copernicus Astronomical Center, ul. Bartycka 18, 00-716 Warszawa, Poland.
[3] Physikalisches Institut der Universität zu Köln, Zülpicher Str. 77, 50937 Köln, Germany
[4] Max-Planck-Institut für Radioastronomie, Auf dem Hügel 69, 53121 Bonn, Germany.
[5] Department of Physics and Astronomy, CIERA, Northwestern University, Evanston, IL 60208, USA.
[6] Radio Astronomy Laboratory, University of California, Berkeley, CA 94720, USA.
[7] National Radio Astronomy Observatory, Charlottesville, VA 22903, USA.

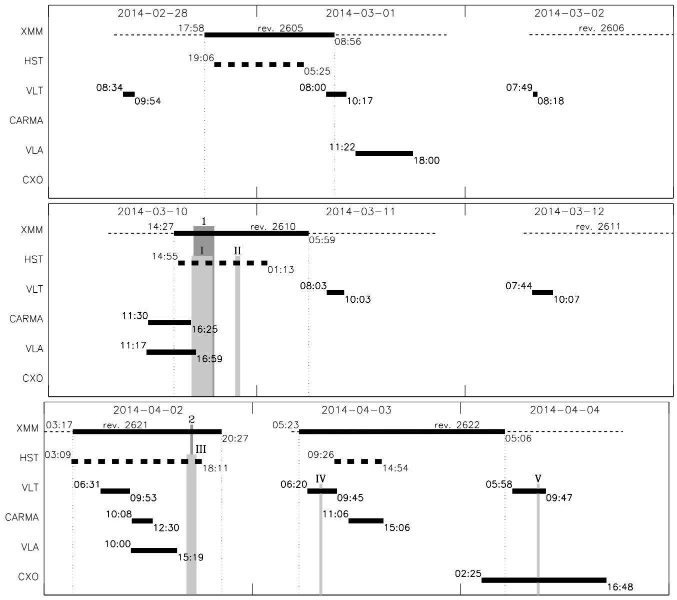


Fig. 1: Time diagram of the 2014 Feb.–Apr. multiwavelength campaign. The horizontal dashed lines are the XMM-Newton orbital visibility times of Sgr A* labeled with revolution numbers. The thick solid lines are the time slot of the observations for each instrument with start and stop hours. The vertical dotted lines are the limits of the XMM-Newton observations. The vertical gray blocks are the detected X-ray (Arabic numerals) and NIR (Roman numerals) flares.

(Eisenhauer et al. 2005; Eckart et al. 2006), the X-ray flare radiative process is still debated with arguments for synchrotron (SYN; Dodds-Eden et al. 2009; Barrière et al. 2014), inverse Compton (IC; Yusef-Zadeh et al. 2012), and synchrotron self-Compton (SSC; Eckart et al. 2008) models. The millimeter and radio flares are delayed by some minutes to hours after the NIR/X-ray flares (Marrone et al. 2008; Yusef-Zadeh et al. 2008, 2009). This behavior is well explained by the adiabatically expanding plasmon model (Van der Laan 1966; Yusef-Zadeh et al. 2006).

On 2011, the G2 object was discovered on its Keplerian orbit toward Sgr A* with a pericenter passage first predicted in mid-2013 (Gillessen et al. 2012). Two hypothesis have been developed on its nature: the first one is that G2 is a compact and ionized cloud of gas (Gillessen et al. 2012, 2013a,b) which would be disrupted during the pericenter passage leading to a putative change of the flare characteristics. The second one is that the G2 is a star with circumstellar matter leading to the name of Dusty S-cluster object (DSO; Eckart et al. 2013; Witzel et al. 2014). In the latter scenario, only a small part of the circumstellar matter would be accreted onto Sgr A*. The best constraints on the DSO/G2 characteristics were reported by Valencia-S. et al. (2015): the DSO/G2 is a pre-main sequence star of $1-2\,M_{\odot}$ with a circumstellar accretion disk emitting a Br$\gamma$ line thanks to the magnetospheric accretion of circumstellar matter on the stellar photosphere. Its pericenter passage was constrained to 2014 Apr. 20 (Mar. 1– Jun. 10) at $2032\,R_{\rm s}$ corresponding to 163 au from Sgr A* (with $R_{\rm s}=1.2\times10^{12}\,{\rm cm}=0.08\,{\rm au}$ the Sgr A* Schwarzschild radius). These NIR observations made after the pericenter passage proved that DSO/G2 was not tidally disrupted which rejects the purely gas cloud model.

We report here the results published in Mossoux et al. (2016) about the 2014 Feb.–Apr. multiwavelength observations for the study of the effect of the DSO/G2 pericenter passage on the flare activity from Sgr A*.

## 2 The 2014 Feb.–Apr. multiwavelength observations and flares detection

The 2014 Feb.–Apr. campaign is composed by joint XMM-Newton/HST/VLT observations (XMM-Newton AO-12; PI: N. Grosso) with coordinated/simultaneous observations with HST/WFC3 (F153M filter), VLT/SINFONI (H+K filter), VLA and CARMA (PI: H. Bushouse; A. Eckart; F. Yusef-Zadeh; R. L. Plambeck). The time diagram and the detected X-ray and NIR flares are represented in Fig. 1.

Two X-ray flares (1–2) were automatically detected using the two-steps Bayesian blocks algorithm (Mossoux et al. 2015) with a false positive rate for the flare detection of 0.1%: one on 2014 Mar. 10 and one on Apr. 2. Five NIR flares (I–V) were detected with a $3\sigma$ detection limit on the aperture- and extinction-corrected flux density light-curve: two on 2014 Mar. 10, one on Apr. 2, one on Apr. 2 and one on Apr. 3. The start of a possible radio (13.37 GHz = 2.2 cm) was also observed with VLA on 2014 Mar. 10. Three small millimeter flares

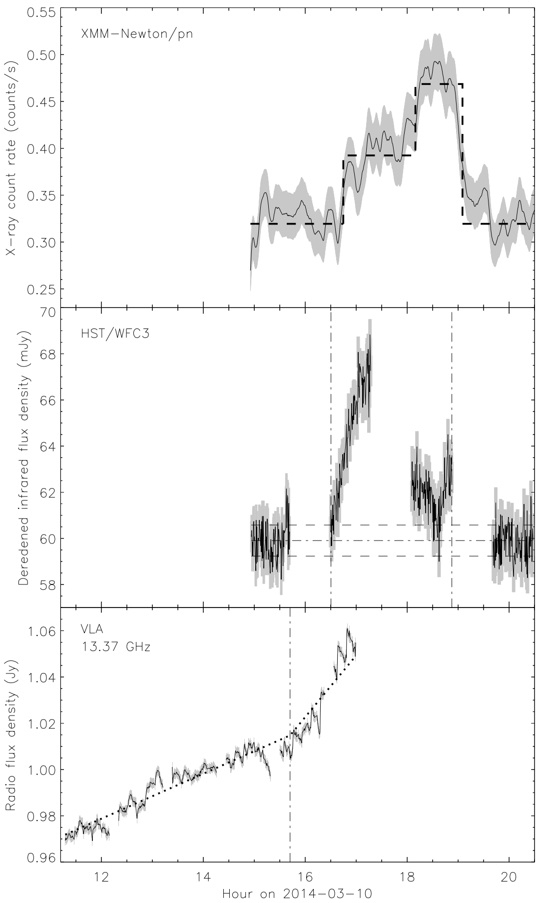


Fig. 2: Simultaneous X-ray, NIR and radio observations of flare I/1 from Sgr A* of 2014 Mar. 10. *Top panel:* The XMM-Newton/EPIC pn smoothed light curve computed with a window width of 500 s and its error in gray. The dashed lines are the Bayesian blocks. *Middle panel:* The deredened HST/WFC3 light curve and its error in gray. The vertical dot-dashed lines are the beginning and the end of the flare. *Bottom panel:* The VLA light curve at 13.37 GHz. The vertical dot-dashed line is the time of the beginning of the flare. The dashed line is the broken slope fit.

(95 GHz = 3.2 mm) were also observed with CARMA: one on 2014 Apr. 2 and two on Apr. 3.

The VLA radio flare of 2014 March 10 begins about 50 min before the NIR/X-ray flare I/1 (Fig. 2) implying that this radio flare is the delayed counterpart of a NIR/X-ray flare occurring before the beginning of the HST and XMM-Newton observations.

The NIR/X-ray flare I/1 is an atypical flare. Indeed, the X-ray light curve is highly asymmetric and characterized by a long rise (7700 s) and a rapid decay (844 s). Moreover, the maximum of the X-ray flare is delayed by $25.5 - 73.9$ min from those of the NIR flare (see Fig. 2). We proposed two interpretations to explain this atypical shape. The first one is the adiabatic compression of a plasmon where the NIR photons are produced by synchrotron radiation and the X-ray photons are due to the SSC process. If the plasmon is compressed, its density increases leading to a more efficient SSC mechanism and thus a lower number of NIR photons reaching the observer. The second interpretation is that the flare I/1 is actually composed by two close subflares (Ia/1a and Ib/1b) produced by their own electron population.

We only observed the decay phase of the NIR flare III on 2014 April 2 just after the occultation of Sgr A* by the Earth (see bottom left panel of Fig. 3). At the end of the previous HST orbit, the flux density from Sgr A* increased slowly.

The first radio flare observed with CARMA on April 3 could be the delayed millimeter counterpart of the NIR flare IV observed with the VLT/SINFONI with a delay of 4.4 h.

## 3 Constraining the physical parameters of the flaring region

To constrain the physical parameters of the flaring regions, we first determined the NIR–to–X-ray amplitude ratio of the flares detected in NIR and X-rays using a Gaussian fit of the NIR and X-ray light curves (see Fig. 3). Two close Gaussian flares (IIIa and IIIb) are needed to reproduce the light curve of the NIR flare III. The NIR flare IIIa is the simultaneous counterpart of the X-ray flare 2 whereas the NIR flare IIIb has no detected X-ray counterpart.

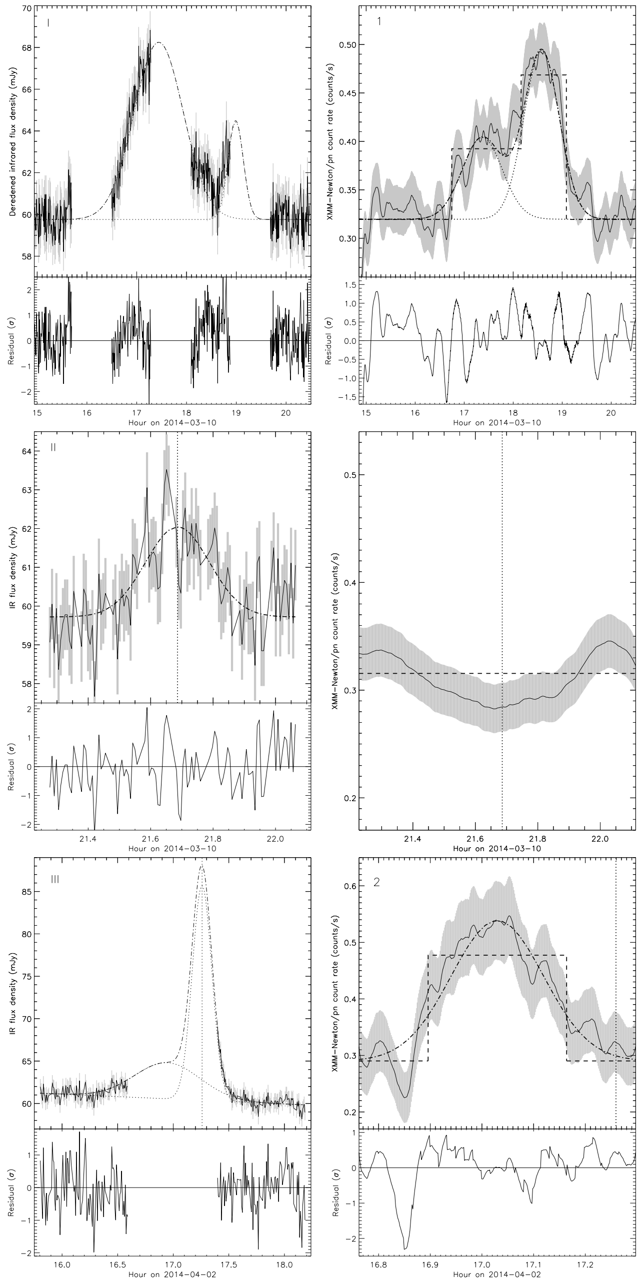

Fig. 3: Gaussian light curve fitting of the HST NIR flares (left panels) and the X-ray counterparts (right panels). The solid lines are the observed light curves with the error bars in gray. The dashed lines in the right panels are the Bayesian blocks. The X-ray light curves are smoothed with an Epanechnikov kernel (parabola shape) with a window width of 500 s and 100 s for 2014 Mar. 10 and Apr. 2, respectively. The dotted lines are the individual Gaussians and the dot-dashed line is the sum of the Gaussians. The vertical dotted lines are the time of the NIR flare peak when there is no detected X-ray counterpart. The residuals are in units of $\sigma$.

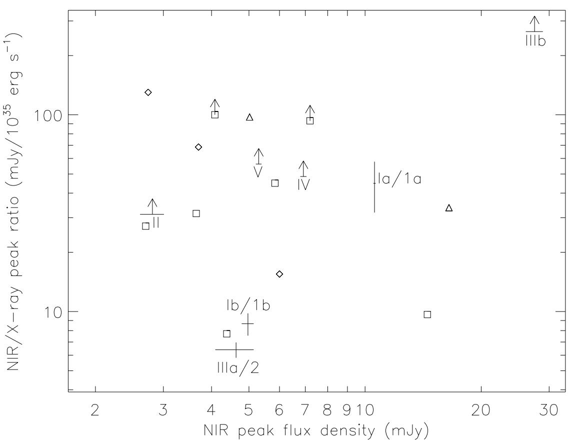


Fig. 4: NIR-to-X-ray peak ratio vs. amplitude of the NIR flares. Squares refer to the flares reported in Table 3 of Eckart et al. (2012). Triangles are the simultaneous NIR/X-ray flares detected on 2007 Apr. 4 and labeled *D* and *E* in Table 2 of Trap et al. (2011). Diamonds are the delayed flares of 2004 Jul. 7, 2008 Jul. 26+27 and 2008 May 5 reported in Table 2 of Yusef-Zadeh et al. (2012). The labeled points are the NIR and X-ray flares observed during this campaign.

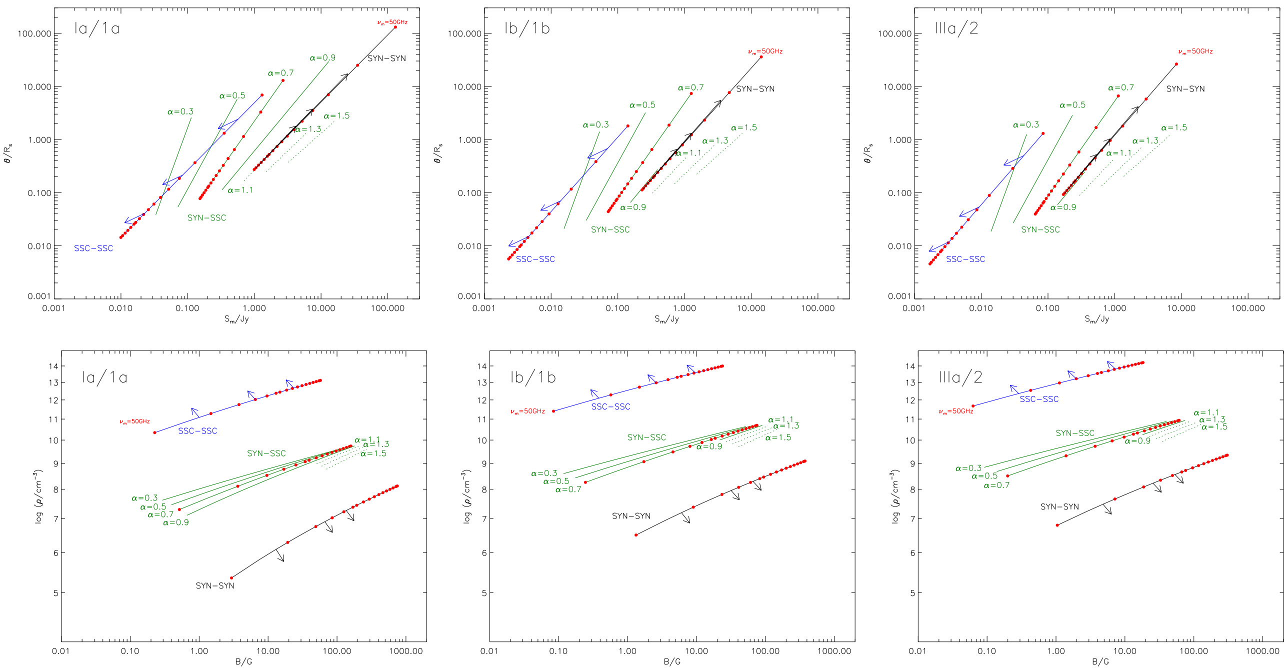


Fig. 5: Physical parameters of the flares observed simultaneously in X-rays and NIR for the three emission models. The flare Ia/1a, Ib/1b and IIIa/2 are in the upper, middle and bottom panels, respectively. Left panels are the size of the flaring-source region ($\theta$) vs. the peak of the spectrum ($S_\mathrm{m}$) at the frequency $\nu_\mathrm{m}$. Right panels are the density of the relativistic electrons vs. the magnetic field. The locii where the Synchrotron Self-Compton−Synchrotron Self-Compton (SSC-SSC), Synchrotron−Synchrotron Self-Compton (SYN-SSC) and Synchrotron-Synchrotron (SYN-SYN) are dominant are shown in black, blue and green, respectively. The red dots represent the turnover frequencies from 50 to 3000 GHz by step of 200 GHz. The arrows show the direction of the curves if the limit on the alternative emission processes is lowered. Dotted lines are locii of SYN-SSC where the MIR emission is larger than the observed upper-limit value of 57 mJy at 11.88 $\mu$m (Dodds-Eden et al. 2009).

For the NIR flares without detected X-ray counterpart (flares II, IIIb, IV and V), we determined an upper limit with a 95% confidence level on the undetected X-ray amplitude using a Bayesian method (Kraft et al. 1991). The NIR–to–X-ray flux ratio vs. resulting NIR amplitudes are represented among the previously observed NIR/X-ray flares in Fig. 4. The NIR flares with a detected X-ray counterpart are in the bulk of the NIR amplitudes and amplitude ratios already observed. The NIR flare IIIb without detected X-ray counterpart has the largest NIR amplitude and the highest NIR–to–X-ray flux ratio ever observed for a NIR/X-ray flare.

We then used the formalism developed by Eckart et al. (2012) to constrain the physical parameters of the flaring region considering the local radiative processes for the NIR and X-rays: SYN-SYN, SSC-SSC, and SYN-SSC. This formalism is described by six parameters. Two of them are fixed: the turnover frequency ($\nu_\mathrm{m}$) and the synchrotron spectral index ($\alpha$). The four remaining parameters (the size of the source region $\theta$, the magnetic field $B$, the electron density $\rho$, and the maximum of the flux density spectrum $S_\mathrm{m}$) are fitted to reproduce the NIR–to–X-ray flux ratio for a given $\nu_\mathrm{m}$ and $\alpha$ and for a given radiative process. The resulting graphs are shown in Fig. 5. The SYN-SYN, SSC-SSC and SYN-SSC radiative processes are the black, blue and green lines. For the SYN-SYN, SSC-SSC mechanisms, $\alpha$ is given by the amplitude ratio between the NIR and the X-ray flares since there spectrum are supposed to be described by the same spectral index. For the SYN-SSC mechanism, the spectral indexes in NIR and X-rays are not necessarily the same since they are produced by different electron populations. We thus computed the physical parameters for seven values of $\alpha$ from 0.3 to 1.5. We see that the larger the X-ray–to–NIR flare amplitude ratio, the better the physical parameters of the flaring region are constrained. For the NIR/X-ray flare IIIa/2 and the SYN/SSC mechanism, the most constrained parameters are $\theta = 0.03 - 7\,R_\mathrm{s}$ and $\rho = 10^{8.5} - 10^{10.2}\,\mathrm{cm^{-3}}$.

## 4 Conclusions

We detected 12 flares during the 2014 Feb.–Apr. campaign: seven NIR flares with HST/WFC3 and VLT/SINFONI, three X-ray flares (simultaneous with the three HST flares) with XMM-Newton, one centimeter flare with VLA whose the NIR/X-ray counterpart was not observable and three small millimeter flares with CARMA whose one could be the delayed radio flare of the first NIR flare observed with VLT/SINFONI. Thanks to the NIR–to–X-ray amplitude ratio, we constrained the physical parameters of the flaring regions using the formalism of Eckart et al. (2012). The larger the X-ray–to–NIR flare amplitude ratio, the better the constraints on the physical parameters of the flaring region.

The X-ray flaring rate observed during this campaign (three flares over 255.6 ks) is statistically consistent with those observed during the 2012 *Chandra XVP* campaign using the Bayesian blocks algorithm for the flare detection (1.5 flare per day) implying that no change of the X-ray flaring rate was observed close to the DSO/G2 pericenter passage. The NIR flaring activity observed during the 2014 Feb.–Apr. campaign is also consistent with those previously observed by Witzel et al. (2012) considering the higher detection threshold of the HST/WFC3 and VLT/SINFONI compared to VLT/NACO.

The typical timescale for the accretion of fresh matter from the DSO/G2 object onto Sgr A* at the pericenter is about three years. This timescale is even larger if we consider the large angular momentum of the matter from the DSO/G2 due to its eccentric orbit. We thus would not see any change in the flare characteristics from Sgr A* before 2017.

## References

Barrière, N. M., Tomsick, J. A., Baganoff, F. K., et al. 2014, ApJ, 786, 46
Dodds-Eden, K., Porquet, D., Trap, G., et al. 2009, ApJ, 698, 676
Eckart, A., Baganoff, F. K., Schödel, R., et al. 2006, A&A, 450, 535
Eckart, A., García-Marín, M., Vogel, S. N., et al. 2012, A&A, 537, A52
Eckart, A., Mužić, K., Yazici, S., et al. 2013, A&A, 551, A18
Eckart, A., Schödel, R., García-Marín, M., et al. 2008, A&A, 492, 337
Eisenhauer, F., Genzel, R., Alexander, T., et al. 2005, ApJ, 628, 246
Falcke, H. & Markoff, S. B. 2013, Classical and Quantum Gravity, 30, 244003
Genzel, R., Eisenhauer, F., & Gillessen, S. 2010, Reviews of Modern Physics, 82, 3121
Ghez, A. M., Salim, S., Weinberg, N. N., et al. 2008, ApJ, 689, 1044
Gillessen, S., Eisenhauer, F., Fritz, T. K., et al. 2009, ApJ, 707, L114
Gillessen, S., Genzel, R., Fritz, T. K., et al. 2013a, ApJ, 763, 78
Gillessen, S., Genzel, R., Fritz, T. K., et al. 2013b, ApJ, 774, 44
Gillessen, S., Genzel, R., Fritz, T. K., et al. 2012, Nature, 481, 51
Kraft, R. P., Burrows, D. N., & Nousek, J. A. 1991, ApJ, 374, 344
Marrone, D. P., Baganoff, F. K., Morris, M. R., et al. 2008, ApJ, 682, 373
Mossoux, E., Grosso, N., Bushouse, H., et al. 2016, A&A, 589, A116
Mossoux, E., Grosso, N., Vincent, F. H., & Porquet, D. 2015, A&A, 573, A46
Neilsen, J., Nowak, M. A., Gammie, C., et al. 2013, ApJ, 774, 42
Schödel, R., Ott, T., Genzel, R., et al. 2002, Nature, 419, 694
Trap, G., Goldwurm, A., Dodds-Eden, K., et al. 2011, A&A, 528, A140
Valencia-S., M., Eckart, A., Zajaček, M., et al. 2015, ApJ, 800, 125
Van der Laan, H. 1966, Nature, 211, 1131
Witzel, G., Eckart, A., Bremer, M., et al. 2012, ApJS, 203, 18
Witzel, G., Ghez, A. M., Morris, M. R., et al. 2014, ApJ, 796, L8
Yusef-Zadeh, F., Bushouse, H., Wardle, M., et al. 2009, ApJ, 706, 348
Yusef-Zadeh, F., Roberts, D., Wardle, M., Heinke, C. O., & Bower, G. C. 2006, ApJ, 650, 189
Yusef-Zadeh, F., Wardle, M., Dodds-Eden, K., et al. 2012, AJ, 144, 1
Yusef-Zadeh, F., Wardle, M., Heinke, C., et al. 2008, ApJ, 682, 361

*SF2A 2016*
*C. Reylé, J. Richard, L. Cambrésy, M. Deleuil, E. Pécontal, L. Tresse and I. Vauglin (eds)*

# WHY CURVATURE RADIATION IN NEUTRON-STAR MAGNETOSPHERES SHOULD BE TREATED IN THE FRAMEWORK OF QUANTUM ELECTRODYNAMICS

G. Voisin[1], S. Bonazzola[1] and F. Mottez[2]

**Abstract.** Curvature radiation is a key phenomenon in pulsar and magnetar magnetospheres. It is classically conceptually very close to synchrotron radiation, however we will show that in ultra-relativistic very-high-magnetic-field environments, the same approximations that lead to its use are also leading quickly to a potential quantized regime where the classical theory may fail. We explain in some details these caveats and give an outline of a quantum-electrodynamics treatment. We show that the internal consistency of the theory of curvature radiation is improved, and some interesting effects due to spin-flip transitions may occur.

Keywords: Neutron stars, pulsars, magnetars, synchrotron, curvature radiation, quantum electrodynamics

## 1 Introduction

Electron and positron states with very low momentum perpendicular to the magnetic field have been of interest in the field of rotating neutron-star magnetospheres almost since their discovery in 1968 Hewish et al. (1968). Indeed, the community soon realized that the extremely intense rotating magnetic fields of those magnetospheres, ranging from $\sim 10^4$ Teslas at the surface of old millisecond pulsars to $\sim 10^{11}$ Teslas at the surface of some magnetars with a typical $\sim 10^8$ Teslas Viganò et al. (2015), could generate extremely large electric-potential gaps along the open magnetic-field lines (see e.g. Arons (2009) for a review) which in turn accelerate charged particles to energies only limited by radiation reaction. It is believed that these magnetospheres are mostly filled with electrons and positrons resulting from a cascade of pair creations : pairs are created by quantum-electrodynamics processes involving gamma rays, and in turn radiate their kinetic energy in gamma-rays that make other pairs. The process of radiation is that of an accelerated charge that inspirals around a curved magnetic field. Because the magnetic field $\vec{B}$ is so intense, radiation reaction quickly forces the particle to follow very closely the field line. It follows that electrons and positrons are believed to radiate mostly because of their motion along the curved field line rather than perpendicular to it. Such motion and radiation are described either by the synchro-curvature regime or the curvature regime (Ruderman & Sutherland 1975), depending on whether the residual perpendicular motion is taken into account or neglected.

We show in section 2 the treatment of curvature radiation within the framework of classical electrodynamics and we demonstrate in section 3 that in neutron-star magnetospheres it quickly leads to apply the classical theory when momentum is already significantly quantized. In section 4 we give an outline of the theory of quantum curvature radiation.

## 2 Consistency of the theory of curvature radiation

In the ultra-relativistic regime, the classical treatment of curvature radiation is fundamentally the same as that of the synchrotron radiation (Jackson 1998). In the extreme environments surrounding pulsars and magnetars we are interested in, the ultra-relativistic approximation is always appropriate. There are mostly two reasons to this similarity. First in the ultra-relativistic regime the beam of emitted light is very collimated with a typical angle $\sim 1/\gamma$ where $\gamma \gg 1$ is the relativistic Lorentz factor. It follows that the light finally catched by an observer

[1] LUTh, Observatoire de Paris, PSL Research University, 5 place Jules Janssen, 92190 Meudon
[2] LUTh, Observatoire de Paris, PSL Research University - CNRS, 5 place Jules Janssen, 92190 Meudon

was necessarily emitted on a very small portion of the trajectory, which in turn needs only be locally circular. The second reason is the neglecting of radiation back-reaction on the motion of the particle, that allows to treat motion and radiation in a completely separated way. Therefore, the fact that the path be curved because of a magnetic field or any other source does not matter. Finally, classical synchrotron radiation appears as a particular case of curvature radiation.

In the context of pulsar magnetospheres, the path followed by electrons and positrons is assumed to be a magnetic-field line, to which one can add the $\vec{E}\times\vec{B}/B^2$ drift, where $\vec{E}$ is the electric field, $\vec{B}$ the magnetic field. This motion is not physical, since it does not follow the usual helicoidal solution of the motion of a charged particle in a magnetic field. In the case of a particle following a magnetic-field line, the Lorentz force $\vec{v}\times\vec{B}$ is the only force acting on the particle and is exactly zero. Therefore, a charged particle cannot follow a magnetic-field line without turning, even slightly, around the field.

However, one assumes such a path as a result of the extreme radiation reaction undergone by a charged particle. Let's take a few numbers that we will consider typical of a pulsar polar cap gap. We consider an accelerating electric field of intensity $E$, assumed collinear to the magnetic field of intensity $B$. Close to the neutron star surface, a dipolar magnetic field locally has a radius of curvature $\rho$ of the order of magnitude of the neutron star radius. Assuming the electric field is given by a force-free condition around a star rotating at $\Omega_*$ (see e.g. (Arons 2009)) one has

$$\rho \sim 10^4\mathrm{m}, \Omega_* \sim 1\mathrm{s}, B \sim 10^8\mathrm{Teslas}, E = \Omega_* R_* B \sim 10^{12}\mathrm{V/m}. \tag{2.1}$$

In these conditions, an electron or a positron accelerates almost instantaneously, that is on a length scale much shorter than the size of the gap, until radiation reaction balances the electric field. If one assumes that losses are only due to curvature radiation then the radiated power is $\propto \Omega_c^2\gamma^4$, with $\Omega_c = c/\rho$ the pulsation of an imaginary circular trajectory of radius $\rho$ traveled at the speed of light $c$, the equilibrium Lorentz factor is (Viganò et al. 2014)

$$\gamma_{\max} = \left(\frac{3}{2}\frac{4\pi\epsilon_0 E\rho}{e}\right) \sim 2\cdot 10^7 E_{12}^{1/4}\rho_4^{1/4}, \tag{2.2}$$

with $-e$ the charge of the electron and $\epsilon_0$ the vacuum electric permittivity (in international system units), and we use the notation $X_n = 10^{-n}X$. If the particle bears an initial momentum perpendicular to the magnetic field, it can only be small compared to the longitudinal momentum, because in the opposite case the dominant losses are from synchrotron which follows the same scaling law but with a pulsation $\Omega_s$ much larger than the curvature pulsation $\Omega_c$

$$\Omega_s = \frac{eB}{\gamma m} \sim 10^{12} B_8\gamma_7^{-1} \gg \Omega_c \sim 10^4\rho_4^{-1}, \tag{2.3}$$

resulting in a dissipation $10^{16}B_8^2\gamma_7^{-2}\rho_4^{-2}$ times more efficient for the same Lorentz factor. That is why an electron or positron cannot have a perpendicular momentum even comparable to its longitudinal momentum. This is the justification of curvature radiation, that assumes that all perpendicular momentum is dissipated.

However, a small perpendicular component must remain. It suggests to compute the radiation of a particle following an helix in the approximation of a small pitch-angle $\alpha$, approximation usually called synchro-curvature radiation (see e.g. Cheng & Zhang (1996), Harko & Cheng (2002), Viganò et al. (2014) or Kelner et al. (2015)). One understands that curvature radiation, however based on an unphysical path, is the natural mathematical limit when $\alpha \to 0$ of synchro-curvature radiation. If one assumes that thanks to relativistic beaming the radiation-reaction force is directed in the exact opposite direction to the velocity of the particle and that radiation-reaction balances the electric field, one can quickly obtain the evolution of the pitch-angle of the particle (See e.g. Viganò et al. (2014) )

$$\sin\alpha = \sin\alpha_0 \exp\left(-\frac{t}{\tau_\alpha}\right) \tag{2.4}$$

where $\alpha_0$ is the initial pitch angle and

$$\tau_\alpha = \frac{\gamma_{\max} mc}{eE} \sim 2\cdot 10^{-8}\gamma_{\max 7}E_{12}^{-1}\mathrm{s} \tag{2.5}$$

is the characteristic decay time.

As a consequence, the classical theory predicts an arbitrary decay of the pitch angle on very short distances.

## 3 Limit of the classical theory

The quantum theory of a relativistic electron in an uniform magnetic field was derived by several authors (Huff (1931), Johnson & Lippmann (1949), Melrose & Parle (1983), Sokolov & Ternov (1968)) . It is applicable to all spin 1/2 particles. However we consider an electron to simplify the presentation. The electron is characterized by the quantified angular momentum around the magnetic field, quantified momentum parallel to the field and two possible spin orientations. The energy of the particle is the sum of the squared perpendicular and longitudinal momenta plus the squared rest mass energy

$$E = \sqrt{m^2c^4 + \underbrace{\hbar\omega_c mc^2 n}_{\text{Perpendicular momentum}} + \underbrace{(cp_\parallel)^2}_{\text{Parallel momentum}}} \tag{3.1}$$

where $n$ is an integer quantifying the perpendicular momentum, $\omega_c = eB/m$ is the cyclotron pulsation and $p_\parallel$ the parallel momentum. The two spin orientations are degenerate with respect to the energy. In quantum theory, the levels are quantified by the number $n$. They are sometimes referred to as Landau levels; we call them perpendicular levels. Transitions between perpendicular levels are at the origin of synchrotron radiation.

The classical limit of a quantum theory means, in particular, that the quantized step of a given quantity is negligible compared the value of this quantity. In the case of perpendicular momentum it means that $1/\sqrt{n} \ll 1$. The step $\sqrt{\hbar\omega_c mc}$ increases with the magnetic-field intensity. Transitions between perpendicular levels then become quasi-continuous, and one finds the classical limit of synchrotron radiation.

The decay of pitch-angle calculated in the previous section corresponds in the quantum theory to the decay of $n$. If one extrapolates a little the theory in a uniform field to a curved magnetic field, one understands that the limit of curvature radiation then corresponds to $n = 0$. This means a regime in which perpendicular momentum cannot be treated classically. But is this regime ever reached ? For an ultra-relativistic particle most of the energy is in the longitudinal term $cp_\parallel \sim \gamma mc^2$, and one can estimate the pitch angle of the first perpendicular state as

$$\alpha_1 \simeq \frac{1}{\gamma}\sqrt{\frac{\hbar\omega_c}{mc^2}} \sim 10^{-8} B_8^{1/2} \gamma_7^{-1}. \tag{3.2}$$

Equation 2.5 implies that this pitch angle would be reached in barely 10 meters if the classical theory is correct. However, as we have seen, we are out of the domain of validity of the classical theory.

## 4 Sketch of a quantum theory

Here we intend to outline the main physical ideas behind a quantum theory of curvature radiation. Detailed calculations and results, including spectra, will be detailed in two upcoming papers (in preparation) and to some extent in Voisin et al. (2016, in press).

The first interesting point, from a qualitative point of view, is that it is possible to make synchrotron-like radiation within the quantum formalism in a way that is relatively independent of the physical ingredients (or classically "forces") that cause the motion, or here the wave function. An - even locally - circular path translates in the vocabulary of quantum mechanics in rotation invariance around the axis of the circle. Therefore, our wave-function must be a proper state of the angular momentum operator around this axis, as it is also the generator of rotations (see e.g. Le Bellac (2003)). Of course, if this is our only requirement. We impose the corresponding arbitrary Hamiltonian $\hat{H}$ which in this case is merely proportional to the angular momentum operator $\hat{J}$,

$$\hat{H} = \Omega\hat{J} \tag{4.1}$$

, where for curvature radiation in the utlra-relativistic limit, $\Omega = \Omega_c = c/\rho$. Proper values are then given by $E = \hbar\Omega l$ where $l$ is a half-integer. This kind of Hamiltonian is found as a limit when the perpendicular term dominates in equation 3.1, for example. One last thing is that our theory can only be one-dimensional since our wave-function is cylindrically symmetric but extends to infinity in space. The one dimension can be parametrized by the angle around the axis of the cylinder. Applying a first-order perturbation theory, sometimes called Fermi golden rule, to our Hamiltonian with the usual interaction Hamiltonian of quantum electrodynamics one finds transitions between proper wave-functions that are identical to the classical curvature radiation of pulsation $\Omega$, up to a prefactor due to the lack of relevant 3-dimensional confinement.

Our theory therefore needs to implement two rotation invariances, one around the axis of the main circular trajectory, and locally around the tangent to this trajectory. Although not intuitive, the two corresponding rotation operators commute with each other allowing an independent treatment. We need a magnetic field to confine the particle on such a trajectory, a possible choice is a field with concentric field lines around the main axis. As known from the uniform-field theory the characteristic confinement length around the magnetic field is given by $\lambda = \left(\frac{2\hbar}{eB}\right)^{1/2}$. In the case of pulsar fields, this length is very small compared to the radius of curvature allowing to expand equations in a small parameter

$$\epsilon = \frac{\lambda}{\rho} \sim 10^{-16} B_8^{-1/2} \rho_4^{-1} \tag{4.2}$$

. At zeroth order, the two previous rotation operators commute with the Hamiltonian and are therefore observables. We need no more. Thus we can separate the two rotations in our physical model. The proper energies are

$$E = \sqrt{m^2c^4 + \underbrace{\hbar\omega_c mc^2 n}_{\text{Perpendicular momentum}} + \underbrace{(\hbar\Omega l)^2}_{\text{Parallel momentum}}}, \tag{4.3}$$

where the only difference with 3.1, quite satisfactorily, is that the parallel momentum is now replaced by the angular momentum around the main axis. $\Omega$ and $l$ are defined as in the toy model of the previous paragraph. One remarks that when motion parallel to the field dominates, this term dominates the energy and we find the same expression as in our toy model at main order.

Classical curvature radiation is recovered in this model by computing transitions between states with $n = 0$ in the ultra-relativistic limit $l \gg 1, \hbar\Omega l \gg mc^2$. The photon energy is taken from a variation of $l$. In this class of states the particle as close as possible to the field line, with a spreading of only $\sim \lambda$. Additionally one shows that these states correspond to a null orbital angular momentum. What was unphysical in the classical theory becomes possible in quantum mechanics. However, there is a trick : the spin of this perpendical "fundamental" state is oriented backward the magnetic field giving a negative total angular momentum of $-1/2\hbar$. Thus, the particle holds on the magnetic field due to the interaction between its spin and the field.

It is interesting to generalize a little the definition of curvature radiation to incorporate different spin orientations. As a result of spin-orbit coupling, this can only be done by taking into account transitions to the first excited perpendicular states. This can be considered a first step towards quantum synchro-curvature radiation or spin-flip curvature radiation. It proves to be not negligible in typical pulsar, young pulsar and potentially magnetar environments.

## 5 Conclusions

An electron in a typical pulsar or magnetar magnetosphere falls very quickly in the synchro-curvature low-pitch-angle regime due to radiation reaction on the particle. Curvature radiation is the natural mathematical and physical limit of synchro-curvature radiation within classical electrodynamics. However, in these very high magnetic fields the momentum perpendicular to the magnetic field very quickly becomes comparable to its quantization step. A quantum theory of the motion of an electron in a curved magnetic field can be devised as a generalization of the existing theory in a uniform magnetic field. In this case, classical curvature radiation survives in a more consistent way, since states with null orbital momentum become physical, thanks to spin-magnetic-field interaction. If one allows spin-flip to happen then new transitions appear that can be not negligible in neutron-star environments.

## References


Arons, J. 2009, in Neutron Stars and Pulsars, ed. W. Becker, Astrophysics and Space Science Library No. 357 (Springer Berlin Heidelberg), 373–420

Cheng, K. S. & Zhang, J. L. 1996, The Astrophysical Journal, 463, 271

Harko, T. & Cheng, K. S. 2002, Monthly Notices of the Royal Astronomical Society, 335, 99

Hewish, A., Bell, S. J., Pilkington, J. D. H., Scott, P. F., & Collins, R. A. 1968, Nature, 217, 709

Huff, L. D. 1931, Physical Review, 38, 501

Jackson, J. D. 1998, Classical Electrodynamics, 3rd Edition

Johnson, M. H. & Lippmann, B. A. 1949, Physical Review, 76, 828

Kelner, S. R., Prosekin, A. Y., & Aharonian, F. A. 2015, The Astronomical Journal, 149, 33, arXiv: 1501.04994

Le Bellac, M. 2003, Physique quantique (Les Ulis; Paris: EDP Sciences)

Melrose, D. B. & Parle, A. J. 1983, Australian Journal of Physics, 36, 755

Ruderman, M. A. & Sutherland, P. G. 1975, The Astrophysical Journal, 196, 51

Sokolov, A. A. & Ternov, I. M. 1968, Synchrotron Radiation (Akademie-Verlag)

Viganò, D., Pons, J. A., Miralles, J. A., & Rea, N. 2015, eprint: arXiv:1501.06735, 90–101

Viganò, D., Torres, D. F., Hirotani, K., & Pessah, M. E. 2014, Monthly Notices of the Royal Astronomical Society, 447, 1164

Voisin, G., Bonazzola, S., & Mottez, F. 2016, in press, in AIP Conference Proceedings (AIP Publishing)

*SF2A 2016*
*C. Reylé, J. Richard, L. Cambrésy, M. Deleuil, E. Pécontal, L. Tresse and I. Vaughlin (eds)*

# MODELS OF MAGNETIZED WHITE DWARFS

M. Oertel[1], D. Chatterjee[1,2], A.F. Fantina[3], N. Chamel[4] and J. Novak[1]

**Abstract.** To explain observations of overluminous Type Ia supernovae, strongly magnetized white dwarfs with masses above $2M_\odot$ have been proposed as their progenitors. This has interesting implications in high-precision cosmology, as Type Ia supernovae have been widely used as standard candles. We compute equilibrium configurations of magnetized white dwarfs, self-consistently determining the structure of a compact object in strong (poloidal) magnetic fields. Our results show that, although the magnetic field can support indeed these massive configurations, they might never be reached in nature since electron capture destabilizes the star already at lower masses. Hence strongly magnetized white dwarfs are unlikely to be the progenitors of overluminous supernovae.

Keywords: stars:white dwarf, magnetic fields, equation of state, methods:numerical

## 1 Introduction

White dwarfs (WDs) are the progenitors of type Ia supernovae (SNIa), which have been used as "standard candles" to measure cosmological distances assuming a unique astrophysical scenario for these events, the thermonuclear explosion of a Chandrasekhar mass WD. The picture of SNIa has much diversified recently, in particular with the discovery of overluminous type Ia supernova (SNIa) (Howell et al. 2006). The progenitors of such events are thought to be "super-Chandrasekhar" WDs with a mass $> 2$ $M_\odot$ (see, e.g., Hillebrandt et al. 2013), resulting either from the merger of two massive WDs, from rapidly (differentially) rotating WDs (Howell et al. 2006), or from strongly magnetized WDs (Kundu & Mukhopadhyay 2012; Das & Mukhopadhyay 2012a).

Therefore it is of utmost importance to determine the structure of magnetized WDs and their maximum mass. Hundreds magnetized WDs have been observed, with surface fields of up to about $10^9$ G (Wickramasinghe & Ferrario 2000). The internal field, not directly observable, might be stronger and have a non negligible influence on the structure of the star. The study of the mass-radius relation of a magnetized WD has a long history and it was recognized early on that the impact of the magnetic field on both its radius and mass could be large. However, simplifying assumptions have been made for convenience. For instance, the pioneering work by Ostriker & Hartwick (1968) considers a vanishing magnetic field at the surface of the star and neglects any magnetic field effect on the euqation of state (EoS) as well as general relativistic (GR) effects and electrostatic interactions. The works of Adam (1986), Das & Mukhopadhyay (2012a), and Kundu & Mukhopadhyay (2012) focus on the effect of the magnetic field on the EoS, including the Landau quantization of the electron gas, but use a Newtonian description of the star's structure in spherical symmetry, i.e. neglecting the deformation of the star by the magnetic field. A similar approach is followed in Suh & Mathews (2000), where, however, the general relativistic (spherical) Tolman-Oppenheimer-Volkoff (TOV) equations are applied to solve for the star's structure. Recent attempts for more realistic WD models include equilibrium configurations in Newtonian framework (Bera & Bhattacharya 2014). Further, Das & Mukhopadhyay (2015a) and Bera & Bhattacharya (2015) computed the mass-radius relation of magnetic WDs for different field geometries in GR.

What all these works have in common is that for strongly magnetized WDs, masses are obtained well above the original Chandrasekhar limit, that are able to explain the overluminous SNIa. However, microscopic

[1] LUTH, Observatoire de Paris, PSL Research University, CNRS, Université Paris Diderot, Sorbonne Paris Cité,5 place Jules Janssen, 92195 Meudon, France
[2] Laboratoire de Physique Corpusculaire, ENSICAEN, 6 Boulevard Maréchal Juin, 14050 Caen Cédex, France
[3] Grand Accélérateur National d'Ions Lourds (GANIL), CEA/DRF - CNRS/IN2P3, Bvd Henri Becquerel, 14076 Caen, France
[4] Institut d'Astronomie et d'Astrophysique, CP-226, Université Libre de Bruxelles (ULB), 1050 Brussels, Belgium

processes like electron captures or pycno-nuclear reactions might induce instabilities and effectively limit the maximum mass (Chamel et al. 2013). Within this work we address these stability issues in a completely self-consistent setup: we solve combined Einstein+Maxwell equations including magnetic field effects in the EoS.

## 2 Model setup

### 2.1 Equation of state

Our EoS follows the model developed in Lai & Shapiro (1991); Chamel et al. (2012), originally for the crust of strongly magnetized neutron stars. The interior of magnetized WDs is assumed to be composed of fully ionized atoms. Moreover, we assume that the internal temperature has dropped below the crystallization temperature so that ions are arranged on a regular crystal lattice and that we can neglect thermal effects. For simplicity, we shall consider crystalline structures made of only one type of ions ${}^A_Z X$, with mass number $A$ and atomic number $Z$ (${}^{12}$C or ${}^{16}$O). The EoS receives thus three contributions: from nuclear masses, from the relativistic Fermi gas of electrons and from the crystalline lattice, i.e. electron-ion interactions.

As in Lai & Shapiro (1991); Chamel et al. (2012), we neglect the change of nuclear masses in the presence of a strong magnetic field and take experimental masses (Audi et al. 2012). The lattice energy, evaluated for point-like ions arranged in a body-centered-cubic (bcc) lattice, is independent of the magnetic field. Magnetic field effects are thus considered only on the dense Coulomb plasma, i.e. Landau quantization of the electron gas is taken into account, see Chatterjee et al. (2016) for more details and explicit expressions. As an example, the EoS for a ${}^{12}$C WD is shown in Fig. 1 for different magnetic fields strengths. De Haas-van Alphen oscillations are clearly visible for field strengths roughly above the critical field $b_{\rm crit} = \frac{m_e^2 c^3}{e\hbar} \approx 4.4 \times 10^{13}$ G. $m_e$ denotes here the electron mass and $e$ its charge, $c$ the speed of light and $\hbar$ the reduced Planck constant.

At some mass density $\rho_\beta$ (or equivalently at some corresponding pressure $P_\beta$), the nucleus ${}^A_Z X$ becomes unstable against the capture of an electron with the emission of a neutrino :

$$ {}^A_Z X + e^- \rightarrow {}^A_{Z-1} Y + \nu_e \, . \tag{2.1} $$

The daughter nucleus ${}^A_{Z-1} Y$ itself may be unstable. As electrons combine with nuclei, further compression of matter does not increase the pressure, thus leading to a global instability of the star. In the absence of magnetic fields, the onset of electron captures occur at mass density $\rho_\beta \simeq 4.16 \times 10^{10}$ g cm$^{-3}$ (pressure $P_\beta \simeq 6.99 \times 10^{28}$ dyn cm$^{-2}$) for ${}^{12}$C and $\rho_\beta \simeq 2.06 \times 10^{10}$ g cm$^{-3}$ ($P_\beta \simeq 2.73 \times 10^{28}$ dyn cm$^{-2}$) for ${}^{16}$O. In the presence of a strong magnetic field, the threshold density and pressure are shifted to either higher or lower values depending on the magnetic field strength Chamel & Fantina (2015).

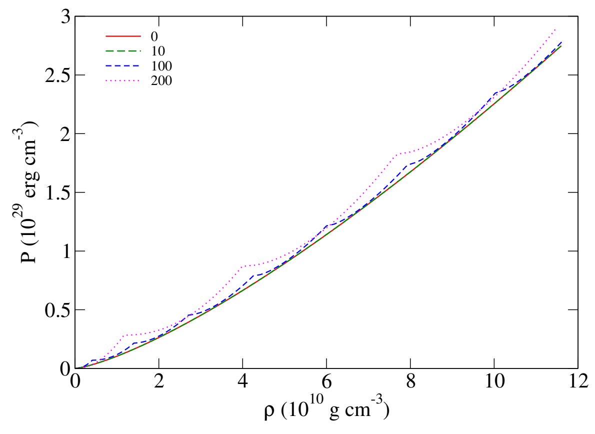


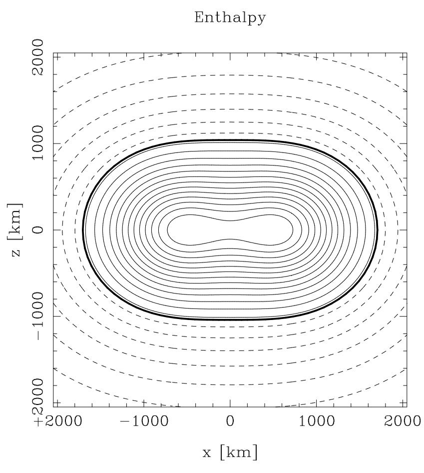


**Fig. 1. Left**: EoS (pressure $P$ vs mass density $\rho$) for a ${}^{12}$C WD, for different magnetic field strengths $b_\star = b/b_{\rm crit}$.**Right**:Enthalpy isocontours of a relativistic ${}^{12}$C WD for $\mathcal{D} = 3{\times}10^{34}$ A m$^2$ resulting in a polar field of $B_p \sim 3{\times}10^{13}$ G.

### 2.2 Stellar structure equations

We compute the WD structure numerically assuming stationarity, axisymmetry, circularity and matter being a perfect conductor. The latter assumption implies that the electric field vanishes in the fluid rest frame.

Magnetostatic equilibrium equations are then solved combined with Maxwell equations for the electromagnetic field and gravity equations, either general relativistic or Newtonian, using the LORENE* numerical library. The magnetic field is purely poloidal by construction (Bocquet et al. 1995), which is not necessarily the most general one, but allows for an easy comparison with observed polar fields. In contrast to other works, our code allows to consistently include the magnetic field effects on the EoS in the structure equations, derived in a coherent way from the energy momentum tensor in presence of an electromagnetic field (Chatterjee et al. 2015). Note in particular that the equations for equilibrium do not contain any contribution from the magnetization. They thus differ from those given in Bera & Bhattacharya (2014), where the magnetization has been artificially included. More details can be found in a forthcoming publication (Chatterjee et al. 2016).

In Fig. 1, as an example of a stellar configuration we show the enthalpy isocontours of a non-rotating $^{12}$C WD, taking a magnetic dipole moment, $\mathcal{D}$ of $3 \times 10^{34}$ A m$^2$. This corresponds to a polar field strength of about $B_p \sim 3 \times 10^{13}$ G. The thick line indicates the stellar surface. The star's deformation due to the magnetic field is clearly visible. It is obvious that the star cannot be treated in spherical symmetry. Increasing further $\mathcal{D}$ (and thus the magnetic field), at some point the density at the center of the star vanishes and the star takes a toroidal shape (Cardall et al. 2001). This is not really a physical instability, although hardly imaginable astrophysically, but it cannot be treated by our code since a nonzero density is assumed at the center. We stop our calculations therefore at the maximally distorted configurations, before the star becomes toroidal.

## 3 Results and discussion

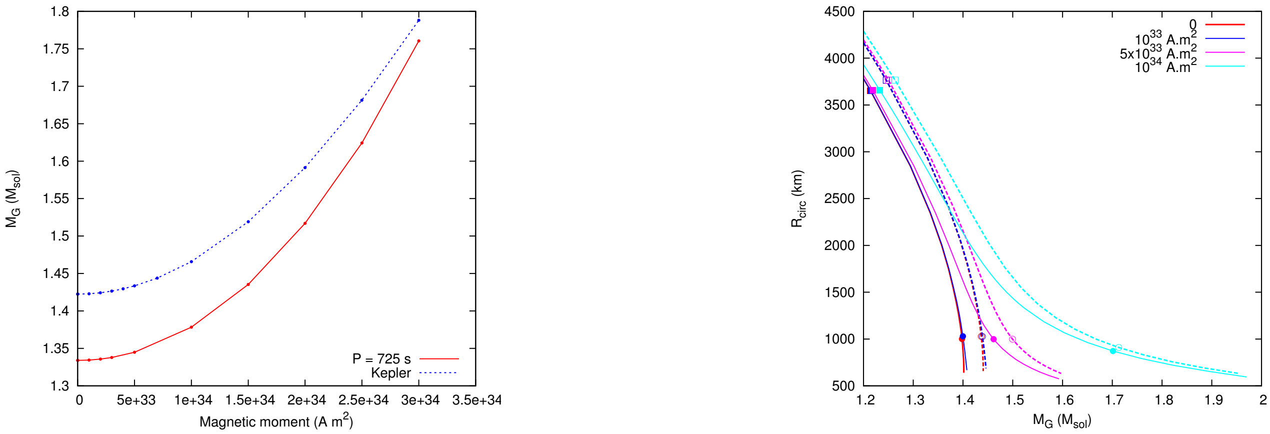


**Fig. 2. Left**: Mass for Newtonian magnetized $^{16}$O WDs rotating at a period of 725 s (solid line) and at Kepler frequency (dashed line) for different values of $\mathcal{D}$. The central density has been chosen such that the mass of the non-rotating, non-magnetized WD is 1.34 $M_\odot$. **Right**: Mass vs radius for Newtonian $^{16}$O WDs for different values of $\mathcal{D}$ with (solid lines) and without (dashed lines) lattice effects. The filled and empty dots mark the onset of electron capture on $^{16}$O with and without lattice effects, respectively, whereas the squares indicate a lower limit for the onset of pycno-nuclear reactions.

Qualitatively the results for equilibrium $^{12}$C and $^{16}$O WDs are very similar and for most quantities the numerical values differ only slightly. Note that we do not consider sequences at fixed magnetic field strength, as in other works, e.g. in Bera & Bhattacharya (2014), since they would suggest artificially a gravitational instability, which disappears if the relevant quantity, $\mathcal{D}$, is kept constant throughout the sequences, see Chatterjee et al. (2016).

In Fig. 2 (right) the mass-radius relation for $^{16}$O WDs is displayed for sequences –varying central density– at different values of $\mathcal{D}$. For the magnetized sequences, the curves end at the corresponding maximally distorted configuration. For even higher values of $\mathcal{D}$, the maximally distorted configuration is reached at approximately the same mass as for $10^{34}$ A m$^2$. Thus, in principle WDs with masses of the order $2M_\odot$ could exist. Accepting toroidal shapes, even higher masses could be reached. In addition, we consider here purely poloidal magnetic fields, which are known to be unstable on long time scales. Therefore a mixed poloidal-toroidal configuration

*http://www.lorene.obspm.fr

would be more realistic, which could again slightly increase the mass. Keep in mind, however, that the magnetic fields for the most massive configurations are orders of magnitude above currently observed values. And, as discussed below, electron capture (EC) and pycno-nuclear reactions might effectively be the main limiting factor.

### 3.1 Influence of different modelling parameters

**Magnetic field dependence of the EoS** : As mentioned in Sec. 2.1 and shown in Fig. 1 (left), the magnetic field dependence of the EoS starts to play a role for field values above roughly $10^{13}$G. Even accepting that polar fields might be orders of magnitude above the currently observed values, such high magnetic fields can be hardly reached inside a WD with a poloidal field structure before the maximally distorted configuration, i.e. before the star takes a toroidal shape. Therefore the influence of the magnetic field dependence of the EoS on the results remains very small.

**Lattice effects within the EoS** : The electrostatic interaction between electrons and ions introduced by Hamada & Salpeter (1961) was found to lower the electron pressure resulting in a softer EoS and hence leads to slightly less massive configurations. We confirm this result. As can be seen from Fig. 2 (right), where results including lattice effects are shown as plain lines and those without as dashed lines, the effect on the radius can, however, be huge. The difference might be as large as factor of 2.

**General relativity** : It is well known that general relativity reduces the maximum mass of non-magnetic WDs by a few percent (see, e.g., Ibáñez 1984). For strongly magnetized WDs the difference between Newtonian and relativistic WDs becomes even smaller since magnetic energy increases and the deformation of the star renders it less compact, leading to less important relativistic effects.

**(Uniform) rotation** : In Fig. 2 (left) we display the masses of uniformly rotating magnetized WDs as function of $\mathcal{D}$. The period of 725 s has been chosen at the lower end of observed values (Ferrario et al. 2015). It is obvious that uniform rotation cannot considerably increase the mass, but that the main effect increasing the mass results from the magnetic field. Even a rotation at mass-shedding limit (Kepler frequency) cannot shift the mass to about $2M_{\odot}$ without magnetic field.

### 3.2 Instabilities induced by EC and pycno-nuclear reactions

The dots on the curves in Fig. 2 (right) mark the onset of EC reactions inside the star, i.e. more massive configurations become unstable. It is obvious that is it thus very improbable that the maximally distorted configuration is ever reached. The situation becomes worse if pycno-nuclear reactions are considered, see the squares in Fig. 2. Since the rates for pycno-nuclear reactions are very uncertain, the squares, however, represent only an estimate of the lower limit for the onset of these type of reactions. We show here results for $^{16}$O, but it should be kept in mind, that threshold densities for the onset of EC and pycno-nuclear reactions are lower for $^{16}$O than for carbon, such that the value of the maximum mass is lower for $^{16}$O WDs than for $^{12}$C ones. But, in most cases the maximally distorted configuration is not reached for $^{12}$C WDs, neither.

We conclude that although the magnetic field in principle allows to support very massive WDs with masses of the order $2M_{\odot}$ or even slightly above, they might never exist as stable objects and are thus unprobable to be the progenitors of overluminous SNIa.

This work has been funded by the SN2NS project ANR-10-BLAN-0503, the “Gravitation et physique fondamentale” action of the Observatoire de Paris, Fonds de la Recherche Scientifique - FNRS (Belgium) and the COST action MP1304 “NewCompstar”.

## References

Adam D., 1986, A&A, 160, 95

Audi G., Wang M., Wapstra A. H., Kondev F. G., MacCormick M., Xu X., Pfeiffer B., 2012, Chin. Phys. C, 36, 1287

Bera P., Bhattacharya D., 2014, MNRAS, 445, 3951

Bera P., Bhattacharya D., 2016, MNRAS, 456, 3375

Bocquet M., Bonazzola S., Gourgoulhon E., Novak J., 1995, A&A, 301, 757

Cardall C. Y., Prakash M., Lattimer J. M., 2001, ApJ, 554, 322

Chamel N. et al., 2012, Phys.Rev. C, 86, 055804
Chamel N., Fantina A. F., Davis P. J., 2013, Phys. Rev. D, 88, 081301
Chamel N., Fantina A. F., 2015, Phys. Rev. D, 92, 023008
Chatterjee D., Elghozi T., Novak J., Oertel M., 2015, MNRAS, 447, 3785
Chatterjee D., Fantina A., Chamel N., Novak J., Oertel M., 2016, submitted to MNRAS.
Das U., Mukhopadhyay B., 2012a, Phys. Rev. D, 86, 042001
Das U., Mukhopadhyay B., 2015, JCAP, 5, 16
Ferrario L., de Martino D., Gänsicke B. T., 2015, Space Sci. Rev., 191, 111
Hamada T., Salpeter E. E., 1961, ApJ, 134, 683
Hillebrandt W., Kromer M., Röpke F. K., Ruiter A. J., 2013, Front. Phys., 8, 116
Howell D. A. et al., 2006, Nature (London), 443, 308
Ibáñez Cabanell J. M., 1984, A&A, 135, 382
Kundu A., Mukhopadhyay B., Mod. Phys. Lett. A, 27, 1250084
Lai D., Shapiro S. L., 1991, ApJ, 383, 745
Ostriker J. P., Hartwick F. D. A., 1968, ApJ, 153, 797
Suh I.-S., Mathews. G. J., 2000, ApJ, 530, 949
Wickramasinghe D. T., Ferrario L., 2000, Publ. Astron. Soc. Pac., 112, 873

*SF2A 2016*
*C. Reylé, J. Richard, L. Cambrésy, M. Deleuil, E. Pécontal, L. Tresse and I. Vauglin (eds)*

# UNDERSTANDING ACTIVE GALACTIC NUCLEI USING NEAR-INFRARED HIGH ANGULAR RESOLUTION POLARIMETRY I : MontAGN - STOKES COMPARISON

L. Grosset[1], F. Marin[2], D. Gratadour[1], R. Goosmann[2], D. Rouan[1], Y. Clénet[1], D. Pelat[3] and P. A. Rojas Lobos[2]

**Abstract.** In this first research note of a series of two, we present a comparison between two Monte Carlo radiative transfer codes: MontAGN and STOKES. Both were developed in order to better understand the observed polarisation of Active Galactic Nuclei (AGN). Our final aim is to use these radiative transfer codes to simulate the polarisation maps of a prototypical type-2 radio-quiet AGN on a wide range of wavelengths, from the infrared band with MontAGN to the X-ray energies with STOKES. Doing so, we aim to analyse in depth the recent SPHERE/IRDIS polarimetric observations conducted on NGC 1068. In order to validate the codes and obtain preliminary results, we set for both codes a common and simple AGN model, and compared their polaro-imaging results.

Keywords: galaxies: active, galaxies: Seyfert, radiative transfer, techniques: polarimetric, techniques: high angular resolution

## 1 Introduction

Polarimetry is a powerful tool as it gives access to more information than spectroscopy or imaging alone, especially about scattering. In particular, indications on the geometry of the distribution of scatterers, the orientation of the magnetic field or the physical conditions can be revealed thanks to two additional parameters: the polarisation degree and the polarisation position angle. Polarimetry can put constraints on the properties of scatterers, like for example spherical grains or oblate grains (Lopez-Rodriguez et al. 2015) and therefore constrain the magnetic field orientation and optical depth of the medium. The downside is that analysis of polarimetric data is not straightforward. The use of numerical simulations and especially radiative transfer codes is a strong help to understand such data (see for instance Bastien & Menard 1990; Murakawa et al. 2010; Goosmann & Matt 2011). It allows us to assess and verify interpretations by producing polarisation spectra/maps for a given structure, which can then be compared to observations.

STOKES and MontAGN are two numerical simulations of radiative transfer both using a Monte Carlo method built to study polarised light travelling through dusty environments (whether stellar or galactic). In both cases, one of the main goal in developing such codes was to investigate the polarisation in discs or tori around the central engine of AGN. While STOKES was designed to work at high energies, from near infrared (NIR) to X rays, MontAGN is optimised for longer wavelength, typically above 1 $\mu$m. Therefore they are covering a large spectral scale with a common band around $0.8 - 1$ $\mu$m. Both approaches are quite different since STOKES is a geometry-based code using defined constant dust (or electrons, atoms, ions ...) three-dimensional structures while MontAGN uses a Cartesian 3D grid sampling describing dust densities.

In this first research note, we want to present our first comparison between the two codes. We opted for a similar toy model that we implemented in the two simulation tools in order to produce polarisation maps to be compared one to each other. The second proceedings of this series of two will focus on the results of the code when applied to a toy model of NGC 1068 (Marin et al. 2016a, hereafter Paper II).

[1] LESIA, Observatoire de Paris, PSL Research University, CNRS, Sorbonne Universités, UPMC Univ. Paris 06, Univ. Paris Diderot, Sorbonne Paris Cité, 5 place Jules Janssen, 92190 Meudon, France
[2] Observatoire Astronomique de Strasbourg, Université de Strasbourg, CNRS, UMR 7550, 11 rue de lUniversité, 67000 Strasbourg, France
[3] LUTh, Observatoire de Paris, CNRS, Université Paris Diderot, Sorbonne Paris Cité, 5 place Jules Janssen, 92190 Meudon, France

## 2 The radiative transfer Codes

### 2.1 *STOKES*

STOKES was initially developed by R. W. Goosmann and C. M. Gaskell in 2007 in order to understand how reprocessing could alter the optical and ultraviolet radiation of radio-quiet AGN (Goosmann & Gaskell 2007; Goosmann et al. 2007). The code was continuously upgraded to include an imaging routine, a more accurate random number generator and fragmentation (Marin et al. 2012, 2015), until eventually pushing the simulation tool to the X-ray domain (Goosmann & Matt 2011; Marin et al. 2016b). STOKES is a radiative transfer code using Mueller Matrices and Stokes vectors to propagate the polarisation information through emission, absorption and scattering. Photons are launched from a source (or a set of sources) and then propagate in the medium until they are eventually absorbed or they exit the simulation sphere. The optical depth is computed based on the geometry given as an input. At each encounter with a scatterer, the photon's absorption is randomly determined from the corresponding albedo; if it is absorbed, another photon is launched from the central source. In a scattering case, the new direction of propagation is determined using phase functions of the scatterer and the Stokes parameters are modified according to the deviation. For a detailed description of the code, see papers of the series (Goosmann & Gaskell 2007; Marin et al. 2012, 2015).

### 2.2 *MontAGN*

Following the observation of NGC 1068 in polarimetric mode at high angular resolution conducted by Gratadour et al. (2015), MontAGN (acronym for "Monte Carlo for Active Galactic Nuclei") was developed to study whether our assumptions on the torus geometry were able to reproduce the observed polarisation pattern through simulations in the NIR. MontAGN has many common points with STOKES. Since the two codes were not designed for the same purpose, the main differences originate from the effects that need to be included in the two wavelength domains, which differ between the infrared and the shorter wavelengths. STOKES includes Thomson scattering, not available in MontAGN, while MontAGN takes into account the re-emission by dust as well as temperature equilibrium adjustment at each absorption to keep the cells temperature up to date, not present in STOKES.

In MontAGN photons are launched in the form of frequency-independent photon packets. If absorption is enabled, when a photon packet is absorbed, it is immediately re-emitted at another wavelength, depending on the dust temperature in the cell. The cell temperature is changed to take into account this incoming energy. The re-emission depends on the difference between the new temperature of the cell and the old one to correct the previous photon emissions of the cell at the former temperature (following Bjorkman & Wood 2001). If re-emission is disabled, all photon packets are just scattered, but we apply the dust albedo as a factor to the energy of the packet to solely keep the non-absorbed fraction of photons (see Murakawa et al. 2010). This disabling allows us to get much more statistics at the end of the simulation as every photon is taken into account. But it also requires to have a lot of photons in each pixel at the end as we may obtain in one pixel only photons with weak probability of existence, a situation that is not representative of the actual pixel polarisation.

## 3 Simulation

We set up a model of dust distribution compatible with the two codes. At the centre of the model, a central, isotropic, point-like source is emitting unpolarised photons at a fixed wavelength (0.8, 0.9 and 1 $\mu$m, only images at 0.9 $\mu$m are shown in this publication). Around the central engine, is a flared dusty disk with radius ranging from 0.05 pc to 10 pc. It is filled with silicate grains and has an optical depth in the V-band of about 50 along the equatorial plane (see Fig. 1). Along the polar direction, a bi-conical, ionised wind with a 25° half-opening angle with respect to the polar axis flows from the central source up to 25 pc. The wind is filled with electrons in STOKES and silicate grains at much lower density in MontAGN*. The conical winds are optically thin ($\tau_V =$ 0.1). We added to these structures a cocoon of silicate grains surrounding the torus, from 10 pc to 25 pc, outside the wind region to account for a simplified interstellar medium in another model. More information about the models can be found in Paper II. Note that re-emission was disabled for MontAGN in these simulations.

*This difference in composition should not affect the polarisation results as the two corresponding phase functions are close, but the flux and polarised flux will be attenuated in the case of dust because of absorption. Thomson scattering should therefore be included in MontAGN to be more realistic.

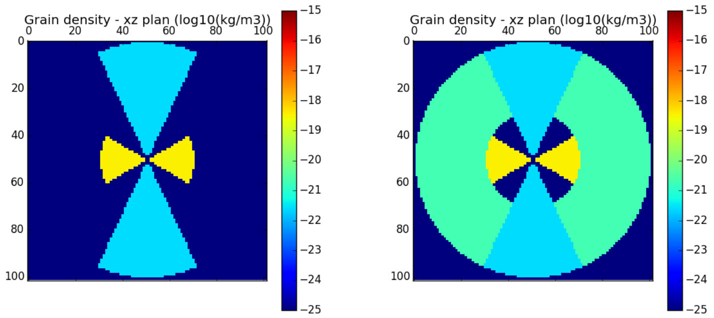


**Fig. 1.** Grain density (in kg/m$^3$) set for both models. Note that in STOKES the polar outflow is constituted of electrons, at a density allowing us to have the same optical depth **Left:** first model : "model I" **Right:** second model with the dust shell : "model II".

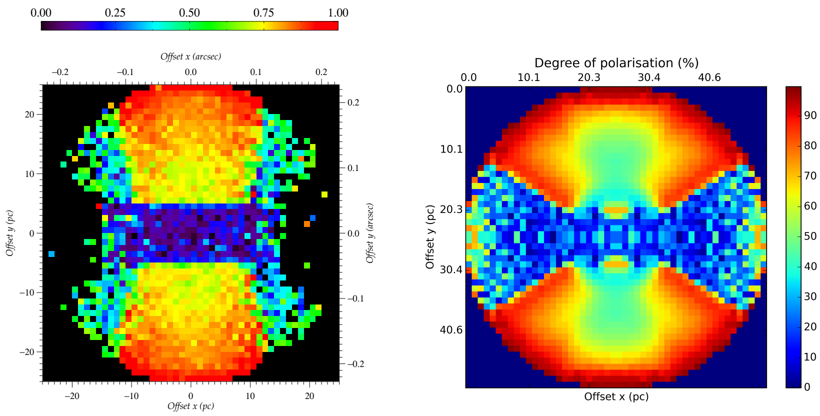


**Fig. 2.** Polarisation degree for model II at 0.9 $\mu$m **Left:** with STOKES **Right:** with MontAGN (in %)

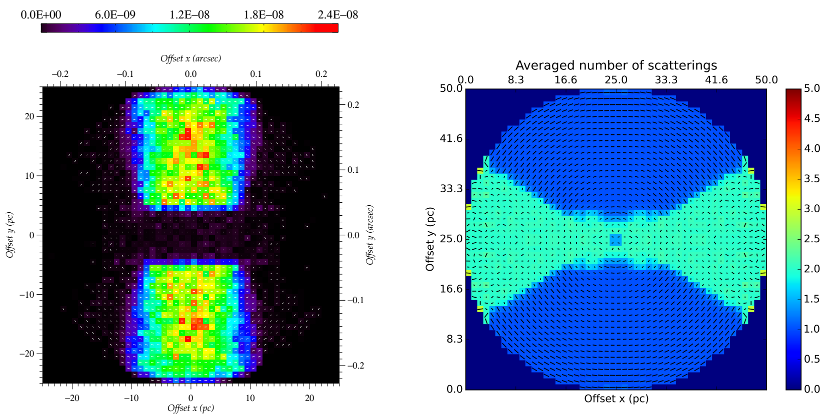


**Fig. 3.** At 0.9 $\mu$m **Left:** Polarised flux (in arbitrary units) with the polarisation position angle superimposed for model II with STOKES. **Right:** Averaged number of scatterings a photon undergo before exiting the medium with polarisation vectors superimposed for model II with MontAGN.

With more than $5{\times}10^6$ photons sampled, we obtain for both models an overall good agreement between the two codes. In the polar outflow region, the similarities are high between the two codes, revealing high polarisation degrees (close to 100%) despite the differences in composition (see Fig. 2). This is expected from single scattered light at an angle close to 90° (see Bastien & Menard 1990), which is confirmed from the maps of averaged number of scatterings (see Fig. 3, right). However in the central region, where the torus is blocking the observer's line-of-sight, the results between MontAGN and STOKES slightly differ (see the equatorial detection of polarisation at large distances from the centre in Fig. 2, right). We interpret this polarisation as arising from the differences in the absorption method between the two codes. Because in MontAGN all photons exit the simulation box, we always get some signal even if it may not be representative of photons reaching this peculiar pixel. If inside a pixel only photons with low probability, i.e. with the energy of their photon packets being low after multiple scatterings, are collected, the polarisation parameters reconstructed from these photons will not be reliable. This is why we need to collect an important number of photons per pixel.

Otherwise, the polarisation structure revealed by polaro-imaging is very similar between the two codes and lead to distinctive geometrical highlights that will be discussed in the second research note of this series (Paper II).

## 4 Concluding remarks

We compared the MontAGN and STOKES codes between 0.8 and 1 $\mu$m for similar distribution of matter and found that many of the polarimetric features expected from one code are reproduced by the second. The only difference so far resides on the detection of polarisation at large distances from the centre of the model, where we need a higher sampling in order for MontAGN to match STOKES results. The next step will be to improve the models, and develop the MontAGN code by including more effects like electron scattering or non spherical grains (ortho- and para-graphite, namely). However we already get a fairly good agreement between the codes which give us confidence to pursue our exploration of the near-infrared signal of AGN together with MontAGN and STOKES. Note that the comparison allowed to detect flaws and bugs, a positive outcome. We intend to explore our first results in Paper II and push the codes towards more complex geometries. Once a complete agreement will be found in the overlapping band (0.8 – 1 $\mu$m), we will run a large simulation ranging from the far-infrared to the hard X-rays for a number of selected radio-quiet AGN. Our targets include the seminal type-2 NGC 1068, as well as a couple of other nearby AGN with published polarimetric data. Forthcoming new infrared polarimetric observations using SPHERE will complement our database and be modelled with MontAGN and STOKES.

The authors would like to acknowledge financial support from the Programme National Hautes Energies (PNHE).

## References

Bastien, P. & Menard, F. 1990, ApJ, 364, 232

Bjorkman, J. E. & Wood, K. 2001, ApJ, 554, 615

Goosmann, R. W. & Gaskell, C. M. 2007, A&A, 465, 129

Goosmann, R. W., Gaskell, C. M., & Shoji, M. 2007, in IAU Symposium, Vol. 238, Black Holes from Stars to Galaxies – Across the Range of Masses, ed. V. Karas & G. Matt, 375–376

Goosmann, R. W. & Matt, G. 2011, MNRAS, 415, 3119

Gratadour, D., Rouan, D., Grosset, L., Boccaletti, A., & Clénet, Y. 2015, A&A, 581, L8

Lopez-Rodriguez, E., Packham, C., Jones, T. J., et al. 2015, MNRAS, 452, 1902

Marin, F., Goosmann, R. W., & Gaskell, C. M. 2015, A&A, 577, A66

Marin, F., Goosmann, R. W., Gaskell, C. M., Porquet, D., & Dovčiak, M. 2012, A&A, 548, A121

Marin, F., Goosmann, R. W., Grosset, L., et al. 2016a, in SF2A-2016: Proceedings of the Annual meeting of the French Society of Astronomy and Astrophysics, ed. L. Cambrésy, M. Deleuil, E. Pécontal, C. Reylé, M. Richard, L. Tresse, & I. Vauglin

Marin, F., Goosmann, R. W., & Petrucci, P.-O. 2016b, A&A, 591, A23

Murakawa, K., Ueta, T., & Meixner, M. 2010, A&A, 510, A30

*SF2A 2016*
*C. Reylé, J. Richard, L. Cambrésy, M. Deleuil, E. Pécontal, L. Tresse and I. Vauglin (eds)*

# FROM FERMI-LAT OBSERVATIONS TO THE BLIND PULSAR SURVEY SPAN512 WITH THE NANÇAY RADIO TELESCOPE

F. Octau[1], G. Desvignes[2], I. Cognard[1, 3], D. Champion[2], P. Lazarus[2], D. Smith[4] and G. Theureau[1,3, 5]

**Abstract.** Since the discovery of the first pulsar in 1967, we know over 2500 pulsars today. Pulsars offer a broad range of studies: from the study of the properties of interstellar medium and of pulsar magnetospheres up to test of gravity in the strong-field regime and the characterisation of the cosmological Gravitation Wave Background. This explains why we keep searching for pulsars nowadays. Such focus was initiated at the Nançay Radio Telescope (NRT) with the observation of unidentified Fermi-LAT sources, which led to the quick discovery of three new millisecond pulsars. In 2012, a blind pulsar survey called SPAN512 (in reference to the large bandwidth of 512 MHz) was initiated and the NRT began to observe the low galactic latitude sky at 1.4 GHz. This survey is still in progress ($\approx 90\%$ of the observations have been made) and, up to now, it has led to the discovery of three pulsars, two of them with millisecond spin periods.

Keywords: pulsar, radio telescope, survey, SPAN512

## 1 The Nançay Radio Telescope

The Nançay Radio Telescope (NRT), inaugurated in 1965, is a transit telescope with a 4'(Right ascension $\alpha$) $\times$ 22' (Declination $\delta$) power beam and is equivalent to a 94-m diameter parabolic dish. With such configuration, a source with a declination $\delta > -39°$ can be observed for at least one hour per day when it passes through the meridian. The telescope was initially designed for the observation of galaxies, comets and star envelopes at 1.4 GHz, which corresponds to the frequency of the emission line of the neutral Hydrogen. An intensive program of pulsar observations is in progress since 2004. The NRT produces high quality data for pulsar timing array (PTA, hereafter) projects whose aim consists in detecting the Gravitational Wave signature of the population of massive binary black holes (Desvignes et al. 2016). The Nançay Ultimate Pulsar Processing Instrument, which started to operate in late 2011, is a baseband recording system using a digitizer made of FPGA board developed by the CASPER group (ROACH, Reconfigurable Open Architecture Computing Hardware*) and a computing machine made of Central Processing Units (CPUs) and Graphics Processing Units (GPUs). Here the analog-to-digital converters firstly sample and digitise (in 8-bit) the signal over a 512 MHz band at the Nyquist rate with dual polarisations. A polyphase filter bank channelises the band into 128 channels, each of 4 MHz width. The channels are then packetised into four sub-bands and sent to four GPU clusters for real-time coherent dedispersion (timing mode). The modularity of the aforementioned system easily allows us to divide the bandwidth into 1024 channels in search mode (survey mode, Desvignes et al. 2013). The raw data are then decimated in time to produce dynamic spectra written into 4-bit PSRFITS format (Hotan et al. 2004).

[1] Laboratoire de Physique et Chimie de l'Environnement et de l'Espace LPC2E CNRS-Université dOrléans, F-45071 Orléans Cedex 02, France
[2] Max-Planck-Institut für Radioastronomie, Auf dem Hügel 69, D-53121 Bonn, Germany
[3] Station de radioastronomie de Nançay, Observatoire de Paris, CNRS/INSU, F-18330 Nançay, France
[4] Université Bordeaux 1, CNRS/IN2P3, CENBG Gradignan, F-33175 Gradignan, France
[5] Laboratoire Univers et Théories LUTh, Observatoire de Paris, CNRS/INSU, Université Paris Diderot, 5 place Jules Janssen, 92190 Meudon, France
*casper.berkeley.edu

The signal received from a pulsar is dispersed by free electrons and ionised material encountered along the line of sight. To correct for this physical phenomenon, a delay proportional to the so-called dispersion measure (DM) and to the inverse square law frequency, is applied to each frequency channel. In survey mode, data are analysed with pulsar searching software like PRESTO (Ransom et al. 2002) and Radio Frequency Interference (RFI) caused by human activities is removed by identifying strong narrow-band signals. At this stage in the analysis, the times of each data acquisition are corrected for the delay between the observatory and the solar system barycentre. Then, the time series produced are Fourier transformed using a fast Fourier transform followed by a harmonic summing routine. A search in acceleration is also performed to look for pulsars in binary system which may be accelerated by a companion star. The output is a list of candidates whose informations like potential periods (P), accelerations, signal-to-noise ratio (S/N), coherent power, number of summed harmonics, etc. are recorded. Candidates with S/N above 6 are folded. As pulsars are generally very weak sources, the addition of many pulses in phase is necessary to increase the S/N and make them detectable. The strategy adopted for pulsar surveys consists in dedispersing data exploring the whole range of dispersion measure (from 0 up to 1800 pc.cm$^{-3}$) and fold candidates with the best signal-to-noise ratio. Such procedure was applied in 2011, pointing at the position of a dozen of unidentified Fermi-LAT sources. This led to the fast discovery of three new millisecond pulsars: PSR J2043+1711 (Guillemot et al. 2012), PSR J2302+4442 and PSR J2017+0603 (Cognard et al. 2011).

## 2 The SPAN512 survey conducted with the Nançay Radio Telescope

Motivated by the aim to discover exotic pulsar systems and, more specifically, millisecond pulsars (MSPs, hereafter), whose spin stability might be very suitable for PTA programs, the pulsar survey SPAN512 (Desvignes et al. 2013) has been conducted at Nançay since 2012. This survey inspects the sky at L-band at intermediate galactic latitudes ($3.5° < |b| < 5°$) away from the inner Galaxy ($74° < l < 150°$). Figure 1 shows the extent of the survey on the sky. The large bandwidth of 512 MHz and the fine time resolution of 64 $\mu$s allow this survey to be sensitive to very faint and distant MSPs. Moreover, the long integration time of 18 minutes increases the likelihood of detecting transient pulsars (Rotating Radio Transients, intermittent pulsars... See Lyne 2009 and Keane & McLaughlin 2011 for reviews) and the total observing time predicts the detection of at least one Fast Radio Burst (Thornton et al. 2013; Petroff et al. 2016). A total of 50 Terabytes of data have been produced from the 6 034 sky pointings which amount to 1740 hours of observing time. All the data were processed at the IN2P3 supercomputer in Lyon[†]. The processing consisted in applying the steps described in Section 1 to analyse survey data. The acceleration search is sensitive to object with an orbital period roughly ten times longer than the observing time. To search for very short orbital period objects, we split the observations into two parts and analyse them separately, making the acceleration search more efficient. After the processing, 750 000 candidates were produced. We then needed to select the most promising ones, to be reobserved and possibly confirm. This selection task may be very laborious and human eye inspection makes it very subjective. One approach was to use a Neural Network algorithm, such as the one developed by Zhu et al. 2014. This Neural Network estimates the probability of a candidate to be a pulsar using Image Pattern Recognition and allows the astronomer to inspect fewer candidates. After inspection, a list of around 60 candidates have been prioritised for re-observation.

## 3 Results: Discovery of three new pulsars

Soon after the beginning of the observations in 2012, the SPAN512 survey revealed two new pulsars: PSR J2048+49 (P $\approx$ 0.56 s and DM $\approx$ 221 pc.cm$^{-3}$) and PSR J2205+60 (P $\approx$ 2.4 ms and DM $\approx$ 157 pc.cm$^{-3}$). The pulse profile of J2205+60 is very thin. This characteristic, together with the expected stability of an MSP could make PSR J2205+60 one of the pulsars used to search for Gravitational Waves through Pulsar Timing Arrays (Desvignes et al, in prep). Recently, using the (Zhu et al. 2014) Neural Network, we have discovered a new 2.08-ms pulsar, PSR J2055+38 (see Fig. 2). From November 2015 up to now, 27 observations of this pulsar have been recorded at 1.4 GHz and a timing analysis is in progress. The position and the period derivative are not yet very well known and more data need to be collected to improve the timing solution. However, the current data allowed us to obtain a phase-connected solution and to assert that the new pulsar discovered is in a Black Widow (BW) system (see Freire 2005 and Roberts 2013 for reviews) where the pulsar is ablating its

[†] `http://cc.in2p3.fr/`

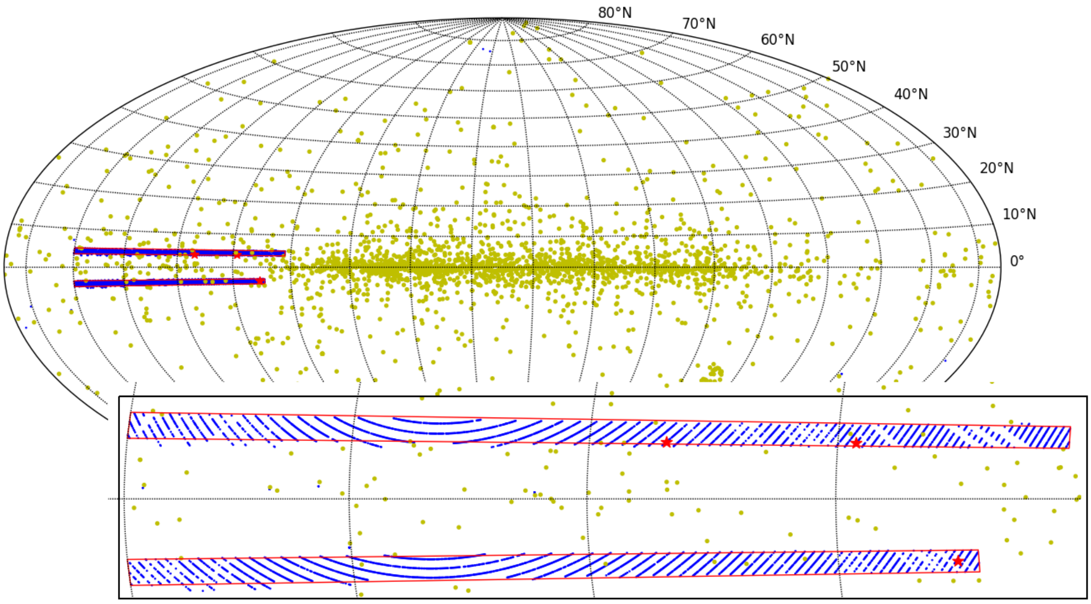


**Fig. 1.** Pulsar survey SPAN512 coverage is shown in the red squares. The blue points represent beams already pointed in the sky. In green, this is the distribution of the already known pulsars. The red stars are the pulsars discovered with the SPAN512 survey.

companion and the mass lost by the companion creates clouds of ionized material. Almost every BW system exhibits more or less variable eclipses in their radio signal. At 1.4 GHz, PSR J2055+38 is no exception, as it found to be eclipsing for around 10% of its orbit around the orbital phase $\phi \approx 0.25$ (see Fig. 2).

## 4 Conclusions and perspectives

A blind pulsar survey SPAN512 is being conducted with the NRT to scan the intermediate Galactic latitudes. Although this survey is not finished, it allowed us to discover three new pulsars, two of them having millisecond spin periods. We need to collect more data to study one of the pulsars discovered, PSR J2055+38, an eclipsing BW pulsar. Even if most of BW pulsars are not suitable for PTAs due to their chaotic nature, the study of the variations of the intra-binary ionised material can help us to have better insights about the formation process of millisecond pulsars and about the pulsar surroundings. Even if there is no source in Fermi-LAT catalogs near the position of PSR J2055+38, most of BW pulsars have a $\gamma$-ray counterpart. Hence, we hope to be able to detect $\gamma$-ray pulsations from this pulsar using the radio timing ephemeris.

## References

Cognard, I., Guillemot, L., Johnson, T. J., et al. 2011, ApJ, 732, 47

Desvignes, G., Caballero, R. N., Lentati, L., et al. 2016, MNRAS, 458, 3341

Desvignes, G., Cognard, I., Champion, D., et al. 2013, in IAU Symposium, Vol. 291, Neutron Stars and Pulsars: Challenges and Opportunities after 80 years, ed. J. van Leeuwen, 375–377

Freire, P. C. C. 2005, in Astronomical Society of the Pacific Conference Series, Vol. 328, Binary Radio Pulsars, ed. F. A. Rasio & I. H. Stairs, 405

Guillemot, L., Freire, P. C. C., Cognard, I., et al. 2012, MNRAS, 422, 1294

Hotan, A. W., van Straten, W., & Manchester, R. N. 2004, PASA, 21, 302

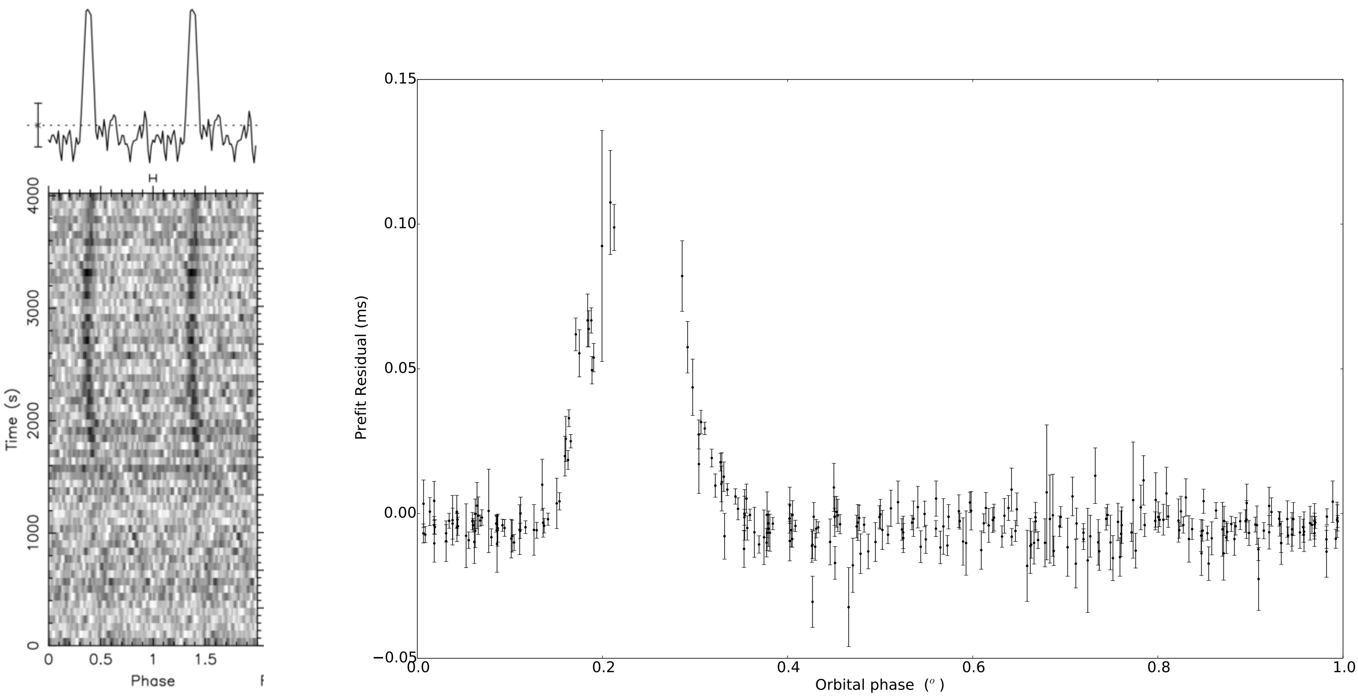


**Fig. 2. Left:** Profile of PSR J2055+38. We can notice the presence of eclipse during the observation. **Right:** Timing residuals for PSR J2055+38, eclipses occur at the orbital phase $\phi \approx 0.25$.

Keane, E. F. & McLaughlin, M. A. 2011, Bulletin of the Astronomical Society of India, 39, 333

Lyne, A. G. 2009, in Astrophysics and Space Science Library, Vol. 357, Astrophysics and Space Science Library, ed. W. Becker, 67

Petroff, E., Barr, E. D., Jameson, A., et al. 2016, PASA, 33, e045

Ransom, S. M., Eikenberry, S. S., & Middleditch, J. 2002, AJ, 124, 1788

Roberts, M. S. E. 2013, in IAU Symposium, Vol. 291, Neutron Stars and Pulsars: Challenges and Opportunities after 80 years, ed. J. van Leeuwen, 127–132

Thornton, D., Stappers, B., Bailes, M., et al. 2013, Science, 341, 53

Zhu, W. W., Berndsen, A., Madsen, E. C., et al. 2014, ApJ, 781, 117

*SF2A 2016*
*C. Reylé, J. Richard, L. Cambrésy, M. Deleuil, E. Pécontal, L. Tresse and I. Vauglin (eds)*

# CONSEQUENCES OF ROTATING OFF-CENTRED DIPOLAR ELECTROMAGNETIC FIELD IN VACUUM AROUND PULSARS

A. Kundu[1] and J. Pétri[1]

**Abstract.** Studying the electromagnetic field of pulsars is one of the key themes in neutron star physics. While most of the works assume a standard central dipolar electromagnetic field model, recently some efforts had been made in explaining how inclusion of higher field components produces drastic consequences in our understanding of these objects.

We put forward the effects of a unique recently presented approach in which the magnetic axis is shifted off from the centre. It is found that the rotating off-centred dipolar electromagnetic field itself reveals the presence of the higher components within. The consequences of this approach on the shape of the polar caps and the emission diagrams are discussed.

Keywords: dipole, magnetic fields, neutron stars, pulsars, off-centred

## 1 Introduction

Pulsars are a special class of neutron stars (Gold (1968)) with strong magnetic fields and rotation period lying between 1.4 ms and 8.5 seconds. Since their discovery (Hewish et al. (1968)), several attempts have been made to understand these mysterious objects. The magnetic field topology of pulsars provides insight into the physical processes and hence, extensive literature focusses on it.

A simple model for the magnetic poles and the magnetic field line structure was put forward by Radhakrishnan & Cooke (1969) and the electromagnetic field equations for a rotating dipole in vacuum were first presented by Deutsch (1955) giving the symmetrical solutions about a magnetic dipole which is inclined to the rotation axis. Most of the followed literature is focussed on these standard assumptions.

However, with the discovery of pulsar J2144-3933 which have a period of 8.51 s, by far the longest of any known radio pulsar, it was realized that this simple assumption needs revision (Young et al. (1999)). It was argued by Gil & Mitra (2001) that to explain this extremal observation, a complicated multi-polar surface magnetic field has to be considered. Gil et al. (2002) modelled surface magnetic field of neutron stars which required strong and non-dipolar surface magnetic field near the pulsar polar cap. The electromagnetic field was considered by them to be a superposition of the global dipole field and a small scale magnetic anomaly. Petri (2015) included multipolar components to the electromagnetic field in a self-consistent way and demonstrated that working with only a dipole field can be very misleading.

It is also assumed by default that the centre of the magnetic dipole coincides with the centre of the rotation axis. However, it has been shown that a deviation from this centred assumption i.e. an off-centred geometry is possible for stars and planets by Stift (1974) and Komesaroff (1976) respectively. The offset idea was applied to the neutron stars by Harding & Muslimov (2011) to investigate the effects of offset polar caps on pair cascades near the surface. Recently, Petri (2016) studied the effect of an offset dipole anchored in the neutron star interior and calculated exact analytical solutions for the electromagnetic field in vacuum outside the star. We use these equations to study the consequences of the off-centred approach.

[1] Observatoire Astronomique de Strasbourg, Université de Strasbourg, CNRS, UMR 7550,
11 Rue de l'université, F-67000 Strasbourg, France

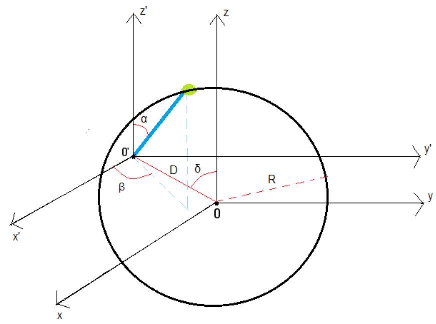


Fig. 1: Geometry of an off-centred Pulsar

## 2 Off-centred geometry

Figure 1 depicts the geometry of an off-centred pulsar of radius $R$. The centre of the unprimed reference frame $xyz$ coincides with the geometrical centre $O$ of the pulsar. Hence, this is the frame which is attached to the rotation axis of the pulsar. The position vector for a random vector in this centred frame is defined as $\mathbf{r} = r\mathbf{n}$ where $\mathbf{n} = (\sin\theta\cos\phi, \sin\theta\sin\phi\cos\theta)$.

We define another reference frame $x'y'z'$ attached to the magnetic axis of the pulsar which is centred at $O'$. The centre of this new frame $O'$ is shifted from $O$ by a distance $D$. Let's call this primed reference frame $x'y'z'$ as the off-centred frame.

The angle of inclination between the two frames w.r.t. the $z - axis$ of the centred frame is $\delta$. The magnetic axis is shown in blue with polar angle and azimuth angle as $\alpha$ and $\beta$ respectively as seen from the off-centred frame. It is defined as $\mathbf{m} = m(\sin\alpha\cos\beta, \sin\alpha\sin\beta, \cos\alpha)$ and its position vector w.r.t. the centred frame is given by $\mathbf{d} = D(\sin\delta, 0, \cos\delta)$

An important condition used throughout the calculations was $D << R$ as the centre of the magnetic axis must lie within Pulsar. A quantity $\epsilon = D/R$ was defined and hence, we have, $\epsilon << 1$. The angles $\alpha, \beta$ and $\delta$ are shuffled to get different orientations for the off-centred geometry. We chose $\epsilon = 0.2$ for the off-centred calculations throughout the discussion.

## 3 Results and Discussions

The exact analytical expressions for dipolar and quadrupolar electromagnetic fields recently published in Appendix C of Petri (2016) are used for all the calculations.

### 3.1 Polar cap geometry

Polar cap is the region mapped out by the foot points of the magnetic field lines touching the light cylinder. Studying polar caps is considered crucial to understand the pulsar radio emission as this is the region which is most likely to be the source of the coherent radio emission. We present a comparison of the polar cap geometry for the centred and the off-centred geometry.

The comparison is shown in Figure 2 where we plot the shapes of the polar caps for various inclination angles. The $x$ and $y$ axis represent the azimuth angle $\phi$ and the polar angle $\theta$ respectively. The centred case (shown in green) has been calculated by considering $\epsilon = 0$ and for the off-centred case (shown in blue) $\epsilon$ is taken to be 0.2.

A broad view distinction depicts that the shape is not affected due to the shift of the centre of the dipole from the geometrical centre but size, apparently, is affected. The size of the polar cap is one of the determining factors for the pulse profile width of pulsar. The larger polar caps as evident in (b) could be used to justify observations with longer pulse widths than expected.

The shift in the location of the polar caps in terms of $\theta$ for aligned geometries defined by $\delta = 0$ are seen in parts (a) to (d) of the Figure 2.

In contrast to the aligned case, the orthogonal geometries defined by $\delta = 90$ show a shift in $\phi$. The shift for each pole is in opposite directions as seen in (e) and (f). This shift in $\phi$ represents a phase delay which could

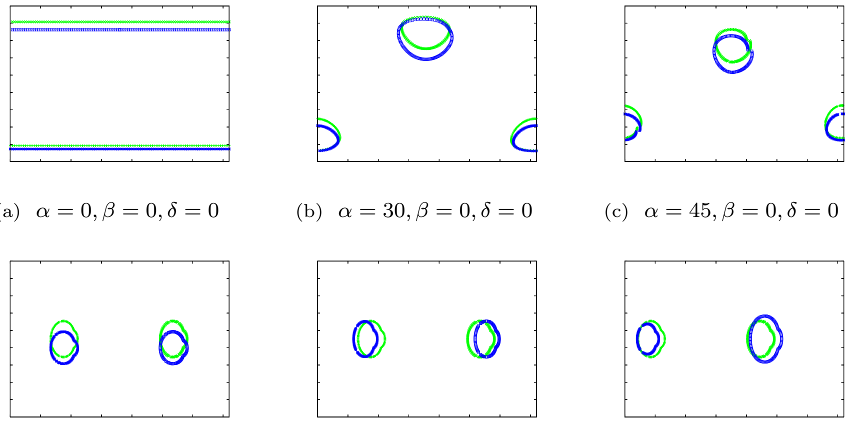

(a) $\alpha = 0, \beta = 0, \delta = 0$ (b) $\alpha = 30, \beta = 0, \delta = 0$ (c) $\alpha = 45, \beta = 0, \delta = 0$

(d) $\alpha = 90, \beta = 90, \delta = 0$ (e) $\alpha = 90, \beta = 90, \delta = 90$ (f) $\alpha = 90, \beta = 45, \delta = 90$

Fig. 2: Polar cap geometry comparison for $\epsilon = 0$ (in green) and $\epsilon = 0.2$ (in blue) for various cases

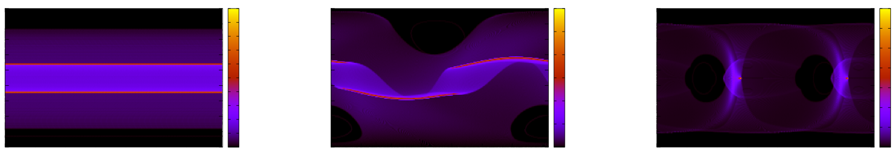

(a) $\alpha = 0, \beta = 0, \delta = 0$ (b) $\alpha = 30, \beta = 0, \delta = 0$ (c) $\alpha = 90, \beta = 90, \delta = 90$

Fig. 3: High energy emission phase diagrams for $\epsilon = 0.2R$ for various cases

serve as a crucial factor to compare observational phase delays in pulse profiles with our approach and hence, explain such observations.

### 3.2 High energy emission phase diagrams

We present the phase diagrams for the high enery emission in this section.

In Figure 3 we show the high energy emission for a shift of $\epsilon = 0.2R$ for several cases. The $x - axis$ spans the phase $\phi$ while the $y - axis$ represents the angle of the line of sight. The key on the right side of each plot represents the intensity. The black region corresponds to the no emission region and moving towards yellow means an increase in the photon count. For all the three cases shown we see the black region close to the poles which specifies the 'no emission' zone. It is in accord with the theory that the high energy emission has its source close to the light cylinder. It is not very easy to precisely conclude things related to the off-centred approach from these phase diagrams so we will plot the light curves in the next section. We also show the light curves for the radio emission.

### 3.3 High energy emission and radio emission light curves

To understand the phase diagrams deeply we need to have a look at the higher resolution which can be attained by extracting light curves from them.

Light curves for high energy and radio regime for $\alpha = 30, \beta = 0, \delta = 0$ and $\alpha = 90, \beta = 90, \delta = 90$ are shown in Figure 4 and Figure 5 respectively.

We see clearly the radio emission complements the high energy emission with the former being the strongest at the poles and the latter in proximity to the light cylinder.

In (a), (b) and (d) parts of Figure 4 we see that the pulse width varies for the two regimes. In (c) it can be noticed that the high energy emission is spread over almost entire range of $\phi$, we do not see a dip close to zero in Figure 4 but we have very clear such dips in the orthogonal case in Figure 5 which is entirely based on

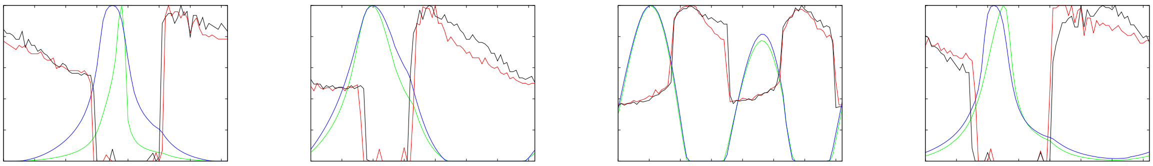

(a) $\theta = 30$ (b) $\theta = 45$ (c) $\theta = 90$ (d) $\theta = 150$

Fig. 4: High energy and radio emission light curves for $\alpha = 30, \beta = 0, \delta = 0$ with $\epsilon = 0$ and $\epsilon = 0.2R$ for various line of sight angles. The high energy emission curves are shown in red and black for the centred and the off-centred case respectively. Similarly, the green and the blue curves represent the emission curves for the radio regime in the same order.

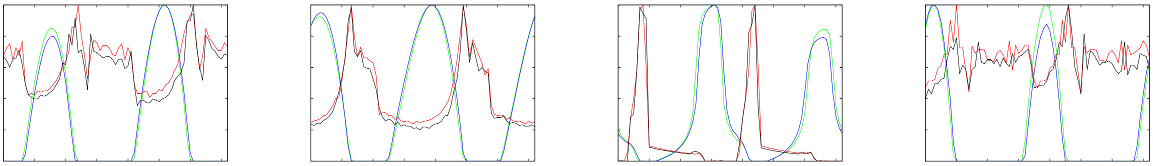

(a) $\theta = 30$ (b) $\theta = 45$ (c) $\theta = 90$ (d) $\theta = 150$

Fig. 5: High energy and radio emission light curves for $\alpha = 90, \beta = 90, \delta = 90$ with $\epsilon = 0$ and $\epsilon = 0.2R$ for various line of sight angles. The high energy emission curves are shown in red and black for the centred and the off-centred case respectively. Similarly, the green and the blue curves represent the emission curves for the radio regime in the same order.

geometry and the angle of line of sight. Also, the number of peaks for radio emission curve depends on our angle of line of sight and hence, we see one peak in some cases while from both the poles in others. Finally, a significant phase delay is observed between the radio and the high energy light curve for both the cases.

## 4 Conclusions

We conclude that the off-centred approach is a reliable candidate to be considered while studying pulsars. On comparison of the shape of the polar caps for the offset case with those of the centred one we see significant differences which could help explain various observational signatures. Study of the emission mechanisms with the phase diagrams and the light curves show the differences in the pulse width and phase delay which could give a better insight in our understanding of the emission mechanism. Our next step is to make an analyis of polarization using this approach.

## References


Deutsch, A. J. 1955, Annales d'Astrophysique, 18, 1

Gil, J. & Mitra, D. 2001, The Astrophysical Journal, 550, 383, arXiv: astro-ph/0010603

Gil, J. A., Melikidze, G. I., & Mitra, D. 2002, Astronomy and Astrophysics, 388, 235, arXiv: astro-ph/0111474

Gold, T. 1968, Nature, 218, 731

Harding, A. K. & Muslimov, A. G. 2011, The Astrophysical Journal, 743, 181, arXiv: 1111.1668

Hewish, A., Bell, S. J., Pilkington, J. D. H., Scott, P. F., & Collins, R. A. 1968, Nature, 217, 709

Komesaroff, M. M. 1976, Proceedings of the Astronomical Society of Australia, 3, 51

Petri, J. 2015, Monthly Notices of the Royal Astronomical Society, 450, 714, arXiv: 1503.05307

Petri, J. 2016, Monthly Notices of the Royal Astronomical Society, 463, 1240, arXiv: 1608.01015

Radhakrishnan, V. & Cooke, D. J. 1969, Astrophysical Letters, 3, 225

Stift, M. J. 1974, Monthly Notices of the Royal Astronomical Society, 169, 471

Young, M. D., Manchester, R. N., & Johnston, S. 1999, Nature, 400, 848

*SF2A 2016*
*C. Reylé, J. Richard, L. Cambrésy, M. Deleuil, E. Pécontal, L. Tresse and I. Vauglin (eds)*

# STEADY-STATE MODEL OF ACCRETION COLUMNS IN MAGNETIC CATACLYSMIC VARIABLES

L. Van Box Som[2,4,1], É. Falize[1,2], J.-M. Bonnet-Bidaud[2], M. Mouchet[3], C. Busschaert[1] and A. Ciardi[4]

**Abstract.** The standard model of accretion columns in magnetic cataclysmic variables is investigated through semi-analytical solutions in the steady-state regime. The balance between bremsstrahlung and cyclotron cooling is studied and the effects of the white dwarf gravitational field are analysed.

Keywords: magnetic cataclysmic variables, radiative shocks, accretion processes, high-energy processes

## 1 Introduction

Among the different binary systems, cataclysmic variables provide the best environment to study high-energy radiation in the accretion processes. As possible progenitors of type Ia supernovae, understanding these complex systems is crucial to explain the initial conditions of these explosions (Maoz et al. 2014). Magnetic cataclysmic variables (mCVs) are close binary systems composed of a magnetised white dwarf accreting matter from a late type Roche-lobe filling companion star (Warner 1995). Depending on the white dwarf magnetic field, mCVs are classified into intermediate polars (IPs) when $B_{WD} < 10$ MG and polars when $B_{WD} \sim 10 - 230$ MG. In polars and some IPs, the accreting matter coming from the companion is channelled by the magnetic field onto the white dwarf magnetic poles. This leads to the creation of an accretion column (Cropper 1990; Wu 2000). The impact of the free-falling flow at supersonic velocities ($v_{ff} \sim 5000$ km.s$^{-1}$) creates a radiative reverse shock which heats the coming matter to typical temperatures of about 50 keV. This high-energy environment is structured by the cooling processes which shape the density and the temperature profiles of the post-shock region and produce strong gradients near the white dwarf photosphere. According to the current acknowledged model of accretion columns, the radiative shock is expected to reach an equilibrium height determined by the cooling processes. To determine the mCVs properties, particularly to infer the white dwarf mass, the knowledge of the spatial profiles of this high-energy radiative region is fundamental. Although integrated luminosities can be observed from mCVs, the spatial scales, associated with the accretion shock, are largely smaller than the white dwarf radius, which prevents direct observations. To obtain analytical and semi-analytical solutions from the radiation hydrodynamics equations which model the accretion column, a steady-state regime is frequently assumed. Steady-state models are crucial to forecast the column behaviour and to determine the white dwarf mass. Particularly to correctly model the accretion onto high mass white dwarfs ($M_{WD} > 0.8$ M$_\odot$), taking into account the white dwarf gravitational field is essential. In this paper, we present solutions of the radiative hydrodynamics equations with gravitation.

## 2 Steady-state model of the post-shock region

For mCVs, the main cooling processes in the post-shock region are bremsstrahlung and cyclotron emission (Wu et al. 1994). Other processes such as Compton cooling and thermal conductivity are negligible. In order to

[1] CEA-DAM-DIF, F-91297 Arpajon,France
[2] CEA Saclay, DSM/Irfu/Service d'Astrophysique, F-91191 Gif-sur-Yvette,France
[3] LUTH, Observatoire de Paris, PSL Research University, CNRS, Université Paris Diderot, Sorbonne Paris Cité, F-92195 Meudon, France
[4] LERMA, Observatoire de Paris, PSL Research University, CNRS, Sorbonne Universités, UPMC Univ. Paris 06, F-75005, Paris,France

model the post-shock region, we assume a plane-parallel and collisional shock which can be described by a single temperature medium. In the one-temperature approximation and in the steady-state regime, the post-shock region is described by the equations of radiation hydrodynamics:

$$\frac{d}{dx}[\rho v] = 0 \tag{2.1}$$

$$\frac{d}{dx}[\rho v^2 + P] = \rho \frac{GM_{WD}}{(x_0 - x)^2} \tag{2.2}$$

$$v[\frac{dP}{dx} - \gamma \frac{P}{\rho}\frac{d\rho}{dx}] = -(\gamma - 1)\Lambda(\rho, P) \tag{2.3}$$

where $x$, $\rho$, $v$, $P$, $G$, $M_{WD}$, $x_0$, $\gamma$ and $\Lambda$ are respectively the spatial coordinate, the density, the velocity, the pressure of the flow, the gravitational constant, the white dwarf mass, a spatial constant, the adiabatic index and the cooling function. The constant $x_0$ is defined as $x_0 = x_s + R_{WD}$ where $x_s$ is the steady-state height of the post-shock region and $R_{WD}$ is the white dwarf radius. The latter is related to the white dwarf mass by the Nauenberg relation (Nauenberg 1972). The spatial axis has its origin at the shock front and its direction is the one of the accreting flow. In this model, the cooling function is expressed as the sum of the two radiative processes: $\Lambda = \Lambda_{brem} + \Lambda_{cycl}$. Each process can be described by a power-law function : $\Lambda_i = \Lambda_{0,i}\rho^{\alpha_i}P^{\beta_i}$ where $\Lambda_{0,i}$, $\alpha_i$ and $\beta_i$ are three characteristic constants of the radiative mechanism. This form models the exact bremsstrahlung cooling ($\Lambda = \Lambda_0^{brem}\rho^{1.5}P^{0.5}$) and an effective cyclotron cooling function ($\Lambda = \Lambda_0^{cycl}(B_{WD})\rho^{-2.35}P^{2.5}$) (Wu et al. 1994).

## 3 Semi-analytical solutions of the post-shock region

To solve the equations (2.1), (2.2), and (2.3) in the steady-state regime, an intermediate variable $\eta$ is introduced (Bertschinger 1989; Falize et al. 2009) defined by the following equations:

$$\rho(x) = \frac{\rho_0}{\eta(x)}, \qquad v(x) = v_{ff}\eta(x) \tag{3.1}$$

where $\rho_0$ and $v_{ff}$ are respectively the density and the velocity of the supersonic-upstream flow. The upstream velocity is the free-fall velocity given by $v_{ff} = \sqrt{2GM_{WD}/x_0}$ and the upstream density is inferred from the accretion rate, $\dot{M}$, as $\rho_0 = \dot{M}/(Sv_{ff})$ where $S$ is the column cross-section. At the shock front, the post-shock variables are related to the pre-shock variables by the Rankine-Hugoniot conditions. The white dwarf photosphere is assumed to be a cold and solid wall at which temperature and velocity tend to zero. After some algebraic manipulations, equations (2.1), (2.2), and (2.3) lead to a system of two coupled differential equations obtained on the intermediate variable $\eta$ and the variable $P$:

$$\frac{dP}{dx} = \frac{\rho_0}{\eta}\frac{GM_{WD}}{(x_0 - x)^2} - \rho_0 v_{ff}^2 \frac{d\eta}{dx} \tag{3.2}$$

$$\frac{d\eta}{dx}\left[\gamma P v_{ff} - \rho_0 v_{ff}^3 \eta\right] = -(\gamma - 1)\Lambda(\eta, P) - v_{ff}\rho_0 \frac{GM_{WD}}{(x_0 - x)^2} \tag{3.3}$$

The transformation (3.1) allows us to simplify the reductions of the equations [(2.1), (2.2), (2.3)] in a more direct way than in previous studies (Cropper et al. 1999). This system [(3.2), (3.3)] is solved by a dichotomy method coupled with a fourth-order Runge-Kutta method. The shock height is extracted iteratively from the boundary condition: $v = 0$ at the white dwarf photosphere. In Fig. 1a and Fig. 1b, the spatial profiles of the post-shock region variables (density, velocity, pressure and temperature) are presented, in the case of the bremsstrahlung cooling, obtained with this method (filled color lines). When $x_s/R_{WD} << 1$, the gravitational field of the white dwarf can be assumed constant in the post-shock region and then it is negligible compared to the cooling processes. In this case, the system [(3.2), (3.3)] can be simplified in a single differential equation on $\eta$ and an ordinary function for the pressure. The resulting differential equation admits analytical solutions when only one cooling process is taken into account (Falize et al. 2009). The inferred profiles from the analytical solution for the bremsstrahlung cooling are presented in dotted black lines. They are compared to the semi-analytical solution obtained from the system [(3.2), (3.3)] when gravitation is not taken into account (dashed color lines). In Fig. 1a, the post-shock region properties are calculated for a white dwarf mass of $M_{WD} = 0.4$

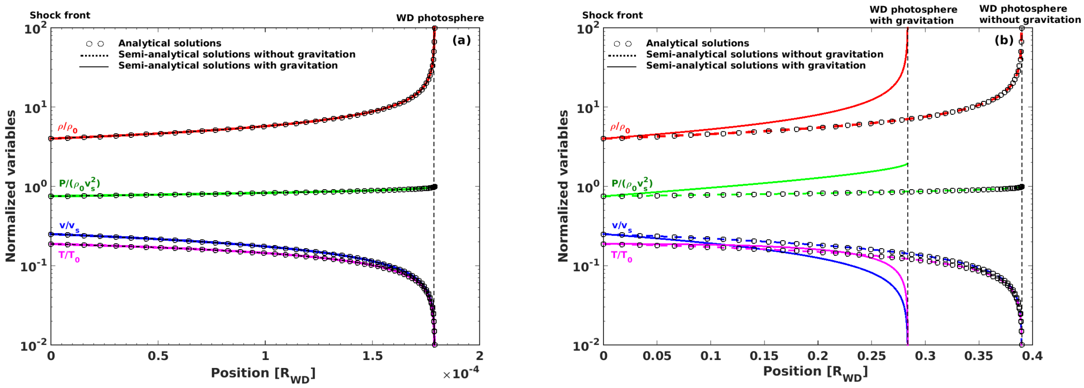


**Fig. 1.** Normalized profiles of the density, pressure, velocity and temperature of the post-shock region with only bremsstrahlung process. The shock front is located to the origin of the x-axis and the white dwarf photosphere is located at the dotted black lines. **(a)** Profiles when gravitation is negligible: $M_{WD} = 0.4\ M_{\odot}$, $\dot{M} = 10^{16}$ g.s$^{-1}$, and $S = 10^{14}$ cm$^2$. **(b)** Profiles when gravitation can not be neglected: $M_{WD} = 1\ M_{\odot}$, $\dot{M} = 10^{15}$ g.s$^{-1}$, and $S = 10^{15}$ cm$^2$.

$M_{\odot}$, an accretion rate of $\dot{M} = 10^{16}$ g.s$^{-1}$ and a column cross-section of $S = 10^{14}$ cm$^2$. In this case, the white dwarf gravitational field can be neglected because $x_s/R_{WD} = 1.8 \times 10^{-4} << 1$ with $x_s = 2$ km. All the physical profiles perfectly match the analytical solutions which describe the high-energy region. In Fig. 1b, the spatial profiles are presented when the white dwarf gravitation strongly modifies the gradient of the post-shock region characterized by a white dwarf mass of $M_{WD} = 1\ M_{\odot}$, an accretion rate of $\dot{M} = 10^{15}$ g.s$^{-1}$ and a column cross-section of $S = 10^{15}$ cm$^2$. When gravitation is not taken into account, $x_s/R_{WD} = 0.39$ with $x_s = 2130$ km whereas when gravitation is taken into account, $x_s/R_{WD} = 0.28$ with $x_s = 1550$ km. Gravitation tends to decrease the steady-state height due to the release of gravitational energy which is in agreement with the results presented by Cropper et al. (1999). In this case, gravitation is essential to correctly model the radiative region.

## 4 Steady-state shock height as function of mCVs parameters

As shown by the radiation hydrodynamics equations, the physics of the accretion column in the steady-state regime is strongly dependent on the four mCVs parameters: the white dwarf mass $M_{WD}$, the white dwarf magnetic field $B_{WD}$, the accretion rate $\dot{M}$ of the accretion flow and the column cross-section $S$. In Fig. 2a, Fig. 2b and Fig. 2c, the behaviour of the steady-state shock height is extracted as a function of the white dwarf mass for $M_{WD} = 0.2 - 1.4\ M_{\odot}$ and for different set of parameters [$B_{WD}$, $\dot{M}$ and $S$] whose values are taken in the observed parameters range (Bonnet-Bidaud et al. 2015). Each curve has a resolution of a hundred points. The filled lines correspond to the case with gravitation and the dashed lines without gravitation. In Fig. 2a, the variation of the magnetic field for different values (0, 30, 60, 90 MG) is shown assuming a representative accretion rate at $10^{15}$ g.s$^{-1}$ and a cross-section at $10^{14}$ cm$^2$. In Fig. 2b, the evolution for different accretion rates ($10^{14}$, $10^{15}$, and $10^{16}$ g.s$^{-1}$) is studied for an assumed magnetic field at 30 MG and a column cross-section at $10^{14}$ cm$^2$. Finally in Fig. 2c, the variation of different values of cross sections ($10^{14}$, $10^{15}$ and $10^{16}$ cm$^2$) is studied for an assumed 30 MG magnetic field and accretion rate value at $10^{15}$ g.s$^{-1}$.

An analytical expression of the steady shock height as a function of the mCVs parameters is possible only in the most simple case: with only bremsstrahlung cooling and no gravitation (Falize et al. 2009). When the model takes into account the cyclotron cooling and the gravitational field, there is no analytical solution of the steady-state height. For very low white dwarf masses, strong accretion rates and small column cross-section, the bremsstrahlung cooling is dominant and the shock height strictly increases ($x_s \sim S\dot{M}^{-1}M_{WD}^{3/2}R_{WD}^{-3/2}$) as a function of the white dwarf mass. When the cyclotron cooling starts becoming dominant, the shock height reaches a peak and decreases as the white dwarf mass increases. This maximum is due to the balance between the two radiative cooling processes and is the result of the inversion of the dominant cooling process in the post-shock region. The accretion rate and the column cross-section modify the position of this maximum by modifying the radiative balance. As shown before, $x_s$ obviously decreases with the gravitational field. For very strong magnetic fields ($B_{WD} >> 30$ MG), the radiative processes, in particular the cyclotron cooling, is so

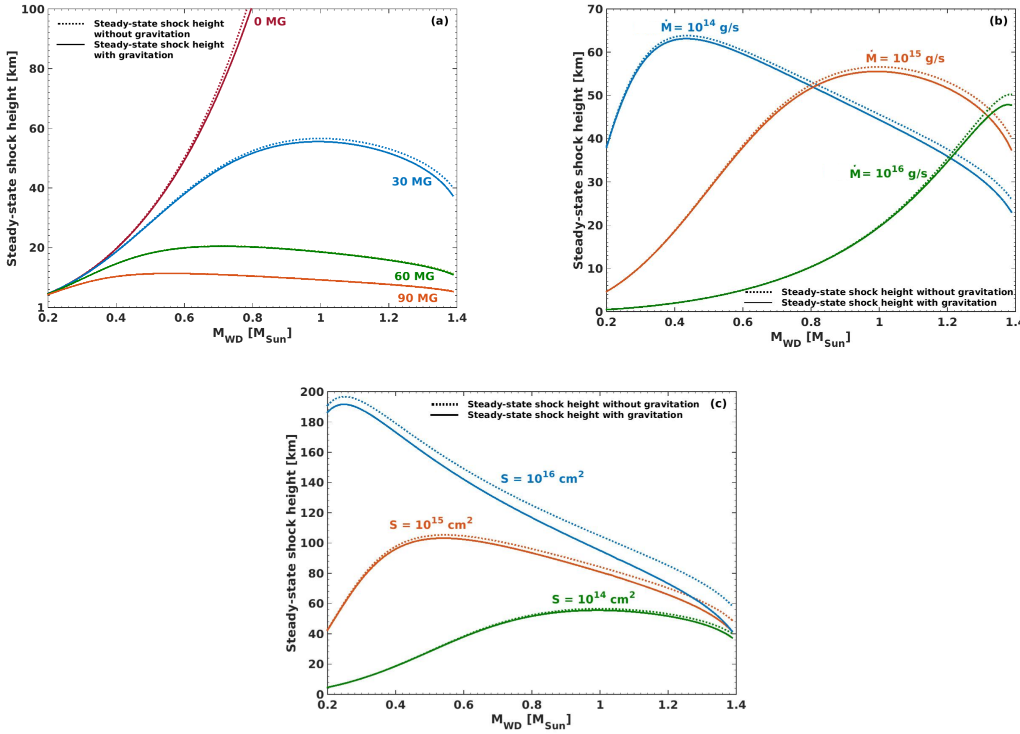


**Fig. 2.** Evolution of the steady-state shock height as a function of the white dwarf mass $M_{WD} = 0.2-1.4\ M_{\odot}$ for different mCVs parameters. The resolution without gravitation is given in dashed line and the resolution with gravitation in filled line. **(a)** An accretion rate of $10^{15}$ g.s$^{-1}$ and a section of $10^{14}$ cm$^2$ are assumed. **(b)** A magnetic field of 30 MG with a cross-section of $10^{14}$ cm$^2$ is assumed. **(c)** A magnetic field of 30 MG with an accretion rate of $10^{15}$ g.s$^{-1}$ is assumed.

strong that the shock height becomes very small ($x_s < 10$ km) and the gravitational field is saturated, not playing a role anymore.

## 5 Conclusions

We have presented solutions of the radiation hydrodynamics equations with gravitation which model the accretion column and particularly onto high mass white dwarfs. We have compared them with analytical and semi-analytical solutions which validates our resolution in the case where gravitation is negligible and in the case where gravitation is essential to correctly model the post-shock region. An extensive study of the steady-state shock height as functions of mCVs parameters has been presented. We have highlighted the wide range of shock height behaviours, and in particular the inversion of the balance between the two radiative cooling processes in this high-energy region generates a maximum of the shock height.

## References

Bertschinger, E. 1989, ApJ, 340, 666
Bonnet-Bidaud, J. M., Mouchet, M., Busschaert, C., Falize, E., & Michaut, C. 2015, A&A, 579, A24
Cropper, M. 1990, Space Sci. Rev., 54, 195
Cropper, M., Wu, K., Ramsay, G., & Kocabiyik, A. 1999, MNRAS, 306, 684
Falize, E., Michaut, C., Cavet, C., et al. 2009, Ap&SS, 322, 71
Maoz, D., Mannucci, F., & Nelemans, G. 2014, ARA&A, 52, 107
Nauenberg, M. 1972, ApJ, 175, 417
Warner, B. 1995, Cambridge Astrophysics Series, 28
Wu, K. 2000, Space Sci. Rev., 93, 611
Wu, K., Chanmugam, G., & Shaviv, G. 1994, ApJ, 426, 664

*SF2A 2016*
*C. Reylé, J. Richard, L. Cambrésy, M. Deleuil, E. Pécontal, L. Tresse and I. Vauglin (eds)*

# ENERGY DEPENDENT VARIABILITY AND OUTBURST EVOLUTION IN BLACK HOLE X-RAY BINARIES

H. Stiele[1] and A. K. H. Kong[1]

**Abstract.** Almost all low mass black hole X-ray binaries are transient sources. Most of these sources show a certain pattern during outburst: the evolution from low hard state through intermediate state(s) into high soft state and the returning to the hard state at lower luminosity. However, there are outbursts that remain in the hard state (so called "failed" outbursts).

Using the technique of covariance spectra we can investigate the variability of individual spectral components on different time scales. Comprehensive studies of covariance spectra for a sample of black hole X-ray binaries observed in the rising low hard state of "normal" outbursts revealed an increase of the covariance ratios towards lower energies that has been interpreted as the sign of additional disc variability on long time scales.

There are now two sources (H 1743-322 and GS 1354–64) that do not show an increase towards lower energies in their covariance ratio. Both sources have been observed during "failed" outbursts and showed photon indices much harder than what is usually observed in black hole X-ray binaries.

Keywords: X-rays: binaries, binaries: close, black hole physics

## 1 Introduction

In low-mass black hole X-ray binaries (BHBs), a stellar mass black hole accretes matter from its low-mass, early type companion star through Roche-lobe overflow. Most of the time, these systems are too faint to be studied with current X-ray instruments. Through the monitoring of BHBs during outbursts with the RXTE satellite for about 15 years a detailed phenomenological picture of the spectral and timing properties of these sources has emerged (Belloni 2010; McClintock & Remillard 2006). We learned that BHBs typically begin and end their outbursts in the low hard state (LHS), and that most sources show transitions to a high soft state (HSS). In the LHS, the energy spectrum is dominated by a hard component, which fitting with simple models extends up to a cut-off energy of $\sim 50-100$ keV. In addition, a much softer component associated to a thermal accretion disc is sometimes observed when the interstellar absorption is not too high. Strong ($30-40\%$) band-limited noise as well as low frequency quasi-periodic oscillations (LF-QPOs) is observed in the Power Density Spectrum (PDS). In the HSS, the energy spectrum is dominated by a thermal component, usually modeled with a disc-blackbody with a temperature of $1-2$ keV. A weak power-law component is present, with a steeper and strongly variable photon index. No apparent high-energy cut-off is observed in high signal-to-noise spectra. The PDS shows weak (few %) power-law noise.

This picture has been challenged in recent years. Investigations of power density spectra at softer energies showed that in the hard intermediate state two distinct power spectral shapes coexist simultaneously in the soft and hard energy band (Yu & Zhang 2013; Stiele & Yu 2014).

There are about ten X-ray binaries (including neutron stars and black holes; Capitanio et al. 2009, and references therein) that have only been observed during outbursts where they did not make the transition to the soft state. This type of outburst has been dubbed "failed" outburst. In the case of H 1743-322 both type of outbursts have been observed (Capitanio et al. 2009; Stiele & Yu 2016). Capitanio et al. (2009) supposed that "failed" outbursts are connected to a premature decrease of the mass accretion rate. At the moment, the physical reason why some outbursts make it to the soft state, while other remain in the hard state, is elusive.

[1] National Tsing Hua University, Department of Physics and Institute of Astronomy, No. 101 Sect. 2 Kuang-Fu Road, 30013, Hsinchu, Taiwan

## 2 Observations and data analysis

We used *XMM-Newton* observations of the 2004 and 2009 outbursts of GX 339–4 (Wilkinson & Uttley 2009; Stiele & Yu 2015), of Swift J1753.5–0127 taken in 2006 and 2012 (Wilkinson & Uttley 2009; Stiele & Yu 2015), of the "failed" outbursts in 2008 and 2014 of H 1743–322 (Motta et al. 2010; Stiele & Yu 2016), and of GS 1354–64 during its outburst in 2015 (Stiele & Kong 2016). All observations were taken during the LHS. We filtered and extracted the pn event files, using standard SAS tools, paying particular attention to extract the list of photons not randomized in time. For our study we selected the longest, continuous exposure available in each observation. We used the SAS task `epatplot` to investigate whether the observations are affected by pile-up, and in the case of pile-up excluded the column(s) with the highest count rate until the selection results in an observed pattern distribution that follows the theoretical prediction quite nicely. We selected single and double events (PATTERN<=4) for our study. More details on individual observations can be found in Stiele & Yu (2015, 2016) and Stiele & Kong (2016).

We produced PDS in several energy bands. We subtracted the contribution due to Poissonian noise (Zhang et al. 1995), normalised the PDS according to Leahy et al. (1983) and converted to square fractional rms (Belloni & Hasinger 1990). The PDS were fitted with models composed of zero-centered Lorentzians for BLN components, and Lorentzians for QPOs following Belloni et al. (2002).

We also extracted the averaged energy spectra and corresponding redistribution matrices and ancillary response files. Background spectra have been extracted from columns 3 to 5. Since energy spectra obtained from EPIC/pn fast-readout mode data are known to show excess emission below ∼1 keV (see e. g. Martocchia et al. 2006) we limited our spectral studies to energies above 0.8 keV. We fit the averaged EPIC/pn spectra within ISIS V. 1.6.2 (Houck & Denicola 2000) in the 0.8 − 10 keV range, grouping the data to ensure that we have at least 20 source counts in each bin. We included a systematic uncertainty of 1 per cent. We used a model consisting of an absorbed (TBABS; Wilms et al. 2000) disc blackbody plus thermal Comptonisation component (NTHCOMP; Zdziarski et al. 1996; Życki et al. 1999), including a high-energy cut-off. If needed, a Gaussian was added to attribute for emission of the Fe line at ∼6.4 keV. We included an additional Gaussian component to model the features caused by gain shift due to Charge-transfer inefficiency around 1.8 and 2.2 keV (Hiemstra et al. 2011; Díaz Trigo et al. 2014). The individual spectral parameters of GX 339-4, Swift J1753.5–0127, and GS 1354–64 are given in Table 1.

**Table 1.** Spectral parameters of GX 339-4, Swift J1753.5–0127, and GS 1354–64.

| param. | GX 339/04 | GX 339/09 | Sw1753/06 | Sw1753/12/2 | GS1354 |
|---|---|---|---|---|---|
| $N_{dbb}$ | $40922^{+15215}_{-13085}$ | $10825^{+5996}_{-3448}$ | $1526^{+676}_{-771}$ | $5526^{+1511}_{-1630}$ | $486^{+104}_{-63}$ |
| $T_{in}$ [keV] | $0.202^{+0.013}_{-0.009}$ | $0.223^{+0.014}_{-0.012}$ | $0.213^{+0.033}_{-0.040}$ | $0.257^{+0.014}_{-0.009}$ | $0.50^{+0.01}_{-0.02}$ |
| $\Gamma$ | $1.65 \pm 0.01$ | $1.53^{+0.03}_{-0.05}$ | $1.73 \pm 0.03$ | $1.60^{+0.01}_{-0.06}$ | $1.51^{+0.05}_{-0.03}$ |
| $E_{cutoff}$ [keV] | $7.6 \pm 0.2$ | $7.4 \pm 0.2$ | $> 9.3$ | $7.3^{+0.1}_{-0.2}$ | $6.82 \pm 0.08$ |
| $E_{fold}$ [keV] | $17.8^{+6.5}_{-3.8}$ | $19.8^{+5.6}_{-2.4}$ | – | $15.4 \pm 2.2$ | $9.4 \pm 0.5$ |
| $\chi^2_{red}$ | 0.61 | 0.64 | 0.69 | 1.15 | 0.97 |

## 3 Covariance spectra and ratios

We derived covariance spectra following the approach described in Wilkinson & Uttley (2009). Taking a look at the PDS we selected short time scales related to the decaying part of the PDS, and long time scales related to the top-flat part. As reference band we used the energy range between 1 and 4 keV, taking care to exclude energies from the reference band that are in the channel of interest. To investigate the variability in a model independent way, we derived covariance ratios by dividing the long timescale covariance spectrum by the short timescale one.

The covariance ratios of GX 339-4 and Swift J1753.5–0125 are shown in Fig.1. At soft energies (below 1 keV) an increase of the ratio with decreasing energy is visible. This increase has been interpreted as the sign of additional disc variability on longer timescales (Wilkinson & Uttley 2009). The covariance ratio of GS 1354–64

(Fig.2 left panel) is flat at energies above 1 keV, while at lower energies it decreases with decreasing energy. This behaviour clearly differs from the increase of the covariance ratio towards lower energies, which has been found in later phases of the LHS in GX 339-4 and Swift J1753.5-0125. The covariance ratios observed in the 2008 and 2014 outbursts of H 1743-322 are rather flat (Fig.2 right panel).

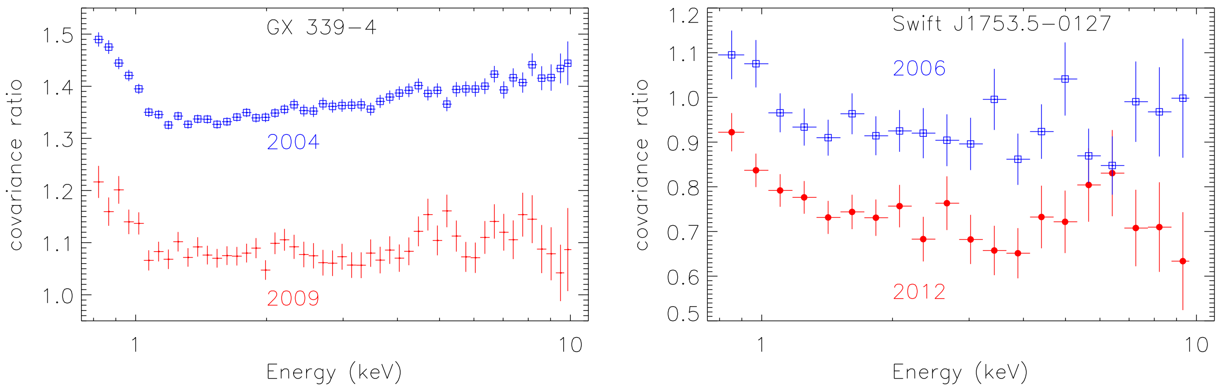


**Fig. 1.** Covariance ratios obtained in the LHS during outburst rise of GX 339-4 (**left**) and Swift J1753.5-0125 (**right**). The ratios show an increase towards lower energies, interpreted as sign of additional disc variability on longer time scales.

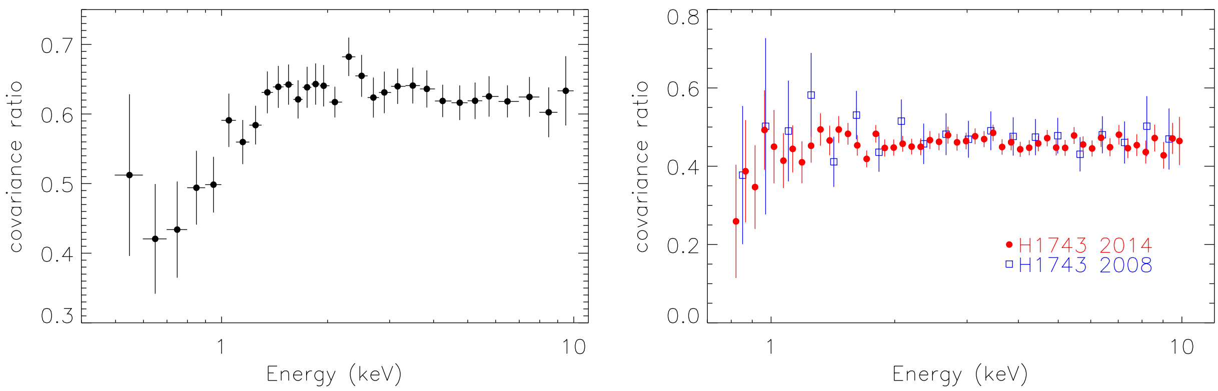


**Fig. 2.** Covariance ratios obtained during "failed" outbursts of GS 1354–64 (**left**) and H 1743-322 (**right**). These ratios do *not* show an increase towards lower energies.

## 4 Discussion

We used *XMM-Newton*/EPIC pn timing mode data of a sample of BHBs to study variability on different time scales and energy ranges using covariance spectra.

The covariance ratio obtained from the *XMM-Newton* observation of GS 1354–64 decreases with decreasing energy below 1 keV (Stiele & Kong 2016), while the one obtained for LHS observations of GX 339–4 and Swift J1753.5–0125 increases with decreasing energy (Wilkinson & Uttley 2009; Stiele & Yu 2015). The increase of the covariance ratio towards lower energies has been interpreted as a sign of additional disc variability on longer timescales. Thus the decrease observed in GS 1354–64 can be either regarded as a sign of missing disc variability on longer timescales or as a sign of additional variability on short timescales. For two observations of H 1743-322 taken during the 2008 and 2014 "failed" outbursts we also found covariance ratios that do not show an increase at lower energies. In case of H 1743-322 the covariance ratios remained rather flat (Stiele & Yu 2016).

Fitting the energy spectra in the $0.8-10$ keV range with the model given in Sect. 2, we found that the energy spectrum of GS 1354–64 differed significantly from the ones of GX 339-4 and Swift J1753.5–0125 (Stiele

& Kong 2016). The inner disc temperature of GS 1354–64 is significantly higher than the temperatures found in the previous study, while the disc blackbody normalisation, photon index, and cut-off and fold energies are lower. With a higher inner disc temperature and a smaller inner disc radius the observed covariance ratio cannot be explained by a faint disc component and it is more likely that the differences in covariance ratio are related to some changes in the accretion process. We note that all three observations that do not show increasing covariance ratio towards lower energies have energy spectra that require a rather low photon index and were taken during "failed" outbursts. Therefore different shapes of covariance ratio, although observed at soft energies, might be driven by changes in the Comptonizing component or they indicate changes in the accretion geometry that determine if a BHB goes into a "normal" or "failed" outburst. We want to mention that in the case of H 1743-322 the different shape of the covariance ratio can also be related to the higher inclination angle of this source in comparison to the inclination of GX 339–4 or Swift J1753.5-0125 (Stiele & Yu 2016). For GS 1354–64 the inclination angle is not known.

A further investigation of these different possibilities must be the aim of future studies as more data are needed. Further insight can be obtained by observations of other sources during a "failed" outburst or at high inclination to extent the size of the sample or by an observation of H 1743-322 in an early LHS during a "normal" outburst with *XMM-Newton*.

This work is based on observations obtained with *XMM-Newton*, an ESA science mission with instruments and contributions directly funded by ESA Member States and NASA. Data used in this work are available from the *XMM-Newton* Science Archive (http://www.cosmos.esa.int/web/xmm-newton/xsa). This work was supported by the National Natural Science Foundation of China under grant Nos. 11073043, 11333005, and 11350110498, by Strategic Priority Research Program "The Emergence of Cosmological Structures" under grant No. XDB09000000 and the XTP project under grant No. XDA04060604, by the Shanghai Astronomical Observatory Key Project and by the Chinese Academy of Sciences Fellowship for Young International Scientists Grant. This project was supported by the Ministry of Science and Technology of the Republic of China (Taiwan) through grants 103-2628-M-007-003-MY3 and 104-281-M-007-060.

## References

Belloni, T. & Hasinger, G. 1990, A&A, 227, L33

Belloni, T., Psaltis, D., & van der Klis, M. 2002, ApJ, 572, 392

Belloni, T. M. 2010, in Lecture Notes in Physics, Berlin Springer Verlag, Vol. 794, Lecture Notes in Physics, Berlin Springer Verlag, ed. T. Belloni, 53

Capitanio, F., Belloni, T., Del Santo, M., & Ubertini, P. 2009, MNRAS, 398, 1194

Díaz Trigo, M., Migliari, S., Miller-Jones, J. C. A., & Guainazzi, M. 2014, A&A, 571, A76

Hiemstra, B., Méndez, M., Done, C., et al. 2011, MNRAS, 411, 137

Houck, J. C. & Denicola, L. A. 2000, in Astronomical Society of the Pacific Conference Series, Vol. 216, Astronomical Data Analysis Software and Systems IX, ed. N. Manset, C. Veillet, & D. Crabtree, 591

Leahy, D. A., Elsner, R. F., & Weisskopf, M. C. 1983, ApJ, 272, 256

Martocchia, A., Matt, G., Belloni, T., et al. 2006, A&A, 448, 677

McClintock, J. E. & Remillard, R. A. 2006, Black hole binaries (Compact stellar X-ray sources), 157–213

Motta, S., Muñoz-Darias, T., & Belloni, T. 2010, MNRAS, 408, 1796

Stiele, H. & Kong, A. K. H. 2016, MNRAS, 459, 4038

Stiele, H. & Yu, W. 2014, MNRAS, 441, 1177

Stiele, H. & Yu, W. 2015, MNRAS, 452, 3666

Stiele, H. & Yu, W. 2016, MNRAS, 460, 1946

Wilkinson, T. & Uttley, P. 2009, MNRAS, 397, 666

Wilms, J., Allen, A., & McCray, R. 2000, ApJ, 542, 914

Yu, W. & Zhang, W. 2013, ApJ, 770, 135

Zdziarski, A. A., Johnson, W. N., & Magdziarz, P. 1996, MNRAS, 283, 193

Zhang, W., Jahoda, K., Swank, J. H., Morgan, E. H., & Giles, A. B. 1995, ApJ, 449, 930

Życki, P. T., Done, C., & Smith, D. A. 1999, MNRAS, 309, 561

*SF2A 2016*
*C. Reylé, J. Richard, L. Cambrésy, M. Deleuil, E. Pécontal, L. Tresse and I. Vauglin (eds)*

# GCT, THE GAMMA-RAY CHERENKOV TELESCOPE FOR MULTI-TEV SCIENCE WITH THE CHERENKOV TELESCOPE ARRAY

H. Sol[1], J.-L. Dournaux[2], P. Laporte[2] and the GCT Team and CTA Consortium[3]

**Abstract.** GCT is a gamma-ray telescope proposed for the high-energy section of the Cherenkov Telescope Array (CTA). A GCT prototype telescope has been designed, built and installed at the Observatoire de Paris in Meudon. Equipped with the first GCT prototype camera developed by an international collaboration, the complete GCT prototype was inaugurated in December 2015, after getting its first Cherenkov light on the night sky in November. The phase of tests, assessment, and optimisation is now coming to an end. Pre-production of the first GCT telescopes and cameras should start in 2017, for an installation on the Chilean site of CTA in 2018.

Keywords: high energy astrophysics, gamma-ray astronomy, Cherenkov telescope, prototype for CTA

## 1 Introduction

CTA, the Cherenkov Telescope Array, is the main global project of ground-based gamma-ray astronomy for the coming decades. Performance will be significantly improved relatively to present instruments, especially with an increase by a factor of ten of the sensitivity and a larger spectral range (Acharya et al. 2013). To achieve such goal, the CTA array will consist of several tens of Cherenkov telescopes of different types and sizes, with 23m, 12m and 4m telescopes respectively devoted to the low-energy sub-TeV domain down to 20 GeV, the intermediate TeV range, and the high-energy domain from a few TeV up to 300 TeV (see Fig. 1). To provide access to the whole sky, two arrays are going to be implemented, one in La Palma, Canary Islands, and one in Chile near Paranal. Pre-production and deployment of the first telescopes on sites are foreseen for 2017-2018. The production phase will then last a few years, with routine user operation expected to start in 2022 and for about 30 years. The nominal CTA southern array will include a sub-array of seventy 4m telescopes spread over a few square kilometres to study the sky at extremely high energies. The Gamma-ray Cherenkov Telescope (GCT) is one of the proposed telescope designs for that sub-array.

## 2 Which science at multi-TeV?

Large field of view instruments like MILAGRO and HAWC have shown that our cosmos harbours some sources emitting in the highest part of the electromagnetic spectrum, above tens of TeV. Extrapolating from present IACT (Imaging Atmospheric Cherenkov Telescopes) like HESS, MAGIC and VERITAS also suggests a variety of phenomena to study at such energies. However this electromagnetic cosmic window is still very poorly known due to limited current sensitivity and angular resolution. CTA, thanks to its large sub-array of 4m telescopes, will allow for the first time a detailed exploration and deep analysis of this extreme domain, from 3 to 300 TeV (Fig. 1). It combines the guarantee of important astrophysical results with a large discovery potential in cosmology and fundamental physics. We give three examples hereafter.

The search for PeVatrons, cosmic accelerators of particles at PeV energies ($10^{15}$ eV) in our Galaxy and in the Large Magellanic Cloud (LMC), will be a key area in this regard, with the pending question of the origin of the most energetic galactic cosmic rays and their impact on their environment. Indeed, recent results by

[1] LUTH, Observatoire de Paris, PSL Research University, CNRS, Place J. Janssen, 92 195, Meudon, France
[2] GEPI, Observatoire de Paris, PSL Research University, CNRS, Place J. Janssen, 92 195, Meudon, France
[3] See `http://www.cta-observatory.org` for full author list and affiliations

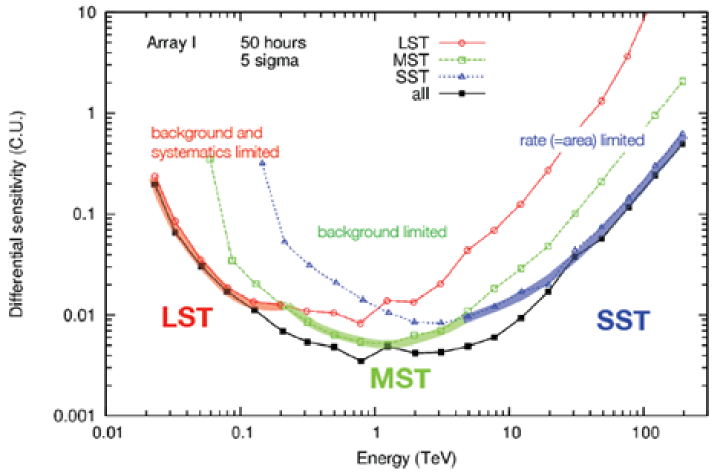


**Fig. 1.** Differential sensitivity of the future CTA array over its spectral range. The LST, MST and SST, respectively large sized, medium sized and small sized telescopes, dominate the sensitivity at low (in red), medium (in green) and high (in blue) energies (Bernlohr et al. 2013) .

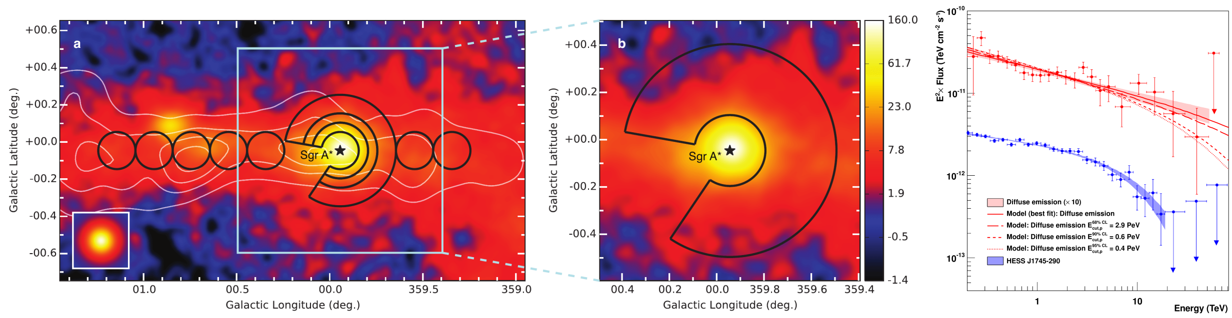


**Fig. 2. Left:** Very high energy (VHE) gamma-ray image of the Galactic Center region in coded colors. White contours indicate the density distribution of molecular gas. The zoomed view of the inner part shows the region used to extract the spectrum of the diffuse emission. **Right:** VHE gamma-ray spectra of the diffuse emission (in red; multiplied by 10) and of the central compact source HESS J1745-290 (in blue). Reproduced from Abramowski et al. (2016).

HESS suggest the first evidence of a cosmic hadronic PeVatron in the Galactic Center as illustrated in Fig. 2. Data show a power-law spectrum without any cutoff or break, up to tens of TeV, from the diffuse emission within the central 10 parsecs of the Milky Way (Abramowski et al. 2016). The galactic central black hole Sagittarius A* could be the source at the origin of this potential PeVatron, but this clearly deserves further investigation. Exceptionnally powerful VHE sources have also been detected in the LMC. Among them, 30DorC is the first unambiguous detection of a superbubble in the TeV range. It exhibits extreme conditions and could be another type of PeVatron to analyse with CTA (Abramowski et al. 2015). In the remote extragalactic space, the multi-TeV range will allow to explore the most powerful acceleration mechanisms in nearby Active Galactic Nuclei (AGN) and in AGN flares, and will open the search for signatures of hadronic versus leptonic processes around supermassive black holes (Sol et al. 2013). Studying the propagation along the line of sight of extremely high energy photons from cosmic sources will offer in addition the opportunity to analyse the diffuse extragalactic background light (EBL) and to probe the fine structure of spacetime, looking for potential clues of Lorentz Invariance Violation (LIV) and of axion-like particles (ALP). Indeed several versions of quantum gravity theories imply that LIV can significantly reduce the EBL opacity to gamma-rays above 10 TeV. The detection of such anomalies in the cosmic opacity could be reachable by CTA with the search for LIV upturn in the multi-TeV spectra of bright blazars (Tavecchio & Bonnoli 2016). Extending the spectral range up to extreme energies should also facilitate the studies of arrival time delays of VHE photons with their energy, which is another possible signature of LIV phenomena.

## 3 The early phase of the GCT project

The GCT is an alt-azimuth dual-mirror telescope based on a Schwarzschild-Couder (SC) optical design never built in astronomy before the advent of CTA. Such SC design offers many advantages for ground-based gamma-ray astronomy, with large field of view and reduced focal length allowing compact and lightweight telescope and camera equipped with Multianode Photo-multiplier (MAPM) or Silicon Photo-multiplier (SiPM) detectors. The camera has been developed by a collaboration involving teams from Australia, Germany, Japan, Netherlands and UK. Conception work and FEA simulations of the telescope started in Meudon in 2011 (Dumas et al. 2014; Dournaux et al. 2016a,b). The mechanical structure has been designed so as to facilitate production, transport, assembly and maintenance. It is composed of the telescope base (tower), the entrainment system (AAS), the dishes and arms supporting the mirrors (OSS), the camera support with the system of camera loading and unloading, and the counterweight. The 4m primary mirror is segmented in six aspherical petals, while the 2m secondary mirror is monolithic. Three on-board cabinets are implemented on the telescope for the telescope control system, as well as a chiller for the cooling of the camera (see Fig. 3).

To test the true performance of the SC design and validate the studies and processes, a complete prototype of the GCT telescope and cameras has been implemented. A first camera and its fast electronics was developed and built by the international collaboration and integrated in laboratory in UK. Foundations were completed in 2012 and a shelter installed early 2013 in Meudon. The manufacturing of the main telescope sub-systems was subcontracted to industries between 2013 and 2015. Meanwhile a control room has been arranged near the site on the Meudon campus.

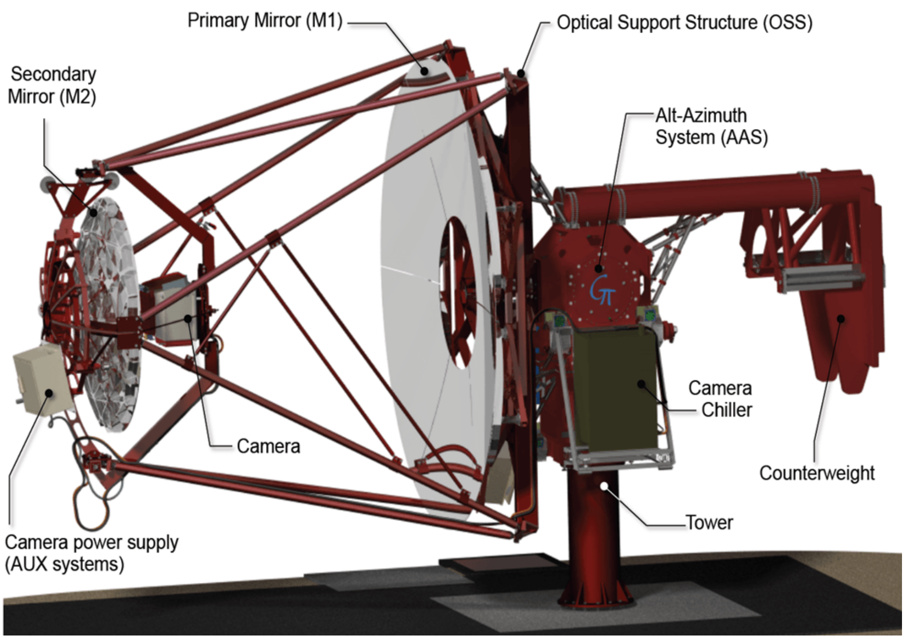


**Fig. 3.** A compact Schwarzschild-Couder telescope: the GCT design and its main sub-systems.

## 4 Assembly of the GCT prototype

Once the production and integration of every sub-system completed, the assembly of the telescope went very quickly in 2015 (see Fig. 4). The mechanical structure was installed in two days by a small team in April. Two days were also needed to mount the secondary mirror and two segments of the primary mirror on the telescope in August. The camera arrived in Meudon mid-November and was installed for the first time on the telescope in less than one week, with all connections operational (power and optical fibre, chiller pipes). The process of loading the camera on the telescope lasted by itself less than 15 minutes thanks to the specific loading-unloading mechanism. The Fig. 5 illustrates various steps of the prototype assembly.

**Fig. 4.** The GCT telescope and camera prototype assembled on the Meudon site (November 2015).

**Fig. 5. Integration of the complete prototype.** From left to right: (I) mounting the OSS on the tower and the AAS in April 2015, (II) the secondary mirror during its installation on the mechanical structure in August 2015, (III) first loading of the camera on the telescope in November 2015, (IV) the main cabinet for the slow control of the instrument.

## 5 First Cherenkov light and inauguration

The week following the installation of the camera on the telescope and after preliminary tests performed under the shelter, the instrument was tested on the Meudon night sky in the evening of November 26th, one day after the full moon. Clouds, city lights, and the almost full moon resulted in a night background rate estimate of about 500 MHz (photoelectrons/sec/pixel), typically 50 times higher than that expected on the Chilean site of CTA. Despite these difficulties, several Cherenkov events characteristic of an air shower signal were detected in a few minutes (Fig. 6). They were the first detection of air showers by a CTA prototype, and the very first Cherenkov light for a dual-mirror Schwarzschild-Couder telescope, never achieved before in astronomy. These results obtained during poor weather and light conditions, and before any optimisation of the instrument, appeared as very promising. They have been an important step towards the validation of the concepts and technologies, and for the preparation of CTA, recognised by the international community (Dournaux et al. 2016c). The GCT prototype was inaugurated a few days after its first light, in the presence of representatives of institutes and agencies and with the participation of CTA and VHE scientists (Fig. 6).

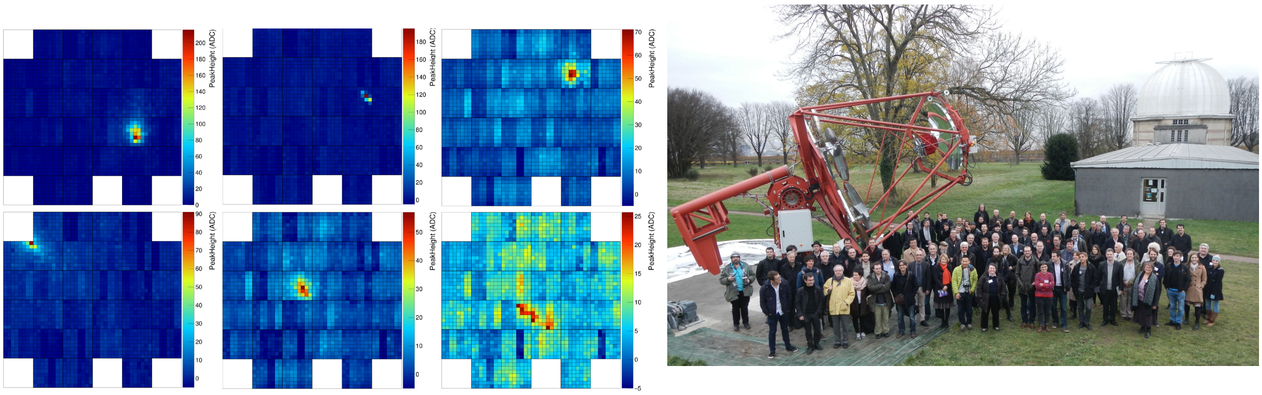

**Fig. 6. Left:** The first Cherenkov light, with integrated images of some atmospheric showers detected on the night sky in Meudon on November 26th, 2015 (extracted from Watson et al. (2016)). Such events typically last about ten nanoseconds (see for instance a short video available at cta.obspm.fr). **Right:** The inauguration of the GCT prototype on December 1st, one week after the first light. @The GCT Consortium

## 6 Test phase and assessment

After the commissioning of the complete prototype, several tests and developments were performed in 2016 both for the camera and for the telescope. Following the Design Verification Document and conformity matrix, about 300 tests were necessary in mechanics, optics, electronics and RAMS to check that the telescope structure, mirrors, slow control and security meet all specifications and CTA requirements. A preliminary virtual model of the telescope has been developed with the TPOINT software, after pointing observations of bright stars and planets with a CCD camera installed at the focal surface. Residual misalignments and flexures can then be deduced and modelled, which allows for further correction of geometrical effects and tube flexure.

The test phase is now coming to an end. Most of the time it has validated the performance, as for instance the alignment accuracy of axes as well as azimuth and elevation angular velocities (see Fig. 7), maximum power, pointing accuracy, emergency stop, etc. No technological barrier and specific risks have been identified. Some components not yet implemented on the prototype need to be added, like actuators and baffles for the mirrors, and some others need to be slightly modified for various reasons, like the camera support to improve the telescope-camera interface after some change in the mechanical structure. A special attention is payed to mirrors in order to select the best industrial solution before starting mass production. Work is now in progress to optimise the detailed design plans for GCT-1, the first GCT telescope to be built in pre-production for the southern array of CTA, based on knowledge and expertise gained during the prototyping and assessment phase.

Detailed simulations of the instrument performance are now available (Costantini et al. 2016) and both telescope and camera are better known and calibrated than last year. Slow control for the telescope and data handling for the Cherenkov camera have been improved. A second observational campaign with the Cherenkov camera is planned in Meudon before the end of 2016. It should complete our knowledge of the overall behaviour of the equipment while operating on the night sky.

## 7 Conclusion and perspectives

The international GCT consortium aims to build 35 telescopes equipped with Cherenkov cameras as in-kind contribution to the CTA Observatory. For the telescope structure, slow control and secondary mirror, the intent is to launch a call for tender in early 2017 and to select an industrial prime for the production of a first telescope unit GCT-1, in order to install it in Chile in the first part of 2018. It will allow validation of the whole industrialisation process as well as of assembly and operation on site. A number of other telescope units will be ordered afterwards following the schedule presented in Fig. 8, when France decides to start the funding of the construction phase of CTA. The project ensures the participation of the French CTA community and its direct involvement on site from the beginning of the implementation of the southern array. It should contribute to the first partial operations of the CTA array under construction in about two years from now, with the obtention of the first experimental data. Full operations of CTA are foreseen for the horizon 2022 and for 30 years.

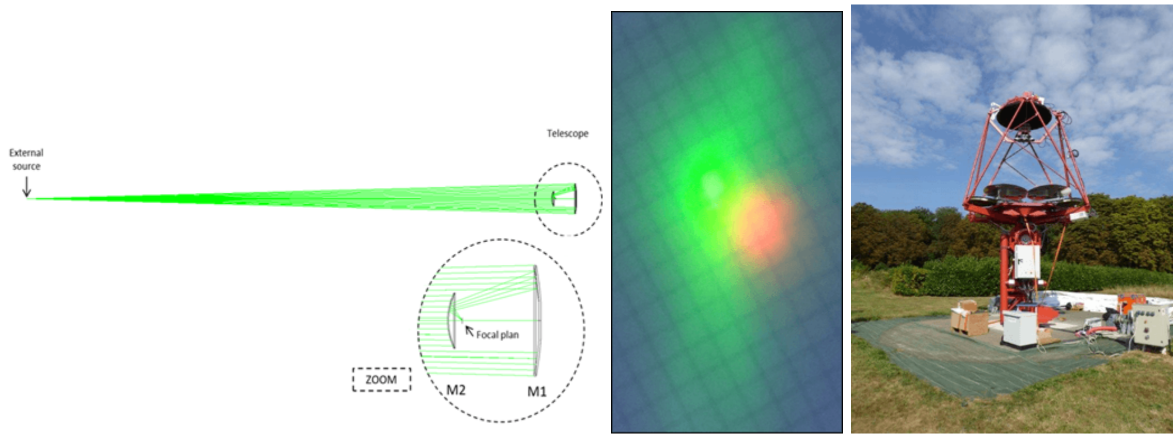


**Fig. 7. Left:** Test of the alignment of the mechanical and optical axes. A green laser at 77 m distance illuminates segments of the primary mirror and materialises the optical axis on the focal surface. A red laser is attached along the mechanical axis. **Middle:** Image of the two axes on the focal surface, with squares of side 5 mm. Axes are coincident within tolerance, prior to any adjustment of the mirror alignement with actuators. **Right:** Testing the motorisation and entrainment of the telescope. Here the telescope is at 91 degrees in elevation.

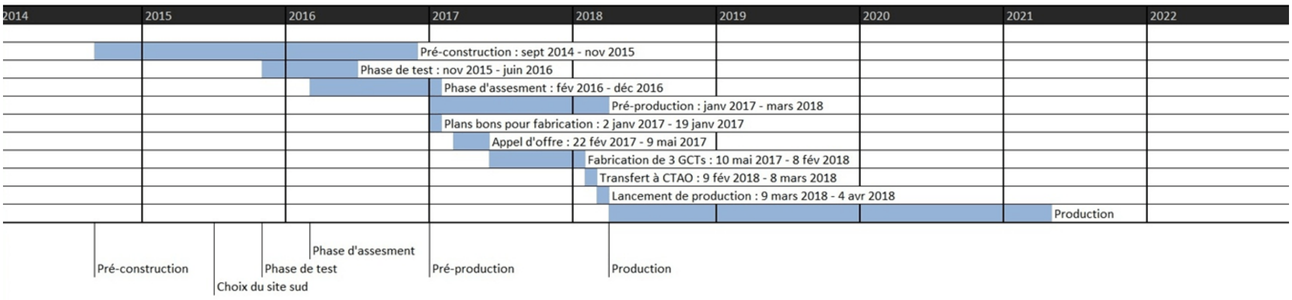


**Fig. 8.** Indicative agenda of the GCT array implementation for the CTA production and deployment.

**Acknowledgements:** We gratefully acknowledge support from the agencies and organisations listed under Funding Agencies at this website: `http://www.cta-observatory.org/` and the Programme National Hautes Energies (PNHE) of the CNRS.

## References

Abramowski, A., et al, 2015, Science, 347, 406

Abramowski, A., et al, 2016, Nature, 531, 476

Acharya, B.S., et al, 2013, Astroparticle Physics, 43, 3

Bernlohr, K., et al, 2013, Astroparticle Physics, 43, 171

Costantini, H., Dournaux, J.-L., Ernenwein, J.-P., Laporte, P., Sol, H., et al, 2016, Proceedings of the Gamma 2016 symposium, Heidelberg (in press; arXiv:1610.01427v1)

Dournaux, J.-L., Amans, J.P., Dangeon, L., Fasola, G., et al, 2016a, Proceedings SPIE 9912 (in press)

Dournaux, J.-L., Gironnet, J., Huet, J.M., Laporte, P., et al, 2016b, Proceedings SPIE 9912 (in press)

Dournaux, J.-L., De Franco, A., Laporte, P., White, R., Greenshaw, T., Sol, H., et al, 2016c, Nuclear Instruments and Methods in Physics Research A, `http://dx.doi.org/10.1016/j.nima.2016.05.059`

Dumas, D., Huet, J.-M., Dournaux, J.-L., et al, 2014, Proceedings SPIE 9145

Sol, H., Zech, A., Boisson, C., et al, 2013, Astroparticle Physics, 43, 215

Tavecchio, F., Bonnoli, G., 2016, A&A, 585, A25

Watson, J.J., De Franco, A., Abchiche, A., et al, 2016, Proceedings of the Gamma 2016 symposium, Heidelberg (in press; arXiv:1610.01452v1)

*SF2A 2016*
*C. Reylé, J. Richard, L. Cambrésy, M. Deleuil, E. Pécontal, L. Tresse and I. Vauglin (eds)*

# MODELS OF FAST RADIO BURSTS AT COSMOLOGICAL DISTANCES

F. Mottez[1], C. Guépin[2], K. Kotera[2, 3], G. Voisin[1] and P. Zarka[4]

**Abstract.** Fast radio bursts are isolated radio pulses of high amplitude, with a frequency / time delay relation that can be interpreted as the dispersion measure (DM) of a source at cosmological distances (several hundreds of Mpc). Up to 2015, the only known FRBs all had different locations on the sky, and different DM. Many theoretical explanations of FRBs have been proposed. Some of them are associated to unique cataclysmic events, others are compatible with the repetition of bursts from the same source. The recent publication of the repeating FRB 121102 shows that at least some of the FRB must be compatible with non-cataclysmic events. A model based on the interaction of a highly relativitic pulsar wind with a body orbiting the pulsar (planet, big asteroid, white dwarf) could explain FRBs. It is briefly compared with other models of repeating FRBs.

Keywords: fast radio bursts, pulsars, wind, cyclotron maser

## 1 Introduction

Fast radio bursts are isolated radio pulses ($\sim$ GHz) similar to a pulsar pulse but of high amplitude (several Janskys). Their duration is typically $\sim$ 5 ms at a given frequency. About 30 FRBs have been observed at the Parkes, Arecibo and Greenbank radio-telescopes since the first discovery in 2006. Their distribution in the sky is not uniform, but not enhanced in the galactic plane (Petroff et al. 2016).

Like pulsar signals, FRBs have a dispersion measure (DM). The DM is a number relating a time delay from the source (at distance $d$) to observer that depends on the frequency,

$$(\frac{t}{s}) = 4.2 \times 10^3 (\frac{\nu}{MHz})^{-2} DM, \quad \text{and} \quad DM = \int_0^d n_e dz, \tag{1.1}$$

where $n_e$ is the electron number density, and the integral is computed along the line of sight. A large DM implies a lot of electrons encountered. The DM of FRBs (>300 pc.cm$^{-3}$) is much larger than those of pulsars (typically less than 150 pc.cm$^{-3}$, even for the most distant ones). There can be two explanations to a large DM : (1) the distance $d$ is large. The source is outside our galaxy, and only "normal" ISM and inter galactic medium (IGM) is met. Or (2) electron density $n_e$ is unusually high somewhere between the source and us. The source can be inside the Galaxy, but there is a somehow dense nebulae/corona... between the source and us. With FRBs, the first hypothesis leads to distances $d \sim 100 - 1000$ Mpc (Lorimer et al. 2007). Let us notice that a few FRBs exhibit scattering; this is characteristic of turbulence in interstellar an/or intergalactic medium (Katz 2016b).

[1] LUTH, Observatoire de Paris, PSL Research University, CNRS, Université Paris Diderot, 5 place Jules Janssen, 92195 Meudon
[2] Sorbonne Universités, UPMC Univ. Paris 6 et CNRS, UMR 7095, Institut d'Astrophysique de Paris, 98 bis bd Arago, 75014 Paris, France
[3] Laboratoire AIM-Paris-Saclay, CEA/DSM/IRFU, CNRS, Université Paris Diderot, F-91191 Gif-sur-Yvette, France
[4] LESIA, Observatoire de Paris, PSL Research University, CNRS, Université Paris Diderot, Université Pierre et Marie Curie, 5 place Jules Janssen, 92195 Meudon

## 2 Constraining the models of FRBs

What make FRBs so mysterious is their high dispersion measure. Nevertheless, the models of FRB should also explain their brevity, their production rate (extrapolated to $10^3$ to $10^4$ per sky per day), their location in galactic coordinates, and their lack of counterpart (up to now) at other frequencies.

A few special FRBs that could help to validate/invalidate models. For instance, FRB 140514 has 21% circular polarization (Petroff et al. 2015), and FRB 121102 is a repeating one ! Spitler et al. (2016); Scholz et al. (2016).

The repeating FRB 121102 is especially interesting because it is compatible with none of the (many) models based on cataclysmic events. For a total of 60 hours of observation between 2012 and 2016, 17 bursts of FRB 121102 have been observed with Arecibo at 1.4 GHz, 1 in Parkes, 5 with GBT at 2 GHz. None were seen in Lovell, Jansky VLA, and Effelsberg.

The distribution of the bursts is not "regular" : 6 bursts were seen during a 10-min period, and 4 in a 20-min period. All these bursts have the same DM=599 pc cm$^{-3}$ (but two), and the same $\delta$ and RA. The bursts have varied amplitudes, varied spectral shapes that do not exhibit power law Spitler et al. (2016). Bursts number 8 and 10 are double peaked. The bursts of FRB 121102 have no circular nor linear polarization. No periodicity was found. No hard X /soft $\gamma$-ray burst counterpart was found with Swift, Fermi, MAXI, and INTEGRAL.

## 3 Models versus locations of FRB

The models of FRB are numerous, and they correspond to sources at various distances. For instance, models invoking giant flares from a star or compact binary stars suppose a thick plasma layer near the source in order to cause the DM (Loeb et al. 2014). The weak point with this models is the distribution of FRBs in the sky : the galactic disk is not a privileged direction.

The same requirement of DM near the source is associated with models of FRB in nearby galaxies : flares from a magnetar near a galactic nucleus (Pen & Connor 2015), or the interaction of a young pulsar with its supernova remanent (Connor et al. 2016).

For sources in $z \sim 0.2 - 1$ galaxies, the DM excess can come from the inter galactic medium (IGM). Many of these models are based on unique cataclysmic events: NS star collapse into BH, NS merger, but they are not compatible with the repeating FRB 121102.

A popular model since the discovery of the repeating FRB is based on super-giant flare from magnetar Katz (2016a). It explains the DM, the possibility of repeating bursts. But magnetar giant flares are usually bright in X-rays or gamma-rays, and it is not very clear yet why the ones that cause FRB would only be seen in radio waves (Tendulkar et al. 2016).

Another very popular model considers a super-giant-Crab-like pulse (Katz 2014). It is compatible with the random succession of bursts, and the excess of DM can be caused partly in the vicinity of the source, and partly in the IGM. The idea of super-giant-Crab-like pulses is particularly interesting because the Crab giant pulses are random radio signals without couterpart at other wavelengths, as is the case with FRBs.

Actually, this model, and the model of super-giant flare from magnetar, are based on extrapolation of the properties of well known signals, but not yet on a well founded theoretical explanation. For instance, there are explanations to the giant pulses of the Crab, but not to the 1000 times more energetic pulses that would correspond to the FRB. It seems that some more theoretical work must be done.

Other models of very distant sources of FRB invoke bodies orbiting or falling on pulsars. Geng & Huang (2015); Dai et al. (2016) have developped a model of FRB caused by asteroids falling on a neutron star. This model is partly inspired from an old (and finaly discarded) model of gamma-ray burst developped by Colgate & Petschek (1981). It can explain the release of energy, possibly in the form of radio waves.

Mottez & Zarka (2014) have developed a model that invoke planets, large asteroids, or white dwarfs, orbiting a pulsar in interaction with the pulsar wind. This model is compatible with sources at cosmological distances, despite the relatively low amount of energy that they require (see section 4).

The models of magnetar super-giant flares, of Crab-like-super-giant pulses, or asteroid fallback, and pulsar orbiting bodies are all compatible with a repeating source of FRB at cosmological distance, or a least in another galaxy.

We outline now the main concepts associated to the Mottez & Zarka (2014) model.

## 4 Pulsar companions and the extreme collimation of radiation when the radio-source comes at relativistic speed

When a source of radiation propagates at relativistic speed, the radiation is focused in the direction of the motion of the source, along a cone that, for high Lorentz factors has a characteristic angle $\sim 1/\gamma$. This means that (1) the signal is perceptible from a narrower range of angles, (2) all the energy is focussed a narrow solid angle $\sim 1/\gamma^2$, therefore it corresponds to a strong amplification of the received signal, in comparison to what would be obsered in the reference frame of the source.

Active nuclei galaxies provide a well-known example of relativistic aberration. Many active galactic nuclei are associated with a relativistic jet with a Lorentz factor about $\gamma \sim 10$. When we, observers, are along the axis of the jet, we observe very bright emissions, called BL Lac, and this brightness is caused by the relativitic aberration.

Pulsars are surrounded by winds of electron and positron plasmas (possibly also with ions) with Lorentz factors that could reach values up to $10^6$ or more... Let us suppose that this wind is perturbed by a solid body orbiting into it. If the perturbation is directly attached to the planet, the source moves with the planet, and is not relativistic, and nothing is expected to be observed over long distances. But the planet can develop a structure that extends far from the solid planet into the wind. If the planet is magnetized, and if the wind is super-Alfvénic, this can take the form of a magnetosphere. But we know that the pulsar wind, as long as the magnetic energy is not dissipated, is sub-Alfvénic (Mottez & Heyvaerts 2011b). (Both the Alfvén velocity $v_A$ and the plasma speed $v_W$ are close to $c$ but $v_W < v_A$.)

In that case, two stationnary Alfvén waves anchored to the planet are long structures that extend very far from the solid planet into the wind. They are called Alfvén wings*. Their angle with the wind direction is very small (Mottez & Heyvaerts 2011b,a).

Therefore when the pulsar wind crosses this structure, it is perturbed by it during a short fraction of a second (in the observer/planet frame). Then, it is the source of radio emission triggered by a cyclotron maser instability. Therefore, the source composed of this perturbed pulsar wind propagates at the highly relativistic velocity of the pulsar wind. This represents an extreme case of relativistic aberration, where a signal of moderate amplitude (compared to a cataclysmic event, or a flare) that is emitted continuously, can give rise to a FRB like radio-signal that is observables hundreds of Mpc away, during the few milliseconds during which the neutron star, the planet (more precisely, the associated Alfvén wing) and the observer on Earth are aligned Mottez & Zarka (2014, 2015).

## 5 Models invoking asteroids are plausible because small bodies can survive near a neutron star

Two of the above cited models consider that small bodies can approach a pulsar, and possibly fall onto it. Considering the amount of energy radiated by a pulsar, it may seem strange that they are not quickly evaporated at low distances. Actually, most of the energy is released in the form of a pulsar wave (Deutsch 1955). This is a strong magnetic wave radiating at the pulsar rotation period $P_*$ in the range $10^{-3} - 10$ s. This is a high rotation frequency, but a very low electromagnetic wave frequency corresponding to wavelengths much larger than the size of a small pulsar companion. This makes absorption of wave energy very inefficient. Following the Mie theory, the absorption rate of energy of a $\sim 1$ km asteroid is smaller than those of a large companion by about six orders of magnitude. Then, asteroids can survive hundred of thousand years at close distance from a pulsar, when larger bodies cannot (Kotera et al. 2016).

## 6 The pulsar companion model of FRB: compatibility with recent observations

According to this model, a single body orbiting a pulsar would be the cause of a signal (a few ms long) that is repeated periodically, at every revolution of the body (a few hours to a few months or years). Up to now, no periodic FRB repeater has been observed. But we have no proof that the known FRBs are non periodic, because none of them has been observed continuously over periods covering days... or months.

The repeating FRB 121102 could be caused, not by a single body orbiting a pulsar, but with a stream of large asteroids that could, for instance be the result of the tidal disruption of a planet. We have said that 6 burst were seen during a 10-min period, and 4 in a 20-min period. This is compatible with the fact that some of

*Alfvén wings exist with non-magnetized as well as with magnetized bodies.

these asteroids could remain gravitationally bound, like the many asteroids seen in the solar system that evolve in groups of two or three (126 groups of two in the asteroid belt, 7 groups of three).

The model also shows that bursts would be typically composed of four or two peaks would be emitted. More if the body cross the line of sight in a time longer than the pulsar period. The bursts intensities depend on the size of the body, on its distance to the neutron star and on the Lorentz factor of the wind. The two brightest peaks can have the same amplitude, or very different ones. This is compatible with pulses with a single peak (the majority of the observed pulses), if the two bursts are not resolved in time, or if only one peak amplitude is above the detector noise level. The model of Mottez & Zarka (2014) is also compatible with the two double peaked bursts observed with FRB 121102.

## 7 The pulsar companion model of FRB: compatibility with other models

The model of FRB caused by bodies orbiting pulsar have a common point with those of FRB caused by asteroids falling onto the neutron star : they both involve a neutron star and objects orbiting it. But there are many differences. The Mottez & Zarka (2014) model is like those of a light-house, with a continuously emitted radiation that we capture only when the observer is in the (extremly narrow) emission-beam. The Geng & Huang (2015) model suppose that the time during which the radio-waves are emitted corresponds to the destruction of the asteroid near the star surface, and there is no relativistic aberration induced beam focusing.

The Mottez & Zarka (2014) model has nothing either in common with the popular model of magnetar super-flares. The flares are supposed to be caused by restructurations that are internal to the neutron star.

Conversely, the Mottez & Zarka (2014) model could be compatible with those of the super-giant-Crab-like pulses. Indeed, if we consider the young Crab pulsar as a neutron star surrounded by a high amount of small-size asteroids (condensed debris from the supernova), each of these asteroids in the Crab wind could be associated with Alfvén wings. Consequently, each of those asteroids would be a radio source that would behave like a mini-FRB.

Actually, the Geng & Huang (2015) model would be also compatible with a model of Crab giant pulses, if each pulse is caused by an asteroid falling onto the Crab neutron star. But the Mottez & Zarka (2014) would have the advantage of explaining why the Crab giant pulses are only seen in radio, when counterparts at other wavelengths could be expected from asteroids falling onto the star[†].

This work is supported by the PNHE/CNRS/INSU. C. Guépin is supported by a fellowship from the CFM Foundation and acknowledges support from the Labex ILP (reference ANR-10-LABX-63, ANR-11-IDEX-0004-02). G. Voisin is supported by a fellowship from the École Normale Supérieure de Cachan.

## References

Colgate, S. A. & Petschek, A. G. 1981, ApJ, 248, 771

Connor, L., Sievers, J., & Pen, U.-L. 2016, MNRAS, 458, L19

Dai, Z. G., Wang, J. S., Wu, X. F., & Huang, Y. F. 2016, The Astrophysical Journal, 829, 27

Deutsch, A. J. 1955, Annales d'Astrophysique, 18, 1

Geng, J. J. & Huang, Y. F. 2015, The Astrophysical Journal, 809, 24

Katz, J. I. 2014, Phys. Rev. D, 89, 103009

Katz, J. I. 2016a, ApJ, 826, 226

Katz, J. I. 2016b, ApJ, 818, 19

Kotera, K., Mottez, F., Voisin, G., & Heyvaerts, J. 2016, A&A, 592, A52

Loeb, A., Shvartzvald, Y., & Maoz, D. 2014, MNRAS

Lorimer, D. R., Bailes, M., McLaughlin, M. A., Narkevic, D. J., & Crawford, F. 2007, Science, 318, 777

Mottez, F. & Heyvaerts, J. 2011a, Astronomy and Astrophysics, 532, A22+

Mottez, F. & Heyvaerts, J. 2011b, Astronomy and Astrophysics, 532, A21+

Mottez, F. & Zarka, P. 2014, A&A, 569, A86

Mottez, F. & Zarka, P. 2015, in SF2A-2015: Proceedings of the Annual meeting of the French Society of Astronomy and Astrophysics, ed. F. Martins, S. Boissier, V. Buat, L. Cambrésy, & P. Petit, 237–240

[†]The first model by Colgate & Petschek (1981) of asteroids falling onto a neutron star was designed to explain gamma-ray bursts!

Pen, U.-L. & Connor, L. 2015, ApJ, 807, 179

Petroff, E., Bailes, M., Barr, E. D., et al. 2015, MNRAS, 447, 246

Petroff, E., Barr, E. D., Jameson, A., et al. 2016, PASA, 33, e045

Scholz, P., Spitler, L., Hessels, J., et al. 2016, in AAS/High Energy Astrophysics Division, Vol. 15, AAS/High Energy Astrophysics Division, 105.03

Spitler, L. G., Scholz, P., Hessels, J. W. T., et al. 2016, Nature, 531, 202

Tendulkar, S. P., Kaspi, V. M., & Patel, C. 2016, ApJ, 827, 59

*SF2A 2016*
*C. Reylé, J. Richard, L. Cambrésy, M. Deleuil, E. Pécontal, L. Tresse and I. Vauglin (eds)*

# MODELING THE REVERBERATION OF OPTICAL POLARIZATION IN AGN

P. A. Rojas Lobos[1], R. Goosmann[1] and F. Marin[1]

**Abstract.** According to the standard paradigm, the strong and compact luminosity of active galactic nuclei (AGN) is due to multi-temperature black body emission originating from an accretion disk formed around a supermassive black hole. This central engine is thought to be surrounded by a dusty region along the equatorial plane and by ionized winds along the poles. The innermost regions cannot yet be resolved neither in the optical nor in the infrared and it is fair to say that we still lack a satisfactory understanding of the physical processes, geometry and composition of the central (sub-parsec) components of AGN. Like spectral or polarimetric observations, the reverberation data needs to be modeled in order to infer constraints on the AGN geometry (such as the inner radius or the half-opening angle of the dusty torus). In this research note, we present preliminary modeling results using a time-dependent Monte Carlo method to solve the radiative transfer in a simplified AGN set up. We investigate different model configurations using both polarization and time lags and find a high dependency on the geometry to the time-lag response. For all models there is a clear distinction between edge-on or face-on viewing angles for fluxes and time lags, the later showing a higher wavelength-dependence than the former. Time lags, polarization and fluxes point toward a clear dichotomy between the different inclinations of AGN, a method that could help us to determine the true orientation of the nucleus in Seyfert galaxies.

Keywords: Galaxies: active, galaxies: nuclei, polarization, radiative transfer

## 1 Introduction

Active galactic nuclei (AGN) are the strongest steady sources in the Universe. While being extremely spatially compact, they produce enough bolometric luminosity to eventually outshine their host galaxy. It is an accepted paradigm that such strong and compact emission is due to accretion onto a supermassive black hole (SMBH, Salpeter 1964; Lynden-Bell 1969). In thermal, radio-quiet AGN the SMBH is surrounded by an accretion disk producing the optical and UV continuum radiation (see Shields 1978, Shakura and Sunyaev 1973 and Pringle, Rees and Pacholczyk 1973). This emission is reprocessed by other structures surrounding the disk, such as the so-called broad line emission region (BLR), or a circumnuclear dusty medium often called the "dusty torus" (Antonucci 1993). This dusty region extends to a spatial scale of a few parsecs for a $10^7 M_\odot$ SMBH, but only in very few objects the circumnuclear dust is barely resolvable by near-IR interferometry techniques. The innermost parts cannot yet be resolved neither in the optical nor the infrared and it is fair to say that we still lack a satisfactory understanding of the physical processes, geometry and composition of the central (sub-parsec) components of AGN.

Both, the BLR and the dusty torus are somewhat confined to the equatorial plane that is defined by the accretion disk. The dusty torus is opaque to optical light (Gaskell 2009) and therefore obscures the BLR at all lines of sight intercepting it. Observers at such equatorial viewing angles do not see broad optical emission lines and therefore observe a so-called type-2 AGN. At polar viewing angles, the BLR is visible and the optical spectrum denotes a type-1 object. This is a fundamental axis of the so-called Unified Model of AGN that attempts to explain the observational diversity of active galaxies as an orientation effect. To verify this scenario the role of polarimetry was crucial. Antonucci (1984) and Antonucci and Miller (1985) observed polarized broad lines in highly inclined Seyfert galaxies and found a relation between low inclination (type-1) and high-inclination sources (type-2). They thus postulated that both AGN types share the same morphology but are

[1] Observatoire Astronomique de Strasbourg, Université de Strasbourg, CNRS, UMR 7550, 11 rue de l'Université, 67000 Strasbourg, France

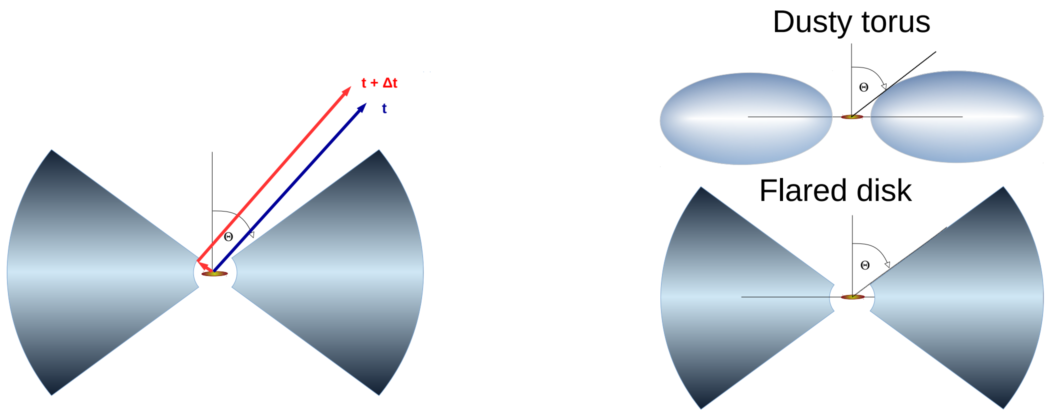


Fig. 1: Left: Reverberation principle – the blue line traces unpolarized photons coming directly from the source. The red line shows photons scattered inside the equatorial scattering region (polarized light). Right: model geometries – the doughnut-shaped torus (top) and the extended flared-disk geometry (bottom).

seen at a different system inclination. Since then, a lot of effort has been put into understanding the complex polarization signal observed in the optical band. In particular, Smith et al. (2004) suggested that a flattened equatorial scattering region could explain the specific polarization observed in type-1 AGN: a low polarization degree $P$ (inferior to 1% in most of the cases) associated with a polarization position angle parallel to the symmetry axis of the circumnuclear dust region. It was shown by our collaboration that also a wide half opening angle of the dusty torus produces the polarization characteristics of type-1 AGN Marin et al (2012).

Knowing that flattened scattering regions in type-1 AGN produce continuum polarization should make it possible to conduct polarization reverberation mapping as introduced by Gaskell et al. (2012). The reverberation lag is due to a difference in light travel time between continuum radiation coming directly from the accretion disk and scattered radiation coming from structures farther away (e.g., from the torus, see Fig. 1, left). It is obtained by cross-correlating the optical continuum lightcurve with the polarized spectrum. The latter is obtained by multiplying the polarization fraction with the spectral intensity. The polarized time lag holds information on the average distance between the continuum source and the scattering regions. In this way, Gaskell et al. (2012) were able to infer the size of the inner scattering regions in the Seyfert-1 galaxy NGC 4151.

Like spectral or polarimetric observations, the reverberation data needs to be accurately modeled to infer constraints on the AGN geometry (such as the inner radius or the half-opening angle of the dusty torus). In this research note, we present preliminary modeling results using a time-dependent Monte Carlo method to solve the radiative transfer in a simplified AGN set up. We present results for polarization and time lags assuming different model configurations.

## 2 Modeling the circumnuclear region

The STOKES code is a Monte-Carlo radiative transfer code written by Goosmann and Gaskell (2007), Marin et al (2012) and Marin, Goosmann and Gaskell (2015) that computes the Stokes parameters of light, from which we can derive the polarization percentage, position angle, and total flux. In its latest public version, it also stores the time information in order to compute time-lags. The code allows the user to define different geometries and opacities for emission and scattering structures around a set of emitting regions. A free-to-download version of the code (v1.2 at this moment) can be found at: http://www.stokes-program.info/ . A recent review of the code performance is given in Marin & Goosmann (2014).

To investigate how polarized reverberation mapping can improve our knowledge of the morphology and composition of the dusty region at the center of AGN, we constructed a toy-model representative of the inner few parsecs of a Seyfert galaxy. At the center of the model, we implemented an irradiating continuum source using an isotropic point-like region emitting an unpolarized flux according to a power-law spectrum $F_* \propto \nu^\alpha$ with $\alpha = 1$. Around it we defined a flattened dust distribution that could take two distinct forms: either a flared-disk or an elliptically-shaped torus. An illustration of the two geometries can be seen in Fig. 1 (right). The filling of the equatorial region was either uniform (volume filling factor equal to unity) or non-uniform, i.e.

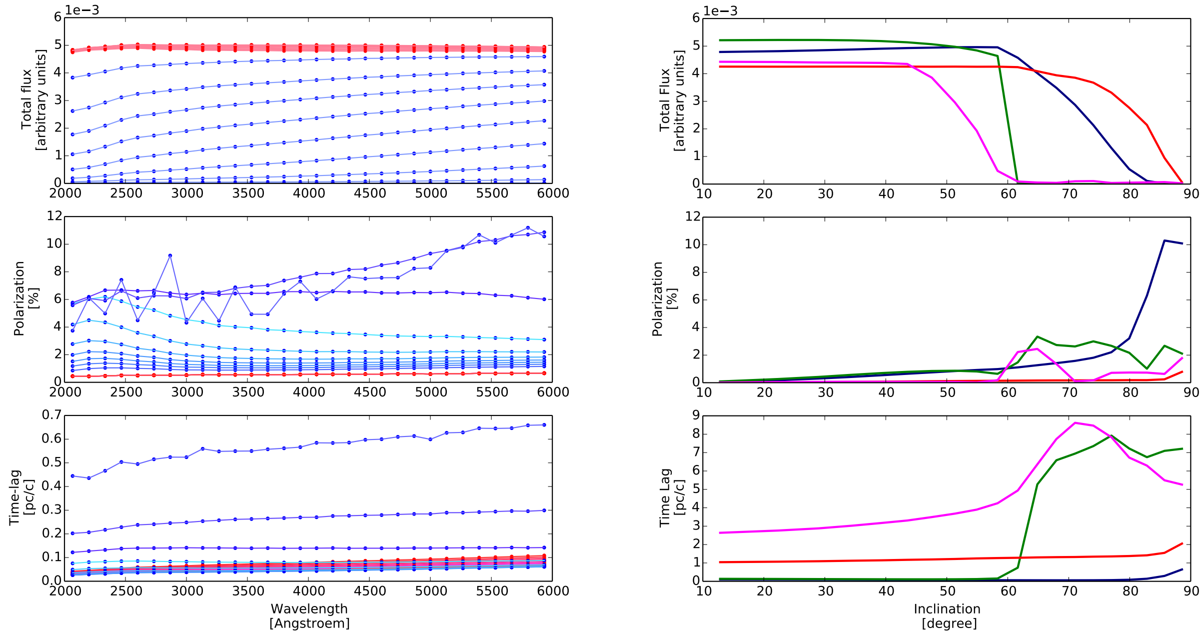


Fig. 2: Total flux (top), polarization percentage (middle) and time lag (bottom). The red dots show viewing angles lower than 60° (type-1) and blue dots show viewing angles above 60° (type-2). Left: Plots as a function of wavelength (left) for a uniform-density torus. Right: V-band data as a function of the system inclination. Blue line: uniform-dusty-torus, green line: uniform-flared-disk, red line: clumpy-dusty-torus, magenta line: clumpy-flared-disk.

clumpy (volume filling factor = 25). For all models, we considered the same torus dimensions: distance from the center: 0.0067 pc, external radius: 15.0067 pc, and inclination angle: 30° from the symmetry axis. The inner radius was set according to the time lag of 8 light-days found by Gaskell et al. (2012) for NGC 4151. The outer torus radius and the half-opening angle are based on near-infrared polarimetric observations by Ruiz et al. (2003). The dusty region is optically thick, as is expected from observations with a total optical depth of $\sim 150$ along the observer's line-of-sight. Both models (flared-disk and toroidal geometries) were tested with two dust prescriptions: "AGN-dust" presented in Gaskell et al. (2004) and "MilkyWay-dust" ("MW-dust") as prescribed by Mathis, Rumpl & Nordsieck (1977). AGN-dust is composed of 85% silicate and 15% graphite; MW-dust is composed of 62.5% silicate and 37.5% graphite. The grain radius, $a$, varies from 0.005$\mu$m to 0.250$\mu$m following a distribution $n(a) \propto a^s$ with $s = -2.05$ for AGN and $s = -3.5$ for MW dust.

## 3 Results

We first study the case of a uniform-density torus. In Fig. 2 (left), we plot the spectral flux, polarization and time lag as a function of wavelength. The spectral results can be compared to earlier work given in (Goosmann and Gaskell 2007). It turns out that both the strong direct emission seen at type-1 viewing angles and the significantly weaker scattered emission seen at type-2 orientations are mostly independent of wavelength. A slight depression is seen below 3000 Å, which can be related to Mie scattering becoming more prominent versus Rayleigh scattering as well as to the presence of the dust-related 2175 Å feature. Apart from a similar variation in the near-UV and a slight overall rise towards longer wavelengths, the time lag is mostly insensitive to wavelength. This behavior is confirmed for the other modeling geometries studied in this work. Furthermore, it was discussed in (Goosmann and Gaskell 2007) that the polarization properties induced by dust scattering in toroidal geometries do not vary much with wavelength. Next, we focus on the results as a function of the system inclination (Fig. 2 right). It turns out that the time lag of the polarized emission is not affected when modifying the dust prescription. Thus, we only present modeling results for the case of standard "Milky Way" dust. A discussion on the dust prescription and polarization effects is given in Goosmann and Gaskell (2007).

The total flux and polarization as a function of inclination confirm what was shown in previous papers (Goosmann and Gaskell 2007; Marin et al 2012; Marin, Goosmann and Gaskell 2015). The flux must be much stronger at polar viewing angles (such as expected from type-1 AGN) than below the torus horizon (type-2) where only scattered radiation is seen. The scattered radiation is more strongly polarized but also accumulates a larger time lag. Notice that a time lag of zero corresponds to the direct emission from the source seen by the observer without any deviation. The fact that the time lag and the polarization fraction at type-1 inclinations are still larger than zero is due to the superimposed scattered component. At type-2 viewing angles the observed radiation must scatter inside the torus funnel before it escapes, increasing the time lag significantly.

The angular profile of the total flux, polarization and the time lag differ between the four geometries. We find a difference in the angular flux distribution between flared and toroidal shapes: the flared disk allows less radiation to be scatted towards type-2 viewing angles than the doughnut-shaped torus. A similar effect was found and discussed before when comparing the scattering properties between a large and a compact torus for the same half-opening angle (see section 4.2 and figure 7 in Goosmann and Gaskell 2007, for more details). For a given overall geometry, i.e. either flared or toroidal, the total flux and time lag are only in rough agreement with each other. Introducing clumpiness leads to a somewhat smoother and broader transition around the torus horizon and strongly lowers the polarization fraction and therefore the polarized flux.

## 4 Summary and conclusion

We modeled the polarization properties and time dependence of radiation scattered by circumnuclear dust in AGN. The inner radius of the dust region was fixed from polarization reverberation measurements in NGC 4151 (Gaskell et al. 2012). At type-1 viewing angles we find almost no variation in shape for all models, but we find a clear difference in the angular flux distribution depending on the geometry. Our results extend the work in Goosmann and Gaskell (2007) in terms of time lags.

There are additional differences in the polarization signature between a torus and a flared disk. While the torus models, either uniform or clumpy, do not show large differences in time-lag between type-1 or type-2 viewing angles, the case is different for flared geometries. The time lag is almost seven times larger at type-2 viewing angles than at polar inclinations. A flared disk structure leads to more important delays at edge-on inclinations, together with lower fluxes and polarization than for a toroidal dusty torus.

In conclusion, time-resolved polarimetry adds independent constrains to the unresolved structure of AGN and we aim to investigate in further detail these differences in a forthcoming paper.

This work was supported by CONICYT PFCHA/BecasCHILE Doctorado en el extranjero 72150573.

## References

Antonucci, R. 1984, ApJ, 278, 499

Antonucci, R. 1993, ARA&A, 31, 473

Antonucci, R. and Miller, J.S., 1985, ApJ, 297, 621A

Gaskell, C. M., Goosmann, R. W., Antonucci, R. R. J., & Whysong, D., 2004, ApJ, 616, 147

Gaskell, C. M. 2009, NewAR 53, 140

Gaskell, C. M. and Goosmann, R. W. and Merkulova, N. I. and Shakhovskoy, N. M. and Shoji, M. 2012, ApJ, 749, 148

Goosmann, R. W.and Gaskell, C. M. 2007, A&A, 465, 129

Lynden-Bell, D. 1969, Nature 223, 690

Marin, M., Goosmann, R. W., Gaskell, C. M., Porquet, D. and Dovciak, M. 2012, A&A, 548, 121

Marin, F., & Goosmann, R. W. 2014, SF2A-2014: Proceedings of the Annual meeting of the French Society of Astronomy and Astrophysics, 103

Marin, F., Goosmann, R. W. and Gaskell, C. M. 2015, A&A, 577, 66

Mathis, J. S., Rumpl, W., & Nordsieck, K. H., 1977, ApJ, 217, 425

Pringle, J. E. and Rees, M. J. and Pacholczyk, A. G., 1973, A&A, 29, 179

Ruiz, M. and Young, S. and Packham, C. and Alexander, D. M. and Houghg, J. H. 2003, MNRAS, 340, 733R

Salpeter, E. E. 1964, ApJ, 140, 796

Shakura, N. I. And Sunyaev, R. A. 1973, A&A, 24, 337

Shields, G. A., 1978, Nature, 272, 706

Smith, J. E. et al., 2004, MNRS, 350, 1405

*SF2A 2016*
*C. Reylé, J. Richard, L. Cambrésy, M. Deleuil, E. Pécontal, L. Tresse and I. Vauglin (eds)*

# MULTIWAVELENGTH STUDY OF FERMI-LAT BLAZARS VARIABILITY AND RADIATION PRODUCTION MECHANISMS

R. J. Britto[1, 2], E. Bottacini[1, 3], M. Böttcher[4], D. A. H. Buckley[5], S. Buson[1, 6], B. Lott[1, 7], J. P. Marais[2], P. J. Meintjes[2], S. Razzaque[1, 8] and B. van Soelen[2]

**Abstract.** Quasars constitute a subclass of radio-loud active galactic nuclei that release a tremendous amount of non-thermal radiation through a pair of twin jets. When one of these jets is aligned close to the direction of the Earth, the object is then called a blazar. A consistent monitoring of these sources can help to unveil physical mechanisms at the origin of the radiation production that spreads throughout the whole electromagnetic spectrum, from radio waves to $\gamma$ rays. The goal of this paper is to report some current works being undertaken in term of both spectral studies and time domain analyses of bright blazars which are observed with the *Fermi* Gamma-Ray Space Telescope and by South Africa-based optical telescopes. In particular, we present our recent and current studies on blazars 3C 454.3 and NVSS J141922-083830 respectively.

Keywords: Quasars: general – Quasars: individual: 3C 454.3 – Telescopes – Gamma rays: general – Methods: data analysis

## 1 Introduction

Understanding the nature of Active Galactic Nuclei (AGNs) has been a fascinating challenge of astrophysics since the middle of the 20$^{\text{th}}$ century. Though the so-called unified model of AGNs gives a comprehensive representation of Seyfert galaxies, radio galaxies, quasars, blazars, etc., we still have a lot to understand concerning the radiation production mechanisms which are the origin of the broadband spectral energy distributions (SEDs) that spread over the whole electromagnetic spectrum. In Figure 1 the unified model of AGNs is represented, consisting of a supermassive black hole (SMBH) surrounded by an accretion disk of hot plasma emitting visible and ultraviolet radiation, a relatively dense region of high-velocity gas clouds and radiation field, called the broad-line region (BLR), a pair of twin relativistic plasma jets that are probably formed by material ejected from the accretion disk, while a significant part of the matter is falling towards the SMBH in rotation in an intense magnetic fiels (Urry & Padovani 1995). In the rest of this paper we will present studies on blazars, which are the most luminous sources in the Universe, apart from $\gamma$-ray bursts. Blazars are radio-loud AGNs with one of their jets directed close to the direction of the Earth. Most of the radiation we detect from these sources is the Doppler boosted non-thermal radiation emitted within the jets. Blazars are divided into two main categories: the flat spectrum radio quasars (FSRQs) and the BL Lacs. Several recent reviews describe the current understanding as well as challenges in the AGN and blazar physics (Massaro et al. 2016; Dermer & Giebels 2016; Finke 2016).

Though it is widely accepted that the low energy component of blazar SEDs is due to the electron synchrotron emission mechanism, it is still debated whether the origin of the high energy (HE) component is produced

[1] (on behalf of the *Fermi-LAT Collaboration)*
[2] Department of Physics, University of the Free State, PO Box 339, Bloemfontein 9300, South Africa
[3] W. W. Hansen Experimental Physics Laboratory, Stanford University, Stanford, CA 94305, USA
[4] Centre for Space Research, North-West University, Potchefstroom 2520, South Africa
[5] South African Astronomical Observatory, PO Box 9, Observatory 7935, Cape Town, South Africa
[6] Astrophysics Science Division, NASA Goddard Space Flight Center, Greenbelt, MD 20771 USA; University of Maryland Baltimore County/CRESST, Baltimore, MD 21250, USA
[7] Univ. Bordeaux, Centre d'Études Nucléaires de Bordeaux-Gradignan, UMR 5797, CNRS/IN2P3, 33175 Gradignan, France
[8] Department of Physics, University of Johannesburg, PO BOX 524, Auckland Park 2006, South Africa

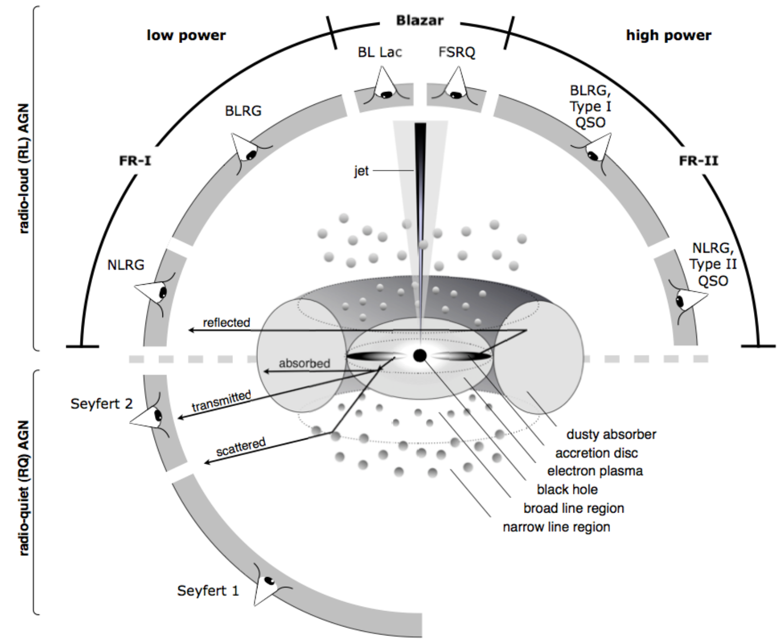


**Fig. 1.** The unified model of Active Galactic Nuclei (AGNs). Credit: Beckmann & Shrader (2012).

through leptonic or through hadronic processes. We presented in Britto et al. *(submitted to PoS)* a short review of some current understandings and investigations of *leptonic versus hadronic* scenarios of radiation production mechanisms in blazar jets.

The *Fermi* Gamma-Ray Space Telescope was lauched on 11 June 2008, and has observed the whole sky for the last eight years. Its main instrument, the LArge Area Telescope (LAT), is sensitive to photons between 20 MeV and >300 GeV. Most of the time the LAT is observing in survey mode, which allows us to have a scan of the whole sky every three hours (Atwood et al. 2009). This observing strategy is of particular interest for the monitoring of variable sources such as AGNs, and particularly blazars that exhibit dramatic variabilty patterns on sub-day time scales.

We present in Section 2 our previous work on searching for $\gamma$-ray absorption in the *Fermi*-LAT data of 3C 454.3, and in Section 3 our study of 3C 454.3 during its June 2014 outburst. We report in Section 4 our on-going study on blazars NVSS J141922-083830 and our projects of using optical South Africa based telescopes in complementarities to $\gamma$-ray observations.

## 2 Probing absorption in the BLR

**Note.** The results and the discussion presented in this section are taken from a previous work presented by R. J. Britto, S. Razzaque and B. Lott (Britto et al. 2015a).

FSQR 3C 454.3 is a well studied blazar, with observations spanning over many years, and particularly since it has exhibited some of the brightest blazar flares ever detected in the MeV-GeV range: in December 2009 (Striani et al. 2010; Ackermann et al. 2010), April 2010 (Ackermann et al. 2010), in November 2010 (Abdo et al. 2011, still currently the record for blazars), in June 2014 (Britto et al. 2016), and in June 2016 (Lucarelli et al. 2016; Bulgarelli et al. 2016; Ojha 2016)*. We studied the $\gamma$-ray SED of this source between 100 MeV and several tens of GeV by using Pass 8 data from the *Fermi*-Large Area Telescope (*Fermi*-LAT). It is expected that $\gamma$-ray photons in the ~10-100 GeV range undergo absorption through interaction with ultraviolet photons of the BLR by electron-positron pair production ($\gamma\gamma \rightarrow e^+e^-$). If we can quantify the expected absorption for

*See also: `http://fermi.gsfc.nasa.gov/ssc/data/access/lat/msl_lc/`

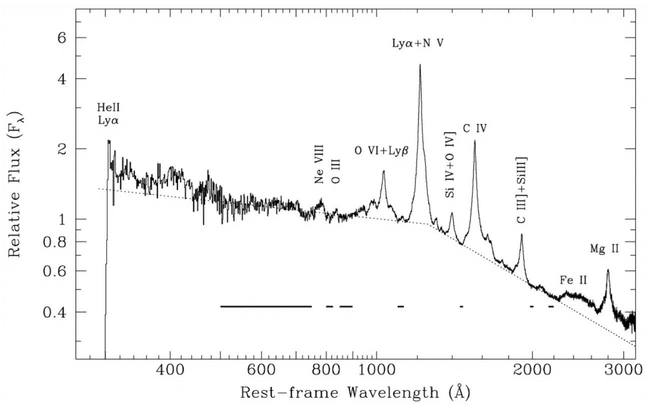


**Fig. 2.** Mean quasar spectrum in 1 Å bins. The dotted line represents the best-fit broken power-law continuum, excluding the region below 500 Å. The bottom lines indicate the continuum windows used in the fit. Figure 4 from Telfer et al. (2002).

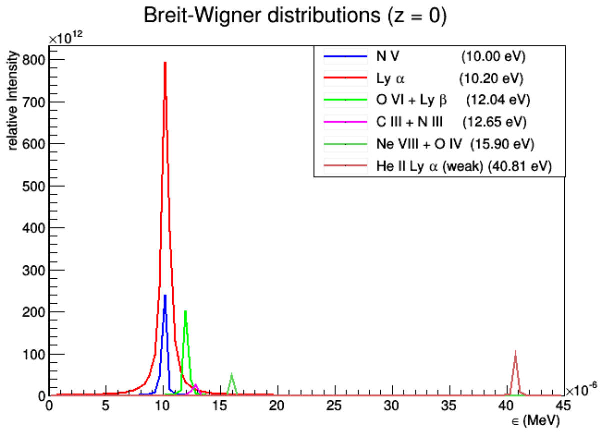


**Fig. 3.** Modelling of six bright ultraviolets lines of the BLR, using a Breit-Wigner distribution. Figure from Britto et al. (2015b).

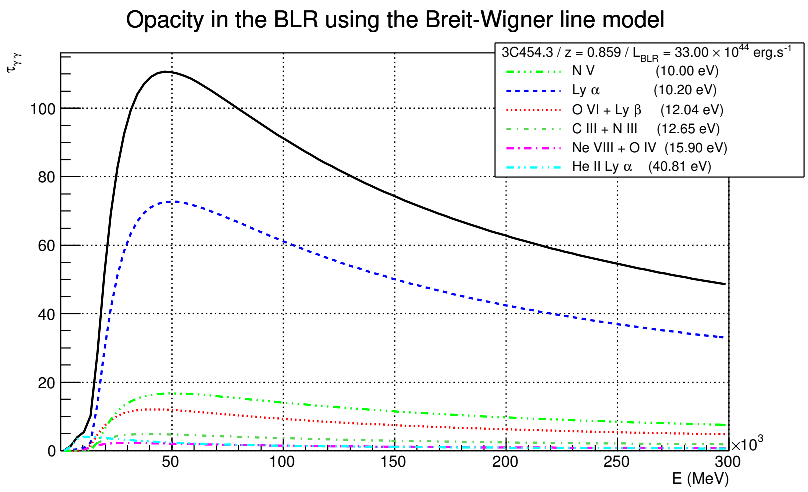


**Fig. 4.** Opacity $\tau_{\gamma\gamma}(E, z)$ *versus* Energy, for 3C 454.3. The opacity sum on the 6 lines is represented in plain black. Figure 1 from Britto et al. (2015a).

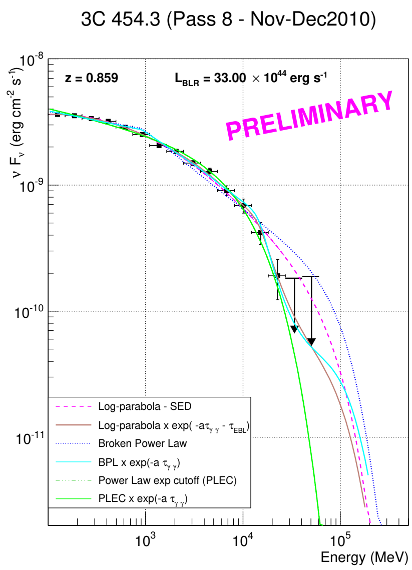


**Fig. 5.** SEDs of 3C 454.3 during its November-December 2010 outburst period. Figure 4 from Britto et al. (2015a).

a certain width and within a certain density of material of the BLR, it may be a precious tools to constrain the location of the $\gamma$-ray emission region: within or beyond the BLR.

We modeled the opacity of the BLR between 1 and 100 GeV, using eight prominant lines from the composite ultraviolet spectrum of radio-loud quasars compiled by Telfer et al. (2002): NV, Ly$\alpha$, OVI, Ly$\beta$, CIII, NIII, NeVIII and OIV (Figure 2). We also added the HeII Ly$\alpha$ line in our model, under a certain assumption of its width and intensity, in order to model the $\gamma\gamma$ absorption at lower energy. These six lines correspond to an ultraviolet emission from $\sim$10 to 41 eV respectively. We modeled them using a *Breit-Wigner* distribution (Figure 3). In Figure 4 is shown the opacity, $\tau_{\gamma\gamma}$, of each line and the total opacity used in our model.

We fitted the *Fermi*-LAT SED of 3C 454.3 during its giant flare (02 November–05 December 2010 — MJD 55502.5-55535.5, Abdo et al. 2011) using successively the following functions: a log-parabola (LP), a broken power law (BPL), and a power law with an exponential cutoff (PLEC). To all these functions we also added

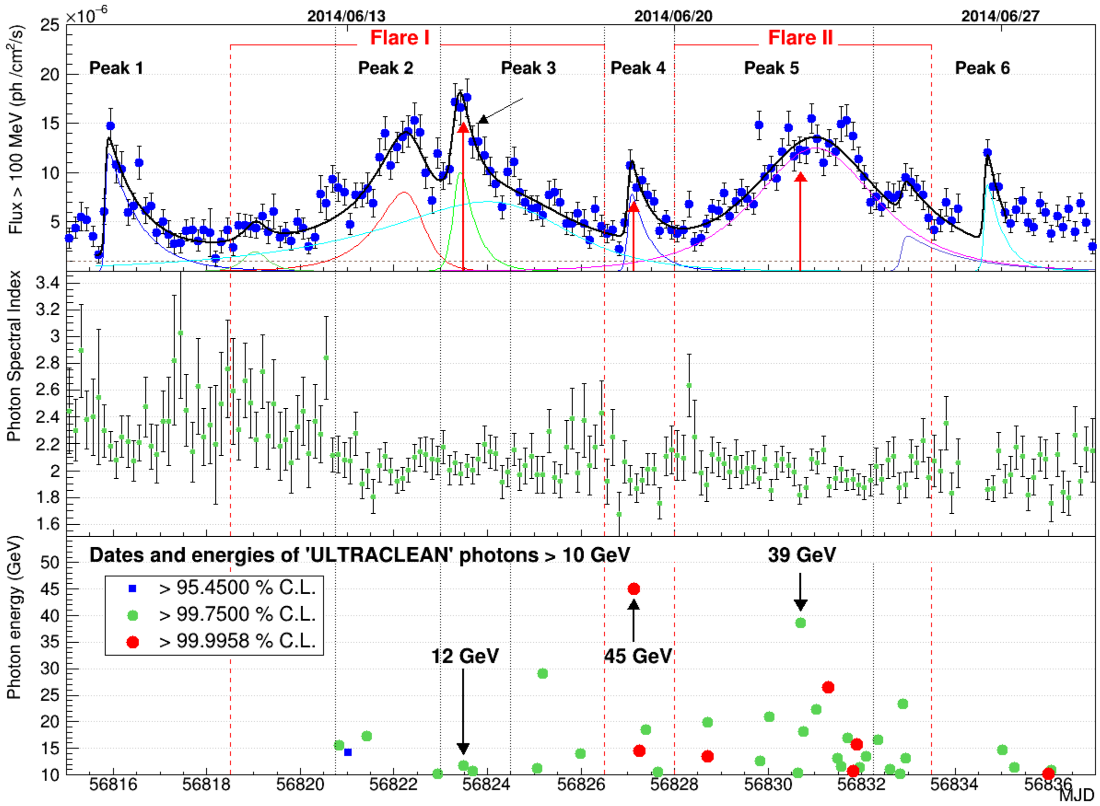


**Fig. 6.** *Top panel: Fermi*-LAT light-curve of the flare phase with 3-hr binning. The thin color lines correspond to the contribution of single peaks in the total fit, which is represented by the thick black line. The red arrows indicate the arrival time of the three high-energy photons used to calculate the Doppler factor, and whose energies are labeled in the bottom panel. Due to an instrumental problem, the MJD 56834.375 bin contains no data. *Middle panel:* Photon spectral index ($\Gamma$) of the PL fits of data. *Bottom panel:* Arrival time and energy of E>10 GeV photons with three different significance levels of source association (2-, 3-, and 4-$\sigma$ Gaussian equivalent). Vertical red dash lines indicate the two major flaring phases (I and II), and black dotted lines indicate Peaks 2, 3, 4 and 5. Figure 2 of Britto et al. (2016).

a exponential component to model absorption by the extragalactic background light ($\tau_{EBL}$, from the model of Finke et al. (2010)). We then compared these fits with those that do not include $\tau_{\gamma\gamma}$ (Figure 5).

The observed spectrum $F_{obs}(E)$ was given by:

$$F_{obs}(E) = e^{-\tau_{EBL}(E,z)}\ e^{-a\ \tau_{\gamma\gamma}(E,z)}\ F_{int}(E), \tag{2.1}$$

where $F_{int}(E)$ is the LP, BPL or PLEC fitting function. The parameter $a$ is kept free in the $[10^{-5}, 1]$ range to account for the fraction of radius of the BLR in which $\gamma$ rays may be absorbed.

We report a $\tau_{\gamma\gamma}$-like dip with a significance close to 3 $\sigma$ in the discrepancy between $F_{obs}(E)$ and $F_{obs}(E)/e^{-\tau_{\gamma\gamma}}$, when using the BPL model only.

We found that the $\gamma\gamma$ absorption in the BLR is not significant enough to claim a discovery for the models of BLR and spectral functions we have investigated. In Britto et al. (2015a), we presented this modelling for 12 FSRQs, using 5.5 years of Pass 8 data, and also during three flaring periods. We reported hints of absorption in the case of 3C 454.3, at 3.9 $\sigma$ for the 5.5 year data set, and close to 3 $\sigma$ during the Nov-Dec 2010 flare (the one presented in this section). An implication of our results could be that the $\gamma$-ray emission zone in this FSRQ might be located outside or at the outer edge of the BLR (parameter $a \lesssim 0.01$). However, further investigation on binning effects on the SED fits are required. Future work is also expected to improve the modelling of the BLR. Based on another modelling of the BLR, Poutanen & Stern (2010) and Stern & Poutanen (2014) also discussed evidence of GeV $\gamma$-ray absorption in the BLR for several bright FSRQs.

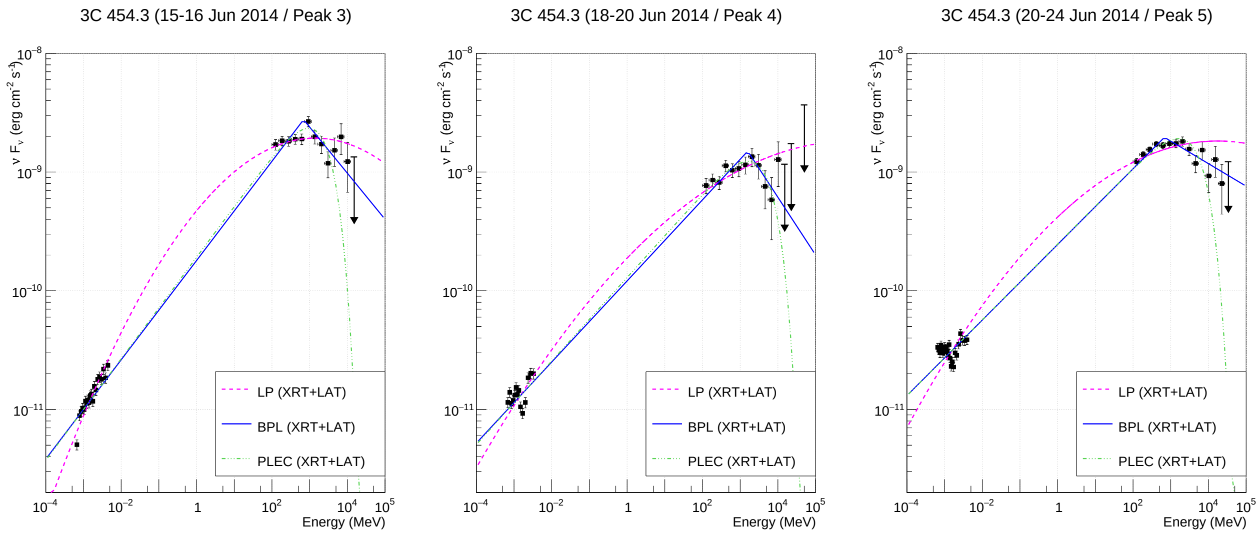


**Fig. 7.** SEDs of 3C 454.3 in the 1 keV-100 GeV range, with *Swift*-XRT and *Fermi*-LAT data points fitted with LP, BPL and PLEC functions, for Peak 3 (left), Peak 4 (middle) and Peak 5 (right). Figure 7 from Britto et al. (2016).

**Table 1.** Calculated limits of the values of $\delta$, $\beta_{\rm jet} = \sqrt{\Gamma_{\rm jet}^2 - 1}/\Gamma_{\rm jet}$, $R'$, $\Gamma_{\rm jet}$ and $r$, corresponding to the Peak 3, Peak 4 and Peak 5 subflaring events.

| Subflaring events | $\delta$ | $\beta_{\rm jet}$ | $\Gamma_{\rm jet}$ | $R'$ [cm] | $r$ [cm] |
|---|---|---|---|---|---|
| Peak 3 ($T_r = 2.1$ hr) | 19 | 0.995 | 10 | $2.3 \times 10^{15}$ | $2.5 \times 10^{16}$ |
| Peak 4 ($T_r = 1200$ s) | 29 | 0.998 | 16 | $5.6 \times 10^{14}$ | $1.0 \times 10^{16}$ |
| Peak 5 ($T_r = 27.8$ hr) | 14 | 0.991 | 7 | $2.3 \times 10^{16}$ | $1.8 \times 10^{17}$ |

## 3 Fast variability of FSRQ 3C 454.3 during June 2014 and constrain on the location of the $\gamma$-ray emitting region

**Note.** The results and the discussion presented in this section are taken from a previous work published by R. J. Britto, E. Bottacini, B. Lott, S. Razzaque and S. Buson (Britto et al. 2016).

We studied the flare of FSRQ 3C 454.3 during its May–July 2014 outburst, using the Pass 8 data representation (analysis procedure described in Britto et al. 2016). In Figure 6 is shown the light-curve of 3C 454.3 during its main flare (7–29 June 2014). We reported fast variability and the detection of HE photons above 10 GeV, mainly during the second half of the flare. Several individual flaring structures (called “Peaks”) were identified.

A time-unbinned likelihood algorithm has been developed for a better estimate of the flux rise times, compared to a simple fiting of the binned light-curve (Lott et al. 2012). This allowed us to report a rise time $T_r = 1.2 \pm 0.7$ ks for Peak 4.

We calculated the opacity of the X-ray–$\gamma$-ray radiation field in the flaring blobs — associated to individual peaks — to HE photons emiting during these peaks, in order to constrain the value of the jet Doppler factor $\delta$. We required the opacity to be equal to unity for the highest energy photon of each blob, in order to give a lower limit on $\delta$. The X-ray–$\gamma$-ray radiation field was modelled by phenomenological fitting of the near-simultaneous *Swift*-XRT and *Fermi*-LAT data that we analysed (Figure 7). Lower limits on the jet Lorentz factor $\Gamma_{\rm jet}$, the radius of the blob $R'$, and on its distance $r$ from the central supermassive black hole were calculated, according the formulae $\delta = [\Gamma_{\rm jet}(1 - \beta_{\rm jet}\cos\theta)]^{-1}$, $R' \approx \delta c t_v/(1+z)$, and $r \simeq 2\Gamma_{\rm jet}^2 c t_v/(1+z)$ respectively. Our results are summarised in Table 1. Considering the radius of the canonical BLR of 3C 454.3 to be $R_{BLR} < 10^{18}$ cm (Bonnoli et al. 2011; Sbarrato et al. 2012), we get a constraint on the location of the three blobs correspondng to Peak 3, 4 and 5 to be located on the outer layers of the BLR.

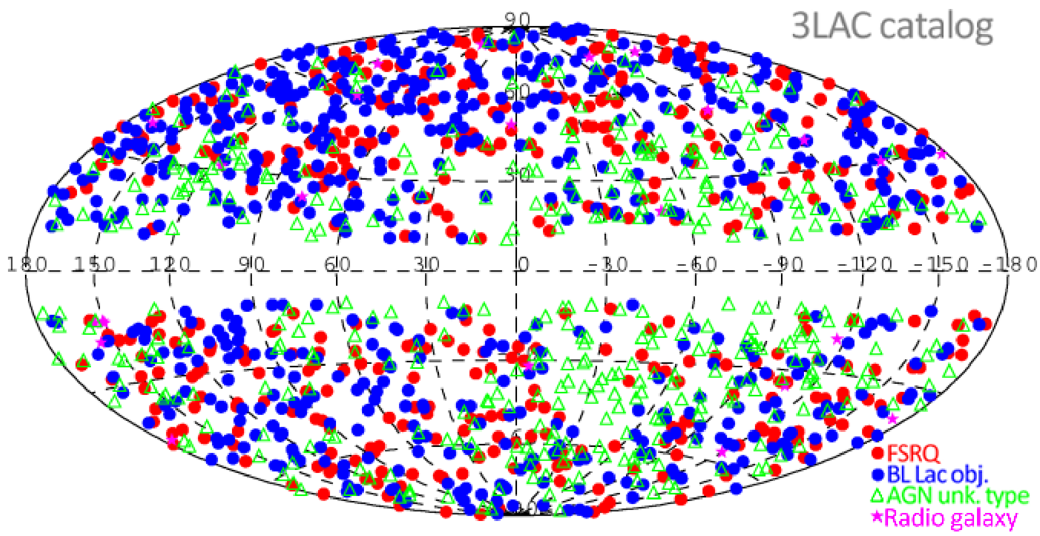


**Fig. 8.** Sky map of the Third *Fermi*-LAT AGN Catalog (3LAC), in Galactic coordinates. Figure 5 from Ackermann et al. (2015).

## 4 Observations of Fermi-LAT blazars using South Africa-based telescopes and the case of NVSS J141922-083830

The observing strategy of the *Fermi* Gamma-Ray Spece Telescope we mentioned above is of particular interest for the monitoring of variable sources such as AGNs, and particularly blazars that exhibit dramatic variabilty patterns on sub-day time scales.

The Third *Fermi*-LAT Point Source Catalog (3FGL, Acero et al. 2015), based of the analysis of the first four years of data, contains 3033 sources. The Third LAT AGN Catalog (3LAC, Ackermann et al. 2015) gives more details on the $\gamma$-ray properties of 3FGL AGNs for Galactic latitudes $|b| > 10°$. This catalogue contains 632 BL Lacs, 467 FSRQs and 460 blazar candidates of uncertain types (or BCUs), as represented in Figure 8. The vast majority of these BCU objects do not have redshift. Most of them are faint, which explains the lack of detailed optical spectra that could enable their classification.

Optical spectroscopy is used for determinating the blazar type and its redshift, whenever spectral lines can be identified. Also, in order to monitor blazar outbursts over several days, optical photometry is used to study the correlations between optical and $\gamma$-ray light-curves (see Britto 2015; Britto et al.) *(submitted to PoS)*.

The *South African Astronomical Observatory* (SAAO) was established in 1972 in the suburb of Cape Town as the merging of several South African observatories. Its offices are located on the site of the *Royal Observatory, Cape of Good Hope*, in Cape Town, but its major astronomical observations are conducted a few kilometers outside Sutherland, a small town in the Northern Cape, about 370 km North-East of Cape Town (Figures 9 and 10). It is run today by the *National Research Fondation* (NRF) of South Africa. Several telescopes operate on this site, including some that are part of collaborative effort with other countries. The biggest telescope in Africa is the *Southern African Large Telescope* (SALT), a 10-m class telescope funded by a consortium of international partners from South Africa, the United States, Germany, Poland, India, the United Kingdom and New Zealand (Buckley et al. 2006). Though SALT has been fully operational since 2011 for science observation, its upgrade is still continuing.

From all the 3LAC sources (at Galactic latitudes $|b| > 10$ deg) that are variable, belonging to the BL Lac or FSRQ or BCU classes, and that are observable by SALT in South Africa ($-75° \lesssim$ Decl $\lesssim +10°$), we have listed $\gtrsim 280$ target sources. Among this list, $\sim$50 % of them ($\sim$140) have a V mag brighter than 19. Among this rather large pool of target sources, we have undertaken the observation of several BCUs from 3LAC by using the *SpUpNIC* spectrograph of the SAAO 1.9-m telescope, Sutherland, and the *Robert Stobie Spectrograph* (RSS) of SALT, also based in Sutherland. The initial phases of this work were reported in Klindt et al. (2016b,a), and the continuing project in Van Soelen et al. *(submitted to PoS)*. We also consider the use of the *HIgh speed Photo-Polarimeter (HIPPO)* on the 1.9-m telescope.

**Fig. 9.** Telescope site at SAAO, Sutherland, South Africa. The 10-m class telescope SALT is visible in the backgound, in the middle of the picture. Picture from `http://www.saao.ac.za/`.


**Fig. 10.** Location of the major telescopes in Southern Africa: the High Energy Stereoscopy System (HESS) in Namibia; the MeerKAT radio telescope array in Karoo, South Africa — also the site of the core array of the Square Kilometer Array (SKA) radio telescope array; the Watcher robotic telescope, next to the Boyden 1.5-meter telescope, Free State, South Africa; the HartRAO radio telescope near Pretoria. Many telescopes are located at the South Africa Astronomical Observatory near Suthernland (SAAO), including the 1.9-m telescope and SALT, from which we get spectroscopy data, and MASTER-OT, etc. Credit: Google Maps, `https://maps.google.com/`.

Beside our project to perform systematic observations of BCUs during their quiescent stage for the determination of redshift and classification, we are also observing flaring blazars. An interesting example of the multiwavelength study of flaring blazars using South-Africa based telescopes is our current work on the BCU NVSS J141922-083830 (2FGL J1419.4-0835). This object is very faint in its quiescent state (magnitude V$\sim$18) and hardly detected in $\gamma$-ray in a three-day binned light-curve. On 21 February 2015, the telescope based in Kislovosk (from *Mobile Astronomical System of the TElescope-Robots–Optical Transcient* [MASTER-OT]) detected a flare of this source with a white magnitude of 14.6 (Lipunov et al. 2015). A SALT-RSS spectrum was obtained on 1 March 2015, and a redshift z=0.903 was reported, if the observed emision line is the Mg II 5325 Å, (Figure 11 and Buckley et al. 2015).

We are currently undertaking the $\gamma$-ray long term monitoring of NVSS 141922-083830 with *Fermi*-LAT, and more specifically the multiwavelength study of the source during its February-March 2015 flare (Figure 12 and Buckley et al., *(in preparation)*.

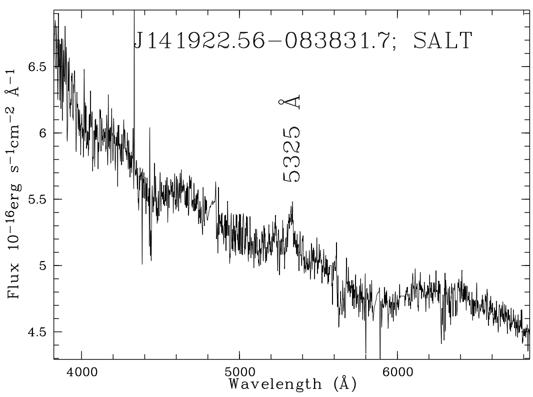


**Fig. 11.** SALT RSS spectrum of NVSS J141922-083830 obtained on 2015-03-01.01 UT using the PG900 lines/mm grating at an angle of 14.00 degrees, with a 1100 s exposure. The spectral window is 3780–6850 Å at a resolution of 4.8 Å with a 1.25 arcsec slit. Figure from Buckley et al. (2015).

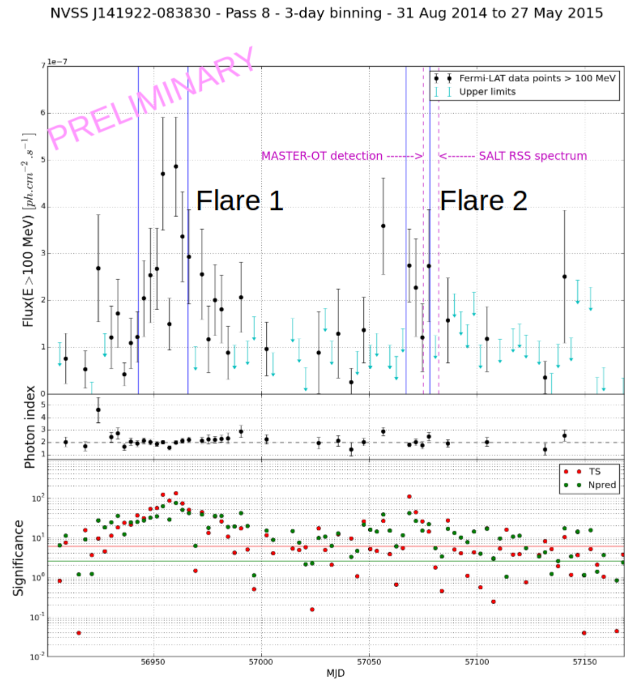


**Fig. 12.** Upper: *Fermi*-LAT light-curve of NVSS J141922-083830, in 3-day binning, during its two main recent outbursts (October 2014 and February–March 2015.) Dashes vertical lines indicate the date of one detection by MASTER-OT and the SALT observation. Middle: Power-law spectral index variation. Bottom: Number of photons associated to the source (predicted by the model–$N_{\rm pred}$) and significance of the detection (Test Statistics–$TS$). The horizontal plain lines represents the thresholds of these two quantities below which an upper limit was drawn if at least one is below its threshold.

## 5 Conclusions

Considering the large number of $\gamma$-ray blazars and their potential flaring outbursts, the continuous monitoring of the $\gamma$-ray sky above 20 MeV by *Fermi*-LAT, and the possibility to use South Africa based telescopes for optical photometry and spectroscopy, constitute a great potential for investigating time-domain and spectral characteristics of a large number of Southern Hemisphere sources, for which constraints on some of their physical parameters can be given.

**Note added.** A paper with a similar material was presented at the *MONDELLO WORKSHOP 2016. Frontier Research in Astrophysics - II (FRAPWS 2016)*. However, the conference proceeding of the Mondello conference was written to be complementary to this one. The reader may be interested to refer to Britto et al. *(submitted to PoS)*.

## Acknowledgments

The *Fermi*-LAT Collaboration acknowledges support for LAT development, operation and data analysis from NASA and DOE (United States), CEA/Irfu and IN2P3/CNRS (France), ASI and INFN (Italy), MEXT, KEK, and JAXA (Japan), and the K.A. Wallenberg Foundation, the Swedish Research Council and the National Space Board (Sweden). Science analysis support in the operations phase from INAF (Italy) and CNES (France) is also gratefully acknowledged. The authors acknowledge support from the National Research Foundation, South Africa and the South African Gamma-ray Astronomy Programme (SA-GAMMA).

## References


Abdo, A. A., Ackermann, M., Ajello, M., et al. 2011, ApJ, 733, L26

Acero, F., Ackermann, M., Ajello, M., et al. 2015, ApJS, 218, 23

Ackermann, M., Ajello, M., Atwood, W. B., et al. 2015, ApJ, 810, 14

Ackermann, M., Ajello, M., Baldini, L., et al. 2010, ApJ, 721, 1383

Atwood, W. B., Abdo, A. A., Ackermann, M., et al. 2009, ApJ, 697, 1071

Beckmann, V. & Shrader, C. R. 2012, Active Galactic Nuclei

Bonnoli, G., Ghisellini, G., Foschini, L., Tavecchio, F., & Ghirlanda, G. 2011, MNRAS, 410, 368

Britto, R. J. 2015, in Proceedings of Science: SALT Science Conference 2015 (SSC2015), 32

Britto, R. J., Bottacini, E., Lott, B., Razzaque, S., & Buson, S. 2016, ApJ, 830, 162

Britto, R. J., Marais, J. P., Meintjes, P. J., Van Soelen, B., & on behalf of the Fermi-LAT Collaboration. , in FRAPWS2016: Frontier Research in Astrophysics II, 23–28 May 2016, Mondello (Palermo), Italy, submitted to *Proceedings of Science*

Britto, R. J. G., Razzaque, S., Lott, B., & on behalf of the Fermi-LAT Collaboration. 2015a, in Proceedings of the *Fifth International Fermi Symposium*, October 20–24, 2014, Nagoya, Japan (arXiv:1502.07624 [astro-ph.HE])

Britto, R. J. G., Razzaque, S., Lott, B., & on behalf of the Fermi-LAT Collaboration. 2015b, in Poster of the *Fifth International Fermi Symposium*, October 20–24, 2014, Nagoya, Japan, `https://confluence.slac.stanford.edu/display/LSP/Fermi+Symposium+2014` [Poster_AGN_Britto_Nagoya_corrected.pdf])

Buckley, D. A. H., Breytenbach, J. B., Kniazev, A., et al. 2015, The Astronomer's Telegram, 7167

Buckley, D. A. H., Britto, R. J., Chandra, S., et al. , in preparation, to be submitted to MNRAS

Buckley, D. A. H., Swart, G. P., & Meiring, J. G. 2006, in Proc. SPIE, Vol. 6267, Society of Photo-Optical Instrumentation Engineers (SPIE) Conference Series, 62670Z

Bulgarelli, A., Parmiggiani, N., Fioretti, V., et al. 2016, The Astronomer's Telegram, 9176

Dermer, C. D. & Giebels, B. 2016, Comptes Rendus Physique, 17, 594

Finke, J. 2016, in *Proceedings of Science*, arXiv:1602.05965 [astro-ph.HE], Proceedings of the 3rd Annual Conference on High Energy Astrophysics in Southern Africa (HEASA 2015), 18–20 June 2015, Johannesburg, South Africa, Eds. M. Böttcher, D. Buckley, S. Colafrancesco, P. Meintjes and S. Razzaque, 6

Finke, J. D., Razzaque, S., & Dermer, C. D. 2010, ApJ, 712, 238

Klindt, L., Van Soelen, B., Meintjes, P. J., & de Witt, A. 2016a, in *Proceedings of Science*, Proceedings of the 3rd Annual Conference on High Energy Astrophysics in Southern Africa (HEASA 2015), 18–20 June 2015, Johannesburg, South Africa, Eds. M. Böttcher, D. Buckley, S. Colafrancesco, P. Meintjes and S. Razzaque, 8

Klindt, L., Van Soelen, B., Meintjes, P. J., & Väisänen, P. 2016b, in *Proceedings of Science*, SAIP2015: the 60th Annual Conference of the South African Institute of Physics, ISBN: 978-0-620-70714-5, 302

Lipunov, V., Gorbovskoy, E., Kornilov, V., et al. 2015, The Astronomer's Telegram, 7133

Lott, B., Escande, L., Larsson, S., & Ballet, J. 2012, A&A, 544, A6

Lucarelli, F., Pittori, C., Verrecchia, F., et al. 2016, The Astronomer's Telegram, 9157

Massaro, F., Thompson, D. J., & Ferrara, E. C. 2016, A&A Rev., 24, 2

Ojha, R. 2016, The Astronomer's Telegram, 9190

Poutanen, J. & Stern, B. 2010, ApJ, 717, L118

Sbarrato, T., Ghisellini, G., Maraschi, L., & Colpi, M. 2012, MNRAS, 421, 1764

Stern, B. E. & Poutanen, J. 2014, ApJ, 794, 8

Striani, E., Vercellone, S., Tavani, M., et al. 2010, ApJ, 718, 455

Telfer, R. C., Zheng, W., Kriss, G. A., & Davidsen, A. F. 2002, ApJ, 565, 773

Urry, C. M. & Padovani, P. 1995, PASP, 107, 803

Van Soelen, B., Klindt, L., Marais, J. P., et al. , in *Proceedings of Science*, FRAPWS2016: Frontier Research in Astrophysics II, 23–28 May 2016, Mondello (Palermo), Italy, submitted

*SF2A 2016*
*C. Reylé, J. Richard, L. Cambrésy, M. Deleuil, E. Pécontal, L. Tresse and I. Vauglin (eds)*

# UNDERSTANDING ACTIVE GALACTIC NUCLEI USING NEAR-INFRARED HIGH ANGULAR RESOLUTION POLARIMETRY II: PRELIMINARY RESULTS

F. Marin[1], L. Grosset[2], R. Goosmann[1], D. Gratadour[2], D. Rouan[2], Y. Clénet[2], D. Pelat[3] and P. A. Rojas Lobos[1]

**Abstract.** In this second research note of a series of two, we present the first near-infrared results we obtained when modeling Active Galactic Nuclei (AGN). Our first proceedings showed the comparison between the MontAGN and STOKES Monte Carlo codes. Now we use our radiative transfer codes to simulate the polarization maps of a prototypical, NGC 1068-like, type-2 radio-quiet AGN. We produced high angular resolution infrared (1 $\mu$m) polarization images to be compared with recent observations in this wavelength range. Our preliminary results already show a good agreement between the models and observations but cannot account for the peculiar linear polarization angle of the torus such as observed. Gratadour et al. (2015) found a polarization position angle being perpendicular to the bipolar outflows axis. Further work is needed to improve the models by adding physical phenomena such as dichroism and clumpiness.

Keywords: galaxies: active, galaxies: Seyfert, radiative transfer, techniques: polarimetric, techniques: high angular resolution

## 1 Introduction

Understanding the morphology, composition and history of each AGN component is a non-trivial goal that requires a strong synergy between all observational techniques. The role of polarimetric observations was highlighted in the 80s thanks to the discovery of broad Balmer lines and Fe II emission sharing a very similar polarization degree and position angle with the continuum polarization in NGC 1068, a type-2 AGN (Antonucci & Miller 1985). The resemblance of the polarized flux spectrum with respect to the flux spectrum of typical Seyfert-1s lead to the idea that Seyfert galaxies are all the same, at zeroth-order magnitude (Antonucci 1993). Observational difference would arise from a different orientation of the nuclei between pole-on and edge-on objects; this is due to the presence of an obscuring dusty region situated along the equatorial plane of the AGN that will block the direct radiation from the central engine for observers looking through the optically thick circumnuclear material. This is the concept of the so-called "dusty torus", first conceived by Rowan-Robinson (1977) and later confirmed by (Antonucci & Miller 1985).

Since then, a direct confirmation for the presence and structure of this dusty torus was an important objective for the AGN community. The closest evidence for a dusty torus around the central core of NGC 1068 was first obtained by Jaffe et al. (2004) and Wittkowski et al. (2004), using mid-infrared (MIR) and near-infrared (NIR) interferometric instruments coupled to the European Southern Observatory's (ESO's) Very Large Telescope interferometer (VLTI). Jaffe et al. (2004) were able to spatially resolve the MIR emission from the dusty structure and revealed that 320 K dust grains are confined in a 2.1 $\times$ 3.4 pc region, surrounding a smaller hot structure. The NIR data obtained by Wittkowski et al. (2004) confirm the presence of this region, with the NIR fluxes arising from scales smaller than 0.4 pc. Since then, long-baseline interferometry became a tool used to explore the innermost AGN dusty structure extensively at high angular resolution (typically of the order of milli-arcsec, see e.g., Kishimoto et al. 2009, 2011).

[1] Observatoire Astronomique de Strasbourg, Université de Strasbourg, CNRS, UMR 7550, 11 rue de l'Université, 67000 Strasbourg, France
[2] LESIA, Observatoire de Paris, PSL Research University, CNRS, Sorbonne Universités, UPMC Univ. Paris 06, Univ. Paris Diderot, Sorbonne Paris Cité
[3] LUTH, Observatoire de Paris, CNRS, Universit Paris Diderot, 92190 Meudon, France

Coupling adaptive-optics-assisted polarimetry and high angular resolution observations in the infrared band, Gratadour et al. (2015) exploited the best of the two aforementioned techniques to obtain strong evidence for an extended nuclear torus at the center of NGC 1068. Similarly to previous optical (Capetti et al. 1995) and infrared (Packham et al. 1997; Lumsden et al. 1997) polarimetric observations, Gratadour et al. (2015) revealed an hourglass-shaped biconical structure whose polarization vectors point towards the hidden nucleus. By subtracting a purely centro-symmetric component from the map of polarization angles, an elongated (20 × 50 pc) region appeared at the assumed location of the dusty torus. If the signal traces the exact torus extension, high angular resolution polarization observations would become a very powerful tool to study the inner core of AGN.

In this lecture note, the second of the series, we will show the preliminary results obtained by running Monte Carlo radiative transfer codes for a NGC 1068-like AGN. Our ultimate goal is to reproduce the existing UV-to-infrared polarimetric observations using a single coherent model in order to constrain the true three-dimensional morphology of the hard-to-resolve components of close-by AGN.

## 2 Building an NGC 1068 prototype

Our primary model is powered by a central, isotropic, point-like source emitting an unpolarized spectrum with a power-law spectral energy distribution $F_* \propto \nu^{-\alpha}$ and $\alpha = 1$. Along the polar direction, a bi-conical, ionized wind with a 25° half-opening angle* with respect to the polar axis flows from the central source to 25 pc. The wind is assumed to be ionized and therefore filled with electrons. It is optically thin (optical depth in the V-band along polar direction $\tau_V = 0.1$). Along the equatorial plane, a flared disk sets on at 0.05 pc (a typical dust sublimation radius, see Kishimoto et al. 2007) and ends at 10 pc. The half-opening angle of the dust structure is fixed to 30° (Marin et al. 2012) and its V-band optical depth is of the order of 50. The dust is composed of 100 % silicates with grain radii ranging from 0.005 $\mu$m to 0.25 $\mu$m, together with a size distribution proportional to $a^{-3.5}$ ($a$ being the grain radius).

The observer's viewing angle is set to 90° with respect to the symmetry axis of the model. More than $10^7$ photons were sampled to obtain polarimetric images with a pixel resolution of 1 pc (9 milli-arcsec at 14.4 Mpc). For this proceedings note, we selected the images computed at 1 $\mu$m and used the Monte Carlo code STOKES.

### 2.1 *Results of our baseline model*

The polarimetric maps for our baseline model are shown in Fig. 1. The left image shows the polarization position angle superimposed to the 1 $\mu$m polarized flux. The polarization vectors show the orientation of polarization but are not proportional to the polarization degree (which is shown in the right image).

The polar outflows, where electron scattering occurs at a perpendicular angle, shows the strongest polarization degree (up to 90 – 100 %) associated with a centro-symmetric polarization angle pattern. This in perfect agreement with the polarization maps taken by the optical and infrared polarimeters in the 90s and recently upgraded by Gratadour et al. (2015). At the center of the model, the photon flux is heavily suppressed by the optically thick material, but scattered radiation from the cones to the surface of the torus leads to a marginal flux associated with a weak polarization degree† (< 8 %). Such degree of polarization is in very good agreement with the values observed by Gratadour et al. (2015) at the location of the nucleus (5 – 7 %). However, compared to the results of the previous authors, the polarization position angle from the modeling is almost centro-symmetric rather than aligned/anti-aligned with the circumnuclear dusty structure. It is only on the highest point of the torus morphology that a $\sim$ 50 % polarization degree associated with a higher flux can be found, due to a lesser amount of dust facing the wind-scattered photon trajectories. When the whole picture is integrated, the resulting polarization degree is of the order of 60 %.

### 2.2 *Accounting for the ISM*

To test multiple configurations, we ran a second series. Based on the previous setup, we included interstellar matter (ISM) around the model. The ISM dust grains share the same composition as the dust in the circum-

*The half-opening angle of our model is smaller than what is observed (Goosmann & Matt 2011). We will change this value when the comparison between MontAGN and STOKES will be completed, see Paper I.

†Polarization degrees quoted in the text are for the scattered-induced polarization only. Dilution by the interstellar polarization, host galaxy starlight and starburst light will drastically reduce the observed polarization degree.

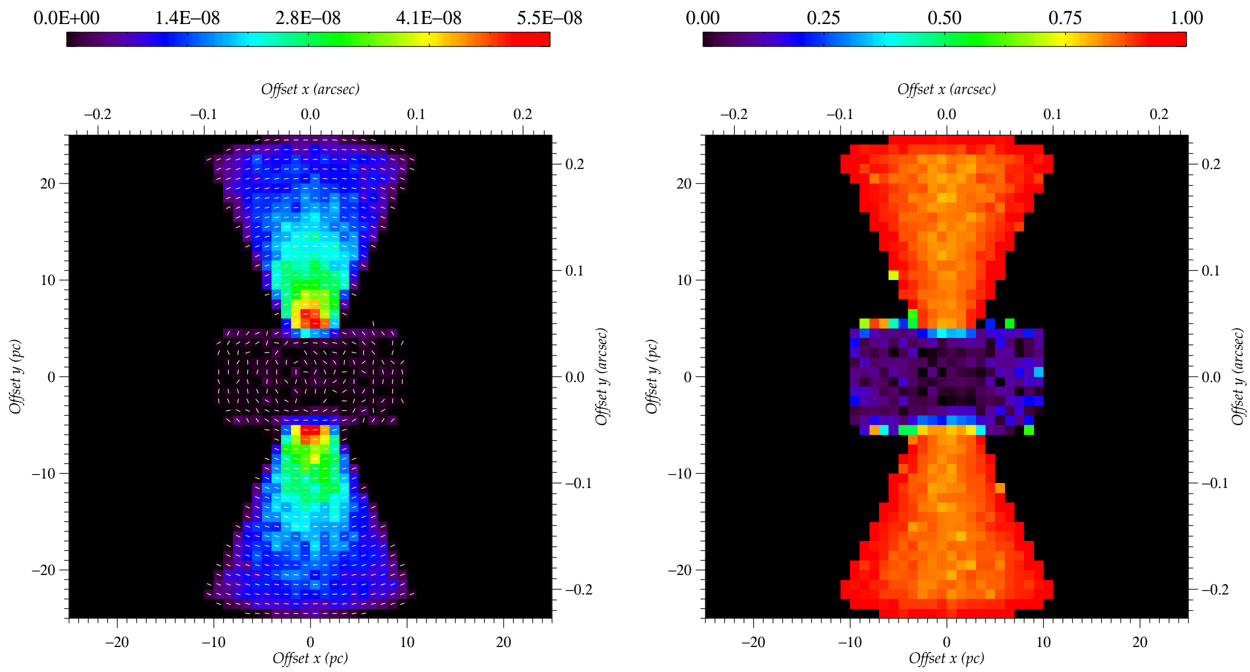


**Fig. 1.** 1 $\mu$m polarimetric simulations of NGC 1068. Left figure shows the color-coded polarized flux in arbitrary units with the polarization position angle superimposed to the image. Right figure shows the color-coded degree of polarization (from 0, unpolarized, to 1, fully polarized).

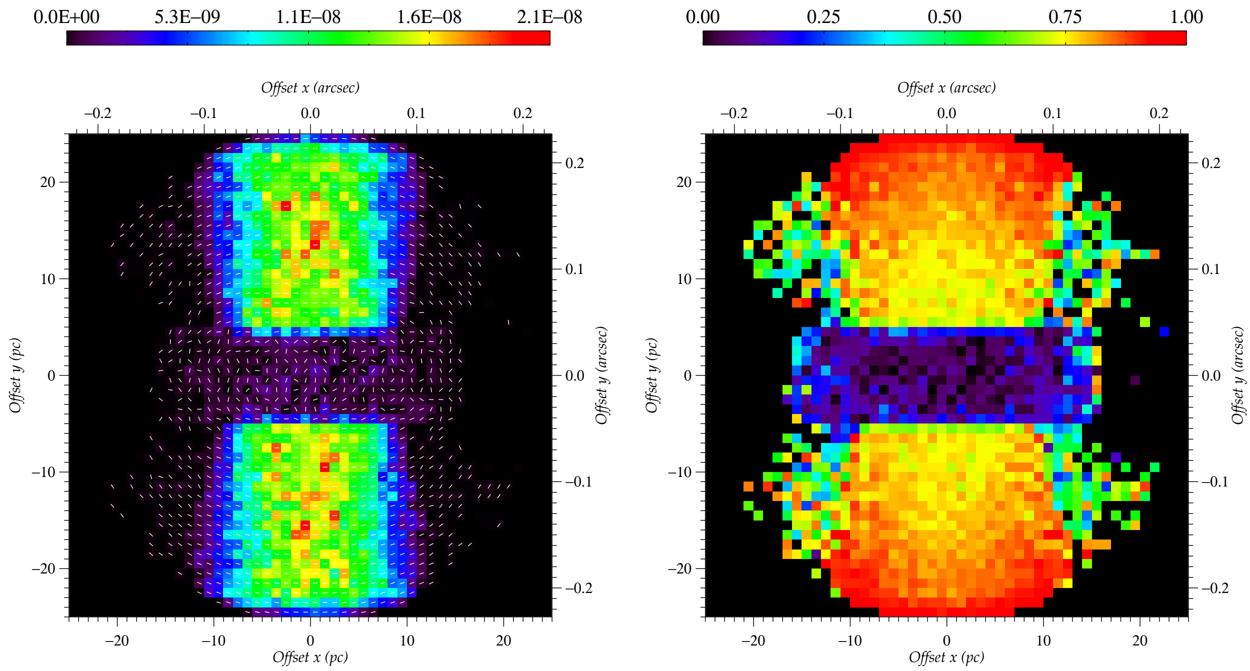


**Fig. 2.** Same as Fig. 1 with the addition of optically thin interstellar matter around the model

nuclear AGN region and the ISM is optically thin in all directions ($\tau_V = 0.5$). Our new polarimetric images are shown in Fig. 2

A striking difference between the ISM-free (Fig. 1) and the ISM-included (Fig. 2) polarimetric maps is the shape of the outflowing winds seen in transmission through the dust. The perfect hourglass shape observed when the AGN was in vacuum is now disturbed. The global morphology is more similar to a cylinder, with no flux gradient observed as the photons propagate from the central engine to the far edges of the winds. The overall flux distribution is more uniform throughout the winds, which seems to be in better agreement with what has been observed in the same band, at least for sub-arcsec scales (Packham et al. 1997). At better angular resolutions, polarized flux images are still needed. The polarization position angle has retained its centro-symmetric pattern but the polarization angle is more chaotic at the location of the torus, due to additional dust-scattering. The degree of polarization at the center of the AGN is the same as previously but the integrated map shows a slightly smaller polarization degree (58 %) due to depolarization by multiple scattering.

## 3 Discussion

Running our radiative transfer codes at 1 $\mu$m, we found that a NGC 1068-like model produces the centro-symmetric polarization angle pattern already observed in the optical and infrared bands. Disregarding additional dilution by other sources, the polarization position angle pinpoints the source of emission. Including the ISM in the model does not change the results but tends to decrease the final polarization degree. It also changes the flux repartition in the outflowing winds that act like astrophysical mirrors, scattering radiation from the hidden nucleus. Compared to what has been shown in Gratadour et al. (2015) in the H (1.6 $\mu$m) and K (2.2 $\mu$m) bands, we find very similar levels of linear polarization at the center of the model, where the central engine is heavily obscured by dust. However, we do not retrieve the distinctive polarization position angle of the torus found by the authors. According to our models, the pattern is at best centro-symmetric rather than directed perpendicular to the outflowing wind axis.

Additional work is needed to explore how such a distinctive pattern can arise at the location of the torus. In particular, adopting the most up-to-date morphological and composition constraints from literature is mandatory to built a coherent NGC 1068 model. Including effects such as polarization by absorption (dichroism) will be necessary. Comparing our results with past linear and circular polarization measurements (e.g, Nikulin et al. 1971; Gehrels 1972; Angel et al. 1976) will drive our models towards the right direction. Finally, the broadband coverage of the codes, from the X-rays to the far infrared, will allow us to robustly test our final model against spectroscopic and polarimetric observations in many wavebands.

The authors would like to acknowledge financial support from the Programme National Hautes Energies (PNHE).

## References

Angel, J. R. P., Stockman, H. S., Woolf, N. J., Beaver, E. A., & Martin, P. G. 1976, ApJ, 206, L5
Antonucci, R. 1993, ARA&A, 31, 473
Antonucci, R. R. J. & Miller, J. S. 1985, ApJ, 297, 621
Capetti, A., Macchetto, F., Axon, D. J., Sparks, W. B., & Boksenberg, A. 1995, ApJ, 452, L87
Gehrels, T. 1972, ApJ, 173, L23
Goosmann, R. W. & Matt, G. 2011, MNRAS, 415, 3119
Gratadour, D., Rouan, D., Grosset, L., Boccaletti, A., & Clénet, Y. 2015, A&A, 581, L8
Jaffe, W., Meisenheimer, K., Röttgering, H. J. A., et al. 2004, Nature, 429, 47
Kishimoto, M., Hönig, S. F., Antonucci, R., et al. 2011, A&A, 527, A121
Kishimoto, M., Hönig, S. F., Antonucci, R., et al. 2009, A&A, 507, L57
Kishimoto, M., Hönig, S. F., Beckert, T., & Weigelt, G. 2007, A&A, 476, 713
Lumsden, S., Bland-Hawthorn, J., Moore, T., et al. 1997, Ap&SS, 248, 287
Marin, F., Goosmann, R. W., Gaskell, C. M., Porquet, D., & Dovčiak, M. 2012, A&A, 548, A121
Nikulin, N. S., Kuvshinov, V. M., & Severny, A. B. 1971, ApJ, 170, L53
Packham, C., Young, S., Hough, J. H., Axon, D. J., & Bailey, J. A. 1997, MNRAS, 288, 375
Rowan-Robinson, M. 1977, ApJ, 213, 635
Wittkowski, M., Kervella, P., Arsenault, R., et al. 2004, A&A, 418, L39

*SF2A 2016*
*C. Reylé, J. Richard, L. Cambrésy, M. Deleuil, E. Pécontal, L. Tresse and I. Vauglin (eds)*

# HALL-MHD SIMULATIONS OF THE KELVIN-HELMHOLTZ INSTABILITY AT THE SOLAR WIND/MAGNETOSPHERE INTERFACE

M. H. J. Leroy[1] and R. Keppens[1]

**Abstract.** The process feeding the development of the boundary layer at the interface between the solar wind (SW) and the magnetosphere (MS) during northward interplanetary magnetic field is still not fully understood, though the Kelvin-Helmholtz instability (KHI) being the major actor is in good agreement with the observations so far. In this work, we study different configurations than can occur in the KHI scenario in a three-dimensional (3D) Hall-MHD setting, where the double mid-latitude reconnection (DMLR) process exposed by Faganello, Califano et al. is triggered by the equatorial roll-ups. Their previous work is extended here with a larger simulation box and the addition of a density contrast. The influence of the parameters on the growth rate of the KHI and thus the efficiency of the DMLR is assessed. The effect of the Hall term on the physical processes is also investigated.

Keywords: solar wind, magnetosphere, Kelvin-Helmholtz, Hall-MHD

## 1 Introduction

The plasma at the SW/MS interface is described by the resistive Hall-MHD set of equations. The introduction of the Hall term take into account the possibility that ions can demagnetise at the ion inertial length $\delta_i = c/\omega_{pi} \approx$ 100 km and break the 'frozen-in' condition, leading to an additional current term, while the magnetic resistivity will allows for the plasma to break fields lines and account for reconnection processes. These contributions appear explicitly in the Ohm's law $\mathbf{E} = -(\mathbf{v} - (\eta_H/\rho)\mathbf{J}) \times \mathbf{B} + \eta\mathbf{J}$, which has been rewritten to make the parameter $\eta_H = \rho/(n_e e)$ appears. The KHI will develop faster around the equatorial plane as the shear between the SW and the MS is stronger in this region, after the dispersion relation from Chandrasekhar (1961). Due to the 'frozen-in' property of the plasma, the differential advection of field lines along the latitude will induce twisting, leading to stressed field lines regions at symmetrical positions on each side of the equatorial plane. This process has been demonstrated by Faganello et al. (2012) and has been branded the DMLR. Magnetic reconnection then happens inside these regions above and below the equatorial plane, exchanging field lines from the MS and the SW with each other, continuously provoking the entry of SW matter into the MS. A specific configuration used by Faganello et al. (2012) will be reproduced here while extending the domain and duration of the simulation to see how vortex mergers in the mid-plane could alter the DMLR. The box size is chosen as $L_x$=70, $L_y$=188, $L_z$=377, given in ion inertial lengths and the number of points in the simulations is $N^3 = 200^3$. $L_y$ is twice larger than in Faganello et al. (2012) so that the domain is large enough for two pairs of KH vortices to appear. The $z$-direction corresponds to the latitude, the $y$-direction follows the interface and the $x$-direction is across the shear layer. The boundary conditions are periodic in the $y$- and $z$-directions, while in the $x$-direction the fields are extrapolated in a continuous fashion and corrected for a discrete monopole control. The initial fields are derived from a solution of a simplified Grad-Shafranov equation with ignorable $y$-direction that allows for equilibrium at the start and respects the $\nabla \cdot \mathbf{B}$=0 constraint and the velocity field is destabilized by the addition of incompressible perturbations.

[1] Centre for mathematical Plasma-Astrophysics, Department of Mathematics, KU Leuven, Celestijnenlaan 200B, B-3001 Leuven, Belgium

## 2 Parameters exploration

### 2.1 Modifications of the initial settings

The value of several initial physical quantities are modified to assert their influence on the growth rate and development of the KHI. The results are summed up in Fig.1 which displays the time evolution of the volume averaged values of $V_x^2$ and the maximum value of the current $J_{max}$ in the whole domain. This last value is always found the current sheets. The twisting of the field lines leads to the current sheets and is a clue to potential reconnection sites. For $M_A$=1/2, the lower velocity shear reduces the growth rate of the instability. In the case $M_A$=2, the instability does not develop as fast as the reference run. However it still appears at a later time with a stronger growth rate and reaches a larger $J_{max}$. Doubling the density jump to $\Delta_\rho = 7$ allows to determine if secondary RTI compete with the KHI. While the growth rate remains close to the reference run, the maximum current value reached is larger, indicating an enhanced compression of field lines. The last changes are the reduction of the shear layer width and the introduction of a shift between the velocity and density jumps. The result is that the KHI is triggered much sooner for $L_u$=1, as well as large values of the current, but the final stage displays a lower $< V_x^2 >$, and $J_{max}$ similar to the reference run. This comes from the fact that the velocity perturbation has a greater impact on a smaller and steeper gradient across the shear layer, but the situation becomes similar once the boundary layer between the SW and MS is fully developed. The more interesting point is that the combination of the narrow shear layer and the enhanced density jump on a shifted location yields the largest growth rate and highest values of $J_{max}$. The time evolution is also more dynamical with large variations in $< V_x^2 >$ and $J_{max}$.

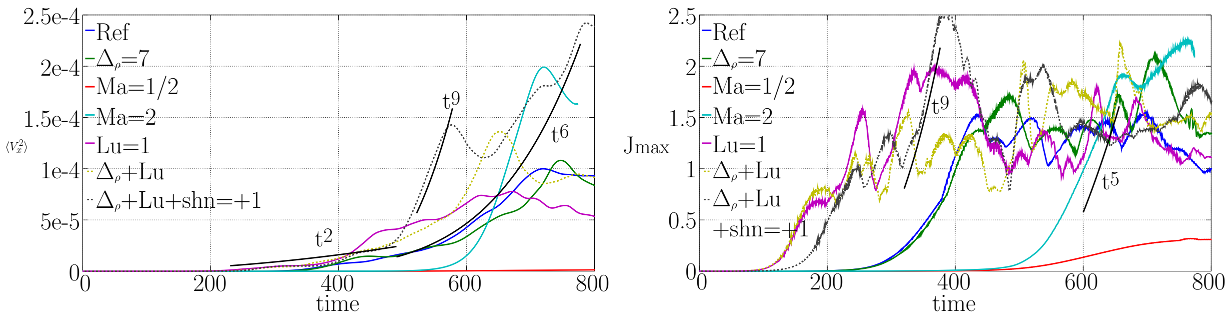


**Fig. 1. Left:** Time evolution of $< V_x^2 >$ for different alterations of an initial parameter. **Right:** Time evolution of $J_{max}$.

#### 2.1.1 Initial density jump

We then focus on the effect of the initial density jump in $\Delta_\rho$=[2 3.7 5 7 9]. It allows to clearly identify the effects of potential Rayleigh-Taylor instabilities (RTI), developing and competing with the KHI, fed by the centrifugal force generated by the vortices forming at the interface. All the curves fit the $t^6$ slope and $< V_x^2 >$ develops at the same time, but it seems to have an optimal value around $\Delta_\rho$=5. It has an effect afterwards as after a similar increase of $J_{max}$ following a $t^9$ slope, it increases the maximum value of the current found in the domain during the non linear stage. The first element to notice is that the largest values of the current magnitude can be found in the runs with the largest $\Delta_\rho$, up to $J_{max}$ = 1.3 compared to $J_{max}$ = 1.11 for the reference run. The second point is that this maximum value is not found at the same time between the runs. This comes from the fact that the twisting/reconnection process is quite dynamical in our simulations and that the magnetic gradients, hence the maximum of the current, increase until reaching a value where the reconnection of several field lines happens.

#### 2.1.2 Initial shear layer width

Next is the effect of the modification of the shear layer width from $L_u$=3 to $L_u$=1. This will create steeper initial velocity and density gradients and cause the KHI to appear faster than for the reference setting even keeping the other parameters at their reference values, and this is confirmed by Fig.3. The KHI and current sheets appear much sooner for $L_u$=1 than for $L_u$=3 and the first one reaches current values 30% higher even before the $L_u$=3

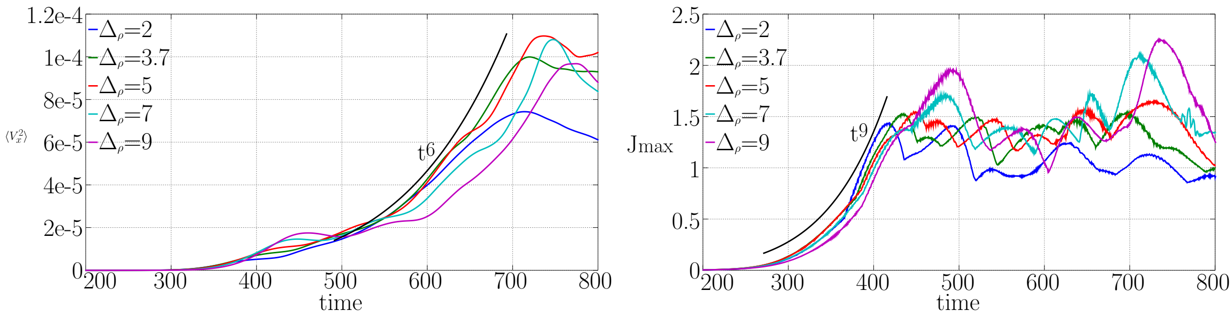


**Fig. 2. Left:** Time evolution of $< V_x^2 >$ for different $\Delta_\rho$. **Right:** Time evolution of $J_{max}$.

run reaches its first maximum. Nevertheless, the picture changes after some time as the $L_u$=1 simulation, while still reaching larger current values than the reference run, reaches its value maximum of $< V_x^2 >$ around $t_A$=600 and remains at a lower value than the reference run. What can be observed here is that the boundary layer is formed faster for $L_u$=1 and saturate in its non-linear evolution but since the current values are equal or higher than for the reference run, it shows that the $< V_x^2 >$ and $J_{max}$ are not linked in a simple way, but that the magnetic topology induced by the flow variation at the linear stage has consequences at later stages even if the general process remains the same in both cases. The $L_u$=2 run presents a most interesting variation of this development since it displays the fastest and largest growth of $< V_x^2 >$ while reaching values of $J_{max}$ no larger than the reference run in the linear stage. But at later stages after a drop in current magnitude and then in velocity, both increase to the largest values reached by the simulations in this set, showing a restart of the braiding/reconnection process. The addition of the shift between the velocity and density jump has a more diverse effect on the KHI evolution. The run with a negative shift see the KHI developing sooner than any other simulations but then saturates after its initial surge in a similar fashion to the $L_u$=1 run. The positive shift has quite the opposite effect as it seems to start the same way the $L_u$=1 run does, then reaches very large values of $< V_x^2 >$, becoming similar to the $L_u$=2 run, and presents a $J_{max}$ evolution with the largest variations.

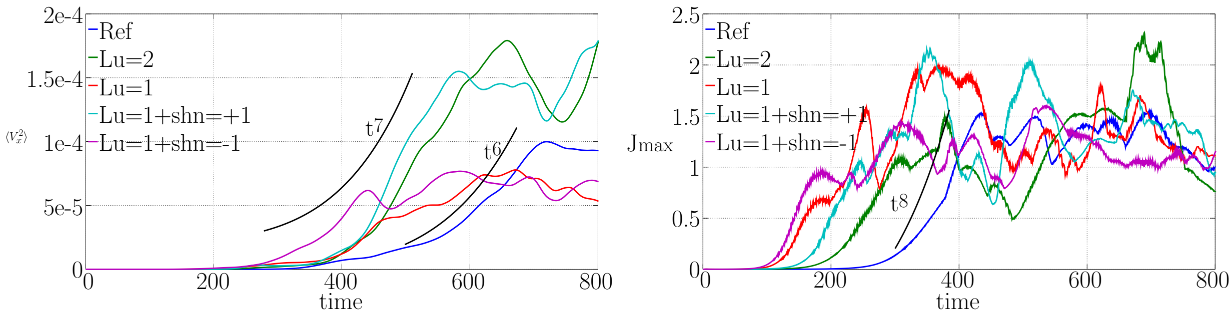


**Fig. 3. Left:** Time evolution of $< V_x^2 >$ for different $L_u$. **Right:** Time evolution of $J_{max}$.

### *2.2 Influence of the Hall term*

We also look into the influence of the Hall term by varying the magnitude of the parameter $\eta_H$ in Ohm's law. The actual normalized value the parameter should have in our setup is $\eta_H$=$V_{A0}/(\Omega_{ci0}\delta_i)$=6.25. Previous studies argued that the Hall term usually enhances the instability and transport properties of the flow like Chacón et al. (2003). This trend is confirmed in Fig.4, where the more realistic $\eta_H$=6.25 case attains almost twice the maximum value of $< V_x^2 >$ presented by the other simulations. The growth rate in this case is also much larger than for the lower values of $\eta_H$ following a $t^6$ slope. Despite this enhancement of the flow in the $x$-direction, all Hall-MHD simulations share the same effect on the current magnitude. This influence of the Hall term on the current is backed by Fig.4 where the maximum value of the current decreases steadily with the increasing value of $\eta_H$ while still retaining roughly the same evolution.

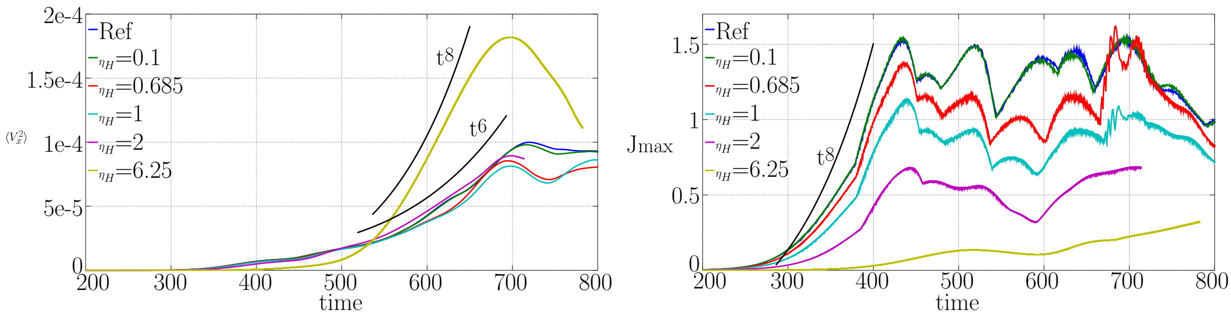


**Fig. 4. Left:** Time evolution of $< V_x^2 >$ for different $\eta_H$. **Right:** Time evolution of $J_{max}$.

## 3 Conclusions

The Kelvin-Helmholtz instability is one of the best candidate to explain the expansion of the low-latitude boundary layer forming between the shocked solar wind and the magnetosphere during northward IMF as more and more theoretical and observational studies points out. However, the precise characteristics of the mechanism remains unclear. The development of vortices on the equatorial plane do not only affect the boundary layer at this location but can also have consequences for the SW/MS interface at a distance as the DMLR hypothesis shows. In this paper we experimented on the different configurations the DMLR can adopt depending on the initial value of different physical parameters. The first observation is that the density contrast, neglected for the sake of clarity in many previous works, is an important feature of the KHI in those conditions. It can greatly affect the profile of the boundary layer, and by extension the efficiency of the DMLR as an exchange mechanism for field lines, and thus matter, between the SW and the MS. The second point is that the initial width and location of the shear layer and density contrast have a significant effect on the growth rate and size of the emerging boundary layer between SW and MS, again notably affecting the mixing on the equatorial plane and the topology of the current sheets at mid-latitude. At last some attention must be kept on the influence of the Hall term and the resolution used in simulation. Though the enhancement of the growth rate of the instability by the Hall term is recovered, it presents here an inhibiting effect on the magnitude of the current sheets, while not affecting much the general topology of the flow. A more detailed analysis, also including the effect of the resolution and the simulation of spacecrafts data can be found in Leroy & Keppens (2016).

This research was supported the Interuniversity Attraction Poles Programme initiated by the Belgian Science Policy Office (IAPP7/08 CHARM). We acknowledge access to the K.U.Leuven Tier-2 High Performance Computing cluster Thinking and UGent Tier-1 High Performance Computing cluster Muk. We thank Francesco Califano and Claudia Rossi for fruitful discussions. The figures in this paper were realised using the GNU software OctaveEaton et al. (2014).

## References

Chacón, L., Knoll, D., & Finn, J. 2003, Physics Letters A, 308, 187

Chandrasekhar, S. 1961, Hydrodynamic and hydromagnetic stability (Clarendon Press)

Eaton, J. W., Bateman, D., Hauberg, S., & Wehbring, R. 2014, GNU Octave version 3.8.1 manual: a high-level interactive language for numerical computations (CreateSpace Independent Publishing Platform), ISBN 1441413006

Faganello, M., Califano, F., Pegoraro, F., Andreussi, T., & Benkadda, S. 2012, Plasma Physics and Controlled Fusion, 54, 124037

Leroy, M. & Keppens, R. 2016, Physics of Plasmas *In review*

# FROM AUGER TO AUGERPRIME: UNDERSTANDING ULTRAHIGH-ENERGY COSMIC RAYS

F. Montanet, for the Pierre Auger Collaboration[1]

**Abstract.** Ultrahigh-energy cosmic rays (UHECRs), whose origin is still mysterious, provide a unique probe of the most extreme environments in the universe, of the intergalactic space and of particle physics beyond the reach of terrestrial accelerators. The Pierre Auger Observatory started operating more than a decade ago. Outperforming preceding experiments both in size and in precision, it has boosted forward the field of UHECRs as witnessed by a wealth of results. These include the study of the energy spectrum beyond 1 EeV with its spectral suppression around 40 EeV, of the large-scale anisotropy, of the mass composition, as well as stringent limits on photon and neutrino fluxes.
But any harvest of new results also calls for new questions: what is the true nature of the spectral suppression: a propagation effect (so-called Greisen, Zatsepin and Kuz'min or GZK cutoff) or cosmic accelerators running out of steam? What is the composition of UHECRs at the highest energies? In order to answer these questions, the Auger Collaboration is undertaking a major upgrade program of its detectors, the AugerPrime project. The science case and motivations, the technical strategy and the scientific prospects are presented.

Keywords: Cosmic rays, UHECRs, Pierre Auger Observatory

## 1 Introduction

Ultrahigh-energy cosmic rays have been studied at the Pierre Auger Observatory for more than 10 years by recording the associated extensive air showers (EASs). The Observatory (The Pierre Auger Collaboration 2015a) comprises a surface detector (SD) consisting of an array of 1600 water-Cherenkov stations with a spacing of 1500 m, covering an area of $\approx 3000$ km$^2$ and an air-fluorescence detector (FD) with a total of 24 telescopes in four sites on the perimeter of this array. The SD samples at ground level the particle components of extensive air showers with a duty cycle of nearly 100%, while the FD measures the longitudinal development of showers along their path in the atmosphere during clear moonless nights (with a duty cycle of $\sim$15%). The 1500 m spacing of the SD makes it 100% efficient to showers with energies above $3 \times 10^{18}$ eV. A denser infill array, with 61 water-Cherenkov detectors on a grid of 750 m spacing, extends the energy range down to $3 \times 10^{17}$ eV. Energies as low as $10^{17}$ eV are measured by means of 3 additional high-elevation Auger telescopes (HEAT). A sub-array of 124 radio sensors (Auger Engineering Radio Array, or AERA) working in the MHz range is employed to study radio emission from EASs and to identify mass-sensitive radio parameters.
The collected data provide information on the nature and origin of the primary cosmic rays and their astrophysical interpretation. From the point of view of particle physics, the measured observables allow us to set constraints on hadronic interactions and test their modelling in an energetic and kinematic region not reachable at accelerators. A selection of some the most important results is presented in this paper; for most of them, we refer the reader to the latest updates summarized in (The Pierre Auger Collaboration 2015b),(Ghia 2015).

## 2 Selected results

The energy spectrum above 3 $\times 10^{17}$ eV has been measured with unprecedented precision and statistics using 4 different data sets: the SD 'vertical' data up to a zenith angle of $\theta = 60^o$, the 'horizontal' data beyond

[1] LPSC, Université Grenoble-Alpes, CNRS/IN2P3, Grenoble, France
Observatorio Pierre Auger, Malargüe, Argentina
(Full author list : `http://www.auger.org/archive/authors_2016_06.html`)

$\theta = 60^{\rm o}$, the infill data and the "hybrid" data, the latter consisting of all events detected simultaneously by both the SD and FD. The hybrid data set is used to obtain the energy calibration directly from the data (The Pierre Auger Collaboration 2014a; Pesce 2011; Ravignani 2013). The resulting spectrum, shown in Fig. 1, flattens from a power law with index $3.29 \pm 0.02({\rm stat}) \pm 0.05({\rm sys})$ to one with index $2.60 \pm 0.02({\rm stat}) \pm 0.1({\rm sys})$ at $E_{\rm ankle} = 4.8 \pm 0.1 \pm 0.8$EeV. A clear suppression is observed at a significance in excess of $20\sigma$ beyond $E_{\rm s} = 42.1 \pm 1.7 \pm 7.6$EeV, energy at which the differential flux is reduced to one-half of the expected one from the extrapolation of the power-law above the ankle. The dominant systematic uncertainty of the spectrum stems from a 14% overall uncertainty in the energy scale.

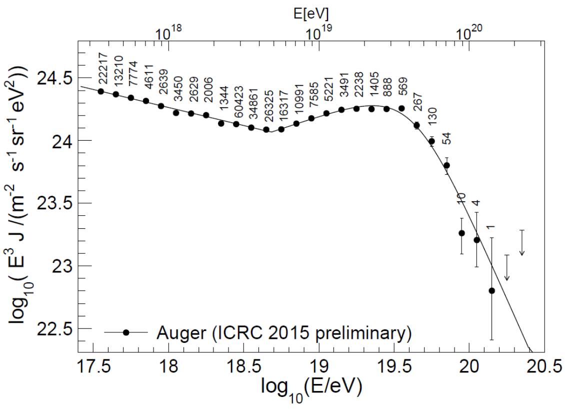


**Fig. 1.** The combined Auger energy spectrum.

Different observables can be used to obtain information on the primary composition, the most direct of which is the depth $X_{\rm max}$ of maximum development of the longitudinal shower profile, measured by the FD. Its first two moments $\langle X_{\rm max}\rangle$ and root-mean squared RMS($X_{\rm max}$) are related to the depth of the first interaction of the primary and to the subsequent development of the shower. The interpretation in terms of composition is inferred through the comparison with simulated data obtained using different hadronic interactions models. It is therefore affected by the rather large theoretical uncertainties of theses models. Having been corrected for the detector resolution, $\langle X_{\rm max}\rangle$ and its RMS can be directly compared to the predictions of air-shower simulations using recent hadronic interaction models, as shown in Fig. 2. Our measurements are clearly at variance with model predictions for a pure composition; assuming no change in hadronic interactions at these energies, they point to a composition getting heavier above the ankle.

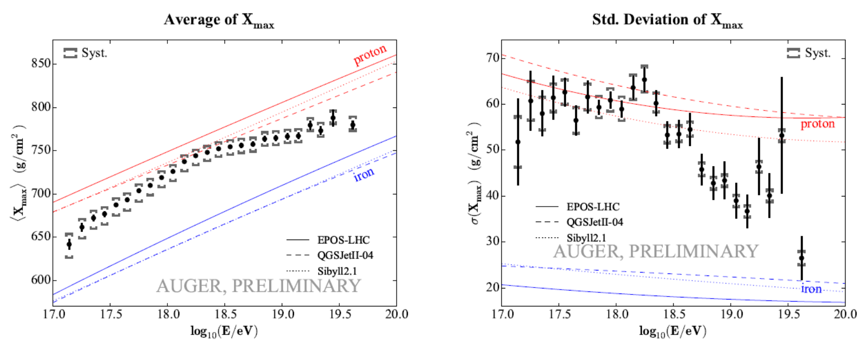


**Fig. 2.** First two moments of the $X_{\rm max}$ distribution, compared to model predictions, assuming either an all-proton or all-iron composition.

A deeper insight can be obtained by studying the shape of the $X_{\rm max}$ distributions (The Pierre Auger Collaboration 2014b): comparing them with those expected for different mass fractions (using different hadronic interaction models), the best fitting mixture of nuclei can be derived. This study shows that the data can be best reproduced with the inclusion of intermediate nuclei, the proton fraction strongly decreasing above $10^{19}$ eV, a 10-15% proton contribution seeming to appear again above $\approx 2.5\times10^{19}$eV. The high fraction of protons in the ankle region, together with the anisotropy limits derived from our data (The Pierre Auger Collaboration 2015c) suggest that already below $10^{18.5}$eV protons are mainly extragalactic and could point to an interpretation of the ankle as being due to the energy loss of extragalactic protons through electron-positron pair production during propagation in the cosmic microwave background Berezinsky & al. (2005, 2006). However, exploiting the correlation between $X_{\max}$ and the number of muons produced in the EAS at energies around $10^{19}$ eV, which is sensitive to the mixture of primary masses, we showed that the composition around the ankle is actually mixed, thus disfavouring that hypothesis.

An attempt to understand the origin of the suppression was made by simultaneously fitting both the spectrum and the evolution of $X_{\max}$ above $10^{18.7}$ eV. A simple astrophysical model was used assuming identical sources, homogeneously distributed in a comoving volume, injecting protons, He, N and Fe nuclei. The spectrum at the source was described as a broken power law with a rigidity-dependent exponential cutoff. The best fit to the spectrum was obtained by subsequent cutoffs of the different groups of elements, with $R_{\text{cut}} = 10^{18.67}$V and a very hard source spectrum with slope $\gamma = 0.94$, thus pointing to a flux suppression partly due to the reach to the maximum energy within the source. A second local minimum, with $\gamma = 2$ and larger maximum rigidity, similar to that expected for energy-loss effects due to propagation, can fit the spectrum, but the $X_{\max}$ distributions are too wide to agree with those measured. The best-fit position strongly depends on the details of propagation and of the air-shower development, the uncertainties of which are much larger than the statistical uncertainty of the measured data.

## 3 The AugerPrime upgrade

In the past 10 years, the Auger results have led to major breakthroughs in the study of cosmic rays. Different models have been built trying to reproduce our results (Caprioli & al. 2015; Unger & al. 2015; Globus & al. 2015), but the many unknowns about source distribution, composition, galactic and extragalactic magnetic fields, etc, prevent the emergence of a uniquely consistent picture. New information on the nature of the primaries is mandatory to address the problem of the origin of ultrahigh-energy particles. As discussed above, the origin of the flux suppression is still unknown, whether it be due to propagation effects or to exhaustion of the sources. We need mass-composition information above 40 EeV, currently not available due to the intrinsic duty cycle of the FD. Furthermore, the direct detection of cosmogenic photons or neutrinos would be direct evidence of the GZK effect. Studies of the arrival directions of UHECRs with composition-related selections will be most important to understand the reasons for the lack of small-scale anisotropy at the highest energies. The evaluation of the proton fraction above a few times $10^{19}$ eV is the decisive ingredient for estimating the physics potential of existing and future cosmic-ray, neutrino, and $\gamma$-ray detectors. From the particle physics point of view, direct measurements of the muon component of EASs will allow the study of hadronic interactions in an energy and kinematic region not explorable by terrestrial accelerators.

The AugerPrime upgrade of the Observatory has been specifically designed to improve the composition-sensitive information (The Pierre Auger Collaboration 2016). Along the lines of a hybrid design, each SD will be equipped with a top scintillator layer (Fig. 3a). Shower particles will be sampled by two detectors (scintillators and water-Cherenkov stations) having different responses to the muonic and electromagnetic components, thus allowing us to reconstruct each of them separately. The muonic component will be derived in each station by subtracting the signal observed in the scintillator from that seen in the water-Cherenkov tank. By fitting the muon lateral distribution, the muon signal at 800 m from the core $S(800)$ can be used as a composition-related observable. More sophisticated methods, based on multivariate analyses or on shower universality (Ave & al. 2011; Lipari 2008) will allow us to correlate the detector signals at different lateral distances and exploit the information of the arrival time of the EAS and of the temporal structure of the measured signals.

A preliminary demonstration of the potentials of AugerPrime can be obtained by taking two extreme and opposite assumptions fitted to the Auger flux and composition data: a maximum-rigidity (scenario 1) and a photo-disintegration one (scenario 2). The muon number relative to that expected for an equal mix of p-He-CNO-Fe as primary particles, the mean $X_{\max}$ and its RMS are shown in Fig. 3(b-d). Their values are quite similar in the region below $10^{19.2}$eV, covered by data of the FD, but the two scenarios can be distinguished with high significance and statistics in the GZK suppression region, where the models predict significantly different extrapolations.

The upgrade of the SD will also include newer electronics, with faster digitizers (120 MHz sampling compared to the current 40 MHz) and an increased dynamic range, allowing us to extend the measure to the larger signals closer to the shower core. To complement the SD upgrade, a network of underground muon detectors, each

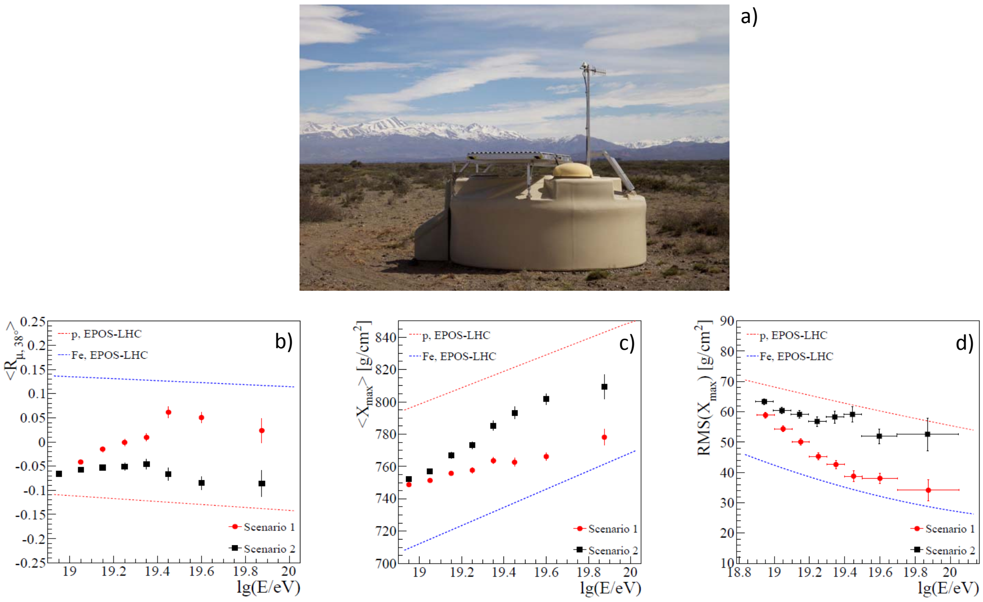


**Fig. 3.** (a) One of the first AugerPrime upgraded surface detectors; (b-d) reconstructed relative muon number $R_\mu$, $X_{\rm max}$ and RMS ($X_{\rm max}$) for the 2 considered scenarios (see text).

of 30m$^2$ area, is now being deployed in the infill area, for mass-composition studies in the sub-ankle region and direct verification of the extraction of the muonic signals from the combination of top scintillators and water-Cherenkov tanks. An upgrade of the FD is also foreseen: the operation mode of the FD will be changed to extend measurements into night periods with a higher light background, in order to reach a 50% increase of the on-time. The AugerPrime upgrade is now undergoing its engineering array phase. Its full operation is foreseen from 2018 until 2025, when event statistics will more than double compared with the existing Auger data set, adding event-by-event mass information.

## References

Ave, M. & al. 2011, Proc. 32nd ICRC, Beijing, 2, 178

Berezinsky, V. & al. 2005, Phys. Lett. B, 612, 147

Berezinsky, V. & al. 2006, Phys. Rev. D, 74, 043005

Caprioli, D. & al. 2015, Astrophys. J. Lett, 811, 2

Ghia, P. L. 2015, for The Pierre Auger Collaboration, Proc. 34th ICRC, The Hague, PoS(ICRC 2015)034

Globus, N. & al. 2015, Phys. Rev. D, 92, 021302

Lipari, P. 2008, Phys. Rev. D, 79, 063001

Pesce, R. 2011, for The Pierre Auger Collaboration, ArXiv:1107.4809, Proc. 32nd ICRC, Beijing, 2, 214

Ravignani, D. 2013, for The Pierre Auger Collaboration, ArXiv:1307.5059, Proc. 33rd ICRC, Rio de Janeiro

The Pierre Auger Collaboration. 2014a, JCAP, 019, 140808

The Pierre Auger Collaboration. 2014b, Phys. Rev. D, 90122006

The Pierre Auger Collaboration. 2015a, Nucl. Instrum. Meth. A, 798, 172

The Pierre Auger Collaboration. 2015b, Proc. 34th ICRC, The Hague, ArXiv:1509.03732

The Pierre Auger Collaboration. 2015c, Astrophys. J., 802, 111

The Pierre Auger Collaboration. 2016, Upgrade - Preliminary Design Report, ArXiv:1604.03637

Unger, M. & al. 2015, Phys. Rev. D, 92, 123001

*SF2A 2016*
*C. Reylé, J. Richard, L. Cambrésy, M. Deleuil, E. Pécontal, L. Tresse and I. Vauglin (eds)*

# WHICH MECHANISM FOR GAMMA-RAY FLARES OF THE CRAB NEBULA ?

T. Akramov[1] and H. Baty

**Abstract.** We report preliminary results using two dimensional (2D) classical MagnetoHydroDynamic (MHD) simulations with the aim to investigate the physical mechanism underlying gamma-ray flares. We explore the explosive reconnection mechanism proposed by Baty et al. (2013) in order to confirm its ability to produce flares when located in the stripped wind region. In particular, the time scale of the process is shown to be independent of the unkown dissipation, enforcing the robustness of the model. A considerable particle acceleration is also obtained, involving a potentially important non thermal contribution for the resulting synchrotron radiation.

Keywords: plasma - reconnection - high-energy - gamma-rays

## 1 Introduction

The Crab pulsar and its surrounding nebula is a well-known relic of a massive star that exploded in 1054 AD. The Crab nebula was generally believed to be a good standard candle in gamma rays. Recently, this view has been challenged by sudden increases in the gamma-ray flux in a narrow spectral band within a few hundred MeV, as observed in gamma-rays by Fermi/LAT. These flares are short but powerful; their duration is between a few hours and up to several days with a rising/falling time of a few hours/days [Striani et al. (2013)]. To date it is neither clear what mechanism powers these flares nor where exactly in the nebula they should be located.

Magnetic reconnection could be an efficient mechanism to explain these flares [Clausen-Brown & Lyutikov (2012)]. The tearing instability of current sheets is the simplest way of triggering magnetic reconnection [Lyutikov (2003)]. Recently, Baty et al. (2013) proposed an explosive mechanism based on the double tearing mode (DTM). The favoured site for the radiation emission corresponds to a region situated in the stripped wind close to the light cylinder radius ($r \simeq 50r_L$). Indeed, the DTM is a magnetohydrodynamic (MHD) instability that is known to develop in multiple current sheets, as expected from the magnetic structure of pulsars magnetosphere with the presence of a current sheet wobbling around the equatorial plane [Coroniti (1990)].

The aim of our work is to explore into more detail the physical mechanism underlying the DTM mode, with a particular emphasis on the time scale giving the fast and explosive character of the process. This is investigated by means of two dimensional (2D) classical resistive MHD simulations. We also explore the consequences for particles using an independent test-particle acceleration code. Preliminary results are presented in this paper.

## 2 MHD model and numerical setup

We use the resistive MHD model in the non relativistic framework; and the two-dimensional cartesian geometry $(x, y)$ is considered. The initial magnetic structure consists of a double Harris current sheet configuration in static equilibrium:

$$B_x = 0, B_y = B_0[1 - \tanh(\frac{x + x_0}{a}) + \tanh(\frac{x - x_0}{a})], \tag{2.1}$$

where $a$ is the half-width of each current sheet and $x_0$ gives the location of the current sheets. An isothermal plasma with a small $\beta$-parameter is considered here as $\beta = 0.2$. We set the ratio of specific heats $\gamma$ equal to $5/3$ and choose units such that the magnetic permeability is unity, $\mu_0 = 1$. We also set $B_0 = 1$ and $a = 0.2$ to

[1] Observatoire Astronomique de Strasbourg, Université de Strasbourg, CNRS, UMR 7550, 11 rue de l'université, F-67000 Strasbourg, France

define our normalization. The velocity is normalized by the characteristic Alfvén speed $v_A$ given by $B_0/\sqrt{4\pi\rho_0}$ and we set $v_A = 1$. The current sheets are located at $x = \pm x_0$ with $x_0 = 0.5$. A divergence-free magnetic field ($\delta B \sim 10^{-3}B_0$) is used to perturb the system at the initial time. The simulations are carried out using the shock-capturing MPI-AMRVAC code with the finite-volume method [Porth et al. (2014)] in a square box of dimensions $[-2:2] \times [-2:2]$ including $960 \times 960$ grid cells. In order to investigate the scaling law of the explosive DTM growth, a high number of resistivity values ($\eta$) will be considered, $\eta$ beeing here the parameter of the unkown magnetic dissipation.

In addition, we perform test-particle calculations to investigate particle acceleration mechanisms during the DTM evolution at the different MHD times. For the sake of simplicity, a single particle with an effective mass $m = 10m_e$ is introduced ($m_e$ being the electron mass). A standard second-order (Boris-Buneman) time integrator is used to solve the motion equation. The integration time is $t_{int} = 4.4 \times 10^3 \tau_g$ (leading to $t_{int} \simeq \tau_A$), where $\tau_g = m/(qB_0)$ is the gyro-period and $\tau_A = 2x_0/v_A$ is the Alfvén transit time. The energy spectra are obtained with $10^4$ initially mono-energetic ($|\mathbf{v}_0| = 10^{-3}v_A$) particles, initiated in arbitrary directions with random coordinates within $x \in [-1:1]$ and $y \in [-2:2]$. The electromagnetic structure is assumed to be invariant for the time integration in the $z$-direction.

## 3 MHD simulation results

### 3.1 *Typical evolution*

The typical behaviour of the system is obtained through four successive DTM phases as illustrated in Fig. 1 (for $\eta = 5 \times 10^{-5}$) using the magnetic field lines. In order to measure the growth rate of DTM instabilities, we use the maximum absolute value of velocity $y$-component ($v_{y,max}$) in the domain, and its typical evolution is shown in Fig. 2. We are particularly interested in the explosive phase which is characterized by the coalescence of two initial magnetic islands (see Fig. 1-c and the time interval $200 \leq t \leq 250$ in Fig. 2). During this phase, the velocity $v_{y,max}$ increases very dynamically with an instantaneous growth rate, $v_{y,max} \propto e^{\sigma(t)\cdot t}$, where $\sigma(t)$ is the growth rate defined as $d\ln(v_{y,max})/dt$. Note that we have obtained $\sigma(t) \simeq \alpha t + \beta$ ($\alpha$ and $\beta$ are constants), illustrating the explosive character of the phase.

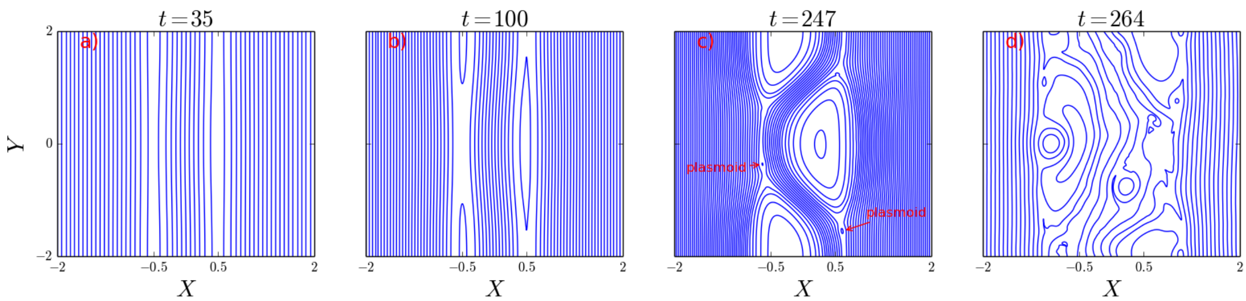


**Fig. 1.** Typical DTM evolution for $\eta = 5 \times 10^{-5}$: Magnetic filed lines corresponding to different phases of the DTM development (see Fig. 2). The explosive phase is represented in panel (c) at a given time where plasmoids are visible.

### 3.2 *Scaling law with* $\eta$

Since the growth rate $\sigma$ evolves with time, one can measure the average and maximum growth rates of the explosive phase. This is done for different resistivity values in the range $[\,2 \times 10^{-6} : 2.5 \times 10^{-4}]$. Fig. 3 shows these results. As an important point, we obtained that the maximum rate ($\sigma_{max}$) increases very weakly with the resistivity as $\sigma_{max} \sim \eta^{0.05\pm0.04}$ (bottom panel of Fig. 3). In other words, $\sigma_{max}$ is nearly independent of $\eta$. Moreover, secondary islands or "plasmoids" can be observed during this phase for cases where the local Lundquist number ($S_c = lv_A/\eta$ with a current sheet length $l$) exceeds a critical value, $S_c \gtrsim 10^4$, in agreement with theory [Loureiro et al. (2007)]. However, they appear as transient structures and disappear during the coalescence of primary islands. Consequently, they do not affect the explosive reconnection phase.

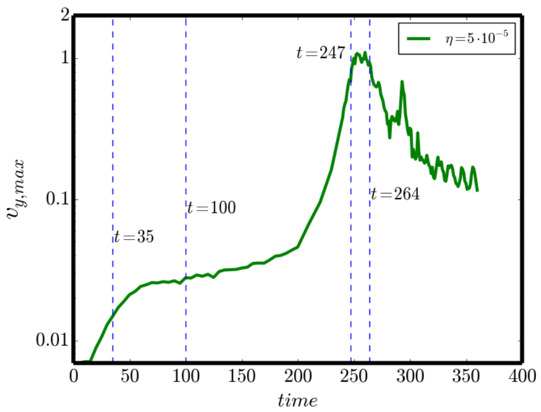


**Fig. 2.** Typical DTM evolution for $\eta = 5\times10^{-5}$: maximum value of $|\mathbf{v}_y|$ as a function of time. The times corresponding to panels of Fig. 1 are indicated by vertical lines.

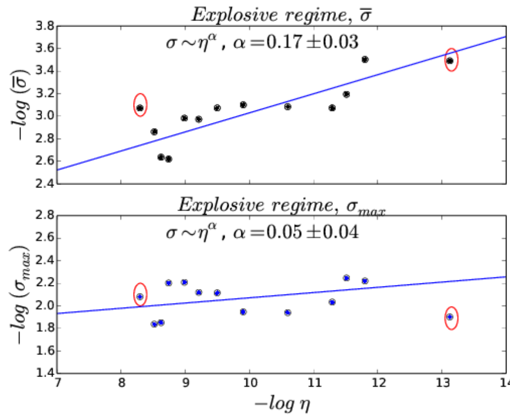


**Fig. 3.** Average (top panel) and maximum (bottom panel) measured growth rates of the explosive phase, as a function of the resistivity value. The two extreme points (with circles) are excluded from the linear fit.

## 4 Test-particle calculation results

In order to evaluate the efficiency of particle acceleration during the DTM phase, we have obtained energy spectra using $10^4$ particles at different MHD times. Firstly, the so-called "saturation phase" (see Fig. 1-b and the time interval $80 \leq t \leq 180$ in Fig. 2) is chosen for comparison. The spectrum for this phase is plotted on left panel of Fig. 4. Secondly, the explosive phase is investigated at three different times ($t = 241, 247$ and 250). The results are shown on right panel of Fig. 4. One can see the considerable non-thermal acceleration ($3 - 4$ orders of magnitude higher in kinetic energy) process potentially contributing to the resulting synchrotron radiation with a spectral index of 1.75. The conclusion holds whatever is the resistivity value.

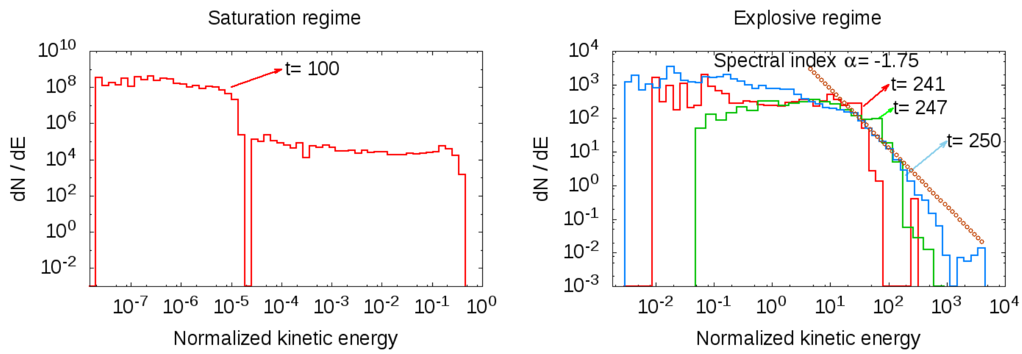


**Fig. 4.** Energy spectra obtained for the saturation phase at $t = 100$ (left panel) and for the explosive phase at $t = 241, 247, 250$ (right panel), using MHD configuration for a simulation with $\eta = 5 \times 10^{-5}$.

## 5 Conclusion

Our MHD results confirm the robustness of the DTM mechanism due to the very weak resistivity dependence of the explosive instabilty. Our results of test-particle acceleration show that an important non-thermal energization could also contribute to the resulting synchrotron radiation in addition to the thermal component (see synthetic synchrotron spectra obtained by Takamoto et al. (2015) in highly relativistic regime). Thus, the DTM instability of the magnetic structure in the striped wind region is a viable mechanism to explain Crab MeV flares. As the present results were obtained with newtonian MHD, we are actually extending our work to the more relevant relativistic MHD regime.

H. Baty acknowledges support by French National Research Agency (ANR) through Grant ANR-13-JS05-0003-01 (Project EMPERE). We also acknowledge computational facilities available at Equip@Meso of the Université de Strasbourg.

## References

Baty, H., Petri, J., & Zenitani, S. 2013, MNRAS, 436, L20

Clausen-Brown, E. & Lyutikov, M. 2012, MNRAS, 426, 1374

Coroniti, F. V. 1990, ApJ, 349, 538

Loureiro, N. F., Schekochihin, A. A., & Cowley, S. C. 2007, Physics of Plasmas, 14, 100703

Lyutikov, M. 2003, MNRAS, 346, 540

Porth, O., Xia, C., Hendrix, T., Moschou, S. P., & Keppens, R. 2014, ApJs, 214, 4

Striani, E., Tavani, M., Vittorini, V., et al. 2013, ApJ, 765, 52

Takamoto, M., Pétri, J., & Baty, H. 2015, MNRAS, 454, 2972

# Session SF2A

# Numerical simulations in astrophysics

*SF2A 2016*
*C. Reylé, J. Richard, L. Cambrésy, M. Deleuil, E. Pécontal, L. Tresse and I. Vauglin (eds)*

# NUMERICAL RELATIVITY AND SPECTRAL METHODS

P. Grandclement[1]

**Abstract.** The term numerical relativity denotes the various techniques that aim at solving Einstein's equations using computers. Those computations can be divided into two families: temporal evolutions on the one hand and stationary or periodic solutions on the other one. After a brief presentation of those two classes of problems, I will introduce a numerical tool designed to solve Einstein's equations: the KADATH library. It is based on the the use of spectral methods that can reach high accuracy with moderate computational resources. I will present some applications about quasicircular orbits of black holes and boson star configurations.

Keywords: Gravitation, Methods: numerical

## 1 Introduction

In the strong field regime, gravitation must be studied in the framework of general relativity. The geometry of the spacetime is described by the metric which gives the distance between neighboring points. It is a four-dimensional, second order, symmetric tensor and so consists of ten components. This metric depends on the energy content of the spacetime and the link between geometry and energy is given by the famous Einstein's equations. They consist of a set of ten highly coupled non-linear equations. Those equations are not easy to solve and analytic solutions are known in only very few cases. Most of the time one relies on semi-analytically methods (like the famous post-Newtonian expansion) or on computers to find solutions. This proceeding is concerned with the latter case. In particular, I will briefly introduce a class of numerical techniques known as spectral methods. Then I will present a numerical tool that enables the use of those methods: the KADATH library.

The fields of astrophysics where general relativity must be taken into account are numerous. One can think about coalescing compact binaries, especially with the first direct detection of the gravitational waves in September 2015. General relativity in also important in supernovae simulations and for studying the structure of neutron stars. There are also a lot of other applications that concerns more theoretical physics than classical astrophysics. One can mention the study of critical phenomena or the stability of ADS spacetime. I will present two applications, one about quasicircular configurations of compact binaries and one about objects that could be a viable alternative to black holes: the boson stars.

## 2 3+1 formalism

The 3+1 formalism is a rewriting of Einstein's equations in order to make them suitable for numerical resolution (see Gourgoulhon (2012) for a review). It is essentially a splitting of the four spacetime dimensions into space (the 3) and time (the 1). In order to do so one has to introduce a family of spatial hypersurfaces $\Sigma_t$ such that the full spacetime is given by the union of all those hypersurfaces. At each point of $\Sigma_t$ one introduces the normal $\mathbf{n}$ which is a timelike vector. The choice of $\Sigma_t$ is not unique but is merely a choice of time coordinate. Under those assumptions, the metric reads :

$$\mathrm{d}s^2 = -\left(N^2 - N^i N_i\right)\mathrm{d}t^2 + 2N_i \mathrm{d}t\mathrm{d}x^i + \gamma_{ij}\mathrm{d}x^i\mathrm{d}x^j,$$

[1] LUTH, Observatoire de Paris, 5 place J. Janssen, 92195 Meudon

where $N$ is the lapse, $N^i$ the shift vector and $\gamma_{ij}$ the spatial metric. All those objects are purely three dimensional objects that live on the hypersurfaces $\Sigma_t$. It implies that the Latin indices range from 1 to 3 only. However those quantities do depend on the hypersurface considered, meaning they do depend on time. So, to summarize, instead of working with four-dimensional quantities, the 3+1 formalism describes the spacetime by temporal sequences of purely spatial quantities.

The next step is then to project Einstein's equations onto the hypersurfaces and on the normal $\mathbf{n}$. Doing so, one translates the four dimensional equations into a set of equations involving only spatial quantities. This leads to the 3+1 equations of general relativity. They are given below, along with the Maxwell ones, for comparison purposes.

| Type | Einstein | Maxwell |
|---|---|---|
| Constraints | Hamiltonian $R + K^2 - K_{ij}K^{ij} = 0$ | $\nabla \cdot \vec{E} = 0$ |
| | Momentum : $D_j K^{ij} - D^i K = 0$ | $\nabla \cdot \vec{B} = 0$ |
| Evolution | $\frac{\partial \gamma_{ij}}{\partial t} - \mathcal{L}_{\vec{N}} \gamma_{ij} = -2NK_{ij}$ | $\frac{\partial \vec{E}}{\partial t} = \frac{1}{\varepsilon_0 \mu_0} \left(\vec{\nabla} \times \vec{B}\right)$ |
| | $\frac{\partial K_{ij}}{\partial t} - \mathcal{L}_{\vec{N}} K_{ij} = -D_i D_j N + N\left(R_{ij} - 2K_{ik}K^k_j + KK_{ij}\right)$ | $\frac{\partial \vec{B}}{\partial t} = -\vec{\nabla} \times \vec{E}$ |

$D_i$ and $R_{ij}$ denote, respectively the covariant derivative and Ricci tensor associated to $\gamma_{ij}$. $K_{ij}$ is the so-called extrinsic curvature tensor and can be seen as being the velocity of the metric, in the sense that it is closely related to the first time derivative of the metric. Indeed the first evolution equation is not one of Einstein's equation but merely the kinematic definition of $K_{ij}$.

Solving this set of equations proceeds in two steps. First one needs to solve the *initial value problem*, meaning one needs to find the values of $\gamma_{ij}(t = 0)$ and $K_{ij}(t = 0)$ that fulfill the constraint equations and that describe accurately the physical situation one wants to study. Mathematically speaking it involves solving a set of four elliptic coupled equations. The second step is the *evolution problem* where one uses the evolution equations to get the values of $\gamma_{ij}$ and $K_{ij}$ at later times. Let us mention that the second order system is written as a set of two first order equations, as it can be done in Newtonian dynamics if one rewrites Newton's equation as $\partial_t x = v$ and $\partial_t v = f/m$. If the constraint equations are fulfilled at $t = 0$ and if the evolution equations are solved properly, it can be demonstrated that the constraints equations are going to be true for all times. One says that they are transported by the evolution equations. Solving the evolution equations means having the ability to maintain stability and accuracy and that requires good choice of coordinates, choice that is being done via the lapse and shift.

## 3 Spectral methods

Spectral methods are a class of numerical techniques where the various fields are described by finite sums of known functions called the *basis functions*. An introduction to those methods can be found in Grandclément & Novak (2009).

In one dimension, consider an interval $\Lambda$ and a set of orthogonal basis functions $\Phi_i$ on $\Lambda$. The spectral theory gives then a recipe to approximate any function $f$ of $\Lambda$ by its interpolant of degree $N$ :

$$f \approx I_N f \equiv \sum_{i=0}^{N} a_i \Phi_i,$$

where the $a_i$ are called the coefficients of $f$. Standard choices for the basis functions include orthogonal polynomials like Legendre of Chebyshev or trigonometrical functions. In this second case, the spectral expansion is nothing else than the usual discrete Fourier transform of $f$.

An important feature of the spectral expansion is the existence of the so-called *collocation points*. One can show that there exist $N + 1$ points $x_i$ in $\Lambda$ such that $f$ and its interpolant coincide at those points : $f(x_i) = I_N f(x_i)$. It follows from that property that one has two ways of describing a function on $\Lambda$: either by its coefficients $a_i$ or by its values at the various collocations points $f(x_i)$. There is a bijection between the two descriptions and one can go back and forth between the two without any loss of precision. Depending on the mathematical operation that one needs to perform on $f$ it may be easier to work with one description or the other. For instance, derivation is much easier to perform using the coefficients description for it only requires to know the derivative of the basis functions.

The main reason for using spectral methods is the very fast convergence of $I_N f$ to the real function $f$. One can show that, if $f$ is $\mathcal{C}^\infty$, then the convergence is faster than any power-law of $N$. This is called *spectral convergence*. This is to be compared with finite difference schemes where only a power-law convergence is achieved. For less regular functions however, spectral convergence is lost. In that case a multi-domain decomposition can be used: by setting the domains such that the discontinuities lie at the interface, one can hope to recover spectral convergence (the functions being $\mathcal{C}^\infty$ by parts).

Figure 1 shows an example of spectral expansion. The blue curve corresponds to the function $u(x) = \cos^3(\pi x/2) - (x+1)^3/8$, which is not polynomial but is $\mathcal{C}^\infty$. The red curve denote the true projection of $u$ onto the set of Chebyshev polynomials and the green one the interpolant $I_N u$. All those three functions differ. The circles show the location of the collocation points where, indeed, $u$ and $I_N u$ coincide. The left panel is for $N = 4$ and the right one for $N = 8$. The convergence of $I_N u$ to $u$ is clearly illustrated.

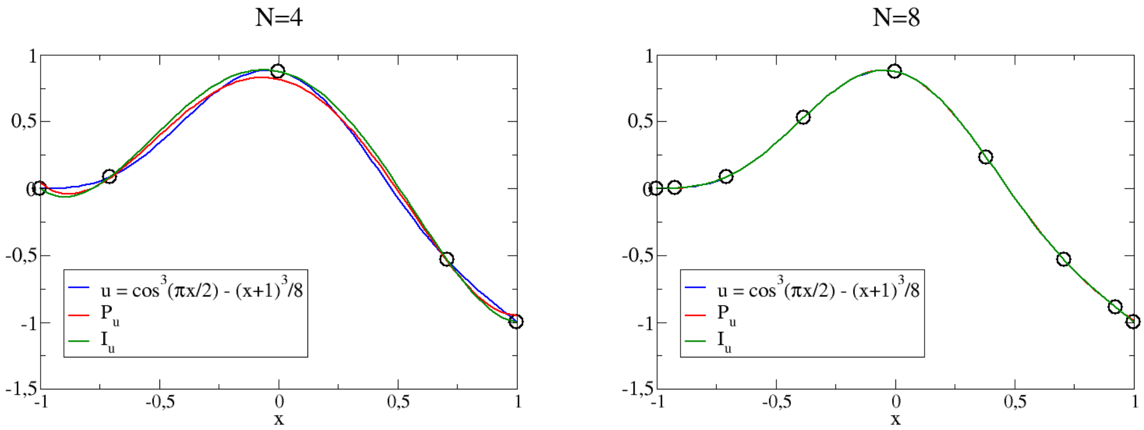


**Fig. 1. Left:** Function (blue curve), its true projection onto the basis functions (red curve) and its spectral representation (green curve). for $N = 4$. The circles denote the location of the collocation points.**Right:** Same thing for $N = 8$.

Figure 2 shows the maximum difference between $u$ and its interpolant $I_N u$, as a function of $N$, for the same function $u$ as in Fig. 1. The error decreases exponentially until it reaches a saturation of about $10^{-14}$, coming from the fact that the code works in double precision.

In order to solve differential equations using spectral methods, one relies on a class of techniques known as the *weighted residual methods*. Consider a field equation written as $R = 0$, where $R$ is given as a function of some unknown fields (for instance $R = \Delta f - S$ for solving a Poisson equation). The weighted residual methods provide a way of transforming this field equation into a set of discrete equations by demanding that $(R, \xi_i) = 0$. Here $(,)$ denotes the same scalar product as the one used for the spectral expansion. The $\xi_i$ are called the test functions and various choices are possible. For instance, if one chooses as test functions the basis functions themselves, the weighted residual method is called the $\tau$-method. Some of the discrete equations must usually be relaxed in order to enforce appropriate matching and boundary conditions.

## 4 The KADATH library

It is a library designed to enable the use of spectral methods in various context arising in the fields of astrophysics and theoretical physics. It is written in C++ and makes an extensive use of object programming. The library is intended to be very modular both in term of the geometry considered and the type of equations it can solve. The equations are passed to the code with a text interface inspired by LateX that should be easy to grasp for most researchers. A description of the library can be found in Grandclément (2010) and it can be downloaded freely at `http://luth.obspm.fr/~luthier/grandclement/kadath.html`.

KADATH implements various choices of geometry and coordinates (spherical, bispherical etc...) and additional cases are relatively easy to add. When the library is used to solve a system of equations, the unknowns

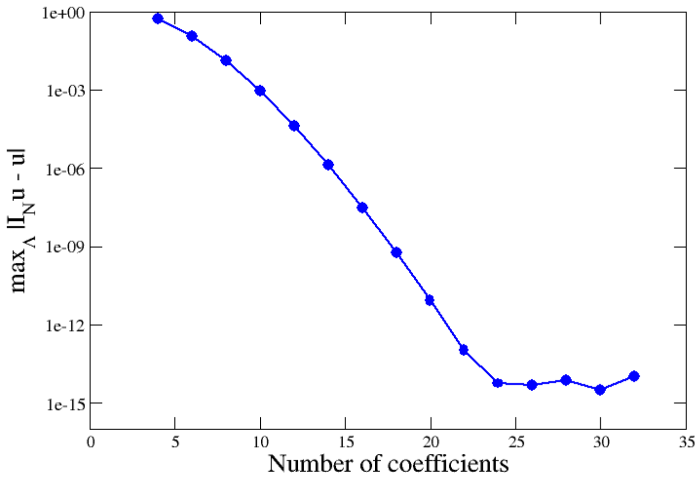


**Fig. 2.** Maximum difference between $u$ and its interpolant, as a function of the number of coefficients.

are the coefficients of all the unknown fields in the whole space. Let us denote those coefficients by a vector $\vec{x}$. The equations are dealt with using the weighted residual method and they lead to a discrete system $\vec{F}\left(\vec{x}\right) = 0$.

In general, the system considered is non-linear and the solution must be sought be means of a Newton-Raphson method. One starts from an initial guess $\vec{x}_0$ and the true solution is approached by successive steps. Each iteration requires the inversion a linear approximation of the system. More precisely the approximation $\vec{x}_{i+1}$ relates to the previous one by $\vec{x}_{i+1} = \vec{x}_i - \vec{\delta x}$, where $\vec{\delta x}$ is the solution of $J\left(\vec{x^i}\right) \times \vec{\delta x} = \vec{F}\left(\vec{x}_i\right)$, where $J$ is the Jacobian of the system (computed here at the position $\vec{x}_i$).

The Jacobian must be computed at each step of Newton-Raphson algorithm. In KADATH this is done via a numerical technique called *automatic differentiation*. Basically, each quantity (here each coefficient) is supplemented by its variation. One then talks about dual numbers. All the arithmetic is then redefined on those dual number. Let us consider the dual form of the unknown vector denoted by $\left\langle \vec{u}, \vec{\delta u} \right\rangle$. The action of $\vec{F}$ in its dual form leads to $\left\langle \vec{F}, \delta\vec{F} \right\rangle$. It is possible to show that the variation $\delta\vec{F}$ gives some information on the Jacobian. More precisely one has $\delta\vec{F} = J \times \vec{\delta u}$. So, the Jacobian itself can be obtained by taking all the possible values of $\vec{\delta u}$.

One of the main difficulty comes from the fact that the size of the Jacobian can be big. For three-dimensional problems, one can have to deal with a matrix of size $200,000 \times 200,000$. Because of this, KADATH has to be run in parallel. Thanks to the automatic differentiation, the Jacobian is obtained column by column, each computation being independent of the the others, so that this can be easily parallelized. The inversion of the Jacobian is also performed in a parallel manner using the library `scalapack`. KADATH has been successfully used with several thousands processors.

One of the main limitation of the library concerns explicit time evolutions. They are virtually non-existent and the library is only concerned with solutions having some symmetry with respect to time (either stationary or periodic solutions). The simplest way to deal with explicit time evolutions is to use a Runge-Kutta integration with respect to time, using the spectral approximation only for the spatial dimensions. This is widely used and seems to yield good results. An alternative is to use a spectral expansion also in time. For instance one can expand the fields onto Chebyshev polynomials in time and integrate the evolution equation on a given interval $[0, \Delta T]$, once the initial value of the fields are given (and possibly their first time derivative). The fields are then known on $[0, \Delta T]$ and the procedure can then be repeated. The choice of the numerical parameter $\Delta T$ is obviously important. Very preliminary tests indicate that this procedure works fine. However the resulting code is much longer than its counterpart based on Rugge-Kutta. Whether there are some cases where spectral expansion in time is really needed is still an open question.

As seen before, most of the computational time is spent when calculating the Jacobian and solving the associated linear system. There exists a class of alternative methods that could reduce this cost. They aim at finding the solution of a linear system iteratively. There are various versions of those techniques (GMRES, Bicgstab ...) but they are all based on the notion of Krylov subspace. Essentially the solution of the system is assumed to be given by successive powers of $J : \sum_n J^n \times S$. Using this property, one can show that each step of the iteration requires only to be able to compute products like $J \times f$ where $f$ is given (by the method and the iteration...). It follows that, if the procedure converges with a number of iteration much smaller than the size of the Jacobian, those iterative techniques would be much faster than the direct inversion. Also they do not require to store the matrix $J$ and so are usually less expensive in terms of memory usage. However the main limitation of those iterative techniques is that convergence is far from being guarantied. Most of the time it requires a carefully preconditioning of the system and q fine-tuning of the various computational parameters. Those methods are probably not general enough to be used for all the applications of KADATH. Nevertheless, for some particular cases, it may be useful to allow the user to have access to those techniques and there are plans to include them in the KADATH library. A detailed presentation of various iterative methods can be found in Saad (2003).

## 5 Some applications

### 5.1 Boson star models

Boson stars are one of the alternative to black holes, especially in the context of supermassive objects at the center of galaxies. By this one means that they can have a great mass inside a small radius, without the presence of an event horizon. Boson stars are described by a complex scalar field coupled to gravity. The structure of those objects is then given by the solution of Einstein's equations (for the gravity) coupled to the Klein-Gordon one (for the scalar field).

Boson stars are obtained when considering the following ansatz for the scalar field $\phi = \phi_0 \exp\left[i\left(\omega t - k\varphi\right)\right]$. Doing so, the quantity $\phi_0$ is real and only depends on $(r, \theta)$. The metric fields are also axisymmetric and stationary. The various boson star models are labelled by the winding number $k$ which is an integer, and the real pulsation $\omega$. InGrandclément et al. (2014) we solved the equations using a two-dimensional setting in KADATH (i.e. the *Polar* space). The left panel of Fig. 3 shows the configuration of the field $\phi_0$ in the case $k = 2$ and $\omega = 0.8$.

Numerical models can be used to deduce observational constraints on the existence of boson stars. For instance, Vincent et al. (2016) have simulated the image of an accretion disk around such an object and see if there are some differences with accretion disk around a black hole. This is what is done on the right panel of Fig. 3. In this particular case however, it was noted that the two images were very close, even if the geometry of spacetime is different. Nevertheless, the study of various physical effects around boson stars should lead to several observational tests that could be used, in the future, to rule out or confirm the existence of such objects.

### 5.2 Quasi-circular compact binaries

This application is concerned with the computation of binary black hole configurations. It is assumed that the two holes are on closed circular orbit. This cannot be exact: due to gravitational wave emission the orbit is rather a spiral. However, in the early stages of the binary this is probably a good approximation. From the practical point of view it greatly simplifies the problem by removing any explicit time evolution (the problem becomes three-dimensional only). An additional approximation that is used is the so-called *conformal flatness approximation* which assumes that the spatial metric is conformally flat. Not only does it simplify the equations but it also kills the gravitational waves.

Under those assumptions, the mathematical problem reduces to solving five coupled non-linear elliptic equations for five unknown fields. Non-trivial boundary conditions must be enforced on the horizon of the holes. The system is solved using the bispherical coordinates of the KADATH library (see Uryũ et al. (2012)). Figure 4 shows one particular configuration where the mass ratio of the two objects is two. The upper panel shows the value of the surface gravity on the two holes. As expected, this quantity is inversely proportional to the mass of each hole. Also, as seen on the lower panel, it is almost constant on each horizon. This is a numerical confirmation of what is know as the zeroth law of black hole thermodynamics.

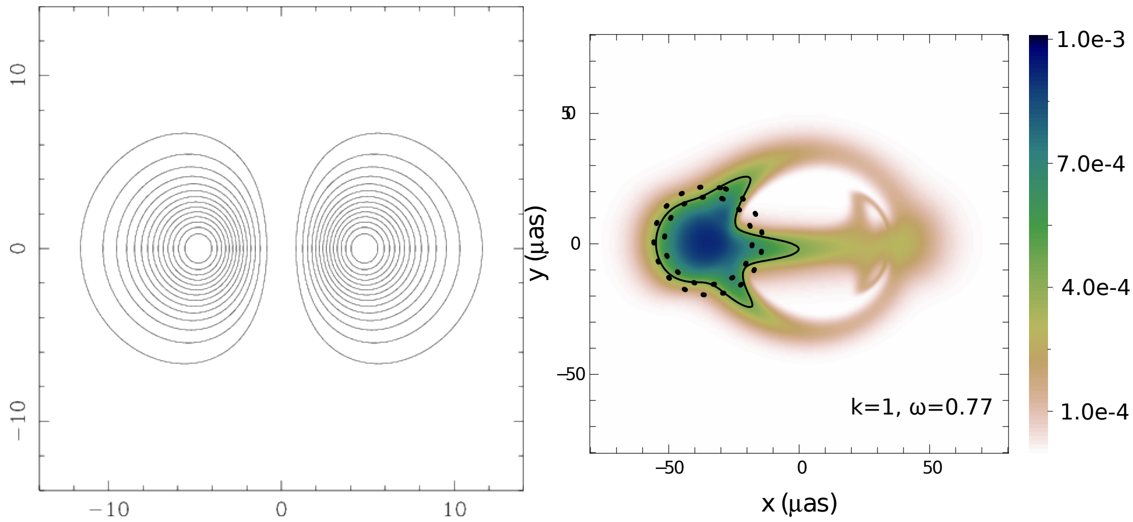


**Fig. 3. Left:** Isocountours of $\phi_0$ in the $(x, z)$ plane. The field is symmetric around the $z$-axis.**Right:** Image of an accretion disk around a $k = 4$, $\omega = 0.77$ boson star.

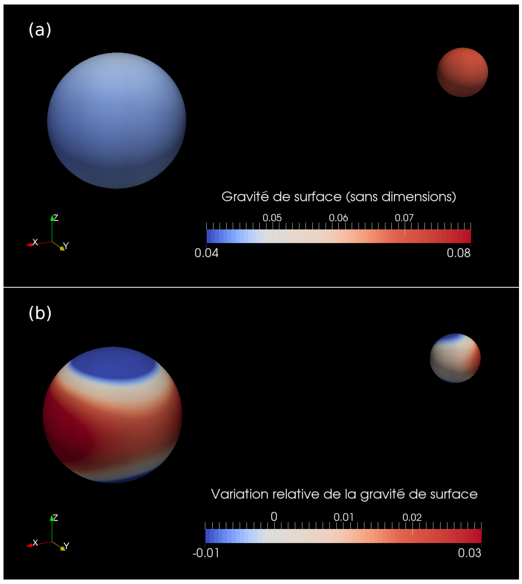


**Fig. 4.** Surface gravity of black holes in circular orbit. The mass ratio is two. The upper panel shows the surface gravity itself and the lower one its relative variation on each hole.

## 6 Conclusions

After years of struggles numerical relativity is able to produce meaningful results. Nevertheless there are still some work that needs to be done. One can mention the computation of more realistic initial data or the study of alternative models to black holes. Spectral methods are a powerful tool to do so. I have presented a library that enables the use of such methods, in a very modular manner: the KADATH library. It has already produced results in various fields, from compact objects to theoretical physics. Future developments of the library are planed, for instance by providing alternative mathematical methods to solve the discrete system resulting from the spectral approximation. An effort should also be made to make this tool easier to use, by providing better documentation, examples and tutorials.

## References

Gourgoulhon, E. 2012, 3+1 Formalism in General Relativity ; Bases of Numerical Relativity (berlin: springer)
Grandclément, P. 2010, J. Comp. Phys., 229, 3334
Grandclément, P. & Novak, J. 2009, Liv. Rev. Relat., 12
Grandclément, P., Somé, C., & Gourgoulhon, E. 2014, Phys. Rev. D, 90, 024068
Saad, Y. 2003, Iterative methods for sparse linear systems (Society of Industral and Applied Mathematics)
Uryũ, K., Tsokaros, A., & Grandclément, P. 2012, Phys. Rev. D, 86, 104001
Vincent, F., Meliani, Z., Grandclḿent, P., Gourgoulhon, E., & Straub, O. 2016, Class. Quant. Grav., 33, 105015

# HALL MAGNETO-HYDRODYNAMICS IN PROTOPLANETARY DISCS

W. Béthune[1], G. Lesur[2] and J. Ferreira[1]

**Abstract.** Protoplanetary discs exhibit large-scale, organised structures. Because they are dense and cold, they should be weakly ionized, and hence concerned by non-ideal plasma effects, such as the Hall effect. We perform numerical simulations of non-stratified Keplerian discs, in the non-ideal magnetohydrodynamic framework. We show that the Hall effect causes self-organisation through three distinct stages. A weak Hall effect enhances turbulent transport. At intermediate strength, it produces magnetized vortices. A strong Hall effect generates axisymmetric zonal flows. These structures may trap dust particles, and thus influence planetary formation. The transport of angular momentum is quenched in the organised state, impugning the relevance of magneto-rotational turbulence as a driving mechanism of accretion in Hall dominated regions.

Keywords: protoplanetary discs, magnetohydrodynamics (MHD), turbulence

## 1 Introduction

Observations of young stellar objects reveal signatures of accretion at a rate $\dot{M} \sim 10^{-8} M_{\odot}\,\mathrm{yr}^{-1}$ onto the star. This calls for a mechanism to efficiently transport angular momentum through the protoplanetary disc. The magneto-rotational instability (MRI, Balbus & Hawley 1991) provides such a mechanism. It was originally studied in the context of fully ionised discs, threaded by a weak magnetic field. Under these conditions, it saturates in sustained turbulence, which exerts a net torque on the flow (Hawley et al. 1995).

However, protoplanetary discs are optically thick, so ionising stellar radiations and cosmic rays can hardly reach the densest regions. The ionisation fraction typically drops below $n_e/n \lesssim 10^{-10}$ within the disc (Fromang et al. 2002), whence non-ideal' magnetohydrodynamic (MHD) effects come into play. Ohmic and ambipolar diffusions can damp, and potentially quench the MRI (Jin 1996; Kunz & Balbus 2004). The Hall effect induces different behaviours depending on its intensity. A weak Hall effect can enhance or kill the turbulent transport, depending on the orientation of the large-scale magnetic field (Balbus & Terquem 2001; Sano & Stone 2002). A strong Hall effect was shown to generate self-organised flows in local simulations (Kunz & Lesur 2013).

Recent observations of the dust emission disclosed large-scale structures in discs, such as horseshoe-shaped traps (van der Marel et al. 2013) or axisymmetric rings (Brogan et al. 2015). It is tempting to ask whether these structures could emerge from Hall-MHD turbulence, without resorting to planet-disc interactions. Numerical simulations including the Hall effect were mostly carried in the local, shearing-box approximation. We address the ability of the Hall effect to produce self-organised structures in a global context (Béthune et al. 2016).

[1] Univ. Grenoble Alpes, IPAG, 38000 Grenoble, France
[2] CNRS, IPAG, 38000 Grenoble, France

## 2 Framework

### 2.1 Model

Protoplanetary discs obey the equations of non-ideal magnetohydrodynamics (MHD); the evolution of density, momentum and magnetic fields are thus given by (Balbus & Terquem 2001):

$$\frac{\partial \rho}{\partial t} + \nabla \cdot [\rho \boldsymbol{v}] = 0, \tag{2.1}$$

$$\frac{\partial}{\partial t}[\rho \boldsymbol{v}] + \nabla \cdot [\rho \boldsymbol{v} \otimes \boldsymbol{v} + P\boldsymbol{I}] = \boldsymbol{J} \times \boldsymbol{B} - \rho \boldsymbol{\nabla} \Phi, \tag{2.2}$$

$$\frac{\partial \boldsymbol{B}}{\partial t} = \nabla \times \left[ \boldsymbol{v} \times \boldsymbol{B} - \eta \boldsymbol{J} - \frac{1}{n_e e} \boldsymbol{J} \times \boldsymbol{B} + \frac{1}{c\gamma \rho_i \rho} \boldsymbol{J} \times \boldsymbol{B} \times \boldsymbol{B} \right]. \tag{2.3}$$

The 'non-ideal' character comes from the low ionisation degree of the gas, and brings about the last three terms in equation (2.3). From left to right, they respectively correspond to Ohmic diffusion, the Hall effect, and ambipolar diffusion. Their relevance to protoplanetary discs is discussed by, for example, Wardle (2007).

We are primarily interested by the influence of the Hall effect. The intensity of this term is inversely proportional to the charge number density $n_e$. It follows that the Hall effect is strongest in the midplane. As a first step, we only consider the deepest layers of the disc, neglecting its vertical density stratification. The thermal stratification is ignored as well, the gas being considered as isothermal for simplicity.

### 2.2 Method

The PLUTO code (Mignone et al. 2007) is used to integrate the dynamical equations in time. We define a cylindrical computational domain, with the radius $r$ extending from $r_0$ to $5r_0$, and the height $z$ from zero to $h$. Periodic boundary conditions are applied in the vertical and azimuthal directions; outflow conditions are applied at the radial boundaries. The thin disk approximation requires $h/r_0$ to be small; we set it to $1/4$. The isothermal pressure scale height $H \equiv c_s/\Omega$ is made comparable to the geometrical height $h$, by setting the isothermal sound speed $c_s = 10\%$ of the inner Keplerian velocity $\Omega_0 r_0$. The initial density has a constant value. The initial magnetic field $B_0$ is axial and constant too, with a plasma $\beta \gg 1$, and with $\Omega \cdot B > 0$. The opposite polarity simply produces a stable, laminar flow (Balbus & Terquem 2001).

With $v_{\mathrm{A}} \equiv B/\sqrt{\rho}$ the Alfvén velocity, the Hall induction term in equation (2.3) can be written as

$$\frac{1}{n_e e} \boldsymbol{J} \times \boldsymbol{B} = \ell_{\mathrm{H}} v_{\mathrm{A}} \boldsymbol{J} \times \boldsymbol{e_B}, \tag{2.4}$$

where $\boldsymbol{e_B}$ is the unit vector along the magnetic field. The Hall length $\ell_{\mathrm{H}}$ defines the scale below which the Hall effect becomes dynamically important (Kunz & Lesur 2013). We normalise it to the geometrical height of the computational domain, $\mathcal{L} \equiv \ell_{\mathrm{H}}/h$. This number is also set to a constant value in each simulation.

## 3 Results

### 3.1 Self-organisation

We perform a series of simulations, varying the magnitude of the initial magnetic field $B_0$ and Hall length $\ell_{\mathrm{H}}$. We show in Fig. 1 the result of three runs having the same initial magnetic field, but different values of $\mathcal{L}$.

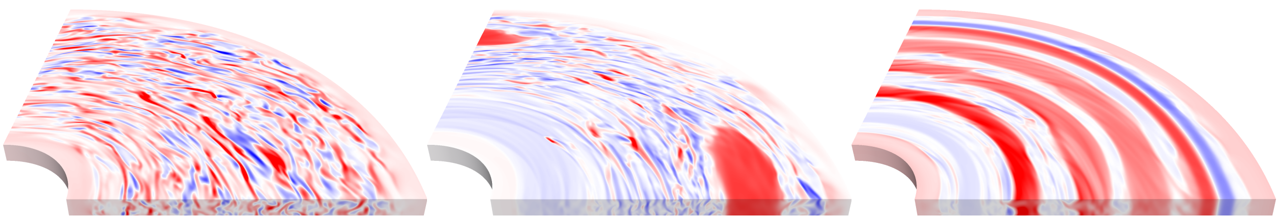

**Fig. 1.** Distribution of axial magnetic field $B_z$ for three values of $\mathcal{L}$. **Left:** turbulence in the ideal MHD case $\mathcal{L} = 0$. **Center:** magnetized vortex in the intermediate case $\mathcal{L} = 0.4$. **Right:** zonal flows in the strong Hall regime $\mathcal{L} = 1$.

The case $\mathcal{L} = 0$ (*left panel*) corresponds to ideal MHD. Due to the weak, axial magnetic field, the magneto-rotational instability operates in this disc (Balbus & Hawley 1991). The instability saturates into turbulence, as known from local, shearing-box simulations (Hawley et al. 1995). When increasing $\mathcal{L}$ from zero to $\mathcal{L} = 0.4$ (*center panel*), the spatial scale of magnetic fluctuations increases, until leaving one single magnetic flux concentration. When increasing $\mathcal{L}$ beyond unity (*right panel*), the magnetic field gets confined into axisymmetric rings, with no flux between. For $\mathcal{L} \geq 1$, increasing $B_0$ or $\ell_{\rm H}$ will increase the number of rings, their width remaining $\sim h$.

While causing these magnetic structures, the Hall effect also affects the velocity and pressure fields of the flow. The equations of incompressible Hall-MHD admit the conserved flux

$$\varpi \equiv \nabla \times \boldsymbol{v} + \frac{1}{\rho \ell_{\rm H}} \boldsymbol{B}. \tag{3.1}$$

As a consequence, a local increase in magnetic flux must come with a local decrease in vorticity flux, and vice versa. In the case $\mathcal{L} = 0.4$, the patch of accumulated magnetic flux has its vorticity lowered compared to the surrounds. In other words, it is an anti-cyclonic vortex in the disc. Vortices may play a role in the process of planetary formation, as they can attract dust particles (Barge & Sommeria 1995). The rings found for $\mathcal{L} = 1$ also induce radial oscillations of the orbital velocity, called zonal flows. The gas transits from super to sub-Keplerian rotation in these rings, making them potential dust traps too (Weidenschilling 1977).

### *3.2 Transport of angular momentum*

The accretion of matter from a Keplerian disc onto its central star requires a removal of angular momentum. One way to transport angular momentum is given by turbulence, customarily described by its diffusivity $\nu = \alpha \Omega h^2$ (Shakura & Sunyaev 1973). We show in Fig. 2 how the Hall effect modifies the transport coefficient $\alpha$.

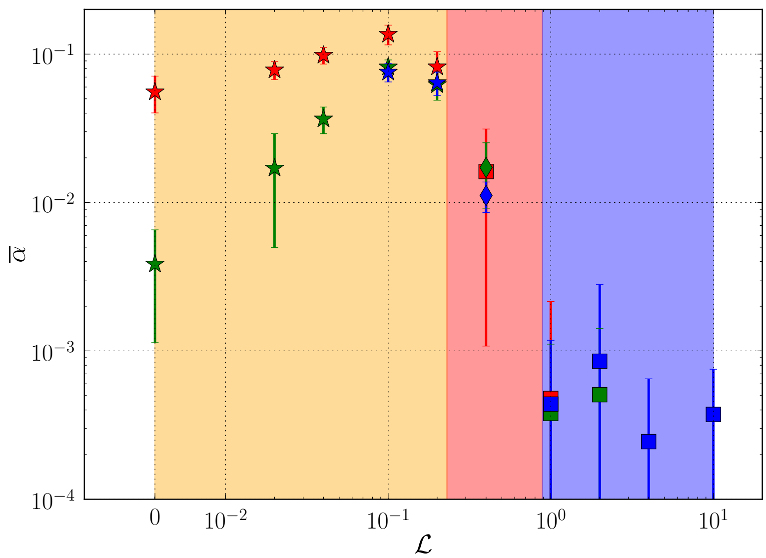


**Fig. 2.** Volume-averaged, normalised stress $\bar{\alpha}$ as a function of the Hall strength $\mathcal{L}$. The three coloured regions delineate the turbulence (orange), vortex (red) and zonal flow (blue) regimes. The symbols color corresponds to the initial magnetic field intensity $B_0$, being weak (blue), intermediate (green) or strong (red).

In the turbulent regime $\mathcal{L} \lesssim 0.2$ (orange area), the transport of angular momentum is increased by the Hall effect. As in ideal MHD, it also increases with the initial magnetic field (Hawley et al. 1995). The maximum $\alpha \approx 0.1$ is attained for $\mathcal{L} \approx 0.1$. The level of transport steeply decreases for $\mathcal{L} \in [0.1, 1]$, where vortices are observed. In the zonal flow regime $\mathcal{L} \geq 1$, the transport coefficient is stalled at $\alpha \lesssim 10^{-3}$. This stress is in fact caused by spiral density waves, excited near the inner radial boundary, where the sound speed $c_s < \Omega h$. The magnetic contribution alone would produce $\alpha \lesssim 10^{-5}$, insufficient to explain the observed accretion rates.

## 4 Conclusions

The Hall effect tends to organise the magnetic and vorticity fluxes threading a non-stratified Keplerian disc. When increasing its intensity, the flow transits trough three distinct structural states. A weak Hall effect $\mathcal{L} \ll 1$ enhances turbulent transport. For moderate strengths $\mathcal{L} \lesssim 1$, the disc features large-scale, magnetized vortices. A strong Hall effect $\mathcal{L} \gtrsim 1$ produces axisymmetric zonal flows, and kills angular momentum transport. These structures were found to hold when adding Ohmic and ambipolar diffusion with realistic intensities.

Both vortices and zonal flows induce local pressure maxima, which could attract dust particles and hence influence the course of planetary formation. In the strong Hall limit, the absence of turbulent transport raises questions regarding the driving mechanism of accretion. Stratified simulations by Lesur et al. (2014) suggest that the overall stress could be laminar in this regime. The self-organisation threshold depends solely on the ratio $\ell_{\mathrm{H}}/h \approx 0.1$, but the geometrical height $h$ was introduced for modelling purposes. These results must therefore be confronted to global, stratified simulations.

This work was granted access to the HPC resources of IDRIS under the allocation 2015- 042231 made by GENCI.

## References

Balbus, S. A. & Hawley, J. F. 1991, ApJ, 376, 214
Balbus, S. A. & Terquem, C. 2001, ApJ, 552, 235
Barge, P. & Sommeria, J. 1995, A&A, 295, L1
Béthune, W., Lesur, G., & Ferreira, J. 2016, A&A, 589, A87
Brogan, C. L., Perez, L. M., Hunter, T. R., et al. 2015, ApJ, 808, L3
Fromang, S., Terquem, C., & Balbus, S. A. 2002, MNRAS, 329, 18
Hawley, J. F., Gammie, C. F., & Balbus, S. A. 1995, ApJ, 440, 742
Jin, L. 1996, ApJ, 457, 798
Kunz, M. W. & Balbus, S. A. 2004, MNRAS, 348, 355
Kunz, M. W. & Lesur, G. 2013, MNRAS, 434, 2295
Lesur, G., Kunz, M. W., & Fromang, S. 2014, A&A, 566, A56
Mignone, A., Bodo, G., Massaglia, S., et al. 2007, ApJS, 170, 228
Sano, T. & Stone, J. M. 2002, ApJ, 577, 534
Shakura, N. I. & Sunyaev, R. A. 1973, A&A, 24, 337
van der Marel, N., van Dishoeck, E. F., Bruderer, S., et al. 2013, Science, 340, 1199
Wardle, M. 2007, Ap&SS, 311, 35
Weidenschilling, S. J. 1977, MNRAS, 180, 57

*SF2A 2016*
*C. Reylé, J. Richard, L. Cambrésy, M. Deleuil, E. Pécontal, L. Tresse and I. Vauglin (eds)*

# PERSPECTIVES IN NUMERICAL ASTROPHYSICS: TOWARDS AN EXCITING FUTURE IN THE EXASCALE ERA

V. Reverdy[1]

**Abstract.** In this discussion paper, we investigate the current and future status of numerical astrophysics and highlight key questions concerning the transition to the exascale era. We first discuss the fact that one of the main motivation behind high performance simulations should not be the reproduction of observational or experimental data, but the understanding of the emergence of complexity from fundamental laws. This motivation is put into perspective regarding the quest for more computational power and we argue that extra computational resources can be used to gain in abstraction. Then, the readiness level of present-day simulation codes in regard to upcoming exascale architecture is examined and two major challenges are raised concerning both the central role of data movement for performances and the growing complexity of codes. Software architecture is finally presented as a key component to make the most of upcoming architectures while solving original physics problems.

Keywords: numerical astrophysics, exascale, cosmology, simulations

## 1 Introduction

Over the last decades, numerical simulations have progressively become a central element of modern astrophysics. The fact that astrophysical processes are often difficult to reproduce in laboratories and the fact that these processes are often complex multiscale multiphysics problems have helped numerical simulations to acquire this role. In the meantime, astrophysics has become together with climate science (Lapenta et al. 2013; Towns et al. 2014), one the biggest user of supercomputing resources. However, again and again, the same pattern keeps happening in numerical astrophysics: 1) To answer a specific question, a numerical project is designed. 2) Because existing codes do not allow to answer the exact question, a new physics module needs to be developed. 3) But as parallelization techniques are often complex to implement, a lot of work needs to be put into making the physics module compatible with the existing code architecture. 4) However, as the project has been defined as a physics project and not as an applied mathematics or computer science project, the simplest implementation technique is chosen: the code is forked into a specific version dedicated to the problem, and the new physics is integrated thanks to quick and dirty hacks. 5) Because astrophysical processes often involve multiphysics aspects or high-dimensional parameter spaces, simulation are run and their parameters are progressively adjusted to fit observational results. 6) The conclusion is generally that a set of parameters fitting the observational data can be found, but answering the original question would require more resolution or more data points. 7) A paper is published presenting these conclusions, but because the code has been implemented through quick and dirty hacks, the authors judge that their code is not mature enough to be publicly released on a open-source license, therefore preventing any possibility of cross validation by a larger community. 8) To investigate the problem with more resolution and more data points, more funding is requested, the process restart at step 1), and the code is forked again. Even though the steps we just listed are intentionally exaggerated, some elements of this list can be found, at least partially, in many large scale simulation projects. As the numerical astrophysics community is now aiming for exascale simulations in the coming years (Berczik et al. 2013), and as porting codes to the exascale will be a major challenge involving a lot of resources and time (Dongarra et al. 2011), we offer a quick review of some of the questions numerical astrophysics will have to face while trying to ensure original, high-quality, reliable, and reproducible science results.

[1] University of Illinois at Urbana-Champaign, Department of Astronomy, MC-221, 1002 W. Green Street, Urbana, IL 61801

## 2 On astrophysics simulations

### 2.1 What is an astrophysics simulation? Why running high performance simulations?

Before going any further one has to define what an astrophysics simulation is. Is there any conceptual difference between solving a single equation on a computer, fitting data to compute model parameters or to produce mock catalogs, quickly exploring or test an hypothesis using a script or a high-level language, and running high performance simulations on supercomputers? Technically, all these tasks boil down to solving a problem algorithmically using a Turing machine. However, they differ vastly in terms of motivation and implementation.

In the first case, computers are just used as powerful calculators to get a numerical value from solving a symbolic equation. In the second case, when we use computers to fit data and produce mock catalogs, are we actually simulating anything? The question is worth asking because a significant fraction of present-day simulations are run to produce mock catalogs to prepare observational surveys and check experimental data (Lowing et al. 2015; Fosalba et al. 2015). But fitting and producing mock catalogs that emulate real observations, does not require any understanding of the underlying physics derived from its firsts principles. Trained properly on large existing data sets, machine learning algorithms and neural networks are perfectly suited to produce mock catalogs (Xu et al. 2013; Kamdar et al. 2016) while using far less computing resources, and being sometimes more accurate than high performance numerical simulations. As they will become more and more widely used, and as they may outperform traditional simulations to mimic observational and experimental results, machine learning techniques are likely to raise interesting epistemological questions regarding the very notion of understanding in science.

Then how do the third and fourth case described in the first paragraph differ? Present-day personal computers and modern high-level languages allow to quickly prototype, design and implement simulations to test hypotheses on toy models. These simulations are generally very relevant to explore analytical models and provide qualitative results about them. But if personal computers can allow to investigate analytical models, and if machine learning can provide very accurate fitting solutions to mimic real observational results, why are we still doing high performance simulations in 2016? We argue that one of the main point of high performance simulations is to investigate the emergence of complexity from fundamental principles (Anderson et al. 1972) to: 1) test these principles, 2) verify how less fundamental models can be derived from first principles, and 3) understand how complex physical processes actually work. According to this view, the goal of high performance simulations is not to mimic what we observe, but to understand how the fundamental laws of physics are connected to what we observe. Increasing the number of free parameters in simulations increase the likelihood of being able to reproduce observations, but it provides no guarantee that the underlying physics is correct. On the contrary, gaining in abstraction following a traditional reductionist approach would allow to simulate a wider range of astrophysical processes from a smaller set of laws, and would limit the problem of degenerated solutions.

### 2.2 Why more computing power?

As noted in the introduction, numerical astrophysics is currently on a race towards more and more computing power. The first petascale supercomputer was tested in 2008 (Barker et al. 2008), and we are likely to enter in the exascale era during the next decade. But why more computing power is even required? Common motivations for more computing power can fit into one of two categories. The first category corresponds to the case in which the level of physics complexity remain the same but either larger simulations in time or in space, more resolution, or more simulations to improve statistical accuracy are required (Alimi et al. 2012). In that case, code scalability is of primary concern. The second category corresponds to the case in which more complex problems need to be solved either regarding the number of physical phenomena that has to be taken into account (Vogelsberger et al. 2014), or regarding the geometry of the problem. In that case, as entirely new modules often need to be developed, genericity and modularity of software architectures is of primary concern.

But there is a third category: using more computing power to gain in abstraction and genericity while reducing the number of free parameters. For example, in numerical cosmology, over the years, several techniques have been developed to analyze light propagation: some have been focusing on weak lensing (Jain et al. 2000), some others on the late-time integrated Sachs-Wolfe effect and some others on the accurate computation of redshifts in cosmological simulations. However, all these effects do not need separate modelling as they all originate from the same phenomenon: the propagation of photons according to general relativity. Directly integrating the geodesics equations instead of implementing completely different approaches depending on the effect allow to use a single code for a wide range of analyses while reducing the parameter count and improving the accuracy of results (Reverdy 2014).

Over the years, to cover more and more physics domains, and to target more and more platforms, astrophysics codes have grown to an unprecedented scale. Because this growth has often been the result of an unplanned community effort, it has lead to an increase of code complexity. Adding new physics aspects to these codes therefore requires a deep knowledge of the implementation including data structure, algorithms, and parallelism, and often involves far more work on the computational and technical aspects than on the implementation of solvers and actual physics equations. On the top of the above-mentioned advantages, gaining in abstraction also offers the opportunity to drastically reduce code complexity, making further developments easier, more modular, and more maintainable in the long run.

## 3 Challenges for the exascale era

As already pointed out, as the computing power of supercomputers keeps growing, an exascale supercomputer is very likely to become reality within the next decade, regardless of the readiness status of astrophysical codes. In the next sections, we discuss two major challenges astrophysics codes will face in their race to the exascale.

### *3.1 Pure computing power and data movement*

Very few present-day codes are able to fully leverage petascale supercomputers. One of the main reason is that most of these codes inherited from codes that were designed in the 2000's (Teyssier 2002; Springel 2005) with computing power as a primary focus. The democratization of multithreading has deeply affected supercomputing, and a major effort has been put into exploiting efficiently both inter and intra-node parallelism. Even though hybrid MPI/OpenMP or MPI/pthread parallelism is more common in 2016 than in 2006 (Bryan et al. 2014), not all parallel codes exploit these techniques. But this is not the main reason why petascale supercomputers are underused. While numerical astrophysics was focusing on pure computing power, the main bottleneck of high performance computing was silently moving away from it. A quick comparison between the 2004 and 2014 world's top supercomputer according to the TOP500 ranking lead to the following numbers: while the pure computing power has grown by three orders of magnitude in a decade, the total memory available on these systems has grown by two order of magnitude, less than two orders of magnitude for the storage system, and even less when it comes to compare cache and random access memory speed. Unless a revolutionary memory technology emerges in the coming years, leveraging supercomputers will rely more and more on how to feed processing units with a constant flow of data (Reed & Dongarra 2015). In other words, the pure computing power is not the problem anymore, the problem is how to store and efficiently access data. And most astrophysics codes were not originally designed with this problem in mind.

On modern platforms, L1 cache access is roughly two orders of magnitude faster than RAM access. Therefore when a CPU needs elements that have not been put in cache due to complex access patterns or complex branching strategies, hundreds of cycles can be lost for doing nothing except waiting. Making the most of current and upcoming architectures involve improving cache friendliness and data access patterns for both optimizing data transfer between random access memory and central processing units, and facilitating vectorization and the use of SIMD instruction sets. In that regard, data structures have a major role to play (Hartmann et al. 2008), as they often represent the backbone of simulation codes. These codes will not be able to scale up to the exascale without solving issues regarding the storage of massive amount of data with predictable access patterns.

### *3.2 Code complexity*

The second major challenge simulation codes will face concern their growing complexity. This complexity arises from the conflict between the need of low-level development for optimization purpose and the need of high-level development to incorporate more and more numerical methods, algorithms, solvers, and physical phenomena. Because most of these aspects are orthogonal to each other, one should be able to compose them to design their code. But how to achieve modularity, genericity and efficiency at the same time? For now, many of the most used codes in numerical astrophysics focus on a particular set of physics problems, with a particular set of numerical methods and target specific architectures. Moreover, all aspects of the computation are very intertwined. One of the direct consequences of this intertwining is encountered by many scientist: slightly modifying the physics of an existing code often involves weeks or months of technical work, because the physics cannot be easily changed without impacting the entire code.

If the hardware has changed a lot over the last decades, programming approaches have, on the contrary, and for the most part, stayed the same. Developing a script to visualize data and compute some statistics on a personal computer is not the same as developing high performance libraries involving years of effort. In the second case, the choice of a programming language, the choice of a particular design or interface, and even the choices of function signatures including function names and arguments are everything but technical details. Original architecture decisions can have tremendous impacts on the overall design years later. This can be illustrated through the design of something as simple as a data cube, in other words a cube defining a region of a discretized space and containing values of physical quantities. At first, the problem seems simple: a cube can be defined through the coordinates of its center and its edge length. But soon, design questions arise: How to store coordinates? How to manage the precision on the coordinates? Should fixed-point be preferred to floating-point representation to avoid non homogeneous precision around 0? Can the number of dimensions be made arbitrary? In that case, how to compute the number of cells, faces, edges, and vertices recursively at compile-time? Should the cube be also stored as the coordinates of its vertices so that cells, faces and edges can be referenced recursively as independent objects built on top of the same underlying vertices? Should the coordinates be allocated on the stack or on the heap? Regarding to the storage of an array of data cubes, can the array of structures be converted into a structure of arrays to provide better vectorization opportunities? How to deal with different system of coordinates and affine transformation? Do data cubes own physical quantities or do they contain links to them? etc... In the end, designing a data cube happen to be a very complex problem, with fundamental consequences in terms of genericity, ease-of-use and efficiency. When a simulation stores billions of data cubes to manage space discretization, all these design decisions can have a major impact on the overall performances and memory usage of a code. In the end, investigating complex physics problems in the exascale era will require modular codes because otherwise, adjusting the slightest element will require months of development and make exascale codes unmaintainable.

## 4 Conclusions

As we illustrated throughout this paper, designing astrophysics codes capable of leveraging exascale architectures will not be an easy task. Designing codes to answer original questions instead of simply aiming at improving resolutions will be even more complicated. However, investigating the emergence of complexity from fundamental laws using extra computing power offers plenty of room for originality. In that context, software architecture have a central role to play to achieve, at the same time, genericity, efficiency and ease-of-use. Accomplishing this task will require, at least, astrophysics, computer science, applied mathematics and software engineering aspects. But because all these aspects are interrelated, and because the design of the most fundamental software components can have drastic implications in the long run, only a transdisciplinary – not a multidisciplinary – approach will succeed.

Vincent Reverdy has been supported by the National Science Foundation Grant AST-1313415.

## References

Alimi, J.-M., Bouillot, V., Rasera, Y., et al. 2012, The International Conference for High Performance Computing, Networking, Storage and Analysis, Salt Lake City, Utah, USA, 10-16 November 2012

Anderson, P. W. et al. 1972, Science, 177, 393

Barker, K. J., Davis, K., Hoisie, A., et al. 2008, in Proceedings of the 2008 ACM/IEEE Conference on Supercomputing, SC '08 (Piscataway, NJ, USA: IEEE Press), 1:1–1:11

Berczik, P., Spurzem, R., Zhong, S., et al. 2013, Up to 700k GPU Cores, Kepler, and the Exascale Future for Simulations of Star Clusters Around Black Holes, ed. J. M. Kunkel, T. Ludwig, & H. W. Meuer (Springer), 13–25

Bryan, G. L., Norman, M. L., O'Shea, B. W., et al. 2014, ApJS, 211, 19

Dongarra, J. et al. 2011, International Journal of High Performance Computing Applications, 25, 3

Fosalba, P., Crocce, M., Gaztañaga, E., & Castander, F. J. 2015, MNRAS, 448, 2987

Hartmann, J., Krahnke, A., & Zenger, C. 2008, Applied Numerical Mathematics, 58, 435

Jain, B., Seljak, U., & White, S. 2000, ApJ, 530, 547

Kamdar, H. M., Turk, M. J., & Brunner, R. J. 2016, MNRAS, 455, 642

Lapenta, G., Markidis, S., Poedts, S., & Vucinic, D. 2013, Computing in Science and Engineering, 15, 68

Lowing, B., Wang, W., Cooper, A., et al. 2015, MNRAS, 446, 2274

Reed, D. A. & Dongarra, J. 2015, Commun. ACM, 58, 56
Reverdy, V. 2014, PhD thesis, Paris Observatory
Springel, V. 2005, MNRAS, 364, 1105
Teyssier, R. 2002, A&A, 385, 337
Towns, J., Cockerill, T., Dahan, M., et al. 2014, Computing in Science and Engineering, 16, 62
Vogelsberger, M., Genel, S., Springel, V., et al. 2014, MNRAS, 444, 1518
Xu, X., Ho, S., Trac, H., et al. 2013, ApJ, 772, 147

*SF2A 2016*
*C. Reylé, J. Richard, L. Cambrésy, M. Deleuil, E. Pécontal, L. Tresse and I. Vauglin (eds)*

# THE GASEOUS PROTO-CLUSTER: BETTER CHARACTERIZING THE INITIAL CONDITIONS OF STELLAR CLUSTER FORMATION?

Y.-N. Lee[1] and P. Hennebelle[1, 2]

**Abstract.** Cluster formation simulations have always been numerically challenging due to the large range of spatial and temporal scales that vary by orders of magnitudes and multiple physical mechanisms involved. The simulation box is typically of parsec (pc) scale while resolution down to a few astronomical units (AUs) is needed to well resolve individual stars. However, studies of this kind are important for the understanding of the interaction between gravity and turbulence that guides the star formation and the mechanisms through which the possibly self-regulated initial mass function (IMF) is shaped by stellar feedback. Most simulation works have initial conditions that correspond to molecular clouds (MCs), while the actual star formation occurs in a very small volume fraction of the whole simulation box. We present a series of simulations to characterise the early stage of cluster formation, of which a primary stage of gas concentration is noticed. We denote this stage as the gaseous proto-cluster, which forms from gravo-turbulent collapse of the MC. This high-density region is indeed the principle site of star formation. The existence of this primary stage implies that the cluster formation environment is somewhat universal and cluster formation studies could therefore set out from more local conditions, therefore reducing the computational demand.

Keywords: ISM, turbulence, gravity, cluster formation

## 1 Introduction

Stars are the building blocks of the Universe. Assembled, they form associations, clusters, and galaxies. Individually, they harbour planetary systems which can eventually breed living being. Due to the hierarchical nature of astronomical structures. Star formation is complex in such a way that large scales and small scales are inter-connected and both play important roles. Galactic dynamics at scales up to a few kilo-parsec (kpc) create molecular clouds (MCs) through shearing or turbulent movements. Pre-stellar cores (10s of astronomical units) form within MCs and eventually form stars. During and at the end of their lives, stars inject energy and materials back into the environment through various feedback mechanisms including the proto-stellar jet, ionising radiation, stellar wind, and super novae.

In terms of numerical simulation, the computational box must be large enough so that the large-scale dynamic is not neglected and that the small-scale dynamics can be generated self-consistently. Meanwhile, this guarantees that the boundary condition should not have a strong artificial impact on the results. In the context of stellar cluster formation, this often leads us to a setup with a MC, or part of a MC (a few pcs) containing at least 100 solar masses ($M_\odot$), or sometimes up to a few thousands. As to correctly follow the cluster formation, at least the star-forming core scale (10s of AU or $10^{-4}$ pc) has to be resolved. The resolution of this kind of simulations, therefore, needs to be very high (equivalent $2^{13-15}$ cells in each dimension on a cartesian grid). On the other hand, different forms of energy such as the thermal motion, turbulence, magnetic field, radiation, and cosmic rays all have similar strength of $\sim 1$ eV cm$^{-3}$. The interactions amongst them are therefore important. Considering all these, a simulation of cluster formation is extremely expensive if we want to accurately follow all the physics. At the same time, it means that it is difficult for us to isolate individual problems and study them in a simplified setup. To reduce the complexity, the study of star formation is often decomposed into hierarchical steps. Stars are frequently observed to be born in clusters and many studies stress the importance

[1] Laboratoire AIM, Paris-Saclay, CEA/IRFU/SAp – CNRS – Université Paris Diderot, 91191 Gif-sur-Yvette Cedex, France
[2] LERMA (UMR CNRS 8112), Ecole Normale Supérieure, 75231 Paris Cedex, France

of understanding star formation in this context (Lada & Lada 2003; Longmore et al. 2014). In this study, we focus on the formation of a gaseous proto-cluster, the gas assembly phase and the beginning of star formation, with a view to better characterise the star formation environment and to prescribe more precisely the physical mechanisms at play.

Murray (2009) pointed out the relation $R \propto M^{1/3 \sim 1/2}$ for low-mass embedded clusters, where $R$ and $M$ are the gas radius and mass, with the catalog reported by Lada & Lada (2003). Adams et al. (2006) also compiled data from Lada & Lada (2003) and Carpenter (2000) and showed a number-size relation $R_* \propto N_*^{1/2}$ between the radius of the cluster and the number of objects it contains. The results of Gutermuth et al. (2009) are also compatible with this relation. The number-size relation is reasonably equivalent to the mass-size relation if we adopt a universal initial mass function (IMF) and thus similar characteristic mass among clusters. Larger data sets of star-forming clumps also exhibit a mass-size relation $R \propto M^n$ (Fall et al. 2010; Urquhart et al. 2014, $n = 0.38$ or $0.50$). These results are obtained from molecular lines and dust continuum observations of the star-forming gas, suggesting that the mass-size relation and probably some other properties of the stellar cluster are established as early as the gas-dominated phase. Pfalzner et al. (2016) pointed out that the mass-size relation for embedded clusters and gaseous proto-clusters follow the same trend with a shift in absolute value, which could be explained with star formation efficiency or cluster expansion. The existence of this mass-size relation suggests that the gaseous proto-cluster is very likely in some equilibrium state governed by the MC environment in which it resides, and is crucial for understanding the nature of the cluster and, more generally, star formation. We emphasise here a global equilibrium, which does not imply that the structure is not locally collapsing.

Many numerical studies of star or core formation inside MCs have been performed to understand the impact of turbulence and gravity on star formation and the origin of the IMF (Padoan et al. 2007; Schmidt et al. 2010; Girichidis et al. 2011, 2012; Klessen et al. 1998; Klessen & Burkert 2000; Bonnell et al. 2003, 2008; Smith et al. 2009; Ballesteros-Paredes et al. 2015). In this study, we focus on understanding the gas-dominated phase of early cluster formation inside MCs, and show the properties of the gaseous proto-cluster are determined by those of its parent MC and are subsequently inherited by the stellar cluster. We focus on the transition between the global collapse at larger scales and the energy equilibrium that is reached for this gas-dominated object through gravo-turbulent interaction. The dense proto-cluster provides a favorable environment for star formation, and certain characteristics of the stellar cluster are therefore determined at the gas-dominated phase. In order to characterise the gaseous proto-cluster formed in MCs collapsing under self-gravity, we perform a series of simulations of gaseous proto-cluster formation inside a MC with various levels of initial turbulent support. We identify such gaseous proto-cluster regions and analyse their properties to examine whether these structures are indeed objects in equilibrium and if they coincide with observations of star-forming clumps. We also discuss the sink particles forming therein and compare the sink cluster with observations of embedded clusters. Once the nature of the clusters is known, we can investigate star formation given this recipe of a cluster environment to gain knowledge of the star formation rate, the star-forming mechanisms, the IMF, etc. From a numerical point of view, the wide range of temporal and spatial scales concerned in star formation simulations have always been computationally challenging. The knowledge of how a gaseous proto-cluster forms in a MC could serve as a valuable tool for initialising a more realistic star formation simulation without having to include the whole cloud into the simulation box, and thus could help gaining computation time or resolution.

## 2 Simulations: self-gravitating molecular cloud

We perform numerical simulations of a collapsing MC under self-gravity with the magneto-hydrodynamic (MHD) adaptive mesh refinement (AMR) code RAMSES (Teyssier 2002; Fromang et al. 2006). The evolution of the cloud is governed by ideal MHD equations with a cooling function of the interstellar medium (ISM) considered, as that described by Audit & Hennebelle (2005). A series of MCs with different levels of initial turbulence is simulated. Simulations are initialised with a Bonnor-Ebert-like spherical cloud of $10^4$ M$_\odot$ that has a density profile $\rho(r) = \rho_0 / \left[1 + \left(\frac{r}{r_0}\right)^2\right]$ with ten times density contrast between the center and the edge, where $\rho_0 = 822$ cm$^{-3}$ and $r_0 = 2.5$ pc. The cloud has 15 pc diameter and the computational box is twice the size of the cloud. The space surrounding the cloud is patched with diffuse gas of uniform density $\rho_0/100$. The initial temperature is set by the cooling function and it is about 10 K in the dense gas. A turbulent velocity field is generated with a Kolmogorov spectrum with random phase and is scaled in such a way that the initial Mach numbers are 2.7, 6, 7.3, and 10, respectively. A weak magnetic field with uniform mass-to-flux ratio in the $x$

Table 1: Simulation parameters: the cloud is specified with varying level of the ratio $t_{ff}/t_{vct}$. We list corresponding turbulent velocity and virial parameter $\alpha_{vir} = 2E_{kin}/E_{grav}$.

| Label | $t_{ff}/t_{vct}$ | $v_{rms}$ (km/s) | Mach | $\alpha_{vir}$ |
|---|---|---|---|---|
| A | 0.4 | 0.6 | 2.7 | 0.12 |
| B | 0.9 | 1.5 | 6.0 | 0.64 |
| C | 1.1 | 1.8 | 7.3 | 0.96 |
| D | 1.5 | 2.4 | 10 | 1.78 |

direction is applied. Its highest value is about 8 $\mu$G at the cloud center. The ratios of characteristic timescales at the central plateau region ($r < r_0$) are used as parameters to specify the initial conditions. The ratio of free-fall time to sound crossing time $t_{ff}/t_{sct} = 0.15$ and the ratio of free-fall time to Alfvén crossing time $t_{ff}/t_{act} = 0.2$, which corresponds to mass-to-flux over critical mass-to-flux ratio of 8, are fixed for all runs. Both thermal and magnetic energy are small compared to the gravitational potential energy. The ratio between free-fall time and turbulent crossing time $t_{ff}/t_{vct}$ is varied in each run, giving different levels of kinetic support against self-gravity. In Table 1, we provide the values of $t_{ff}/t_{vct}$ and the corresponding turbulent rms velocity, Mach number, and virial parameter $\alpha_{vir} = 2E_{kin}/E_{grav}$ to characterise the initial energy state of the MC.

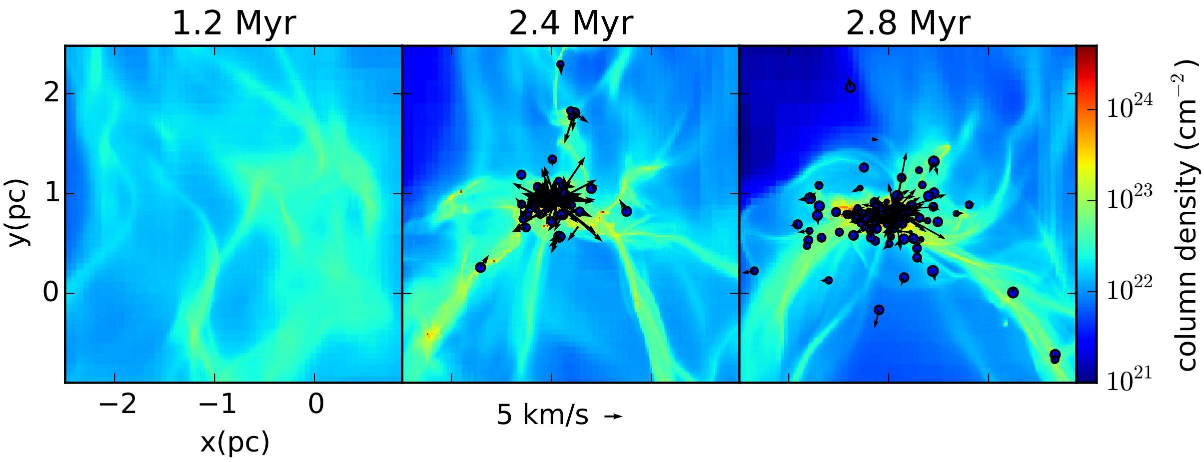


Fig. 1: Zoomed images of run B at times 1.2, 2.4, and 2.8 Myr. Sink particles over-plotted on column density. The circles represent the sink particles with the size proportional to the log of their masses and the arrows indicate their velocity. The origin of corresponds to the center of the simulation box.

We start with a $128^3$ base grid and allow seven levels of refinement (equivalent to $16384^3$) using an AMR scheme to ensure that the Jean's length is always resolve by 10 cells. This corresponds to resolution of 0.23 pc on the coarse grids and 0.002 pc (or 400 AU) at the densest regions. Neumann boundary conditions with imposed zero gradients are used, which allows the gas to outflow freely. Sink particles (Bleuler & Teyssier 2014) are used in our simulations, and the densest region unresolved with a fluid description is replaced with a sink particle to economise computational power and to follow accretion onto Lagrangian mass. These particles are formed when density exceeds $10^8$ cm$^{-3}$, while the flow is convergent and gravitationally bound. After their formation, the sink particles continue to accrete mass from their surrounding. As these high density regions represent possible star formation sites, they furnish dynamical and statistical hints on stellar cluster properties. We caution that although our resolution is very small with respect to the cluster size, ensuring good description of the cluster itself, the sink particle size is too large for the sinks to represent individual stars. The typical mass of our sink particles is on the order of $\simeq 10$ M$_{\odot}$.

Figures 1 and 2 show zoomed views of the central region of run B where the proto-cluster is forming in column density with sink particles and in density sliced map with velocity over-plotted from two angles of view. The cloud is globally collapsing, while filamentary structures are forming under gravo-turbulent interactions. A pc-scale prominent entity of relatively high density emerges in the central region, and its size is slowly varying in time. A general rotational motion becomes evident as the collapse proceeds, since there is no dissipative mechanism at this scale strong enough to remove large amount of angular momentum. The global infalling

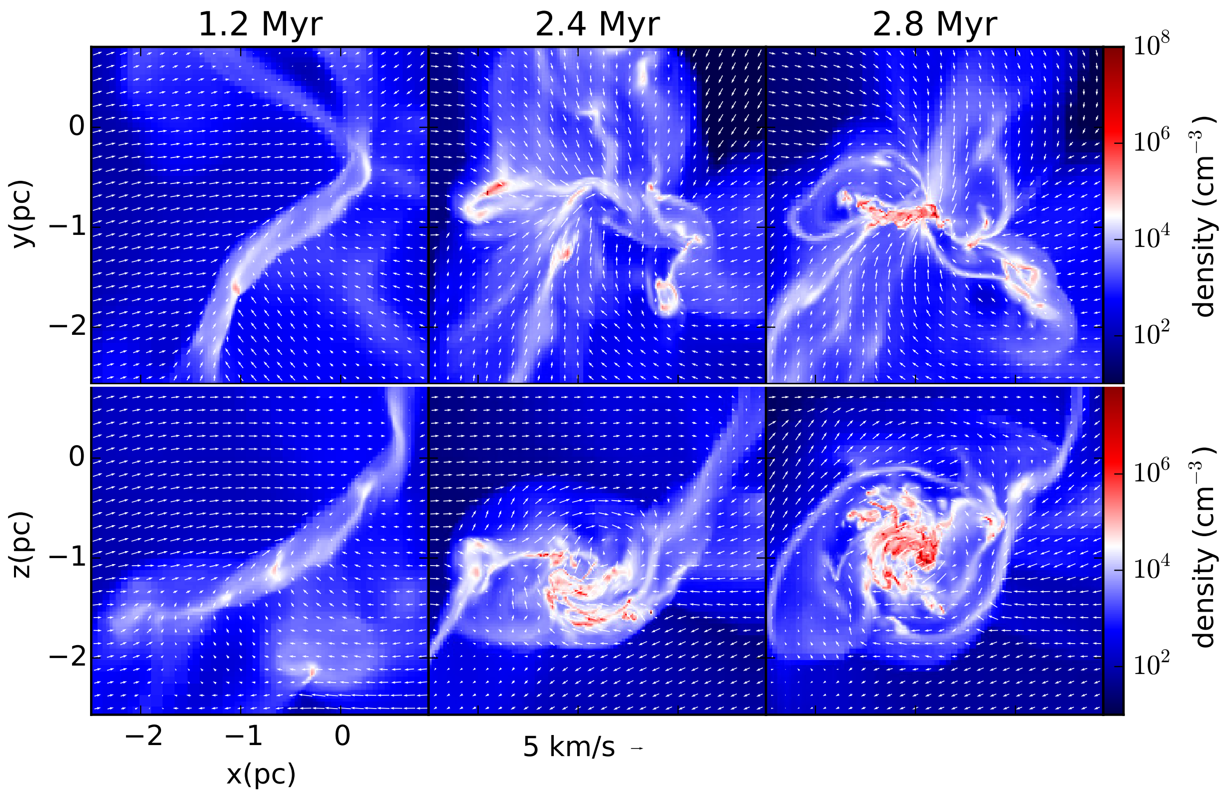


Fig. 2: Zoomed images of run B at times 1.2, 2.4, and 2.8 Myr focusing on the central dense objet with two views showing the flattened shape. **Top:** velocity field overplotted on density sliced map of the flattened rotating proto-cluster, edge-on view. **Bottom:** same as top, face-on view .

motion is noticeably reduced upon striking the central objet, forming highly irregular shocks at the seemingly ill-defined border. For the first stage of this work, simple scenario without stellar feedback is employed, in which nothing except the depletion of cloud gas can stop sink accretion. We therefore stop the simulations when about half of the initial cloud mass has been accreted onto the sink particles, since the results are less likely to be physical in this stage. This corresponds to physical time of about three million years. While some of the sink particles form in the filamentary structures feeding the central cluster, most of the sinks are observed to form within the gaseous proto-cluster, hence strongly suggesting that this central region is an important site for understanding star properties such as the IMF.

## 3 Identifying the proto-cluster from simulation results

Using the gas dynamics to characterize the proto-cluster and the sink distribution for the embedded cluster, respectively, we develop algorithms to identify the cluster region with highly irregular border.

### 3.1 The gaseous proto-cluster

In the density maps shown in Fig. 2, we see a dense, flattened structure forming at the center that is dominated by rotation. The infalling motion is stopped by a shock at the border, where we see an abrupt change in flow directions. Despite the accreting mass, the size is relatively stationary. The turbulent nature of this region prevents us from studying the detailed gas behaviour, and we, therefore, calculate integrated quantities to get rid of pronounced fluctuations. We first determine a series of ellipsoids, and then decide which one best represents the cluster.

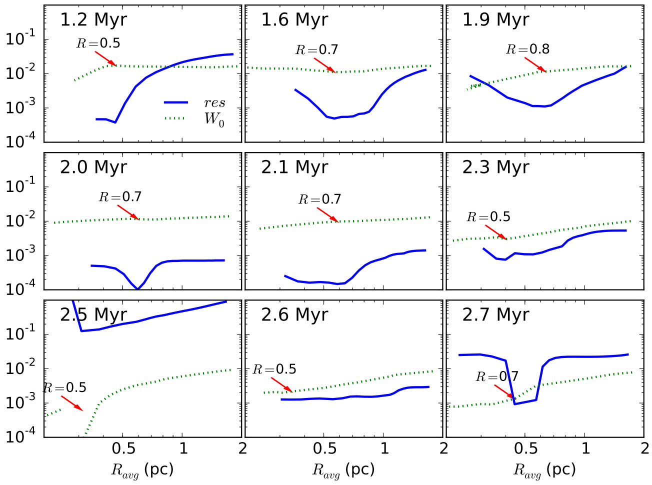


Fig. 3: Examples of the piecewise fit at nine time steps for the run with $t_{\rm ff}/t_{\rm vct}$=0.9. The normalized residual is plotted as function of cluster characteristic radius $R_{\rm avg} = (R^2H)^{\frac{1}{3}}$ in blue solid curves, of which the optimal value is such that the fit is the best. The infall moment $W_0(R_{\rm avg})$ is shown in arbitrary units with green dotted curves. The gaseous proto-cluster radius at which there exists a change in slope is indicated with a red arrow and the size of the semimajor axis is indicated.

#### 3.1.1 Step 1: Integrated gas properties of an ellipsoid

In order to define the cluster, we calculate the center of mass, total angular momentum, and moment of inertia in an oblate ellipsoidal region of semi-major axis $R$ and semi-minor axis $H$. For a series of $R$ values, we compute iteratively to find the corresponding $H$ by replacing *1)* the geometrical center with the center of mass, *2)* the minor axis with the axis of rotation, and *3)* the geometrical aspect ratio with that obtained from mass distribution, i.e., the inertia momenta, until convergence is reached. We find that the procedure typically converges in around ten iterations leading to a variation of less than $10^{-4}$ and gives reasonable results. The ellipsoids attained therefore satisfy the following criteria:

$$\vec{x}_{\rm center} = \frac{\sum \vec{x}_i m_i}{\sum m_i}, \qquad \vec{a}_H \,/\!\!/ \sum m_i \vec{v}_i \times \vec{r}_i, \qquad (\frac{H}{R})^2 = \frac{\lambda_1}{\sqrt{\lambda_2\lambda_3}}. \tag{3.1}$$

The quantities $x$ and $m$ with subscript $i$ indicate the position and mass of each cell inside the ellipsoid; $\vec{a}_H$ is the vector representing the direction of the minor axis. The eigenvalues of the moment of inertia are $\lambda_{1,2,3}$ in increasing order. This procedure defines a series of self-consistent ellipsoids contained within each other. The disordered nature of the flow causes the ellipsoids to be not necessarily similar nor aligned.

#### 3.1.2 Step 2: The fitting procedure

A cloud forming a central cluster features a collapsing envelope and a quasi-stationary core with minor infalling motion. To distinguish between the two, we define a quantity

$$W_0 = \int_{V(R)} \vec{v} \cdot \vec{n} \; dm \; / \; \| \int_{V(R)} \vec{v} \times \vec{n} \; dm \| \tag{3.2}$$

for the series of ellipsoids of different size to observe the change in the collapsing motion, where $\vec{v}$ is the velocity and $\vec{n}$ the unit vector pointing from the ellipsoid center to the cell position. While the envelope is expected to be globally infalling, the gaseous proto-cluster itself should be relatively stationary with more prominent rotation. The quantity $W_0$ thus follows different radial dependence inside and outside the proto-cluster. We propose a simple piecewise power-law description that differentiates the flow properties inside and outside the gaseous proto-cluster. As shown in Fig. 3, the infall moment exhibits a change in slope in log scale. Inside the cluster, the gas is no longer necessarily collapsing and $W_0$ can even change signs. A piecewise fit is performed and the residual calculated to define the semimajor axis $R_*$ of the gaseous proto-cluster. This expression is

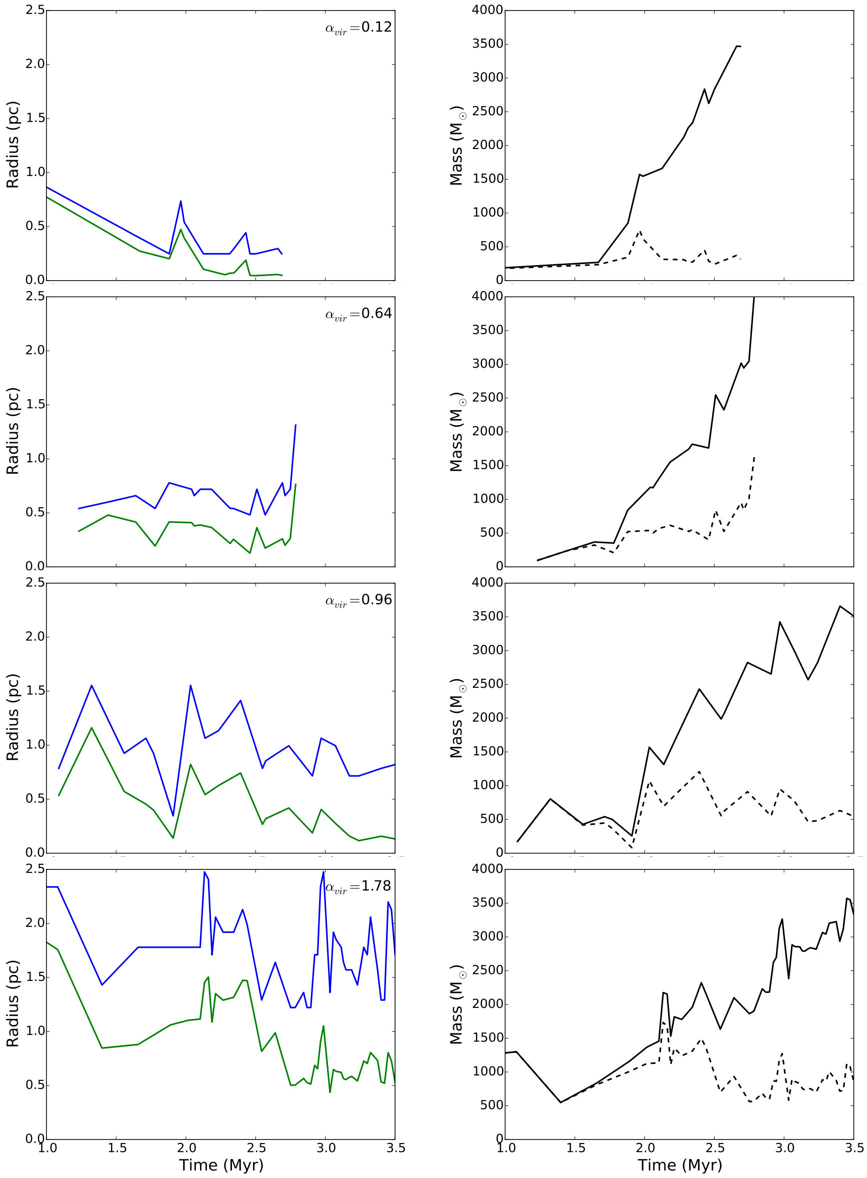


Fig. 4: **Left:** Time evolution of the semiaxes $R$ and $H$ of the ellipsoidal gas cluster. **Right:** Cluster mass shown as function of time. The two curves represent the gas mass (dashed) and that plus the sink mass (solid) inside the ellipsoidal region defined with gas kinematics. From top to bottom are runs A, B, C, and D with increasing levels of turbulence. The proto-cluster size increases with turbulence level. Most of the mass is accreted onto the sinks while the cluster mass increases in time, therefore the gas mass stays roughly constant.

written as

$$W_{0,\mathrm{fit}}(R_{\mathrm{avg}}, r_*) = \begin{cases} a_c R_{\mathrm{avg}}^{b_c} & \text{for} \quad R_{\mathrm{avg}} < r_* \\ a_e R_{\mathrm{avg}}^{b_e} & \text{for} \quad R_{\mathrm{avg}} > r_* \end{cases} \tag{3.3a}$$

$$res(r_*) = \frac{1}{n_R} \sum_R \left[ \frac{W_{0,\mathrm{fit}}(R_{\mathrm{avg}}, r_*) - W_0(R)}{W_0(R)} \right]^2 \tag{3.3b}$$

$$R_* = \arg\min res(r_*). \tag{3.3c}$$

The average radius of the ellipsoid $R_{\mathrm{avg}} = (R^2 H)^{\frac{1}{3}}$ is used to perform the power-law fit. Other combination of $R$ and $H$ are tested and the results have no strong dependence on this choice. The inner part of the fitted function is put to zero when there are fluctuations around zero, and the negative points are omitted when fitting the outer part. The size of the gaseous proto-cluster is defined as the radius at which the minimal local minimum occurs.This normalised residual of the best fit is usually smaller than $10^{-3}$, and its square root implies an error of a few percentage of the fit. The fit residual is large when there are changes in sign of $W_0$ as a result of our definition of the functions, but the radius is on the contrary very well defined in such cases. A local minimum of the fit residual cannot always be found. This might be because the gas is highly turbulent and that there is a fluctuating shock zone between the envelope and gaseous proto-cluster, which deteriorates the fit if it is included in either of the two domains. Nonetheless, when it exists, it marks well the transition between the two regimes. Moreover, the obtained result is in good coherence of the dense region seen from the visualisations.

The inferred evolution of the size and mass of the cluster are presented in Fig. 4. Despite its turbulent nature, the size of the gaseous proto-cluster stays relatively constant while mass is accreted. The more turbulent the initial cloud is, the larger the proto-cluster is. The mass evolution is plotted with the gas mass and total mass (sinks inside the ellipsoid included). The gas mass stays roughly constant while the total mass increases, implying that most of the mass accreted onto the cluster ends up in the sinks. As expected, the radius drops with $\alpha_{\rm vir}$ because of the weaker rotational and turbulent support. This is reproduced by the analytical model developed in (Lee & Hennebelle 2016b). It is important to note that these simulations are performed without stellar feedback. With feedback considered, the sink formation and accretion could be substantially delayed and/or reduced.

### 3.2 *The embedded sink cluster*

The sink particles trace the dense region, where stars formation occurs, therefore the sink particle distribution is representative of the stellar cluster and can be used to infer the cluster size.This is carried out by computing the three eigenvalues of the rotational inertia matrix of sink particles with respect to their center of gravity. The eigenvalues represent not only the size but also the shape of the sink particle cluster. The rotational inertia matrix and the inferred radii are

$$I_{\rm rot} = \sum_i m_i \begin{bmatrix} x_i^2 & x_i y_i & x_i z_i \\ x_i y_i & y_i^2 & y_i z_i \\ x_i z_i & y_i z_i & z_i^2 \end{bmatrix}, \quad \text{and} \quad r_i = \beta \sqrt{\frac{5\lambda_i}{M}},\ i = 1, 2, 3, \tag{3.4}$$

where $i$ is the index of sink particles, $M$ the total mass of sinks, and $\lambda_1, \lambda_2, \lambda_3$ three eigenvalues of $I_{\rm rot}$. The factor 5 comes from the uniform mass distribution assumption, and a correctional factor $\beta \geq 1$ accounts for the fact that the mass might be centrally concentrated. From a first calculation (see dashed lines in Fig. 5), it is clear that the sink particles are very extendedly distributed, and that the concentration in certain directions gives a relative large eigenvalue compared to the other two. However, sinks forming inside the filaments feeding the cluster or those ejected by N-body interactions should not be taken into account when studying the cluster itself. We thus refine the calculation by omitting the sink particles that have larger distances than the largest semi-axis from the first calculation and repeating the same procedure. We search for convergence by increasing $\beta$ starting from unity. We employ the smallest $\beta$ value that yields convergence, which is always between 1 and 1.5. The convergence is reached in a couple of iterations. This yields a cluster which is more spherical and stays roughly constant in size as the total sink mass increases. The evolution of the sink cluster radius and mass are plotted in Fig. 5. The total mass of all sinks is plotted in dotted curves while that of those inside the cluster is plotted with dashed curves. The total mass including the gas is also plotted in solid curves. The selection of clustered sinks is not always robust, and the inferred size shows spiky fluctuations despite the generally stable trend it exhibits. However, the significantly reduced size and relatively mild decrease in mass suggest that the distant sinks,which make up only a small fraction of the mass, are effectively rejected.

### 3.3 *The cluster mass-size relation*

The mass-size relation is one of the important characteristics of proto-clusters that can be compared with observations. On the left of Fig. 6, the mass-size relations of gaseous proto-clusters defined with gas kinematics are over-plotted with observations of star-forming clumps (Fall et al. 2010; Urquhart et al. 2014), and the number-size relations of clusters obtained from sink distributions are over-plotted with embedded cluster observations (Adams et al. 2006; Gutermuth et al. 2009). Early time steps (before 2 Myr) are plotted with thinner lines. As the gaseous proto-cluster accretes mass, it arrives on the observed sequence. The larger the turbulence in the parent cloud, the more expanded the proto-cluster since the mass feeding the proto-cluster has higher kinetic energy and the rotation is also more important. For the sake of comparison with observations, we also show the

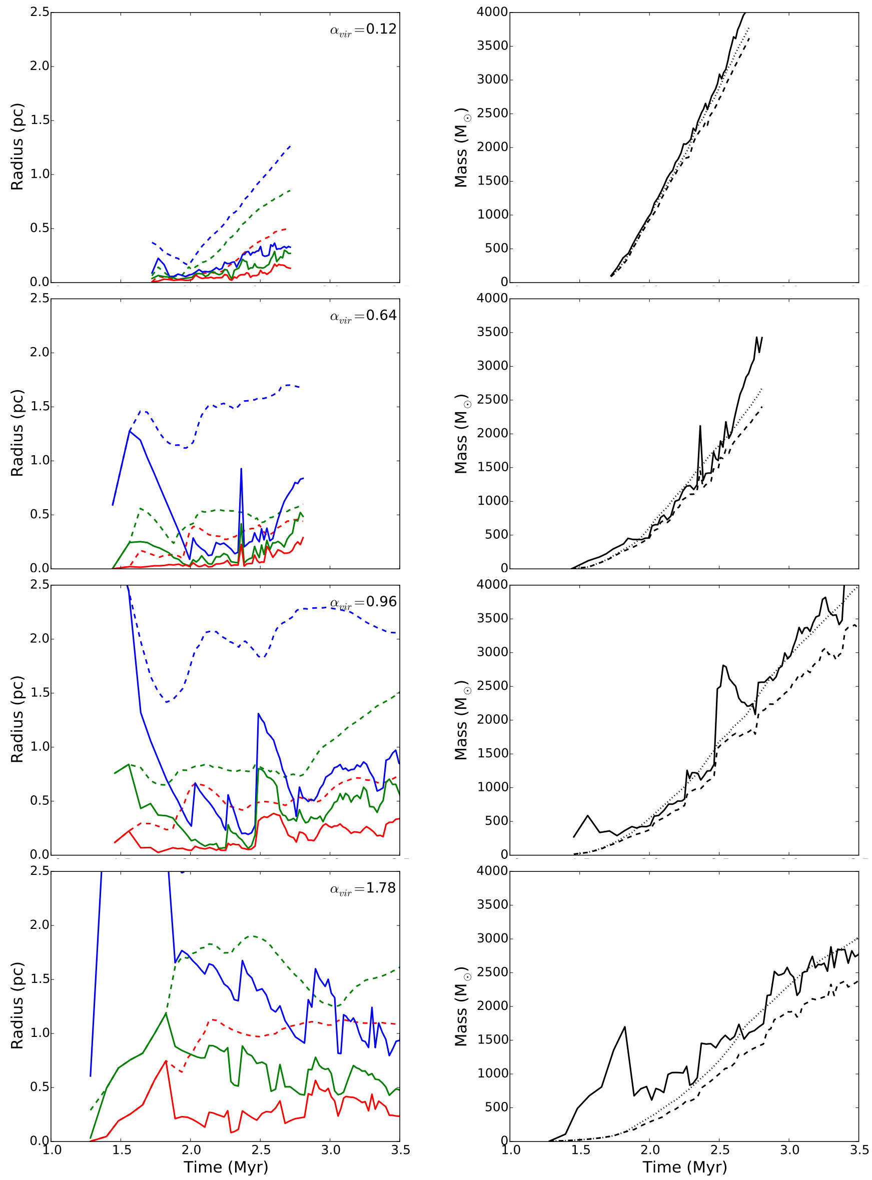


Fig. 5: **Left:** Time evolution of the three semi-axes of the cluster determined with sink particles. The dashed curves and solid curves represent the values calculated with all sinks and the reduced values with distant sinks omitted, respectively. **Right:** Sink mass (dashed) and total mass (solid) inside cluster region defined with sink distributions plotted against time. The dotted line represents the sink mass before sink removal. Removing the sink particles far away from the center drastically reduces the size while only mildly decreasing the total mass. From top to bottom are runs A, B, C, and D with increasing levels of turbulence.

relation obtained by Adams et al. (2006) $R$ (pc) $\propto (N/300)^{1/2}$. The sink clusters come close to this sequence after sufficient evolution. At a later stage, they form fewer new sinks and start increasing in radius. Further discussion is needed, however, as our sinks are massive and do not represent individual stars. The number-size (or mass-size) relation inferred with sink particles is thus biased and not exactly representative of the embedded cluster itself. Observationally speaking, Pfalzner et al. (2016) plotted the number-size relation for different star-forming regions and found that, even though this relation follows the same trend inside different regions, its absolute value in number can vary by a factor 20 (their Fig. 3). The cluster definition and distance of the object could play important roles. On the other hand, we see that the sink cluster radius does not change very much with time, at least implying that at the early stage of cluster formation, the stars should still somewhat be correlated to and regulated by their natal gas. If we assume a 0.5 M$_\odot$ averaged mass for the stars inside

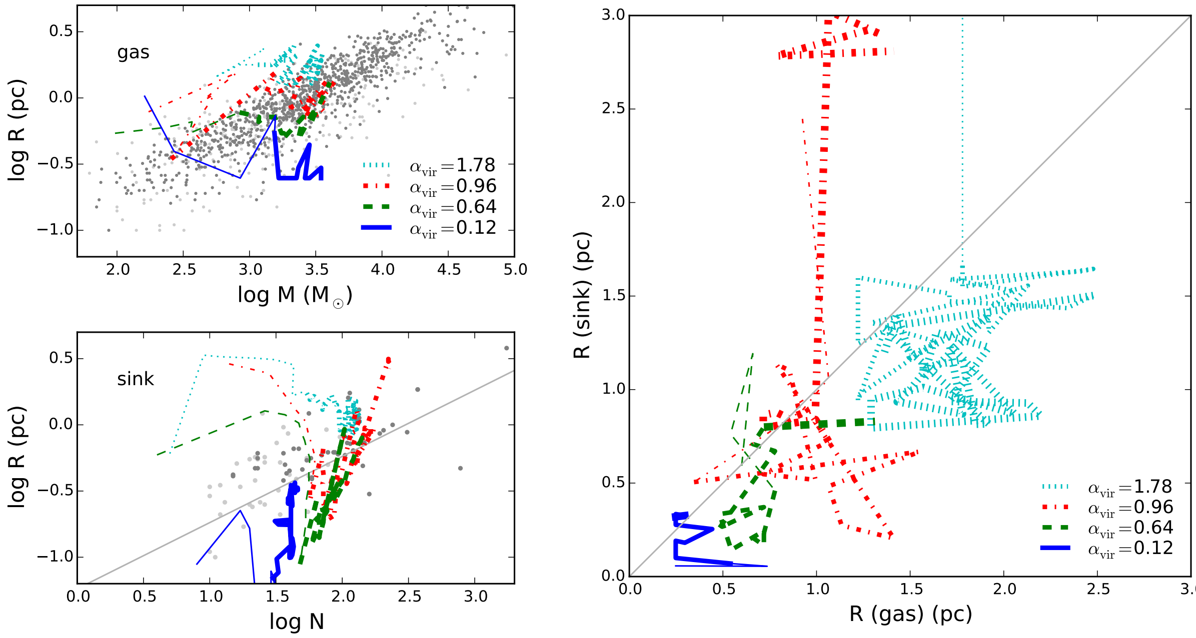


Fig. 6: **Left top:** Gaseous proto-cluster mass-size relation defined with gas kinematics over-plotted with measurements of star-forming clumps (Fall et al. 2010; Urquhart et al. 2014). The total mass of the cluster is used (gas plus sinks). **Left bottom:** Sink cluster number-size relation over-plotted with embedded cluster (Adams et al. 2006; Gutermuth et al. 2009). The gray line indicates the number-size relation $R$ (pc) $\propto (N/300)^{1/2}$ (Adams et al. 2006). Simulations with four different levels of turbulent support are plotted. The blue solid, green dashed, red dot-dashed, and cyan dotted curves have virial parameters $\alpha_{\rm vir}$ = 0.12, 0.64, 0.96, 1.78, respectively. The curves represent the time sequence. As the proto-clusters accrete, they gain in mass and move from left to right in the figure. Time steps before 2 Myr are plotted with thinner lines. **Right:** Radius of sink clusters plotted against radius of gas proto-clusters for four runs. The relations are plotted with thinner lines for time before 2 Myr and with thicker lines after 3 Myr. The gas and sink cluster sizes show good correlation in general, while the sink cluster size is slightly smaller than that of the gas cluster.

the clusters, a star formation efficiency of less than 10% is required to reconcile the two relations given that the cluster size does not evolve. Alternatively, this could also be explained by an expansion after the cluster formation. We inferred the cluster size for gas and sinks, which enables a comparison between the two and allows us to compare the cluster size with observations as well. We stress that according to our analysis, the link between the gaseous proto-cluster radius and that of the embedded cluster is not a trivial matter. Therefore, the 20% efficiency that is usually inferred should be regarded with great care.

We compare the cluster size inferred with gas and sinks in the right panel of Fig. 6. The sink clusters generally are smaller in size than the gas clusters. This implies that the stars are formed in the inner region of the gaseous proto-cluster. The relations are plotted with a line thickness that increases with time. We can see in both the green and red curves that at early time the sink cluster radius is large probably due to the bad definition of a cluster with very few sinks. Once the cluster becomes steadily established (after 2 Myr), they show a radius that is smaller than the gaseous proto-cluster size. At an even later time (after 3 Myr with the thickest lines), the sink cluster radius shows a growth with respect to the gas radius. This might be a sign of the dynamical decoupling and expansion of the stellar cluster. Longmore et al. (2014) concluded that the gas-star coevolution cannot continue over a dynamical time, on the one hand, because the gas is dissipative while stars are ballistic and, on the other hand, because stars form from gravitational collapse of gas and create a local, gas-free environment for themselves. Parker & Dale (2015) perform a Q-parameter analysis (Cartwright & Whitworth 2004) of gas and stars in simulations and suggest that their spatial distributions are not trivially linked. This sheds light on the importance of correctly following both gas and particle dynamics in simulations and the necessity of pertinent theories of early stellar cluster formation.

To conclude, our simulations successfully reproduce the mass-size regions that we define as gaseous proto-clusters. When the cloud is too weakly supported (small $\alpha_{\rm vir}$), the gaseous proto-cluster is strongly accreting

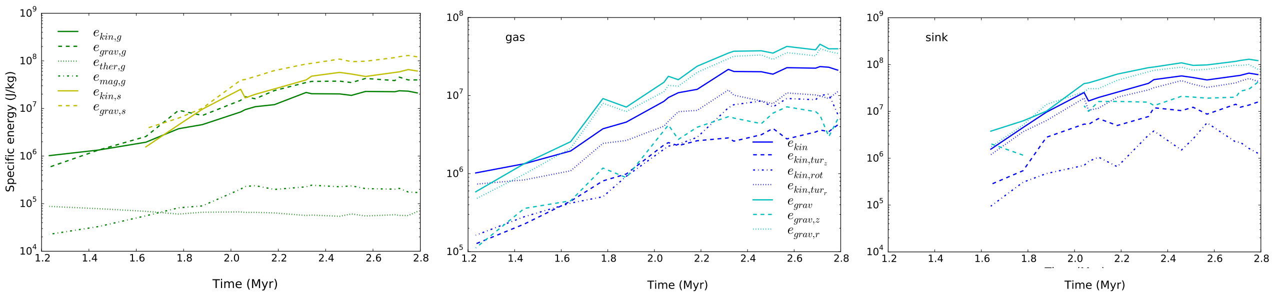


Fig. 7: **Left:** different forms of specific energy of the cluster defined with gas kinematics plotted against time. The gas component is plotted in green and the sinks are plotted in yellow. The solid, dashed, dotted, and dash-dotted lines represent kinetic, gravitational, thermal, and magnetic energies respectively. The gravitational energy is plotted in absolute value. **Middle and Right:** kinetic (blue) and gravitational energy (cyan) decomposition of the gas component (middle panel) and the sink component (bottom panel) of the proto-cluster plotted in specific values. Total energy, energy along $z$-axis, rotational energy, and energy perpendicular to $z$-axis are plotted with solid lines, dashed lines, dash-dotted lines, and dotted lines respectively.

and has a small radius and this should probably not be compared to the observations. For other runs of clouds with $\alpha_{\rm vir}$ close to unity, a good agreement of the mass-size relation between observations and simulations is reached. As gaseous proto-clusters accrete mass, they arrive on the observed sequence, which very likely implies a stationary and quasi-equilibrium state. Although we have performed simulations of $10^4$ $M_\odot$ clouds, giving gaseous proto-clusters of a few thousands $M_\odot$, the gas is almost isothermal and the results could then be rescaled to the observed mass range. The simulations are parametrised by the following two non-dimensional numbers:

$$\alpha_{\rm vir} \propto \frac{\sigma^2 R}{M} \quad \text{and} \quad \mathcal{M} = \frac{\sigma}{c_{\rm s}}. \tag{3.5}$$

If we rescale the MC in the simulation to different mass, size, and temperature such that

$$M' = AM \quad , \quad R' = A^{\frac{1}{3-\gamma}} R \quad \text{and} \quad c_{\rm s}' = A^{\frac{2-\gamma}{6-2\gamma}} c_{\rm s}, \tag{3.6}$$

where $\gamma = 1$ or 0.7 is the exponent in the Larson relation $\rho \propto R^{-\gamma}$ (Larson 1981; Falgarone et al. 2004, 2009; Hennebelle & Falgarone 2012; Lombardi et al. 2010) and $A$ is a scaling factor. With this rescaling, $\alpha_{\rm vir}$ and $\mathcal{M}$ stay unchanged, and the new MC also follows the Larson relation. The gaseous proto-cluster inside the cloud is therefore rescaled, following $R_* \propto M_*^{\frac{1}{3-\gamma}} \sim M_*^{0.5}$. This implies that given parent clouds that follow Larson relations, the gaseous proto-clusters formed therein follow relation reported by Fall et al. (2010) and Urquhart et al. (2014). We also develop an analytical model to predict the mass-size relation of gaseous proto-clusters (Lee & Hennebelle 2016b). As long as the condition that stellar feedback is not very important stays valid, our simulations and analytical model match the observations.

## 4 Properties of the proto-cluster and prospectives

The goal of this study is to well characterise the star-forming gas. Having identified the cluster from simulations, we perform some analysis of their internal properties.

### 4.1 *Energy equilibrium*

Once the proto-cluster is identified, we calculate the energies in different forms inside this region and examine the balance. Since we are discussing the gas-dominated early phase of cluster formation, we use the proto-clusters previously defined with gas kinematics, which indeed show good correspondence with observations. The specific kinetic, gravitational, thermal, and magnetic energies are plotted at several time steps in the left panel of Fig. 7 for the run with $t_{\rm ff}/t_{\rm vct} = 0.9$. The gravitational energy is plotted in absolute value. For the gas component (green), the thermal and magnetic energies are a few percent of the gravitational energy, which is consistent with that initialised in the parent cloud and, therefore, do not contribute much to supporting against self-gravity at the cluster scale. The specific thermal energy stays roughly constant and decreases mildly, indicating a slight temperature decrease due to density increase. The specific magnetic energy increases slightly as a result of magnetic flux concentration. On the other hand, the kinetic energy, which has contributions from turbulence and rotation, acts largely to support against gravitational contraction. The cluster satisfies $2E_{\rm kin,g}+E_{\rm grav,g} \approx 0$, indicating the gas component is in virial equilibrium during mass accretion. The particle component (yellow), on the other hand, begins to have higher specific kinetic and gravitational energies a short while after the sinks start forming. This implies that the sink particles are more centrally concentrated than the gas and lie in a deeper potential well, which is consistent with our previous finding that the radius determined with sinks is smaller (Fig. 6 right). This is compatible with the discovery by Bate et al. (2003) that the stars have velocity dispersion that is three times higher than that of the gas. It is remarkable that the sinks are bound almost at virial and also satisfy the relation $2E_{\rm kin,s} + E_{\rm grav,s} \approx 0$, indicating that the cluster energy properties are largely inherited from its natal gas and are determined at the early formation stage. Walker et al. (2016) suggested that clusters very likely form in a conveyor-belt mode, in which the core of the star-forming cloud accumulates mass at the same time as stars form. This is perfectly in coherence with our simulation results that stars form in the dense, gaseous proto-cluster, of which the mass and energy is sustained by accretion.

### 4.2 Rotation and turbulence anisotropy

The rotation makes up an important proportion of the kinetic energy of the proto-cluster and a flattened form is thus a natural consequence. We estimate the rotational energy of the proto-cluster and separate it from its turbulent counterpart. This allows us to compare the proportions of rotational and turbulent energies and also examine whether turbulence is isotropic. The rotational energy is estimated as $E_{\rm kin,rot} = \frac{1}{2} J I^{-1} J$, where $J$ is the angular momentum the cluster, and $I$ is its rotational inertia matrix. This allows us to eliminate turbulence by summing up various motions. Uncertainties remain, in particular, since we do not take into account the differential rotation, this is probably an underestimation. The one-dimensional turbulent energy along the rotational axis of the cluster $E_{{\rm kin},z}$ is also calculated. The turbulent energy perpendicular to the rotational axis could be thus estimated as $E_{{\rm kin},r} = E_{\rm kin} - E_{\rm kin,rot} - E_{{\rm kin},z}$. We display the energies for the run with $t_{\rm ff}/t_{\rm vct} = 0.9$. In the middle panel of Fig. 7, we plot the total kinetic energy, rotational energy, turbulence parallel and perpendicular to the rotational axis, respectively, for the gas component in blue. The proportion of rotational energy increases as the gaseous proto-cluster accretes, while that of $E_{{\rm kin},z}$ is slightly decreasing. The rotational energy grows to become comparable to the turbulent energy in the same plane and makes up nearly a third of the total kinetic energy. The turbulence shows anisotropy since $E_{{\rm kin},r}/E_{{\rm kin},z} > 2$, although there remain uncertainties in the estimation of the rotation. The rotation flattens the proto-cluster and this anisotropy in geometry thus makes the kinetic energy distribution anisotropic in turn. We also plot in cyan the gravitational energy of the cluster ($E_{\rm grav}$).The gravitational energy is calculated by integrating the inner product of the gravity and the position vector with respect to cluster center over the cluster volume (as is carried out in the virial theorem). With this definition, we can separate the gravitational energy into two contributions by calculating respectively with the gravitational acceleration parallel ($E_{{\rm grav},z}$) and perpendicular ($E_{{\rm grav},r}$) to the cluster minor axis. This points out the fact that not only the proto-cluster is generally in virial equilibrium, but it also satisfies a modified virial theorem that accounts for the two dimensions, i.e., $2E_{{\rm kin},z}+E_{{\rm grav},z} \approx 0$ and $2E_{{\rm kin},r} + 2E_{\rm kin,rot} + E_{{\rm grav},r} \approx 0$. This motivates the decomposition of the virial theorem into two dimensions in the analytical model by Lee & Hennebelle (2016b). The right panel of Fig. 7 shows the same plot as that in the middle for the sink component of the proto-cluster. The sink particles show similar trends to the gas in general. A very different behaviour is that the rotational energy calculated for the whole system is not increasing like that of the gas. Moreover, $E_{\rm kin,rot} \ll E_{\rm kin}$, indicating that the stars are giving angular momentum to the gas and there is less a general rotation.

### 4.3 Density PDF

The star formation is a result of collapse induced by local over-density, therefore, essential information is imprinted in the density probability density function (PDF) of the star-forming environment, which is in turn a result of interaction between turbulence and gravity. The density PDF is important for theoretical prediction of the IMF (Padoan & Nordlund 2002; Hennebelle & Chabrier 2008, 2009; Hopkins 2012). We plot the volume-weighted density PDFs of the gaseous proto-clusters identified in the previous section and that of the parent MC in Fig. 8, and show that there are indeed fundamental differences. At the beginning of the simulation, the PDF is very close to a log-normal distribution, which is a natural consequence of the turbulence, while the gravity

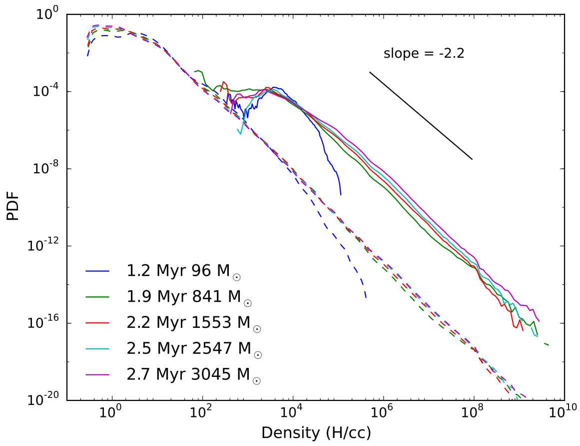


Fig. 8: In solid curves for the gaseous proto-cluster and in dashed curves for the parent cloud, the PDF at several time steps for run B with $t_{\rm ff}/t_{\rm vat} = 0.9$. The normalisation is performed such that the integral is equal to one. The distribution is close to lognormal at the beginning as a result of turbulence interaction. The gravity soon dominates and creates a prominent power-law tail. The slope -2.2 is the average of the cluster PDF slopes evaluated at the same density range as the black line except for the first time step.

soon dominates. The gaseous proto-cluster shows the same power-law high-mass tail as the parent MC with slope $-2.2$, which is a signature of local gravitational collapse. This is a common feature of star-forming region as first mentioned observationally by Kainulainen et al. (2009). The major difference lies in that the gaseous proto-cluster region is denser than the original cloud environment with a density peak around $10^4$ cm$^{-3}$. The density PDF of the MC stays almost unchanged while a gaseous proto-cluster develops within. This emphasises the fact that when the stars form, their environment is already not the same as the MC in which they reside. The gaseous proto-cluster stage, of which the gas properties are modified by the interaction of gravity and turbulence, should therefore be taken into account when linking the MC to the stellar cluster.

### *4.4 Stellar feedback*

To have a fully physical description of a realistic self-regulation of star mass accretion and cluster formation, stellar feedbacks such as radiations (Bate 2009; Price & Bate 2009; Commerçon et al. 2011; Bate 2012; Krumholz et al. 2012), protostellar jets and outflows (Wang et al. 2010; Nakamura & Li 2011, 2014; Federrath et al. 2014; Federrath 2015; Dale et al. 2013c, 2015), HII regions (Krumholz et al. 2007; Peters et al. 2010; Dale et al. 2013a,b, 2015), and supernovae (Iffrig & Hennebelle 2015; Walch & Naab 2015) should be incorporated. Here we show results of gaseous proto-cluster formation in a simulation with the ionising HII region (Geen et al. 2015) in Fig. 9. The early evolution of the proto-cluster is barely influenced by stellar feedback since massive star have not yet formed and have not been exerting energy output into the ISM. In the left panel we see that at early time the cluster forms similarly to that in the simulation without feedback. At later time, the HII region heats up proto-cluster and eventually disperses all the gas available for star formation. The cluster survives from the gas expulsion and become gas free. An interesting event is also observed in this simulation that at the expansion front of the ionising wave, a secondary cluster formation is triggered. On the right panel of Fig. 9, we calculated the radius of the gaseous proto-cluster with the previously developed method, the evolution is very similar to that without feedback until that the gas starts flowing outwards and our method becomes no longer valid. A next step of this study is to include the feedback from lower mass stars such as the proto-stellar jet.

## 5 Conclusions

With a set of simulations of self-gravitating MCs under global collapse, we demonstrated that star do not form uniformly in MCs. Instead, they form inside gaseous proto-cluster environments, which occupy a small volume fraction of the MC. The gaseous proto-cluster forms from the quasi-static equilibrium between the turbulence-driving accretion from the global infall and the turbulence cascade that dissipates energy. The gas inside

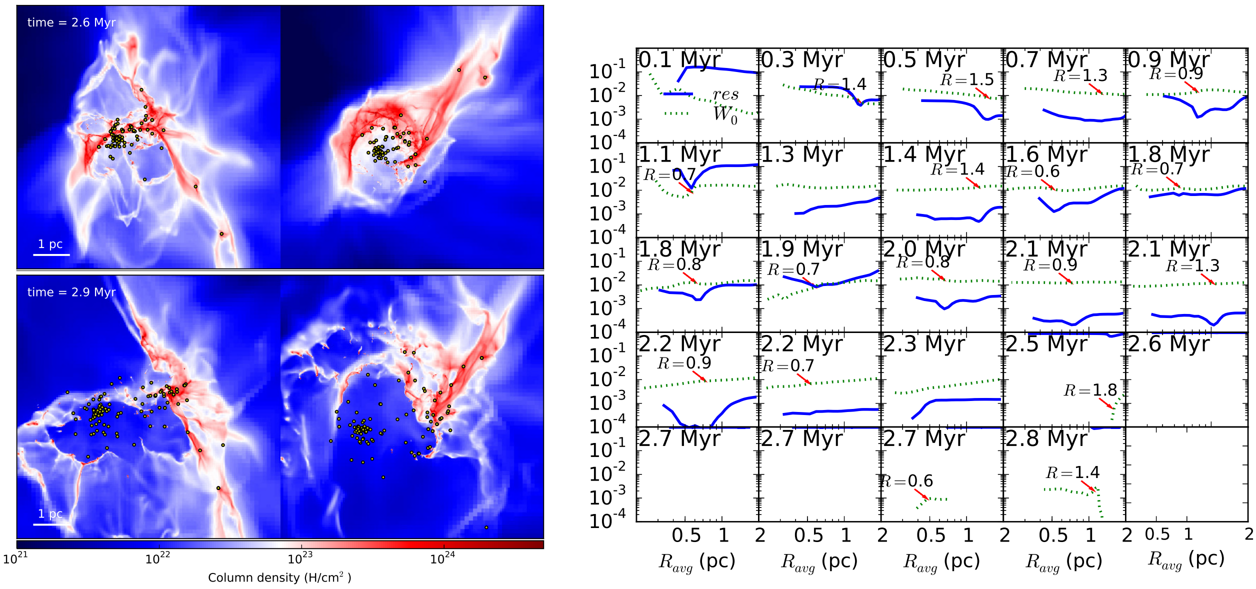


Fig. 9: **Left:** Column density of simulation with HII feedback at two time steps. Circles show the stellar cluster that survives the gas expulsion. **Right:** Radius identification of the gaseous proto-cluster at several time steps.

the gaseous proto-cluster is reprocessed and is denser, more turbulent than the averaged MC. The gaseous proto-cluster mass and size could be inferred from its parent MC and there exists a mass-size relation from observations that is reproduce with our simulations. The proto-clusters inferred with gas and sink components are compared to the observed star-forming clumps and embedded clusters, respectively. Both the gas and sink clusters show stationary behaviour in size and are coherent with observations. We stress that although the stellar cluster radius and the gaseous proto-cluster radius are correlated, their exact values are sensitive to the definition adopted. Therefore, this implies that any interpretation in terms of gas removal or efficiency should be taken with care. Energy analyses show that the proto-cluster is in virial equilibrium such that the rotation and turbulence support against self-gravity. As turbulence is driven by the accretion from the collapsing MC, a new balance is established in this emerging entity. This is obviously prescribed by the properties of the parent MC and the nature of its collapse. The initial turbulence level in the parent MC is also imprinted in that of the gaseous proto-cluster and, consequently, determines its size.

This study shows that stellar clusters from very likely inside an environment that has universal properties and is to some extent disentangled from the parent MC, which allows us to focus on the dense regions and possibly set up a more realistic and economic initial condition for cluster formation simulations. Last but not least, we started to include stellar feedback mechanisms, such as ionising HII (Geen et al. 2016) regions and supernova (Iffrig & Hennebelle 2015), into the simulations. These kinds of high energy processes disperse that gas inside the gaseous proto-cluster and terminates star-formation at later stages, while the conclusions from earlier studies without stellar feedback stays unchanged. We conclude that the gaseous proto-cluster is indeed an important intermediate step of stellar cluster formation from MCs, and that star formation should be studied in this context. Interested readers are invited to refer to Lee & Hennebelle (2016a) for more detailed informations.

This work was granted access to HPC resources of CINES under the allocation x2014047023 made by GENCI (Grand Equipement National de Calcul Intensif). This research has received funding from the European Research Council under the European Community's Seventh Framework Programme (FP7/2007-2013 Grant Agreement no. 306483).

## References

Adams, F. C., Proszkow, E. M., Fatuzzo, M., & Myers, P. C. 2006, ApJ, 641, 504

Audit, E. & Hennebelle, P. 2005, A&A, 433, 1

Ballesteros-Paredes, J., Hartmann, L. W., Pérez-Goytia, N., & Kuznetsova, A. 2015, MNRAS, 452, 566

Bate, M. R. 2009, MNRAS, 392, 1363

Bate, M. R. 2012, MNRAS, 419, 3115
Bate, M. R., Bonnell, I. A., & Bromm, V. 2003, MNRAS, 339, 577
Bleuler, A. & Teyssier, R. 2014, MNRAS, 445, 4015
Bonnell, I. A., Bate, M. R., & Vine, S. G. 2003, MNRAS, 343, 413
Bonnell, I. A., Clark, P., & Bate, M. R. 2008, MNRAS, 389, 1556
Carpenter, J. M. 2000, AJ, 120, 3139
Cartwright, A. & Whitworth, A. P. 2004, MNRAS, 348, 589
Commerçon, B., Hennebelle, P., & Henning, T. 2011, ApJ, 742, L9
Dale, J. E., Ercolano, B., & Bonnell, I. A. 2013a, MNRAS, 431, 1062
Dale, J. E., Ercolano, B., & Bonnell, I. A. 2013b, MNRAS, 430, 234
Dale, J. E., Ercolano, B., & Bonnell, I. A. 2015, MNRAS, 451, 987
Dale, J. E., Ngoumou, J., Ercolano, B., & Bonnell, I. A. 2013c, MNRAS, 436, 3430
Falgarone, E., Hily-Blant, P., & Levrier, F. 2004, Ap&SS, 292, 89
Falgarone, E., Pety, J., & Hily-Blant, P. 2009, A&A, 507, 355
Fall, S. M., Krumholz, M. R., & Matzner, C. D. 2010, ApJ, 710, L142
Federrath, C. 2015, MNRAS, 450, 4035
Federrath, C., Schrön, M., Banerjee, R., & Klessen, R. S. 2014, ApJ, 790, 128
Fromang, S., Hennebelle, P., & Teyssier, R. 2006, A&A, 457, 371
Geen, S., Hennebelle, P., Tremblin, P., & Rosdahl, J. 2015, MNRAS, 454, 4484
Geen, S., Hennebelle, P., Tremblin, P., & Rosdahl, J. 2016, MNRAS
Girichidis, P., Federrath, C., Banerjee, R., & Klessen, R. S. 2011, MNRAS, 413, 2741
Girichidis, P., Federrath, C., Banerjee, R., & Klessen, R. S. 2012, MNRAS, 420, 613
Gutermuth, R. A., Megeath, S. T., Myers, P. C., et al. 2009, ApJS, 184, 18
Hennebelle, P. & Chabrier, G. 2008, ApJ, 684, 395
Hennebelle, P. & Chabrier, G. 2009, ApJ, 702, 1428
Hennebelle, P. & Falgarone, E. 2012, A&A Rev., 20, 55
Hopkins, P. F. 2012, MNRAS, 423, 2037
Iffrig, O. & Hennebelle, P. 2015, A&A, 576, A95
Kainulainen, J., Beuther, H., Henning, T., & Plume, R. 2009, A&A, 508, L35
Klessen, R. S. & Burkert, A. 2000, ApJS, 128, 287
Klessen, R. S., Burkert, A., & Bate, M. R. 1998, ApJ, 501, L205
Krumholz, M. R., Klein, R. I., & McKee, C. F. 2012, ApJ, 754, 71
Krumholz, M. R., Stone, J. M., & Gardiner, T. A. 2007, ApJ, 671, 518
Lada, C. J. & Lada, E. A. 2003, ARA&A, 41, 57
Larson, R. B. 1981, MNRAS, 194, 809
Lee, Y.-N. & Hennebelle, P. 2016a, A&A, 591, A30
Lee, Y.-N. & Hennebelle, P. 2016b, A&A, 591, A31
Lombardi, M., Alves, J., & Lada, C. J. 2010, A&A, 519, L7
Longmore, S. N., Kruijssen, J. M. D., Bastian, N., et al. 2014, Protostars and Planets VI, 291
Murray, N. 2009, ApJ, 691, 946
Nakamura, F. & Li, Z.-Y. 2011, ApJ, 740, 36
Nakamura, F. & Li, Z.-Y. 2014, ApJ, 783, 115
Padoan, P. & Nordlund, Å. 2002, ApJ, 576, 870
Padoan, P., Nordlund, Å., Kritsuk, A. G., Norman, M. L., & Li, P. S. 2007, ApJ, 661, 972
Parker, R. J. & Dale, J. E. 2015, MNRAS, 451, 3664
Peters, T., Banerjee, R., Klessen, R. S., et al. 2010, ApJ, 711, 1017
Pfalzner, S., Kirk, H., Sills, A., et al. 2016, A&A, 586, A68
Price, D. J. & Bate, M. R. 2009, MNRAS, 398, 33
Schmidt, W., Kern, S. A. W., Federrath, C., & Klessen, R. S. 2010, A&A, 516, A25
Smith, R. J., Clark, P. C., & Bonnell, I. A. 2009, MNRAS, 396, 830
Teyssier, R. 2002, A&A, 385, 337
Urquhart, J. S., Moore, T. J. T., Csengeri, T., et al. 2014, MNRAS, 443, 1555
Walch, S. & Naab, T. 2015, MNRAS, 451, 2757
Walker, D. L., Longmore, S. N., Bastian, N., et al. 2016, MNRAS
Wang, P., Li, Z.-Y., Abel, T., & Nakamura, F. 2010, ApJ, 709, 27

*SF2A 2016*
*C. Reylé, J. Richard, L. Cambrésy, M. Deleuil, E. Pécontal, L. Tresse and I. Vauglin (eds)*

# HOW BARYONIC FEEDBACK PROCESSES CAN AFFECT DARK MATTER HALOS: A STOCHASTIC MODEL

J. Freundlich[1], A. El-Zant[2] and F. Combes[1]

**Abstract.** Feedback processes from stars and active galactic nuclei result in gas density fluctuations which can contribute to 'heating' dark matter haloes, decrease their density at the center and hence form more realistic 'cores' than the steep 'cusps' predicted by cold dark matter (CDM) simulations. We present a theoretical model deriving this effect from first principles: stochastic density variations in the gas distribution perturb the gravitational potential and hence affect the halo particles. We analytically derive the velocity dispersion imparted to the CDM particles and the corresponding relaxation time, and further perform numerical simulations to show that the assumed process can indeed lead to the formation of a core in an initially cuspy halo within a timescale comparable to the derived relaxation time. This suggests that feedback-induced cusp-core transformations observed in hydrodynamic simulations of galaxy formation may be understood and parametrized in relatively simple terms.

Keywords: Dark matter, Galaxies: halos, Galaxies: evolution, Galaxies: formation

## 1 Introduction

Despite its huge success at explaining the large scale structure of the Universe, the cold dark matter (CDM) model of structure formation faces different challenges at galactic scales. In particular, while CDM numerical simulations predict steep, 'cuspy' density profiles for dark matter halos, observations of dark matter dominated galaxies favor more shallower 'cores' (e.g., Moore 1994; de Blok et al. 2008; Oh et al. 2011).

Proposed solutions to this 'core-cusp' discrepancy and the related challenges of CDM cosmology, such as the 'too big to fail' problem, can be broadly divided into those considering fundamental changes in the physics of the model and those focusing on the baryonic processes at stake during galaxy formation and evolution. The first category of solutions comprises alternatives to CDM such as warm dark matter, self-interacting dark matter and models that fundamentally change the gravitational law like Mordechai Milgrom's MOND theory. Solutions invoking baryonic processes within the CDM framework are motivated by the fact that the discrepancies between model and observations precisely occur at the scale at which baryons start to play an important role, notably through powerful stellar and active galactic nuclei (AGN) feedback processes and outflows. Moreover, hydrodynamical simulations with different feedback implementations are able to reproduce dark matter cores (e.g., Governato et al. 2010; Teyssier et al. 2013). However, such complex simulations do not necessarily specify the physical mechanisms through which baryons affect the dark matter distribution.

Baryons can mostly affect the dark matter halo through their own gravity and by modifying the gravitational potential. Such is the case with adiabatic contraction (when the accumulation of cold gas at the center of the halo steepens its potential well and causes the dark matter to contract; Blumenthal et al. 1986) and with the dynamical friction through which a massive object such as a satellite galaxy or a clump of gas can transfer part of its kinetic energy to the dark matter background (Chandrasekhar 1943). This latter process can 'heat' the dark matter halo and remove the central cusp (El-Zant et al. 2001). Alternatively, repeated gravitational potential fluctuations induced by stellar winds, supernova explosions and AGN could also dynamically heat

[1] LERMA, Observatoire de Paris, PSL Research University, CNRS, Sorbonne Universités, UPMC and Collège de France, F-75014, Paris, France
[2] Centre for Theoretical Physics, The British University in Egypt, Sherouk City 11837, Cairo, Egypt

the dark matter and lead to the formation of a core (Pontzen & Governato 2012). In this case, variations in the baryonic mass distribution induce violent potential fluctuations which progressively disperse dark matter particles away from the center of the halo.

To isolate further the physical mechanism at stake during core formation, we present and test an *a priori* theoretical model in which the gravitational potential fluctuations leading to core formation arise from feedback-induced stochastic density variations in the gas distribution. Dark matter particles experience successive 'kicks' from the potential fluctuations, which cumulatively induce them to deviate from their trajectories as in a diffusion process or as two-body relaxation does for stellar systems. This work is described in more details in Freundlich (2015), Chapter 4, and El-Zant et al. (2016).

## 2 Theoretical model

### 2.1 Stochastic density fluctuations

We assume that the potential fluctuations leading to core formation arise from stochastic density perturbations in a gaseous medium of mean density $\rho_0$ confined within a sphere of radius $d$ corresponding to the inner region of the halo. The density contrast $\delta(\boldsymbol{r}) = \rho(\boldsymbol{r})/\rho_0 - 1$ can be Fourier decomposed over $V = d^3$ such that

$$\delta(\boldsymbol{r}) = \frac{V}{(2\pi)^3} \int \delta_{\boldsymbol{k}} e^{-i\boldsymbol{k}.\boldsymbol{r}} d\boldsymbol{k}. \tag{2.1}$$

The perturbations are assumed to be isotropic, stationary and described by a power-law power spectrum

$$\mathcal{P}(k) = V \langle |\delta_k|^2 \rangle \propto k^{-n}. \tag{2.2}$$

Turbulent media such as the interstellar medium are indeed expected to display power-law power spectra as fluctuations initiated at large scale cascade down to the dissipation scale. For the sake of our calculations, we also assume minimum and maximum cutoff scales $2\pi/k_{\rm max} \ll 2\pi/k_{\rm min}$.

### 2.2 Repetitive kicks on the dark matter particles

Each perturbation mode $\delta_{\boldsymbol{k}}$ induces a small 'kick'

$$\boldsymbol{F}_{\boldsymbol{k}} = 4\pi i \; G\rho_0 \; \boldsymbol{k} \; k^{-2} \; \delta_{\boldsymbol{k}} \tag{2.3}$$

on the dark matter particles, the cumulative effect of these kicks leading the particles to deviate from their trajectories by a mean velocity variation after a time $T$ such that

$$\langle \Delta v^2 \rangle = 2 \int_0^T (T-t) \, \langle F(0) F(t) \rangle \; dt. \tag{2.4}$$

This description is analogous to two-body relaxation in stellar systems, in which the kicks correspond to the successive interactions of the particles with one another.

### 2.3 Relaxation time in the diffusion limit

In the diffusion limit where $2\pi/k_{\rm min} \ll R$, i.e., where the density perturbations are small compared to the distance $R$ traveled during $T$ by the dark matter particles with respect to the fluctuation field, we analytically obtain a relaxation time

$$t_{\rm relax} = \frac{n v_r \langle v \rangle^2}{8\pi (G\rho_0)^2 V \langle |\delta_{k_{\rm min}}|^2 \rangle}, \tag{2.5}$$

where $v_r = R/T$ is the mean velocity of the dark matter particles with respect to the fluctuating field and $\langle v \rangle$ their initial orbital velocity. This expression assumes that the spatial statistical properties of the perturbations expressed through the force autocorrelation function $\langle \boldsymbol{F}(0).\boldsymbol{F}(r) \rangle$ can be transported into the temporal domain such that $\langle \boldsymbol{F}(0).\boldsymbol{F}(t) \rangle = \langle \boldsymbol{F}(0).\boldsymbol{F}(r = v_r t) \rangle$ (e.g., Wilczek et al. 2014, and references therein). The resulting relaxation time does not depend on the minimum and maximum cutoff scales, and only linearly on the power law exponent $n$. It mainly depends on the gas mass fraction through $\rho_0$ and the normalization of the power spectrum of the density fluctuations.

### 2.4 Application to a fiducial dwarf galaxy

We evaluate the relaxation time for a fiducial dwarf NFW halo, assuming orbital velocities $\langle v(l)\rangle \sim l\sqrt{G\rho(<l)}$ and gas movements dominated by those at the largest fluctuation scale, with $v_r \sim d\sqrt{G\rho(<d/2)}/2$, $\rho(<l)$ being the average density inside radius $l$. The halo is assumed to have a scalelength $R_s = 0.9$ kpc and a total mass $M_{\rm vir} = 2.26\ 10^{11}$ $M_\odot$ inside $R_{\rm vir} = 30$ kpc. The gas mass fraction inside $d/2 = 5$ kpc is $f(d/2) \equiv \rho_0/\rho(<d/2) = 0.17$ and we assume a power spectrum with $n = 2.4$ and $\langle|\delta_{k_{\rm min}}|^2\rangle \approx 0.005$. Eq. 2.5 yields a relaxation time of about 3.5 Gyr within $d/2$, decreasing towards the very center of the halo. This gives a timescale at which the density variations are expected to affect the trajectories of the dark matter particles, but does not specify the global response of the system.

## 3 Numerical test

### 3.1 Numerical test setup

In order to test the effects of power-law density fluctuations as in our theoretical model on the dark matter distribution of a galactic halo, we use the self-consistent field (SCF) method developped by Hernquist & Ostriker (1992). This algorithm was designed to describe the evolution of collisionless stellar systems by computing the gravitational potential at each time step and advancing the trajectories of the particles one by one accordingly. The density and the potential are expanded in a set of basis functions deriving from spherical harmonics with radial and angular maximal cutoff numbers $n_{\rm max}$ and $l_{\rm max}$.

We carry out such a simulation for the fiducial dwarf halo described in section 2.4, adding force and potential perturbations as in our theoretical model. The direction of each kick is random, and the total force is rescaled *a posteriori* to match the assumed power spectrum normalization. We further assume that the pulsation frequency associated to a mode $k$ is either defined with a constant propagation velocity as $\omega(k) = v_r k$ or from Larson's relation (Solomon et al. 1987) as $\omega(k) = 2\sqrt{k}$, both choices yielding similar results.

### 3.2 Spherical case: a flattening of the cusp as expected from the theoretical model

To neglect non-radial modes and match more closely the analytical calculations, we start by considering the case where strict spherical symmetry is maintained by imposing $l_{\rm max} = 0$. The resulting evolution of the halo density profile is shown on the left panel of Fig. 1: the assumed stochastic density fluctuations do lead to the formation of a core in an initially cuspy configuration within a timescale comparable to the relaxation time derived analytically. As expected from Eq. 2.5, the effect mostly depends on the fluctuation level and the gas fraction, with a weak dependence in $n$ and no variations with $k_{\rm min}$ and $k_{\rm max}$ (cf. El-Zant et al. 2016).

### 3.3 General case: an accelerated cusp-core transformation due to non-radial modes

In the general case, $l_{\rm max} \neq 0$ and no spherical symmetry is imposed on the system. An optimal choice for a simulation with $\sim 10^5$ particles is $n_{\rm max} = 10$ and $l_{\rm max} = 4$ (Vasiliev 2013). In this case, the cusp-core transformation is significantly faster than in the previous case but its parametrization remains unchanged, which can be seen on the right panel of Fig. 1. As the perturbations imposed on the halo particles are the same as when spherical symmetry is enforced, the difference must stem from how the imparted energy is transported and redistributed within the halo. This suggests that azimuthal modes significantly boost core formation and that the processes through which the energy stemming from the fluctuations is redistributed are largely non-isotropic. Such a conclusion is in agreement with Pontzen et al. (2015), who also show that the non-sphericity of dark matter haloes is a key ingredient for an efficient cusp-core transition.

## 4 Conclusion

We presented and tested through simple collisionless simulations an *a priori* theoretical model to describe the cusp-core transformation of dark matter haloes in which gravitational potential fluctuations arise from stochastic density variations in the gas distribution. Different stellar and AGN feedback mechanisms can account for such density variations. Their dynamical effects are modeled as a diffusion process in which repetitive kicks to the dark matter particles contribute to heating the halo and to forming a core. This model provides a relatively simple parametrization of the cusp-core transformation, mostly depending on the gas fraction and the fluctuation level.

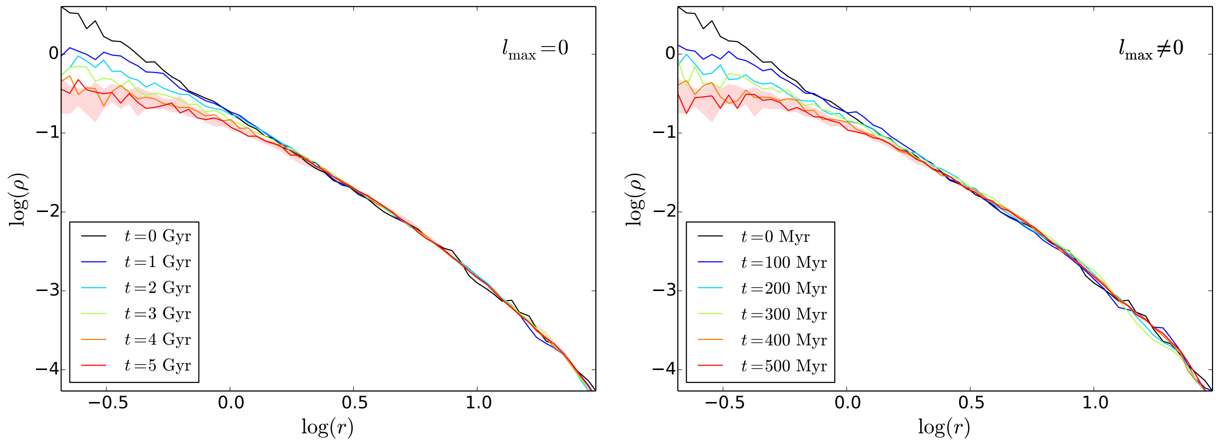


**Fig. 1. Left:** Evolution of the dark matter density profile for the fiducial halo described in section 2.4 with strict spherical symmetry imposed at each time step through $l_{\max} = 0$. The halo is submitted to a fluctuating gravitational potential stemming from power-law density fluctuations as in our theoretical model, presented in section 2, and forms a core from an initially cuspy NFW profile within a few Gyr. **Right:** A similar evolution is observed on a much smaller timescale when no strict spherical symmetry is imposed. On both sides, the shaded area highlights the scatter at $t = 500$ Myr between 10 random realization of the simulation with $l_{\max} \neq 0$.

A detailed comparison with hydrodynamical simulations is left to a future study. Different feedback implementations are likely to change the statistical properties of the fluctuating density field and hence the efficiency of the cusp-core transformation, which we could compare with our parametrization. Other theoretical models attempt at describing this transformation, with differences but also some similarities. Amongst them, Dutton et al. (2016) propose a spherical model based on a succession of global inflows and violent outflows, while Fouvry et al. (2016) focus on a diffusion mechanism not unlike ours but described by a dressed Focker-Planck equation. The predictions of these different models should be compared together with hydrodynamical simulations, the importance of non-radial modes and asphericity being one of the issues to be investigated more thoroughly.

This work benefited from the Franco-Egyptian Partenariat Hubert Curien (PHC) Imhotep and the ERC-Momentum-267399.

## References


Blumenthal, G. R., Faber, S. M., Flores, R., & Primack, J. R. 1986, ApJ, 301, 27

Chandrasekhar, S. 1943, ApJ, 97, 255

de Blok, W. J. G., Walter, F., Brinks, E., et al. 2008, AJ, 136, 2648

Dutton, A. A., Macciò, A. V., Dekel, A., et al. 2016, MNRAS, 461, 2658

El-Zant, A., Shlosman, I., & Hoffman, Y. 2001, ApJ, 560, 636

El-Zant, A. A., Freundlich, J., & Combes, F. 2016, MNRAS, 461, 1745

Fouvry, J.-B., Bieri, R., Pichon, C., & Dubois, Y. 2016, in prep.

Freundlich, J. 2015, PhD thesis, LERMA, Observatoire de Paris, CNRS, Sorbonne Universités, UMPC Univ. Paris 06, Collège de France, PSL Research University

Governato, F., Brook, C., Mayer, L., et al. 2010, Nature, 463, 203

Hernquist, L. & Ostriker, J. P. 1992, ApJ, 386, 375

Moore, B. 1994, Nature, 370, 629

Oh, S.-H., de Blok, W. J. G., Brinks, E., Walter, F., & Kennicutt, Jr., R. C. 2011, AJ, 141, 193

Pontzen, A. & Governato, F. 2012, MNRAS, 421, 3464

Pontzen, A., Read, J. I., Teyssier, R., et al. 2015, MNRAS, 451, 1366

Solomon, P. M., Rivolo, A. R., Barrett, J., & Yahil, A. 1987, ApJ, 319, 730

Teyssier, R., Pontzen, A., Dubois, Y., & Read, J. I. 2013, MNRAS, 429, 3068

Vasiliev, E. 2013, MNRAS, 434, 3174

Wilczek, M., Xu, H., & Narita, Y. 2014, Nonlinear Processes in Geophysics, 21, 645

*SF2A 2016*
*C. Reylé, J. Richard, L. Cambrésy, M. Deleuil, E. Pécontal, L. Tresse and I. Vauglin (eds)*

# KINETIC SIMULATIONS OF COLLISIONLESS MAGNETIC RECONNECTION

N. Aunai[1], J. Dargent[1, 2], B. Lavraud[2,], A. Ciardi[3], M. Drouin[3,] and R. Smets[1]

**Abstract.** This paper focuses on magnetic reconnection and its role in magnetospheric physics, where collisions are inexistant. In this context, the presence of a very cold ion population of ionospheric origin is known to have an important contribution to the particle density at the magnetopause. However, besides this mass loading effect, consequences of their extremely low temperature, and therefore of their must smaller gyroscale, have not yet been addressed from a modeling viewpoint. This study presents two fully kinetic simulations with and without cold ions in the magnetosphere and highlights how their small Larmor radius can change signatures expected to be proxy of the X line in spacecraft measurements. In a second part, this paper addresses shortly the problem of the X line orientation in an asymmetric system. Using this time hybrid kinetic simulations, we show the X line aligned with the bisector of upstream magnetic field vectors results in faster reconnection rate. This have consequences regarding where reconnection at the magnetopause, although models here do not include large scale dynamics. We conclude with perspectives regarding future developments to address multi-scale magnetic reconnection dynamics at the magnetopause.

Keywords: magnetic reconnection, Particle-In-Cell, magnetopause

## 1 Introduction

Magnetic reconnection is undoubtedly one of the most important process in astrophysical plasma physics. First, by suddenly releasing magnetic energy stored in large scale systems for long times it often is an interesting candidate for acceleration and heating events observed in the universe. Second, by enabling large scale magnetic connectivity to be changed, it can drastically impact plasma transport. The Earth magnetosphere and nearby solar wind constitute the best environments to study the phenomenon, since theories and models can directly be compared to in situ spacecraft measurements. Numerical models have and continue to be a major asset in understanding basics mechanisms at the root of the complex nonlinear reconnection dynamics, and an important source of data to interpret in situ measurements. The goal of this paper is to highlight in a small review the main conclusion of recent studies we did on the magnetic reconnection process occurring at the magnetopause. We first discuss recent numerical results regarding how an often observed very cold ionospheric ion population impacts expected signatures of the X-line region and may enable us to assert its identification in spacecraft in situ data(Dargent et al. 2016). We will then focus on hybrid kinetic modeling, which, by neglecting the kinetic nature of electrons, enable us to model larger domain for longer times to understand how is the reconnection X-line oriented in the general case of asymmetric magnetopause reconnection. The full details of this study have been published recently (Aunai et al. 2016). We will then conclude our paper with perspectives regarding large scale modeling of magnetopause magnetic reconnection.

## 2 Fully kinetic simulations: role of cold ions in magnetopause reconnection

In collisionless systems, particle dynamics is the result of collective effects, and populations are free to mix without any bulk energetization (heating). Whenever reconnection occurs in current sheets separating different

[1] Laboratoire de Physique des Plasmas, Ecole Polytechnique, CNRS, UPMC, Université Paris Sud, route de Saclay, 91128 Palaiseau Cedex
[2] Institut de Recherche en Astrophysique et Planétologie, CNRS, Toulouse, France
[3] LERMA, Universite Pierre et Marie Curie, Observatoire de Paris, Meudon, France c Ecole Normale Superieure, Paris, France. UMR 8112 CNRS

plasma sources, it unavoidably mix particle populations otherwise separated. Interpreting the overall dynamics with a fluid (macroscopic) formalism, becomes questionable. The Earth magnetopause is one such environment, as it separates the solar wind plasma, from the comparatively hot and tenuous magnetospheric one. The so-called *asymmetric reconnection* process taking place here is far richer and more complex than *symmetric reconnection* where reconnected plasmas have identical field and particle properties. The numerical modeling of Solar wind/ magnetosphere reconnection has been the topic of intense research over the last decade, including comparisons to in situ spacecraft measurements(Mozer & Pritchett 2011; Mozer et al. 2008). One ingredient has however been neglected so far in models though it may play an important role at the magnetopause: the omnipresence of very cold ions of ionospheric origin on the magnetosphere side of the boundary(Sauvaud et al. 2001; André & Cully 2012; Walsh et al. 2014; Toledo-Redondo et al. 2015; Fuselier et al. 2016). Although here most of the time, and in important proportions (if not dominant), these particles are almost always forgotten because their low energy make them almost invisible to particle detectors. What is the consequence of accounting for this population in addition to the hot magnetospheric population in reconnection models? An immediate answer is that they bring more material than otherwise and should therefore lower the reconnection rate(Borovsky & Denton 2006; Borovsky et al. 2008; Wang et al. 2015). This so-called *mass loading* effect has been noticed several times already. However the fact that this additional population has an extremely low temperature, and therefore brings lots of particles with a tiny gyroradius has yet been unexplored and should lead to sensible changes in the microphysics of reconnection. In this study, we therefore performed two fully kinetic Particle-In-Cell (PIC) simulations in a two-dimensional geometry, differing only by the velocity distribution function of magnetospheric ions. Keeping both identical total density, current and temperature profiles through the initial current sheet, and so ruling out the previously observed mass-loading effect, we represent, in run **A**, the magnetosphere protons as a single locally maxwellian population, while run **B** represents them as two distinct populations, one being 500 times colder than the other. In both simulations, the ratio between the plasma density in the magnetosphere and in the magnetosheath is 0.25, and the magnetic field is twice stronger in the magnetosphere side than in the magnetosheath side. Simulations are ran until reaching a quasi-steady state, i.e. a time at which upstream magnetic flux is reconnected at constant rate. Both simulations reach that point after $\approx 120$ inverse cyclotron frequencies and reveal very similar reconnection rate and overall evolution. This great similarity is expected since, although enabled by small scale microphysics processes, reconnection overall mostly depends on macroscopic quantities and two-fluid effects, which are here identical in both runs. However, when looking carefully at small scale signatures, the two simulations differ noticeably in an interesting way.

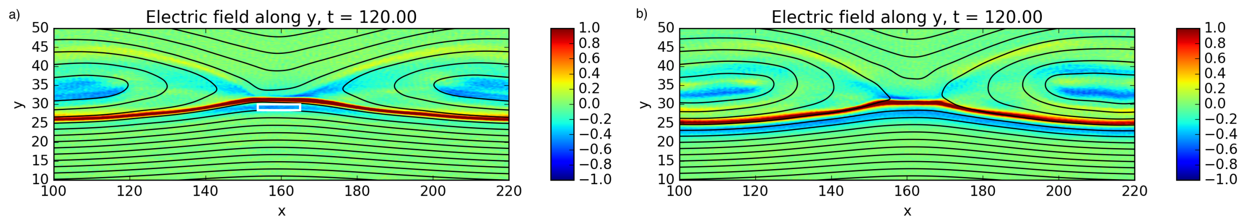


**Fig. 1.** $E_y$ component of the electric field represented in color, with superimposed in-plane magnetic field lines as solid black lines. **Left:** snapshot from run A **Right:** Snapshot from run B.

Figure 1 shows the vertical component ($E_y$) of the electric field of both simulations. As very well known now, the magnetospheric separatrix is the locus of an intense electric field pointing towards the magnetosheath. This field, already noticed in spacecraft measurements, easily allows observers to discriminate the magnetosheath separatrix from the magnetospheric one. However, it exists all along the separatrix and is useless to identify the X-line region. More recently, another electric field structure has been pointed out as an interesting proxy of the X-line. The so-called Larmor electric field, is a small area, confined to the X-line region, on the magnetospheric side, where the vertical component of the electric field reverses and points towards the magnetosphere(Malakit et al. 2010). Although its amplitude (much weaker than the strong magnetospheric peak) and width can vary from one case to the other, PIC simulations of asymmetric reconnection consistently show this structure, which is therefore actively searched in spacecraft data when trying to identify X-line crossings. Interestingly however, when cold ions are present in the simulation (panel b), this negative electric field is not confined to the X line region anymore and extends all along the separatrix too, therefore becoming useless as an X-line proxy. Careful analysis of the simulations revealed the negative electric field arises from the initial phase of the simulation when reconnection had not started yet. It is associated with the bouncing of magnetosheath ions at the field reversal, which happen to mostly all make their U-turn at the same distance from the mid-plane. This statistically results in an apparent out-of-plane bulk velocity which, associated with the positive horizontal magnetic field here results in a vertical negative electric field. Once reconnection starts, it broadens the current sheet and this ion bounce mechanism becomes impossible everywhere but around the X line, where the current sheet stays thin, and the electric field disappears everywhere but there. However when cold ions are present, their Larmor radius is so small that the width of the initial electric field structure is actually larger. They therefore just $\mathbf{E} \times \mathbf{B}$ drift there thus maintaining the electric field. The full analysis would be too long to describe in this short review and can be found in (Dargent et al. 2016). An important conclusion to this study is that the presence of cold ions at the magnetopause should carefully be checked as their density is non negligible and their extremely low temperature will make them evolve quite differently from other ions, therefore modifying expected signatures.

## 3 Hybrid kinetic simulations: X-line orientation in asymmetric magnetic reconnection

Magnetopause reconnection involves vastly different plasmas, but also occurs on a surface where the magnetic shear strongly and continuously varies. The latter property leads to the very basic yet unsolved question of what is the local orientation of the reconnection X line, i.e. how is the line joining reconnection sites on the magnetopause surface oriented locally? Is this orientation set-up by the large scale interaction of the solar wind magnetic field and plasma with the magnetosphere ? Locally fixed by the reconnection process itself as a function of local relevant parameters such as the magnetic shear, amplitude jump and plasma asymmetry? Or is it the result of both large and small scale dynamics? Both ends of the problem have been addressed over the past, from global magnetohydrodynamic simulations to two-dimensional PIC models. Hybrid models, assuming an adequate dissipation mechanism is chosen(Aunai et al. 2013a), seem to result in reconnection rates and overall dynamics similar to those observed in full PIC models (Aunai et al. 2013b). In this work we take advantage of this to do a parametric study investigating what the orientation of the X line is as a function of the magnetic shear angle. Due to computing limitations, we restrict ourselves to 2D simulations, looking for the reconnection plane, given a magnetic and plasma configuration, maximizing the reconnection rate, and assuming that nature chooses the plane having the larger reconnection rate as the local orientation.

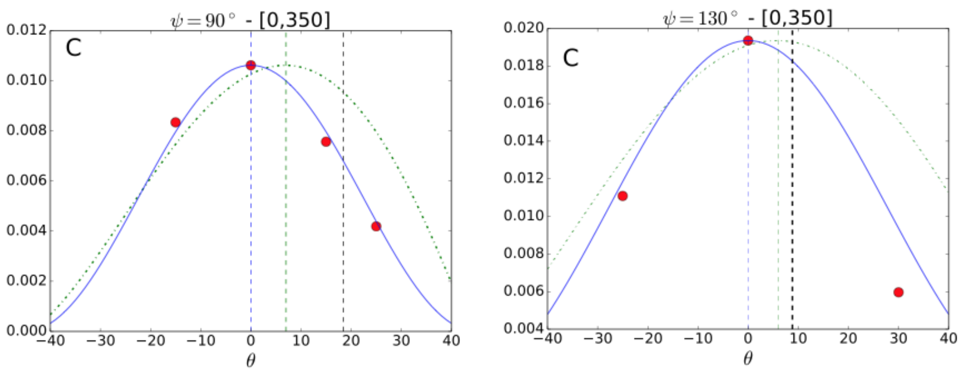


**Fig. 2.** Red points represent the reconnection rate, averaged over the entire simulation time, as a function of $\theta$, the angle by which the simulation plane is rotated with respect to the magnetic configuration. The solid blue curve shows $B_1^2(\theta)B_2^2(\theta)$, the dashed-dotted green curves shows the Cassak-Shay scaling law for asymmetric reconnection rates based on upstream in-plane magnetic field amplitudes(Cassak & Shay 2007). The blue and green vertical lines represent the maximum of the blue and green curve, respectively. The black vertical line denotes the plane orientation for which the out-of-plane magnetic component is symmetric. This last orientation is the one routinely used in observations as the one of the reconnection plane, but is not, by far in the present results, the plane maximizing the reconnection rate.

Figure 2 shows, for two different magnetic shears, the average reconnection rate of an otherwise identical system, rotated around the direction normal to the current sheet. As we can see by looking at the red points on the plots, in either case the reconnection rate presents a strong variation as the simulation plane is rotated, and this variation presents a maximum. This trend, obtained from simulation data, is compared to different models, all predicting the most probable reconnection plane. Among the different models, the best fit is the blue curve, which is the product of the in-plane magnetic energy on each side of the current sheet $B_1^2(\theta)B_2^2(\theta)$, which incidentally is maximized for the plane defined by the bisector of upstream magnetic field vectors(Hesse et al. 2013). Other models either fit less the data or are completely off. An immediate conclusion of this study is that if reconnection evolves in 2D or quasi-2D fashion, that is that large scale inhomogeneities pre-existing reconnection and those developed by reconnection are dominantly contained in a plane, the reconnection rate will drastically change depending on what that plane is. Other studies seems to indicate this trend survives in full-PIC, in 2D as in 3D simulations. Whether the global path X-lines draw on the magnetopause surface strongly or marginally depend on this trend imposed locally, is an important question to solve. This will likely require multi-scale simulations, including a maximum of relevant microphysical effects as well as global solar wind / magnetosphere interaction.

## 4 Towards multi-scale kinetic modeling

The coupling of the solar wind and the earth magnetosphere is largely controlled by magnetopause reconnection. Although it has been clear for several decades now, that southward IMF leads to dayside reconnection and larger geo-effectiveness of solar wind structures than northward IMF, knowing of where, when and how reconnection occurs on the magnetopause surface clearly remains poorly understood. It is very likely that both microphysics and large scale dynamics play key roles in this interaction. Hybrid models represent an interesting compromise between the too computationally demanding description of the full Vlasov-Maxwell system and the rough solutions obtained from single or two fluid approaches. Moreover hybrid PIC models offer the advantage (over Vlasov hybrid approaches) to very easily account for multiple relevant ion populations as we have seen can co-exist. However, state of the art hybrid codes suffer from having to resolve propagation of dispersive waves coming with Hall physics which drastically limit simulation domains and times if one wants to have good separation between the ion gyroscale processes and well resolved dissipation scales. Therefore so far, most hybrid simulations either focus on detailed process modeling requiring high resolution and therefore can't include large scale dynamics, or on large scale physics but then usually badly resolve key processes enabled and largely controlled at small scales. An interesting fact about hybrid codes, that comes from calculating the electric field from an Ohm's law rather than using Maxwell's equations, is that they actually don't need to resolve Hall and smaller spatial scales to be stable. One only needs to resolve these terms where they are needed. This is a great advantage, compared to fully kinetic codes that usually have to resolve intrinsic plasma scales such as the Debye length. Based on these observations, we are currently working on designing a massively parallel hybrid code with block adaptive mesh refinement. Such a code should be able to focus space time resolution dynamically on regions that need it, and therefore confine intense computational load in small regions of space, while keeping a lighter resolution elsewhere. In the case of magnetopause reconnection for instance, such code would enable to account for both a good separation of ion and dissipation scales around X-lines and at the same time include large scale geometry and dynamics at a coarser level. Using the Multi-Level-Multi-Domain method, different levels of refinements are evolving in a rather independent way. This lets us imagine that within this decade, the hierarchy of levels could not only involve mesh refinement but also physics refinement, i.e. coarse levels could also be treated with a lighter formalism. For instance, regions involving only weak gradients in comparison to the local ion Larmor radius will not only see their mesh size increased but at some point should fall in a regime where the fluid approximation is more acceptable. Such multi-scale multi-physics developments are imperiously needed for more realistic simulations of systems having even larger scale separations such as the solar corona environment.

The authors acknowledge the ANR for funding the project MON-ANR (ANR-13-PDOC-0027) and the LabEx Plas@Par (project PHARE) supporting this research. The authors also thank the SMILEI development team. This work was granted access to the HPC resources of IDRIS and CINES under the allocation i2015047231.

## References

André, M. & Cully, C. M. 2012, Geophysical Research Letters, 39, n/a

Aunai, N., Hesse, M., Black, C., Evans, R., & Kuznetsova, M. 2013a, Phys. Plasmas, 20, 042901

Aunai, N., Hesse, M., Lavraud, B., Dargent, J., & Smets, R. 2016, Journal of Plasma Physics, 82, 535820401

Aunai, N., Hesse, M., Zenitani, S., et al. 2013b, Phys. Plasmas, 20, 2902

Borovsky, J. E. & Denton, M. H. 2006, Geophysical Research Letters, 33, n/a, l20101

Borovsky, J. E., Hesse, M., Birn, J., & Kuznetsova, M. M. 2008, Journal of Geophysical Research: Space Physics, 113, n/a, a07210

Cassak, P. A. & Shay, M. A. 2007, Physics of Plasmas, 14, 102114

Dargent, J., Aunai, N., Lavraud, B., & Toledo-Redondo, S. 2016, submitted to J. Geophys. Res.

Fuselier, S. A., Burch, J. L., Cassak, P. A., et al. 2016, Geophysical Research Letters, 43, 1435, 2015GL067358

Hesse, M., Aunai, N., Zenitani, S., Kuznetsova, M., & Birn, J. 2013, Physics of Plasmas, 20

Malakit, K., Shay, M. A., Cassak, P. A., & Bard, C. 2010, Journal of Geophysical Research (Space Physics), 115, 10223

Mozer, F., Pritchett, P., Bonnell, J., Sundkvist, D., & Chang, M. 2008, J. Geophys. Res., 113

Mozer, F. S. & Pritchett, P. L. 2011, Space Science Reviews, 158, 119

Sauvaud, J.-A., Lundin, R., Rème, H., et al. 2001, Annales Geophysicae, 19, 1523

Toledo-Redondo, S., Vaivads, A., André, M., & Khotyaintsev, Y. V. 2015, Geophys. Res. Lett., 42, 6146

Walsh, B. M., Phan, T. D., Sibeck, D. G., & Souza, V. M. 2014, Geophysical Research Letters, 41, 223

Wang, S., Kistler, L. M., Mouikis, C. G., & Petrinec, S. M. 2015, Journal of Geophysical Research: Space Physics, 120, 6386, 2015JA021524

*SF2A 2016*
*C. Reylé, J. Richard, L. Cambrésy, M. Deleuil, E. Pécontal, L. Tresse and I. Vauglin (eds)*

# CHEMISTRY AND DYNAMICS: A POST-PROCESSING TOOL TOWARDS A REAL COUPLING

V. Valdivia[1], B. Godard[2], P. Hennebelle[1], M. Gerin[2] and P. Lesaffre[2]

**Abstract.** Chemistry plays a key role in the comparison between observations and theoretical predictions, but its treatment in numerical simulations is a real challenge. In particular the full treatment of the chemistry requires to solve simultaneously hundreds to thousands of reactions, constraining the time-steps to be as small as the smallest one. Fortunately, several species reach the chemical equilibrium much faster than others, and careful choices allow to describe the chemical state in a simpler manner. Here we present a hybrid approach to treat the chemistry of the interstellar medium.

Keywords: Methods: numerical, ISM: clouds, abundances, Astrochemistry

## 1 Introduction

Chemistry is an essential component in the modelling of molecular clouds, but its complex description, which is coupled to the dynamics of the gas, makes it a commonly neglected issue.

Chemistry plays a key role in determining the thermal state of the gas. While the heating is ensured by the photoelectric heating (Bakes & Tielens 1994) on grains, in the case of molecular clouds, the cooling is realised by the line emission from atoms and molecules. Emission lines, and thus the ability to cool the gas, strongly depend on the abundance of the emitting atom or molecule, and thus on the chemical composition of the gas. On the other hand, the chemical structure of the gas is determined by the dynamics and the physical structure of the cloud. As different chemical tracers are sensitive to different physical conditions, the observed abundances not only allow to probe the medium, but also allow to link models to observations.

Even though the chemical state of the gas is crucial to predict its evolution, most of numerical simulations avoid the explicit treatment of the chemistry. Instead, heating and cooling functions are used to describe the thermal state of the gas. The advantage of using these functions is that they allow to produce realistic structures, being even able to reproduce the multiphase structure of the interstellar medium (ISM) (Audit & Hennebelle 2005; Valdivia & Hennebelle 2014; Valdivia et al. 2016c). These cooling functions can include several processes, such as the cooling by fine structure lines of CII, OI, and CI, cooling by H through the Lyman $\alpha$ emission, and the cooling due to electron recombination onto positively charged grains. These are usually subgrid models, which are functions of the local gas parameters. Furthermore, turbulence and magnetic fields not only controls the dynamics and the physical structure of the gas, but also influences the transport of atoms and molecules within the cloud.

In order to compare with available observations and make predictions, synthetic observables, such as synthetic spectra or synthetic maps, are needed. A simple approach consists in post-processing numerical simulations to obtain the expected abundances of atoms and molecules. These approaches can be as simple as applying a density threshold to estimate the molecular fraction of hydrogen (Heiner et al. 2015), or as sophisticated as the calculation of a full equilibrium using photon dominated regions (PDR) codes, for example (Levrier et al. 2012). The main advantage of this kind of approach is that exhaustive chemical networks (that depend on the local physical conditions of the gas), along with radiative transfer strategies, can be used. But this approach is not flawless. The main problem related to this approach is the fact that the chemistry does not evolve with

[1] Laboratoire AIM, CEA/DSM-CNRS, Université Paris Diderot, IRFU/SAp, 91191 Gif-sur-Yvette, France
[2] LERMA (UMR CNRS 8112), Ecole Normale Supérieure, 75231 Paris Cedex, France

the gas, and the abundances miss some dynamical effects, or the underlying dynamics is imposed, as in the turbulent dissipation region (TDR) code (Joulain et al. 1998; Godard et al. 2009, 2014).

It is only very recently that the computational ressources have permitted to simulate 3-dimensional structures including explicit treatments for the chemistry. In recent years several efforts to couple the chemical evolution to the dynamical evolution of the gas have been attempted, either by including dedicated chemical networks into widely used codes (Glover & Mac Low 2007a,b; Glover et al. 2010; Koyama & Inutsuka 2000; Clark et al. 2012; Dobbs et al. 2008; Ziegler 2016), or either by developing general chemistry packages that can be plugged to them (Grassi et al. 2014). Time dependent chemistry has the advantage that the chemical abundances evolve with the gas, where they are not only formed and destroyed, but they can also be advected or diffused during the simulation, and thus capture the effect of the dynamics. But this kind of simulations is extremely prohibitive. The computation of the abundances can reveal itself extremely expensive. Computation times can be as high as several hundreds of times the usual computation time even for a modest chemical network. To deal with this problem most simulations use reduced chemical networks (Glover & Mac Low 2007a,b; Hocuk & Cazaux 2015; Hocuk et al. 2016), and uses further approximations to deal with complicated calculations, such as the computation of column densities and shielding parameters (Richings & Schaye 2016).

So the question that arises is how to take into account the dynamical effects on the chemical abundances, including good estimates of shielding parameters, and without excessively increasing the computation time? Even though the questions seems to have no answer, it is possible to address it by making clever choices.

Here we describe a hybrid strategy that can help to deal with this problem in numerical simulations in the context of the evolution of molecular clouds.

## 2 Hybrid strategy

### 2.1 General idea

Chemical species have very different evolution times. Species with long evolution times are most likely influenced by the gas motions, and consequently can be found out-of-equilibrium. On the other hand, species with short evolution times quickly react to variations in their environment, and are prone to be at equilibrium and to follow the evolution of other dominant species. This behaviour allows us to propose a strategy to treat the chemical evolution of molecular clouds minimising the calculation time.

The first step is to identify the species with the longuest evolution times. These species need to be calculated on-the-fly, and ideally including good, but fast estimates for the parameters such as the shielding. The second step is to post-process the simulation using a chemical network, where the abundances of the species dynamically calculated in the simulation can be fixed. The rest of the species in the chemical network is calculated at equilibrium using the physical conditions of the cloud.

### 2.2 On-the-fly treatment: $H_2$ chemistry

In the context of the interstellar medium a key molecule is the molecular hydrogen ($H_2$). This molecule has a very long evolution time on the order of $t \sim \frac{10^9}{n\ [\mathrm{cm}^{-3}]}$ yr (Hollenbach & Salpeter 1971), where $n$ is the number density of the gas. This molecule is of crucial interest because it precedes the formation of other molecules. The evolution of its abundance is well described by

$$\frac{\partial n_{\mathrm{H}_2}}{\partial t} + \nabla \cdot (n_{\mathrm{H}_2}\mathbf{v}) = k_1 n(n - 2n_{\mathrm{H}_2}) - k_2 n_{\mathrm{H}_2}, \tag{2.1}$$

where $n$ is the total density of the gas, $n_{\mathrm{H}_2}$ is the number density of $H_2$, $\mathbf{v}$ is the velocity field, $k_1$ is the formation rate on grains, and $k_2$ is the photodissociation rate by ultraviolet (UV) photons. Equation 2.1 includes the evolution of the density of $H_2$ due to the formation and destruction processes, as well as an advection term. It is able to reproduce the evolution of $H_2$ without needing a costly chemical network. In a previous work (Valdivia et al. 2016c) we implemented the evolution of $H_2$ in the RAMSES code (Teyssier 2002), using our tree-based method (Valdivia & Hennebelle 2014) to estimate column densities, as well as the visual extrinction $A_V$, and the $H_2$ shielding parameter $f_{\mathrm{sh,H}_2} = \exp(-\tau) \times f_{\mathrm{shield}}(\mathcal{N}_{\mathrm{H}_2})$, due to the combined action of the dust and the selfshielding (Draine & Bertoldi 1996) by $H_2$. In this expression $\tau$ is the optical depth, and $\mathcal{N}_{\mathrm{H}_2}$ is the $H_2$ column density. Numerical simulations show an important fraction of $H_2$ out of equilibrium that can play an important role in the chemical evolution of the cloud (Valdivia et al. 2016c).

### 2.3 Post-treatment: the chemical solver

The rest of the abundances in the chemical network (described later) is calculated by post-processing using a chemical solver. The chemical solver used in this work is a modified version of the solver used by the Meudon PDR code (Le Petit et al. 2006), that allows us to fix the abundance of $H_2$. It solves a coupled system of equations using a Newton-Raphson scheme to find the equilibrium for the chemistry. The equilibrium is defined by the following set of equations:

$$\begin{aligned}
&\frac{dn(\mathrm{X}_i)}{dt} = \sum_j^{N_\mathcal{R}} \left( \prod_k n(\mathrm{R}_{j,k}) \right) \kappa_j \; s_j(\mathrm{X}_i) = 0, && \forall i \in [1:N_X] \\
&\sum_j^{N_X} n(\mathrm{X}_j)\; m(\mathrm{A}_i, \mathrm{X}_j) = n_{\mathrm{A}_i} && \forall i \in [1:N_A] \\
&\sum_j^{N_X} n(\mathrm{X}_j)\; c(\mathrm{X}_j) = 0,
\end{aligned} \tag{2.2}$$

where $n(\mathrm{X}_i)$ is the number density of the $i-th$ species, $n_\mathrm{A}$ is the number density of atom A, $N_\mathcal{R}$ is the number of reactions, $\mathrm{R}_{j,k}$ stands for the reactants, $\kappa_j$ is the reaction rate of reaction $j$, $s_j(\mathrm{X})$ the stoichiometric coefficient of X in reaction $j$, $m(\mathrm{A},\mathrm{X})$ the multiplicity of atom A in species X, and $c(\mathrm{X})$ the charge of X.

The main input parameters are the total gas density $n$, the kinetic temperature $T_k$, the external UV radiation field $\chi$, the visual extinction $A_V$, the cosmic ray ionisation rate $\zeta_{\mathrm{H}_2}$, and optionally the $H_2$ number density $n(\mathrm{H}_2)$, the shielding parameters $f_{\mathrm{sh},\mathrm{H}_2}$, $f_{\mathrm{sh},\mathrm{CO}}$, and the ion-neutral drift velocity $v_\mathrm{d}$.

When the $H_2$ abundance is fixed the system of equations is overdetermined and at least one other species must be fixed to guarantee the conservation. We assume that atomic hydrogen is the only species out-of-equilibrium, along with $H_2$, due to its high abundance and because it is the main H-bearer besides $H_2$.

## 3 On the validity of the hybrid strategy

### 3.1 Evolution time

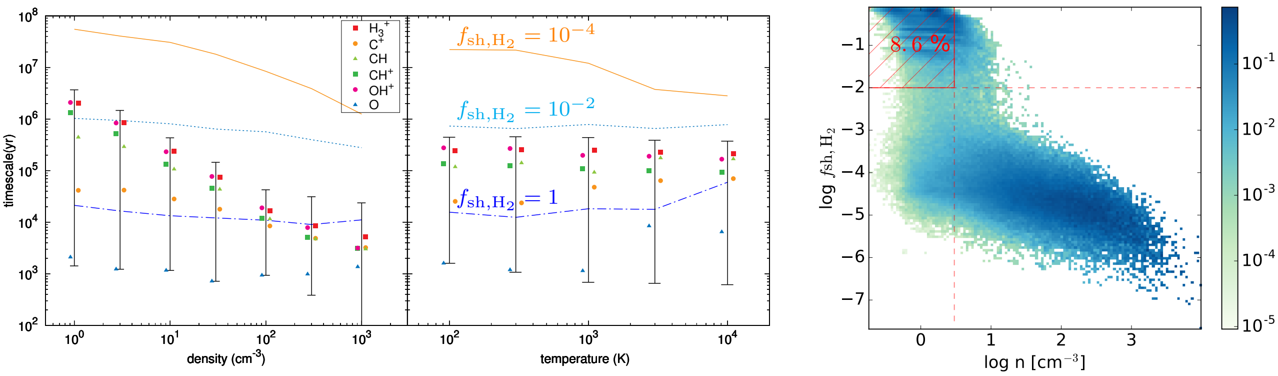


**Fig. 1. Left:** Chemical timescale averaged over random initial conditions. Lines correspond to the $H_2$ timescales computed for different shielding parameters: $f_{\mathrm{sh,H_2}} = 10^{-4}$ (solid), $10^{-2}$ (dotted), and 1 (dashed dotted). Vertical segments correspond to the interval of timescales for other molecules. Timescales for single species are shown for reference. **Right:** Gas mass distribution as a function of the density and the $H_2$ shielding parameter for a high-resolution simulation of a realistic molecular cloud.

Our approach is only valid if the evolution time of $H_2$ is longer than for the rest of the species. To test the validity of our approach in a range of different physical conditions we use a chemical network containing a total of 149 species and 2692 reactions, very similar to the one used by the Meudon PDR code. We computed the equilibrium timescales for all the species in the network under a wide range of physical conditions. Figure 1 shows the range of timescales for the species in the chemical network compared to the timescales for $H_2$. This figure helps us to constrain the conditions under which our approach is valid.

From the left-hand side panel of Fig. 1 we can identify a safe region, where the $H_2$ evolution timescale is always longer than (or comparable to) the evolution timescale of any other species in a wide range of physical conditions. As long as the gas number density is $n \gtrsim 3$ cm$^{-3}$ or the $H_2$ shielding factor is $f_{\mathrm{sh,H_2}} \lesssim 10^{-2}$ the evolution time of $H_2$ will be long enough to guarantee that other species will have the time to reach their equilibrium.

To know whether this strategy is valid for numerical simulations of realistic molecular clouds it is essential to know the amount of matter that fullfils these conditions. The right-hand side panel of Fig. 1 shows the mass-weighted distribution of the gas in the high-resolution numerical simulation of Valdivia et al. (2016c, Appendix A). This figure shows that for a realistic molecular cloud these conditions are fulfilled in more than 91% of the mass of the gas.

### *3.2 Convergence*

An issue of a different nature is the convergence of the solver. Fixing a species can prevent the existence of a solution for the equilibrium, or it can make it more difficult to reach. To determine under which conditions our approach is able to provide reliable results we performed a test covering a grid of 2.56 millions models in the 4D parameter space: density $n$, gas temperature $T$, $H_2$ fraction $f(H_2)$, and visual extinction $A_V$.

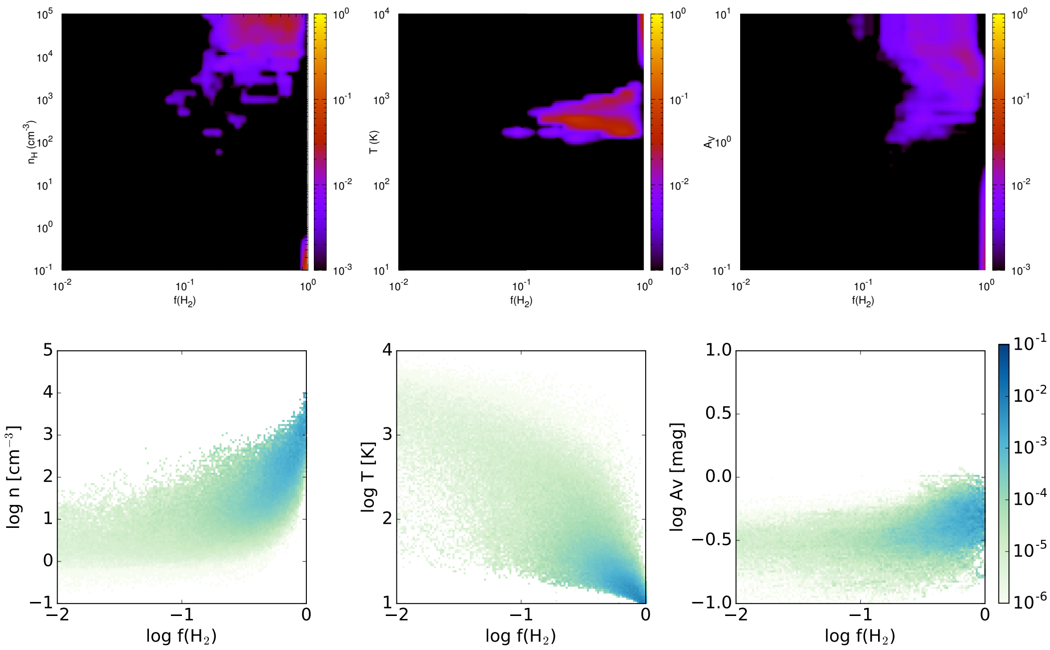


**Fig. 2. Top:** Fraction of convergence failures for $2.56 \times 10^6$ models in the 4D parameter space. **Bottom:** Mass fraction distribution in the simulation as a function of the same parameters.

The top panel of Fig. 2 shows the fraction of cases where the chemical solver fails to converge. This figure clearly shows two problematic regions in the parameter space. The most extended one corresponds to regions where the gas is dense ($n \gtrsim 10^3$ cm$^{-3}$), well shielded ($A_V \gtrsim 1$), with molecular fractions higher than $10^{-1}$, and gas temperatures comprised between 300 K and few $10^3$ K. These same models were tested without fixing the $H_2$ fraction showing similar results, which means that the failure is related to the algorithm and topology of the equation system. The second region, much more compact than the precedent one, corresponds to low density gas ($n \lesssim 1$ cm$^{-3}$), almost fully molecular ($f(H_2) \gtrsim 0.95$), illuminated ($A_V \lesssim 0.5$), and warm ($T \gtrsim 10^3$ K). In this case the chemical solver fails to converge due to the large abundance of $H_2$, which prevents the H conservation by other H-bearing species. The bottom panel shows the distribution of mass of the gas as a function of the same parameters. This figure shows that these cases are very unlikely to arise under realistic conditions for molecular clouds, and that our approach provides reliable results.

## 4 Conclusions

We showed that this approach is well adapted to treat numerical simulations of molecular clouds as long as the $H_2$ evolution time and the hydrodynamical time-step remain longer than the evolution time of the rest of the species. We assessed the convergence rate of the chemical solver for a wide variety of parameters. We showed the existence of two regions in the parameter space where the convergence fails.

We showed that a typical multiphase molecular cloud, submerged in the ISRF, displaying a wide variety of densities, temperatures, $H_2$ fractions, and shielding parameters, does not present gas in those problematic regions, and thus the solver is well adapted.

We conclude that our approach can be used to treat the chemistry of molecular clouds at a minimal cost compared to a time-dependent treatment of the chemistry. In a companion article we apply this hybrid approach to study the abundance of the methylidine cation ($CH^+$ molecule) in diffuse molecular clouds (Valdivia et al. 2016a,b).

We acknowledge the finantial support of the Agence National pour la Recherche through the COSMIS project. This research has received funding from the European Research Council under the European Communitys Seventh Framework Program (FP7/2007-2013 Grant Agreement No. 306483). We thank the French Programme Physique Chimie du Milieu Interstellaire (PCMI). This work was granted access to HPC resources of CINES under the allocation x2014047023 made by GENCI (Grand Equipement National de Calcul Intensif). This work was granted access to the HPC resources of MesoPSL financed by the Region Ile de France and the project Equip@Meso (reference ANR-10-EQPX-29-01) of the programme Investissements dAvenir supervised by the Agence Nationale pour la Recherche.

## References

Audit, E. & Hennebelle, P. 2005, A&A, 433, 1

Bakes, E. L. O. & Tielens, A. G. G. M. 1994, ApJ, 427, 822

Clark, P. C., Glover, S. C. O., Klessen, R. S., & Bonnell, I. A. 2012, MNRAS, 424, 2599

Dobbs, C. L., Glover, S. C. O., Clark, P. C., & Klessen, R. S. 2008, MNRAS, 389, 1097

Draine, B. T. & Bertoldi, F. 1996, ApJ, 468, 269

Glover, S. C. O., Federrath, C., Mac Low, M.-M., & Klessen, R. S. 2010, MNRAS, 404, 2

Glover, S. C. O. & Mac Low, M.-M. 2007a, ApJS, 169, 239

Glover, S. C. O. & Mac Low, M.-M. 2007b, ApJ, 659, 1317

Godard, B., Falgarone, E., & Pineau Des Forêts, G. 2009, A&A, 495, 847

Godard, B., Falgarone, E., & Pineau des Forêts, G. 2014, A&A, 570, A27

Grassi, T., Bovino, S., Schleicher, D. R. G., et al. 2014, MNRAS, 439, 2386

Heiner, J. S., Vázquez-Semadeni, E., & Ballesteros-Paredes, J. 2015, MNRAS, 452, 1353

Hocuk, S. & Cazaux, S. 2015, A&A, 576, A49

Hocuk, S., Cazaux, S., Spaans, M., & Caselli, P. 2016, MNRAS, 456, 2586

Hollenbach, D. & Salpeter, E. E. 1971, ApJ, 163, 155

Joulain, K., Falgarone, E., Pineau des Forêts, G., & Flower, D. 1998, A&A, 340, 241

Koyama, H. & Inutsuka, S.-I. 2000, ApJ, 532, 980

Le Petit, F., Nehmé, C., Le Bourlot, J., & Roueff, E. 2006, ApJS, 164, 506

Levrier, F., Le Petit, F., Hennebelle, P., et al. 2012, A&A, 544, A22

Richings, A. J. & Schaye, J. 2016, MNRAS, 458, 270

Teyssier, R. 2002, A&A, 385, 337

Valdivia, V., Godard, B., Hennebelle, P., Gerin, M., & Lesaffre, P. 2016a, to appear in the Proceedings of the SF2A

Valdivia, V., Godard, B., Hennebelle, P., Gerin, M., & Lesaffre, P. 2016b, manuscript submitted for publication

Valdivia, V. & Hennebelle, P. 2014, A&A, 571, A46

Valdivia, V., Hennebelle, P., Gérin, M., & Lesaffre, P. 2016c, A&A, 587, A76

Ziegler, U. 2016, A&A, 586, A82

*SF2A 2016*
*C. Reylé, J. Richard, L. Cambrésy, M. Deleuil, E. Pécontal, L. Tresse and I. Vauglin (eds)*

# SIMULATING THE LOCAL UNIVERSE

J. G. Sorce[1]

**Abstract.**
In the local Universe, cosmic structures can be observed down to very small scales, scales on which the standard cosmological model might fail. Such detailed observations have to be compared with simulations in order to verify the predictions of different cosmological models. However, the cosmic variance can obscure the tests. More precisely, comparisons on a one-to-one basis are feasible only with simulations that look like the local Universe. Constrained by observed positions and peculiar velocities of galaxies, the simulations presented here reproduce locally the three-dimensional distribution of matter. Within a sphere of radius 100 $h^{-1}$ Mpc, the observed nearby Large and Small Scale Structure is simulated with an accuracy of a few megaparsecs. These simulations include our nearest cluster neighbor, Virgo, allowing a detailed study of its formation history. It follows that the Virgo cluster has had a quiet merging history within the last seven gigayears. In the near future, zoom-in hydrodynamical simulations of the later will permit deeper comparisons with observations.

Keywords: cosmology: large-scale structure of universe, galaxies: clusters: individual, methods: numerical, n-body simulations

## 1 Introduction

Cosmological simulations of structure formation rely on the cosmological principle which assumes the homogeneity of the Universe on large enough scales. The random nature of the primordial Gaussian perturbation field however implies that properties of patches of a few megaparsecs vary widely. To overcome this cosmic variance, statistical comparisons between observations and simulations to test cosmological models are based on large observational datasets (e.g. Stoughton et al. 2002; Abazajian et al. 2003, 2009) and large cosmological simulations (e.g., Klypin et al. 2011; Alimi et al. 2012; Prada et al. 2012; Angulo et al. 2012; Watson et al. 2014; Klypin et al. 2014; Skillman et al. 2014; Dubois et al. 2016). An alternative approach is to reduce the cosmic variance by focusing on the nearby Universe and by reproducing the local Large Scale Structure numerically.

This approach has two advantages: 1) the local Universe is without any doubt the best-observed volume of the Universe and as such allows very detailed comparisons with simulations down to the small scales; 2) a very large box size is not required to simulate our neighborhood, hence high resolutions required to study the smallest scales can be achieved without being overly time consuming. Still, while standard cosmological simulations are obtained straightforwardly from a random realization of the primordial perturbation field within a cosmological framework, local observational datasets are required as additional constraints in order to get simulations that resemble our neighborhood.

Generating constrained initial conditions consists in reconstructing first the density field today from sparse and noisy observational data of the local galaxies like positions and radial peculiar velocities (Kolatt et al. 1996; Kravtsov et al. 2002; Klypin et al. 2003; Sorce et al. 2014) or redshift catalogs (Heß et al. 2013). Second, the initial linear density field or initial conditions must be retrieved either backwards as in the POTENT reconstruction method (Dekel et al. 1990; Bertschinger et al. 1990; Nusser & Dekel 1992) or in the CLUES project[*] (Constrained Local Universe Simulations, Gottlöber et al. 2010; Yepes et al. 2014) with the Constrained Realizations technique (Hoffman & Ribak 1991; Ganon & Hoffman 1993) or forwards as recently proposed by Kitaura (2013); Heß et al. (2013); Jasche & Wandelt (2013); Wang et al. (2013). In the latter case, the initial

[1] Leibniz-Institut für Astrophysik, 14482 Potsdam, Germany
[*]`http://www.clues-project.org/`

field is sampled from a probability distribution function consisting of a Gaussian prior and a likelihood (see Wang et al. 2014, for a complete overview).

This paper uses the backward technique and focuses on using peculiar velocities as constraints. Indeed, although measuring peculiar velocities is challenging, such velocities are highly linear, correlated on large scales and excellent tracers of the underlying gravitational field as they account for both the baryonic and the dark matter. The results are presented as follows. In the second section, the methodology widely described in Sorce et al. (2014, 2016); Sorce (2015) is briefly reviewed. The third section compares the observed and the simulated local Large Scale Structure at redshift zero and presents the reduction of the cosmic variance using sets of random and constrained simulations. Before concluding, in the fourth section, the merging history of the dark matter halo unique candidate for the Virgo cluster is studied.

## 2 Methodology & Data

### 2.1 Radial peculiar velocity catalogs

The second generation observational catalog of radial peculiar velocities, built by the Cosmicflows[†] collaboration and used as constraints within the CLUES project is abundantly described in Tully et al. (2013). In short, 8,000 accurate galaxy peculiar velocities constitute this catalog. They are derived from distance measurements obtained mostly with the Tully-Fisher (Tully & Fisher 1977) and Fundamental Plane relations (Colless et al. 2001). Cepheids (Freedman et al. 2001), Tip of the Red Giant Branch (Lee et al. 1993), Surface Brightness Fluctuation (Tonry et al. 2001), supernovae of type Ia (Jha et al. 2007) and other miscellaneous methods provide the rest.

### 2.2 Techniques: grouping, minimization of biases, WF, CR, etc

The catalog undergoes a series of treatment to produce constrained initial conditions as reported in the following text:

- it is grouped to remove non-linear, virial motions (e.g. Tully 2015b,a) that would backfire when using the linear reconstruction method to produce the linear density field. More precisely, datapoints belonging to a single cluster are collapsed into one observational datapoint in the catalog.
- biases are minimized (Sorce 2015) within the catalog to erase the spurious infall on the local Volume observed in the reconstruction. Briefly, positions and peculiar velocities are corrected.
- the cosmic displacement field is reconstructed with the Wiener-Filter technique (linear minimal variance estimator abridged to WF, Zaroubi et al. 1995, 1999) applied to the catalog of constraints.
- the noisy radial peculiar velocity constraints are relocated at the positions of their progenitors via the reconstructed cosmic displacement field to ensure the proper location of the structures at z=0 (Doumler et al. 2013c,a,b) and they are replaced with their WF 3D reconstructions (Sorce et al. 2014).
- the Constrained Realization technique (schematically WF+Random field=CR, Hoffman & Ribak 1991, 1992) combines the modified observational peculiar velocities with a random realization to restore statistically the missing structures to produce constrained linear density fields.
- the density fields are rescaled to higher redshifts and possibly the resolution is increased by adding small scale features (with e.g. GINNUNGAGAP code[‡]) to complete the construction of constrained initial conditions.

### 2.3 Set of Constrained Simulations

A set of 25 constrained simulations with $512^3$ particles and a box size of 500 $h^{-1}$ Mpc are performed based on initial conditions obtained with this full process and the N-body code GADGET (Springel 2005). Fifteen of these simulations are based on different random realizations of Gaussian fields. They are called hereafter different-RR simulations. The remaining ten simulations share the same random large scale field but different small scale features have been added to increase the resolution (see Sorce et al. 2016, for a more detailed explanation). From now on, they are referred to the same-RR simulations. The two subsets allow us to evaluate to which extent the large and the small (non-linear and thus unconstrained) scales influence the evolution and formation history of the large scale structure and of the Virgo candidate studied further in this paper. Two simulations

[†] `http://www.ipnl.in2p3.fr/projet/cosmicflows/`

[‡] `https://github.com/ginnungagapgroup/ginnungagap`

with $1024^3$ particles with the same box size have been run to check that results shown here are not affected by the mass resolution. Simulations are run within the framework of Planck cosmology ($\Omega_m$=0.307, $\Omega_\Lambda$=0.693, $H_0$=67.77, $\sigma_8 = 0.829$, Planck Collaboration et al. 2014). The starting redshift is z=60 and the force resolution is set to 25 $h^{-1}$ kpc.

## 3 The local Large Scale Structure

### 3.1 Observations, Reconstructions and Simulations

To orientate similarly observations, reconstructions and simulations of the local Universe for comparison purposes, an observer is assumed to be at the center of the reconstructed and simulated boxes and the three supergalactic coordinates are defined similarly to observational ones. Before comparisons, a brief description of the local observed structures is a must. For that purpose, a simulation is drawn randomly from the set of 25 simulations and shown in Figure 1. Note that the choice of the simulation has no impact on the following discussion as simulations all reproduce the local Large Scale structure within a ~200 $h^{-1}$ Mpc radius area. While the left panel of Figure 1 presents the WF reconstructed linear density (contour) and velocity (arrows) fields in a 5 $h^{-1}$ Mpc thick slice of the XY supergalactic plane, the right panel shows the randomly selected simulated non-linear density (contour) and velocity (arrow) fields[§] in the same slice. On top of the fields, red dots stand for galaxies from the 2MASS redshift catalog (Huchra et al. 2012) in a 10 $h^{-1}$ Mpc thick slice. Several well-known structures and voids can be identified like Perseus-Pisces (PP), Shapley, Coma superclusters and the Sculptor void. In addition to the major structures and voids, the Zone of Avoidance (ZOA) due to our Milky-Way dust is marked highlighting the importance of the simulations over the reconstruction. While no reconstructed structures are visible beyond 50 $h^{-1}$ Mpc from the center of the box due to a lack of information in the observed data, the simulated ZOA hosts structures, in particular connections between objects above and below the ZOA.

Comparing observations, reconstructions and simulations is not straightforward. There are some limitations involved: 1) the observed galaxy surveys are magnitude limited and suffer from the luminosity bias, the reconstruction presents only the linear fields and tends to the null field in absence of data or in presence of noisy data. Actually, these limitations highlight again the importance of the simulations: they give access not only to the formation history but also to the non-biased full (including non-linearities) fields of the local Universe.

Qualitative comparisons reveal a good agreement between the 2MASS redshift catalog, the reconstruction and the simulation on Figure 1. This agreement can be quantified with the cosmic web (e.g. gravitational tidal, displacement and velocity shear tensors, Hahn et al. 2007; Lavaux & Wandelt 2010; Hoffman et al. 2012). Focusing on the velocity shear tensor, its eigenvalues permit to distribute cells into knots, filaments, sheets and voids. It is thus straightforward to determine the environment of a galaxy in the cosmic web. With a null threshold and the definition used in Hoffman et al. (2012) for the velocity tensor, three negative eigenvalues correspond to a void while three positive values stand for a knot. Two negative and one positive values constitute a sheet while the opposite configuration reveals a filament. Observationally, filaments and sheets should host more or less the same large amount of galaxies (~ 35-45 %) while knots and voids should shelter only a small fraction of them (~ 10 %) (e.g. Forero-Romero & González 2015; Libeskind et al. 2012, who showed that the fractions are quasi independent of the threshold choice as long as it is reasonable). The results averaged over the fifteen different-RR constrained simulations give 6±1 % of the galaxies in knots, 35±2 % in filaments, 48±2 % in sheets and 10±1 % in voids. The galaxies are distributed as expected. In addition, the derivation of the standard deviations between the simulated and reconstructed velocity fields reveals that reconstructions and simulations agree at about 100-150 km s$^{-1}$ (i.e. 2-3 $h^{-1}$ Mpc, the linear theory threshold, in terms of displacement). From these comparisons, it can be concluded that the major attractors and voids of the local Universe are properly simulated.

### 3.2 Reduction of the cosmic variance

The primary goal of constrained simulations is to reduce cosmic variance to allow detailed comparisons between simulations and observations to test cosmological models. In the previous section, the simulations have been shown to resemble the local Universe implying a qualitative reduction of the cosmic variance. In this section,

[§]obtained with a cloud-in-cell scheme applied to the distribution of particles

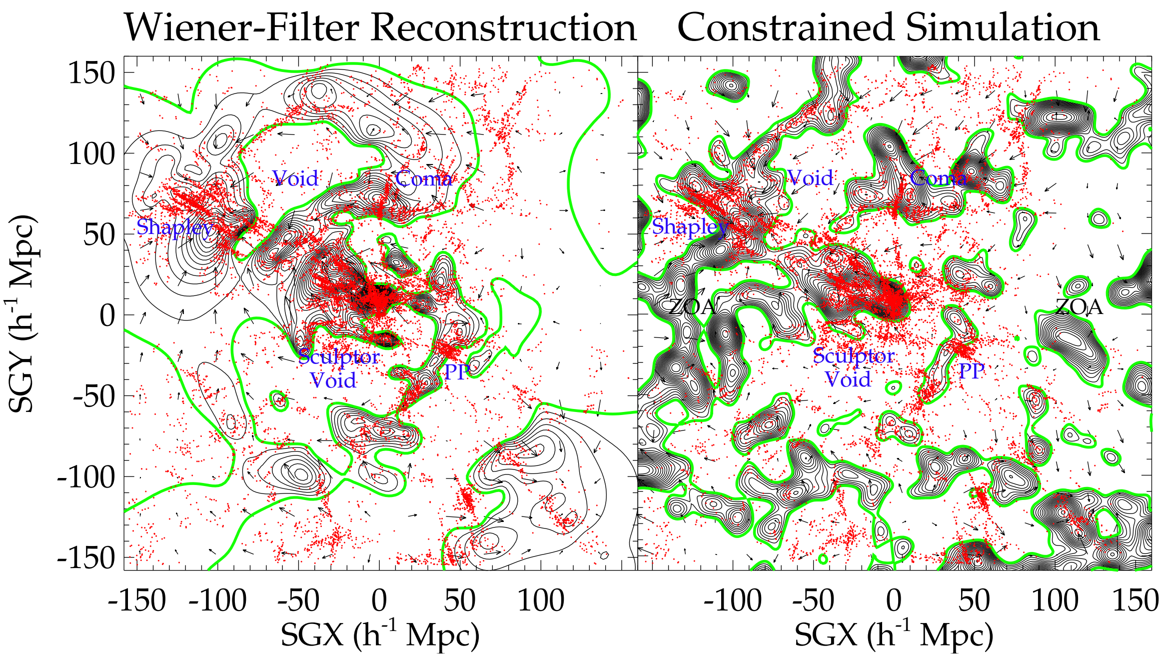


**Fig. 1.** XY supergalactic plane of the reconstructed overdensity (contours) and velocity fields of the local Universe obtained with the Wiener-Filter technique (left) and of the simulated density (contours) and velocity fields of one constrained simulations (right).The green color stands for the mean density. Arrows represent velocity fields. To facilitate the comparison, the simulation has been smoothed at 5 $h^{-1}$ Mpc and the reconstruction at 2 $h^{-1}$ Mpc which gives in both cases grid cells of $\sim$ 5 $h^{-1}$ Mpc. Galaxies from the 2MASS redshift catalog, in a $\pm$ 5 $h^{-1}$ Mpc thick slice, are superimposed as red dots. Structures, voids and flows of the local Universe are well recovered and simulated. A few of them are identified (blue names). While the Wiener-Filter reconstructs fairly well the local Universe in the center of the box, the simulation allows to go farther in distances and deeper into the Zone of Avoidance (ZOA) and, more importantly, it supplies the whole density field (including non-linearities).

the reduction of the cosmic variance is quantified between the different sets of simulations, i.e. constrained and random, to determine the constrained power of the method used. To this end, a cloud-in-cell scheme on a $512^3$ grid is applied to the particle distributions of the simulations at z=0 with a subsequent Gaussian smoothing on a scale of 5 $h^{-1}$ Mpc and a normalization by the mean density. A density-density plot (the density field of a first simulation versus the density field of a second simulation) is built from a cell-to-cell comparison of any pair of constrained simulations. The same is done with the random simulations. If the two simulations were identical all points would follow the 1:1 relation. The cosmic variance between two simulations can then be defined as the one-sigma, hereafter $1\sigma$, scatter (or standard deviation) around this 1:1 relation. Mean and variance of the $1\sigma$ scatters are calculated for the 105 pairs of the 15 random simulations and those of the 15 constrained simulations as well as for the 45 pairs of the 10 constrained simulations sharing the same RR. In the left panel of Figure 2, this procedure gives three points (filled dark grey, black and light grey circles for each one of the simulation types: random, constrained, constrained sharing the same RR) with error bars at the x-axis value of 500 $h^{-1}$ Mpc at z=0. The same is done in smaller sub-boxes of size 400, 300, 250 $h^{-1}$ Mpc, etc, centered on the original box in order to measure the cosmic variance in the smaller central volumes where most of the observational data are, i.e. where they are the most effective.

The effect of the non-linear clustering is visible on small scales. As the system evolves and becomes more non-linear, a larger fraction of the sub-box is filled with low density regions (voids) rather than with high density regions (clusters). The densities of these nearly empty regions tend asymptotically to zero regardless of the initial field while that of high density regions, rising from small but positive differences in the initial field, are magnified. Consequently, the probability to compare a cell in a low density region with one in another low density region, with similar values, increases. This method limit explains the decrease of the $1\sigma$ scatters for sub-box smaller than 100 $h^{-1}$ Mpc in the random simulations. Still the variance of these scatters increases because the probability to find a high density region in one of the pair simulation versus a low density region in the other simulation of the pair is non zero. The effect is (quasi-)inexistent for constrained simulations as by construction structures (such as the Great Attractor and the Virgo cluster) are present close to the center of the box. The cosmic variance, defined as the $1\sigma$ scatter of cell-to-cell comparisons, is considerably reduced for constrained simulations, by a factor 2 to 3 on a scale of 5 $h^{-1}$ Mpc in the inner part of the box, when compared to that of random simulations. In addition, the error bars of the constrained $1\sigma$ scatters are smaller by a factor at least 2 with respect to the random ones. The same procedure for the three components of the velocity field results in the same conclusion. As an example, taking a sub-box of 150 $h^{-1}$ Mpc, the cosmic variance is decreased from 0.5 to 0.3 for the density fields normalized by the mean density at z=0 and from 150 to 50 km $s^{-1}$ for the velocity fields. As a reference to assess the low values of the $1\sigma$ scatters and thus the small discrepancies between the constrained simulated velocity fields, one can consider the validity of the Wiener-Filter reconstructed velocity field which is ± [100-150] km $s^{-1}$ (Sorce 2015).

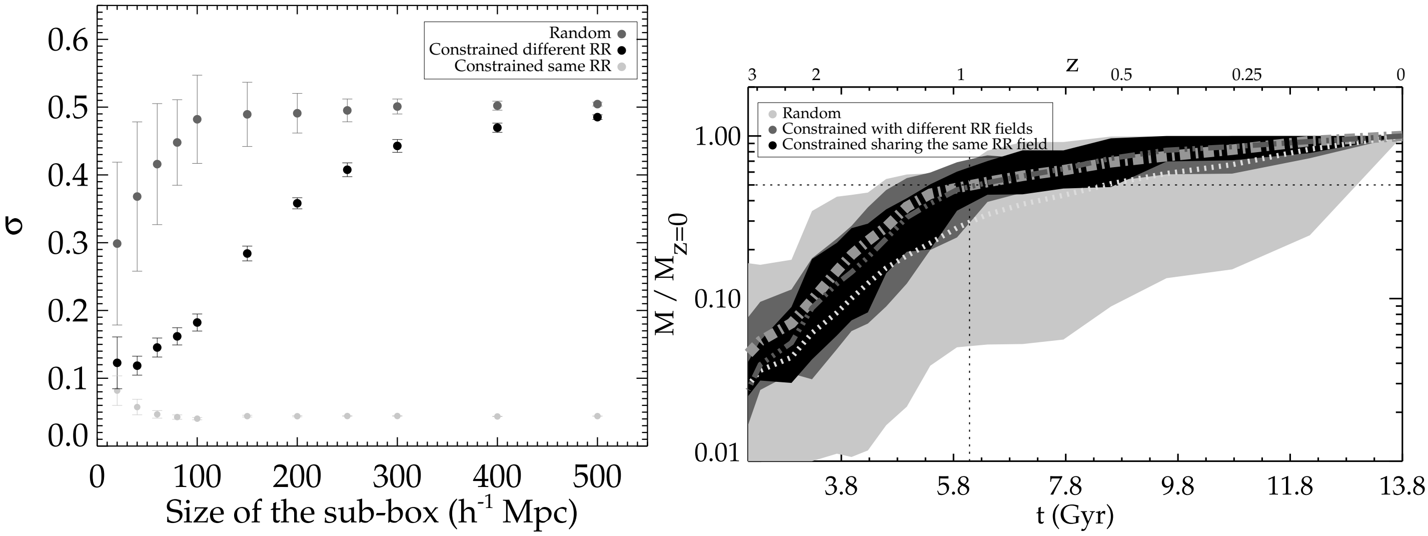


**Fig. 2. Left:** Mean (circles) and scatter (error bars) of one-sigma scatters (standard deviations) obtained with cell-to-cell comparisons carried out on pairs of density fields normalized by the mean density smoothed on a 5 $h^{-1}$ Mpc scale at z=0. Scatters are given as a function of the sub-box size. Pairs are constituted of two random (dark grey), two constrained (black) and two constrained sharing the same random realization field (light grey) simulations. **Right:** Zones of possible merging histories obtained with 100 random halos sharing the same mass range as constrained halos (light grey), 15 Virgo halos from simulations built with different large scale random fields (dark grey) and 10 Virgo halos from simulations sharing the same large scale random field (black). The mean merging histories are plotted on top of the regions (dotted line for random, dot-dashed line for constrained with different large scale random fields and triple dot-dashed line for constrained sharing the same large scale random field). Masses at every redshift have been divided by the mass at redshift zero.

Since the variance between the different constrained simulations is relatively low, the local large scale environment is robustly simulated. Since this large scale environment has been suggested to play an essential role in the formation and evolution of local objects (e.g. Garrison-Kimmel et al. 2014), these constrained simulations are ideal to study local objects. The next subsection takes our nearest neighbor cluster, Virgo as an example.

### *3.3 An example: our nearest neighbor cluster, Virgo*

For each simulation, a list of halos and their properties is established using Amiga Halo Finder (AHF, Knollmann & Knebe 2009) and the definition based on $M_{200}$ ( i.e the mass enclosed in a sphere with a mean density of 200 times the critical density of the Universe). The Virgo counterpart in each simulation is identified as the unique dark matter halo of reasonable mass (same order of magnitude) in spherical regions of 5 $h^{-1}$ Mpc radius centered on the observed position of Virgo. The characteristics (position, mass, velocity) of the identified halos are within 10-20% of those of the observed Virgo.

Merging histories of the 25 Virgo halos are compared with those of 100 halos, selected randomly in the same mass range, at redshift zero, as the former. To this end, halos are split into three samples: the 15 Virgo halos from the different-RR simulations, the 10 Virgo halos from the same-RR simulations and the 100 randomly selected halos. At a given redshift, minimum and maximum mass of any progenitor in a given sample are identified and the corresponding interval is plotted in the upper panel of Figure 2 once normalized by the mass at redshift zero. Therefore, these regions define the possible merging histories of the three different samples (dark grey, black and light grey respectively). For each sample, the mean merging history is plotted on top of the corresponding area with dot-dashed, triple dot-dashed and dotted lines.

Virgo halos present a smaller scatter in their merging histories than the 100 unconstrained randomly selected halos spanning over the same mass range (dark grey against light grey areas). At low redshifts, the variance of constrained halos' merging histories is decreased by a factor $\sim 2$ when compared to that of the merging histories of random halos. The 10 Virgo halos from the simulations sharing the same RR (black) present an even narrower range of merging histories as expected.

Moreover, random and Virgo halos do not share the same mean merging history: there is a break at redshift $\sim 1$ in the mean merging history of Virgo halos indicating that the accretion of material onto halos becomes smoother with time. At approximately the same redshift, Virgo halos have acquired about 50% of their redshift zero masses while the average random halo has gathered only about 30% of its mass. Namely, the large scale environment of the Virgo cluster considerably constrains its possible evolution.

## 4 Conclusions

Although the Universe is homogeneous on large scales, it is known not to be on the small scales rendering detailed one-to-one comparisons between observations and simulations difficult. A remedy to the problem consists in performing simulations that look like the local Universe to reduce the cosmic variance. Such simulations are produced with initial conditions constrained by observational data.

This paper presents and analyzes a set of such constrained simulations built with a refined technique applied to a catalog of local galaxy radial peculiar velocities. To measure efficiently the reduction of the cosmic variance, a set of 15 random simulations are compared to 15 constrained simulations. These simulations contain $512^3$ particles within 500 $h^{-1}$ Mpc. A check with two $1024^3$-particles simulations showed that the results presented here are not affected by the number of particles. First, the general agreement of these simulations with our cosmic neighborhood is checked. Then the cosmic variance is shown to be reduced. To this end, a cloud-in-cell scheme is applied to the different simulated distribution of particles. The resulting fields undergo a 5 $h^{-1}$ Mpc Gaussian smoothing and are normalized by their mean value. Defining the cosmic variance as the one-sigma scatter (or standard deviation) in density-density plots (field of a first simulation versus field of a second simulation), cell-to-cell comparisons between pairs of simulations of the same nature (random or constrained) are conducted. $1\sigma$ scatters obtained for the same nature pairs of simulations are averaged. Not only are these average $1\sigma$ scatters minimal when comparing the inner part of the simulated boxes, where most of the constraints are, but they are also smaller by a factor 2 to 3 with respect to those found for random simulations. The best constrained part of the simulations is the inner box within approximately 100 $h^{-1}$ Mpc for the smallest (clusters) scales, the resemblance extends to 300 $h^{-1}$ Mpc on larger scales (5 to a few tens of megaparsecs). This agreement meets expectations as the observational catalog used as constraints extends to 230 $h^{-1}$ Mpc with 98% of the distance measurements within 160 $h^{-1}$ Mpc and a median distance of 61 $h^{-1}$ Mpc.

The variance between the different constrained simulations is relatively low implying that the local large scale environment is robustly simulated. Since this large scale environment has been suggested to play an essential role in the formation and evolution of local objects, these constrained simulations are ideal to study local objects. Our nearest neighbor cluster, Virgo constitutes such an example.

Applying a halo finder to the constrained simulations, a unique dark matter halo candidate for the Virgo cluster is identified in each one of the simulations. These halos share properties (position, velocity, mass) in common with the observed cluster at the 10-20% level. Studying their merging history and comparing it with that of random halos within the same mass range at redshift zero reveal that here again the cosmic variance is reduced by a factor 2 at low redshifts for the constrained halos: merging histories of randomly chosen halos of the same masses as the Virgo halos span over twice a larger range of possible histories. Interestingly, at around redshift 1, Virgo halos have already accreted 50% of their mass while an average random halo of the same mass has only accreted 30% of its mass. This suggests that the Virgo cluster has had a quiet merging history within the last seven gigayears compared to a random cluster of the same mass. This knowledge may be of extreme importance for observational analyses. In the near future, zoom-in hydrodynamical simulations of the Virgo candidates will allow deeper comparisons with observations.

The author gratefully acknowledges the Gauss Centre for Supercomputing e.V. (www.gauss-centre.eu) for providing computing time on the GCS Supercomputers SuperMUC at LRZ Munich and Jureca at JSC Juelich. JS acknowledges support from the Alexander von Humboldt Foundation and thanks her collaborators.

## References

Abazajian, K., Adelman-McCarthy, J. K., Agüeros, M. A., et al. 2003, AJ, 126, 2081

Abazajian, K. N., Adelman-McCarthy, J. K., Agüeros, M. A., et al. 2009, ApJS, 182, 543

Alimi, J.-M., Bouillot, V., Rasera, Y., et al. 2012, ArXiv e-prints: 1206.2838

Angulo, R. E., , V., White, S. D. M., et al. 2012, MNRAS, 426, 2046

Bertschinger, E., Dekel, A., Faber, S. M., Dressler, A., & Burstein, D. 1990, ApJ, 364, 370

Colless, M., Saglia, R. P., Burstein, D., et al. 2001, MNRAS, 321, 277

Dekel, A., Bertschinger, E., & Faber, S. M. 1990, ApJ, 364, 349

Doumler, T., Courtois, H., Gottlöber, S., & Hoffman, Y. 2013a, MNRAS, 430, 902

Doumler, T., Gottlöber, S., Hoffman, Y., & Courtois, H. 2013b, MNRAS, 430, 912

Doumler, T., Hoffman, Y., Courtois, H., & Gottlöber, S. 2013c, MNRAS, 430, 888

Dubois, Y., Peirani, S., Pichon, C., et al. 2016, MNRAS

Forero-Romero, J. E. & González, R. 2015, ApJ, 799, 45

Freedman, W. L., Madore, B. F., Gibson, B. K., et al. 2001, ApJ, 553, 47

Ganon, G. & Hoffman, Y. 1993, ApJ, 415, L5

Garrison-Kimmel, S., Boylan-Kolchin, M., Bullock, J. S., & Lee, K. 2014, MNRAS, 438, 2578

Gottlöber, S., Hoffman, Y., & Yepes, G. 2010, ArXiv e-prints: 1005.2687

Hahn, O., Carollo, C. M., Porciani, C., & Dekel, A. 2007, MNRAS, 381, 41

Heß, S., Kitaura, F.-S., & Gottlöber, S. 2013, MNRAS, 435, 2065

Hoffman, Y., Metuki, O., Yepes, G., et al. 2012, MNRAS, 425, 2049

Hoffman, Y. & Ribak, E. 1991, ApJ, 380, L5

Hoffman, Y. & Ribak, E. 1992, ApJ, 384, 448

Huchra, J. P., Macri, L. M., Masters, K. L., et al. 2012, ApJS, 199, 26

Jasche, J. & Wandelt, B. D. 2013, MNRAS, 432, 894

Jha, S., Riess, A. G., & Kirshner, R. P. 2007, ApJ, 659, 122

Kitaura, F.-S. 2013, MNRAS, 429, L84

Klypin, A., Hoffman, Y., Kravtsov, A. V., & Gottlöber, S. 2003, ApJ, 596, 19

Klypin, A., Yepes, G., Gottlöber, S., Prada, F., & Hess, S. 2014, ArXiv e-prints: 1411.4001

Klypin, A. A., Trujillo-Gomez, S., & Primack, J. 2011, ApJ, 740, 102

Knollmann, S. R. & Knebe, A. 2009, ApJS, 182, 608

Kolatt, T., Dekel, A., Ganon, G., & Willick, J. A. 1996, ApJ, 458, 419

Kravtsov, A. V., Klypin, A., & Hoffman, Y. 2002, ApJ, 571, 563

Lavaux, G. & Wandelt, B. D. 2010, MNRAS, 403, 1392

Lee, M. G., Freedman, W. L., & Madore, B. F. 1993, ApJ, 417, 553

Libeskind, N. I., Hoffman, Y., Knebe, A., et al. 2012, MNRAS, 421, L137

Nusser, A. & Dekel, A. 1992, ApJ, 391, 443

Planck Collaboration, Ade, P. A. R., Aghanim, N., et al. 2014, A&A, 571, A16

Prada, F., Klypin, A. A., Cuesta, A. J., Betancort-Rijo, J. E., & Primack, J. 2012, MNRAS, 423, 3018

Skillman, S. W., Warren, M. S., Turk, M. J., et al. 2014, ArXiv e-prints: 1407.2600

Sorce, J. G. 2015, MNRAS, 450, 2644

Sorce, J. G., Courtois, H. M., Gottlöber, S., Hoffman, Y., & Tully, R. B. 2014, MNRAS, 437, 3586

Sorce, J. G., Gottlöber, S., Yepes, G., et al. 2016, MNRAS, 455, 2078

Springel, V. 2005, MNRAS, 364, 1105

Stoughton, C., Lupton, R. H., Bernardi, M., et al. 2002, AJ, 123, 485

Tonry, J. L., Dressler, A., Blakeslee, J. P., et al. 2001, ApJ, 546, 681

Tully, R. B. 2015a, AJ, 149, 54

Tully, R. B. 2015b, AJ, 149, 171

Tully, R. B., Courtois, H. M., Dolphin, A. E., et al. 2013, AJ, 146, 86

Tully, R. B. & Fisher, J. R. 1977, A&A, 54, 661
Wang, H., Mo, H. J., Yang, X., Jing, Y. P., & Lin, W. P. 2014, ApJ, 794, 94
Wang, H., Mo, H. J., Yang, X., & van den Bosch, F. C. 2013, ApJ, 772, 63
Watson, W. A., Iliev, I. T., Diego, J. M., et al. 2014, MNRAS, 437, 3776
Yepes, G., Gottlöber, S., & Hoffman, Y. 2014, New Astr. Rev., 58, 1
Zaroubi, S., Hoffman, Y., & Dekel, A. 1999, ApJ, 520, 413
Zaroubi, S., Hoffman, Y., Fisher, K. B., & Lahav, O. 1995, ApJ, 449, 446

# Session SF2A

# Stellar physics

# INFLUENCE OF PLUME-INDUCED INTERNAL GRAVITY WAVES ON THE ROTATION PROFILE OF LOW-MASS STARS

C. Pinçon[1], K. Belkacem[1] and M. J. Goupil[1]

**Abstract.** High-quality seismic data due to the space-borne missions CoRoT and *Kepler* provide precious information on the core rotation of thousands of stars from the subgiant to the red giant stages. We know today that current stellar evolution codes need for an additional physical mechanism to extract angular momentum from the core to the envelope of evolved low-mass stars and explain the low observed internal rotation. In this framework, internal gravity waves generated by penetrative convection at the top of the radiative region may play a role. In this work, we investigate whether the transport of angular momentum by plume-induced gravity waves may counteract the accelereration due the the strong contraction of the innermost layers. On the red giant branch, we find that the strong radiative damping near the H-burning shell prevents these waves from slowing down the core, so that another process should operate in these stars. Nevertheless, we show that plume-induced gravity waves are a good candidate to regulate the amplitude of the differential rotation in subgiant stars.

Keywords: stars: rotation - waves - convection - hydrodynamics

## 1 Introduction

Asteroseismology reveals the internal structure of stars and bring stringent constraints for stellar modeling. Since the achievement of the space-borne missions CoRoT and *Kepler*, a large amount of seismic data for stars from the subgiant to the red giant branches have been made available. Among the main scientific results, the detection of mixed modes, which are oscillation modes with amplitude both in the core and the envelope, made the measurement of the mean core rotation possible for thousands of stars. It thus provided a step forward towards a better understanding of the angular momentum redistribution through the post-main sequence evolution. From these observations, it turns out that the mean core rotation moderately increases on the subgiant branch (Deheuvels et al. 2012, 2014) and then strongly drops as soon as the beginning of the red giant branch, while the central layers are still contracting (Mosser et al. 2012).

Theoretical predictions made by the current stellar evolution codes including transport by meridional circulation and shear-induced mixing are far from reproducing the observations (e.g. Marques et al. 2013; Ceillier et al. 2013). In addition, we know for more than one decade that stellar modeling still fails to predict the quasi solid-body rotation measured in the solar radiative zone (e.g. García et al. 2007). All these discrepancies between theory and observations stress out the need for an additional mechanism to extract angular momentum from the core to the envelope of the stars.

In this framework, internal gravity waves (hereafter, IGW), which are buoyancy waves propagating through the radiative zone of the stars, may have a significative role to play. They are generated at the lower edge of the convective zone, either by turbulent stresses or by the penetration of convective plumes, as observed in geophysics or in numerical simulations (e.g. Dintrans et al. 2005). IGW can then travel in depth before being radiatively damped and thus deposit their angular momentum into the medium. In one hand, IGW generated by turbulent pressure, following the excitation model by Kumar et al. (1999), have already been shown to be able to explain the flat rotation profile observed in the solar radiative zone (Zahn 1997; Talon et al. 2002). However, they seem to rapidly decouple from the core as soon as the beginning of the subgiant branch because of an increasing radiative damping that prevents them from reaching the innermost layers (Fuller et al. 2014).

[1] LESIA, Observatoire de Paris, PSL Research University, CNRS, Université Pierre et Marie Curie, Université Paris Diderot, 92195 Meudon, France

In the other hand, a semianalytical estimate of the generation of IGW by penetrative convection is now available and has already demonstrated the ability of these waves to efficiently affect the rotation of the solar radiative zone (Pinçon et al. 2016). Nevertheless, a similar study on more evolved stars has not been undertaken yet.

In this work, we investigate the ability of plume-induced waves to modify a given rotation profile in subgiant and red giant stars. As a first step, our study is based on the comparison of the dynamical wave-driven timescale with the contraction/expansion timescale throughout a $1M_\odot$ star. Moreover, the role of the differential rotation amplitude on the transport by IGW is stressed out.

## 2 Characteristic timescale and plume-induced wave flux

### 2.1 Wave-driven timescale

Transport of angular momentum in stars is governed by an advection-diffusion equation. Therefore, the local timescale associated with the transport of angular momentum by IGW, given a rotation profile $\Omega(r)$ (within the shellular approximation), is equal to the ratio of the density of angular momentum in the star to the radial divergence of the angular momentum wave flux, i.e.

$$t_w(r) \sim \left|\frac{\rho r^2 \Omega}{\dot{J}}\right| , \tag{2.1}$$

with $r$ the radius, $\rho$ the density at the equilibrium and $\dot{J}$ the divergence of the mean radial wave flux of angular momentum. At this stage, the angular momentum extraction by IGW, in a shell at the radius $r$, will be said to be efficient compared to the acceleration caused by the core contraction if $t_w(r) < t_{cont}(r)$, with $t_{cont}$ the local contraction timescale. As shown in Eq. (2.1), the computation of $t_w$ requires the knowledge of the wave flux throughout the star via the term $\dot{J}$.

### 2.2 Wave flux generated by penetrative convection

To estimate the wave energy flux emitted at the top of the radiative zone, Pinçon et al. (2016) considered the pressure exerted by an ensemble of incoherent convective plumes in the penetration zone as the source term in the wave equation. By assuming a high Péclet number and a very sharp thermal transition at the base of the convective zone, they derived a simplified expression for the mean radial wave energy flux per unit of frequency, for an angular degree $l$ and an azimuthal number $m$ at the top of the radiative zone,

$$\mathcal{F}_{E,w}(r_t,\omega,l,m) \sim \frac{1}{4\pi r_t^2}\frac{\mathcal{A}\mathcal{S}_p}{2}\frac{\rho_b V_b^3}{2} F_{R,l}\frac{e^{-\omega^2/4\nu_p^2}}{\nu_p} e^{-l(l+1)b^2/2r_t^2} , \tag{2.2}$$

where $r_t$ is the radius at the top of the radiative zone, $\mathcal{A}$ is the plumes filling factor in the excitation region, $\mathcal{S}_p = \pi b^2$ is the horizonthal area occupied by one single plume, with $b$ the plume radius, $\rho_b$ and $V_b$ are respectively the density and the plume velocity at the base of the convective region, $F_{R,l} = \sqrt{l(l+1)}V_b/r_t N_0$, with $N_0$ the Brunt-Väisälä frequency at the top of the radiative zone, and $\nu_p = 1/\tau_p$, with $\tau_p$ the plume lifetime.

To go further, the total wave flux of angular momentum at each radius in the radiative zone is deduced from the sum of all the contributions to the wave energy flux emitted from the top of the radiative zone and modulated by a damping term (Zahn 1997)

$$\mathcal{F}_{J,w}(r) = \sum_l \sum_{m=-l}^{m=+l} \int_{-\infty}^{+\infty} \frac{m}{\omega}\frac{r_t^2}{r^2}\mathcal{F}_{E,w}(r_t,\omega,l,m) e^{-\tau(r,\hat{\omega},l)} \mathrm{d}\omega , \tag{2.3}$$

with

$$\tau(r,\hat{\omega},l) = [l(l+1)]^{3/2}\int_r^{r_t} K\frac{N N_T^2}{\hat{\omega}^4}\left(\frac{N^2}{N^2-\hat{\omega}^2}\right)^{1/2}\frac{\mathrm{d}r}{r^3} , \tag{2.4}$$

where $N$ is the Brunt-Väisälä frequency, with its thermal part $N_T$, $K$ is the radiative diffusion coefficient, and

$$\hat{\omega}(r,\omega,m) = \omega - m\delta\Omega(r) \tag{2.5}$$

is the Doppler-shifted intrinsic frequency. Note that $\delta\Omega(r) = \Omega(r) - \Omega_t$ where $\Omega_t$ is the rotation rate at the top of the radiative zone. Near a critical layer (i.e. where $\hat{\omega} = 0$), we will suppose that the considered wave component is totally dissipated and deposit all the angular momentum that they carry into the medium, so that they cannot go deeper in the star.

## 3 Ability of plume-induced waves to extract angular momentum from the core

### 3.1 Input physics and assumed rotation profile

We consider two $1\mathrm{M}_\odot$ stellar models computed with the evolution code CESTAM (Marques et al. 2013) localized on the subgiant branch and at the beginning of the ascent of the red giand branch. The chemical composition follows the solar mixture as given in Asplund et al. (2009), with the initial helium and metal abundances $Y_0 = 0.261$ and $Z_0 = 0.0146$. We used the NACRE nuclear reaction rates and the OPAL2005 equation of states and opacity tables. The convection was modeled by the mixing-length theory parametrized with $\alpha_{MLT} = 1.75$. We did not consider microscopic diffusion, overshooting and rotation. To compute Eq. (2.2), we assume that the plume lifetime is close to the convective timescale at the base of the convective zone as given by the MLT, i.e. $\nu_p \approx \omega_{MLT}$. In addition, we fix the plumes filling factor at a reasonable value $\mathcal{A} \approx 0.1$, as observed in the uppermost layers of numerical simulations of the Sun (e.g. Stein & Nordlund 1998). All the other quantities are directly estimated using the equilibrium internal structure from the stellar models (see Pinçon et al. 2016, for details).

As seen in Eq. (2.3), the total wave flux depends on the differential rotation in the radiative zone via Eq. (2.4). As shown by Pinçon et al. (2016) in the solar case, its amplitude can have strong consequences on the transport by IGW. We will then assume a given rotation profile for each stellar model. Doing so, we assume that the rotation rate is low enough to have no effect on the internal structure of the stellar models. Nevertheless, little is known about the shape of the rotation profile in evolved stars. By assuming a priori, first, that an efficient mechanism prevents the core contraction from developing a strong differential rotation in the radiative zone, and second, that this latter forces a quite smooth profile, it leads us to consider a rotation profile in the form

$$\delta\Omega(r) = \Delta\Omega \cos^2\left(\frac{\pi}{2}\frac{r}{r_t}\right) \quad \text{for} \quad r < r_t \ , \tag{3.1}$$

with $\Delta\Omega$ the amplitude of the differential rotation between the center and the top of the radiative zone. We thus assume a decreasing rotation rate from the core to the envelope and the $\cos^2$ function ensures a smooth profile at the center and near the base of the convective zone. Using such a synthetic profile is questionable, but it will give us a first hint about the efficiency of the transport by IGW in subgiant and red giant stars while considering different values for $\Delta\Omega$.

### 3.2 Efficiency of the transport by plume-induced IGW

We now have all the ingredients to compute $t_w$ and compare it to $t_{cont}$ throughout the radiative zone of the stellar models. For each of them, we vary the amplitude of the differential rotation $\Delta\Omega$ in a range between 0 and 12 µrad s$^{-1}$, which is representative of the observations of evolved low-mass stars (Mosser et al. 2012; Deheuvels et al. 2012, 2014).

#### 3.2.1 RGB stars

For red giant stars, all our computations show that the wave-driven timescale is well larger than the contraction timescale below the H-burning shell ($t_w \gg t_{cont}$). This is illustrated in Fig.1 *(left panel)* for a $1\mathrm{M}_\odot$ model at the beginning of the ascent of the RGB with $\log T_{eff} = 3.68$ and $\log L/L_\odot = 0.55$. Since this result is conservative over a range that is representative of the observed values for $\Delta\Omega$, we can conclude that IGW alone are inefficient to slow down the core rotation and that another process should operate in these stars in order to explain the observations. Indeed, as pointed out by Fuller et al. (2014), the wave damping rate, which is locally proportional to $N^3$, strongly increases as the innermost layers contract. Near the H-burning shell, where $N$ is maximum, IGW suffer a serious damping preventing them to go deeper and affect the core rotation in these stars. Nevertheless, we cannot exclude that damped IGW near and above the H-burning-shell, which have deposited their angular momentum in the medium (see the low values of $t_w$ in this region), could play a role by interacting with meridional circulation and boosting the extraction of angular momentum from the stellar core to the envelope. This hypothesis will need to be checked using a more complete calculation.

#### 3.2.2 Subgiant stars

On the subgiant branch, the situation is similar to RGB stars for very low differential rotations. Nevertheless, as $\Delta\Omega$ increases, the wave-driven timescale decreases. This is illustrated in Fig.1 *(right panel)* for a $1\mathrm{M}_\odot$ subgiant

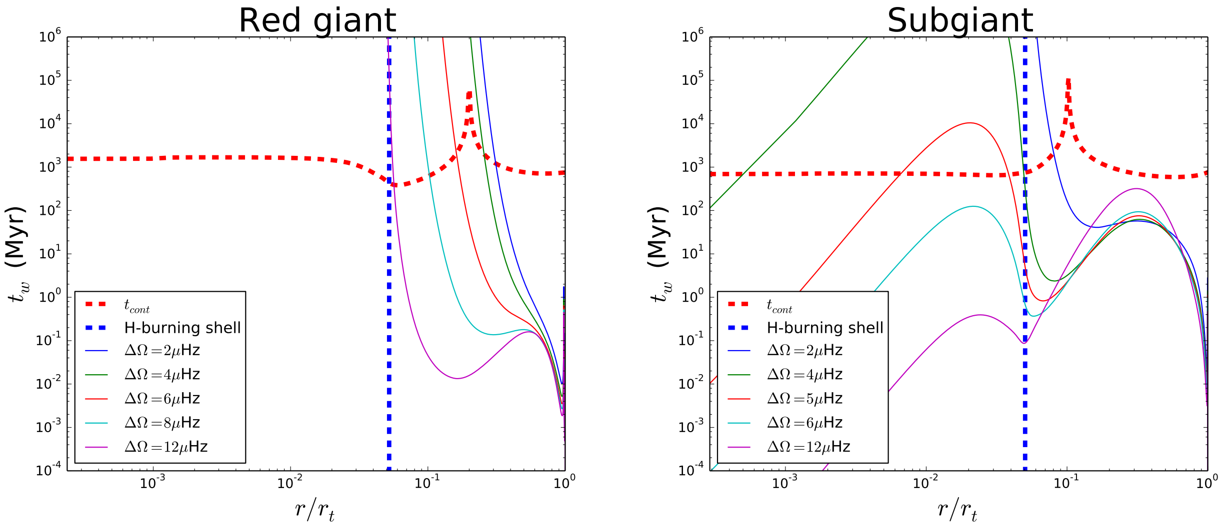


**Fig. 1. Left:** Wave-driven timescale, $t_w$, computed using Eq. (2.1) as a function of the normalized radius in the radiative zone, for a 1M$_\odot$ model at the beginnng of the ascent of the RGB with $\log T_{eff} = 3.68$ and $\log L/L_\odot = 0.55$. The contraction timescale and the location of the H-burning shell are represented by the red and blue dashed lines, respectively. Different amplitudes for $\Delta\Omega$ are considered. **Right:** Same as the previous figure, but for a 1M$_\odot$ subgiant model with $\log T_{eff} = 3.72$ and $\log L/L_\odot = 0.3$.

model with $\log T_{eff} = 3.72$ and $\log L/L_\odot = 0.3$. It even gets lower than the contraction timescale throughout the region below the H-burning shell as soon as $\Delta\Omega$ is larger than a threshold. This trend is mainly due to the asymmetry between prograde (m>0) and retrograde (m<0) components that is enhanced and the radiative damping of the retrograde waves that decreases as $\Delta\Omega$ increases. In the example of Fig.1 *(right panel)*, we can see that IGW are able to counteract the acceleration due to the core contraction as soon as $\Delta\Omega \gtrsim 6$ μHz. We note that this theoretical threshold value is consistent with the mean core rotation observed in subgiant stars. Therefore, we demonstrate here that IGW generated by penerative convection may be a major actor in the transport of angular momentum on the sugiant branch before the radiative damping becomes too strong as the stars evolve on the RGB. Obviously, they have to be taken into account in stellar modeling.

## 4 Conclusions

Internal gravity waves generated by penetrative convection cannot be responsible alone for the low rotation rates observed in the red giant stars. Indeed, the strong radiative damping near the H-burning shell prevents them from modifying the core rotation, as it has already been shown in previous works for turbulence-induced IGW. Nevertheless, in subgiant stars, these waves seem to be a good candidate to limit the amplitude of the differential rotation in the radiative zone. The results of this work are preliminary and have to be confirmed by a more thorough study. This will be subject to a near future work. Efforts will have also to be done to properly include transport by IGW in a stellar evolution code, which is a necessary step to study their interaction with the other transport processes and their effect along the stellar evolution.

## References


Asplund, M., Grevesse, N., Sauval, A. J., & Scott, P. 2009, ARA&A, 47, 481

Ceillier, T., Eggenberger, P., García, R. A., & Mathis, S. 2013, A&A, 555, A54

Deheuvels, S., Doğan, G., Goupil, M. J., et al. 2014, A&A, 564, A27

Deheuvels, S., García, R. A., Chaplin, W. J., et al. 2012, ApJ, 756, 19

Dintrans, B., Brandenburg, A., Nordlund, Å., & Stein, R. F. 2005, A&A, 438, 365

Fuller, J., Lecoanet, D., Cantiello, M., & Brown, B. 2014, ApJ, 796, 17

García, R. A., Turck-Chièze, S., Jiménez-Reyes, S. J., et al. 2007, Science, 316, 1591

Kumar, P., Talon, S., & Zahn, J.-P. 1999, ApJ, 520, 859

Marques, J. P., Goupil, M. J., Lebreton, Y., et al. 2013, A&A, 549, A74

Mosser, B., Goupil, M. J., Belkacem, K., et al. 2012, A&A, 548, A10

Pinçon, C., Belkacem, K., & Goupil, M. J. 2016, A&A, 588, A122

Stein, R. F. & Nordlund, A. 1998, ApJ, 499, 914

Talon, S., Kumar, P., & Zahn, J.-P. 2002, ApJ, 574, L175

Zahn, J.-P. 1997, in Astrophysics and Space Science Library, Vol. 225, SCORe'96 : Solar Convection and Oscillations and their Relationship, ed. F. P. Pijpers, J. Christensen-Dalsgaard, & C. S. Rosenthal, 187–200

*SF2A 2016*
*C. Reylé, J. Richard, L. Cambrésy, M. Deleuil, E. Pécontal, L. Tresse and I. Vauglin (eds)*

# MAGNETIC ACTIVITY OF SEISMIC SOLAR ANALOGS

D. Salabert[1], R. A. García[1], P. G. Beck[1] and the SSA team

**Abstract.** We present our latest results on the solar–stellar connection by studying 18 solar analogs that we identified among the *Kepler* seismic sample (Salabert et al. 2016a). We measured their magnetic activity properties using observations collected by the *Kepler* satellite and the ground-based, high-resolution HERMES spectrograph. The photospheric ($S_{\rm ph}$) and chromospheric ($\mathcal{S}$) magnetic activity proxies of these seismic solar analogs are compared in relation to solar activity. We show that the activity of the Sun is actually comparable to the activity of the seismic solar analogs. Furthermore, we report on the discovery of temporal variability in the acoustic frequencies of the young (1 Gyr-old) solar analog KIC 10644253 with a modulation of about 1.5 years, which agrees with the derived photospheric activity (Salabert et al. 2016b). It could actually be the signature of the short-period modulation, or quasi-biennal oscillation, of its magnetic activity as observed in the Sun and the 1-Gyr-old solar analog HD 30495. In addition, the lithium abundance and the chromospheric activity estimated from HERMES confirms that KIC 10644253 is a young and more active star than the Sun.

Keywords: solar-type, activity, evolution, data analysis, observational

## 1 Introduction

The Mount Wilson spectroscopic observations of main-sequence G and K stars (Wilson 1978; Duncan et al. 1991) have suggested the existence of two distinct branches of cycling stars, the active and inactive (Saar & Baliunas 1992; Soon et al. 1993), and that the Sun lies squarely between the two, thus appearing as a peculiar outlier (Böhm-Vitense 2007). Today, whether the solar dynamo and the related surface magnetic activity are typical or peculiar still remains an open question (Metcalfe et al. 2016). Finding solar-analog stars and studying their surface magnetic activity is a very promising way to understand solar variability and its associated dynamo (Egeland et al. 2016). Moreover, the study of the magnetic activity of solar analogs is also important for understanding the evolution of the Sun and its environment in relation to other stars and the habitability of their planets.

The unprecedented quality of the continuous four-year photometric observations collected by the *Kepler* satellite (Borucki et al. 2010) allowed the measurements of acoustic oscillations in hundreds of solar-like stars (Chaplin et al. 2014). Moreover, the length of the *Kepler* dataset provides a unique source of information for detecting magnetic activity and the associated temporal variability in the acoustic oscillations. Indeed, it is well established that in the case of the Sun, p modes are sensitive to changes in the surface magnetic activity (Woodard & Noyes 1985). Moreover, the p-mode frequencies are the only proxy that can reveal inferences on sub-surface changes with activity that is not detectable at the surface by standard proxies (e.g., Salabert et al. 2009, 2015; Basu et al. 2012).

Cayrel de Strobel (1996) provided a definition of a solar-analog star based on the fundamental parameters (e.g., $M$ and $T_{\rm eff}$). Here, we took advantage of the combination of asteroseismology with high-resolution spectroscopy which substantially improves the accuracy of the stellar parameters and reduces their errors (Mathur et al. 2012; Chaplin et al. 2014; Metcalfe et al. 2014). We selected stars for which solar-like oscillations were detected in order to avoid very active stars (Salabert et al. 2003; Mosser et al. 2009; Chaplin et al. 2011). This is what we called a seismic solar-analog star. We included in the sample only stars with measured rotation (García et al. 2014) to ensure the presence of magnetic activity. A total of 18 seismic solar analogs were identified from the photometric *Kepler* observations (Salabert et al. 2016a).

## 2 Photospheric and chromospheric magnetic activity of seismic solar analogs

The photospheric activity $S_{\rm ph}$ index corresponds to a proxy of the global stellar magnetic variability derived by means of the surface rotation $P_{\rm rot}$ (Mathur et al. 2014b). It is defined as the mean value of the light-curve fluctuations over sub

[1] Laboratoire AIM, CEA/DRF-CNRS, Université Paris 7 Diderot, IRFU/SAp, Centre de Saclay, 91191 Gif-sur-Yvette, France

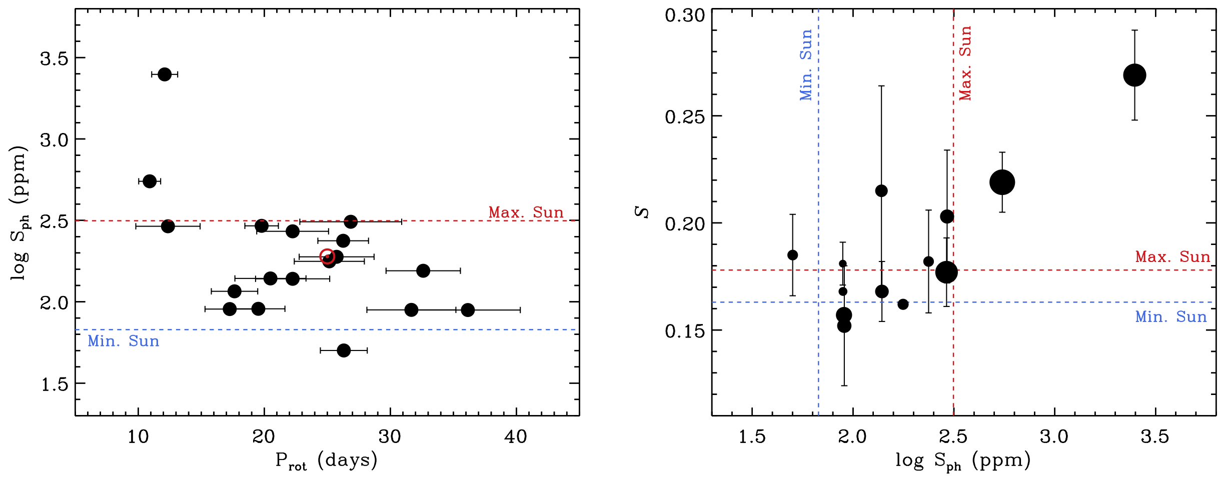


**Fig. 1.** (Left panel) Photospheric index $S_{\rm ph}$ as a function of the rotation period $P_{\rm rot}$ of the 18 seismic solar analogs observed with *Kepler*. (Right panel) Chromospheric $\mathcal{S}$ index derived from HERMES observations and calibrated into the MWO system as a function of the photospheric index $S_{\rm ph}$. The symbol size is inversely proportional to the rotation. Adapted from Salabert et al. (2016a).

series of length $5 \times P_{\rm rot}$. We note however that $S_{\rm ph}$ represents a lower limit of the photospheric activity as it depends on the inclination angle. It was estimated here through the analysis of the *Kepler* long-cadence observations calibrated as described in García et al. (2011). The chromospheric activity $\mathcal{S}$ index is a proxy of the strength of the plasma emission in the cores of the Ca II H&K lines in the near ultra violet (Wilson 1978). In this work, the $\mathcal{S}$ index was measured from spectroscopic observations collected with the HERMES spectrograph (Raskin et al. 2011) mounted on the 1.2-m MERCATOR telescope at the Observatorio del Roque de los Muchachos (La Palma, Canary Islands, Spain). A detailed description of the data processing of the HERMES observations can be found in Beck et al. (2016a). We note that the result is dependent on the instrumental resolution and on the spectral type. However, as the selected stars were chosen for all having comparable stellar properties to the Sun, the estimated values of the $\mathcal{S}$ index can be thus safely compared between each other.

The left panel of Fig. 1 shows the $S_{\rm ph}$ of the 18 seismic solar analogs as a function of their rotation $P_{\rm rot}$. The mean value of the solar $S_{\rm ph}$ over cycle 23 calculated from the photometric VIRGO/SPM observations (Fröhlich et al. 1995) is also indicated, as well as the corresponding values at minimum and maximum of activity. The $S_{\rm ph}$ of the identified solar analogs is comparable to the Sun, within the range of activity covered over a solar cycle. Moreover, the two youngest solar analogs in our sample below 2 Gyr-old (Chaplin et al. 2014; Metcalfe et al. 2014), which rotate in about 11 days, are the most active. The comparison between the $S_{\rm ph}$ and the $\mathcal{S}$ magnetic activity proxies is shown on the right panel of Fig. 1 for a subset of 13 stars with a S/N(Ca) > 15 in the spectroscopic data (for more explanations, see Salabert et al. 2016a). The values of $\mathcal{S}$ were calibrated to the Mount Wilson Observatory (MWO) system using the HERMES scaling factor derived by Beck et al. (2016a). The mean values at minimum and maximum of solar activity are also represented. The resulting activity box corresponds to the range of change in solar activity along the 11-year magnetic cycle. Although the sample of stars is small, the $S_{\rm ph}$ and $\mathcal{S}$ indices are observed to be complementary, within the errors. We note also that both proxies were not estimated from contemporaneous *Kepler* and HERMES observations, introducing a dispersion partly related to possible temporal variations in stellar activity. Nevertheless, it confirms that $S_{\rm ph}$ can complement the classical $\mathcal{S}$ index for activity studies.

## 3 Magnetic variability in the young solar analog KIC 10644253

With a rotation of ~ 11 days, the solar analog KIC 10644253 (BD+47 2683, $V = 9.26$) is the youngest solar-like pulsating star observed by *Kepler* with an age of $1.07 \pm 0.25$ Gyr (Metcalfe et al. 2014) and one of the most active (García et al. 2014). It is thus an excellent candidate for investigating the magnetic activity of a young Sun with asteroseismic data. In addition to the Sun, temporal variations of p-mode frequencies related to magnetic activity were so far observed in only three stars: the F-type stars HD 49933 (García et al. 2010) and KIC 3733735 (Régulo et al. 2016), and the solar-analog G-type KIC 10644253 (Salabert et al. 2016b).

To study the temporal variations of the low-degree, p-mode oscillation frequencies observed in KIC 10644253, the

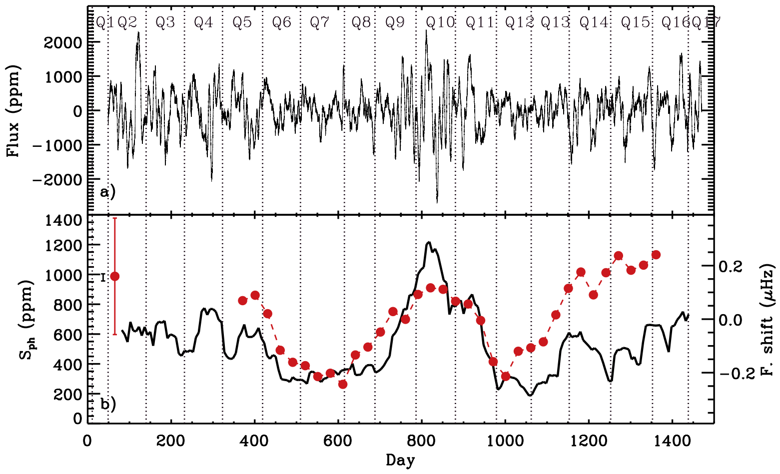


**Fig. 2.** (Top panel) Photometric long-cadence observations of KIC 10644253 collected over 1411 days by *Kepler* as a function of time. (Bottom panel) Photospheric index $S_{\rm ph}$ (black) of KIC 10644253 as a function of time compared to the frequency shifts obtained from the cross-correlation analysis (red circles). The frequency shifts were extracted from the continuous short-cadence observations from Q5 to Q17. The associated mean uncertainties are illustrated in the upper left-hand corner using the same color code. In the two panels, the vertical dotted lines represent the observational length of each *Kepler* quarter from Q1 to Q17. Adapted from Salabert et al. (2016b).

*Kepler* short-cadence dataset was split into contiguous 180-day-long sub series (Salabert et al. 2016b). The associated power spectra were analyzed using both peak-fitting (Ballot et al. 2011; Salabert et al. 2011) and cross-correlation (Régulo et al. 2016) independent methods and the corresponding frequency shifts $\langle \delta\nu \rangle$ extracted. In addition, the light curve was analyzed to estimate the $S_{\rm ph}$ over sub series of $5 \times P_{\rm rot} = 54.55$ days. Figure 2 shows that both the photospheric $S_{\rm ph}$ and the frequency shifts $\langle \delta\nu \rangle$ present the signature of magnetic activity variability. A modulation of about 1.5 years is measured in both observables of about 900 ppm for $S_{\rm ph}$ and 0.5 $\mu$Hz for the frequency shifts. It could be the signature of the short-period modulation, or quasi-biennal oscillation, of its magnetic activity as observed in the Sun (see, e.g., Fletcher et al. 2010). The variations found in KIC 10644253 at a rotation period of ~ 11 days is analogous to what is found by Egeland et al. (2015) from the study of the temporal variations of the $\mathcal{S}$ index in the solar analog HD 30495 falling on the inactive branch (Böhm-Vitense 2007). Moreover, the comparison between magnitude and frequency dependence of the frequency shifts measured for KIC 10644253 with the ones obtained for the Sun indicates that the same physical mechanisms are involved in the sub-surface layers in both stars.

In addition, the analysis of the Hermes spectroscopic observations shows that KIC 10644253 is ~ 18% chromospherically more active than the Sun with an $\mathcal{S}$ index of $0.213 \pm 0.008$. Moreover, the high lithium abundance of $2.74 \pm 0.03$ dex and the effective temperature of $6006 \pm 100$ K mean that the lithium at the surface has not been depleted yet by internal processes (Ramírez et al. 2012). This is validating its young age estimated from seismology and in agreement with a rotation of ~ 11 days from gyrochronology (Meibom et al. 2011; van Saders et al. 2016). Furthermore, among the 18 solar analogs in this sample, KIC 10644253 has the highest lithium abundance (Beck et al., Submitted).

## 4 Conclusions

The study of the characteristics of the surface activity of solar analogs can provide new constraints in order to better understand the magnetic variability of the Sun, and its underlying dynamo during its evolution. We analyzed here the sample of main-sequence stars observed by the *Kepler* satellite for which solar-like oscillations were detected and rotational periods measured and from published stellar parameters, we identified 18 seismic solar analogs. We then studied the properties of the photospheric and chromospheric magnetic activity of these stars in relation of the Sun. The photospheric index $S_{\rm ph}$ was derived through the analysis of the *Kepler* observations, while the chromospheric proxy $\mathcal{S}$ was measured with follow-up, ground-based Hermes spectroscopic observations. We showed that the magnetic activity of the Sun is comparable to the activity of the seismic solar analogs studied here, within the maximum-to-minimum activity variations of the Sun during the 11-year cycle. As expected, the youngest and fastest rotating stars are observed to be the most active of our sample. Furthermore, the comparison of the photospheric index $S_{\rm ph}$ with the well-established chromospheric $\mathcal{S}$ index shows that $S_{\rm ph}$ can be used to provide a suitable magnetic activity proxy. We established the existence of a temporal variability of the magnetic activity was observed in the young (1 Gyr-old) solar analog KIC 10644253. A significant modulation of about 1.5 years was measured in the low-degree, p-mode frequencies and in the photospheric index $S_{\rm ph}$.

The rest of the Seismic Solar Analogs (SSA) team consists by alphabetic order of: J. Ballot, L. Bigot, O. L. Creevey, R. Egeland, S. Mathur, T. S. Metcalfe, J.-D. do Nascimento Jr., P. L. Pallé, F. Pérez Hernández, and C. Régulo. The authors wish to thank the entire *Kepler* team. Funding for this Discovery mission is provided by NASA Science Mission Directorate. The spectroscopic observations are made with the Mercator Telescope, operated by the Flemish Community at the Spanish Observatorio del Roque de los Muchachos (La Palma) of the Instituto de Astrofísica de Canarias. This work utilizes data from the National Solar Observatory/Sacramento Peak Monitoring Program, managed by the National Solar Observatory, which is operated by the Association of Universities for Research in Astronomy (AURA), Inc. under a cooperative agreement with the National Science Foundation. The research leading to these results has received funding from the European Community's Seventh Framework Program ([FP7/2007-2013]) under grant agreement no. 312844 (SPACEINN). DS and RAG acknowledge the financial support from the CNES GOLF and PLATO grants. PGB acknowledges the ANR (Agence Nationale de la Recherche, France) program IDEE (no. ANR-12-BS05-0008) "Interaction Des Etoiles et des Exoplanètes".

## References

Ballot, J., Gizon, L., Samadi, R., et al. 2011, A&A, 530, A97

Basu, S., Broomhall, A.-M., Chaplin, W. J., & Elsworth, Y. 2012, ApJ, 758, 43

Beck, P. G., Allende Prieto, C., Van Reeth, T., et al. 2016a, A&A, 589, A27

Beck, P. G., Do Nascimento Jr., J.-D., Duarte, T., et al., A&A, Submitted

Böhm-Vitense, E. 2007, ApJ, 657, 486

Borucki, W. J., Koch, D., Basri, G., et al. 2010, Science, 327, 977

Cayrel de Strobel, G. 1996, A&A Rev., 7, 243

Chaplin, W. J., Bedding, T. R., Bonanno, A., et al. 2011, ApJ, 732, L5

Chaplin, W. J., Basu, S., Huber, D., et al. 2014, ApJS, 210, 1

Duncan, D. K., Vaughan, A. H., Wilson, O. C., et al. 1991, ApJS, 76, 383

Egeland, R., Metcalfe, T. S., Hall, J. C., & Henry, G. W. 2015, ApJ, 812, 12

Egeland, R., Soon, W., Baliunas, S., et al. 2016, arXiv:1609.04756

Fletcher, S. T., Broomhall, A.-M., Salabert, D., et al. 2010, ApJ, 718, L19

Fröhlich, C., Romero, J., Roth, H., et al. 1995, Sol. Phys., 162, 101

García, R. A., Mathur, S., Salabert, D., et al. 2010, Science, 329, 1032

García, R. A., Hekker, S., Stello, D., et al. 2011, MNRAS, 414, L6

García, R. A., Ceillier, T., Salabert, D., et al. 2014, A&A, 572, AA34

Mathur, S., Metcalfe, T. S., Woitaszek, M., et al. 2012, ApJ, 749, 152

Mathur, S., García, R. A., Ballot, J., et al. 2014a, A&A, 562, AA124

Mathur, S., Salabert, D., García, R. A., & Ceillier, T. 2014b, Journal of Space Weather and Space Climate, 4, A15

Meibom, S., Barnes, S. A., Latham, D. W., et al. 2011, ApJ, 733, L9

Metcalfe, T. S., Creevey, O. L., Doğan, G., et al. 2014, ApJS, 214, 27

Metcalfe, T. S., Egeland, R., & van Saders, J. 2016, ApJ, 826, L2

Mosser, B., Michel, E., Appourchaux, T., et al. 2009, A&A, 506, 33

Ramírez, I., Fish, J. R., Lambert, D. L., & Allende Prieto, C. 2012, ApJ, 756, 46

Raskin, G., van Winckel, H., Hensberge, H., et al. 2011, A&A, 526, A69

Régulo, C., García, R. A., & Ballot, J. 2016, A&A, 589, A103

Saar, S. H., & Baliunas, S. L. 1992, The Solar Cycle, 27, 150

Salabert, D., Jiménez-Reyes, S. J., & Tomczyk, S. 2003, A&A, 408, 729

Salabert, D., García, R. A., Pallé, P. L., & Jiménez-Reyes, S. J. 2009, A&A, 504, L1

Salabert, D., Régulo, C., Ballot, J., García, R. A., & Mathur, S. 2011, A&A, 530, A127

Salabert, D., García, R. A., & Turck-Chièze, S. 2015, A&A, 578, A137

Salabert, D., Garcia, R. A., Beck, P. G., et al. 2016a, arXiv:1608.01489

Salabert, D., Régulo, C., García, R. A., et al. 2016b, A&A, 589, A118

Soon, W. H., Baliunas, S. L., & Zhang, Q. 1993, ApJ, 414, L33

van Saders, J. L., Ceillier, T., Metcalfe, T. S., et al. 2016, Nature, 529, 181

Wilson, O. C. 1978, ApJ, 226, 379

Woodard, M. F., & Noyes, R. W. 1985, Nature, 318, 449

*SF2A 2016*
*C. Reylé, J. Richard, L. Cambrésy, M. Deleuil, E. Pécontal, L. Tresse and I. Vauglin (eds)*

# THE GASEOUS PROTO-CLUSTER AS A PRODUCT OF GRAVO-TURBULENT INTERACTION: MODIFIED LOCAL ENVIRONMENT FOR STELLAR CLUSTER FORMATION?

Y.-N. Lee[1] and P. Hennebelle[1, 2]

**Abstract.** Stars are often observed to form in clusters, while the formation of the gaseous proto-cluster precedes that of the stellar cluster. We discuss the assembly of gas via gravo-turbulent reprocessing inside collapsing molecular clouds, and demonstrate that virial equilibrium is established for the gaseous proto-cluster, of which the higher density is favorable for clustered star formation, and that some physical characteristics of the stellar cluster are inherited from the gaseous proto-cluster. We introduce an analytical two-dimensional virial model to account for the quasi-stationary accreting gaseous proto-cluster which has non-negligible rotation. Results are compared to observations and simulations and the fact that gaseous proto-clusters lie on an equilibrium sequence may imply that star formation could be to some extent disentangled from larger scale physics, offering an encouraging explanation for the universality of IMF.

Keywords: proto-cluster, star formation, cluster, gravity, IMF

## 1 Introduction

Star formation is a hierarchical process with involves a density change over orders of magnitude. Galaxy dynamics at kilo-parsec scales causes density concentrations through shocks and shearing forces. The structure forms from giant molecular associations or HI super-clouds down to parsec-scale molecular clouds (McKee & Ostriker 2007). Inside molecular clouds, further density concentration creates site of clustered star formation. These mass concentrations are often referred to as star-forming clumps, in which high star formation activity is observed while the stars are stilled embedded inside the gas. At a later stage of the stellar activities, massive stars start to combust violently or even reach the end of the lives, and therefore blowing the gas away by injecting energy into the interstellar medium (ISM). The formation phase of a cluster is thus terminated by expulsion of all the gas available for forming stars. It has been suggested in previous studies that most stars are formed in clusters (Lada & Lada 2003; Allen et al. 2007; McKee & Ostriker 2007). Depending on the amount of energy, the end product of this process is either an open cluster, which is gas free, with the stars directly observable, or individual stars dissociated from the cluster, becoming field stars. This mode of clustered star formation is, therefore, important for understanding the origin of stellar statistical properties, such as the initial mass function (IMF), which has a fundamental impact on the amount of feedback energy available from massive stars and also the number solar-type stars that can harbor life.

Given the large variation in density, which translates into free-fall time, and the spatial scales concerned. In order to properly address the physical processes that are important at different scales, star formation is often studied step by step. This study is focused on the gas assembly phase of cluster formation, where the interaction between gravity and turbulence are most dominating physical processes. The tight correlation between the mass-size relation of star-forming clumps and that of the stellar clusters (Pfalzner et al. 2016) also suggest that star formation should be studied in conditions that correspond to these dense entities*. Fall et al. (2010) inferred from observational results of molecular lines and dust continuum a stellar cluster mass-size relation $R \propto M^{0.38}$

[1] Laboratoire AIM, Paris-Saclay, CEA/IRFU/SAp – CNRS – Université Paris Diderot, 91191 Gif-sur-Yvette Cedex, France
[2] LERMA (UMR CNRS 8112), Ecole Normale Supérieure, 75231 Paris Cedex, France

*Both the terms star-forming clump and gaseous proto-clusters refer to dense substructures inside molecular clouds, where most star formation takes place, and are used indifferently inside this text.

for mass range from $10^2$ to $10^4$ solar masses. Similar studies from the ARLASGAL survey (Urquhart et al. 2014) concluded $R \propto M^{0.50}$. Given the data dispersion, this power-law exponent is compatible with value between 0.4 and 0.6. Previous studies (Hennebelle 2012; Matzner & Jumper 2015) tried to analytically describe the quasi-static growth of proto-cluster by balancing gravitational and turbulent forces, and studies the the proto-stellar population resulting from such environment. Meanwhile, Pfalzner (2011) regarded this mass-size relation as a growth sequence. So far these models have ignored rotation, which, however, has been observed in several stellar clusters (Hénault-Brunet et al. 2012; Davies et al. 2011; Mackey et al. 2013). Indeed structures forming from collapse usually show important rotation due to angular momentum conservation. We therefore follow a similar idea to Hennebelle (2012), while taking the rotation and turbulence into account to develop an analytical model to infer gaseous proto-cluster properties from those of the parent molecular cloud. Given the small infall and the observed sequence (Fall et al. 2010; Urquhart et al. 2014), an equilibrium, at globally equilibrium assumption is highly plausible. Our model applies to low-mass clusters, and those with mass above $10^4$ are beyond the scope of our discussion since more massive clumps tend to evolve more quickly and form massive stars that, in turn, disrupt the cloud via feedback. We caution that although we refer to this gaseous proto-cluster as the first phase of stellar cluster formation, this is actually a continuous process: the stars start to form as the gas proto-cluster is still accreting and finally take over after the gas expulsion. In this picture, the gaseous proto-cluster is globally in equilibrium, while density fluctuations therein cause local infall to form stars. This study is restricted to the earliest stage where the effects of the stars are less important.

## 2 Two-dimensional model: Modified virial theorem

We present a simple analytical model to describe the gaseous proto-cluster formation from a collapsing molecular cloud: a virial model, adapted to the turbulent and rotational kinematics of the cluster under mass accretion. We propose that a gaseous proto-cluster is in global virial equilibrium, and the rotational and turbulent kinetic energy support against self-gravity and ram pressure confinement. The rotation results from angular momentum conservation under collapse, while the turbulence is sustained by the accreting gas and dissipates through turbulent cascade. We start by deducing the two-dimensional virial theorem for an ellipsoidal structure with rotation and turbulence, and then discuss the energy balance from accretion and turbulent dissipation. The mass accretion rate and the specific angular momentum are evaluated as properties of the parent cloud. Finally, we present the mass-size relation predicted by the model.

### 2.1 Two-dimensional virial theorem of the gaseous proto-cluster

Rotation introduces non-isotropic motions which makes that the geometry is no longer spherical. We consider an oblate ellipsoid that has its minor-axis coinciding with the rotational axis. The three semi-axes are $R = R > H$. Neglecting the thermal and magnetic terms terms for simplicity, we calculate the virial integral of the system in two dimensions, by taking the inner product of the momentum equation $\rho d_t \vec{v} = -\rho \nabla \phi$ with the $\vec{r}$ and $\vec{z}$ vectors in the cylindrical coordinate before integrating over the volume of the ellipsoid. The integration of the inner product with $\vec{r}$ gives:

$$\frac{1}{2}\partial_t^2 \int_V \rho r^2 dV + \frac{1}{2}\partial_t \int_S \rho\ r^2 \vec{v}\cdot d\vec{S} + \int_S v_r r \rho \vec{v}\cdot d\vec{S} - \int_V \rho v_{2\mathrm{d}}^2 dV = -\frac{3}{5}\frac{GM^2}{R}\left[\frac{\cos^{-1}(\eta)}{(1-\eta^2)^{\frac{3}{2}}} - \frac{\eta}{1-\eta^2}\right] = -\frac{GM^2}{R}u_r(\eta), \tag{2.1}$$

where $v_{2\mathrm{d}}$ is the velocity dispersion in the $x-y$ plane, and $v_r$ is the velocity dispersion in the $\vec{r}$ direction; $\eta = \frac{H}{R}$ represents the aspect ratio of the ellipsoid. In the $\vec{z}$ direction we obtain

$$\frac{1}{2}\partial_t^2 \int_V \rho z^2 dV + \frac{1}{2}\partial_t \int_S \rho\ z^2 \vec{v}\cdot d\vec{S} + \int_S v_z z \rho \vec{v}\cdot d\vec{S} - \int_V \rho v_{1\mathrm{d}}^2 dV = -\frac{3}{5}\frac{GM^2}{R}\left[\frac{\eta}{1-\eta^2} - \frac{\eta^2\cos^{-1}(\eta)}{(1-\eta^2)^{\frac{3}{2}}}\right] = -\frac{GM^2}{R}u_z(\eta), \tag{2.2}$$

where $v_{1d} = v_z$ is the velocity dispersion in the $\vec{z}$ direction.

Virial equilibrium is reached when the time derivative terms are zero. The third term on the left-hand side of both equations is the counterpart of the ram pressure term in the spherical model (Hennebelle 2012), while the geometry renders its interpretation less obvious since we are ignorant of the mass infall pattern. But its impact is effectively less import and is neglected in this discussion. Therefore we have the equations for virial equilibrium in two dimensions by simplifying Eqs. (2.1) and (2.2) as

$$Mv_{2\mathrm{d}}^2 = \frac{GM^2}{R}u_r(\eta) \quad \text{and} \quad Mv_{1\mathrm{d}}^2 = \frac{GM^2}{R}u_z(\eta). \tag{2.3}$$

### 2.2 The energy equilibrium of an ellipsoidal cluster

In an accreting system, the turbulence is driven by the gravitational energy released from the accreted material (Klessen & Hennebelle 2010; Goldbaum et al. 2011), and it dissipates through the turbulent cascade on the timescale of the crossing time of the system. The turbulent energy is found by balancing the driving and the dissipation. Considering our ellipsoid with uniform density, the gravitational potential energy is given by the Legendre elliptical integral of the first kind $F(\varphi|k) = \int_0^{\varphi} \frac{d\theta}{\sqrt{1-k^2\sin\theta^2}}$:

$$E_{\mathrm{grav}} = \frac{3}{10}GM^2\frac{2}{\sqrt{R^2-H^2}}\cos^{-1}\left(\frac{H}{R}\right) = \frac{3}{5}\frac{GM^2}{R}\frac{\cos^{-1}(\eta)}{\sqrt{1-\eta^2}} = \frac{GM^2}{R}u_g(\eta).$$

The rate of gravitational that transforms into turbulent energy is

$$\dot{E}_{\mathrm{grav}} = \epsilon\frac{GM^2}{R}u_g(\eta)\left(\frac{2\dot{M}}{M} - \frac{\dot{R}}{R} + \frac{u_g'(\eta)\dot{\eta}}{u_g(\eta)}\right), \tag{2.4}$$

where the unknown factor $\epsilon \leq 1$ stands for the turbulence-driving efficiency, while part of the energy is dissipated at the accretion shock. Absorbing the second and third terms in the parenthesis into the uncertainties of accretion driving efficiency, we obtain a simplified expression

$$\dot{E}_{\mathrm{grav}} = \epsilon_{\mathrm{acc}}\frac{2GM\dot{M}}{R}u_g(\eta). \tag{2.5}$$

The turbulence dissipates via turbulent cascade on the crossing time of the system $\tau_{\mathrm{diss}}$, while the directional energy distribution and the relevant scale is less well understood in ellipsoidal geometry. We discuss two assumptions, which introduces two sets of equations with similar form but different coefficients. Firstly, we assume that the turbulence is anisotropic and that the turbulent energy follows the inertial regime of the Kolmogorov spectrum even though the structure is not spherically symmetric, that is, the energy cascades down length scales at the same rate and is eventually dissipated.

$$\dot{E}_{\mathrm{diss}} = \frac{3}{2}M\sigma_H^2/\tau_{\mathrm{diss}} = \frac{3}{2}M\sigma_H^2/\frac{2H}{\sigma_H} = \frac{3}{4}M\sigma_R^3/R. \tag{2.6}$$

Secondly, we make an alternative assumption that the inertial range at which the energy is dominating is reached at scales smaller than the cluster size, the turbulence should be isotropic. By assuming the dominating scale $\epsilon_{\mathrm{diss}}H < H$, we obtain

$$\dot{E}_{\mathrm{diss}} = \frac{3}{2}M\sigma_R^2/\tau_{\mathrm{diss}} = \frac{3}{2}M\sigma_R^2/\frac{2\epsilon_{\mathrm{diss}}H}{\sigma_R} = \frac{3}{4}M\sigma_R^3/\epsilon_{\mathrm{diss}}\eta R. \tag{2.7}$$

The rotation provides support only in the directions perpendicular to the rotational axis. Using the averaged specific angular momentum $j$, the rotational energy of the cluster is $2E_{\mathrm{rot}} = \frac{5}{2}M\left(\frac{j}{R}\right)^2$. The factor $\frac{5}{2}$ comes from uniform density and rigid body assumptions, which we verified with simulations to be not far from being realistic. Using Eqs. (2.3, 2.5, 2.6), and (2.7) while splitting the two-dimensional motion perpendicular to the short axis into rotation and turbulence, we obtain the equation set to be solved, i.e.,

$$\frac{5}{2}\left(\frac{j}{R}\right)^2 + s_r(\eta)\sigma^2 = \frac{GM}{R}u_r(\eta) \tag{2.8a}$$

$$s_z(\eta)\sigma^2 = \frac{GM}{R}u_z(\eta) \tag{2.8b}$$

$$\dot{E}_{\mathrm{diss}}/M = d(\eta)\frac{\sigma^3}{4R} = \dot{E}_{\mathrm{grav}}/M = \epsilon_{\mathrm{acc}}\frac{2G\dot{M}}{R}u_g(\eta), \tag{2.8c}$$

where the geometrical factors $s_r$, $s_z$, and $d$ are described in Eqs. (2.6) and (2.7) for two cases. The factors $u_r$, $u_z$, and $u_g$ are functions of $\eta$ of the ellipsoid, as shown in Fig. 1. The essential idea is to decompose the gravitational potential resulting from force in different directions. It could be readily verified that $u_r(\eta) + u_z(\eta) = u_g(\eta)$ and that $u_g(1) = \frac{3}{5}$, which corresponds to the spherical case.

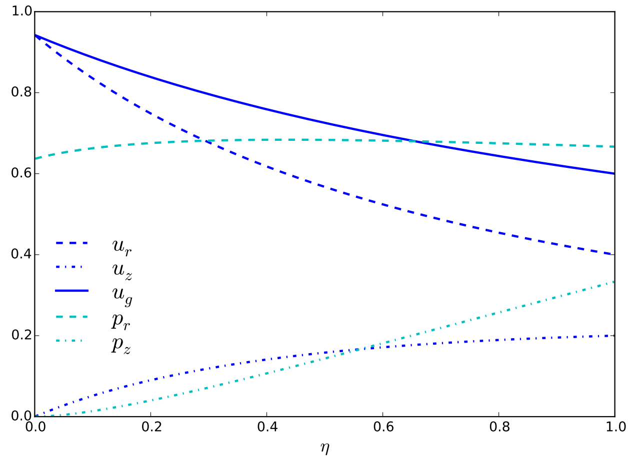


Fig. 1: Gravitational potential in blue curves (solid: complete potential $u_g$, dashed: $u_r$, dot-dashed: $u_z$) and the ram pressure factors in cyan as functions of the ellipsoid aspect ratio $\eta$.

### 2.3 Accretion rate and angular momentum

In order to solve the equilibrium equations, we estimate the mass accretion rate and angular momentum as functions of the cluster mass, or more precisely, the cloud mass.

The mass accretion rate can be estimated through simple free fall arguments, while assuming that in a cloud experiencing inside-out collapse, the mass-flux rate is almost constant at any radius and comparable to the cloud surface. This could be verified with some analytical calculations as well as from simulations. The left panel of Fig. 2 shows the gaseous proto-cluster mass accretion rate plotted against mass in a molecular cloud of $10^4$ solar mass collapsing onto several final radii $r_f$, corresponding to the range of the proto-cluster radius in our simulations. After the gaseous proto-cluster mass reaches over $10^3$ M$_\odot$, the accretion rate becomes weakly dependent on the cluster mass for any cluster radius and approaches a value that is characteristic of the cloud mass. It is therefore reasonable to estimate the cluster accretion rate with the cloud mass and from we obtain

$$\dot{M}_0 \propto M_\mathrm{c}\sqrt{\rho_\mathrm{c}}, \tag{2.9}$$

where $M_\mathrm{c}$ and $\rho_\mathrm{c}$ are the cloud mass and density. Consider a molecular cloud following the Larson relations (Larson 1981; Falgarone et al. 2004, 2009; Hennebelle & Falgarone 2012; Lombardi et al. 2010)

$$\rho_\mathrm{c} \propto R_\mathrm{c}^{-\gamma} \quad \text{and} \quad \sigma_\mathrm{c} \propto \sqrt{\frac{M}{R}} \propto R_\mathrm{c}^{1-\frac{\gamma}{2}}, \tag{2.10}$$

where different values of $\gamma$ (typically around 0.7 or 1) are quoted in the literature. We obtain

$$\dot{M}_0 \propto M_\mathrm{c}\sqrt{\rho_\mathrm{c}} \propto R_\mathrm{c}^3\,\rho_\mathrm{c}^{1.5} \sim R_\mathrm{c}^{3-1.5\gamma} \propto M_c^{(6-3\gamma)/(6-2\gamma)}. \tag{2.11}$$

With $\gamma = 1$ or 0.7, we get $\dot{M}_0 \propto M_c^{\gamma_{\dot{M}}}$, where $\gamma_{\dot{M}} = 0.75$ or 0.85, respectively. We multiply this accretion rate by an empirical correction in the presence of turbulence, which behaves like a dilution factor $(1-\kappa)$, where $\kappa = E_\mathrm{turb}/E_\mathrm{grav}$ is the ratio between turbulent kinetic energy and gravitational energy of the cloud. A numerical evaluation is made for the cloud of $10^4$ solar mass, obtaining

$$\dot{M} = \dot{M}_0\sqrt{1-\kappa} = 4.0\times 10^{-3}\ \mathrm{M}_\odot\ \mathrm{yr}^{-1}\left(\frac{\alpha_{*,c}M_*}{10^4\mathrm{M}_\odot}\right)^{\gamma_{\dot{M}}}\sqrt{1-0.35\left(\frac{\sigma_\mathrm{rms}}{\sigma_\mathrm{vir}}\right)^2}, \tag{2.12}$$

where $\alpha_{*,\mathrm{c}} = M_\mathrm{c}/M_*$ is the cloud-cluster mass ratio. An example of mass accretion rate evaluated at radius 1 pc, corresponding to $r_f/r_0 = 0.13$, is shown in the right panel of Fig. 2 for four simulations with different levels of turbulent support. This empirical correction for turbulent support is very simplistic but gives an error within a factor 2, and the four turbulence levels cover a large range of accretion rates, which all give reasonable mass-size relations. Thus this accretion rate approximation does not affect the results too much.

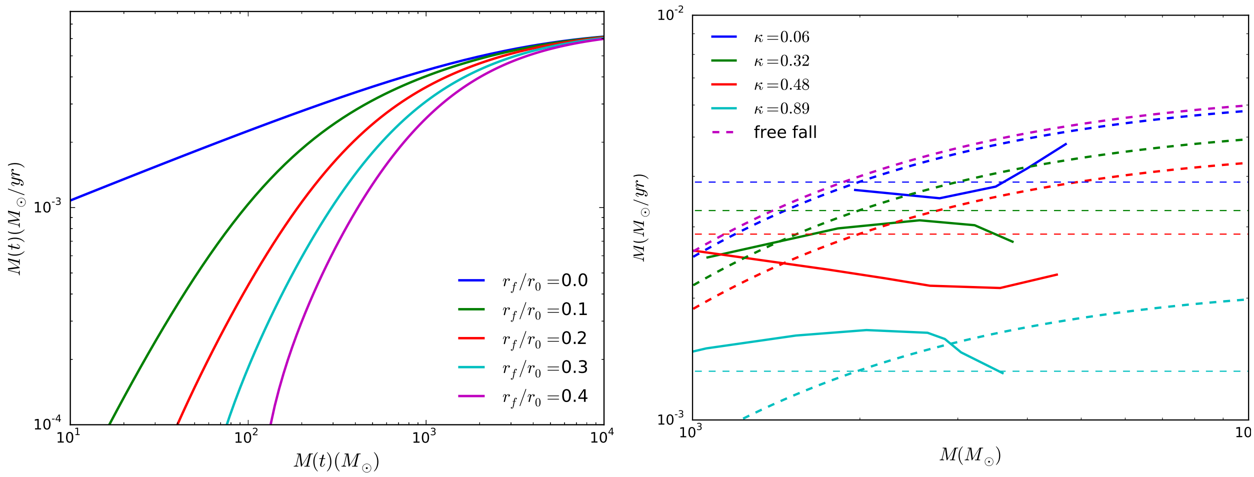


Fig. 2: **Left:** Mass accretion rate plotted against mass for several final radius values $r_f/r_0$ inside a $10^4$ $\mathrm{M}_\odot$ cloud, assuming the interior of the cloud collapses in free fall. The radius at which $\dot{M}$ is evaluated increases from the top to the bottom curve. **Right:** Mass accretion rate plotted against mass at $r = 1$ pc. The solid curves represent values evaluated in simulations with different levels of turbulent support. The dashed curve in magenta is the analytical solution for a $10^4$ $\mathrm{M}_\odot$ cloud in free fall. The empirically corrected accretion rate $\sqrt{1-\kappa}$ is plotted in dashed curves. The accretion rate is approximated to be constant at its value at $M_* = 2 \times 10^3$ $\mathrm{M}_\odot$.

The estimation of angular momentum follows the cancelation between turbulent vortices, which usually results in some residual rotation, that is then amplified by the collapse of the molecular cloud. We take a characteristic rotational velocity proportional to the turbulent velocity dispersion and follows the scaling law $v_{\mathrm{rot}} \propto v_{\mathrm{rms}}(r/r_0)^{0.5}$ (Dib et al. 2010; Burkert & Bodenheimer 2000). Using the Bonnor-Ebert-like density profile in our simulations (Lee & Hennebelle 2016a)

$$\rho(r) = \frac{\rho_0}{1+\xi^2},\ \xi = \frac{r}{r_0} \in [0, \xi_{\mathrm{ext}}], \tag{2.13}$$

where $\xi_{\mathrm{ext}} = r_{\mathrm{ext}}/r_0 = 3$ and assuming random rotational axis in spherical shells, we have the averaged specific angular momentum inside a sphere of radius $r$ with the density profile described in Eq. (2.13),

$$\bar{j}(r) = \left[\frac{\int\limits_{M(r)} (v_{rot} r)^2 dm}{\int\limits_{M(r)} dm}\right]^{\frac{1}{2}} = 0.22\ v_{\mathrm{rms}}\ r_0\ \frac{1}{2}\left[\frac{\xi^4 - 2\xi^2 + 2\log(1+\xi^2)}{\xi - \arctan(\xi)}\right]^{\frac{1}{2}}. \tag{2.14}$$

The constant is calibrated with the simulations. The average specific angular momentum plotted against mass at varying radius is plotted in Fig. 3 for the initial condition of four runs (solid curves) with varying levels of turbulent support, as well as the analytical solutions (dashed curves) with corresponding $v_{\mathrm{rms}}$. The specific angular momentum roughly has the dependence $\bar{j}(r) \propto M(r)^{0.59}$ in the mass range of our interest ($10^3 - 10^4$ $\mathrm{M}_\odot$). We do the consider the lost by angular momentum transport in our model since this effect is not very important at the cluster scale. The averaged specific angular momentum in the gaseous proto-cluster thus has the form:

$$j_* \ \propto\ j_{\mathrm{c}} \left(\frac{M_*}{M_{\mathrm{c}}}\right)^{0.59} \ \propto\ \sigma_{\mathrm{c}}\ R_{\mathrm{c}}\ \alpha_{*,\mathrm{c}}^{-0.59} \ \propto\ M_c^{(4-\gamma)/(6-2\gamma)}\ \alpha_{*,\mathrm{c}}^{-0.59}. \tag{2.15}$$

The last approximation comes from the Larson relations (Eqs. (2.10)). Applying physical values gives

$$j_* = 6.7 \times 10^{19} \mathrm{m}^2\mathrm{s}^{-1} \frac{\sigma_{\mathrm{rms}}}{\sigma_{\mathrm{vir}}} \left(\frac{\alpha_{*,c} M_*}{10^4 \mathrm{M}_\odot}\right)^{\gamma_j} \alpha_{*,\mathrm{c}}^{-0.59}, \tag{2.16}$$

where $\gamma_j = 0.75$ or $0.72$ corresponding to $\gamma = 1$ or $0.7$.

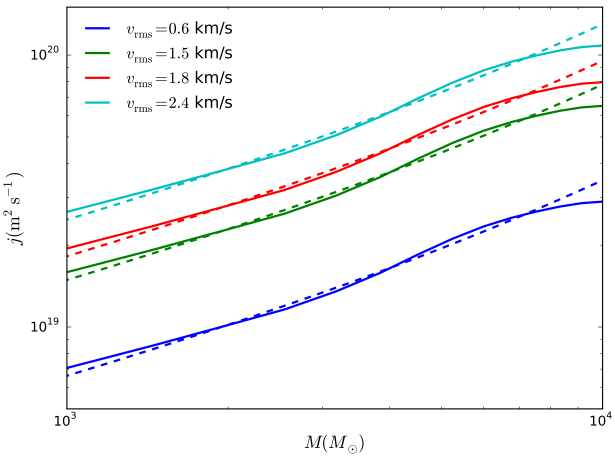


Fig. 3: Specific angular momentum plotted against mass contained inside varying radius. Solid curves represent the values calculated from the initial condition of the simulation. Dashed curves show the values estimated analytically. Values from four simulations with various initial turbulent supports are shown, and the specific angular momentum scales with the velocity dispersion.

### *2.4 Results and comparisons*

Given the parameters $\dot{M}$ and $j$, solving Eqs. (2.8) to infer the three variables $R$, $\eta$, $\sigma^2$ for a given mass in equilibrium is equivalent to solving for $\eta$ and $R$ from equations

$$f(\eta) = \frac{8\frac{5}{2}^{\frac{3}{2}} j^3 \dot{M}}{G^2 M^3} = \begin{cases} u_z^{\frac{3}{2}}\left(u_r - \frac{1+\eta^{\frac{2}{3}}}{\eta^{\frac{2}{3}}} u_z\right)^{\frac{3}{2}}(1+2\eta^{\frac{2}{3}})/(\epsilon_{\rm acc}\eta u_g) \\ u_z^{\frac{3}{2}}(u_r - 2u_z)^{\frac{3}{2}}3/(\epsilon_{\rm diss}\epsilon_{\rm acc}\eta u_g) \end{cases} \text{and } R = \frac{5j^2}{2GM} r(\eta) = \begin{cases} \frac{5j^2}{2GM}\left(u_r - \frac{1+\eta^{\frac{2}{3}}}{\eta^{\frac{2}{3}}} u_z\right)^{-1} \\ \frac{5j^2}{2GM}\left(u_r - 2u_z\right)^{-1} \end{cases}, \tag{2.17}$$

where the upper row is the anisotropic solution and the bottom row the isotropic one. The functions $f(\eta)$ and $r(\eta)$ are geometrical factors that depend on $\eta$. The solution occurs at the intersection of $f(\eta)$ and a constant determined by $M$, $\dot{M}$, and $j$ as seen in Eqs. (2.17). Since $f(\eta)$ is first increasing and then decreasing in the interval $\eta \in [0, 1]$, two solutions coexist when there are solutions. The solution with a higher value of $\eta$ is physical because it reduces to the spherical case when the angular momentum goes to zero. The recovered $\eta$ value in turn gives the radius of the gaseous proto-cluster.

The gaseous proto-cluster mass-size relation is governed by several parameters. We apply some canonical values to illustrate the solution properties in Fig 4. Three cloud-cluster mass ratios $\alpha_{*,\rm c} = 1, 2, 3$ are used for virialized molecular clouds, i.e., $\sigma_{\rm rms}/\sigma_{\rm vir} = 1$, in Eqs. (2.12 and 2.16). The canonical turbulence driving efficiency $\varepsilon = 0.5$ is used; see Eqs. (2.7, 2.8, and 2.17), $\varepsilon = \epsilon_{\rm acc}$ and $\varepsilon = \epsilon_{\rm diss}\epsilon_{\rm acc}$, respectively. The resulting mass-size relation is shown in Fig. 4 for two $\gamma$ values. The dispersion of observations is compatible with a large range of the model parameters, guaranteeing the robustness of our model prediction regardless of some poorly controlled factors. Our model yields a $R \propto M^{0.5}$ relation for $\gamma = 1$ and $R \propto M^{0.42-0.44}$ for $\gamma = 0.7$. These power-law exponents are compatible with those from Fall et al. (2010, 0.38) and Urquhart et al. (2014, 0.50). We overplot the model with their star-forming clumps. The trend is very closely reproduced. The mass-size relations that we obtained is thus robust despite our ignorance of the properties of the turbulence, which only introduces a slight change in aspect ratio of the proto-clusters. The curves do not represent evolutionary sequences. After a gaseous proto-cluster reaches equilibrium, it evolves toward sequences with smaller $\alpha_{*,\rm c}$ presuming that the parent cloud is not accreting mass much faster than the gaseous proto-cluster. We trace in yellow the gaseous proto-cluster formed inside a $10^4$ $\rm M_\odot$ cloud in Fig. 4, which is indicative as an evolutionary sequence following $R \propto M$. A clump does not migrate too much on this equilibrium sequence during their lifespan, and the mass-size relation observed for star-forming clumps is rather a result of gaseous proto-clusters forming from a range of different gas reservoir than an evolutionary track.

We evaluate the proto-cluster mass and size from simulations and over plot the results on the model predictions in Fig. 5. The level of turbulent support is represented by the virial parameter $\alpha_{\rm vir} = 2E_{\rm kin}/E_{\rm grav}$.

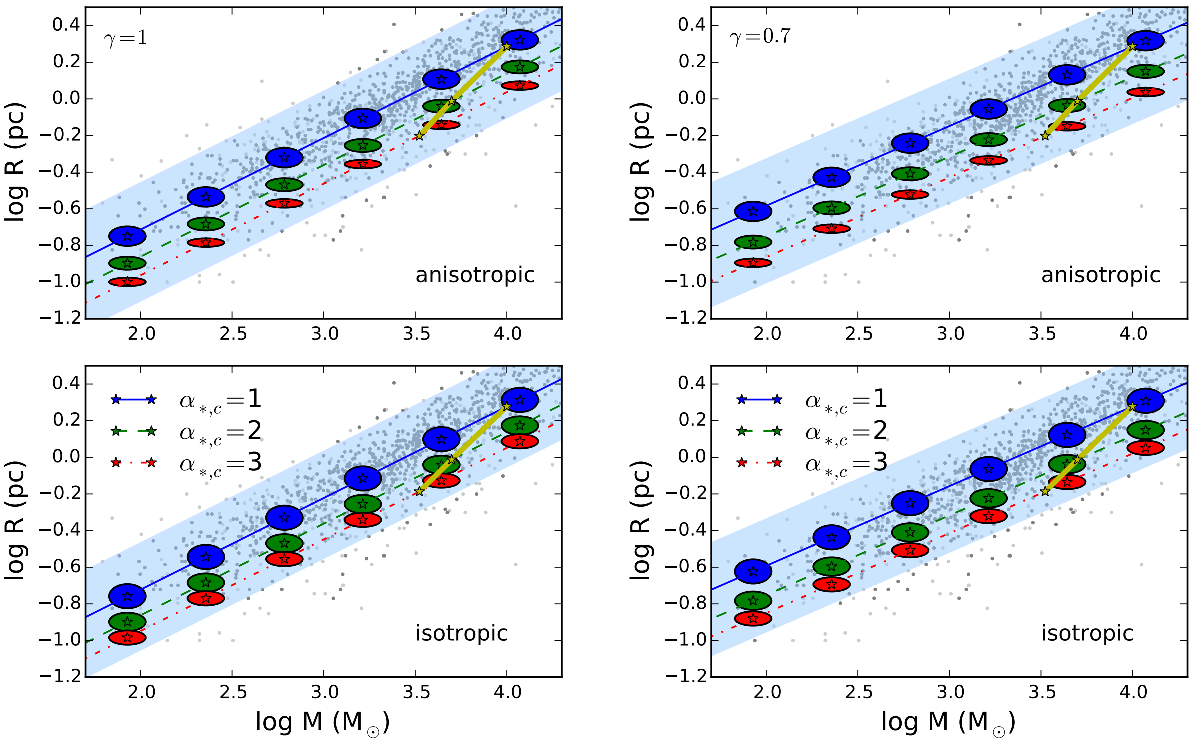


Fig. 4: **Left:** Mass-size relation of ellipsoidal clusters, shown with cloud-cluster mass ratio $\alpha_{*,\mathrm{c}} = 1, 2, 3$, plotted with blue solid, green dashed, red dot-dashed lines, respectively, using anisotropic turbulence following Kolmogorov spectrum (upper panel) and isotropic turbulence (lower panel). The turbulence efficiency $\varepsilon = 0.5$ is used, and the shadowed region represents the range of solutions for $\varepsilon \in [0.2, 0.7]$. The radius of the cluster decreases with increasing $\varepsilon$. The elliptical patches represent the form of the clusters. With the molecular cloud density-size relation $\rho \propto R^{-1}$, the clusters follow a $R \propto M^{0.5}$ trend for a given $\alpha_{*,\mathrm{c}}$. The gaseous proto-cluster corresponding to $10^4$ $\mathrm{M}_\odot$ parent cloud is traced in yellow, indicating of an evolutionary sequence roughly following $R \propto M$. The radius of the gaseous proto-cluster does not depend too much on the underlying assumption of the turbulent energy distribution, while the aspect ratio is smaller in the anisotropic case since there is relatively less turbulent support in the vertical direction. The dots are the observed star-forming clumps from Fall et al. (2010) and Urquhart et al. (2014). **Right:** Same plots as figures on the left for gaseous proto-clusters inside parent clouds following $\rho \propto R^{-0.7}$ relation. The mass-size relation follows $R \propto M^{0.42-0.44}$.

The angular momentum and mass accretion rate are calculated accordingly for each case. We show models with values $\gamma = 1$ and 0.7. The results show that the proto-cluster could be identified at a relative early stage when the mass is still small, and that as it accretes mass, it arrives on the sequence where virial equilibrium is reached. The model is not in good coherence with simulation results at early time, possibly because the time-dependent terms and ram pressure are still relatively important and should not be neglected, while we use quasi-stationary assumptions. Once the mass is large enough, the simulations are in good agreement with the model. The case with $\alpha_{\mathrm{vir}} = 0.12$ is probably too strongly accreting owing to the weak kinetic support, thus this case does not correspond well to the quasi-stationary model.

### 2.5 *The IMF peak position*

The theoretical prediction of the core mass function (CMF) peak position (Hennebelle & Chabrier 2013) depends on the Jeans mass and the Mach number of the star-forming gas. We calculate the Jeans mass $M_{\mathrm{J}} = \pi^{5/2} c_s^3 / 6\sqrt{G^3 \rho}$ (thin curves) and the predicted CMF peak mass $M_{\mathrm{peak}} = M_{\mathrm{J}}/(1 + b^2 \mathcal{M}^2)$ (thick curves), which are shown in Fig. 6, from the proto-cluster properties predicted by our model. A canonical value $b = 0.5$ is used (Federrath et al. 2010). We present the result with two $\gamma$ values (see Eq. (2.10)) and two polytropic equation of state $P \propto \rho^{\Gamma}$ with $\Gamma = 1$ or 0.85. With increasing mass, the Jeans mass increases with decreasing density. On the other hand, the turbulence increases with gaseous proto-cluster mass and gives a reasonable IMF peak prediction assuming that CMF and IMF peaks coincide. In the mass range between $10^2$ and $10^4$

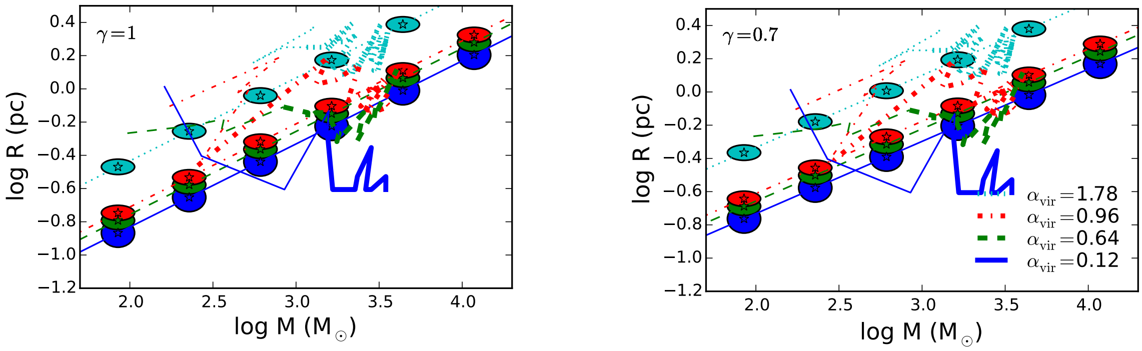


Fig. 5: **Left:** Mass-size relation of ellipsoidal clusters. The proto-cluster identified from simulations are overplotted with models of the corresponding levels of turbulence with $\gamma = 1$ . Canonical values of cloud-cluster mass ratio $\alpha_{*,\rm c} = 3$ and $\varepsilon = 0.5$ are used along with isotropic turbulence. The velocity dispersion increases from the bottom to the top curve. Simulation results at time before 2 Myr are plotted with thin lines. The model is in good agreement with simulation only after the proto-cluster gains enough mass, possibly implying that the time dependent terms and ram pressure should not be neglected at early stage. **Right:** Same as left panel but with $\gamma = 0.7$.

solar mass, where most clusters are observed, the predicted IMF peak value is around $0.1 - 0.3$ $\mathrm{M}_\odot$ with less than 1 dex variation.

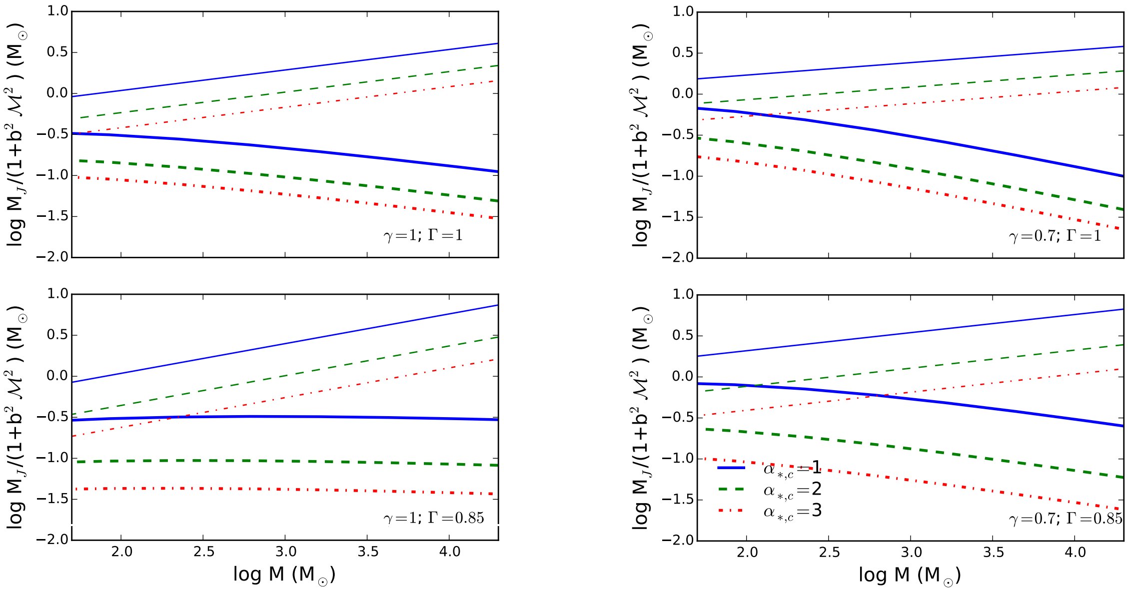


Fig. 6: Initial mass function peak prediction from proto-cluster model with isotropic turbulence for cloud-cluster mass ratio $\alpha_{*,\rm c} = 1, 2, 3$ plotted against proto-cluster mass. The values 1 and 0.7 are used for the Larson relation $\rho \propto R^{-\gamma}$. As for the polytropic index $\Gamma$ of gas inside the proto-cluster, values 1 (isothermal) and 0.85 are considered. The Jeans mass is plotted with thin curves, and the IMF peak mass is plotted with thick curves. Color codings are same as those in Fig. 4.

## 3 Conclusions

One important message is that stars do not form uniformly in molecular clouds. In this study, we confronted observations and simulations with a simple analytical model. We showed that before stars start forming, the molecular cloud gas is reprocessed through gravo-turbulent interaction and a gaseous proto-cluster environment in global equilibrium is established, which is much more favorable for star formation than the diffuse large-scale molecular clumps. This gaseous proto-cluster sets a more general condition for stellar cluster formation and to some extent decouples star formation from the large-scale molecular clump. This is supports the idea that stellar clusters form in similar environments and that the IMF is regulated by more local conditions. We developed a two-dimensional model for a system with rotation, turbulence, and accretion, which predicts the radius, aspect ratio, and velocity dispersion given the mass, angular momentum, and accretion rate of the system. Readers interested by more details are invited to refer to Lee & Hennebelle (2016b).

The gaseous proto-clusters lie on an equilibrium sequence that is governed by the interaction of gravity and turbulence, which yields a mass-size relation similar to the Larson relation, while a gaseous proto-cluster is roughly ten times more massive than a molecular cloud of the same size. Such a resemblance is seen in the two relations since both are outcomes of turbulence and gravity interaction. Notwithstanding, we emphasize that in the case of a gaseous proto-cluster, accretion is relatively important in concentrating mass and sustaining turbulence, thus creating an environment different from that of the molecular cloud. As most stars form in clusters, the gaseous proto-cluster properties should be indeed used for understanding star formation. Using a simple estimate for the peak position of the CMF, we show that because of various compensations, it depends only weakly on the cluster mass, which suggests that the physical conditions of gaseous proto-clusters may be, at least in part, responsible for the apparent universality of the IMF.

This work was granted access to HPC resources of CINES under the allocation x2014047023 made by GENCI (Grand Equipement National de Calcul Intensif). This research has received funding from the European Research Council under the European Community's Seventh Framework Programme (FP7/2007-2013 Grant Agreement no. 306483).

## References

Allen, L., Megeath, S. T., Gutermuth, R., et al. 2007, Protostars and Planets V, 361
Burkert, A. & Bodenheimer, P. 2000, ApJ, 543, 822
Davies, B., Bastian, N., Gieles, M., et al. 2011, MNRAS, 411, 1386
Dib, S., Hennebelle, P., Pineda, J. E., et al. 2010, ApJ, 723, 425
Falgarone, E., Hily-Blant, P., & Levrier, F. 2004, Ap&SS, 292, 89
Falgarone, E., Pety, J., & Hily-Blant, P. 2009, A&A, 507, 355
Fall, S. M., Krumholz, M. R., & Matzner, C. D. 2010, ApJ, 710, L142
Federrath, C., Roman-Duval, J., Klessen, R. S., Schmidt, W., & Mac Low, M.-M. 2010, A&A, 512, A81
Goldbaum, N. J., Krumholz, M. R., Matzner, C. D., & McKee, C. F. 2011, ApJ, 738, 101
Hénault-Brunet, V., Gieles, M., Evans, C. J., et al. 2012, A&A, 545, L1
Hennebelle, P. 2012, A&A, 545, A147
Hennebelle, P. & Chabrier, G. 2013, ApJ, 770, 150
Hennebelle, P. & Falgarone, E. 2012, A&A Rev., 20, 55
Klessen, R. S. & Hennebelle, P. 2010, A&A, 520, A17
Lada, C. J. & Lada, E. A. 2003, ARA&A, 41, 57
Larson, R. B. 1981, MNRAS, 194, 809
Lee, Y.-N. & Hennebelle, P. 2016a, A&A, 591, A30
Lee, Y.-N. & Hennebelle, P. 2016b, A&A, 591, A31
Lombardi, M., Alves, J., & Lada, C. J. 2010, A&A, 519, L7
Mackey, A. D., Da Costa, G. S., Ferguson, A. M. N., & Yong, D. 2013, ApJ, 762, 65
Matzner, C. D. & Jumper, P. H. 2015, ApJ, 815, 68
McKee, C. F. & Ostriker, E. C. 2007, ARA&A, 45, 565
Pfalzner, S. 2011, A&A, 536, A90
Pfalzner, S., Kirk, H., Sills, A., et al. 2016, A&A, 586, A68
Urquhart, J. S., Moore, T. J. T., Csengeri, T., et al. 2014, MNRAS, 443, 1555

*SF2A 2016*
*C. Reylé, J. Richard, L. Cambrésy, M. Deleuil, E. Pécontal, L. Tresse and I. Vauglin (eds)*

# THE CHANGING MAGNETIC FIELDS OF INTERMEDIATE-MASS T TAURI STARS

F. Villebrun[1], E. Alecian [1], J. Bouvier [1], G. Hussain [2,3] and C. P. Folsom [2]

**Abstract.** Through their pre-main sequence phase (PMS phase), intermediate-mass stars evolve from a fully convective structure to a radiative structure in their interiors. During this transition, the occurence of strong magnetic fields drops from 100% to 7-8%. The reasons for this drop are yet unclear, and in order to understand it we need to characterise the magnetic fields of these intermediate-mass PMS stars, and compare them with the fundamental and evolutionary properties of the stars. As a first step, we determined their effective temperatures and luminosities. We show here the ESPaDOnS and HARPSpol spectra processing that brought up our results.

Keywords: intermediate-mass stars, pre-main sequence stars, fossil magnetic fields, dynamo fields

## 1 Introduction

Stars at all masses appear on the HR diagram along the birthline. They start fully convective, then for more massive stars a radiative core forms and grows until the stars become fully radiative. A small convective core then develops right before they reach the Zero-Age-Main-Sequence (ZAMS). Such structural changes have important implications: during the convective phase, where the stars are either fully convective or have a convective envelope (orange and green regions in Fig. 1), magnetic fields are presumably generated via a dynamo process. In the radiative phase (the blue and pink regions in Fig. 1), no strong fields are generated in the envelope, while the dynamo field of the core takes too long to appear at the surface (e.g. Moss 2001).

The magnetic field properties of main sequence intermediate-mass stars (1.5 to 8$M_\odot$, of spectral type A and late-B, A/B stars hereafter) are now well established. Strong magnetic fields are found in 5 to 10% of these stars. They are mainly dipolar, stable over many years and even decades (Donati & Landstreet 2009) with strengths of the order of 1 kG. Such stable and large-scale fields are called fossil fields (i.e. they are not continuously sustained from dissipation). Studies of the PMS progenitors of A/B stars, the Herbig Ae/Be (HAeBe) stars, have shown that fossil fields are present as early as the PMS phase (Alecian et al. 2013). One of the challenges today is to understand the origin of such fossil fields. The current leading theory considers that fossil fields are remnants of fields generated during the convective phase of the PMS stellar evolution. Theoretical and numerical works have demonstrated that fields generated in a previous convective phase can relax into stable fields during the transition from the convective to the radiative phase, under peculiar conditions involving the rotation rate and the proportion of poloidal to toroidal fields (Duez & Mathis 2010; Emeriau & Mathis 2015; Gaurat et al. 2015).

In addressing these issues, it is instructive to consider T Tauri stars. T Tauri stars are PMS stars of spectral types FGKM (Herbig 1962). They possess large circumstellar disks and many are still actively accreting. Intermediate-mass T Tauri stars (IMTTS, 1.2 to 4 $M_\odot$) are precursors to HAeBe stars. Spectropolarimetric studies of over 15 low-mass T Tauri stars have revealed that - unlike in HAeBes - magnetic fields are ubiquitous in these systems and of dynamo type (Hussain et al. 2009; Donati et al. 2008, 2010, 2011). No equivalent study has ever been performed in IMTTS. We thus want to determine the magnetic fields characteristics of IMTTS

[1] Université Grenoble Alpes, CNRS, IPAG, F-38000 Grenoble, France
[2] Institut de Recherche en Astrophysique et Planétologie, Université de Toulouse, UPS-OMP, F-31400 Toulouse, France
[3] European Southern Observatory, Karl-Schwarzschild-Str. 2, 85748 Garching bei München, Germany e-mail: ghussain@eso.org

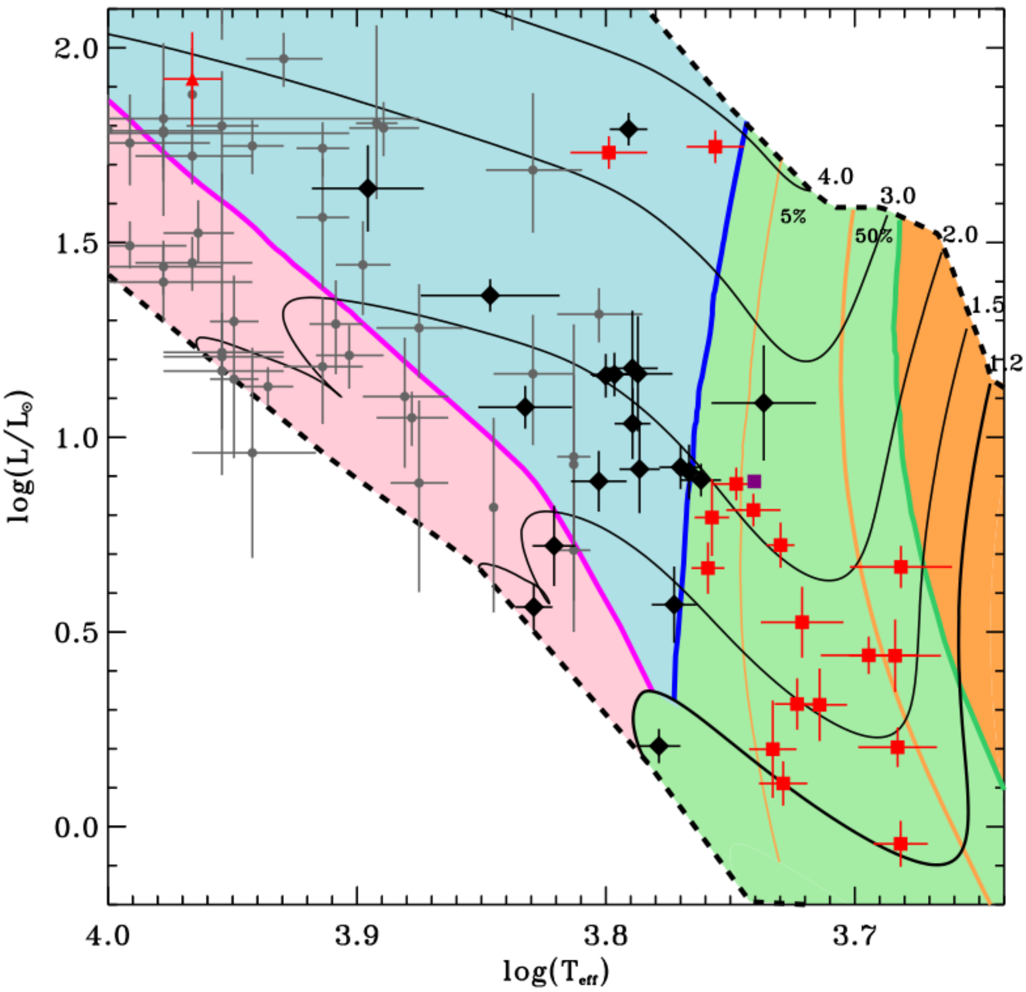


**Fig. 1.** IMTTS (large symbols) and some of the HAeBes (small dots) plotted in an HR diagram. Red squares are the IMTTS observed in 2012 in which a magnetic field has been detected. Black diamonds are the IMTTS observed in 2012 in which no magnetic field has been detected. The purple square (without error bars) is CV Cha, the only IMTTS with a well-constrained magnetic map (Hussain et al. 2009). The youngest magnetic HAeBe star (HD 190073) is indicated with a red triangle. The PMS evolutionary tracks (full black line) for labelled mass ($M_\odot$) and the ZAMS (thick dashed-line) are also overplotted. The shaded areas have the following meaning; orange: fully convective; green: radiative core + convective envelope; blue: fully radiative; and pink: convective core + radiative envelope. The thick coloured lines represent the limit between each of these regions. The 2 orange lines mark the ratio $M_{\rm conv.env.}/M_{\rm star}$ of 50% and 5%, tracing the changing internal structure of the stars. Figure updated from fig. 6 in Hussain & Alecian (2014).

(topologies, strengths and stabilities) from the fully convective region (orange) to the fully radiative region (blue). If the magnetic topology is simple, and predominantly dipolar, the field is likely fossil in origin as this is the topology found in nearly all fossil field stars. If the field is complex, multipolar, and/or has a significant toroidal component, then it is likely dynamo generated. We will thus be able to determine the time-scales and conditions in stellar interiors under which fossil fields are maintained.

Before reconstructing the surface magnetic fields of these IMTTS, we first need to determine two of their fundamental parameters : their effective temperatures $T_{\rm eff}$ and their luminosities $L$. $T_{\rm eff}$ and $L$ will enable us to accurately position them in the HR diagram, providing strong constraints on their internal structure. We used the 114 ESPaDOnS and HARPSpol (respectively at CFHT and at 3.6m ESO La Silla) spectropolarimetric data of 44 IMTTS we acquired in 2012 for detecting magnetic fields in these stars. The data have been reduced using Libre-Esprit and the REDUCE software adapted for HARPSpol (e.g. Alecian et al. 2011).

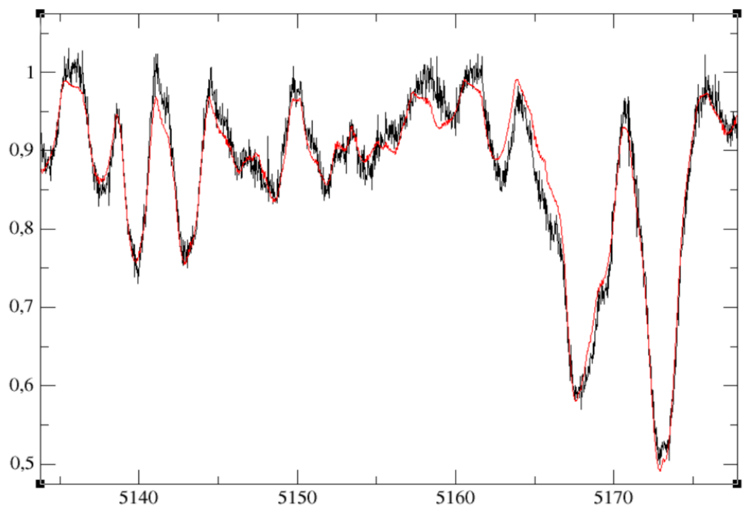


**Fig. 2.** Spectrum of COUP 1350 (black) measured by ESPaDOnS, and the best fit we get using the ZEEMAN spectrum synthesis code (red). Only a small portion of the spectrum is shown. As an example, for this star, we get $T_{\rm eff}$=5592.6K ($\sigma$=127.5K) and $v\sin i$=61.80km/s ($\sigma$=1.03km/s).

## 2 Spectra processing

### 2.1 Spectra renormalization

To derive the stars' effective temperatures, the spectrum synthesis code ZEEMAN (Landstreet 1988; Wade et al. 2001; Folsom et al. 2012) needs accurately normalized spectra. The normalization provided by the data reduction pipeline being insufficient for our work, we used a polynomial renormalization routine (C. Folsom, PhD Thesis, Sect 5.1). This routine determines continuum points in the stellar spectrum order by order, and then fits a polynomial function based on these continuum points. The original spectrum is then divided by the fitted polynomial function, making sure that the spectrum is sufficiently well-normalized for our study. For high-$v\sin i$ stars, renormalization can be challenging as line broadening can make the continuum difficult to determine. We therefore need to be much more cautious when continuum-fitting the spectra of rapidly rotating stars ($v\sin i > 80$km/s) by selecting continuum points with more demanding standards.

### 2.2 Spectra fitting

Once properly normalized, we used the spectrum synthesis code ZEEMAN and stellar atmospheric models from MARCS (Gustafsson et al. 2008) to derive stellar parameters. By a $\chi^2$-minimization procedure (see Fig. 2) ZEEMAN makes every non-fixed stellar parameter converge to its best solution. To get a better accuracy on the parameters we were interested in ($T_{\rm eff}$ and $v\sin i$) we reduced the number of degrees of freedom by setting all the other stellar parameters to the reference quantities used for these stars: log(g)=4.0, $v_{\rm macro}$ = 2km/s, and solar abundances (Asplund et al. 2009). We discarded wavelength windows that fall into one of the following cases: potentially affected by telluric lines, potentially affected by emission lines, bad quality fits (with a high RMS difference with respect to the rest of the spectrum), close to the blue-edge (noise is high here), close to the red-edge (many telluric lines at high $\lambda$). By using as much spectral information as possible for each spectrum, 2-6 spectra for each IMTTS of our sample, and by excluding bad quality fits with a 1 or 2 $\sigma$-clipping, we derived $T_{\rm eff}$ and $v\sin i$ with typical uncertainties of $\sim$ 120K and $\sim$ 1.5km/s respectively (450K and 20km/s for the most challenging cases, respectively).

### 2.3 Luminosity determination

To position our sample of IMTTS in the HR diagram, we also needed to compute their luminosities. We based our calculations on the (V-J) band, (B-V) being more affected by accretion and circumstellar extinction. We took the J magnitudes from the 2MASS survey (Cutri et al. 2003) and the V magnitudes mainly from Kharchenko (2001), or from the NOMAD catalog (Zacharias et al. 2004). We used theoretical $(V\text{-}J)_o$ of 5-30 Myr intermediate-mass stars from Pecaut & Mamajek (2013) to compute the color excesses E(V-J) and extinctions $A_J$. The total to selective extinction $R_J$=0.437 has been determined from the color excesses and extinctions relationships shown in Casagrande et al. (2010). We then used new GAIA parallaxes (Gaia Collaboration et al. 2016) to determine the absolute magnitudes $M_J$ of our stars, and theoretical bolometric corrections $(BC)_J$ from

Pecaut & Mamajek (2013) to get their bolometric magnitudes. Finally, using $M_{bol\odot}$=4.74 from Cox (2000), we determined their bolometric luminosities. For a dozen of stars, GAIA parallaxes were not available: we thus used the best distance estimate of their corresponding star-forming region/cluster found in the literature.

## 3 Conclusion

Our estimates of $T_{\rm eff}$ and luminosities are displayed on the HR diagram with their associated error bars (see Fig 1.). Preliminary studies of our spectropolarimetric data indicate that about half of our IMTTS are magnetic (red) contrary to the non-magnetic ones (black). We find that almost all stars in the convective regions (orange and green) are magnetic. Once the envelope of the stars becomes fully radiative (blue and pink regions) the magnetic incidence drops dramatically, implying that a drastic selection must be made.

To determine the circumstances of this selection, we plan to map the surface magnetic fields of IMTTS in the convective region (green). Mapping the surface magnetic fields of IMTTS at different stages of their evolution through the PMS will enable us to compare these magnetic fields with the fundamental and evolutionary properties of these stars, which are now better constrained thanks to the determination of $T_{\rm eff}$ and $L$ that we performed.

This work has made use of data from the European Space Agency (ESA) mission *Gaia* (`http://www.cosmos.esa.int/gaia`), processed by the *Gaia* Data Processing and Analysis Consortium (DPAC, `http://www.cosmos.esa.int/web/gaia/dpac/consortium`). Funding for the DPAC has been provided by national institutions, in particular the institutions participating in the *Gaia* Multilateral Agreement.

Villebrun F. is financed by the AGIR program of the Université Grenoble Alpes.

## References

Alecian, E., Kochukhov, O., Neiner, C., et al. 2011, A&A, 536, L6

Alecian, E., Wade, G. A., Catala, C., et al. 2013, MNRAS, 429, 1001

Asplund, M., Grevesse, N., Sauval, A. J., & Scott, P. 2009, ARA&A, 47, 481

Casagrande, L., Ramírez, I., Meléndez, J., Bessell, M., & Asplund, M. 2010, A&A, 512, A54

Cox, A. N. 2000, Allen's astrophysical quantities

Cutri, R. M., Skrutskie, M. F., van Dyk, S., et al. 2003, VizieR Online Data Catalog, 2246

Donati, J.-F., Bouvier, J., Walter, F. M., et al. 2011, MNRAS, 412, 2454

Donati, J.-F., Jardine, M. M., Gregory, S. G., et al. 2008, MNRAS, 386, 1234

Donati, J.-F. & Landstreet, J. D. 2009, ARA&A, 47, 333

Donati, J.-F., Skelly, M. B., Bouvier, J., et al. 2010, MNRAS, 402, 1426

Duez, V. & Mathis, S. 2010, A&A, 517, A58

Emeriau, C. & Mathis, S. 2015, in IAU Symposium, Vol. 307, New Windows on Massive Stars, ed. G. Meynet, C. Georgy, J. Groh, & P. Stee, 373–374

Folsom, C. P., Bagnulo, S., Wade, G. A., et al. 2012, MNRAS, 422, 2072

Gaia Collaboration, Brown, A. G. A., Vallenari, A., et al. 2016, ArXiv e-prints

Gaurat, M., Jouve, L., Lignières, F., & Gastine, T. 2015, A&A, 580, A103

Gustafsson, B., Edvardsson, B., Eriksson, K., et al. 2008, A&A, 486, 951

Herbig, G. H. 1962, Advances in Astronomy and Astrophysics, 1, 47

Hussain, G. A. J. & Alecian, E. 2014, in IAU Symposium, Vol. 302, Magnetic Fields throughout Stellar Evolution, ed. P. Petit, M. Jardine, & H. C. Spruit, 25–37

Hussain, G. A. J., Collier Cameron, A., Jardine, M. M., et al. 2009, MNRAS, 398, 189

Kharchenko, N. V. 2001, Kinematika i Fizika Nebesnykh Tel, 17, 409

Landstreet, J. D. 1988, ApJ, 326, 967

Moss, D. 2001, in Astronomical Society of the Pacific Conference Series, Vol. 248, Magnetic Fields Across the Hertzsprung-Russell Diagram, ed. G. Mathys, S. K. Solanki, & D. T. Wickramasinghe, 305

Pecaut, M. J. & Mamajek, E. E. 2013, ApJS, 208, 9

Wade, G. A., Bagnulo, S., Kochukhov, O., et al. 2001, A&A, 374, 265

Zacharias, N., Monet, D. G., Levine, S. E., et al. 2004, in Bulletin of the American Astronomical Society, Vol. 36, American Astronomical Society Meeting Abstracts, 1418

*SF2A 2016*
*C. Reylé, J. Richard, L. Cambrésy, M. Deleuil, E. Pécontal, L. Tresse and I. Vauglin (eds)*

# FORMATION HISTORY OF OLD OPEN CLUSTERS CONSTRAINED BY DETAILED ASTEROSEISMOLOGY OF RED GIANT STARS OBSERVED BY KEPLER

E. Corsaro[1,2,3], Y.-N. Lee[1], R. A. García[1], P. Hennebelle[1], S. Mathur[4], P. G. Beck[1], S. Mathis[1], D. Stello[5,6] and J. Bouvier[7]

**Abstract.** Stars originate by the gravitational collapse of a turbulent molecular cloud, often forming clusters of thousands of stars. Stellar clusters therefore play an important role in our understanding of star formation, a fundamental problem in astrophysics that is difficult to investigate because pre-stellar cores are typically obscured by dust. Thanks to a Bayesian analysis of about 50 red giants of NGC 6791 and NGC 6819, two old open clusters observed by NASA Kepler, we characterize thousands of individual oscillation modes. We show for the first time how the measured asteroseismic properties lead us to a discovery about the rotation history of these clusters. Finally, our findings are compared to 3D hydrodynamical simulations for stellar cluster formation to put strong constraints on the physical processes of turbulence and rotation, which are in action in the early formation stage of the stellar clusters.

Keywords: open clusters and associations: individual (NGC 6791, NGC 6819) – stars: oscillations – stars: late-type – stars: formation – stars: rotation – techniques: Bayesian – methods: numerical

## 1 Introduction

Most of the star formation in the Galaxy is occurring within massive giant molecular clouds Lee et al. (2012). Giant molecular clouds are expected to form hundred of thousands of stars that can originate stellar clusters if the system is able to remain gravitationally bound well beyond its formation phase. This shows that investigating the early dynamical evolution of the molecular clouds is crucial for understanding the star and planet formation processes at different epochs and by taking into account the diversity of environments in the Galaxy (Lada & Lada 2003; Longmore et al. 2014). However, the star forming regions are obscured by dust, hence direct observations are limited to the infrared and radio bands. Stellar clusters, which are born embedded to giant molecular clouds, therefore represent important benchmarks to test stellar and planetary formation, and stellar evolution theories. Open clusters in particular generally contain a small amount or no interstellar medium, which makes them well suitable for studies involving a broad range of wavelengths other than the infrared and radio ones. In addition, conversely to globular clusters, stars in open clusters are sparse enough, with a density of at least 1 $M_\odot$ pc$^{-3}$, thus providing the opportunity to perform detailed analyses on individual stellar members. The great advantage of this approach is that the stars in a cluster — as opposed to field stars that often originate from the dissolution of small stellar systems — can preserve the signature of the initial conditions of the progenitor cloud.

Little is known on the role of angular momentum on the early stage formation of stars in open clusters. It is believed that molecular clouds satisfying the Jeans instability undergo a gravitational collapse in which

[1] Laboratoire AIM Paris-Saclay, CEA/DRF — CNRS — Université Paris Diderot, IRFU/SAp Centre de Saclay, F-91191 Gif-sur-Yvette Cedex, France
[2] Instituto de Astrofísica de Canarias, E-38200 La Laguna, Tenerife, Spain
[3] Departamento de Astrofísica, Universidad de La Laguna, E-38205 La Laguna, Tenerife, Spain
[4] Space Science Institute, 4750 Walnut street Suite 205, Boulder, CO 80301, USA
[5] Sydney Institute for Astronomy (SIfA), School of Physics, University of Sydney, Sydney, New South Wales 2006, Australia
[6] Stellar Astrophysics Centre, Department of Physics and Astronomy, Aarhus University, Ny Munkegade 120, DK-8000 Aarhus C, Denmark
[7] Université Grenoble Alpes, IPAG, F-38000 Grenoble, France; CNRS, IPAG, F-38000 Grenoble, France

the internal motions are strongly influenced by turbulence (Shu et al. 1987). This implies that the angular momentum from the progenitor gas cloud cannot leave any significant imprint of their action in the resulting stars of the cluster. From a theoretical point of view, if the angular momentum vector of the cloud is transferred to the individual pre-stellar cores then rotation and possibly magnetic fields could be responsible of guiding the gravitational accretion of mass along preferential directions in space. For understanding this aspect, reliable measurements of the space orientation of the stellar-spin axis are required. Previous analyses conducted on young open clusters support no evidence of stellar-spin alignment (Jackson & Jeffries 2010), but they relied on a combination of measurements for stellar rotational periods from light curves, projected equatorial velocities from spectroscopy, and stellar radii based on the cluster distance. As a result, the adopted methodology could be prone to significant systematics, and it is not applicable for distant and old populations of stars, whereas the required primary information will lack.

Asteroseismology, the study of stellar oscillations, has proven to be a powerful tool to extract direct information on the stellar interiors, and in particular on the stellar angular momentum vector, thus allowing for accurate and detailed results, especially in the case of red giant stars (Huber et al. 2013). Red giants are low- and intermediate-mass stars that have evolved off the main sequence to settle in either a hydrogen-shell-burning or helium-core-burning phase of the stellar evolution. Many red giants exhibit stellar oscillations that can be analyzed through a Fourier spectrum of the light curve. Such a Fourier spectrum contains a regular pattern of tens and sometimes more than a hundred of radial and non-radial stellar oscillation modes (Bedding et al. 2011). Each oscillation mode can be identified by means of an angular degree $l$ and an azimuthal number $m$, the latter related to the degeneracy lifted by the stellar rotation to form a multiplet of $(2l + 1)$ components (Gizon & Solanki 2003; Beck et al. 2012). The dipolar $(l = 1)$ mixed modes (Beck et al. 2011) are the most suited for measuring the orientation of the spin axis.

## 2 Data analysis & results

Here we investigate 48 oscillating red giant members of the open clusters NGC 6791 and NGC 6819 (Basu et al. 2011; Stello et al. 2011; Corsaro et al. 2012), with masses spanning from 1.1 to 1.7 $M_\odot$ (Miglio et al. 2012). Both clusters are old, with NGC 6791 one of the oldest known in our Galaxy (Brogaard et al. 2012). Despite their distance (on galactic scales up to $\sim$4 kpc), thanks to the high luminosity of the red giants, the individual stellar members could be monitored by the photometric space mission NASA *Kepler* for a period of about 4 years. By performing detailed asteroseismic analyses on each star (García et al. 2011, 2014; Mathur et al. 2010; Corsaro & De Ridder 2014; Corsaro et al. 2015), we obtain a total of about 380 rotationally split dipolar mixed modes — identified from a set of more than 3900 oscillation modes — and we use them to measure the spin inclination angles.

The analysis of the rotationally split dipolar mixed modes shows that about 70% of the stars in each cluster has a strong preferential spin orientation, with inclination angles between 20° and 30°. This is contrary to what would be expected by assuming an uniform 3D distribution of spin vectors, where most of the inclination angles would then be found close to 90°. The spatial distribution of the stars also guarantees that they adequately sample the observed spherical morphology of the two stellar clusters.

Existing N-body simulations for old open clusters (Geller et al. 2013) show that the stellar angular momentum can influence the evolution of colliding stars and of the orbital configurations of multiple stellar systems, e.g. the orbital eccentricities and periods of binaries. In the case of single stars we instead observe only a spin down over time (Meibom et al. 2015). Because of the larger average distances among the star members of an open cluster, the N-body interactions cannot produce any appreciable effect on redistributing stellar spin inclinations and yielding a spin alignment even for timescales of several Gyr. As a consequence, the spin alignment that is observed in the stars of our sample should have a different origin, linked to the formation epoch of the cluster.

We have performed 3D hydrodynamical simulations that reproduce the collapse of a dense molecular cloud forming a proto-cluster (Lee & Hennebelle 2016). The simulations show that when we consider a cloud dominated by turbulent kinetic energy, $E_{\rm tur}$, over that of global rotation, $E_{\rm rot}$ (yielding the condition $E_{\rm rot}/E_{\rm tur} < 1$), no significant stellar spin alignment is produced in the final pre-stellar cores and the distribution of spin inclinations resembles that of a uniform orientation in 3D space. The scenario becomes comparable to that of our observations when $E_{\rm rot}/E_{\rm tur} \simeq 1$ instead. In addition, when considering masses below 0.7 $M_\odot$, even an energy equipartition between rotational and turbulent kinetic energy is not able to produce a significant spin alignment in the resulting pre-stellar cores.

## 3 Conclusion

Our results indicate that a mass above $0.7\,M_{\odot}$, accreted into a pre-stellar core from the progenitor molecular cloud, would be required in order to allow the cloud's average angular momentum to be transferred from the scale of the molecular cloud to those of individual stars. At least 50 % of the cloud's rotational kinetic energy can be responsible of efficiently aligning the spin axes within the stellar members of a cluster. Therefore, the two open clusters NGC 6791 and NGC 6819 are likely to be originating from a formation process that involved a dense collapsing molecular cloud with a strong rotational energy component. Through the measurement of stellar spin inclinations for stars with masses comparable to that of our Sun and belonging to open clusters we can obtain information on the initial energy budget of the progenitor molecular cloud, its global rotation, and the efficiency by which the cloud's averaged angular momentum is transferred to the individual stellar members of the clusters. This will lead to the exploration and reconstruction of the dynamical evolution of galactic star forming regions that have originated clusters with ages up to several Gyr.

E.C. is funded by the European Community's Seventh Framework Programme (FP7/2007-2013) under grant agreement n°312844 (SPACEINN). Y.-N.L. and P.H. acknowledge funding by the European Research Council under the European Community's Seventh Framework Programme (FP7/2007-2013 Grant Agreement no. 306483) and the HPC resources of CINES under the allocation x2014047023 made by GENCI (Grand Equipement National de Calcul Intensif). R.A.G. received funding from the CNES GOLF and PLATO grants at CEA. R.A.G. and P.G.B. received funding from the ANR (Agence Nationale de la Recherche, France) program IDEE (n ANR-12-BS05-0008) "Interaction Des Étoiles et des Exoplanètes". Sa.M. acknowledges support from the NASA grant NNX12AE17G. St.M. acknowledges funding by the European Research Council through ERC grant SPIRE 647383. D.S. is the recipient of an Australian Research Council Future Fellowship (project number FT140100147). J.B. acknowledges financial support from grant ANR 2011 Blanc SIMI5-6 020 "Toupies: Towards understanding the spin evolution of stars". This work has received funding from the CNES grants at CEA.

## References

Basu, S., Grundahl, F., Stello, D., et al. 2011, ApJ, 729, L10

Beck, P. G., Bedding, T. R., Mosser, B., et al. 2011, Science, 332, 205

Beck, P. G., Montalban, J., Kallinger, T., et al. 2012, Nature, 481, 55

Bedding, T. R., Mosser, B., Huber, D., et al. 2011, Nature, 471, 608

Brogaard, K., VandenBerg, D. A., Bruntt, H., et al. 2012, A&A, 543, A106

Corsaro, E. & De Ridder, J. 2014, A&A, 571, A71

Corsaro, E., De Ridder, J., & García, R. A. 2015, A&A, 579, A83

Corsaro, E., Stello, D., Huber, D., et al. 2012, ApJ, 757, 190

García, R. A., Hekker, S., Stello, D., et al. 2011, MNRAS, 414, L6

García, R. A., Mathur, S., Pires, S., et al. 2014, A&A, 568, A10

Geller, A. M., Hurley, J. R., & Mathieu, R. D. 2013, AJ, 145, 8

Gizon, L. & Solanki, S. K. 2003, ApJ, 589, 1009

Huber, D., Carter, J. A., Barbieri, M., et al. 2013, Science, 342, 331

Jackson, R. J. & Jeffries, R. D. 2010, MNRAS, 402, 1380

Lada, C. J. & Lada, E. A. 2003, ARA&A, 41, 57

Lee, E. J., Murray, N., & Rahman, M. 2012, ApJ, 752, 146

Lee, Y.-N. & Hennebelle, P. 2016, A&A, 591, A30

Longmore, S. N., Kruijssen, J. M. D., Bastian, N., et al. 2014, Protostars and Planets VI, 291

Mathur, S., García, R. A., Régulo, C., et al. 2010, A&A, 511, A46

Meibom, S., Barnes, S. A., Platais, I., et al. 2015, Nature, 517, 589

Miglio, A., Brogaard, K., Stello, D., et al. 2012, MNRAS, 419, 2077

Shu, F. H., Adams, F. C., & Lizano, S. 1987, ARA&A, 25, 23

Stello, D., Meibom, S., Gilliland, R. L., et al. 2011, ApJ, 739, 13

*SF2A 2016*
*C. Reylé, J. Richard, L. Cambrésy, M. Deleuil, E. Pécontal, L. Tresse and I. Vauglin (eds)*

# PAIX THE FIRST ROBOTIC ANTARCTICA POLAR MISSION

M. Chadid[1]

Stellar pulsations and Asteroseismogy are currently among the fundamental techniques to improve our understanding of the internal structure of stars and the hydrodynamics of their atmosphere. On the observational side, progress is limited by the data accuracy needed to detect numerous modes of oscillations with small amplitudes and by the discontinuous nature of typical groundbased data strings which often introduce ambiguities in the determination of oscillation frequencies. Space missions such as MOST, CoRoT and KEPLER enable to overcome both difficulties, and indeed have considerably enhanced the scope of pulsation and asteroseismology methods. However, the outcome of the space missions on the stellar oscillation fields shows large gaps in terms of the flexibility during the observing runs, the choice of targets, the repair of failures and the inexorable high costs. Now the time has come to implement a new way to study the stellar oscillations with long uninterrupted and continuous observations over 150 days from the ground. PAIX –Photometer AntarctIca eXtinction– is a polar programme made of the lowcost commercial components, and achieves astrophysical measurement time–series of stellar fields, challenging photometry from space. PAIX gives a new insight to cope with unresolved stellar enigma and stellar oscillation challenges and offers a great opportunity to benefit from an access of the best astronomical site on Earth –Dome C– where the seeing reaches a median value of 1 arcsec during the polar night. PAIX is attached to the Cassegrain focus of a 40–cm Ritchey-Chrétien optical telescope, with a F/D ratio of 10, located at Dome C in the open field, without any shelter, installed at ice level. PAIX challenges space telescopes and even has more advantages than CoRoT and KEPLER in observing in $UBVRI$ bands and then collecting simultaneously multicolor light curves of several targets within the same 12.4 x 8.3 arcmin field of view. PAIX has been antarctized to run under extreme weather conditions with temperatures as low as -80 deg.C, and has been robotized, designed and built by PaixTeam whose operating headquarters are located at Université Nice Sophia-Antipolis and Observatoire de la Cote d'Azur.

I acknowledge financial supports from the French National Program of Stellar Physics (PNPS).

[1] Université Nice Sophia-Antipolis, Observatoire de la Côte d'Azur, UMR 7293, Parc Valrose, 06108 Nice Cedex 02, France

*SF2A 2016*
*C. Reylé, J. Richard, L. Cambrésy, M. Deleuil, E. Pécontal, L. Tresse and I. Vauglin (eds)*

# HR8844: A NEW HOT AM STAR?

R. Monier[1, 2], M. Gebran[3] and F. Royer[4]

**Abstract.** Using one archival high dispersion high quality spectrum of HR8844 (A0V) obtained with the echelle spectrograph SOPHIE at Observatoire de Haute Provence, we show that this star is not a superficially normal A0V star as hitherto thought. The model atmosphere and spectrum synthesis modeling of the spectrum of HR8844 reveals large departures of its abundances from the solar composition. We report here on our first determinations of the elemental abundances of 41 elements in the atmosphere of HR8844. Most of the light elements are underabundant whereas the very heavy elements are overabundant in HR8844. This interesting new chemically peculiar star could be a hybrid object between the HgMn stars and the Am stars.

Keywords: stars: individual, stars: Chemically Peculiar

## 1 Introduction

HR8844 currently assigned an A0V spectral type, is one of the 47 northern slowly rotating early-A stars studied by Royer et al. (2014). This star has been little studied: only 32 references can be found in ADS although it is fairly bright (V=5.89). The low projected rotational velocity of HR8844 can either be due to i) a very low inclination angle ($i \simeq 0$) or ii) a very low equatorial velocity $v_e$ . In this second case, the star could develop large over and underabundances and be a new Chemically Peculiar (CP) star. We have recently synthesized several lines of 41 elements present in the SOPHIE spectrum of HR8844 using model atmospheres and spectrum synthesis including hyperfine structure of various isotopes when necessary. These synthetic spectra were iteratively adjusted to the archival high resolution high signal-to-noise spectrum of HR8844 in order to derive the abundances of these elements. This abundance analysis yields underabundances of the light elements (He, C, N and O) and overabundances of the iron-peak elements and of the very heavy elements (VHE whose atomic number Z is greater than 30). This definitely shows that HR884 should be reclassified as a new CP star. We present here preliminary determinations of the elemental abundances in HR8844.

## 2 Observations and reduction

HD 30085 has been observed at the Observatoire de Haute Provence using the High Resolution (R =75000) mode of SOPHIE in August 2009. One 10 minutes exposures was secured with a $\frac{S}{N}$ ratio of about 269. We did not observe HR8844 ourselves but fetched the spectrum from the SOPHIE archive.

## 3 Model atmospheres and spectrum synthesis

The effective temperature and surface gravity of HR8844 were first evaluated using Napiwotzky et al's (1993) UVBYBETA calibration of Stromgren's photometry. The found effective temperature Teff is 9750 $\pm$ 200 K and the surface gravity $\log g$ is 3.80 $\pm$ 0.25 dex.

A plane parallel model atmosphere assuming radiative equilibrium, hydrostatic equilibrium and local thermodynamical equilibrium has been first computed using the ATLAS9 code (Kurucz 1992), specifically the

[1] LESIA, UMR 8109, Observatoire de Paris Meudon, Place J.Janssen, Meudon, France
[2] Lagrange, UMR 7293, Universite de Nice Sophia, Nice, France
[3] Department of Physics and Astronomy, Notre Dame University - Louaize, PO Box 72, Zouk Mikael, Lebanon
[4] GEPI, UMR 8111, Observatoire de Paris Meudon, Place J.Janssen, Meudon, France

linux version using the new ODFs maintained by F. Castelli on her website*. The linelist was built starting from Kurucz's (1992) gfhyperall.dat file † which includes hyperfine splitting levels. This first linelist was then upgraded using the NIST Atomic Spectra Database ‡ and the VALD database operated at Uppsala University (Kupka et al. 2000)§. A grid of synthetic spectra was then computed with SYNSPEC48 (Hubeny & Lanz 1992) to model the lines. The synthetic spectrum was then convolved with a gaussian instrumental profile and a parabolic rotation profile using the routine ROTIN3 provided along with SYNSPEC48. We adopted a projected apparent rotational velocity $v_e \sin i = 27$ km.s$^{-1}$ and a radial velocity $v_{rad} = 4.50$ km.s$^{-1}$ from Royer et al. (2014).

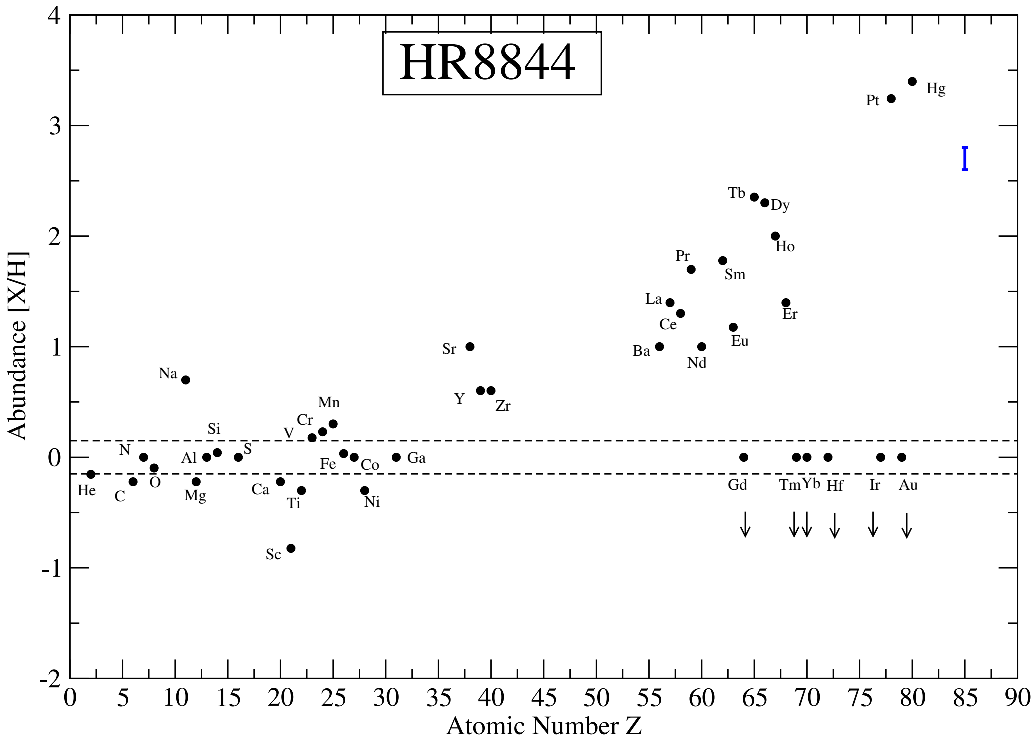


**Fig. 1.** The derived elemental abundances for HR8844

## 4 The derived abundance pattern for HR8844

The derived abundances for the 41 elements studied are displayed in Fig. 1. For a given element, we display actually the difference of the abundance in HR8844 relative to the solar value. A null value therefore means a solar abundance, a negative value an underabundance and a positive value an overabundance for that element in HR8844. We have depicted 2 horizontal lines at ± 0.15 dex of the null values to display a representative error bar. Any abundance situated above or below these lines represent real over or underabundances. We find that HR8844 displays underabundances in the light elements He, C, O, Mg, Ca, Sc, Ti and Ni. It has solar abundances for N, Al, Si, S and Fe and only mild overabundances for V, Cr, Mn. It has large overabundances in several very heavy elements:Sr, Y, Zr, Ba, La, Ce, Pr, Nd, Sm, Eu, Tb, Dy, Er, Ho, Pt and Hg. The heaviest elements Pt and Hg seem to be the most overabundant however their abundance determinations should be taken with caution as they rely on one line only for each element. The abundance pattern of HR8844 somehow

*http://www.oact.inaf.it/castelli/
†http://kurucz.harvard.edu/linelists/
‡http://physics.nist.gov/cgi-bin/AtData/linesform
§http://vald.astro.uu.se/ vald/php/vald.php

resembles that of the hot Am stars, Sirius A and HD72660 which have effective temperatures and surface gravities very close to that of HR8844. However much work remains to be done to establish the differences and similarities of surface composition in these three stars.

## 5 Conclusions

The derived abundance pattern of HR8844 strongly departs from the solar composition which definitely shows that HR8844 is not a superficially normal early A star but is actually another new CP star. We have already reported on the discovery of 5 new CP stars of the HgMn type in Monier et al. (2015) and Monier et al. (2016). HR8844 has overabundances of both the rare earths and possibly of the VHE Hg and Pt and therefore resembles both a very hot Am star and a very cool HgMn star. It could be a hybrid object intermediate between these two classes of objects. We are currently planning more observations of HR8844 with SOPHIE in order to complement the abundances derived here and search for line variability. This will help us adddress the relationship of HR8844 to the 2 other hot Am stars, Sirius A and HD72660 and constrain the nature of this interesting new CP star.

The authors acknowledge use of the SOPHIE archive (`http://atlas.obs-hp.fr/sophie/`) at Observatoire de Haute Provence. They have used the NIST Atomic Spectra Database and the VALD database operated at Uppsala University (Kupka et al., 2000) to upgrade atomic data.

## References

Hubeny, I., Lanz, T. 1992, A&A, 262, 501

Kupka F., Ryabchikova T.A., Piskunov N.E., Stempels H.C., Weiss W.W., 2000, Baltic Astronomy, vol. 9, 590-594

Kurucz, R.L. 1992, Rev. Mexicana. Astron. Astrofis., 23, 45

Monier, R., Gebran, M., Royer, F. 2015, A&A, 577A, 96M

Monier, R., Gebran, M., & Royer, F. 2016, Ap&SS, 361, 139

Napiwotzki, R., Schoenberner, D., Wenske, V. 1993, A&A, 268, 653

Royer, F., Gebran, M., Monier, R., Adelman, S., Smalley, B., Pintado, O., Reiners, A., Hill, G., Gulliver, G. 2014 , A&A, 562A, 84R

*SF2A 2016*
*C. Reylé, J. Richard, L. Cambrésy, M. Deleuil, E. Pécontal, L. Tresse and I. Vauglin (eds)*

# HD 30963: A NEW HGMN STAR

R. Monier[1,2], M. Gebran[3] and F. Royer[4]

**Abstract.** Using high dispersion high quality spectra of HD 30963 obtained with the echelle spectrograph SOPHIE at Observatoire de Haute Provence in November 2015, we show that this star, hitherto classified as a B9 III superficially normal star, is actually a new Chemically Peculiar star of the HgMn type. Spectrum synthesis reveals large overabundances of Mn, Sr, Y, Zr , Pt and Hg and pronounced underabundances of He and Ni which are characteristic of HgMn stars. We therefore propose that this interesting object be reclassified as a B9 HgMn star.

Keywords: stars: individual, stars: Chemically Peculiar

## 1 Introduction

HD 30963 (V =7.23 mag), currently assigned an B9 III spectral type, is one of the slowly rotating late B we are currently observing. This star has been little studied: one only finds 10 references in SIMBAD for HD 30963. The incentive of this project is to reclassify the late B stars in the northern hemisphere brighter than V=7.5 mag with low apparent projected velocities (less than 60 km s$^{-1}$). We have previously undertaken a similar survey of the slowly rotating early A stars, whose results are published in Royer et al. (2014). An abundance analysis of high resolution well exposed spectra of these objects has sorted out the sample into 17 chemically normal stars (ie. whose abundances do not depart more than ± 0.20 dex from solar values), 12 spectroscopic binaries and 13 Chemically Peculiar stars (CP). Among the new CP stars, Monier et al. (2015) and Monier et al. (2016) have identified 5 new HgMn stars. We present here new abundance determinations for HD 30963, a slowly rotating late B star and show that this star is another new HgMn late B star.

## 2 Observations and reduction

HD 30963 has been observed on five consecutive days at Observatoire de Haute Provence (OHP) using SOPHIE in its high resolution mode (R=75000) in November and December 2015. A log of the observations appears in Tab. 1. Four 1800 and one 2400 seconds exposures were obtained with a signal-to-noise ratio varying from 78 up to 167. As we do not see conspicuous radial velocity variations on these spectra taken over five days, we have shifted all spectra onto a common wavelength scale (that of the first spectrum) and we have coadded the individual spectra into a mean spectrum. Assuming a radius for HD 30963 of about 3 to 4 $R_{\odot}$ and using the $v_e \sin i$ of Zorec & Royer (2012), we derive an upper limit of 4.12 days for the rotational period of HD 30963. The observations which we secured over 5 days separated by about 24 hours each therefore cover the rotational period of HD 30963.

## 3 Reassigning a proper spectral type to HD 30963

The following spectral regions have been used to readdress the spectral type of HD 30963. First, the red wing of $H_{\epsilon}$ from 3980 Å up to 4000 Å harbours the Hg II line at 3984 Å and two Zr II and one Y II lines likely to

[1] LESIA, UMR 8109, Observatoire de Paris Meudon, Place J.Janssen, Meudon, France
[2] Lagrange, UMR 7293, Universite de Nice Sophia, Nice, France
[3] Department of Physics and Astronomy, Notre Dame University - Louaize, PO Box 72, Zouk Mikael, Lebanon
[4] GEPI, UMR 8111, Observatoire de Paris Meudon, Place J.Janssen, Meudon, France

| Observations log for HD 30963 | | |
|---|---|---|
| Date | UT start exposure | $\frac{S}{N}$ |
| 2015-11-28 | 00:00:35.307 | 118 |
| 2015-11-28 | 23:44:20.941 | 78 |
| 2015-11-30 | 00:25:54.328 | 140 |
| 2015-11-30 | 23:24:27.855 | 101 |
| 2015-12-01 | 22:29:32.033 | 167 |

**Table 1.** Log of SOPHIE observations of HD 30963

| Derived abundances for HD 30963 | | |
|---|---|---|
| Wavelengths (Å) | Identification | Abundance |
| 3982.60 | Y II | 1000.0 $\odot$ |
| 3983.93 | Hg II | 150000.0 $\odot$ |
| 3990.96 | Zr II | 150.0 $\odot$ |
| 3998.82 | Zr II | 150.0 $\odot$ |
| 4067.04 | Ni II | 0.10 $\odot$ |
| 4077.70 | Sr II | 35.0 $\odot$ |
| 4471.48 | He I | 0.20 $\odot$ |
| 4478.64 | Mn II | 50.0 $\odot$ |
| 4481.15 | Mg II | 2.50 $\odot$ |
| 4500.00 | Fe II | 2.00 $\odot$ |
| 4514.17 | Pt II | 2500.0 $\odot$ |
| 4554.01 | Ba II | 10.00 $\odot$ |

**Table 2.** Abundances derived for the 11 lines used in this work.

be strengthened in a late B-type star of the HgMn type (Fig. 1). Second, the region from 4470 Å to 4490 Å contains the Mg II triplet near 4481.15 Å, the He I line at 4471.48 Å and the Mn II line at 4478.64 Å(Fig. 2). We have also looked for peculiarities in the Ni II line at 4067.04 Å and the Sr II resonance line at 4077.70 Å and in the Pt II line at 4514.17 Å and the Ba II resonance line at 4554.01 Å. The eleven lines used are collected in Tab. 2 with their identifications and abundances (see Sec. 4.2) expressed as multiples of the corresponding solar abundances (labeled with the symbol $\odot$). Their positions are marked by vertical lines in both figures (after a correction for the radial velocity).

## 4 Abundance determinations

### *4.1 Model atmospheres and spectrum synthesis*

The effective temperature Teff and surface gravity $\log g$ of HD 30963 were taken from Huang et al. (2010) survey of field B stars. These authors have derived Teff = 11476 K and $\log g = 3.66$ for HD 30963 by adjusting the observed $H_\gamma$ profile to grids of synthetic spectra. A 72 layers plane parallel model atmosphere assuming radiative equilibrium and hydrostatic equilibrium has been first computed for these values of Teff and $\log g$ using the ATLAS9 code (Kurucz 1992), specifically the linux version using the new ODFs maintained by F. Castelli on her website. The linelist was built starting from Kurucz's (1992) gfhyperall.dat* file which includes hyperfine splitting levels. This first linelist was then upgraded using the NIST Atomic Spectra Database † and the VALD‡ database operated at Uppsala University (Kupka et al. 2000). A grid of synthetic spectra was then computed with SYNSPEC48 (Hubeny & Lanz 1992) to model the eleven lines listed in Table 1 adopting a null microturbulent velocity. The synthetic spectra were further convolved using the routine ROTIN3 provided along with SYNSPEC48 using $v_e \sin i = 37$ km s$^{-1}$ (Zorec & Royer 2012) and the appropriate FWHM for SOPHIE. The unknown abundance $[\frac{X}{H}]$ was varied until minimisation of the chi-square between the observed

*http://kurucz.harvard.edu/linelists/
†http://physics.nist.gov/cgi-bin/AtData/linesform
‡http://vald.astro.uu.se/ vald/php/vald.php

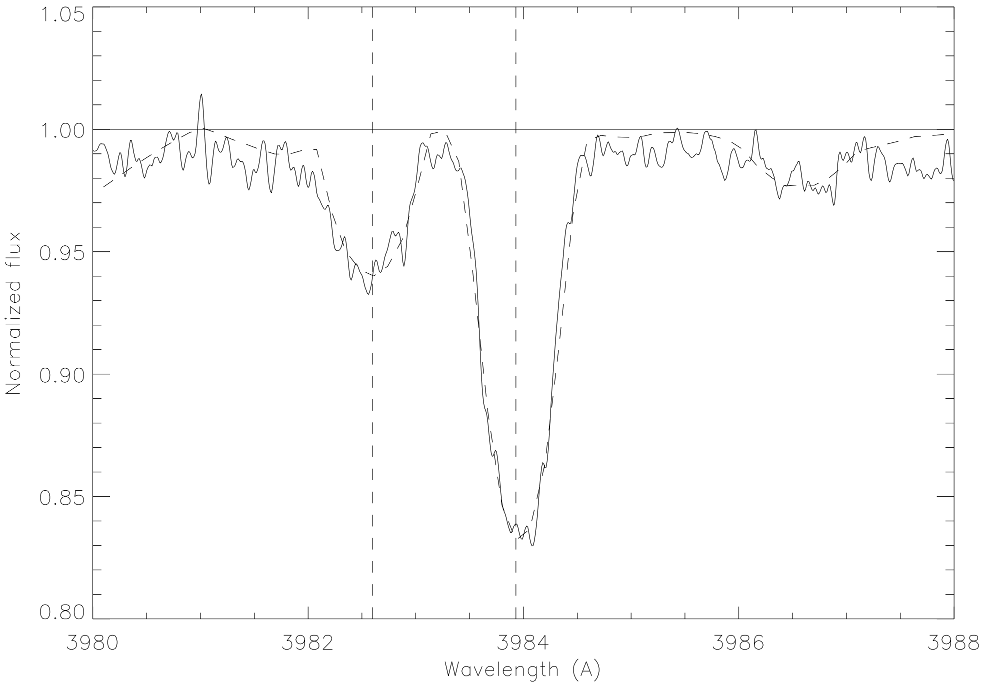


**Fig. 1.** Synthesis of the Hg II 3983.93 Å line (observed: thick line, models: dashed lines)

and synthetic spectrum.

### *4.2 Evidence for strong excesses in Mn, Y, Zr, Pt and Hg*

We find that five elements, Mn, Y, Zr, Pt and Hg, have strong excesses, ie. larger than 50 times the solar values The synthesis of the Mn II line at 4478.64 Å in Fig. 2 yields an overabundance of 50 times the solar abundance. This is a substantial excess and it may be revised to a lower value when we will model Mn II lines having atomic data for several isotopes and hyperfine structure. The Hg overabundance is derived from the synthesis of 11 transitions next to 3983.84 Å representing the hyperfine structure of various isotopes of Hg in a similar manner as (Castelli & Hubrig 2004) modeled HD 175640. The abundance that best fits the observed line profile is very large (150000 $\odot$) as can be seen in Fig. 1. This is one of the strongest Hg excess we found in the new HgMn stars (Monier et al. 2015; Monier et al. 2016).

The abundance of Zr derived from the 2 lines in Table 1 is about 150 $\odot$. The Yttrium abundance derived from Y II 3932.44 Å is also very important (1000 $\odot$). While modeling the Fe II lines in the 4500 Å- 4600Å region, we noticed a 1.5 % feature at about 4514.15 Å which we identify as one of the strongest Pt II line expected at 4514.17 Å listed in VALD. No other "easier" identification (ie. in terms of a lighter element) can reproduce the observed line depth at this wavelength. We are currently looking for other lines of Pt II lines at shorter wavelengths to confirm the presence of platinum in HD 30963. We also checked that a model computed for a solar platinum abundance and one without the Pt II line yield no absorption at all at 4514.17 Å. From the 4514.17 Å line only, a provisional excess of platinum is derived to be about 2500 $\odot$. We also find considerable deficiencies in He (0.2 $\odot$) and Ni (0.1 $\odot$). The excesses in Mn, Y, Zr, Pt and Hg and the deficiencies in He and Ni are characteristic of an HgMn star.

## 5 Conclusions

Whereas it was up to now classified as a normal late B9 III star, our analysis of HD 30963 shows that it has very peculiar over and underabundances. The overabundances in Mn, Sr, Y, Zr, Pt and Hg are characteristic of an HgMn star. It displays large overabundances of the Sr, Y and Zr triad which is however inverted compared

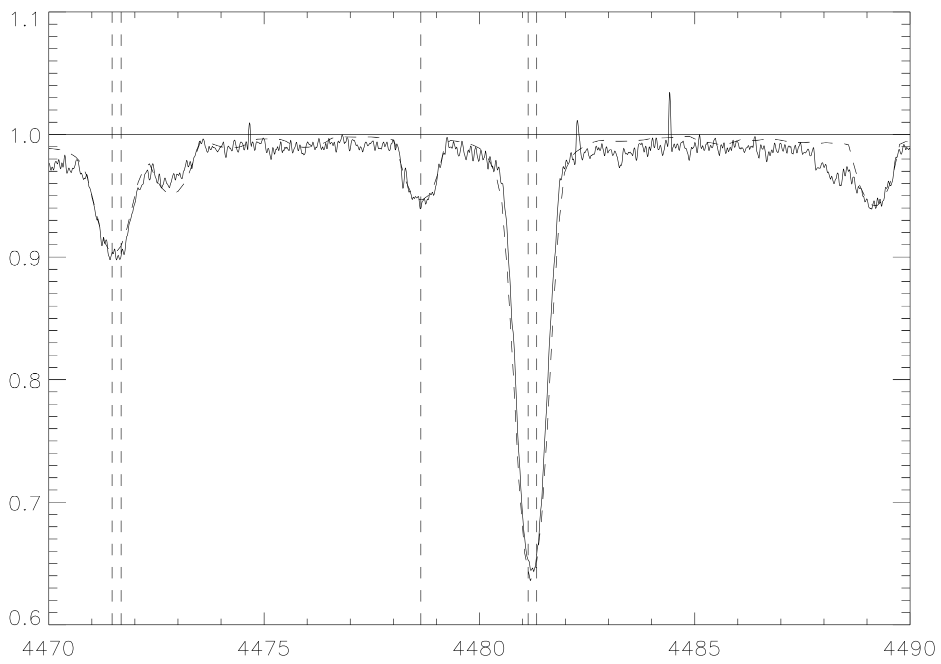


**Fig. 2.** Synthesis of the He I (4471.4 Å) ,Mn II ( 4478.64 Å) and Mg II (4481.15 Å) lines

to the solar system triad. The synthesis of the Hg II and Pt II lines reveals large overabundances of Pt and Hg. We are currently performing a detailed abundance analysis of HD 30963 to complement the first abundances presented here.

The authors acknowledge the efficient help of the night assistants at Observatoire de Haute Provence. They have used the NIST Atomic Spectra Database and the VALD database operated at Uppsala University (Kupka et al., 2000) to upgrade atomic data.

## References

Castelli, F., Hubrig, S. 2004, A&A, 425, 265

Huang, W., Gies, D. R., & McSwain, M. V. 2010, ApJ, 722, 605

Hubeny, I., Lanz, T. 1992, A&A, 262, 501

Kupka F., Ryabchikova T.A., Piskunov N.E., Stempels H.C., Weiss W.W., 2000, Baltic Astronomy, vol. 9, 590-594

Kurucz, R.L. 1992, Rev. Mexicana. Astron. Astrofis., 23, 45

Monier, R., Gebran, M., Royer, F. 2015, A&A, 577A, 96M

Monier, R., Gebran, M., & Royer, F. 2016, Ap&SS, 361, 139

Napiwotzki, R., Schoenberner, D., Wenske, V. 1993, A&A, 268, 653

Royer, F., Gebran, M., Monier, R., Adelman, S., Smalley, B., Pintado, O., Reiners, A., Hill, G., Gulliver, G. 2014 , A&A, 562A, 84R

Zorec, J., & Royer, F. 2012, A&A, 537, A120

*SF2A 2016*
*C. Reylé, J. Richard, L. Cambrésy, M. Deleuil, E. Pécontal, L. Tresse and I. Vauglin (eds)*

# INTERNAL ROTATION OF $\gamma$ DORADUS STARS

R.-M. Ouazzani[1], S. J. A. J. Salmon[3], V. Antoci[1], T. R. Bedding[1,4] and S. J. Murphy[1,4]

**Abstract.** Thanks to the exquisite *Kepler* data, resulting from four years of quasi-continuous photometric observations, we are now able to use g-modes in order to reveal the internal structure of $\gamma$ Doradus stars. In particular, it is now possible to detect series of g-modes with non-uniform period spacing, which carry the signature of internal rotation. In a theoretical work published earlier this year, we have defined a new seismic diagnostic for rotation in the $\gamma$ Doradus stars that are rotating too rapidly to present rotational splitting. It is based on a new observable that is the slope of the period spacing when plotted againt the period. Here we recall the one-to-one relation between this observable and the internal rotation rate. We explain how it can be used without any additional constraint in order to retreive the rotation rate in the cavity probed by the observed g-modes. Finally we evaluate the uncertainty induced by the use of the asymptotic formulation of the traditional approximation, and we give a word of caution concerning retrograde modes.

Keywords: asteroseismology, stellar interiors, stellar rotation, $\gamma$ Doradus stars

## 1 Introduction

$\gamma$ Doradus ($\gamma$ Dor) stars are late A- to early F-type stars, of masses between 1.3 and 2 $M_\odot$, on the main sequence. Thanks to the four years of nearly continuous photometry from *Kepler*, we were finally able to measure their g mode pulsations to the precision level required to perform seismic modelling. These g modes probe the innermost regions and in particular the interface between the convective core and the radiative envelope, where transport of chemical elements and angular momentum is expected to occur. Whether this transport is caused by overshooting, shear induced turbulence or gravity waves is still matter of debate. In this context, the determination of internal rotation rates in $\gamma$ Dor stars constitutes a valuable constraint.

These stars typically have projected rotation velocities of around 100 km $s^{-1}$, but that can reach up to 250 km $s^{-1}$ (see for instance Abt & Morrell 1995; Royer 2009). Rotation lifts the degeneracy of pulsation frequencies. For slow rotation, g modes in $\gamma$ Dor stars can exhibit splittings which can be used in order to determine the rotation rate in their propagation cavity (see Kurtz et al. 2014; Saio et al. 2015; Schmid et al. 2015; Keen et al. 2015; Murphy et al. 2016). In the case of moderate to rapid rotation, the structure of the frequency spectrum differs drastically. The prograde modes are shifted towards higher frequencies, whereas the retrogrades are shifted towards lower frequencies, to such an extent that they appear in the spectrum as clusters of modes, each with given angular degree ($\ell$) and azimuthal order ($m$), and varying radial orders. Moreover, each of these clusters show a period spacing with a linear trend (Bouabid et al. 2013) which is related to the identity of the modes $\{\ell, m\}$, and the rotation velocity in their cavity.

Based on this and making use of an approximate treatment of rotational effects, the traditional approximation (TAR), Van Reeth et al. (2016) performed seismic determination of rotation in a sample of $\gamma$ Dor stars observed by *Kepler*. We opted for the development of seismic diagnostics which are model independent, and are therefore not affected by the lack of knowledge of the stellar structure. To establish such diagnostics, we make use of non-perturbative calculations for the effect of rotation on $\gamma$ Dors g modes (implemented in the ACOR code, see Ouazzani et al. 2012, 2015).

[1] Stellar Astrophysics Centre, Department of Physics and Astronomy, Aarhus University, Aarhus C, Denmark
[2] Laboratoire AIM, CEA/DSM-CNRS-Université Paris 7, Irfu/Service d'Astrophysique, CEA-Saclay, France
[3] Institut d'Astrophysique et de Géophysique de l'Université de Liège, Liège, Belgium
[4] Sydney Institute for Astronomy (SIfA), School of Physics, University of Sydney, Australia

## 2 A new asteroseismic diagnostic for internal rotation in $\gamma$ Doradus stars

As mentioned above, in $\gamma$ Dor stars that are moderate to rapid rotators, the modes gather by $\ell$ and $m$, and their period spacings ($\Delta P$) vary linearly with modes periods. In Ouazzani et al. (2016) we have shown that the slope of this trend, which we named $\Sigma_{\ell,m}$ strongly depends on the rotation in the probed cavity, and marginally on other aspects of the stellar structure. This is illustrated in Fig. 1 (left), which represents the slope $\Sigma$ as a function of the rotation rate, for dipolar ($\ell = 1$) modes. The solid lines are the average of $\Sigma$, calculated with the non perturbative method, for three representative models of $\gamma$ Dor stars, which have been computed by the CLES code (Code Liégeois d'Évolution Stellaire, Scuflaire et al. 2008): the model 1z is 1.4 $M_\odot$ on the zero-age-main-sequence (ZAMS), the model 2m is 1.6 $M_\odot$ mid-way on the main-sequence (MS), and the model 3t, a 1.86 $M_\odot$ star on the terminal-age-main-sequence (TAMS). We used the asymptotic formulation of the TAR to evaluate the scatter caused by the difference in structure encountered in the $\gamma$ Dor instability strip (see Ouazzani et al. 2016, for more details). This yields the dispersion areas in colour in Fig. 1 (left).

Hence, we established a one-to-one relation between the observable $\Sigma_{\ell,m}$ and the average rotation velocity in the cavity probed by the g modes of angular degree $\ell$ and azimuthal order $m$. The largest spread is obtained for the retrograde modes, this is treated is further details in Sect. 3.2. As a proof of concept, we chose four stars which have been quasi-continuously observed by observed by *Kepler* for 18 quarters (*Kepler* input catalog number KIC 4253413 and KIC 6762992), 17 quarters (KIC 5476299) and 15 quarters (KIC 4177905), respectively. Their measured oscillation periods were extracted using the classical pre-whitening procedure (Period04, Lenz & Breger 2005) and are plotted against their period spacings in Fig. 1 (right). We rely on the combined knowledge of the range of observed periods, their period spacings, as well as the slope $\Sigma$ in order to identify the angular degree $\ell$ and azimuthal order $m$ of the ridges. The four sequences of modes were identified as belonging to dipolar prograde modes. The slopes of the period spacings series were determined using a simple linear fit of the data points. By reporting these slopes in the diagram given in Fig. 1 (left), we directly retreive the average rotation frequency in the cavity probed by these modes. The results are the following: 7.1 $\pm$ 0.9 $\mu$Hz for KIC 6762992, 9.8 $\pm$ 0.9 $\mu$Hz for KIC 4177905, 10.7 $\pm$ 1.4 $\mu$Hz for KIC 4253413, and 17.8 $\pm$ 2.9 $\mu$Hz for KIC 5476299.

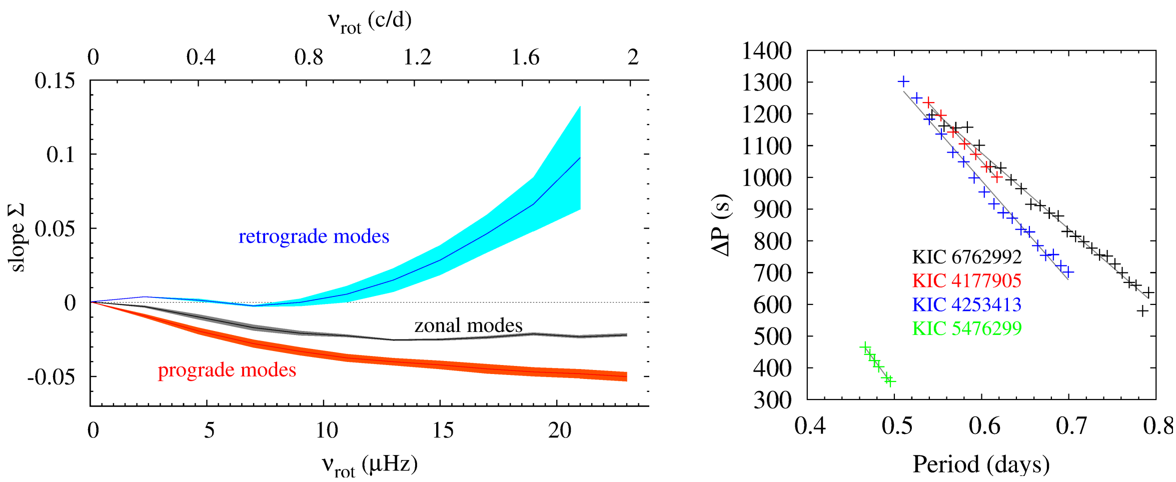


**Fig. 1. Left:** Diagram giving the one-to-one relation between the slope of the period spacing, i.e. the observable $\Sigma$, and the rotation frequency established as an average of the non-perturbative calculations for models 1z, 2m, and 3t. It is given here for dipolar modes: prograde modes in red, zonal modes in black and retrograde modes in blue. The dispersions correspond to the variations of $\Sigma$ due to the mass, age on the main sequence, metallicity, and type of mixing on the edge of the convective core, computed using the asymptotic formula at each rotation rate for a grid of models covering the $\gamma$ Dor stars instability strip. **Right:** Period spacing as a function of the period for four sequences of modes observed in four stars observed by *Kepler*: KIC 6762992 in black points, KIC 4177905 in red points, KIC 4253413 in blue points, and KIC 5476299 in green points. The grey lines correspond to the linear fits used to determine the slope of the respective ridge.

## 3 A word of caution

In the previous section, we give the one-to-one relation between the slope of the period spacing series, and the internal rotation rate in $\gamma$ Dor stars, as introduced by Ouazzani et al. (2016). In this section, we evaluate the uncertainties induced by using the asymptotic formulation of the TAR for the determination of the rotation rate from $\Sigma$. Moreover, we investigate more closely the specificity of retrograde modes.

### *3.1 Uncertainties related to the use of the Asymptotic formulation of the TAR*

In rotating stars, the equation system for pulsations is not separable in terms of the radial and horizontal coordinates, unlike for the non rotating case. The TAR is not a perturbative method. This is an approximate treatment which conserves the separability of the system by making specific assomptions. The first one is that the stars is rotating as a solid body. The centrifugal distortion is neglected, i.e. the spherical symmetry is assumed. Moreover, considering the properties of high radial order g modes, the TAR neglects the Coriolis force associated with radial motion, and radial component of the Coriolis force associated with horizontal motion. Finally, the Cowling approximation is made (Cowling 1941). Under the TAR, the simplification of the problem allows for an asymptotic formulation derived from the Tassoul (1980) formula for g-mode periods, where $\ell(\ell+1)$ is replaced by $\lambda$. This eigenvalue depends on $\ell$, m and the spin parameter $s = 2\nu_{rot}/\nu_{co}$, $\nu_{co}$ being the frequency of the modes in the corotating frame. The asymptotic formula gives:

$$P_{\rm co}(n) = \frac{2\pi^2(n+\frac{1}{2})}{\sqrt{\lambda_{\ell,m,s(n)}}\int_{r_0}^{r_1}\frac{N}{r}{\rm dr}} \quad \text{and} \quad \langle\Delta {\rm P_{co}}\rangle \simeq \frac{2\pi^2}{\sqrt{\lambda_{\ell,{\rm m},{\rm s(n+1)}}}\int_{\rm r_0}^{\rm r_1}\frac{\rm N}{\rm r}{\rm dr}\left(1+\frac{1}{2}\frac{\rm d\ln\lambda}{\rm d\ln s}\right)} \tag{3.1}$$

The asymptotic formulation requires very little computational resources and time. For that reason it is often used in order to study the pulsational properties of grids of stellar models. However, the aim here is to investigate its validity when used to model the diagnostic $\Sigma$, compared to the non-perturbative method. To do so, we computed the slopes $\Sigma$ of dipolar modes period spacing series computed with the two methods for the three representative models 1z, 2m, 3t mentioned before. The largest uncertainties arise for the model 1z, which is chosen to be shown in Fig.2. The period spacing is plotted against the period for model 1z with a rotation frequency ranging from 11 to 23 $\mu$Hz, computed with the non-perturbative method (lines with points), and with the asymptotic formulation (solid lines).

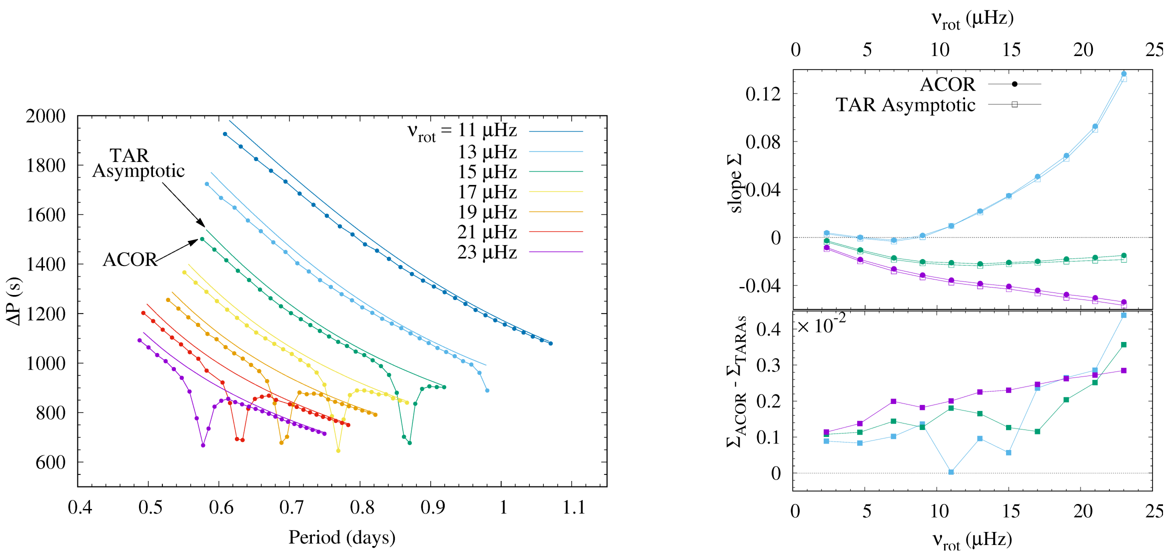


**Fig. 2. Left:** Period spacing as a function of the period for model 1z, computed with the asymptotic formulation (solid lines) and with the non perturbative method (ACOR lines with points) for rotation frequencies ranging from 11 to 23 $\mu$Hz. **Right, top:** Slope $\Sigma$ of the period spacing series as a function of the rotation frequencie of the model 1z, computed with the TAR asymptotic formulation (open squares), and with the non-perturbative method (ACOR, filled circles), for prograde (purple), zonal (green), and retrograde modes (blue). **Right, bottom:** Discrepancy between the two computations.

One striking difference between these two series of curves is the occurence of dips for the non-perturbative series, around the same period spacing value whatever the rotation rate. These dips occur preferentially at higher rotation frequencies (from $\nu_{rot} = 13\mu$Hz upwards). After exploring the pulsation spectrum of modes with higher $\ell$ values, it turns out that these features in the $\ell = 1$ series appear in the frequency range where g modes of $\ell = 3$ are increasingly numerous in the spectrum. Even if conserving a dominant $\ell = 1$ character, modes in this region are bumped into and perturbed by their $\ell = 3$ counterparts. These dips appear for the retrograde and zonal modes, because for prograde modes the shift in frequency due to rotation is such that g modes of different $\ell$ do not lie in the same frequency range at all.

These features are not at all reproduced by the asymptotic formulation, and they seem to modify the overall slope of the ridges noticeably towards negative values. However, let us compare the period spacing series, when the dips are removed from the ridges, i.e. far from the dips. The result is given in Fig.2 (right). Apart from an overall increasing trend with rotation, the discrepancy it is not negligible at low rotation frequency (around 10 % at $\nu_{rot} = 2.5\mu$Hz), and can reach up to approximately 20 % for zonal modes at high rotation.

### 3.2 The case of retrograde modes

In the inertial frame of reference, the effect of rotation of g modes is twofold: the intrinsic effect of the Coriolis and centrifugal forces, and the change of reference from the corotating frame to the inertial one. Zonal modes are not impacted by this change of frame, but retrograde modes are shifted towards shorter periods, whereas prograde modes are shifted towards longer ones respectively. For retrograde modes, this shift substracts from the intrinsic effect of rotation. The specificity of retrograde modes resides in the competition between these two effects. Although quantitatively inaccurate, the asymptotic for the period spacing helps understand this phenomenon. Following Eq. (3.1) the period spacing in the inertial frame can be written as:

$$\Delta P_{in} \propto \frac{1}{\sqrt{\lambda_{\ell,m,s}}\left(1 - m\frac{P_{co}}{P_{rot}}\right)}, \tag{3.2}$$

where the factor $\sqrt{\lambda_{\ell,m,s}}^{-1}$ comes from the TAR and stands for the Coriolis effect on the pulsations in the corotating frame, and $\left(1 - m\frac{P_{co}}{P_{rot}}\right)^{-1}$ for the change of reference frame. As rotation varies, three regimes can be identified for the behaviour of $\Delta P_{in}$:

- *Slow rotation*: when the pulsation periods are significantly smaller than the rotation period, $\Delta P_{in}$ follows the behaviour given by the Ledoux (1951) perturbative formalism at first order. This is illustrated in Fig. 3, with the two green ridges, computed for models rotating at 2.33 $\mu$Hz (4.97 days). The green open triangles are obtained with the Ledoux formula, whereas the green open circles are obtained with the non-perturbative calculations. For inertial periods shorter than $P_{rot}/4$ (straight dashed green line), the $\Delta P_{in}$ follows the first order perturbative formula.

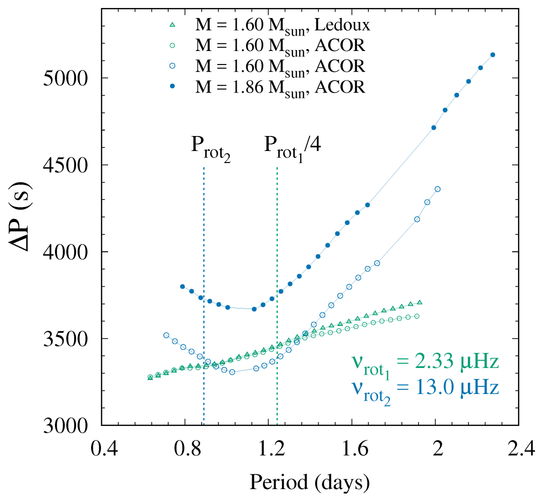


**Fig. 3.** Period spacing as a function of period in the inertial frame for retrograde modes computed for a 1.86 $M_\odot$ (filled symbols), and a 1.60 $M_\odot$ (open symbols) stellar models, with the ACOR code (circles), or with the Ledoux splitting (triangles), for slow rotation ($\nu_{\rm rot1}$ =2.33 $\mu$ Hz, green) and rapid rotation ($\nu_{\rm rot2}$ =13.0 $\mu$ Hz, blue). The two vertical dashed lines stand for the period in the inertial frame that equals the rotation period $P_{\rm rot2} = 0.89$ days for the rapid rotation case, and when it equals a quarter of the rotation period for the slowly rotating case $P_{\rm rot1}/4 = 1.24$ days. Some modes are discarded for not presenting a clear $\ell = 1$ character.

- For *inertial periods* $P_{in}$ *longer than* $P_{rot}/4$, the rotational effect is determined by Eq. (3.2). For $P_{in}$ shorter than $P_{rot}$, i.e. in the superinertial regime, the behaviour of $\Delta P_{in}$ is dominated by the factor $\sqrt{\lambda_{\ell,m,s}}^{-1}$, which causes a decreasing trend of $\Delta P_{in}$ with respect to $P_{in}$. This is illustrated in Fig. 3 by the part of the blue ridges which are leftward of the dashed blue line.
- For $P_{in}$ *longer than* $P_{rot}$, i.e. in the subinertial regime, the effect of the change of reference frame dominates under the form of an asymptotic behaviour towards infinity.

The spread in $\Sigma$ for retrograde modes, shown in Fig. 1, is explained by the difference between the two blue ridges (open and filled circles) in Fig. 3. The difference between the two ridges resides in the period of modes of given radial order: for the 1.6 $M_\odot$ model (blue open circles), the modes are more numerous on the decreasing part of the ridge than for the 1.86 $M_\odot$ model (blue filled circles). As a result, when performing a linear fit of these points, the slope of the ridge corresponding to the 1.6 $M_\odot$ model is smaller than for the 1.86 $M_\odot$ model. In other words, because these ridges are not linear, the periods change of the excited modes (radial orders n between -50 and -15) due to a change of the model's parameters impacts $\Sigma$. Therefore, should the diagnostic given in Fig. 1 be used on observed series of retrogrades modes, we would recommend a more detailed modelling accounting for the period range on which the parameter $\Sigma$ is determined.

## 4 Conclusions

We have reported on the establishment of a new seismic diagnostic of rotation for g modes when the rotational splitting cannot be extracted correctly: $\Sigma$, the slope of the period spacing when plotted against the period. We give the one-to-one relation between $\Sigma$ and the internal rotation rate. We then explore the relevance of using the asymptotic formulation of the TAR in order to establish the one-to-one relation mentioned above. It appears that the asymptotic method fails to reproduce features that are related to the multiple $\ell$ character of the modes. When these features are removed, the uncertainties can be significant, but lower than the spread in $\Sigma$ due to the differences of internal structures encountered in the $\gamma$ Dor instability strip. Finally we give a word of caution concerning the use of the $\Sigma$ diagnostic with retrograde mode, and explain in details the peculiar nature of these modes.

Funding for the Stellar Astrophysics Centre is provided by The Danish National Research Foundation (Grant DNRF106). The research was supported by the ASTERISK project (ASTERoseismic Investigations with SONG and Kepler) funded by the European Research Council (Grant agreement no.: 267864).

## References

Abt, H. A. & Morrell, N. I. 1995, ApJS, 99, 135
Bouabid, M.-P., Dupret, M.-A., Salmon, S., et al. 2013, MNRAS, 429, 2500
Cowling, T. G. 1941, MNRAS, 101, 367
Keen, M. A., Bedding, T. R., Murphy, S. J., et al. 2015, MNRAS, 454, 1792
Kurtz, D. W., Saio, H., Takata, M., et al. 2014, MNRAS, 444, 102
Ledoux, P. 1951, ApJ, 114, 373
Lenz, P. & Breger, M. 2005, Communications in Asteroseismology, 146, 53
Murphy, S. J., Fossati, L., Bedding, T. R., et al. 2016, MNRAS, 459, 1201
Ouazzani, R.-M., Dupret, M.-A., & Reese, D. R. 2012, A&A, 547, A75
Ouazzani, R.-M., Roxburgh, I. W., & Dupret, M.-A. 2015, A&A, 579, A116
Ouazzani, R.-M., Salmon, S. J. A. J., Antoci, V., et al. 2016, ArXiv e-prints
Royer, F. 2009, in Lecture Notes in Physics, Berlin Springer Verlag, Vol. 765, The Rotation of Sun and Stars, 207–230
Saio, H., Kurtz, D. W., Takata, M., et al. 2015, MNRAS, 447, 3264
Schmid, V. S., Tkachenko, A., Aerts, C., et al. 2015, A&A, 584, A35
Scuflaire, R., Théado, S., Montalbán, J., et al. 2008, Ap&SS, 316, 83
Tassoul, M. 1980, ApJS, 43, 469
Van Reeth, T., Tkachenko, A., & Aerts, C. 2016, A&A, 593, A120

*SF2A 2016*
*C. Reylé, J. Richard, L. Cambrésy, M. Deleuil, E. Pécontal, L. Tresse and I. Vauglin (eds)*

# THE PHOENIX MODEL ATMOSPHERE GRID FOR STARS

F. Allard[1]

**Abstract.** We present a new project for a 1D static though full NLTE model atmosphere grid ranging $T_{\rm eff} = 15,000$ to 1500 K in 100K steps, surface gravities ranging from $\log g = -0.5$ to 6.0 in steps of 0.25 dex, and metallicity ranging from [M/H]=-2.5 to +0.5 in steps of 0.25 dex accounting for alpha element enrichment of [$\alpha$/H]= +0.0, +0.2, +0.4 and C/O enhancement.

Keywords: stars, red dwarfs, M Dwarfs, Very Low Mass stars, model atmosphere, spectroscopy

## 1 Introduction

The PHOENIX model atmosphere code has been created in 1994 in Phoenix, Arizona from merging the M Dwarf model atmosphere code (Allard 1990, molecules in equilibrium chemistry, molecular opacities, convection) with the supernovae radiative transfer code (Hauschildt 1991, spherical symmetry radiative transfer with scattering, full NLTE, Opacity Sampling, Expansion Velocity treatment). The resulting PHOENIX code has been since then developed for additional atmospheric physics such as radiative diffusion (Leblanc & Monin 2005), Quasi-molecular Alkali line profiles (Allard et al. 2007), non-local chemical equilibrium (NLCE) (Barman et al. 2011), and cloud formation(Allard et al. 2001, 2003a, 2011; Allard & Homeier 2012; Allard et al. 2012, 2013b,a; Allard 2014; Allard et al. 2014). More recently, a 3D version of PHOENIX has been developed that include all this complexity (Hauschildt & Baron 2014).

M dwarfs were the last stars to be fully understood due to an SED dominated by molecular opacities (MgH, CaOH, CaH, TiO, VO, FeH, $H_2O$, CO) and cloud formation below 3000 K. But recently, Rajpurohit et al. (2012, 2013, 2014, 2016) and Baraffe et al. (2015) have demonstrated that the most up-to-date code version reproduce for the first time the overall spectral energy distribution (SED) of M dwarfs down to the hydrogen burning minimum mass. The revised temperature scale has been confirmed by independent research based on interferometry Mann et al. (2016). And Veyette et al. (2016) have demonstrated the importance to account for carbon enhancement for the thermal structure of M Dwarfs. The revised solar abundances and the possibility to use all the lines of complete and accurate molecular line lists made also the difference.

Time as come to provide detailed and uniform model atmosphere grids for the analysis of the GAIA survey, in preparation of the PLATO 2.0 mission, and for the CARMENES and SPIRou survey among others. I present here the 2017 PHOENIX model atmosphere grid project.

## 2 Model description

In recent years the possibility to model the atmospheres of stars with Radiation HydroDynamical (RHD) simulations and 3D radiative transfert has progressed for Red Supergiant stars (Chiavassa et al. 2016) and main dwarf stars (Asplund 2014; Ludwig & Steffen 2016) improving our knowledge on stars and revised solar abundances (Asplund et al. 2009; Caffau et al. 2011) in time for the GAIA survey.

However, most of the parameter determination is still done using more available and rapid to compute 1D static model atmospheres avec iSpec (Blanco-Cuaresma et al. 2014) ou encore les services en ligne de bases de donnes POLLUX (http://or.lcpc.fr/pollux/) par exemple. The most important is to take into account the findings of the afore mentioned 3D work in doing so. However, all these codes are not NLTE codes, and NLTE has proven difficult if not impossible in the frame of 3D work. The role of full NLTE codes such as `PHOENIX` is

[1] Univ Lyon, Ens de Lyon, Univ Lyon1, CNRS, Centre de Recherche Astrophysique de Lyon UMR5574, F-69007, Lyon, France

therefore to provide control on the question of the importance of NLTE effects, to provide thermal structures to the large variety of radiative transfer codes being operated, and provide large uniform model atmosphere grids also for the transcription of the predictions of interior and evolution models in the observational plane.

PHOENIX also includes the hyperfine structure for some NLTE atoms and solves the radiative transfer in spherical geometry that is mandatory for extended atmospheres. Instead of using a fixed microturbulence velocity, mixing length, radius and mass throughout the computation of the grid, our use of PHOENIX is therefore to interpolate these informations for each model of the grid from RHD simulation studies (Ludwig et al. 1999, 2002; Ludwig 2006; Ludwig et al. 2006; Freytag et al. 2010b, 2012) and interior and evolution model (Baraffe et al. 2015, 2003; Chabrier et al. 2000; Baraffe et al. 1998, 1997).

This is the intention of the current project, to use the multi-purpose PHOENIX code in its full NLTE capacity and compute a complete and uniform model atmosphere grid with parameters ranging from $T_{\rm eff} = 15,000$ to 1500 K in 100K steps, surface gravities ranging from $\log g = -0.5$ to 6.0 in steps of 0.25 dex, and metallicity ranging from [M/H]=-2.5 to +0.5 in steps of 0.25 dex accounting for alpha element enrichment of $[\alpha/H]= +0.0$, +0.2, +0.4 and C/O enhancement.

In PHOENIX atmosphere models, a trial atmospheric profile is applied (usually using a previously calculated model), the equations of hydrostatic and radiative transfer are solved, and the solution is tested until convergence is reached. The model is considered converged when the energy is conserved within one tenth of a percent from layer to layer. At each of the model iterations, a spectrum with typically over 30,000 points is generated which samples the bolometric flux from 0.01 to 500 $\mu$m with a step of 0.01 to 2 Å in the region where most of the flux is emitted (i.e. 0.1 to 50 $\mu$m). When the model is converged, a final spectrum is generated with maximum sampling of around 0.01 Å throughout the SED. The final spectrum must be degraded to the instrumental resolution and applied rotation and macroturbulence corrections before being compared to spectroscopic observations.

The PHOENIX version 15.5 model atmospheres developed by Allard & Hauschildt (1995); Allard et al. (1994, 1997, 2001, 2003b, 2007, 2011); Allard & Homeier (2012); Allard et al. (2012, 2013b,a); Allard (2014); Allard et al. (2014) are characterized by the following parameters: (i) the surface gravity, $\log(g)$, (ii) the effective temperature, $T_{\rm eff}$, (iii) the mixing length to scale height ratio, $\alpha/H_p$, (iv) the micro-turbulent velocity $\xi$, and (v) the initial element abundances, $\epsilon_i$. Cloud formation is based on the Rossow (1978) cloud model and used the results of RHD simulations of M-L-T dwarfs atmospheres by Freytag et al. (2010a) and Freytag et al. (2017, in prep.) to calibrate the mixing length, the overshoot, the dynamical velocity and micro-turbulence, and the diffusion coefficient. We also use the most recent solar abundance composition by Asplund et al. (2009) and Caffau et al. (2011). The most important opacities that have been updated since Allard et al. (2001) are: i) all atomic lines are now included from hydrogen to uranium (Kurucz database 2006), ii) we have migrated from the AMES (Partridge & Schwenke 1997; Langhoff 1997) to the BT2 (Barber et al. 2006) water vapor and (Plez 1998) TiO line lists, ii) the VO, MgH, and CaH line lists by (Plez 1998) replace the remaining JOLA approximations, iv) $NH_3$ opacities from the ExoMol project (Yurchenko et al. 2011), v) All bands of $H_2$-$H_2$ CIA tables (Borysow 2002; Abel et al. 2011), $H_2$-H CIA tables (Gustafsson & Frommhold 2003), and He-H CIA tables (Gustafsson & Frommhold 2001) for the most recent version implemented, vi) polarizability wavelength distributions have been added for several additional types of grains bringing our database from 30 to 43, vii) 5 different grain size distributions to choose from have been added, viii) a cloud model has been added, and finally ix) we include detailed profiles for most of the important alkali lines based on the unified theory of collisional quasi-molecular broadening Allard et al. (2007, and references therein). The CE calculations are treated as in Allard et al. (2001) with additional condensates added to serve low temperature brown dwarf atmospheres. See Ferguson et al. (2005) for a detailed description of our opacity database and its application to Rosseland and Planck mean calculations.

## 3 Model grids already available

We have been posting on our online web site (https://phoenix.ens-lyon.fr/simulator/) several model atmosphere grids reflecting the evolution in the development of PHOENIX version 15.5 code version since the original publications to the more recent developments of the BT-Settl grids thanks to funding by the Agence Nationale de la Recherche (Projects Extrasolar planets 2005-2009, GUéPARD 2010-2014). These are :

- NextGen (Allard et al. 1994; Hauschildt et al. 1997) : breakthrough opacity sampling model atmospheres,
- AMES-Cond/Dusty (Allard et al. 2001; Chabrier et al. 2000; Baraffe et al. 2003): first complete dust condensation model atmospheres i.e. models with dust in equilibrium with gas phase while the Cond

models neglect the dust opacity to simulate full sedimentation,

- BT-NextGen (Allard 2010; Allard et al. 2011, 2012): NextGen models with revised modern molecular opacities (Ferguson et al. 2005) and the BT2 water vapor line list bu Barber et al. (2006),
- BT-Cond/Dusty (Allard 2010; Allard et al. 2011, 2012): same as former AMES-Cond/Dusty, but with revised opacities as above,
- BT-Settl GNS93 (Husser et al. 2013): first extremely extended grid of model atmospheres (a former version to that published) with modern opacities,
- BT-Settl AGSS2009 (Allard et al. 2011; Allard & Homeier 2012; Allard et al. 2012): using the Asplund et al. (2009) solar abundances,
- BT-Settl CIFIST2011(Allard et al. 2011; Allard & Homeier 2012; Allard et al. 2012): using the Caffau et al. (2011) solar abundances and adding the computation of the supersaturation on-the-fly rather then using a fixed value suggested by Rossow in the cloud model,
- BT-Settl CIFIST2011b (Allard et al. 2013a,b) : accounting also for a calibration of the mixing length based on RHD simulations by Ludwig et al. (1999, 2002); Ludwig (2006); Ludwig et al. (2006),
- BT-Settl CIFIST2011bc (Allard et al. 2013b,a; Allard 2014; Allard et al. 2014) : accounting for the calibration of the mixing length, overshoot and diffusion coefficient based on RHD simulations by Freytag et al. (2010b, 2012) and account of the grain size distribution and nucleation in the cloud model,
- BT-Settl CIFIST2011c (Allard 2014; Allard et al. 2014) : Aditonnal adjustments of the calibration of the MLT, overshoot, and diffusion coefficient based on RHD simulations by Freytag et al. (in prep.),
- BT-Settl CIFIST2011_2015 (Allard et al. (en prep.), Baraffe et al. 2015) : The MLT equations were revised from (or MLT, see Kippenhahn & Weigert 1994) to the formulation according to Mihalas et al. (1978) (See also Mihalas 1978).

These models are available via the PHOENIX web server (https://phoenix.ens-lyon.fr/simulator/) and the OSU Archive (http://osubdd.ens-lyon.fr/phoenix/).

Since the model atmospheres are using spherical radiative transfer the interior+atmosphere problem becomes iterative, and future versions of the synthetic spectra grid will use the radius and the lithium abundance of the current evolution models.

## 4 Conclusions and propectives

Model atmosphere grids accounting for full NLTE, the calibration of the mixing length, and cloud formation are already available via the Phoenix Web Server (https://phoenix.ens-lyon.fr/simulator), but there exist at this point no comprehensive version including all the recent developments. With the mission GAIA, the need for a complete and comprehensive and uniform grid of models is high.

The PHOENIX model atmosphere project will provide a uniform grid ranging over $T_{\rm eff} = 15,000$ to 1500 K in 100K steps, surface gravities from $\log g = -0.5$ to 6.0 in steps of 0.25 dex, and metallicity from [M/H]=-2.5 to +0.5 in steps of 0.25 dex accounting for alpha element enrichment of $[\alpha/\mathrm{H}] = +0.0$, +0.2, +0.4 and C/O enhancement, and of synthetic spectra valid across the HR diagram down to the substellar regime. This corresponds to more then 500,000 models to calculate, each with 10h or computing time per cpu, or over 5 million CPU hours of computation.

Our priority in term of future development of the models is the molecular opacity upgrade. Since the ExoMol project has revised most of the molecular opacities important for the atmospheres of stars, we are planing the integration of all the molecular opacities of the ExoMol project and from other authors in a later revision of this model atmosphere grid that will be performed on the *Pôle Scientifique de Modélisation Numérique* (PSMN) and on national computing centers.

The research leading to these results has received funding from the "Programme National de Physique Stellaire" (PNPS) of CNRS (INSU). The computations are performed at the *Pôle Scientifique de Modélisation Numérique* (PSMN) at the *École Normale Supérieure* (ENS) in Lyon.

## References


Abel, M., Frommhold, L., Li, X., & Hunt, K. L. C. 2011, J. Chem. Phys., 134, 076101

Allard, F. 1990, PhD thesis, Ruprecht Karls Univ. Heidelberg

Allard, F. 2010, Highlights of Astronomy, 15, 695

Allard, F. 2014, in IAU Symposium, Vol. 299, Exploring the Formation and Evolution of Planetary Systems, ed. M. Booth, B. C. Matthews, & J. R. Graham, 271–272

Allard, F., Allard, N. F., Homeier, D., et al. 2007, A&A, 474, L21

Allard, F., Guillot, T., Ludwig, H.-G., et al. 2003a, in IAU Symposium, Vol. 211, Brown Dwarfs, ed. E. Martín, 325

Allard, F., Guillot, T., Ludwig, H.-G., et al. 2003b, in IAU Symposium, Vol. 211, Brown Dwarfs, ed. E. Martín, 325

Allard, F. & Hauschildt, P. H. 1995, ApJ, 445, 433

Allard, F., Hauschildt, P. H., Alexander, D. R., & Starrfield, S. 1997, ARA&A, 35, 137

Allard, F., Hauschildt, P. H., Alexander, D. R., Tamanai, A., & Schweitzer, A. 2001, ApJ, 556, 357

Allard, F., Hauschildt, P. H., Miller, S., & Tennyson, J. 1994, ApJ, 426, L39

Allard, F. & Homeier, D. 2012, Mem. Soc. Astron. Ital., Astroph:1206.1021

Allard, F., Homeier, D., & Freytag, B. 2011, in ASPCS, Vol. 448, CS16, ed. C. Johns-Krull, M. K. Browning, & A. A. West, 91

Allard, F., Homeier, D., & Freytag, B. 2012, Royal Society of London Philosophical Transactions Series A, 370, 2765

Allard, F., Homeier, D., & Freytag, B. 2013a, Mem. Soc. Astron. Italiana, 84, 1053

Allard, F., Homeier, D., & Freytag, B. 2014, in Astronomical Society of India Conference Series, Vol. 11, Astronomical Society of India Conference Series

Allard, F., Homeier, D., Freytag, B., Schaffenberger, W., & Rajpurohit, A. S. 2013b, ArXiv e-prints

Asplund, M. 2014, in American Institute of Physics Conference Series, Vol. 1632, American Institute of Physics Conference Series, 58–87

Asplund, M., Grevesse, N., Sauval, A. J., & Scott, P. 2009, ARA&A, 47, 481

Baraffe, I., Chabrier, G., Allard, F., & Hauschildt, P. H. 1997, A&A, 327, 1054

Baraffe, I., Chabrier, G., Allard, F., & Hauschildt, P. H. 1998, A&A, 337, 403

Baraffe, I., Chabrier, G., Barman, T. S., Allard, F., & Hauschildt, P. H. 2003, A&A, 402, 701

Baraffe, I., Homeier, D., Allard, F., & Chabrier, G. 2015, A&A, 577, A42

Barber, R. J., Tennyson, J., Harris, G. J., & Tolchenov, R. N. 2006, MNRAS, 368, 1087

Barman, T. S., Macintosh, B., Konopacky, Q. M., & Marois, C. 2011, ApJ, 733, 65

Blanco-Cuaresma, S., Soubiran, C., Heiter, U., & Jofré, P. 2014, A&A, 569, A111

Borysow, A. 2002, A&A, 390, 779

Caffau, E., Ludwig, H.-G., Steffen, M., Freytag, B., & Bonifacio, P. 2011, Sol. Phys., 268, 255

Chabrier, G., Baraffe, I., Allard, F., & Hauschildt, P. 2000, ApJ, 542, 464

Chiavassa, A., Caldas, A., Selsis, F., et al. 2016, ArXiv e-prints

Ferguson, J. W., Alexander, D. R., Allard, F., et al. 2005, ApJ, 623, 585

Freytag, B., Allard, F., Ludwig, H., Homeier, D., & Steffen, M. 2010a, A&A, 513, A19

Freytag, B., Allard, F., Ludwig, H.-G., Homeier, D., & Steffen, M. 2010b, A&A, 513, A19

Freytag, B., Steffen, M., Ludwig, H.-G., et al. 2012, J.Comp.Phys., 231, 919

Gustafsson, M. & Frommhold, L. 2001, J. Chem. Phys., 115, 5427

Gustafsson, M. & Frommhold, L. 2003, A&A, 400, 1161

Hauschildt, P. 1991, Non-LTE Modellatmosphären für Novae und Supernovae.

Hauschildt, P. H., Allard, F., Alexander, D. R., & Baron, E. 1997, ApJ, 488, 428

Hauschildt, P. H. & Baron, E. 2014, A&A, 566, A89

Husser, T.-O., Wende-von Berg, S., Dreizler, S., et al. 2013, A&A, 553, A6

Kippenhahn, R. & Weigert, A. 1994, Stellar Structure and Evolution (Springer; Study edition ISBN-13: 978-0387580135)

Langhoff, S. R. 1997, ApJ, 481, 1007

Leblanc, F. & Monin, D. 2005, JRASC, 99, 139

Ludwig, H.-G. 2006, A&A, 445, 661

Ludwig, H.-G., Allard, F., & Hauschildt, P. H. 2002, A&A, 395, 99

Ludwig, H.-G., Allard, F., & Hauschildt, P. H. 2006, A&A, 459, 599

Ludwig, H.-G., Freytag, B., & Steffen, M. 1999, A&A, 346, 111

Ludwig, H.-G. & Steffen, M. 2016, Astronomische Nachrichten, 337, 844
Mann, A. W., Feiden, G. A., Gaidos, E., Boyajian, T., & von Braun, K. 2016, ApJ, 819, 87
Mihalas, D. 1978, Stellar atmospheres, 2nd edn. (W. H. Freeman and Co., San Francisco)
Mihalas, D., Auer, L. H., & Mihalas, B. R. 1978, ApJ, 220, 1001
Partridge, H. & Schwenke, D. W. 1997, J. Comp. Phys., 106, 4618
Plez, B. 1998, A&A, 337, 495
Rajpurohit, A. S., Reylé, C., Allard, F., et al. 2016, A&A, 596, A33
Rajpurohit, A. S., Reylé, C., Allard, F., et al. 2013, A&A, 556, A15
Rajpurohit, A. S., Reylé, C., Allard, F., et al. 2014, A&A, 564, A90
Rajpurohit, A. S., Reylé, C., Schultheis, M., et al. 2012, A&A, 545, A85
Rossow, W. B. 1978, Icarus, 36, 1
Veyette, M. J., Muirhead, P. S., Mann, A. W., & Allard, F. 2016, ArXiv e-prints
Yurchenko, S. N., Barber, R. J., & Tennyson, J. 2011, MNRAS, 413, 1828

# THE PHOTOMETRIC VARIABILITY OF $\zeta$ ORI AA OBSERVED BY BRITE* **

B. Buysschaert[1, 2], C. Neiner[1] and BEST

**Abstract.** Using BRITE photometry, we investigated the photometric variability of the magnetic O-type supergiant $\zeta$ Ori Aa. We found two independent frequencies, leading to several higher harmonics and simple linear combinations. One frequency is related to the rotation period, $f_{\rm rot} = 0.15 \pm 0.02\,{\rm d}^{-1}$. The derived rotation period from this frequency and its higher harmonics, $P_{\rm rot} = 6.65 \pm 0.28\,{\rm d}$, is compatible with the literature value ($P_{\rm rot} = 6.83 \pm 0.08\,{\rm d}$). Thanks to simultaneous CHIRON spectroscopy, we locate the origin of the second frequency, $f_{\rm env} = 0.10 \pm 0.02\,{\rm d}^{-1}$, at the circumstellar environment. We propose mass-loss events as the underlying origin.

Keywords: Stars: massive - Stars: mass loss - Stars: rotation - Stars: individual: $\zeta$ Orionis

## 1 Introduction

$\zeta$ Ori comprises several components organised in a hierarchical system. $\zeta$ Ori A and $\zeta$ Ori B orbit each other every 1509 years with an eccentricity of 0.07 (Mason et al. 2001; Turner et al. 2008), while the moderately eccentric Aa+Ab system, with $e = 0.338 \pm 0.004$, has an orbital period of $2687.3 \pm 7.0$ d (Hummel et al. 2013). We present the stellar parameters of these three components in Table 1.

In addition, $\zeta$ Ori Aa is currently the only known magnetic O-type supergiant. Its magnetic field was first detected by Bouret et al. (2008). Later, Blazère et al. (2015) confirmed and characterized its magnetic field, while accounting for the recently detected Ab component by means of spectral disentangling. The authors deduced $\zeta$ Ori Aa's magnetic field to be dipolar with a polar strength of about 140 G. Moreover, the star's rotation period was determined to $6.83 \pm 0.08$ d. No evidence for a (strong) magnetic field was found for the Ab component. Lastly, their calculations and H$\alpha$ observations were compatible with a weak dynamical magnetosphere around $\zeta$ Ori Aa, indicating only weak interactions between the large scale magnetic field and the circumstellar environment.

## 2 Data analysis

$\zeta$ Ori was monitored during two observing campaigns by the BRIght Target Explorer (BRITE)-Constellation, which aims to observe the majority of stars brighter than $V \approx 5$ (Weiss et al. 2014). The constellation consists of five different nano-satellites, two Austrian, one Canadian, and two Polish, of which three satellites are equipped with a red bandpass filter and two have a blue filter. We have analysed these observations to unravel the photometric variability of $\zeta$ Ori Aa.

[1] LESIA, Observatoire de Paris, PSL Research University, CNRS, Sorbonne Universités, UPMC Univ. Paris 06, Univ. Paris Diderot, Sorbonne Paris Cité, 5 place Jules Janssen, F-92195 Meudon, France

[2] Instituut voor Sterrenkunde, KU Leuven, Celestijnenlaan 200D, 3001 Leuven, Belgium

* Based on data collected by the BRITE Constellation satellite mission, designed, built, launched, operated and supported by the Austrian Research Promotion Agency (FFG), the University of Vienna, the Technical University of Graz, the Canadian Space Agency (CSA), the University of Toronto Institute for Aerospace Studies (UTIAS), the Foundation for Polish Science & Technology (FNiTP MNiSW), and National Science Centre (NCN).
** Based on CHIRON spectra collected under CNTAC proposal CN2015A-122.

**Table 1.** Stellar parameters of the three main components of $\zeta$ Ori, determined by Hummel et al. (2013) unless noted differently. Stellar masses and radii were determined from the photometric distance. (*a*: Sota et al. (2014); *b*: Simón-Díaz & Herrero (2014); *c*: Blazère et al. (2015); *d*: Bouret et al. (2008))

| | Aa | Ab | B |
|---|---|---|---|
| $m_V$ (mag) | 2.08 | 4.28 | 4.01 |
| SpT | O9.2Ib Nwk $^a$ | B1IV | B0III |
| $M\,(M_\odot)$ | $33 \pm 10$ | $14 \pm 3$ | – |
| $R\,(R_\odot)$ | $20 \pm 3.2$ | $7.3 \pm 1.0$ | – |
| $v \sin i$ (km/s) | 127 $^b$ | $< 100$ $^c$ | 350 |
| $T_{\rm eff}$ (kK) | $29.5 \pm 1.0$ $^d$ | 29 $^c$ | – |
| $\log g$ (dex) | $3.25 \pm 0.10$ $^d$ | 4.0 $^c$ | – |

### 2.1 Data preparation

The individual BRITE nano-satellites monitored a large part of the Orion constellation from mid-September 2013 until mid-March 2014, and from late-September 2014 until mid-March 2015. These two campaigns lasted ~130 d and ~170 d, respectively, and are now known as Orion I and Orion II. During the Orion I run, the two Austrian BRITE nano-satellites (BAb and UBr) were used, while the Canadian (BTr), the Polish (BLb and BHr), and one Austrian (UBr) nano-satellites were employed for Orion II. Once the images are downlinked and the observing campaign has finished, lightcurves are extracted from the CCD frames, using circular apertures (Popowicz et al., submitted). The raw lightcurve files have been corrected for intrapixel sensitivity, and provide additional meta-data such as CCD centroid positions and CCD temperature. We continue to improve upon this extracted photometry by adjusting the timing to mid-exposure times, accounting for different cadences, and by cleaning the data for any flux and meta-data outliers. Lastly, we performed a decorrelation for instrumental effects, which are in part related to the changing on-board temperature, affecting both the CCD and the optical path. We show these temperature variations for all four satellites during the Orion II campaign in Fig. 1. The corrected and studied BRITE photometry for $\zeta$ Ori is shown in Fig. 2. Simultaneous blue and red observations agree well with each other.

### 2.2 Time-series analysis

Since we intended to perform a time-series analysis on the BRITE photometry, only data with the highest duty cycle and the best root-mean-square flux stability were considered for further analysis. As a consequence, we discarded the BTr and BAb observations obtained during the Orion II campaign. During the initial analysis, we also noted that the photometry of the two campaigns is variable on different timescales. Therefore, we continued to analyse Orion I and Orion II data separately.

To study the brightness variations in the selected BRITE photometry, we followed an iterative prewhitening approach (see e.g. Degroote et al. 2010). We determined the most significant frequency peak in the frequency diagram, fitted a sine model with that frequency to the data, calculated the residuals, and repeated this process on the residuals until no significant variability remained. Lomb-Scargle periodograms (Lomb 1976; Scargle 1982) were used for frequency diagrams, with ten times oversampling over the region of 0 - 10 $\mathrm{d}^{-1}$. We used the signal-to-noise criterion (Breger et al. 1993) to deduce the significance of a peak in the periodogram, using a 4 $\mathrm{d}^{-1}$ frequency window and a threshold of four times the noise level. Lastly, the extracted frequency sets per BRITE lightcurve were compared with each others, and only frequencies appearing in at least two lightcurves were accepted.

## 3 Results

We extracted the main significant frequencies for $\zeta$ Ori, which are harmonics or linear combinations of two independent frequencies. These two frequencies are $f_{\rm rot} = 0.15 \pm 0.02\,\mathrm{d}^{-1}$ and $f_{\rm env} = 0.10 \pm 0.02\,\mathrm{d}^{-1}$, which we discuss in more detail below. We attributed these variabilities to $\zeta$ Ori Aa and its environment, because it produces about 80 % of the measured flux (Hummel et al. 2013).

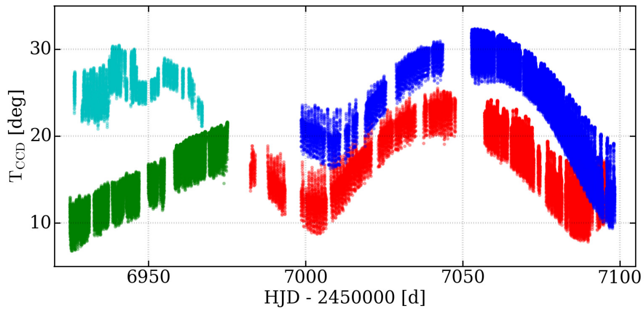


**Fig. 1.** On-board temperature variations for four nano-satellites during the Orion II campaign. The color represents the nano-satellite of the BRITE-Constellation: cyan for BAb, green for BTr, red for BHr, and blue for BLb.

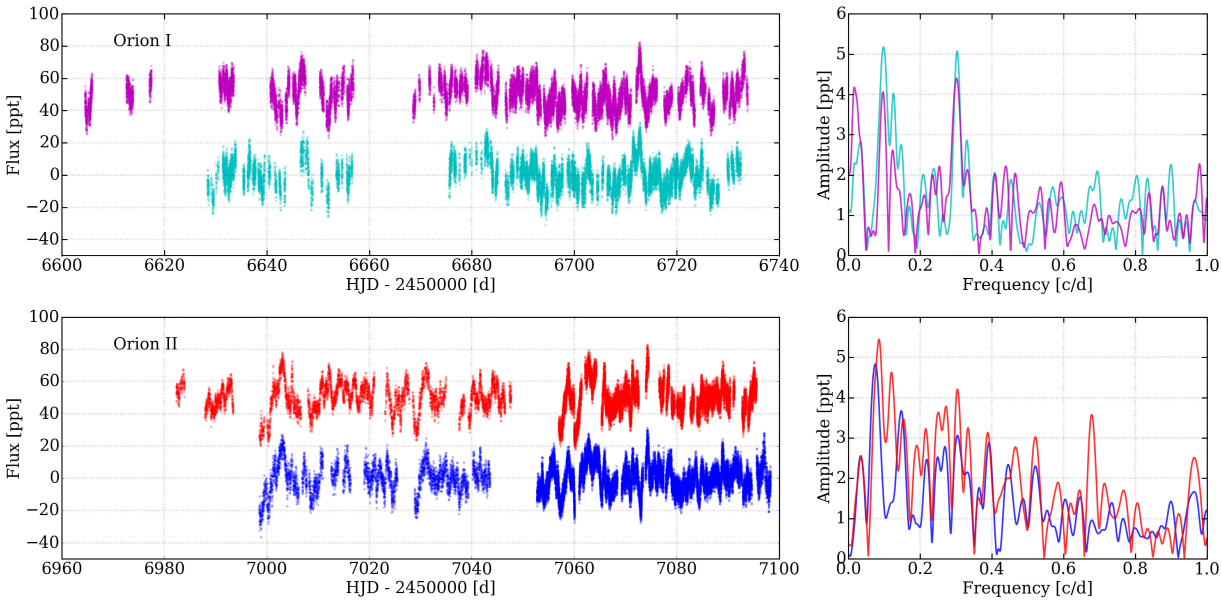


**Fig. 2.** *Left*: Studied BRITE photometry for $\zeta$ Ori, fully detrended and corrected for instrumental effects for the Orion I (*top*) and Orion II (*bottom*) observing campaigns. The color represents which nano-satellite of the BRITE-Constellation monitored $\zeta$ Ori: cyan for BAb, red for BHr, blue for BLb, and magenta for UBr. The flux variations are given in parts-per-thousand (ppt). Observations taken by a red nano-satellite (UBr, BHr) have an offset of 50 ppt for increased visibility. *Right*: Corresponding Lomb-Scargle periodograms of the photometry. The amplitude of the variability is marked in ppt. No significant variability was found outside the region of 0 to 1 $\mathrm{d}^{-1}$.

### 3.1 Rotation

Both the Orion I and Orion II photometry of $\zeta$ Ori Aa show variations with $f_{\mathrm{rot}}$ and its higher harmonics, irrespectively of the color. Of these harmonics, $2f_{\mathrm{rot}}$ is the most pronounced, and is most likely related to the magnetic poles coming twice into view per rotation cycle. This is often observed for magnetic massive stars (e.g. $\sigma$ Ori E Oksala et al. 2015). The amplitudes of the variations related to the rotation and its harmonics differ per observing campaign. $2f_{\mathrm{rot}}$ is the strongest of the rotational variation for Orion I data, while it is $f_{\mathrm{rot}}$ itself for Orion II. Combining the measurements of $f_{\mathrm{rot}}$ and its higher harmonics to increase the precision, we obtain $P_{\mathrm{rot}} = 6.65 \pm 0.28$ d. This value is consistent within the error bars with the rotation period of Blazère et al. (2015, i.e. $6.83 \pm 0.08$ d).

### 3.2 Circumstellar environment

The origin of the photometric variations with $f_{\mathrm{env}}$ can be understood by performing a comparison with high-resolution CHIRON spectroscopy (Tokovinin et al. 2013), simultaneously taken with the second part of the

Orion II campaign (Fig. 3). In particular, we investigated the variability of the P Cygni profile of the H$\alpha$ line and changes of its equivalent width with respect to time. Both analyses confirmed the presence of the variability with $f_{\rm env}$ in the H$\alpha$ emission line, indicating that the circumstellar environment of $\zeta$ Ori Aa is causing the brightness changes seen in the BRITE photometry. Since the timescale is not related to the rotation period of the star, we consider it unlikely that the magnetosphere is causing the variations. Instead, we propose that periodic mass loss produces these variations, although the exact mechanism remains unknown at present. Discrepancies in the circumstellar behaviour could also explain why the BRITE lightcurves of the Orion I and Orion II campaigns display significant differences, with stronger activity in Orion II.

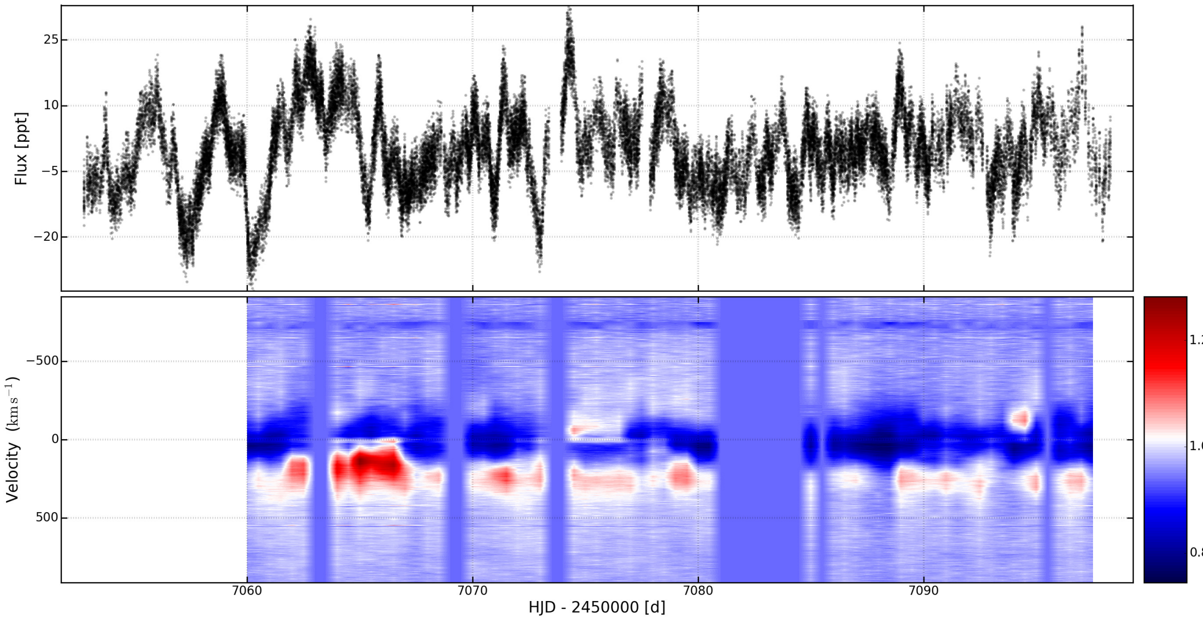


**Fig. 3.** *Top*: BRITE photometry during the second half of the Orion II campaign, with merged blue and red color information. *Bottom*: Dynamical plot of the H$\alpha$ line observed in the simultaneous CHIRON spectroscopy.

## 4 Conclusions

We analysed two-color BRITE photometry of $\zeta$ Ori, taken during two observing campaigns. The data indicates the star is photometrically variable. Thanks to an iterative prewhitening approach, we recover several significant frequencies, which can be explained as higher harmonics and simple linear combinations of two fundamental frequencies. The first frequency is $f_{\rm rot} = 0.15 \pm 0.02\,{\rm d}^{-1}$, the rotation period of $\zeta$ Ori Aa, and agrees well with the literature value. The second frequency is $f_{\rm env} = 0.10 \pm 0.02\,{\rm d}^{-1}$. Thanks to simultaneous spectroscopy of the H$\alpha$ line, we show that it has its origin in the circumstellar environment of $\zeta$ Ori Aa. Period mass loss is the proposed driving mechanism for these variations. Additional variability remains present in the residuals.

## References

Blazère, A., Neiner, C., Tkachenko, A., Bouret, J.-C., & Rivinius, T. 2015, A&A, 582, A110

Bouret, J.-C., Donati, J.-F., Martins, F., et al. 2008, MNRAS, 389, 75

Breger, M., Stich, J., Garrido, R., et al. 1993, A&A, 271, 482

Degroote, P., Aerts, C., Samadi, R., et al. 2010, Astronomische Nachrichten, 331, 1065

Hummel, C. A., Rivinius, T., Nieva, M.-F., et al. 2013, A&A, 554, A52

Lomb, N. R. 1976, Ap&SS, 39, 447

Mason, B. D., Wycoff, G. L., Hartkopf, W. I., Douglass, G. G., & Worley, C. E. 2001, AJ, 122, 3466

Oksala, M. E., Kochukhov, O., Krtička, J., et al. 2015, MNRAS, 451, 2015

Scargle, J. D. 1982, ApJ, 263, 835

Simón-Díaz, S. & Herrero, A. 2014, A&A, 562, A135

Sota, A., Maíz Apellániz, J., Morrell, N. I., et al. 2014, ApJS, 211, 10
Tokovinin, A., Fischer, D. A., Bonati, M., et al. 2013, PASP, 125, 1336
Turner, N. H., ten Brummelaar, T. A., Roberts, L. C., et al. 2008, AJ, 136, 554
Weiss, W. W., Rucinski, S. M., Moffat, A. F. J., et al. 2014, PASP, 126, 573

# Session SF2A

# Users meeting os the French telescopes - TBL/OHP193

*SF2A 2016*
*C. Reylé, J. Richard, L. Cambrésy, M. Deleuil, E. Pécontal, L. Tresse and I. Vauglin (eds)*

# TELESCOPE BERNARD LYOT: OPERATION, INSTRUMENTATION, PERSPECTIVES

R. Cabanac[1] and TBL Team[2]

**Abstract.** This talk is the TBL director report at the 3rd French national telescopes Users Meeting of 2016. Telescope Bernard Lyot, the 2-m at Pic du midi (2870m), is dedicated to spectro-polarimetric studies since 2007 with the instrument Narval. This paper presents TBL operation, science highlights and statistics of the past 10 years of operation. It also opens perspectives for the coming 10 years with the funding of Neo-Narval (Narval stabilized to $v_r < 3$m/s) and SPIrou at Pic du midi (aka SPIP) for the study of the young exoplanetary systems.

Keywords: Telescope operation, instrumentation, spectropolarimetry, stellar magnetism, exoplanets

## 1 Introduction

Before describing the details of Telescope Bernard Lyot operations, it is important to recall the users that Pic du midi Observatory is still used for science observations today because of the partnership with an independent administration, a public syndicate, funded by Occitanie Region, departmental and local governments. That public administration is responsible for maintaining the buildings, the access to the summit via a cable car, and the hotel and restaurant logistics. The public administration also runs a museum and a planetarium in the historic part of the summit and manage an average of 100,000 public visitors per year. A leasing treaty running until 2029 is regulating the partnership between the Observatory Midi-Pyrenees (University of Toulouse, Paul Sabatier) and the public administration. This partnership is extremely successful and few common projects are on tracks, an international Dark Sky reserves covering 3000 km$^2$ around Pic du midi, and a World Heritage UNESCO series is on track (High Mountain Observatories, with Spanish, Chilean and US partners).

## 2 TBL administrative status in 2016

At the beginning of the last contract (2012-2015), CNRS INSU has proposed to delegate the administrative management of the National Telescopes (OHP T2M and TBL) to their local Universities (Aix-Marseille and U Toulouse), which both have an Observatory (OSU Pytheas and OMP). The date of TBL adminitrative transfer to OMP was set to the end of the contract (31 dec 2015). Starting in 2013, A working group have extensively discussed and prepared to fusion of TBL to the OMP staff, and proposed a working solution for TBL to continue its science observations in optimal conditions. Since January 1st, TBL is therefore managed by OMP Executive Science Director at Pic du midi and Tarbes (R. Cabanac until Sept 6, 2016, Eric Josselin from Sept 7, 2016).

### *2.1 TBL budget in 2016*

The University Paul Sabatier funding to TBL is 40 keuros per year, the CNRS contribution is 80 keuros. This budget barely covers costs for operating the telescope in service mode, and TBL still needs project-oriented funding for instrumentation upgrades and dome maintenance. The staff is divided between 11 University staff and 9 CNRS staff for a global budget (including salaries) of ∼1 million euros.

[1] IRAP, University of Toulouse, CNRS, France
[2] OMP-TBL, University of Toulouse, CNRS, France

### 2.2 TBL staff

TBL staff has gained 2 new telescope operators to increase the number of observable nights to 320, but the electronic TBL specialists are now requested to support all Pic du midi telescope and experiments, the staff is now 8 operators, 5.5 electronicians, and 5.5 support staff (2 software, 1 secretary, 1 instrument specialist, 1 technical director).

## 3 Science operations

### 3.1 Service observing

TBL is operated in full service mode since semester 2009B. Philippe Mathias, CNAP AA SO3, is responsible of this service that covers all aspects of observations. A team of 4 CNAP support astronomers (SO3) shares the task of preparing observing queues each night for the service observers. Service observateurs are hired among Masters and PhD students all over France, post-docs who wish to gain experience in telescope observations and among a team of volunteers (TBL associated observers) who are trained for observations at TBL.
Service observing at TBL includes the proposal phase (through Northstar interface), 2 calls for proposals per year in semesters A (March 1-August 31) and semesters B (Sept 1- Feb 28), the Time allocation phase then done by the French national TAC, the observations performed by TBL science team after successful PI have filled their Phase 2 program definition (Protected link to PH2), the release of all observations, which are reduced and released to the PIs after a quality check and validation process is done by the support astronomer, at the end of each night of observations (using automated software). A PH2 night log allows PI to follows the progress of their program during the semester. Finally, TBL /Narval data is kept proprietary for one year is spectroscopic mode and 2 years for polarimetric mode, after which data is released on the Public TBL Legacy database and Polar Base database.

### 3.2 TBL users

TBL observing time is mostly reserved to the French astronomical community that have performed 208 science programs between 2007A and 2015B, 10 Large programs running for 4 consecutive semesters and covering 50% of the observing time, and 188 PI programs of one semester. The science themes of the programs are mostly stellar physics (188), interstellar medium (4), and planetology (16).
TBL also participates to European Transnational access program OPTICON that buys nights at consolidated cost to 22 european-managed 2 to 4-m telescopes. Between 2007A and 2015B, 19 programs where selected and funded by OPTICON.
Finally, TBL can sell nights (at consolidated costs) to foreign PIs or Agencies, 3 such foreign programs were 'allocated' since 2007A (for Bulgarian Academy of Science, and Netherland).
The following table summarizes the statistics of proposals and pressure on the offered clear times.

Source des demandes TBL/NARVAL depuis 2007:

Mode service

| | 2006B | 2007 | 2008 | 2009 | 2010 | 2011 | 2012 | 2013 | 2014 | 2015 | 2016 |
|---|---|---|---|---|---|---|---|---|---|---|---|
| PNPS | 173 | 407 | 386 | 282 | 200.5 | 145.5 | 156 | 138.5 | 138 | 168 | 167 |
| PNP | 0 | 0 | 41 | 55 | 37 | 12 | 0 | 10.5 | 14.5 | 15 | 3 |
| PCMI | 0 | 32 | 0 | 1 | 5 | 0 | 0 | 0 | 1 | 5 | 4 |
| OPTICON | 0 | 33 | 48 | 25 | 7.5 | 21 | 28 | 5.5 | 13.5 | 23 | 14.5 |
| AUTRE | | | | | | | | 4 | | | 3.5 |
| | 173 | 472 | 475 | 363 | 250 | 178.5 | 184 | 158.5 | 167 | 211 | 192 |
| PRESSION | - | 2.0 | 2.0 | 4.8 | 3.3 | 2.4 | 2.5 | 2.1 | 2.2 | 2.8 | **2.6 (PI<2)** |

### 3.3 Science highlights in 2016

Any non-exhaustive science highlight is necessarily biased by an arbitrary selection function, the one chosen here is to mention works that underline the notable quality of Narval used in synergy with other instruments. In this respect, two papers are worth mentioning, the first one is a work of Hébrard et al. (2016), that made a detailled analysis of the correlation observed in magnetic M dwarf stars between their phometric jitter and magnetic fields, five stars were followed (GJ 205, GJ 358, GJ 410, GJ 479, GJ 846) with HARPS-Pol and NARVAL (see Figure 1).

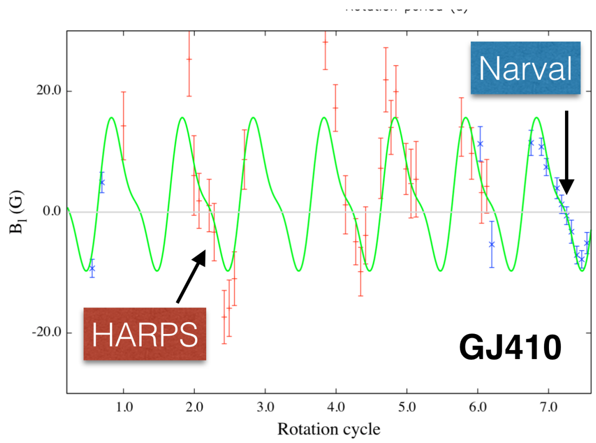


**Fig. 1.** Periodogram of M dwarf GJ410, observed with both HARPS-Pol and Narval Hébrard et al. (2016). Note that despite being mounted on a 2-m telescope, Narval data are significantly more accurate than HARPS-Pol data (@ ESO 3.6m). This underlines the importance of designing dedicated spectro-polarimeters, instead of adding polarimetric module to an existing spectrograph.

Aurière et al. (2016) have been studying the supergiant Betelgeuse for many years. The most recent paper of the team shows a remarkable detection of a linearly polarized spectrum for Betelgeuse. This linear polarization signature is interpreted as a depolarization of the continuum by the absorption lines. The linear polarization of the Betelgeuse continuum is due to the anisotropy of the radiation field induced by brightness spots at the surface and Rayleigh scattering in the atmosphere. Aurière et al. (2016) have developed a geometrical model to interpret the observed polarization, from which they infer the presence of two brightness spots and their positions on the surface of Betelgeuse. Their study of the linearly polarized spectrum of Betelgeuse provides a novel method for studying the evolution of brightness spots at its surface and complements quasi-simultaneous observations obtained with PIONIER at the VLTI, cf Figure 2.

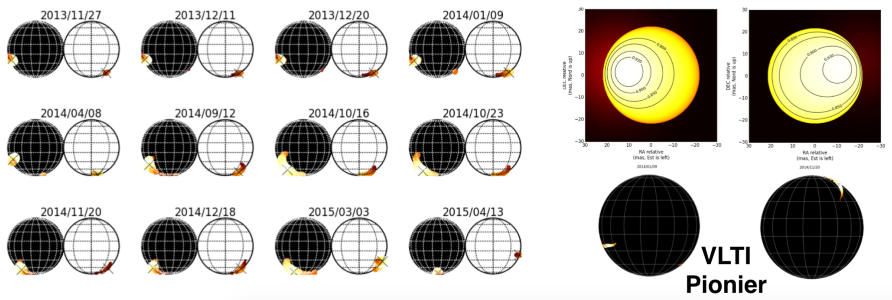


**Fig. 2.** Comparison between the models of spot evolution on Betelgeuse based on Narval data (**left**), and VLTI/PIONIER data (**right**). The two models are remarkably concordant.

### *3.4 TBL publication record*

A more quantitave account of TBL/Narval impact in the field of stellar magnetism over the years (2007-2015) is its publication record based on the new ADS interface ui.adsabs.harvard.edu shown in the following table that summarizes the record as of June 2016.

| Papers | Total | Refereed |
|---|---|---|
| Number of papers | 441 | 275 |
| Normalized paper count | 111.9 | 54.1 |
| Total number of reads | 121446 | 105687 |
| Average number of reads | 275.4 | 384.3 |
| Median number of reads | 172 | 312 |
| Total number of downloads | 66400 | 58644 |
| Average number of downloads | 150.6 | 213.3 |
| Median number of downloads | 94 | 166 |
| **Citations** | **Total** | **Refereed** |
| Number of citing papers | 3212 | 3158 |
| Total citations | 7118 | 6835 |
| self-citations | 1585 | 1478 |
| Average citations | 16.1 | 24.9 |
| Median citations | 4 | 12 |
| Normalized citations | 1155.1 | 1082.9 |
| Refereed citations | 5089 | 4913 |
| Average refereed citations | 11.5 | 17.9 |
| Median refereed citations | 3 | 8 |
| Normalized refereed citations | 821.8 | 778.7 |
| **Indicators** | **Total** | **Refereed** |
| h index | 46 | 46 |

### 3.5 *More decenal statistics*

A detailled set of observing statistics computed over the period 2007-2015 have been published on TBL web site: http://spiptbl.bagn.obs-mip.fr/observation/statistiquesobservations. The salient results per semester are shown in the table below.

total numbers a dark time per semester (Nautical twilight): from **~74000 science fits**.
semester A: 1391.36097228 h semester B: 2067.81753856

| Name | Science h (% SROP) | Readout h (% SROP) | Overhead h (% SROP) | Pointing h (% SROP) | S+R+O+P h (% SROP) | Close h | Total h |
|---|---|---|---|---|---|---|---|
| 2007A | 281.0 (74) | 25.7 (6.8) | 17.0 (4.5) | 54.5 (14.4) | 378.0 (41) | 475.1 | 1391.4 |
| 2008A | 268.5 (70) | 37.3 (9.8) | 16.4 (4.3) | 60.0 (15.7) | 382.2 (46) | 564.2 | 1391.4 |
| 2009A | 310.2 (72) | 28.9 (6.7) | 13.3 (3.1) | 76.2 (17.8) | 428.5 (49) | 511.0 | 1391.4 |
| 2010A | 272.0 (64) | 49.3 (11.7) | 34.5 (8.2) | 67.2 (15.9) | 423.0 (46) | 479.2 | 1391.4 |
| 2011A | 245.9 (63) | 29.4 (7.6) | 22.6 (5.8) | 89.9 (23.2) | 387.7 (41) | 448.7 | 1391.4 |
| 2012A | 283.6 (65) | 39.9 (9.2) | 38.3 (8.8) | 71.8 (16.6) | 433.7 (45) | 431.4 | 1391.4 |
| 2013A | 208.2 (67) | 29.0 (9.4) | 27.9 (9.0) | 45.1 (14.5) | 310.2 (36) | 535.9 | 1391.4 |
| 2014A | 205.7 (61) | 38.1 (11.3) | 37.6 (11.2) | 54.5 (16.2) | 335.9 (37) | 480.9 | 1391.4 |
| 2015A | 219.8 (62) | 41.3 (11.6) | 42.6 (11.9) | 53.6 (15.0) | 357.4 (36) | 399.3 | 1391.4 |
| 2006B | 283.7 (66) | 26.6 (6.2) | 13.3 (3.1) | 105.6 (24.6) | 429.2 (21) | 0.0 | 2067.8 |
| 2007B | 646.8 (75) | 65.7 (7.6) | 48.5 (5.6) | 99.3 (11.5) | 860.3 (53) | 449.7 | 2067.8 |
| 2008B | 289.1 (71) | 39.2 (9.7) | 18.4 (4.5) | 59.3 (14.6) | 405.9 (30) | 694.1 | 2067.8 |
| 2009B | 299.9 (70) | 33.0 (7.7) | 19.7 (4.6) | 78.3 (18.2) | 431.0 (31) | 674.6 | 2067.8 |
| 2010B | 387.8 (71) | 45.5 (8.3) | 34.2 (6.3) | 78.0 (14.3) | 545.4 (39) | 654.7 | 2067.8 |
| 2011B | 410.2 (68) | 61.0 (10.2) | 49.8 (8.3) | 78.7 (13.1) | 599.7 (45) | 725.3 | 2067.8 |
| 2012B | 196.4 (65) | 20.1 (6.7) | 18.8 (6.2) | 65.4 (21.7) | 300.7 (22) | 700.0 | 2067.8 |
| 2013B | 325.5 (71) | 37.2 (8.1) | 40.6 (8.8) | 56.2 (12.2) | 459.5 (32) | 631.6 | 2067.8 |
| 2014B | 265.9 (62) | 42.4 (9.9) | 49.9 (11.6) | 72.1 (16.8) | 430.3 (29) | 597.1 | 2067.8 |
| 2015B | 326.9 (59) | 48.4 (8.7) | 74.8 (13.5) | 104.6 (18.9) | 554.7 (35) | 496.9 | 2067.8 |

## 4 What's next for TBL?

### *4.1 New instruments*

Narval has been the dedicated instrument of TBL for almost ten years, it is now approaching the end of its scheduled scientific life. Although the pressure on the instrument is still high for a 2-m telescope, The TBL science committee (CS TBL, chair D Mouillet) was mandated to explore future instrumentation for TBL and actual interest of the community to continue using TBL beyond Narval. A call for idea was published in 2012 by the CS TBL. Letters of intent were received for two instruments. One was Neo-Narval (PI T Boehm), an upgraded version of Narval providing a stabilized spectrograph ($\sim$2m/s) for velocimetry and polarimetric studies in the visible range, and SPIP (PI Hebrard/Donati), a copy of SPIRou, a velocimetry-stabilized spectropolarimeter ($\sim$1m/s) in the near infrared to be installed at CFHT in the coming years. The two projects were presented in 2013-2014 at the Prospective exercise of INSU-AA Hyres. The stellar physics community expressed a strong support and interest for both instruments, stating the complementary of the two projects, although no funding was available at the time. In 2015, the two projects were funded on CPER with 500 keuros Neo-Narval and 4 Meuros SPIP (cf talk of T. Boehn on Neo-Narval).
The science cases and technical documents of the two instruments are available online, at spiptbl.bagn.obs-mip.fr/INSTRUMENTATION2/neonarval for Neo-Narval, and http://spirou.irap.omp.eu/ for SPIRou.
Neo-narval is scheduled to be commissioned in 2018 and SPIP by 2021.

### *4.2 TBL operation with Neo-Narval and SPIP*

Assuming one can disregard decommissioning of Neo-Narval because the stellar community has expressed a concern that Neo-Narval will be the only spectropolarimeter in operation in the northern hemisphere when SPIROU replace Espadons at CFHT, diverse operation modes can be proposed when Neo-Narval and SPIP are both available at TBL.
A first mode would be to mount one instrument on the telescope based on a fixed calendar. This mode is the most straightforward, but is arguably not very efficient. A second mode could be to have both polarimeters mounted on the telescope with a system switching the beam from one instrument to the other in a timely fashion. This would require the TBL to redesign the bonnette. A third solution would be to used both instruments at the same time, while one would be used in full spectropolarimetry mode, and the other in spectroscopic mode. Finally, a fourth solution would be to use both spectropolarimeters in full mode simultaneously. Mode 2, 3 and 4 would require more and more complex redesign of the bonnette and some R&D for the fourth one, none of those implementations being funded, yet.

## 5 Conclusion

Thanks to its existing and future instrumentation Telescope Bernard Lyot is still a competitive internationally acclaimed telescope in 2016, and promise to be very successful in the coming years. This was possible because of the dedication of a very competent and enthusiastic technical team working without counting hours, days and nights, for maintaining both the telescope and its instrumentation. This was also possible thanks to the dynamic scientific community pushing for the best performing instruments and asking for challenging programs, and finally this was possible because of the financial support of local and regional governments, which year after year support science at the summit of Pic du midi. Would any of those three legs disappear, TBL would be doomed. As a leaving director I express my gratitude to all those people and wish you clear skies!

## References

Aurière, M., López Ariste, A., Mathias, P., et al. 2016, A&A, 591, A119
Hébrard, É. M., Donati, J.-F., Delfosse, X., et al. 2016, MNRAS, 461, 1465

*SF2A 2016*
*C. Reylé, J. Richard, L. Cambrésy, M. Deleuil, E. Pécontal, L. Tresse and I. Vauglin (eds)*

# FOLLOW-UP AND CHARACTERIZATION OF THE TESS EXOPLANETS WITH SOPHIE, SPIROU, AND JWST

N. Crouzet[1], X. Bonfils[2], X. Delfosse[2], I. Boisse[3], G. Hébrard[4], T. Forveille[2], J.-F. Donati[5], F. Bouchy[3,6], C. Moutou[3,7], R. Doyon[8,9], E. Artigau[8,9], L. Albert[8,9], L. Malo[7,8,9], A. Lecavelier des Etangs[4] and A. Santerne[3]

**Abstract.**
The NASA *TESS* mission will deliver hundreds of transiting exoplanet candidates orbiting bright stars. The spectrometers SOPHIE at OHP and SPIRou at CFHT will be ideal to obtain radial velocities of these candidates, confirm their nature, and derive the planets' masses. These measurements will be crucial to deliver the best targets for atmospheric characterization with *JWST*. Here, we calculate the required observing time with SOPHIE, SPIRou, and *JWST* for each of the *TESS* targets in order to prepare follow-up observations. To infer their potential for *JWST*, we restrict the calculations to the case of transmission spectroscopy with NIRISS. The radial velocity follow-up of the giant planets ($R_p > 4\,\mathrm{R_E}$) could be achieved with SOPHIE, with a median observing time of 3.47 hours per target, and a total observing time of 305 hours that includes the 80% most favorable cases. Several small planets ($R_p < 4\,\mathrm{R_E}$) could also be confirmed, but most of them would require an unrealistic time investment. On the other hand, SPIRou is ideally suited to the follow-up of the small planets, with a median observing time of 2.65 hours per target, and a median observing time of 4.70 hours for the terrestrial planets in the habitable zone ($R_p < 2\,\mathrm{R_E}$, $S < 2\,\mathrm{S_E}$). With *JWST*, the 10% most favorable small planets have a median observing time of 16.2 hours, and the 10% most favorable habitable zone terrestrial planets have a median observing time of 59.7 hours. Overall, this study will help define a follow-up strategy and prepare observation programs with SOPHIE and SPIRou before the first planet candidates are delivered by *TESS*.

Keywords: Surveys, Planets and satellites: detection, Planets and satellites: atmospheres, Methods: observational, Techniques: radial velocities, Techniques: spectroscopic

## 1 Introduction

Exoplanets transiting in front of bright stars offer the best prospects for their physical characterization: by delivering more photons, bright stars increase the efficiency of follow-up observations and more information can be obtained on the systems compared to fainter stars. *TESS* (*Transiting Exoplanet Survey Satellite*, launch: 2017, PI: G. Ricker, Ricker et al. 2014) is a NASA mission to detect transiting exoplanets around bright stars ($4 < I_{mag} < 13$) by high precision wide field photometry. One year later, *JWST* (*James Webb Space*

[1] Dunlap Institute for Astronomy and Astrophysics, University of Toronto, 50 St Georges Street, Toronto, ON M4Y 2K2, Canada
[2] Université Grenoble Alpes, CNRS, IPAG, 38000 Grenoble, France
[3] Aix-Marseille Université, CNRS, LAM (Laboratoire d'Astrophysique de Marseille) UMR 7326, 13388 Marseille, France
[4] Institut d'Astrophysique de Paris, UMR 7095 CNRS, Université Pierre & Marie Curie, 98bis boulevard Arago, 75014 Paris, France
[5] Université de Toulouse, UPS-OMP, IRAP, 14 avenue E. Belin, Toulouse, F-31400 France & CNRS, IRAP/UMR 5277, Toulouse, 14 avenue E. Belin, F-31400 France
[6] Observatoire de Genève, Université de Genève, 51 ch. des Maillettes, 1290 Sauverny, Switzerland
[7] Canada-France-Hawaii Telescope Corporation, CNRS, 65-1238 Mamalahoa Hwy, Kamuela, HI 96743, USA
[8] Département de physique and Observatoire du Mont-Mégantic, Université de Montréal, Montréal, QC H3C 3J7, Canada
[9] Institut de Recherche sur les Exoplanètes (iREx), Université de Montréal, Département de Physique, C.P. 6128 Succ. Centre-ville, Montréal, QC H3C 3J7, Canada

*Telescope*, launch: 2018) will provide a unique opportunity to probe the atmospheres of transiting exoplanets by spectroscopy at infrared wavelengths. Most of the exoplanet targets for *JWST* are expected to come from *TESS*. With such a tight schedule, efficient follow-up of the *TESS* planet candidates is crucial. The spectrometers SOPHIE (Bouchy et al. 2009) at OHP (Observatoire de Haute-Provence) and SPIRou (Delfosse et al. 2013) at CFHT (Canada-France-Hawaii Telescope) will be ideal to confirm the planetary nature of these candidates and to measure their masses by radial velocities. SOPHIE has been successfully used for the follow-up of *CoRoT* and *Kepler* candidates, and the *TESS* targets will be significantly brighter. SOPHIE operates at visible wavelengths (3872-6943 Å). SPIRou is a near-infrared spectro-polarimeter that will enable radial velocity measurements at high precision ($< 1$ m s$^{-1}$) and high resolving power ($> 70{,}000$) in the 0.98-2.35 $\mu$m bandpass in one shot. One of its main goals is the detection of low-mass exoplanets around low-mass stars, and the first light is planned for the end of 2017, early 2018. The small size of M dwarfs also favours the detection and characterization of small planets through their transits, and *TESS* will detect many more planets around M dwarfs than *Kepler* and *K2* thanks to its almost full sky coverage. In this work, we present estimates of the observing time required with SOPHIE and SPIRou to follow-up the *TESS* simulated planets in radial velocity, and the time required with *JWST* to characterize their atmospheres. This study will be useful to define follow-up strategies and to prepare observation campaigns before the first *TESS* candidates are delivered. The observation chain and the simulations are described in Section 2. Section 3 gives estimates of the required observing time per target. Section 4 presents the cumulative observing time with SOPHIE and SPIRou for each planet category in order to prepare follow-up programs.

## 2 Observation chain and description of the simulations

### 2.1 Transiting planet candidates with TESS

The main goal of the NASA *TESS* mission is to detect transiting exoplanets orbiting around bright stars. We use the catalog of simulated *TESS* detections presented in Sullivan et al. (2015) as an input of our simulations. We consider the expected yield of planets around the $2 \times 10^5$ target stars: about 70 Earths, 486 Super-Earths, 1111 Sub-Neptunes, and 67 giant planets; these numbers are only indicative as they differ for each simulation. We do not consider detections from the full frame images (see Figure 18 of Sullivan et al. 2015, for more details). This catalog provides several physical parameters of the simulated systems: planetary radius $R_p$, orbital period $P$, insolation $S$, host star radius $R_\star$, effective temperature $T_{eff}$, magnitude in several bandpasses, and radial velocity semi-amplitude $K$. We derive other quantities: the planet mass $M_p$ using the empirical mass-radius relation provided by Weiss et al. (2013), the host star mass $M_s$, the semi-major axis $a$, the transit depth $\delta$ and duration $\tau$, the planet equilibrium temperature $T_{eq}$, density $\rho_p$, surface gravity $\log g_p$, and atmospheric scale height $H$. We assume equatorial transits (inclination $i = 0$) and circular orbits (eccentricity $e = 0$). We do not consider planet multiplicity in this study.

### 2.2 Radial velocity follow-up with SOPHIE and SPIRou

Radial velocity follow-up of the *TESS* candidates will be necessary to confirm their planetary nature and measure their masses. The spectrometers SOPHIE in the visible and SPIRou in the near-infrared are ideal in that purpose. For each *TESS* target, we calculate the observing time $t_{RV}$ that would be necessary to measure $K$ with a given signal to noise ratio $S/N$ with these two instruments. We use a reference radial velocity precision $K_{ref}$ of 6 m s$^{-1}$ at a magnitude $V_{ref}$ of 12 in an exposure time $t_{ref}$ of 15 minutes for SOPHIE in the high resolution mode (G. Hébrard, private communication), and an expected precision $K_{ref}$ of 1 m s$^{-1}$ at a magnitude $J_{ref}$ of 9.5 in an exposure time $t_{ref}$ of 15 minutes for SPIRou (Delfosse et al. 2013). We scale these reference precisions to the magnitudes of the *TESS* targets according to Poisson noise. We impose a minimum exposure time of 10 minutes to average stellar pulsations, and a floor precision per point of 2 m s$^{-1}$ for SOPHIE and 1 m s$^{-1}$ for SPIRou. We assume that the measurements are made at quadratures of the radial velocity curves, and we consider that a planet is detected if $K$ is measured with a $S/N$ of 3. In this study, we do not consider stellar rotation and stellar activity which may limit the radial velocity precision.

### 2.3 Atmospheric characterization with JWST

The atmosphere of transiting exoplanets can be characterized by transmission and emission spectroscopy during their transits and eclipses, respectively. Here, we consider the case of transit spectroscopy of the *TESS* planets with *JWST*, and we calculate the observing time $t_{JWST}$ that is necessary to detect molecules in their atmospheres. We use the *JWST*/NIRISS instrument in the SOSS mode (Single-Object Slitless Spectroscopy) which is dedicated to exoplanet spectroscopy, through the online NIRISS SOSS 1-D Simulator*. We run a reference simulation using a set of parameters corresponding to the mean of the *TESS* small planets ($R_p < 4\,\mathrm{R_E}$, where $\mathrm{R_E}$ is the Earth's radius). Then, we scale the results to each *TESS* target: we calculate the target's flux in the NIRISS bandpass from its $T_{eff}$ and $J$-band magnitude using a blackbody spectral energy distribution, and we assume that the noise scales as the Poisson noise. We assume the same observing time in and out of transit, and we use the 1st order spectrum only. The observation efficiency, defined as integration time / total observing time, is 33% in the reference simulation. We keep this value for all the targets for simplicity, because it is optimized during the simulation and the simulator can only be ran on individual targets. A future improvement, if available, would be to run the simulator on all the *TESS* targets. For the atmospheric signal, we calculate the fractional loss of light $\delta_H$ due to molecular absorption from an atmospheric annulus of thickness $H$:

$$\delta_H = \frac{\mathrm{d}\delta}{\mathrm{d}R_p} \times H = \frac{2HR_p}{R_\star^2} \tag{2.1}$$

This metric allows us to estimate the characteristic amplitude of a molecular absorption feature without relying on a theoretical transmission spectrum. Instead, we consider a single spectral feature with an amplitude $\delta_H$, a width $\Delta\lambda = 100$ nm, and a central wavelength $\lambda_c = 1.8$ $\mu$m corresponding to the center of the NIRISS SOSS order 1 spectrum. Then, we calculate the observing time that is necessary to detect this 1-scale height amplitude feature with a $S/N = 1$. In practice, a molecular feature is expected to span several scale heights and a spectrum may contain several features, which would increase the $S/N$ (for example, an amplitude of 3 scale heights would yield $S/N = 3$). These calculations are made for each wavelength tabulated in the NIRISS simulation output and we take the median of the observing times as an estimate for $t_{JWST}$. We also set a lower limit for $t_{JWST}$ as twice the transit duration, because the observations will span at least one full transit including an out-of-transit baseline.

## 3 Observing time per target

### 3.1 SOPHIE and SPIRou

We split the target star population into those harbouring giant planets ($R_p > 4\,\mathrm{R_E}$) and those harbouring small planets ($R_p < 4\,\mathrm{R_E}$) including the terrestrial planets in the habitable zone ($R_p < 2\,\mathrm{R_E}$, $S < 2\,\mathrm{S_E}$), where $\mathrm{R_E}$ and $\mathrm{S_E}$ are the Earth radius and insolation respectively. In this definition, the habitable zone has no outward limit, but most of the *TESS* targets will be observed for 30 days only which will reduce the number of long period, cold planets. We consider only the targets that can be observed with an airmass lower than 2 ($-16.07° < DEC < +90°$ for SOPHIE, $-40.17° < DEC < +79.83°$ for SPIRou). Figure 1 shows the required observing time $t_{RV}$ as a function of stellar magnitude. The follow-up of the giant planets could be achieved with SOPHIE, with a median $t_{RV}$ of 3.47 h per target, and a total time of 305 h after excluding 17 planets with $t_{RV} > 25$ h (the total time varies significantly depending on the limit adopted for $t_{RV}$). Some small planets could also be confirmed by SOPHIE, with a median of 5.92 h and a maximum of 10.71 h for the 10% most favorable cases (103 planets). However, most of the small planets would require an unrealistic time investment, with a median of 116 h per target. On the other hand, SPIRou is ideally suited to the follow-up of the small planets, with a median $t_{RV}$ of 2.65 h, and a median of only 4.70 h for the terrestrial planets in the habitable zone. As limitations, these calculations do not take into account the observational overheads, and constraining the eccentricity will require taking some data points out of quadratures. Thus, the actual observing times will be slightly larger than the estimates presented here.

### 3.2 JWST

To calculate $H$ and $\delta_H$, we consider a H/He-dominated atmosphere for the giant planets ($\mu = 2.32$ u, where $\mu$ is the atmospheric mean molecular mass), a $H_2O$-dominated atmosphere for the hot and warm small planets ($\mu = 18$ u), and an Earth-like atmosphere for the cold small planets ($\mu = 29$ u). We define hot, warm, and cold according to the planets' insolation: $S > 10\,\mathrm{S_E}$, $2\,\mathrm{S_E} < S < 10\,\mathrm{S_E}$, and $S < 2\,\mathrm{S_E}$ respectively (with this

*`http://maestria.astro.umontreal.ca/niriss/simu1D/simu1D.php`

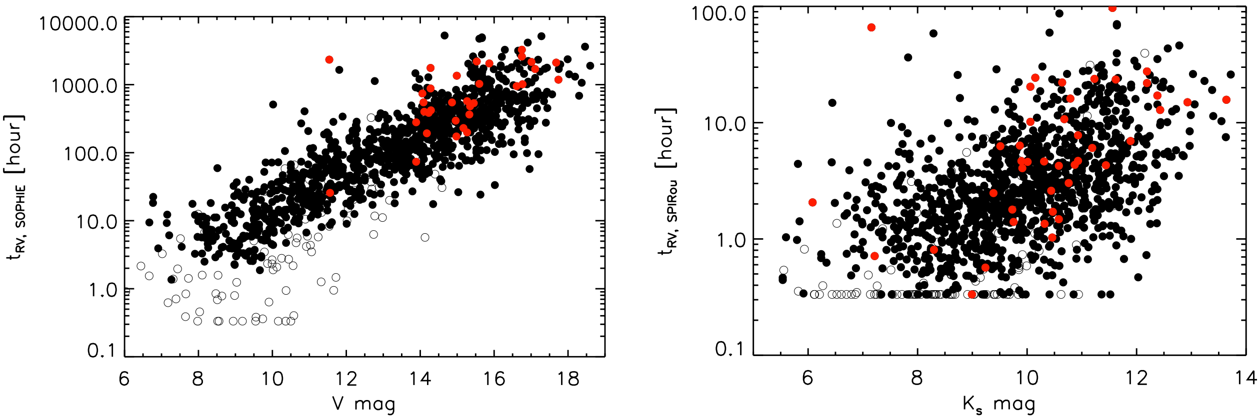


**Fig. 1.** Observing time required with SOPHIE (left) and SPIRou (right) for each *TESS* target as a function of the $V$ and $K_s$ magnitude, respectively. Giant planets are indicated as open circles, small planets are indicated as filled black circles, and terrestrial planets in the habitable zone are indicated as filled red circles. See text for definitions.

definition, "cold" is equivalent to "habitable zone"). We consider all the targets, with no restriction on $DEC$. Figure 2 shows the observing time $t_{JWST}$ required to detect the molecular absorption feature. Interestingly, we find that $t_{JWST}$ increases only weakly with the $K_s$ magnitude for the small planets. This is because $R_\star$ decreases as a function of $K_s$ (M dwarfs are fainter than more massive, larger stars) and as a result $\delta_H$ increases with $K_s$ (the relative transit depth is larger for small stars). We note that $R_\star$ and $R_p$ appear uncorrelated for the *TESS* simulated small planets. Whether this only weak correlation between the time required for transit spectroscopy and the stellar magnitude is generally true for planets around M-dwarfs remains to be investigated. The median observing time $t_{JWST}$ is 13.5 h for the giant planets and is set by twice the transit duration. The small planets have a median of 201 h, and the 10% most favorable ones have a median of 16.2 h and a maximum of 28.6 h. The 10% most favorable habitable zone terrestrial planets have a median of 59.7 h and a maximum of 80.3 h. These planets are highly valuable but will require a significant *JWST* time investment, thus identifying the best ones with SPIRou is crucial. If we assume H/He-dominated atmospheres for all the planets, the median observing time drops to 8 h for the small planets and is limited by twice the transit duration, and to 13.1 h for the habitable zone terrestrial planets.

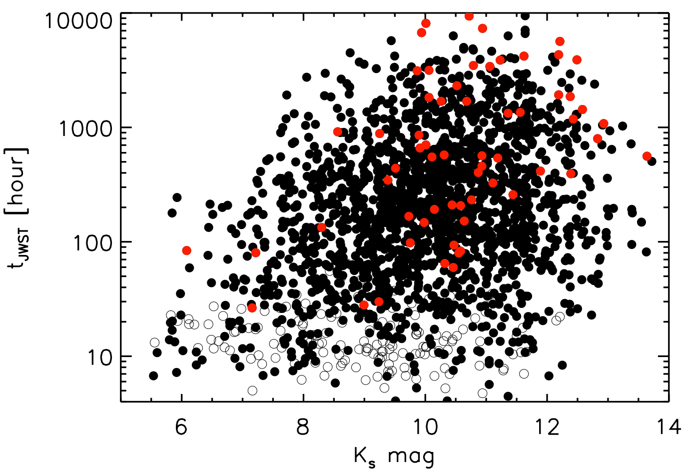


**Fig. 2.** Observing time required with *JWST* NIRISS for each *TESS* planet as a function of the $K_s$ magnitude. The color code is the same as in Figure 1. We set a lower limit on $t_{JWST}$ as twice the transit duration, which is the limiting factor for the giant planets. We show the full *TESS* sample, although targets requiring more than ~100 hours will probably not be observed by *JWST*.

## 4 Preparing radial velocity follow-up programs

In this section, we estimate the cumulative observing time that would be necessary with SOPHIE and SPIRou for the radial velocity follow-up of the *TESS* planet candidates, in order to prepare and optimize observation campaigns. We split the planets into giants ($R_p > 4\,\mathrm{R_E}$), sub-Neptunes and Super-Earths ($2\,\mathrm{R_E} < R_p < 4\,\mathrm{R_E}$), and terrestrial planets ($R_p < 2\,\mathrm{R_E}$), and into hot, warm, and cold planets as defined in Section 3.2. We sort the planets by increasing $t_{RV}$ and compute its cumulative distribution. The results are shown in Figure 3. We exclude planets with $t_{RV} > 25$ hours, which would extend the cumulative distributions on the right hand side. These diagrams can be used to define a follow-up strategy: they give directly the number and type of planets that could be followed-up in a given amount of telescope time. Placing the *TESS* candidates on these diagrams as they are being discovered (from an initial guess) will also help decide on their follow-up. Finally, they are useful to define a combined strategy between SOPHIE and SPIRou: an obvious split would be to observe the giant planets with SOPHIE and the small planets around M-dwarfs with SPIRou. These estimates are based on the *TESS* planet simulations: the uncertainties in the number of planets could be as large as 50% (Sullivan et al. 2015), and we do not account for false positive discrimination. As a future improvement, the targets' potential for observations with *JWST* could be included quantitatively in defining the radial velocity follow-up samples, for example by means of a unique merit function taking into account $t_{RV}$ and $t_{JWST}$.

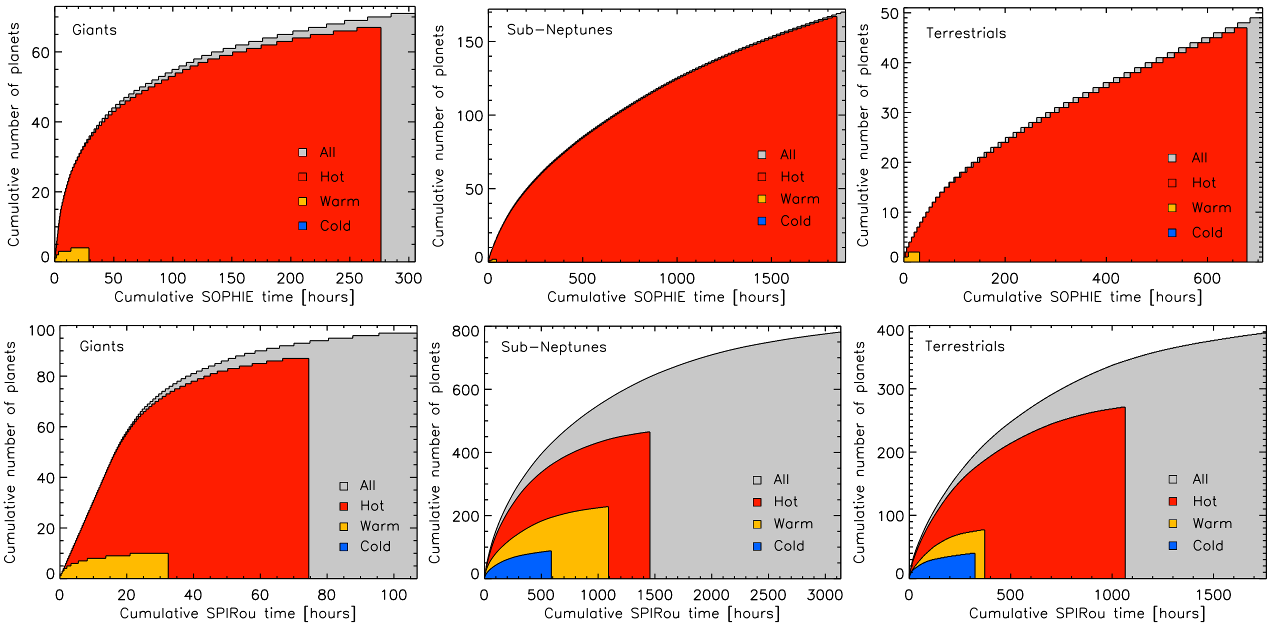


**Fig. 3.** Cumulative number of *TESS* planets that can be followed-up in radial velocity as a function of the cumulative observing time for SOPHIE (top) and SPIRou (bottom), for the giant planets (left), Sub-Neptunes and Super-Earths (middle), and terrestrial planets (right). We show the full sample (grey), as well as the hot (red), warm (yellow), and cold (blue) samples. The planets are sorted by increasing $t_{RV}$. See text for definitions.

## 5 Conclusion

The observing time estimates provided in this study will help define the *TESS* planet candidate samples to observe in radial velocity with SOPHIE and SPIRou as well as their potential for atmospheric characterization with *JWST*. Practically, this approach will help us decide which candidates to observe with SOPHIE and SPIRou while they are being identified by *TESS* and deliver the best targets for *JWST* during the process. This could be particularly important in the context of a large SPIRou program at CFHT, the SPIRou Legacy Survey, which would aim at ∼500 nights in the first 5 years of operation. This program would be shared into several science topics and could include the follow-up of the *TESS* low-mass exoplanet candidates around M-dwarfs. Finally, in the coming years, SOPHIE may be upgraded with a new detector in order to improve its sensitivity and extend its wavelength coverage. This would result in a gain equivalent to one magnitude for mid- and early-M-dwarfs.

The Dunlap Institute is funded through an endowment established by the David Dunlap family and the University of Toronto.

## References

Bouchy, F., Hébrard, G., Udry, S., et al. 2009, A&A, 505, 853

Delfosse, X., Donati, J.-F., Kouach, D., et al. 2013, in SF2A-2013: Proceedings of the Annual meeting of the French Society of Astronomy and Astrophysics, ed. L. Cambresy, F. Martins, E. Nuss, & A. Palacios, 497–508

Ricker, G. R., Winn, J. N., Vanderspek, R., et al. 2014, in Proc. SPIE, Vol. 9143, Space Telescopes and Instrumentation 2014: Optical, Infrared, and Millimeter Wave, 914320

Sullivan, P. W., Winn, J. N., Berta-Thompson, Z. K., et al. 2015, ApJ, 809, 77

Weiss, L. M., Marcy, G. W., Rowe, J. F., et al. 2013, ApJ, 768, 14

*SF2A 2016*
*C. Reylé, J. Richard, L. Cambrésy, M. Deleuil, E. Pécontal, L. Tresse and I. Vauglin (eds)*

# GROUND-BASED FOLLOW-UP OF THE GAIA-RVS RADIAL VELOCITY STANDARDS

C. Soubiran[1], G. Jasniewicz[2], C. Zurbach[2], F. Crifo[3], P. Sartoretti[3], D. Katz[3], O. Marchal[3], P. Panuzzo[3] and S. Udry[4]

**Abstract.** The RVS spectrograph on board of Gaia having no calibration device, radial velocity standards are needed to calibrate the zero-point of the instrument. We have prepared a list of 2798 such stars, well distributed over the sky, and compiled ∼25 000 individual RV measurements from ground-based velocimeters. For a fraction of these stars, their stability at the 300 m s$^{-1}$ level during the Gaia mission has still to be assessed. The catalogue and follow-up programme are presented.

Keywords: stars, radial velocity, Gaia

## 1 Introduction

After a successful launch on 19 December 2013 and several months of commissioning activities, Gaia started its regular observations in July 2014. Gaia is currently continuously scanning the sky in TDI (Time Delay Integration) mode, observing all objects brighter than G = 20.7, including the bright objects down to magnitude 2-3. In addition to the position, parallax and proper motion being measured for one billion stars, radial velocity (RV) is also determined for the ∼100 million brightest stars (down to G ∼ 16) with the Radial Velocity Spectrometer (RVS, Katz et al. 2004; Cropper & Katz 2011). RV measurements will start to be published in the second Gaia Data Release expected end 2017. The RVS is an integral-field spectrograph with resolving power of ∼11 500 covering the near infra-red wavelength range 845 to 872 nm. The RVS will record 40 epochs on average per source during the 5 years of the mission. At the end of the mission in 2019, the RV precision is expected to be 1 km s$^{-1}$ for GK stars down to G = 12-13. Fig. 1 shows the RVS spectrum of one of our targets compared to a NARVAL spectrum of the same star convolved at the RVS resolution. The latest news about Gaia can be found on the ESA website*, together with the science performances updated after the commissioning.

The RVS has no calibration device. The internal calibration uses all bright, well behaved and stable FGK stars to establish the wavelength scale. The zero-point of the RVs needs however to be calibrated with RV standards (RV-STDs) known in advance and proved to be stable during the Gaia observations at the level of 300 m s$^{-1}$. When we started to look for suitable RV-STDs in 2006, no catalogue was existing, fulfilling the RVS requirements in terms of number of stars, magnitude range, sky coverage and precision. Crifo et al. (2010) estabished a list of 1420 RV-STD candidates, all part of the Hipparcos catalogue and selected in 3 sources of RVs : 'Radial velocities of 889 late-type stars' (Nidever et al. 2002), 'Radial velocities for 6691 K and M giants' (Famaey et al. 2005), and 'The Geneva-Copenhagen Survey of Solar neighbourhood' (Nordström et al. 2004), complemented with IAU standards (Udry et al. 1999). All these stars were observed between 2006 and 2012 with ELODIE and SOPHIE at OHP, NARVAL at TBL and CORALIE at the Swiss Euler telescope at La Silla. The archives of these instruments, as well as the HARPS archive, have been queried to complement our observations. These velocimeters all use the same cross-correlation pipeline and masks, so their measurements are homogeneous. The resulting pre-launch version of the catalogue of RV-STDs for Gaia includes 10 214 RV measurements for 1 420 stars, and is presented in Soubiran et al. (2013). The catalogue is made of 2 tables available at the CDS, one with the basic information on the stars and mean RVs and errors, the other one displays the individual measurements.

[1] Laboratoire d'astrophysique de Bordeaux, Univ. Bordeaux, CNRS, 33615 Pessac, France
[2] Laboratoire Univers & Particules de Montpellier, Université de Montpellier, CNRS, 34095 Montpellier, France
[3] GEPI, Observatoire de Paris, 92195 Meudon, France
[4] Observatoire de Genève, CH-1290 Versoix, Switzerland
*`http://www.cosmos.esa.int/web/gaia/`

## 2 The updated catalogue of RV standards for Gaia

The need of additional RV-STDs was expressed in December 2013 by the scientists in charge of the RVS pipeline. In 2006, the first estimate of ∼1000 necessary stars was based on the fact that Gaia should observe one RV-STD per hour. Later studies showed that the RVS calibration needs at least twice more RV-STDs. Our group was in charge of finding these additional candidates. They were searched in the archives of ELODIE (Moultaka et al. 2004), of SOPHIE and of HARPS taking advantage of the large number of FGK stars followed-up in exoplanet programmes, the observations of which are now public. There are indeed many stable stars in the archives, nicely fulfilling the RVS requirements.

Briefly the RV-STDs must be FGK stars brighter than V = 11, with no other star within 20 arcsec (80 arcsec initially). The RV stability at the level of 300 m $s^{-1}$ was assessed by considering stars with at least 2 consistent RV measurements over a minimum time baseline of 300 days. The potential binaries, identified as such in Simbad or XHIP (Anderson & Francis 2012), were eliminated. Then we considered the stars showing a standard deviation, $\sigma_{\rm RV}$, lower than 100 m $s^{-1}$ (corresponding to the stability level of $3\sigma_{\rm RV} \leq 300$ m $s^{-1}$). Note that all the measurements were transformed into the SOPHIE scale, the small offsets between the different instruments being corrected as explained in Soubiran et al. (2013). As a consequence the RVS final RVs will be in the SOPHIE scale.

We have now a total of 2 798 RV-STD candidates, shown on the celestial sphere in Fig. 2 : 1209 are from the initial catalogue, 1589 are new ones. Fig. 3 shows typical examples of stable stars found in the combined archives.

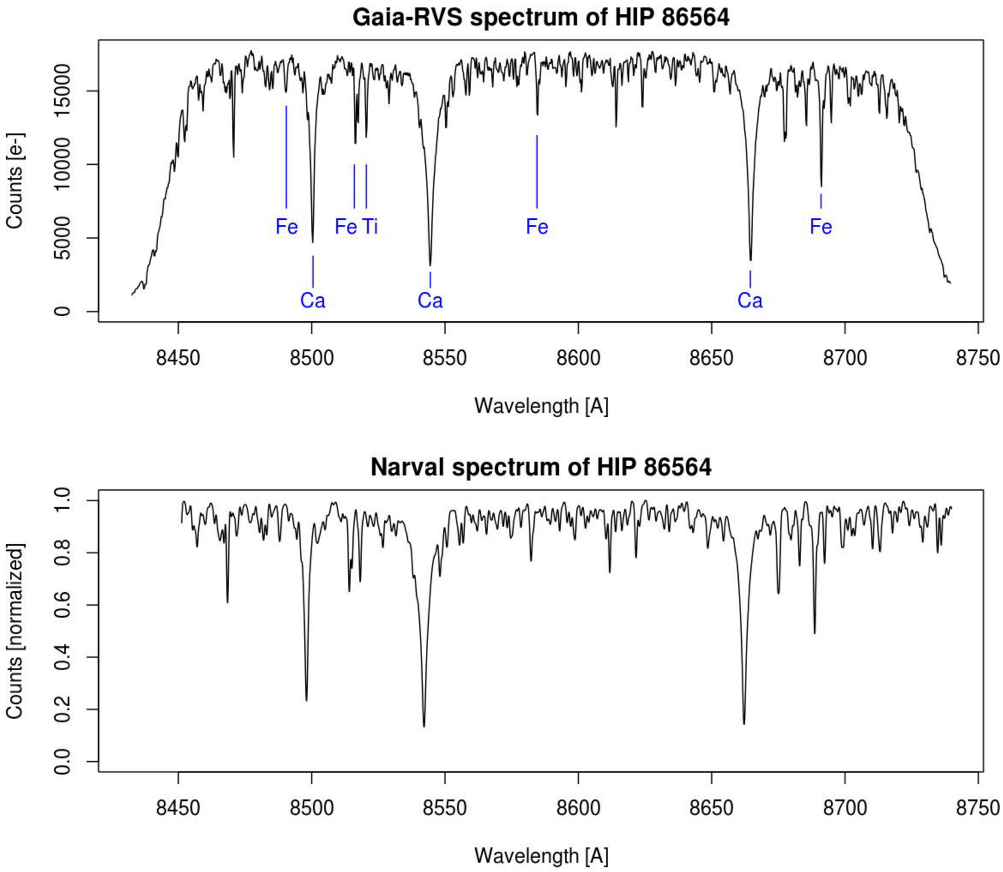


**Fig. 1.** HIP086564 is a bright V=6.64 K5 star observed by the RVS during the commissioning phase, and previously observed by us with NARVAL. This image has been published on the ESA web site as "Image of the Week" in June 2014.

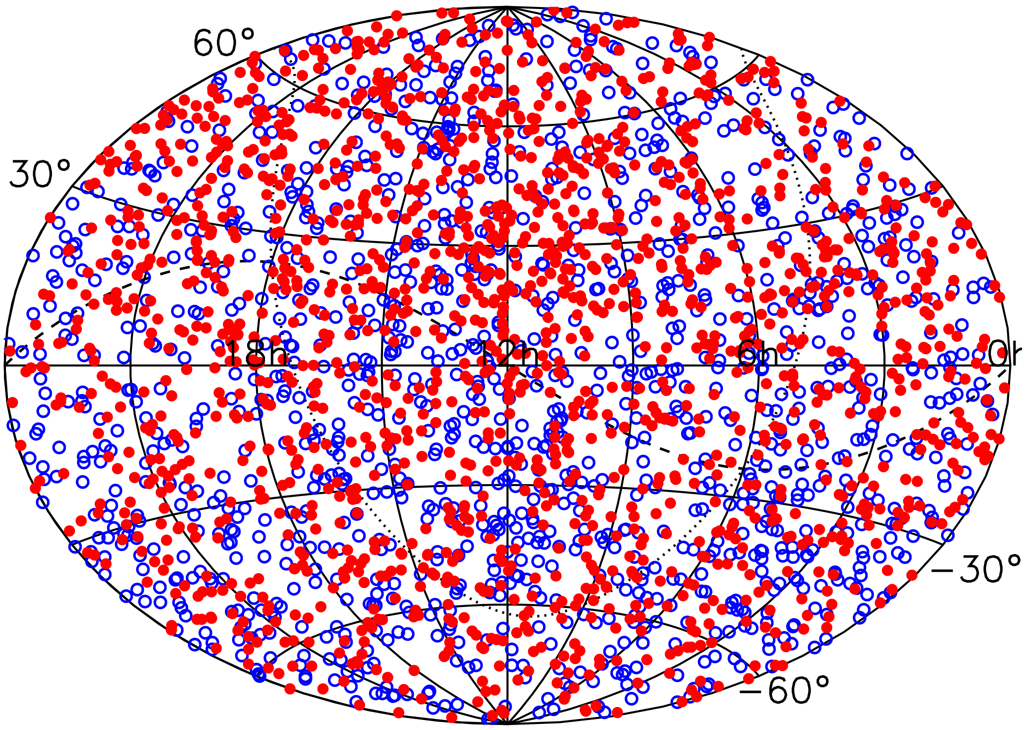


**Fig. 2.** Distribution of the RV-STD candidates on the celestial sphere in equatorial coordinates : blue open circles for the initial catalogue (Soubiran et al. 2013), red dots for the new ones. The dashed line indicates the projection of the Ecliptic plane, the dotted line that of the Galactic plane.

## 3 Follow-up programme

At this stage, most of the selected stars are only RV-STD candidates. Their stability at the level of 300 m s$^{-1}$ during the Gaia mission (end in 2019) has still to be confirmed with new ground based observations (Crifo et al. 2015). There are 1 632 stars for the northern follow-up programme, already observed with ELODIE, SOPHIE, or NARVAL. We have already gathered a total of 24 865 individual RV measurements for these stars. However, not all the 1 632 stars have to be re-observed, depending on the number and time baseline of the already available RV measurements, and the date of the last observations. A total of 1072 northern stars have been selected to be re-observed with SOPHIE because they lack recent observations. This is a higher limit since the number of stars is revised each semester by querying the SOPHIE archive for public observations of our stars made by other groups. The follow-up of the 1072 northern stars started in September 2014, and is ongoing at a rate of 6 nights per semester. About 30% of the programme is achieved, with only one star found to exhibit variations larger than 300 m s$^{-1}$.

For the Southern programme we will use CORALIE. In addition, we will query again the HARPS archive to complement our own observations.

## 4 Conclusion

The catalogue of RV-STDs is mandatory for Gaia, for the RVS calibration, but it will also be useful for other projects. It is a unique dataset considering the number of stars, the homogeneity and precision of the RV measurements and their time baseline up to 20 years. For instance, the Gaia ESO survey (Gilmore et al. 2012) has already observed some of our RV- STDs for the validation of their Giraffe and UVES radial velocities. The USNO Astronomical Almanach lists our most stable stars in their section about Radial Velocity Standard Stars. This work is also an example of exploitation of the archives of spectrometers.

We thank the Programme National Cosmologie et Galaxies for supporting the observations at OHP.

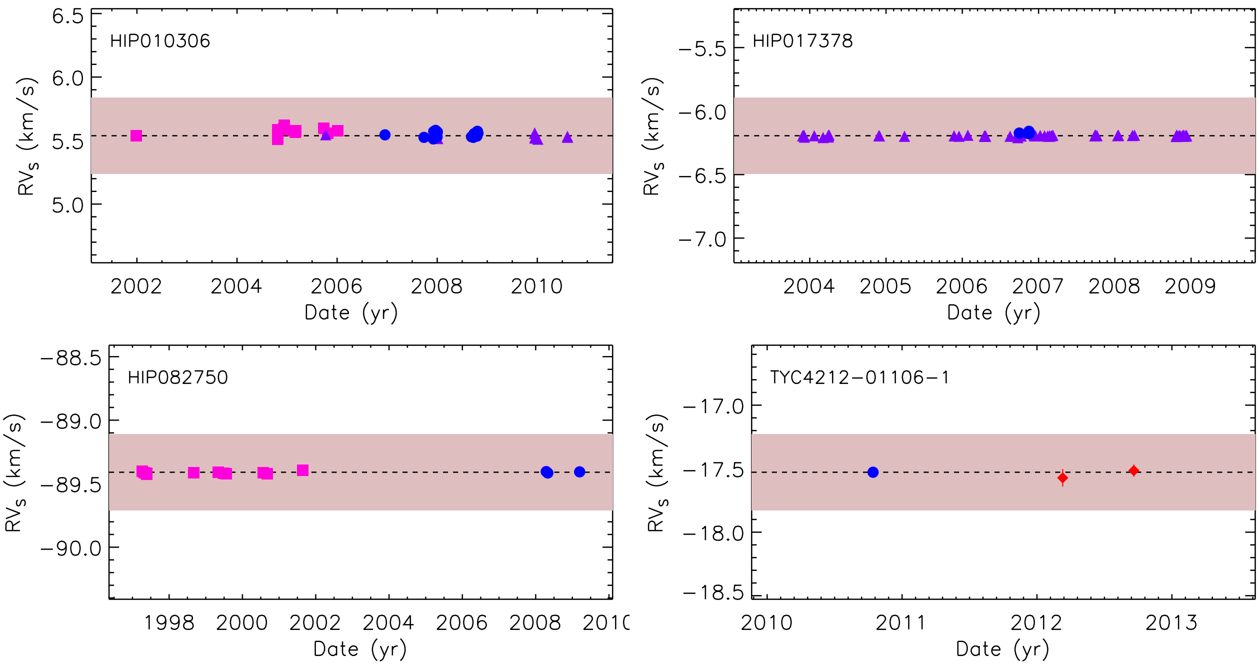


**Fig. 3.** RV measurements for some of the new RV-STD candidates. The pink squares, blue dots, red diamonds and purple triangles are respectively ELODIE, SOPHIE, NARVAL and HARPS measurements. The RV axis is centered on the mean RV and spans 2 km s$^{-1}$. The shaded area represents the 300 m s$^{-1}$ stability limit.

## References


Anderson, E. & Francis, C. 2012, Astronomy Letters, 38, 331

Crifo, F., Jasniewicz, G., Katz, D., et al. 2015, in SF2A-2015: Proceedings of the Annual meeting of the French Society of Astronomy and Astrophysics, ed. F. Martins, S. Boissier, V. Buat, L. Cambrésy, & P. Petit, 359–362

Crifo, F., Jasniewicz, G., Soubiran, C., et al. 2010, A&A, 524, A10

Cropper, M. & Katz, D. 2011, in EAS Publications Series, Vol. 45, EAS Publications Series, 181–188

Famaey, B., Jorissen, A., Luri, X., et al. 2005, A&A, 430, 165

Gilmore, G., Randich, S., Asplund, M., et al. 2012, The Messenger, 147, 25

Katz, D., Munari, U., Cropper, M., et al. 2004, MNRAS, 354, 1223

Moultaka, J., Ilovaisky, S. A., Prugniel, P., & Soubiran, C. 2004, PASP, 116, 693

Nidever, D. L., Marcy, G. W., Butler, R. P., Fischer, D. A., & Vogt, S. S. 2002, ApJS, 141, 503

Nordström, B., Mayor, M., Andersen, J., et al. 2004, A&A, 418, 989

Soubiran, C., Jasniewicz, G., Chemin, L., et al. 2013, A&A, 552, A64

Udry, S., Mayor, M., & Queloz, D. 1999, in Astronomical Society of the Pacific Conference Series, Vol. 185, IAU Colloq. 170: Precise Stellar Radial Velocities, ed. J. B. Hearnshaw & C. D. Scarfe, 367

*SF2A 2016*
*C. Reylé, J. Richard, L. Cambrésy, M. Deleuil, E. Pécontal, L. Tresse and I. Vauglin (eds)*

# A NEW FAMILY OF MAGNETIC STARS: THE AM STARS

A. Blazère[1,2], C. Neiner[1], P. Petit[2] and F. Lignières[2]

**Abstract.**
We presented the discovery of an ultra-weak field in three Am stars, $\beta$ UMa, $\theta$ Leo, and Alhena, thanks to ultra-deep spectropolarimetric observations. Two of the three stars of this study shown peculiar magnetic signatures with prominent positive lobes like the one of Sirius A that are not expected in the standard theory of the Zeeman effect. Alhena, contrary to Sirius A, $\beta$ UMa and $\theta$ Leo, show normal signatures. These detections of ultra-weak fields in Am stars suggest the existence of a new family of magnetic intermediate-mass stars: the Am stars. However the various shapes of the signatures required further observation to identify the physical processes at work in these stars. A preliminary explanation is based on microturbulence.

Keywords: Stars: magnetic fields,

## 1 Introduction

Magnetic fields play an important role in the evolution of intermediate-mass stars. However, the properties of these magnetic hot stars are still poorly understood. About 10% of intermediate mass stars are found to be strongly magnetic with a longitudinal magnetic field in excess of 100 G (Aurière et al. 2007).

A first ultra-weak magnetic field was discovered on the normal A star Vega (Lignières et al. 2009). The magnetic maps constructed thanks to Zeeman Doppler Imaging (ZDI) show a magnetic spot close to the pole. This discovery raises the question of the existence of ultra-weak magnetic fields in the $\sim$ 90% of stars that do not host a strong field.

A first weakly magnetic Am star (i.e. chemically peculiar stars showing metallic lines), Sirius A, was discovered by Petit et al. (2011). However, the observed signature in circular polarization is not of null integral over the line profile as in other intermediate-mass stars, since the Stokes V line profile exhibits a positive lobe dominating the profile. This signature shape is not expected in the normal Zeeman theory. Therefore, the abnormal shape of the polarized profile remained a puzzle and required further investigation.

As a consequence, we observed three Am stars: $\beta$ UMa, $\theta$ Leo, and Alhena. Detecting ultra-weak fields in Am stars is challenging due to the weakness of the expected signatures. The fundamental parameters of all targets are presented in Table 1. The three objects are early A-type targets and have similar stellar parameters.

## 2 Observations

The targets were observed with the Narval spectropolarimeter, installed at the 2-meter Bernard Lyot Telescope (TBL) at the summit of Pic du Midi Observatory in the French Pyrénées. We used the polarimetry mode to measure circular polarization (Stokes V).

We obtained 149 spectra of $\beta$ Uma collected in 2010 and 2011, 171 spectra of $\theta$ Leo collected in 2012, 2013, and 2014 and 20 spectra of Alhena gathered in October 2014 and between September 2015 and April 2016 in the frame of the BritePol project (see Neiner et al. 2015).

[1] LESIA, Observatoire de Paris, PSL Research University, CNRS, Sorbonne Universités, UPMC Univ. Paris 06, Univ. Paris Diderot, Sorbonne Paris Cité, 5 place Jules Janssen, 92195 Meudon, France
[2] Université de Toulouse, UPS-OMP, Institut de Recherche en Astrophysique et Planétologie, Toulouse, France

**Table 1.** Fundamental parameters of $\beta$ UMa, $\theta$ Leo and Alhena

| | $\beta$ UMa | $\theta$ Leo | Alhena | Sirius A |
|---|---|---|---|---|
| spectral type | A1Vm | A2Vm | A2Vm | A1Vm |
| $T_{\rm eff}$ (K) | $9600^a$ | $9350^b$ | $9260^e$ | 9900 |
| log g | $3.6^a$ | $3.83^c$ | $3.65^b$ | 4.33 |
| Mass $M_\odot$ | $2.7\ ^d$ | $2.7\ M^d$ | $2.5\ ^d$ | 2.12 |
| Radius $R_\odot$ | $3.9\pm0.1\ ^d$ | $3\ ^a$ | 4.3 | $1.7\ ^a$ |
| Microturbulence | $2.0\text{-}2.65^e$ | $2.1\text{-}2.4^d$ | $1.0\text{-}1.4^d$ | $1.8\text{-}2.0^f$ |

[a] Boyajian et al. (2012)
[b] Smith & Dworetsky (1993)
[c] Monier (2005)
[d] Adelman et al. (2015)
[e] Adelman (2014)
[f] Landstreet (2011)

## 3 Data Analysis

To test whether the stars are magnetic, we applied the well-known and commonly used Least-Squares Deconvolution (LSD) technique (Donati et al. 1997) on each spectra and computed LSD pseudo line profiles from all available photospheric lines. The line-lists used for LSD were created from a list of lines extracted from the VALD data base (Piskunov et al. 1995; Kupka & Ryabchikova 1999) using the respective effective temperature and log g of each star (Table 1). We removed the H lines, the lines blended with the H lines and the lines that are not visible in the spectra.

For $\beta$ UMa and $\theta$ Leo, we did not obtain detection in the individual LSD profiles. To further improve the signal-to-noise ratio, we then co-added all LSD profiles of this star, resulting in one single averaged LSD profile for each star. The result are shown in Fig. 1.

The Stokes profiles of the $\beta$ UMa and $\theta$ Leo display peculiar signatures with a prominent positive lobe (see Fig. 1) similar to the signatures of Sirius A. This kind of signatures is not expected in the normal Zeeman theory, and required investigations to confirm or infirm the magnetic origin of these signatures. For $\beta$ UMa and $\theta$ Leo, we demonstrated thanks to several tests that the peculiar signatures are due to a magnetic field (see Blazère et al. 2016b for more details).

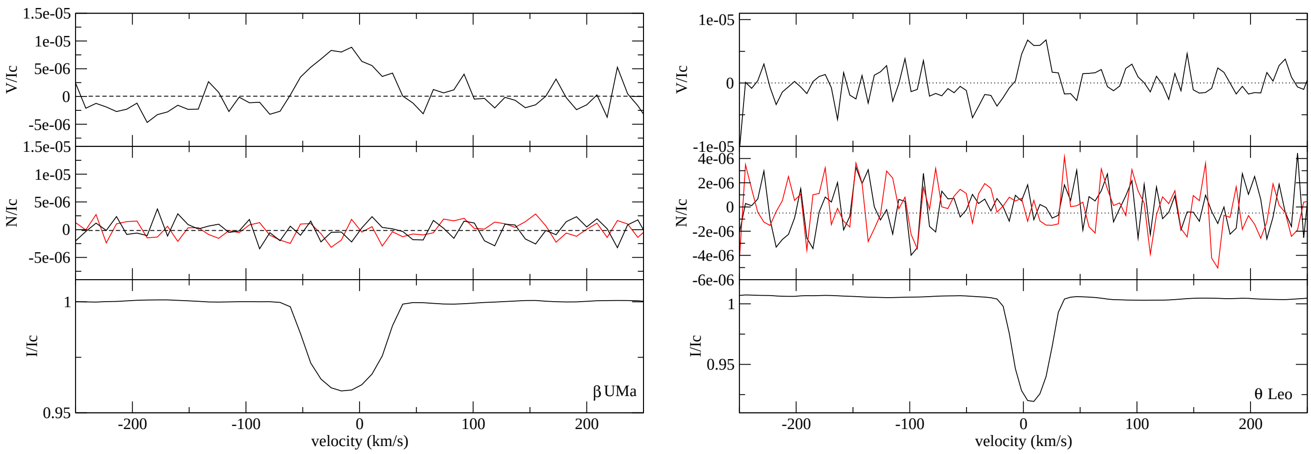


**Fig. 1.** Co-added LSD profiles in Stokes I (bottom) and V (top). The two available "null" control parameters Null1 and Null2 are shown in the middle panel. Top: $\beta$ UMa observations. Bottom: Same figure for $\theta$ Leo. All profiles are normalized to the continuum level. Taken from Blazère et al. (2016b)

For Alhena, contrary for $\beta$ UMa and $\theta$ Leo, we obtain detections in the individual LSD profiles. Examples of the LSD profiles are shown in Fig. 2. The shape of the Stokes V signatures is as expected in the standard Zeeman theory, like the one of Vega, and change slightly with time (see Blazère et al. 2016a for more details). The measured longitudinal magnetic fields is between -5 G and -10 G, which implies a minimal dipolar field strength of ~30 G. That is weak but higher than the one of Vega (~ 7 G, Petit et al. 2010).

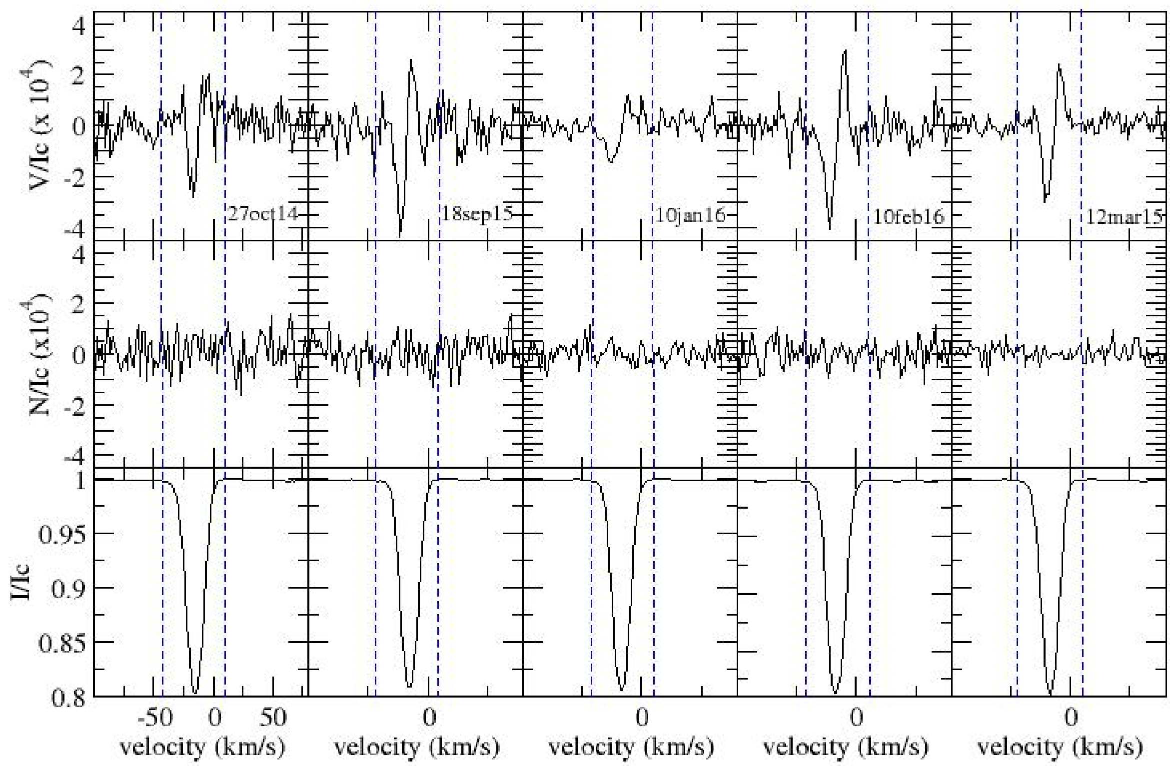


**Fig. 2.** Example of LSD profiles in Stokes I (bottom), Stokes V (top), and "null" polarization (center) for different nights of Alhena observations. All profiles are normalized to the continuum level.

## 4 Conclusion

Only 4 Am stars were observed with the required precision to detect ultra-weak magnetic fields, and all of them host a weak magnetic field. These stars belong to a new family of magnetic stars: the magnetic Am stars. Three of them (Sirius A, $\beta$ UMa and $\theta$ Leo) show peculiar magnetic signatures with a prominent positive lobe and one star (Alhena) shows a normal Zeeman signature. The preliminary explanation for the peculiar signatures observed in most Am stars is a combination of a gradient in velocity and in magnetic field. This explanation is sustained by the fact that these Am stars have a high microturbulence and host a superficial layer of convection. The Am star that hosts a normal signature (Alhena) has a lower microturbulence compared to the other Am stars. Its microturbulence is close to the one of Vega, which also displays a normal signature. Therefore, microturbulence could be an explanation for the peculiar versus normal signatures in Am stars. All Am stars observed so far have similar spectral parameters (temperature, mass, radius, metallicity,...), they are hot and their Am character is weak. Observing cooler Am stars and stronger Am stars could help us to understand the physical processes that produce the peculiar signatures and determine if the amplitude and shape of the magnetic signatures depend on particular stellar parameters.

## Acknowledgements

We acknowledge ANR funding for the Imagine project.

## References

Adelman, S. J. 2014, PASP, 126, 505
Adelman, S. J., Gulliver, A. F., & Kaewkornmaung, P. 2015, PASP, 127, 340
Aurière, M., Wade, G. A., Silvester, J., et al. 2007, A&A, 475, 1053
Blazère, A., Neiner, C., & Petit, P. 2016a, MNRAS
Blazère, A., Petit, P., Lignières, F., et al. 2016b, A&A, 586, A97
Boyajian, T. S., McAlister, H. A., van Belle, G., et al. 2012, ApJ, 746, 101
Donati, J.-F., Semel, M., Carter, B. D., Rees, D. E., & Collier Cameron, A. 1997, MNRAS, 291, 658
Kupka, F. & Ryabchikova, T. A. 1999, Publications de l'Observatoire Astronomique de Beograd, 65, 223
Landstreet, J. D. 2011, A&A, 528, A132
Lignières, F., Petit, P., Böhm, T., & Aurière, M. 2009, A&A, 500, L41
Monier, R. 2005, A&A, 442, 563
Neiner, C., Grunhut, J., Leroy, B., De Becker, M., & Rauw, G. 2015, A&A, 575, A66
Petit, P., Lignières, F., Aurière, M., et al. 2011, A&A, 532, L13
Petit, P., Lignières, F., Wade, G. A., et al. 2010, A&A, 523, A41
Piskunov, N. E., Kupka, F., Ryabchikova, T. A., Weiss, W. W., & Jeffery, C. S. 1995, A&AS, 112, 525
Smith, K. C. & Dworetsky, M. M. 1993, A&A, 274, 335

# Session SF2A

# WEAVE

*SF2A 2016*
*C. Reylé, J. Richard, L. Cambrésy, M. Deleuil, E. Pécontal, L. Tresse and I. Vauglin (eds)*

# WEAVE-QSO: A MASSIVE INTERGALACTIC MEDIUM SURVEY FOR THE WILLIAM HERSCHEL TELESCOPE

M. M. Pieri[1], S. Bonoli, J. Chaves-Montero, I. Pâris, M. Fumagalli, J. S. Bolton, M. Viel, P. Noterdaeme, J. Miralda-Escudé, N. G. Busca, H. Rahmani, C. Peroux, A. Font-Ribera, S. C. Trager and The WEAVE Collaboration

**Abstract.** In these proceedings we describe the WEAVE-QSO survey, which will observe around 400,000 high redshift quasars starting in 2018. This survey is part of a broader WEAVE survey to be conducted at the 4.2m William Herschel Telescope. We will focus on chiefly on the science goals, but will also briefly summarise the target selection methods anticipated and the expected survey plan.

Understanding the apparent acceleration in the expansion of the Universe is one of the key scientific challenges of our time. Many experiments have been proposed to study this expansion, using a variety of techniques. Here we describe a survey that can measure this acceleration and therefore help elucidate the nature of dark energy: a survey of the Lyman-$\alpha$ forest (and quasar absorption in general) in spectra towards $z > 2$ quasars (QSOs). Further constraints on neutrino masses and warm dark matter are also anticipated. The same data will also shed light on galaxy formation via study of the properties of inflowing/outflowing gas associated with nearby galaxies and in a cosmic web context. Gas properties are sensitive to density, temperature, UV radiation, metallicity and abundance pattern, and so constraint galaxy formation in a variety of ways. WEAVE-QSO will study absorbers with a dynamic range spanning more than 8 orders of magnitude in column density, their thermal broadening, and a host of elements and ionization species. A core principal of the WEAVE-QSO survey is the targeting of QSOs with near 100% efficiency principally through use of the J-PAS ($r < 23.2$) and Gaia ($r \lesssim 20$) data.

Keywords: large-scale structure of Universe, distance scale, dark energy, intergalactic medium, quasars: absorption lines, cosmology: observations

## 1 Introduction

The WEAVE is a new multi-object survey spectrograph for the 4.2m William Herschel Telescope (WHT) with 1000 fibres over a 3.1 deg$^2$ field of view. The WEAVE spectrograph offers two possible resolutions R=5000 and R=20000 (Dalton et al. 2012, 2014; Dalton et al. 2016). WEAVE-QSO survey is designed to optimise quasar absorption science through the measurement of Lyman-$\alpha$ absorption and other intergalactic medium (IGM) absorbers. The science objectives form two pillars; probing cosmological parameters through measurements of baryon acoustic oscillations through quasar absorption, and a wider variety of IGM science and smaller-scale structure cosmology. The former is contingent on WEAVE-QSO's unrivalled number density of Lyman-$\alpha$ (Ly$\alpha$) forest quasars, the latter rests on unprecedented resolution and signal-to-noise massive spectroscopic survey.

Observations in the late 1990s unexpectedly showed that the expansion of the universe is accelerating at the present epoch. This is usually termed dark energy and one of the challenges of our time is determining the cause of this acceleration. These observations indicate that either our understanding of gravity is flawed on cosmological scales or that the majority of mass-energy in the Universe tends to push objects apart on these scales. One way to explore this phenomenon is to measure the expansion history of the Universe. There is a convenient standard ruler to achieve this, called Baryon Acoustic Oscillations (BAOs; e.g. Seo & Eisenstein 2003). BAOs arise from acoustic waves in the early universe, and from these early perturbations large-scale

E-mail:matthew.pieri@lam.fr

[1] Aix Marseille Univ, CNRS, LAM, Laboratoire d'Astrophysique de Marseille, Marseille, France

structures were formed. Measuring the scale of BAOs in the distribution of large-scale structure at various epochs allows us to probe the expansion of the Universe.

The Baryon Oscillation Spectroscopic Survey (BOSS, Dawson et al. 2013) provides on average 17 QSOs deg$^{-2}$ (from 40 targets deg$^{-2}$) down to limiting apparent magnitude g=22 with single epoch data. This provides completeness of around 50% in the critical redshift ranges $2.2 < z < 3.5$ (Ross et al. 2012). An average exposure of 45 min on a 2.5m telescope provides a median signal-to-noise in the Ly$\alpha$ forest of around 2Å. The extended version of BOSS (eBOSS, Dawson et al. 2016) is in the process of increasing the number density to 25 QSOs deg$^{-2}$ by adding 60,000 QSO at $z > 2.1$, while it will also improve the S/N on a further 60,000 $z > 2.1$ QSOs. In the process it is expected to obtain root-2 improvement on the BAO precision.

In a similar manner to SDSS and the survey for the Dark Energy Spectroscopic Instrument (DESI), the WEAVE-QSO survey will devote a small proportion of WEAVE fibres towards obtaining high redshift QSO spectra over a large footprint. However, we do not propose to duplicate the DESI Ly$\alpha$ forest survey (which will occur on a similar timescale to WEAVE); rather we intend to use a complementary approach: WEAVE will narrow the redshift range and footprint providing a better BAO precision over this redshift range, and will open up the redshift and footprint for brighter QSOs for which WEAVE's higher spectral resolution will be most impactful. For both faint QSOs ($r < 23.2$) and the bright QSOs ($r \lesssim 20$), we expect a near complete sample for their respective footprint and redshift cuts. This level of redshift and signal-to-noise selectivity is expected with near 100% fibre efficiency for QSOs over from a single pass. A single pass is an efficient survey mode but it is also a necessity give a fibre reconfiguration time of approximately an hour for the WEAVE spectrograph. For comparison, DESI will take multi-pass approach to obtaining 90% fibre efficiency on any $z > 2.1$ QSOs. Excellent target selection is clearly a key element to the execution of the WEAVE-QSO survey.

The steepness of the QSO luminosity function limits the viable number density of targets, but makes a survey of many thousands of square degrees desirable. Hence the WEAVE-QSO cannot dominate the fibre budget in any single field and must share fields with other programs. Key to this flexibility is the fact that a survey of structure in intervening absorbers such as this one is not sensitive to an uneven angular selection functions - i.e., we are free to target QSOs wherever they are available. High surface density of targets with sufficient signal to noise is desirable for cosmology though. Our proposed fields are predominately at high galactic latitudes in the NGC and as a result we expect to share fields with both the with the WEAVE Galactic Archaeology science in both high- and low-resolution modes, and the WEAVE-LOFAR survey, both of which are also presented in these proceedings (Hill et al. *in prep* and Smith et al. 2016 respectively).

In the following we briefly set out a WEAVE-QSO survey science goals, and a brief summary of the current expected target selection and survey plan.

## 2 Baryon acoustic oscillations in quasar absorption

The measurement of clustering in diffuse intergalactic gas is an emerging method for measuring BAO and therefore dark energy. This measurement is performed using the Ly$\alpha$ forest, a forest of absorption lines seen along the line-of-sight to distant QSOs caused by the intergalactic medium (IGM) on large scales. When the QSO has sufficiently high redshift ($z > 2$), some of this forest of absorption falls in the optical window. Each QSO spectrum may, in principal, provide hundreds of megaparsecs of structure information along the line-of-sight in isolation, but moderate-resolution data, with low signal-to-noise, is limited by systematics on large-scales (related to uncertain continuum normalisation) and only provides structure information below $\leq 10h^{-1}$ Mpc (e.g. McDonald et al. 2006).

The BOSS survey overcame such limitations by building a sample of $\sim$150000 QSO Ly$\alpha$ forest spectra over 5 years. BOSS provides, for the first time, a sufficiently high surface density of QSOs to characterise large-scale structures in the intergalactic gas between different lines of sight, thus reducing the impact of errors in any one line-of-sight (Slosar et al. 2011). The Ly$\alpha$ forest BAO feature has been detected (Busca et al. 2013; Slosar et al. 2013) using a third of the expected BOSS QSO sample (Data Release 9: DR9). This provides the first measurement of the matter-dominated epoch where the expansion of the Universe was slowing. Recently, the autocorrelation measurement has been updated with twice the data (Delubac et al. 2015), giving a 3% precision measurement of BAO. The cross-correlation of quasars and the Ly$\alpha$ forest has also been measured (Font-Ribera et al. 2014a), generating an additional probe that is more sensitive to the angular diameter distance and with only limited correlation in errors with the forest autocorrelation. When combined, observations provide the most precise measurement to date of the Hubble parameter since the formation of the cosmic microwave background (CMB) and are in tension with the latest model based on CMB data from the Planck satellite at the $2.5\sigma$ level.

There are currently no physically motivated models (Aubourg et al. 2015) to explain this tension and no known significant sources of systematic error. As a result we must obtain greater precision to either ease this tension or accept that we are driven to new physics.

The WEAVE-QSO survey will measure BAO in the large-scale distribution of intergalactic gas by taking advantage of the excellent completeness and purity of target selection provided by the Javalambre Physics of the Accelerating Universe Survey (J-PAS; Benitez et al. 2014). This targeting will be available for approximately 6000deg$^2$ of the WEAVE-QSO survey, which can roughly be approximated by the overlap between J-PAS and SDSS survey boundaries shown in figure 3 of Smith et al. (2016). Figure 1 shows that the greatest boost in BAO precision upon achieving a near complete sample is provided by a data with $z > 2.7$. Despite the fact that the J-PAS targeting is only expected to cover 6000deg$^2$ of the WEAVE-QSO survey, the survey is still expected to provide unrivalled intergalactic absorption BAO precision at $2.7 < z < 3.5$ to approximately 0.5% precision. Note also that the HETDEX survey (Hobby-Eberly Telescope Dark Energy Experiment, Adams et al. 2011) is expect to achieve sub-percent precision on BAO with $2 < z < 4$ Lyman-$\alpha$ emitting galaxies.

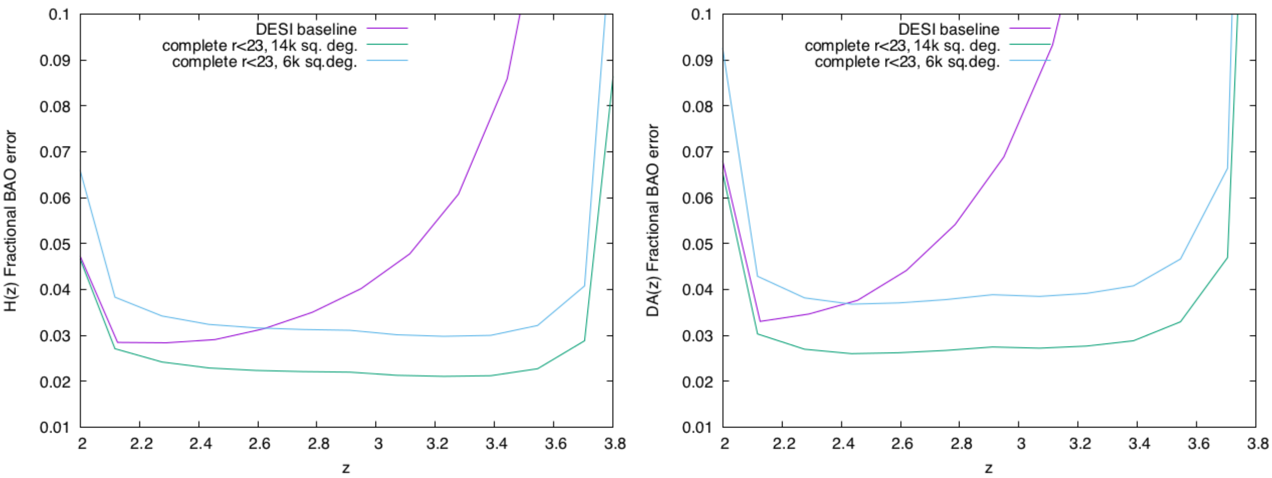


**Fig. 1.** Fisher forecasts of BAO precision expected for **Left:** the Hubble parameter, and **Right:** the angular diameter distance. This is shown for three survey scenarios (noting that DESI and WEAVE will produce spectra with similar signal-to-noise): the DESI baseline QSO absorption survey over 14,000 deg$^2$ to a depth of $r < 23$, a complete QSO sample to $r < 23$ over $14,000$deg$^2$, and a complete QSO sample to $r < 23$ over 6000 deg$^2$. It is clear that for a survey complete to this depth, high BAO precision can be achieved for $z > 2.7$ which is also highly complementary to DESI. It should be noted that WEAVE-QSO also expected to survey $\Delta r \approx 0.2$ fainter. These forecasts were produced following the method of Font-Ribera et al. (2014b).

## 3 Other cosmology

The Ly$\alpha$ forest is currently providing the tightest limits on the total neutrino masses and on dark matter particle velocities (i.e. distinguishing between cold dark matter and warm dark matter models). A cosmological background of neutrinos is a prediction of the standard model and an important goal in modern cosmology is to detect it and constrain neutrino properties. The combination of cosmic microwave background data by Planck with the 1D Lyman-$\alpha$ flux power spectrum as measured from the SDSS-III survey (Palanque-Delabrouille et al. 2013) has provided a tight upper limit of 0.15 eV at $2\sigma$ confidence level on the total neutrino masses (Palanque-Delabrouille et al. 2015). The data consists of a set of about 15,000 quasar spectra from BOSS DR9 among those that have high signal-to-noise ratios, which allowed to measure flux power in 12 redshift bins between z=2.2 and z=4.4 and at the scales between 0.002 km s$^{-1}$ and 0.02 km s$^{-1}$. These results show that we are on the verge of discriminating between the two possible neutrino hierarchies (inverted or normal). Furthermore, these findings have strong implications for particle physics experiments aiming at measuring neutrino masses or detecting the cosmic neutrino background.

WEAVE spectra in the low resolution mode have resolution nearly double that of SDSS (R=5000 as oppose to R=2000) and with this systematic effects will be better modelled and quantified. In particular, the metal contamination could be more quantitatively addressed; adding smaller scales to the Lyman-$\alpha$ flux power would allow also to probe further the neutrino induced suppression and its redshift and scale dependence (at the expenses of a more careful modelling from the theoretical side); a larger sample would result in similar statistical error bars on the flux power (though the statistical error contribution is still sub-dominant compared to the systematic ones); measuring the flux power to small scales $< 100$ km s$^{-1}$) would allow to constrain the thermal state of the IGM more precisely; and this in turn will impact on the final constraints, since the thermal state history is usually marginalized over, and it is one of the main uncertainties in the modelling.

Regarding the coldness of dark matter, the Ly$\alpha$ forest can also place tight constraints on the nature of dark matter by probing small-scales at relatively high redshift. Warm dark matter has been advocated in order to solve the small-scale crisis of the standard $\Lambda$CDM model presents, i.e., that there appear to be more low mass haloes, that are too dense and whose dynamical properties may be odds with observations. By possessing a non-negligible thermal velocity, warm dark matter significantly suppresses structure formation below a given scale. To constrain the particle mass it is mandatory to reach small scales (unlike neutrinos discussed above that have also an effect at larger scales) and also relatively high redshift, where non-linearities have had less time to erase primordial information in the power spectrum. The tightest constraints have been presented in Viel et al. (2013) who found a lower limit of $> 3.3$ keV for a thermal warm dark matter relic, using a set of 25 $z > 4$ Keck High Resolution Echelle Spectrometer and the Magellan Inamori Kyocera Echelle QSO spectra in combination with the SDSS 1D flux power at lower redshifts. This analysis shows that the flux power is consistent with very massive particles that are indistinguishable at this level from cold dark matter, while masses of 1-2 keV that are usually advocated to solve the small scale tensions present in the standard model are not supported by this data and analysis. WEAVE QSO spectra in the R$\sim$20000 are sufficient to measure the cut-off induced by the thermal state to a much more precise degree than the one which is usually measured by the few tens of high resolution spectra at similar redshifts that have been used so far. The possibility of probing other dark matter models such as wave (or fuzzy or quantum) dark matter (e.g. Schive et al. 2014; Hui et al. 2016) present themselves.

## 4 Cosmic web tomography and circumgalactic medium science

A key facet of galaxy formation is its environmental context. In order to develop a thorough understanding of galaxy formation and intergalactic gas we must map structures in which they reside (Pichon et al. 2001). How do galaxy and gas properties differ in knots, filaments, sheets and voids and how do they evolve in these different environments? These are fundamental questions we are currently unable to address, although early attempts are being made in narrow, deep surveys (Lee et al. 2014). Instrumentation for next-generation ELT class telescopes is being developed with this specific science goal in mind. WEAVE will pursue cosmic web mapping in three distinct programs; one wide and low resolution, another one deeper with higher resolution, and a third making use of rare close groups of structure skewers.

Wide cosmic web mapping will make complete use of the whole deep-wide sample including faint QSOs. This sample allows IGM 3D mapping, where we expect to obtain $< 15$ Mpc h$^{-1}$ resolution over this 6000 deg$^2$ footprint (Ozbek et al. 2016). This resolution will be sufficient to identify large-scale voids useful for void-counting and a measurement of the Alcock-Paczynski effect through void shape, both of which have demonstrated cosmological value in galaxy surveys (Pisani et al. 2015 and Sutter et al. 2014 respectively). While not sufficient to place the following studies of legacy astrophysics in a filamentary context, this will allow us to reconstruct of large-scale peaks and voids of structure and explore IGM properties and galaxy formation in the context of large-scale environment. J-PAS will provide a large number of Lyman-$\alpha$ emitting galaxies (around 300,000). In the best cases they will be detected with a redshift precision of $\Delta z = 0.01$, this is also insufficient to resolve filamentary structure but may supplement low resolution tomography for a void/non-void separation.

Higher resolutions can be obtained using the highly complementary galaxy called HETDEX. This survey provides galaxies identified in Ly$\alpha$ emission (known as 'Lyman-$\alpha$ emitters') at redshifts $z > 2$, and so are highly complementary with this survey of Ly$\alpha$ absorption. HETDEX begins this year (2016) and will cover 450 deg$^2$ within the proposed WEAVE survey footprint. This area will be filled with IFUs with a filling factor of 1/4.5 each with R=700 providing 1 Mpc precision on galaxy locations. Each IFU is 1' wide and is separated from others by $\sim$1'. Each IFU will be filled with Lyman-$\alpha$ emitters tracing structure and each can be thought of as providing a skewer of structure analogous to quasar absorption. WEAVE-QSO will reobserve $r < 21$ QSOs in the HETDEX footprint, doubling the integration time and supplementing the S/N>5/Å sample. Ly$\alpha$ forest data will improve the mapping resolution by improving the filling factor of large-scale structure skewers, provide an alternative tracer for these structure to (aiding with the understanding of the use of LAEs as a tracer) and allow the possibility of studying the large-scale gaseous context of galaxy formation, feedback and the feeding of star formation. It is evident that mapping of the cosmic web with galaxies, while probing the Ly$\alpha$ forest, will also generate a variety of legacy science of placing both galaxies and their circumgalactic media in a cosmic web context.

SDSS quality spectra have proven a rich source of information about metals associated with the optically thin gas of the Ly$\alpha$ forest. This is despite the fact that the moderate resolution and S/N of such data render confident identifications of individual systems all but impossible. Progress was made by adapting the measurement of weak, distributed metal absorption through pixel-based techniques (e.g. Cowie et al. 1995; Schaye et al. 2003) to data of this quality. This has been demonstrated by directed measurements of a particular species (Pieri et al. 2010a) and blind searches that result from composite spectra produced by stacking forest lines (Pieri et al. 2010b, 2014). These composite spectra displayed unprecedented precision, providing the potential to measure gas column density, metallicity, elemental abundances pattern (resulting largely from stellar populations that give rise to them), and ionization fractions (arising due to UV background shape and intensity, density, temperature, and recombination time scale). Pieri et al. (2014) showed that strong, blended forest lines on 138 km s$^{-1}$ scales are typically associated with circumgalactic regions of Lyman break galaxies such as those found in the KBSS survey (Rudie et al. 2012). When such systems are stacked, the densities inferred force one to conclude that gas clumping on scales up to 30 pc and near-solar metallicity is seen.

WEAVE data will enrich such Ly$\alpha$ forest studies through larger samples with greater signal-to-noise and resolution. However, the combination of these measurements in combination with cosmic web mapping and Lyman-$\alpha$ emitter locations will be transformative for this science. The combination of WEAVE and HETDEX surveys in particular will provide a wealth of information on the circumgalactic medium of Lyman-$\alpha$ emitting galaxies. These Lyman-$\alpha$ emitters are thought to reside in haloes of mass roughly an order of magnitude lower than the KBSS survey. Such haloes are more abundant and are predicted to dominate the volume fraction of the universe enriched by metals (Pieri & Martel 2007; Booth et al. 2012). The HETDEX IFUs will be sufficiently close to WEAVE quasars to probe CGM regions for approximately a third of WEAVE quasars over the 450 deg$^2$ footprint of HETDEX, this corresponds to approximately 4000 quasars with S/N/Å $> 5$ with full CGM information. This large statistical survey approach to studying the CGM of with Lyman-$\alpha$ emitters will complement ongoing focussed studies (e.g. Fumagalli et al. 2016; Wisotzki et al. 2016) conducted with Multi-Unit Spectroscopic Explorer (MUSE). This sample promises to be a rich source of gas inflow/outflow around galaxies at an epoch where quasar absorption spectra are a font of information (due primarily to a dense Ly$\alpha$ forest observed in the optical window). This sample will allow the forest stacking techniques described above to be as discriminating as they are precise. Furthermore many Lyman limit systems (LLS) and damped Lyman-$\alpha$ (DLA) systems will be placed in a circumgalactic context boosting the science described below.

LLSs are optically-thick absorbers with column densities $> 10^{17}$ cm$^{-2}$. Due to the characteristic absorption at the Lyman limit, they are easy to identify even in modest SN spectra, provided that the 912 Å break in the system's rest-frame enters the spectral range of the survey ($z > 3.01$ for WEAVE). LLSs are much more abundant than DLAs. At $z \sim 3$, there are $\sim$5 times more LLSs than DLAs per unit redshift, and are impactful for both cosmological and galaxy evolution studies. By selecting quasars with narrow-band photometry, WEAVE will provide the first bias-free estimate of the number of LLSs and the mean free path of ionizing radiation in the $z \sim 3$ universe, drastically reducing the uncertainties on current estimates the mean free path for ionizing photons. From the point of view of galaxy evolution, LLSs have recently been the subject of many studies, as they are believed to be associated to galaxy haloes. LLSs have in fact physical densities comparable to the density of halo gas ($< 0.01$ cm$^{-3}$), and show a range of metal properties indicative of multiple gas phases in galaxy haloes (i.e. nearly pristine systems suggestive of gas accretion and highly enriched systems suggestive of outflows). The numbers of LLSs expected and the high resolution of the data allow the prospect of measurements of LLS bias and so their association with galaxies. Moreover, the resolution of WEAVE compared to sister surveys like DESI or BOSS allows the study of the metal enrichment of these absorbers, for the first time directly in a large survey. Furthermore WEAVE resolution offers the prospect of identifying more metal poor (or even metal free) DLAs, large samples of $z > 3.5$ DLAs, and resolving metal velocity structure in both LLSs and DLAs.

## 5 IGM thermal history

The relationship between temperature and density in the intergalactic medium (IGM) is a fundamental quantity, which describes the physical state of the baryons in the early universe. Observations of the Ly$\alpha$ forest in the spectra of high-redshift quasars are the primary approach used to obtain constraints on the IGM thermal history. Gas heating effects act as astrophysical nuisance parameters (Viel et al. 2013). Improved measurements of the IGM thermal history will aid in refining these cosmological measurements (see Section 3).

Photoionization heating impacts on the dynamical state of gas in the IGM by raising the gas pressure. This increases the scale over which small-scale structure is smoothed (Gnedin & Hui 1998). As there is a finite amount of time required for the gas to dynamically respond to a change in pressure, the precise amount of smoothing depends on when the gas was first heated and the hydrogen reionized. This Jeans smoothing acts on larger scales (a few hundred proper kpc) relative to thermal (Doppler) broadening and smooths the gas in physical rather than velocity space (Peeples et al. 2010). However, the pressure smoothing scale in the IGM at $2 < z < 3$ has not yet been measured precisely using line-of-sight Ly$\alpha$ forest data. In principle, when combined with measurements of the instantaneous temperature, constraints on the IGM pressure smoothing scale from quasars may yield insights into the timing and duration of the reionization history.

The most widely used approach for studying the structure of the IGM in low to moderate resolution Ly$\alpha$ forest spectra is the power spectrum of the transmitted flux. Combining the power spectrum with other statistics, such as the distribution of the transmitted flux, can further tighten constraints and help break parameter degeneracies (Viel et al. 2009). However, existing measurements are either based on data from the Sloan Digital Sky Survey, which consists of thousands of low to moderate resolution ($R \sim 2000$), low signal-to-noise (S/N/Å$\sim$5) spectra (McDonald et al. 2006), or 10-m class telescope data consisting of several tens of high resolution (R$\sim$40000) high signal-to-noise (S/N/pixel>50) spectra (e.g. Kim et al. 2004). The former data have achieved constraints on the Ly$\alpha$ forest power spectrum that have small statistical error bars, while the latter, higher quality data are better suited to studying astrophysical effects on small scales. An independent sample of hundreds of moderate resolution (R$\sim$20000), moderate to high signal-to-noise (S/N/Å>30) spectra at $2.4 < z < 3.4$ obtained with the WEAVE survey will probe an intermediate complementary regime. While resolving the thermal broadening requires higher resolution (R$\sim$40000) spectroscopy, R$\sim$20000 data will capture changes in the ionization state of the gas associated with evolution in the temperature-density relation.

A precise measurement of the temperature-density relation will help to place further constraints on the tail end of He-II reionization at $z \sim 3$ (e.g. McQuinn et al. 2009). He-II reionization is expected to result in large ($> 30\mathrm{Mpc}h^{-1}$) fluctuations in the ionization and thermal state of the intergalactic gas (McQuinn et al. 2009). These fluctuations are a potential systematic uncertainty in cosmological measurements. Ionization fluctuations will result in additional large-scale power in the three dimensional power spectrum of the Ly$\alpha$ forest forest transmission (White et al. 2010; Gontcho A Gontcho et al. 2014; Pontzen 2014). The WEAVE survey will provide a very large sample of low resolution ($R \sim 5000$, cf. $R \sim 2000$ for BOSS), moderate signal-to-noise spectra, with around 20 quasars per square degree to a limiting magnitude of $r = 22.5$. Greig et al. (2015) estimate temperature fluctuations imprinted during He-II reionization at $z \sim 3$ will impact at the 20-30% level on the three-dimensional flux power spectrum at $k \sim 0.02\mathrm{Mpc}^{-1}$ for a BOSS-like survey with 15 quasars per deg$^{-2}$ and S/N/Å$\sim$5. The WEAVE data will therefore be well-suited to this purpose, assuming that observational systematics (e.g. continuum fitting) and degeneracies with other astrophysical effects are well controlled and understood. This would provide a direct way to probe the expected patchy nature of He-II reionization, which is inaccessible with line-of-sight data alone. Similarly, exploring the impact of ionization fluctuations on the (even larger) scales associated with the mean free path for hydrogen ionizing photons, $k < 0.01\mathrm{Mpc}^{-1}$, will also provide independent constraints on the distribution of ionizing sources (i.e. quasars or star forming galaxies) at $2 < z < 3$ (Pontzen et al. 2014).

## 6 Target Selection and Survey Size

Our goal of near-100% completeness and efficiency will be achieved by use of data from J-PAS. This is a narrow band imaging survey set to begin science verification in summer of 2016 and begin survey mode operations in mid-2017 and as such it leads the WEAVE survey approximately 1-2 year. These filters and provide a resolution of $R = 50$. This survey will cover $> 8500\mathrm{deg}^2$ at high galactic latitudes, and will cover all trays over the course of 8 years. The boundary is dictated by a combination of observability and at Javalambre in Spain and limits on dust extinction. Given the location of the WHT, surveying the highest declination portion of this footprint is not possible. The observable portion of the J-PAS footprint can be approximated by its overlap with the SDSS DR8 imaging footprint, and amounts to approximately 6000 deg$^2$. This defines our deep-wide survey area. The study of QSO clustering and QSO science is already a core aspect of J-PAS science (e.g. Abramo et al. 2012), and in coordination with the J-PAS team we have explored the identification of QSOs in J-PAS data.

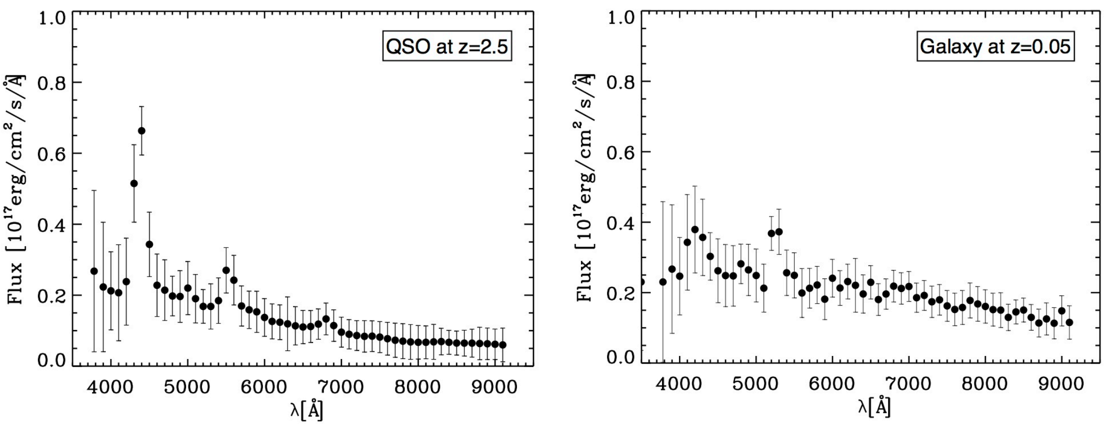


**Fig. 2.** An illustration of purity to galaxy interlopers. In both cases the points show perfect data and error bars indicating expected J-PAS uncertainty at a magnitude of r=23.2. **Left:** a $z = 2.5$ QSO, exhibiting detectable Lyman-$\alpha$, CIV and perhaps CIII in emission **Right:** a mock z=0.05 galaxy spectrum that, in combination with a realisation of noise, is identified by a draft automated identification scheme as a z=2.5 QSO. The galaxy spectrum shows OIII emission that mimics CIV emission and a combination of nearby absorption lines which appears to mimic a weak Lyman-$\alpha$ emission line. However, the amplitude of these mimicking effects is both too weak with respect to continuum emission and one another to be mistaken for a z=2.5 QSO in a refined procedure.

In order to test QSO identification in J-PAS we have built a library of 500 QSO templates to which we have added redshift dependent realisations of the Ly$\alpha$ forest taken from BOSS cosmological mocks (Bautista et al. 2015). These spectra then have the J-PAS filter response functions applied to them and a level as noise expected based on their assumed r-band magnitude. Recovery of high-z QSOs has then been tested through a visual inspection of QSOs and through automatic identification. In both cases the goal is to test for purity and completeness of QSOs with $2.2 < z < 2.9$ in J-PAS data, and to learn the faint limit of this identification. This current test assumes that stars and galaxies have no impact on purity. We justify this due to the lack of strong emission lines that would pose a problem for identification in J-PAS data. As shown in Figure 2, a galaxy and a z=2.5 QSO are easy to distinguish by eye despite our current automated methods identifying them as a z=2.5 QSO. Automated fitting algorithms are being developed, but visual inspection provides near perfect completeness and efficiency in current tests to $r < 23$. If necessary visual inspection can be used to support automated approaches to achieve targeting of this quality.

## 7 Summary

WEAVE-QSO is a massive spectroscopic survey of the intergalactic medium seen in absorption to background QSOs in absorption set to begin in 2018. A deep-wide survey of Ly$\alpha$ forest QSOs $r < 23.2$ will be targetted using J-PAS data with 95% completeness and purity within the 6000 deg$^2$ of overlapping footprint with the J-PAS survey. Throughout this footprint the WEAVE-QSO survey will take spectra of with $z > 2.7$ QSOs down to this faint limit will constitute a signal-to-noise limit of S/N/Å> 0.5. This will be supplemented by QSOs with $2.1 < z < 2.7$ to a higher signal-to-noise limit for non-BAO science. In total this will provide 350,000 spectra of Ly$\alpha$ forest QSOs.

This will be supplemented by survey of bright ($r < 20$) QSOs with $z > 2.1$ covering a further 4000 deg$^{-2}$ of Gaia targeted QSO giving S/N/Å = 7. This provides 5 QSOs/deg$^{-2}$ or 16 per WEAVE field. By default this supplementary bright survey will be conducted in the low resolution mode, but a subset of this sample will be observed in the WEAVE high-resolution mode. This will be subject to fibre cross-talk constraints, sky brightness limits and redshift constraints based on science value and the limited wavelength coverage.

This work has been carried out thanks to the support of the A*MIDEX project (ANR- 11-IDEX-0001-02) funded by the Investissements dAvenir French Government program, managed by the French National Research Agency (ANR).

## References


Abramo, L. R., Strauss, M. A., Lima, M., et al. 2012, MNRAS, 423, 3251

Adams, J. J., Blanc, G. A., Hill, G. J., et al. 2011, ApJS, 192, 5

Aubourg, É., Bailey, S., Bautista, J. E., et al. 2015, Phys. Rev. D, 92, 123516

Bautista, J. E., Bailey, S., Font-Ribera, A., et al. 2015, J. Cosmology Astropart. Phys., 5, 060

Benitez, N., Dupke, R., Moles, M., et al. 2014, ArXiv e-prints

Booth, C. M., Schaye, J., Delgado, J. D., & Dalla Vecchia, C. 2012, MNRAS, 420, 1053

Busca, N. G., Delubac, T., Rich, J., et al. 2013, A&A, 552, A96

Cowie, L. L., Songaila, A., Kim, T.-S., & Hu, E. M. 1995, AJ, 109, 1522

Dalton, G., Trager, S., Abrams, D. C., et al. 2016, Final design and progress of WEAVE: the next generation wide-field spectroscopy facility for the William Herschel Telescope

Dalton, G., Trager, S., Abrams, D. C., et al. 2014, in Proc. SPIE, Vol. 9147, Ground-based and Airborne Instrumentation for Astronomy V, 91470L

Dalton, G., Trager, S. C., Abrams, D. C., et al. 2012, in Proc. SPIE, Vol. 8446, Ground-based and Airborne Instrumentation for Astronomy IV, 84460P

Dawson, K. S., Kneib, J.-P., Percival, W. J., et al. 2016, AJ, 151, 44

Dawson, K. S., Schlegel, D. J., Ahn, C. P., et al. 2013, AJ, 145, 10

Delubac, T., Bautista, J. E., Busca, N. G., et al. 2015, A&A, 574, A59

Font-Ribera, A., Kirkby, D., Busca, N., et al. 2014a, J. Cosmology Astropart. Phys., 5, 027

Font-Ribera, A., McDonald, P., Mostek, N., et al. 2014b, J. Cosmology Astropart. Phys., 5, 023

Fumagalli, M., Cantalupo, S., Dekel, A., et al. 2016, MNRAS, 462, 1978

Gnedin, N. Y. & Hui, L. 1998, MNRAS, 296, 44

Gontcho A Gontcho, S., Miralda-Escudé, J., & Busca, N. G. 2014, MNRAS, 442, 187

Greig, B., Bolton, J. S., & Wyithe, J. S. B. 2015, MNRAS, 447, 2503

Hui, L., Ostriker, J. P., Tremaine, S., & Witten, E. 2016, ArXiv e-prints

Kim, T.-S., Viel, M., Haehnelt, M. G., Carswell, R. F., & Cristiani, S. 2004, MNRAS, 347, 355

Lee, K.-G., Hennawi, J. F., White, M., Croft, R. A. C., & Ozbek, M. 2014, ApJ, 788, 49

McDonald, P., Seljak, U., Burles, S., et al. 2006, ApJS, 163, 80

McQuinn, M., Lidz, A., Zaldarriaga, M., et al. 2009, ApJ, 694, 842

Ozbek, M., Croft, R. A. C., & Khandai, N. 2016, MNRAS, 456, 3610

Palanque-Delabrouille, N., Yèche, C., Baur, J., et al. 2015, J. Cosmology Astropart. Phys., 11, 011

Palanque-Delabrouille, N., Yèche, C., Borde, A., et al. 2013, A&A, 559, A85

Peeples, M. S., Weinberg, D. H., Davé, R., Fardal, M. A., & Katz, N. 2010, MNRAS, 404, 1281

Pichon, C., Vergely, J. L., Rollinde, E., Colombi, S., & Petitjean, P. 2001, MNRAS, 326, 597

Pieri, M. M., Frank, S., Mathur, S., et al. 2010a, ApJ, 716, 1084

Pieri, M. M., Frank, S., Weinberg, D. H., Mathur, S., & York, D. G. 2010b, ApJ, 724, L69 P10

Pieri, M. M. & Martel, H. 2007, ApJ, 662, L7

Pieri, M. M., Mortonson, M. J., Frank, S., et al. 2014, MNRAS, 441, 1718

Pisani, A., Sutter, P. M., Hamaus, N., et al. 2015, Phys. Rev. D, 92, 083531

Pontzen, A. 2014, Phys. Rev. D, 89, 083010

Pontzen, A., Bird, S., Peiris, H., & Verde, L. 2014, ApJ, 792, L34

Ross, N. P., Myers, A. D., Sheldon, E. S., et al. 2012, ApJS, 199, 3

Rudie, G. C., Steidel, C. C., Trainor, R. F., et al. 2012, ApJ, 750, 67

Schaye, J., Aguirre, A., Kim, T.-S., et al. 2003, ApJ, 596, 768

Schive, H.-Y., Chiueh, T., & Broadhurst, T. 2014, Nature Physics, 10, 496

Slosar, A., Font-Ribera, A., Pieri, M. M., et al. 2011, J. Cosmology Astropart. Phys., 9, 1

Slosar, A., Iršič, V., Kirkby, D., et al. 2013, J. Cosmology Astropart. Phys., 4, 26

Smith, D. J. B., Best, P. N., Duncan, K. J., et al. 2016, ArXiv e-prints

Sutter, P. M., Pisani, A., Wandelt, B. D., & Weinberg, D. H. 2014, MNRAS, 443, 2983

Viel, M., Becker, G. D., Bolton, J. S., & Haehnelt, M. G. 2013, Phys. Rev. D, 88, 043502

Viel, M., Bolton, J. S., & Haehnelt, M. G. 2009, MNRAS, 399, L39

White, M., Pope, A., Carlson, J., et al. 2010, ApJ, 713, 383

Wisotzki, L., Bacon, R., Blaizot, J., et al. 2016, A&A, 587, A98

*SF2A 2016*
*C. Reylé, J. Richard, L. Cambrésy, M. Deleuil, E. Pécontal, L. Tresse and I. Vauglin (eds)*

# WEAVE AN OVERVIEW AND STATUS UPDATE

P. Bonifacio[1], G. Dalton[2,3], S. Trager[4], A. L. Aguerri[5], E. Carrasco[6], A. Vallenari[7], D. C. Abrams[8], K. Middleton[2], F. Sayède[1] and the WEAVE Instrument Consortium

**Abstract.** The WHT Enhanced Area Velocity Explorer is a high multiplex, multi-object spectrograph that will equip the prime focus of the WHT 4.2m telescope. The instrument is currently in the construction phase and several components have already been procured. I will give a short overview of the instrument and of the project and its status. The French participation is done through CNRS - Institut National des Sciences de l'Univers and the technical activity is carried out, at this stage, at GEPI, Observatoire de Paris.

Keywords: Instrumentation: spectrographs, Surveys

## 1 Introduction

The need for a high multiplex spectrograph on a 4m class telescope has been clearly identified in the European strategic Astronet documents (Kauffmann 2005; Drew et al. 2008). The urgency of such a development was driven by the upcoming Gaia mission (Gaia Collaboration 2016), when it became obvious that, as a consequence of budget-driven descoping the Radial Velocity Spectrograph on-board of Gaia (Katz et al. 2004) would have magnitude limits brighter than expected Katz (2009). This of course, notwithstanding the expressed needs of such an instrument also for extragalactic science. The French community was very reactive in looking for a solution and launched on a fast track the study for GYES, a multi-object spectrograph for the prime-focus of the Canada-France-Hawaii Telescope (Bonifacio et al. 2010; Mignot et al. 2010; Bonifacio et al. 2011) that was completed in only ten months. In spite of a very positive report on the phase A study the instrument was not retained for phase B mainly based on what was felt the community interest*. The GYES project allowed to develop to a considerable degree the science case and some technical solutions, like a two-arm spectrograph with Volume Phase Holographic gratings as dispersing media, and a pick-and-place positioner based essentially on -off-the-shelf components. This was also the occasion when the teams of GEPI and Oxford began to collaborate. The idea of a multi-object spectrograph for the WHT was presented at the SPIE meeting in San Diego (Balcells et al. 2010), with a strong support from the British, Dutch and Spanish communities. From the French perspective it was thus natural, once the GYES project was stopped, to divert the forces to join the WEAVE project. For the French community it has been very important that we were immediately welcomed in the project, even though France is not a member of the Isaac Newton Group (ING). This same open policy was the basis on which the project was opened to the Italian and Mexican contributions. In the following I will give a technical overview of the instrument and provide an update of its status. I will also provide an update of the French support to the project.

[1] GEPI, Observatoire de Paris, PSL Research University, CNRS, Univ. Paris Diderot, Sorbonne Paris Cité, Place Jules Janssen, 92195 Meudon, France
[2] RALSpace, STFC Rutherford Appleton Laboratory, OX11 0QX, UK
[3] Dept. of Physics, University of Oxford, Keble Road, Oxford, OX1 3RH, UK
[4] Kapteyn Institut, Rijksuniversiteit Groningen, Postbus 800, NL-9700 AV Groningen,Netherlands
[5] Instituto de Astrofisica de Canarias, 38200 La Laguna, TF, Spain
[6] INAOE, Luis Enrique Erro 1, Tonantzintla, Puebla, Mexico
[7] Osservatorio Astronomico di Padova, INAF, Vicolo Osservatorio 5, 35122, Padova, Italy.
[8] Isaac Newton Group, 38700 Santa Cruz de La Palma, Spain

*`http://www.cfht.hawaii.edu/en/science/SAC/reports/SAC_report_Nov_2010.php`

## 2 Overview of the instrument

The final design of the instrument can be found in Dalton et al. (2016), this supersedes previous designs (Dalton et al. 2012, 2014). The capabilities of the instrument are summarized in Table 1 of Dalton et al. (2016). WEAVE can deploy up to 960 single fibres over a field-of-view of $2^\circ$ diameter, each fibre has an on-sky aperture of $1.3''$. Alternatively 20 integral-field units of $11'' \times 12''$, with $1.3''$ spaxels can be deployed on the same field. Finally a large integral-field unit with a field of view of $1.3' \times 1.5'$ and $2.6''$ spaxels can be used to study extended objects. Through a slit-exchange mechanism each fibre system can feed the WEAVE spectrograph. To accommodate the large number of fibres we have a single spectrograph with two arms, red and blue, and the light is split by a dichroic at 590 nm. The dispersing elements are Volume Phase Holographic gratings. A pair of gratings provides the low-resolution mode, with a mean resolving power R$\sim$ 5750 and a full spectral coverage betwen 366 nm and 959 nm. The resolving power is not constant over each arm, but ranges between 3000 and 7500, the highest resolving power being attained at the red end of each arm. For stellar studies this is convenient since two very important spectral features, the MgI b triplet at 518 nm and the CaII at 850 nm will be observed at the red end of the blue and red arms respectively at a resolving power around 7000. The high-resolution mode of WEAVE is obtained by inserting another pair of gratings in the optical path that provide a resolving power of $\sim$ 21000 over two non-contiguous spectral ranges in the red and blue arms. In the blue arm one has a choice between a blue range (404 nm – 465 nm) and a green range (473 nm – 545 nm). In the red arm the range is 595 nm – 685 nm.

The positioner relies on two robots that cooperate to pick-and-place the fibres in such a way that a full plate configuration can be prepared a little less than one hour. Like similar positioners, 2dF (Taylor et al. 1997; Lewis et al. 1998) and OzPoz (Gillingham et al. 2000), WEAVE has two plates, while one is being configured by the robot, the other is observing. The plates are exchanged by tumbling the positioner around an axis orthogonal to the optical axis of the telescope. This optimizes the observation time, however it also fixes the minimum integration time on a given plate, if a full plate configuration is requested on the next plate. WEAVE has been conceived as an instrument for deep surveys so that a 1h total integration on each plate configuration is appropriate. Of course the total integration may be split into several shorter integrations. As long as each integration attains a signal from the targets well above the read-out noise, this strategy is beneficial since it will allow for cosmic-ray removal and avoid saturation of bright targets.

## 3 Current status

At the time of writing most of the WEAVE subsystems are in the stage of procurement and building. All the large blanks necessary for the prime focus corrector have been acquired. The largest lens, 1.1 m in diameter is fused silica and was created from a blank delivered by Corning to Kiwistar Optics that has started its polishing. Lens 4 has been polished and is now being tested. Lens 3 is close to completion on ine surface. The prime focus translation system has been delivered and tested at IAC in June 2016 and will be shipped to La Palma later this year. A very important step has been made in mid-July when the top-end ring of WHT was removed and replaced successfully. This manoeuvre will become routine when WEAVE is to be replaced by another instrument. The fibres for the single objects and small IFUs ($1.3''$) on the sky have been delivered to France and are ready to be integrated into fibre bundles (24 fibres/bundles). The project appears to be on-schedule for a first-light in the first half of 2018.

## 4 French participation to WEAVE

From the technical point of view the French participation has been carried out at the GEPI and Lagrange laboratories. The scientific participation is much wider and involves most of the INSU laboratories. Lagrange did most of the design of the prime focus corrector in phase A, GEPI is responsible for design and procurement of the fibre systems, in collaboration with the University of Gröningen for the IFUs. The total French effort to the fibre system amounts to 8.3 Full Time Equivalents throughout the project. From the scientific point of view the French community is strongly involved in the Galactic Archeology Survey (Survey Leader V. Hill) and in the QSO survey (Survey leader M. Pieri), and a small involvement exists also in the LOFAR Survey.

From the institutional point of view it is very important that INSU has labelised two national observation services (Actions Nationales pour l'Observation, ANO) related to WEAVE. One for the WEAVE construction (WEAVE-ANO2, responsible P. Bonifacio) and one for the WEAVE survey (WEAVE-ANO4, responsible V.

Hill). This is very important, because, firstly, it allows astronomers of the Conseil National des Astronomes et Physiciens (CNAP) to work on either of the WEAVE aspects having their work recognised as observation service, secondly it opens up the opportunity of recruiting CNAP astronomers to work on WEAVE.
From the funding point of view, at this stage, CNRS and Observatoire de Paris are providing all of the FTEs necessary for the fibre system. The equipment costs are mostly covered by two genereous allocations of Région Île de France that funded WEAVE through the 'Domaine d'Intrt Majeur Astrophysique et Conditions pour l'Apparition de la Vie' (DIM-ACAV†), for a total of 756 500 euro. A very important contribution has also come from the Région Franche Comté and the remaining from CNRS and Observatoire de Paris. Funding requests to the two latter organisms for 2017 are pending, upon successful outcome of these requests the hardware cost of the fibre systems should be covered.

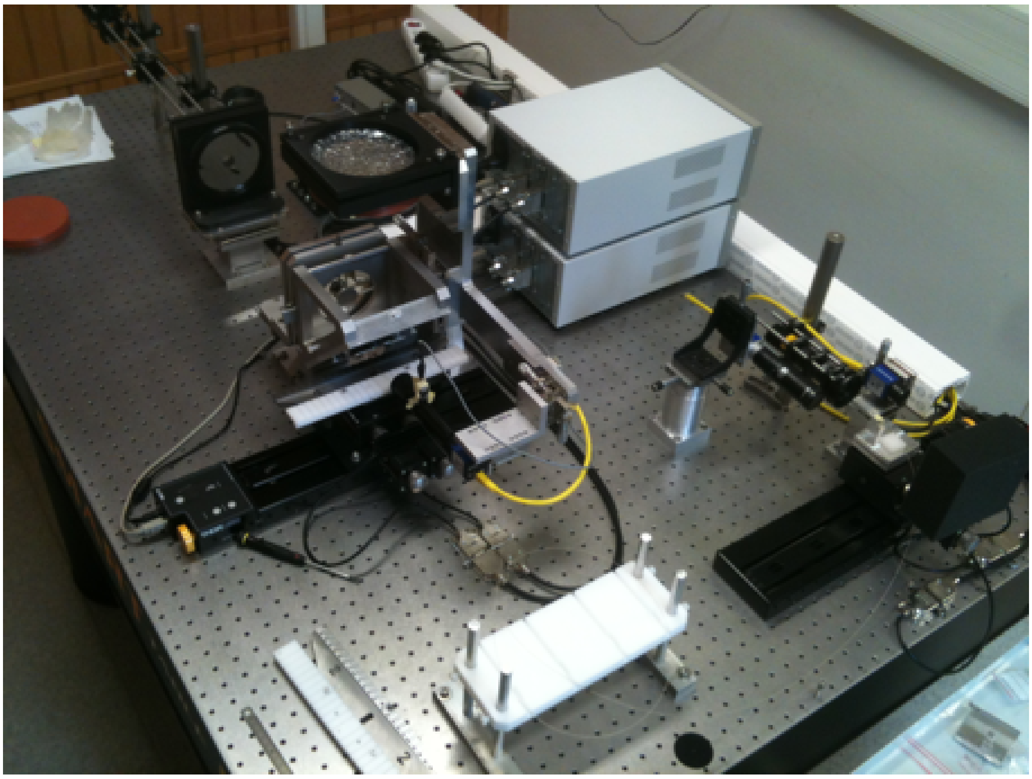

**Fig. 1.** The optical bench for testing the WEAVE fibres at GEPI.

## 5 Conclusions

WEAVE is an important opportunity for the French community, it will provide access to observational capabilities that are not otherwise available. It is quite remarkable that the bulk of the funding of the hardware does not come from traditional sources, but rather from regional funds. This is a virtuous example on how regions can boost their scientific potential through moderate, but well aimed, investment in science. In this respect a system like that of the DIMs introduced by Région Île de France appears to be extremely effective. It would certainly be positive if other French Regions would put in place similar structures.
The WEAVE project is proceeding as planned, all the subsystems are making considerable project. There are very exciting times ahead of us!

The French participation to WEAVE is coordinated by CNRS Institut National de Sciences de l'Univers (INSU) with the support of the Programme National de Cosmologie et Galaxies. We acknowledge funding from Région Île de France, through DIM-ACAV, Région Franche Comté through the institute UTINAM , INSU, and Observatoire de Paris.

† `https://dimacav.obspm.fr/`

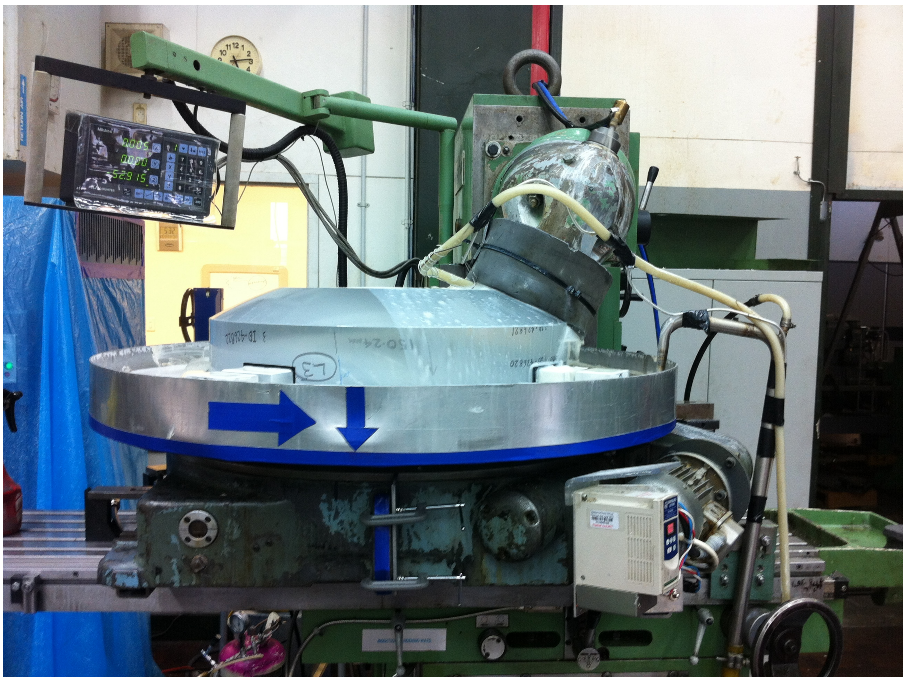

**Fig. 2.** Lens L3 of the prime focus corrector being polished at Kiwistar optics.

## References


Balcells, M., Benn, C. R., Carter, D., et al. 2010, in Proc. SPIE, Vol. 7735, Ground-based and Airborne Instrumentation for Astronomy III, 77357G

Bonifacio, P., Arenou, F., Babusiaux, C., et al. 2010, in Proc. SPIE, Vol. 7735, Ground-based and Airborne Instrumentation for Astronomy III, 77350E–77350E–9

Bonifacio, P., Mignot, S., Dournaux, J.-L., et al. 2011, in EAS Publications Series, Vol. 45, EAS Publications Series, 219–222

Dalton, G., Trager, S., Abrams, D. C., et al. 2016, in Proc. SPIE, Vol. 9908, Ground-based and Airborne Instrumentation for Astronomy VI, 9908–53

Dalton, G., Trager, S., Abrams, D. C., et al. 2014, in Proc. SPIE, Vol. 9147, Ground-based and Airborne Instrumentation for Astronomy V, 91470L

Dalton, G., Trager, S. C., Abrams, D. C., et al. 2012, in Proc. SPIE, Vol. 8446, Ground-based and Airborne Instrumentation for Astronomy IV, 84460P

Drew, J., Bergeron, J., Bouvier, J., et al. 2008, Report by the European Telescope Strategic Review Committee on Europes 2-4m telescopes over the decade to 2020, Tech. rep., ASTRONET

Gaia Collaboration. 2016, A& A in press, ArXiv e-prints

Gillingham, P. R., Miziarski, S., & Klauser, U. 2000, in Proc. SPIE, Vol. 4008, Optical and IR Telescope Instrumentation and Detectors, ed. M. Iye & A. F. Moorwood, 914–921

Katz, D. 2009, in SF2A-2009: Proceedings of the Annual meeting of the French Society of Astronomy and Astrophysics, ed. M. Heydari-Malayeri, C. Reyl'E, & R. Samadi, 57

Katz, D., Munari, U., Cropper, M., et al. 2004, MNRAS, 354, 1223

Kauffmann, G. 2005, Report on a wide field, highly multiplexed spectrograph, Tech. rep., ASTRONET

Lewis, I. J., Glazebrook, K., & Taylor, K. 1998, in Proc. SPIE, Vol. 3355, Optical Astronomical Instrumentation, ed. S. D'Odorico, 828–833

Mignot, S., Cohen, M., Dalton, G., et al. 2010, in Proc. SPIE, Vol. 7735, Ground-based and Airborne Instrumentation for Astronomy III, 77354H

Taylor, K., Cannon, R. D., & Watson, F. G. 1997, in Proc. SPIE, Vol. 2871, Optical Telescopes of Today and Tomorrow, ed. A. L. Ardeberg, 145–149

*SF2A 2016*
*C. Reylé, J. Richard, L. Cambrésy, M. Deleuil, E. Pécontal, L. Tresse and I. Vauglin (eds)*

.

# THE WEAVE-LOFAR SURVEY

D. J. B. Smith[1], P. N. Best[2], K. J. Duncan[3], N. A. Hatch[4], M. J. Jarvis[5], H. J. A. Röttgering[3], C. J. Simpson[6], J. P. Stott[5], R. K. Cochrane[2], K. E. Coppin[1], H. Dannerbauer[7], T. A. Davis[8], J. E. Geach[1], C. L. Hale[5], M. J. Hardcastle[1], P. W. Hatfield[5], R. C. W. Houghton[5], N. Maddox[9], S. L. McGee[10], L. Morabito[5], D. Nisbet[2], M. Pandey-Pommier[11], I. Prandoni[12], A. Saxena[3], T. W. Shimwell[3], M. Tarr[13], I. van Bemmel[14], A. Verma[5], G. J. White[15], W. L. Williams[1] and the WEAVE Consortium

**Abstract.** In these proceedings we highlight the primary scientific goals and design of the WEAVE-LOFAR survey, which will use the new WEAVE spectrograph on the 4.2m William Herschel Telescope to provide the primary source of spectroscopic information for the LOFAR Surveys Key Science Project. Beginning in 2018, WEAVE-LOFAR will generate more than $10^6$ R=5000 365-960nm spectra of low-frequency selected radio sources, across three tiers designed to efficiently sample the redshift-luminosity plane, and produce a data set of enormous legacy value. The radio frequency selection, combined with the high multiplex and throughput of the WEAVE spectrograph, make obtaining redshifts in this way very efficient, and we expect that the redshift success rate will approach 100 per cent at $z < 1$. This unprecedented spectroscopic sample – which will be complemented by an integral field component – will be transformational in key areas, including studying the star formation history of the Universe, the role of accretion and AGN-driven feedback, properties of the epoch of reionisation, cosmology, cluster haloes and relics, as well as the nature of radio galaxies and protoclusters. Each topic will be addressed in unprecedented detail, and with the most reliable source classifications and redshift information in existence.

Keywords: surveys, galaxies: formation, evolution, active, clusters.

[1] Centre for Astrophysics Research, School of Physics Astronomy and Mathematics, University of Hertfordshire, College Lane, Hatfield, Hertfordshire, AL10 9AB, United Kingdom
[2] Institute for Astronomy, Royal Observatory, Blackford Hill, Edinburgh, EH9 3HJ, United Kingdom
[3] Leiden Observatory, Universiteit Leiden, Huygens Laboratory/J.H. Oort Building, Niels Bohrweg 2, NL-2333 CA Leiden, The Netherlands
[4] The Centre for Astronomy & Particle Theory, School of Physics & Astronomy, Nottingham University, University Park, Nottingham, NG7 2RD, United Kingdom
[5] Oxford Astrophysics, Denys Wilkinson Building, Keble Road, Oxford, OX1 3RH, United Kingdom
[6] Gemini Observatory, Northern Operations Center, 670 North A'ohōkū Place, Hilo, HI 96720-2700, USA
[7] Instituto de Astrofsica de Canarias (IAC), E-38205 La Laguna, Tenerife, Spain & Universidad de La Laguna, Dpto. Astrofsica, E-38206 La Laguna, Tenerife, Spain
[8] School of Physics & Astronomy, Cardiff University, Queens Buildings, The Parade, Cardiff, CF24 3AA, UK
[9] ASTRON, the Netherlands Institute for Radio Astronomy, Postbus 2, 7990 AA, Dwingeloo, The Netherlands
[10] School of Physics and Astronomy, University of Birmingham, Edgbaston, Birmingham, B15 2TT, UK
[11] Univ Lyon, Univ Lyon1, Ens de Lyon, CNRS, Centre de Recherche Astrophysique de Lyon UMR5574, 9 av Charles André, F- 69230, Saint-Genis-Laval, France
[12] INAF-IRA, Via P. Gobetti 101, 40129 Bologna, Italy
[13] ICG, Dennis Sciama Building, Burnaby Road, Portsmouth, PO1 3FX, United Kingdom
[14] Joint Institute for VLBI ERIC, PO Box 2, 7990 AA Dwingeloo, The Netherlands
[15] Department of Physics and Astronomy, The Open University, Walton Hall, Milton Keynes, MK7 6AA, UK & RAL Space, STFC Rutherford Appleton Laboratory, Chilton, Didcot, Oxfordshire, OX11 0QX, UK

## 1 Introduction & Motivation

The International LOFAR Telescope offers a transformational increase in survey speed compared to existing radio telescopes, as well as opening up one of the few poorly explored regions of the electromagnetic spectrum. An important driver for LOFAR, since its inception, has been to carry out a series of surveys of the low-frequency radio sky to advance, in particular, our understanding of the formation and evolution of galaxies, clusters, and active galactic nuclei (AGN).

The LOFAR Surveys Key Science Project (KSP) is described in Röttgering et al. (2011), but to summarise, LOFAR is carrying out surveys in a wedding-cake strategy, with three tiers of observations to be completed over the next $\sim 5$ years. Tier-1 is the widest tier, and includes low-band (LBA; between 10-80 MHz) and high-band (HBA; between 120-240 MHz) observations across the whole $2\pi$ steradians of the northern sky to a depth approximately 10 times that of the FIRST survey (Becker et al. 1995), or $\sim 600$ times deeper than the VLA Low-frequency Sky Survey (Cohen et al. 2007). Deeper Tier-2 and Tier-3 observations are proposed over smaller areas (Tier-3 will cover $\sim 100\,\mathrm{deg}^2$ to a depth greater than that of the deepest current radio imaging), focusing on fields with the highest quality multi-wavelength datasets available across a broad range of the electromagnetic spectrum. The effectiveness of new direction-dependent calibration techniques (necessary to account for the large confusing influence of the ionosphere on low-frequencies) has been demonstrated by several publications (e.g. Hardcastle et al. 2016; Shimwell et al. 2016; van Weeren et al. 2016; Williams et al. 2016), while LOFAR's ability to rapidly survey large areas has also been demonstrated (Shimwell et al. *submitted*).

Whilst the high sensitivity of low-frequency radio surveys to AGN is well known, figure 1 shows that the LOFAR Surveys KSP data are also supremely sensitive to star-formation, assuming standard relationships between radio flux density and star formation rate (SFR) from Bell (2003). LOFAR is able to detect star-forming systems that are beyond the reach of even confusion limited observations with the *Herschel Space Observatory* (Pilbratt et al. 2010) and SCUBA-2 (Holland et al. 2013, despite the negative $K$-correction at sub-millimetre wavelengths).

The William Herschel Telescope Enhanced Area Velocity Explorer instrument (WEAVE; Dalton et al. 2012, 2014) is a next-generation spectroscopy facility, which has been designed with follow-up of LOFAR targets as one of the primary goals. WEAVE is a multi-object (MOS) and multi-integral field unit (IFU) fibre-fed spectrograph, which allows 1,000 fibres to be positioned robotically over a field of view 2 degrees in diameter. In "low resolution" mode, WEAVE produces spectra at $R = 5,000$ over a contiguous wavelength range between 365-960 nm in a single exposure, ideal for the efficient detection, redshifting and classification of radio sources.

WEAVE-LOFAR is therefore tasked with being the primary source of spectroscopic information for the LOFAR surveys. Spectra are required for much more than simply estimating redshifts; it is only using these data that we are able to robustly distinguish between star forming galaxies (SFGs) and AGN, and between accretion modes in those AGN themselves. Spectra also permit us to measure velocity dispersions, estimate metallicities and derive virial black hole mass estimates; many thousands of WEAVE-LOFAR spectra thus offer an unique insight into the relationship between star formation and accretion over a huge swathe of cosmic history. In addition, since we target sources selected at radio frequencies (which are unaffected by dust obscuration), WEAVE-LOFAR will be much less biased against obscured sources than samples selected at optical/near-infrared wavelengths, providing a representative view of the galaxy and AGN populations. Furthermore, the unique capability offered by the suite of WEAVE integral field units (IFUs) enables us to investigate the onset of cluster formation in the early Universe (putting proto-clusters into cosmological context for the first time), allows us to probe the gas supply of massive high-redshift galaxies, and provides the opportunity to measure the impact of AGN-driven feedback on galaxy evolution.

Some of the key areas that WEAVE-LOFAR will address include:

- the star-formation history of the Universe,
- accretion and AGN-driven feedback,
- the epoch of reionisation,
- cosmology,
- cluster haloes and relics,
- radio galaxies and protoclusters.

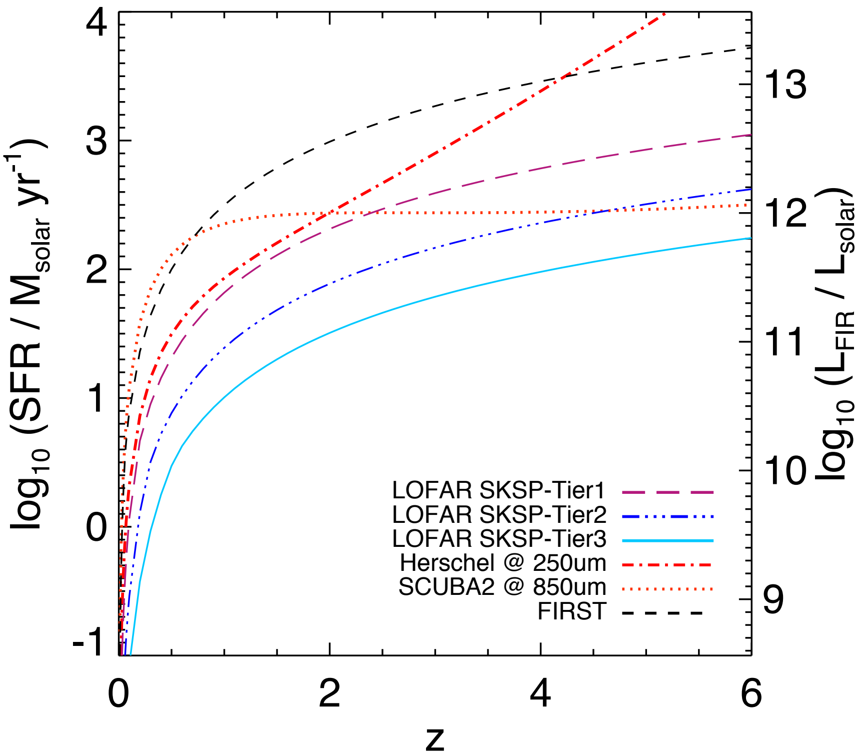


**Fig. 1.** A comparison between the star formation rate sensitivity of the $5\sigma$ limits of each tier of the LOFAR Surveys KSP (purple long-dashed, blue dot-dot-dot-dashed and light-blue solid lines for Tiers 1, 2 & 3, respectively), and selected other surveys, including FIRST (Becker et al. 1995, shown as the dashed black line), and five times the confusion noise limit of *Herschel Space Observatory* at 250 $\mu$m (taken from Rigby et al. 2011, red dot-dashed line, assuming a canonical isothermal template with $T = 35K$ and $\beta = 1.5$), and from SCUBA-2 at 850 $\mu$m (dotted red line, assuming the same template SED and the confusion noise estimate taken from Geach et al. 2016). We assume an universal radio spectral index of $\alpha = 0.71$ from Mauch et al. (2013), adopting the convention that $S_\nu \propto \nu^{-\alpha}$.

The WEAVE-LOFAR survey will be described in a future publication (Smith et al. in prep), but in section 2 we discuss the survey design and expected redshift success rate, while in section 3 we discuss some key areas of the science case in more detail. We conclude in section 4.

## 2 Survey Design

### 2.1 Tier strategy and choice of fields

WEAVE-LOFAR will adopt a tiered strategy, designed to efficiently sample the redshift-luminosity plane. In this way, the survey will obtain statistical samples of both the rarest bright sources (e.g. radio galaxies in the epoch of reionisation) and the star-forming galaxies that dominate the source counts at the faintest flux densities. WEAVE-LOFAR will have three tiers named Deep, Mid and Wide, which mimic the enumerated tiers of the LOFAR Surveys KSP, though targeting only a subset of the sources in each. The targeting strategy will be:

- Deep: $S_{150\mathrm{MHz}} > 100\,\mu$Jy,
- Mid: $S_{150\mathrm{MHz}} > 1\,$mJy,
- Wide: $S_{150\mathrm{MHz}} > 10\,$mJy.

Together, the three tiers fill the redshift-luminosity plane as shown in figure 2, which are based on realisations of a single WEAVE field of view for each tier of our survey in the SKA simulated skies from Wilman et al.

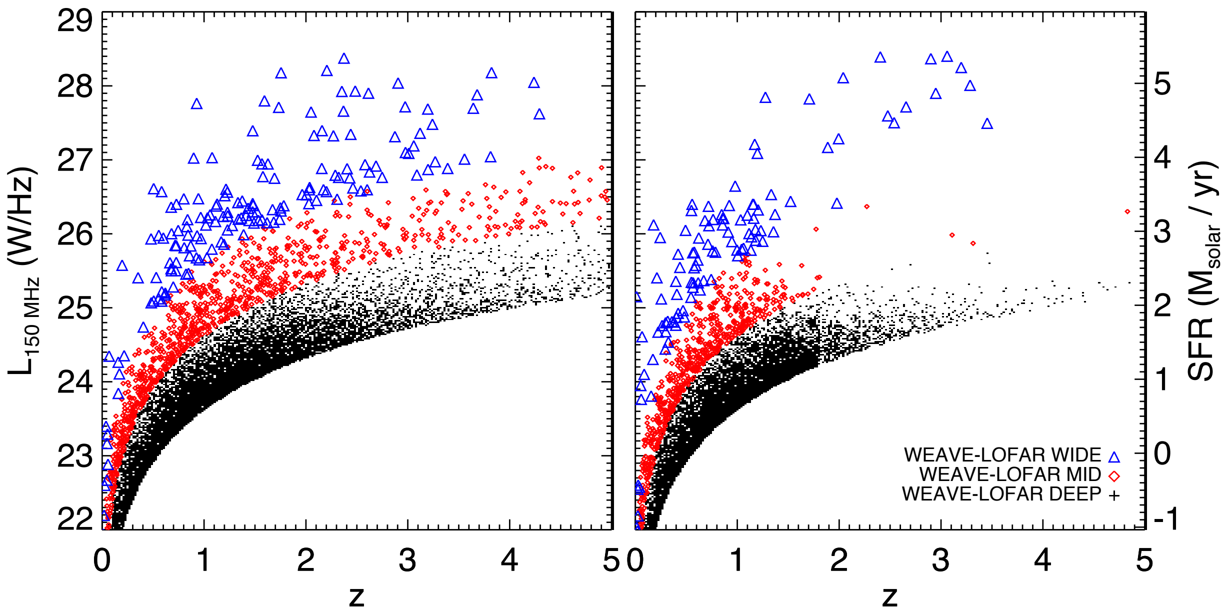


**Fig. 2. Left:** The luminosity redshift plane as sampled by fields drawn from each of the three tiers of the WEAVE-LOFAR survey. Targets in the Wide tier are shown as blue triangles, while those in the mid tier are shown as red diamonds. The faintest, most numerous sources in the Deep tier are shown as black points. The right-hand axis has been scaled to reflect the star-formation rates associated with the values on the left-hand y-axes, though clearly the more luminous sources' radio emission is not powered by star formation, but by AGN. **Right:** As for the left panel, but only those sources for which we expect – based on our simulations – to obtain successful redshifts are shown. The expected redshift success rate in each tier is 75.6, 60.8 and 67.1 per cent in the Deep, Mid and Wide tiers, respectively.

(2008). The source density above the flux limit in each tier is 15,000/1,100/160 per $\pi\,\mathrm{deg}^2$ WEAVE field of view for the Deep/Mid/Wide tiers respectively. In the Deep and Mid tiers, this is high enough to enable us to define our own dedicated pointings (since the number of available targets exceeds the number of fibres in the MOS spectrograph). We have chosen those fields visible by both WEAVE and LOFAR that have the best available multi-wavelength ancillary data; these are detailed in table 1, and plotted in figure 3 (light-blue regions represent the Mid tier fields, while the deep fields are shown as pink circles).

In the Wide tier, the low source density of the brightest and rarest sources (including samples of high redshift powerful AGN, as well as the ultra-rare radio galaxies within the Epoch of Reionisation, the EoR) means that we must share fibres with other WEAVE surveys to efficiently use the instrument. Fortunately the WEAVE Galactic Archaeology (GA; Hill et al. *in prep*) survey and the WEAVE QSO survey (Pieri et al. *in prep*) also require wide areal coverage, and we intend to follow this strategy to cover the widest possible area (up to $10{,}000\,\mathrm{deg}^2$ over the initial five years of survey operations). The LOFAR Surveys KSP observations to date are shown as the blue circles in figure 3), and the necessity of observing fields in common with the GA and QSO teams has been a key ingredient in identifying the regions to observe in recent LOFAR cycles.

### *2.2 Expected redshift success rates*

The redshift distribution of each sub-component of the faint radio source population, estimated using the SKA simulated skies (Wilman et al. 2008) is shown for each tier of WEAVE-LOFAR in figure 4, from left to right in order of decreasing source density. The star forming galaxies are shown as red lines, the radio-quiet AGN are shown in black, while the high- and low-excitation radio galaxies are shown as blue and light-blue lines, respectively. Also overlaid are the redshift success rates that we expect to obtain in 1hr integrations for each population, indicated by the dotted lines of each colour.

The redshift success rates have been estimated by taking the SKA simulated skies, alongside a simple but realistic model for each component of the faint radio source population, and accounting for a realistic sky spectrum, instrument throughput, fibre size, dust reddening and wavelength coverage, and assuming a default

**Table 1.** Field names and approximate centres (in the standard format, HHMM+DD) for the WEAVE-LOFAR Deep and Mid tiers. The Wide tier will be co-located with the WEAVE-GA and WEAVE-QSO surveys, spread over regions in the galactic halo, primarily at $|b| > 30$.

**Mid Tier:**

| Name | Pointing Centre |
|---|---|
| HETDEX | 1200+55 |
| *H*-ATLAS NGP | 1300+29 |
| *H*-ATLAS GAMA | 0900/1200/1430+00 |
| SDSS Stripe 82 | 0000+00 |
| XMM-LSS | 0219-05 |
| COSMOS | 1000+02 |
| Total Area: | $\sim$1,250 deg$^2$ |

**Deep Tier:**

| Name | Pointing Centre |
|---|---|
| Boötes | 1430+34 |
| Lockman Hole | 1050+57 |
| ELAIS-N1 | 1610+54 |
| NEP | 1800+66 |
| Total Area: | $\sim$100 deg$^2$ |

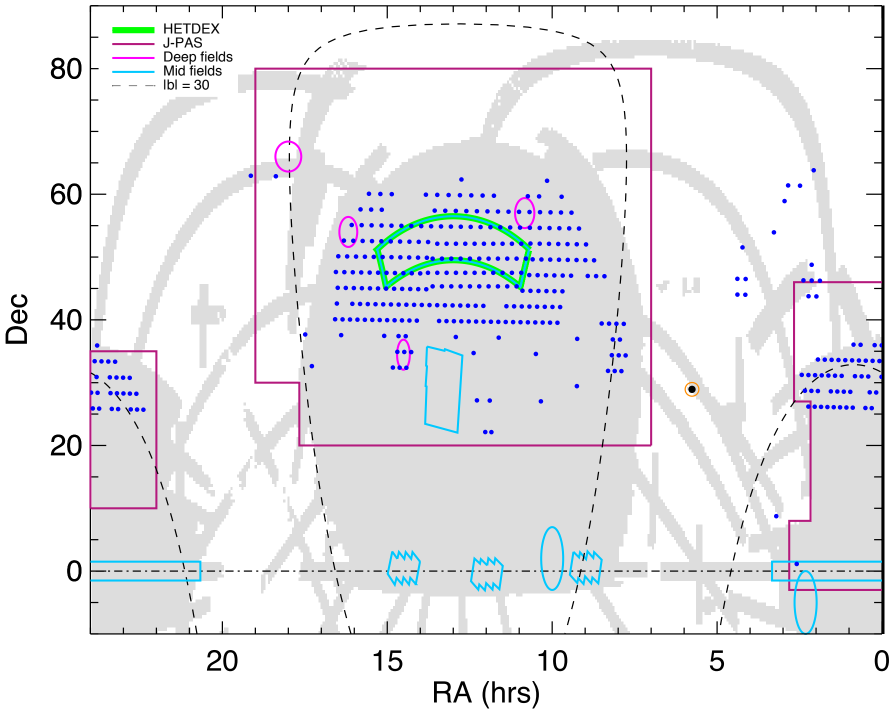


**Fig. 3.** The primary fields for the WEAVE-LOFAR survey detailed in table 1, overlaid on the outline of the SDSS imaging (grey). The Mid-tier fields are outlined in light blue, alongside the Deep fields (pink circles). The primary Mid-tier field, the HETDEX northern field (Hill et al. 2008), is outlined in green, while the outline of the J-PAS survey (Benitez et al. 2014) is shown in purple. The fields observed as part of the LOFAR Surveys KSP up to the end of observing cycle 6 are shown as the blue circles. The black circle outlined in orange shows the location of the galactic anti-centre, while the the black dashed lines correspond to galactic latitudes $|b| = 30$.

1 hr integration on every source (though we plan to include deeper integrations of targets in the deep tier which don't yield a redshift in the first hour). The high redshift success rate in these simulations (which approaches 100 per cent at $z < 1$) is due to the fact that radio sources are predominantly emission line galaxies, or luminous ellipticals with strong 4000 Å breaks. The redshift success rate is also included in the right-hand panel of figure 2, which shows that the WEAVE-LOFAR sample will be predominantly star-forming galaxies at $z < 1.5$ and high redshift radio galaxies at $z > 2$.

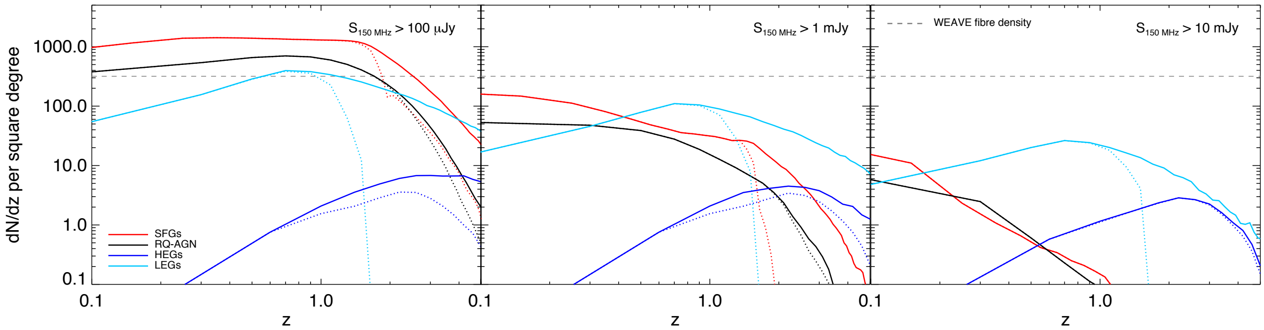


**Fig. 4.** The expected redshift distributions for each tier of WEAVE-LOFAR, including the Deep tier, at $S_{150} > 100\,\mu$Jy (**Left**), the Mid tier ($S_{150} > 1$ mJy; **Centre**), and the Wide tier ($S_{150} > 10$ mJy; **Right**). Solid lines show the model redshift distribution while dotted lines of the same colour show the distribution of successful redshifts that we expect. The population has been divided to reveal the expected redshift distributions for each constituent of the source population according to the SKA Simulated Skies (Wilman et al. 2008), including star-forming galaxies (SFGs, in red), radio-quiet AGN (RQ-AGN, in black), high excitation radio galaxies (HEGs, in blue) and low-excitation radio galaxies (LEGs, light blue).

## 3 Science Highlights

The science case for WEAVE-LOFAR will be presented in more detail in Smith et al. (in prep), however in this section we present brief highlights from four of the main areas.

### *3.1 The star formation history of the Universe*

As figure 1 shows, the LOFAR surveys offer arguably the most effective way of tracing star formation in the Universe, since radio luminosity is roughly proportional to SFR (e.g. Bell 2003). Radio emission is unaffected by dust obscuration, and the high angular resolution available means that confusion effects do not limit the sensitivity (unlike with Herschel, e.g. Oliver et al. 2012). While photometric, rather than spectroscopic, redshifts would be sufficient to trace the star formation density of the Universe, such redshifts are only reliable for objects with high signal-to-noise-ratio broadband detections and well-defined continuum breaks. Photometric redshifts are therefore inadequate for low-mass galaxies and/or those suffering from dust extinction, or indeed for those with bright emission lines, which comprise a large majority of the faint radio source population. The WEAVE spectra will also allow us to cleanly distinguish star forming galaxies from AGN, which can have similar flux densities at a range of redshift; spectra are therefore critical if we wish to unleash the immense power of LOFAR for studying star formation.

WEAVE LOFAR is designed in such a way as to allow us to study the properties of star formation in galaxies as a function of stellar mass, environment, and redshift simultaneously, and with large statistical samples in every bin. This will enable us to study the influence of each factor on key properties of the galaxy population including the star formation rate density of the Universe (e.g. Madau et al. 1998; Madau & Dickinson 2014), the star formation rate function (e.g. Smit et al. 2012; Cai et al. 2014), the fundamental metallicity relation (e.g. Mannucci et al. 2010; Stott et al. 2013), and provide a new insight on the physics behind the far-infrared radio correlation (e.g. Yun et al. 2001; Murphy 2009; Murphy et al. 2011; Smith et al. 2014). Whilst we expect that individual spectra will detect only emission lines (i.e. not continuum), the uniformity of the WEAVE spectra, combined with the very large samples that we will observe, enables us to statistically detect the continuum properties of star-forming galaxies as well, reaching higher redshifts in better detail than has been previously possible. Those individual sources with continuum detections will also allow us to search for e.g. velocity offset absorption lines, thought to represent a 'smoking gun' of stellar/AGN feedback (e.g. Chen et al. 2010; Davis et al. 2012; Geach et al. 2014), and it will also be possible to search for this signal statistically, averaging across populations (e.g. Bradshaw et al. 2013).

### 3.2 Accretion and AGN-driven feedback

Since deep radio surveys can identify not only the classical double radio-loud sources, but also the much more abundant population of radio-quiet AGN at $z > 1$ (Jarvis & Rawlings 2004; Simpson et al. 2006; Seymour et al. 2008; Smolčić et al. 2008), they offer the opportunity to explore all aspects of AGN activity and evolution. By detecting radio-quiet AGN, independent of obscuration (and knowing that most black hole growth is obscured; e.g. Martínez-Sansigre et al. 2005), radio surveys have the ability to make the most complete census of black hole accretion, including Compton-thick objects missed by X-ray surveys, allowing the poorly understood relationship between star formation and accretion to be studied further. WEAVE-LOFAR will provide new insight on the origin of the radio loud/quiet dichotomy (e.g. Ivezić et al. 2002; Cirasuolo et al. 2003; Martínez-Sansigre & Rawlings 2011). Furthermore, obtaining large and complete samples of AGN ensures that we are able to study the interplay between key properties of the AGN themselves, such as jet power (probed by the radio luminosity; e.g. Hardcastle et al. 2007; Gürkan et al. 2015), or accretion rate (as probed by emission line luminosity; e.g. Heckman et al. 2004), as well as their large-scale environments, and how these relationships vary with redshift. The complete redshift information for the radio-loud AGN population provided by WEAVE-LOFAR will be essential for determining the jet kinetic luminosity function, quantifying the amount of energy injected by jets of various powers into the intergalactic medium of their host galaxies.

Spectroscopy is essential if we wish to reliably discriminate between radiatively-efficient and -inefficient accretion (the so-called "quasar" and "radio" modes; Croton et al. 2006) through the presence or absence of high ionisation emission lines (see e.g. O'Sullivan et al. 2015; Best & Heckman 2012). Here again, spectroscopy provides vital input for testing galaxy formation models, which often assume that AGN feedback controls the evolution of galaxies. In our current understanding of the AGN feedback phenomenon, the quasar mode can drive gas out of the galaxy to terminate star-formation activity (Silk & Rees 1998), while the radio (or "jet") mode provides a lower rate of energy input that balances gas cooling, maintaining massive galaxies as "old, red and dead" (Best et al. 2006). Recent studies have shown a decline in the space density of radio-mode AGN at $z < 1$, and it has been suggested that this is related to the merger history of these galaxies (Rigby et al. 2011; Simpson et al. 2012) and their gas supply (e.g. Best et al. 2014; Williams & Röttgering 2015). WEAVE spectroscopy is required to determine radio-selected AGN accretion mechanisms and provides essential data for testing models of AGN-galaxy co-evolution (e.g., the relationship between star formation and accretion over cosmic history). For example, tracking the evolution of radio-mode AGN and comparing it with the evolution of massive quiescent galaxies (i.e. their likely hosts) will be key for studying the quenching mechanism itself.

### 3.3 The epoch of reionisation

The recent discovery and subsequent study of a QSO at $z > 7$ have suggested that reionisation is incomplete 750 Myr after the Big Bang (Mortlock et al. 2011; Bolton et al. 2011). However, the large cross-section for Lyman-$\alpha$ absorption means that the intergalactic medium becomes opaque for neutral fractions as low as $\sim$0.1 per cent, limiting the usefulness of optical studies. The 21 cm hyperfine transition, by contrast, has a cross-section around $10^7$ times smaller, and LOFAR will be able to map the distribution of neutral gas at $z > 6$ provided sufficiently bright radio sources can be found at high redshift (Carilli et al. 2002; Mack & Wyithe 2012). Current models predict one $S_{150\mathrm{MHz}} > 10\,\mathrm{mJy}$ source at $z > 6$ every $\sim$200 deg$^2$, but these extremely valuable, ultra- rare sources are difficult to isolate from the overall population and will be more efficiently identified as part of a large-scale survey effort rather than through single-object follow-up, and LOFAR will be able to discover and identify them due to its large field of view and high survey speed. Assuming conservative $z > 6$ source densities (though recent work by Saxena et al. *in prep* suggests that the true numbers may be higher), a 10,000 deg$^2$ survey would be expected to find $\sim 50$ $z > 6$ radio galaxies (giving multiple lines of sight into this critical era of cosmic history), and would permit us to conduct 21 cm absorption experiments. Larger samples are highly desirable, given that the brighter and higher-redshift sources are easier to probe for 21 cm absorption, and that they provide more information about the reionisation process. A statistical sample of EoR sources will enable us to answer some of the most interesting questions about the reionisation process, such as "how long did it take?", "how clumpy was it?", and "which sources were responsible?".

WEAVE-LOFAR will also be able to probe the demographics of the black hole population at these very large redshifts to answer important questions such as "how do massive black holes and galaxies form?" and enabling us to determine the relationship between the black hole itself and the long-pursued massive and metal free stars (i.e. "population III" stars). This approach is complementary to other searches for QSOs in the Epoch of Reionisation as the low-frequency radio surveys are also sensitive to the highly dust-obscured sources that may be missed by optical/near-IR or X-ray survey data.

### 3.4 Radio galaxies and protoclusters

Studying the formation of galaxy clusters and their member galaxies is key to our understanding of cosmology and galaxy evolution as they are ideal laboratories to test the standard model of structure and galaxy formation (Kravtsov & Borgani 2012). The most important epoch to study is the 3 Gyr period around $z \approx 2$. During this period, the first cluster-sized halos collapsed (Chiang et al. 2013), forming the nuggets that will grow into massive clusters by the present day. Furthermore, cluster galaxies underwent a rapid period of star formation during this time, forming the bulk of the stars that now reside in massive cluster ellipticals (De Lucia et al. 2006). The evolution of galaxies is affected by their surroundings, so by $z \approx 1$ there exists an intimate relationship between the properties of galaxies and their environments (e.g. Dressler 1980; Behroozi et al. 2010; Peng et al. 2010; Houghton 2015). Observations of forming galaxies in this critical phase are therefore essential to obtain a complete understanding of how clusters and their member galaxies form.

This cluster formation process is still shrouded in mystery, despite a handful ($\sim 15$) of protoclusters having been observed in detail. This is because current studies have not been able to place protoclusters in cosmological context: we do not know what their current halo mass is, nor how large each protocluster will grow. Without these key pieces of information it is hard to interpret what these galaxy overdensities are and how they fit into our theory of structure formation. The WEAVE-LOFAR IFU survey will transform our understanding of the early stages of cluster formation by measuring the already collapsed mass and estimating the present-day descendant cluster mass of 50 protoclusters at $1 < z < 2.5$. The protoclusters will be identified as groups of two or more radio galaxies within 1.5 arc min from the WIDE tier of the WEAVE-LOFAR MOS survey, where we have the best sensitivity to the rarest objects. Both observational evidence (e.g. Venemans et al. 2007; Wylezalek et al. 2013; Hatch et al. 2014) and the latest simulations (in particular those by Orsi et al. 2016) agree that high redshift radio galaxies are beacons for protoclusters.

Numerical simulations show that the progenitors of massive galaxy clusters consist of many separate halos spread over 25 Mpc at $z > 2$ (Chiang et al. 2013; Muldrew et al. 2015; Contini et al. 2016). The most massive of these halos could reach a few times $10^{13}$ to $10^{14}\,M_{\odot}$, and be signposted with a radio galaxy (Orsi et al. 2016). The rarest of the rare, ultra-massive protoclusters will contain several massive halos, each of which may be signposted with a radio-galaxy. Hence the association of several radio galaxies implies the presence of an agglomeration of several $> 10^{13}\,M_{\odot}$ dark matter haloes that will eventually combine to form some of the most massive clusters in the Universe. The WEAVE-LOFAR IFU survey will not only locate them, but also put them into cosmological context for the first time. We will measure the collapsed dark matter halo mass of the radio galaxies by cross correlating the radio galaxies with the surrounding emission line galaxy population (either Lyman-$\alpha$ at $z > 2.1$ or [OII] at $z < 1.5$, taking advantage of WEAVE's broad wavelength coverage). The final descendant cluster mass can only be measured with a high-spectral resolution instrument, such as WEAVE.

## 4 Conclusions

We have described the WEAVE-LOFAR survey, which will use the thousand-fold multiplex and large contiguous wavelength coverage of the WEAVE instrument (Dalton et al. 2012, 2014), scheduled for first light on the William Herschel Telescope in 2018, to produce more than $10^6$ spectra of sources selected at 150 MHz from the LOFAR Surveys Key Science Project (Röttgering et al. 2011). WEAVE-LOFAR will have three tiers, in order to efficiently sample the luminosity-redshift plane, and to representatively probe the whole faint radio source population. WEAVE-LOFAR will be the primary source of spectroscopic redshifts and source classifications that are required to harness the vast star formation and accretion sensitivity of LOFAR, and will allow a very wide range of science topics to be addressed. These topics include the star formation history of the Universe, the interplay between different accretion modes, and their relationships with AGN-driven feedback, probing the epoch of reionisation, cosmology, and understanding cluster haloes and radio relics. The vast spectroscopic data set that will be produced will have immense legacy value, including e.g. allowing the necessary calibration of photometric redshifts for the *Euclid* mission and LSST. WEAVE-LOFAR will also include resolved spectroscopy of protocluster targets, essential for putting these growing overdensities into their cosmological context, and studying the influence of powerful AGN on their surrounding galaxies. Due to the demographics of the faint radio source population, we expect that observing low-frequency selected sources will have a high redshift success rate, approaching 100 per cent at $z < 1$.

TS acknowledges support from the ERC Advanced Investigator programme NewClusters 321271. H.D. acknowledges financial support from the Spanish Ministry of Economy and Competitiveness (MINECO) under the 2014 Ramn y Cajal program MINECO RYC-2014-15686.

## References

Becker, R. H., White, R. L., & Helfand, D. J. 1995, ApJ, 450, 559

Behroozi, P. S., Conroy, C., & Wechsler, R. H. 2010, ApJ, 717, 379

Bell, E. F. 2003, ApJ, 586, 794

Benitez, N., Dupke, R., Moles, M., et al. 2014, ArXiv e-prints

Best, P. N. & Heckman, T. M. 2012, MNRAS, 421, 1569

Best, P. N., Kaiser, C. R., Heckman, T. M., & Kauffmann, G. 2006, MNRAS, 368, L67

Best, P. N., Ker, L. M., Simpson, C., Rigby, E. E., & Sabater, J. 2014, MNRAS, 445, 955

Bolton, J. S., Haehnelt, M. G., Warren, S. J., et al. 2011, MNRAS, 416, L70

Bradshaw, E. J., Almaini, O., Hartley, W. G., et al. 2013, MNRAS, 433, 194

Cai, Z.-Y., Lapi, A., Bressan, A., et al. 2014, ApJ, 785, 65

Carilli, C. L., Gnedin, N. Y., & Owen, F. 2002, ApJ, 577, 22

Chen, H.-W., Wild, V., Tinker, J. L., et al. 2010, ApJ, 724, L176

Chiang, Y.-K., Overzier, R., & Gebhardt, K. 2013, ApJ, 779, 127

Cirasuolo, M., Magliocchetti, M., Celotti, A., & Danese, L. 2003, MNRAS, 341, 993

Cohen, A. S., Lane, W. M., Cotton, W. D., et al. 2007, AJ, 134, 1245

Contini, E., De Lucia, G., Hatch, N., Borgani, S., & Kang, X. 2016, MNRAS, 456, 1924

Croton, D. J., Springel, V., White, S. D. M., et al. 2006, MNRAS, 365, 11

Dalton, G., Trager, S., Abrams, D. C., et al. 2014, in Proc. SPIE, Vol. 9147, Ground-based and Airborne Instrumentation for Astronomy V, 91470L

Dalton, G., Trager, S. C., Abrams, D. C., et al. 2012, in Proc. SPIE, Vol. 8446, Ground-based and Airborne Instrumentation for Astronomy IV, 84460P

Davis, T. A., Krajnović, D., McDermid, R. M., et al. 2012, MNRAS, 426, 1574

De Lucia, G., Springel, V., White, S. D. M., Croton, D., & Kauffmann, G. 2006, MNRAS, 366, 499

Dressler, A. 1980, ApJ, 236, 351

Geach, J. E., Dunlop, J. S., Halpern, M., et al. 2016, ArXiv e-prints

Geach, J. E., Hickox, R. C., Diamond-Stanic, A. M., et al. 2014, Nature, 516, 68

Gürkan, G., Hardcastle, M. J., Jarvis, M. J., et al. 2015, MNRAS, 452, 3776

Hardcastle, M. J., Evans, D. A., & Croston, J. H. 2007, MNRAS, 376, 1849

Hardcastle, M. J., Gürkan, G., van Weeren, R. J., et al. 2016, MNRAS, 462, 1910

Hatch, N. A., Wylezalek, D., Kurk, J. D., et al. 2014, MNRAS, 445, 280

Heckman, T. M., Kauffmann, G., Brinchmann, J., et al. 2004, ApJ, 613, 109

Hill, G. J., Gebhardt, K., Komatsu, E., et al. 2008, in Astronomical Society of the Pacific Conference Series, Vol. 399, Panoramic Views of Galaxy Formation and Evolution, ed. T. Kodama, T. Yamada, & K. Aoki, 115

Holland, W. S., Bintley, D., Chapin, E. L., et al. 2013, MNRAS, 430, 2513

Houghton, R. C. W. 2015, MNRAS, 451, 3427

Ivezić, Ž., Menou, K., Knapp, G. R., et al. 2002, AJ, 124, 2364

Jarvis, M. J. & Rawlings, S. 2004, New A Rev., 48, 1173

Kravtsov, A. V. & Borgani, S. 2012, ARA&A, 50, 353

Mack, K. J. & Wyithe, J. S. B. 2012, MNRAS, 425, 2988

Madau, P. & Dickinson, M. 2014, ARA&A, 52, 415

Madau, P., Pozzetti, L., & Dickinson, M. 1998, ApJ, 498, 106

Mannucci, F., Cresci, G., Maiolino, R., Marconi, A., & Gnerucci, A. 2010, MNRAS, 408, 2115

Martínez-Sansigre, A. & Rawlings, S. 2011, MNRAS, 414, 1937

Martínez-Sansigre, A., Rawlings, S., Lacy, M., et al. 2005, Nature, 436, 666

Mauch, T., Klöckner, H.-R., Rawlings, S., et al. 2013, MNRAS, 435, 650

Mortlock, D. J., Warren, S. J., Venemans, B. P., et al. 2011, Nature, 474, 616

Muldrew, S. I., Hatch, N. A., & Cooke, E. A. 2015, MNRAS, 452, 2528

Murphy, E. J. 2009, ApJ, 706, 482
Murphy, E. J., Condon, J. J., Schinnerer, E., et al. 2011, ApJ, 737, 67
Oliver, S. J., Bock, J., Altieri, B., et al. 2012, MNRAS, 424, 1614
Orsi, Á. A., Fanidakis, N., Lacey, C. G., & Baugh, C. M. 2016, MNRAS, 456, 3827
O'Sullivan, S. P., Gaensler, B. M., Lara-López, M. A., et al. 2015, ApJ, 806, 83
Peng, Y.-j., Lilly, S. J., Kovač, K., et al. 2010, ApJ, 721, 193
Pilbratt, G. L., Riedinger, J. R., Passvogel, T., et al. 2010, A&A, 518, L1
Rigby, E. E., Maddox, S. J., Dunne, L., et al. 2011, MNRAS, 415, 2336
Röttgering, H., Afonso, J., Barthel, P., et al. 2011, Journal of Astrophysics and Astronomy, 32, 557
Seymour, N., Dwelly, T., Moss, D., et al. 2008, MNRAS, 386, 1695
Shimwell, T. W., Luckin, J., Brüggen, M., et al. 2016, MNRAS, 459, 277
Silk, J. & Rees, M. J. 1998, A&A, 331, L1
Simpson, C., Martínez-Sansigre, A., Rawlings, S., et al. 2006, MNRAS, 372, 741
Simpson, C., Rawlings, S., Ivison, R., et al. 2012, MNRAS, 421, 3060
Smit, R., Bouwens, R. J., Franx, M., et al. 2012, ApJ, 756, 14
Smith, D. J. B., Jarvis, M. J., Hardcastle, M. J., et al. 2014, MNRAS, 445, 2232
Smolčić, V., Schinnerer, E., Scodeggio, M., et al. 2008, ApJS, 177, 14
Stott, J. P., Sobral, D., Bower, R., et al. 2013, MNRAS, 436, 1130
van Weeren, R. J., Williams, W. L., Hardcastle, M. J., et al. 2016, ApJS, 223, 2
Venemans, B. P., Röttgering, H. J. A., Miley, G. K., et al. 2007, A&A, 461, 823
Williams, W. L. & Röttgering, H. J. A. 2015, MNRAS, 450, 1538
Williams, W. L., van Weeren, R. J., Röttgering, H. J. A., et al. 2016, MNRAS, 460, 2385
Wilman, R. J., Miller, L., Jarvis, M. J., et al. 2008, MNRAS, 388, 1335
Wylezalek, D., Galametz, A., Stern, D., et al. 2013, ApJ, 769, 79
Yun, M. S., Reddy, N. A., & Condon, J. J. 2001, ApJ, 554, 803

*SF2A 2016*
*C. Reylé, J. Richard, L. Cambrésy, M. Deleuil, E. Pécontal, L. Tresse and I. Vauglin (eds)*

# THE WEAVE DISK DYNAMICS SURVEY

B. Famaey[1], T. Antoja[2], M. Romero-Gomez[3], A. Siebert[1], C. Babusiaux[4], P. Di Matteo[4], F. Figueras[3], F. Fragkoudi[4], F. Garzon-Lopez[3], C. Gonzalez-Fernandez[5], I. Martinez-Valpuesta[6], G. Monari[1], R. Mor-Crespo[3], V. Hill[7] and the WEAVE Survey Consortium

**Abstract.** WEAVE is the next-generation wide-field survey facility for the William Herschel Telescope. It consists of a multi-object fibre spectrograph with a 2°-diameter field of view that can obtain $\sim 1000$ spectra simultaneously. The "WEAVE Galactic Archaeology survey" is the survey focused on the Milky Way, as a complement to the Gaia space mission, and will start operating in early 2018. This survey is subdivided in four sub-surveys, among which the "WEAVE disk dynamics survey". This survey plans to measure the radial velocities (and abundances as far as possible) of $\sim 10^6$ stars with magnitude $15 < V < 20$ in the Milky Way disk to unravel the detailed features of its gravitational potential. In particular, the non-axisymmetric perturbations such as the bar and spiral arms, are among the main drivers of the evolution of the Galactic disks. Questions (i) about their nature – e.g., are these features transient, quasi-stationary, or do both types co-exist? – (ii) about their detailed structure and dynamics – e.g., is the bar short or long, what is its pattern speed? –, as well as (iii) about their influence on secular processes such as stellar radial migration are essential elements for a better understanding of the chemo-dynamical evolution of our Galaxy, and of galaxies in general. This survey is designed to answer these questions.

Keywords: Galaxy: kinematics and dynamics – Galaxy: evolution

## 1 Introduction

The Milky Way is a unique laboratory in which to test our models of galaxy formation, structure, and evolution. The story of the efforts to obtain stellar kinematic data in the solar neighbourhood during the XXth century has culminated with ESA's Hipparcos astrometric catalogue (Perryman et al. 1997), and with the complementary ground-based spectroscopic surveys that have provided the missing information on the line-of-sight velocities (e.g., Nordström et al. 2004; Famaey et al. 2005). Now, ESA's Gaia satellite (Gaia Collaboration 2016) will perform astrometry and photometry of more than 1 billion objects up to a magnitude $V \sim 20$, as well as spectrosocopy for some 150 million objects up to $V \sim 16$. In order to get six-dimensional phase-space information for fainter stars, the mission will have to be completed with ground-based spectrosocpic surveys. Such a ground-based survey is precisely what WEAVE is (Dalton et al. 2014). It consists of a multi-object fibre spectrograph with a 2°-diameter field of view. The spectrograph measures 1000 spectra simultaneously at a spectral resolution of $R \sim 5000$ over an instantaneous wavelength range $370 - 1000$ nm. In high-resolution mode, it reaches $R \sim 20000$ over two more limited wavelength regions.

The "WEAVE Galactic Archaeology survey" is the survey focused on the Milky Way, as a complement to the Gaia space mission, and will start operating in early 2018. This survey is divided into 4 sub-surveys focusing on

[1] Observatoire astronomique de Strasbourg, Université de Strasbourg, CNRS UMR 7550, 67000 Strasbourg, France
[2] Directorate of Science, ESA-ESTEC, PO Box 299, 2200 AG Noordwijk, The Netherlands
[3] Dept. dAstronomia i Meteorologia, Institut de Ciències del Cosmos, Universitat de Barcelona, IEEC, Martí i Franquès 1, E08028 Barcelona, Spain
[4] GEPI, Observatoire de Paris, CNRS, Université Paris Diderot, 5 place Jules Janssen, 92190 Meudon, France
[5] Institute of Astronomy, University of Cambridge, Madingley Road, Cambridge, CB3 0HA, UK
[6] Instituto de Astrofísica de Canarias, E-38205 La Laguna, Tenerife, Spain
[7] Laboratoire Lagrange, Université de Nice Sophia-Antipolis, Observatoire de la Côte d'Azur, CNRS, Bd de lObservatoire, CS 34229, 06304 Nice cedex 4, France

Galactic open clusters, the Galactic halo, the chemical labelling of Galactic populations (HR chemodynamical survey), and the disk dynamics.

The latter "WEAVE disk dynamics survey" is intended to be complementary to Gaia (and a Northern complement to the spectroscopic survey 4MOST in the South) and competitive with APOGEE. This survey therefore needs to be continuous in terms of spatial coverage, and to comprise of the order of $10^6$ stars. We proposed to observe red clump stars with high priority, for $V > 15$. We therefore will cover a significant fraction of the Galactic disk to a depth well suited for gaining new insights on the disks structure and history.

We divide the WEAVE disk dynamics survey into four goals and two sub-surveys. The four goals are:

i) Global phase-space structure of the disk (see Sect. 2);

ii) Nature and dynamics of the bar and spiral arms (see Sect. 3);

iii) Radial migration (see Sect. 4);

iv) Interface between thin, thick disk and halo (see Sect. 5).

These goals can be achieved through measuring and studying:

a) The global phase-space distribution function of disk populations, including the spatial disk structure, mean velocity field and the velocity dispersion;

b) The substructure in phase-space associated to the distinct processes acting on the disk (mergers and/or resonances of non-axisymmetric perturbations);

c) The distribution of abundances and its relation to the aforementioned dynamical constraints.

The constraints set by the answers to our goals should ultimately help to determine the relative importance and actual efficiency of the various processes acting on the disk.

This science case is divided into two sub-surveys with different observing strategies to cover the different goals (see Sect. 6):

1) The Inner Milky Way LR disk (IMWD),

2) The Outer Milky Way LR-HR disks (OMWD) surveys.

The IMWD survey consists in the coverage of the inner Galactic disk ($20° < l < 135°$) at latitudes lower than 6°. It will consist fully of red clump stars for which photometric distances will be obtained even when Gaia parallaxes will be very uncertain at large distances. The innermost part of the disk ($20° < l < 90°$) will have continuous coverage. The main motivation of the survey is a detailed understanding of the effects of the bar and spiral arms on stellar dynamics in the inner Galaxy, which is essential to better understand the secular evolution of the disk. This will be complemented by a slightly sparser coverage of the disk between $90° < l < 135°$, in order to follow the effects of the bar and spirals beyond the suspected location of the bar's Outer Lindblad Resonance.

On the other hand, the effects of mergers and interactions of satellites or dark matter clumps on the disk is expected to become more important in the outer Galaxy. There these processes can lead to flaring, corrugation waves, the presence of accretion debris, etc, at the interface between the thin, thick disk and the halo. Studying the detailed dynamics of the outer disk is thus going to be of tremendous importance to understand the build-up history of the Galaxy. The interface between the disk and the halo is particularly important there, hence higher Galactic latitudes should be probed than in the inner disk. The OMWD survey plans to observe giant stars in the longitude range $135° < l < 225°$ at latitudes up to 10°. High latitude fields with relatively low extinction down to $b = 5°$ will be probed in HR mode while the lower latitude fields will be observed in LR mode.

## 2 Global phase-space structure of the disk

We need to know the radial and vertical kinematical structure of the Galactic disk in order to disentangle various kinematical subpopulations, and to measure the scale-length of the Galactic disk dynamically. This is particularly important in view of testing predictions of the standard cosmological model and of alternatives (e.g. Bienaymé et al. 2009; Bovy & Rix 2013), and in order to determine the shape of the putative dark matter halo around the Galaxy (e.g., Binney & Piffl 2015), as well as the possible existence of a dark disk. This main objective will be achieved through dynamical models of the Galaxy relying on the 0th order assumptions of axisymmetry and equilibrium. These very legitimate assumptions allow us to make use of Jeans' theorem constraining the phase-space distribution function to depend only on three isolating integrals of motion. In this context, the action integrals are the best suited, since they are adiabatically invariant and are, with their conjugate angle variables, the natural coordinates of perturbation theory. By constructing distribution functions depending on these action integrals, one can, e.g., disentangle the various stellar populations such as the thin and thick disk in a much more reliable way than with naive kinematic decomposition. One can then iterate the fits with different gravitational potentials until the best-fitting potential is found, giving access to the underlying mass distribution including dark matter. It will also be important to determine the extension of the Milky Way disk and the location of the break in the disk surface density in the outer Galaxy, as well as the characteristics of the warp and flare.

## 3 Nature and dynamics of the bar and spiral arms

With the approach presented in the previous section, the consequences of assuming axisymmetry and equilibrium when it is not actually the case might bias the results. In this respect, it will be extremely useful to test this type of modelling on non-equilibrium models from simulations. But the WEAVE data themselves will actually allow us to characterize the first-order perturbations of the global non-axisymmetric components, including the central bar and main spiral arms. These non-axisymmetries drive the position of the main mode of the velocity distribution in the radial direction (Siebert et al. 2011). This will be measured at all positions inside the inner Galactic disk thanks to the IMWD survey, and can leave a signature from line-of-sight velocities and photometric distances for red clump stars alone, as illustrated in Monari et al. (2016a, their Fig. 12). Starting from an axisymmetric equilibrium distribution function in action space, one can then apply linear perturbation theory to analytically determine the perturbed distribution function in terms of actions and angles in the presence of a single main perturber (Monari et al. 2016b). This technique breaks down close to first-order resonances, where stellar populations should rather be modelled in terms of new action and angle variables obtained from a well-chosen canonical transformation suited to the given resonance. Such equilibrium distribution functions in the presence of a main perturber such as the bar can then be themselves perturbed with the technique outlined in Monari et al. (2016b) in the presence of secondary non-axisymmetric perturbers such as spiral arms. Data allowing measurement of the mean radial and vertical motions as a function of position, combined with more local determinations of the positions of resonantly generated moving groups in velocity space (e.g., Antoja et al. 2011), will then place stringent constraints on the form of the perturber potentials themselves. Different models of spiral arms can e.g. be tested through comparison between accurate line-of-sight velocities together with astrometry from Gaia and existing spiral models (e.g., Lin et al. 1969; Romero-Gomez et al. 2011; Antoja et al. 2011; Grand et al. 2012). This will also allow the disentangling of the dynamical effects of a bar as measured with COBE/DIRBE (see e.g. Monari et al. 2016c) versus those with a slowly-rotating bar, like the one suggested by Wegg et al. (2015) and Portail et al. (2015). The WEAVE disk dynamics survey is particularly well-suited for this task as it will nicely cover the region of the Galactic disk where the tip of the bar and its long flat extension - whose nature remains to be determined with certainty - are located, and the region ahead of it in terms of rotation contrary to surveys based in the Southern hemisphere which will rather probe the region behind the bar in term of its rotation.

## 4 Radial migration

In classical chemical evolution models, stars are postulated to live their entire lives at the same radius. Even when heating is taken into account, the range of radii which individual stars in the disk explore was generally thought to be small, of the order 1.5 kpc. This seemingly natural assumption was shattered when Sellwood & Binney (2002) showed that stars can migrate over large distances while retaining essentially circular orbits. The mechanism governing this migration is the trapping of stars at the co-rotation resonance of transient spirals. This can be enhanced if the spirals are co-rotating in a large radial range (Grand et al. 2012). Migration is also triggered where the resonances of the bar and the spiral pattern overlap: stochasticity can force stars to rapidly migrate radially away from their place of birth (Minchev & Famaey 2010; Weinberg 2015). Radial migration is a key component driving the secular evolution of the disk, and has important consequences for understanding galactic evolution (e.g., Minchev et al. 2014), including issues such as the age-metallicity relation and the G-dwarf problem. There are several probes of radial migration. First, a direct dynamical probe is the dynamics in the Scutum-Crux window at $l = +27°$, which samples the overlap region between the suspected co-rotation of the bar and the 4:1 inner resonance of an inner spiral. This resonance overlap could cause stellar migration, as suggested by Minchev & Famaey (2010), which would lead to specific streaming along the spiral arm, and could be directly compared to other proposed processes such as trapping by a transient co-rotating spiral (Grand et al. 2012). The outer disk of the Milky Way is another important stellar repository reflecting the history of any migration that may have occurred in our Galaxy. Do we find that stars there are on nearly circular orbits (favouring either an in situ or a spiral migration mechanism) or are they on elongated orbits (favouring heating by satellites or the bar)? The chemistry will also be important to distinguish the processes: is the chemistry of the outer disk vastly different from that of coeval stars in the inner disk? (e.g., Haywood et al. 2013). A strong age-metallicity relation will be very suggestive of in situ star formation, which can help distinguish this scenario from migration. Different mechanisms causing the radial migration would leave drastically different signatures in the elemental abundance pattern of stars and in the age-metallicity relation across the disk, reflecting the variation in star-formation history and chemical evolution across the region of migration. The combination of dynamics and chemistry of stars in the disk, which for the foreseeable future is only possible in the Milky Way, will provide important new constraints on the evolution of disk galaxies. WEAVE is the ideal instrument to probe this important effect on disk evolution, as metallicities, alpha-element abundances and stellar kinematics at high precision can be obtained simultaneously.

## 5 Interface between thin, thick disk and halo

Recent studies have shown that several processes that were traditionally thought to act on the different Galactic components are, in fact, influencing also the whole Galaxy. For instance, there has been a debate on whether the non-axisymmetric components can influence or even cause the formation of the thick disk (Schönrich & Binney 2009; Minchev et al. 2012; Solway et al. 2012), with an emerging consensus that non-axisymmetries alone cannot induce the appropriate thickening (Minchev et al. 2012; Aumer et al. 2016). But in any case, it has been demonstrated that non-axisymmetries have at present non-negligible effects on the thick disk stellar populations (Monari et al. 2013; Antoja et al. 2015) and not only on the thin disk as traditionally believed. Another example: the study of the effects of the external perturbations by satellites has been traditionally focused on the thick disk. However, such interactions can also cause non-axisymmetric patterns in the outer disk. Moreover, the interplay between these and the vertical imprint of the external perturbations can create complex combinations of breathing modes (from the non-axisymmetries, Williams et al. 2013; Faure et al. 2014) and bending modes (from the impact of satellites themselves, Widrow et al. 2012; Gomez et al. 2013; Carlin et al. 2013; Laporte et al. 2016) of the thin disk populations. There is, thus, a complex interface between the thin, thick disks, and halo, and the mechanisms acting on them. This is particularly visible in the outer disk (Slater et al. 2014), where the density of stars exhibits a complex morphology with both stream-like features and a sharp edge to the structure in both the North and the South. This has been interpreted both in terms of tidal streams and a distorted disk structure creating stream-like features close to the disk, but none of these models seem satisfactory yet. Studying velocity gradients in combination with North-South density asymmetries (corrugation patterns) should allow us to disentangle these various effects. The outer disk directions covered in the OMWD sub-survey is an especially suitable place to test and measure all the above-mentioned effects. It is in this last goal of our sub-survey that the objectives of the whole Galactic archeology survey mix and become a single one: understand the formation and evolution history of our Galaxy as a whole.

## 6 Footprint

The footprint of the WEAVE disk dynamics survey is presented in Figure 1. Targets will now be selected essentially from IPHAS and VPHAS photometry, as well as Gaia. Selection of red clump stars in the magnitude range $15 < V < 20$ will be prioritized. The stars will be selected using the simplest criteria possible to allow for an easy estimation of the target selection bias a posteriori. The aim is to follow the red clump extension locus on the colour- magnitude diagram induced by correlated increase of distance and extinction. Additional criteria based on the Gaia DR2 will later on be used to remove close red dwarfs that could fall in some fields in this locus depending on the extinction.

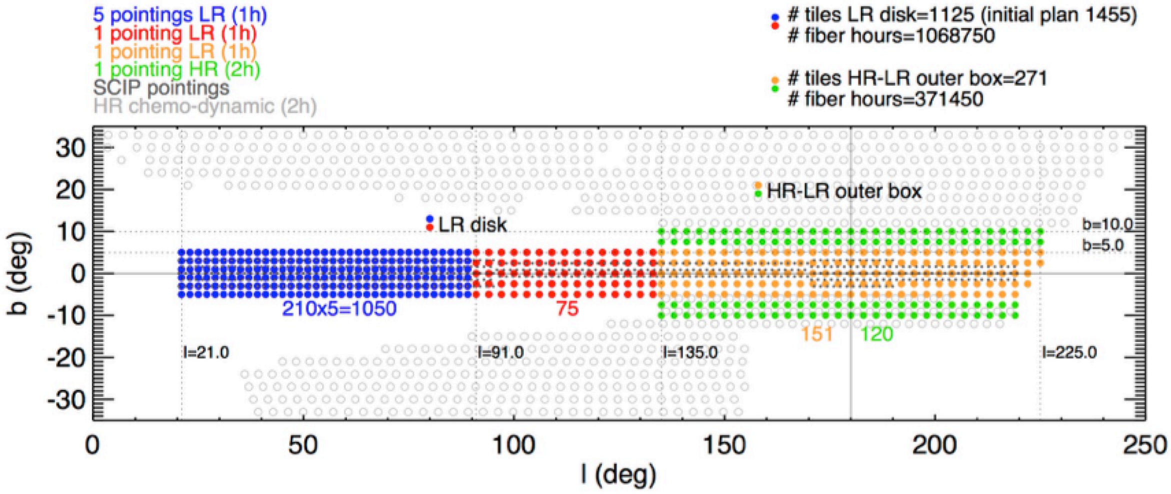


**Fig. 1.** The WEAVE disk dynamics survey footprint. IMWD 5 pointings: blue; IMWD 1 pointing: red; OMWD LR: orange; OMWD HR: green. Open circles are the original lines-of-sight for the HR chemodynamical survey.

## References


Antoja T., et al., 2011, MNRAS, 418, 1423

Antoja T., et al., 2015, ApJ, 800, L32

Aumer M., et al. MNRAS, 459, 3326

Bienaymé O., et al., 2009, A&A, 500, 801

Binney J., Piffl T., 2015, MNRAS, 454, 3653

Bovy J., Rix H.-W., 2013, ApJ, 779, 115

Carlin J. L., et al., 2013, ApJ, 777, L5

Dalton G., et al., 2014, SPIE, 9147, 0L

Famaey B., et al., 2005, A&A, 430, 165

Faure C., et al., 2014, MNRAS, 440, 2564

Gaia Collaboration, et al., 2016, eprint arXiv:1609.04172

Gomez F., et al., 2013, MNRAS, 429, 159

Grand R. J. J., et al., 2012, MNRAS, 426, 167

Haywood M., et al., 2013, A&A, 560, A109

Laporte C. F. P., et al., 2016, eprint arXiv:1608.04743

Lin C. C., et al., 1969, ApJ, 155, 721

Minchev I., Famaey B., 2010, ApJ, 722, 112

Minchev I., et al., 2012, A&A, 548, A127

Minchev I., et al., 2014, A&A, 572, A92

Monari G., et al. 2013, eprint arXiv:1306.2632

Monari G., et al., 2016a, MNRAS, 461, 3835

Monari G., et al., 2016b, MNRAS, 457, 2569

Monari G., et al., 2016c, eprint arXiv:1609.02557

Nordström B., et al., 2004, A&A, 418, 989

Perryman M., et al., 1997, A&A, 323, L49

Portail M., et al. 2015, MNRAS, 448, 713

Romero-Gomez M., et al., 2011, MNRAS, 418, 1176

Schönrich R., Binney J., 2009, MNRAS, 399, 1145

Sellwood J., Binney J., 2002, MNRAS, 336, 785

Siebert A., et al., 2011, MNRAS, 412, 2026
Slater C. T., et al., 2014, ApJ, 791, 9
Solway M., et al., 2012, MNRAS, 422, 1363
Wegg C., et al., 2015, MNRAS, 450, 4050
Weinberg M. D., 2015, eprint arXiv:1508.06855
Widrow L. M., et al., 2012, ApJ, 750, L41
Williams M. E. K., et al., 2013, MNRAS, 436, 101

*SF2A 2016*
*C. Reylé, J. Richard, L. Cambrésy, M. Deleuil, E. Pécontal, L. Tresse and I. Vaughlin (eds)*

# RED-GIANT STARS: CHEMICAL CLOCKS IN THE MILKY WAY

N. Lagarde[1], A.C. Robin[1], C. Reylé[1] and G. Nasello[1]

**Abstract.** A broad effort is ongoing with large spectroscopic surveys such as APOGEE, ESO-Gaia, RAVE from which stellar parameters, radial velocities and detailed chemical abundances can be measured for CoRoT, Kepler, and K2 targets. In addition, asteroseismic data of red-giants stars observed by the space missions CoRoT and Kepler allow determination of stellar masses, radii, and can be used to determine the position and ages of stars. This association between spectroscopic and asteroseismic constraints provide a new way to understand galactic and stellar evolutions. To exploit all potential of this combination it would be crucial to develop our approach of synthetic populations. We compute stellar populations synthesis with the Besançon Galactic model including the asteroseismic and chemical properties from stellar evolution models. These synthetic populations can be compared with sinificant large surveys as APOKASC (APOGEE+Kepler) or CoRoGEE (CoRoT+APOGEE). We focus here on the carbon and nitrogen surface abundances of Kepler red-giant stars. We underline the importance of transport processes occurring in red-giant stars as rotation and thermohaline instability to understand chemical properties of stellar populations in the Galaxy. The future for this area also starts taking shape with the launch of Gaia, futur spectroscopic surveys such as 4MOST and WEAVE, and the future space mission PLATO that will provide seismic data for more than 100 000 red-giants. Such synthetic population model is a key tool to investigate future observations and better understand the evolution of the Milky Way.

Keywords: Stellar evolution, red giant stars, population synthesis, Galactic evolution

## 1 Introduction

Understanding stellar evolution is crucial to improve our knowledge of chemical and evolution properties of galaxies. As shown by the initial mass function (e.g. Salpeter 1955; Scalo 1986; Kroupa 2001; Luhman et al. 2000), low- and intermediate-mass stars are the most numerous stars in our Galaxy. They form the dominant stellar component of our Galaxy and represent a very important astrophysical interest. In their advanced phases, these stars undergo important changes of their structure and chemical composition. Due to strong winds during the superwind phase, which leads to the emergence of planetary nebula, they contribute significantly to the enrichment of the interstellar medium and to the chemical evolution of galaxies. They have a rich nucleosynthesis, with a large part of enrichment in $^{4}$He, and they dominate the production of $^{13}$C, $^{14}$N, and main s-process elements. Red-giant stars cover a large domain in mass, age, chemical composition and evolutionary states. They are cool and high luminous stars making them easily observable. The oscillation spectrum of red-giant stars are very rich providing informations of deep stellar interior.

The observations of red-giant stars have been rised during the last decade. The very large surveys APOGEE (Majewski et al. 2015; SDSS Collaboration et al. 2016), and Gaia-ESO (Gilmore et al. 2012), provide global (gravity, effective temperature or radial velocity) and chemical properties for a large number of giants. The two satellites CoRoT (Baglin et al. 2006) and *Kepler* (Borucki et al. 2010) observed ∼20 000 giant stars, probing their stellar interior thanks to asteroseismology, and given their evolutionary states, stellar mass, radius, age and distance. In addition, the satellite Gaia (Perryman 2002) observe 1 billion stars in the Milky Way will provide accurate distances, proper motions or abundances. To exploit all potential of these different kind of observations, it is crucial to combine them together, and to develop the population synthesis approach. We show here the preliminarily results from the Besançon Galaxy model which take into account new stellar evolution models including rotation and thermohaline instability (Lagarde et al. 2012).

[1] Institut Utinam, CNRS UMR6213, Université de Franche-Comté, OSU THETA Franche-Comté-Bourgogne, Observatoire de Besançon, BP 1615, 25010 Besançon Cedex, France

## 2 Population synthesis with the Besançon Galaxy model

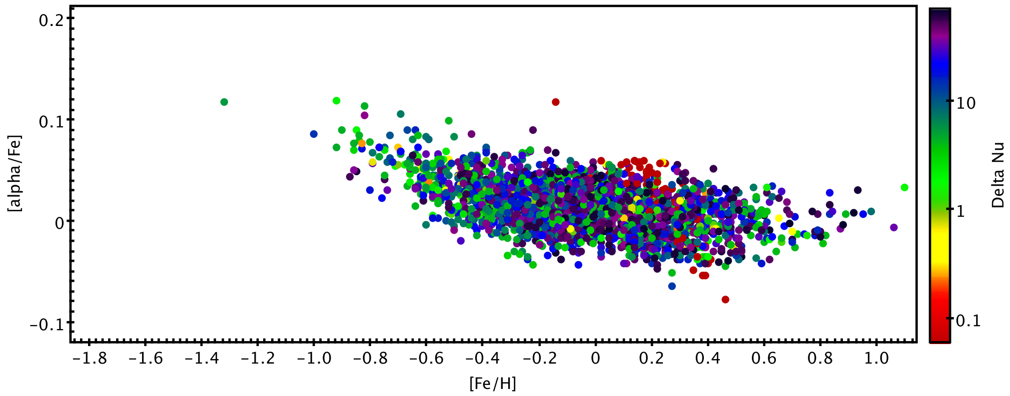


**Fig. 1.** Color-coded [$\alpha$/Fe] abundance as a function of metallicity for the thin disc. The color code represents the values of the large separation $\Delta\nu$ provided by classical stellar evolution models.

The Besançon Galaxy model is a stellar population synthesis model (Robin et al. 2003; Czekaj et al. 2014) intended to put together the formation and evolution scenarios of the Galaxy, stellar formation and evolution theory, models of stellar atmospheres as well as dynamical constraints in order to make a consistent picture of available observations (photometry, asteroseismology, astrometry, and spectroscopy) at different wavelengths. Each stellar population (thin and thick discs, halo, and bulge) was calculated given a particular initial mass function, star formation rate, age-metallicity relation, and evolutionary tracks.

To fully exploit the potential of recent asteroseismic and spectroscopic surveys, we use the stellar evolution models computed with the stellar evolution code STAREVOL (Lagarde et al. 2012) for low- and intermediate-mass stars (1.0M$_\odot$ $\leq$M$\leq$6.0M$_\odot$). These models provide the relevant classical stellar parameters together with global asteroseismic properties and following 54 stable and unstable species from $^1$H to $^{37}$Cl at the surface of stars all along the stellar evolution. This is done from the pre-main sequence to the early-asymptotic giant branch. This stellar evolution grid contains models computed with rotation-induced mixing and thermohaline instability, along with standard models without mixing outside convective regions for comparison purposes (for more details see Lagarde et al. 2012).

Such population synthesis provides for the first time the seismic properties such as the large separation $\Delta\nu$, the frequency with the maximum amplitude $\nu_{max}$, or the asymptotic period spacing of g-modes $\Delta\Pi$ for stars observed by CoRoT and *Kepler* in the thin disc. Figure 1 illustrates the alpha abundance ratio versus iron abundance for a sample of thin disc stars, colour-coded by the value of $\Delta\nu$ along the thin disc. Moreover, asteroseismology using the value of $\Delta\Pi$ help us to distinguish between clump and red-giant stars (Mosser et al. 2012). We can also compute the surface chemical properties of these stars to interpret large spectroscopic surveys (Figure 2).

Transport processes occuring in stellar interiors have a significant impact on global (e.g. luminosity, effective temperature, age), chemical, and seismic properties (e.g. Palacios et al. 2006; Lagarde et al. 2012; Bossini et al. 2015). Population synthesis simulations are powerful tools to study these processes using survey data. As discuss in litterature (e.g. Palacios et al. 2003; Charbonnel & Lagarde 2010), rotation-induced mixing and, more particularly for low-mass stars, thermohaline instability change the photospheric composition of giant stars. Thermohaline mixing induces the changes of surface abundances of $^3$He, $^7$Li, C and N for stars brighter than the RGB-bump luminosity (Charbonnel & Lagarde 2010). Rotation-induced mixing modifies the internal chemical structure of main sequence stars. A dispersion of initial stellar rotational velocity explains the observed dispersion of chemicals surface abundances in subgiant stars (Palacios et al. 2003, 2006). Figure 2 shows the effects of rotation-induced mixing and thermohaline instability on the surface $^{12}$C/$^{13}$C of clump stars along the thin disc.

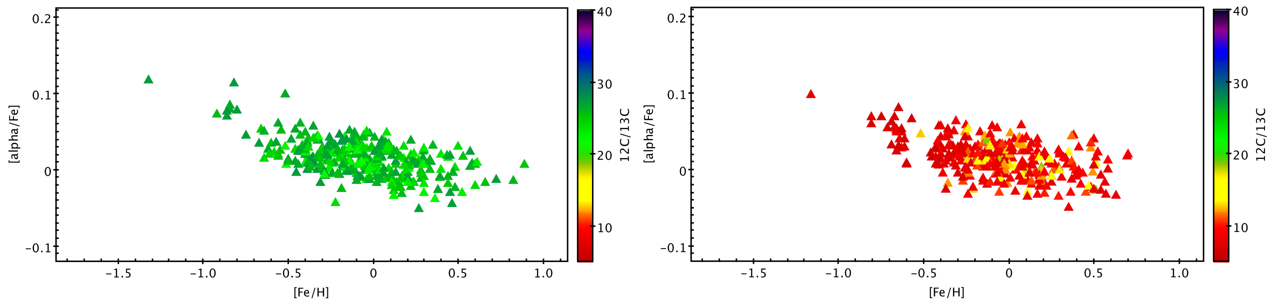


**Fig. 2.** Color-coded [$\alpha$/Fe] abundance as a function of metallicity for the clump stars simulated in the thin disc. The color code represents the surface abundances of carbon isotopic ratio, using standard stellar evolution models (left panel), and using models including the effects of rotation-induced mixing and thermohaline instability all long the evolution (right panel).

## 3 Perspectives

Computations for a larger grid in stellar masses, metallicities, initial velocities, $\alpha$-enrichments are now being performed in order to compare with large surveys (Lagarde et al 2016 in prep.). We plan to extend this study to all Galactic stellar populations, beginning with the thick disc. Thanks to WEAVE, 4MOST, and PLATO the future looks extremely bright in terms of collecting spectroscopic and seismic data for a large number of stars. The Besançon Galaxy model will be a key tool to exploit APOKASC and CoRoGEE catalogues and to prepare theses future instruments and missions as well as to give a better understanding of stellar and galactic evolution.

We acknowledge financial support from the french Programme National de Physique Stellaire (PNPS) of CNRS/INSU. N.L. acknowledges financial support from the CNES fellowship.

## References

Baglin, A., Auvergne, M., Boisnard, L., et al. 2006, in 36th COSPAR Scientific Assembly, Vol. 36, 3749
Borucki, W. J., Koch, D., Basri, G., et al. 2010, Science, 327, 977
Bossini, D., Miglio, A., Salaris, M., et al. 2015, MNRAS, 453, 2290
Charbonnel, C. & Lagarde, N. 2010, A&A, 522, A10
Czekaj, M. A., Robin, A. C., Figueras, F., Luri, X., & Haywood, M. 2014, A&A, 564, A102
Gilmore, G., Randich, S., Asplund, M., et al. 2012, The Messenger, 147, 25
Kroupa, P. 2001, MNRAS, 322, 231
Lagarde, N., Decressin, T., Charbonnel, C., et al. 2012, A&A, 543, A108
Luhman, K. L., Rieke, G. H., Young, E. T., et al. 2000, ApJ, 540, 1016
Majewski, S. R., Schiavon, R. P., Frinchaboy, P. M., et al. 2015, ArXiv e-prints
Mosser, B., Goupil, M. J., Belkacem, K., et al. 2012, A&A, 540, A143
Palacios, A., Charbonnel, C., Talon, S., & Siess, L. 2006, A&A, 453, 261
Palacios, A., Talon, S., Charbonnel, C., & Forestini, M. 2003, A&A, 399, 603
Perryman, M. A. C. 2002, Ap&SS, 280, 1
Robin, A. C., Reylé, C., Derrière, S., & Picaud, S. 2003, A&A, 409, 523
Salpeter, E. E. 1955, ApJ, 121, 161
Scalo, J. M. 1986, Fund. Cosmic Phys., 11, 1
SDSS Collaboration, Albareti, F. D., Allende Prieto, C., et al. 2016, ArXiv e-prints

# Session SF2A

# National and international synergies in space meteorology

*SF2A 2016*
*C. Reylé, J. Richard, L. Cambrésy, M. Deleuil, E. Pécontal, L. Tresse and I. Vauglin (eds)*

# METEOSPACE, SOLAR MONITORING AND SPACE WEATHER AT CALERN OBSERVATORY

T. Corbard[1], J.-M. Malherbe[2], D. Crussaire[2], F. Morand[1], F. Ruty[3], L. Biree[4], J. Aboudarham[2], N. Fuller[2], C. Renaud[1] and M. Meftah[5]

**Abstract.** METEOSPACE is a new partnership project between the Paris Observatory (OP), the Observatoire de la Côte d'Azur (OCA), the French Air Force and a service company (LUNA technology) for the development and operation of a set of small telescopes H$\alpha$ / Ca II K / Ca II H / G band to be installed at on the Calern plateau (OCA). The objective is to monitor solar activity for both research and its applications in space weather through continuous optical observations of the dynamic phenomena that are visible in the chromosphere: eruptions, destabilization of the filaments triggering coronal mass ejections and associated Moreton waves.

Keywords: Sun, Chromosphere, Space-Weather, H$\alpha$

## 1 Introduction - Short history of solar monitoring at Calern and Meudon observatories

A long term solar monitoring program has started at Calern observatory in 1974 (Laclare 1975). It is dedicated to solar astrometry and aims to detect and monitor possible solar diameter variations. The first instrument hosted by this solar astrometric station was a visual astrolabe. Over the years the observer's eye was replaced by analogic and digital cameras and in 1999 a new instrument called DORAYSOL was built which included a variable prism in order to record transit data all along the day (Morand et al. 2010). In 2010 the CNES PICARD satellite was lauched with the SODISM telescope onboard which was fully dedicated to solar astrometry (solar diameter and shape) (Meftah et al. 2014b, 2016). In 2011, the qualification model of SODISM called SODISM-2 was installed at Calern (Meftah et al. 2014a) and a day-time turbulence monitor was developped that allows simultaneous record of the spatio-temporal parameters of atmospheric turbulence (Ikhlef et al. 2016). SODISM-2 is a multi-wavelength imager providing full-disk images of the photosphere in the continuum at 535.7 nm, 607.1 nm , 782.2 nm and 1025.0 nm, and of the chromosphere in the Ca II K-line at 393.37 nm. Since 2011 more than 138000 images have been recorded and distributed via our local server `https://solar-data.oca.eu/` and the Multi Experiment Data and Operation Center (MEDOC). Continuum wavelength avoiding Fraunhofer lines were specificaly chosen in order to avoid the influence of magnetic activity on diameter measurements. The Ca II K filter is a broadband filter (0.7 nm) that covers the whole chromosphere from the temperature minimum 500 km above the photosphere up to about 1800 km and the transition region. It is used to detect large scale activity features on the solar disk.

Observations at Calern are fully complementary to those performed in Meudon since 1909. The climate of Ile-de-France allows to get daily images (280 days per year) but it is impossible to perform there continuous observations and monitor solar activity with temporal resolution compatible with transient and fast phenomena as flares, filament disturbances and Coronal Mass Ejecta. Hence, the scientific objective at Meudon is to follow solar activity along the solar cycle, and for that purpose, daily images are sufficient. From another point of

[1] Université Côte d'Azur , Observatoire de la Côte d'Azur, CNRS, Laboratoire Lagrange, 06304 Nice, France
[2] LESIA, Observatoire de Paris, Section de Meudon, 92195 Meudon, France
[3] Société Luna, 75011 Paris, France
[4] Armée de l'Air CDAOA / COSMOS, 69250 Lyon Mont-Verdun, France
[5] Université Paris Saclay, CNRS, Laboratoire Atmosphères, Milieux, Observations Spatiales (LATMOS), 78280 Guyancourt, France

view, Meudon operates a spectrograph which provides full line profiles (of H$\alpha$, CaII K) over the full disk with 0.02 nm spectral resolution typical; profiles can be used for probing the solar atmosphere as they contain depth information. On the contrary, most instruments in the world operate with monochromatic filters, corresponding to only one layer in the chromosphere. Another spectrograph operates the same way in the world at Coimbra (Portugal): it is a copy of Meudon spectrograph.

## 2 METEOSPACE Scientific Objectives

The goal of the new project presented here is to install a set of small telescopes at Calern observatory dedicated to the continuous observation of the chromosphere. This project will benefit from the existing solar station equipment and staff at Calern observatory. Monitoring solar activity both in real time and in the long term are needed for both research and for applications in space weather through the detection of rapid and transient solar phenomena:

- instabilities in solar filaments, eruptive filaments being partly associated with the onset of coronal mass ejections (CME)
- solar flares, also associated with CME
- chromospheric Moreton wave, also associated with the coronal wave which also appears in the lower corona radio radiation and in the high corona coronographic observations (SOHO / LASCO).

The hydrogen H$\alpha$ line is the most suitable line for monitoring solar phenomena from their birth, low in the solar atmosphere, the chromosphere, the root of solar eruptive activity. Images taken in narrow band filters of Ca II K and Ca II H lines will also complement these observations. These lines of singly ionized calcium are the strongest absorption lines in the visible solar spectrum and among the most sensitive indicators of the chromospheric structure and magnetic features of the Sun.

## 3 National and international context

Because H$\alpha$ images of the Sun are potentially very useful for predicting eruptions, observatories around the world observe the sun at that wavelength for both the scientists and space-weather applications. This led to the Global High Resolution H$\alpha$ Network `http://swrl.njit.edu/ghn_web/` but also to the H$\alpha$ program of the Global Oscillation Network Group (GONG) `http://halpha.nso.edu/` which, in addition to its helioseismology products, provides since 2012, in real time, H$\alpha$ images throughout its network for civilian and military applications.

The FEDOME* project managed by the French Air Force that aims to gather observations useful for space-weather prediction has already signed agreements with the Nancay station for radio observations (ORFEES† antenna) and the 'Institut de Physique du Globe de Paris' (IPGP) for their magnetometric data. It also uses optical data from CLIMSO‡ (Koechlin 2015) which is an associative operation led at Pic du Midi Observatory under the Research Institute in Astrophysics and Planetology (IRAP) scientific supervision. CLIMSO comprises 2 telescopes and 2 coronographs on the same equatorial table. It provides images of the solar disk in H$\alpha$ and Ca II, and images of the low corona in H$\alpha$ and singly ionized helium (He II) when the weather allows.

Meudon observatory provides H$\alpha$ and Ca II spectroheliograms at low cadence, typically a single image of each type per day suitable for studies at the scale of the 11 year solar cycle. Because of climate, this site does not allows monitoring solar activity continuously. The only European station conducting continuous observations in H-alpha is GONG station on the Canary Islands with a cadence of one image per minute. The Kanzelhöhe observatory in Austria and the Royal Observatory of Belgium also have an H$\alpha$ observation program and their images are made available through the space weather web portal of the European Space Situational Awareness (SSA) program `http://swe.ssa.esa.int/swe`.

From space, the Hinode/SOT instrument (Tsuneta et al. 2008) provides high resolution images with a limited field of view of the chromosphere notably in H$\alpha$ and Ca II H. It also provides photospheric network diagnostic through the CH molecular G-band. The Solar Dynamic Observatory instruments continuously provide full

*FÉdération des DOnnées Météorologiques de l'Espace
†Observation Radio Fréquences pour l'Etude des Eruptions Solaires
‡ Christian Latouche IMageur Solaire.

images of the photosphere and corona at different heights (Pesnell et al. 2012). The only channel covering partially the chromosphere is the one of He II line in extreme ultraviolet (at 30.4 nm) which probes the upper chromosphere and lower transition region.

## 4 METEOSPACE Instruments

METEOSPACE will propose several 80 mm or 100 mm aperture small telescopes operating either in spectral lines as H$\alpha$, CaII K, CaII H or G band (4 instruments maximum). H$\alpha$ will be provided by a Fabry Perot from DayStar Filters (USA) with 0.05 nm bandwidth. CaII K and H will be obtained using Barr Associates narrow interference filters (0.15 nm). G band will use a 0.8 nm Andover filter. The telescopes will be mounted in a box maintained at 25 degrees temperature (active heating, passive cooling). The CCD cameras use interline Sony sensors of 2750 x 2200 pixels (4.54 microns and 20000 electrons full well capacity) with electronic shutter. The pixel size will be 1 arc sec on the sun. The temporal resolution will be 10 s for H$\alpha$ and 60 s for other lines. Data will be provided in FITS format after data treatment using an automated pipeline. Real time data will be available for operational purposes for solar weather forecasting. Several gigabytes will be produced every day. The instruments will run in automatic mode. The equatorial mount is made by Valmeca (France). The computer will drive the mount, filters and cameras and will direct raw data towards the Calern server. The pre-processing will be done automatically at Calern before transfer do the database in Nice. A small part will be directed daily to the national solar survey archive BASS2000 `http://bass2000.obspm.fr/`. The telescopes ($\sim$350 k€) and the building ($\sim$50 k€) to host them at Calern are already financed by Direction Générale de l'Armement with contributions from Observatoire de Paris and Région Ile-de-France. However, to be successful and to have a chance to join the existing international programs gathering data for space-weather from ground-based observatories, the project needs to be totally automated and to be able to handle the real time processing of the images. For this we need to have an automatized roof for the building, to control the environment (weather station, rain sensor, wide field camera) and to insure the continuity of the observations by provisioning spare cameras and computers. Several funding requests are underway for these aspects.

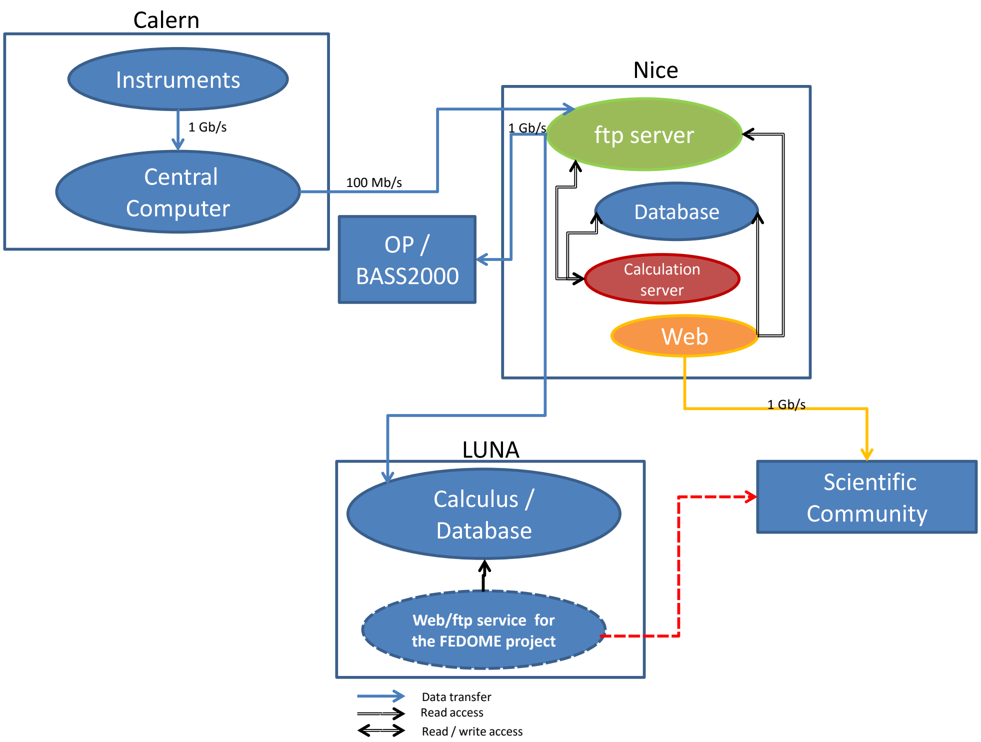


**Fig. 1.** Data acquisition, reduction and distribution system

## 5 Data processing and distribution

Data will be processed and distributed in near real-time. The system shown on Fig. 1 is made of three main units: a central computer close to the instruments at Calern observatory, a cluster located in Nice with nodes for computing, hosting a database ftp and web servers and a cloud service developed and maintained by LUNA for operational space weather applications and its use by the FEDOME project. The central computer reads raw data from the instruments, build level 0 FITS files and quick-look jpeg files and continuouly transfers these data to the cluster in Nice. The computing nodes of the cluster will implement real-time data selection, build the level 1 (calibrated) data when relevant, run the real time solar features extraction codes and populate the database. Automation of the filament tracking was previously developped in the framework of the HELIO project (Bonnin et al. 2013) and will be adapted for these new data. The ftp server is dimensioned to serve 5 TB per year and uses redundant array of independent disks (RAID 6) for insuring raw data security. Data will remain accessible on the server for three years after which a long term archive possibly hosted by BASS2000 should be developped and used. The web interface to the database and ftp server will be developped in collaboration with LUNA and made fully open to the scientific community and general public. All data will be fully open and made accessible as soon as they are produced without any retention period. A service for space-weather applications developped by LUNA for the FEDOME project will gather data from these servers. Part of the tools developped for this service will also contribute to the pipeline hosted by the Nice cluster.

## 6 Conclusion

The possibility of installing this instrumentation at the Calern station of OCA with local scientific and technical team on an existing platform of solar observations is a unique opportunity in continental Europe in complementarity with Nançay for radio astronomy and solar coronography at Pic du Midi. The METEOSPACE project will provide unique high cadence images of the chromosphere to the community and our goal is to join and contribute to the major international networks distributing optical ground-based solar data for both the fundamental study of chromospheric activity and space-weather applications. A workshop is held in Nice[§] to discuss and gather community input on science requirements and to discuss the existing and futur instrumentation for ground-based solar observing programs in the framework of space-weather studies and applications.

We thank Région Ile-de-France, the 'Programme National Soleil-Terre' (PNST) of CNRS-INSU, the Lagrange Laboratory and the ESTERS [¶] federative axis of Paris Observatory for their support.

## References

Bonnin, X., Aboudarham, J., Fuller, N., Csillaghy, A., & Bentley, R. 2013, Sol. Phys., 283, 49

Ikhlef, R., Corbard, T., Morand, F., et al. 2016, MNRAS, 458, 517

Koechlin, L. 2015, in SF2A-2015: Proceedings of the Annual meeting of the French Society of Astronomy and Astrophysics, ed. F. Martins, S. Boissier, V. Buat, L. Cambrésy, & P. Petit, 21–24

Laclare, F. 1975, Academie des Sciences Paris Comptes Rendus Serie B Sciences Physiques, 280, 13

Meftah, M., Corbard, T., Hauchecorne, A., et al. 2016, in Proc. SPIE, Vol. 9904, Society of Photo-Optical Instrumentation Engineers (SPIE) Conference Series, 99040Z

Meftah, M., Corbard, T., Irbah, A., et al. 2014a, A&A, 569, A60

Meftah, M., Hochedez, J.-F., Irbah, A., et al. 2014b, Sol. Phys., 289, 1043

Morand, F., Delmas, C., Corbard, T., et al. 2010, Comptes Rendus Physique, 11, 660

Pesnell, W. D., Thompson, B. J., & Chamberlin, P. C. 2012, Sol. Phys., 275, 3

Tsuneta, S., Ichimoto, K., Katsukawa, Y., et al. 2008, The Solar Optical Telescope for the Hinode Mission: An Overview, ed. T. Sakurai (New York, NY: Springer New York), 113–142

[§] http://meteospace.sciencesconf.org

[¶] Environnement Spatial de la Terre : Recherche et Surveillance http://esters.obspm.fr/

*SF2A 2016*
*C. Reylé, J. Richard, L. Cambrésy, M. Deleuil, E. Pécontal, L. Tresse and I. Vauglin (eds)*

# SPACE-WEATHER ASSETS DEVELOPED BY THE FRENCH SPACE-PHYSICS COMMUNITY

A. P. Rouillard[1,2], R. F. Pinto[1,2], A. S. Brun[3], C. Briand[4], S. Bourdarie[5], T. Dudok De Wit[6], T. Amari[7], P.-L. Blelly[1,2], E. Buchlin[8], A. Chambodut[9], A. Claret[3], T. Corbard[10], V. Génot[1,2], C. Guennou[4], K. L. Klein[4], L. Koechlin[1,2], M. Lavarra[1,2], B. Lavraud[1,2], F. Leblanc[11], J. Lemorton[5], J. Lilensten[12], A. Lopez-Ariste[1,2], A. Marchaudon[1,2], S. Masson[4,13], E. Pariat[4], V. Reville[3], L. Turc[14], N. Vilmer[4] and F. P. Zucarello[4,15]

**Abstract.** We present a short review of space-weather tools and services developed and maintained by the French space-physics community. They include unique data from ground-based observatories, advanced numerical models, automated identification and tracking tools, a range of space instrumentation and interconnected virtual observatories. The aim of the article is to highlight some advances achieved in this field of research at the national level over the last decade and how certain assets could be combined to produce better space-weather tools exploitable by space-weather centres and customers worldwide. This review illustrates the wide range of expertise developed nationally but is not a systematic review of all assets developed in France.

Keywords: solar wind, energetic particles, space weather

## 1 Introduction

The near-Earth environment is continually perturbed by magnetised plasma, beams of energetic particles and ionising radiations (X-rays, extreme ultraviolet) produced by the solar atmosphere. Solar winds and powerful ejections propagate to Earth through the interplanetary medium and can drive strong geomagnetic activity. The fastest solar wind (>500 km/s) originates in coronal holes that are visible as dark regions in ultraviolet images of the corona, while the origin of the slowest winds (<500 km/s) is still debated. Intense solar storms,

[1] Centre National de la Recherche Scientifique, UMR 5277, Toulouse, France
[2] Institut de Recherche en Astrophysique et Planétologie, Université de Toulouse III (UPS), France
[3] AIM, CEA/CNRS/University of Paris 7, Service dAstrophysique, CEA-Saclay, 91191 Gif-sur-Yvette, France
[4] LESIA, Observatoire de Paris, PSL Research University, CNRS, Sorbonne Universités, UPMC Univ. Paris 06, Univ. Paris Diderot, Sorbonne Paris Cité
[5] ONERA (The French Aerospace Laboratory), Centre de Toulouse, 31055 Toulouse, France
[6] Laboratoire de Physique et Chimie de l'Environnement et de l'Espace (LPC2E), CNRS and University of Orlans, Orlans, France
[7] Centre de Physique Théorique, Ecole Polytechnique, CNRS, F-91128 Palaiseau Cedex, France
[8] Institut d'Astrophysique Spatiale, CNRS, Univ. Paris-Sud, Université Paris-Saclay, Bt. 121, 91405 Orsay, France
[9] Institut de Physique du Globe de Strasbourg UMR7516; Université de Strasbourg/EOST, CNRS ; 5 rue rené descartes 67084 Strasbourg Cédex, France
[10] Université Côte d'Azur, Observatoire de la Côte d'Azur, CNRS, Laboratoire Lagrange, Nice, France
[11] LATMOS/IPSL, UPMC Univ. Paris 06 Sorbonne Universités, UVSQ, CNRS, Paris, France
[12] IPAG, UGA - CNRS-INSU, UMR 5274, Grenoble, F-38041, France
[13] Station de Radioastronomie de Nançay, Observatoire de Paris, PSL Research University, CNRS, Universitd́'Orléans, 18330 Nançay, France
[14] Scientific Support Office, Directorate of Science, European Space Research and Technology Centre (ESA/ESTEC), Noordwijk, The Netherlands
[15] Centre for mathematical Plasma-Astrophysics, KU Leuven, Belgium

known as Coronal Mass Ejections (CMEs), are mostly the result of abrupt changes in magnetic fields situated near active regions on the solar surface. The strongest geomagnetic storms are induced by CMEs (Gosling et al. 1990) but the interaction between the slow and fast solar winds during their propagation to Earth, creates Corotating Interaction Regions (CIRs) that drive frequent weaker geomagnetic storms of which the cumulated effect represents a dominant transfer of energy between the interplanetary medium and the magnetosphere (Borovsky and Denton 2006). The continual battering of the magnetosphere by the solar winds modifies the properties of the radiation belts, and forces motions and reconfigurations of the geomagnetic field lines through magnetospheric convection and substorms (Akasofu 1964; Axford 1969). All these contribute to changing the properties of the ionosphere/thermosphere system and induce currents on the ground.

Our modern society depends heavily on a variety of technologies that are vulnerable to intense geomagnetic storms and solar energetic particle events with very different effects at different locations on the globe. For instance major elements of the power grid are exposed and particularly vulnerable to space weather at high latitudes but this is less true in France and southern Europe. In the last decades, our modern society (worldwide) has become critically dependent on Global Navigation Satellite System (GNSS) systems to direct and control our transport systems. Solar storms generate GHz radio emission and upon impact with the geospace, ionospheric density disturbances that interfere with high-frequency, very-high-frequency, and ultra-high-frequency radio communications and navigation signals from GNSS systems. Exposure of spacecraft to energetic particles during Solar Energetic Particles (SEP) events and radiation belt enhancements can cause temporary operational anomalies, degrade solar arrays, damage critical electronics and blind optical systems such as imagers and star trackers (Baker et al. 2008).

A report from the United States National Academy of Sciences estimated the economic and societal costs attributable to impacts of a major geomagnetic storm in the range of 1000-2000 billion of Euros for the United States alone during the first year following the severe geomagnetic storm with recovery times of 4 to 10 years (Baker et al. 2008). An executive order of the White House was put in place by the president of the United States on 13 October 2016 to coordinate efforts to prepare the United States for a space-weather events.

The following review aims at summarising the assets available in France that are useful for space-weather forecasting. This review summarises the twenty presentations and discussions held at the assembly of the French Astronomical Society in Lyon on 15 June 2016[1]. This article provides an overview of space-weather assets developed by the French space-physics community. It is limited to the effects of space weather in the geospace environment and does not review effects on other planets of the solar system.

## 2 Space-weather assets in France:

### 2.1 Ground-based observatories:

**Solar observatories:** The Pic Du Midi[2] (alt. 2877m), Calern[3] (alt.1270m) and Meudon[4] (alt.162m) observatories record images of the solar surface and corona in the H-alpha and CaII-K and CaII-H lines on an almost daily basis.

The CLIMSO instrumentation[5] at the Pic du Midi is a suite of two solar telescopes and two coronagraphs, taking one frame per minute in four channels, weather permitting of course: observations of the solar disk in H-alpha (656.28 nm) and in Ca II (393.3 nm), the coronagraphs take images of prominences in He I (1083 nm) and in H-alpha (656.28 nm), all year long (Figure 1). A new detector is being installed to observe the corona in the FeXIII line (1074.7nm), this will complemented with additional instrumentation to measure the coronal magnetic field. Such observations are routinely taken by the Coronal Multi-Channel Polarimeter (CoMP; Tomczyk et al. 2008) coronagraph in Hawaii, this type of instrumentation measures the coronal magnetic field through the Hanle effect. Images taken in FeXIII line can be exploited to infer some properties of the corona using reconstruction techniques (Rachemeler et al. 2014). CLIMSO (Long. 00° West) combined with the CoMP coronagraph in Hawaii (Long. 155° West) will provide more continuous observational coverage of the structure of the coronal magnetic field.

[1] http://2016.sf2a.eu/
[2] http://www.obs-mip.fr/pic-du-midi
[3] https://www.oca.eu/
[4] http://solaire.obspm.fr/
[5] https://climso.fr/

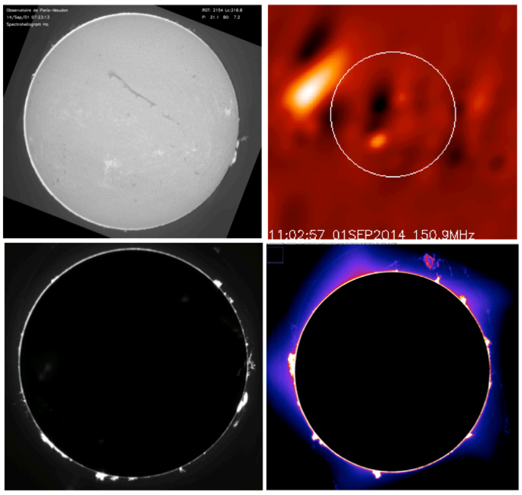


**Fig. 1.** Observations of the solar disk in H-alpha (656.28 nm) by the Meudon observatory and of the corona at radio wavelength by the NRH at 150.9MHz, HeI (1083nm) and and H-alpha (656,28nm) by the CLIMSO instruments at the Pic Du Midi. The two top images were taken during a major solar storm on 1 September 2014 that erupted behind the East limb of the Sun but caused intense SEP even at Earth (Plotnikov et al. 2016).

A suite of three telescopes to observe the chromosphere in H-alpha, CaII K and Ca II H, G-band is being installed at the Calern Observatory with funding from the Direction Générale de l'Armement as an extension in the optical lines of the French Air Force space-weather project (FEDOME) that currently exploits solar radio observations. These telescopes will record high-cadence H-alpha images of the Sun to be included in the international H-alpha network ([6]). Furthermore the use of the same H-alpha filter and image resolution will ease the merge of these images with those of the Global Oscillation Network Group (GONG). Currently the GONG H-alpha network ([7]) retrieves data at a cadence of one image per minute from only one European observatory in Tenerife. Calern H-alpha observations will provide real-time monitoring of quiescent and eruptive prominences at a cadence up to 10 images per minute allowing also the study of fast evolving phenomena such as the Moreton waves which are believed to be the chromospheric signature of the coronal pressure waves associated with flares/CMEs.

The Nançay radioastronomy station provides a unique set of radio data that can be used for space weather. The Radiohliographe (NRH) provides radio images of the full Sun for 10 frequencies between 100 and 400 MHz. The Nançay Decametric Array (NDA) and ORFEES spectrographs provide radio spectrum respectively between 30-80 MHz and 120-1000 MHz. The high frequencies provide crucial information on the early formation of CMEs low in the corona where plasma density is high and the perturbations of the corona induced by these CMEs such as shock formation (type II bursts) and particles beams from flares (type III bursts). These observations are used continuously by the French Air Force (FEDOME project). The NRH, ORFEES, and NDA are part of a radio survey project called the Radio Monitoring [8] as a joint effort of the Paris Observatory and other solar radio observatories around the world. These radio observations provide in real-time information on the earliest effects of flares, CMEs and particle propagation in the interplanetary medium.

**Magnetometers and geomagnetic indices:** Continuous monitoring of geomagnetic activity has been carried out in France for many decades. France hosts the headquarters of the International Service of Geomagnetic Indices[9] (ISGI) appointed by the International Association of Geomagnetism and Aeronomy (IAGA); ISGI is the reference service for validation, dissemination and stewardship of geomagnetic indices through its official

[6] `http://swrl.njit.edu/ghn_web/`
[7] `http://halpha.nso.edu/`
[8] `http://radio-monitoring.obspm.fr`
[9] `http://isgi.unistra.fr/`

Web portal. The *aa* and *am* indices are currently produced by the School and Observatory of Earth Sciences (EOST) in Strasbourg. New indices are currently being constructed by EOST to capture global geomagnetic activity on timescales of substorms (30 minutes), shorter timescales than the widely used geomagnetic range indices (3 hours).

**Ionospheric radars:** Monitoring of ionospheric perturbations during geomagnetic storms is carried out worldwide using the SUPERDARN radars. France maintains one radar in the Kerguelen island and is helping with the installation of a new radar in Lannemezan, south of France. SUPERDARN is currently not used for space-weather but could be exploited in the future to provide near-real time updates of the state of ionospheric convection to numerical models through data assimilation techniques. A workshop is held in Nice to discuss and gather community inputs on the organisation of the French ground-based solar observing facilities providing either real time data or long synoptic observing programs able to produce the needed statistic on various events relevant for space-weather ([10]).

**Neutron monitors:** Providing measurement of the most energetic particles produced during some solar storm. France is in charge of two neutrons monitors, located in Kerguelen and Terre Adélie, which are part of a worldwide neutron monitor network. French neutrons monitors are used on a regular basis for the SIEVERT program (collaboration Aviation Civile - Observatoire de Paris), evaluating the radiation dose for the civil flying personal.

### 2.2 *Space instrumentation designed for space weather:*

Among the most important hazards to humans and electronics in space is high-energy particle radiation. Damages to electronics are numerous in kind, so that particle radiation is a main source of operational anomalies on-board spacecraft. The monitoring of particle fluxes in various near-Earth orbits is thus critical to the understanding of these effects, and their potential forecasting. The ICARE_NG instrument, which was flown for instance on the Jason-2 and 3 spacecraft, measures for that purpose electrons and protons in the ranges 250 keV - 4 MeV and 8 - 100 MeV, respectively. Along a similar line of thought, but this time for monitoring the surface electrostatic charging of spacecraft which can lead to significant damages through ensuing discharges (e.g., to electronics, solar panels), one needs to measure the fluxes of low energy ions and electrons (0 - 40 keV range). In addition, the obtained data permit to measure the actual charging over time (providing key information during a potential anomaly). The AMBRE instrument currently flying on the Jason-3 spacecraft was developed for that purpose, and an even smaller version AMBRE 2.0 is currently under development.
Finally, coronagraph imagers for spacecraft have long been developed in France (e.g., LASCO C2 on SOHO). New developments are on-going in this area as well with space-weather applications. This concerns in particular developments in the UV wavelengths for monitoring the UV solar irradiance or the polarisation of the Lyman-alpha line, the latter being able to shed new light on the magnetic structure of the corona and thus of ensuing CMEs and geomagnetic storms. Such spacecraft instrumentation would be directly complementary to the Hanle observations of the corona soon to be made by CLIMSO in the forbidden lines of Fe XIII.

### 2.3 *Numerical models and tools:*

Figure 2 provides a flow chart summarising the origins and consequences of major space-weather effects and the numerical models developed by the national community that have either reached sufficient maturity or else showing great potential for space-weather forecasting. Some are being integrated within the European Space-Situational Awareness (SSA, [11]) program and the Virtual Space Weather Modelling Center[12]. These models simulate specific regions of the Sun-Earth system starting from the generation of magnetic fields inside the Sun, to their eruption on the surface, the formation of Coronal Mass Ejections and of the solar wind, the propagation of the solar wind in the interplanetary medium and the evolution of geomagnetic and ionospheric

[10] `https://meteospace.sciencesconf.org/`
[11] `http://swe.ssa.esa.int/`
[12] `https://esa-vswmc.eu/`

activity. Radio-wave propagation models are then used to evaluate or predict the impact on radio systems such as HF/VHF/UHF communications, radars or GNSS receivers. Although many regions of the Sun to Earth system are already modelled, they are not yet coupled together to produce a unique and integrated Sun to Earth numerical model. Many numerical models developed over the last decades have reached sufficient maturity to be useful for space-weather forecasting, their relevance to the different components of the Sun-Earth system are highlighted in Figure 2.

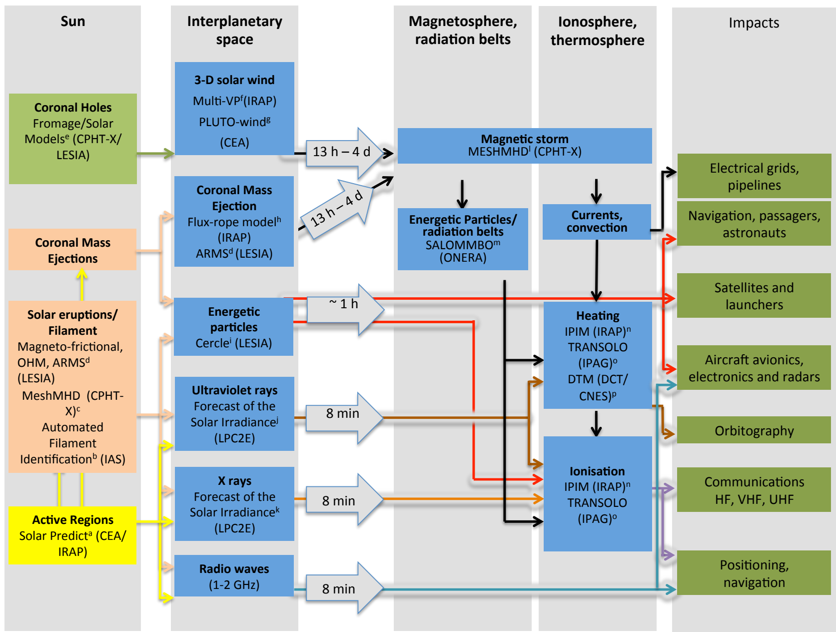


**Fig. 2.** A flow chart showing the causes and effects of space-weather events. The figure also lists the assets/numerical models developed in France that are capable of simulating a particular phenomena. The numerical techniques include: (a.) Jouve et al. (2011) Hung et al. (2015), (b.) Buchlin et al. (2012), (c.) Amari et al. (2014), (d.) Masson et al. (2009), Zucarello et al. (2015), Masson et al. (2013), (e.) Amari et al. (2014), (f.) Pinto et al. (2016), (g.) Reville et al. (2015), (h.) Rouillard et al. (2016), (i.) Lantos et al. (2005), (j. k.) Vieira et al. 2010, (l.) Amari et al. (2014), (m.) Bourdarie et al. (1996), (n.) Marchaudon and Blelly (2015), (o.) Lilensten et al. (1989), (p.) Bruisma et al. (2003). The links to the internet pages of the various facilities are given in the text.

To be useful for space-weather forecasting, a particular model must run sufficiently fast to provide a prediction of the future state of a particular region of the Sun-Earth system. The complexity of the system usually forces simplifications of the problem to be carried out by breaking down the problem into a sequence of manageable components. Each component may be dealt with completely different approaches instead of implementing a self-consistent integrated numerical approach. For instance, modelling the effect of solar activity on the interplanetary medium is usually separated into two components -; one - is the background solar wind —- the large-scale structure of which is regulated by the slowly varying topology of the coronal magnetic field and by solar rotation, and the second component, superposed to the first one, are the CMEs that are sudden, often dramatic, transitions in the structure of the corona with the release of complex magnetic structures in the interplanetary space. These CMEs will interact strongly with the background solar wind sometimes increasing their geoeffectiveness' (Lavraud and Rouillard, 2015). The slowly varying structure of the background solar wind co-rotates with the Sun allowing numerical models to forecast the properties of the near-Earth environment many days in advance. However CMEs are not only harder to forecast because of their complex structure but also because they can reach the Earth in the matter of hours only. This often forbids some more accurate but too long numerical computations. Of course, all these phenomena are modulated by the 11-yr solar cycle (e.g. Pinto et al. 2011) and by even longer modulation cycles such as the Gleissberg cycle.

**Recent numerical advances:** Between the low corona and 1AU, the characteristic scales over which transients evolve change by several orders of magnitude imposing formidable challenges to theorists wishing to model the corona-interplanetary medium in a single numerical domain. Several approaches are at hand to surmount these challenges including adaptive mesh refinement on structured and unstructured mesh. The latter is used by a number of models recently developed to model CMEs. Unstructured mesh is a tessellation of the numerical domain into simple geometrical shapes (triangular, tetrahedral), while computationally intensive, it permits more accurate finite-element analysis to be carried out in certain regions where plasma parameters have strong gradients. At the Sun, these regions are critical because they correspond to regions where strong non-potential fields can develop and lead to CMEs. A reconstruction of the coronal magnetic field driven by photospheric magnetic fields was recently successful at modelling the pre-eruptive phase of a CME and its free energy (Amari et al. 2014), this tool is potentially useful as a forecasting tool of CME eruptions. MHD codes using Adaptive mesh refinement such as ARMS are also very promising for the next generation of solar storm modelling. Event though it is computationally intensive, it allows to resolve the small-scale while keeping the large scale dynamics, i.e., study the CME initiation and follow it through the heliosphere. To become more tractable, the evolution of a CME is often split into different manageable sequences of physical processes. Grid modelling is another possible mean of using numerical simulation in space-weather application. Ahead of an eruptive event, grids of parametrised numerical runs, using simplified approximations are executed. When an observed event is triggered, the model which best fits a selection of observable is selected. This observationally-constrained model can then be used as a reliable element in the space weather modelisation pipeline. Recent numerical work exploiting a magneto-frictional approach and force-free field models driven by measured photospheric magnetic field have successfully capture the dynamics of observed emission and the loss of equilibrium of CMEs in the early phase of the eruption process (Savcheva et al. 16). Parametric simulations can also be used to constrain the eruptivity criterions of solar magnetic fields (Zuccarello et al. 2015). In order to predict the eruptivness of an active region and capture the loss of equilibrium of a filament, a promising and challenging solution is to perform data-driven and/or data- inspired simulation, capabilities possessed by the OHM (LESIA) code, i.e., which can use the observed magnetogram as initial condition (Masson et al. 09). When CMEs reach the heights imaged by coronagraphs, CME properties such as speed and flux rope orientations can be inferred, the propagation of CMEs from the upper corona to the typical heights where interplanetary models take over (20 Rs) may also be modelled using other semi-analytical models exploiting coronographic observations. In a similar manner to terrestrial-weather forecasting, we often resort to parametrisation, empirical laws and data assimilation techniques so that a particular numerical model becomes useful for space-weather forecasting.

**Parameterisation and analytical approaches:** The process of parameterisation is used to capture and account more instantaneously for the effect of CERTAIN processes by relating them to variables on scales that can be resolved by a particular model. Parameterisation is employed in all numerical models of the Sun-Earth system either when a physical model is still lacking, when the processes at play are too complex and forbid a physics-based approach or when processes occur on scales unresolved by the numerical grid but have macroscopic effects. For instance, instead of modelling the complex structure of a CME space-weather applications usually resort to the parameterisation of CME properties (dimensions, direction of propagation, speed and internal magneto-plasma properties) and use simple analytical representations of CMEs, such as the 'ice-cream cone' model widely used to inject hydrodynamic CME in global 3-D MHD simulations. This speeds up computation considerably. Novel and fast prototype models with great potential for faster forecasting of CME formation and eruption are being developed by a number of research groups in France, they include magneto-frictional models (Pariat et al. 2016) and simple flux-rope models[13]. Parameterisation is also used to fold in the heating of the solar corona that ultimately leads to the solar wind; this is done in the new 1-D hydrodynamic MULTI-VP model of the solar wind[14] (Pinto et al. 2016) and the 3-D MHD PLUTO stellar wind models (Reville et al. 2016). Parameterisation is also used to model geomagnetic activity, magnetospheric convection, solar irradiance and particle precipitation that will drive advanced models of the ionosphere such as the kinetic/kinetic-fluid codes IPIM (Marchaudon and Blelly 2015) and TRANSOLO (Lilensten et al. 1989), or to model source and loss rates of certain particle populations in the radiation belts in the SALAMMBO transport code (Bourdarie et al. 1996; Maget et al. 2015).

[13] `http://spaceweathertool.cdpp.eu`
[14] https://stormsweb.irap.omp.eu/

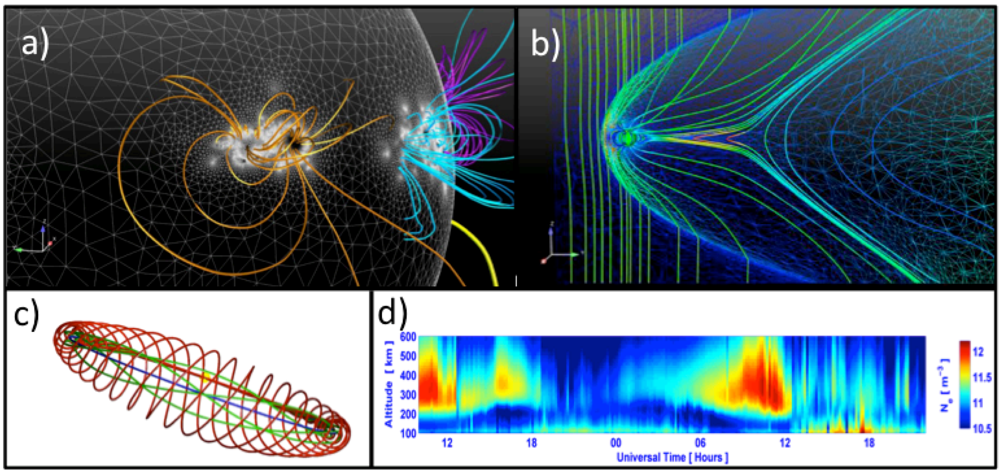


**Fig. 3.** (a) Magnetic reconstruction of the active regions based on a nonlinear force-free field model on an unstructured grid (Amari et al. 2015), (b) meridional cut of the global 3-D MHD simulation of a magnetosphere on a unstructured grid (source: courtesy of Tahar Amari), (c) a semi-analytical magnetic flux rope 3-D model (Rouillard et al. 2016), (d) simulated ionospheric densities using the IPIM 16-moment kinetic-fluid code (Marchaudon and Blelly 2016).

**Data assimilation:** The output of a numerical model will depend critically on the quality of the input data, the validity of the assumptions used in the model and the level of predictability of the system. The error involved in measuring the initial conditions, and an incomplete understanding of processes at play in space weather requires us to use advanced data assimilation techniques. Data assimilation is used to provide continually fresh input data and to test and correct a numerical model against the most up to date data. These data may be direct measurements of physical quantities such as magnetic fields measured in-situ or through remote-sensing observations (e.g. solar magnetograms). A number of models in France have made major progress in this field, these include the solar-cycle forecasting codes exploiting 4-D variational data assimilation techniques to constrain advanced solar dynamo models (Jouve et al. 2011; Hung et al. 2015), the SALAMMBO model that exploits proven methods to reconstruct aspects of the energetic electron environment through direct insertion, which runs a physics-based code that substitutes the in situ measurements as they become available and transports particles to regions of interest that may not have direct measurements (Maget et al. 2015). Of course the forecasting improvements brought by data assimilation techniques will depend on how well the measurements to be assimilated resolve the characteristic scales over which the system varies in space and time. There is considerable interest within the community in placing instrumentation (c.f. section before) on numerous platforms including nano-satellites to obtain more comprehensive measurements of the near-Earth environment that would be assimilated to numerical models. A workshop gathering space- and terrestrial-weather forecasters will be held in Toulouse to identify potential collaborations between the two communities on the subject of data assimilation[15].

**Ensemble forecasting:** In an effort to quantify the large amount of inherent uncertainty remaining in numerical predictions, ensemble forecasts have been used in terrestrial weather forecasting since the 1990s to help

[15]https://meteo-2016.sciencesconf.org/

gauge the confidence in the forecast, and to obtain useful results farther into the future than otherwise possible. This approach is at its infancy in space-weather forecasting but some first projects are in place to exploit multiple realisations of solar magnetograms from the US Air Force Air Force Data Assimilative Photospheric Flux Transport (ADAPT) (Arge et al. 2010) maps to run the Solar Models[16] and the MULTI-VP[17] solar wind model.

**Possible synergies between numerical models:** A number of synergies between the different numerical models developed nationally were identified during the workshop. For instance, forecasts of the electromagnetic radiation emitted by the Sun could be be used to drive advanced models of the global ionosphere-thermosphere system. Numerical models of the coronal magnetic field could be exploited by solar wind models extending from the Sun to 21.5 Rs, and beyond 21.5 Rs 3-D MHD models of the wind model could take over.

### *2.4 National Data Centers: assets for post-event analysis*

Reliable access to a wide range of datasets is of prime importance for post-event analysis and validation of numerical models. The French heliophysics community is heavily involved in the development of three complementary databases, which are: (1) which are BASS2000[18], for ground-based solar observations (including Pic du Midi, Meudon, and Calern), MEDOC[19] for space solar observations (including SoHO, STEREO, PICARD, and SDO), and the CDPP[20] (Plasma Physics Data Center) for in-situ plasma measurements and radio observations of natural plasma in the solar system. They ensure the archiving, redistribution and valorisation of these datasets relating to the heliosphere, the Sun, the interplanetary medium, and the planetary magnetospheres. These datasets are of prime importance for post-event analysis and validation of numerical models.

The data centres have a long-standing expertise at developing fast and reliable services to the different space-physics communities. In addition to the archiving and redistribution of data from observations or measurements, they also provide derived data products of added value, as well as tools to explore and use the data. For example, MEDOC distributes temperature and emission measure maps[21] derived from SDO/AIA data, and provides a HelioViewer server to be used from a web interface[22] or from the JHelioViewer client;this tool can be used to browse solar data associated to space weather events. For heliospheric plasma measurements, the CDPP provides the AMDA[23] (Automated Multi-Dataset Analysis) advanced data-mining tool, in which users can interactively handle online data (real-time and archived), combine various physical parameters, conduct conditional searches, and interface data with other community tools. The CDPP Propagation Tool helps calculate the trajectory of solar disturbances (such as coronal mass ejections) and energy particles, and highlights the link between solar and heliospheric events. For a given observation date at the Sun, users obtain the estimated times of the corresponding in situ observations, and they can be automatically directed either to MEDOC movies and observations, or to in situ measurements hosted on the AMDA. Such a tool is extremely valuable for space-weather studies.

## 3 Conclusion:

The interest in exploiting French national assets and learning about the effects of space weather is rapidly growing among major French national agencies, including Météo France, L'Armée de l'Air (FEDOME project), la Direction Générale de l'Aviation Civile (projet SIEVERT), EDF (centre de recherche et développement, EDF Energy). The CNRS via the National Institute for the Sciences of the Universe (INSU) and the CNES recognise a large number of our national space-weather assets however there is little funding available to go beyond pure science and to convert our assets into useful space-weather forecasting tools. In response to a request from governmental institutions in France, including the Ministry of Research, a report prepared by a team of scientists and engineers, called the GTME, lists the current space-weather assets in France, the impact of space weather

[16]http://solarmodels.cpht.polytechnique.fr/
[17]https://stormsweb.irap.omp.eu/
[18]http://bass2000.obspm.fr/
[19]https://idoc.ias.u-psud.fr/MEDOC
[20]http://cdpp.eu
[21]http://medoc-dem.ias.u-psud.fr/
[22]http://helioviewer.ias.u-psud.fr/
[23]http://amda.cdpp.eu/

at the latitudes of the French territories and the current deficiencies in the space-weather program in France.

The strong interest of the French science community for space weather covers major corner stones of space-weather activities:

- To further test and develop our numerical models: indeed space-weather forecasting is the ultimate test for many of our theories and numerical models: forecasting solar storms formation, propagation and interaction with the Earths environment in real time is a powerful way of validating many home-grown models.
- To study and promote the launch of space-weather observatories such as the Carrington project to monitor the Sun and the Sun-Earth line from a vantage point situated outside the Sun-Earth line and smaller observatories to monitor in real-time the state of the Sun-Earth system.
- To promote and expand our data processing and assimilation techniques via our unique set of interconnected data centers (MEDOC, CDPP, BASS2000),
- To further develop our space and ground-based instrumentation that represents a formidable contribution for space-weather predictions. The community would like to develop and integrate these assets in the rapidly growing network of international space-weather assets.

It was concluded at the workshop held in Lyon that the SSA programme is the right framework to promote these national space-weather assets. The community maintains collaborations at the European level through funded projects such as the H2020 FlareCast project aiming to improve solar eruptions. The space-weather segment of SSA currently includes Expert Service Centres in Solar and Heliospheric Weather, Space Radiation, Ionospheric Weather, and Geomagnetic Conditions. France's contribution to SSA would strengthen Europe's effort at constructing a space-weather prediction center. A conclusion of the workshop was that the community should coordinate its space-weather activities more efficiently. The idea was proposed that a new national entity, officially recognised by the National Institute for Sciences of the Universe (INSU) should be created that would promote synergies and help coordinate the various space-weather projects listed in this paper.

## References

Akasofu, S.-I. 1964, Planet. Space Sci., 12, 273
Amari, T., Canou, A., Aly, J.J. 2014, Nature, 514, 465
Arge, N.., Henney, C.J., et al. 2010, Twelfth International Solar Wind Conference, 1216, 343
Axford, I. 1969, Rev. Geophys. Space Phys., 7, 421
Baker, D.N. et al. 2008, Severe Space Weather Events, The National Academies Press.
Borovsky, J.., Denton, M.H. 2006, J. Geophys. Res., 111, A07S08, A07S08
Bourdarie, S. et al. 1996, J. Geophys. Res., 101, 27171
Bruinsma, S., Thuillier, G. and Barlier, F. 2003, JASTP, 65, 1053
Buchlin, E., Mercier, C., Vial, J.-C. 2012, AES Publ. Series, 55, 175
Hung, C. P., Jouve, L., Brun, A. S., Fournier, A., Talagrand, O., 2015, ApJ., 814, 151
Gosling, J.T., Bame, S.J., McComas, D.J. et al. 1990, Geophys. Res. Lett., 17, 901
Jouve, L., Brun, A.S., Talagrand, O. 2011, Astrophys. J., 735, 31
Lantos, P. et al. 2005, Sol. Phys., 229, 373
Lavraud, B. & Rouillard, A.P. 2014, Proc. of IAU Symposium, 300, 273
Lilensten, J. et al. 1989, Ann. Geophys., 7, 83
Maget, V. et al. 2015, J. Geophys. Res. (Space Phys.), 120, 5608
Marchaudon, A. & Blelly, P.L. 2015, J. Geophys. Res. (Space Phys.), 120, 5728
Masson, S., Pariat, E., Aulanier G., et al., 2009, ApJ, 700, 559
Masson, S., Antiochos, S.K., DeVore, C. R., 2013, ApJ, 771, 82
Pariat, E. et al. 2016, to be submitted to ApJ.
Pinto, R., Rouillard, A.P. et al. 2016, to be submitted

Réville, V., Folsom, C. P., Strugarek, A., Brun, A. S. 2016, ApJ, In Press
Rouillard, A.P. et al. 2016, to be submitted
Savcheva, A., Pariat E.,et al., 2016, ApJ, 817, 43 Plotnikov, I. et al. 2016, to be submitted to ApJ.
Vieira, L.E., de Wit, Dudok, et al. 2016, Proc. 38th COSPAR Scientific Assem., 38, 5
Zuccarello, F. P.; Aulanier, G.; Gilchrist, S. A., 2015, ApJ, 814, 126

# Session SF2A

# Cosmic rays and interstellar medium

*SF2A 2016*
*C. Reylé, J. Richard, L. Cambrésy, M. Deleuil, E. Pécontal, L. Tresse and I. Vauglin (eds)*

# CONSEQUENCES OF WARM $H_2$ ON THE CHEMISTRY OF DIFFUSE MOLECULAR CLOUDS: THE CASE OF $CH^+$

V. Valdivia[1], B. Godard[2], P. Hennebelle[1], M. Gerin[2] and P. Lesaffre[2]

**Abstract.** The large abundances of $CH^+$ observed in the local diffuse interstellar gas have been a longstanding problem. The main formation path is the ion-neutral reaction between $C^+$ and $H_2$, which is highly endothermic. This reaction requires either warm reactants or non-thermal processes to occur efficiently. Our main goal is to evaluate the relative roles of the presence of warm $H_2$, and the increased formation rate due to the ion-neutral drift in the production of $CH^+$. We performed a hybrid approach using magnetohydrodynamical simulations with the RAMSES code, where the formation of $H_2$ is included, along with a post-treatment of the chemistry. We explore the role of the cosmic ray ionisation rate on the chemistry. We find that the warm $H_2$ is a key ingredient in the formation of $CH^+$

Keywords: ISM: clouds, $CH^+$, $H_2$, Methods:numerical

## 1 Introduction

Molecular clouds display a wide range of physical conditions, where the two main phases known as warm neutral medium (WNM) and the cold neutral medium (CNM) coexist at pressure equilibrium (Field 1965). Turbulent motions within molecular clouds have a multifaceted role. They create density fluctuations, where the chemistry can proceed faster, they intermingle the two phases maintaining gas in the thermally unstable phase (Audit & Hennebelle 2005), and they transport long-lived molecules to environments where they are not expected to be produced. This is the case of molecular hydrogen ($H_2$) which can be produced in transitory cold and dense structures created by the turbulence, and then trasported to warmer regions where it is shielded by the structure of the molecular cloud (Valdivia et al. 2016c). Such warm $H_2$ can eventually participate in endothermic reactions.

An interesting related problem is the formation of $CH^+$, which requires molecular hydrogen to be formed efficiently. $CH^+$ has been observed in the interstellar medium (ISM) of our galaxy in visible wavelenghs (Crane et al. 1995; Gredel 1997; Weselak et al. 2008), and $^{13}CH^+$ has been detected deeper in the Galactic disc in infrared wavelengths (Falgarone et al. 2005, 2010; Godard et al. 2012). In the diffuse ISM, $CH^+$ is easily destroyed by reactions with electrons, hydrogen atoms and hydrogen molecules, and the only reaction able to efficiently produce $CH^+$ under such conditions is

$$C^+ + H_2 \rightarrow CH^+ + H \qquad (\Delta E/k = -4300\ \mathrm{K}), \tag{1.1}$$

which is a highly endothermic ion-neutral reaction (Agúndez et al. 2010). Two effects can increase the efficacity of this reaction. The first one is the presence of warm reactants, or in other words, the presence of warm $H_2$, and the second one is the drift between neutrals and ions (Myers et al. 2015).

## 2 Numerical methods

In order to evaluate the importance of these two effects under realistic conditions, we post-process a high-resolution magnetohydrodynamical (MHD) multiphase simulation of a molecular cloud, where the formation

[1] Laboratoire AIM, CEA/DSM-CNRS, Université Paris Diderot, IRFU/SAp, 91191 Gif-sur-Yvette, France
[2] LERMA (UMR CNRS 8112), Ecole Normale Supérieure, 75231 Paris Cedex, France

and destruction of $H_2$, as well as the thermal feedback, are included (Valdivia et al. 2016c). The dust and $H_2$ selfshieldings are estimated using our tree-based method (Valdivia & Hennebelle 2014). We post-process a snapshot (at 15 Myr) using a chemical solver that we developed (Valdivia et al. 2016b), which is able to prescribe the $H_2$ abundance, while computing the rest at equilibrium. The validity of our approach is justified in a companion work (Valdivia et al. 2016a).

## 3 Results

### 3.1 *Role of warm $H_2$*

To assess the importance of warm $H_2$ in the abundance of $CH^+$ we calculate the abundance of $CH^+$ in two ways. In the first case we calculate the chemical equilibrium by fixing the $H_2$ abundance to the value obtained in the simulation (out-of-equilibrium), while in the second case we do it for all the species, including $H_2$. The left panel of Fig. 1 shows that the out-of-equilibrium $H_2$ found at the edge of the clumps locally increases the abundance of $CH^+$ up to 2-3 orders of magnitude. The panel on the right shows that the integrated column densities are 3-10 times higher than those obtained when $H_2$ is considered to be at equilibrium.

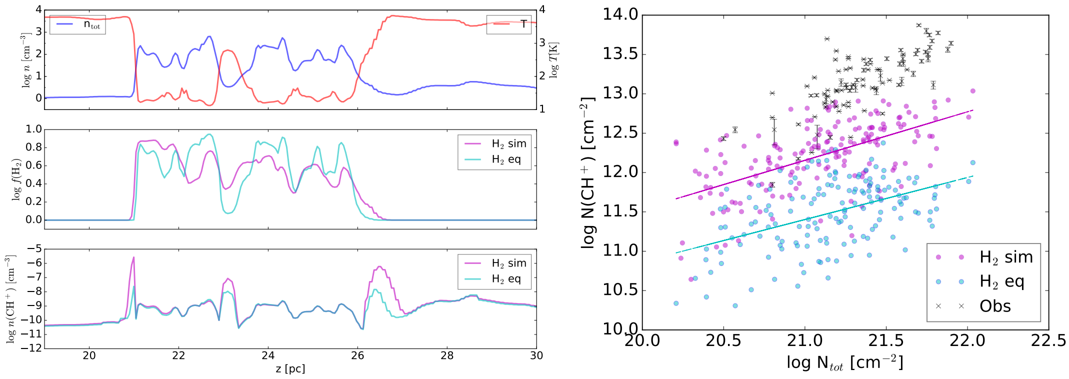


**Fig. 1. Left:** Line-of-sight showing the effect of warm $H_2$. From the top to the bottom panels show the density and temperature, the $H_2$ fraction obtained from the simulation and what is expected at equilibrium, and the associated CH+ number density. **Right:** Comparison of the column densities of $CH^+$ as a function of the total column density obtained for the case when $H_2$ is fixed from the simulation and for the case where it is calculated at equilibrium. The crosses are the observational data (Crane et al. 1995; Gredel 1997; Weselak et al. 2008).

### 3.2 *Role of the ion-neutral drift*

The drift between ions and neutrals can increase the reaction rate of highly endothermic ion-neutral reactions, acting as an increase of the effective temperature $T_{\rm eff}$ (Draine 1980; Draine et al. 1983; Flower et al. 1985):

$$T_{\rm eff} = T + \Delta T; \qquad \Delta T = \frac{\mu}{3k} v_{\rm d}^2, \tag{3.1}$$

where $T$ is the gas temperature, and the increase in temperature $\Delta T$ depends on the ion-neutral drift velocity $v_{\rm d}$. In this expression $\mu$ is the reduced mass for the reaction, and $k$ is the Boltzmann constant. The reaction rate of the ion-neutral drift is proportional to $\exp(-\max\{\beta/T_{\rm eff}, (\beta - 3\Delta T)/T\})$.

As our simulation is ideal, the ion-neutral drift velocity is estimated from the balance between the Lorentz force with the ion-neutral drag as

$$v_{\rm d} \approx \frac{(\nabla \times \vec{B}) \times \vec{B}}{4\pi \sum_{jk} n_j n_k \mu_{jk} K_{jk}} \tag{3.2}$$

where $\vec{B}$ is the magnetic field, $n_j$ and $n_k$ are the number densities of the neutral and ionic species, $\mu_{jk}$ is the reduced mass and $K_{jk}$ is the momentum transfer coefficient of species $j$ and $k$. We consider H, $H_2$ as the neutral species, and $H^+$, $He^+$, $C^+$, and $S^+$ as the ionic species. For the momentum transfer coefficients we use the values of Pinto & Galli (2008), and the Langevin rates whenever more accurate expressions were not available.

Figure 2 shows the distribution of ion-neutral drift velocities obtained for our simulation, which peaks around 0.04 km $s^{-1}$, with a tail that decays very fast for high velocities, producing a negligible effect on the effective temperature distribution, as shown in the central panel of the same figure. The effect on the abundance of $CH^+$ is also negligible, as shown in the right panel in Fig. 2.

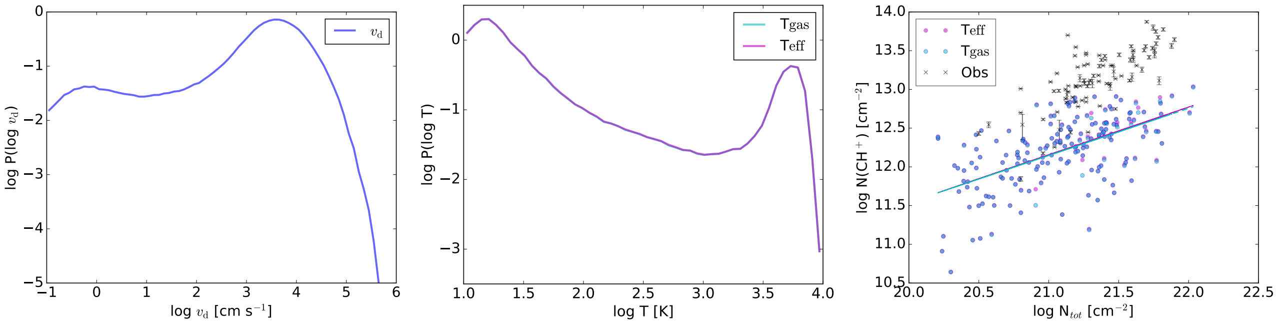

**Fig. 2. Left:** Normalised volume-weighted drift velocity distribution obtained for our simulation. **Centre:** Normalised mass-weighted distribution of the gas temperature and the effective temperature. **Right:** Comparison of the column densities of $CH^+$ as a function of the total column density for the cases where the ambipolar diffusion is not included and including this effect.

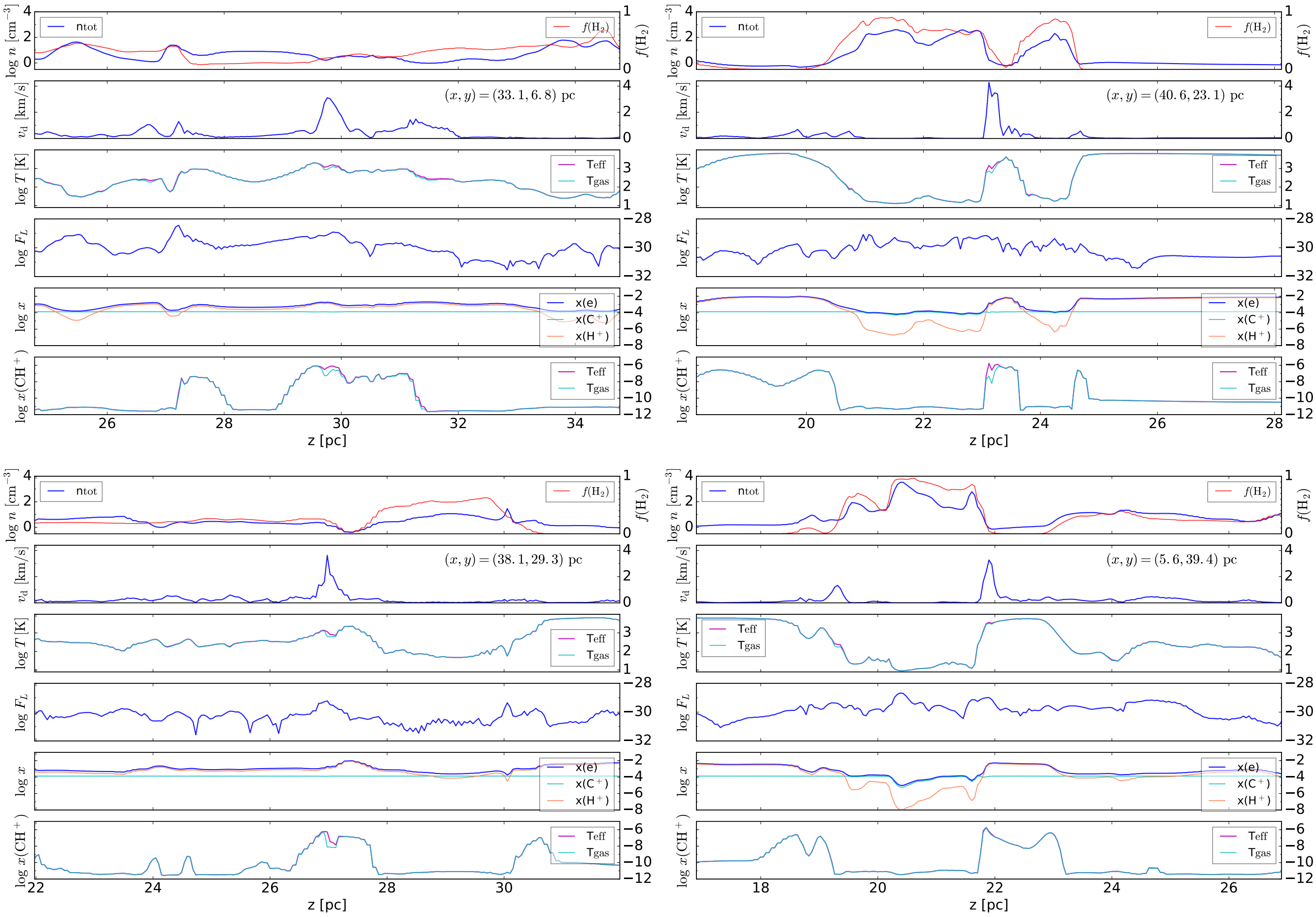

**Fig. 3.** Lines-of-sight with high ion-neutral drift velocities. Each panel shows (from the top to the bottom) the total number density and the $H_2$ fraction, the drift velocity, the gas temperature and the effective temperature, the Lorentz force, the electronic fraction, and the $CH^+$ abundance.

To better see the effect of the ion-neutral drift, we select four lines of sight that present drift velocities of at least 3 km $s^{-1}$, shown in Fig. 3. These lines-of-sight show that high drift velocities arise in low density and warm gas, as expected from Eq. 3.2. These regions of high $v_{\rm d}$ are very localised, and the ion abundance is close to $10^{-3} - 10^{-2}$ and dominated by $H^+$. Despite producing small differences in the effective temperature, the ion-neutral drift can locally increase the abundance of $CH^+$ up to one order of magnitude. Unfortunately, regions with high drift velocities are very uncommon and thus the effect is negligible.

### *3.3 Role of the cosmic ray ionisation rate*

Cosmic rays can alter the chemistry of the ISM by producing species such $H^+$, $He^+$, and $H_2^+$, that can participate in ion-neutral reactions, which proceed at rates much faster than reactions between neutrals. Even though our simulation uses a cosmic ray ionisation rate of $\zeta = 3 \times 10^{-16}$ $s^{-1}$, we explore the role of different values of $\zeta$ in our post-processing for the chemistry. The left panel of Fig. 4 shows the results for a line-of-sight for three different values of $\zeta = 3 \times 10^{-17}, 3 \times 10^{-16}$, and $3 \times 10^{-15}$ $s^{-1}$. This line-of-sight shows that even though the ion fraction increases for higher values of $\zeta$, the abundance of $CH^+$ is less sensitive. However, the variation in $CH^+$ is systematic, and smaller values of the cosmic ray ionisation rate can slightly increase the $CH^+$ abundances.

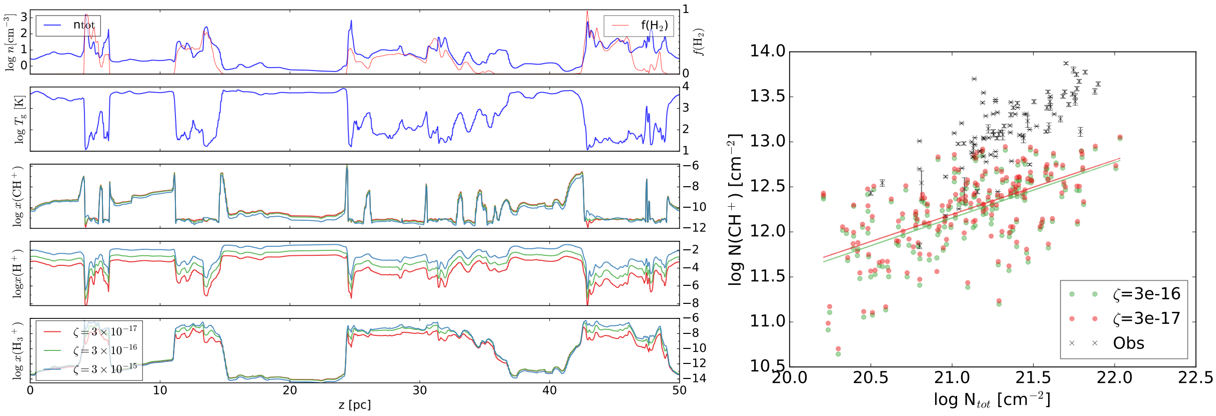


**Fig. 4. Left:** Line-of-sight showing the effect of the cosmic ray ionisation rate $\zeta$. **Right:** Comparison of the column densities of $CH^+$ as a function of the total column density for two values of $\zeta$. In both cases the values of $\zeta$ are given in $s^{-1}$

## 4 Conclusions

Out-of-equilibrium (warm) $H_2$ is crucial to form $CH^+$ efficiently in the diffuse ISM, nevertheless it is not enough to explain the observed abundances. High ion-neutral drift velocities can boost the $CH^+$ formation, but as these events are extremely rare, at least at the resolution of our simulation, the global effect of our distribution of $v_{\rm d}$ is statistically negligible. Nevertheless, as our simulation lacks of a description of small scale processes, such as the intermitent dissipation of energy or ambipolar diffusion, future works must address this issue. The cosmic ray ionisation rate has a moderate impact on the abundance of $CH^+$, but it can play a central role on the abundances of other species.

We are grateful to Alexandre Faure, who kindly provided us with the Langevin rates, and to Edith Falgarone and Eva Ntormousi for valuable discussions. We acknowledge the finantial support of the Agence National pour la Recherche through the COSMIS project. This research has received funding from the European Research Council under the European Community Seventh Framework Programme (FP7/2007-2013 Grant Agreement No. 306483). We thank the French Programme Physique Chimie du Milieu Interstellaire (PCMI). This work was granted access to HPC resources of CINES under the allocation x2014047023 made by GENCI (Grand Equipement National de Calcul Intensif). This work was granted access to the HPC resources of MesoPSL financed by the Region Ile de France and the project Equip@Meso (reference ANR-10-EQPX-29-01) of the programme Investissements d'Avenir supervised by the Agence Nationale pour la Recherche.

## References

Agúndez, M., Goicoechea, J. R., Cernicharo, J., Faure, A., & Roueff, E. 2010, ApJ, 713, 662
Audit, E. & Hennebelle, P. 2005, A&A, 433, 1
Crane, P., Lambert, D. L., & Sheffer, Y. 1995, ApJS, 99, 107
Draine, B. T. 1980, ApJ, 241, 1021
Draine, B. T., Roberge, W. G., & Dalgarno, A. 1983, ApJ, 264, 485
Falgarone, E., Godard, B., Cernicharo, J., et al. 2010, A&A, 521, L15
Falgarone, E., Phillips, T. G., & Pearson, J. C. 2005, ApJ, 634, L149
Field, G. B. 1965, ApJ, 142, 531
Flower, D. R., Pineau des Forêts, G., & Hartquist, T. W. 1985, MNRAS, 216, 775
Godard, B., Falgarone, E., Gerin, M., et al. 2012, A&A, 540, A87
Gredel, R. 1997, A&A, 320, 929
Myers, A. T., McKee, C. F., & Li, P. S. 2015, MNRAS, 453, 2747
Pinto, C. & Galli, D. 2008, A&A, 484, 17
Valdivia, V., Godard, B., Hennebelle, P., Gerin, M., & Lesaffre, P. 2016a, to appear in the Proceedings of the SF2A
Valdivia, V., Godard, B., Hennebelle, P., Gerin, M., & Lesaffre, P. 2016b, manuscript submitted for publication
Valdivia, V. & Hennebelle, P. 2014, A&A, 571, A46
Valdivia, V., Hennebelle, P., Gérin, M., & Lesaffre, P. 2016c, A&A, 587, A76
Weselak, T., Galazutdinov, G., Musaev, F., & Krełowski, J. 2008, A&A, 479, 149

*SF2A 2016*
*C. Reylé, J. Richard, L. Cambrésy, M. Deleuil, E. Pécontal, L. Tresse and I. Vauglin (eds)*

# H.E.S.S. AND CTA, PRESENT AND PERSPECTIVES IN GROUND-BASED GAMMA-RAY ASTRONOMY

H. Sol[1]

**Abstract.** Very high energy (VHE) gamma-ray astronomy emerged as a new branch of astronomy about ten years ago with the major discoveries achieved by the High Energy Stereocopic System (H.E.S.S.) operating in Namibia, quickly followed by the Major Atmospheric Gamma Imaging Cherenkov Telescopes (MAGIC) in the Canary Islands and the Very Energetic Radiation Imaging Telescope Array System (VERITAS) in the USA. These experiments succeeded to start exploring the cosmos at TeV energies, with the present detection of 178 sources in this range, mostly pulsar wind nebulae, supernova remnants, binary systems, blazars, and a variety of other types of sources. Based on these promizing results, the scientific community soon defined a next generation global project with significantly improved performance, the Cherenkov Telescope Array (CTA), in order to implement an open observatory at extreme energies, allowing a deep analysis of the sky in the highest part of the electromagnetic spectrum, from 20 GeV to 300 TeV. The CTA preparation phase is now completed. Production of the first telescopes should start in 2017 for deployment in 2018, in the perspective of an array fully operational at the horizon 2022.

Keywords: very high energy astrophysics, gamma-ray astronomy, cosmic accelerators, compact sources

## 1 Introduction

During the last decade, the IACT (Imaging Atmospheric Cherenkov Telescope) experiments H.E.S.S., MAGIC and VERITAS showed the richness of our cosmos when seen in the TeV range, with the detection of several tens of sources of various types, pulsars and pulsar wind nebulae (PWN), supernova remnants (SNR), binary stellar systems, star clusters, diffuse interstellar medium, galactic center, blazars, radio galaxies, starburst galaxies and a number of new VHE sources still unidentified. The sample of confirmed sources detected in the VHE range should soon reach 200 objects. Current experiments are continuously gathering new results. However their relatively poor sensitivity limits their possibilities of investigation. CTA, the next generation main instrument of ground-based gamma-ray astronomy will have improved performance, especially with an increase by a factor of ten of the sensitivity, a large spectral range, and a large field of view of about 8 degrees (Acharya et al. 2013). CTA array will consist of several tens of Cherenkov telescopes of different types and sizes, with 23m, 12m and 4m telescopes in order to cover a very large domain in energy from 20 GeV up to 300 TeV. Two arrays are going to be implemented, one in La Palma, Canary Islands, and one in Chile near Paranal to have access to the whole sky. Lifetime should be 30 years. At least a thousand of cosmic sources should be reachable with CTA. Production and deployment of the first telescopes on sites are foreseen for 2017-2018. Routine user operation open to general observer is expected to start in 2022.

## 2 A few recent H.E.S.S. discoveries in galactic science

With about 3000 hours of observation, the H.E.S.S. Galactic Plane Survey provided the first survey of the Milky Way at VHE energies with a resolution of about 0.1 degree and a sensitivity of 2% of the Crab nebula point source. It has recorded up to 77 VHE galactic sources, revealing a large variety of cosmic accelerators in our Galaxy (Lemoine et al. 2015). A diffuse large scale galactic gamma-ray emission has also been detected for the first time in regions off known VHE sources along the galactic plane (Abramowski et al. 2014). It can be

[1] LUTH, Observatoire de Paris, PSL Research University, CNRS, Place J. Janssen, 92 195, Meudon, France

interpreted as a mix of diffuse hadronic and Inverse-Compton VHE emission and contributions from unresolved sources, and clearly deserves further investigation.

An increasing sample of pulsar wind nebulae, the dominant class of TeV galactic sources, is now allowing the first statistical studies. A general picture is currently emerging, constraining further the theoretical models which still have difficulties to fully describe the current PWN populations and to study their link to young pulsars expected to power them and their interaction with the ambient interstellar medium.

Several new detections have also been achieved by H.E.S.S. in relation with supernova remnants. One example which perfectly illustrates the power of a multi-wavelength approach is the case of the complex region close to the SNR W41 in sky projection (Abramowski et al. 2015a). A new VHE source HESS J1832-093 has been discovered, located on the edge of the radio shell of a neighbouring remnant SNR G22.7-0.2 (see Fig. 1). The multi-lambda data suggest that this is the signature of escaping cosmic-rays illuminating a nearby molecular cloud. However there are some alternatives such as the presence of a PWN or of a VHE binary system. Deeper observations should allow to distinguish between the different scenarios.

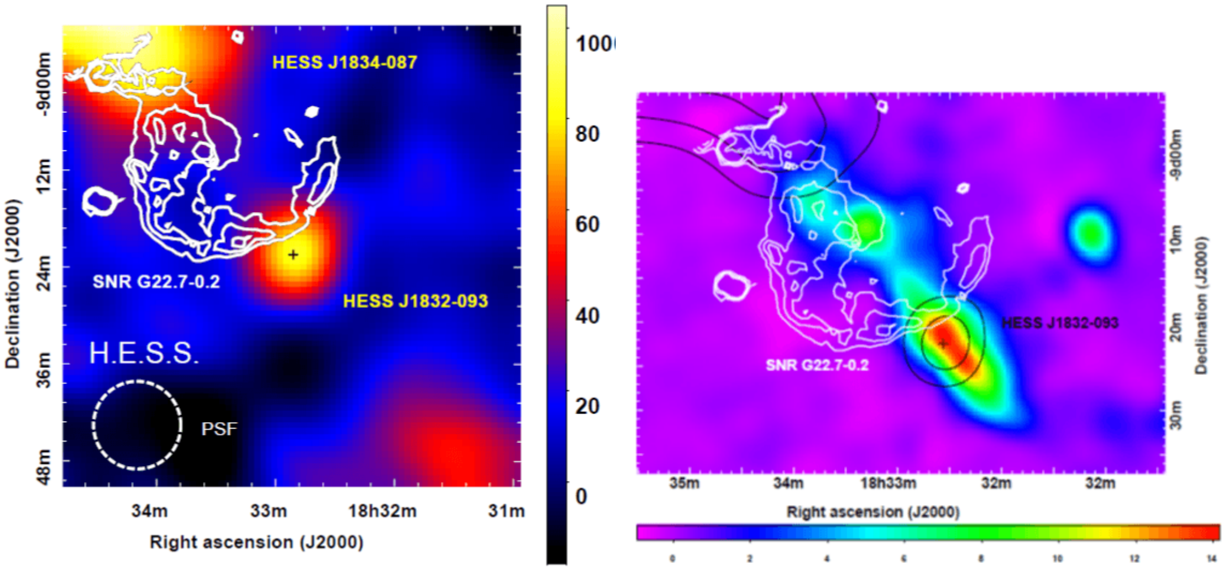


**Fig. 1. Left:** H.E.S.S. excess map of the region around the SNR G22.7-0.2 in coded colors. **Right:** Integrated $^{13}CO$ antenna temperature map in arbitrary units. Overlaid black contours show the gamma-ray excess. In the two maps white contours correspond to the 1.4 GHz radio map (Abramowski et al. 2015a)

The search with H.E.S.S. for PeVatrons, cosmic accelerators of particles at PeV energies ($10^{15}$ eV), appeared to be quite promizing in our Galaxy and in the Large Magellanic Cloud (LMC). The experiment found the first evidence of a cosmic hadronic PeVatron in the Galactic Center with the obtention of a power-law spectrum without any cutoff or break, up to tens of TeV, from the diffuse emission within the central 10 parsecs of the Milky Way around the VHE point source of the Galactic Center (Abramowski et al. 2016). Exceptionnally powerful VHE sources have also been detected in the LMC (Abramowski et al. 2015b). Among them, 30DorC is the first unambiguous detection of a superbubble in the TeV range. It exhibits extreme conditions and could be another type of PeVatron deserving further analysis (see Fig. 2).

## 3 The Cherenkov Telescope Array project

The CTA project was launched ten years ago, motivated by the success of the new IACT instruments at that time (see Fig. 3). Supported at the european level and by national agencies, the CTA consortium now brings together 32 countries, with almost 200 institutes and 1300 members. On June 14th, 2016, the CTA council selected the city of Bologna in Italy to host the CTA headquarters and DESY-Zeuthen near Berlin to host the Science Management Centre. Massive simulations (Bernlohr et al. 2013) have been done to optimize the layout and its performance in terms of sensitivity, spectral resolution and angular resolution (see Fig. 4). A special issue of Astroparticles Physics, volume 43, has been devoted to the CTA science case in 2013, with a large part

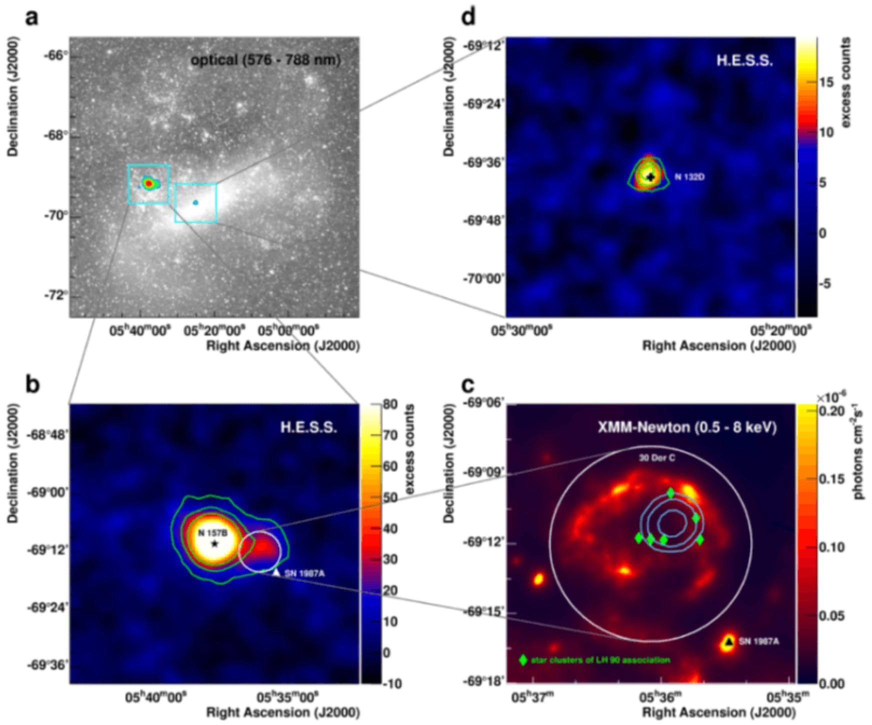


**Fig. 2.** Powerful TeV emitters detected in the Large Magellanic Cloud: N123D, an old TeV radio-loud SNR, possibly interacting with dense shocked interstellar cloud (upper right); N157B, a PWN associated to the most powerful known pulsar PSR J0537-6910 (lower left); 30DorC, the first unambiguous detection of superbubble in VHE (lower right). With its size of about 47 pc, 30DorC harbours extreme conditions and appears as a possible PeVatron (Abramowski et al. 2015b).

dedicated to galactic science.

Several prototypes of telescopes and cameras have been implemented in the world especially in France, Germany, Italy, Poland, Switzerland and UK and are under construction in Spain and USA. Their first Cherenkov light has been obtained by the 4m prototype built and installed at the Observatoire de Paris in Meudon at the end of 2015 (Sol et al. 2016). The prototyping and assessment phase is coming to an end and the pre-production of first telescopes and cameras to be installed on the two CTA sites is starting. First partial operations of the arrays and commissioning data can be expected in about two years. A number of key science projects (KSP) which have been worked out by the CTA consortium for the guaranteed time will soon be published. The first call for general observer proposals will be launched when the arrays are near completion. The CTA Observatory will provide support and services to the user (softwares, instrument response functions, data management and pipelines, dissemination, data archive, observer access).

## 4 Conclusion and perspectives

Full operations of CTA are planned for 2022 and should last at least until 2050. CTA high sensitivity will ensure access to VHE sources in all parts of our Galaxy, while present instruments are basically limited to nearby sources, or extremely bright ones. Further improvement in angular and spectral resolution will provide detailed maps and high-quality spectra. Several observational modes will be operational (targetted sources, surveys, observing with full array or with sub-arrays, alarms and targets of opportunity). Fast re-positionning of the telescopes and good temporal resolution, below the minute scale, will be very adapted to study transient phenomena and to get light curves over several time scales. In this regard, a global alarm network is being developped between the large research infrastructures of the coming decades in astrophysics and astroparticle physics.

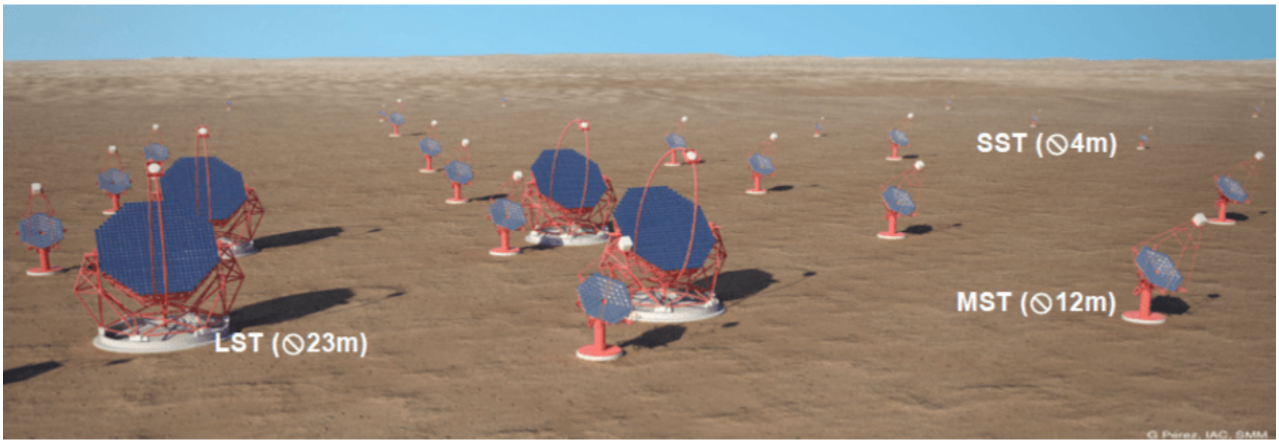


**Fig. 3.** Artist's view of the future southern Cherenkov Telescope Array with telescopes of three different sizes, covering a large spectral range from 20 GeV to 300 TeV.

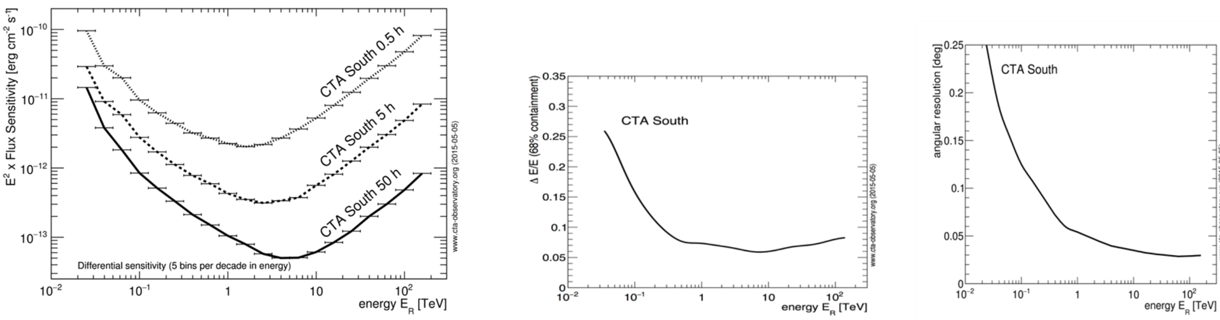


**Fig. 4. Left:** Differential sensitivity aimed for the nominal southern CTA array. **Middle:** Typical spectral resolution with the same array. **Right:** Typical angular resolution with the same array. (Extracted from *http : //portal.cta − observatory.org/CTA_Observatory/performance/SitePages/Home.aspx* ).

**Acknowledgements:** We gratefully acknowledge the H.E.S.S. collaboration and the CTA consortium, as well as support from the agencies and organisations listed under Funding Agencies at the websites https://www.mpi-hd.mpg.de/hfm/HESS/ and http://www.cta-observatory.org/.

## References

Abramowski, A., et al, 2014, Phys.Rev.D, 90, id.122007
Abramowski, A., et al, 2015a, MNRAS, 446, 1163
Abramowski, A., et al, 2015b, Science, 347, 406
Abramowski, A., et al, 2016, Nature, 531, 476
Acharya, B.S., et al, 2013, Astroparticle Physics, 43, 3
Bernlohr, K., et al, 2013, Astroparticle Physics, 43, 171
Lemoine-Goumard, M., 2015, Proceedings of Science, 34th ICRC (arXiv:1510.01373v1)
Sol, H., Dournaux, J.-L., Laporte, P., et al, 2016, these proceedings

# Session SF2A

# Exogenous inputs and origin of life

*SF2A 2016*
*C. Reylé, J. Richard, L. Cambrésy, M. Deleuil, E. Pécontal, L. Tresse and I. Vauglin (eds)*

# COMPLEX ORGANIC MOLECULES TOWARD LOW-MASS AND HIGH-MASS STAR FORMING REGIONS

C. Favre[1], C. Ceccarelli[1], B. Lefloch[1], E. Bergin[2], M. Carvajal[3], N. Brouillet[4], D. Despois[4], J. Jørgensen[5] and I. Kleiner[6]

**Abstract.** One of the most important questions in molecular astrophysics is how, when, and where complex organic molecules, COMs ($\geq$ 6 atoms) are formed. In the Interstellar-Earth connection context, could this have a bearing on the origin of life on Earth? Formation mechanisms of COMs, which include potentially prebiotic molecules, are still debated and may include grain-mantle and/or gas–phase chemistry. Understanding the mechanisms that lead to the interstellar molecular complexification, along with the involved physicochemical processes, is mandatory to answer the above questions. In that context, active researches are ongoing in theory, laboratory experiment, chemical modeling and observations. Thanks to recent progress in radioastronomy instrumentation for both single-dish and millimeter array (e.g. Herschel, NOEMA, ALMA), new results have been obtained. I will review some notable results on the detection of COMs, including prebiotic molecules, towards star forming regions.

Keywords: astrochemistry, ISM: molecules, Submillimeter: ISM

## 1 Introduction

Of the over 180 molecules that have been detected toward the interstellar and circumstellar media*, about 63 are complex species (i.e. that contain 5-6 or more atoms including carbon Herbst & van Dishoeck 2009). It is noticeable that both simple and complex molecules are present during each phase of the star and planet formation: from the molecular cloud to the planetary system including embedded protostar and circumstellar disk. However, one the major question of astrochemistry is how, when and where complex organic molecules, including the so-called prebiotic molecules, are formed? This leads one to ask *i)* which are the physicochemical processes that are involved in their production/destruction? and *ii)*, whether grain surface processes or gas phase reactions prevail in their formation. In order to get strong insight into the understanding of their production, it is necessary – from an astronomical point of view – to perform systematic surveys of both simple and complex molecules toward a large sample of low-mass and high-mass star forming regions. Nonetheless, to get a full overview, it is necessary to couple astronomical observations to chemical modeling, theory, spectroscopy and laboratory experiments on interstellar ice analogs. In this proceeding, a brief review on the observed interstellar complexity will be given in Section 2. Observational limitations and advances will be discussed together with notable results in Section 3. In Section 4, we will discuss the necessity of a direct interaction between the different scientific communities for the study of the astrochemistry.

[1] Univ. Grenoble Alpes, CNRS, IPAG, F-38000 Grenoble, France
[2] Department of Astronomy, University of Michigan, 311 West Hall, 1085 S. University Ave, Ann Arbor, MI 48109, USA
[3] Dpto. Fìsica Aplicada, Unidad Asociada CSIC, Facultad de Ciencias Experimentales, Universidad de Huelva, E-21071 Huelva, Spain
[4] Laboratoire d'astrophysique de Bordeaux, Univ. Bordeaux, CNRS, B18N, allée Geoffroy Saint-Hilaire, 33615 Pessac, France
[5] Centre for Star and Planet Formation, Niels Bohr Institute & Natural History Museum of Denmark, University of Copenhagen, Denmark
[6] LISA, Univ. de Paris-Est et Paris Diderot, Créteil, France
*http://www.astro.uni-koeln.de/cdms/molecules

## 2 The interstellar molecular complexity

Complex organic molecules (hereafter COMs), such as methyl formate ($HCOOCH_3$) and dimethyl ether $(CH_3)_2O$, are present toward both high-mass and low-mass star forming regions, including in prestellar cores (e.g. Turner 1989, 1991; Ziurys & McGonagle 1993; Nummelin et al. 2000; Remijan et al. 2002, 2003, 2004; Bottinelli et al. 2007; Schilke et al. 2001; Beuther et al. 2005; Jørgensen et al. 2005, 2011; Bisschop et al. 2008; Favre et al. 2011a,b, 2014; Bacmann et al. 2012; Pineda et al. 2012; Tercero et al. 2012, 2013; Peng et al. 2013; Brouillet et al. 2013, 2015; Vastel et al. 2014; López-Sepulcre et al. 2015; Taquet et al. 2015, etc). Of the over 63 complex species detected in the interstellar and circumstellar media (Herbst & van Dishoeck 2009), the so-called prebiotic molecules are of particular interest, especially in the context of an exogenous delivery of organic matter that might have made possible the appearance of life on Earth. Such molecules, can either be *i)* biological molecules, that are molecules used by life on Earth (such as the glycine, which is the simplest amino acid) and/or *ii)* precursors molecules that, in the network of reactions, can lead to truly biotic molecules such as sugars and amino acids, known to be found in meteorites originating from the very early Solar System (e.g. Caselli & Ceccarelli 2012; Pizzarello et al. 2006). In that context, Glycolaldehyde ($CH_2OHCHO$) is considered as a species of prebiotic interest since via a formose reaction involving formaldehyde ($H_2CO$) it will lead to 3-carbon sugars [$C_3H_6O_3$] such as glyceraldehyde. Then, a second reaction involving both glycolaldehyde and a 3C-sugar will give rise to ribose ($C_5H_{10}O_5$, 5C-sugar), the backbone of RNA. This molecule has been detected toward the hot core sources, such as Sgr B2(N) (e.g. Beltrán et al. 2009; Hollis et al. 2000, 2001) and, recently around a solar-type young star through the use of ALMA observations (Jørgensen et al. 2012, 2016). Regarding amino-acids, Belloche et al. (2008) have reported the detection of the amino acetonitrile ($NH_2CH_2CN$) toward the high mass-star forming region SGRB2(N). This molecule can lead to the formation of the biological molecule glycine. This latter has been detected in the Murchison meteorite (Pizzarello et al. 2006; Kvenvolden et al. 1970) and in the Wild 2 and Tchouri comets by Sandford et al. (2006) and Altwegg et al. (2016), respectively but not in the ISM. Incidentally, at the present time 4 complex species have been detected toward circumstellar disks: $HC_3N$, c-$C_3H_2$, $CH_3CN$ and $CH_3OH$ (Chapillon et al. 2012; Qi et al. 2013; Öberg et al. 2015; Walsh et al. 2016), implying that chemistry leading to complex organic molecules likely takes place in those objects.

These findings lead one to ask which degree of complexity can be reached in the ISM. In that context, the detection of a branched molecule iso-propyl cyanide (i-$C_3H_7CN$), which is not a straight-chain carbon molecule has been reported by Belloche et al. (2014). More recently, the propylene oxide ($CH_3CHCH_2O$), a chiral molecule (see Marloie et al. 2010, for chiral molecules that can likely be searched for in the ISM together with spectroscopic characterization), has been detected in the ISM by McGuire et al. (2016). As a consequence, observations of the chemical complexity and the diversity that offer star-forming regions make possible to access the physico-chemical conditions in which simple and complex molecules form and evolve.

## 3 Search for complex organic molecules and spectral confusion

In this section, we just focus on the spectral analysis on observational data of COMs and, in particular, on the problem of spectral confusion in line surveys and how to reduce it. For further details on the detection of complex molecules, we refer to the full review on complex molecules by Herbst & van Dishoeck (2009). COMs harbor a multitude of rotational lines in the (sub)millimeter windows, that leads to spectral confusion in the data: some transitions appear to be blended and/or partially blended with the emission from another molecule for example. In addition, this also results in a forest of weak lines in astronomical surveys. This latter point is illustrated in the Figure 4 of Tercero et al. (2010). To clearly assign a bunch of transitions to a given molecule (so to partially reduce the confusion) and accurately derive a reliable abundance, accurate spectroscopy is obviously needed as pointed out by Favre et al. (2014) and Vastel et al. (2015). Nonetheless, recent progress in radioastronomy instrumentation for both single-dish and millimeter array (e.g. Herschel, NOEMA, ALMA, IRAM-30m) help to lower the confusion level as described below.

### *3.1 High angular and spectral resolution*

High-resolution observations help to reduce spectral confusion. It is actually evident that the use of high spectral resolution help to separate the emission arising from different molecules in a spectrum. Regarding observations performed with high angular resolution, the use of the spatial information together with the synthesized beam (may) allow the observer to spatially isolate where the molecule is emitting from and thus, to spatially and spectrally lower the confusion level. Indeed, the spectrum resulting from single-dish observations gives the average signal integrated over a large beam area that may include the emission from different species. Alternatively, the spectrum that results from interferometric observations gives the average signal integrated over a smaller integrated area that may exclude the spatial contamination from another molecule.

### 3.2 Spectral Surveys

The use of actual published line surveys likely help to lower the spectral confusion level. For example, the sensitive broadband observations of the Orion-KL star-forming region acquired with the Heterodyne Instrument for the Far-Infrared (HIFI) instrument on the Herschel Space Observatory as part of the HEXOS key program (Bergin et al. 2010) is among the most completed molecular line surveys of this region. Indeed, the high spectral resolution (1.1 MHz) and the wide frequency range covered by these observations (480 GHz to 1907 GHz) have allowed us to identify ∼13,000 features and model a total of 39 molecules (79 isotopologues) toward Orion-KL (see Crockett et al. 2014) and, the HIFI spectral fit of these simple and complex molecules are available to the community. The observer can thus use these fit template model spectra to make reliable line identifications and to appreciate where potential line blends may exist.

### 3.3 High sensitivity

The search for COMs, including prebiotic molecules, is difficult because of their relatively low abundance and line intensity. Especially, in very rich molecular sources such as Orion-KL, high spectral confusion makes it difficult to detect the weakest lines. Regarding the detection of these weak lines, high sensitivity is key. Indeed, the high sensitivity that is available in the radioastronomy instruments (IRAM-30m, ALMA) has allowed new salient detection, such that as follows:

- **PO and PN**. Phosphorus is one of the main biogenic elements (it is part of the adenosine triphosphate, ATP) and one of the major question is to know whether PO is the main gas phase reservoir of phosphorus in molecular clouds (Thorne et al. 1984). Until recently, P-bearing molecules have been detected in some objects of the Solar System (e.g. Altwegg et al. 2016), in evolved stars: HCP, $PH_3$, CP, CCP, PO, PN (e.g. Agúndez et al. 2007) and, towards high-mass star forming regions: PN (Ziurys 1987; Fontani et al. 2016) and PO (Rivilla et al. 2016). Recently, as part of the Large Program dedicated to Astrochemical Surveys At IRAM (ASAI; Lefloch & Bachiller, in preparation) and thanks to the high sensitivity of the IRAM 30-m telescope, Lefloch et al. (2016) have reported the first detection of PO and PN in the direction of L1157, a solar-type star forming region.
- **Glycolaldehyde and its isotopologues**. The high sensitivity and angular resolution that offers ALMA, allowed us to observe and measure the emission from species with low abundances with respect to methanol for example. In that context, using ALMA observations as part as the the ALMA Protostellar Interferometric Line Survey (PILS), Jørgensen et al. (2012) and Jørgensen et al. (2016) have reported the first discovery of this precusor of sugar, together with its $^{13}$C- and deuterated flavors, towards IRAS 16293-2422, a solar-type protostar.

## 4 Astrochemistry: astronomical observations, chemical modeling, theory, spectroscopy and laboratory experiments

The direct interaction between the different scientific communities is key for the study of the astrochemistry. Indeed, to get a complete overview and understand the physicochemical processes that are involved in the production and/or destruction of interstellar molecules, it is necessary to couple observations to chemical modeling and laboratory experiments on interstellar ice analogs.

### 4.1 The gas phase vs grain surface chemistry controversy

Formation mechanisms of complex molecules are the subject of active debate. Indeed, they could be formed on ice grain mantles via radical-radical surface reactions (e.g. the Langmuir-Hinshelwood mechanism, see Hasegawa et al. 1992; Garrod & Herbst 2006) and/or in the gas-phase. In that context, formation of methyl formate ($HCOOCH_3$) and dimethyl ether ($CH_3OCH_3$) is still subject to controverse. Indeed, both of these species are detected in the ISM: in cold ($\leq$20K) and warm (∼100K) sources. A notable result is that their abundances are about the same over a large range of abundances and sources. This correlation between methyl formate and dimethyl ether in ISM objects is pointed by Jaber et al. (2014). This findings suggests that either these molecules present a common precursor or that they have a mother–daugther relation. Nonetheless, chemical models are unable to reproduce the observed abundances (Taquet et al. 2012). Indeed, different routes can lead to their formation: *i)* they could be formed on ice grain mantles through the following successive processes: hydrogenation of CO, CR-induced photo-dissociation and finally warm-up (Garrod & Herbst 2006; Garrod et al. 2008; Öberg et al. 2009; Kalvāns 2015) and/or *ii)* they can be produced through gas-phase reactions involving the radical methoxy $CH_3O$ (see Balucani et al. 2015). At the present time, the following question is still unresolved : are dimethyl ether and methyl formate synthesized through gas phase chemistry and/or at the icy surface of grain mantle? To reply the above question it is necessary to couple observations with chemical models and Laboratory experiments in order to investigate *i)* which pathway may dominate in their production and that, according to the physical conditions of the environment in which they are observed and *ii)* to measure the rate coefficient of the different routes to reproduce, via the use of chemical model, the observed abundances.

### 4.2 Systematic surveys

From an astronomical point of view, understanding the mechanisms that lead to the interstellar molecular complexification implies to perform systematic surveys of simple and complex species toward a large sample of sources. This is crucial to *i)* investigate the different possible formation/destruction pathways and, *ii)* to understand the influence of the environmental conditions.

In that light, there is the ongoing NOEMA Large Program Seeds Of Life In Space (SOLIS[†], C. Ceccarelli & P. Caselli, in preparation). This large NOEMA program aims to understand how, when and where complex organic molecules form during the early stages of solar-type stars formation. To answer the above questions, this program intends to perform systematic surveys with NOEMA of a bunch of COMs (and many other molecules) toward a sample of low–mass and intermediate–mass objects. It is important to note that the SOLIS project involves an international team composed of specialists in astrophysical observations, modeling, laboratory experiments and theoretical chemistry calculations.

## 5 Conclusions

Complex molecules, including those of prebiotic interest, are present toward high and low mass star-forming regions. From an astronomical point of view, molecular line surveys are key to get an overview and to access considerable insight into the physicochemical processes that are involved in their production/destruction. In that light, ALMA and NOEMA are 2 key interferometers for astronomical studies because they both provide high sensitivity together with high angular resolution. Nonetheless, it is important to note that understanding the mechanisms that lead to the interstellar molecular complexification requires to couple astronomical observations to chemical modeling, theory, spectroscopy and laboratory experiments on interstellar ice analogs.

## References

Agúndez, M., Cernicharo, J., & Guélin, M. 2007, ApJ, 662, L91

Altwegg, K., Balsiger, H., Bar-Nun, A., et al. 2016, Science Advances, 2

Bacmann, A., Taquet, V., Faure, A., Kahane, C., & Ceccarelli, C. 2012, A&A, 541, L12

Balucani, N., Ceccarelli, C., & Taquet, V. 2015, MNRAS, 449, L16

Belloche, A., Comito, C., Hieret, C., et al. 2008, ArXiv e-prints

Belloche, A., Garrod, R. T., Müller, H. S. P., & Menten, K. M. 2014, Science, 345, 1584

Beltrán, M. T., Codella, C., Viti, S., Neri, R., & Cesaroni, R. 2009, ApJ, 690, L93

Bergin, E. A., Phillips, T. G., Comito, C., et al. 2010, A&A, 521, L20

Beuther, H., Zhang, Q., Greenhill, L. J., et al. 2005, ApJ, 632, 355

Bisschop, S. E., Jørgensen, J. K., Bourke, T. L., Bottinelli, S., & van Dishoeck, E. F. 2008, A&A, 488, 959

Bottinelli, S., Ceccarelli, C., Williams, J. P., & Lefloch, B. 2007, A&A, 463, 601

[†]SOLIS Large Program website: http://solis.osug.fr/

Brouillet, N., Despois, D., Baudry, A., et al. 2013, A&A, 550, A46
Brouillet, N., Despois, D., Lu, X.-H., et al. 2015, A&A, 576, A129
Caselli, P. & Ceccarelli, C. 2012, A&A Rev., 20, 56
Chapillon, E., Dutrey, A., Guilloteau, S., et al. 2012, ApJ, 756, 58
Crockett, N. R., Bergin, E. A., Neill, J. L., et al. 2014, ApJ, 787, 112
Favre, C., Carvajal, M., Field, D., et al. 2014, ApJS, 215, 25
Favre, C., Despois, D., Brouillet, N., et al. 2011a, A&A, 532, A32
Favre, C., Wootten, H. A., Remijan, A. J., et al. 2011b, ApJ, 739, L12
Fontani, F., Rivilla, V. M., Caselli, P., Vasyunin, A., & Palau, A. 2016, ApJ, 822, L30
Garrod, R. T. & Herbst, E. 2006, A&A, 457, 927
Garrod, R. T., Weaver, S. L. W., & Herbst, E. 2008, ApJ, 682, 283
Hasegawa, T. I., Herbst, E., & Leung, C. M. 1992, ApJS, 82, 167
Herbst, E. & van Dishoeck, E. F. 2009, ARA&A, 47, 427
Hollis, J. M., Lovas, F. J., & Jewell, P. R. 2000, ApJ, 540, L107
Hollis, J. M., Vogel, S. N., Snyder, L. E., Jewell, P. R., & Lovas, F. J. 2001, ApJ, 554, L81
Jaber, A. A., Ceccarelli, C., Kahane, C., & Caux, E. 2014, ApJ, 791, 29
Jørgensen, J. K., Bourke, T. L., Myers, P. C., et al. 2005, ApJ, 632, 973
Jørgensen, J. K., Bourke, T. L., Nguyen Luong, Q., & Takakuwa, S. 2011, A&A, 534, A100
Jørgensen, J. K., Favre, C., Bisschop, S. E., et al. 2012, ApJ, 757, L4
Jørgensen, J. K., van der Wiel, M. H. D., Coutens, A., et al. 2016, ArXiv e-prints
Kalvāns, J. 2015, ApJ, 806, 196
Kvenvolden, K., Lawless, J., Pering, K., et al. 1970, Nature, 228, 923
Lefloch, B., Vastel, C., Viti, S., et al. 2016, MNRAS, 462, 3937
López-Sepulcre, A., Jaber, A. A., Mendoza, E., et al. 2015, MNRAS, 449, 2438
Marloie, G., Lattelais, M., Pauzat, F., Pilmé, J., & Ellinger, Y. 2010, Interdisciplinary Sciences: Computational Life Sciences, 2, 48
McGuire, B. A., Carroll, P. B., Loomis, R. A., et al. 2016, Science
Nummelin, A., Bergman, P., Hjalmarson, Å., et al. 2000, ApJS, 128, 213
Öberg, K. I., Garrod, R. T., van Dishoeck, E. F., & Linnartz, H. 2009, A&A, 504, 891
Öberg, K. I., Guzmán, V. V., Furuya, K., et al. 2015, Nature, 520, 198
Peng, T.-C., Despois, D., Brouillet, N., et al. 2013, A&A, 554, A78
Pineda, J. E., Maury, A. J., Fuller, G. A., et al. 2012, ArXiv e-prints
Pizzarello, S., Cooper, G. W., & Flynn, G. J. 2006, The Nature and Distribution of the Organic Material in Carbonaceous Chondrites and Interplanetary Dust Particles
Qi, C., Öberg, K. I., Wilner, D. J., & Rosenfeld, K. A. 2013, ApJ, 765, L14
Remijan, A., Shiao, Y., Friedel, D. N., Meier, D. S., & Snyder, L. E. 2004, ApJ, 617, 384
Remijan, A., Snyder, L. E., Friedel, D. N., Liu, S., & Shah, R. Y. 2003, ApJ, 590, 314
Remijan, A., Snyder, L. E., Liu, S., Mehringer, D., & Kuan, Y. 2002, ApJ, 576, 264
Rivilla, V. M., Fontani, F., Beltrán, M. T., et al. 2016, ApJ, 826, 161
Sandford, S. A., Aleon, J., Alexander, C. M. O., et al. 2006, Science, 314, 1720
Schilke, P., Benford, D. J., Hunter, T. R., Lis, D. C., & Phillips, T. G. 2001, ApJS, 132, 281
Taquet, V., Ceccarelli, C., & Kahane, C. 2012, ApJ, 748, L3
Taquet, V., López-Sepulcre, A., Ceccarelli, C., et al. 2015, ApJ, 804, 81
Tercero, B., Cernicharo, J., Pardo, J. R., & Goicoechea, J. R. 2010, A&A, 517, A96
Tercero, B., Kleiner, I., Cernicharo, J., et al. 2013, ArXiv e-prints
Tercero, B., Margulès, L., Carvajal, M., et al. 2012, A&A, 538, A119
Thorne, L. R., Anicich, V. G., Prasad, S. S., & Huntress, Jr., W. T. 1984, ApJ, 280, 139
Turner, B. E. 1989, ApJS, 70, 539
Turner, B. E. 1991, ApJS, 76, 617
Vastel, C., Ceccarelli, C., Lefloch, B., & Bachiller, R. 2014, ApJ, 795, L2
Vastel, C., Yamamoto, S., Lefloch, B., & Bachiller, R. 2015, A&A, 582, L3
Walsh, C., Loomis, R. A., Öberg, K. I., et al. 2016, ApJ, 823, L10
Ziurys, L. M. 1987, ApJ, 321, L81
Ziurys, L. M. & McGonagle, D. 1993, ApJS, 89, 155

# Session SF2A

# Services and databases in spectroscopy

*SF2A 2016*
*C. Reylé, J. Richard, L. Cambrésy, M. Deleuil, E. Pécontal, L. Tresse and I. Vauglin (eds)*

# DESIRABLE EVOLUTIONS OF STELLAR SPECTROSCOPIC SERVICES IN THE LIGHT OF CURRENT STUDIES OF REMOTE STELLAR POPULATIONS.

A. Lançon[1], P. Prugniel[2], M. Powalka[1] and I. Vauglin[2]

**Abstract.** Recent and future surveys have improved the precision and the accuracy of photometric and spectroscopic observations of remote galaxies. By examining the difficulties encountered in the modelling of these stellar populations, we identify a few key requests to future libraries of stellar spectra and to the related spectroscopic services. Beside providing data access, future services should increasingly focus on the associated on-line and off-line tools required to model and analyse galaxy spectra.

Keywords: stars, stellar populations

## 1 Introduction

Over the last decade, the tremendous progress of the quality of observational data has in some areas left model developments behind. The uncertainties in galaxy observations, for instance, have become small compared to the errors in population synthesis models. Although models can be fitted to high quality spectra of galaxies with residuals as low as two or three percent, these deviations are often significantly larger than the observational errors, implying systematic errors in the estimated astrophysical properties. It is by digging into these residuals that our understanding of the star formation and metal enrichment histories of stellar populations will progress. Some of the recurrent difficulties can be traced back to the adopted stellar spectral libraries, or to the algorithms used to associate a spectrum with any point along a stellar evolution track.

Stellar spectral libraries, a core ingredient of population synthesis tools, come in a variety of flavours. Some are theoretical, others empirical, and semi-empirical combinations are also common. The properties most important for the synthesis of stellar populations are a broad spectral coverage, an extensive coverage of the natural range of stellar physical parameters, and a good accuracy of the stellar energy distributions. A high spectral resolution is desirable for studies of nearby populations, that can be resolved into individual stars, but an intermediate resolution ($\lambda/\delta\lambda \sim 10000$) is satisfactory to study even the lowest mass unresolved galaxies.

The list of existing stellar spectral libraries is too long to be given here. The access to these public data is not anymore a bottleneck, and we are now facing other difficulties: (i) the description of these data is sometimes limited, (ii) the sampling of physical parameter space could be improved, and (iii) the tools, be they associated to the on-line archives or imbedded in public software packages for an off-line usage, lack the detailed descriptions that are needed to unveil the causes of the differences between stellar population model predictions.

In the following, we explicit a few of the practical difficulties met today when comparing the predictions of population synthesis codes with observations, and we identify paths along which work directly related to spectroscopic services could help achieve significant improvements. These future services shall not only focus on the data access, but also on all the on-line and off-line tools needed for the usage and interpretation of spectra.

## 2 Spectroscopy

Two recent empirical spectroscopic libraries successfully used in the analysis of optical spectra of stellar populations are Miles (Sánchez-Blázquez et al. 2006) and Elodie (Prugniel & Soubiran 2001). Both cover a wide

[1] Observatoire astronomique de Strasbourg, UMR 7550, Université de Strasbourg, CNRS, 67000 Strasbourg, France
[2] Univ Lyon, Univ Lyon1, Ens de Lyon, CNRS, Centre de Recherche Astrophysique de Lyon UMR5574, F-69230, Saint-Genis-Laval, France

range of stellar parameters, thus allowing studies of populations of all ages and metallicities. The libraries carry the chemical signatures of the Milky Way, in particular the anti-correlation between [Fe/H] and [$\alpha$/Fe], but methods have been devised to correct for this bias based on the differential effects of $\alpha$-enhancements in theoretical spectra (Prugniel & Koleva 2012; Vazdekis et al. 2015). The spectra are available through web sites that also provide estimated parameters, and articles describe their intrinsic properties (signal-to-noise ratio, line spread function). Last but not least, successful interpolators are available for these libraries (Prugniel & Soubiran 2001; Vazdekis et al. 2010; Sharma et al. 2016).

Interpolators, once trained on the available spectra, predict spectra for any position in the space of stellar parameters (effective temperature, gravity, metallicity, etc.). The polynomial form of the imbedded predictive model ensures numerical efficiency in the generation of population synthesis models, and is also a key to efficient fitting of new spectra (Koleva et al. 2009; Rix et al. 2016). With the Miles or Elodie libraries and the corresponding interpolators, fit residuals to star and stellar population spectra are regularly seen to stay below 2% (Prugniel et al. 2007). Internal errors on derived population parameters are small, and in particular much smaller than the systematic differences between the results obtained using different population synthesis codes (Koleva et al. 2008).

So where is improvement needed? An obvious path is the extension to non-optical wavelength. A few models have included empirical extensions to the ultraviolet or the near-infrared, but as yet for a restricted range of metallicities (e.g. Mouhcine & Lançon 2002; Maraston 2005; Lançon et al. 2007a; Vazdekis et al. 2016; Röck et al. 2016). The Xshooter Spectral Library XSL, with more than 600 spectra at $\lambda/\delta\lambda \sim 10000$ between 310 and 2400 nm, is designed to allow more variety (Chen et al. 2014). The ongoing studies of these spectra highlight that it is difficult to find theoretical spectra that will match the data satisfactorily at all wavelengths. The fundamental parameters of the stars usually determined from a restricted spectral range are not usually sufficient to obtain a good model fit everywhere else, and this suggests there may be biases in the parameter estimates as a consequence of inadequate assumptions for other ingredients of the models (e.g. turbulent velocities). Also, it is clear that despite steady advances much progress is still needed in lists of atomic and molecular data. The fits of observed spectra (of stars or galaxies) with purely theoretical spectra still have much larger residuals than fits with interpolated empirical spectra.

Two or three technical issues could be solved in the nearby future.

One is interpolation. The interpolators that work satisfactorily for empirical libraries do not seem to perform as well when applied to the regular grids of theoretical models. The analysis of new spectra with the latter tend to produce distributions in parameter space (such as the HR diagram) that show systematic local deviations from the loci expected from stellar theory. One of the reasons may be that parameter space is undersampled in certain parts, while unnecessary models exist for parameters that do not occur in natural stars. This aspect has been discussed recently by Ting et al. (2016), and more work is needed to identify an optimal sampling strategy for future calculations of synthetic spectra in the case of broad wavelength ranges, extended temperature and gravity ranges, and spectra that are not normalised to a continuum of one. The nature of the interpolation should also be optimised: what prior normalisation of complete UV-to-infrared spectra is adequate? can transformations of the flux variable (for instance the use of its logarithm) be useful in certain regimes? Finally, the synthetic spectra themselves must still be questioned. When large grids of such spectra are computed, local convergence problems may go unnoticed, leading to small amplitude artificial discontinuities in the variations of fluxes with certain physical parameters.

Another path of progress is the choice of abundance patterns in synthetic libraries, and the description thereof. The surface abundances of stars are known to vary with time, for instance via diffusion and convection (dredge-up). In contrast, the vast majority of grids of synthetic stellar spectra provide grids for the whole HR diagram at constant abundance ratios. Considering the importance of C, N, O in shaping the spectra of luminous red stars (e.g. Lançon et al. 2007b; Aringer et al. 2016), variants with evolutionary-driven abundance patterns should be computed more systematically. Light element abundances variations add to those of $\alpha$-elements, for which more information is fortunately available in the literature. Finally, we note that the role of helium may still be underestimated when computing synthetic spectra, although its importance in shaping stellar evolution tracks is clear. A brief study was presented by Girardi et al. (2007), using grids in which Y was varied at a given Z. The reference grid in this study had the same Y for all Z (i.e. $\Delta Y/\Delta Z = 0$). The recent grid of Husser et al. (2013) offers spectra for a broad range of [Fe/H] and [$\alpha$/Fe], but with constant [He/H] (i.e. $\Delta Y/\Delta Z < 0$). In contrast, stellar evolution models usually assume positive (and sometimes quite large) values of $\Delta Y/\Delta Z$. This makes it difficult to map points along evolutionary tracks to spectra in the theoretical grids. Fortunately, the awareness of the need for consistency with known evolutionary trends is

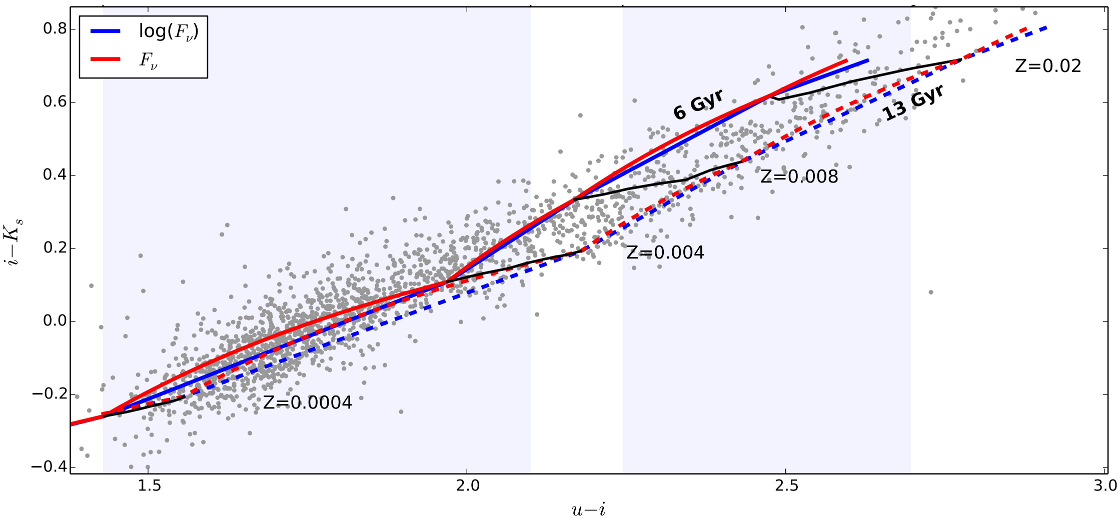


**Fig. 1.** Colors of globular clusters in the core of the Virgo cluster (grey dots, from Powalka et al. 2016), and population synthesis predictons at ages of 6 Gyr (solid) and 13 Gyr (dashed). The intrinsic metallicity sampling of the models is indicated. It is scarce at low Z. Red and blue lines are obtained, respectively, when interpolating fluxes or their logarithms. At low metallicity, choosing one or the other leads to large age differences.

rising (e.g. Coelho 2014). Future spectroscopic services could usefully include tools to standardise the chemical information provided by the authors, for instance to convert [Fe/H] and a reference for the solar composition into a full list of elemental abundances.

## 3 Photometry

Although photometric studies of stellar populations are plagued by stronger degeneracies than spectroscopic studies, they will remain necessary, being the only way to assess faint remote galaxies or to obtain an exhaustive coverage of a large area of the sky. To predict the colours of galaxies in the local universe, tables of stellar bolometric corrections are sufficient, but broad baseline spectral libraries remain necessary for the computation of $k-$corrections (i.e. photometry at non-zero redshift).

Colors of galaxies or star clusters are already available with a precision better than a percent, and an accuracy thought to be better than 2 %. Differences between the predictions of various families of population synthesis models are much larger. Powalka et al. (2016) demonstrated this in a comparison between various model sequences and $\sim$ 1700 globular clusters (GC) of the core of the Virgo galaxy cluster, showing that none our of 11 model families was able to match the locus of the GC in $u, g, r, i, z, K_s$. Analogous difficulties were found for younger star clusters, local galaxies or redshifted galaxies, e.g. by Wofford et al. (2016), Hansson et al. (2012), Taylor et al. (2011).

Not all the difficulties come from the stellar spectral libraries or the way these are implemented, but some definitely do. A very careful flux calibration of empirical libraries is necessary to match optical colours of stellar populations (Ricciardelli et al. 2012; Maraston & Strömbäck 2011). The XSL project is still working on extending this effort to the near-infrared. On the theoretical side, Coelho (2014) emphasise that stellar radiative transfer calculations designed for the prediction of high resolution spectra or of broad band fluxes are not always consistent: lists of lines with uncertain theoretical properties (strength and wavelength) are sometimes left out from high resolution calculations to avoid confusion, while they are included at low resolutions. Differences between the resulting broad band flux levels exceed 20 % at optical and near-UV wavelengths in some temperature regimes.

Direct ways of testing the photometric accuracy of synthetic stellar libraries are available. The colours of dwarfs can be tested against the stellar locus of deep multi-band surveys. For instance, Powalka et al. (2016) showed that the $u, g, r, i, z, K_s$ colours of Phoenix-based models (Husser et al. 2013) are in good agreement with those measured in the NGVS survey (Ferrarese et al. 2012), provided the variations of mean [Fe/H] and [$\alpha$/Fe] along the locus are properly taken into account (however this does not guarantee all spectral features are well-modelled in detail). HST and ground-based observations of numerous star clusters make it possible to extend such studies to giants.

Finally, Figure 1 illustrates how interpolation choices may affect photometric age estimates, in regimes where the sampling step in the stellar libraries are large. Progress on interpolation strategies combined a better sampling of stellar parameter space, will help photometric studies as much as spectroscopic ones.

## 4 Conclusions

Coming extensions of libraries of stellar spectra (wavelength range, number of spectra) will improve stellar population models, but we have identified a number of studies that will need to be conducted in parallel in order to achieve the accuracy required for the analysis of modern galaxy data. Interpolation tools will have to be developed even further, and photometric accuracy ensured. Emerging strategies for the sampling of parameter space in the calculation of new grids of theoretical spectra will need to be extended into the regime of multi-wavelength spectrophotometric data useful for population synthesis, taking into account the evolution of stellar surface chemistries. Spectroscopic services around the on-line data can play a decisive role by making tools and descriptions available that will facilitate the intercomparison between data sets and between library implementation methods.

This contribution is based in part on work supported by the French Programme National Cosmologie & Galaxies (2016) and by the French-Chilean ECOS-Sud/Conicyt project C15U02.

## References

Aringer, B., Girardi, L., Nowotny, W., Marigo, P., & Bressan, A. 2016, MNRAS, 457, 3611
Chen, Y.-P., Trager, S. C., Peletier, R. F., et al. 2014, The Messenger, 158, 30
Coelho, P. R. T. 2014, MNRAS, 440, 1027
Ferrarese, L., Côté, P., Cuillandre, J.-C., et al. 2012, ApJS, 200, 4
Girardi, L., Castelli, F., Bertelli, G., & Nasi, E. 2007, A&A, 468, 657
Hansson, K. S. A., Lisker, T., & Grebel, E. K. 2012, MNRAS, 427, 2376
Husser, T.-O., Wende-von Berg, S., Dreizler, S., et al. 2013, A&A, 553, A6
Koleva, M., Prugniel, P., Bouchard, A., & Wu, Y. 2009, A&A, 501, 1269
Koleva, M., Prugniel, P., Ocvirk, P., Le Borgne, D., & Soubiran, C. 2008, MNRAS, 385, 1998
Lançon, A., Gallagher, J. S., de Grijs, R., et al. 2007a, in IAU Symposium, Vol. 241, Stellar Populations as Building Blocks of Galaxies, ed. A. Vazdekis & R. Peletier, 152–155
Lançon, A., Hauschildt, P. H., Ladjal, D., & Mouhcine, M. 2007b, A&A, 468, 205
Maraston, C. 2005, MNRAS, 362, 799
Maraston, C. & Strömbäck, G. 2011, MNRAS, 418, 2785
Mouhcine, M. & Lançon, A. 2002, A&A, 393, 149
Powalka, M., Lançon, A., Puzia, T. H., et al. 2016, ApJ, in press
Prugniel, P. & Koleva, M. 2012, in IAU Symposium, Vol. 284, The Spectral Energy Distribution of Galaxies - SED 2011, ed. R. J. Tuffs & C. C. Popescu, 16–19
Prugniel, P., Koleva, M., Ocvirk, P., Le Borgne, D., & Soubiran, C. 2007, in IAU Symposium, Vol. 241, Stellar Populations as Building Blocks of Galaxies, ed. A. Vazdekis & R. Peletier, 68–72
Prugniel, P. & Soubiran, C. 2001, A&A, 369, 1048
Ricciardelli, E., Vazdekis, A., Cenarro, A. J., & Falcón-Barroso, J. 2012, MNRAS, 424, 172
Rix, H.-W., Ting, Y.-S., Conroy, C., & Hogg, D. W. 2016, ApJ, 826, L25
Röck, B., Vazdekis, A., Ricciardelli, E., et al. 2016, A&A, 589, A73
Sánchez-Blázquez, P., Peletier, R. F., Jiménez-Vicente, J., et al. 2006, MNRAS, 371, 703
Sharma, K., Prugniel, P., & Singh, H. P. 2016, A&A, 585, A64
Taylor, E. N., Hopkins, A. M., Baldry, I. K., et al. 2011, MNRAS, 418, 1587
Ting, Y.-S., Conroy, C., & Rix, H.-W. 2016, ApJ, 826, 83
Vazdekis, A., Coelho, P., Cassisi, S., et al. 2015, MNRAS, 449, 1177
Vazdekis, A., Koleva, M., Ricciardelli, E., Röck, B., & Falcón-Barroso, J. 2016, MNRAS, 463, 3409
Vazdekis, A., Sánchez-Blázquez, P., Falcón-Barroso, J., et al. 2010, MNRAS, 404, 1639
Wofford, A., Charlot, S., Bruzual, G., et al. 2016, MNRAS, 457, 4296

*SF2A 2016*
*C. Reylé, J. Richard, L. Cambrésy, M. Deleuil, E. Pécontal, L. Tresse and I. Vauglin (eds)*

# RE-GROUPING STARS BASED ON THE CHEMICAL TAGGING TECHNIQUE: A CASE STUDY OF M67 AND IC4651

S. Blanco-Cuaresma[1] and C. Soubiran[2]

**Abstract.** The chemical tagging technique proposed by Freeman & Bland-Hawthorn (2002) is based on the idea that stars formed from the same molecular cloud should share the same chemical signature. Thus, using only the chemical composition of stars we should be able to re-group the ones that once belonged to the same stellar aggregate. In Blanco-Cuaresma et al. (2015), we tested the technique on open cluster stars using iSpec (Blanco-Cuaresma et al. 2014a), we demonstrated their chemical homogeneity but we found that the 14 studied elements lead to chemical signatures too similar to reliably distinguish stars from different clusters. This represents a challenge to the technique and a new question was open: Could the inclusion of other elements help to better distinguish stars from different aggregates? With an updated and improved version of iSpec, we derived abundances for 28 elements using spectra from HARPS, UVES and NARVAL archives for the open clusters M67 and IC4651, and we found that the chemical signatures of both clusters are very similar.

Keywords: stars, chemical abundances, metallicity, chemical tagging

## 1 Introduction

The chemical composition of a star provides an invaluable source of information about its history, the stellar aggregate were it was born (in some cases, still gravitationally bounded), the molecular cloud from which it was formed and, finally, the characteristics of that region and time of the Galaxy. It is accepted that most of the stars are born in groups and, if we assume that the original giant molecular cloud was homogeneous and well-mixed, then we can expect that the stars born together share a common chemical fingerprint that may be different from other stellar aggregates (born in different places and times). The chemical tagging technique (Freeman & Bland-Hawthorn 2002) consists in identifying stars that were born together by only looking into their chemical abundances, thus, re-construct the history of our Galaxy.

In Blanco-Cuaresma et al. (2015), we designed and executed an experiment using open clusters (most of them with solar metallicities) to test the limits of the chemical tagging technique. We compiled a large dataset of high-resolution stellar spectra from stars in clusters, then we treat each of them as individual isolated stars, we homogeneously derived the chemical abundances for 14 elements and we tried to re-group the stars based only on their chemical information. We found that, given the level of precision that we obtained because of to the spectra quality and the limits of the methods, the differences between different open clusters for the selected elements were not significant enough to correctly disentangle their stars.

In this study, we concentrated our efforts in only two clusters (M67 and IC4651) and we explore the possibility of using more elements to overcome the problems we found in Blanco-Cuaresma et al. (2015). Additionally, we developed a new spectroscopic pipeline that takes advantage of the latest improvements implemented in iSpec* (Blanco-Cuaresma et al. 2014a).

## 2 Open clusters

M67 and IC4651 are open clusters with a chemical composition similar to the Sun. They are located in the galactic anti-center (M67: $l = 215.70°$, $b = 31.90°$; IC4651: $l = 340.09°$, $b = -7.91°$) with a distance from the Sun of 790 pc and 890 pc, respectively (Dias et al. 2002; Paunzen & Netopil 2006).

[1] Observatoire de Genève, Université de Genève, CH-1290 Versoix, Switzerland
[2] Laboratoire d'astrophysique de Bordeaux, Univ. Bordeaux, CNRS, 33615 Pessac, France
*http://www.blancocuaresma.com/s/

## 3 Data

Our initial dataset contained 103 spectra for M67 (52 from the UVES archive Dekker et al. 2000; 51 from the HARPS archive Mayor et al. 2003) and 41 for IC4651 (33 from UVES; 8 from HARPS; 1 from NARVAL Aurière 2003). We measured their radial velocities and compared them to the average velocities reported by HARPS: 33.77 km/s for M67 and -30.36 km/s for IC4651. The criteria to accept a star as member of the cluster was that its velocity should be within the $\pm 2$ km/s margin. Only 1 star belonging to IC4651 did not match the criteria and was discarded.

Then, we corrected the radial velocities, co-added spectra for common stars coming from the same instrument and setup, and we selected only those with a signal-to-noise (S/N) higher than 100. We could use spectra with a lower S/N but for this study we wanted to minimize problems originated by low S/N and not linked to real physical features of each star. Once the processing was completed, the dataset was reduced to 22 M67 spectra (all of them observed with UVES) and 16 IC4651 spectra (8 UVES, 7 HARPS and 1 NARVAL) which correspond to 21 M67 stars and 11 IC4651 stars.

## 4 Method

The spectroscopic analysis was done with an automatic pipeline based on iSpec. In a first step, the atmospheric parameters (i.e. effective temperature, surface gravity and metallicity) were determined for all the co-added spectra by using a selection of absorption lines in the visual range (i.e. 480 to 680 nm). We used SPECTRUM (Gray & Corbally 1994) as radiative transfer code, MARCS[†] (Gustafsson et al. 2008) as model atmosphere and Grevesse et al. (2007) as solar abundances. The lines were chosen based on a previous analysis of a solar spectrum (with a resolution of 47 000) obtained from the Gaia FGK Benchmark Stars library[‡] (Blanco-Cuaresma et al. 2014b) where, starting from an atomic line list extracted from VALD (Kupka et al. 2011), we derived abundances ([El/X]) for all the observed absorption lines and we discarded those with a [El/H] greater/smaller than +/-0.05 dex.

In our dataset we found 12 dwarfs, 3 turn-off stars and 8 giants for M67; while for IC4651 we had 3 dwarfs and 8 giants. The criteria to separate dwarfs from giants was based on its surface gravity, stars with gravities greater than 4 dex were considered dwarfs and smaller than 3 dex were classified as giants (in between these limits the star is considered in the turn-off).

Once the atmospheric parameters were fixed, individual chemical abundances were derived using an extensive collection of observed absorption lines which were cross-matched with a VALD atomic line list. For each line, the following abundances were determined:

1. Fixed atmospheric parameters (main iteration).
2. Artificially higher metallicity (+0.10 dex).
3. New realisation of the spectrum using a poisson distribution and the flux errors (S/N iteration).
4. New atomic line list where only the line of interest is present (i.e. no blends will be modeled).

We discarded all the lines where the difference with the main iteration is greater than 0.10 dex when using a greater metallicity, greater than 0.10 when checking the S/N or greater than 0.50 dex when synthesized without blends. The accepted lines were combined using the median, a robust statistic to minimize the impact of outliers. Errors were computed using the standard deviation, we avoided the use of more robust statistics (such as the median absolute deviation or MAD) to remain on the conservative side of the estimation.

To achieve the maximum precision, it is common to perform differential analysis. This means that all abundances are computed differentially line-by-line using a star of reference. Typically this is done using a solar spectrum, but this strategy brings up a problem: not all the stars in the dataset have similar atmospheric parameters to those of the Sun.

Giants and dwarfs are at different stages of their life and there are processes that may have affected their chemical abundances (such as atomic diffusion). Also, assumptions in our analysis (e.g. LTE) may not apply equally (e.g. NLTE effects), or simply continuum normalization is going to be different because the typical

[†] http://marcs.astro.uu.se/
[‡] http://www.blancocuaresma.com/s/

spectrum is different (e.g. absorption lines in dwarfs are broader). If we use the Sun as reference, we would derive different chemical signatures for dwarfs and giants, even if they belong to the same cluster. In front of this situation, in Blanco-Cuaresma et al. (2015) we had to treat giants and dwarfs separately. This is a valid solution but it has the inconvenient of decreasing the statistics.

In this study we tried a different approach, instead of using the Sun as reference for all the stars, we took the giant M67 No164 and the dwarf M67 No1194 as reference stars for the giants and dwarfs in our sample. We assumed that these two stars have the same chemical abundance and that their differences are originated mainly due to assumptions in our models and biases in our analysis, thereby we were able to mix the differential abundances coming from giants and dwarfs.

## 5 Results

In Blanco-Cuaresma et al. (2015) we were not able to disentangle stars from different clusters by using the chemical signature of 14 elements. The following question was raised: Could a different combination of elements help? In this study we have increased the number of elements to 28 for the open clusters M67 and IC4561 as shown in Fig. 1. Most of the elements have a dispersion smaller than 0.05 dex, demonstrating that the level of precision is high and that the strategy for mixing giants and dwarfs is working properly. Nevertheless, the chemical signatures remain extremely similar between the two clusters. The elements showing the larger differences, such as barium, praseodymium or sulfur, are those which have the largest dispersion, preventing a clear separation of both populations.

Checking directly the individual abundances per star (Fig. 2) shows the great level of overlapping. If we ignore the color coding, it is not feasible to identify what stars belong to what cluster. In this chemical space of 28 elements, M67 and IC4651 are not located in clearly different places.

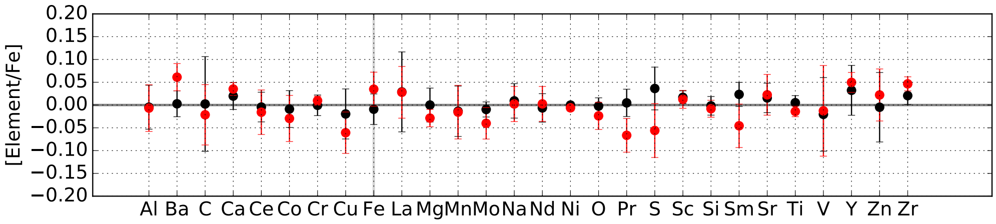


**Fig. 1.** Combined differential chemical abundances with M67 No164 and M67 No1194 as reference for giants and dwarfs, respectively. The chemical signature corresponds to the open clusters M67 (black) and IC4651 (red). All the abundances are respect to iron (i.e. [E/Fe]), except iron which is represented in respect to hydrogen (i.e. [Fe/H]). Error bars correspond to the standard deviation of the abundances.

## 6 Conclusions

We showed how a chemical signature composed of 28 different elements with a general precision better than 0.05 dex does not seem enough to chemically separate stars from the open clusters M67 and IC4651. Is this result still challenging the chemical tagging technique or these two cluster do have a common past?

Both clusters are located towards the galactic anti-center at a similar distance from the Sun, although they are separated by more than 100°. Additionally, some studies found that M67 is several Gyr[§] older than IC4651 (Paunzen & Netopil 2006). Could these clusters be born from the same molecular cloud but at different moments? This would required the cloud to be fragmented in two without triggering star formation and remaining chemically unaltered during a long time. Another possibility would be that it is common to have different molecular clouds with very similar compositions, which could mean that both were enriched in the same measure by different past events. The similarities between these two clusters should be further studied.

This work would not have been possible without the support of Laurent Eyer from the University of Geneva.

[§] 1 Gyr represents $10^9$ years.

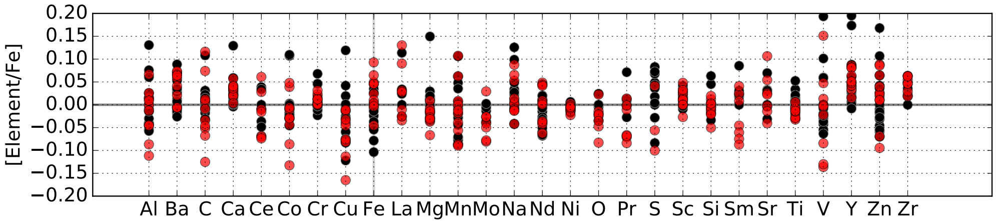


**Fig. 2.** Individual differential chemical abundances with M67 No164 and M67 No1194 as reference for giants and dwarfs, respectively. The abundances correspond to individual stars from the open clusters M67 (black) and IC4651 (transparent red). All the abundances are respect to iron (i.e. [E/Fe]), except iron which is represented in respect to hydrogen (i.e. [Fe/H]).

## References


Aurière, M. 2003, in EAS Publications Series, Vol. 9, EAS Publications Series, ed. J. Arnaud & N. Meunier, 105

Blanco-Cuaresma, S., Soubiran, C., Heiter, U., et al. 2015, A&A, 577, A47

Blanco-Cuaresma, S., Soubiran, C., Heiter, U., & Jofré, P. 2014a, A&A, 569, A111

Blanco-Cuaresma, S., Soubiran, C., Jofré, P., & Heiter, U. 2014b, A&A, 566, A98

Dekker, H., D'Odorico, S., Kaufer, A., Delabre, B., & Kotzlowski, H. 2000, in Society of Photo-Optical Instrumentation Engineers (SPIE) Conference Series, Vol. 4008, Society of Photo-Optical Instrumentation Engineers (SPIE) Conference Series, ed. M. Iye & A. F. Moorwood, 534–545

Dias, W. S., Alessi, B. S., Moitinho, A., & Lépine, J. R. D. 2002, A&A, 389, 871

Freeman, K. & Bland-Hawthorn, J. 2002, ARA&A, 40, 487

Gray, R. O. & Corbally, C. J. 1994, AJ, 107, 742

Grevesse, N., Asplund, M., & Sauval, A. J. 2007, Space Sci. Rev., 130, 105

Gustafsson, B., Edvardsson, B., Eriksson, K., et al. 2008, A&A, 486, 951

Kupka, F., Dubernet, M.-L., & VAMDC Collaboration. 2011, Baltic Astronomy, 20, 503

Mayor, M., Pepe, F., Queloz, D., et al. 2003, The Messenger, 114, 20

Paunzen, E. & Netopil, M. 2006, MNRAS, 371, 1641

# Session SF2A

# SKA-LOFAR

# THE NOIRE STUDY

B. Cecconi[1], A. Laurens[2], C. Briand[1], J. Girard[3], M. Bucher[4], D. Puy[5], B. Segret[6], M. Bentum[7] and the NOIRE team[8]

**Abstract.** NOIRE (Nanosats pour un Observatoire Interférométrique Radio dans l'Espace; Nanosats for a space borne interferometric radio observatory) is an ongoing feasibility study with CNES and in collaboration with Dutch colleagues. The goal is to assess the feasibility of a low frequency space radio interferometer using nanosatellites.

Keywords: Radioastronomy, Interferometry, Space, Nanosatellites

## 1 Introduction

During the last decades, space physics and radioastronomy have dramatically changed our knowledge of the Universe and his evolution. However our view is still incomplete at the lowest frequencies range (below 30 MHz), which remains the last unexplored spectral band. Below 30 MHz, ionospheric fluctuations strongly perturb ground based radioastronomy observations. They are impossible below 10 MHz due to the ionospheric cutoff. Furthermore, man made radio interferences make these observations even more difficult. Deploying a space borne radio observatory is the only way to open the last window on the Universe. This spectral window starts at a few kHz, which is the local solar wind radio cutoff frequency and ends between 10 and 30 MHz. The science objectives of this observatory are diverse and numerous: the dark ages of the Universe, the mapping of the Galaxy, pulsars and astrophysical transients, space weather, the atmosphere and magnetospheres of solar system planets and exoplanets. Figure 1 is illustrating the cosmological science objectives.

NOIRE (Nanosats pour un Observatoire Interfromtrique Radio dans l'Espace; Nanosats for a space borne interferometric radio observatory) is an ongoing feasibility study with PASO (Plateau d'Architecture des Systèmes Orbitaux; Space Systems Architecture Service) at CNES that assesses the feasibility of a low frequency space radio interferometer using nanosatellites.. It is conducted in collaboration with Dutch colleagues involved in several space borne low frequency radio interferometers projects (OLFAR, DEx, SURO, DSL...) Bentum et al. (2011). The goal spectral range of NOIRE is 0.1 to 100 MHz. The technologies and methods (particularly interferometric imaging) developed for LOFAR, NenuFAR or SKA are useful ingredients for such a project.

## 2 Low Frequency Radio Signal in Space nearby Earth

In the low frequency range (namely below 100 MHz), the sky brightness temperature can be as high as $10^7$ K at about 1 MHz. Figure 2 is showing the main radio sources and components observable in space near Earth.

[1] LESIA, Observatoire de Paris, PSL, Meudon, France
[2] PASO, CNES, Toulouse, France
[3] SAp-AIM, Univ. Denis Diderot Paris 7, Saclay, France
[4] APC, Univ. Denis Diderot Paris 7, Paris, France
[5] LUPM, Univ. Montpellier, Montpellier, France
[6] ESEP, LESIA, Observatoire de Paris, PSL, Meudon, France
[7] Technical Univ. Twente, Twente, the Netherlands
[8] M. Agnan, W. Baan, F. Barbiero, A. Basset, M. Bentum, C. Boniface, A.-J. Boonstra, P.-M. Brunet, M. Bruno, M. Bucher, R. Camarero, C. Cénac-Morthe, M.-F. Del Castillo, M. Delpech, P. Desgreys, C. Dudal, T. Dudok de Wit, L. Dusseau, S. Engelen, Y. Gargouri, M. Giard, Y. Giraud-Heraud, P. Gélard, T. Graba, J.-M. Griessmeier, H. Halloin, Y. Hello, S. Katsanevas, M. Klein-Wolt, A. Lamy, L. Lamy, C. Loisel, S. Loucatos, P. Loumeau, M. Maksimovic, S. Mancini, R. Mohellebi, ?M. Moncuquet, B. Monna, B. Mosser, Q. Nenon, E. Nuss, J. Panh, G. Patanchon, H. Petit, A. Petiteau, J.-L. Pinçon, H. Pourshaghaghi, D. Puy, J. Rotteveel, B. Segret, F. Saigné, A. Sicard-Piet, A. Tartari, C. Tasse, F. Vacher, D. Valat, P. K. A. van Vugt, G. Vasileiadis, P. Zarka, A. Zaslavsky

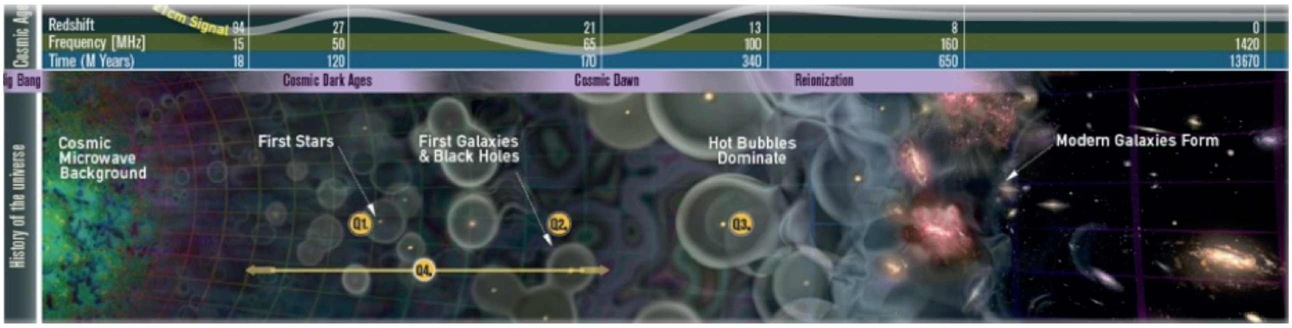


**Fig. 1.** Cosmological science objectives for low frequency observations, adapted from Klein-Wolt & Falcke (2013)

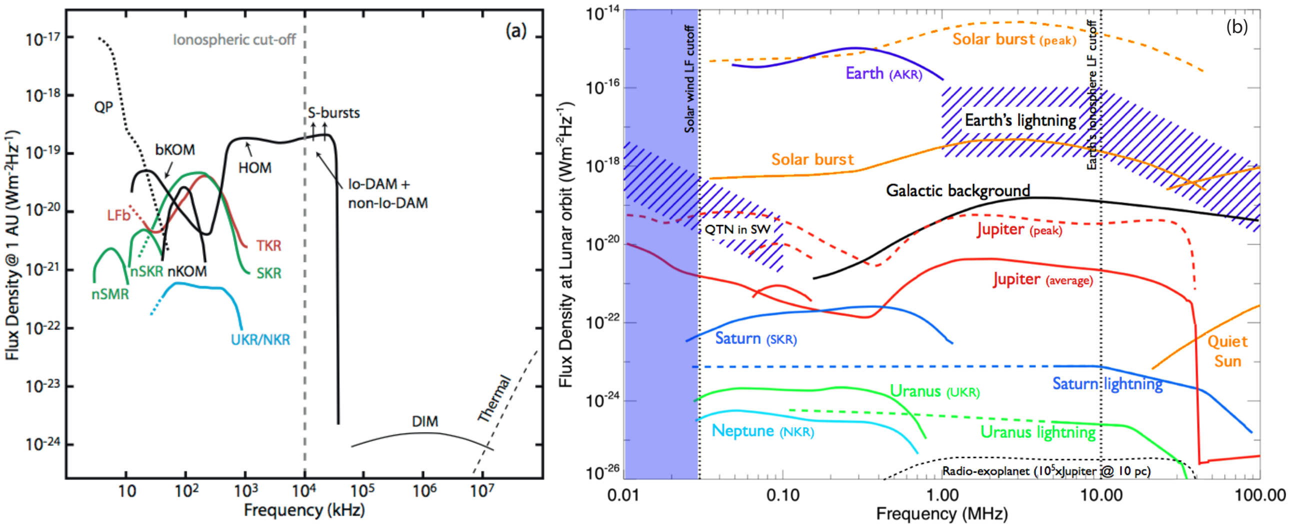


**Fig. 2.** (a) Solar system radio source normalized spectra, as observed from a distance of 1 AU (Astronomical Unit). Radio emission spectra from Jupiter, Saturn, Earth, Uranus/Neptune are traced in black, green, red and blue. (b) The radio component spectra observed from Earth, including solar radio emissions, earth and planetary auroral and atmospheric radio emissions, galactic emission and local plasma noise on the antenna. Figure adapted from Zarka et al. (2012) and Cecconi (2014).

## 3 Science Opportunities

Astrophysical science objectives start with the low frequency sky mapping, see the discussion Cecconi et al. (2016) in this issue, followed by the monitoring of radio sources (radio galaxies, large scale structures, clusters with radio halos, cosmological filaments), including polarization, down to a few MHz. NOIRE would provide pathfinder measurements of the red-shifted HI line that originates from before the formation of the first stars (dark ages, recombination). In case NOIRE is in lunar orbit, ultra-high energy cosmic rays and neutrinos will be studied through their interaction with the lunar surface. The detection of pulsars down to very low frequencies has implications with interstellar radio propagation. The low frequency cutoff of the temporal broadening would provide information on the largest scale of turbulence in the interstellar medium, putting limits on low frequency transient observation capabilities.

Solar and planetary science objectives are focussed on the magnetized and electrified environments. The low frequency radio bursts from the Sun are probing the interplanetary medium from 1.5 Rs (Solar Radii) to 1 AU. Imaging these radio bursts will provide completely new insights on the inner heliosphere, with application in Space Weather. Monitoring the terrestrial and planetary auroral radio emissions are also a key element of the understanding of the interaction between the solar wind and the magnetospheres. The four the giant planets magnetospheres are very dynamical objects, and long term studies are required to understand their rotation periods, the modulations by satellites and the solar wind or the seasonal effects. Such an observatory would

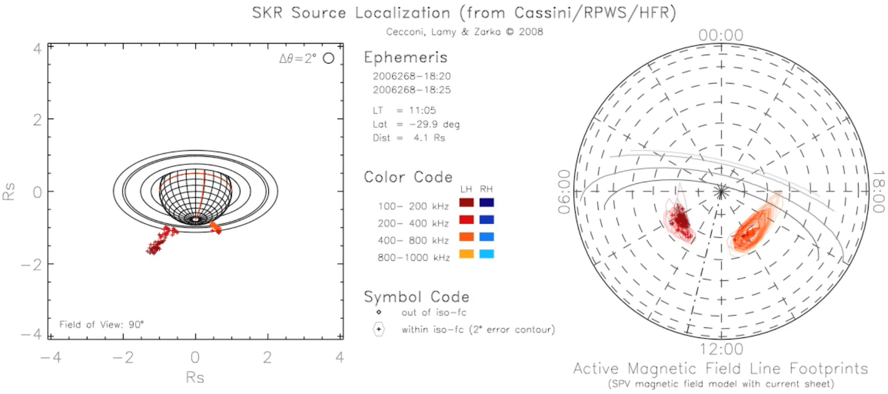


**Fig. 3.** Saturn auroral kilometric radiation observed with Cassini/RPWS. The direction of arrival and polarization retreived with goniopolarimetric analysis are shown on the left-hand side panel (directions projected on the plane of the sky, and polarization coded in color). The right-hand side panel shows an extra step derivation where the radio sources are mapped in the atmosphere, in order to be compared with observation of atmospheric aurora. Figure adapted from Cecconi et al. (2009).

be a first opportunity in decades to study Uranus and Neptune magnetospheres. The terrestrial and planetary radiation belts can also be observed and imaged. The local plasma at the place of the observatory can also be studied through: (i) quasi thermal noise spectroscopy (Meyer-Vernet & Perche 1989) and (ii) sampling the raw waveforms of local plasma waves (Briand et al. 2016).

Finally, the unknown remains to be discovered in this unexplored spectral band.

## 4 Space Radio Instrumentation

Current radio instrumentation with goniopolarimetric capabilities is described in Cecconi (2014) and references therein. Goniopolarimetric instruments are using a triad of electric short dipoles to derived polarization and direction of arrival characteristics of radio waves on a single spacecraft. Figure 3 shows the result of a goniopolarimetric analysis conducted with the Cassini/RPWS radio receiver (Gurnett et al. 2004) at Saturn. Current radio instrumentation characteristics (BepiColombo/MMO/RPW or SolarOrbiter/RPW radio receivers) are summarized as follows: superheterodyne radio receiver with 3 MHz bandwidth, sensitivity about 5 $\mathrm{nV}/\sqrt{\mathrm{Hz}}$, 80 to 100 dB dynamical range, about 1 W power consumption and a few 100 g. Future instruments (JUICE/RPWI or SolarProbePlus/Fields) are proposing base band radio receiver clocked at 100 MHz. Developments are ongoing (Mohellebi et al. 2014) to try to reduce the front-end power consumption while keeping performances.

## 5 Design of of Radio Interferometry

Current space radio instruments are capable of deriving direction of arrival, flux and polarization of radio waves passing at the place of a spacecraft. Imaging capabilities require interferometric instrumentation. The characteristics of such observatory must derives from a sound and detailed assessment of the science objectives, described in terms of measurement performance resulting into instrument, platform and system requirements. In case of a swarm of interferometric nodes, the instrument itself is the combination of the radio receivers, the nodes (platform) and the swarm (system).

Some preliminary requirements specific to radioastronomy can be stated easily. The nodes must be clean of radio frequency interferences (RFI). The current space engineering standard for electromagnetic compatibility (ECSS secretariat 2012) is not setting any constraint in most of the NOIRE observation band, so that most COTS (commercial off-the-shelf) components are unlikely to be suitable for NOIRE. Automated RFI mitigation software could be implemented, but its effect and interferometric processing must be assessed.

The NOIRE study team has drafted the science objectives and derived the corresponding measurement performance requirements. The translation into instrument specification is ongoing. The instrument parameter space includes at receiver level: sensitivity, temporal, and spectral sampling and resolution; at system level: number of nodes, knowledge and/or control of attitude, absolute location and relative location, clock synchronisation and ranging, inter-spacecraft communication and uplink/downlink capabilities, algorithms, etc. The current status of the assessment is not showing fundamental show stoppers. For all pieces of the system technologies are available, but not necessarily space qualified. Should the current design goal (a swarm of identical nodes) be disqualified, escape routes are also kept in mind.

This assessment is also making use of existing studies done for previous projects, such as OLFAR (Orbiting Low Frequency Array, see Rajan et al. (2010)) or DEx (Dark Ages Explorer, see Klein-Wolt & Falcke (2013)). Discussions with teams in the USA are also ongoing.

Concerning the ultimate goal of the Dark Ages of the Universe, the preliminary discussions show that the current sensitivity and calibration stability of the space radio receivers are not suitable, requiring specification studies and instrumental developments.

## 6 Conclusion

The NOIRE concept is very promising and innovative. Similar concepts are studied by many teams in the world. The current status of the study is not showing any show stopper. The study will resulting in a road map drafting a series a demonstrators towards a full scale observatory.

The NOIRE team acknowledges support from the PASO (Plateau d'Architecture des Systèmes Orbitaux) team at CNES. The NOIRE team members also acknowledge support from their institutions (Centre National de la Recherche Scientifique (CNRS) Observatoire de Paris, Univ. Paris 7 Denis Diderot, Univ. de Montpellier, Commissariat l'Energie Atomique (CEA), ONERA, Univ. Paul Sabatier, Univ. d'Orléans and Telecom Paris Tech) as well as their associated space campuses (Centre Spatial Universitaire de Montpellier-Nîmes, Univ. de Montpellier; Fondation Van Allen, Institut d'Electronique du Sud, Univ. de Montpellier; Campus Spatial Diderot, UnivEarthS, Sorbonne Paris Cité; and C2ERES, ESEP/PSL). They also thank the Dutch OLFAR teams (ASTRON, Radboud Univ. Nijmegen, TU Twente and TU Delft) for fertilizing discussions.

## References

Bentum, M., Boonstra, A.-J., & Baan, W. 2011, IEEE, 1

Briand, C., Henri, P., Génot, V., et al. 2016, J. geophys. Res. Space Physics, 121, 1062

Cecconi, B. 2014, Comptes Rendus Physique, 15, 441

Cecconi, B., Lamy, L., Zarka, P., et al. 2009, J. Geophys. Res., 114

Cecconi, B., Laurens, A., Briand, C., et al. 2016, in SF2A 2016, ed. L. Cambrésy, M. Deleuil, E. Pécontal, C. Reylé, J. Richard, L. Tresse, & V. L. (SF2A), this issue

ECSS secretariat. 2012, Electromagnetic Compatibility, Space Engineering Standard ECSS-E-ST-20-07C, rev. 1, ESA

Gurnett, D., Kurth, W. S., Kirchner, D., et al. 2004, Space Sci. Rev., 114, 395

Klein-Wolt, M. & Falcke, H. 2013, Dark Ages Explorer, White Paper, Radboud University Nijmegen

Meyer-Vernet, N. & Perche, C. 1989, J. Geophys. Res., 94, 2405

Mohellebi, R., Petit, H., Loumeau, P., et al. 2014, in New Circuits and Systems Conference (NEWCAS), 2014 IEEE 12th International, Trois-Rivieres, QC, 109–112

Rajan, R. T., Engelen, S., Bentum, M., & Verhoeven, C. 2010, IEEE AC, 1

Zarka, P., Bougeret, J.-L., Briand, C., et al. 2012, Planetary and Space Science, 74, 156

*SF2A 2016*
*C. Reylé, J. Richard, L. Cambrésy, M. Deleuil, E. Pécontal, L. Tresse and I. Vauglin (eds)*

# MAPPING THE RADIO SKY FROM 0.1 TO 100 MHZ WITH NOIRE

B. Cecconi[1], A. Laurens[2], C. Briand[1], J. Girard[3], M. Bucher[4], D. Puy[5], B. Segret[6], M. Bentum[7] and the NOIRE team[8]

**Abstract.** The goal of the NOIRE study (Nanosats pour un Observatoire Interférométrique Radio dans l'Espace) is to assess the scientific interest and technical feasibility of a space borne radio interferometer operating from a few kHz to a few 10 MHz. Such observatory would be able to build a global sky map with an unprecedented spatial resolution depending on the selected technical implementation. We present a review of our understanding of the Galactic mapping, assessing the instrument requirement for such observations.

Keywords: Radioastronomy, Interferometry, Space, Nanosatellites, Galaxy

## 1 Introduction

The radio sky at the low frequencies is bright. Its brightness temperature peaks at about 1 MHz with a value of $10^7$ K. The source of this radiation is the free-free synchrotron radiation of electron spiraling in the Galactic magnetic field (de Oliveira-Costa et al. 2008, and references therein). Hence the mapping of the low frequency radio sky is not only a science objective by itself, but also a crucial input for foreground radio sources observations (e.g., radio sources in the Solar System), as well as faint background sources (Dulk et al. 2001). The current space borne low frequency radio instruments such as those onboard Cassini (Gurnett et al. 2004) or STEREO (Bougeret et al. 2008) space mission have been calibrated using a model of the Galactic background emission (Zarka et al. 2004; Zaslavsky et al. 2011).

Mapping the sky is the first step for any observatory that opens an unexplored spectral band. For instance, the LOFAR (Low Frequency Array, van Haarlem et al. (2013)) team recently published its MSSS (Multifrequency Snapshot Sky Survey) (Heald et al. 2015), which covers the whole Northern sky from 30 to 160 MHz with an angular resolution $\leq$ 100 arcsec. NOIRE (Nanosats pour un Observatoire Interférométrique Radio dans l'Espace) is a feasibility study for a radio interferometer similar to LOFAR, but in space and covering the 0.1 to 100 MHz spectral band. A dedicated paper presents this study in this volume (Cecconi et al. 2016). It is lead by the French space agency CNES (Centre National d'Études Spatiales) and is assessing the possibility to use nanosatellites. The nanosatellite concept is a promising platform for distributed instrumentation. However due to the limitation of power resources, the feasibility assessment is not straightforward. Careful evaluation of science objectives linked with instrument and platform requirements are thus necessary.

[1] LESIA, Observatoire de Paris, PSL, Meudon, France
[2] PASO, CNES, Toulouse, France
[3] SAp-AIM, Univ. Denis Diderot Paris 7, Saclay, France
[4] APC, Univ. Denis Diderot Paris 7, Paris, France
[5] LUPM, Univ. Montpellier, Montpellier, France
[6] ESEP, LESIA, Observatoire de Paris, PSL, Meudon, France
[7] Technical Univ. Twente, Twente, the Netherlands
[8] M. Agnan, W. Baan, F. Barbiero, A. Basset, M. Bentum, C. Boniface, A.-J. Boonstra, P.-M. Brunet, M. Bruno, M. Bucher, R. Camarero, C. Cénac-Morthe, M.-F. Del Castillo, M. Delpech, P. Desgreys, C. Dudal, T. Dudok de Wit, L. Dusseau, S. Engelen, Y. Gargouri, M. Giard, Y. Giraud-Heraud, P. Gélard, T. Graba, J.-M. Griessmeier, H. Halloin, Y. Hello, S. Katsanevas, M. Klein-Wolt, A. Lamy, L. Lamy, C. Loisel, S. Loucatos, P. Loumeau, M. Maksimovic, S. Mancini, R. Mohellebi, ?M. Moncuquet, B. Monna, B. Mosser, Q. Nenon, E. Nuss, J. Panh, G. Patanchon, H. Petit, A. Petiteau, J.-L. Pinçon, H. Pourshaghaghi, D. Puy, J. Rotteveel, B. Segret, F. Saigné, A. Sicard-Piet, A. Tartari, C. Tasse, F. Vacher, D. Valat, P. K. A. van Vugt, G. Vasileiadis, P. Zarka, A. Zaslavsky

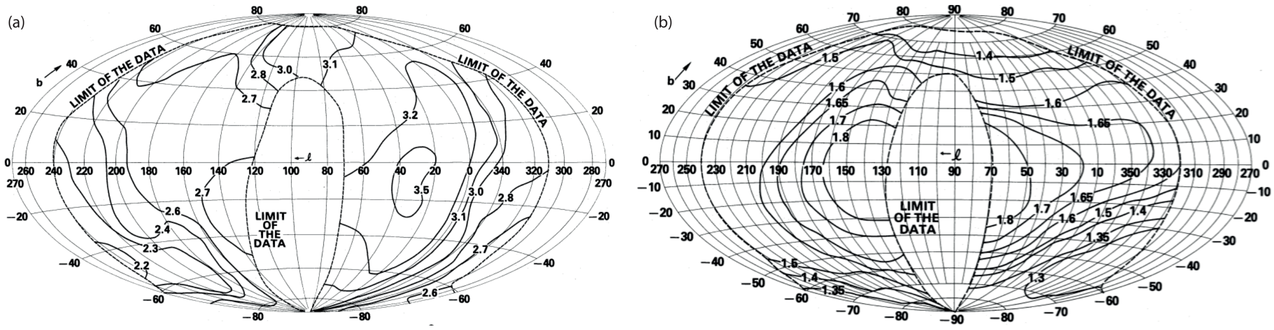


**Fig. 1.** Coutour map in galactic coordinates of the nonthermal emission as published by Novaco & Brown (1978). Panels (a) and (b) are showing maps at 3.93 and 1.31 MHz respectively. The contours are in units of $10^6$ and $10^7$ K, respectively.

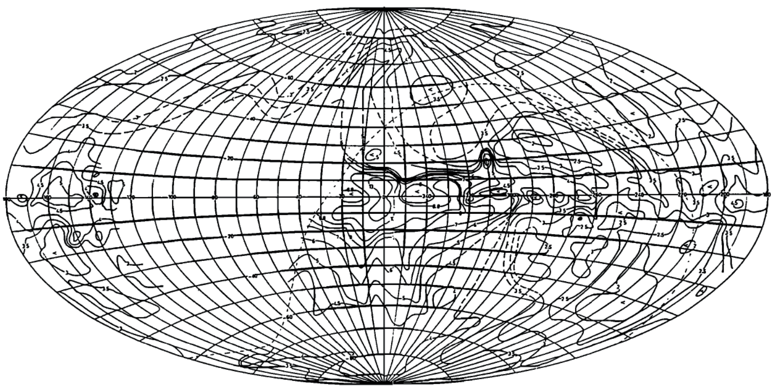

**Fig. 2.** A 10 MHz map of the galaxy based upon data from several surveys that were convolved to a common anluar resolution of 5°. Contours are in units of $8 \times 10^4$ K. Figure extracted from Cane & Erickson (2001).

## 2 Review of known galactic background characteristics

The first map of the Galaxy is published by Novaco & Brown (1978). They have built maps and spectra from 1 to 10 MHz using RAE-2 (Radio Astronomy Explorer 2) data (Alexander et al. 1975). Figure 1 is showing the sky maps at 3.93 and 1.31 MHz. However it is very difficult to use these maps for calibration of low frequency radio instruments since: (i) the RAE-2 data are not readily available (NSSDC is holding microfilms and tapes*, but no digitized version is available); (ii) the maps are not complete, as shown on Fig. 1; and finally (iii) the Novaco & Brown (1978) paper is not explaining the methodology used to derive the radio maps. Cane & Erickson (2001) are providing a combined map at 10 MHz, see Fig. 2. This map has a better coverage and resolution than that of Novaco & Brown (1978) at 10 MHz, but it is still not complete. A complete map at 30 MHz has been published by Cane (1978). For higher frequencies, Guzmán et al. (2010) is proposing a map at 45 MHz, which is reproduced on Fig. 3. This paper is also providing a map of spectral indices from 45 to 408 MHz. In the recent years, Global Sky Models have been developed and improved but their spatial coverage is still scarce below 100 MHz (de Oliveira-Costa et al. 2008; Zheng et al. 2016), although the MSSS is filling the gap down to 30 MHz in the Northern hemisphere.

The integrated spectrum of the galatic radiation has also been published Cane (1979); Dulk et al. (2001); Manning & Dulk (2001). Figure 4 is showing a compilation of published spectra and an measure of galactic background anisotropy from WIND/Waves data (Manning & Dulk 2001).

*http://nssdc.gsfc.nasa.gov/nmc/datasetSearch.do?spacecraft=RAE-B

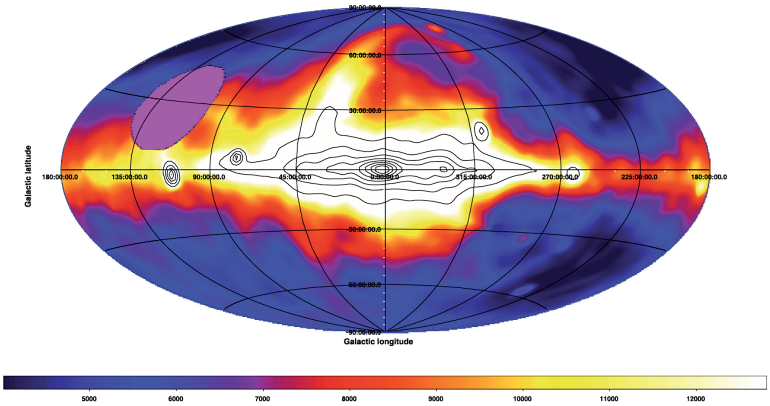


**Fig. 3.** Hammer-Aitoff projection of the 45 MHz full sky map. Eight contours are drawn between 15 000 and 60 000 K. The map does not cover the $\delta > +65°$ zone. Figure extracted from Guzmán et al. (2010).

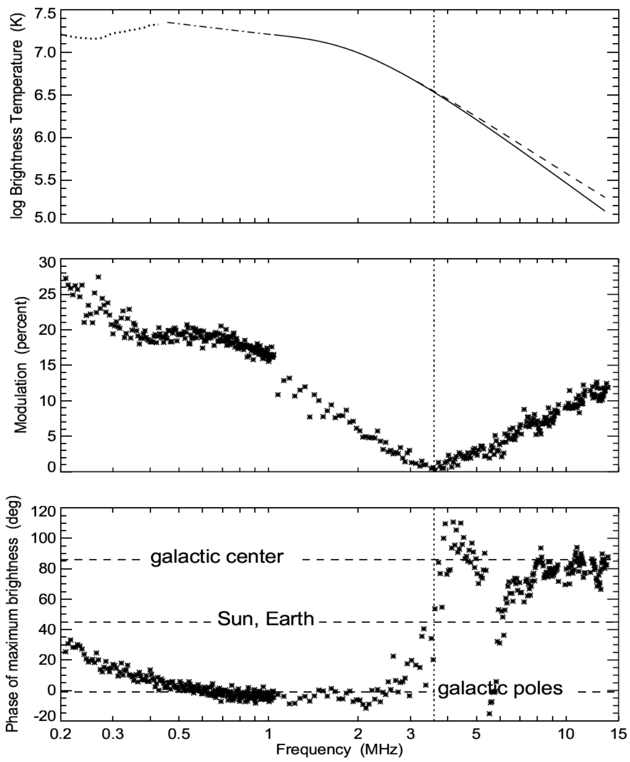


**Fig. 4.** Top panel: Estimated spectrum of brightness temperature of the Galactic background radiation obtained from sources described in the text. Middle panel: Wind/WAVES measurements of the degree of modulation (peak minus average power) of the signal from the Galactic background. The measurement uncertainty is evident from the variation from one frequency to another. Bottom panel: Spin phase of maximum intensity. The ordinate is ecliptic longitude, with an ambiguity of 180° inherent in reception by a dipole antenna. Figure extracted from Manning & Dulk (2001).

## 3 Requirements for NOIRE

The performance requirements shall be defined for the spectral, temporal, spatial scales, as well as for the signal amplitude and fluctuations (sensitivity and dynamical range) and for the polarization degrees. Figure 4 provides preliminary spectral performance requirements. The lowest observable frequencies, above the local background is about 100 to 300 kHz (see also Figs. 1 and 2 of Zarka et al. (2012)). In order to correctly sample the peak of the emission, the frequency resolution should be set to 100 kHz below 5 MHz. At higher frequencies, a 1 MHz sampling resolution is sufficient up to 100 MHz. Considering the temporal scale, as we want to build a static map, the longer integration times the better signal to noise ratio. The aimed spatial scales are of the order of $1^\circ$ or better. The observed signal is reaching $10^7$ Jy at 3 MHz. The fluctuations on spatial scales still remain to be evaluated. As far as polarization is concerned, no significant component is expected due to Faraday rotation depolarization in the interstellar medium.

The previous statements can be turned into instrumental, platform and system requirements. The temporal, spectral, sensitivity and dynamical range performances directly relates to the radio receiver design. The performance requirements drafted here are fully compatible with current space radio receivers. The spatial resolution is proportional to the $\lambda/B$ ratio, where $\lambda$ is the wavelength and $B$ the interferometric baseline. With a 100 km baseline, the reachable spatial resolutions are 20.6 arcsec, 1 arcmin and 10.3 arcmin at 30, 10 and 1 MHz, respectively.

The interferometer could work as a full sky imager using the 3D interferometry inversion (Carozzi 2015) or in a beam-forming mode, as done for the LOFAR/MSSS.

Although the measurement, system and platform requirements presented here are not strongly driving the design of NOIRE, it is noticealbe as other science objectives are putting more stringent constraints on each of the addressed parameters.

## 4 Conclusions

This work is still under development, and a support from an experienced team in galactic background modeling and observations would be very helpful. This support would help the NOIRE team to assess the constraints drafted in this paper, and would be very welcome for the science analysis when data are available. However, considering this preliminary assessment, the NOIRE concept would provide a suitable observation platform for this science objective.

The NOIRE team acknowledges support from the PASO (Plateau d'Architecture des Systèmes Orbitaux) team at CNES. The NOIRE team members also acknowledge support from their institutions (Centre National de la Recherche Scientifique (CNRS) Observatoire de Paris, Univ. Paris 7 Denis Diderot, Univ. de Montpellier, Commissariat l'Energie Atomique (CEA), ONERA, Univ. Paul Sabatier, Univ. d'Orléans and Telecom Paris Tech) as well as their associated space campuses (Centre Spatial Universitaire de Montpellier-Nîmes, Univ. de Montpellier; Fondation Van Allen, Institut d'Electronique du Sud, Univ. de Montpellier; Campus Spatial Diderot, UnivEarthS, Sorbonne Paris Cité; and C2ERES, ESEP/PSL). They also thank the Dutch OLFAR teams (ASTRON, Radboud Univ. Nijmegen, TU Twente and TU Delft) for fertilizing discussions.

## References

Alexander, J. K., Kaiser, M. L., Novaco, J. C., Grenu, F. R., & Weber, R. R. 1975, Astron. Astrophys., 40, 365

Bougeret, J.-L., Goetz, K., Kaiser, M. L., et al. 2008, Space Sci. Rev., 1–4, 487

Cane, H. 1979, Mon. Not. R. astr. Soc., 189, 465

Cane, H. V. 1978, Aust. J. Phys., 31, 561

Cane, H. V. & Erickson, W. C. 2001, Radio Science, 36, 1765

Carozzi, T. D. 2015, MNRAS, 451, L6

Cecconi, B., Laurens, A., Briand, C., et al. 2016, in SF2A 2016, ed. L. Cambrésy, M. Deleuil, E. Pécontal, C. Reylé, J. Richard, L. Tresse, & V. L. (SF2A), this issue

de Oliveira-Costa, A., Tegmark, M., Gaensler, B. M., et al. 2008, MNRAS, 388, 247

Dulk, G., Erickson, W., Manning, R., & Bougeret, J.-L. 2001, Astrophys. J., 365, 294

Gurnett, D., Kurth, W. S., Kirchner, D., et al. 2004, Space Sci. Rev., 114, 395

Guzmán, A. E., May, J., Alvarez, H., & Maeda, K. 2010, Astronomy and Astrophysics, 525, A138

Heald, G. H., Pizzo, R. F., Orrú, E. Breton, R. P., et al. 2015, Astron. Astrophys., 582, 1

Manning, R. & Dulk, G. 2001, Astrophys. J., 372, 663

Novaco, J. C. & Brown, L. W. 1978, Astrophys. J., 221, 114

van Haarlem, M. P., Wise, M. W., Gunst, A. W., et al. 2013, Astron. Astrophys., 556, A2

Zarka, P., Bougeret, J.-L., Briand, C., et al. 2012, Planetary and Space Science, 74, 156

Zarka, P., Cecconi, B., & Kurth, W. S. 2004, J. Geophys. Res., 109, A09S15

Zaslavsky, A., Meyer-Vernet, N., Hoang, S., Maksimovic, M., & Bale, S. D. 2011, Radio Sci., 46

Zheng, H., Tegmark, M., Dillon, J. S., et al. 2016, MNRAS

*SF2A 2016*
*C. Reylé, J. Richard, L. Cambrésy, M. Deleuil, E. Pécontal, L. Tresse and I. Vauglin (eds)*

# OBSERVATIONS OF FAST RADIO BURSTS AND PERSPECTIVES AT LOW FREQUENCIES

P. Zarka[1] and F. Mottez[2]

**Abstract.** We briefly summarize the characteristics of the elusive Fast Radio Bursts from existing observations. Then we emphasize the interest of low-frequency observations, e.g. with NenuFAR. In order to define the best observing parameters and detection scheme, we have built a simulation program of FRB at low-frequencies, that proceeds in 2 steps: (i) FRB generation and dilution in a dynamic spectrum with given characteristics, and (ii) definition of the FRB spectrum, and detection on the galactic radio background by means of parametric dedispersion. We carry on a preliminary simulation study, that allows us to draw first conclusions, among which the possibility to detect Lorimer-like FRB with NenuFAR.

Keywords: Fast radio burst, radio astronomy, dynamic spectrum, low frequencies, dedispersion, NenuFAR

## 1 Introduction

The first Fast Radio Burst (FRB) was discovered in 2007 (Lorimer et al. 2007), and about 20 have been detected since then (Petroff et al. 2016), all but one at $\sim$1.4 GHz, and one down to 700 MHz (Masui et al. 2015). They consist of a single broadband pulse, of a few milliseconds duration at a given frequency sometimes including an exponentially decreasing tail, and of flux density between 0.1 and 30 Jy at $\sim$1 GHz. Their main characteristic is that they are dispersed, like pulsar signals but much more dispersed. The signal slides from high to low frequencies with a delay $\delta t(f)$ following very closely the law proportional to $\mathrm{DM}/f^2$ that characterizes radio propagation in a plasma (with DM the dispersion measure, i.e. the integrated electron content along the wave path, in pc.cm$^{-3}$, and $f$ the frequency of observation). The two main differences between an FRB and pulsar pulses are that (i) an FRB is a unique event (not periodic, although in some cases repetition was observed at variable but generally long intervals (Spitler et al. 2016), and (ii) the dispersion measure DM generally does not exceed $\sim$100 pc.cm$^{-3}$ for sources out of the galactic plane, whereas the DM of FRB is several hundreds to $\geq$1000, also for sources out of the galactic plane. After a few years of debate, it is now accepted that FRB are extragalactic signals from sources at hundreds of Mpc to Gpc distances, the large dispersion of which is indeed due to a very large propagation path. As the detected signal is quite intense (0.1$-$30 Jy), all but one theories proposed for FRB that assume an isotropic emission, require a large energy source $\sim 10^{33}$ J. One theory involves radio beaming in a very narrow angle, of order of 1"$^2$, and consequently requires a much less energetic emission $\sim 10^{21}$ J (Mottez & Zarka 2014).

Although only $\sim$20 FRB have been detected until now, the estimated FRB rate is of several thousands/sky/day (e.g. Connor et al. 2016). And basically nothing is known about the FRB spectra, i.e. their spectral slope (Oppermann et al. 2016) or low-frequency cutoff that would provide useful information for constraining their emission mechanism. Observations at GHz frequencies are usually performed in small fields of view ($\ll 1^{\circ 2}$), which explains the low detection rate until now. Al lower frequencies, instruments such as LOFAR (van Haarlem et al. 2013) or NenuFAR (Zarka et al. 2012) have large fields of view, up to $\sim 100^{\circ 2}$. But the FRB signals will be dispersed on much longer times, as the propagation delay varies as $f^{-2}$. The scattering effect (in $f^{-4.4}$) will also be much stronger. And the galactic background spectrum steeply rises towards low frequencies, as $f^{-2.55}$. It is thus difficult to estimate quantitatively what should be the observations parameters for an optimal low frequency search of FRB, or even if they will be detectable at all.

[1] LESIA & USN, Observatoire de Paris, CNRS, PSL
[2] LUTh, Observatoire de Paris, CNRS, PSL

## 2 Simulation of low-frequency observations

For that purpose, we have built a simulation program of low-frequency observations aiming at FRB detection. It runs in two steps.

In step 1, we build the dynamic spectrum of a dispersed FRB observed in a selected spectral range $[f_{min}, f_{max}]$ with spectral resolution $\delta f$ and temporal resolution $\delta t$. The FRB is defined by its intrinsic fixed frequency duration (excluding any scattering tail) and temporal profile (square, gaussian), its DM, and the e-folding time of its scattering tail if any. The overall duration of the simulated dynamic spectrum must be longer than the dispersion delay from $f_{max}$ to $f_{min}$, that amounts e.g. to 17870 sec ($\sim$5 hours) through the band [15,85] MHz for DM=1000. The FRB may occur (at $f_{max}$) at any arbitrary time after the beginning of the dynamic spectrum, but in practice we make it occur before t$\sim$100 sec in order to limit the length (and thus the volume) of the simulated dynamic spectrum. In order to avoid the dilution of the FRB signal in $\delta t \times \delta f$ bins, resolutions better than $\delta t$=1 msec and $\delta f$=1 kHz should in principle be used. But an observation of 5 hours duration in the [15,85] MHz range with 1 msec$\times$1 kHz duration represents a dynamic spectrum of 1.26 Terapixels. It is thus necessary to observe with coarser resolutions (e.g. $\delta t$=10-100 msec and $\delta f$=5-25 kHz), with which the large dispersion drift and scattering will indeed cause strong FRB signal dilution. Step 1 of our simulation computes this dilution by using a super-resolved $(t, f)$ grid at 0.1 msec $\times$ 0.1 kHz that tracks the burst in the $(t, f)$ plane. The burst shape is computed consecutively for each channel of width $\delta f$: the burst is generated undispersed at the above super-resolution with its selected temporal profile and flux density set to 1; then a scattering tail is added (if requested), conserving the total power (or fluence) of the burst, that is the integral of its time profile before scattering; finally, the burst is dispersed with the selected DM, and the dynamic spectrum is rebinned at the chosen $\delta t \times \delta f$. With DM=1000, $\delta t$=10-100 msec and $\delta f$=25 kHz we find, for an FRB signal of intrinsic fixed-frequency duration 5 msec, a dilution by a factor $\sim$67 in the resulting dynamic spectrum. The maximum contribution of the FRB, of initial intensity 1 at super-resolution, to a $\delta t \times \delta f$ bin is thus $\sim$0.015. This dilution, mainly due to the very large dispersion of the signal across the channel width, goes down to a factor $\sim$13 with $\delta f$=5 kHz. An FRB simulated in NenuFAR's range is displayed in Fig. 1.

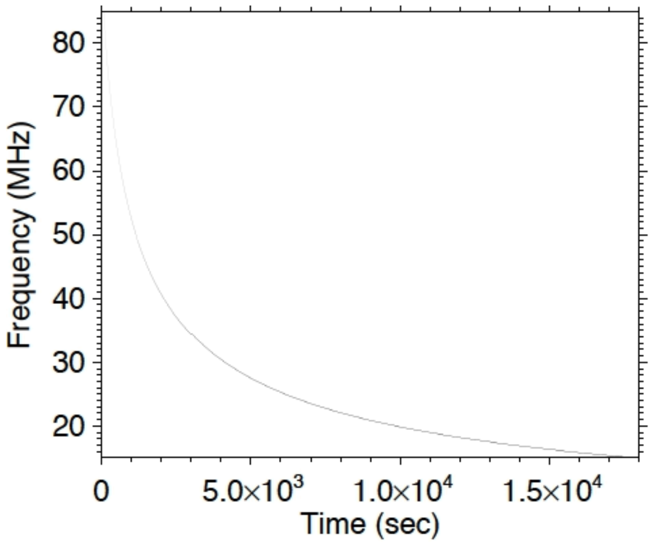


**Fig. 1.** Simulated FRB in the frequency range of NenuFAR. The burst has a fixed-frequency duration of 5 msec, plus a scattering tail, a DM=1000, and it occurs at $t_\circ$=100 sec at 85 MHz. The dynamic spectrum has resolutions $\delta t$=100 msec $\times$ $\delta f$=25 kHz.

Step 2 starts from the FRB dynamic spectrum generated in step 1. It allows us to define the peak flux density and spectrum of the FRB (flat, power law) that is applied to the dynamic spectrum. Then, the unpolarized sky background is added at each frequency, as an average value plus a random noise representing its statistical fluctuations. The average value at frequency $f$ (i.e. wavelength $\lambda$(m)=300/$f$(MHz)) is: $S_{sky} = 2kT_{sky}/A_{eff}$ with $k$ the Boltzmann constant, $T_{sky}$(K)=$60\lambda^{2.55}$, and $A_{eff}$ is computed for various user-selected arrays (of dipoles, of LOFAR HBA tiles (van Haarlem et al. 2013), or of NenuFAR mini-arrays (Zarka et al. 2012)). The standard deviation of the random fluctuations is: $\sigma = S_{sky}/(\delta f \times \delta t)^{1/2}$. The FRB hidden in the sky background fluctuations is then blindly searched for via parametric dedispersion: a ramp of trial DM is tested; for each test DM value, the dynamic spectrum is dedispersed and integrated in frequency to obtain a time series $x(t)$, converted to SNR$(t) = ((x(t) - < x(t) >)/\sigma_x)$, where peaks are then identified. The dynamic spectrum FRB+Sky can be first rebinned to simulate observations with $(t, f)$ resolutions lower than simulated at step 1, and the frequency range of the search can be reduced compared to the range $[f_{min}, f_{max}]$ simulated at step 1. Optionally, the dynamic spectrum can be "flattened" (i.e. each spectrum is divided by the average sky background) and smoothed (each fixed-frequency time series is "smoothed" by the dispersive spread within the corresponding channel at the tested DM value) prior to dedispersion.

## 3 Results

Examples of simulation results are presented in Fig. 2. All panels correspond to an FRB with DM=1000 occurring at $t_\circ$=100 sec (at $f_{max}$=85 MHz), of duration 5 msec plus a scattering tail of 2 msec at 85 MHz (increasing as $f^{-4.4}$ at lower frequencies), observed with resolutions $\delta t$=100 msec (rows #1 to #4) or 10 msec (rows #5 and #6) and $\delta f$=25 kHz, in the range 15−85 MHz with the NenuFAR array (at completion, with 96 arrays of 19 dipoles (Zarka et al. 2012)). Row #1 (top) corresponds to an FRB with a flat spectrum of flux density $S$=1000 Jy. It is easily detected in the 15−85 MHz range, applying flattening and smoothing, with SNR>80. Row #2 corresponds to similar results for $S$=100 Jy: here the SNR is only ∼7. Note that in both cases DM and $t_\circ$ are biased toward slightly larger values than those used at step 1, due to the scattering tail. Rows #3 and #4 are similar to row #2 except that no smoothing is applied. The strongest peak is obtained at a time different from $t_\circ$ and DM=990 (row #3). A peak with lower SNR is found at $\sim t_\circ$ and DM∼1000 (row #4). However, it can be noticed that the shape of the peak in the (DM,$t$) plane (panel 4a) as well as in the time series SNR($t$) (panel 4b) in row #4 is similar to those in rows #1 and #2, which is not the case for the spurious peak of row #3. Thus discrimination of real signal peaks should be possible. But this also shows that smoothing improves detectability. With a flat spectrum at $S$=30 Jy, the FRB is no more detected in the range 15−85 MHz with NenuFAR. Row #5 shows the results obtained with a similar simulation but with $\delta t$=10 msec, for an FRB with a spectrum $S$(Jy)=30×($f$/85 MHz)$^{-0.7}$, searched for in the 32−85 MHz range. As in row #3 the main peak is not the FRB at $t_\circ$=100 sec and DM=1000, but a spurious peak at another time (panel 5b) and DM=1006 (panels 5a and 5c), but one of the few detected peaks with highest SNR is indeed the simulated FRB (row #6).

## 4 Conclusions

This is a preliminary simulation study, as the parameter space to explore is vast. But the developed tools have been tested and validated. This study shows that:

- a good spectral resolution, better than a few kHz, is important for reducing the FRB signal dilution ;
- a time resolution of ∼10 msec/spectrum is acceptable for an FRB search ;
- smoothing (by the dispersive spread in each spectral channel) improves SNR and thus detectability ;
- an FRB with flux density ∼30 Jy and fixed-frequency duration 5 msec (similar to the Lorimer burst (Lorimer et al. 2007), but with DM up to 1000), can be detected with NenuFAR ; note that although this flux density corresponds to the strongest FRB detected at ∼1.4 GHz, it is a modest flux density at the much lower frequency studied here as the spectrum may rise toward low frequencies ;
- analysis of the shape of the detected peaks in the (DM,$t$) plane and in a time series SNR($t$) should allow us to discriminate between genuine FRB and spurious peaks.

The present analysis assumes no effect from RFI (interference) nor ionospheric fluctuations. The latter should not strongly influence detectability, and the residual effect of the former (that should be mitigated prior to dedispersion) will be much reduced by the dedispersion with a large DM. We conclude that FRB search will be worth to carry on at low frequencies, e.g. with NenuFAR. If detection occurs, it will bring important information about FRB occurrence, distribution in the sky, spectrum, low-frequency cutoff, and polarization. The developed simulation program may be used for optimizing the observations of FRB, RRAT (Rotating RAdio Transients (McLaughlin et al. 2006)), or pulsar single pulses with various low-frequency instruments.

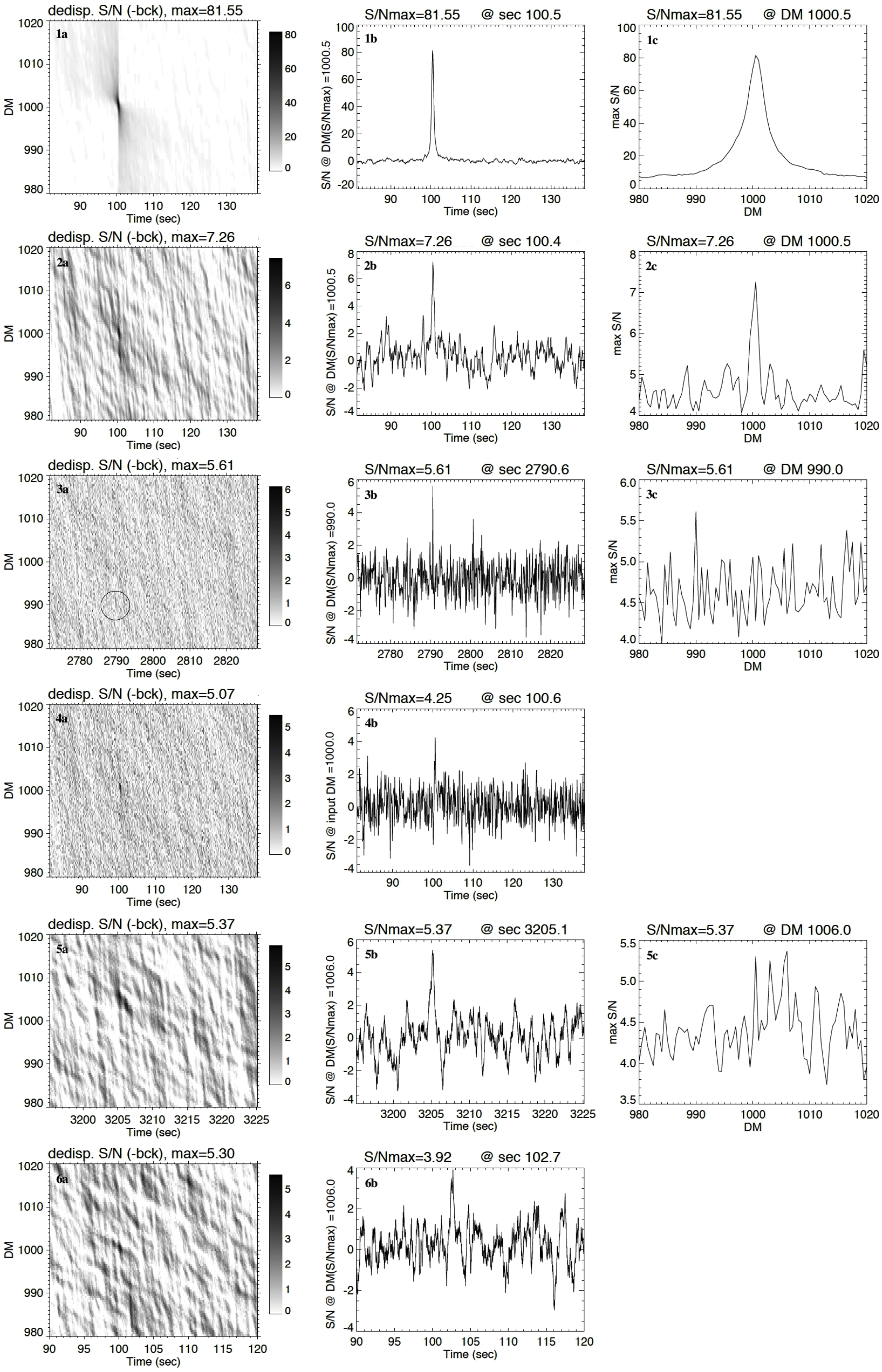


**Fig. 2.** Simulation tests of detection of the FRB of Fig. 1. Row #1: the FRB has a flat spectrum of 1000 Jy. Row #2: the FRB has a flat spectrum of 100 Jy. Rows #3 and #4: same as row #2 but no smoothing applied in the detection scheme. Rows #5 and #6: the dynamic spectrum (of Fig. 1) has a time resolution $\delta t$=10 msec and is restricted to the 32−85 MHz range. The FRB has a flux density spectrum of $30\times(f/85\ \mathrm{MHz})^{-0.7}$. Column *a*: dedispersed and integrated time series as a function of the DM (on panel 3a, the peak SNR value is an isolated pixel near the center of the circle). Column *b*: time profile obtained by dedispersion with the DM indicated on the y-axis and spectral integration, around the time of maximum SNR (rows #1,2,3,5) as well as around $t_\circ$ (rows #1,2,4,6). Column *c*: maximum SNR of the time series obtained for each DM. See text (section 3) for details.

## References

Connor, L., Lin, H.-H., Masui, K., et al. 2016, MNRAS, 460, 1054

Lorimer, D. R., Bailes, M., McLaughlin, M. A., Narkevic, D. J., & Crawford, F. 2007, Science, 318, 777

Masui, K., Lin, H.-H., Sievers, J., et al. 2015, Nature, 528, 523

McLaughlin, M. A., Lyne, A. G., Lorimer, D. R., et al. 2006, Nature, 439, 817

Mottez, F. & Zarka, P. 2014, A&A, 569, A86

Oppermann, N., Connor, L. D., & Pen, U.-L. 2016, MNRAS, 461, 984

Petroff, E., Barr, E. D., Jameson, A., et al. 2016, PASA, 33, e045

Spitler, L. G., Scholz, P., Hessels, J. W. T., et al. 2016, Nature, 531, 202

van Haarlem, M. P., Wise, M. W., Gunst, A. W., et al. 2013, A&A, 556, A2

Zarka, P., Girard, J. N., Tagger, M., & Denis, L. 2012, in SF2A-2012: Proceedings of the Annual meeting of the French Society of Astronomy and Astrophysics, ed. S. Boissier, P. de Laverny, N. Nardetto, R. Samadi, D. Valls-Gabaud, & H. Wozniak, 687–694

*SF2A 2016*
*C. Reylé, J. Richard, L. Cambrésy, M. Deleuil, E. Pécontal, L. Tresse and I. Vaughlin (eds)*

# FARADAY TOMOGRAPHY WITH LOFAR: NEW PROBE OF THE INTERSTELLAR MAGNETIC FIELD

M. I. R. Alves[1], V. Jelić[2,3], K. Ferrière[1] and F. Boulanger[4]

**Abstract.** Magnetic fields are a key constituent of the interstellar medium of our Galaxy. However, their exact role in the Galactic ecosystem is still poorly understood since we do not yet have a complete view of its structure in the Galaxy. This is about to change with the Faraday tomography technique, which allows us to derive the magnetic field in separate regions along the line of sight. We first describe the principle of Faraday tomography and illustrate the power of this novel technique with some of the latest results from the LOw Frequency ARray (LOFAR). We present preliminary results of our LOFAR project, aimed at investigating the origin of the filamentary-like structures revealed by Faraday tomography observations.

Keywords: ISM: general, magnetic fields, structure – radio continuum: ISM – techniques: polarimetric, interferometric

## 1 Introduction

Since interstellar magnetic fields were discovered in our Galaxy (Hall 1949; Hiltner 1949), it has been established that magnetism is pervasive in the Universe. Planets, stars, and galaxies all show the presence of magnetic fields, which span a large range in strength and change considerably in structure. The properties of Galactic interstellar magnetic fields, in different environments and objects, have been inferred throughout the years from a variety of observational methods. These are based on polarization of starlight and dust thermal emission, Zeeman splitting, Faraday rotation, and synchrotron emission (e.g. see reviews by Ferrière 2011; Haverkorn 2015). Not only from observations but also from a theoretical point of view, it became clear that magnetic fields are a vital constituent of the interstellar medium. However, the details of their role in the Galactic ecosystem, for instance in star formation, in the distribution and dynamics of interstellar matter, or in the evolution of supernova remnants, are still poorly known.

A great limitation of most of the aforementioned methods is that they provide line-of-sight integrated quantities, with no details on how the integrands vary along the sightline. Moreover, they probe different components of the magnetic field in different phases of the interstellar medium. For instance, dust polarization (either in emission or extinction) traces the orientation of the plane-of-the-sky magnetic field in the dusty (mostly neutral) medium, while synchrotron emission and its polarization give the same field component but in the general, cosmic-ray filled interstellar medium. The line-of-sight magnetic field can be obtained from Zeeman splitting and Faraday rotation in the neutral and ionized medium, respectively. The key to make progress in studies of Galactic magnetism is thus to combine complementary tracers.

The Faraday tomography method is based on this approach: it relies on a combination of Faraday rotation and synchrotron emission. The observed synchrotron emission from the Galaxy is produced by different regions along the line of sight. The emission produced by each region undergoes Faraday rotation and the amount of rotation increases with distance to the emitting region. The idea is thus to exploit Faraday rotation to locate the different regions along the line of sight. Moreover, the amount of Faraday rotation increases with wavelength squared ($\lambda^2$). Therefore, observing at large wavelengths, or low frequencies, is very efficient to

[1] IRAP, Université de Toulouse, CNRS, 9 avenue du Colonel Roche, BP 44346, 31028, Toulouse Cedex 4, France
[2] Ruđer Bošković Institute, Bijenička cesta 54, 10000 Zagreb, Croatia
[3] ASTRON - The Netherlands Institute for Radio Astronomy, PO Box 2, 7990 AA Dwingeloo, The Netherlands
[4] IAS, Université Paris-Sud 11, CNRS, Bâtiment 121, 91405 Orsay, France

probe the nearby interstellar medium in detail. On the other hand, observations at smaller wavelengths are more suitable to probe the interstellar medium over large distances. Faraday tomography is being increasingly used, thanks to the high-quality data, with wide wavelength coverage and high angular resolution, provided by recent radio telescopes such as the LOw Frequency ARray (LOFAR). The few studies available for various sightlines reveal a rich interstellar medium, filled with a number of synchrotron emitting regions interspersed with Faraday rotating screens (e.g. Iacobelli et al. 2013; Jelić et al. 2014, 2015).

## 2 Faraday tomography

Faraday tomography exploits the Faraday rotation of synchrotron polarized emission. The amount of Faraday rotation of the polarized emission produced at a point P with line of sight depth $L$ is equal to the wavelength squared times the Faraday depth ($\phi$) of point P. The latter is proportional to the line-of-sight integral of the free-electron density times the line-of-sight magnetic field ($\phi = \int_0^L n_e B_{||} dz$). The synchrotron emissivity at a given wavelength is a function of the plane-of-the-sky magnetic field ($\vec{B_\perp}$) times the density of cosmic-ray electrons. Essentially, one measures the synchrotron polarized intensity at a large number of different wavelengths and converts its variation with $\lambda^2$ into a variation with $\phi$ (alike a Fourier transform, Brentjens & de Bruyn 2005).

Consider a line of sight that intersects four interstellar clouds, as Fig. 1 depicts: two Faraday-rotating (light grey) and two synchrotron-emitting (dark blue) clouds. The top panel shows how these are located as a function of distance from the observer, $z$, placed at the far left. The red arrows give the direction of the magnetic field in each Faraday-rotating cloud. As per the above equation, $\phi$ increases or decreases across the rotating clouds according to whether the magnetic field points towards or away from the observer. This is illustrated in the middle panel, which shows the variation of $\phi$ with $z$: $\phi_1$ corresponds to the Faraday thickness of the closer Faraday-rotating cloud and $\phi_2$ is the cumulated Faraday thickness of both Faraday-rotating clouds. The bottom panel shows the Faraday spectrum, $|F(\phi)|$, where the two peaks at $\phi_1$ and $\phi_2$ represent the polarized emission from the closer and the farther synchrotron-emitting clouds, respectively. In Fig. 1-left the Faraday-rotating and the synchrotron-emitting clouds are spatially separated; in Fig. 1-right the closer synchrotron-emitting cloud is embedded in the closer Faraday-rotating cloud, and hence it has a finite Faraday thickness that extends over a range of Faraday depths (up to nearly $\phi_1$). Regions that are extended in $\phi$ are called Faraday thick. However, this definition is wavelength dependent and in practice the shape of the Faraday spectrum depends on the instrument's wavelength coverage and resolution (Brentjens & de Bruyn 2005).

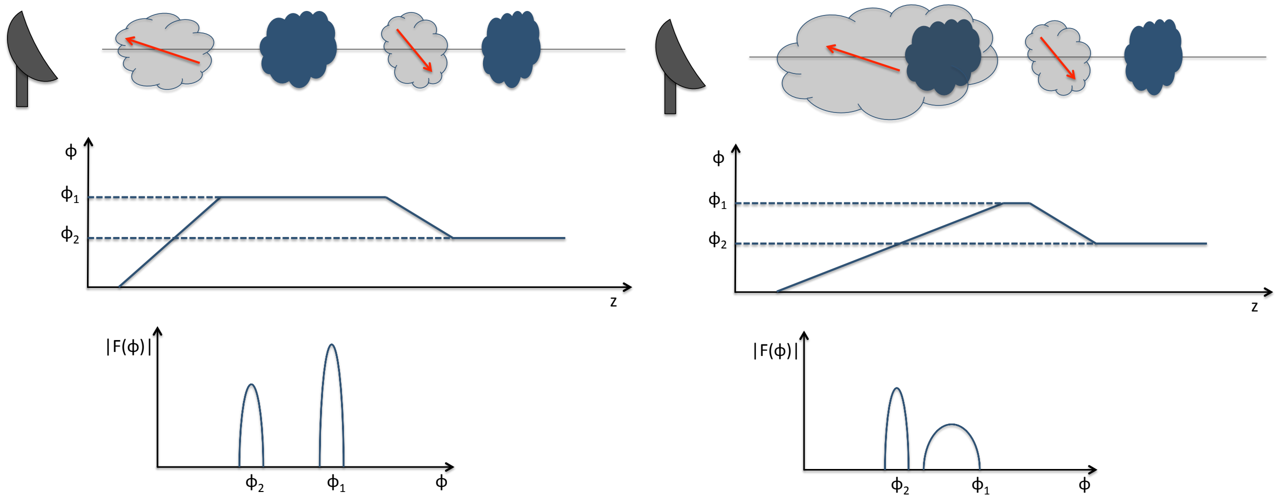


**Fig. 1.** Illustration of the principle of Faraday tomography. See main text for details. **Left:** The Faraday-rotating clouds (light grey) and the synchrotron-emitting clouds (dark blue) are spatially separated. **Right:** The closer synchrotron-emitting cloud is embedded in the closer Faraday-rotating cloud.

In practice one applies the technique to all the lines of sight in a given field, obtaining a Faraday depth cube: synchrotron polarized intensity as a function of position-position-Faraday depth, or $\alpha$ - $\delta$ - $\phi$. The challenge consists in identifying the structures detected in the Faraday depth cube with physical structures in the interstellar medium for which we know the position in real space, $\alpha$ - $\delta$ - $z$ (from e.g. H I and H$\alpha$ line observations, dust extinction measurements from stellar redenning). If such a correlation is found then we can derive (i) the intensity and orientation of $\vec{B}_\perp$ from the synchrotron polarized intensity and (ii) the mean line-of-sight magnetic field $\vec{B}_{||}$ in the ionized regions from their Faraday depth. Or, as is often the case, the structures seen in the Faraday cube reveal the presence of Faraday screens located in front of the background Galactic synchrotron emission, which is then displaced in Faraday depth $\phi$ (Sect. 3.1). In this case, we can measure the Faraday thickness, $\Delta\phi$, of the structure and estimate its mean $\vec{B}_{||}$.

## 3 Towards the physical properties of "Faraday filaments"

### 3.1 The richness of Faraday tomography

Recent LOFAR Faraday depth cubes revealed a bewildering variety of structures in the interstellar medium. In particular, long and linear features that are likely associated with physical structures of ionized gas. A prominent example is the 4° long and 7.′5 wide straight filamentary feature detected in a high Galactic latitude field centred on the quasar 3C196 (labelled A in Fig. 2, Jelić et al. 2015). Figure 2 shows the polarized intensity of the different structures seen at distinct Faraday depths, between $-3$ and $+5\,\mathrm{rad/m^2}$, in the 3C196 field. Structure A (in orange) is a perfect example of a Faraday screen, mentioned above: it displaces the background synchrotron emission (in purple) from $\phi \simeq +2\,\mathrm{rad/m^2}$, where it leaves a hole, to lower Faraday depths of about $+0.5\,\mathrm{rad/m^2}$. The Faraday thickness of structure A is thus $1.5\,\mathrm{rad/m^2}$. Since this feature is not seen in the total intensity maps nor in the currently available H$\alpha$ surveys (typical tracer of ionized gas), which do not have the angular resolution to reveal such a narrow structure, it is hard to determine its physical properties (e.g. distance and free-electron density). Consequently, Jelić et al. (2015) could only use the measured Faraday thickness to place lower limits in the product $n_e B_{||}$. Assuming that feature A is indeed a filament and is located nearby, say within 200 pc (it is unlikely located much beyond this distance, given its large angular size), Jelić et al. estimated a path length $ds = 0.3\,\mathrm{pc}$. As a result, $n_e B_{||} > 6.2\,\mathrm{cm^{-3}}\,\mu\mathrm{G}$ in this Faraday, filamentary, screen.

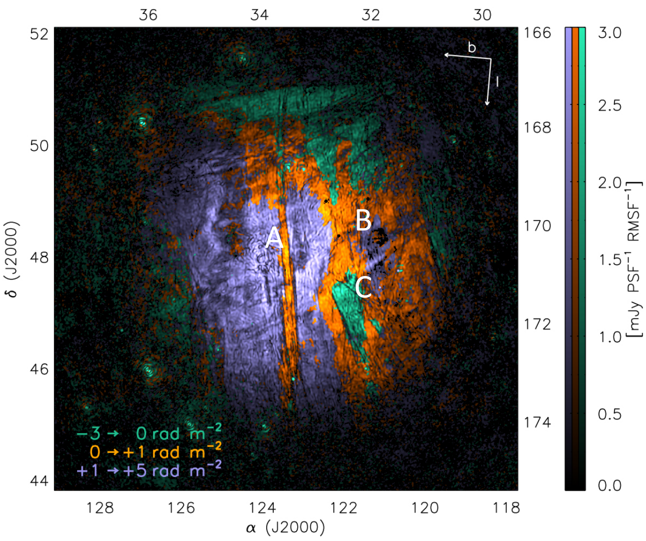


**Fig. 2.** The polarized intensity at different Faraday depth intervals, as indicated in the figure, in the LOFAR 3C196 observations of Jelić et al. (2015). The labels A, B, and C identify noticeable structures in the field.

The primary question that arises from this study is: what is the origin of such filaments that are (so far) only seen in Faraday rotation? To explore their origin we need to know their physical properties, i.e., to associate them with physical structures in the interstellar medium. Indeed, filaments of similar sizes to those detected in Faraday tomography studies are found in H I and H$\alpha$ observations of the interstellar medium (e.g. McCullough & Benjamin 2001; Clark et al. 2014). We are currently carrying out different observational projects with LOFAR, with the goal of investigating the possible connection between "Faraday filaments" and interstellar filaments.

### 3.2 The McCullough & Benjamin interstellar filament

We selected a narrow (20″) and long (2°) filament of ionized gas detected serendipitously in high-resolution H$\alpha$ observations by McCullough & Benjamin (2001) to perform Faraday tomography with LOFAR. From the observed H$\alpha$ intensity of 0.5 R we can estimate its free-electron density, for a given electron temperature and size. Assuming a typical electron temperature of $10^4$ K, that the filament is cylindrical and located within 200 pc (as suggested by its radial velocity), we obtain an electron density of $2\,\mathrm{cm}^{-3}$. Further assuming a typical magnetic field strength in the ionized gas of 0.5–2 $\mu$G, yields a Faraday thickness of 0.3–1.1 rad/m$^2$ for the filament. This is similar to the Faraday thickness of filament A in the LOFAR observations of Jelić et al. (2015).

We used the LOFAR high-band antennas to measure the polarization, between 115 and 175 MHz, of a $\sim 5° \times 5°$ region of the sky centred on the McCullough & Benjamin interstellar filament, at $(l, b) \simeq (140°, 38°)$. After a first data reduction iteration, we produced the Faraday depth cube that covers $\phi = [-40, 40]\,\mathrm{rad/m}^2$ in steps of 0.25 rad/m$^2$. While no signature of the filament is seen, we do detect diffuse polarized emission across the field at high (and negative) Faraday depths, $\phi \sim -33$ to $-28\,\mathrm{rad/m}^2$. We are currently re-processing the LOFAR observations to produce a higher angular resolution Faraday depth cube (better than the present $3'$).

If we do detect the H$\alpha$ filament in the Faraday depth cube, it will represent the first association between a LOFAR Faraday filament and a gaseous structure in the interstellar medium. We will then be able to estimate its magnetic field, combining LOFAR with the ancillary H$\alpha$ observations. In the case of a non-detection, we will give lower limits on the filament's magnetic field. The results will allow us to examine the possible formation scenarios of this structure. McCullough & Benjamin (2001) argue that the most probable origin of the filament is an ionized trail left by photoionization from a star or a compact object, which would also explain its straightness. The authors also consider the possibility that this is an unusual linear filament associated with a large-scale nearby bubble. Indeed, observational and numerical studies (e.g. Planck Collaboration Int. XXXII. 2016; Hennebelle 2013) have shown that interstellar filaments can be formed from turbulent motions in the atomic medium, which stretch/compress the gas into filaments or sheets, thereby stretching/compressing the magnetic field in the same direction. The magnetic field structure is thus a clue to the filament's origin.

## 4 Conclusions

Faraday tomography is proving to be a powerful technique for Galactic magnetism studies. Its main asset is the capability to probe the magnetic field in different regions along the line of sight. LOFAR Faraday tomography studies have started to provide new views into the structure of the interstellar medium, although still incomplete and puzzling. Notably, the detection of long and narrow filamentary structures that are most likely associated with physical structures of ionized gas. Still, it has not yet been possible to establish a connection between, what we name, "Faraday filaments" and gaseous filaments in the interstellar medium. This is precisely the goal of our LOFAR project in which we perform Faraday tomography of a region of the sky that contains an interstellar filament of ionized gas, seen in H$\alpha$ observations. The data are currently being analysed.

M.I.R. Alves acknowledges the support by the Centre National d'Études Spatiales (CNES postdoctoral fellowship). LOFAR, the Low Frequency Array designed and constructed by ASTRON, has facilities in several countries, that are owned by various parties (each with their own funding sources), and that are collectively operated by the International LOFAR Telescope (ILT) foundation under a joint scientific policy.

## References

Brentjens, M. A. & de Bruyn, A. G. 2005, A&A, 441, 1217

Clark, S. E., Peek, J. E. G., & Putman, M. E. 2014, ApJ, 789, 82

Ferrière, K. 2011, Mem. Soc. Astron. Italiana, 82, 824

Hall, J. S. 1949, Science, 109, 166

Haverkorn, M. 2015, in Astrophysics and Space Science Library, Vol. 407, Magnetic Fields in Diffuse Media, ed. A. Lazarian, E. M. de Gouveia Dal Pino, & C. Melioli, 483

Hennebelle, P. 2013, A&A, 556, A153

Hiltner, W. A. 1949, ApJ, 109, 471

Iacobelli, M., Haverkorn, M., & Katgert, P. 2013, A&A, 549, A56

Jelić, V., de Bruyn, A. G., Mevius, M., et al. 2014, A&A, 568, A101

Jelić, V., de Bruyn, A. G., Pandey, V. N., et al. 2015, A&A, 583, A137

McCullough, P. R. & Benjamin, R. A. 2001, AJ, 122, 1500

Planck Collaboration Int. XXXII. 2016, A&A, 586, A135

# ALGORITHMIC ASPECTS FOR THE RECONSTRUCTION OF SPATIO-SPECTRAL DATA CUBES IN THE PERSPECTIVE OF THE SKA

D. Mary[1], A. Ferrari[1], C. Ferrari[1], J. Deguignet[1] and M. Vannier[1]

**Abstract.** With millions of receivers leading to TerraByte data cubes, the story of the giant SKA telescope is also that of collaborative efforts from radioastronomy, signal processing, optimization and computer sciences. Reconstructing SKA cubes poses two challenges. First, the majority of existing algorithms work in 2D and cannot be directly translated into 3D. Second, the reconstruction implies solving an inverse problem and it is not clear what ultimate limit we can expect on the error of this solution. This study addresses (of course partially) both challenges. We consider an extremely simple data acquisition model, and we focus on strategies making it possible to implement 3D reconstruction algorithms that use state-of-the-art image/spectral regularization. The proposed approach has two main features: (i) reduced memory storage with respect to a previous approach; (ii) efficient parallelization and ventilation of the computational load over the spectral bands. This work will allow to implement and compare various 3D reconstruction approaches in a large scale framework.

Keywords: SKA, radio, inverse problems, parallelization, spatio-spectral cubes.

## 1 Introduction

The SKA* is an ambitious international project aimed at building the world's largest radio telescope. The full array will be built over two sites in Australian and African deserts. The frequency range that the SKA is expected to cover is unprecedented, from approximately 50 MHz to 15 GHz (and possibly up to $\sim$ 30 GHz in its final phase).

In the Murchison desert of Western Australia will reside the lowest frequency part of the instrument ($\sim$50 to 350 MHz). The telescope will consist there of hundreds of thousands of log–periodic dual–polarised antenna elements, which will be arranged in hundreds of stations of a few metres in diameters. The signals of all elements within one station will be combined numerically and all the stations will be combined together, forming a so-called "aperture array". The inter-station distances will range from a few tens of meters in the central core area to several tens (even hundreds) of kilometres in the outer distribution, which will probably include spiral arms.

In the Karoo desert (800 km North of Cape Town) will be built the part of SKA operating at higher frequencies (above 350 MHz). The array will consist of hundreds of 15 m diameter dishes, with a distribution eventually spreading in different states of Africa. The maximum baselines will be progressively increased from several tens to at least several hundreds of kilometres. Further technical developments are planned, aiming to cover the intermediate frequency part of the SKA also with dense aperture arrays.

Extending significantly the performances of other contemporary antenna arrays in radio, SKA will allow for increased survey speed, sensitivity, angular resolution and for observing simultaneously in a large number of frequency bands. In turn, imaging algorithms will have to be able to reconstruct high fidelity and high dynamic range sky cubes. The final quality of the astrophysical data of SKA rely heavily on joint efforts from radioastronomy, signal processing, optimization and computer sciences. Owing to the gigantic complexity of SKA telescope, this is perhaps more critical than for any other ground-based astronomical instrument.

The purpose of this communication is first to outline the organization, development and challenges posed by the SKA. We focus in these points in Sec. 2.

---

[1] Lab. J.-L. Lagrange, Université de Nice Sophia Antipolis, CNRS, Observatoire de la Côte d'Azur, Parc Valrose, F-06108 Nice cedex 02, France

*For an extended version of information presented below on SKA see Ferrari (2016).

We then turn to the reconstruction of SKA cubes, which poses two challenges. First, the majority of existing algorithms work in 2D. Even if the spectral dimension can be tackled with similar methods as for the spatial dimensions, similar algorithms cannot be translated into 3D. The reason is that when the number of data and optimization variables is too large, classical algorithms suffer from one of two opposite, but equally lethal issues: an immediate stop (related to memory overflows) or an endless iterative process (related to computational load). Second, the reconstruction implies solving an inverse problem and it is not clear what ultimate limit we can expect on the error of this solution.

The study below addresses (partially of course) both challenges. We consider an extremely simplistic data acquisition model (Sec. 3), ignoring for instance calibration errors, direction depending effects or gridding issues. The focus here is on strategies allowing to make possible the implementation of large-scale 3D reconstruction algorithms benefitting from state-of-the-art image/spectral reconstruction methods (Sec. 4). We present some results and perspectives in Sec. 5.

The present paper is a review of some contributions from (Ferrari et al. 2015; Ferrari 2016; Deguignet et al. 2016).

## 2 SKA organization, developments and challenges

### 2.1 Project organization

The current status of this ambitious international project is the result of a quite long development history. Planning future infrastructures and data processing strategies is a major management challenge, involving engineers, astronomers, and project managers (see Ferrari (2016) and references therein), and requiring governance.

The SKA governance, called SKA Organisation (SKAO) includes today ten formal members (Australia, Canada, China, India, Italy, New Zealand, South Africa, Sweden, the Netherlands and the United Kingdom), with in addition several countries that have expressed their potential interest in joining the Organisation.

In the case of France, the SKA project is completing the pre-construction phase without France as a formal partner, but France is invited as an observer to International SKA Organisation meetings. During 2014, the French astronomy community developed a roadmap for future research at the CNRS - National Institute for Science of the Universe (INSU). Recognizing the undeniable scientific and technological interest of the SKA, the CNRS-INSU, together with national Observatories and Universities already involved in the SKA project, created in 2016 the SKA-France organization[†], which coordinates the activities of scientific, technological and industrial participants from France. SKA-France is intended to complement the work done by the CNRS Action Spécifique SKA-LOFAR, which has a mandate to encourage the scientific involvement of the French community in current and future radio astronomical facilities.

The general director of SKAO chairs a board, which includes representatives of member countries and which is called to take all relevant decisions for the development of the project. A scientific director is responsible for the parallel and complementary advancement of the SKA scientific preparation.

In agreement with SKA technical, methodological and scientific ambitions, the SKAO has identified several key work packages[‡] (WP). These WP will allow for assembling the different telescope components, building the necessary infrastructures, dealing with data transport, energy issues related to this “big machine”, managing the telescope, and, last but not least, processing the data, store them and making them usable by the astronomical community.

For technical WP, the SKA largely builds on the construction and operation of precursors and pathfinders instruments: SKA precursors are the three instruments that are located on the future SKA sites (MWA, ASKAP and MeerKAT), while SKA pathfinders are radio telescopes engaged in SKA related technology and science studies (a census of these instruments is available at the SKA web page[§]). Through the huge progress in antenna design and wide bandwidth feeds, as well as in the ability to transport and process massive amounts of data, a new generation of radio telescopes is being built with these instruments, that pave the way to SKA.

At low frequencies, instruments such as the Low-Frequency Array (LOFAR, in Europe, with its major extension NenuFAR, in France) and the Murchison Widefield Array (MWA, in Australia) employ several thousands of inexpensive dipole antennas arranged within stations without moving parts; the signals from these stations are digitized, transported to a central processor and combined to emulate a conventional dish antenna. These

[†] see `https://ska-france.oca.eu/index.php/en/home-ska-en`

[‡] see `https://www.skatelescope.org/wp/` for a list of the SKA Work Packages

[§] `https://www.skatelescope.org/precursors-pathfinders-design-studies/`

telescopes process the signal on sufficiently short time scales to correct for the ionospheric changes, severely affecting radio observations below a few hundreds MHz.

At higher frequencies (from hundreds of MHz to a few GHz), two major arrays are being built, which are formed by tens of big ($\sim$12-15m diameter) dishes: ASKAP in Australia and MeerKAT in South Africa. In addition, several major radio facilities have been recently upgraded to improve their performance, including, for instance the Jansky Very Large Array (JVLA, in New Mexico), the Giant Meterwave Radio Telescope (GMRT, in India) and the Westerbork Synthesis Radio Telescope (WSRT, in the Netherlands).

### 2.2 SKA development

In 2012 the SKA board proceeded to the selection of the SKA construction sites. Both Australia and South African deserts, sites of the three precursors, were considered as excellent locations for building the arrays covering the low- and mid-frequency part of the electromagnetic spectrum. At that phase, in particular, both precursors going to GHz frequencies (ASKAP and MeerKAT) were planned to be integrated to the future SKA antennas. In 2015, however, a redefinition of the design needed to be developed (known as "re-baselining") due to cost issues. This led to the definition of the first phase of SKA (generally referred to as "SKA1"), that will consist of two arrays:

- **SKA1-LOW** in Australia, including $\sim$131,000 dipoles covering the frequency range from $\sim$50 MHz to $\sim$350 MHz. The array will be in the same region of ASKAP and will have a maximum baseline of approximately 80 km;
- **SKA1-MID** in South Africa, including $\sim$130 15m diameter dishes and observing frequencies from 350 MHz to 13.8 GHz, with a $\Delta\nu \approx 3$ GHz hole around 1.5 GHz. The instrument will integrate the MeerKAT antennas, for a total number of $\sim$200 dishes, separated by a maximum distance of $\sim$150 km.

Based on these decisions, the construction of SKA1, which corresponds to $\approx$10% of the full final instrument, is planned to start in 2018, with the first science operations beginning in early 2020's. SKA1 will be a single observatory built over three sites, among which one will host the head-quarter (at Jodrell Bank, in UK, site decision taken in 2015) and the other the two telescopes, SKA1-LOW in Australia and SKA1-MID in South Africa.

After 2023, the instrument is planned to be further developed towards the full square kilometre total collecting area. This will of course require the necessary preparation from the technological and scientific point of view, for which SKA1 will play a crucial role, but also a likewise important budget and managing strategy. In order to provide a long-term government commitment and funding stability, the SKAO is thus currently evolving towards an intergovernmental organisation (IGO), similar to other big research infrastructures (such as ESO, ESA and CERN).

### 2.3 Challenges

The power of the SKA comes from the large number of receivers, the large fields of view made available and the high numbers of spectral bands. The large scale nature of this instrument poses automatically several challenges, which make mandatory dedicated research in various fields working in close connexion:

- ***Computer sciences***. An immediate challenge is that of the processing and storage of the data produced simultaneously by myriads of receivers. In its first phase (SKA1), when the total collecting area will be approximately one tenth of the final expected array, the total raw data output for the low- and mid-frequency parts of the telescope will be of the order of 150 and 2 Tbytes per second, respectively. This results in several Zbytes ($10^{21}$ bytes) of raw data per year, which exceeds the total global internet traffic rate at present day. Even after data reduction, the archived data rate for astronomical exploitations is expected to be of the order of 50 to 300 Pbytes per year. Data processing and storage will require by early 2020's super–computers characterised by about 10 times better performances than the fastest machines available today.
- ***Signal Processing***. An instrument like SKA requires the outputs of many different elements to be combined. Beyond issues related to the data rate, all array elements must be modeled and calibrated for this massive combination to be reliable. The calibration part of the array must estimate two main quantities. First, the gain response and noise power of each antenna (or group of dipoles) (Wijnholds &

van der Veen 2009; van der Veen & Wijnholds 2013; van der Tol et al. 2007). Second, the atmospheric perturbation on the propagation of radio waves, especially the phase delays caused by the ionosphere, which are time and wavelength dependent (van der Tol 2009; Thompson et al. 2001; Intema et al. 2009). Many calibration models and algorithms have been devised in the signal processing litterature. Another important branch where Signal Processing is very active is the imaging part, where sparsity based models in particular have proved very useful in radiointerferometric imaging (see below).

- ***Optimization***. Optimization techniques express problems in mathematical form by means of objectives and constraints. These techniques allow to address some properties of the solution (*e.g.* existence, unicity,...), to derive systematic methods to solve the problem, and to study the convergence rate towards the solution (see *e.g.* Canu et al. (2016) for an introduction). Optimization consequently plays a central role for designing calibration, imaging or more generally processing algorithms that are both computationally efficient and able to cope with several disturbance sources, see *e.g.* Brossard et al. (2016) and references therein.

The success of the interplay between the expertises above in the context of large scale data is recognized as a crucial point from the SKAO, which has proposed several grants within the program *AstroCompute in the Cloud* in conjunction with Amazon Web Services (AWS). This program encourages development and code optimization for massive data for image analysis, calibration and data mining, visualization, management and sharing.

The study below reflects some works going in the direction of allying signal processing, optimization and parallelization tools. Our focus here is not on the data model, which is taken very simple and ignores for instance calibration, gridding issues or direction dependent effects. Our focus is on devising reconstruction methods able to cope with large (multiband) data while using efficient regularization techniques. In fact, building algorithms that are both able to reconstruct large data cubes with affordable computing power and high fidelity is a challenge *per se* and this work is a step in this direction.

## 3 Data model and reconstruction approach

The considered data acquisition model is sketched in Fig. 1. The unknown reference sky is discretized and represented by means of parameters (pixels or voxels values) corresponding to fluxes integrated over some sky patch and spectral band. The interferometer samples information on the Fourier spectrum of $\boldsymbol{x}^\star$ (bottom left panel) at locations specified by the antennas positions and the observing wavelength (bottom right panel). The samples are called complex visibilities. Because the antennas are sparsely disseminated on the ground, the sampling in the Fourier space is sparse as well. When observing in a set of $L$ frequency bands, the interferometer provides $L$ radially aligned Fourier samples for each antenna/station baseline (in fact twice this number by symmetry). As Earth rotates, the position of the antennas with respect to the sky changes and the number of collected samples increases. A grey image of the sky $\boldsymbol{i}^d$ can be formed by computing the inverse Fourier Transform (top right panel). We shall assume that this image is related to the grey image by $\boldsymbol{i}^d = \boldsymbol{H}\boldsymbol{x}^\star$, and that $\boldsymbol{H}$ represents a convolution.

Of course, it is also possible to produce $L$ narrow band sky images $\{\boldsymbol{i}_\ell^d\}, \ell = 1, \ldots, L$, by considering only the samples in a given spectral band (Fig. 2). In this case, the dirty image in each channel is $\boldsymbol{i}_\ell^d = \boldsymbol{H}_\ell \boldsymbol{x}_\ell^\star$, where $\boldsymbol{H}_\ell$ and $\boldsymbol{x}_\ell^\star$ represent respectively the convolution matrix and the reference sky image in band $\ell$. For convenience, the $L$ reconstructed images ($N$ pixels each) will be stacked in an $N \times L$ matrix $\boldsymbol{X} := [\boldsymbol{x}_1, \ldots, \boldsymbol{x}_\ell]$, whose $\ell^{th}$ column represents the optimization variables (voxel values) for channel $\ell$. Inverting the operators $\boldsymbol{H}_\ell$ to retrieve $\mathbf{x}_\ell^\star$ from $\boldsymbol{i}_\ell^d$ is not possible owing to the 'holes' in the Fourier space: the system is blind to some frequency contents and simply provides no information on it. (The problem is even worse in practice, because samples are never on regular grids and the operator from image to complex visibilities often departs from a simple Fourier Transform, which increases the causes of non invertibility.)

In such situations a classical approach is to formulate the reconstruction problem as an inverse, ill-posed problem and to a introduce a cost function balancing a data fidelity term and a regularization term. This function will be minimized with dedicated optimization techniques. In the current description, we consider a cost function leading to a minimization problem of the type

$$\min_{\boldsymbol{X}} \sum_{\ell=1}^{L} \frac{1}{2\sigma_\ell^2} \|\mathbf{i}_\ell^d - \boldsymbol{H}_\ell \boldsymbol{x}_\ell\|^2 + f_{\mathrm{reg}}(\boldsymbol{X}) \tag{3.1}$$

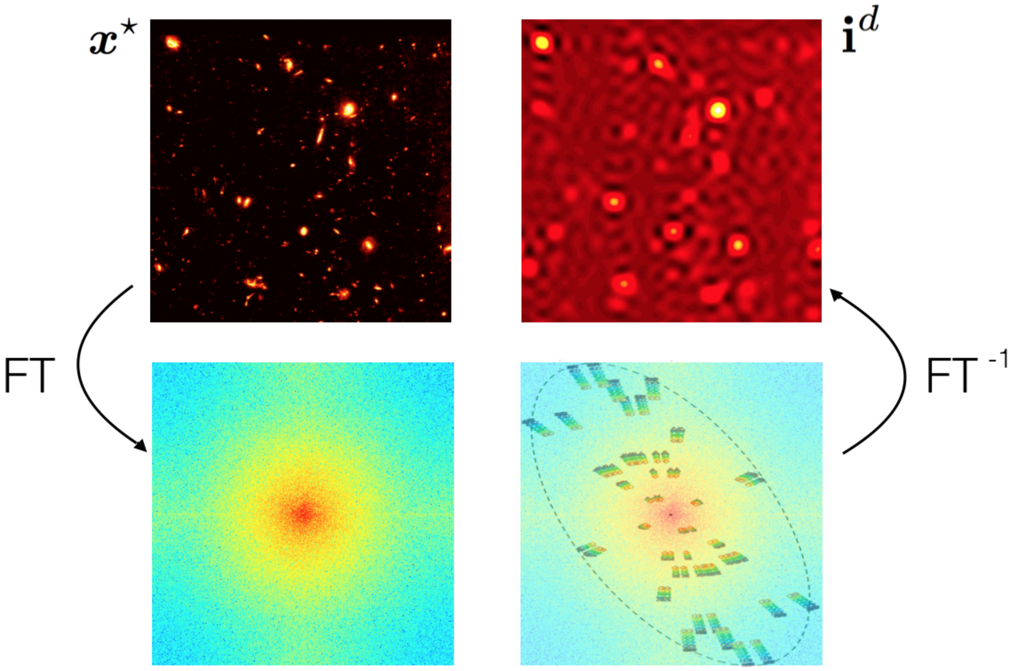


**Fig. 1. Top left**: the reference sky $\boldsymbol{x}^\star$ (sum over several bands). **Bottom left:** modulus of the Fourier Transform of $\boldsymbol{x}^\star$. The origin is at the center of the image. **Bottom right**: Sketch of an interferometric sampling pattern. The Fourier samples collected by the radio array are located by color points (from red to blue). Points of the same color correspond to samples acquired in the same spectral band. **Top right**: Sky estimate by inverse Fourier transform considering all samples available (*i.e.*, the $L$ subsets if there are $L$ bands) and setting missing samples to 0: 'grey' dirty image, $\boldsymbol{i}^d$.

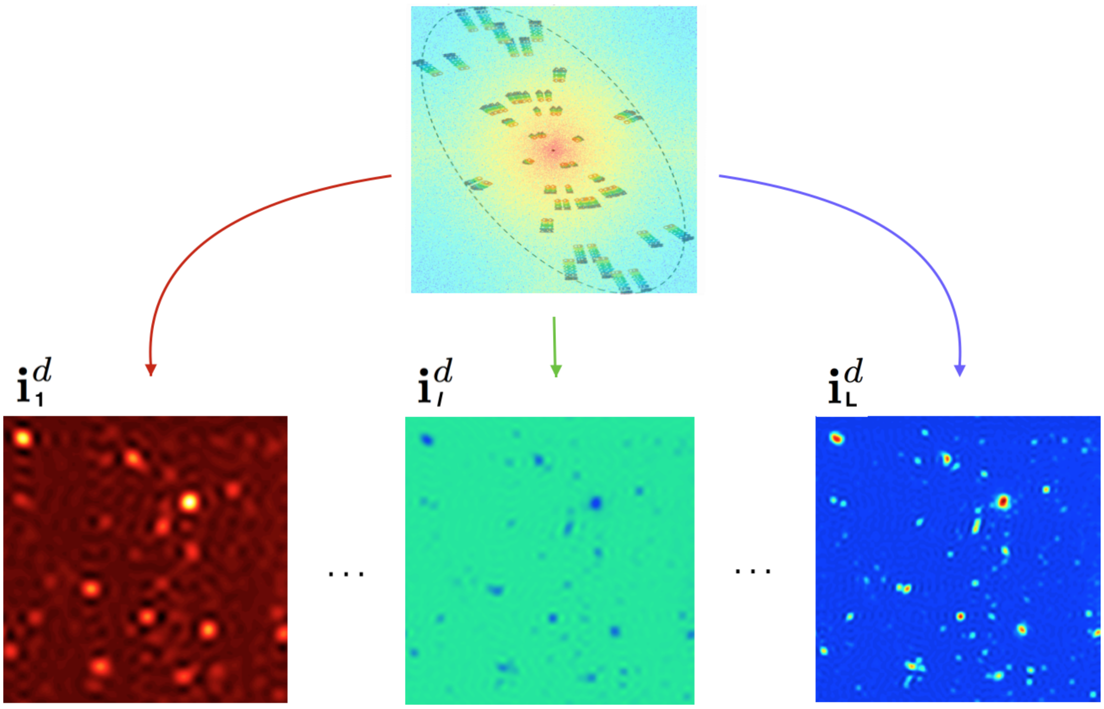


**Fig. 2.** $L$ narrow band dirty images produced from the $L$ subsets of complex visibilities.

where $\sigma_\ell^2$ is the noise variance in dirty image $\boldsymbol{y}_\ell$, and where a positivity constraint can be further imposed on $\boldsymbol{X}$. The first term of (3.1) guarantees that the proposed solution is in agreement (in the specified $\ell_2$ sense) with the data. This term alone is not sufficient, because infinitely many sky models may fulfill any fixed level of data agreement (for a given candidate solution $\boldsymbol{x}_\ell$, adding anything in the kernel of $\boldsymbol{H}_\ell$ does not change anything to the first term). The role of the second term is to help choosing among all solutions one that is compatible with respect to some regularity criterion. The last decade has shown that regularization based on sparse representations in appropriate transform domains can be very effective. Such regularization terms can be formulated in an analysis or in a synthesis framework. These two formalisms are discussed and compared e.g. in Elad et al. (2007). For both approaches, redundant dictionaries improve over non redundant (orthogonal) ones. For narrow-band radio-interferometric imaging, state-of-the-art results appear so far to be obtained with union of bases (Carrillo et al. 2012, 2014; Onose et al. 2016) and IUWT (Garsden et al. 2015; Dabbech et al. 2015). We consider a regularization of the form:

$$f_{\mathrm{reg}}(\boldsymbol{X}) := \mathbf{1}_{\mathbb{R}^+}(\boldsymbol{X}) + \mu_S \sum_{\ell=1}^{L} \|\mathbf{W}_S \boldsymbol{x}_\ell\|_1 + \mu_\nu \sum_{n=1}^{N} \|\mathbf{W}_\nu \boldsymbol{x}^n\|_1. \tag{3.2}$$

In (3.2), $\boldsymbol{x}_\ell$ (the $\ell^{th}$ column of $\boldsymbol{X}$) corresponds to the image at wavelength $\ell$ and $\boldsymbol{x}^n$ (the $n^{th}$ row of $\boldsymbol{X}$) is the spectrum associated to pixel $n$. $\mathbf{W}_S$ and $\mathbf{W}_\lambda$ are the operators corresponding to the spatial and spectral decomposition respectively. IUWT will here be considered for the spatial regularization and a cosine decomposition (DCT) for the spectral model.

Note that the first sum in (3.2) decouples into $L$ terms (one per image) and this is also true for the sum in (3.1). In contrast, the second sum in (3.2) decouples into $N$ terms, each related to one spectrum. This structure is important as it allows to parallelize some computations spectrally and other spatially. Note, however, that each voxel is tied spatially to all voxels at the same wavelength (through the first two sums above) and also tied spectrally to all voxels in the same spectrum (through the second sum). Hence, the problem cannot be globally decoupled and it is truly spatio-spectral.

It is interesting to compare the few existing multi-frequency reconstruction algorithms with approach (3.2). Most of the existing approaches rely on a physical model for the spectral dependence of astrophysical radio sources. Rau & Cornwell (2011) use a Taylor expansion of a model power-law. Other (parametric) models for this spectral dependence have been proposed by Junklewitz et al. (2014), who address the estimation problem using a Bayesian framework and by Bajkova & Pushkarev (2011), who propose a constrained maximum entropy estimation algorithm.

These methods rely on spectral models and thus clearly offer advantages and estimation accuracy when the model is indeed appropriate. However, across the broad frequency coverage of current radio facilities, radio sources exhibiting complex spectral shapes (not simple power laws) are expected. For instance, the works of Kellermann (1974) evidence that some sources may exhibit one or more relative minima, breaks, and turnovers. For the new generation of low frequency telescopes such as LOFAR, recent studies have also shown that second order broadband spectral models are often insufficient (Scaife & Heald 2012). Attempts to relax the spectral power-law model are thus necessary. One such attempt, by Wenger & Magnor (2014), formulates the problem as an inverse problem with a smooth spectral regularization allowing for local deviations. The present approach is another attempt of this kind, as it does not either rely on a spectral power-law model. Examples of situations where this approach can be advantageous are shown in Deguignet et al. (2016).

## 4 Optimization

One drawback of the works by Ferrari et al. (2015) was the necessity to solve a large linear system at each iteration during the minimization. This was kept computationally tractable by using for $\boldsymbol{W}_S$ a concatenation of orthogonal wavelet bases in (Ferrari et al. 2015; Carrillo et al. 2014). Another drawback is the amount of memory. In order to reduce the required memory, we have proposed in (Deguignet et al. 2016) to use the primal-dual optimization algorithm by Condat (2014) and Vũ (2011). Application of Condat (2014) and Vũ (2011) to (3.1, 3.2) leads to Algorithm 1, where:

$$\mathrm{sat}(u) := \begin{cases} -1 & \text{if} \quad u < -1 \\ 1 & \text{if} \quad u > 1 \\ u & \text{if} \quad |u| \leq 1 \end{cases} \tag{4.1}$$

and $(\cdot)_+$ is the projection on the positive orthant. Parameters $\rho$, $\sigma$ and $\tau$ are fixed according to Condat (2014) in order to guarantee the convergence of the algorithm.

---

**Algorithm 1:** MUFFIN algorithm.

**Initialize**: $\boldsymbol{x}$, $\mathbf{U}$ and $\mathbf{V}$

1 **repeat**

2 $\quad \boldsymbol{\nabla} = \left(\boldsymbol{H}_1^\dagger(\boldsymbol{H}_1\boldsymbol{x}_1 - \mathbf{i}_1^d) \,|\, \cdots \,|\, \boldsymbol{H}_\ell^\dagger(\boldsymbol{H}_\ell\boldsymbol{x}_\ell - \mathbf{i}_\ell^d)\right)$ $\tilde{\boldsymbol{X}} = \left(\boldsymbol{X} - \tau(\boldsymbol{\nabla} + \mu_S\boldsymbol{W}_S^\dagger\boldsymbol{U} + \mu_\nu\boldsymbol{V}\boldsymbol{W}_\nu^\dagger)\right)_+$

$\quad \tilde{\boldsymbol{U}} = \mathrm{sat}\left(\boldsymbol{U} + \sigma\mu_S\boldsymbol{W}_S(2\tilde{\boldsymbol{X}} - \boldsymbol{X})\right)$ $\tilde{\boldsymbol{V}} = \mathrm{sat}\left(\boldsymbol{V} + \sigma\mu_\nu(2\tilde{\boldsymbol{X}} - \boldsymbol{X})\boldsymbol{W}_\nu\right)$

$\quad (\boldsymbol{X},\boldsymbol{U},\boldsymbol{V}) = \rho(\tilde{\boldsymbol{X}},\tilde{\boldsymbol{U}},\tilde{\boldsymbol{V}}) + (1-\rho)(\boldsymbol{X},\boldsymbol{U},\boldsymbol{V})$

3 **until** *stopping criterion is satisfied*;

**Return** : $\boldsymbol{X}$

---

Algorithm 1 requires 6 variables $(\tilde{\boldsymbol{X}},\boldsymbol{X},\tilde{\boldsymbol{U}},\boldsymbol{U},\tilde{\boldsymbol{V}},\boldsymbol{V})$ in addition to the gradient and 5 if $\rho = 1$, while 10 variables were necessary in the previous approach (Ferrari et al. 2015). Moreover, in contrast to Ferrari et al. (2015) and Carrillo et al. (2014), Algorithm 1 does not require to solve at each iteration large linear systems. This allows the use of highly redundant, translation invariant wavelet transforms like, for instance, IUWT (Starck et al. 2007).

A major advantage of Algorithm 1 is that the most demanding steps are separable with respect to the wavelengths, leading to the following parallel implementation. MUFFIN is distributed on a cluster where the master node centralises the reconstructed data cube and each wavelength is associated to a compute node $\ell$. The algorithm iterates as follows:

1. The master node computes $\boldsymbol{T} = \mu_\lambda\boldsymbol{V}\boldsymbol{W}_\lambda^\dagger$ and sends the column $\ell$ of $\boldsymbol{T}$, denoted as $\boldsymbol{t}_\ell$, to node $\ell$.

2. Each node $\ell = 1\ldots L$ computes sequentially:

$$\boldsymbol{\nabla}_\ell = \boldsymbol{H}_\ell^\dagger(\boldsymbol{H}_\ell\boldsymbol{x}_\ell - \boldsymbol{y}_\ell) \tag{4.2}$$
$$\boldsymbol{s}_\ell = \mu_S\boldsymbol{W}_S^\dagger\boldsymbol{u}_\ell \tag{4.3}$$
$$\tilde{\boldsymbol{x}}_\ell = (\boldsymbol{x}_\ell - \tau(\boldsymbol{\nabla}_\ell + \boldsymbol{s}_\ell + \boldsymbol{t}_\ell))_+ \tag{4.4}$$
$$\tilde{\boldsymbol{u}}_\ell = \mathrm{sat}\,(\boldsymbol{u}_\ell + \sigma\mu_S\boldsymbol{W}_S(2\tilde{\boldsymbol{x}}_\ell - \boldsymbol{x}_\ell)) \tag{4.5}$$
$$(\boldsymbol{x}_\ell,\boldsymbol{u}_\ell) = \rho(\tilde{\boldsymbol{x}}_\ell,\tilde{\boldsymbol{u}}_\ell) + (1-\rho)(\boldsymbol{x}_\ell,\boldsymbol{u}_\ell) \tag{4.6}$$

3. Each node sends $\boldsymbol{x}_\ell$ and $\tilde{\boldsymbol{x}}_\ell$ to the master and the master computes sequentially:

$$\tilde{\boldsymbol{V}} = \mathrm{sat}\left(\boldsymbol{V} + \sigma\mu_\lambda(2\tilde{\boldsymbol{X}} - \boldsymbol{X})\boldsymbol{W}_\lambda\right) \tag{4.7}$$
$$\boldsymbol{V} = \rho\tilde{\boldsymbol{V}} + (1-\rho)\boldsymbol{V} \tag{4.8}$$

Note that the particularly time consuming steps associated to (4.2,4.3,4.5) are computed in parallel at each wavelength. This is particularly important for (4.3) when the transform is not orthogonal. In such cases, the adjoint operator differs from the perfect reconstruction synthesis operator and its implementation may not benefit from the same fast algorithm.

A distributed memory implementation of MUFFIN should be available soon¶. The algorithm has been implemented in *Julia* (Bezanson et al. 2014).

## 5 Some results and future works

We show here one example illustrating the efficiency of using a joint spatio-spectral approach with respect to a channel per channel reconstruction. Simulations use PSFs obtained with the HI-inator package‖ based on MeqTrees software (Noordam & Smirnov 2010) with MeerKAT arrays configuration. The Fourier coverage

---

¶`https://github.com/andferrari/muffin.jl`

‖`https://github.com/SpheMakh/HI-Inator`

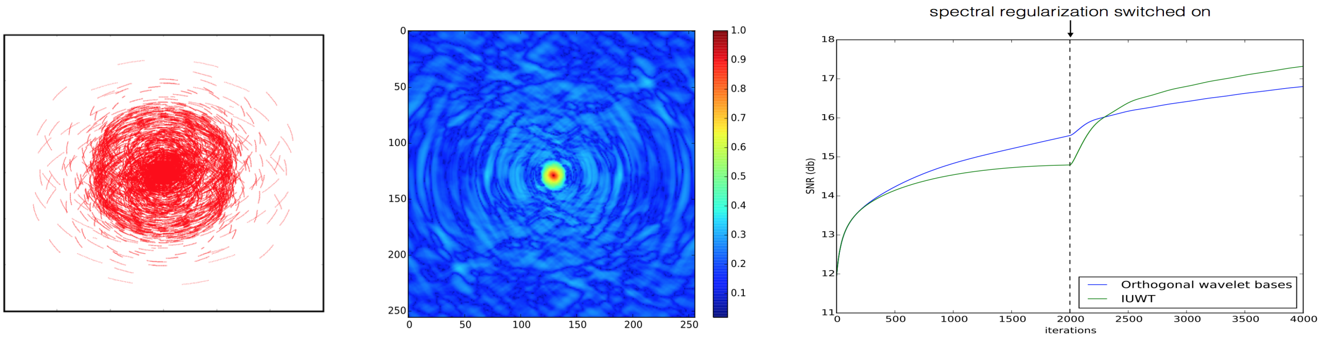


**Fig. 3. Left:** considered $(u, v)$ coverage. **Center:** PSF in one band. **Right:** Comparison of the SNR for union of orthogonal bases and IUWT. Spectral regularization is turned on at iteration 2000.

correspond to a total observation time of 8 hours. For the purpose of making Monte Carlo simulations, we simulated small cubes of 15 frequency bands with images of $256 \times 256$ pixels.

In Algorithm 1, we compare the case where $\boldsymbol{W}_S$ in (4.5) corresponds to "$2^{nd}$ generation" IUWT (Starck et al. 2007) (and $\boldsymbol{W}_S^\dagger$ in (4.3) is the exact corresponding adjoint operator), or to the union of orthogonal bases used by Ferrari et al. (2015). The sky corresponds to the radio emission of an HII region in the M31 galaxy. A sky cube is computed from this real sky image by applying a first order power-law spectrum model. The $256 \times 256$ map of spectral indices was constructed following the procedure detailed in Junklewitz et al. (2014): for each pixel, the spectral index is a linear combination of an homogeneous Gaussian field and the reference sky image. A Gaussian noise corresponding to 10 dB was finally added to the dirty images to simulate instrumental and model errors. The parameters of the optimization algorithm are set to $\rho = 1$, $\sigma = 1$ and $\tau = 10^{-5}$.

A critical problem for the deconvolution of large data cubes is the calibration of the regularization parameters $\mu_S$ and $\mu_\lambda$. We decouple the calibration in two steps:

1. $\mu_\lambda$ is first set to 0: the problem is separable with respect to the wavelengths and each node independently iterates Eqs. (4.2-4.6) with $\boldsymbol{t}_\ell = \boldsymbol{0}$. This setting avoids data transfers with the master node. It is relatively fast and allows for multiple runs to calibrate $\mu_S$, *e.g.* by cross-validation.

2. The second step keeps $\mu_S$ and the $\boldsymbol{X}$ estimated in step 1) and calibrates $\mu_\lambda$ using the full algorithm with $\boldsymbol{X}$ as an initial condition.

Fig. 3 compares the reconstruction Signal to Noise Ratio (SNR) for the union of bases (blue) and IUWT (green) as a function of the iterations. SNR is here defined as:

$$\mathrm{SNR}(\boldsymbol{X}, \boldsymbol{X}^\star) := 10 \log_{10} \left( \frac{\|\boldsymbol{X}^\star\|_2^2}{\|\boldsymbol{X} - \boldsymbol{X}^\star\|_2^2} \right) \tag{5.1}$$

where $\boldsymbol{X}$ is the estimated solution and $\boldsymbol{X}^\star$ the "sky truth". The first 2000 iterations correspond to step 1) with $\mu_\lambda = 0$ and $\mu_S = 0.25$, and the subsequent iterations to step 2) with $\mu_S = 0.25$ and $\mu_\lambda = 3.0$. The value of $\mu_S = 0.25$ in 1) and $\mu_\lambda = 3$ in 2) were set, for both types of wavelets, after trials and errors in the range $[10^{-4}\ 10^1]$ and best performances were retained.

The evolution of the SNRs after iteration 2000, i.e. when $\mu_\lambda > 0$ clearly evidences the gain obtained through a joint spatio-spectral reconstruction for both approaches. We see that while performances of both approaches are comparable, they relative behavior depend on the regularization and on the number of iterations (which is an important point in a large scale framework). Indeed, such questions deserve further studies. Those are outside the scope of the present paper but are made possible with the parallel implementation proposed in this contribution.

## 6 Acnkowledgements

This work was supported by ANR project MAGELLAN (ANR-14-CE23-0004-01).

## References

Bajkova, A. & Pushkarev, A. 2011, Monthly Notices of the Royal Astronomical Society, 417, 434

Bezanson, J., Edelman, A., Karpinski, S., & Shah, V. B. 2014, CoRR, abs/1411.1607

Brossard, M., El Korso, M. N., Pesavento, M., et al. 2016, ArXiv e-print: 1609.02448

Canu, S., Flamary, R., & Mary, D. 2016, in Introduction to Optimization with Applications in Astronomy and Astrophysics, EAS Publications series, ed. D. Mary et al., 127–162

Carrillo, R., McEwen, J., & Wiaux, Y. 2012, Monthly Notices of the Royal Astronomical Society, 426, 1223

Carrillo, R., McEwen, J., & Wiaux, Y. 2014, Monthly Notices of the Royal Astronomical Society, 439, 3591

Condat, L. 2014, Signal Processing Letters, IEEE, 21, 985

Dabbech, A., Ferrari, C., Mary, D., et al. 2015, Astronomy and Astrophysics, 576, A7

Deguignet, J., Ferrari, A., Mary, D., & Ferrari, C. 2016, in Proceedings EUSIPCO 2016

Elad, M., Milanfar, P., & Rubinstein, R. 2007, Inverse Problems, 23, 947

Ferrari, A., Deguignet, J., Ferrari, C., et al. 2015, in SKA Pathfinders Radio Continuum Surveys (SPARCS)

Ferrari, C. 2016, in The Renaissance of Radio Astronomy: towards the SKA, EAS Publications Series, ed. D. Mary et al., Vol. 78-79, 21–44

Garsden, H., Girard, J. N., Starck, J.-L., et al. 2015, Astronomy and Astrophysics, 575, A90

Intema, H. T., van der Tol, S., Cotton, W. D., et al. 2009, Astronomy & Astrophysics, 501, 1185

Junklewitz, H., Bell, M., & Enßlin, T. 2014, arXiv.org, 4711

Kellermann, K. I. 1974, Radio Galaxies and Quasars, ed. G. L. Verschuur, K. I. Kellermann, & V. van Brunt, 127

Noordam, J. & Smirnov, O. 2010, Astronomy and Astrophysics, 524, A61

Onose, A., Carrillo, R. E., Repetti, A., et al. 2016, MNRAS, 462, 4314

Rau, U. & Cornwell, T. J. 2011, Astronomy and Astrophysics, 532, 71

Scaife, A. & Heald, G. 2012, Monthly Notices of the Royal Astronomical Society: Letters, 423, L30

Starck, J.-L., Fadili, J., & Murtagh, F. 2007, Image Processing, IEEE Transactions on, 16, 297

Thompson, A. R., Moran, J. M., & Swenson, G. W. 2001, Interferometry and Synthesis in Radio Astronomy; 2nd ed. (Wiley-VCH)

van der Tol, S. 2009, PhD thesis, Delft University of Technology

van der Tol, S., Jeffs, B. D., & van der Veen, A. J. 2007, IEEE Transactions on Signal Processing, 55, 4497

van der Veen, A.-J. & Wijnholds, S. J. 2013, in Handbook of Signal Processing Systems (Springer), 421–463

Vũ, B. C. 2011, Advances in Computational Mathematics, 38, 667

Wenger, S. & Magnor, M. 2014, A Sparse Reconstruction Algorithm for Multi-Frequency Radio Images, Tech. rep., Computer Graphics Lab, TU Braunschweig

Wijnholds, S. J. & van der Veen, A.-J. 2009, IEEE Transactions on Signal Processing, 57, 3512

*SF2A 2016*
*C. Reylé, J. Richard, L. Cambrésy, M. Deleuil, E. Pécontal, L. Tresse and I. Vauglin (eds)*

# NON-THERMAL EMISSION AND DYNAMICAL STATE OF MASSIVE GALAXY CLUSTERS FROM $CLASH$ SAMPLE

M. Pandey-Pommier[1], J. Richard[1], F. Combes[2], A. Edge[3], B. Guiderdoni[1], D. Narasimha[4], J. Bagchi[5] and J. Jacob[6]

**Abstract.** Massive galaxy clusters are the most violent large scale structures undergoing merger events in the Universe. Based upon their morphological properties in X-rays, they are classified as un-relaxed and relaxed clusters and often host (a fraction of them) different types of non-thermal radio emitting components, viz., 'haloes', 'mini-haloes', 'relics' and 'phoenix' within their Intra Cluster Medium (ICM). The radio haloes show steep ($\alpha = -1.2$) and ultra steep ($\alpha < -1.5$) spectral properties at low radio frequencies, giving important insights on the merger (pre or post) state of the cluster. Ultra steep spectrum radio halo emissions are rare and expected to be the dominating population to be discovered via LOFAR and SKA in the future. Further, the distribution of matter (morphological information), alignment of hot X-ray emitting gas from the ICM with the total mass (dark + baryonic matter) and the bright cluster galaxy (BCG) is generally used to study the dynamical state of the cluster. We present here a multi wavelength study on 14 massive clusters from the CLASH survey and show the correlation between the state of their merger in X-ray and spectral properties (1.4 GHz - 150 MHz) at radio wavelengths. Using the optical data we also discuss about the gas-mass alignment, in order to understand the interplay between dark and baryonic matter in massive galaxy clusters.

Keywords: Clusters: lensing:individual: CLASH - intracluster medium: radio: X-ray - dark matter

## 1 Introduction

Galaxy clusters are multiple gravitationally bound systems in our Universe that exist at the dense nodal regions of the cosmic web. They are continuously fed with galaxy groups, sub clusters, gas, dust etc. via filaments, giving rise to massive systems of the order of $10^{15} M_{\odot}$. While $\sim 70-80\%$ of the total mass in massive galaxy clusters is dominated by dark matter, followed by $\sim 15-20\%$ of hot gas ($T \sim 10^{8} K$) in the ICM, the remaining is in the form of a few percent of baryonic matter in the galaxies. The dark matter dominates the cluster potential and is expected to be interacting through gravity only, thus collision less. While, the in-falling baryonic matter in the central region of galaxy clusters undergoes mergers that dissipate a huge amount of energy giving rise to turbulence, cold fronts and shocks within the ICM. The dissipated energy causes heating of the ICM gas that emits in X-rays via thermal bremsstrahlung radiation and accelerates the cosmic ray electrons within the ICM upto relativistic energies giving rise to non-thermal radio synchrotron radiation in the presence of magnetic fields (Brunetti et al. 2014).
Depending upon the intensity of merger activity within the cluster central region, the non-thermal synchrotron emission can be classified into strongly polarized peripheral 'relics' (a few kpc - Mpc scale) and central 'Phoenix' (a few kpc scale) caused via shocks or compression respectively, encountered within the ICM. In addition, the turbulence caused via mergers or gas sloshing gives rise to central un polarized haloes (> 500 kpc upto 1 Mpc

[1] Univ Lyon1, Ens de Lyon, CNRS, Centre de Recherche Astrophysique de Lyon UMR5574, 9 av Charles André, F- 69230, Saint-Genis-Laval, France
[2] LERMA, 61 Av. de l'Observatoire, F-75 014, Paris, France
[3] Department of Physics, University of Durham, South Road, Durham DH1 3LE
[4] Theoretical Astrophysics Group, Tata Institute of Fundamental Research, Homi Bhabha Road, 400 005 Bombay, India
[5] Inter University Centre for Astronomy and Astrophysics, Pune University Campus, Postbag 4, Pune 411007, India
[6] Newmann College, Thodupuzha, Kerala, 685584, India

**Table 1.** Multi wavelength properties of CLASH clusters

| Source | z | X-ray morphology | $L^*_{Bol}$ $10^{44} ergs^{-1}$ | $Temp^*$ keV | sub groups, BCG | Radio morphology | $\alpha_{Halo}$ |
|---|---|---|---|---|---|---|---|
| Non cool-core clusters | | | | | | | |
| MACS $J0416.1-2403$ | 0.39 | extended | 16.0±0.9 | 7.5±0.8 | 4,2 | Halo (USSR) | $\alpha_{235}^{1400}=-1.50\pm0.80^a$ |
| MACS $J1149.5+2223$ | 0.54 | extended | 30.2±1.2 | 8.7±0.9 | 4,1 | Halo (Giant USSR) + Relic | $\alpha_{235}^{1400}=-2.10\pm0.22^a$ |
| MACS $J0717.5+3745$ | 0.55 | extended | 55.8±1.1 | 12.5±0.7 | 5, multiple | Halo (Giant) + Phoenix | $\alpha_{235}^{1400}=-0.98\pm0.03^a$ |
| Cool-core Clusters | | | | | | | |
| RX $J1532.9+3021$ | 0.36 | compact | 20.5±0.9 | 5.5±0.4 | 1,1 | mini-Halo | $\alpha_{235}^{1400}=-1.10\pm0.07^a$ |
| MACS $J0329.7-0211$ | 0.45 | compact | 17.0±0.6 | 8.0±0.5 | 1,1 | mini-Halo (USSR) | $\alpha_{610}^{1400}=-2.40\pm0.04^a$ |
| MACS $J1931.8-2635$ | 0.35 | compact | 20.9±0.6 | 6.7±0.4 | 1,1 | mini-Halo? (USSR) | $\alpha_{150}^{1400}=-2.10\pm0.10^b$ |
| RX $J2129.7+0005$ | 0.23 | compact | 11.4±2.0 | 5.8±0.4 | 1,1 | mini-Halo | $\alpha_{235}^{1400}=-0.60\pm0.00^c$ |
| RX $J1347.5-1145$ | 0.45 | compact | 90.8±1.0 | 15.5±0.6 | 1,1 | mini-Halo | $\alpha_{235}^{1400}=-0.92\pm0.03^d$ |
| MACS $J1206.2-0847$ | 0.44 | compact | 43.0±1.0 | 10.8±0.6 | 1,1 | mini-Halo$^e$? | - |
| MACS $J1115.9+0129$ | 0.35 | compact | 21.1±0.4 | 8.0±0.4 | 1,1 | mini-Halo (USSR) | $\alpha_{235}^{1400}=-1.80\pm0.20^a$ |
| Abell 611 | 0.29 | compact | 11.7±0.2 | 7.9±0.3 | 1,1 | No detection$^c$ | - |
| Abell 1423 | 0.21 | compact | 7.8±0.2 | 7.1±0.6 | 1,1 | No detection$^c$ | - |
| Abell 2261 | 0.22 | compact | 18.0±0.2 | 7.6±0.3 | 1,1 | No detection$^c$ | - |
| Abell 209 | 0.21 | slightly extended | 12.7±0.3 | 7.3±0.54 | 1,1 | Halo (Giant) | $\alpha_{610}^{1400}=-1.20\pm0.20^f$ |

*: Postman et al. 2012, a: Pandey-Pommier et al. 2016, 2014, 2013, b: Giacintucci et al. 2014, c: Kale et al. 2013, 2015, d: Gitti et al. 2007, e: Young et al. 2015, f: Venturi et al. 2008.

scale) in unrelaxed elongated 'non cool clusters' (NCC) and mini-haloes ($<$ 500 kpc) in relaxed compact 'cool clusters' (CC), respectively. CC clusters tend to host a central bright radio loud BCG, while NCC clusters host multiple ellipticals in their center associated to each sub group under collision. In spite of more than 100s of radio detection to-date of the diffuse synchrotron emission from the ICM in massive galaxy clusters, their origin still remains unclear (Ferreti et al. 2012). Thus multi wavelength study is extremely important in order to unravel the correlation between the dynamical state of the cluster and the origin of the non-thermal emission from their ICM.

## 2 Dynamical state and Non-thermal emission in massive galaxy clusters

In this paper we present radio analysis on a sample of 14 massive CLASH clusters (Table 1) (Postman et al. 2012) where deep Giant Metrewave Radio Telescope (GMRT) observations are available. The low frequency radio observations (+ archive and TGSS survey) with the GMRT down to 150 MHz has confirmed detection of radio haloes, mini-haloes and emission from the BCG in all the 14 systems. Combined high frequency data at 1.4 GHz with the Very Large Array (VLA) has been used to derive their spectral information. These clusters are very luminous ($L_{Bol} = 10^{44}$ $erg\ s^{-1}$, T $>$ 5 keV) at X-ray wavelength and show lensing properties at optical wavelength. The result of our multi wavelength analysis are listed below and in Table 1:

- 3 merging NCC massive clusters hosts radio haloes that trace the extent of X-ray emission along with the shock regions (phoenix and relics) and radio emission from the BCGs.
- MACS $J0416.1-2403$ shows 2 bright BCGs and multiple sub-groups under collision with an Ultra Steep Spectrum Radio (USSR) halo (Fig. 1) ($S_\nu = \nu^\alpha$, $\alpha < -1.5$, where $S$ is the flux density (mJy), $\nu$ the frequency (MHz) and $\alpha$ the spectral index). The USSRH are rare population of radio haloes that are relatively brighter at lower frequencies and caused by non-thermal emission from the population of old electrons after the less-common post-major merger or more frequent and less energetic pre-minor merger events in the Universe (Pandey-Pommier et al. 2015, Ogrean et al. 2015, Cassano et al. 2010). These USSR haloes have low surface brightness and are expected to be the dominant population that will be discovered via new generation low frequency interferometer arrays like LOw Frequency ARray (LOFAR) and Square Kilometer Array (SKA), thanks to their high ($\mu$Jy) sensitivity and resolution (arcsec) at MHz-range(Cassano et al. 2015).
- MACS $J1149.5+2223$ shows a bright BCG in the center and multiple sub-groups undergoing collision. It hosts a possible giant USSR halo with shocked relic region (see Fig. 1), suggesting a post violent merger phase (Bonafede et al. 2013, Pandey-Pommier et al. 2016, Golovich et al. 2016).

- MACS $J0717.5+3745$ shows multiple bright galaxies associated to several sub-groups under collision in the center of the cluster. It hosts the most powerful giant radio halo ($\alpha > -1.2$) known in galaxy clusters and a shocked phoenix region at the center (Fig. 1, Pandey-Pommier et al. 2013, van Weeren et al. 2008). The spectral and dynamical properties of the cluster suggest that its in a state of on-going merger.
- 11 CC massive clusters in our list either host mini-haloes or emission from the central radio loud BCG. Using high resolution observations (2") at 1.4 GHz and low resolution observation down to 150 MHz, we were able to marginally differentiate the emission from the jet of the AGN as well as the mini-halo.
- 3 CC clusters (RX$J1532.9+3021$, RX$J2129.7+0005$, RX$J1347.5-1145$) show one central bright BCG and a radio mini-halo caused due to gas sloshing in the central region with $\alpha > -1.2$ as shown in Fig. 2 top panel (Pandey-Pommier et al. 2016, Kale et al. 2013, 2015, Gitti et al. 2007). These clusters are in relaxed state with on-going minor merger activities.
- 3 CC clusters (MACS $J1115.9+0129$, MACS$J0329.7-0211$, MACS$J1931.8-2635$) show one central bright BCG and rare USSR mini-haloes with $\alpha < -1.5$ as seen in Fig. 2 bottom panel, indicating that these clusters are entering a post merger phase, with the population of old electrons mainly emitting at lower frequencies (Pandey-Pommier et al. 2016, Giacintucci et al. 2014).
- 4 CC clusters (MACS$J1206.2-0847$, Abell 611, Abell 1423, Abell 2261) show a bright BCG with no associated mini-halo emission, however emission from the central BCG is clearly detected in these clusters In the case of MACS$J1206.2-0847$, diffuse radio emission was detected a few arsec away from the central BCG, suggesting the presence of a possible mini-halo, however deep radio observations are needed to confirm this result (Young et al. 2007, Kale et al. 2013, 2015). An upper limit derived from the GMRT maps is plotted in Fig. 3, top panel for the mini-haloes and the BCGs. The non detection of mini-haloes indicates that the cluster has entered a relaxed state with no further merger activity in process.
- Abell 209 shows a giant radio halo and an associated central bright BCG (see Fig. 3 bottom panel). This CC cluster is exceptional with slightly extended morphology indicating the end of a massive merger stage or a beginning of a relaxed phase (Venturi et al. 2008).

## 3 Gas-mass alignment and interplay between dark and baryonic matter in massive galaxy clusters

The multiple probes (X-ray, radio, BCG) of matter distribution in galaxy clusters can be used to study their gas-mass alignment as well as the interaction between their dark and baryonic matter. Dark matter dominating the cluster gravitational potential, binds the hot, X-ray emitting and non-thermal radio emitting intra cluster gas to the cluster center. While CC clusters tend to show homogeneous distribution in the total mass map

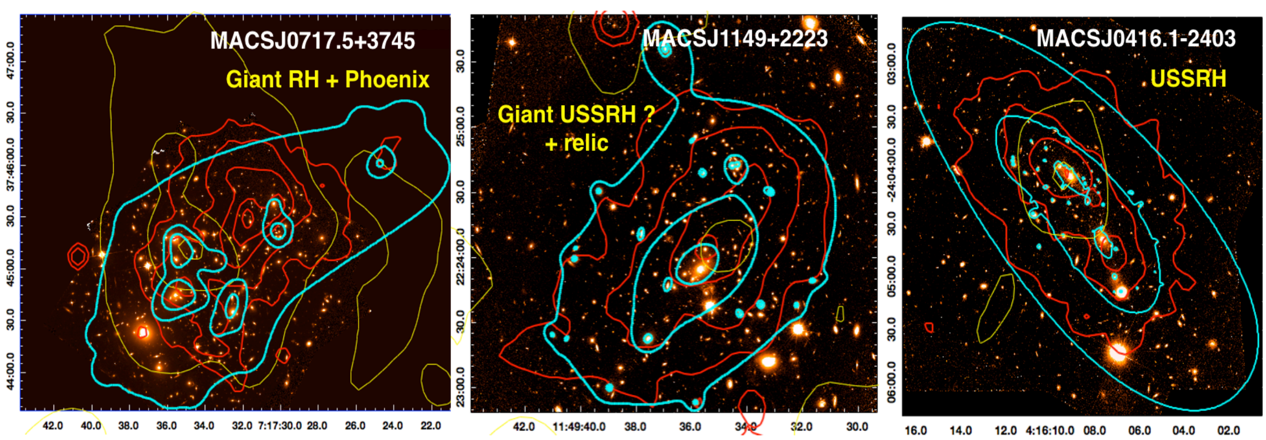


**Fig. 1.** Dark and baryonic matter coupling in NCC clusters. X-ray (red), HST total mass map (cyan) and GMRT (yellow) contours are overlaid on background HST map. The radio haloes are marked as 'RH' and Ultra steep spectrum radio haloes as 'USSRH'. The total mass map for MACS $J0416.1-2403$ is constructed with MUSE data.

(dark + baryonic matter, constructed from the HST/MUSE data) and positional coincidence in the central baryonic mass concentration versus the Centroid of the cluster, the NCC often show in-homogeneous total mass distribution with non-coincidence (offset) in the central baryonic mass concentration versus the Centroid (Limousin et al. 2012). This is mainly due to the violent dynamical interaction in the NCC clusters, that produces shocks or pressure waves disturbing the gas (Cassano et al. 2010). In the following section we will discuss the interaction of dark and baryonic matter in our sample of 14 massive CLASH clusters.

- The baryonic matter (X-ray + radio emitting gas and BCG) in 3 NCC massive clusters namely, MACS $J0717.5+3745$, MACS $J1149.5+2223$ and MACS $J0416.1-2403$ shows no well defined center or positional coincidence in the multi wavelength data. In the case of MACS $J0416.1-2403$, the total mass map was constructed with the MUSE data providing a better constraint on the extent of the cluster mass, thanks to its high sensitivity to detect faint sources (see Fig. 1, last panel). Further, a shift (a few arcsec) in the peak of optical total mass map, X-ray peak from the thermal gas and radio peak from the non-thermal gas in the ICM is detected, suggesting an ongoing merger activity in these clusters (Fig. 1). The shift in the peak also indicates the decoupling of dark matter and baryonic matter gas components suggesting a post-merger scenario for MACS $J1149.5+2223$ and MACS $J0416.1-2403$ clusters with USSR haloes and on-going merger scenario for MACS $J0717.5+3745$ cluster with less- steep radio halo.

- In the case of 6 (RX $J1532+3021$, RX $J2129+0005$, RX $J1347-1145$, MACS $J1115+0129$, MACS $J1931-2635$, MACS $J0329-0211$) CC clusters the central region shows aligned X-ray, radio and total mass peak, suggesting that the clusters are in relaxed phase with minor merger activity and coupled dark and baryonic matter (Fig. 2).

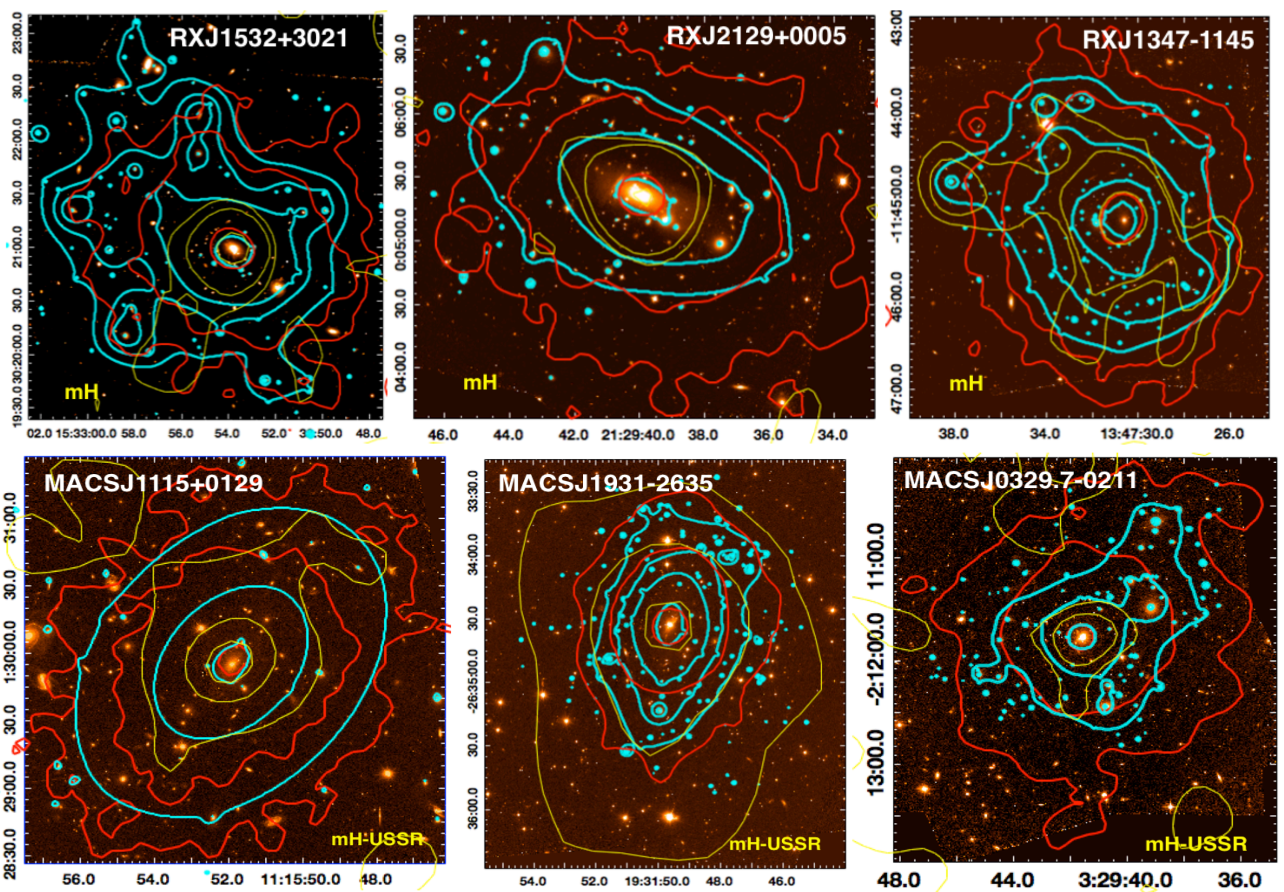


**Fig. 2.** Dark and baryonic matter coupling in CC galaxy clusters. X-ray (red), HST total mass map (cyan) and GMRT (yellow) contours are overlaid on background HST map. The mini-haloes are marked as 'mH' and Ultra steep spectrum radio mini-haloes as 'mH-USSR'.

- In the case of 4 CC clusters a coincidence in the peaks of X-ray and total mass map is seen. The radio emission from the BCG, wherever detected is aligned with the X-ray/total mass map peak, suggesting no more on-going merger activity (Fig. 3).

- Finally, the exceptional CC cluster Abell 209 hosting a giant radio halo shows an offset in the peak of radio and total mass map with a coincidence in the peak of total mass and X-ray (Fig. 3, bottom middle panel), suggesting its transition stage from the NCC to CC phase. The cluster appears to be cooling down after a violent merger phase.

- The morphological and spectral information from the multi wavelength data was used to infer the state of relaxation of galaxy clusters as well as the interplay between their dark and baryonic matter. The X-ray and total mass map concentration (ratio between the light within a circular aperture of minimum 100 kpc and maximum 500 kpc) of each cluster in our list is plotted with respect to the shift in their X-ray Centroid (standard deviation of the projected separation between the X-ray peak and Centroid estimated within circular aperture of maximum 500 kpc) in Fig. 3, bottom right panel. It is clear from the figure that the concentration of CC clusters is higher near the central region and they show smaller shift in their X-ray Centroid compared to the NCC clusters, confirming their non relaxed nature. Further, the mass concentration in X-rays is higher in general for both the CC and NCC clusters compared to the total mass map (with dominating dark matter) derived from the optical data, confirming the collisional nature of the baryonic matter traced via X-ray observations at the cluster center. The lower mass concentration at the cluster center in the total mass map suggests its collision less nature, thus minimally affected via merger events.

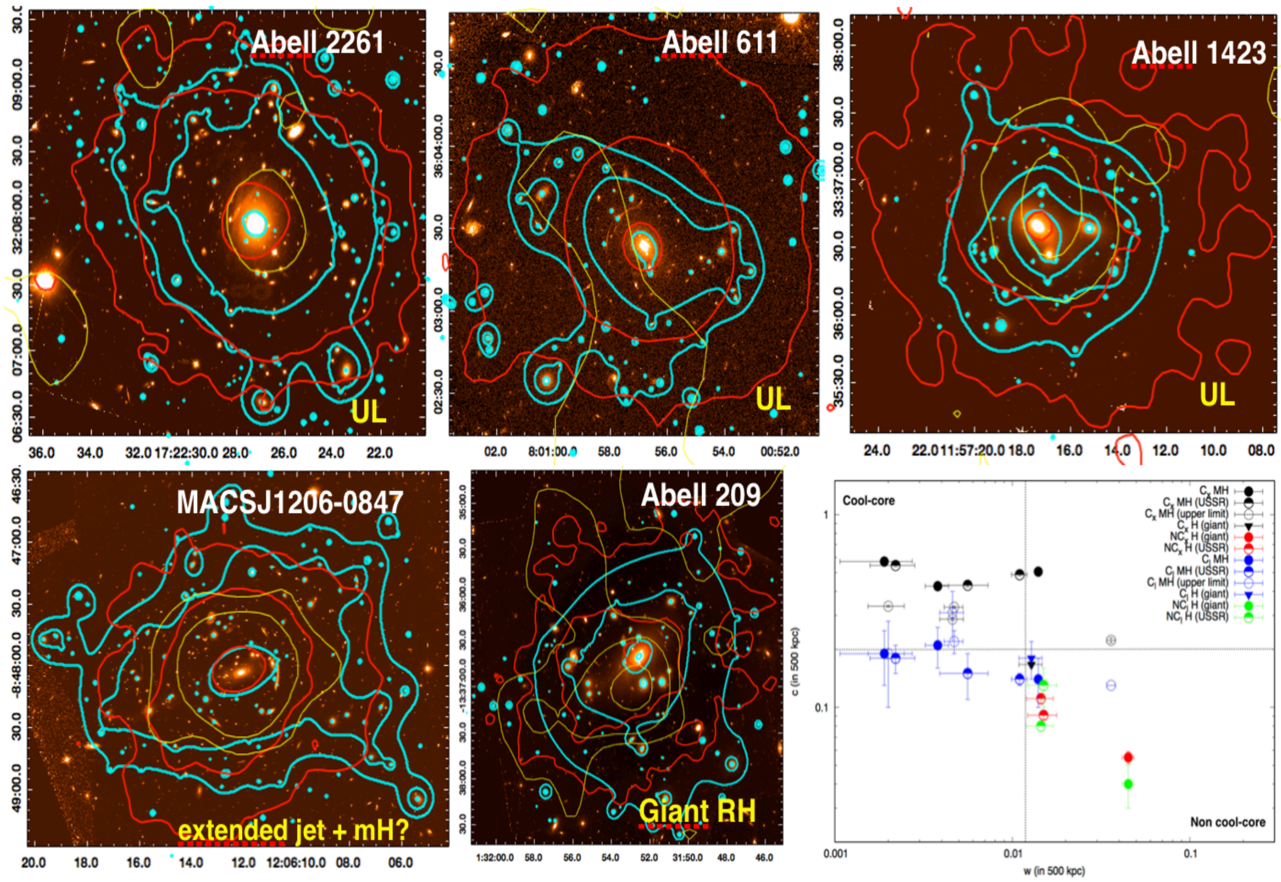


**Fig. 3.** Dark and baryonic matter coupling in CC galaxy clusters. X-ray (red), HST total mass map (cyan) and GMRT (yellow) contours are overlaid on background HST map. The non-detection upper limits are marked as 'UL', radio halo as 'RH', X-ray concentration in cool-core as '$C_x$', X-ray concentration in non cool-core as '$NC_x$', concentration in total mass map via lensing analysis as '$C_l$' in cool-cores and '$NC_l$' in non cool-core clusters.

## 4 Conclusions

Massive galaxy clusters provide the most interesting astrophysical laboratories to study the merger activity and emission processes in the dense regions of the Universe. In this paper, we present a multi wavelength (GMRT, Chandra, HST/MUSE) analysis of morphological and spectral properties on a sample of 14 massive galaxy clusters in the CLASH catalog. The multi wavelength data was used to derive a correlation between the dynamical state and the non-thermal emission from the cluster ICM and study the dark and baryonic matter interaction in their central region. The main results derived in this paper are listed below:

- Low frequency observations (down to 235 or 150 MHz) not only confirm the presence of mini-haloes and haloes in massive galaxy clusters but also provide information about their dynamical state.
- Radio morphology gives the information about the violent or less energetic merger activity in the cluster and the spectral index gives information about the pre- or post- merger state of the cluster.
- The radio (non-thermal) halo and X-ray (thermal) emission are generally coincident and originate from the ICM.
- The peak in mass distribution at X-ray and total mass map is coincident for CC clusters while non-coincident in NCC clusters.
- An offset in the peak of radio and total mass map as well as X-ray is detected in clusters hosting haloes, where the merger is still active.
- Combined multi wavelength analysis of the mass distribution in galaxy clusters suggests that dark matter is loosely interacting while the baryonic matter is tightly interacting during merger events in the cluster central regions.

We thank the staff of GMRT, who made these observations possible. The GMRT is run by the National Centre for Radio Astrophysics of the Tata Institute of Fundamental Research. The authors are thankful to the research grant received from the Franco-Indian CEFIPRA organization. This research has made extensive use of the data available from the public archive from HST, Chandra, VLA and GMRT observatory. MP thanks Dr. Adi Zitrin for useful discussion.

## References

Bonafede, A.; Bruggen, M.; et at.; 2012; MNRAS; 426; 40

Brunetti, G. and Jones, T.; 2014; International Journal of Modern Physics 23; 30007

Cassano, R.; Ettori, E.; et al.; 2010; ApJ; 721 ; 82

Cassano, R.; Bernardi, G.;...Pandey-Pommier, M.; et al.; 2015; Advancing Astrophysics with the Square Kilometre Array (AASKA14), 73

Feretti, L.; Giovannini, G.; et al.; 2012; A&A Rev.; 20; 54

Giacintucci, S.; Markevitch, M.; et al.; 2014; ApJ; 781; 9

Gitti, M.; et al.; 2007; A&A; 470; L25

Golovich, N.; Dawson, W.; et al.; 2016; ApJ; 831; 110

Kale, R.; Venturi, T.; et al.; 2013; A&A; 557; 99

Kale, R.; Venturi, T.; et al.; 2015; A&A; 581; 23

Limousin, M.; Ebeling, H.; et al.; 2015; A&A; 544; 71

Ogrean, G.; van Weeren, R.;...Pandey-Pommier, M.; et al.; 2015;ApJ; 812; 153

Pandey-Pommier, M.; Richard, J.; et al.; 2013; A&A; 557; 117

Pandey-Pommier, M.; van Weeren, R.; et al.; 2015; in Proc. SF2A-2015; 247

Pandey-Pommier, M.; Richard, J.; et al.; arXiv:1612.00225

Postman, M.; Coe, D.; et al.; 2012; ApJ; 199; 25

van Weeren, R.; Rottgering, H.; et al.; 2009; A&A; 505; 991

Venturi, T.; Giacintucci, S.; et al.; 2008; A&A; 484; 327

Young, A.; Mroczkowski, T.; et al. 2015; ApJ; 809; 185

*SF2A 2016*
*C. Reylé, J. Richard, L. Cambrésy, M. Deleuil, E. Pécontal, L. Tresse and I. Vauglin (eds)*

# THE LOW-FREQUENCY RADIO EMISSION IN BLAZAR PKS2155-304

M. Pandey-Pommier[1], S. Sirothia[2,3], P. Chadwick[4], J.-M. Martin[5], P. Colom[5], W. van Driel[5], F. Combes[6], P. Kharb[2], P.-J. Crespeau[1], J. Richard[1] and B. Guiderdoni[1]

**Abstract.** We report radio imaging and monitoring observations in the frequency range 0.235 - 2.7 GHz during the flaring mode of PKS 2155-304, one of the brightest BL Lac objects. The high sensitivity GMRT observations not only reveal extended kpc-scale jet and FRI type lobe morphology in this erstwhile 'extended-core' blazar but also delineate the morphological details, thanks to its arcsec scale resolution. The radio light curve during the end phase of the outburst measured in 2008 shows high variability (8.5%) in the jet emission in the GHz range, compared to the lower core variability (3.2%) seen at the lowest frequencies. The excess of flux density with a very steep spectral index in the MHz range supports the presence of extra diffuse emission at low frequencies. The analysis of multi wavelength (radio/optical/gamma-ray) light curves at different radio frequencies confirms the variability of the core region and agrees with the scenario of high energy emission in gamma-rays due to inverse Compton emission from a collimated relativistic plasma jet followed by synchrotron emission in radio. Clearly, these results give an interesting insight of the jet emission mechanisms in blazars and highlight the importance of studying such objects with low frequency radio interferometers like LOFAR and the SKA and its precursor instruments.

Keywords: Radio galaxies: AGNs: BL Lacertae objects: PKS 2155-304-galaxies: jets-radiation mechanism: synchrotron emission: intracluster medium

## 1 Introduction

Blazars are active galactic nuclei (AGN) powered by accretion onto super massive black holes and mostly associated with BL Lacertae objects (no emission lines) (Urry & Padovani 1995). They show ultra-relativistic outflows and diverse timescale flaring activities from radio (100 MHz) up to Gamma-rays (tens of TeV)(Foschini et al. 2007, 2008). The jets in blazars are characterized as compact morphology, flat spectral core regions of high degree of polarization with superluminal speed (Angel & Stockman 1980). It is believed that the recurrent flaring episodes in AGNs may give rise to large-scale diffuse emission around them that may finally terminate into lobes. These radio lobes show very steep spectra and can be used to probe the AGN duty cycle, their activity history as well as surrounding environmental properties. High sensitivity, arcsec scale resolution observations at low radio frequencies are needed to detect such diffuse emission in blazars and disentangle the details of their morphology. Kharb et al. (2010) carried out a detailed search with the Very Large Array (VLA) at 1.4 GHz for the extended jet (kpc-scale) emission in a sample of 135 radio loud blazars from the MOJAVE sample and detected extended jet emission in the majority of the sources, with only 7% of the sources exhibiting compact core emission. The kpc-scale jet emission in a large fraction of MOJAVE BL Lac objects showed radio power and jet morphology typical of FRII type AGNs (contrary to conventional results), while a substantial number

[1] Univ Lyon, Univ Lyon1, Ens de Lyon, CNRS, Centre de Recherche Astrophysique de Lyon UMR5574, 9 av Charles André, 69230, Saint-Genis-Laval, France
[2] National Centre for Radio Astrophysics - Tata Institute of Fundamental Research, Pune University Campus, Post Bag 3, Ganeshkhind Pune 411007, India
[3] SPT, Cape Town, Square Kilometre Array-South Africa
[4] Department of Physics, Institute for Computational Cosmology, Durham University, South Road, Durham DH1 3LE, United Kingdom
[5] GEPI, Observatoire Paris CNRS, 5 Pl Jules Janssen, 92195 Meudon, France & Station de Radioastronomie de Nançay, Observatoire de Paris, 18330 Nançay, France
[6] LERMA, Observatoire de Paris, CNRS, 61 rue de l'Observatoire, 75014 Paris, France

of blazars associated with quasars had possessed a radio power intermediate between FRIs (core with inflated jet morphology) and FRIIs (core with jet terminating into hotspots)(Kharb et al. 2010, Fanaroff & Riley 1974). In addition to the kpc-scale jet structures, BL Lacs exhibit rapid variable emission (less than an hour to several days) from their core region due to relativistic beaming effects of the jets and are therefore frequently monitored during outburst. In this paper we will discuss the extended faint emission in PKS 2155-304 discovered in high sensitivity GMRT observations in the MHz range and the flux variability in comparison with the single-dish Nançay Radio Telescope (NRT) observations in the GHz range during the end phase of the 2008 flaring episode.

## 2 Low frequency diffuse emission in PKS 2155-304

PKS 2155-304 is one of the most luminous and highly variable BL Lac object located at a redshift of $z$=0.117 (Urry et al. 1993, 1997; Aharonian 2005, 2007, 2009). It was detected as a high energy TeV Gamma-ray source in 1996-1997 by the University of Durham Mark 6 Telescope and later confirmed by the High Energy Spectroscopic System (H.E.S.S.) instrument (Chadwick et al. 1999, Abramoski et al. 2012, Djannati-Atai et al. 2003). The optical and near-IR data show that the object is hosted by a dominant luminous elliptical surrounded by a rich group of galaxies at a similar redshift as PKS 2155-304 (Falomo et al. 1991, 1993). In high resolution ($\sim 0.12''$) NIR $J$ and $K$ band images made with the Multi Conjugate Adaptive Optics Demonstrator (MAD) system at the ESO (European Southern Observatory) VLT (Very Large Telescope) a search was made for the NIR counterparts in order to investigate the properties of the close environment of the source and associated radio counterparts. The observations confirmed the association of a poor galaxy group with the target, but no radio emission was detected from these galaxies, except for the central host (Liuzzo et al. 2013). The central elliptical host in PKS 2155-305 exhibits slightly resolved morphology at radio wavelengths with a core and surrounding halo region extending up to $94''$ or 132 kpc in $8.4'' \times 3.8''$ maps with the VLA at 1.5 GHz and a probable very faint extension up to $\sim 200''$ or 375 kpc in size, in low resolution maps ($26'' \times 10''$), which is apparently over-resolved or undetected in most of the GHz-range observations (Ulvestad et al. 1986, Laurent-Muehleisen et al. 1993). Liuzzo et al. (2013) made VLA radio continuum images from 1.4 to 22.5 GHz and found old radio jet emission at $\sim 20$ kpc from the center of PKS 2155-304 and a jet-like structure of $\sim 2$ kpc size in the eastern direction. A knot of $10''$ in the NW direction was also detected in a high resolution ($\sim 0.6''$) map (Piner et al. 2010). The extended radio power measured at 1.5 GHz was $\log(\mathrm{P}_{ext}) = 25$ W Hz$^{-1}$ (Laurent-Muehleisen et al. 1993).

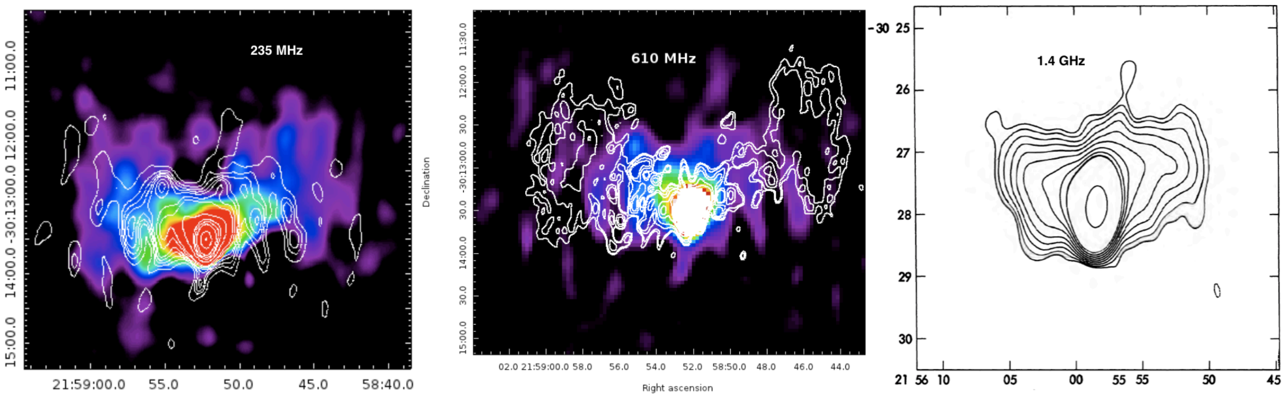


**Fig. 1.** PKS 2155-304: GMRT radio continuum images: (**left**) contours (white) at 235 MHz with resolution $21''$ and rms noise 0.8 mJy/beam overlaid on the 610 MHz color map, (middle:) 610 MHz contours (white) with resolution $5''$ and rms noise 0.04 mJy/beam overlaid on the 235 MHz color map and (**right**) VLA map at 1420 MHz with resolution $26'' \times 10''$, extracted from Ulvestad et al. (1986).

We carried out deep GMRT observations on PKS 2155-304 at 610 and 235 MHz for almost 20 hours and confirmed the presence of a roughly 4.5 arcmin (575 kpc, for a cosmological model with $\Omega_M$= 0.28 and $h$ = 69.6 km/s/Mpc) sized extended structure down to 235 MHz and resolved the structural details– core, halo, jet and lobe regions (Pandey-Pommier et al. 2015). Parts of diffuse emission of different size scales (few 10s of kpc) had already been detected in less sensitive maps previously at different locations in PKS 2155-304 (Beuchert et al. 2010; Liuzzo et al. 2013). However, low frequency GMRT data was able to discover the overall extent of the diffuse emission and resolve the details, in order to give a complete morphological profile of PKS 2155-304, for the first time- thanks to its high sensitivity and resolution. Further, the spectral index analysis between 610 and 235 MHz GMRT data suggests that the emission is steepest in the radio lobe, with $-1 < \alpha < 0$, while the core region shows flatter spectral index with $\alpha = -0.2$, in agreement with VLA observations. Detailed analysis of the spectral properties of diffuse jet emission in PKS 2155-304 will be presented in a future publication (Pandey-Pommier et al. 2016).

## 3 Core variability in PKS 2155-304

PKS 2155-304 is known to exhibit significant variability, on both long (months) and short (days to hours) time scales from radio up to Gamma-ray wavelengths (see Fig. 2, Aharonian et al. 2009). In August 2008, a multi wavelength monitoring campaign was performed on this blazar during the end phase of a bright flare detected at gamma-rays with H.E.S.S. The RXTE X-ray and H.E.S.S. data showed correlation during the high state of the source, but no good correlation was seen with the longer radio wavelength data. Nevertheless, a correlation in the radio data from the NRT, Australian Telescope Compact Array (ATCA), Hartebeesthoek Radio Astronomy Observatory (HartRAO) and optical (*Swift* UVOT) data was seen following the decay in the peak at very high energy (VHE, refer Fig. 2 in Abramowski et al. 2012).

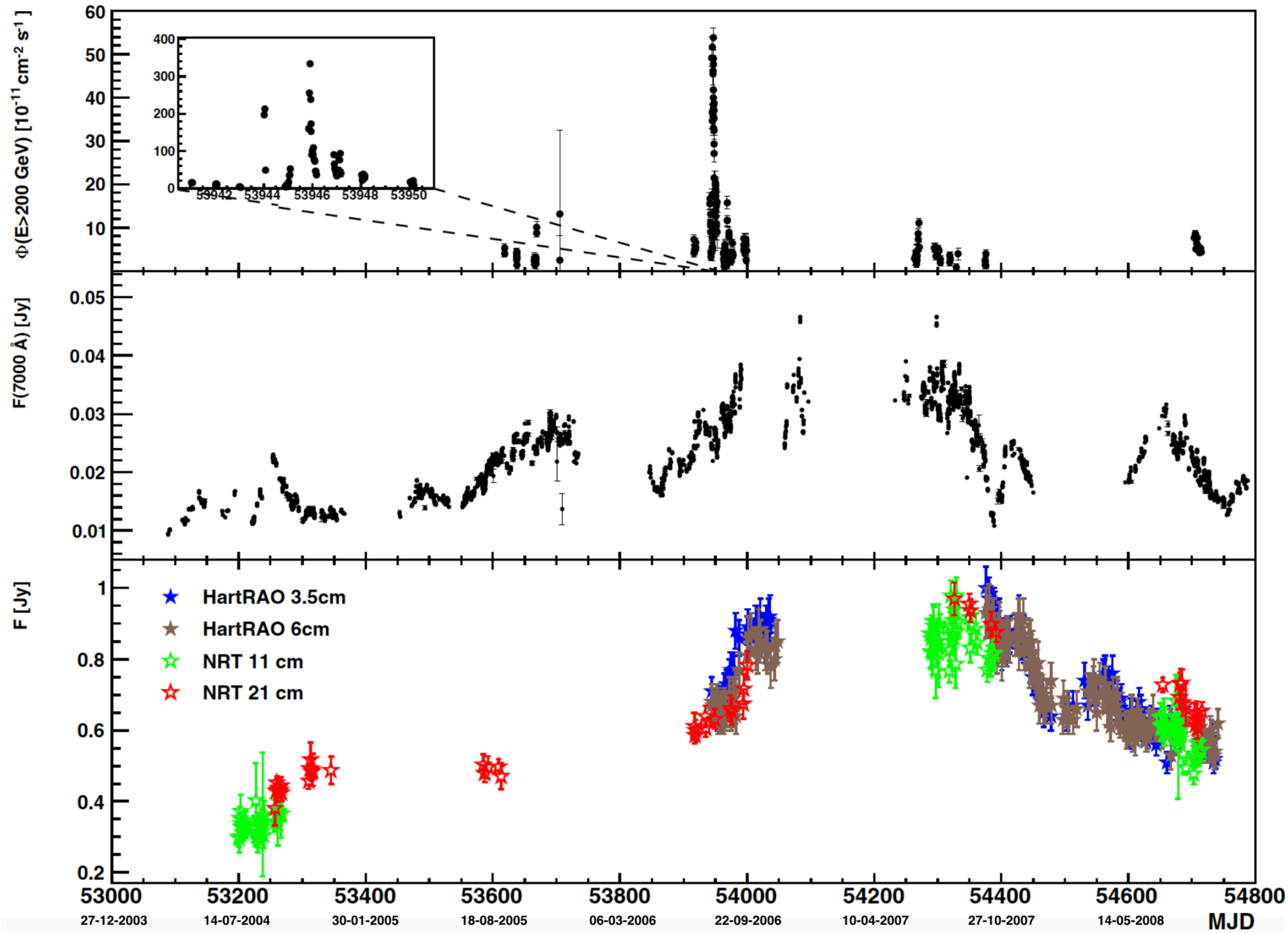


**Fig. 2.** Multi wavelength light curve of PKS 2155-304 during the 2006-2008 flaring episode (extracted from Abramowski et al. 2012).

The radio flux density data collected from 1.4 GHz up to 9 GHz shows that the source was in an active state since 2006 had reached the end of the outburst state by August 2008. The average flux density measured by the NRT was 0.49±0.04 Jy at 2.7 GHz and 0.65±0.02 Jy at 1.4 GHz, suggesting an excess in emission at lower frequency for an assumed radio spectral index of -0.8. The long term variability monitoring multi wavelength data were explained via three different emission models, viz., (i) a one-zone synchrotron self Compton (SSC) model, where the X-ray and Gamma-ray bumps are generated due to synchrotron and Inverse Compton (IC) emission from a population of relativistic electrons in a spherical plasma blob inside the jet medium, (ii) a two-zone and stratified jet SSC model, where high energy emission is generated from the relativistic electrons and positrons in an extended, in homogeneous jet and a dense plasma blob traveling along the jet axis. The dense inner blob being more energetic gives rise to VHE flux and rapid variability in SSC emission, while the extended jet emission gives rise to underlying continuous outflow. Thus two different jet components emitting synchrotron radiation are considered in this model, and (iii) a stratified jet scenario, where only one radiative MHD jet component is considered to be launched by the accretion disk. This jet surrounds a highly relativistic plasma of electron-positron pairs long its axis. The MHD jet plays the role of a collimator and energy reservoir for the pair plasma being injected at the base of the jet. The plasma is re-accelerated along the jet to compensate for synchrotron and IC cooling, which are responsible for observed high enery emission following the SSC scenario. In spite of detailed modeling at high frequencies of the variability in PKS2155-304, none of the above scenarios were able to describe the poor correlation between VHE and the long term radio evolution. The multi wavelength light curve suggested that the rapid activity at high energies on short time scales directly contributes to an averaged, long-term signature at lower energies (see Fig. 2, Abramowski et al. 2012).

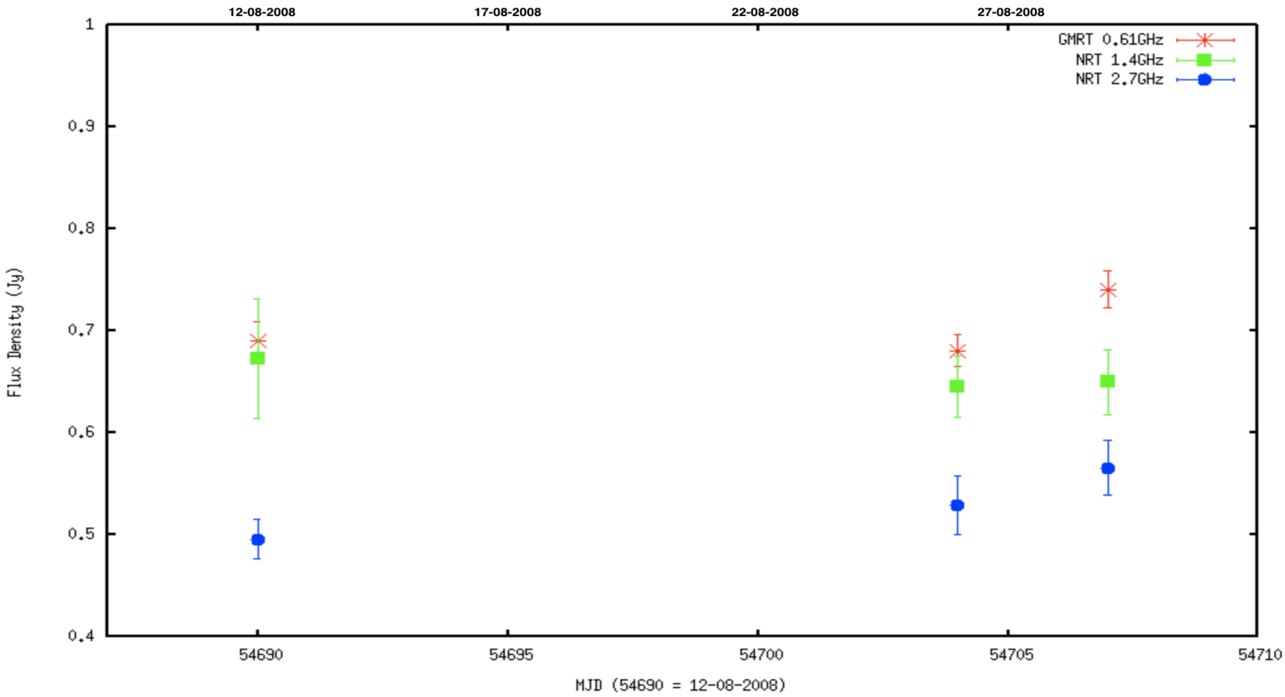


**Fig. 3.** Radio light curve in 2008 during the end of the flaring episode.

The radio light curve derived from the simultaneous data available at 610 and 235 MHz with the GMRT and at 1.4 GHz and 2.7 GHz with the NRT suggests that the low frequency radio emission shows reduced flux variability (3.2%) of the compact core component as compared to that at higher frequencies (8.5%) and that there is an excess in the low frequency flux by almost ∼34% (see Fig. 3). At 235 MHz very marginal variability was seen. This clearly supports the scenario that low frequency emission is dominated by emission from the non variable extended jet-lobe structure that tends to be more luminous at lower frequencies. Furthermore the reduced variability seen at lower frequencies is due to new radio emitting blobs of plasma ejected within the jet medium that are initially opaque to radio waves dues to synchrotron self absorption and then slowly expand adiabatically and cool, causing emission in the MHz range with a certain delay. The longer cooling times at lower frequencies leads to a longer timescale of radio emission as compared to very rapid high energy emission flares. The reduced (or diluted) variability in the radio light curve in the MHz range is due to combined emission from the inner core-jets, superimposed by the dominant low frequency radio emission from the extended outer lobe regions, in agreement with above proposed models.

## 4 Square Kilometre Array (SKA) survey capabilities

Radio monitoring of blazars along with multi wavelength data provides an important constraint on their synchrotron self Compton (SSC) emission models as well as kpc-scale jet properties (Aharonian et al. 2009, Band and Grindly 1985, Kharb et al. 2016, Pandey-Pommier et al. 2015). Thanks to the upcoming radio facilities with high sensitivity and resolutions like the LOw Frequency ARray (LOFAR, 10-240 MHz) and the SKA (50 MHz - 10 GHz), operating at low frequencies, it will be possible to detect many more such faint jet structures in blazars (see Fig. 4, Kharb et al. 2016).

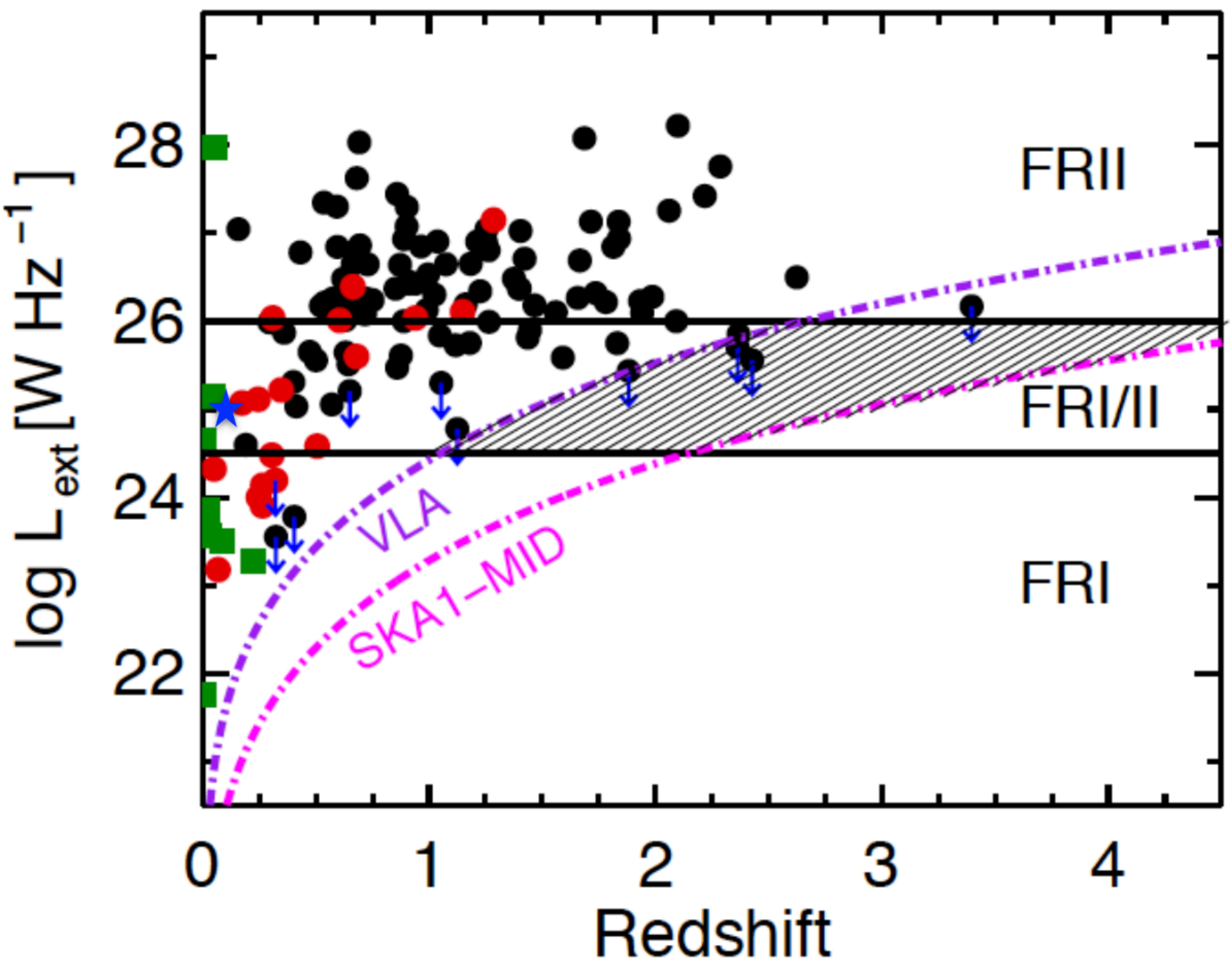


**Fig. 4.** Radio luminosity as a function of redshift for quasars (black circles), blazars (red circle), radio galaxies (green squares) and core-only sources (upper limits with downward arrows). PKS 2155-304 is indicated as a blue star. The FRI-FRII radio power divide is marked with a solid black line and sensitivity limits for the VLA and the SKA Phase 1 mid-range frequency (1.65 to 3.05 GHz) component are shown as dashed lines (adapted from Kharb et al. 2016).

The higher sensitivity of SKA1-MID Band 3 (1.65 to 3.05 GHz) at high frequencies is expected to detect twice as many extended diffuse radio jet emission in blazars than previously known with the VLA (Kharb et al. 2016). SKA1-MID will offer a factor of 10 to 70 overall increase in the sensitivity (0.7 $\mu$Jy beam$^{-1}$) and will be able to delineate the full extent of diffuse lobe emission in blazars and radio galaxies, that were missed out with the previous VLA survey at 1.4 GHz having less sensitivity (10-50 $\mu$Jy beam$^{-1}$). Thus SKA survey will not only discover new kpc-scale persistent diffuse jet emission in blazars, but also help to classify their "intermediate" or "hybrid FRI/II" Type morphology. It will also confirm if the "core-only" blazars are a different population that exhibit episodic jet activity and demonstrate an unresolved core morphology during switched off.

## 5 Conclusions

We list below the results achieved from studying the non-thermal radio emission from the most luminous blazar PKS 2155-304 down to 0.235 GHz with the GMRT and multi wavelength monitoring of flaring activity in 2008.

- Low frequency radio emission at 235 MHz is dominated by emission from an extended, diffuse jet-lobe of 575 kpc size discovered with the GMRT;
- We have confirmed the variability of the source down to 610 MHz during the 2008 flaring episode and its decreased variability at lower frequencies (235 MHz);
- The compact core is highly variable over time scales of a few hours to days down to 610 MHz and has a flat spectral index;
- The SKA will play an important role in detecting new populations of FRI/II sources as well as faint blazar jets.

We thank the staff of GMRT, who made these observations possible. The GMRT is run by the National Centre for Radio Astrophysics of the Tata Institute of Fundamental Research. MP is thankful to the research grant received from the Franco-Indian CEFIPRA organization. The Nançay Radio Telescope is operated as part of the Paris Observatory, in association with the CNRS and partially supported by the Région Centre in France.

## References

Abramowski, A; Acero, F.; et al.; 2012; A&A; 539; A149
Aharonian, F.; Akhperjanian, A.; et al.; 2005; A&A; 430; 865-875
Aharonian, F.; Akhperjanian, A.; et al.; 2007; ApJ; 664; L71
Aharonian, F.; Akhperjanian, A.; et al.; 2010; ApJ; 696; L150
Angel, J. & Stockman, H.; 1980; ARA&A; 18; 321
Band, D. & Grindlay, J.; 1985; ApJ; 298; 128
Beuchert, T., PhD thesis, 2010
Chadwick, P. M.; Lyons, K.; et al. 1999, ApJ, 513, 161
Djannati-Atai, A.; H.E.S.S. Collaboration; 2003; ICRC; p2575
Falomo, R.; Giraud, E.; et al.; 1991; ApJ; 380; L67
Falomo, R.; Pesce, J.; et al.; 1993; ApJ; 411; L63
Fanaroff, B. & Riley, J.; 1974; MNRAS; 167; 31P
Foschini, L.; Ghisellini, G.; et al.; 2007; ApJ; 657; L81
Foschini, L.; Treves, A.; et al.; 2008; A&A; 484; 35
Kharb, P.; Lal, D. V.; et al.; 2016; JoAA; 37; 34
Kharb, P.; Lister, M.; et al.; 2010; ApJ; 710; 764
Laurent-Muehleisen, S.; Kollgaard, R.; et al.; 1993; AJ; 106; 875
Liuzzo, E.; Falomo, R.; et. al.; 2013, AJ, 145, 3
Pandey-Pommier, M., et al.; 2015; 'The multi wavelength Universe' BASI conference proceedings, in press
Piner, B.; Pant; N.; et al.; 2010; ApJ; 723; 1150
Ulvestad, J. & Antonucci, R.; 1986; AJ; 92; 6
Urry, C. & Padovani, P.; 1995; PASP; 107; 803
Urry, C.; Maraschi, L.; et al.; 1993; ApJ; 411; 614
Urry, C.; Treves, A.; et al.; 1997; ApJ; 486; 799

*SF2A 2016*
*C. Reylé, J. Richard, L. Cambrésy, M. Deleuil, E. Pécontal, L. Tresse and I. Vauglin (eds)*

# AGN DUTY CYCLE AND RELIC EMISSION IN THE LOW FREQUENCY SKY

M. Pandey-Pommier[1], H. Intema[2], G. Heald[3, 4, 5] and on behalf of the MSSS team and the LOFAR collaboration

**Abstract.** Active Galactic Nuclei (AGNs) are amongst the brightest sources in the radio sky that deposit large amount of energy in the interstellar and intergalactic medium (ISM, IGM) via their jets. Recurrent flaring episodes in the AGN jets can terminate at large-scale faint diffuse 'relic' emission around them. These relic emissions are rare and represent the end stage of their life cycle. They show very steep spectrum giving insights of AGN duty cycle, their past activity history and surrounding environment properties. High sensitivity and arcsec scale observations at very low frequencies are needed to detect such rare relic emission and disentangle the details of their morphology. In this paper we highlight the important database provided by low frequency surveys to search for relic radio sources and discuss in particular the relic emission from the AGNs detected in the LOFAR Multi frequency Snapshot Sky Survey (MSSS) and TIFR GMRT Sky Survey (TGSS), both surveys performed with SKA pathfinder telescopes. The radio spectrum from 2 different types of relic radio galaxies (B2 0924+30 and 4C 35.06) are investigated and a correlation between the mean particle age of the relic emission and the central AGN properties is derived.

Keywords: Radio galaxies: AGNs: jets - intracluster medium: diffuse emission: relics

## 1 Introduction

Radio galaxies experience continuous evolution throughout their lifetimes, starting from compact, synchrotron self-absorbed sources to well evolved classical double jet radio sources. They host a bright central AGN, that may show recurrent flaring activities giving rise to kpc up to Mpc scale jet structures. Based upon the morphology of the double jets, the radio galaxies are further classified into either Fanaroff-Riley Class I (FR I with disrupted and flared jets) or Class II (FR II with collimated jets and hotspots, Fanaroff and Riley, 1974). A class of FR I and IIs towards the extreme end of their life cycle may extend upto a giant linear (Mpc) scale structure with an active or passive central AGN. As the central AGN activity shuts down in these extreme systems, the ejected plasma in their jets ages and loses energy through synchrotron radiation as well as inverse Compton (IC) scattering of electrons via cosmic microwave background (CMB) photons. This aged plasma further gives rise to relic emission or radio fossils from an earlier episode of central AGN activity. Such relic emission representing the end stage of AGN life cycle has been rarely detected, only ∼50 are known as of now, due to their faint nature at high radio frequencies (Shulevski et al. 2015). Further they are often detected in dense cluster environments where the losses in the energy of synchrotron emitting plasma are delayed due to the external pressure experienced via the cluster environment (Shulevski et al. 2015). Thus, they show steep spectral properties ($-2 < \alpha < -1$) and can be classified into 2 broad categories i.e. fading and restarted (Cordey et al. 1987). In the case of fading galaxies, the central AGN is inactive with no on-going feeding of the jets with new energetic radio emitting plasma. Whereas, in the case of restarted galaxies, the extended radio emission is continuously fueled via the active central core (AGN), showing multiple phase (core, lobes, relics etc.) of evolution in their morphology.

[1] Univ Lyon, Univ Lyon1, Ens de Lyon, CNRS, Centre de Recherche Astrophysique de Lyon UMR5574, 9 av Charles André, F-69230 St-Genis-Laval, France
[2] Leiden Observatory, Leiden University, the Netherlands
[3] CSIRO Astronomy and Space Science, 26 Dick Perry Ave., Kensington WA 6151, Australia
[4] ASTRON, the Netherlands Institute for Radio Astronomy, Postbus 2, 7990 AA Dwingeloo, the Netherlands
[5] Kapteyn Astronomical Institute, University of Groningen, PO Box 800, NL-9700 AV Groningen, the Netherlands

In this paper we emphasize the importance and compare the efficiency (sensitivity and resolution) of different low frequency radio surveys like VLA-VLSSr 74 MHz (resolution= 80 arcsec and rms noise = 100 mJy/beam, Lane et al. 2012, 2014, Cohen et al. 2007), GMRT-TGSS 150 MHz (resolution= 25 arcsec and rms noise = 3.5 mJy/beam, Intema et al. 2016, Sirothia et al. 2010), LOFAR-MSSS 135 MHz (resolution= 108 arcsec and rms noise = 5 mJy/beam, Heald et al. 2015), WSRT-WENSS 325 MHz (resolution= 54 arcsec and rms noise = 3 mJy/beam, Rengelink et al. 1997) and VLA-NVSS 1420 MHz (resolution= 45 arcsec and rms noise = 0.45 mJy/beam, Condon et al. 1998), in order to discover relic radio galaxies. Radio analysis at meter-wavelength is presented for 2 different types of radio galaxies hosting relic emission, complemented with high resolution GHz-range radio observation to study their morphological and spectral properties. The low frequency radio observations (including archive) down to 74 MHz confirms the presence of relic emission around the radio jets of the 2 galaxies discussed here.

## 2 Relic emission in fading radio galaxy: B2 0924+30

B2 0924+30 is a relic radio source hosted by the galaxy, IC2476 that resides centrally into a group of 8 galaxies and a member of a nearby poor cluster WBL224 (Mahdavi et al. 1999, White et al. 1999, Jamrozy et al. 2004). IC2476 is associated to a bright E/S0 type galaxy located at a redshift of z = 0.0261 with no emission line indicative of a passive elliptical as shown in Fig. 1. The radio morphology from the multi-frequency radio data from 0.151-10 GHz confirms that the source is a remnant of an edge-brightened FR II type radio galaxy with no radio jet or core features (Shulevski et al. 2015, Jamrozy et al. 2004, Cordey et. al. 1987, Colla et al. 1975, Ekers et al. 1981). The relic shows bright regions in the lobes with relatively flat spectral index ($\alpha = -1$), whereas the overall spectrum is very steep ($\alpha < -1$). The radio luminosity of the source is about $L_{1.4GHz} = 10^{23.8}$ W.Hz$^{-1}$ as normally seen in the case of low luminosity FR I radio galaxies, suggesting that the AGN had a powerful progenitor in the past but after the central AGN activity has diminished, its luminosity is fading out due to synchrotron and inverse Compton losses. Shulevski et al. (2015) mapped the low frequency emission from B2 0924+30 using the LOFAR HBA band and computed a spectral index of $\alpha = -1$ for the lobes, down to $\alpha = -1.8$ for the inner regions of the lobe in this source, confirming that it is a radio relic of a terminated FRII. There is no sign of restarted AGN activity suggesting that the relic emission is due to the fading of aged plasma. Further, the radiative ageing model suggests that, the age of the outer lobe is around 20 Myr and that towards the host galaxy is 100 Myr, the time elapsed since the AGN has turned off (Shulevski et al. 2015, Jaffe and Perola 1973).

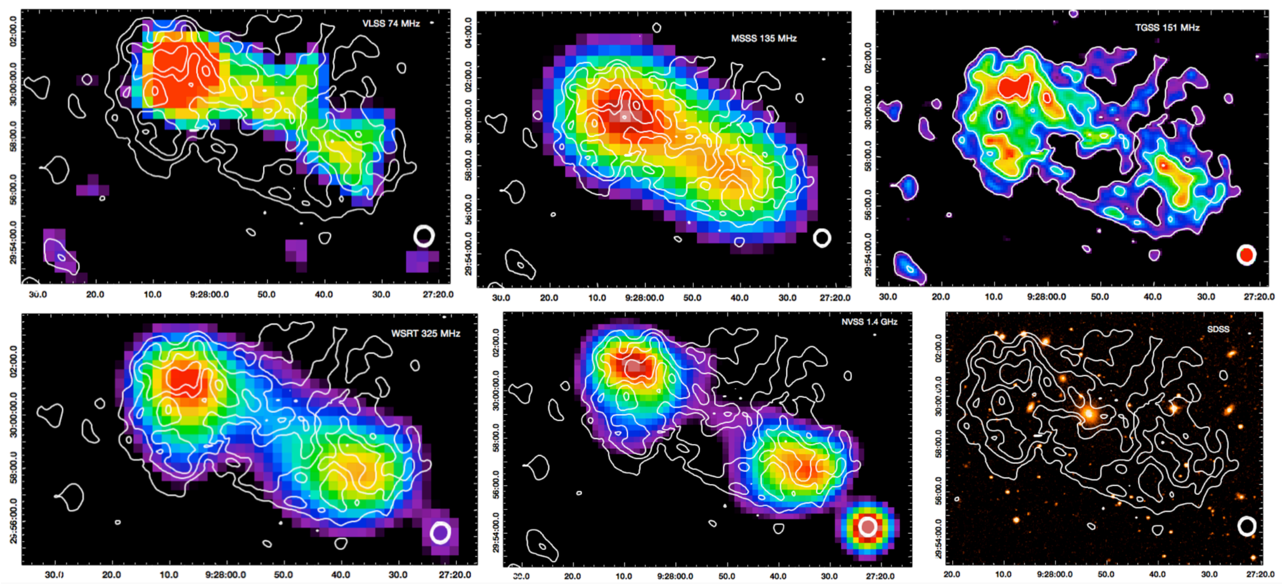


**Fig. 1.** Radio images of B2 0924+30 from various surveys in color scale with TGSS survey high resolution contour overlaid in white.

Low frequency surveys like, VLA-VLSSr, GMRT-TGSS, LOFAR-MSSS, WSRT-WENSS and VLA-NVSS 1420 have clearly detected the 440 kpc relic emission in B2 0924+30 down to 74 MHz (refer Fig. 1 top panel).

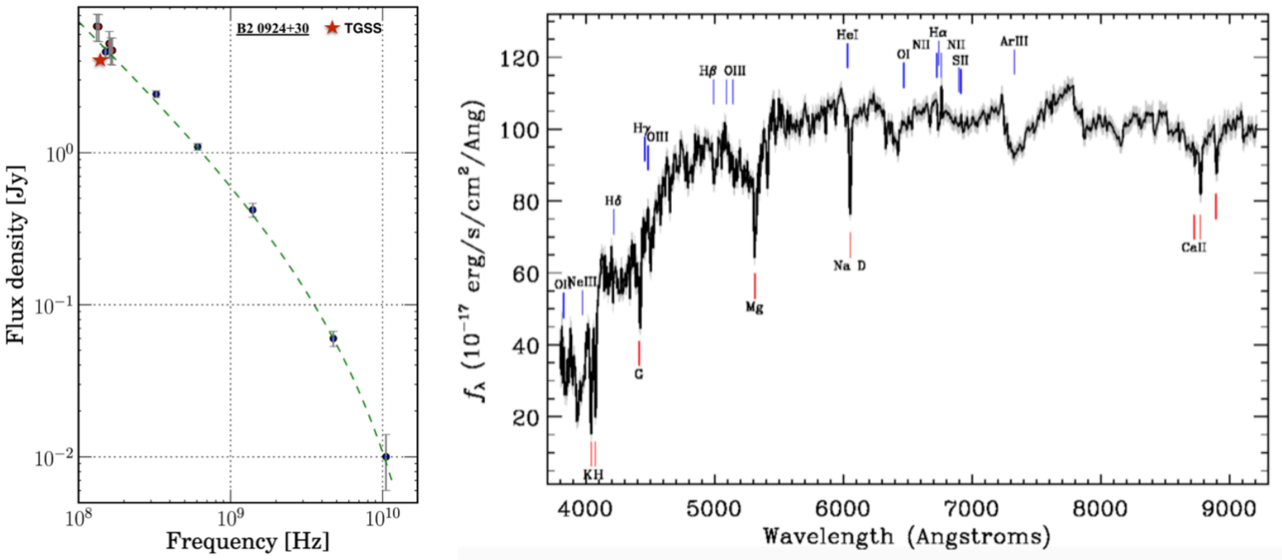


**Fig. 2.** Left panel shows multi frequency radio spectra extracted from Shulevski et al. (2015) with TGSS flux density marked in red and right panel with SDSS spectra of the host optical galaxy IC2476.

The radio galaxy shows a double lobe morphology with no bright core in the center in all the survey images. The TGSS survey being higher in resolution and better in sensitivity at meter wavelength regime has been able to map the morphological details like the faint central region, bended jet structures and overall diffuse radio emission in the radio lobes efficiently, giving better estimate on the source size. The VLSSr survey having lower sensitivity detects only the bright regions in the radio lobes, whereas the MSSS survey being better in sensitivity detects more diffuse emission in the lobes. The high frequency NVSS survey detects only the bright lobe regions but no diffuse extended emission (which tends to be visible only at lower frequencies). The high frequency emission from the bright regions is mainly due to young population of electrons, that tentatively age and loose energy due to adiabatic losses and finally emit mainly at lower frequencies. The integrated flux density measured in the TGSS and MSSS images are in agreement with the available data from the literature and shows that the emission from the overall relic regions dominate the spectrum rather then those from the central region (see Fig. 2).

## 3 Relic emission in restarted radio galaxy: 4C 35.06

4C 35.06 resides in the core of a cD galaxy UGC 2489 that lies at the center of Abell 407 cluster of galaxies (Schneider and Gunn 1982). The radio luminosity of 4C 35.06 is, $L_{1.4GHz}$ = 2.5 $\times 10^{24}$ W Hz$^{-1}$ as typically seen in FR I, lies at a redshift of z = 0.046726 and shows no emission line in the optical spectra suggesting that the host is an elliptical galaxy (Shulevski et al. 2015, Biju et al. 2016). The SDSS optical image of UGC 2489 shows multi-component (9 galaxies) core structure with a stellar halo around the core of roughly 40 kpc in extent (see Fig. 3). High resolution VLA (Liuzzo et al. 2010), GMRT (Biju et al. 2016) and LOFAR (Shulevski et al. 2015) images shows a central unresolved core with radio emission from multiple galaxies, twisted helix dual jet structure scaling upto 435 kpc with no clear hotspots and extended diffuse relic emission at the end of the jet suggesting a FRI type radio galaxy. The twisted jet pattern suggest that the AGN has been active recently and has produced helical structure due to merger or interaction with the other AGNs in the core region (Biju et al. 2016).

The low resolution observations map the unresolved core and extended jet structure down to 74 MHz maps, as seen in Fig. 3. The GMRT-TGSS survey being higher in resolution and good in sensitivity not only maps the connected core and twisted jet morphology but also the underlying diffuse relic emission at the edge of the jets. The relic emission has a steep spectral index $\alpha$ = -2, indicative of a fossil of old plasma. The relic emission has been also measured with the LOFAR and GMRT at higher resolution by Shulevski et al. (2015) and Biju et al. (2016). The high sensitivity MSSS LOFAR survey not only confirms the presence of relic emission in 4C 35.06, but also shows hints of more extended diffuse relic emission at the edge of the jets than previously

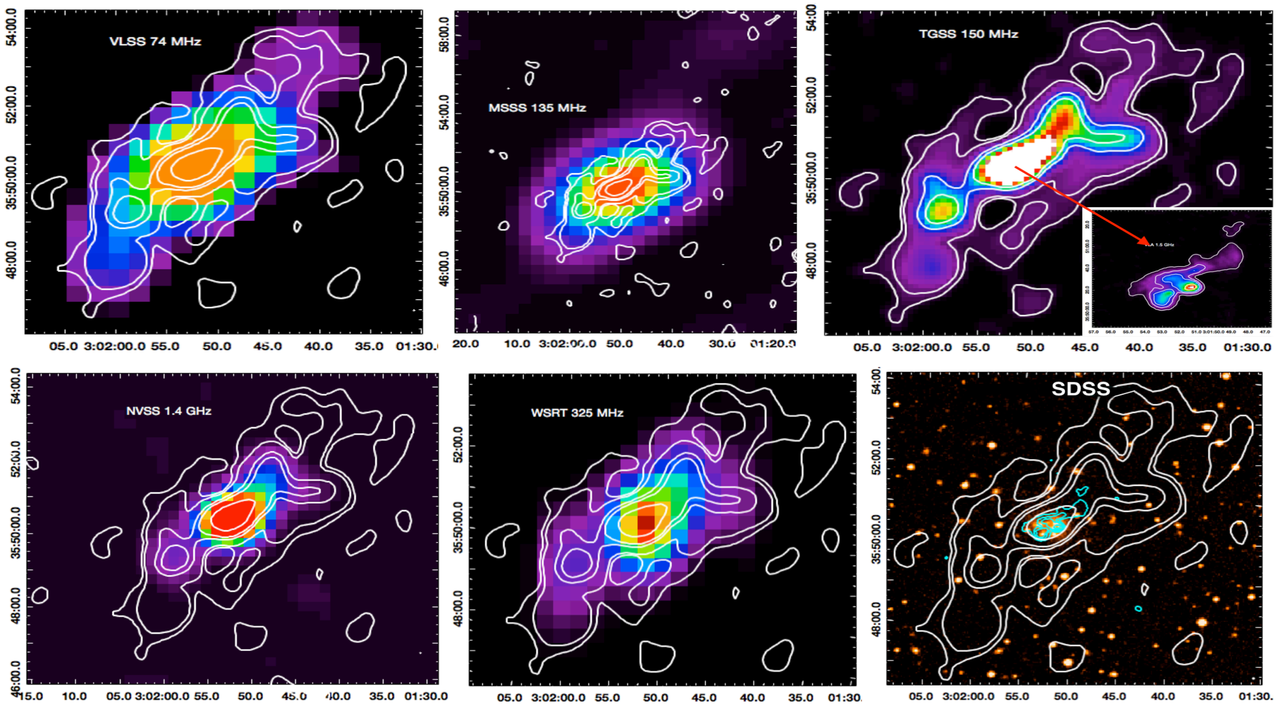


**Fig. 3.** Radio images from various surveys in color scale with TGSS survey high resolution contour overlaid in white. The high resolution VLA image of the core region is shown in the inset image of top 3rd panel.

measured. Deep observations with higher sensitivity below ∼300 MHz are needed to confirm this result. The radio morphology and spectral index suggest that the AGN is intermittently active as it moves in the dense cluster environment.

The broad-band radio spectra suggests that the source has a steep spectral index ($\alpha <$ -1). Integrated flux densities measured in the TGSS survey is in agreement with earlier measurements (see Fig. 4). The average flux from the MSSS survey more or less agrees with the SED. The age of the relic plasma is estimated to be

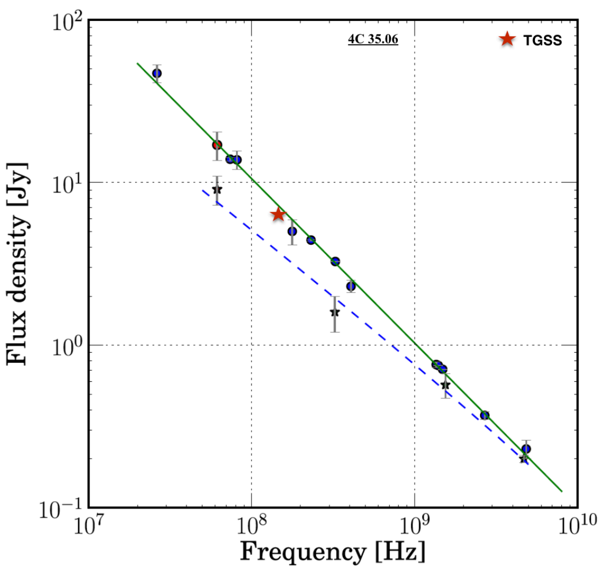


**Fig. 4.** Integrated flux density spectra of 4C 35.06 with TGSS flux density marked in red extracted from Shulevski et al. (2015).

$\sim$70 Myr (elapsed time since last injection of relativistic electrons in the emission region) with 2 different phases (shutdown and restart) of AGN activity in 4C 35.06, suggesting a delay between the 2 phases of 35 Myr each (Shulevski et al. 2015).

## 4 Conclusions

In this paper we demonstrate the importance of database provided by new low frequency radio surveys like TGSS and MSSS to search for relic sources in the meter-wavelength sky, thanks to their unique combination of high sensitivity and resolution. Relic radio galaxies have been rarely detected (at GHz range) and expected to shine efficiently at low radio frequencies as they are sources at the end stage of their life cycle with a fossil of old population electrons. Relics in FR II type radio galaxies are longer lived due to their powerful progenitors as compared to less luminous FR I type galaxies. They show steep spectral properties and extended decay phase as compared to their active phase, due to pressure imposed by the dense cluster environment.

The LOFAR MSSS survey is efficient in detecting low surface brightness regions likes radio lobes, relics etc. however, its low resolution makes it difficult to disentangle the morphological details. The GMRT TGSS survey has better resolution and point source sensitivity than MSSS, but less surface brightness sensitivity and is equally efficient in detecting diffuse emission in AGNs. A large population of relic radio sources are yet to be discovered and the Square Kilometer Array (SKA) will be the ideal interferometer to discover such low surface brightness objects, thanks to its unique combination of high sensitivity, arcsec scale angular resolution and broad (15 MHz- 50 GHz) frequency coverage.

We thank the staff of GMRT, who made these observations possible. The GMRT is run by the National Centre for Radio Astrophysics of the Tata Institute of Fundamental Research. MP is thankful to the research grant received from the Franco-Indian CEFIPRA organization. This research has made extensive use of the data available from the public archive from SDSS, WSRT, VLA and GMRT observatory.

## References

Biju, K. G., et al., arXiv:1607.05080v1

Cohen, A. S., et al. 2007, AJ, 134, 1245

Condon, J. J., et al. 1998, AJ, 115, 1693

Colla, G., et al. 1975, A&AS, 20, 1

Cordey, R. A. 1987, MNRAS, 227, 695

Eckers, R., et al. 1981, A&A, 101, 194

Heald, G. R. et al. 2015, A&A, 582, 123

Fanaroff, B. L., Riley, J. M. 1974, MNRAS, 167, 31

Intema, H. et al., arXiv:1603.04368

Jamrozy, M. et al. 2004, A&A, 427, 79

Jaffe, W. J. and Perola, G. C. 1973, A&A, 26, 423

Lane, W. M., Cotton, W. D., Helmboldt, J. F., Kassim, N. E. 2012, RaSc, 47, 0K04

Lane, W. M., et al. 2014, MNRAS, 440, 327

Liuzzo et al. 2010, A&A, 516, 1

Maddavi, A. et al. 1999, ApJ, 518, 69

Rengelink, R. et al. 1997, A&AS, 124, 259

Schneider, D. P. and Gunn, J. E. 1982, ApJ, 263, 14

Shulevski, A. et al. 2015, A&A, 579, 27

Sirothia, S. K. 2010, PhD thesis

White, R. A. et al. 1999, AJ, 118, 2014

*SF2A 2016*
*C. Reylé, J. Richard, L. Cambrésy, M. Deleuil, E. Pécontal, L. Tresse and I. Vauglin (eds)*

# RADIO MODE FEEDBACK VIA BCGS IN COOL CORE CLUSTERS

S.-L. Hamer[1], M. P. Pommier[1], A.-C. Edge[2] and F. Combes[3]

**Abstract.** Brightest Cluster Galaxies (BCGs) are the most extreme and interesting population of luminous and massive galaxies known within the cluster environment. Nearly all BCGs tend to show radio emission with radio jets varying in size from a few kpc to Mpc scale with various morphological and spectral details (FRI, FRII, WAT, NAT, twisted jets, relic emission etc.). At optical wavelengths many BCGs show ionised emission line (H-alpha) nebula with a range of different morphological structures (extended filaments, one directional plumes, centrally concentrated, extended but quiescent, etc.) but often have an inner disc region with rotational velocities ranging from 100 to several hundred km/s whose axis of rotation is aligned with the radio jets. We perform a combined optical (VIMOS, MUSE) /radio (GMRT, VLA) study of BCGs and derive a correlation between the disc and jet properties (alignment, radio power, rotational velocity, dominance of the disc etc.). We then discuss these correlations in the context of feedback and mergers in the cluster environment. This study is intended to understand the duty cycle (birth, evolution and death) of AGNs in cool core clusters and highlight the importance of low frequency observations in this field with sensitive instruments like LOFAR and SKA precursors (MeerKAT and ASKAP), that are now beginning to operate.

Keywords: Galaxies: clusters: general, Galaxies: clusters: intracluster medium, Radio galaxies:clusters:individual:Hydra-A:Abell194:Abell2566:RXJ 0821+07:Abell 2052, Intracluster medium, Diffuse emission:relics, Galaxies:ellipticals and cD

## 1 Introduction

The central regions of massive galaxy clusters show intense X-ray emission suggesting that significant radiative cooling is occurring within the Intra Cluster Medium (ICM) (Fabian et al. 1981). This suggests that the gas should quickly lose energy, cool down and condense into cold gas clouds and/or form stars on timescales much shorter than the age of the cluster (Fabian 1994). However, the observed star formation rates (McNamara & O'Connell 1989) and cold gas masses (Braine & Dupraz 1994; McNamara & Jaffe 1994; O'Dea et al. 1994; Edge 2001; Salomé & Combes 2003) are insufficient to be consistent with the rate of gas cooling estimated from the X-ray data. Studies of highly sensitive X-ray spectral observations (Peterson et al. 2001; Tamura et al. 2001; Peterson et al. 2003) failed to detect the spectral signatures of gas cooling at $\sim$1 keV. Most importantly the FeXVII line, emitted by gas at 0.5–1 $\times$ $10^6$ K, is weak or absent in many cooling flow clusters. This suggests that some process is truncating the cooling of gas below $\sim frac1,3$ $T_{cluster}$ (one third of the clusters X-ray temperature), preventing the production of cooler gas (see review by Peterson & Fabian 2006).

The fact that the ICM core is rapidly radiating away most of its energy but shows significantly reduced cooling below a critical threshold ($\sim 10v$K) suggests that there must be some process injecting energy back into the cooling gas. Radio mode "feedback" from AGN is the only process consistent enough and energetic enough to provide the energy required to offset the energy loss in the most rapidly cooling cluster cores. This mechanical feedback, occurring as the radio jets (up to Mpc-scale) inflate massive cavities in the ICM (McNamara et al. 2005; McNamara & Nulsen 2007) is central to the growing consensus within the community. This hypothesis is further confirmed by the fact that almost all the BCGs tend to host radio jets. In the case of gas rich cool-core clusters, repeated radio outburst activity gives rise to rare relic emission (with $\alpha < -1.5$) usually in

[1] CRAL, Observatoire de Lyon, CNRS, Universit Lyon 1, 9 Avenue Charles Andr, F-69561 Saint Genis-Laval, France
[2] Department of Physics, Institute for Computational Cosmology, Durham University, South Road, Durham DH1 3LE, UK
[3] LERMA Observatoire de Paris, CNRS, 61 rue de l'Observatoire, F-75014 Paris, France

the peripheral regions of the jet that emits predominantly at lower frequencies Lane et al. (2004). However, the most rapidly cooling cluster cores ubiquitously contain optical line emitting nebula (at $\sim 10^4$ K) surrounding the BCG (Heckman et al. 1989; Cavagnolo et al. 2008). This suggests that despite the feedback some residual cooling must be present to produce this cool gas. Indeed this residual production of cool gas can provide the fuel required to drive the AGN outbursts from the BCG providing a potential mechanism to fine tune the radio feedback and maintain the X-ray properties observed.

## 2 The VOICES data

The Vimos Optical Ifu Cluster Emission line Survey (VOICES) was conduced by Hamer et al. (2016) to study the properties of the optical emission line nebula surrounding BCGs in rapidly cooling clusters. VOICES obtained and studied VIMOS IFU observations of 73 cluster cores known to contain optical line emitting nebula allowing these nebula to be studied in a statistically significant way for the first time. The study found that the line emitting nebula could be catagorised into five distinct morphological classes. The most common were quiescent objects, accounting for 62% of the sample, which were elliptical in structure, centrally concentrated and had a H$\alpha$ peak coincident with the continuum peak. Compact objects, making up just 4% of the sample, were similar but only extended on scales comparable to the seeing making their resolved properties difficult to constrain. Disturbed objects, which had made up the bulk of previously studied objects, accounted for just 17% of the sample. These objects had central H$\alpha$ peaks coincident with the continuum peak but show extended line emission with no ordered structure. The other two classifications show extended emission in just one preferential direction. The most common of these were plumes (12% of the sample) which has a H$\alpha$ peak close to the continuum peak and a lower surface brightness "tail" extending away from the BCG. The final classification were offset objects (just 5% of the sample) in which the majority of the H$\alpha$ emission is associated with a peak offset from the continuum peak by greater than twice the seeing.

The resolved kinematics of the sample suggested that the ionised nebula form a kpc scale disc like structure in the cores of many clusters. Kinimetry analysis (Krajnović et al. 2006; Shapiro et al. 2008) shows that 65% of the sample have kinematics which are consistent with discs. These are found in almost all of the quiescent systems but also within some of the compact objects and within the central regions of some disturbed objects. This suggests that such discs are common in cluster cores and may be an important component of the feedback process.

## 3 Optical Nebula and jet properties comparison

Multi wavelength studies of BCGs can give important insights into the role of the BCG in fueling the feedback process through radio outbursts. A combined optical and radio analysis allows us to investigate the impact of the kpc scale discs on the formation and activation of the radio outflows. Massive discs contain sufficient fuel to launch large scale and sustained radio jets while systems without discs (or with disturbed discs) lack a simple mechanism of funneling this fuel into the AGN accretion region. In Hamer et al. (2016) we identified five distinct morphologies of optical nebulae which may represent distinct evolutionary phases of the cluster core. We discuss below the comparison of radio data from 1.4 GHz down to 150 MHz with the optical data (1) for one example object from each of these morphological classifications:

**Hydra–A** is a BCG with a FR–I type radio morphology situated at the centre of a quiescent nebular of ionised gas. It shows the presence of a 5kpc disc of cold molecular and atomic gas whose axis of rotation is aligned with the radio jets (Hamer et al. 2014a). At 1.4 GHz the radio jets extend for ∼100 kpc and show an S-shaped morphology. Deep MUSE observations of the system detect the presence of H$\alpha$ emission along the eastern edge of the high frequency radio emission. This suggests that the radio jets are directly interacting with the cool gas in this system however, the line emission is asymmetric about the jets following only the eastern edge. These observations are not sensitive enough to directly constrain the form of this interaction (entrainment, enhanced cooling from the compressed ICM etc.) nor if lower surface brightness emission is present on the western edge of the jets. At 150 MHz the emission is significantly more extended with lobes extending over 530 kpc retaining the orientation of the higher frequency jets. Lane et al. (2004) studied the low frequency emission of the jets down to 74 MHz with the VLSS data and suggested a presence of relic emission from the jet with a spectral index between 330 to 74 MHz for the core region, $\alpha = -0.48 \pm 0.03$, for the northern lobe region, $\alpha = -1.20 \pm 0.04$ and $\alpha = -1.5 \pm 0.1$ for the southern lobe. Our new GMRT data at 150 MHz confirms the presence of the diffuse relic emission from the lobes and allows us to measure the spectral index

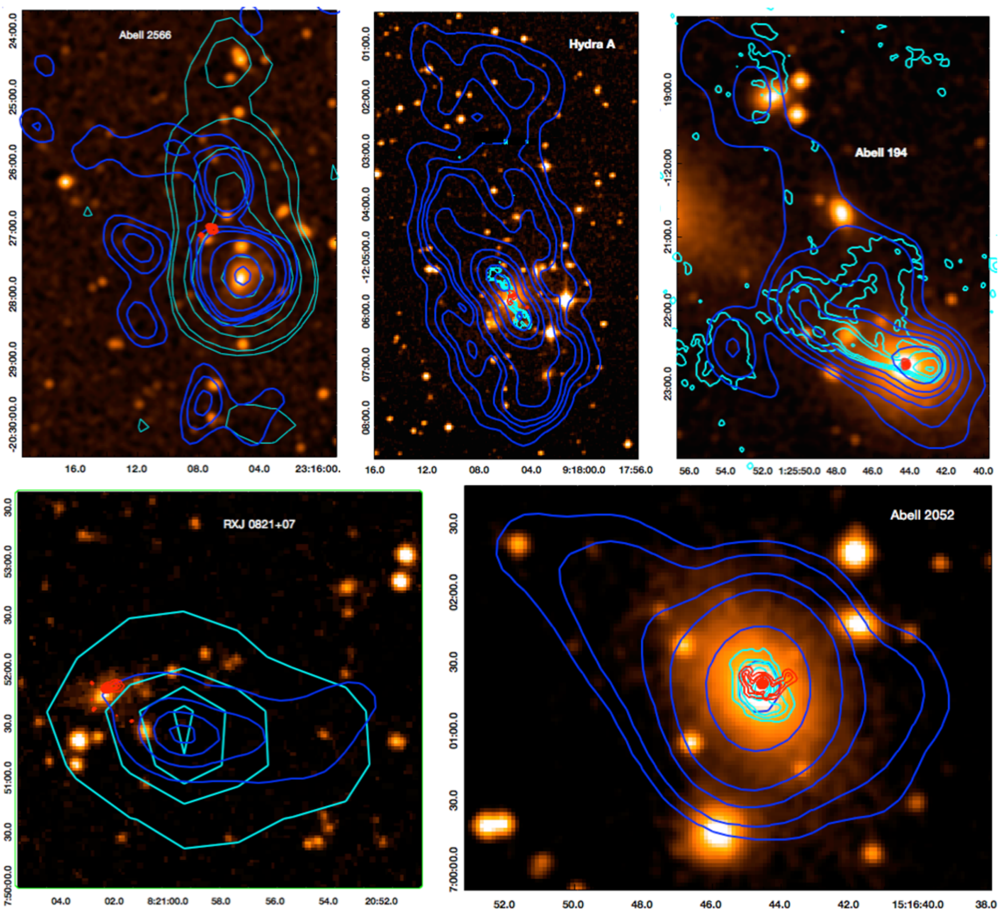


**Fig. 1.** DSS data on cool-core galaxy cluster with overlaid contours from VIMOS H-alpha disc emission (red), TGSS-GMRT 150 MHz (blue) and VLA 1.4 GHz (cyan). From left to right and top to bottom panels- Abell 2566 (offset H$\alpha$), Hydra A (quiescent H$\alpha$), Abell 194 (compact H$\alpha$), RXJ 0821+07 (plumed H$\alpha$) and Abell 2052 (disturbed H$\alpha$). Note that the red contours for the disc emission in Hydra A is measured with the MUSE/VLT.

for the complete structure between 1.4 GHz to 150 MHz at $\alpha = -0.86$. Lane et al. (2004) measure the life time of the lobes to be 47 Myr which is consistent with the age of the outburst estimated from black hole accretion rates and efficiencies (Wise et al. 2007).

**Abell 194** host a BCG with a very compact optical nebula that shows evidence of rotation. The BCG is associated with a narrow angle tailed (NAT) FR–I radio galaxy with jets extending up to 135 kpc at 1.5 GHz. GMRT data at 150 MHz shows a similar extent up to 142 kpc and more clearly traces diffuse emission in the northern jet (Sakelliou et al. 2008). The lobes have a spectral index of $\alpha = -0.51$ between 1.5 GHz and 150 MHz and an estimated age of 1.2 Gyr. The presence of a narrow angled tail in this system suggests that ram pressure is exerted on the radio jets as the galaxy moves through the ICM. This coupled with the central but small ionised nebula implies that this system may be in the late stages of a merger as cold gas begins to re-accumulate in the core.

**Abell 2052** hosts a disturbed optical nebular which shows no ordered velocity structure. The BCG is producing a FR-I type radio galaxy with radio emission at 1.4 GHz that fills the ICM cavities in the North/South direction. The optical nebula shows limbs of emission which extend around the edges of the northern radio lobe. The presence of gas here and the fact that the limbs show no ordered velocity structure suggest that they are likely related to the formation of the X-ray cavity, most likely gas entrained by the radio jet and pulled out of the central nebula. At 150 MHz the structure is much more extended, out to 120 kpc, and shows a sloshing jet morphology which causes spiral structures that can also be seen in the X-ray emission. The spectral index between 1.4 GHz and 150 MHz varies significantly between $\alpha = -0.5$ in the core region and $\alpha = -2.5$ near the edges, suggesting a presence of relic emission surrounding the BCG. However, deep low frequency radio observations are needed to confirm the morphology, size and excess emission at 150 MHz of the jet structure.

**The BCG in RXJ 0821+07** contains a plumed optical nebula with evidence of a disc in the central bright region. The radio source is a head-tail galaxy with an extension of 346 kpc that is barely resolved at 1.2 GHz. At 150 MHz the head-tail structure is clearly resolved and extends from the BCG over a similar extent to the higher frequency data. More diffuse emission at 1.4 GHz is detected as compared to 150 MHz, with a clear offset between the peak of the radio and the optical emission. Further deep radio observations are needed in this BCG, at low radio frequencies in order to confirm the radio counterpart, its morphology and extent of the diffuse emission. The spectral index is -0.9 above 1.4 GHz and gets steeper, $\alpha < -1.2$ at lower frequencies suggesting that there are overlapping regions of plasma with different ages.

**Abell 2566** has a bright centrally peaked nebula that is completely offset from the BCG that shows no evidence of rotation. The BCG hosts an FR-I radio source which is extended in the north/south direction over ∼600 kpc. The presence of line emission offset from the BCG is typically associated with gas sloshing within the core of the BCG (Hamer et al. 2014b) which is possibly being caused by an interaction. The GMRT data shows a bend in the 150 MHz radio morphology to the north of the extent which also suggests sloshing, hence consistent with the optical data. This structure extends over 660 kpc and has a spectral index between 1.4 GHz and 150 MHz of $\alpha = -1.22 \pm 0.02$.

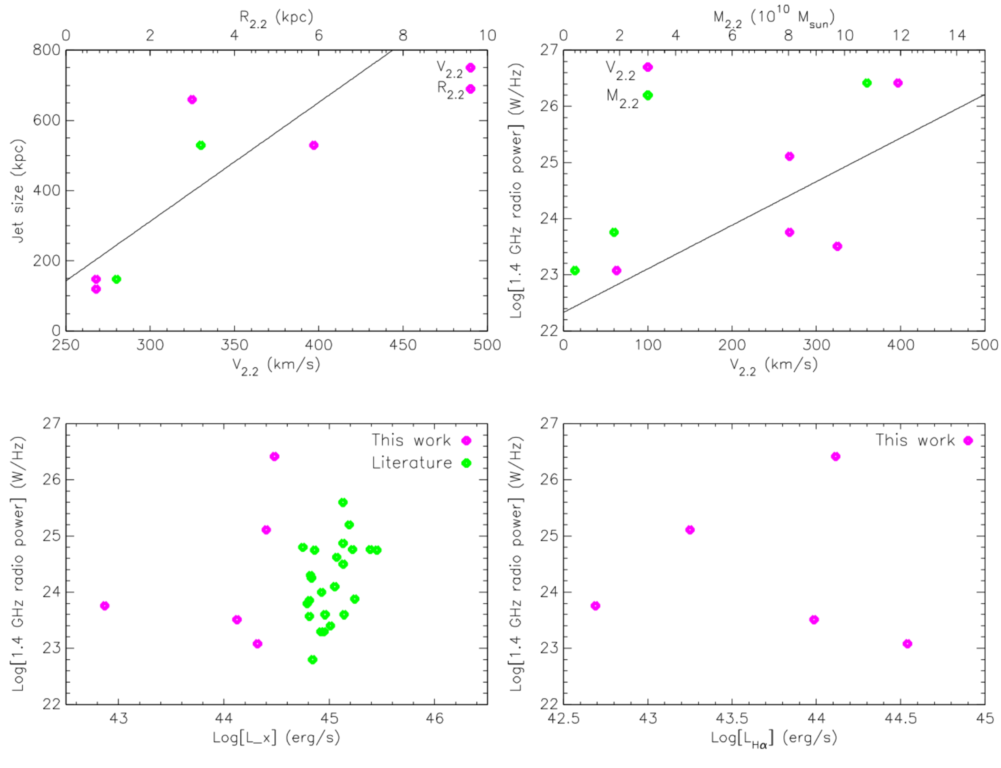


**Fig. 2.** A comparison of the radio properties with the optical and X-ray properties of the cluster. *Top left*: Extent of the jet plotted against the peak rotational amplitude and flattening radius of the disc. *Top right*: 1.4 GHz radio power against the peak rotational amplitude and the dynamical mass of the disc. *Bottom left*: 1.4 GHz radio power against the X-ray luminosity. *Bottom right*: 1.4 GHz radio power against the H$\alpha$ luminosity. Purple points are those derived from this study, green points are taken from the literature.

In figure 2 we compare the properties of the radio jets with those of the optical nebulae and the cluster X-ray emission. We find that the jet size is well correlated with the disc properties (rotational velocity, disc size and dynamical mass) and the radio power increases as the rotational velocity increases. This suggests that more stable discs are launching larger jets while smaller and disturbed discs launch smaller jets. There is some trend of radio power with $L_{H\alpha}$ suggesting the outliers may have a different evolution. This might be expected as more larger more massive discs imply higher orbital angular momentum which will produce a more powerful jet through the BlandfordZnajek process (Blandford & Znajek 1977).

## 4 Conclusions

Radio sources from BCGs have a large variation in size (100–700kpc) with various morphologies (FRI, FRII, WAT, NAT, head-tail etc.). The largest most powerful jets are produced in the most massive and stable discs suggesting discs are an important part of the feedback process. The presence of aged plasma in the ICM suggests that the outbursts are periodic and repeated suggesting feedback is not always on in all systems. We suggest a feedback duty cycle based on the morphological classifications discussed above. Compact objects, which host radio loud AGN are systems which are just beginning to accrete gas and drive outbutrsts. As gas accumulates the disc grows forming a quiescent object driving large radio lobes and retaining some relic emission. Finally the feedback outpaces the accretion disturbing the disc, less fuel is available to drive the outbursts and the system is dominated by relic radio emission. The structure of the H$\alpha$ and radio in the offset and plumed objects are more consistent with mergers and may represent a separate evolution. Further low frequency observations in this field with sensitive instruments like LOFAR and SKA precursors (MeerKAT and ASKAP) will allow us to expand this analysis to more objects improving the statistics of this analysis.

We thank the staff of GMRT, who made these observations possible. The GMRT is run by the National Centre for Radio Astrophysics of the Tata Institute of Fundamental Research. MP is thankful to the research grant received from the Franco-Indian CEFIPRA organization. This research has made extensive use of the data available from the public archive from DSS, VLA and GMRT observatory.

## References

Blandford, R. D. & Znajek, R. L. 1977, MNRAS, 179, 433
Braine, J. & Dupraz, C. 1994, A&A, 283, 407
Cavagnolo, K. W., Donahue, M., Voit, G. M., & Sun, M. 2008, ApJ, 683, L107
Edge, A. C. 2001, MNRAS, 328, 762
Fabian, A. C. 1994, ARA&A, 32, 277
Fabian, A. C., Hu, E. M., Cowie, L. L., & Grindlay, J. 1981, ApJ, 248, 47
Hamer, S. L., Edge, A. C., Swinbank, A. M., et al. 2014a, MNRAS, 437, 862
Hamer, S. L., Edge, A. C., Swinbank, A. M., et al. 2014b, MNRAS, 437, 862
Hamer, S. L., Edge, A. C., Swinbank, A. M., et al. 2016, MNRAS, 460, 1758
Heckman, T. M., Baum, S. A., van Breugel, W. J. M., & McCarthy, P. 1989, ApJ, 338, 48
Krajnović, D., Cappellari, M., de Zeeuw, P. T., & Copin, Y. 2006, MNRAS, 366, 787
Lane, W. M., Clarke, T. E., Taylor, G. B., Perley, R. A., & Kassim, N. E. 2004, AJ, 127, 48
McNamara, B. R. & Jaffe, W. 1994, A&A, 281, 673
McNamara, B. R. & Nulsen, P. E. J. 2007, ARA&A, 45, 117
McNamara, B. R., Nulsen, P. E. J., Wise, M. W., et al. 2005, Nature, 433, 45
McNamara, B. R. & O'Connell, R. W. 1989, AJ, 98, 2018
O'Dea, C. P., Baum, S. A., Maloney, P. R., Tacconi, L. J., & Sparks, W. B. 1994, ApJ, 422, 467
Peterson, J. R. & Fabian, A. C. 2006, Phys. Rep., 427, 1
Peterson, J. R., Kahn, S. M., Paerels, F. B. S., et al. 2003, ApJ, 590, 207
Peterson, J. R., Paerels, F. B. S., Kaastra, J. S., et al. 2001, A&A, 365, L104
Sakelliou, I., Hardcastle, M. J., & Jetha, N. N. 2008, MNRAS, 384, 87
Salomé, P. & Combes, F. 2003, A&A, 412, 657
Shapiro, K. L., Genzel, R., Förster Schreiber, N. M., et al. 2008, ApJ, 682, 231
Tamura, T., Kaastra, J. S., Peterson, J. R., et al. 2001, A&A, 365, L87
Wise, M. W., McNamara, B. R., Nulsen, P. E. J., Houck, J. C., & David, L. P. 2007, ApJ, 659, 1153

# Session SF2A

# The Epoch of Reionisation

*SF2A 2016*
*C. Reylé, J. Richard, L. Cambrésy, M. Deleuil, E. Pécontal, L. Tresse and I. Vauglin (eds)*

# THE INTRINSIC EVOLUTION OF LY$\alpha$ -EMITTING GALAXIES FROM Z $\approx$ 3 TO THE EPOCH OF REIONIZATION

T. Garel[1]

**Abstract.** The evolution of the Ly$\alpha$-emitting galaxy population at z $\gtrsim$ 6 has become a popular tool to probe the reionization of the intergalactic medium. Ly$\alpha$ photons arising from high redshift galaxies and travelling towards the observer can indeed be scattered off the line of sight by hydrogen atoms in the intergalactic medium, such that a rapid change of the observed Ly$\alpha$ properties of galaxies can in principle trace the evolution of the IGM neutral fraction. However, in addition to intergalactic attenuation, the observability of Ly$\alpha$ galaxies may also be (at least partially) driven by the intrinsic evolution of their physical properties and their internal Ly$\alpha$ escape fraction. Here, we use a semi-analytic model of galaxy formation which accounts for the complex travel of Ly$\alpha$ photons through galactic winds but neglects the effect of IGM absorption to discuss how intrinsic evolution alone affects the properties Ly$\alpha$-emitting galaxies at high redshift.

Keywords: galaxies: formation – galaxies: evolution – galaxies: high-redshift – radiative transfer – methods: numerical.

## 1 Introduction

Ly$\alpha$-emitting galaxies are commonly observed from the ground at z $\gtrsim$ 2-3 up to z $\approx$ 7, allowing us to get insight into the first stages of galaxy formation. Of prime interest is the process of reionization which began when the first sources lit up and started heating up the gas and ionizing the intergalactic medium. The exact epoch at which reionization occurred, the nature of the sources responsible for it, as well as its impact on the formation and evolution of galaxies in the early Universe are still questions open to debate. Observationally, Gunn-Peterson trough measurements in quasar spectra show that the Universe was almost fully ionized by z $\gtrsim$ 6, while the analysis of anisotropies in the CMB suggest that reionization started prior to z $\approx$ 10 (Becker et al. 2015; Planck Collaboration et al. 2016). In between (z $\approx 6-8$), most constraints on the (volumetric) neutral fraction of the IGM, $x_{\rm HI}(z)$, have been inferred from Ly$\alpha$ emitter (LAE) observations (e.g. Ouchi et al. 2010; Schenker et al. 2014). Ly$\alpha$ photons being resonantly scattered by HI atoms, the observability of the Ly$\alpha$ line from high redshift galaxies can be strongly affected by IGM attenuation as the redshift increases, in particular when entering the epoch of reionization (z $\approx$ 6). Three main diagnostics have been suggested to probe $x_{\rm HI}(z)$ using Ly$\alpha$-emitting galaxies based on the redshift evolution of (i) the Ly$\alpha$ luminosity function, (ii) the fraction of strong line emitters found in dropout galaxy surveys (i.e. among galaxies selected via their UV continuum magnitudes), and (iii) the clustering of LAEs. The interpretation of these observations with reionization models (e.g. McQuinn et al. 2007) favor an IGM neutral fraction of the order of $\approx$ 50% at z $\approx 6.5-7$. In most cases, the apparent change of the Ly$\alpha$ properties at z $\gtrsim$ 6 is solely attributed to an increase of the neutral fraction of the IGM.

Here, in particular, we will discuss how the *intrinsic* evolution of the physical properties and the internal escape fraction of Ly$\alpha$ photons affect the observability of LAEs at high redshift. We make use of a semi-analytic model of galaxy formation combined with a grid of Ly$\alpha$ radiation transfer models (Garel et al. 2015). The semi-analytic model presented in Garel et al. (2015) is based on an updated version of GALICS (Hatton et al. 2003; Garel et al. 2016). GALICS describes the formation and evolution of galaxies in the cosmological context using (i) a N-body simulation to follow the growth of the dark matter structures and (ii) semi-analytic prescriptions to model the baryonic physics within the dark matter haloes identified in the simulation. We follow Garel et al.

[1] Univ Lyon, Univ Lyon1, Ens de Lyon, CNRS, Centre de Recherche Astrophysique de Lyon UMR5574, F-69230, Saint-Genis-Laval, France

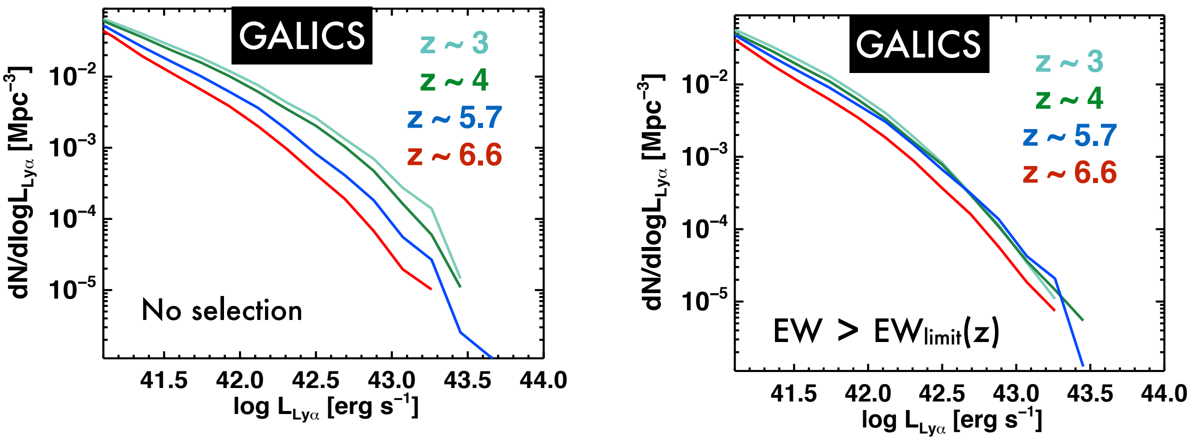


**Fig. 1. Left:** Ly$\alpha$ LFs at z ≈ 3, 4, 5.7 and 6.6 as predicted by the Garel et al. (2015) model without LAE selection. **Right:** Same as the left panel but using an equivalent width limit to select LAEs.

(2012) to predict the Ly$\alpha$ properties of each galaxy. The intrinsic Ly$\alpha$ line is estimated from GALICS and described by a Gaussian profile centered on $\lambda_\alpha$. Observationally, there is growing evidence that the internal Ly$\alpha$ escape fraction and the observed line profiles of galaxies both at low and high-redshift are primarily shaped by the presence of galactic outflows, presumably powered by supernovae (e.g. Steidel et al. 2010). We therefore compute the Ly$\alpha$ radiation transfer using a simple wind model for GALICS galaxies (Garel et al. 2012) coupled with a grid of numerical simulations of Ly$\alpha$ radiative transfer in expanding shells composed of HI gas and dust (Verhamme et al. 2008; Schaerer et al. 2011).

In the following sections, we compare our predictions to various existing Ly$\alpha$ datasets and discuss at which extent *intrinsic* evolution alone can account for the observed evolution of the Ly$\alpha$ luminosity function (LF), the fraction of strong emitters and LAE clustering at z ≈ 6.

## 2 Ly$\alpha$ luminosity functions

In the left panel of Figure 1, we show the raw predictions from the Garel et al. (2015) model in which all LAEs at each redshift are used to construct the Ly$\alpha$ LFs. In the model, the redshift evolution of the Ly$\alpha$ LF is driven by the joint evolution of the star formation rate (SFR) and the Ly$\alpha$ escape fraction of galaxies. On the one hand, the Ly$\alpha$ LF is primarily driven by the evolution of the SFR function (since $L^{\rm intr}_{\rm Ly\alpha} \propto$ SFR) which increases in the model from z = 6 to z = 3 as a result of the growth of galaxies through gas accretion and mergers in a hierarchical Universe. On the other hand, we find that the average $f_{\rm esc}$ does not vary much with redshift, though there is a lot of dispersion from one galaxy to another depending on their own wind properties*.

Based on SUBARU observations, Ouchi et al. (2008) report the non-evolution of the Ly$\alpha$ LF between z = 3.1 and z = 5.7 and a sudden decrease from z = 5.7 to z = 6.6 (often associated to an increase of $x_{\rm HI}$), which is in contrast with our model predictions. In addition, Ouchi et al. (2010) find that the UV LF of LAEs seems to remain unchanged over this period. This suggests that, while the number density of LAEs does not vary, their observed Ly$\alpha$ luminosity is reduced up to ≈ 30 % (Ouchi et al. 2010; Hu et al. 2010; Kashikawa et al. 2011). To interpret the difference between our predictions and the SUBARU data, we now consider the impact of the LAE selection. The NB technique used by Ouchi et al. (2008, 2010) detects LAEs in wide-field surveys using various color criteria on the basis of an excess of flux in the NB. At first order, these criteria will select sources which have a rest-frame Ly$\alpha$ equivalent width (EW) greater than a given limit, $\rm EW_{limit}$. In the study of Ouchi et al. (2008, 2010), these $\rm EW_{limit}$ are higher at lower redshift, i.e. from ≈ 60Å at z ≈ 3 to 15Å at z ≈ 6.6. In the right panel of Figure 1, we show the Ly$\alpha$ LFs predicted by the model once we include this selection (in practice, we allow the $\rm EW_{limit}$ to vary by ≈ 20% around the value quoted by Ouchi et al. (2008, 2010)). We see that the

*To test the additional effect of intervening gas on Ly$\alpha$ fluxes, we used simple empirical prescriptions to model the Ly$\alpha$ attenuation due to intergalactic absorbing systems. As discussed in Garel et al. (2015), we find an IGM transmission of nearly 100% in all cases because most Ly$\alpha$ photons are redshifted away from resonance while escaping the galaxies through gas outflows in our model.

non-evolution of the LF from z = 3 and z = 5.7 can now be reproduced because the selection removes a larger fraction of LAEs at z ≈ 3 than at z ≈ 6. Nevertheless, we note that spectroscopic surveys have also reported a constant Ly$\alpha$ LF evolution from z ≈ 3 and z ≈ 6 using fixed $\mathrm{EW}_{\mathrm{limit}}$ (Cassata et al. 2011), in agreement with the SUBARU data but in contradiction with our interpretation. However, the volume they probed was small so it is plausible that cosmic variance was affecting their results. In addition, we find that the z = 6.6 Ly$\alpha$ LF is decreased by an amount of about 30% in terms of Ly$\alpha$ luminosity compared to the lower redshift LFs, in good agreement with the observed trend. Our results suggest that additional constraints using more homogeneous selection over large samples of LAEs seem necessary to fully exploit the Ly$\alpha$ LF evolution as a probe of $x_{\mathrm{HI}}$.

## 3 LAE fraction

In the last years, many studies have intended to use the fraction of Ly$\alpha$ line emitter, $X_{\mathrm{LAE}}$, in samples of dropout galaxies as a probe of $x_{\mathrm{HI}}(z)$. $X_{\mathrm{LAE}}$ increases from z ≈ 3 to z ≈ 6 and seems to suddenly drop at z ≈ 7 (Stark et al. 2011; Schenker et al. 2014), possibly due to by a sharp increase of neutral IGM opacity at z $\gtrsim$ 6[†]. In Figure 2, we show the redshift evolution of the fraction of strong (EW > 55Å; right panel) and weaker (EW > 25Å; left panel) Ly$\alpha$ emitters among UV-bright dropout galaxies.

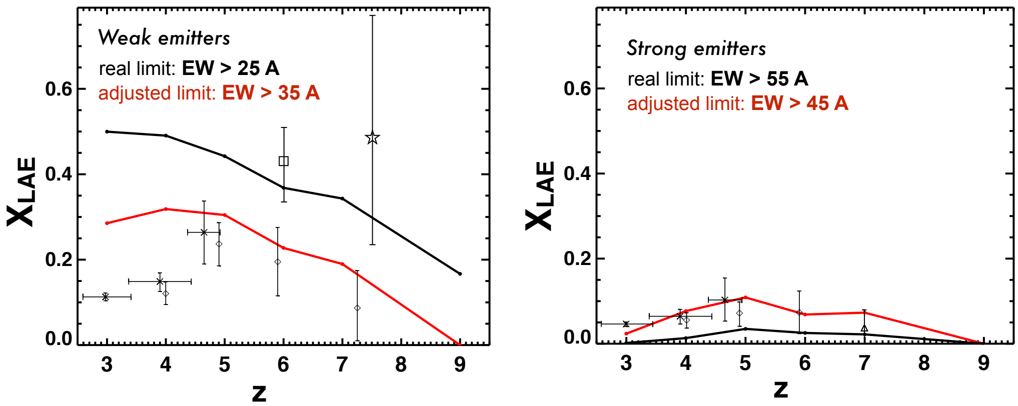


**Fig. 2.** Redshift evolution of the LAE fraction, $X_{\mathrm{LAE}}$, in samples of bright dropout galaxies. The right and left panels show the redshift evolution of $X_{\mathrm{LAE}}$ for strong (EW > 55Å) and weaker (EW > 25Å) Ly$\alpha$ emitters respectively. The black curves represent the model predictions using the same EW limits as the ones used to derive the observational measurements (shown by the various data points; see the Figure 8 of Garel et al. (2015) for the references). The red curves show our predicted $X_{\mathrm{LAE}}$ if these limits are varied by 10Å.

In Figure 2, we show the comparison between observational data points and the predictions from our model (black curves) using the EW cuts that were used to compute $X_{\mathrm{LAE}}$ in the various dropout galaxies samples. We see that the model cannot reproduce the overall trend of $X_{\mathrm{LAE}}(z)$ neither for strong nor weak emitters. Then, we adjust the EW limits in order to get a better match with the observational data (red curves). We find that varying these cuts by only 10Å greatly improves the agreement and that the overall shape of the redshift evolution of $X_{\mathrm{LAE}}$ can be better recovered, i.e. a rise from z ≈ 3 to z ≈ 5 − 6 and then a drop at higher z. This result highlights that $X_{\mathrm{LAE}}$(z) may strongly vary depending on the EW limits and that intrinsic evolution can partially govern the observed trends.

## 4 Clustering of LAEs

An alternative measurement to constrain the ionization state of the IGM can be provided by the 2-point angular correlation function (ACF) of LAEs. Indeed, as first shown by McQuinn et al. (2007), the visibility of LAEs when entering the EoR is favoured if these objects reside in large HII bubbles located at high density peaks, where haloes are strongly clustered. This translates into an apparent *boost* of the ACF, as shown by the results from the simulations of McQuinn et al. (2007) in the left panel of Figure 3: circles and crosses correspond to an IGM neutral fraction $x_{\mathrm{HI}}$ of 30% and 0% respectively. In contrast, the Garel et al. (2015) model does

[†]We note that some surveys have found that $X_{\mathrm{LAE}}$ keeps rising at z $\gtrsim 6-7$.

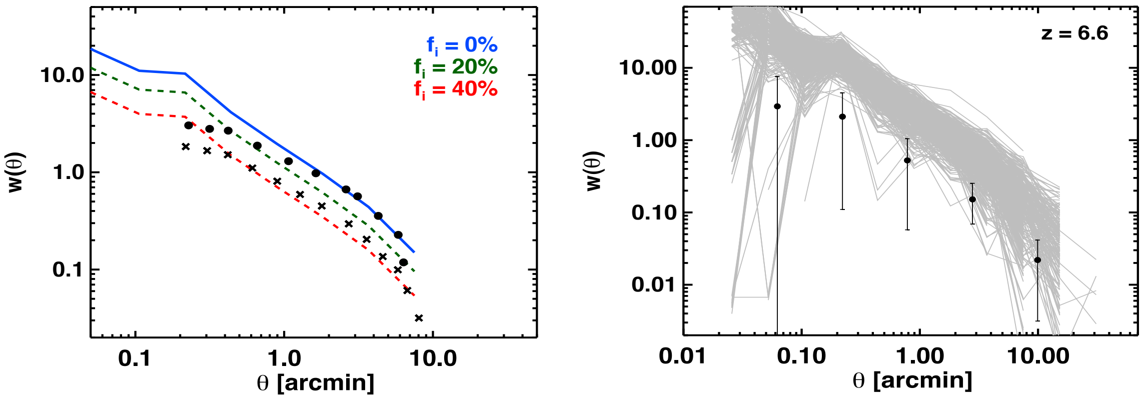


**Fig. 3.** 2-point angular correlation function of LAEs at z = 6.6. **Left:** ACF from the Garel et al. (2015) model for various fractions of interlopers among LAEs. Circles and crosses correspond to the simulations of McQuinn et al. (2007) for which the IGM neutral fraction $x_{\rm HI}$ is 30% and 0% respectively. **Right:** ACFs measured from 500 mock lightcones. Black dots are data points from the survey of Ouchi et al. (2010).

not follow the growth of HII bubbles during the EoR and, as discussed in Section 2, our IGM prescription for Ly$\alpha$ attenuation does not affect the Ly$\alpha$ luminosities. Therefore, here, we only investigate the ACF at z $\gtrsim$ 6 in terms of intrinsic evolution and discuss the expected effects of contamination and cosmic variance on the clustering of LAEs.

As discussed in McQuinn et al. (2007), the contamination of NB-selected samples of LAEs (which can be significant at high redshift; Hu et al. 2010; Kashikawa et al. 2011), may also strongly affect the measurements of the ACF. To test this, we assume that our mock sample of LAEs contains various fractions of low-z interlopers that we model as randomly distributed sources on the sky. We see that the clustering signal is considerably decreased as the contamination fraction becomes larger (blue, green and red curves in the left panel of Figure 3). We find that the *clustering boost* due to reionization imprints the same signature as the effect of contamination on the ACF (at least at scales larger than 0.5 arcminutes). This highlights the importance of measuring ACFs over clean, i.e. spectroscopically confirmed, LAE samples in order to use the ACF as a probe of $x_{\rm HI}$.

The right panel of Figure 3 shows the ACFs measured from 500 hundreds different lightcones mimicking LAE surveys at z = 6.6. We find that there is a strong variance from one realization to another and that the dispersion is of the same order as the error bars of the ACF derived by Ouchi et al. (2010) (black dots). In addition, we note that our simulated box (from which the mock lightcones are generated) is $100h^{-1}$ cMpc on a side so we miss the density fluctuations on the largest scales. Then, on Figure 3, the level of dispersion is underestimated and must be seen as a lower limit. In addition to contamination, we also conclude that cosmic variance is certainly going to affect the detection of the *clustering boost* in LAEs surveys, and that large volumes must be probed in order to derive reliable constraints on $x_{\rm HI}$ using the ACF of LAEs.

## 5 Conclusions

The evolution of the statistical properties of Ly$\alpha$ emitters at z $\gtrsim$ 6 is often used as an indirect observational probe of the evolving neutral fraction of the IGM. Using a semi-analytic model of galaxy formation and numerical simulations of Ly$\alpha$ radiative transfer, we discussed the expected evolution of LAEs, ignoring the effect of reionization on their observability. Although the *intrinsic evolution* scenario as predicted by our model cannot explain quantitatively all the observations, we find that it is, at least in some cases, able to reproduce the general trends that are observed. Our results suggest that the internal evolution of galaxy properties, the LAE selection method, the contamination of photometric samples and uncertainties due to cosmic variance can sometimes account for the apparent evolution of the LAE population seen at z $\gtrsim$ 6, and may be confused with the signature of a change in the ionization state of the IGM.

TG is grateful to the LABEX Lyon Institute of Origins (ANR-10-LABX-0066) of the Université de Lyon for its financial support within the programme 'Investissements d'Avenir' (ANR-11-IDEX-0007) of the French government operated by the National Research Agency (ANR).

## References


Becker, G. D., Bolton, J. S., & Lidz, A. 2015, PASA, 32, e045

Cassata, P., Le Fèvre, O., Garilli, B., et al. 2011, A&A, 525, A143

Garel, T., Blaizot, J., Guiderdoni, B., et al. 2015, MNRAS, 450, 1279

Garel, T., Blaizot, J., Guiderdoni, B., et al. 2012, MNRAS, 422, 310

Garel, T., Guiderdoni, B., & Blaizot, J. 2016, MNRAS, 455, 3436

Hatton, S., Devriendt, J. E. G., Ninin, S., et al. 2003, MNRAS, 343, 75

Hu, E. M., Cowie, L. L., Barger, A. J., et al. 2010, ApJ, 725, 394

Kashikawa, N., Shimasaku, K., Matsuda, Y., et al. 2011, ApJ, 734, 119

McQuinn, M., Hernquist, L., Zaldarriaga, M., & Dutta, S. 2007, MNRAS, 381, 75

Ouchi, M., Shimasaku, K., Akiyama, M., et al. 2008, ApJS, 176, 301

Ouchi, M., Shimasaku, K., Furusawa, H., et al. 2010, ApJ, 723, 869

Planck Collaboration, Adam, R., Aghanim, N., et al. 2016, ArXiv e-prints

Schaerer, D., Hayes, M., Verhamme, A., & Teyssier, R. 2011, A&A, 531, A12

Schenker, M. A., Ellis, R. S., Konidaris, N. P., & Stark, D. P. 2014, ApJ, 795, 20

Stark, D. P., Ellis, R. S., & Ouchi, M. 2011, ApJ, 728, L2

Steidel, C. C., Erb, D. K., Shapley, A. E., et al. 2010, ApJ, 717, 289

Verhamme, A., Schaerer, D., Atek, H., & Tapken, C. 2008, A&A, 491, 89

*SF2A 2016*
*C. Reylé, J. Richard, L. Cambrésy, M. Deleuil, E. Pécontal, L. Tresse and I. Vauglin (eds)*

# STELLAR FEEDBACK DURING THE REIONIZATION WITH EMMA

N. Deparis[1], D. Aubert[1] and P. Ocvirk[1]

**Abstract.** Stellar feedback during the epoch of reionization is a complex problem that is far to be fully understood. The apparition of first stars in the Universe involves highly nonlinear processes that are studied using numerical simulations. We present here a model of star formation, radiation and supernovae feedback, implemented in a new AMR code with fully coupled radiative-hydrodynamic named EMMA. We present a preliminary study concerning the flow of matter and radiation passing through the virial sphere of each halos. We found a class of low-mass halo (less than $10^9 \mathrm{M}_\odot$) getting at the same time gas outflow and radiative inflow, suggesting a photo-heating effect.

Keywords: cosmology: dark ages, reionization, first stars - methods: numerical

## 1 Introduction

Star formation and feedback involve some complex coupling between stars and the intergalactic medium (IGM). By its presence, a star will modify its neighborhood, and then change the state of the medium where futures generation of stars will born. To study this highly nonlinear coupling, we use numerical simulations. Different ways has been explored to implement star formation and feedback (Springel & Hernquist (2003), Stinson et al. (2006), Dubois & Teyssier (2008), Dalla Vecchia & Schaye (2012)). We present one model of star formation, radiative feedback, and supernovae feedback implemented in `EMMA` (Aubert et al. 2015).

During our calibration process, we found that the mass of stellar particle has a drastic effect on how the radiation escapes halos and thus on the reionization history of the simulation. This variation could totally change our interpretation of the simulation, and with the introduction of radiation, we need to take some extra precaution before making conclusions. We also investigate how stellar feedback influences the flow of matter and radiation escaping or falling back around each halo.

## 2 EMMA

`EMMA` is written with the goal of studying the Epoch of Reionization. A full description of the code is given in Aubert et al. (2015), but we briefly summarize it in this section. It follows the evolution of three distinct physics: dark matter (DM), gas, and light in a fully coupled way.

`EMMA` uses a fully treated tree adaptive mesh refinement (AMR) description. Collisionless dynamics – dark matter and stars – use a particle based representation. A cloud in cell (CIC) projection is used to determined gravitational density field from particles. The Poisson equation is solved using a multigrid relaxation method on the base level, and a Gauss-Seidel relaxation on the sub levels. Hydrodynamics solver is based on a piecewise linear method a la MUSCL-Hancock driven by HLLC Riemann solvers. Finally, the radiation propagation is solved using a moment-based description, with the M1 closure approximation. The chemistry module only computes the cooling and ionization processes of atomic hydrogen in the current version.

[1] Observatoire Astronomique de Strasbourg, CNRS UMR 7550, Universite de Strasbourg, Strasbourg, France

## 3 Stellar formation and feedback model

The first part of the stellar models is the star formation process, which occurs in three steps. First, we need to define which region are allowed to form stars, then quantify the amount of gas to convert into stars, and do this conversion.

To flag stars forming regions, we use a simple density threshold.

Some authors use much more complex star formation criterion (see eg Kay et al. (2002) for a detailed comparison about star formation criterion). After some tests, we conclude that at the considered scales (our common resolution is around 1kpc), other criteria (like Jeans unstable or convergent flow) do not make a real difference. This behavior is not true anymore for simulations with sub-galactic scale resolution.

We then compute the star formation rate (SFR) of all the flagged region using a simple Schmidt-Kennicutt observational law (Kennicutt 1998) based on the local gas density :

$$\mathrm{SFR} \propto \rho_{gas}^{1.5}. \tag{3.1}$$

We now have the amount of gas to convert into stars. This conversion consists of taking some gas on the grid and convert it into a particle. A newly formed stellar particle can only have a discrete mass depending on a user parameter. For numerical reasons, we use a quantum based description of stellar particles. To go from the continuous process of star formation to a discrete one in the simulation, we draw the number of particles to inject using a Poisson law (Rasera & Teyssier 2006).

Newly born stars will now start their radiative lives. To constrain the type and the amount of radiation stars will emit, we use the Starburst99 model (Leitherer et al. (1999)). It gives us access to the emissivity spectrum of a stellar population of a given initial mass function (IMF). In this study, we use a Top Heavy IMF and a metallicity of Z=0.001.

During our calibration process, we observed a strong dependence of the stellar quantum mass on the reionization history. We observe that injecting one unit of stellar mass if much more efficient – regarding ionization processes – than injecting eight times one eighth of this mass. It seems that the radiation cannot escape from cells containing low mass stars. We made the experiment of executing two runs, one with the recombination processes shut down in cells containing stars, and another one where we let the recombination happen normally. We do this experiment for different stellar masses and observe that for low stellar particle masses ($10^3 \mathrm{M}_\odot$), reionization histories of runs with free recombination processes, are late compared to constrained one. There is no difference for runs with high stellar masses ($7.10^4 \mathrm{M}_\odot$). In this study, we choose to use heavy stellar particles and let the recombination append normally.

After 17Myrs, stars explode in supernovae, injecting $9.7 \cdot 10^{11} \mathrm{J.kg}^{-1}$, and returning 52% of his mass to the IGM. We can either inject the available energy by heating the medium around the explosion or by modifying its velocity. The thermal energy injection is known to be inefficient due to the efficiency of cooling processes. So we developed a kinetic model which inject the energy by the intermediate of ejecta, and by computing the momentum balance in the cell.

## 4 Halo flow

We develop a tool to analyze what is falling on halos and what is escaping from halos either baryonic matter or radiation. For each halo, we draw a virtual sphere, discretized with Healpix, with a radius corresponding to the associated virial radius and centered on the mass center. The net flow is then compute using :

$$F = \sum_{i=1}^{N} \vec{f_i} \cdot \vec{r_i}, \tag{4.1}$$

with $N$ the number of Healpix point (3072 in this case), $\vec{r_i}$ the radial unit vector at point $i$ and $\vec{f_i}$ the flow of the nearest cell. Normal is oriented outward, so positive values go for outflow and negatives one for inflow. The motion of the center of mass of halos is compensated to reduce environmental effects.

### 4.1 Hydrodynamical flow

Fig. 1 present results for hydrodynamical flows in a 12 cMpc$^3$ simulation. This simulation run with a Planck cosmology (Planck Collaboration et al. 2015), and use $256^3$ dark matter particles for a mass resolution of

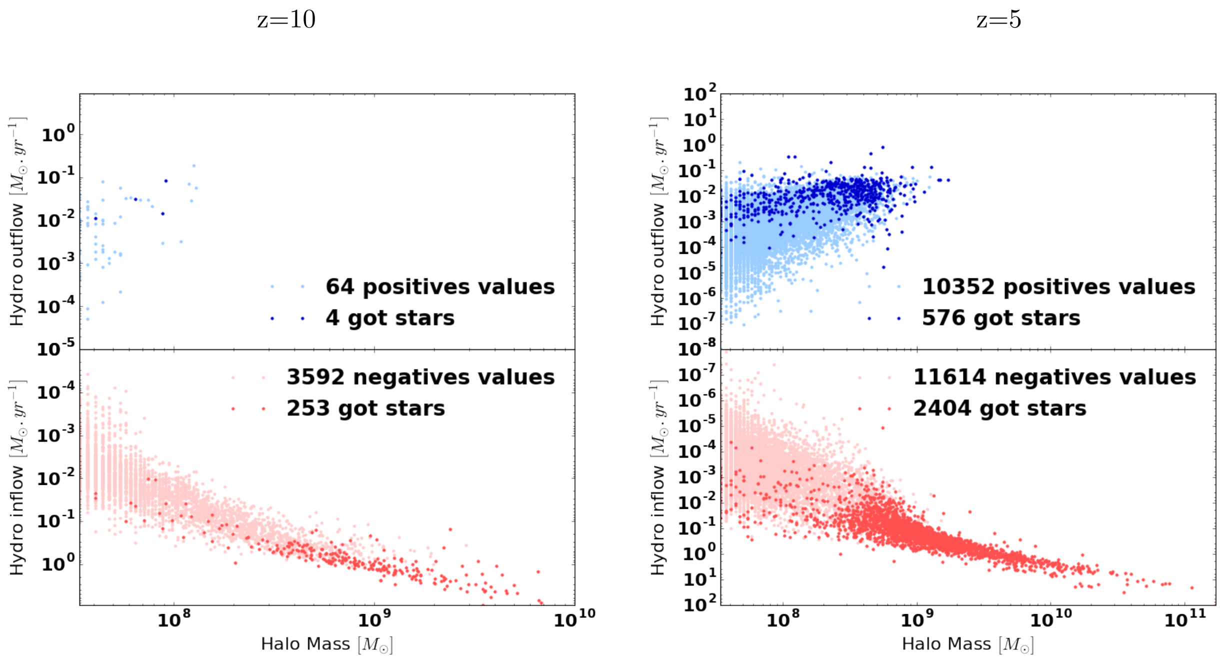


**Fig. 1.** Hydrodynamical flow of halos at redshift 10 (left) and redshift 5 (right). Positives values are for outflow, dark dots represents halos without stars, light dots represents halos with stars. There is much more low mass halos with gas outflow at z=5 than at z=10. Feedback push the baryon outside of lightest halos, who do not have enough gravitational potential to keep their gas inside their virial radius.

$3.4 \cdot 10^6 M_\odot$. Mesh refinement is allowed until resolution reach 500pc. Stellar quantum mass is set to $7.2 \cdot 10^4 M_\odot$ Results are presented at redshift 10 and 5. We see the apparition of a population of low mass halos that get outflow at z=5. This population is not present at z=10. We see here the baryon escaping from low mass halos that do not have enough gravitational potential to hold their gas, heated by radiation or pushed by supernovae feedback. We made the same run excepting that source does not radiate, and this population was considerably reduced (not shown here). We conclude that this effect is at least partially due to radiative feedback. Moreover, this effect became much stronger after the reionization. So, it suggests an outside-in effect. Galaxies get internal radiative sources, even after the end of the reionization, so if the apparition of this population was due to an inside-out effect, it should be present even before the end of the reionization.

### *4.2 Radiative flow and escape fraction*

The left panel of Fig. 2 present the radiative flow obtain in a 12 cMpc$^3$ - 256$^3$ simulation at redshift 5. We see a relation between halo masses and outflow quantities: the more the halo is massive, the more it will emit light. Surprisingly, we see a population of halos without stars, with radiative outflow. We are not able to explain it at this time. However, there is a population of halos less massive than $10^{10} M_\odot$ with radiative inflow. The majority (60%) of theses get stars, but still get more radiation from outside sources than from their inner one. Moreover, there is no halos of more than $10^{10} M_\odot$ with net inflow.

Knowing the age of stars belonging to a halo, we can compute the number of photons produced within its virial radius. Right panel of Fig. 2 present the ratio between the number of photons passing through the R200 over the number of photons injected in the halo by stars. To do this computation for each halo, we only get positives value, corresponding to outflow, on its respective Healpix sphere.

We see that the observed escape fraction tends to be low for low mass halos, presents a maximum for halos around $10^{10} M_\odot$, and decrease for heavier halos. The peak value seems to be at the same mass independently of considered redshift. Halos around the peak value, tend to have an escape fraction increasing with time. It may be due to the increasing ionization fraction around halos, letting the radiation escaping.

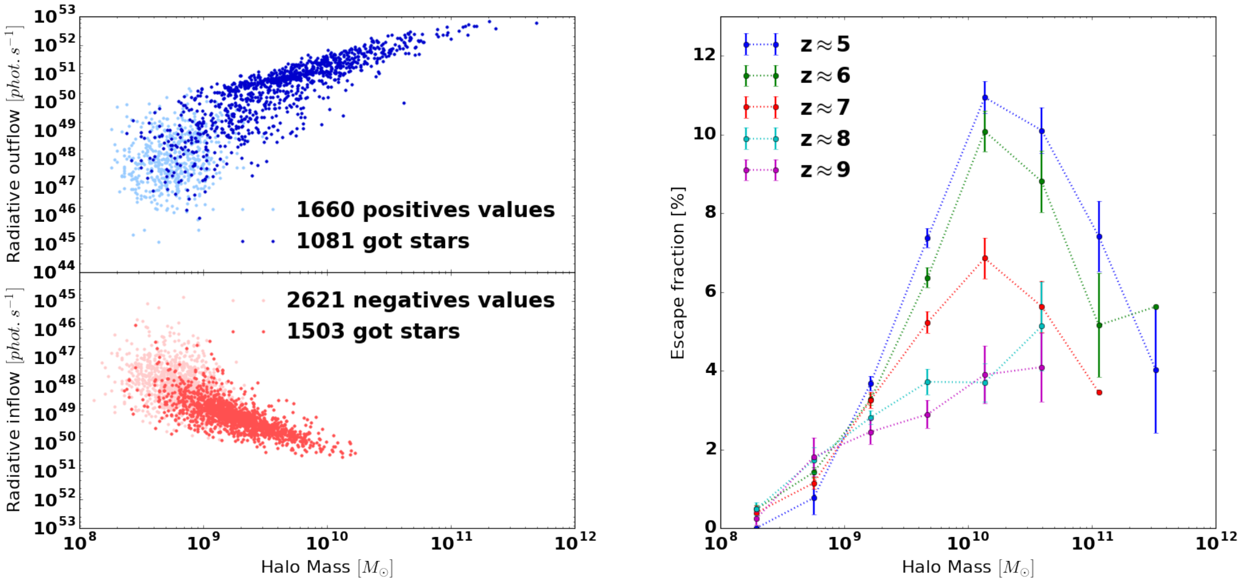


**Fig. 2.** Radiative flow function of halo mass at redshift 5 (left) and escape fraction function of halo mass function of redshift (right). Dark dots represents halos without stars, light dots represents halos with stars.; We observe a population of low mass halos with radiative inflow and a maximum in the escape fraction for halos around $10^{10}\mathrm{M}_{\odot}$.

## 5 Perspectives

We began to compare halo that get hydrodynamical outflow, and the ones with radiative inflow, to explore the link between theses two populations. The goal is to understand if the photo-heating effect can reduce the SFR in low mass halo by pushing baryons out of their virial radius. This study will also be executed on more resolved boxes to increase the resolution of low mass halos, and on bigger boxes to study the influence of bigger halo.

The momentum based method used for supernovae feedback in this study is revealed to be inefficient to regulate star formation. We are currently working on implementing an other scheme for kinetic energy injection, using winds instead of ejecta. This new scheme can change the interpretation of our results has it can modify the amount of gas outflowing from halos and change the way radiation escapes.

## 6 Acknowledgment

This work is supported by the ANR ORAGE grant ANR-14-CE33-0016 of the French Agence Nationale de la Recherche.

## References

Aubert, D., Deparis, N., & Ocvirk, P. 2015, Monthly Notices of the Royal Astronomical Society, 454, 1012

Dalla Vecchia, C. & Schaye, J. 2012, Monthly Notices of the Royal Astronomical Society, 426, 140

Dubois, Y. & Teyssier, R. 2008, in Supernova Feedback in Galaxy Formation, Vol. 390, 388

Kay, S. T., Pearce, F. R., Frenk, C. S., & Jenkins, A. 2002, Monthly Notices of the Royal Astronomical Society, 330, 113

Kennicutt, J. 1998, The Astrophysical Journal, 498, 541, arXiv: astro-ph/9712213

Leitherer, C., Schaerer, D., Goldader, J. D., et al. 1999, The Astrophysical Journal Supplement Series, 123, 3

Planck Collaboration, Ade, P. A. R., Aghanim, N., et al. 2015, ArXiv e-prints, 1502, arXiv:1502.01589

Rasera, Y. & Teyssier, R. 2006, Astronomy and Astrophysics, 445, 1

Springel, V. & Hernquist, L. 2003, Monthly Notices of the Royal Astronomical Society, 339, 289

Stinson, G., Seth, A., Katz, N., et al. 2006, Monthly Notices of the Royal Astronomical Society, 373, 1074

# 21CM BISPECTRUM AS METHOD TO MEASURE COSMIC DAWN AND EOR

H. Shimabukuro[1]

**Abstract.** Cosmological 21cm signal is a promising tool to investigate the state of the Inter Galactic Medium (IGM) during cosmic dawn (CD) and Epoch of Reionization (EoR). Ongoing telescopes such as MWA,LOFAR,PAPER and future telescopes like SKA are expected to detect cosmological 21cm signal. Statistical analysis of the 21cm signal is very important to extract information of the IGM which is related to nature of galaxies and first generation stars. We expect that cosmological 21cm signal follows non-gaussian distribution because various astrophysical processes deviate the distribution from gaussian. In order to evaluate the non-gaussian features, we introduce the bispectrum of the 21cm signal and discuss the property of the 21cm bispectrum such as redshift dependence and configuration dependence. We found that the we can see correlation between large scales and small scales via the 21cm bispectrum and also found that the 21cm bispectrum can give the information of matter fluctuation, neural fraction fluctuation and spin temperature fluctuation by means of its configure dependence.

Keywords: cosmology: dark ages, reionization, first stars

## 1 Introduction

The redshifted 21cm line from neutral hydrogen due to the hyperfine transition is suitable for studying thermal and ionized states of Inter Galactic Medium (IGM) as well as the first objects in the dark age, cosmic dawn (CD) and Epoch of Reionization (EoR) (Furlanetto et al 2006; Pritchard & Loeb 2012). One of the statistical methods to subtract the information about the physical state of IGM at those epochs from 21cm line is the power spectrum analysis of brightness temperature (Furlanetto et al 2006; Pritchard & Furlanetto 2007; Santos et al. 2008; Baek et al. 2010; Mesinger et al. 2013; Pober et al. 2014).

In our previous work Shimabukuro et al. (2015), we gave an interpretation to the time evolution of the 21cm power spectrum and we find that the size of skewness is sensitive to the epoch when X-ray heating becomes effective. Herein we extend this previous work by considering the the bispectrum to investigate the dependence of the skewness on scales because skewness is an integral of the bispectrum with respect to the wave number. In a different work Yoshiura et al. (2015) we have already estimated errors from the thermal noise of detectors in estimating the bispectrum and we found that the 21cm bispectrum would be detectable at large scales at $k \leq 0.1\mathrm{Mpc}^{-1}$ even by the current detectors, such as, the MWA and PAPER. In our study, we focus on non-Gaussianity in 21cm fluctuations induced by astrophysical effects not by cosmological origin. For other probes of non-Gaussianity such as Minkowski functionals, see Gleser et al. (2006); Yoshiura et al. (2016).

## 2 Formulation and set up

A fundamental quantity of 21cm line is the brightness temperature, which is described as the spin temperature offsetting from CMB temperature, given by (see, e.g. Furlanetto et al 2006)

$$\begin{aligned}\delta T_b(\nu) &= \frac{T_\mathrm{S} - T_\gamma}{1+z}(1 - e^{-\tau_{\nu_0}}) \\ &\sim 27 x_\mathrm{H}(1+\delta_m)\left(\frac{H}{dv_r/dr + H}\right)\left(1 - \frac{T_\gamma}{T_\mathrm{S}}\right) \\ &\times \left(\frac{1+z}{10}\frac{0.15}{\Omega_m h^2}\right)^{1/2}\left(\frac{\Omega_b h^2}{0.023}\right)[\mathrm{mK}]. \end{aligned} \tag{2.1}$$

[1] Observatoire de Paris, 61 Avenue de l'Observatoire, 75014 Paris, France

Here, $T_{\rm S}$ and $T_\gamma$ respectively represent gas spin temperature and CMB temperature, $\tau_{\nu_0}$ is the optical depth at the 21cm rest frame frequency $\nu_0 = 1420.4$ MHz, $x_{\rm H}$ is neutral fraction of the hydrogen gas, $\delta_m(\mathbf{x}, z) \equiv \rho/\bar{\rho} - 1$ is the evolved matter overdensity, $H(z)$ is the Hubble parameter and $dv_r/dr$ is the comoving gradient of the gas velocity along the ling of sight. All quantities are evaluated at redshift $z = \nu_0/\nu - 1$.

Let us focus on the spatial distribution of the brightness temperature. The spatial fluctuation of the brightness temperature can be defined as

$$\delta_{21}(\mathbf{x}) \equiv \delta T_b(\mathbf{x}) - \langle \delta T_b \rangle \tag{2.2}$$

where $\langle \delta T_b \rangle$ is the mean brightness temperature obtained from brightness temperature map and $\langle ... \rangle$ expresses the ensemble average. If the statistics of the brightness temperature fluctuations is pure Gaussian, the statistical information of the brightness temperature should be completely characterized by the power spectrum. However, in the era of CD and EoR, it is expected that the spin temperature and the neutral fraction should be spatially inhomogeneous and the statistics of the spatial fluctuations of those quantities would be highly non-Gaussian due to the various astrophysical effects. Here, in order to see the non-Gaussian feature of the brightness temperature fluctuations $\delta_{21}$, we focus on the bispectrum of $\delta_{21}$ which is given by

$$\langle \delta_{21}(\mathbf{k_1})\delta_{21}(\mathbf{k_2})\delta_{21}(\mathbf{k_3}) \rangle = (2\pi)^3 \delta(\mathbf{k_1} + \mathbf{k_2} + \mathbf{k_3}) B(\mathbf{k_1}, \mathbf{k_2}, \mathbf{k_3}). \tag{2.3}$$

In order to characterize the shape of the bispectrum in $k$-space, we use an isosceles ansatz which is defined as $k_1 = k_2 = k = \alpha k_3$ ($\alpha \geq 1/2$). For examples, in case with $\alpha \gg 1$ the shape of the bispectrum is often called as "*squeezed type*" or "*local type*", in case with $\alpha = 1$ it is called as " *equilateral type*", and in case with $\alpha = 1/2$ it is called as "*folded type*".

## 3 Result

In this section, we summarize our result for the 21cm bispectrum.

### 3.1 Redshift evolution of 21cm bispectrum

Next, we consider redshift evolution of 21cm bispectrum. We show ionized evolution and the bispectra as functions of redshift for several $\alpha$ in Fig. 1: the equilateral shape ($\alpha = 1$), the folded shape ($\alpha = 1/2$) and the squeezed shape ($\alpha = 10$) with $k = 1.0$ Mpc$^{-1}$. For the equilateral and folded cases, we can see two peaks located at around $z = 20$ and 12. These peaks can also be seen in the power spectrum of the brightness temperature fluctuations, $P_{21}(k)$, with $k \simeq 1.0$ Mpc$^{-1}$ (see, e.g., our previous paper Shimabukuro et al. 2015). On the other hand, in case with the squeezed shape, three peaks appear at around $z = 23$, 17, and 12. This feature is similar to that of the power spectrum with $k \simeq 0.1$ Mpc$^{-1}$ (Shimabukuro et al. 2015). For the squeezed type, we take the parameter $\alpha$ to be 10 and this means $k_3 = 0.1$ Mpc$^{-1}$. Hence, the squeezed-type 21cm bispectrum is expected to be described in terms of not only the power spectrum with larger two wave number ($k_1$ and $k_2$ in our case) but also that with smaller one wave number ($k_3$ in our case) and also it would have the information about the correlation between the long and short wavelength modes in Fourier space or local non-linearity in real space. The dip at $z \sim 20$ for the $\alpha = 10$ case results in mode coupling between long and short wavelengths. Therefore, we can conclude that the squeezed type bispectrum has information both on large scale and small scale.

### 3.2 Decomposition of 21cm bispectrum

As we saw in Eq. (2.1), the fluctuations in the brightness temperature are contributed not only from the matte density field, but also from the fluctuations of the spin temperature and neutral fraction, aside from the gradient of peculiar velocity which we neglect here. In this section, we decompose the bispectrum into the contributions from these components.

We can rewrite Eq. (2.1) as,

$$\delta T_b(\mathbf{x}) = \overline{\delta T}_b (1 + \delta_{x_{\rm H}}(\mathbf{x}))(1 + \delta_m(\mathbf{x}))(1 + \delta_\eta(\mathbf{x})), \tag{3.1}$$

where $\overline{\delta T_b}$ is the average brightness temperature.

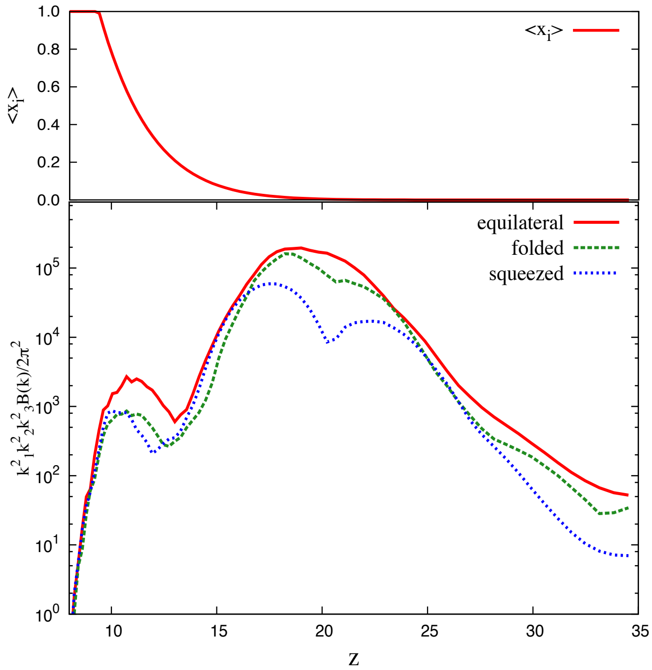


**Fig. 1.** (*Top*) ionization history in our model. (*Bottom*) Comparison of bispectra of typical triangle configurations. We fix $k = 1.0\ \mathrm{Mpc}^{-1}$ and take $\alpha = 1$ (equilateral: red solid line), $\alpha = 1/2$ (folded: green dashed line) and $\alpha = 10$ (squeezed: blue dotted line) for the isosceles ansatz.

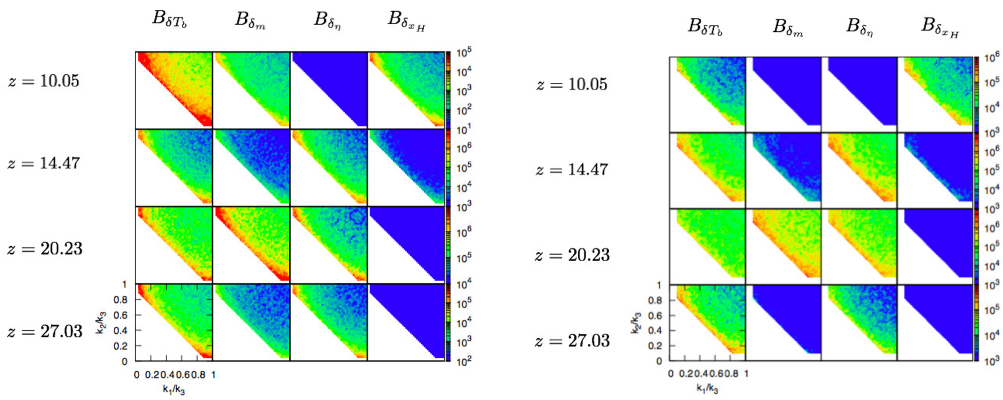


**Fig. 2.** (*Left*) Contours of the total bispectrum and its components in $k_1/k_3$-$k_2/k_3$ plane with $k_3 = 1.0\ \mathrm{Mpc}^{-1}$. (*Right*) Contours of the total bispectrum and its components in $k_1/k_3$-$k_2/k_3$ plane with $k_3 = 0.4\ \mathrm{Mpc}^{-1}$.

Here we characterize the contribution of the spin temperature $T_s$ by a new variable $\eta = 1 - T_\gamma/T_\mathrm{S}$ (Shimabukuro et al. 2015). Using Eq. (3.1), we can decompose the brightness temperature bispectrum into auto- and cross-correlation of $\delta_m, \delta_{x_\mathrm{H}}$ and $\delta_\eta$:

$$\begin{aligned} B_{\delta T_b} \quad = \quad & (\overline{\delta T}_b)^3 [B_{\delta_m \delta_m \delta_m} + B_{\delta_{x_\mathrm{H}} \delta_{x_\mathrm{H}} \delta_{x_\mathrm{H}}} + B_{\delta_\eta \delta_\eta \delta_\eta} \\ & + (\text{cross correlation terms}) \\ & + (\text{higher order terms})]. \end{aligned} \tag{3.2}$$

We focus on the shape dependence of the total bispectrum and its components. Fixing $k_3 = 1.0\ \mathrm{Mpc}^{-1}$, we plot contours of the bispectra in $(k_1/k_3)$-$(k_2/k_3)$ plain in left of Fig. 2. Note that we do not use the normalised bispectrum, $k_1^2k_2^2k_3^2B(k_1,k_2,k_3)$, but the unnormalized bispectrum, $B(k_1,k_2,k_3)$, here. We can see in what configuration of triangle the bispectra are strong. Here it should be noted that the triangle condition is not satisfied in the blank region.

At $z = 10.05$ when EoR has proceeded to some extent($x_i = 0.77$), the total bispectrum is strong at folded and squeezed types. The contribution from neutral hydrogen fraction fluctuations is dominant at these configurations, while matter fluctuation is dominant at equilateral type. At $z = 14.47$, the dominant contribution comes from the spin temperature fluctuations and it is largest at squeezed type. The situation is similar at $z = 27.03$. At $z = 20.23$, both squeezed and folded type of the total bispectrum are strong. The contributions from matter and spin temperature fluctuations are comparable at these configurations, while the former is dominant at equilateral type.

We also show the contour for $k_3 = 0.4$ Mpc$^{-1}$ in the right of Fig.2. Compared with the case of $k_3 = 1.0$ Mpc$^{-1}$, contributions from both matter and spin temperature fluctuations are significant at $z = 20.23$. On the other hand, we find that the contribution from fluctuations of neutral hydrogen fraction at $z = 10.05$ is clear compared with the case of $k_3 = 1.0$ Mpc$^{-1}$. This helps us to subtract the information on neutral hydrogen and it is better to see larger scales if we would like to know the information on neutral hydrogen fluctuations.

## 4 Conclusions

In this proceeding, we introduced the 21cm bispectrum as method to measure non-Gaussianity of brightness temperature field generated by astrophysical processes.

First, we have shown the redshift evolution of the 21cm bispectrum with fixed $k$ for three types of the shape in $k$-space. We found that the redshift evolution of the 21cm bispectrum for the equilateral and folded shapes basically traces that of the 21cm power spectrum, but in case with the squeezed shape, we could see a different behavior and it can be understood by considering the coupling between the large- and small-scale modes.

Next, we studied the 21cm bispectrum by decomposing it into the contributions from the matter density field, the fluctuations in the spin temperature and the neutral fraction. From the redshift evolution, we found the dominant component at each redshift and scale. We also show the shape dependence of each component and compared it with that of total 21cm bispectrum. The shape dependence of each component looks similar to each other, but a slight difference also exists. Hence, by future precise observation it is expected that we would obtain the information about the non-Gaussian feature of these components separately.

## 5 Acknowledements

This work is supported by Grant-in-Aid from the Ministry of Education, Culture, Sports, Science and Technology (MEXT) of Japan, No. 25-3015 and a grant from the French ANR funded project ORAGE (ANR-14- CE33-0016)

## References

S. Baek, B. Semelin, P. Di Matteo, Y. Revaz and F. Combes, arXiv:1003.0834 [astro-ph.CO].

X. H. Fan, C. L. Carilli and B. G. Keating, Ann. Rev. Astron. Astrophys. **44** (2006) 415 [astro-ph/0602375].

S. Furlanetto, S. P. Oh and F. Briggs, Phys. Rept. **433** (2006) 181 [astro-ph/0608032]

L. Gleser, A. Nusser, B. Ciardi, & V. Desjacques 2006, MNRAS, 370, 1329

A. Mesinger, S. Furlanetto, R. Cen,2011, MNRAS, 411, 955

A. Mesinger, A. Ewall-Wice and J. Hewitt, arXiv:1310.0465 [astro-ph.CO]

J. C. Pober, A. Liu, A, J. S. Dillon, et al. 2014, ApJ, 782, 66

J. R. Pritchard and S. R. Furlanetto, Mon. Not. Roy. Astron. Soc. **376** (2007) 1680 [astro-ph/0607234]

Pritchard, J. R., & Loeb, A. 2012, Reports on Progress in Physics, 75, 086901

M. G. Santos, A. Amblard, J. Pritchard et al. 2008, ApJ, 689, 1

H. Shimabukuro, S. Yoshiura, K. Takahashi, S. Yokoyama. & Ichiki, K. 2015, Mon. Not. Roy. Astron. Soc. , 451, 4986

S. Yoshiura, H. Shimabukuro, K. Takahashi, et al. 2015, Mon. Not. Roy. Astron. Soc. 451, 4785

Yoshiura, S., Shimabukuro, H., Takahashi, K., & Matsubara, T. 2016, arXiv:1602.02351

*SF2A 2016*
*C. Reylé, J. Richard, L. Cambrésy, M. Deleuil, E. Pécontal, L. Tresse and I. Vaughlin (eds)*

# FEEDBACK REGULATED ESCAPE OF IONISING RADIATION FROM HIGH REDSHIFT GALAXIES

M. Trebitsch[2,1] and J. Blaizot[2]

**Abstract.** Small galaxies are thought to provide the bulk of the radiation necessary to reionise the Universe by $z \sim 6$. Their ionising efficiency is usually quantified by their escape fraction $f_{\rm esc}$, but it is extremely hard to constrain from observations. With the goal of studying the physical processes that determine the values of the escape fraction, we have run a series of high resolution, cosmological, radiative hydrodynamics simulations centred on three galaxies. We find that the variability of the escape fraction follows that of the star formation rate, and that local feedback is necessary for radiation to escape.

Keywords: radiative transfer, methods: numerical, galaxies: dwarfs, galaxies: formation, galaxies: high redshift, dark ages, reionisation, first stars.

## 1 Introduction

The apparition of the first light sources marks the beginning of the Epoch of Reionisation, during which the intergalactic medium (IGM) transitions from fully neutral to fully ionised around $z \sim 6$. The origin of the bulk of the radiation responsible for reionising the Universe is still subject to debate (e.g. Madau & Haardt 2015; Haardt & Salvaterra 2015): it is unclear that there is enough high-$z$ quasars to provide enough photons, and the contribution of galaxies is poorly constrained. A crucial parameter to account for the galactic contribution to the ionising budget is the *escape fraction* $f_{\rm esc}$, which describe the fraction of photons emitted by stellar sources that can escape from the galaxies to reionise the IGM. The observational determination of $f_{\rm esc}$ is extremely laborious, and is hampered by various selection effects, interloper removals, etc (e.g. Bergvall et al. 2013; Siana et al. 2015). Measurements at low redshift seem to indicate a low value of less than $2-3\%$, but recently Izotov et al. (2016) found Lyman-continuum emitters with $f_{\rm esc} \sim 10\%$. At $z \sim 3$, the IGM is still partially opaque to ionising radiation, which further complicates the measurement of $f_{\rm esc}$, and it will never be possible to directly measure $f_{\rm esc}$ from galaxies during the Epoch of Reionisation, since by definition the Universe is still neutral.

Numerical simulations in the past decade have helped constraining the values of $f_{\rm esc}$ as a function of the redshift and the halo mass $M_{\rm vir}$, but the results are still uncertain. For example, some studies find that $f_{\rm esc}$ increases with $M_{\rm vir}$ (e.g. Gnedin et al. 2008), while some others find the opposite trend (e.g. Yajima et al. 2011; Kimm & Cen 2014; Wise et al. 2014), and Ma et al. (2015) find that there is no clear evolution with the stellar mass of the galaxy. Even within a single study, there is a large scatter in the values of $f_{\rm esc}$ at fixed halo mass. The differences can be accounted by the fact that no two simulations use the same methods: they do not focus on the same galaxies (from minihaloes to Milky-Way progenitors) and do not have the same resolution (from more than 100 pc to subparsec resolution), and more importantly most of the unresolved physical mechanisms like the feedback processes are implemented differently, which is known to lead to different physical properties (e.g. Kimm et al. 2015, for the supernova feedback).

We present here a study of three small galaxies with the goal of understanding the detailed mechanism that can affect the escape of ionising photons during their journey from the star-forming sites to the IGM.

[1] Sorbonne Universités, UPMC Univ Paris 6 et CNRS, UMR 7095, Institut d'Astrophysique de Paris, 98 bis bd Arago, 75014 Paris, France
[2] Univ Lyon, Univ Lyon1, ENS de Lyon, CNRS, Centre de Recherche Astrophysique de Lyon UMR5574, F-69230, Saint-Genis-Laval, France

## 2 Description of the simulations

We performed simulations of galaxies in a cosmological context using the radiative hydrodynamics code Ramses-RT (Teyssier 2002; Rosdahl et al. 2013). The code follows the coupled evolution of gas and radiation, allowing us to track the ionisation state of the gas in the simulation. We use the zoom technique to achieve the very high resolution that we need to start resolving the structure of the ISM. We focus on the three haloes presented in Trebitsch et al. (2015), with masses $M_{\rm vir} \sim 8 \times 10^7 M_\odot$, $6 \times 10^8 M_\odot$, and $2 \times 10^9 M_\odot$.

The haloes were selected in a dark-matter (DM) only simulation using $512^3$ particles in a $10h^{-1}$ Mpc box. We then generated multigrid initial conditions using the Music code (Hahn & Abel 2011), using 3 additional levels of refinement, giving a DM particle mass of $\sim 2000 M_\odot$. We ran the simulation for one billion years, down to $z \sim 5.6$, with a total of 21 levels of refinement, allowing for a cell size of $\Delta x \sim 7$ pc. Radiation is modelled using three photon groups (ionising H I , He I, He II). We use the same supernova (SN) feedback recipe as Kimm & Cen (2014), where after 10 Myr, each star particle deposits in the ISM the amount momentum and metals corresponding to the phase of the SN explosion that can be resolved. We use a new recipe for star formation (Devriendt et al. in prep.), where we account for the turbulence in the star-forming cloud. The stellar particle mass is around $135 M_\odot$, enough to ensure that at least one SN explosion should occur assuming a Chabrier (2003) initial mass function.

## 3 Properties of the simulated galaxies

We present on Fig. 1 the assembly history of the simulated galaxies: the left panel shows the stellar mass to halo mass for the three simulations, each denoted by a different symbol. The colour of the symbols marks the redshift of the snapshot, and for each galaxy a thin grey line guides the eye through the time evolution. By comparing to the diagonal lines indicating constant baryon fractions, we see that roughly 1% to 10% of the baryons are converted in stars in stars. More important, all galaxies exhibit very similar assembly histories, with a series of plateaus indicating periods of time where the halo grows in mass without star formation.

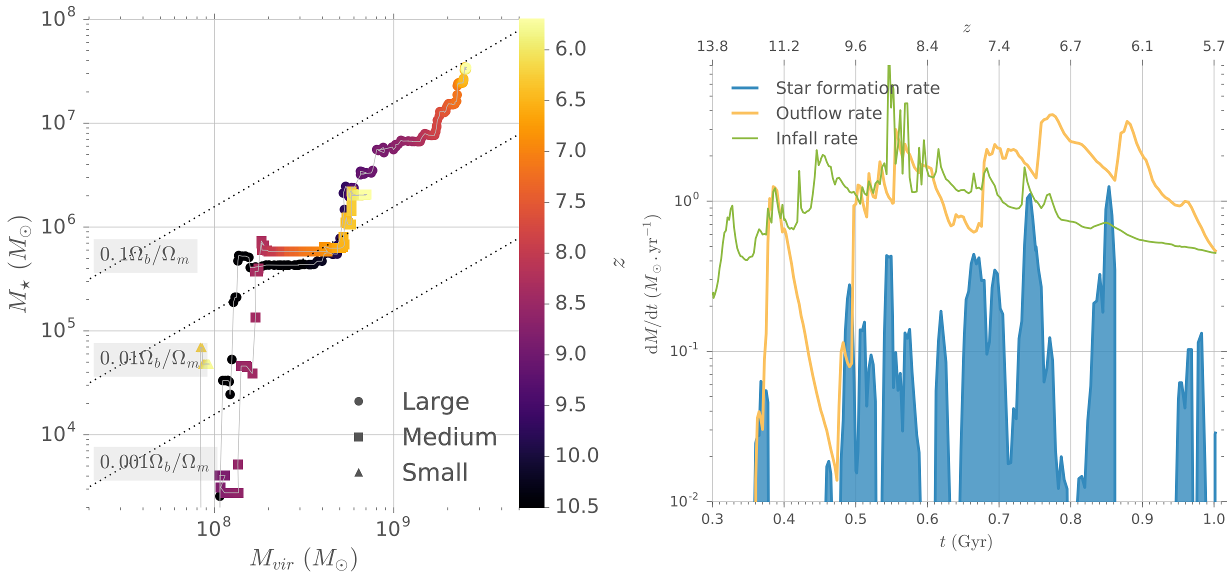


**Fig. 1. Left:** Stellar mass to halo mass relationship for the three haloes. **Right:** Star formation (in blue), outflow (in yellow) and infall (in green) history of the most massive halo. Each SF episode is followed by a massive outflow.

This can be understood with the right panel of Fig. 1, which compares the star formation rate in blue to the the outflow (inflow) rate in yellow (green) measured at the virial radius for the most massive halo of our sample. Each episode of star formation is followed by a dramatic outflow, expelling considerable amounts of gas out of the halo, effectively shutting star formation until the gas reservoir has been refilled.

## 4 Escape of ionising radiation

As the massive stars that produces ionising radiation are very short-lived ($\sim 5$ Myr), the production of ionising photons has a variability that follows that of the star formation rate. However, this is not the end of the story: radiation still needs to escape the halo. We compare on Fig. 2 the time evolution of the escape fraction $f_{\rm esc}$ (in red) to the star formation rate (in blue) and the outflow rate (in yellow). The evolution $f_{\rm esc}$ presents a very bursty behaviour, with values varying quickly from less than 0.1% to more than 60% (e.g. around $t = 850$ Myr). We argue that this can explain the large scatter found in the values of $f_{\rm esc}$ at fixed halo mass in other simulations: in a sample of galaxies of a fixed mass, some will find themselves in a leaking phase while some others will be opaque to ionising radiation.

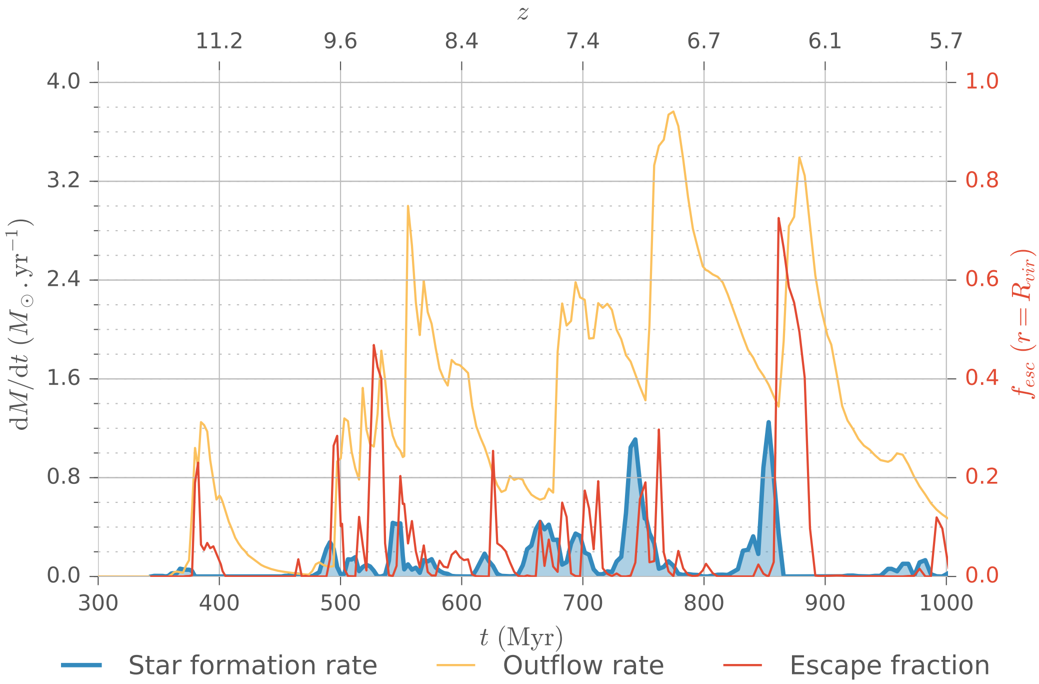


**Fig. 2.** Evolution of the star formation rate (in red), outflow rate (in blue) and escape fraction (in red) for the most massive halo. The escape fraction starts to rise at the same time as the outflow rate, and typically 10 Myr after the beginning of a star formation event.

Interestingly, we note that the peaks of $f_{\rm esc}$ do not correspond exactly to the peaks of star formation, but rather shifted by approximately 10 Myr. We explain this by the fact that radiation can only escape if the interstellar medium (ISM) has been pierced by a feedback event. In our simulations, radiative feedback is not efficient enough, and radiation is trapped in the star-forming cloud until it has been cleaned by a nearby SN. This can be seen on Fig. 3, which compares $f_{\rm esc}$ for the intermediate mass halo for three runs: the run with SN exploding after 10 Myr is shown in blue, the red line shows a run with only 3 Myr delay before the SN, and the yellow line corresponds to a run without any SN feedback. The two runs with SN feedback exhibit similar behaviour, while in the run without SN only very little radiation can escape. It is only when young stars find themselves in an environment transparent enough to ionising radiation that radiation will escape to the IGM.

## 5 Conclusions

Using a series of high resolution RHD simulations of three dwarf galaxies at $z \sim 6$, we have studied the mechanisms that regulate the escape of ionising radiation from galaxies. We found that the assembly of these low mass galaxies is regulated by SN feedback, and that the cycle of star formation episodes followed by SN explosions will result in a highly varying escape of ionising radiation that can explain the scatter found in other studies. We showed that the various feedback processes that are at play in the ISM must be modelled correctly to properly account for the local opacity of the ISM, and feedback is needed for radiation to escape in the IGM.

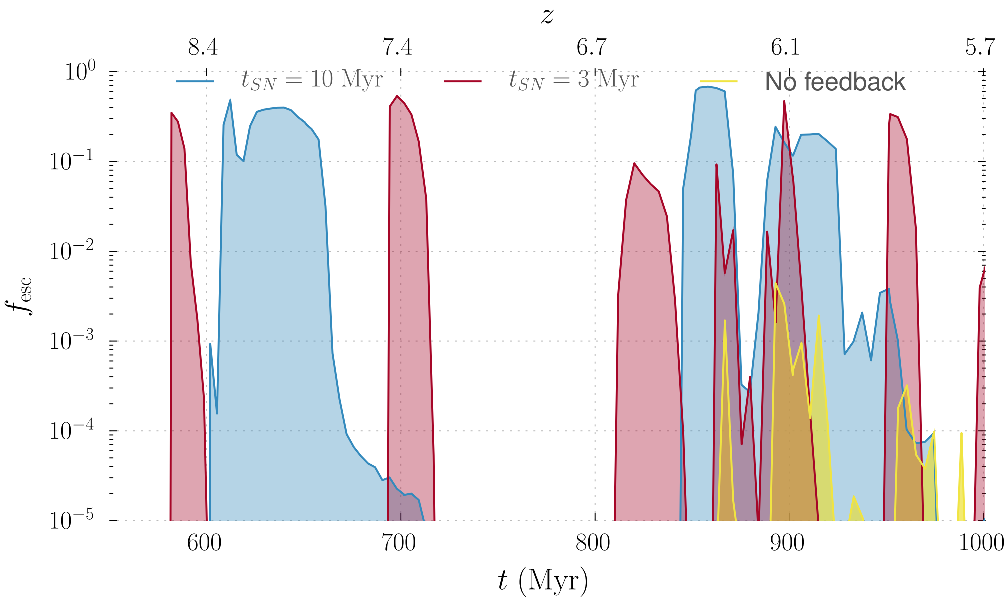


**Fig. 3.** Evolution of $f_{\rm esc}$ for the medium halo with SN feedback and a 10 Myr (3 Myr) time delay between star formation and the supernova in blue (red), and without feedback in yellow.

We will expand this analysis further in an upcoming work (Trebitsch et al. in prep.), as well as discussing some observational consequences.

MT and JB acknowledge support from the Lyon Institute of Origins under grant ANR-10-LABX-66, and from the ORAGE project from the Agence Nationale de la Recherche under grand ANR-14-CE33-0016-03. MT acknowledges funding from the European Research Council under the European Community's Seventh Framework Programme (FP7/2007-2013 Grant Agreement no. 614199, project "BLACK").

## References

Bergvall, N., Leitet, E., Zackrisson, E., & Marquart, T. 2013, A&A, 554, A38

Chabrier, G. 2003, PASP, 115, 763

Devriendt, J., Slyz, A., & Kimm, T. in prep.

Gnedin, N. Y., Kravtsov, A. V., & Chen, H.-W. 2008, ApJ, 672, 765

Haardt, F. & Salvaterra, R. 2015, A&A, 575, L16

Hahn, O. & Abel, T. 2011, MNRAS, 415, 2101

Izotov, Y. I., Schaerer, D., Thuan, T. X., et al. 2016, MNRAS, 461, 3683

Kimm, T. & Cen, R. 2014, ApJ, 788, 121

Kimm, T., Cen, R., Devriendt, J., Dubois, Y., & Slyz, A. 2015, MNRAS, 451, 2900

Ma, X., Kasen, D., Hopkins, P. F., et al. 2015, MNRAS, 453, 960

Madau, P. & Haardt, F. 2015, ApJ, 813, L8

Rosdahl, J., Blaizot, J., Aubert, D., Stranex, T., & Teyssier, R. 2013, MNRAS, 436, 2188

Siana, B., Shapley, A. E., Kulas, K. R., et al. 2015, ApJ, 804, 17

Teyssier, R. 2002, A&A, 385, 337

Trebitsch, M., Blaizot, J., & Rosdahl, J. 2015, in SF2A-2015: Proceedings of the Annual meeting of the French Society of Astronomy and Astrophysics, ed. F. Martins, S. Boissier, V. Buat, L. Cambrésy, & P. Petit, 105–108

Trebitsch, M., Blaizot, J., Rosdahl, J., Devriendt, J., & Slyz, A. in prep.

Wise, J. H., Demchenko, V. G., Halicek, M. T., et al. 2014, MNRAS, 442, 2560

Yajima, H., Choi, J.-H., & Nagamine, K. 2011, MNRAS, 412, 411

# PHOTOMETRIC AND SPECTROSCOPIC ANALYSIS OF LENSED RE-IONISING SOURCES AT THE FRONTIER OF THE UNIVERSE

N. Laporte[1], R. Ellis[1, 2], G. Roberts-Borsani[1], L. Infante [3], W. Zheng[4], F.E. Bauer[3], D. Bina[5], I. Chilingarian[6], S. Kim[3], R. Pelló[5], I. Pérez-Fournon[7], J. Richard[8], P. Troncoso-Iribarren[3] and A. Streblyanska[7]

**Abstract.** Our team is performing an automatic search for very distant sources using HST, VLT, Magellan, Gemini, Spitzer and ALMA dataset around Frontier Fields aiming to study the nature and properties of sources during the epoch of reionization. In this paper, we report on our photometric sample selection, the photometric properties of our $z$>6 candidates and the evolution of galaxy number densities during the first billion years from a statistical point of view. Thanks to the huge depth of HST FF data, we identified several $z$>7 candidates selected in previous HST surveys as mid-$z$ interlopers that could bias our conclusions on the evolution of the first galaxies. We also briefly discuss several interesting objects that will benefit from the arrival of the JWST. The spectroscopic follow-up has just started, and our team is observing a sample of $z$>7 sources with ground-based spectrographs in order to confirm the redshift of these objects and add robust constraints on their physical properties.

Keywords: Galaxies: distances and redshifts, Galaxies: evolution, Galaxies: formation, Galaxies: high-redshift, Galaxies: photometry, Galaxies: star formation

## 1 Introduction

Observations probing the edges of the visible Universe is one of the most intriguing challenges of the coming decade, particularly with respect to detecting the first galaxies at $z$>12 (Bromm & Yoshida 2011) and the first population III stars (eg. O'Shea & Norman 2007). Several telescopes and instruments are under development and have put these topics in their key objectives. Many surveys have been completed in order to push even further the observational limits of the Universe and to strongly increase the number of very high-redshift sources known ($z$>6). Ten years ago, only a dozen objects at $z$> 6 had been discovered (Kneib et al. 2004), with none above $z$>7.5. Nowadays, the number of $z\sim6$, $z\sim7$, and $z\geq8$ galaxies selected in deep surveys count in the 1000s (e.g. Le Fèvre et al. 2015), several 100s (e.g. Bouwens et al. 2015) and $\sim$100 (e.g Oesch et al. 2014), respectively. Thanks to these huge numbers of objects, the evolution and properties of galaxies, as well as their contribution to the reionization process, are relatively well-constrained up to $z\sim6$, with many secure spectroscopic confirmations (Jiang et al. 2013; Smit et al. 2015). Beyond $z\sim6$, spectroscopic follow-up remains extremely challenging due to the decreasing mean brightness of these objects (Oesch et al. 2015; Watson et al. 2015). However, during the last year several groups have demonstrated that a type of very high-redshift candidates systematically shows bright emission lines (e.g. Oesch et al. 2015, Bouwens et al. 2014, Finkelstein et al. 2013) leading to the spectroscopic

[1] Department of Physics and Astronomy, University College London, Gower Street, London WC1E 6BT, UK
[2] European Southern Observatory (ESO), Karl-Schwarzschild-Strasse 2, 85748 Garching, Germany
[3] Instituto de Astrofísica and Centro de Astroingeniería, Pontificia Universidad Católica de Chile, Casilla 306, Santiago 22, Chile
[4] Department of Physics and Astronomy, Johns Hopkins University, Baltimore, MD 21218, USA
[5] CNRS, IRAP, UMR 5277, 9 Av. Colonel Roche, BP 44346, F-31028, Toulouse Cedex 4, France
[6] Smithsonian Astrophysical Observatory, 60 Garden Street MS09, Cambridge, MA 02138, USA and Sternberg Astronomical Institute, M.V.Lomonosov Moscow State University, 13 Universitetsky prospect, 119992 Moscow Russia
[7] Instituto de Astrofsica de Canarias, E-38205 La Laguna, Tenerife, Spain
[8] Centre de Recherche Astrophysique de Lyon UMR5574, F-69230, Saint-Genis-Laval, France

confirmation of objects up to $z$=8.7 (Zitrin et al. 2015; Roberts-Borsani et al. 2016). All these objects display two breaks : one between optical and NIR, the Lyman-break, and another one between 3.6 and 4.5$\mu$m, the 4000Å break that confirms the high-$z$ hypothesis (Smit et al. 2014; Laporte et al. 2014).

In this paper, we report on the photometric selection of bright $z$>7 objects in the latest Hubble flagship program, the *Frontier Fields* (Lotz 2015), the statistical analysis of the sample and on the first stage of the spectroscopic follow-up.

## 2 The HST Frontier Fields

In October 2013, the *Hubble* Space Telescope started observations of six massive galaxy clusters as part of "The Frontier Fields" (hereafter FF, Lotz 2015), aiming to obtain the deepest data using strong gravitational lensing. The *Spitzer* Space Telescope is also involved allowing to increase the wavelength coverage with extremely deep data through 4.5$\mu$m. To date, four clusters have been fully observed by *Hubble* : Abell 2744, MACSJ0416.1-2403, MACSJ0717.5+3745 and MACSJ1149.5+2223 reaching depths of ≈29.0 AB at 5$\sigma$. Our group applied the Lyman Break Galaxy technique (LBG; Steidel et al. 1996) combining non-detections in F435W, F606W, F814W and detections in F125W, F140W, as well as color criteria to select the brightest $z \geq$6.5 candidates in all FF clusters. Compared to others groups, we add one more criteria on the size of the break between F814W and F125W (F814W-F125W > 4.0 mag) in order to remove extreme mid-$z$ interlopers (Hayes et al. 2012, Fig. 1). In the following, we take benefit from public lens models provided in the framework of the Frontier Fields program by the CATS group (Richard et al. 2014; Jauzac et al. 2015).

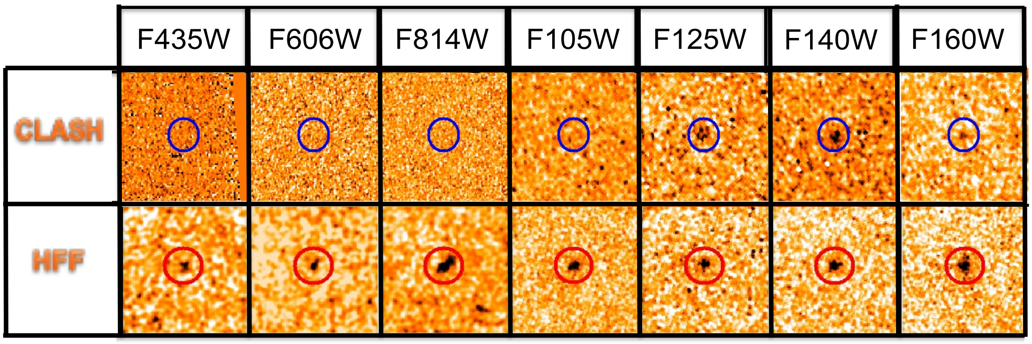


**Fig. 1.** Example of source selected as a good $z$ ∼8 candidate and revealed as mid-$z$ interloper by the *Hubble* Frontier Fields data. The first row shows the shape of this candidate in the CLASH data (Postman et al. 2012) and the second row shows the same object as seen by the Frontier Fields. The detections at ∼0.4, 0.6 and 0.8 $\mu$m demonstrates that this object is not at such high-redshift.

Finally, we selected 39, 22, and 39 $z$>6 candidates in Abell 2744 (Laporte et al. 2014; Zheng et al. 2014), MACS0416 (Laporte et al. 2015; Infante et al. 2015) and MACS0717 (Laporte et al. 2016) respectively. More particularly, we found one of the faintest galaxy at $z$>10 strongly amplified behind MACS0416 (Infante et al. 2015, see section 4) leading to a magnitude of $M_{UV}$ ∼15.5.

## 3 Photometric Analysis of Frontier Fields samples

With the huge number of very high-$z$ lensed galaxies selected in the Frontier Fields survey, we are able to put robust constraints on the faint end of the UV Luminosity Function (LF), and therefore constrain the contribution of the faintest galaxies to the reionization process. However, our selection is only based on photometric criteria (see previous section) and even by using additional criteria on the size of the break limiting the contamination by mid-$z$ interlopers, it is crucial to take into account uncertainties on the photometric redshift to study the evolution of the UV LF. Therefore we used a MC method based on the redshift probability distribution for each source to compute the number density of galaxies in several redshift ranges (see Laporte et al. 2015 for a detailed description of the method). We adopted a Schechter parameterisation (Schechter 1976) and found a clear evolution of $\Phi^{\star}$, more especially between $z$ ∼8 and 9 suggesting a strong decrease in the number of galaxies in this redshift interval, and a relatively small evolution of the faint-end slope $\alpha$ (Fig. 2). The parameterisation of the Schechter function we deduced from half of the Frontier Fields survey is reported in Table 1. We used this

**Table 1.** Schechter parameters for the UV LF at $z \sim 7$, 8 and 9

| $< z >$ | $M^\star$ | $\Phi^\star$ | $\alpha$ |
|---|---|---|---|
| 7 | $-20.33^{+0.37}_{-0.47}$ | $0.37^{+0.12}_{-0.11} \times 10^{-3}$ | $-1.91^{+0.26}_{-0.27}$ |
| 8 | $-20.32^{+0.49}_{-0.26}$ | $0.30^{+0.85}_{-0.19} \times 10^{-3}$ | $-1.95^{+0.43}_{-0.40}$ |
| 9 | -20.45 (*fixed*) | $0.70^{+0.30}_{-0.30} \times 10^{-4}$ | $-2.17^{+0.41}_{-0.43}$ |

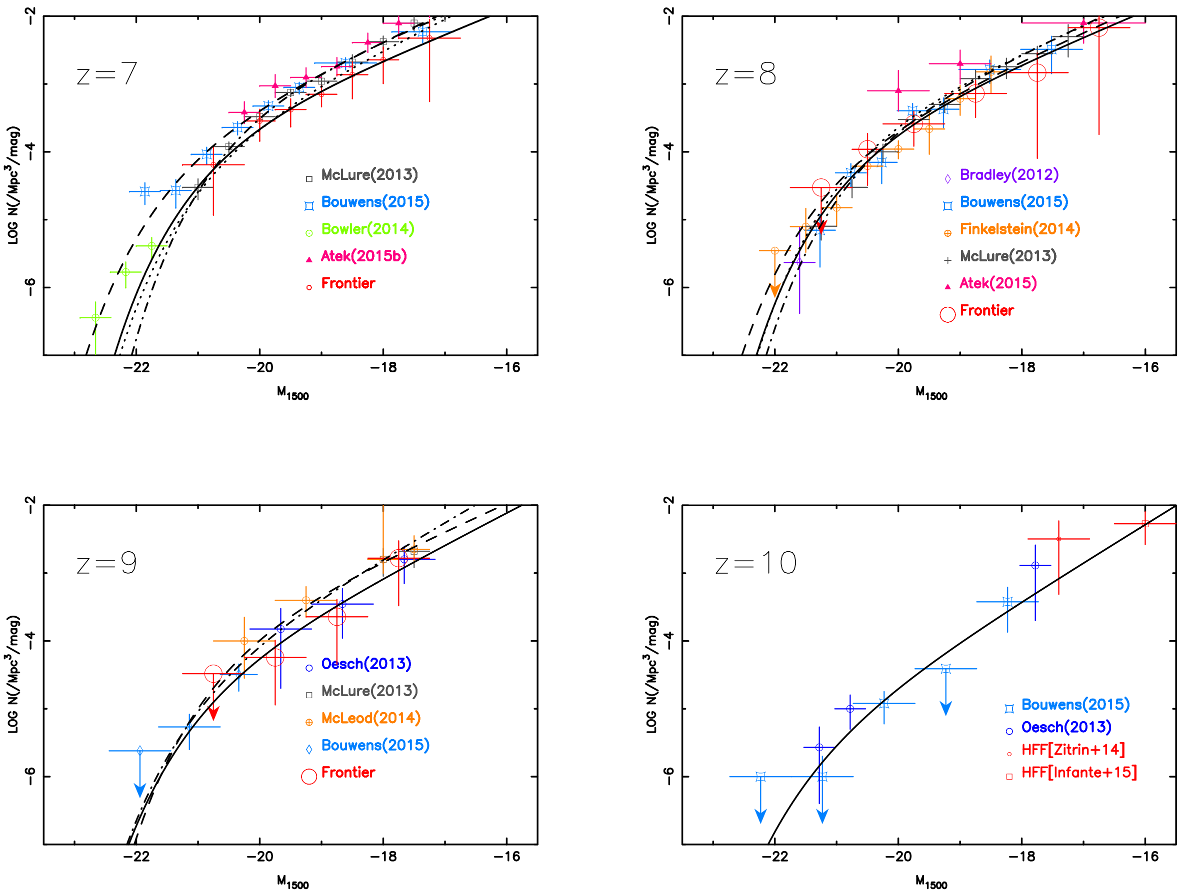


**Fig. 2.** Number densities and best-fit of the Luminosity Function at $z \sim 7$, 8, 9, and 10 using the half of the Frontier Fields data. Our point (in red) are compared with results published in McLure et al. (2013); Bouwens et al. (2015); Bowler et al. (2014); Atek et al. (2015); Bradley et al. (2012); Finkelstein et al. (2015); Oesch et al. (2013); McLeod et al. (2015)

parameterisation to estimate the UV photons density produced by the galaxies at each redshift range covered by this survey, and compared these densities with the UV density required to keep the Universe reionized (Madau et al. 1999). As previously demonstrated, the UV photons density produced by the Lyman Break galaxies is not sufficient to explain the end of the reionization process at $z \sim 6$ (Fig. 3), and therefore others contributors must be considered, such as the Gamma Ray Burst or AGN at very high-redshift.

We also took benefit from the large wavelength range covered by the Frontier Fields data to estimate the physical properties of our very high-$z$ candidates using *iSEDfit* (Moustakas et al. 2013) as described in Infante et al. (2015). We confirmed the trend observed previously in the evolution of the Star Formation Rate (SFR) as function of galaxy mass as well as in the evolution of the size of galaxies as a function of the UV Luminosity at very high-redshift (see Fig. 6 and 10 of Laporte et al. 2016).

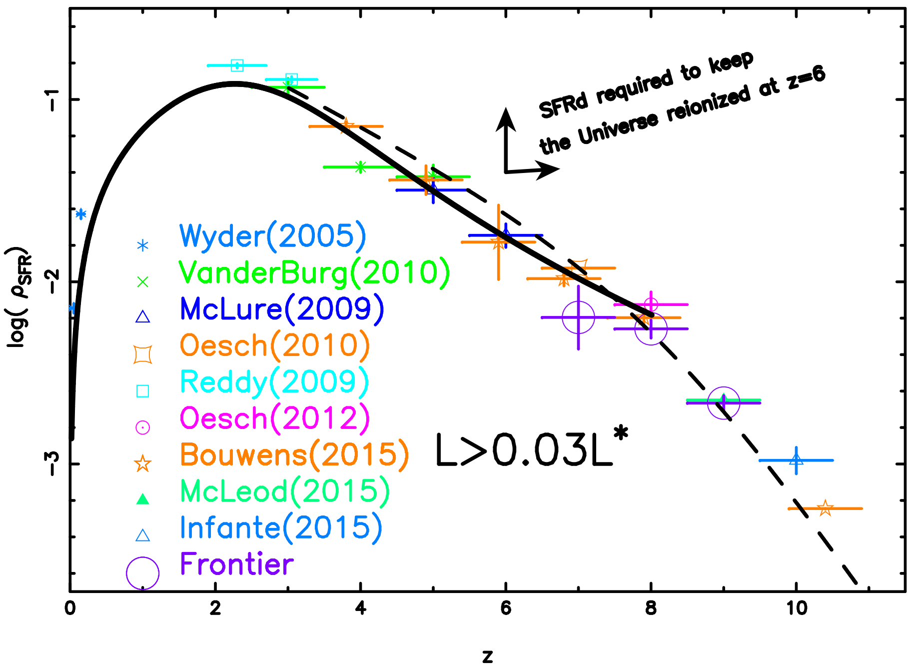


**Fig. 3.** Evolution of the SFRd including densities deduced from the half Frontier Fields data set. Two parameterizations are overplotted: the solid line shows the shape published in Cole et al. (2001) and the dashed line displays the evolution as seen by Ishigaki et al. (2015). The dark arrows show the SFR density required to keep the Universe reionized computed from Madau et al. (1999)

## 4 Spectroscopic follow-up

Our team just started a spectroscopic follow-up of all bright $z \geq 7.5$ objects with several ground based telescopes, such as the *Very Large Telescopes*, *Gemini*, *Magellan* and *Keck*. During the first stage of this program, we observed for $\approx$ 10 hours two of the brightest high-$z$ candidates detected on the Frontier Fields images, namely Abell2744_Y1 (Laporte et al. 2014) and MACS1149_JD1 (Zheng et al. 2012), with MMIRS/Magellan. We reached a $2\sigma$-sensitivity of $10^{-17}$ erg/s/cm$^2$ and detected no line. This non-detection is consistent with the non-detection observed in the GLASS survey (Treu et al. 2015; Schmidt et al. 2016) reaching a flux limit of $10^{-17}$ erg/s/cm$^2$ at $2\sigma$. Others observations are already scheduled with X-Shooter/VLT to push the sensitivity to $2\times10^{-18}$ erg/s/cm$^2$.

## 5 Conclusions

Thanks to the depth of the Frontier Fields survey images, we are able, for the first time, to give robust constraints on the extreme faint-end of the UV Luminosity Function up to $M_{1500}\sim$-15, and therefore start to reveal the role played by the faintest Lyman Break galaxies during the epoch of reionization. However, all these results must be taken with caution since they are based on photometric samples, which could be contaminated by mid-$z$ galaxies displaying a SED similar to the very high-$z$ objects SED. With current facilities, we are only able to observe the brightest objects in the first billion years of the Univers. But the arrival of the *James Webb Space Telescope* in 2018 or the first light of the *European Extremely Large telescope* in 2024 will allow us to explore by spectroscopy a new range of luminosity and therefore definitively determine the major contributors to the reionization process.

We acknowledge support from: European Research Council Advanced Grant FP7/669253 (NL); CONICYT-Chile grants Basal-

CATA PFB-06/2007 (FEB, PT-I, SK, LI), FONDECYT Regular 1141218 (FEB), FONDECYT Postdoctorado 3140542 (PT-I), FONDECYT grant No. 1130528, and "EMBIGGEN" Anillo ACT1101 (FEB); the Ministry of Economy, Development, and Tourism's Millennium Science Initiative through grant IC120009, awarded to The Millennium Institute of Astrophysics, MAS (FEB). This work is based on observations made with the NASA/ESA Hubble Space Telescope, obtained at the Space Telescope Science Institute (STScI), which is operated by the Association of Universities for Research in Astronomy, Inc., under NASA contract NAS 5-26555. The HST image mosaics were produced by the Frontier Fields Science Data Products Team at STScI. This work is based in part on observations made with the *Spitzer* Space Telescope, which is operated by the Jet Propulsion Laboratory, California Institute of Technology under a contract with NASA. This work utilizes gravitational lensing models produced by PIs Bradac, Ebeling, Merten & Zitrin, Sharon, and Williams funded as part of the HST Frontier Fields program conducted by STScI. STScI is operated by the Association of Universities for Research in Astronomy, Inc. under NASA contract NAS 5-26555. The lens models were obtained from the Mikulski Archive for Space Telescopes (MAST).

## References

Atek, H., Richard, J., Jauzac, M., et al. 2015, ApJ, 814, 69

Bouwens, R. J., Bradley, L., Zitrin, A., et al. 2014, ApJ, 795, 126

Bouwens, R. J., Illingworth, G. D., Oesch, P. A., et al. 2015, ApJ, 803, 34

Bowler, R. A. A., Dunlop, J. S., McLure, R. J., et al. 2014, MNRAS, 440, 2810

Bradley, L. D., Trenti, M., Oesch, P. A., et al. 2012, ApJ, 760, 108

Bromm, V. & Yoshida, N. 2011, ARA&A, 49, 373

Cole, S., Norberg, P., Baugh, C. M., et al. 2001, MNRAS, 326, 255

Finkelstein, S. L., Papovich, C., Dickinson, M., et al. 2013, Nature, 502, 524

Finkelstein, S. L., Ryan, Jr., R. E., Papovich, C., et al. 2015, ApJ, 810, 71

Hayes, M., Laporte, N., Pelló, R., Schaerer, D., & Le Borgne, J.-F. 2012, MNRAS, 425, L19

Infante, L., Zheng, W., Laporte, N., et al. 2015, ApJ, 815, 18

Ishigaki, M., Kawamata, R., Ouchi, M., et al. 2015, ApJ, 799, 12

Jauzac, M., Richard, J., Jullo, E., et al. 2015, MNRAS, 452, 1437

Jiang, L., Egami, E., Mechtley, M., et al. 2013, ApJ, 772, 99

Kneib, J.-P., Ellis, R. S., Santos, M. R., & Richard, J. 2004, ApJ, 607, 697

Laporte, N., Infante, L., Troncoso Iribarren, P., et al. 2016, ApJ, 820, 98

Laporte, N., Streblyanska, A., Clement, B., et al. 2014, A&A, 562, L8

Laporte, N., Streblyanska, A., Kim, S., et al. 2015, A&A, 575, A92

Le Fèvre, O., Tasca, L. A. M., Cassata, P., et al. 2015, A&A, 576, A79

Lotz, J. 2015, IAU General Assembly, 22, 2255460

Madau, P., Haardt, F., & Rees, M. J. 1999, ApJ, 514, 648

McLeod, D. J., McLure, R. J., Dunlop, J. S., et al. 2015, MNRAS, 450, 3032

McLure, R. J., Dunlop, J. S., Bowler, R. A. A., et al. 2013, MNRAS, 432, 2696

Moustakas, J., Coil, A. L., Aird, J., et al. 2013, ApJ, 767, 50

Oesch, P. A., Bouwens, R. J., Illingworth, G. D., et al. 2013, ApJ, 773, 75

Oesch, P. A., Bouwens, R. J., Illingworth, G. D., et al. 2014, ApJ, 786, 108

Oesch, P. A., van Dokkum, P. G., Illingworth, G. D., et al. 2015, ApJ, 804, L30

O'Shea, B. W. & Norman, M. L. 2007, ApJ, 654, 66

Postman, M., Coe, D., Benítez, N., et al. 2012, ApJS, 199, 25

Richard, J., Jauzac, M., Limousin, M., et al. 2014, MNRAS, 444, 268

Roberts-Borsani, G. W., Bouwens, R. J., Oesch, P. A., et al. 2016, ApJ, 823, 143

Schechter, P. 1976, ApJ, 203, 297

Schmidt, K. B., Treu, T., Bradač, M., et al. 2016, ApJ, 818, 38

Smit, R., Bouwens, R. J., Franx, M., et al. 2015, ApJ, 801, 122

Smit, R., Bouwens, R. J., Labbé, I., et al. 2014, ApJ, 784, 58

Steidel, C. C., Giavalisco, M., Pettini, M., Dickinson, M., & Adelberger, K. L. 1996, ApJ, 462, L17

Treu, T., Schmidt, K. B., Brammer, G. B., et al. 2015, ApJ, 812, 114

Watson, D., Christensen, L., Knudsen, K. K., et al. 2015, Nature, 519, 327

Zheng, W., Postman, M., Zitrin, A., et al. 2012, Nature, 489, 406

Zheng, W., Shu, X., Moustakas, J., et al. 2014, ApJ, 795, 93

Zitrin, A., Labbé, I., Belli, S., et al. 2015, ApJ, 810, L12

*SF2A 2016*
*C. Reylé, J. Richard, L. Cambrésy, M. Deleuil, E. Pécontal, L. Tresse and I. Vauglin (eds)*

# HIGH-Z GALAXIES & REIONIZATION

R. Pelló[1]

**Abstract.** This paper is a short review on the state of the art regarding the study of sources responsible for the reionization, focusing on the contribution of high-$z$ star-forming galaxies to this process. We discuss the current results on the abundance of this population, coming from deep surveys in lensing and blank fields. A robust estimate of the ionizing emissivity and its evolution with redshift requires a good knowledge on the physical parameters of star-forming galaxies, which in turn relies on detailed multi-wavelength and spectroscopic studies beyond the reach of current facilities for most samples. The complete census of ionizing sources could be facilitated by the use of 3D/IFU spectroscopy without any photometric preselection, as illustrated by recent results obtained with MUSE/VLT. Lensing clusters have become an indispensable tool to push the observational limits, in particular for galaxies formed during the first billion years, waiting for coming facilities such as the JWST and the E-ELT.

Keywords: Galaxies, cosmology, extragalactic surveys, dark ages, reionisation

## 1 Introduction

This paper is intended to be a short review on the state of the art regarding the study of sources responsible for the reionization, focusing on the contribution of high-$z$ star-forming galaxies to this process. The interested reader can find excellent and exhaustive reviews in the literature (see e.g. Barkana & Loeb 2001; Loeb & Barkana 2001; Dijkstra 2014; Ellis 2014). Considerable efforts have been invested during the last decade to understand the process of structure formation in the early universe. The first generation of sources is the result of the growth of linear density fluctuations dominated by dark matter. Gas was attracted by dark-matter halos and cooled down to form stars. The first generation of stars and quasars ended the so-called "dark ages", and started the process of galaxy assembly. UV radiation coming from hot and massive stars progressively photoionized the surrounding hydrogen till the complete reionization about 1 billion years after the Big Bang. Figure 1 presents a schematic illustration of the hydrogen reionization process in the intergalactic medium driven by star-forming galaxies.

There are two main constrains on the reionization history. The first one comes from the evolution in the optical depth of the Lyman absorption series observed in high-$z$ quasars, showing an increase in the optical depth to Lyman-$\alpha$ photons (the Gunn-Peterson effect, Gunn & Peterson 1965) at high z$\sim$6 (see e.g. Fan et al. 2006, and the references therein). However, this approach cannot be used to follow the reionization history beyond z$\sim$6 because saturation rapidly occurs: a tiny volume-averaged fraction of neutral hydrogen of a few $\sim 10^{-4}$ is enough to completely suppress the spectroscopic signal shortward of Lyman-$\alpha$. A large variance is also observed as a function of the line-of-sight, with growing evidence for a "patchy" reionization showing inhomogeneities at $\sim$100 Mpc scales (Pentericci et al. 2014; Becker et al. 2015).

The second constrain comes from the optical depth to electron scattering to cosmic microwave background (CMB) photons, and the correlation of the polarization induced by these electrons and temperature fluctuations (see presentation by M. Langer & M. Douspis, this conference). This effect has been detected since the year-1 WMAP data (see e.g. Komatsu et al. 2011), and improved successively by Planck observations (see e.g. Planck Collaboration et al. 2016; Douspis et al. 2015). The last and best determination from the Planck consortium places the average redshift for reionization between z=7.8 and 8.8, depending on the model, with the a strong constrain on the ionization level of $\sim$10% at z$\sim$10.

[1] Université de Toulouse; UPS-OMP; IRAP; 14, avenue Edouard Belin, F-31400 Toulouse, France

Despite all these recent and spectacular results around the reionization epoch, there is still room for improvement regarding the sources of the reionization and their physical properties, a topic which is closely related to the galaxy-formation process. Also the reionization itself is poorly understood as a detailed physical process, although some interesting models have been published recently (see e.g. Douspis et al. 2015; Manrique et al. 2015).

In Sect. 2 we summarize the methodology and the results obtained from current deep surveys looking for the sources responsible for the reionization in blank and lensing fields. In Section 3 we address the use of 3D/IFU spectroscopy to achieve a complete census of ionizing sources. A general discussion together with the perspectives for future facilities are presented in Section 4. Throughout this article a $\Lambda$-CDM cosmology with $\Omega_\Lambda = 0.7$, $\Omega_m = 0.3$ and $H_0 = 70$ km s$^{-1}$ Mpc$^{-1}$ is assumed, and all magnitudes are quoted in the AB system (Oke & Gunn 1983).

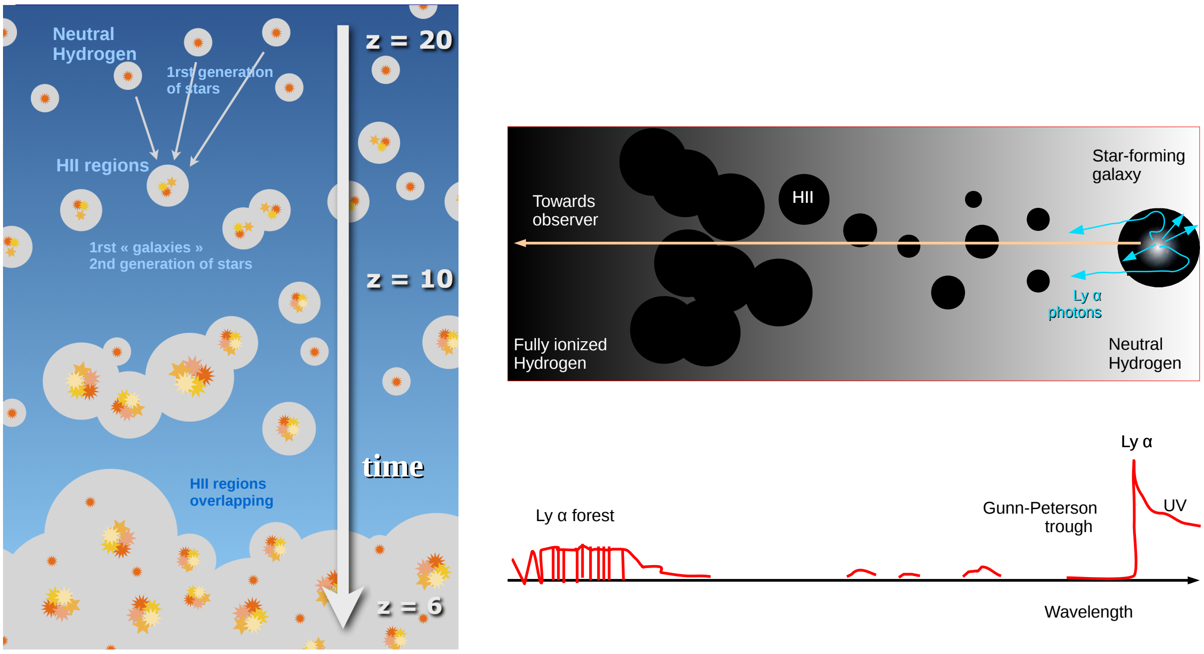


**Fig. 1. Left:** Illustration of the reionization process by star-forming galaxies. Gas is attracted by dark-matter halos and cools down to form stars. With increasing time/decreasing redshift, the HII bubbles increase in size and overlap. **Right:** Figure showing the spectrum expected for a star-forming galaxy observed at a redshift above the reionization.

## 2 From Dark Ages to Reionization: Current constraints on ionizing sources

Star-forming galaxies appear as the main contributors to the reionization. Indeed, luminous quasars show a rapid decline in their Luminosity Function (hereafter LF) beyond z∼5, although there is still some uncertainty on the slope towards the faint end of the LF (McGreer et al. 2013). Regarding the identification of star-forming galaxies around and beyond the reionization epoch, there are two main signatures susceptible to be used for this exercise, as shown in Fig. 1. The first one is the Lyman "drop-out" in the continuum bluewards with respect to Lyman-$\alpha$, due to the combined effect of interstellar and intergalactic scattering by neutral hydrogen. The identification of galaxies at $6 \leq z \leq 12$ requires an homogeneous and deep coverage of the near-IR domain in combination with (ultra-deep) optical data. Different redshift intervals can be defined using the appropriate color-color diagrams or photometric redshifts. An extensive literature is available on this topic since the pioneer work by Steidel et al. (1996) on *Lyman Break Galaxies* (hereafter LBG) (see e.g. Ouchi et al. 2004; Stark et al. 2009; McLure et al. 2009; Bouwens et al. 2015b, and the references therein). Figure 2 provides an example of LBG candidates at z∼8 based on HST (0.3-1.6$\mu$m), VLT/HAWK-I (K$_s$), and Spitzer/IRAC (3.6-4.5$\mu$m) data. The second method is the detection of Lyman-$\alpha$ emission, based on wide-field narrow band surveys, targeting a precise redshift bin (see e.g. Rhoads et al. 2000; Kashikawa et al. 2006; Konno et al. 2014), or efficient 3D/IFU spectroscopy in pencil beam mode (e.g. using MUSE/VLT, Bacon et al. 2015), although the last technique is presently limited to z∼6.7 in the optical domain. It is worth to mention that all photometrically-selected samples, either LBG or *Lyman-α emitters* (hereafter LAE), need a spectroscopic follow up to confirm both the redshift and the nature of these candidates.

Impressive results have been obtained during the last ∼5 years on the determination of the UV LF and its evolution between z∼4 and 10 based on LBG studies (see e.g. Bouwens et al. 2015b). The new instrumentation available on the *Hubble Space Telescope* (HST) on one hand, namely the wide-field WFC3 and its near-IR camera WFC3/IR, and the completion of (ultra)deep and/or wide-field surveys on the other hand (CANDELS, GOODS, HUDF, BoRG, ...), associated to Spitzer/IRAC and deep ground-based observations, have provided a reliable estimate of the UV LF based on ∼1000 arcmin$^2$ effective "deep" survey, reaching m∼27-28 for typical candidates at z∼7-8. In addition to blank field surveys, specific studies have been conducted in lensing clusters (e.g. CLASH* and the Hubble Frontier Fields†, hereafter HFF, still ongoing), taking advantage from the magnification effect to explore the faintest end of the LF. As pointed out by different authors (see e.g. Maizy et al. 2010) lensing clusters are more efficient to conduct detailed (spectroscopic) studies in the sensitive redshift domain, and also to explore the faint-end of the LF, whereas observations in wide blank fields are needed and fully complementary to set reliable constraints on the "bright" end of the LF, given the strong field to field variance in number counts in this regime. Results obtained on the HFF fully confirm the benefit expected from gravitational magnification (Laporte et al. 2014; Atek et al. 2014; Infante et al. 2015; Laporte et al. 2016, see also Laporte, this conference).

The last results on the UV LF for LBGs at z∼4 to 10 are nicely summarized in a recent paper by Bouwens et al. (2015b). This LF exhibits a clear evolution at z≥4, with a depletion of bright galaxies with increasing redshift in one hand, and the slope of the faint end becoming steeper on the other hand. Using a Schechter parametrization for the LF, this trend is consistent with an evolution in the normalization $\Phi^*$ (with constant $M^*_{UV}$) between z∼4 and 7, while the slope $\alpha$ varies between -1.64 at z∼4 and -2.06 at z∼7. The trend in the evolution of the normalization is also seen in lensing clusters (Infante et al. 2015; Laporte et al. 2016). The overall evolution in the UV LF seems to be consistent with expectations for the evolution of the halo mass function. However, samples at z>8 are still dramatically small.

Regarding LAE studies, there is a deficit of strongly-emitting Lyman-α galaxies at z≥6.5, whereas no significant evolution is observed below z∼6 (Kashikawa et al. 2006; Pentericci et al. 2014; Tilvi et al. 2014). This trend is attributed to either an increase in the fraction on neutral hydrogen in the IGM or an evolution of the parent population, and the two trends could be also combined together (see also Sect. 4). LAE studies seem to show that the reionization is still in progress at z∼8 (see Tilvi et al. 2014).

How compatible are these results on the density of ionizing sources with the reionization epoch, as discussed in Sect. 1? Bouwens et al. (2015a) have recently addressed this point. They computed the empirical evolution of the cosmic ionizing emissivity with redshift, taking into account all available observational constraints, and compared it with the evolution of the UV luminosity density derived from the above UV LF. The conversion factor from UV luminosity density into ionizing emissivity is consistent with plausible physical values for the escape fraction and clumping factor, provided that the UV LF is integrated down to M(UV)∼-13. Now, at z∼7, present-day observations are limited to M(UV)∼-17 in the HUDF (record-breaking in a blank field), and can reach as faint as M(UV)∼-15.5 behind lensing clusters (Atek et al. 2015; Infante et al. 2015). Also according to Atek et al. (2015), based on the available candidates at z∼6-8 in the HFF lensing clusters and Parallel fields, the UV luminosity density derived at z∼7 seems sufficient to keep the universe reionized, assuming standard conditions for the escape fraction of ionizing radiation. On the contrary, the faint end of the UV LF is not constrained enough at z∼8.

## 3 Towards a complete census of reionizing sources: the MUSE experience

LBGs and LAEs constitute different observational approaches, partly overlapping, to select ionizing sources. The prevalence of Lyman-α emission in well-controled samples of star-forming galaxies as also a test for the reionization history, as discussed in the next section. The complete census of ionizing sources could be facilitated by the use of 3D/IFU spectroscopy without any photometric preselection, as illustrated by recent results obtained

*http://www.stsci.edu/ postman/CLASH
†http://www.stsci.edu/hst/campaigns/frontier-fields/

with MUSE/VLT in deep blank fields (Bacon et al. 2015) and lensing clusters (Richard et al. 2015; Bina et al. 2016).

Regarding lensing clusters, 17 LAEs were found up to $z \leq 6.7$ behind A1689, with luminosities ranging between 40.5≤log(Ly$\alpha$)≤42.5 after correction for magnification. Figure 2 displays the comparison between the number density of these sources observed with MUSE at $3 \leq z \leq 6.7$, and expectations based on the simple extrapolation of the LF found in the literature towards the low-luminosity regime covered by the MUSE survey (for details see Bina et al. 2016). In this figure we have corrected for an error affecting the determination of the effective covolume. Luminosity bins are independent in this figure, and there is no correction for incompleteness. Contrary to other surveys presented in Figure 2, where the fit is only sensitive to L$^*$ and the normalization, the samples built in lensing clusters are typically ∼10 times fainter than the usual samples available in the literature, in particular at $z \geq 4$, and comparable to the faintest samples currently available at lower redshifts (e.g. the sample Lyman-$\alpha$ emitters observed by MUSE in the HDFS at $z \geq 2.9$ Bacon et al. 2015; Wisotzki et al. 2016). Therefore, they are particularly sensitive to the value of the slope parameter $\alpha$, for which a constant value is often assumed in the literature. Despite the obvious caveats regarding the small size of the present sample, the density of intrinsically-faint sources observed in this field seems roughly consistent with the steepest values used by the different authors to fit their data, namely $\alpha \leq$ -1.5, and inconsistent with flatter values of the slope. Correction for completeness in the faintest bins should exacerbate this trend. The authors acknowledge the need for further investigation to fully confirm this result, based on larger samples of LAE detected in lensing fields.

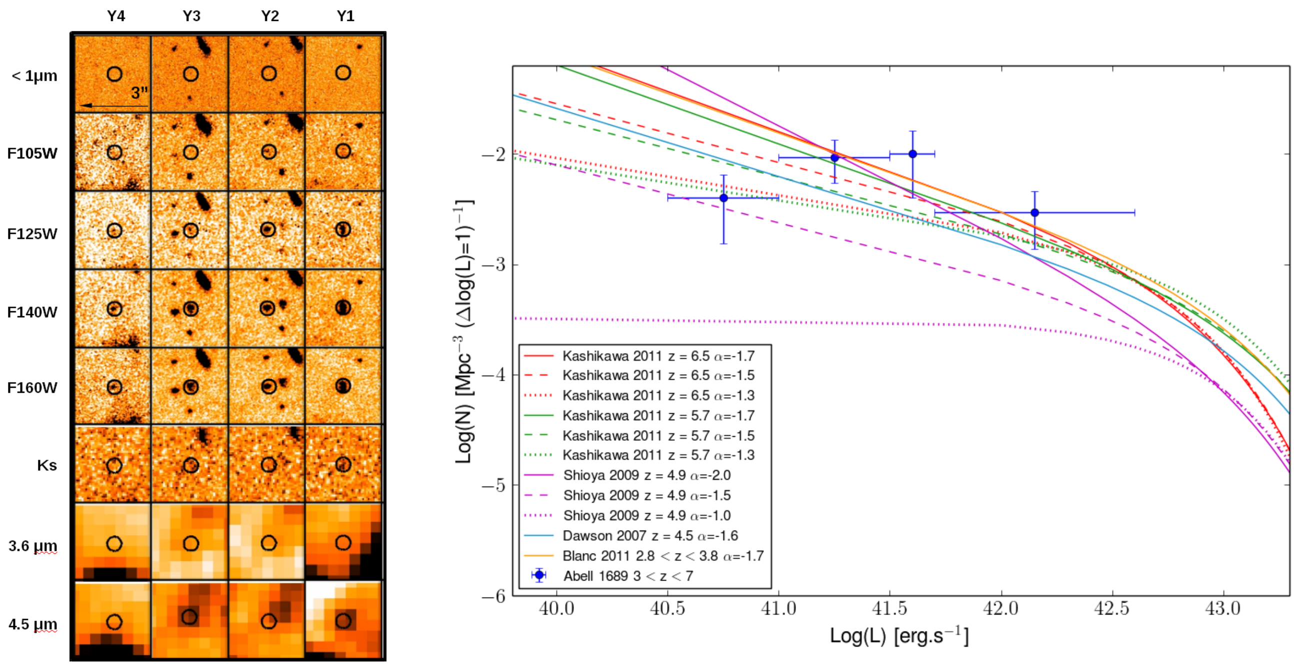


**Fig. 2. Left:** Example of four LBG candidates at z∼8 behind the lensing cluster MACS0416 found by Laporte et al. (2015) based on HST Frontier Fields (0.3-1.6$\mu$m), VLT/HAWK-I (K$_s$), and Spitzer/IRAC (3.6-4.5$\mu$m) data (see also Laporte, this conference). **Right:** Corrected version of Fig. 11 by Bina et al. (2016), showing the comparison between the density of Lyman-$\alpha$ emitters observed at $3 \leq z \leq 6.7$ behind the lensing cluster A1689, and the extrapolation of various LF in the literature towards the low-luminosity regime covered by the MUSE survey (see Bina et al. 2016, and the text for details). References are given in the figure for different redshifts and values of the slope parameter $\alpha$ (Dawson et al. 2007; Shioya et al. 2009; Blanc et al. 2011; Kashikawa et al. 2011). Note that solid lines display the steepest slopes adopted for the LF fit. Error bars include Poisson noise statistics and field-to-field variance.

## 4 Discussion and Perspectives

Present-day results are consistent with the reionization being dominated by faint star-forming galaxies. However, several issues remain to be addressed before a consistent picture of the galaxy-formation process could be achieved, as discussed below. Our current observations are just at the limits, and most of these questions will be answered with the arrival of new instruments and telescopes in the next coming years, such as EMIR/GTC[‡], NIRSpec/JWST[§], NIRCam/JWST[¶] and the E-ELT[‖].

Reionization scenarios emerging from current results need an appreciable fraction of star-formation located in small-size halos to reach a UV photon budget required with a LF integrated down to M(UV)∼-13 (Bouwens et al. 2015a). As pointed out by Boylan-Kolchin et al. (2014), based on simulations of early galaxy formation, this implies a substantial star-formation activity in halos of M(virial)$\sim 10^8$ $M_\odot$ at z∼8, which seems to be in serious tension with galaxy counts in the Local Group. A possible implication to match these counts could be that star-formation became inefficient in halos smaller than M(virial)$\sim 10^9$ $M_\odot$ at early epochs; therefore, the UV LF must break at some point towards M(UV)∼-14. JWST observations are clearly needed to reach such depth, in particular at z∼8, but a first constrain could be also derived from lensing fields (e.g. in the HFF).

When determining the ionizing emissivity for a given population, e.g. when using the UV LF and the density of UV photons to account for the evolution of the cosmic emissivity, the estimate depends on the physical parameters of star-forming galaxies, which is still poorly constrained, in particular for the faint population. Needless to say that the presence of dust in these populations will completely change the interpretation of the UV photon budget. The direct measurement of dust content and UV attenuation at z≥6 requires deep sub-mm data, in particular using ALMA, and very few measurements exist so far (Schaerer et al. 2015). Most samples of photometric candidates presently available from ultra-deep HST data are beyond the reach of current instrumentation for detailed studies. Ideally, multi-wavelength /spectroscopic studies reaching as faint as m(AB)∼30 are needed to make progress in this respect, i.e. reaching the depth of JWST or present HFF (lensing magnification), not only for redshift measurements (based on Lyman-$\alpha$ and other strong emission-lines), but also to determine the precise nature of genuine high-$z$ galaxies and extreme mid-$z$ interlopers. The progress in this area follows the availability of efficient near-IR spectrographs such as ground-based MOSFIRE/Keck, KMOS/VLT or EMIR/GTC, and devoted surveys with these facilities targeting z≥7 candidates (see e.g. Schenker et al. 2014; Oesch et al. 2015; Zitrin et al. 2015), waiting for the JWST.

There is still a large uncertainty on the escape fraction of ionizing photons in the low-luminosity galaxies responsible for the reionization. It is likely that this fraction depends on both the physical properties of galaxies (kinematics, size, star-formation rate, dust, ...) and geometrical considerations (morphology, orientation,...). The physics of Lyman-$\alpha$ emission is particularly complex and could potentially introduce severe biases in the selection function of LAE (see e.g. Verhamme et al. 2012). The prevalence of Lyman-$\alpha$ emission in well-controled samples can be used as a test for reionization history (see e.g. Schenker et al. 2014). The usual assumption is that, on average, the prevalence of Lya emission in galaxies beyond the reionization is a simple extrapolation of observations below the reionization (z<6), and departures from the general trend are interpreted as an increasing fraction of neutral hydrogen. Based on this approach, the "filling factor" of ionized hydrogen is supposed to evolve from ∼66% at z∼7 to <35% at z∼8, with large uncertainties (Pentericci et al. 2014; Tilvi et al. 2014; Schenker et al. 2014). The recent results obtained with MUSE/VLT on the detection of LAE at $3 \leq z \leq 7$, in particular behind lensing clusters, without any photometric preselection, illustrate the efficiency of 3D/IFU spectroscopy in completing the census of ionizing sources. This approach could be extended to the sensitive range at z∼6–12, both in lensing and blank fields, using current or coming facilities (e.g. HARMONI/E-ELT Thatte et al. 2010). There are two main motivations for this approach. In one hand, a large fraction of LAE are not detected in deep photometric surveys up to m∼28-29 (e.g., ∼1/3 of the current LAE detected behind lensing clusters do not exhibit continuum emission); therefore, a pointed survey will miss them. On the other hand, a large fraction (still to be confirmed) of high-$z$ galaxies display extended Lyman-$\alpha$ emission (see e.g. Wisotzki et al. 2016, based on MUSE data). This trend is also found in galaxies observed beyond the reionization, (see e.g. Tilvi et al. 2016), as expected since the pioneer work of Loeb & Rybicki (1999). This means that pointed surveys will miss a large fraction of the Lyman-$\alpha$ emission associated to LBG samples, with strong implications on the reionization budget.

Part of the work presented was supported by the French CNRS, the "Programme National de Cosmologie and Galaxies" (PNCG) of CNRS/INSU, France, the OCEVU Labex (ANR-11-LABX-0060), and the A*MIDEX project (ANR-11-IDEX-0001-02) funded by the "Investissements d'Avenir" French government program managed by the ANR.

[‡] http://www.gtc.iac.es/instruments/emir/emir.php
[§] http://www.stsci.edu/jwst/instruments/nirspec
[¶] http://www.stsci.edu/jwst/instruments/nircam
[‖] https://www.eso.org/sci/facilities/eelt/instrumentation/

## References


Atek, H., Richard, J., Jauzac, M., et al. 2015, ApJ, 814, 69

Atek, H., Richard, J., Kneib, J.-P., et al. 2014, ApJ, 786, 60

Bacon, R., Brinchmann, J., Richard, J., et al. 2015, A&A, 575, A75

Barkana, R. & Loeb, A. 2001, Phys. Rep., 349, 125

Becker, G. D., Bolton, J. S., Madau, P., et al. 2015, MNRAS, 447, 3402

Bina, D., Pelló, R., Richard, J., et al. 2016, A&A, 590, A14

Blanc, G. A., Adams, J. J., Gebhardt, K., et al. 2011, ApJ, 736, 31

Bouwens, R. J., Illingworth, G. D., Oesch, P. A., et al. 2015a, ApJ, 811, 140

Bouwens, R. J., Illingworth, G. D., Oesch, P. A., et al. 2015b, ApJ, 803, 34

Boylan-Kolchin, M., Bullock, J. S., & Garrison-Kimmel, S. 2014, MNRAS, 443, L44

Dawson, S., Rhoads, J. E., Malhotra, S., et al. 2007, ApJ, 671, 1227

Dijkstra, M. 2014, PASA, 31, e040

Douspis, M., Aghanim, N., Ilić, S., & Langer, M. 2015, A&A, 580, L4

Ellis, R. S. 2014, ArXiv e-prints

Fan, X., Carilli, C. L., & Keating, B. 2006, ARA&A, 44, 415

Gunn, J. E. & Peterson, B. A. 1965, ApJ, 142, 1633

Infante, L., Zheng, W., Laporte, N., et al. 2015, ApJ, 815, 18

Kashikawa, N., Shimasaku, K., Malkan, M. A., et al. 2006, ApJ, 648, 7

Kashikawa, N., Shimasaku, K., Matsuda, Y., et al. 2011, ApJ, 734, 119

Komatsu, E., Smith, K. M., Dunkley, J., et al. 2011, ApJS, 192, 18

Konno, A., Ouchi, M., Ono, Y., et al. 2014, ApJ, 797, 16

Laporte, N., Infante, L., Troncoso Iribarren, P., et al. 2016, ApJ, 820, 98

Laporte, N., Streblyanska, A., Clement, B., et al. 2014, A&A, 562, L8

Laporte, N., Streblyanska, A., Kim, S., et al. 2015, A&A, 575, A92

Loeb, A. & Barkana, R. 2001, ARA&A, 39, 19

Loeb, A. & Rybicki, G. B. 1999, ApJ, 524, 527

Maizy, A., Richard, J., de Leo, M. A., Pelló, R., & Kneib, J. P. 2010, A&A, 509, A105

Manrique, A., Salvador-Solé, E., Juan, E., et al. 2015, ApJS, 216, 13

McGreer, I. D., Jiang, L., Fan, X., et al. 2013, ApJ, 768, 105

McLure, R. J., Cirasuolo, M., Dunlop, J. S., Foucaud, S., & Almaini, O. 2009, MNRAS, 395, 2196

Oesch, P. A., van Dokkum, P. G., Illingworth, G. D., et al. 2015, ApJ, 804, L30

Oke, J. B. & Gunn, J. E. 1983, ApJ, 266, 713

Ouchi, M., Shimasaku, K., Okamura, S., et al. 2004, ApJ, 611, 660

Pentericci, L., Vanzella, E., Fontana, A., et al. 2014, ApJ, 793, 113

Planck Collaboration, Adam, R., Aghanim, N., et al. 2016, ArXiv e-prints

Rhoads, J. E., Malhotra, S., Dey, A., et al. 2000, ApJ, 545, L85

Richard, J., Patricio, V., Martinez, J., et al. 2015, MNRAS, 446, L16

Schaerer, D., Boone, F., Zamojski, M., et al. 2015, A&A, 574, A19

Schenker, M. A., Ellis, R. S., Konidaris, N. P., & Stark, D. P. 2014, ApJ, 795, 20

Shioya, Y., Taniguchi, Y., Sasaki, S. S., et al. 2009, ApJ, 696, 546

Stark, D. P., Ellis, R. S., Bunker, A., et al. 2009, ApJ, 697, 1493

Steidel, C. C., Giavalisco, M., Pettini, M., Dickinson, M., & Adelberger, K. L. 1996, ApJ, 462, L17

Thatte, N., Tecza, M., Clarke, F., et al. 2010, in Proc. SPIE, Vol. 7735, Ground-based and Airborne Instrumentation for Astronomy III, 77352I

Tilvi, V., Papovich, C., Finkelstein, S. L., et al. 2014, ApJ, 794, 5

Tilvi, V., Pirzkal, N., Malhotra, S., et al. 2016, ApJ, 827, L14

Verhamme, A., Dubois, Y., Blaizot, J., et al. 2012, A&A, 546, A111

Wisotzki, L., Bacon, R., Blaizot, J., et al. 2016, A&A, 587, A98

Zitrin, A., Labbé, I., Belli, S., et al. 2015, ApJ, 810, L12

*SF2A 2016*
*C. Reylé, J. Richard, L. Cambrésy, M. Deleuil, E. Pécontal, L. Tresse and I. Vauglin (eds)*

# LARGE SCALE OPACITY FLUCTUATIONS IN THE LYMAN ALPHA FOREST: DO QSOS DOMINATE THE UVB AT Z∼5.5-6?

J. Chardin[1], E. Puchwein[1] and M. G. Haehnelt[1]

**Abstract.** The Lyman-alpha forest in the post-reionization Universe shows surprisingly large opacity fluctuations over large (50 cMpc/h) spatial scales at $5.4 \leq z \leq 5.8$. These fluctuations are modelled using a hybrid approach utilizing the large volume Millennium simulation to predict the spatial distribution of QSOs combined with smaller scale post-processed radiative transfer simulations that account for the galaxy contribution. Realictic absorption spectra that account for the contribution of galaxies and QSOs to the ionising UV background are then produced. This improved model confirm our earlier findings that a significant ($\geq$50%) contribution of ionising photons from QSOs can explain the large reported opacity fluctuations on large scales. The inferred QSO luminosity function is thereby consistent with recent estimates of the space density of QSOs at those redshifts.

Keywords: Cosmology: theory - Methods: numerical - diffuse radiation - IGM: structure - Galaxy: evolution - quasars: general

## 1 Introduction

The Ly$\alpha$ forest is the primary probe of the ionisation state of hydrogen in the post-reionization Universe (see Becker et al. 2015a for a recent review). In a recent paper, Becker et al. (2015b) presented measurements of the Ly$\alpha$ opacity PDF averaged over scales of 50 cMpc/h in the redshift range $4 \leq z \leq 6$ based on a sample of QSO absorption spectra. They found large fluctuations of the mean flux at $z \geq 5.4$ and argued that the opacity fluctuations are due to fluctuations of the ionising UV background aided by fluctuations of the mean free path of ionising photons.

Our recent full post-processed radiative transfer simulations of the reionization of hydrogen by (faint) galaxies show only rather moderate fluctuations of the UV background and the mean free path in the post-overlap phase of reionization (Chardin et al. 2015). This led us to suggest that much rarer brighter sources like QSOs with space densities of $\sim 10^{-6}\,\mathrm{Mpc}^{-3}$ may contribute significantly to the ionising background at $z \sim 5.5-6$ and be responsible for the substantial opacity fluctuation at scales of 50 cMpc/h at this redshift. We investigate here in details the implications of this possible explanation by abundance matching the QSO luminosity function in a large volume and by looking at the contribution of QSOs to the ionising UV background at $z > 5$.

In Sect. 2 we present our hybrid approach utilising the large volume Millennium simulation to model the spatial distribution of QSOs combined with smaller scale full hydrodynamical simulations performed with RAMSES and post-processed with the radiative transfer code ATON. Sect. 3 presents our results with regard to spatial fluctuations of the photoionisation rate and the corresponding opacity fluctuations in the Ly$\alpha$ forest. We give our conclusions and outlook in Sect. 4.

## 2 Methodology

### 2.1 *A combined UVB model for galaxies and AGNs*

For the galaxy population, the simulation of the evolution of the dark matter and the hydrodynamics of the gas were performed with the RAMSES code (Teyssier 2002) on a coarse, fixed grid discretized in $512^3$ cells with a

[1] Kavli Institute for Cosmology and Institute of Astronomy, University of Cambridge, Madingley Road, Cambridge, CB3 0HA, UK

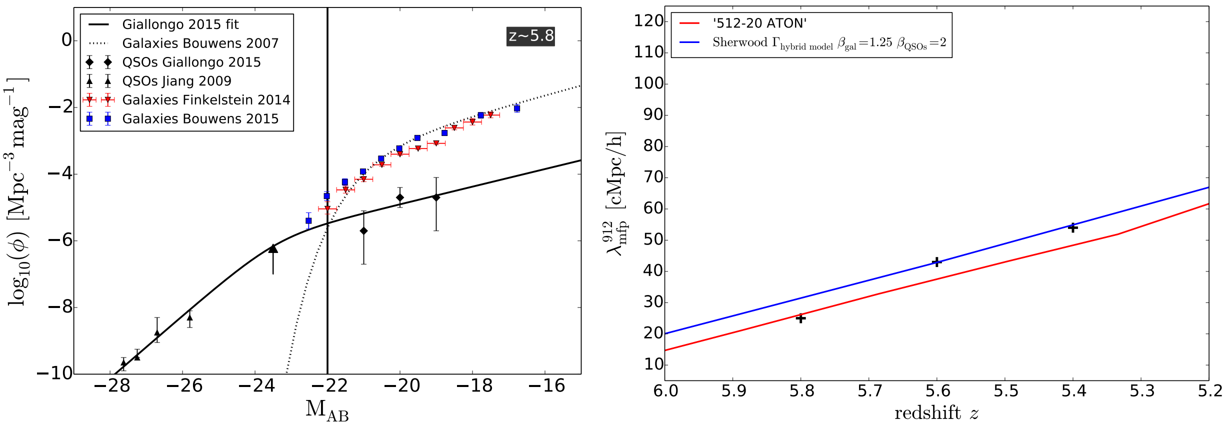


**Fig. 1. Left:** Fit to the QSO luminosity function (solid black) obtained by Giallongo et al. 2015 and a fit to the galaxy luminosity function (dotted balck) obtained by Bouwens et al. (2007). **Right:** The range of mean free path values assumed in our models. The solid red curve shows the evolution of the mean fee path as a function of redshift in our ATON 512-20 radiative transfer simulation. The different black crosses show the values assumed in our different models with fixed mean free path. The blue curve shows the evolution of the mean free path in the Sherwood simulation for different values of the mean photoionization rate in the three redshift bins, using the converged value of $< \Gamma >$ in our hybrid model.

box size of 20 cMpc/h. The radiative transfer calculations were performed in post-processing with the ATON code (Aubert & Teyssier 2008) with a monochromatic treatment that assumes all ionizing photons to have an energy of 20.27 eV. Ionising sources were placed in the dark matter haloes identified in the RAMSES simulation and assumed to emit continuously. The ionising luminosities were calibrated assuming a linear scaling of the ionising luminosity with the mass of dark matter haloes in order to reproduce a reionization history that matches Ly$\alpha$ forest data (see Chardin et al. 2015). The corresponding photoionisation rate due to the galaxy population in this small volume is then called $\Gamma_{\rm gal}^{\rm fiducial}$.

For the AGNs counterpart, we populate DM haloes in the Millennium simulation with sources drawn from a luminosity function guided by the observed space density of QSOs from Giallongo et al. (2015) at these redshifts (see left panel of Fig. 1). We sample the luminosity function from the brightest luminosity present in our $500^3$ $(\mathrm{Mpc/h})^3$ volume which corresponds to $\mathrm{M_{AB}} \sim -27$ and we adopt a lower limit of $\mathrm{M_{AB}} = -22$ for the faintest QSOs and assume that the other QSOs with a fainter luminosity are part of the galaxy population. We then compute the photoionization rate $\Gamma_{\rm QSO}^{\rm fiducial}$ due to these bright sources at every position in the volume assuming a mean free path for the ionising photons with the simple attenuation model used by Becker et al. (2015b).

We then combine the photoionisation rates due to AGNs in this large volume with the ionising UV background due to the much more numerous galaxies driving reionization in our smaller scale ATON simulation. We thereby combine the contributions from galaxies and QSOs as follows: $\Gamma_{\rm gal+QSO} = \Gamma_{\rm gal} + \Gamma_{\rm QSO} = \beta_{\rm gal}\Gamma_{\rm gal}^{\rm fiducial} + \beta_{\rm QSO}\Gamma_{\rm QSO}^{\rm fiducial}$. $\beta_{\rm gal}$ and $\beta_{\rm QSO}$ are the factors by which we need to rescale the luminosities of galaxies and QSOs in order to match the PDF of the Ly$\alpha$ effective optical depth.

In the redshift range we are interested in here, $z = 5.4 - 5.8$, the mean free path of ionising photons is still rather uncertain and we have first explored a range of fixed values as shown by the small crosses in the right panel of Figure 1. Assuming a fixed mean free path is obviously a rather poor approximation as the large UV fluctuations due to QSOs will also result in large fluctuations of the mean free path. Davies & Furlanetto (2016a) argued that the mean free path should depend as a simple power law on the photo-ionisation rate and density,

$$\lambda_{\rm mfp}(\Gamma) = \lambda_0 (\Gamma/\Gamma_0)^{2/3} \Delta^{-\gamma}. \tag{2.1}$$

Here $\Delta$ is the overdensity in the simulation cells and $\gamma$ sets the power law dependance on the overdensity for the mean free path. Davies & Furlanetto (2016b) choose a value of $\gamma = 1$ and we will investigate this model here as well. For the normalisation of the mean free path in equation 2.1 we have chosen $\lambda_0$ and $\Gamma_0$ such that we reproduce the mean free path in the Sherwood simulation (see Bolton et al. 2017) in the limit of a spatially constant UV background. This results in the evolution of the average mean free path shown in the right panel

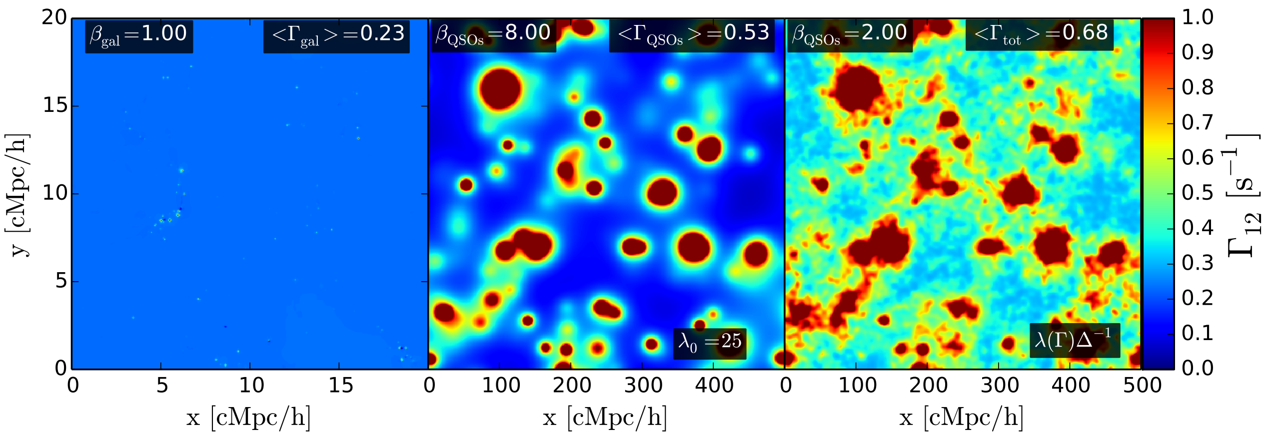


**Fig. 2. Left:** Spacial distribution of the photoionization rate $\Gamma_{\rm gal}$ in a slice of our 20 Mpc/h radiative transfer simulation at redshift $z \sim 5.8$ (galaxies only). **Middle:** Spatial distribution of the photoionization rate ($\Gamma_{\rm QSO}$) due to QSOs through the Millenium simulation at redshift $z \sim 5.8$ for a constant mean free path of $\lambda_0 = 25$ cMpc/h. **Right:** Spatial distribution of the photoionization rate due to QSOs plus galaxies ($\Gamma_{\rm tot} = \Gamma_{\rm QSO} + \Gamma_{\rm gal}$) for a $\Gamma$ dependant parametrization of the mean free path $\lambda(\Gamma)$ according to equation 2.1 with $\lambda_{\rm mfp} \propto \Delta^{-1}$ and $\beta_{\rm gal} = 1.25$.

of Figure 1 as the blue line.

## 3 Results

Figure 2 shows maps of the photoionisation rate $\Gamma_{\rm gal}$ and $\Gamma_{\rm QSO}$ at $z \sim 5.8$ assuming a fixed mean free path. The maps shown are the ones that best match the observed cumulative Ly$\alpha$ effective optical depth PDF as shown in Figure 3. For the fit to the QSO luminosity function as in Giallongo et al. (2015) the luminosities need to be rescaled by a factor $\beta_{\rm QSO} = 8$ in order to match the observed Ly$\alpha$ effective optical depth PDF at redshift z=5.8 for our models with mean free path of 25 cMpc/h. These rather high values of $\beta_{\rm QSO}$ are due to the fact that our assumed mean free path is lower than the (mean) distance between the QSOs in our model. As already discussed neglecting the effect of the QSOs on the mean free path is a bad approximation.

In figure 3, we compare the Ly$\alpha$ effective optical depth PDF for the case of a constant mean free path and with a $\Gamma$ dependant mean free path parametrization as described in section 2.1. The value of $\beta_{\rm QSOs}$ decreases to 2 with the $\Gamma$ dependant mean free path parametrization at z=5.8 if we assume the mean free path to depend on overdensity as $\Delta^{-1}$. Large values of the mean free path close to ionized regions have the effect of increasing the $\langle\Gamma_{\rm QSOs}\rangle$ values. Therefore, for a given luminosity function, adopting a photoionisation dependant mean free path parametrization in the combined UVB model leads to a lower value of $\beta_{\rm QSOs}$ required to generate photoionization rate fluctuations that match the PDF of $\tau_{\rm eff}$. Thus, the recent determination of the AGN luminosity function by Giallongo et al. (2015) only need to be moderately rescaled to be consistent with the Ly$\alpha$ forest PDF data.

## 4 Conclusions

We have combined here high-resolution full radiative transfer simulations with the large volume Millennium simulation to model large scale opacity fluctuations due to a significant contribution of QSOs to the UV background at $z \geq 5$.

We can reproduce the reported broad distribution of the Ly$\alpha$ opacity on scales $\geq 50$ cMpc/h with a contribution $\geq$50% of QSOs to the ionising emissivity. The ionising emissivity of QSO required to reproduce the observed opacity depends rather sensitively on the assumed mean free path and its dependence on the local ionising UV flux and over-density. For assumptions for the mean free path and its dependence suggested by our simulations the required ionising emissivity is similar to that predicted by the recent determination of the QSO luminosity function at this redshift by Giallongo et al. (2015).

The model predicts a strong correlation of low Ly$\alpha$ opacity with the presence of QSOs close to the line-of-sight. This differs strongly from the predictions of alternative models that predict a strong correlation

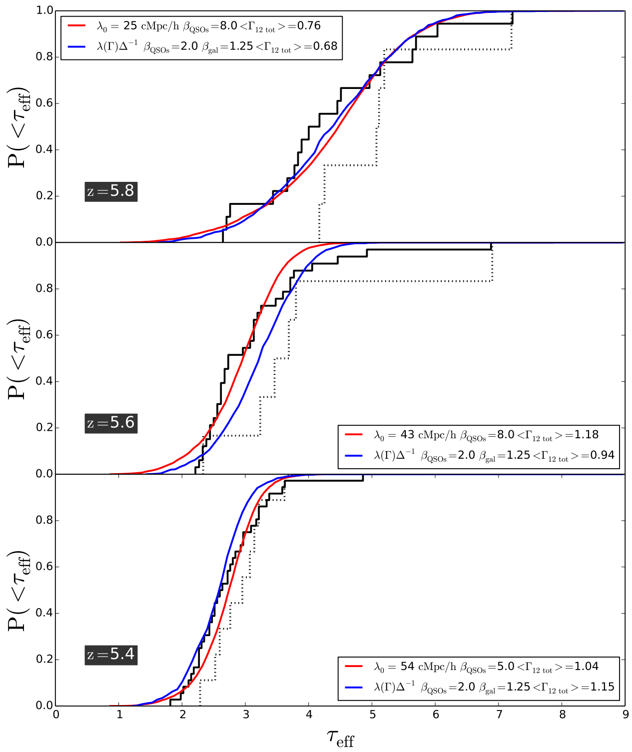


**Fig. 3.** PDF of $\tau_{\rm eff}$ for models with the (rescaled) luminosity funtion of Giallongo et al. 2015 at the three redshifts with values $\beta_{\rm gal}$ and $\beta_{\rm QSOs}$ as indicated in the plots. The red curves shows the case with a constant mean free path $\lambda_{\rm mfp} = \lambda_0$ (with $\beta_{\rm gal} = 1$) while the blue curve show case with a varying mean free path adopting the parametrization chosen in equation 2.1. The black solid step function shows the data from Becker et al. (2015b) based on their own sample of QSO spectra combined with the sample of Fan et al. (2006) while the dotted black step function is for the Becker et al. (2015b) sample only.

or anti-correlation of Ly$\alpha$ opacity with over-density on large scales (see D'Aloisio et al. 2015 and Davies & Furlanetto 2016a). The strength of the correlation should depend on the duty cycle as well as the the possible beaming of the QSOs.

We thank Dominique Aubert for letting us use his code ATON and for helpfull discussions. We thank George Becker for helpful communication regarding his measurements of the flux PDF. We further thank James Bolton and Xiahoui Fan for helpful comments and suggestions. This work was supported by the ERC Advanced Grant 320596 'The Emergence of Structure during the epoch of Reionization'.

## References

Aubert, D. & Teyssier, R. 2008, MNRAS, 387, 295
Becker, G. D., Bolton, J. S., & Lidz, A. 2015a, PASA, 32, e045
Becker, G. D., Bolton, J. S., Madau, P., et al. 2015b, MNRAS, 447, 3402
Bolton, J. S., Puchwein, E., Sijacki, D., et al. 2017, MNRAS, 464, 897
Bouwens, R. J., Illingworth, G. D., Franx, M., & Ford, H. 2007, ApJ, 670, 928
Chardin, J., Haehnelt, M. G., Aubert, D., & Puchwein, E. 2015, MNRAS, 453, 2943
D'Aloisio, A., McQuinn, M., & Trac, H. 2015, ApJ, 813, L38
Davies, F. B. & Furlanetto, S. R. 2016a, MNRAS, 460, 1328
Davies, F. B. & Furlanetto, S. R. 2016b, MNRAS
Fan, X., Strauss, M. A., Becker, R. H., et al. 2006, AJ, 132, 117
Giallongo, E., Grazian, A., Fiore, F., et al. 2015, A&A, 578, A83
Teyssier, R. 2002, A&A, 385, 337

# Session SF2A

# The (sub) millimetric universe at high angular resolution: the ALMA and NOEMA revolution continues

*SF2A 2016*
*C. Reylé, J. Richard, L. Cambrésy, M. Deleuil, E. Pécontal, L. Tresse and I. Vauglin (eds)*

# A NEW INSIGHT OF THE NORTHERN FILAMENTS OF CENTAURUS A

Q. Salomé[1], P. Salomé[1], F. Combes[1 2] and S. Hamer[3]

**Abstract.** We present new APEX observations of the CO(2-1) in the northern filaments of Centaurus A, at the intersection between the radio jet and the northern HI shell. The CO emission was compared with archival FUV (GALEX), FIR (Herschel) and VLT/MUSE data.

The molecular gas mass of the filaments is $(8.2 \pm 0.5) \times 10^7\,\mathrm{M_\odot}$, distributed in two filamentary structures. We found a surprisingly strong molecular filament that lies outside the HI gas. The filaments are mostly molecular, suggesting a scenario where the radio-jet triggers the atomic-to-molecular phase transition.

We then compared the CO masses with the SFR estimates and found very long depletion times ($\sim 75\,$Gyr over the whole filaments), in agreement with the results of Salomé et al. (2016). Analysis of optical excitation lines indicates that the filaments are mostly excited by the AGN or shocks.

Comparison with the H$\alpha$ and HI emission suggests that the three gas phases are spatially and kinematically linked. In particular, the CO emission shows the same velocity gradient as the HI gas.

Keywords: Methods:data analysis, Galaxies:evolution, star formation, Radio lines:galaxies

## 1 Introduction

AGN are supposed to regulate gas accretion and thus slow down star formation (negative feedback). However, evidence of AGN **positive feedback** has also been observed in a few radio galaxies. In a previous work (Salomé et al. 2015), we studied two of the most famous examples of **jet-induced star formation**: 3C 285/09.6 (van Breugel & Dey 1993) and Minkowski's Object (van Breugel et al. 1985). Although CO emission was not detected by the IRAM 30m telescope, we found efficient star formation in both star-forming regions, with molecular depletion times $\leq 1$ Gyr and $\leq 0.02$ Gyr, respectively.

Here we study another famous example: the outer filaments of Centaurus A (Mould et al. 2000; Oosterloo & Morganti 2005). NGC 5128 is a giant nearby early type galaxy that is surrounded by faint arc-like stellar shells (at several kpc around the galaxy). The shells also present HI emission (Schiminovich et al. 1994), CO emission (Charmandaris et al. 2000), and dust continuum (Auld et al. 2012). Along the radio-jet, optically bright filaments (so-called inner and outer filaments) have been observed (Blanco et al. 1975; Graham & Price 1981). These filaments located along the direction of the northern radio jet (at a distance of $\sim 7.7$ kpc and $\sim 13.5$ kpc) are the place of star formation (Auld et al. 2012).

We conducted a multi-wavelength study of the outer filaments based on archival FUV (GALEX), FIR (Herschel) and new CO APEX data. We also looked at optical emission lines (VLT/MUSE) in the filaments.

## 2 Results

**Molecular gas distribution** We mapped the whole northern filaments in CO(2-1) with APEX. The observations cover three regions (figure 1): (1) one within the HI cloud, (2) one outside the HI and within the dust emission, (3) One outside the HI with FUV emission only. CO emission has been detected at almost all the positions observed with APEX, and follows the dust emission. The total molecular mass is $\mathrm{M}^{\mathrm{tot}}_{\mathrm{H_2}} = (8.2 \pm 0.5) \times 10^7\,\mathrm{M_\odot}$. Surprisingly, CO emission is stronger in the eastern part of the filaments, outside the HI shell (figure 1).

[1] LERMA, Observatoire de Paris, CNRS UMR 8112, 61 avenue de l'Observatoire, 75014 Paris, France
[2] Collège de France, 11 place Marcelin Berthelot, 75005 Paris
[3] CRAL, Observatoire de Lyon, CNRS, Université Lyon 1, 9 Avenue Ch. André, 69561 Saint Genis Laval cedex, France

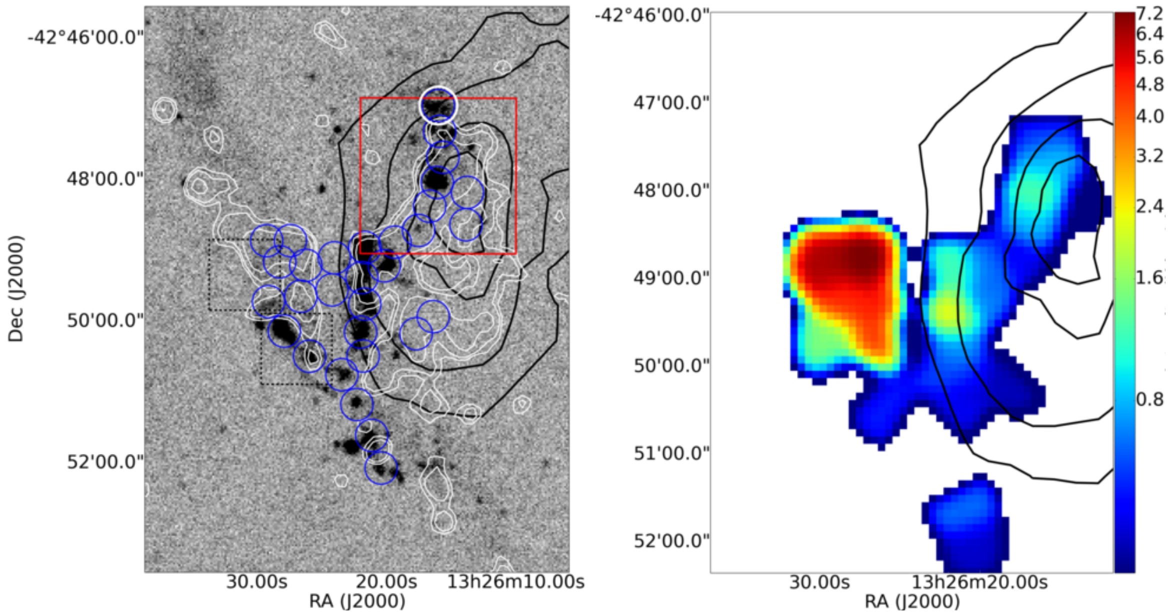


Fig. 1: *Left:* FUV image of the outer filament from GALEX. The black and white contours correspond to the HI and the Herschel-SPIRE 250 $\mu$m emission, respectively. The red box corresponds to the region observed by Charmandaris et al. (2000) with SEST, and the dashed boxes show the field of view of MUSE observations (Santoro et al. 2015). The circles show the positions observed with APEX (blue) and ALMA (white). *Right:* Intensity map of the CO(2-1) emission from APEX in K.km.s$^{-1}$, with the HI emission overlaid in black contours.

**Molecular-to-atomic mass ratio** We compared the APEX CO data with VLA HI data and derive $H_2$/HI mass ratios. However, the resolution of VLA is lower ($40'' \times 78''$), therefore we combined APEX pointings contained in a single VLA beam to simulate a lower resolution. The filaments are mostly molecular, with total masses $M_{H_2} = 7.7 \times 10^7$ $M_\odot$ and $M_{HI} = 2.1 \times 10^7$ $M_\odot$ (ratio of 3.66).

**Star formation efficiency** For each APEX position, we derived the molecular mass from CO, and the star formation rate (SFR) from the FUV and FIR emission. For the whole region, the SFR is $\sim 1.1 \times 10^{-3}$ $M_\odot$.yr$^{-1}$, leading to a molecular depletion time $t_{\rm dep}^{\rm mol} \sim 75$ Gyr. The $\Sigma_{\rm SFR}$ vs $\Sigma_{\rm gas}$ diagram (figure 2; Bigiel et al. 2008; Daddi et al. 2010) shows that the filaments are very inefficient to form stars, compared to disc-like star-forming galaxies.

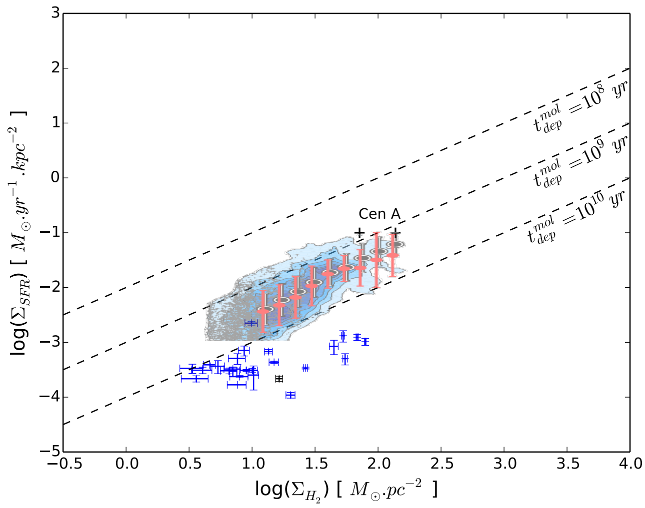


Fig. 2: $\Sigma_{\rm SFR}$ vs. $\Sigma_{\rm H_2}$ for the different regions of CO emission observed with APEX. The black crosses correspond to the central galaxy and the entire filaments ($\Sigma_{\rm H_2} \sim 16.4$ $M_\odot$.pc$^{-2}$; $\Sigma_{\rm SFR} \sim 2.17 \times 10^{-4}$ $M_\odot$.yr$^{-1}$.kpc$^{-2}$). The diagonal dashed lines show lines of constant molecular gas depletion times of, from top to bottom, $10^8$, $10^9$, and $10^{10}$yr. We overlay the contours of Leroy et al. (2013) for nearby spiral galaxies.

**Dynamics of the filaments** The overall CO(2-1) emission of the filaments is blueshifted compared to the central galaxy, the eastern part being bluer than the west. MUSE observations suggest that the molecular and ionised components may be spatially and dynamically associated.

We computed a PV diagram along a slit oriented perpendicularly to the jet. The CO data (figure 3) show (1) a large scale velocity gradient similar to the HI gradient that extends further out to the east side. (2) The break in the slope of the HI velocity gradient (Oosterloo & Morganti 2005) is also seen in CO. Molecular and atomic gas thus seems to be dynamically associated.

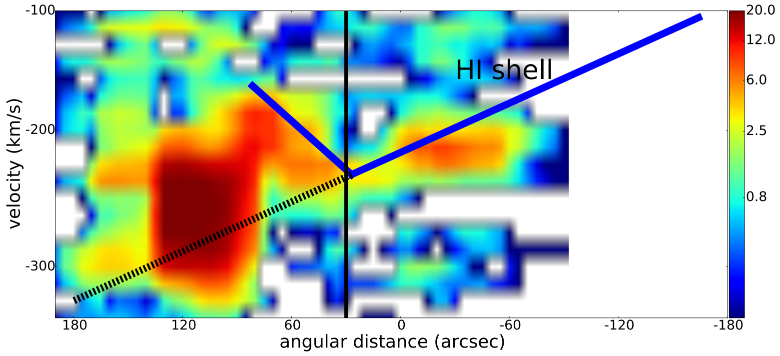


Fig. 3: PV diagram of the CO emission (in mK) centred in $\alpha = 13^{\mathrm{h}}26^{\mathrm{m}}15^{\mathrm{s}}$, $\delta = -42{:}49{:}00$ over the same slit orientation as Oosterloo & Morganti (2005) with a width of $4.2'$ (taking all the CO emission). The blue lines represent the HI cloud velocity gradient. The dashed line represents the continuity of this velocity gradient over the CO emission. The position of the radio jet is shown by the vertical black line.

**Excitation of the filaments** We re-reduce the MUSE data from Santoro et al. (2015) (Program 60.A-9341(A) during the Science Verification). We then computed pixel-by-pixel BPT diagrams (Baldwin et al. 1981; Kewley et al. 2006). Most of the filaments seem to be excited by the radio jet or shocks (figure 4). Those large regions contains smaller inclusions that are excited by star formation, similar to what has been claimed by Santoro et al. (2016).

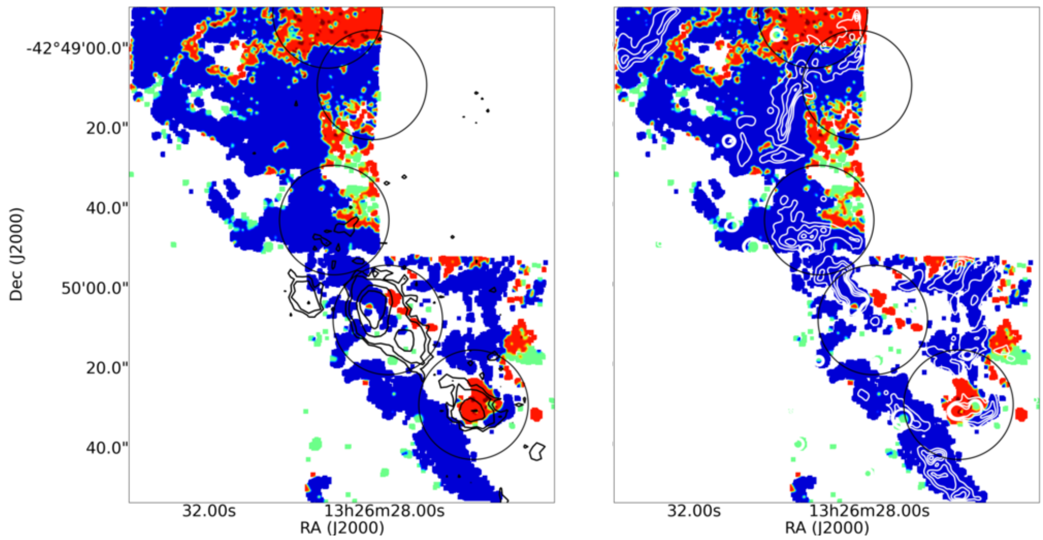


Fig. 4: Map of the excitation processes in the field of view of MUSE. RGB map with star formation in green, AGN/shocks in blue, composite in red. The contours show the UV emission from GALEX (black; *left*) and the H$\alpha$-[NII] emission from MUSE (white; *right*). The APEX beams are represented by the circles.

## 3 Conclusions

APEX was used to map the full region of Centaurus A's northern filaments ($5' \times 4'$). The molecular gas lies in two separated prominent structures: the eastern region (the brightest) and the western region. Those two structures follow the optically identified east and west arms of the northern filaments.

The CO emission in the north is also $\sim 5$ times more massive $\left((8.2 \pm 0.5) \times 10^7\ \mathrm{M}_\odot\right)$ than what was derived by Charmandaris et al. (2000) in the smaller region S1 only $\left(1.7 \times 10^7\ \mathrm{M}_\odot\right)$. The filaments are mostly molecular with a small atomic-to-molecular gas fraction and with the brightest emission being far outside the HI cloud itself.

The star formation efficiency (SFE) is very low in the northern filaments, even if traces of recent star formation are claimed in this region. This suggests that some processes may prevent the star formation to proceed in the cold gas. A possible process that may prevent the molecular gas to form stars is kinetic energy injection from the larger scale dynamics at play in this system.

However, we found that the radio jet could have compressed the gas and triggered the phase transition from atomic to molecular gas. This is certainly a way the AGN and its jets can have a positive feedback effect on the star formation in NGC 5128. Statistical studies with higher resolution CO data all along the filaments are underway (ALMA cycle 3 project) and will shed light on possibly local effects.

## References

Auld, R., Smith, M. W. L., Bendo, G., et al. 2012, MNRAS, 420, 1882
Baldwin, J. A., Phillips, M. M., & Terlevich, R. 1981, PASP, 93, 5
Bigiel, F., Leroy, A., Walter, F., et al. 2008, AJ, 136, 2846
Blanco, V. M., Graham, J. A., Lasker, B. M., & Osmer, P. S. 1975, ApJ, 198, L63
Charmandaris, V., Combes, F., & van der Hulst, J. M. 2000, A&A, 356, L1
Daddi, E., Elbaz, D., Walter, F., et al. 2010, ApJ, 714, L118
Graham, J. A. & Price, R. M. 1981, ApJ, 247, 813
Kewley, L. J., Groves, B., Kauffmann, G., & Heckman, T. 2006, MNRAS, 372, 961
Leroy, A. K., Walter, F., Sandstrom, K., et al. 2013, AJ, 146, 19
Mould, J. R., Ridgewell, A., Gallagher III, J. S., et al. 2000, ApJ, 536, 266
Oosterloo, T. A. & Morganti, R. 2005, A&A, 429, 469
Salomé, Q., Salomé, P., & Combes, F. 2015, A&A, 574, A34
Salomé, Q., Salomé, P., Combes, F., Hamer, S., & Heywood, I. 2016, A&A, 586, A45
Santoro, F., Oonk, J. B. R., Morganti, R., Oosterloo, T. A., & Tadhunter, C. 2016, A&A, 590, A37
Santoro, F., Oonk, J. B. R., Morganti, R., Oosterloo, T. A., & Tremblay, G. 2015, A&A, 575, L4
Schiminovich, D., van Gorkom, J. H., van der Hulst, J. M., & Kasow, S. 1994, ApJ, 423, L101
van Breugel, W., Filippenko, A. V., Heckman, T., & Miley, G. 1985, ApJ, 293, 83
van Breugel, W. J. M. & Dey, A. 1993, ApJ, 414, 563

*SF2A 2016*
*C. Reylé, J. Richard, L. Cambrésy, M. Deleuil, E. Pécontal, L. Tresse and I. Vaughlin (eds)*

# THE AXISYMMETRIC ENVELOPES OF RS CNC AND EP AQR

T. Le Bertre[1], D. T. Hoai[1,2], P. T. Nhung[1,2] and J. M. Winters[3]

**Abstract.** We report on observations obtained at IRAM on two semi-regular variable Asymptotic Giant Branch (AGB) stars, RS Cnc and EP Aqr, undergoing mass loss at an intermediate rate of $\sim 10^{-7}$ M$_{\odot}$ yr$^{-1}$. Interferometric data obtained with the Plateau-de-Bure interferometer (NOEMA) have been combined with On-The-Fly maps obtained with the 30-m telescope in the CO(1-0) and (2-1) rotational lines. The spectral maps of spatially resolved sources reveal an axisymmetric morphology in which matter is flowing out at a low velocity ($\sim 2\,\mathrm{km\,s^{-1}}$) in the equatorial planes, and at a larger velocity ($\sim 8\,\mathrm{km\,s^{-1}}$) along the polar axes. There are indications that this kind of morpho-kinematics is relatively frequent among stars at the beginning of their evolution on the Thermally-Pulsing AGB, in particular among those that show composite CO line profiles, and that it might be caused by the presence of a companion. We discuss the progress that could be expected for our understanding of the mass loss mechanisms in this kind of sources by increasing the spatial resolution of the observations with ALMA or NOEMA.

Keywords: Stars: AGB and post-AGB – *(Stars:)* circumstellar matter – Stars: individual: RS Cnc, EP Aqr – Stars: mass-loss – radio lines: stars.

## 1 Introduction

Stars on the Asymtotic Giant Branch (AGB) are in a short phase of their life (from 1 to a few $10^6$ years). They evolve rapidly owing to their large luminosity (few $10^3$ L$_{\odot}$), and to the ejection of their stellar envelopes. The mechanism by which stars expel their envelopes is essential to the understanding of the terminal phases of stellar evolution, and to a proper description of their contribution to the replenishment of the interstellar medium.

Carbon monoxide (CO) is one of the best tracers of the winds from AGB stars. It originates in the stellar atmospheres and survives up to a few $10^{16-17}$ cm where it is distroyed by UV photons from the interstellar radiation field (Mamon et al. 1988). It thus can be used to probe the region where the winds are shaped and accelerated. The first rotational lines of CO (1-0 and 2-1) are easily accessible from the Plateau-de-Bure (NOEMA), and higher degree lines can be observed from the Atacama desert (ALMA). Modelling of the CO line profiles has provided the best mass loss rate estimates (e.g. Schöier & Olofsson 2001; Teyssier et al. 2006).

In the process of an investigation on the mass loss mechanisms (Winters et al. 2000, 2003), we became interested in sources that exhibit composite CO line profiles, with a narrow component (FWHM $\sim$ 2-3 km s$^{-1}$) overimposed on a broader (FWHM $\sim$ 8-10 km s$^{-1}$) one. These sources were first pointed out by Knapp et al. (1998) who suggested that the peculiar line profiles reveal two different successive winds. We report on our recent work on two such cases, EP Aqr and RS Cnc. We selected these two stars for which a wealth of ancillary data is available, and allows us to characterize their stages of evolution. Although our first investigation on EP Aqr (Winters et al. 2007) tended to support the Knapp et al. interpretation, our study of RS Cnc (Libert et al. 2010) showed that a composite CO line profile might also result from an axi-symmetrical structure, with a slow equatorial wind, and a rapid bipolar outflow. This encouraged us to revisit both sources with a new modelling approach based on the fitting of CO(1-0) and (2-1) spectral maps (Hoai 2015).

[1] LERMA, UMR 8112, CNRS & Observatoire de Paris/PSL, 61 av. de l'Observatoire, F-75014 Paris, France
[2] Department of Astrophysics, Vietnam National Satellite Center, VAST, 18 Hoang Quoc Viet, Ha Noi, Vietnam
[3] IRAM, 300 rue de la Piscine, Domaine Universitaire, F-38406 St. Martin d'Hères, France

## 2 Observations

### 2.1 RS Cnc

RS Cnc is an oxygen-rich S-type star (M6III), with an excess of s-process elements, a $^{12}C/^{13}C$ abundance ratio of 35 (Smith & Lambert 1986), and Tc lines in its optical spectrum (Lebzelter & Hron 1999). It is clearly in the thermally pulsing phase of the AGB (TP-AGB) with dredge-up events. The Hipparcos parallaxe places it at a distance of $143^{+12}_{-10}$ pc (van Leeuwen 2007). The associations with a far-infrared extended source, detected by IRAS and imaged by Spitzer (Geise 2011), and with an H I emission detected with the Nançay Radiotelescope (Gérard & Le Bertre 2003) and imaged with the VLA (Matthews & Reid 2007), show that the central star has been undergoing mass loss for at least $6{\times}10^4$ years (Hoai et al. 2014).

### 2.2 EP Aqr

EP Aqr is an oxygen-rich M-type star (M8III). The Hipparcos parallaxe places it at a distance of $114^{+8}_{-8}$ pc (van Leeuwen 2007). Its luminosity (3450 $L_\odot$) and the low value of its $^{12}C/^{13}C$ abundance ratio ($\sim$ 10, Cami et al. 2000) show that it is at the beginning of its evolution on the TP-AGB. Also, the absence of clear Tc lines in its spectrum (Lebzelter & Hron 1999) suggests that it has not undergone any dredge-up event. It is associated with a far-infrared extended source, detected by IRAS and imaged by Herschel (Cox et al. 2012), which shows that it has been undergoing mass loss for more than a few $10^4$ years.

### 2.3 Observational results and interpretation

We have obtained spectral maps in the (1-0) and (2-1) rotational lines of CO by combining interferometric data from the Plateau-de-Bure Interferometer with short spacing data from the Pico Veleta 30-m telescope. The data for RS Cnc have been presented by Libert et al. (2010) and Hoai et al. (2014). Those for EP Aqr have been presented by Winters et al. (2007), and reanalysed with a new processing by Nhung et al. (2015a).

On the basis of characteristically shaped PV diagrams, the RS Cnc data were interpreted by Libert et al. (2010) as showing evidence for a bipolar geometry. Furthermore, the CO(1-0) channel maps around the central velocity (6.6 km s$^{-1}$), which have been obtained with the extended configurations (A and B) at high angular resolution, reveal a companion at $1''$ north-west of the AGB star (Hoai et al. 2014). As it is not seen in the continuum, it is presently not clear whether this companion is a compact (sub-)stellar object or a cloud in the circumstellar shell.

The EP Aqr data exhibit a rather circular symmetry with enhancements of the emission at some distance from the central star that led Winters et al. (2007) to assume, as first suggested by Knapp et al. (1998), that the mass loss has been variable within the last few $10^3$ years. However, the reanalysis by Nhung et al. (2015a) showed that a morphology similar to that invoked for RS Cnc is also possible, and in fact provides an even better account of the available data.

## 3 Discussion

The spatio-kinematic structure of RS Cnc has been reconstructed by using a model of CO emission adapted to an arbitrary geometry (Hoai et al. 2014; Hoai 2015). We use an axi-symmetric model in which the wind velocity and the flux of matter are smooth functions of the latitude, $\theta$. The wind is assumed to be stationary. The excitation temperature is parametrized as a power of $r$, the distance to the central star.

The parameters of the model and its orientation in space are obtained by minimizing the sum of the square of the deviations (modelled minus observed intensities in the two spectral maps). We obtained a good fit to the data with a model in which the velocity increases smoothly from the equatorial plane to the polar direction (Fig. 1, left), whereas the density is almost independent of the latitude (Fig. 1, right). Another important implication of our study is that matter might still be accelerated at large distances (a few hundred AU, Fig. 2, left).

It is interesting to note that, in this model, the bipolarity is essentially apparent in the kinematics. It illustrates the importance of spectrally resolving emission lines.

There are some slight deviations in the fits as compared to the observations that can be further reduced by introducing a slight asymmetry in the polar flows of the model, with, south, a denser and faster flow than north (Nhung et al. 2015b).

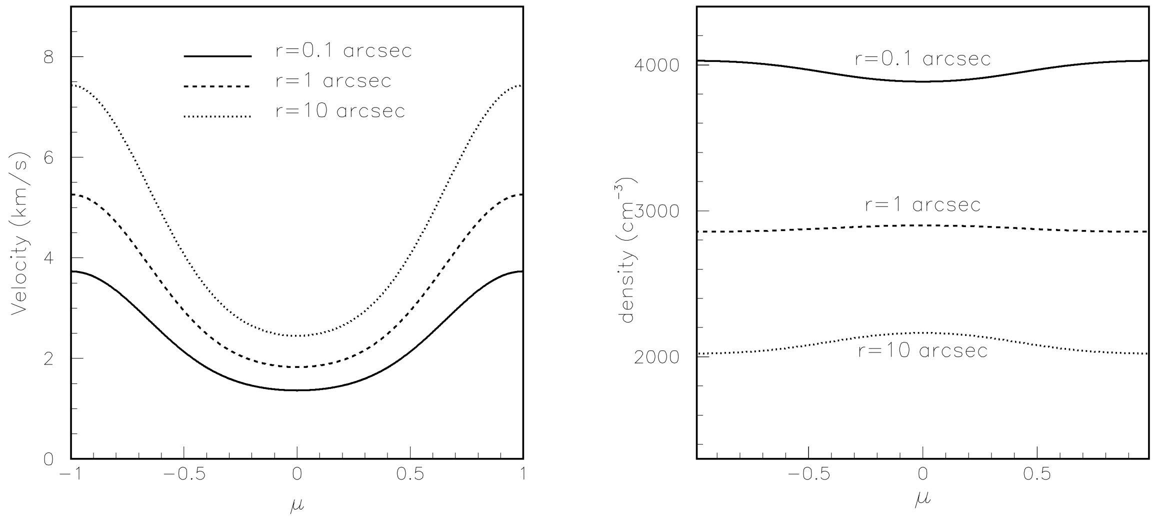


**Fig. 1.** RS Cnc morpho-kinematics (from Hoai et al. 2014). **Left:** velocity as a function of latitude ($\mu = cos\theta$). **Right:** density (in number of hydrogen atoms) as a function of latitude.

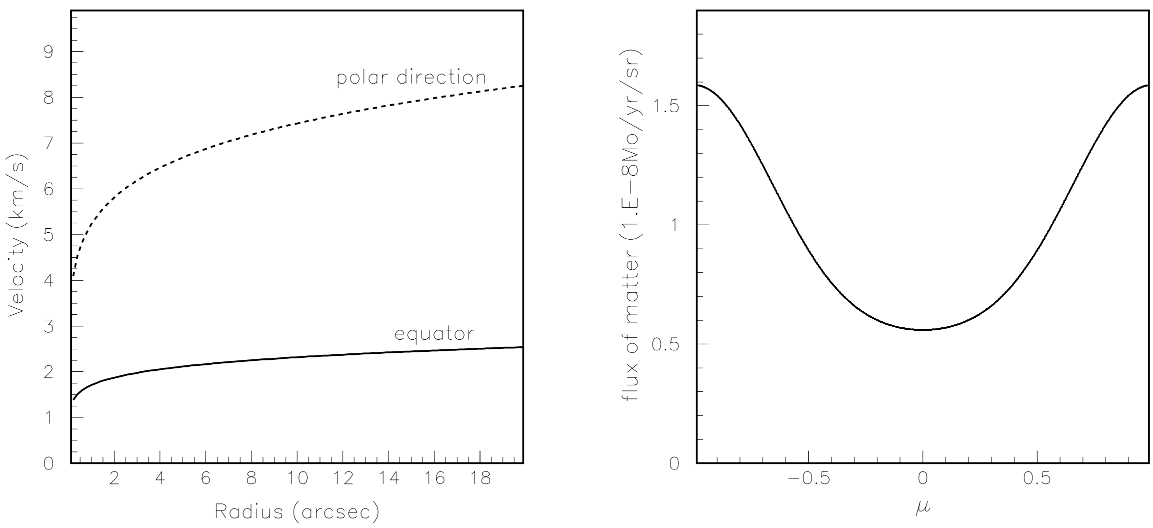


**Fig. 2.** RS Cnc (from Hoai et al. 2014). **Left:** velocity as a function of distance to the central star. **Right:** flux of matter as a function of latitude ($\mu = cos\theta$).

The successful modelling of RS Cnc with an axi-symmetrical geometry called for a reconsideration of our initial interpretation of a variable mass loss for EP Aqr. Indeed, an axi-symmetrical geometry with a polar axis pointing towards the observer could as well be considered for accounting for the symmetry of the images projected on the plane of the sky. In Nhung et al. (2015a) we studied this second option, and concluded that it is more likely than the first one. Interestingly, in the best model, the density does not deviate significantly from spherical symmetry, and, as for RS Cnc, the axi-symmetry shows up only in the velocity field.

It is worth noting that the bipolarity which has been evidenced in RS Cnc and EP Aqr corresponds to an excess of flux of matter along the polar directions (Fig. 2, right), and not to evacuated regions. Magnetic fields and binarity are commonly invoked to explain the bipolarity observed in circumstellar shells. Matt et al. (2010) have shown that a magnetic field should enhance the mass loss towards the equatorial plane. However we observe the opposite (Fig. 2, right), and thus we tend to prefer the second option (i.e. the effect of a companion).

Theuns & Jorissen (1993) and Mastrodemos & Morris (1999) have studied the hydrodynamics of stellar flows in binary systems. They find that for some configurations a three-dimensional shock wave propagates through the circumstellar shell and that it supports a spiral pattern. In the carbon star AFGL 3068, Mauron & Huggins (2006) have found in dust-scattered galactic light a spiral pattern that fits well with the predictions of Mastrodemos & Morris (1999). A spiral structure has also been detected in the CO(3-2) line emission of R Scl by ALMA (Maercker et al. 2015). The model predictions agree with a nearly spherical wind structure in the equatorial plane on which the spiral pattern is imprinted. There are indications in the EP Aqr channel maps of arcs, that may originate through such a mechanism.

Hoai (2015) has also applied the RS Cnc modelling approach to X Her, another AGB star that shows composite CO line-profiles (Knapp et al. 1998). The same kind of model fits satisfactorily well the data obtained at IRAM by Castro-Carrizo et al. (2010) on this source.

## 4 Prospects

To understand better the flow of matter from RS Cnc, we need to investigate the nature of the component (cloud ?, companion ?) located north-west of RS Cnc. Broad-band observations would help to identify the presence of a compact stellar object We need also to investigate the possibility of the presence of a rotating disk, such as those found in some post-AGB stars (Castro-Carrizo et al. 2012). However, presently, there is no evidence of such a kinematic structure in the data.

For EP Aqr, we need also imaging at high spatial resolution ($\sim 0.2''$, or better) to probe the acceleration region of the polar flows, as well as the structures in the equatorial plane (spiral ?), that in principle we should detect from a priviledged almost-polar line of sight.

Although they do not bring the highest spatial resolution, the low-J lines allow to probe matter at large distances from the central star. They are also less affected by deviations from local thermal equilibrium and, especially in the inner regions of circumstellar envelopes, by optical depth effects, than the high-J lines.

## 5 Concluding remarks

Axisymmetry seems to be a common feature in stellar winds, even in the early phases of the TP-AGB. For instance, for EP Aqr the likely absence of Tc in the atmosphere suggests that dredge-up events are still not operating. It shows that non-spherical shapes observed often in planetary nebulae may arise from phenomena that are already active during the AGB phase, although with effects which are less dramatic.

In sources like RS Cnc or EP Aqr, the axi-symmetry becomes apparent only if the kinematical information is available. The two important conclusions for these objects are that (i) the flux of matter is larger along the polar axis than in the equatorial plane, (ii) the stellar winds might still be accelerated at a few hundred AU.

We stress the importance of the high spectral resolution for studying the relatively slow winds from AGB stars. Indeed, we need to resolve spectrally the emission for detecting the axi-symmetry of the source, but also this axi-symmetry may appear only as a kinematic effect (i.e. not as a density effect).

The origin of bipolarity still needs to be identified. The fact that we find sources with a flux of matter larger along the polar axis than in the equatorial plane does not favor magnetic fields. The presence of a companion should produce sub-structures, such as spirals that can be detected in CO lines. It may affect the rate of mass loss, and may play an important role in the ultimate phases of evolution of its primary. The presence of a rotating disk may have a considerable meaning for the mass loss mechanism, that up to now has not been well explored in the models.

High spatial resolution imaging at high spectral resolution of the central parts of these sources where the winds are launched and accelerated with ALMA and NOEMA is clearly essential.

**Acknowledgements**
Based on observations carried out with the IRAM Plateau de Bure Interferometer and the IRAM 30-m telescope. IRAM is supported by INSU/CNRS (France), MPG (Germany) and IGN (Spain). We thank the PCMI and the ASA programmes of the CNRS for financial support.

## References


Cami, J., Yamamura, I., de Jong, T., et al., 2000, A&A, 360, 562

Castro-Carrizo, A., Quintana-Lacaci, G., Neri, R., et al., 2010, A&A 523, A59

Castro-Carrizo, A., Neri, R., Bujarrabal, V., Chesneau, O., Cox, P., & Bachiller, R., 2012, A&A 545, A1

Cox, N. L. J., Kerschbaum, F., van Marle, A. J., et al., 2012, A&A, 537, A35

Geise, K. M., 2011, Master's thesis, University of Denver

Gérard, E., & Le Bertre, T., 2003, A&A, 397, L17

Hoai, D. T., Matthews, L. D., Winters, J. M., et al., 2014, A&A, 565, A54

Hoai, D. T., 2015, PhD thesis (`https://ufe.obspm.fr/theses/rechercher/31`)

Knapp, G. R., Young, K., Lee, E., & Jorissen, A., 1998, ApJS, 117, 209

Lebzelter, T., & Hron, J., 1999, A&A, 351, 533

Libert, Y., Winters, J. M., Le Bertre, T., Gérard, E., & Matthews, L. D., 2010, A&A, 515, A112

Maercker, M., Vlemmings, W. H. T., Brunner, M., De Beck, E., Humphreys, E. M., Kerschbaum, F., Lindqvist, M., Olofsson, H., & Ramstedt, S., 2015, A&A, 586, A5

Mamon, G. A., Glassgold, A. E., & Huggins, P. J., 1988, ApJ, 328, 797

Mastrodemos, N., & Morris, M., 1999, ApJ, 523, 357

Matt, S., Balick, B., Winglee, R., & Goodson, A., 2010, ApJ, 545, 965

Matthews, L. D., & Reid, M. J., 2007, AJ, 133, 2291

Mauron, N., & Huggins, P. J., 2006, A&A, 452, 257

Nhung, P. T., Hoai, D. T., Winters, J. M., et al., 2015a, A&A, 583, A64

Nhung, P. T., Hoai, D. T., Winters, J. M., et al., 2015b, RAA, 15, 713

Schöier, F. L., & Olofsson, H., 2001, A&A, 368, 969

Smith, V. V., & Lambert, D. L., 1986, ApJ, 311, 843

Teyssier, D., Hernandez, R., Bujarrabal, V., Yoshida, H., & Phillips, T. G., 2006, A&A, 450, 167

Theuns, T., & Jorissen, A., 1993, MNRAS, 265, 946

van Leeuwen, F., 2007, "Hipparcos, the New Reduction of the Raw Data", Springer, Astrophysics and Space Science Library, vol. 350

Winters, J. M., Le Bertre, T., Jeong, K. S., Helling, C., & Sedlmayr, E., 2000, A&A, 361, 641

Winters, J. M., Le Bertre, T., Jeong, K. S., Nyman, L.-Å., & Epchtein, N., 2003, A&A, 409, 715

Winters, J. M., Le Bertre, T., Pety, J., & Neri, R., 2007, A&A, 475, 559

*SF2A 2016*
*C. Reylé, J. Richard, L. Cambrésy, M. Deleuil, E. Pécontal, L. Tresse and I. Vauglin (eds)*

# NIKA2, A DUAL-BAND MILLIMETRE CAMERA ON THE IRAM 30 M TELESCOPE TO MAP THE COLD UNIVERSE

F.-X. Désert[1], R. Adam[2,3], P. Ade[4], P. André[5], H. Aussel[5], A. Beelen[6], A. Benoît[7], A. Bideaud[7], N. Billot[8], O. Bourrion[2], M. Calvo[7], A. Catalano[2], G. Coiffard[9], B. Comis[2], S. Doyle[4], J. Goupy[7], C. Kramer[8], G. Lagache[10], S. Leclercq[9], J.-F. Lestrade[11], J.F. Macías-Pérez[2], A. Maury[5], P. Mauskopf[4,12], F. Mayet[2], A. Monfardini[7], F. Pajot[6], E. Pascale[4], L. Perotto[2], G. Pisano[4], N. Ponthieu[1], V. Revéret[5], A. Ritacco[2], L. Rodriguez[5], C. Romero[9], H. Roussel[13], F. Ruppin[2], J. Soler[5], K. Schuster[9], A. Sievers[8], S. Triqueneaux[7], C. Tucker[4] and R. Zylka[9]

**Abstract.** A consortium led by Institut Néel (Grenoble) has just finished installing a new powerful millimetre camera NIKA2 on the IRAM 30 m telescope. It has an instantaneous field-of-view of 6.5 arcminutes at both 1.2 and 2.0 mm with polarimetric capabilities at 1.2 mm. NIKA2 provides a near diffraction-limited angular resolution (resp. 12 and 18 arcseconds). The 3 detector arrays are made of more than 1000 KIDs each. KIDs are new superconducting devices emerging as an alternative to bolometers. The commissionning is ongoing in 2016 with a likely opening to the IRAM community in early 2017. NIKA2 is a very promising multi-purpose instrument which will enable many scientific discoveries in the coming decade.

Keywords: Camera, millimetre astronomy, cosmology, galaxies, star formation, interstellar dust

## 1 Introduction

The golden age of (sub)millimetre astronomy started with the two flagship space missions Herschel and Planck. It is now ongoing with the two world-class (sub)millimetre interferometers ALMA and NOEMA. Whereas Herschel and Planck provided surveys of a large portion or all of the sky at medium angular resolution (35 arcsec. at 500 micron for Herschel and 5 arcmin at 1 mm for Planck), the ground-based interferometers can dig deeply at high angular resolution (sub-arcsecond), but only on very tiny spots (around 20 arcseconds at 1 mm) of the sky. The IRAM 30 m radiotelescope, a leading millimetre facility in Spain, near Granada, can fill the angular scale gap. For that purpose, a wide-field camera is necessary. A consortium of laboratories in France and UK, along with IRAM, has just built and installed such a camera called NIKA2 (more details given in Catalano et al. 2016, see also http://ipag.osug.fr/nika2).

[1] Institut de Planétologie et d'Astrophysique de Grenoble, Univ. Grenoble Alpes, CNRS, IPAG, F-38000 France
[2] Laboratoire de Physique Subatomique et de Cosmologie, Université Grenoble Alpes, CNRS/IN2P3, 53, avenue des Martyrs, Grenoble, France
[3] Laboratoire Lagrange, Université Côte d'Azur, Observatoire de la Côte d'Azur, CNRS, Blvd de l'Observatoire, CS 34229, 06304 Nice cedex 4, France
[4] Astronomy Instrumentation Group, University of Cardiff, UK
[5] Laboratoire AIM, CEA/IRFU, CNRS/INSU, Université Paris Diderot, CEA-Saclay, 91191 Gif-Sur-Yvette, France
[6] Institut d'Astrophysique Spatiale (IAS), CNRS and Université Paris Sud, Orsay, France
[7] Institut Néel, CNRS and Université Grenoble Alpes, France
[8] Institut de RadioAstronomie Millimétrique (IRAM), Granada, Spain
[9] Institut de RadioAstronomie Millimétrique (IRAM), Grenoble, France
[10] Aix Marseille Université, CNRS, LAM (Laboratoire d'Astrophysique de Marseille) UMR 7326, 13388, Marseille, France
[11] LERMA, CNRS, Observatoire de Paris, 61 Avenue de l'Observatoire, Paris, France
[12] School of Earth and Space Exploration and Department of Physics, Arizona State University, Tempe, AZ 85287
[13] Institut d'Astrophysique de Paris, CNRS (UMR7095), Sorbonne Universités, UPMC Univ. Paris 06, 98 bis Boulevard Arago, F-75014, Paris, France

## 2 A description of NIKA2

The camera is based on novel detectors. Kinetic Inductance Detectors (KIDs) are supraconducting devices (Day et al. 2003; Doyle et al. 2006) that see their electrical properties change with incoming light. The kinetic inductance is modified when Cooper pairs are broken by photons of sufficient energy. KIDs are proving to be an alternative to bolometers with specific advantages: time constant (less than a millisecond), low sensitivity to the cooler temperature (a thousand times less than for a bolometer), and ease to manufacture (a single aluminum layer on a silicon wafer). Each detector is wired to be a high-efficiency RLC resonator coupled by a linefeed to the readout. The signal can thus be frequency-multiplexed by a factor of at least 150, each KID having its own resonant frequency. Moreover the detector resonance frequency is linearly dependent on the incoming photon flux. A complex readout system is required to simultaneously measure all the detectors at a sampling rate of up to 100 Hz (Bourrion et al. 2011). Since 2009, these properties have been checked on the sky with the NIKA prototype camera (Monfardini et al. 2010, 2011; Calvo et al. 2013; Catalano et al. 2014) at the IRAM 30 m telescope. Figure 1 (left panel) shows one of the two NIKA2 1 mm arrays. The sampling of the sky by each planar array is of $F.\lambda \simeq 0.7 - 1$.

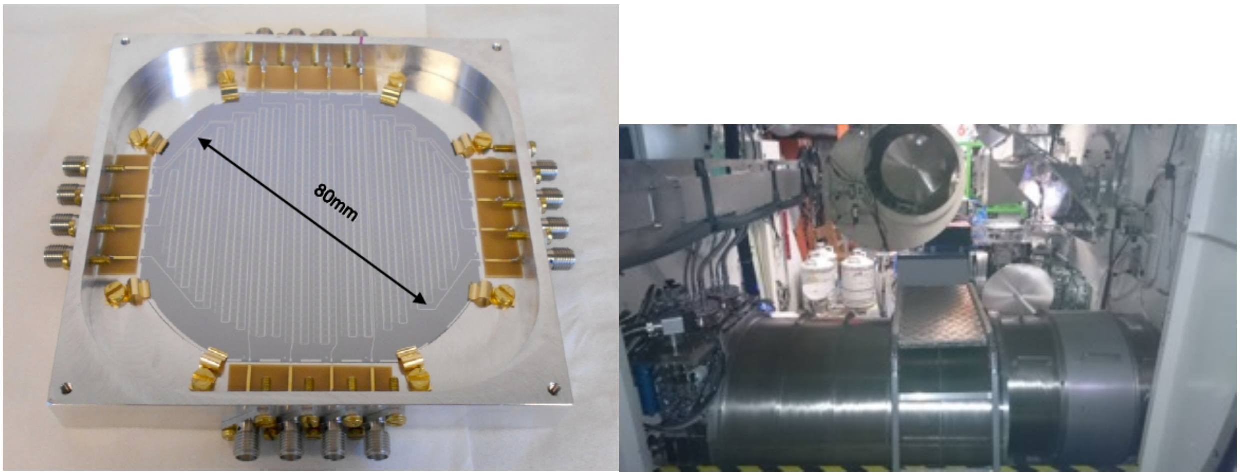


**Fig. 1. Left:** NIKA2 1 mm array containing more than 1000 KIDs. It is made of a single layer of aluminum on a silicon wafer. Aluminum is a supraconductor below 1 K. Feedlines are seen meandering around the detectors. The readout connectors can be seen on the sides: a pair of connectors correspond to the input and output of one feedline and there are 8 readouts needed to read that array. **Right:** The NIKA2 cryostat in the Nasmyth cabin of the IRAM 30 m radiotelescope.

Most of NIKA2 is made of two 4 K pulse-tube cryocoolers and a closed-cycle $^3$He-$^4$He dilution fridge so that these detectors can function at typically 150 mK. The NIKA2 cryostat provides a continuous cooling (no duty cycles) for the whole duration of each observing campaign (up to several months). The optics is made of polyethylene lenses with a near-telecentric system that focuses light on the plane detectors. Filtering (high-frequency cut-off, bandpass) is done via mesh filters (Ade et al. 2006). A dichroic splits the 1 and 2 mm light. Then, a polarizing capability is obtained by having a cold polarizing grid at 45 deg. from the incoming 1 mm light splitting the two linear polarizations onto the two 1 mm arrays. When one wishes NIKA2 to be in the polarization observing mode, a removable half-wave plate can be slid in front of the cryostat. This system was used with NIKA (Ritacco et al. 2016) and provides a continuous rotation of the polarization axis so that Stokes parameters for the linear polarization can be retrieved. Figure 1 (right panel) shows how the heavy cryostat (more than 1.3 tons) fits into the Nasmyth cabin of the IRAM 30 m radiotelescope. A new optical system (M3 and M4 mirrors) had to be designed to accommodate the NIKA2 field-of-view.

## 3 The performance of NIKA2

NIKA2 provides an instantaneous circular field of view with a 6.5 arcmin. diameter on the sky in a simultaneous way in the two broad atmospheric bands at 260 GHz (1.2 mm) and 150 GHz (2.0 mm). The angular resolution is better than 12 and 18 arcsec at resp. 1.2 and 2 mm. The goal sensitivities are resp. 15 and 10 mJy rms for a point-source in one second of integration on average across the whole focal plane. The total number of detectors is about 1100 per array and there are three arrays (two at 1.2 mm and one at 2 mm). The percentage of valid detectors is above 80 % (some detectors cannot be used as their resonant frequencies happen to be too close to each other). The on-going commissioning is assessing these values with thorough calibration campaigns and there are no signs that they cannot be reached.

Maps of the sky can be obtained with a size of up to several degrees by raster scans: the whole telescope is moving with respect to the map center in a zig-zag pattern. The secondary mirror is not wobbling. To illustrate NIKA2 early capabilities, we show the maps obtained at 1 and 2 mm in Fig. 2 around the ultracompact HII region NGC 7538, a secondary calibrator.

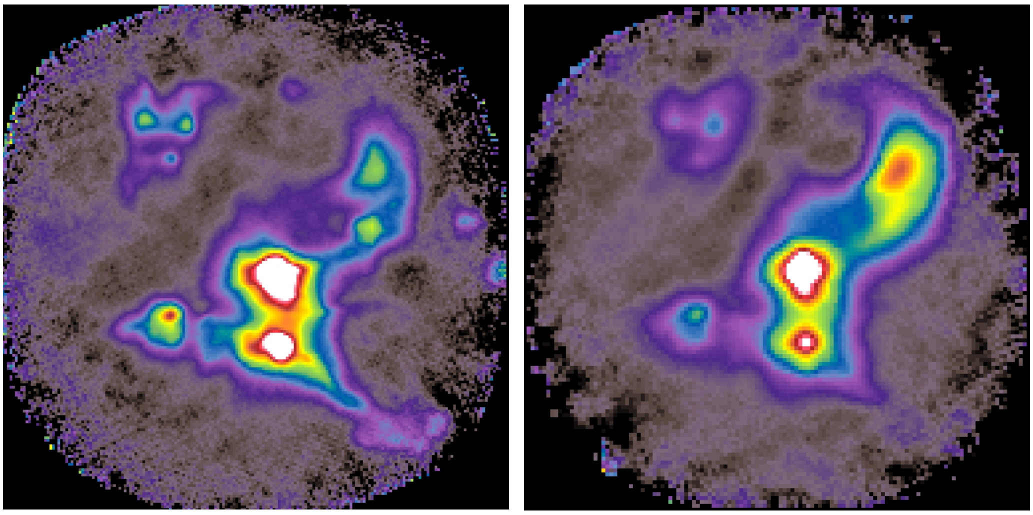

**Fig. 2.** RA-Dec maps centered on the ultracompact HII regions NGC 7538 at **Left:** 1.2 mm and **Right:** 2 mm. The maps were obtained by using the standard NIKA2 IDL-based pipeline and an adaptation of the Scanamorphos map-making algorithm (Roussel 2013) to NIKA2. The integration time was 12 minutes. The size of the mapped square is 10 arcmin. The brightness scale is linear and the maximum is at several Jy per beam. The central calibrator is clearly surrounded by many other bright regions.

## 4 Conclusions

The NIKA2 commissionning is ongoing at the end of 2016. The final configuration of the instrument, which includes improvements in optical elements, filtering, readout electronics and the 2 mm array, still has to be characterised. A science verification phase will begin in early 2017 and the instrument could then be opened to the IRAM community. Five large programs of guaranteed time will be pursued (along with open time proposals): 1) mapping of the hot gas in fifty clusters of galaxies, as already performed on 6 clusters with the prototype camera (Adam et al. 2014, 2015, 2016; Ruppin et al. 2016), 2) a deep survey down to the confusion limit, 3) mapping of nearby galaxies, 4) galactic observations of star formation and dust properties, and 5) polarization of star-forming regions. The observations with NIKA2 will provide several lists of relevant targets to be explored by NOEMA.

We would like to thank the IRAM staff for their support during the campaigns. The NIKA dilution cryostat has been designed and built at the Institut Néel. In particular, we acknowledge the crucial contribution of the Cryogenics Group, and in particular Gregory Garde, Henri Rodenas, Jean Paul Leggeri, Philippe Camus. This work has been partially funded by the Foundation Nanoscience Grenoble, the LabEx FOCUS ANR-11-LABX-0013 and the ANR under the contracts "MKIDS", "NIKA" and ANR-15-CE31-0017. This work has benefited from the support of the European Research Council Advanced Grant ORISTARS under the European Union's Seventh Framework Programme (Grant Agreement no. 291294). We acknowledge fundings from the ENIGMASS French LabEx (R. A. and F. R.), the CNES post-doctoral fellowship program (R. A.), the CNES doctoral fellowship program (A. R.) and the FOCUS French LabEx doctoral fellowship program (A. R.).

## References

Adam, R., Comis, B., Bartalucci, I., et al. 2016, A&A, 586, A122

Adam, R., Comis, B., Macías-Pérez, J.-F., et al. 2015, A&A, 576, A12

Adam, R., Comis, B., Macías-Pérez, J. F., et al. 2014, A&A, 569, A66

Ade, P. A. R., Pisano, G., Tucker, C., & Weaver, S. 2006, in Proc. SPIE, Vol. 6275, Society of Photo-Optical Instrumentation Engineers (SPIE) Conference Series, 62750U

Bourrion, O., Bideaud, A., Benoit, A., et al. 2011, JINST, 6, P06012

Calvo, M., Roesch, M., Désert, F. X., et al. 2013, A&A, 551, L12

Catalano, A., Adam, R., Ade, P., et al. 2016, ArXiv e-prints, 1605.08628

Catalano, A., Calvo, M., Ponthieu, N., et al. 2014, A&A, 569, A9

Day, P. K., LeDuc, H. G., Mazin, B. A., Vayonakis, A., & Zmuidzinas, J. 2003, Nature, 425, 817

Doyle, S., Naylon, J., Cox, J., Mauskopf, P., & Porch, A. 2006, in Proc. SPIE, Vol. 6275, Society of Photo-Optical Instrumentation Engineers (SPIE) Conference Series, 62751O

Monfardini, A., Benoit, A., Bideaud, A., et al. 2011, ApJS, 194, 24

Monfardini, A., Swenson, L. J., Bideaud, A., et al. 2010, A&A, 521, A29

Ritacco, A., Ponthieu, N., Catalano, A., et al. 2016, ArXiv e-prints, 1609.02042

Roussel, H. 2013, PASP, 125, 1126

Ruppin, F., Adam, R., Comis, B., et al. 2016, ArXiv e-prints, 1607.07679, A&A, in press

# Session SF2A

# Observation of the discs with the new generation instruments - ALMA, SPHERE...-

*SF2A 2016*
*C. Reylé, J. Richard, L. Cambrésy, M. Deleuil, E. Pécontal, L. Tresse and I. Vauglin (eds)*

# EVOLUTION OF SOLIDS IN THE JOVIAN SUBNEBULA: IMPLICATIONS FOR THE FORMATION OF THE GALILEAN SATELLITES

T. Ronnet[1], O. Mousis[1] and P. Vernazza[1]

**Abstract.** The four Galilean satellites are thought to have formed within an accretion disk surrounding Jupiter during the late stages of its formation. Here we investigate the fate of solids of different sizes in the accretion disk. The dynamics of the solids is followed along with their thermodynamic evolution. This allows us to track the water ice-to-rock mass fraction of the planetesimals as they sublimate and lose mass when heated in the disk. We then compare our results to the known bulk composition of the Jovian moons and draw some conclusions as regards their formation.

Keywords: Galilean satellites, formation, pebbles, accretion disk

## 1 Introduction

During the late stages of giant planets formation, the gas accreted onto the envelope of the planet must proceed through an accretion disk because of its high angular momentum preventing it to be directly accreted onto the surface of the planet. This process has been illustrated in several studies based on 3D hydrodynamic (e.g, Klahr & Kley 2006; Tanigawa et al. 2012; Szulágyi et al. 2016) and magneto-hydrodynamic (Gressel et al. 2013) simulations. There is little doubt the four Galilean satellites, Io, Europa, Ganymede and Callisto, formed within such a disk surrounding Jupiter in the very end of its formation. The structure of the circumplanetary disk (CPD) however, also called a subnebula, and the size and origin of the solids that eventually formed the satellites, are yet to be constrained. There are currently two main scenarios for the formation of the Jovian moons, one based on a minimum mass subnebula (Mosqueira & Estrada 2003a,b) where all the mass in solids required for forming the satellites is present at one time, and an other one based on an actively-supplied subnebula (Canup & Ward 2002), referred to as the gas-starved disk model, where solids are constantly brought from the surrounding nebula to the sebnubela via the infalling gas flow.

Here we present a lagrangian integrator we developed to track solids evolution within the subnebula of Jupiter. We study planetesimals with a large range of sizes, from $10^{-6}$ up to $10^{6}$ m. The dynamic of the solids is affected by aerodynamic drag due to their relative velocity with the gas and by turbulent diffusion. The evolution of the surface temperature is also computed and allows us to determine the mass ablation rate of the bodies and to follow their ice-to-rock mass fraction accordingly.

The subnebula and solids evolution models are further exposed in the next section, while some results are presented in section 3.

## 2 Models

### 2.1 Subnebula model

The subnebula model derived in Canup & Ward (2002) is a more physically motivated model than minimum mass models which is why we favored it in this study. In this actively supplied accretion disk, or gas starved disk, the repartition of gas in the subnebula is given by considering a balance between the infall of material from the nebula to the CPD and the accretion onto the surface of Jupiter from the CPD. The gas is equally reparted from the inner edge of the disk to the centrifugal radius $r_c$, the distance where the gravitational potential of the

[1] Aix Marseille Univ, CNRS, LAM, Laboratoire d'Astrophysique de Marseille, Marseille, France

central planet balances the angular momentum of the infalling material. Though the position of the centrifugal radius should evolve with time, being farther and farther from Jupiter as the forming planet's mass increases, here we are interested in the very late stages of Jupiter formation. In our model, the mass of the central planet is therefore $1\,M_{\rm Jup}$ and the centrifugal radius is fixed at $26\,R_{\rm Jup}$ while the outer disk edge is placed at $r_d = 150\,R_{\rm Jup}$. The surface density of the gas is then given by:

$$\Sigma_g(r) = \frac{\dot{M}_p}{3\pi\nu} \begin{cases} 1 - \frac{4}{5}\sqrt{\frac{r_c}{r_d}} - \frac{1}{5}\left(\frac{r}{r_c}\right)^2 & \text{for } r \leqslant r_c, \\ \frac{4}{5}\sqrt{\frac{r_c}{r}} - \frac{4}{5}\sqrt{\frac{r_c}{r_d}} & \text{for } r > r_c. \end{cases} \tag{2.1}$$

In the above expression, $\dot{M}_p$ is the mass accretion rate onto Jupiter, which is also the mass accretion rate from the nebula to the CPD, $\nu = \alpha H_g^2 \Omega_K$ is the effective turbulent viscosity, with $\Omega_K$ the keplerian orbital frequency and $H_g$ is the gas scale height calculated from the vertical hydrostatic equilibrium of the gas with an isothermal equation of state $P = c_g^2 \rho_g$, and $c_g^2 = R_g T_d/\mu$. The molecular weight of the gas is $\mu = 2.4\,{\rm g\,mol^{-1}}$ and the temperature distribution in the subnebula is taken from the simple prescription of Sasaki et al. (2010) which gives

$$T_d \simeq 225 \left(\frac{r}{10\,R_{\rm Jup}}\right)^{3/4} \left(\frac{\dot{M}_p}{10^{-7}\,M_{\rm Jup}\,{\rm yr^{-1}}}\right)^{1/4} \ {\rm K}. \tag{2.2}$$

### 2.2 Gas dynamics

Here we are interested in the evolution of solids within the subnebula, whose dynamic is affected by interaction with the gas through friction forces. In order to determine these, we need to calculate the velocity of the gas in the disk.

The most important velocity to determine is actually the azimuthal velocity. Because of the pressure force arising from the density gradient within the disk, the gas rotates at a slightly subkeplerian velocity with a deviation given by

$$v_{\phi,g} \equiv v_K - \eta v_K \approx v_K + \frac{1}{2}\frac{c_g^2}{v_K}\frac{\partial \ln P}{\partial \ln r}\,. \tag{2.3}$$

The keplerian velocity is $v_K = r\Omega_K$ with $\Omega_K = \sqrt{GM_p}/r^3$. Because solids do not feel this pressure force, they would rotate at a slightly higher velocity than the gas and feel a headwind that causes their orbit to decay. Solids dynamics is presented in more details in the next section. It is important to note that the gas rotates at a subkeplerian velocity in the general case of the inward pressure gradient, i.e. outward pressure force opposed to the gravitational attraction of the central planet, but that an outward pressure gradient, such as that created at the outer edge of a gap opened by a planet in a proto-planetary disk (PPD), would result in a gas rotating at a superkeplerian velocity.

We assume that the gas is in hydrostatic equilibrium in the vertical direction and its vertical velocity is therefore zero. Although this is not exactly accurate, the assumption is valid as demonstrated by Keller & Gail (2004) and Takeuchi & Lin (2002). Knowing the vertical and azimuthal velocity of the gas, the radial velocity of the gas can be derived from the azimuthal momentum equation of the viscous gas. We are then able to calculate gas velocity in the CPD in all directions.

### 2.3 Particles dynamics

The motion of solids within the subnebula is affected by interaction with the gas in two different ways. Firstly, solids motion is affected by friction forces due to their relative velocity with the gas. The friction force is expressed through the stopping time $t_s$ of the particle, which contains all the physics of the interaction with the gas. It is separated in two regimes, one where the particle size is much smaller than the mean free path of molecules in the gas and the stopping time does depend on the relative velocity between the gas and the particle, referred to as the Epstein regime, and another one where gas should be regarded as a fluid and the stopping time of the particle depends on its relative velocity with respect with the gas:

$$t_s = \left(\frac{\rho_g v_{th}}{\rho_s R_s}\min\left[1, \frac{3}{8}\frac{v_{rel}}{v_{th}} C_D(Re)\right]\right)^{-1}. \tag{2.4}$$

This stopping time is the characteristic time of angular momentum exchange between the gas and the particle. The drag coefficient $C_D$ is a dimensionless quantity that depends upon the Reynolds number of the flow around the particle.

From this, particles velocity is obtained by numerically integrating their equation of motion. The equation is integrated with an adaptive timestep ODE solver (Brown et al. 1989), using Adams methods for particles with sizes down to $10^{-3}$ m, while an implicit backward differentiation formula scheme is used to integrate the motion of smaller particles whose small stopping times imply a too restrictive timestep for the Adams methods.

The second effect affecting solids motion is turbulence within the CPD. Turbulent eddies are able to entrain particles during their cohesion time, which is approximately the inverse of the local keplerian frequency. Finally, turbulence acts as a diffusion mechanism which we model, following Ciesla (2010, 2011) and Charnoz et al. (2011), with a stochastic motion and advection terms arising from gradients in the diffusivity of particles and density of the gas.

### *2.4 Particles thermodynamics*

An interesting feature of our model is that we also implemented solids thermodynamics. In this study, we restricted ourselves to a mixture of silicates and water ice, but different types of ices can easily be implemented.

All solids, regardless of their sizes, start with a ice-to-rock mass fraction of 0.5, representative of bodies formed beyond the water ice line of the solar nebula. The surface temperature of the planetesimals is calculated using heating and cooling energie sources, following D'Angelo & Podolak (2015). The primary source of energy is the radiation from the surrounding gas. Another heating mechanism is the friction with the gas that heats up the surface of planetesimals. The ablation of ice, on the other end, is an endothermal process which tends to cool down the body.

The theoretical maximum ablation rate of water ice at the surface of the body is given by

$$\frac{dMs}{dt} = -4\pi R_s^2 P_v \sqrt{\frac{\mu_s}{2\pi R_g T_s}}. \tag{2.5}$$

Here, $P_v$ is the equilibrium water vapor pressure of water over water ice at the temperature $T_s$ which is taken from Fray & Schmitt (2009). The mass ablation rate can be used also to determine the change in radius of a particle as it ablates.

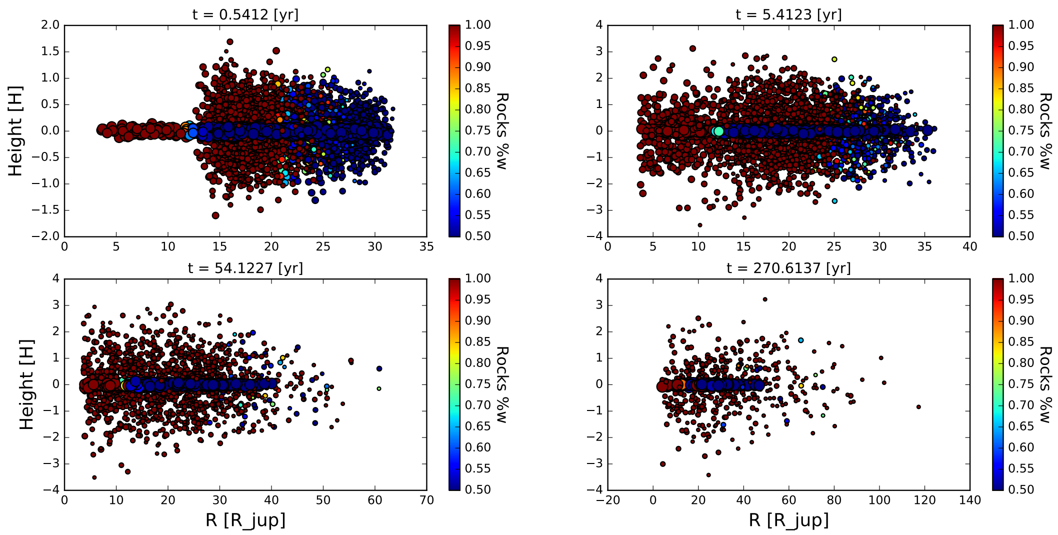


**Fig. 1.** Simulation of $10^4$ particles with initial sizes ranging from $10^{-6}$ up to $10^6$ m. Particles were initially released between 15 and 25 $R_{\mathrm{Jup}}$ and all contained 50% of water ice by mass. All particles also started at the midplane of the disk and their vertical distribution is the result of turbulent transport only. Vertical transport proceeds on shorter timescales than radial diffusion as can be seen from the top left panel where particles are size sorted in the vertical direction already.

The temperature evolution, along with the ablation rate, and thus the change in radius, are solved together with the equation of motion of the particle. We are thus able to consistently follow the evolution of the solids in the Jovian subnebula, including for the first time their water ice content.

## 3 Results

We present in figure 1 an example of simulation with $10^4$ particles with sizes ranging $10^{-6}$–$10^6$ m. All particles were initially released between 15 and 30 $R_{\rm Jup}$ at the midplane of the disk with 50% of water ice by mass. The observed vertical distribution of solids is solely due to turbulent stirring of grains. The settling of larger grains to the midplane of the disk is clearly illustrated, although the reading of the figure is not straight, especially because a very wide range of particle size was used and their representation is uneasy. However, some interesting features are observed. The most important one would probably be that solids of different sizes have a different water ice mass fraction at the same location in the disk, which is clearly identifiable in the top left panel of figure 1 corresponding to the very beginning of the simulation. Although after some time a lot of particles are lost from the simulation and turbulence efficiently mixes the smallest grains, it is clear that bigger bodies are able to carry water further inside the disk.

Further investigations of the presented result will certainly help in better constraining the formation of the Galilean satellites. More specifically, to constrain the size of the building blocks of the moons and their origin by comparing with their bulk composition.

## References


Brown, P. N., Byrne, G. D., & Hindmarsh, A. C. 1989, SIAM J. Sci. Stat. Comput., 10, 1038

Canup, R. M., & Ward, W. R. 2002, AJ, 124, 3404

Charnoz, S., Fouchet, L., Aleon, J., & Moreira, M. 2011, ApJ, 737, 33

Ciesla, F. J. 2010, ApJ, 723, 514

Ciesla, F. J. 2011, ApJ, 740, 9

D'Angelo, G., & Podolak, M. 2015, ApJ, 806, 203

Dwyer, C. A., Nimmo, F., Ogihara, M., & Ida, S. 2013, Icarus, 225, 390

Fray, N., & Schmitt, B. 2009, Planet. Space Sci., 57, 2053

Gressel, O., Nelson, R. P., Turner, N. J., & Ziegler, U. 2013, ApJ, 779, 59

Keller, C., & Gail, H.-P. 2004, A&A, 415, 1177

Klahr, H., & Kley, W. 2006, A&A, 445, 747

Mosqueira, I., & Estrada, P. R. 2003, Icarus, 163, 198

Mosqueira, I., & Estrada, P. R. 2003, Icarus, 163, 232

Sasaki, T., Stewart, G. R., & Ida, S. 2010, ApJ, 714, 1052

Szulágyi, J., Masset, F., Lega, E., et al. 2016, MNRAS, 460, 2853

Takeuchi, T., & Lin, D. N. C. 2002, ApJ, 581, 1344

Tanigawa, T., Ohtsuki, K., & Machida, M. N. 2012, ApJ, 747, 47

*SF2A 2016*
*C. Reylé, J. Richard, L. Cambrésy, M. Deleuil, E. Pécontal, L. Tresse and I. Vauglin (eds)*

# GROWING POROUS GRAINS: A SOLUTION TO THE RADIAL-DRIFT BARRIER

A. J. L. Garcia[1,*], J.-F. Gonzalez[1] and F. C. Pignatale[1]

**Abstract.**
Protoplanetary discs are made of gas and dust orbiting around young stars. Initially submicronic, dust grains can grow by coagulation during collisions until they reach millimetre, then kilometer (planetesimal) and planetary sizes. However, theory indicates that once grains reach a size (between millimetre and meter) for which the planet growth timescale is shorter than the accretion timescale, they drift inwards due to the aerodynamical drag force and are accreted onto the star. This effect goes under the name of radial-drift barrier. Several solutions to this problem have been proposed. In this work, we focus on an intrinsic property of grains: porosity. We investigate the effects porosity can have on grain growth and dynamics using an analytical model. Taking only drift into account (no growth), we find that porous grains are slowed down but also tend to be compressed by the gas in the inner parts of the disc. Analysing growth at fixed distance from the star (no drift), we show that porous grains grow faster and more efficiently than compact ones. Combining drift and growth, we demonstrate that porous grains can overcome the radial-drift barrier and keep growing in the inner parts of the disc while compact grains fall into the star.

Keywords: Protoplanetary discs, Planets and satellites: formation, Star: circumstellar matter, Methods: analytical

## 1 Introduction

The study of planet formation has been revolutionized in the past 20 years as thousands of exoplanets have been discovered (Batalha et al. 2013) with as many different cases as there are planetary systems. We thus need robust tools to understand planet formation. Planets are thought to form in protoplanetary discs, made of gas and dust grains (Lissauer 1993). The growth of very small grains from submicronic monomers to millimeter-sized grains and evolution of large grains from planetesimals to planets are now well known (Blum 2010; Lambrechts & Johansen 2012). However, theoretical and experimental studies demonstrate that when compact grains reach intermediate sizes (from millimetre to meter), they drift quickly, not growing fast enough to decouple from the gas and are accreted into the central star (Weidenschilling 1977). Thus, all the dust reservoir should empty making the growth of planet impossible. Several solutions have been proposed such as particle traps around planet gaps (Paardekooper & Mellema 2004; Fouchet et al. 2010; Gonzalez et al. 2015) or vortices (Barge & Sommeria 1995; Meheut et al. 2012). Porous growth appears to be another solution to the radial-drift barrier (Okuzumi et al. 2012; Kataoka et al. 2013) which could also explain comets' porosity (Lethuillier et al. 2016). In this study, using a model of evolution of porosity during dust growth, we investigate at first the drift of fixed-mass porous and compact grains then growth at fixed distance from the star and finally both drift and growth to study how porosity can influence the grain radial motion, allow grains to reach planetesimal sizes, and overcome the radial-drift barrier.

In section 2, we introduce the different analytical models we have used; in section 3, we present our results and our conclusion in section 4.

## 2 Method

We study the radial motion and evolution of porous and compact grains using the models described in this section.

*e-mail: anthony.garcia@univ-lyon1.fr
[1] Univ Lyon, Univ Lyon1, Ens de Lyon, CNRS, Centre de Recherche Astrophysique de Lyon UMR5574, F-69230, Saint-Genis-Laval, France

### 2.1 T-Tauri disc model

We consider a 1D protoplanetary disc of 0.01 $M_\odot$ mass made of 1% of dust and 99 % of gas, extending from 0.1 to 300 AU around a 1 $M_\odot$ T-Tauri star. The disc physical properties are described by power laws of the distance from the star $R$ and is vertically isothermal with $T(R) \propto R^{-3/4}$ and $T(1\ \mathrm{AU}) = 197$ K. The gas surface density $\Sigma$ is proportionnal to $R^{-3/2}$. In order to represent gas turbulence in the disc, we use the Shakura & Sunyaev (1973) model and set the $\alpha$-parameter to $10^{-2}$ (strong turbulence).

### 2.2 Aerodynamical parameters

Grains evolve in a gaseous environment. As the dust phase is only subject to the gravity of the central star, it rotates with a keplerian velocity. The gas phase is also subject to its own pressure and rotates with a subkeplerian velocity. Therefore, grains undergo a headwind and thus a drag force from the gas. This aerodynamical force can be characterized by the Stokes number St. Two drag regimes can be distinguished according to the radius $s$ of a spherical grain and the mean free path $\lambda$ of the gas molecules: the Epstein regime ($s \leq 9\lambda/4$) where:

$$\mathrm{St} = \frac{\Omega_\mathrm{k}\, \rho_0\, \phi\, s}{\rho_\mathrm{g}\, c_\mathrm{g}} \tag{2.1}$$

where $\rho_0$ is the material density, $\rho_\mathrm{g}$ and $c_\mathrm{g}$ respectively denote the gas density and sound speed, $\Omega_\mathrm{k}$, the Keplerian angular velocity and $\phi$ is the grain filling factor defined as:

$$\phi = \frac{\rho}{\rho_0} \tag{2.2}$$

where $\rho$ is the intrinsic density of the grain. Very porous grains have $\phi$ close to 0 when compact grains have $\phi$ equal to 1. If $s \geq 9\lambda/4$, the grain is in the Stokes regime and has:

$$\mathrm{St} = \frac{4\, \Omega_\mathrm{k}\, \rho_0\, \phi\, s^2}{9\, \lambda\, \rho_\mathrm{g}\, c_\mathrm{g}} \tag{2.3}$$

A grain with St $\sim 1$ physically means that the grain takes a Keplerian orbital period to reach the gas velocity.

### 2.3 Growth and drift

We use the drift model from Weidenschilling (1977) where the grain radial velocity is always directed inwards towards the center of the star:

$$\frac{dR}{dt} = \mathrm{St}\, \frac{1}{\Omega_\mathrm{k}\, \rho_\mathrm{g}}\, \frac{dP_\mathrm{g}}{dR} \qquad \mathrm{St} < 1 \tag{2.4}$$

$$\frac{dR}{dt} = \frac{1}{\mathrm{St}}\, \frac{1}{\Omega_\mathrm{k}\, \rho_\mathrm{g}}\, \frac{dP_\mathrm{g}}{dR} \qquad \mathrm{St} > 1 \tag{2.5}$$

where $P_\mathrm{g}$ is the gas pressure. The radial velocity thus increases with the grain mass for St $< 1$ and decreases for St $> 1$ therefore there is a maximum for St $\sim 1$ corresponding to the radial-drift barrier.

We consider that growth occurs by coagulation during collisions of two identical grains and we use the model from Stepinski & Valageas (1997) where the temporal variation of the grain mass is given by:

$$\frac{dm}{dt} = 4\, \pi\, s^2\, V_\mathrm{rel}\, \rho_\mathrm{d} = m^{2/3} \left( \frac{3\, \sqrt{4\pi}}{\rho_0\, \phi} \right)^{2/3} V_\mathrm{rel}\, \rho_\mathrm{d} \tag{2.6}$$

where $\rho_\mathrm{d}$ is the density of matter concentrated into SPH solid particles. As our work is analytical, we fix $\rho_\mathrm{d} = 0.01\, \rho_\mathrm{g}$ according to the dust-to-gas mass ratio defined in section 2.1. $V_\mathrm{rel}$ is the relative collision velocity between identical grains defined as:

$$V_\mathrm{rel}^2 = 2^{3/2}\, \mathrm{Ro}\, \alpha\, c_\mathrm{g}^2\, \frac{\mathrm{St}}{(\mathrm{St}+1)^2} \tag{2.7}$$

where Ro is the Rossby number for turbulent motions we take equal to 3.

### 2.4 Porosity model

Grains grow by coagulation during collisions and this aggregation makes them become more porous (Okuzumi et al. 2012). As the relative velocity between two colliding aggregates increases with their mass, the tiny aggregates (a few monomers) collide with a small relative velocity and stick without internal reorganization, their intrinsic density $\rho$ thus decreases. It is the 'hit-and-stick' regime. For more massive grains, the shock energy is no longer negligible and is dissipated by compressing the aggregates. It is the 'collisionnal compression' regime. However, Kataoka et al. (2013) have found that static compression may also occur. Indeed, grains have a velocity against the gas and experience a ram pressure which can compress them. This is called the 'gas compression' regime. Moreover, grains can become large enough to have their own gravity and be compacted in the 'self-gravitational compression' regime. We derive the equations for the four regimes and find that the intrinsic density is related to the grain mass $m$ as:

$$\rho \propto \begin{cases} m^{-1/2} & \text{hit-and-stick} \\ m^{0} & \text{collisionnal compression} \\ m^{0} & \text{gas compression (Epstein regime)} \\ m^{-1/14} & \text{gas compression (Stokes regime)} \\ m^{2/5} & \text{self-gravitation} \end{cases} \tag{2.8}$$

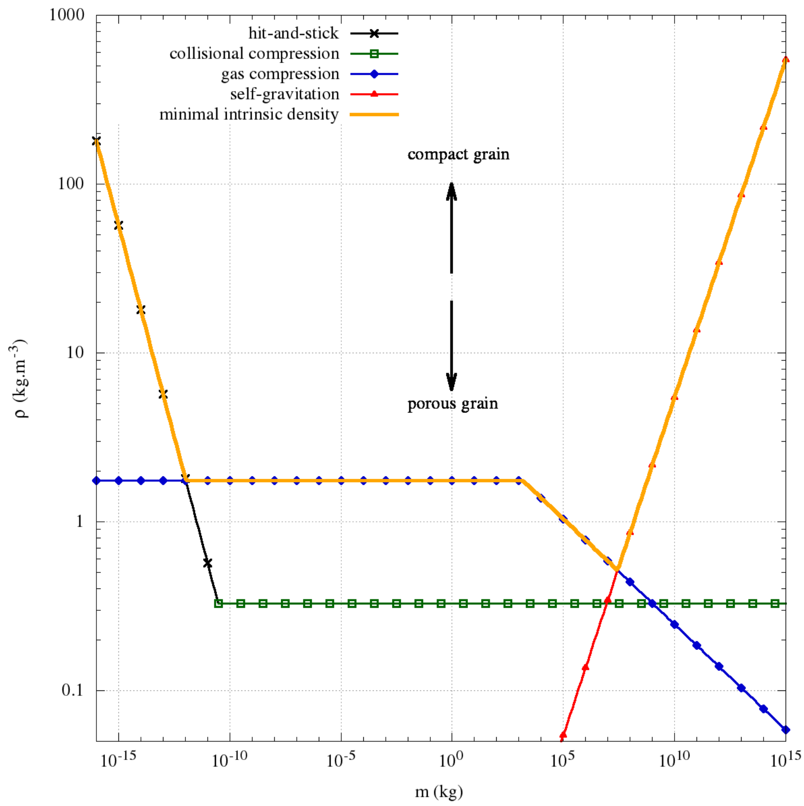


**Fig. 1.** Intrisic densities calculated for the different regimes as a function of grain mass. We consider icy grains ($\rho_0 = 917$ kg.m$^{-3}$) at $R = 10$ AU.

Figure 1 shows the variation of the intrinsic density for the different regimes as a function of grain mass. The grain intrinsic density can only decrease in the hit-and-stick or collisional compression regimes and can only increase because of the gas or self-gravitational compression regimes. If a grain has a density above the curves corresponding to gas or self-gravitation compression, it physically means that the grain is compact enough not to be compressed by those two compression mechanisms. On the other hand, if the grain density is below those curves, the grain is too porous and is staticly compressed by its self-gravitation or by the surrounding gas until it becomes compact enough to be in equilibrium with those two mechanisms. Therefore, the upper curves indicate a minimal intrinsic density.

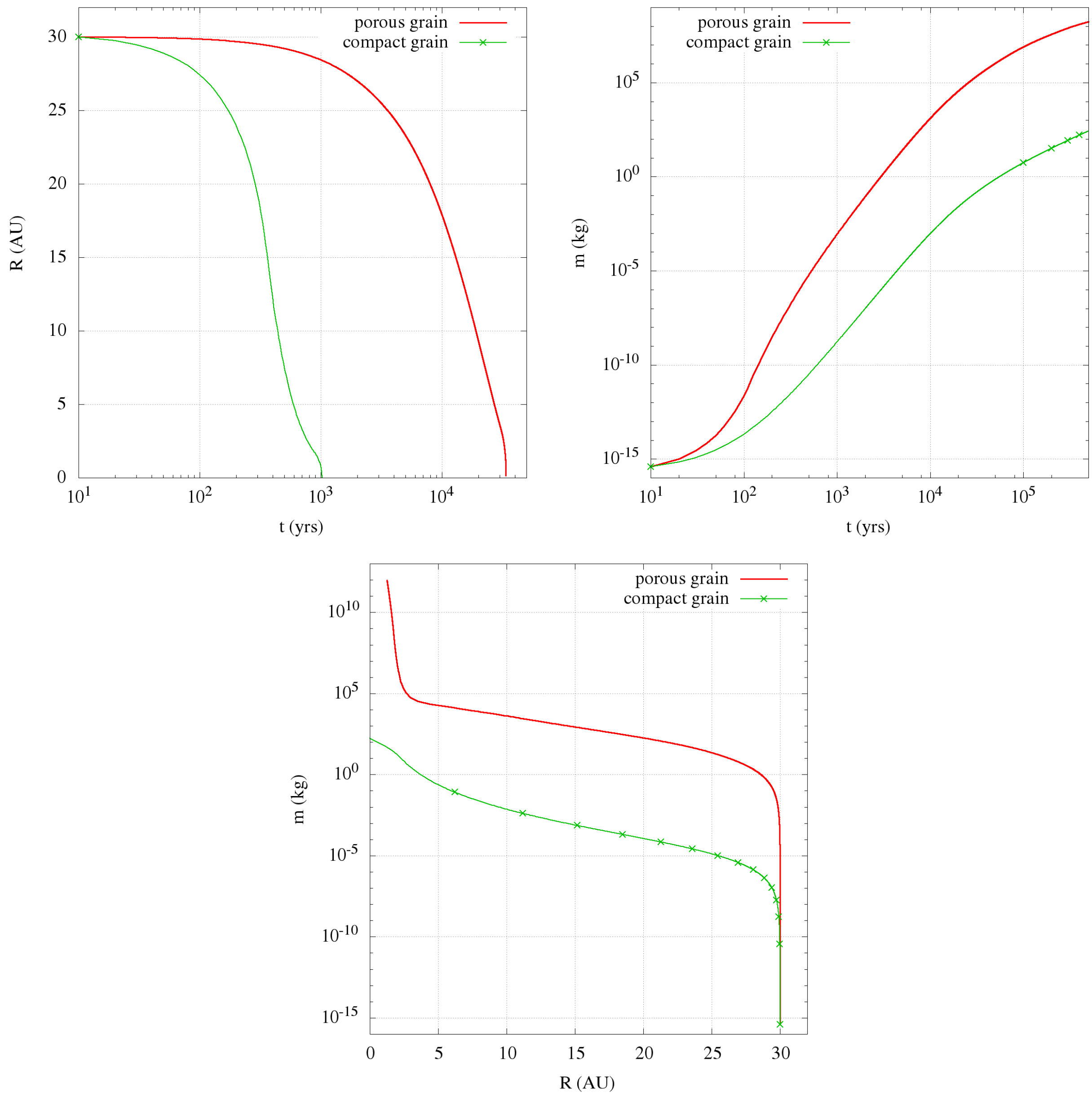


**Fig. 2. (a) Top left:** Only drift: distance from the star $r$ as a function of time for grains with both a constant mass $m = 1$ kg at initial distance $R_{\rm i} = 30$ AU. **(b) Top right:** Only growth: grain mass $m$ as a function of time for grains with an initial mass $m_{\rm i} = 3.84 \mathrm{x} 10^{-16}$ kg at a constant distance from the star $R_{\rm i} = 30$ AU. The porous grain has an initial filling factor $\phi_{\rm i} = 0.1$ . **(c) Bottom center:** Drift and growth: Grain mass $m$ as a function of the distance from the star $R$ for grains with an initial mass $m_{\rm i} = 3.84 \mathrm{x} 10^{-16}$ kg at an initial distance from the star $R_{\rm i} = 30$ AU. The porous grain has an initial filling factor $\phi_{\rm i} = 0.1$. The red curves show the behaviour of an icy grain with the porosity model while the green curves with crosses show that of a compact grain.

## 3 Results & discussion

Figure 2 (a) shows the temporal evolution of the distance from the star for porous (red curve) and compact (green curve) grains with a constant mass $m = 1$ kg starting from $R = 30$ AU. For porous grains, grain density follows the minimal density defined in section 2.4. We can observe that compact grains are quickly accreted ($\sim 10^3$ years) while porous grains are also accreted but within a longer time ($\sim 3 \mathrm{x} 10^4$ years). We can conclude that intermediate-sized porous grains are not able overcome the radial-drift barrier with only drift. For intermediate sizes, a porous grain has a larger area-to-mass ratio than a compact grain with the same mass, and as the intensity of the gas drag is proportional to the area-to-mass ratio, the drag is stronger. This slows down the porous grain. However, porous grains are compressed during the drift: going inwards, they pass through the inner parts of the disc where the hot dense gas can statically compress them and thus their resistance to the drift will be less efficient.

Figure 2 (b) shows the evolution of the mass as a function of time, for compact and porous growing grains with the same initial mass $m_{\rm i} = 3.84{\rm x}10^{-16}$ kg[1] at the same fixed distance from the star ($R_{\rm i}$ = 30 AU). We see that porous grains experience a more efficient growth and become $\sim 10^5$ more massive than compact grains after $5{\rm x}10^5$ years. As an interpretation, for a given mass, porous grains have a larger collisionnal cross section than compact grains therefore their probability to collide with other grains and thus grow is higher than for compact grains. Consequently, porosity could accelerate grain growth.

Figure 2 (c) shows the evolution of the mass as a function of the distance from the star for porous and compact grains with an initial mass $m_{\rm i} = 3.84{\rm x}10^{-16}$ kg[1] and an initial distance from the star $R_{\rm i} = 30$ AU. In this final case, both drift and growth are taken into account. We see that during the first stage of growth (up to $\sim 10^3$ years), both porous grains and compact grains grow without a significant drift but porous grains attain larger masses. When they reach St $\sim 1$, they start to drift but still grow. Even if the growth is more efficient in the inner parts of the disc given the hot and dense gas, compact grains are then accreted into the star. On the other hand, porous grains were already more massive when they start to drift and they reach the inner disc regions with a size which allows them to decouple from the gas, avoiding accretion.

We find that planetesimals[2] can be formed within $\sim 10^4$ years. This can be seen in Figure 2 (c) where the red curve reaches $m = 10^5$ kg, corresponding also to the decoupling of the porous grain close to the star. Even if we continue the growth, our derived timescale and location at which planetesimal size is reached are in a good agreement with Krijt et al. (2016) who have used similar models for porosity and drift. However, planetesimal growth is also driven by accretion of pebbles due to their own gravity (Visser & Ormel 2016) and this type of growth is not taken into account in our model.

## 4 Conclusion

In this work, we investigate if porosity allows grains to overcome the radial-drift barrier. Our calculations show that the growth of porous grains is faster than that one of compact dust. This can be explained by the fact that, for a given mass, porous grains have a larger cross section. This phenomenon can also explain the slower drift of intermediate-sized porous grains illustrated in section 3. Moreover, grains can be compressed because of the static compression by the dense gas when they reach the inner parts. We show that drift of intermediate-sized porous grains with a constant mass cannot overcome the radial-drift barrier. Drift and growth of porous grain could instead overcome the radial drift barrier. Indeed, porous grains grow more efficiently at their initial radius before they drift while still growing and decouple close to the star where the conditions are favorable to reach planetesimal sizes. Conversely, compact grains do not grow fast enough to decouple and are accreted into the star.

In the next work, we will implement this model in our 3D SPH two-phase code (Barrière-Fouchet et al. 2005). This will allow us to investigate mechanisms which are not taken into account in our analytical study such as turbulence of the gas, collective effects of the dust or backreaction of dust on gas. In order to better understand the evolution of the most massive grains, it would be also interesting to include a model of growth by pebble accretion due to their self-gravity.

This research was supported by the Programme National de Physique Stellaire and the Programme National de Planétologie of CNRS/INSU. The authors are grateful to the LABEX Lyon Institute of Origins (ANR-10-LABX-0066) of the Université de Lyon for its financial support within the program "Investissements d'Avenir" (ANR-11-IDEX-0007) of the French government operated by the National Research Agency (ANR). A.G. wants to thank K. Szymanska for her help.

## References

Barge, P., & Sommeria, J. 1995, A&A, 295, L1

[1] corresponding to the mass of a 1 $\mu$m porous grain with a filling factor of 0.1 or that of a 0.46 $\mu$m compact grain
[2] objects with St $> 10^3$ according to the definition of Krijt et al. (2016)

Barrière-Fouchet, L., Gonzalez, J.-F., Murray, J. R., Humble, R. J., & Maddison, S. T. 2005, A&A, 443, 185

Batalha, N. M., Rowe, J. F., Bryson, S. T., et al. 2013, ApJS, 204, 24

Blum, J. 2010, Research in Astronomy and Astrophysics, 10, 1199

Blum, J., & Wurm, G. 2008, ARA&A, 46, 21

Fouchet, L., Gonzalez, J.-F., & Maddison, S. T. 2010, A&A, 518, A16

Gonzalez, J.-F., Laibe, G., Maddison, S. T., Pinte, C., & Ménard, F. 2015, Planet. Space Sci., 116, 48

Kataoka, A., Tanaka, H., Okuzumi, S., & Wada, K. 2013, A&A, 557, L4

Krijt, S., Ormel, C. W., Dominik, C., & Tielens, A. G. G. M. 2016, A&A, 586, A20

Lambrechts, M., & Johansen, A. 2012, A&A, 544, A32

Lethuillier, A., Le Gall, A., Hamelin, M., et al. 2016, A&A, 591, A32

Lissauer, J. J. 1993, ARA&A, 31, 129

Meheut, H., Meliani, Z., Varniere, P., & Benz, W. 2012, A&A, 545, A134

Okuzumi, S., Tanaka, H., Kobayashi, H., & Wada, K. 2012, ApJ, 752, 106

Paardekooper, S.-J., & Mellema, G. 2004, A&A, 425, L9

Shakura, N. I., & Sunyaev, R. A. 1973, A&A, 24, 337

Stepinski, T. F., & Valageas, P. 1997, A&A, 319, 1007

Visser, R. G., & Ormel, C. W. 2016, A&A, 586, A66

Weidenschilling, S. J. 1977, MNRAS, 180, 57

*SF2A 2016*
*C. Reylé, J. Richard, L. Cambrésy, M. Deleuil, E. Pécontal, L. Tresse and I. Vauglin (eds)*

# COULD THE STELLAR MAGNETIC FIELD EXPLAIN THE VERTICAL STRUCTURES IN THE AU MIC DEBRIS DISK?

É. Sezestre[1] and J.-C. Augereau[1]

**Abstract.**
Recent observations of the edge-on debris disk of AU Mic have revealed asymmetric, fast-moving wave-like structures above its disk midplane. Although asymmetries are frequent in debris disks, no model can readily explain these features. In this paper, we present a model aiming to reproduce such structures, particularly the wave morphology and the high projected speeds. We test the hypothesis of dust emitted by a point source, interacting with the stellar wind and the large-scale magnetic field of the star. We perform numerical simulations of test particle trajectories to explore the available parameter space. The impact of the stellar wind and the magnetic field on the dust dynamics is discussed separately, then together. The stellar wind and, to a smaller extent, the magnetic topology, can reproduce the arches. The observed structures cannot be explained by a single trajectory common to all dust grains emitted intermittently by a fixed point source in space. This excludes a giant collision as the emission process. Therefore, our preferred scenario relies on an orbiting source of dust, possibly a planetary companion, emitting at different epochs.

Keywords: stars: individual: AU Mic, planet-disc interactions, magnetic fields

## 1 Introduction

AU Mic is an active M-type star in the $\beta$ Pictoris moving group (23.3 Myr, Mamajek & Bell 2014) with an edge-on debris disk. Recent high contrast imaging with VLT/SPHERE has revealed 5 arch-like structures close to the star (annotated A to E, see fig. 1) in the southeastern side of the disk (Boccaletti et al. 2015). These features have been shown to move away from the star at high speeds, possibly exceeding the local escape velocities. No model can readily explain how to form such fast moving arch-like structures.

In this study, we elaborate on models aiming to explain and reproduce the northwest/southeast asymmetry of the disk, the observed high speeds and the arch-like structures.

We assume that the NW/SE asymmetry can be explained by a local process of dust release, for example emission from a planet or its nearby environment, or because of a dust enhancement due to a giant collision on resonant trapping with a planet. This hypothetic emission source will be called *parent body* in the following, without further specification. The dust is supposed to be exposed to the stellar wind. The resulting wind pressure can put this dust on unbound trajectories, achieving the high projected speeds observed (see sec. 2.1). We explore the interaction between charged dust particles and the stellar magnetic field as a source of vertical elevation for the dust in subsection 2.2. The parametrisation of the model is described in the subsection 2.3. In section 3 we test the influence of the stellar wind (3.1) and the magnetic field (3.2), and then their mutual dependence (3.3).

## 2 Model

### 2.1 Stellar wind and radiation pressure

Dust particules are expected to be exposed to a strong stellar wind and to a lesser extent to the radiation pressure, which exerts a net pressure force that can overcome the stellar gravity. The $\beta$ parameter, the ratio of the pressure to the gravitation forces, quantifies this effect (e.g. Krivov et al. 2006).

[1] Univ. Grenoble Alpes, CNRS, IPAG, F-38000 Grenoble, France

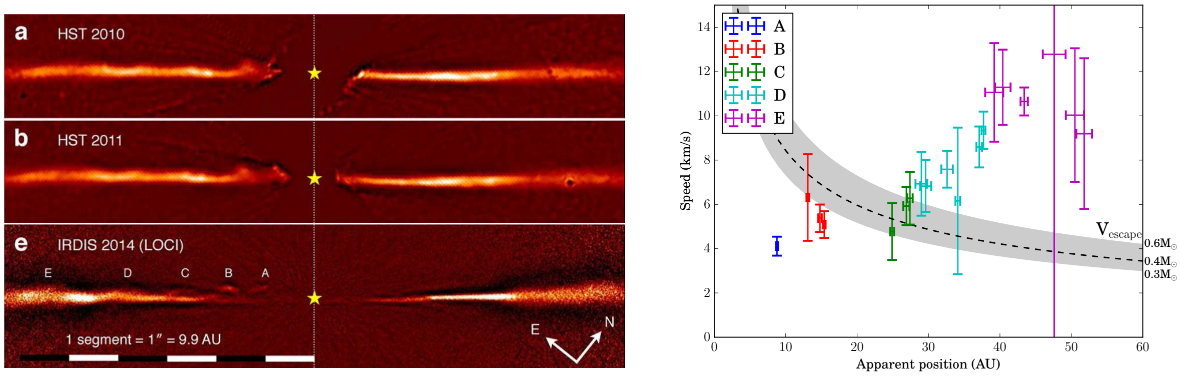


**Figure 1. Left:** Images of the disk in 2010, 2011 and 2014 extracted from Boccaletti et al. (2015). The five structures are labelled from A to E. **Right:** Apparent velocity of the structures as a function of apparent separation. The grey area corresponds to the projected escape velocity of the system assuming a stellar mass between 0.3 and $0.6M_\odot$.

The trajectory of a grain released from a parent body strongly depends on the $\beta$ value. Assuming a parent body on a circular orbit, the $0 < \beta < 0.5$ dust particles will remain on bound orbits, with eccentricities increasing with $\beta$, while $0.5 < \beta < 1$ particles will be placed on parabolic orbits. Dust particles with $\beta > 1$ will follow unbound, "abnormal" parabolic trajectories. These $\beta > 1$ grains are of particular interest in the context of the AU Mic debris disk because their velocity continuously increases while moving outwards, until it reaches an asymptotic value.

### 2.2 *Magnetic field topology*

A 4.2 kG magnetic field has been measured at the stellar surface of AU Mic (Saar 1994). It is supposed to extent at tens of AUs. The interaction *via* the Lorentz force between charged dust particles and a specific magnetic topology can lead to oscillating trajectories around the disk midplane, that may ultimately form arches as observed.

To form an arch, the particle must go upward with respect to the disk midplane, then downward, meaning the net force applied on the grain needs to change sign. These conditions are met if a charged grain evolves in a magnetic field that changes sign on the course of its trajectory.

We suppose that the magnetic axis of the star is misaligned with its rotation axis. We assume that the star has a simple dipole structure but with the field lines emitted from each pole being carried away by the stellar wind. Along the equator, these field lines create a so-called neutral current sheet. At any distance from the star, the neutral current sheet split the disk in two, with one half seeing a magnetic field that has the same strength but an inverse sign compared to the other half of the disk. Due to the misalignment, this current sheet takes the form of a *ballerina skirt* as described in Alfvén (1977). The intersection between the disk midplane and the ballerina skirt is a two-arm spiral as can be seen on figure 2. In the sketch, the brown area corresponds to disk regions located above the current sheet, while the purple area corresponds to regions below the current sheet. In the ideal MHD model, this structure propagates with the stellar wind, as the star rotates. Therefore, the whole structure is in solid rotation with the star, with a period of 4.85 days (Messina et al. 2010).

### 2.3 *Model parameters*

In our model, the dust particles are emitted by a parent body on a circular orbit in the disk midplane. They are released with the keplerian speed plus a vertical component. Their charge is constant over the time. The dust grains feel the gravity of the star, the stellar wind pressure, the radiation pressure and the Lorentz force. The 5 key parameters defining the trajectory are (see fig. 2):

- $\beta$ : the pressure/gravitation forces ratio,
- $q/m$ : the charge/mass ratio,

- $R_0$ : the radius of the parent body orbit assumed to be circular,
- $V_{z0}$ : the initial vertical speed of the particle,
- $\theta_0$ : the angle between the released point and the intersection of the current sheet with the parent body trajectory.

The trajectories are computed with a $4^{th}$-order Runge-Kutta integrator, then rotated and projected to reproduce the images. This leads to an additional free parameter which is the angle $\alpha$ between the observer and the released point.

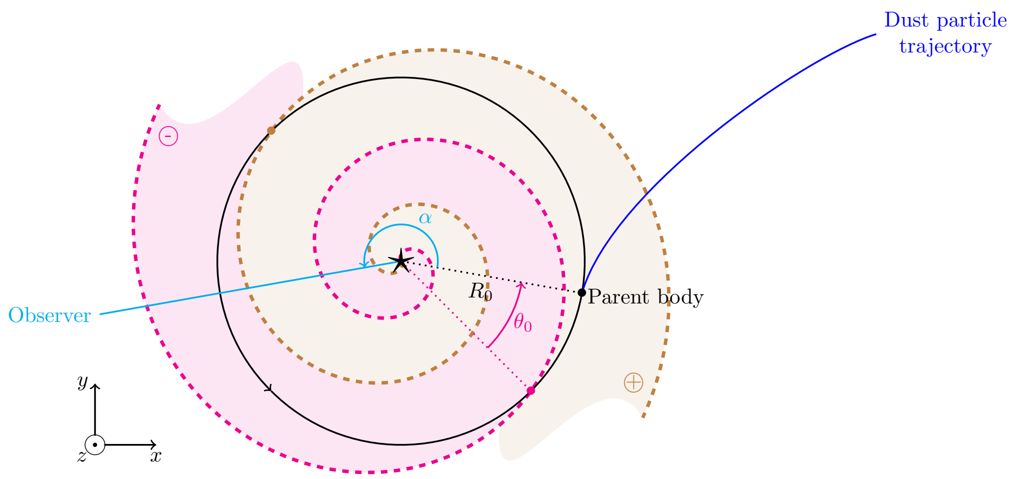


**Figure 2.** Sketch of the system seen from above. The dashed coloured lines mark the sign change of the magnetic field.

## 3 Results

### 3.1 *Ejected dust grains*

In a first step, we ignore the magnetic field and we adjust the observed speeds by projecting the trajectories, considering only $\alpha$, $\beta$ and $R_0$. The movement is thus confined to the disk midplane. We test if a single trajectory can fit all the projected velocities. That supposes a common origin for all the structures, assumed to arise from a static parent body and with self-similar trajectories.

Figure 3 shows the $\chi^2$ map of the speed adjustment. The best fits are obtained for particles emitted at typically 25 AU, with $\beta > 1$ ($\beta \approx 7$). There appears to be a clear dependency between $\beta$ and $R_0$.

While the fit is consistent with all the data points, it appears that the A,B structures may require lower $R_0$ values than the C,D,E structures (for comparison, see fig. 4). That can suggest that either the two groups correspond to two different activity periods for the parent body, or they have a different emission point.

### 3.2 *Arch formation*

In a second step, we examine the vertical position of the dust particles as a function of time to search for extrema as proxies for arch formation. In this case, the magnetic field is switched on, but any projection effect is neglected. Consequently, we have five parameters characterising the trajectory ($\beta, q/m, R_0, V_{z0}, \theta_0$). The number of extrema, noted N in the following, corresponds roughly to twice the number of formed arches.

For each parameter, we select 6 values within a broad range and calculate the resulting 7,776 trajectories. A $\chi^2$ value is assigned to each trajectory, which we here define as the sum of the difference between all the extremum elevations and $\pm 0.5$ AU, divided by the number of extrema. This favours a few oscillations around 0.5 AU above and below the disk midplane rather than numerous arches.

As shown in figure 5, different behaviours are possible. The largest number of extrema is achieved for bound particles (e.g. N=77 for $\beta = 0.4$, figure 5). Unbound particles can only form a smaller number of arches. We

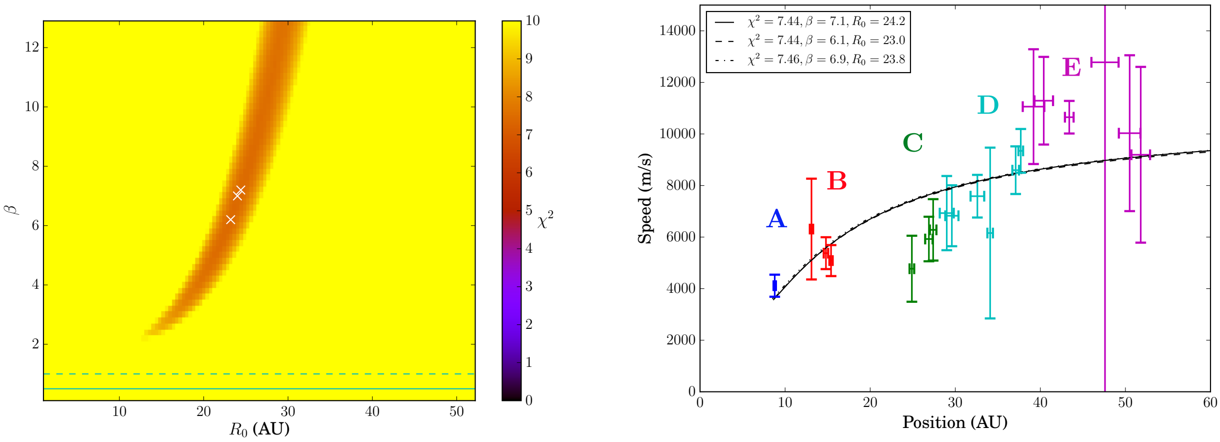


**Figure 3. Left:** Reduced $\chi^2$ map for the fit of the observed speeds of the 5 structures all together. The light blue line and dashed line correspond respectively to $\beta = 0.5$ and $\beta = 1$. **Right:** Best fits for the speeds, corresponding to the white crosses on left panel.

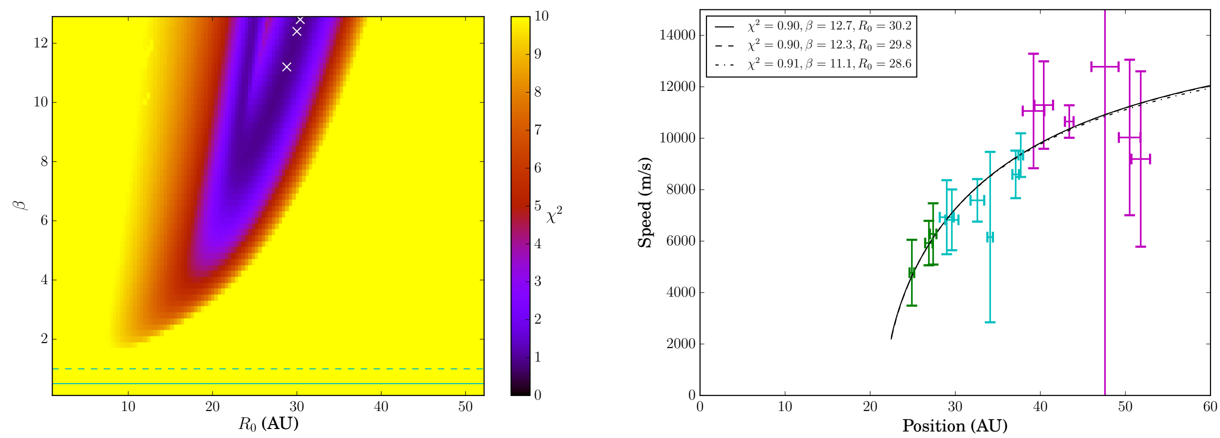


**Figure 4.** Same as fig. 3, but only for the structures C,D,E.

could not form more than 3 arches with unbound particles, and over 4 extrema, the solutions are only small oscillations around the disk midplane, and no longer elevated arches (see N=8 in figure 5).

The 5-dimension $\chi^2$ array is transformed into probability distributions for each parameter of the model, and presented figure 6. The most probable values are $\beta = 0.4$ and $R_0 = 2$ UA. This test is biased toward inclined, bound orbits. In this case, the code detects one arch every revolution, as the particle move from one side of the disk midplane to the other side during one revolution. As the duration of the simulation is constant and does not depend on $R_0$, the closest orbits can do more revolution than farthest orbits. Since one arch is detected every revolution, the closer the orbit, the more arches are formed. This is why the bound, closest orbits give the best results in this case.

### 3.3 *Global Adjustment*

There is a discrepancy between the results of the two precedent tests. The adjustment of the speeds suggests unbound orbits ($\beta \approx 7$), originating from a parent body far from the star ($R_0 \approx 25$ AU). The formation of arches, on the other hand, favours bound ($\beta < 0.5$), close orbits ($R_0 \approx 10$ AU). This simple model might not be complex enough to reproduce the observations. Nevertheless, that excludes a static source of dust with respect to the observer, ruling out a giant collision process of dust emission.

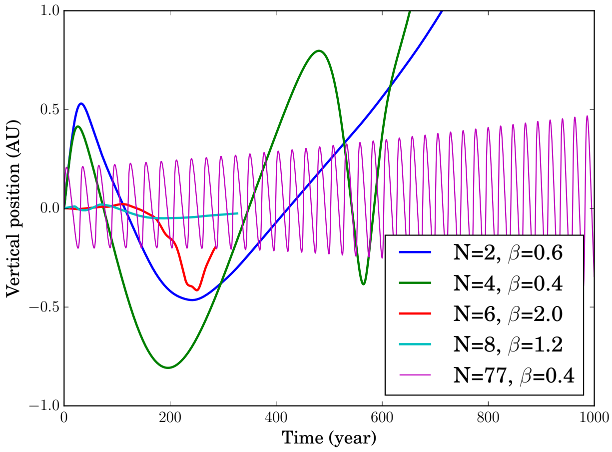


**Figure 5.** Evolution of vertical elevation over the time for the best trajectories at a given number of extrema N.

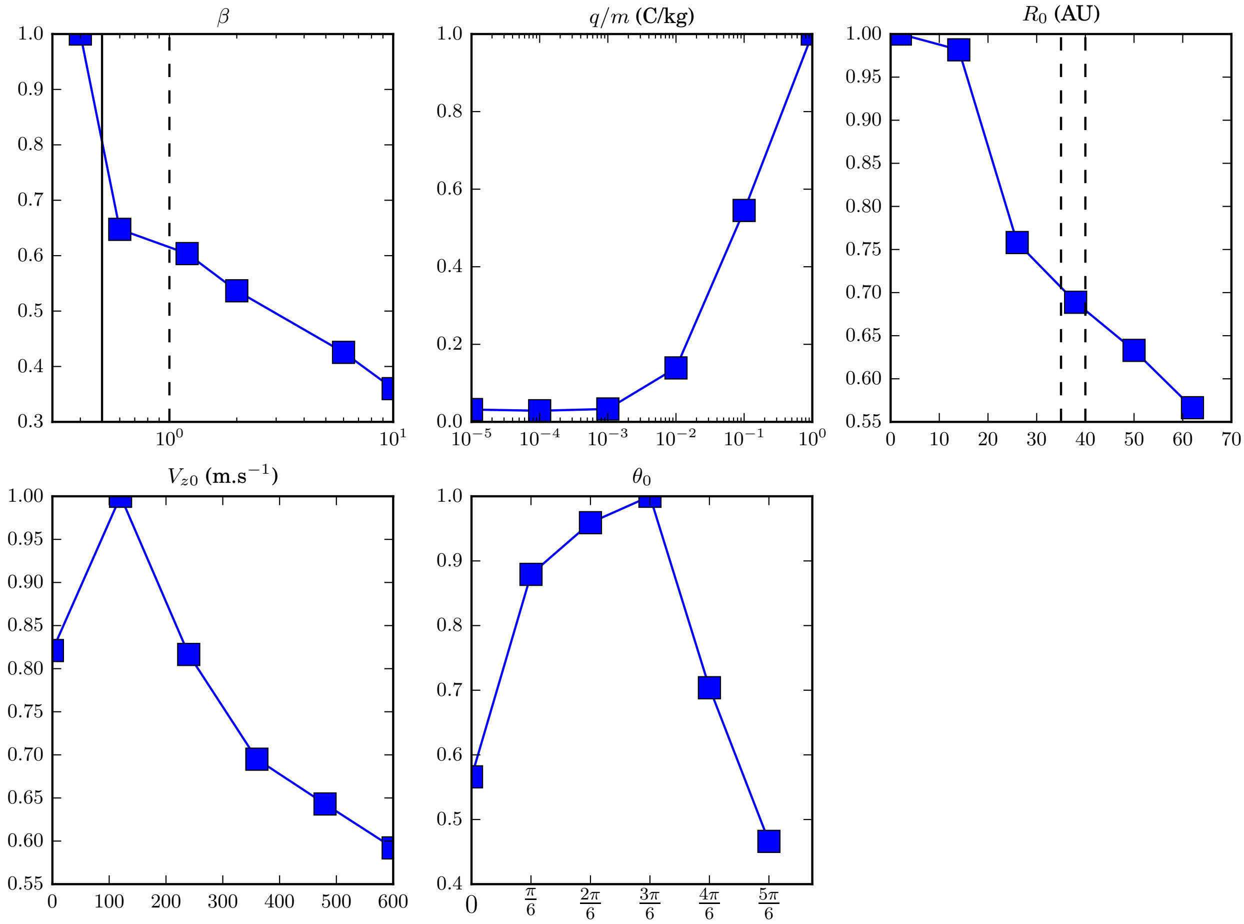


**Figure 6.** Probability distribution for all the parameters derived from the arch formation. The maximal value is normalised. The dashed vertical lines in the $R_0$ panel correspond to the position of the planetesimal belt.

We have developed a more complex model to reproduce the arches and their velocities at the same time. Again, we set a few values for each parameters and calculate the trajectories. The $\chi^2$ calculated for each trajectory describes the ability to form each arch separately, with a morphology similar to what is observed, considering the projection effect to account for the different epochs. The trajectory must fit the elevation above the disk midplane and position of the arch at the observing date, and also go back to the disk midplane consistently with the arch radial extension. Then a non-normalised probability for each parameter is calculated based on the $\chi^2$. The results are presented in figure 7.

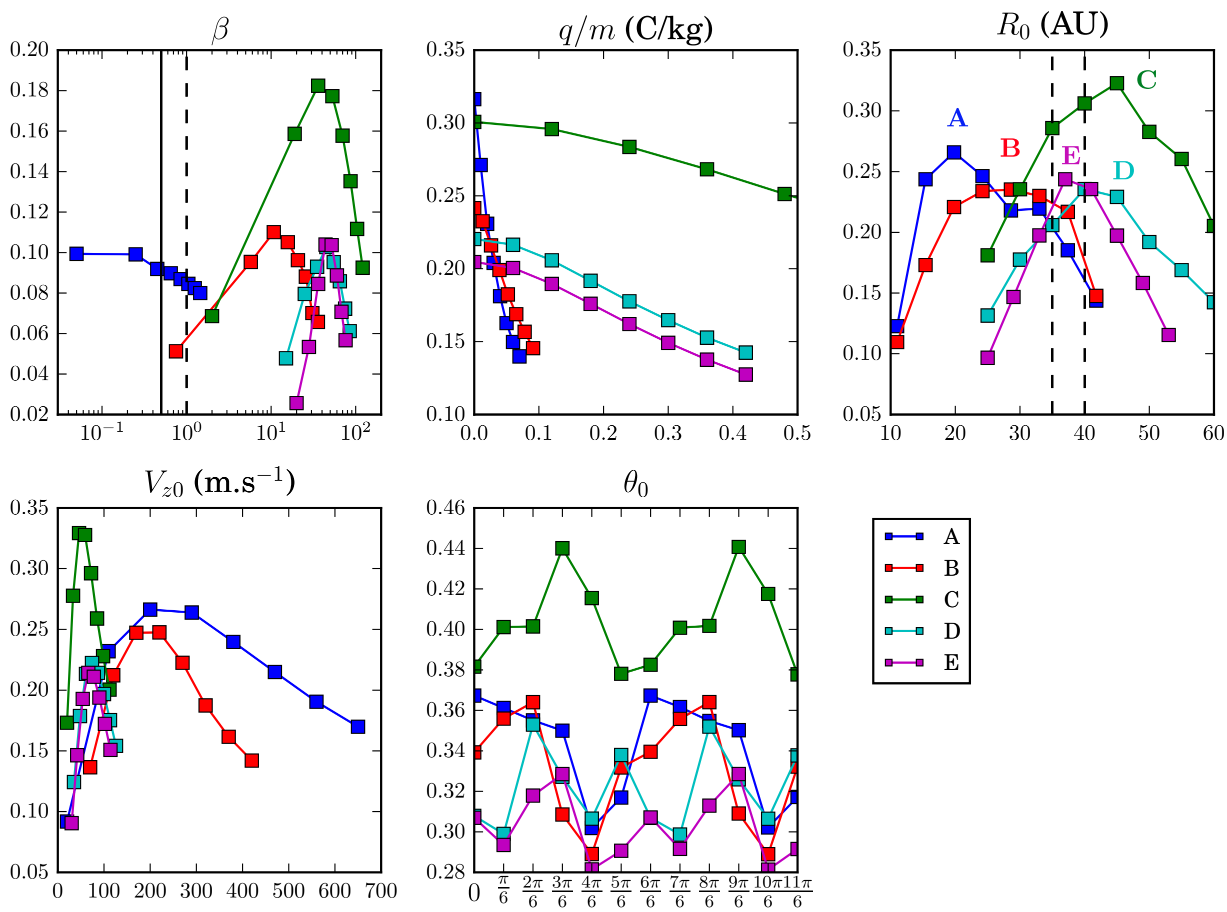


**Figure 7.** Probability distribution of the parameters, for each structure.

For each structure, we see the most probable value of the five parameters in our model. Again, two groups of structures appear. A,B for one side, with low $\beta$, low $R_0$ ($\approx$ 20 AU) and high $V_{z0}$ values ($\approx$ 200 m.s$^{-1}$). They are the closest structures, the most elevated, and are moving slower than the others. On the other side, the C,D,E structures have higher $\beta$ ($\approx$ 30), higher $R_0$ ($\approx$ 40 AU) and lower $V_{z0}$ values ($\approx$ 50 m.s$^{-1}$). These structures seem consistent with a parent body included inside the planetesimal belt, estimated to be at 35-40 AU from the star (Augereau & Beust 2006; Strubbe & Chiang 2006; Schüppler et al. 2015). For all the structures, the charge is very small, meaning that the magnetic field is maybe not the most important component of our model to reproduce the structures, compared to the initial vertical speed. We see also a symmetric behaviour on both sides of the disk for $\theta_0$.

## 4 Conclusion

From the models developed here, we can point out some behaviours for the dust particles:

- We need unbound dust particles to explain the projected speeds: the structures are evolving fast.
- A ballerina skirt magnetic field topology can produce oscillating trajectories, but not 5 arches.
- Several arches formation by a single grain and high velocities seem to require inconsistent $\beta$ values.

- A more complex model seems to argue for two different parent body for the structures, always farthest than 20 AU from the star.

We can set appart the hypothesis of a single point of emission static with respect to the observer, like in the case of a giant collision. A parent body inside the planetesimal belt releasing periodically dust is favoured by the models.

## References

Alfvén, H. 1977, Rev. Geophys., 15, 271

Augereau, J.-C. & Beust, H. 2006, A&A, 455, 987

Boccaletti, A., Thalmann, C., Lagrange, A.-M., et al. 2015, Nature, 526, 230

Krivov, A. V., Löhne, T., & Sremčević, M. 2006, A&A, 455, 509

Mamajek, E. E. & Bell, C. P. M. 2014, Mon. Not. R. Astron. Soc., 445, 2169

Messina, S., Desidera, S., Turatto, M., Lanzafame, A. C., & Guinan, E. F. 2010, Astron. & Astrophys., 520, A15

Saar, S. H. 1994, in Infrared Sol. Phys. Proc. 154th Symp. Int. Astron. Union No. 1, 1–5

Schüppler, C., Löhne, T., Krivov, a. V., et al. 2015, Astron. Astrophys., 97, 1

Strubbe, L. E. & Chiang, E. I. 2006, Astrophys. J., 648, 652

*SF2A 2016*
*C. Reylé, J. Richard, L. Cambrésy, M. Deleuil, E. Pécontal, L. Tresse and I. Vaughlin (eds)*

# REVIEW OF GAS AND DUST IN DEBRIS DISCS

Q. Kral[1]

**Abstract.** This proceeding summarises a talk given on the state-of-the-art of debris disc modelling. We first review the basics of debris disc physics, which is followed by a short overview of the state-of-the-art in terms of modelling dust and gas in debris disc systems.

Keywords: planetary systems - debris discs - circumstellar matter - circumstellar gas

## 1 Introduction

Circumstellar discs are observed around an increasing number of stars. In this proceeding, we are interested in debris discs rather than younger protoplanetary discs still full of gas and where giant planets are still forming. These debris discs are left-overs of planetary formation, old, cold, gas-poor and are detected owing to their infrared (IR) excesses. These discs contain solid bodies with size ranging from a few 100km to a few microns. The mass reservoir is located in the biggest bodies that collide, fragment and create smaller planetesimals. These smaller fragments collide and are ground down to dust. This large cross section of dust or debris can then be observed from Earth, either in thermal emission in the far-infrared or in scattered light in the optical or near-IR. The Kuiper and asteroid belts are the debris disc of our Solar System. However, our debris disc is critically different from observed debris discs; it is less massive and less collisionally active and thus would be impossible to detect with current instruments.

We observe thousands of such debris discs in extrasolar systems. We estimate that at least 25% of stars show an IR-excess (and therefore possess a debris disc), but this number could be much higher if we were able to detect very tenuous Kuiper belt-like systems (e.g. Matthews et al. 2014). For the closest and/or the brightest debris discs, we are able to resolve them. As of today, $\sim 90$ debris discs are resolved at different wavelengths. On the resulting images, we observe that debris discs are not simple symmetric circular discs but rather, they show many structures such as warps, clumps, spirals, depleted zones, shifts of the centre of the disc compared to the star, asymmetric needle-like shapes, ... (see Fig. 1). These structures inform us about the interactions between the disc and its environment. The main question that now drives debris disc science is to try to understand where these structures originate from. To do so, complex models are being developed and I will summarise here the state-of-the-art in terms of modelling debris discs.

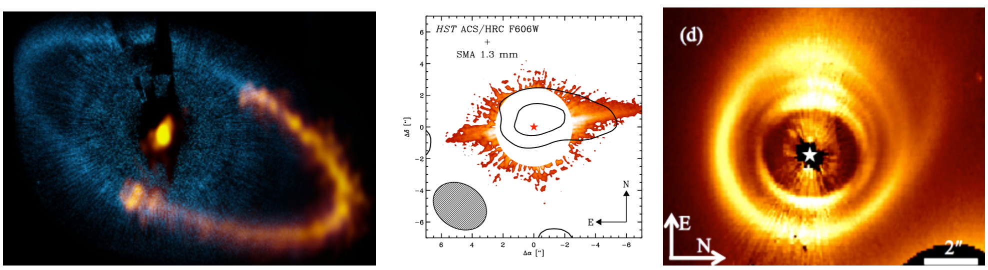


**Fig. 1. Left:** Fomalhaut (Boley et al. 2012; Kalas et al. 2013). **Centre:** HD 15115 (MacGregor et al. 2015). **Right:** HD 141569 (Konishi et al. 2016)

[1] Institute of Astronomy, University of Cambridge, Madingley Road, Cambridge CB3 0HA, UK

Over the past few years, an increasing number of gaseous species (atoms and molecules) have been detected around debris discs (in more than 10 systems). The gas is at low levels, critically different from protoplanetary discs. However, it is surprising as debris discs were thought to be gas-free after the protoplanetary disc phase and subsequent dispersal of the primordial gas via accretion and photoevaporation (e.g. Pringle 1981; Clarke et al. 2001). However, many progresses have been made to understand where the gas may originate from and to model its thermodynamical evolution that might solve the conundrum.

I will first explain in more details the physics of debris discs and how complicated it can be to model numerically (section 2). I will then focus on dust modelling (section 3) before ending on the new hot topic in our field focusing on understanding gas observations in debris discs (section 4).

## 2 Debris disc physics

We here summarise the most important forces and effects that, in an ideal world, should be taken into account when modelling debris discs. We will find out in section 3 that due to a lack of CPU-power, some concessions have to be made concerning which effects are most important to include in our codes.

The equation of motion describing the evolution of a solid body of mass $m$ located at a distance $r$ from the central star of mass $M_\star$ is given by

$$m\frac{\mathrm{d}^2\vec{r}}{\mathrm{d}t^2} = -\frac{GmM_\star}{r^2}\vec{e_r} + \vec{F}_{\mathrm{rad}} + \vec{F}_{\mathrm{drag}} + \vec{F}_{\mathrm{others}}, \tag{2.1}$$

where the first term of the right-hand side of the equation is the gravitational force from the central star $\vec{F_g}$, $\vec{e_r}$ is the radial unit vector, $G$ is the gravitational constant, $\vec{F}_{\mathrm{rad}}$ is the force due to radiation pressure from the star, $\vec{F}_{\mathrm{drag}}$ are for all the drag forces and $\vec{F}_{\mathrm{others}}$ are other forces that can be exerted on this mass $m$ in a debris disc environment. In Eq. 2.1, the collisions are not taken into account. Subsection 2.3 explains what can be their effect on the solid-body dynamics. We now describe each term of the equation of motion.

### 2.1 Stellar gravity and radiation pressure

The photons coming from the central star transfer angular momentum to the orbiting dust grains. Only the smallest dust grains are affected by this purely radial force (Burns et al. 1979) and this translates as the overall gravitational force becoming

$$\vec{F_g} + \vec{F}_{\mathrm{rad}} = -\frac{GmM_\star(1-\beta)}{r^2}\vec{e_r}, \tag{2.2}$$

where $\beta = |\vec{F}_{\mathrm{rad}}/\vec{F_g}|$. When $\beta > 0$, it is as if the grains felt a star with a smaller mass $M_\star(1-\beta)$. $\beta$ is usually modelled as being $\propto 1/s$, the grain size. In reality, it can be more complicated as there are other dependencies, more precisely

$$\beta = \frac{3L_\star \langle Q_{\mathrm{rad}} \rangle}{16\pi G M_\star c\rho s}, \tag{2.3}$$

where c is the light speed, $\rho$ the bulk density of grains, $L_\star$ the star's luminosity and $\langle Q_{\mathrm{rad}} \rangle$ the mean radiation pressure coefficient (averaged over wavelengths). $Q_{\mathrm{rad}}$ depends on the grain compositions and can vary steeply for one composition to another, or as a function of $s$. One can show that if a grain with $\beta > 0.5$ is created from a parent body on a circular orbit at a distance $a_0$, it will become unbound and will be blown out on a hyperbolic orbit. If $\beta < 0.5$, the dust grain will have an eccentric orbit and its new semi-major axis and eccentricity are given by $a = a_0\frac{1-\beta}{1-2\beta}$ and $e = \frac{\beta}{1-\beta}$. These different orbits are well described in Fig. 2. Therefore, there will be a radial segregation of sizes as the smallest grains with the largest eccentricities will reach farther out in the system whilst bigger bodies that are less pushed by radiation pressure will stay close to the parent belt where they are produced.

We note here that we do not take into account any gravitational disturbances that could be created by a planet located close to the disc. The effects of planets are discussed further in subsection 2.4.

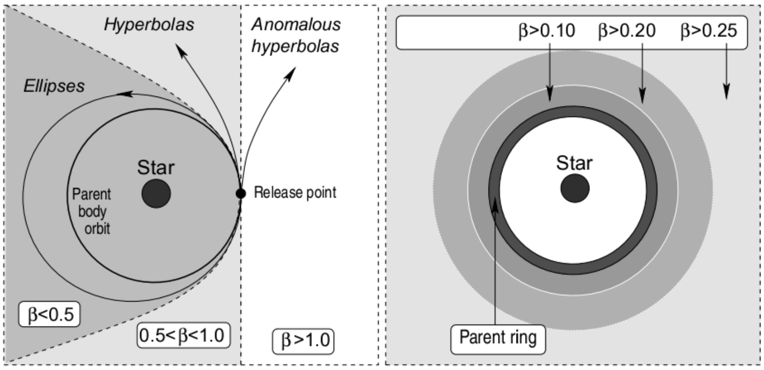


**Fig. 2.** Different types of orbits in a debris disc resulting from different values of $\beta$ (see subsection 2.1). From Krivov (2010).

### 2.2 Drag forces

The radiation pressure force has also an orthoradial component described by the Poynting-Robertson effect. This tangential force is dissipative and opposes the motion, one can show that this force is (Burns et al. 1979)

$$\vec{F}_{\rm PR} = -\beta \frac{GmM_\star}{r^2}\left(\frac{v_r}{c}\vec{e_r} + \frac{\vec{v}}{c}\right), \tag{2.4}$$

where $\vec{v}$ is the velocity vector of the dust grain and $v_r$ its radial component. Under this force alone (no collisions), a dust grain spirals towards the central star on a timescale equal to $t_{\rm PR} = 400\beta^{-1}(r/a_\oplus)^2(M/M_\odot)^{-1}$, where $a_\oplus$ is the semi-major axis of the Earth (Wyatt 2008). If collisions were taken into account the equilibrium would be changed as a particle migrating in by PR-drag could get destroyed by collisions much before reaching the central star. Fig. 3 shows the radial variation of the optical depth for different dynamical excitations (parameterized by $\eta_0$) of a narrow belt at $r_0$. To do so, Wyatt (2005) uses a simple analytical model where all the grains have the same size. The parameter $\eta_0$ used in Fig. 3 is proportional to the optical depth in the parent belt and describe the dynamical excitation of the belt. When $\eta_0$ is small, collisions are unimportant and the surface density of the transport-dominated tenuous belt is constant with distance to star. When $\eta_0$ is large, the system is collision-dominated and the dust is confined to a narrow belt as it gets destroyed before reaching further in Fig. 3 also shows intermediate cases for the evolution of the optical depth with radial distance to star. More complicated models can get rid of the same size assumption and work out the profile at steady-state or as a function of time (e.g. Wyatt et al. 2011; Löhne et al. 2008; Kral et al. 2013).

Around late-type stars where the radiation pressure is smaller, stellar wind particles can matter. Similarly to the radiation pressure forces, stellar wind forces can be decomposed into a radial and tangential force. Eq. 2.4 also applies, replacing $c$ by $v_s$, the stellar wind velocity. Stellar wind drag can then become important as $v_s \ll c$ (e.g. Reidemeister et al. 2011).

Finally, when a dust grain orbits in a gas disc, it feels a gas drag that can be modelled by the Epstein force (Takeuchi & Artymowicz 2001). The gas drag timescale is given by $\rho s/(\rho_g v_{\rm th})$, where $\rho_g$ is the gas number density, $\rho$ the bulk density of grains and $v_{\rm th}$ is the thermal velocity. Around the gas-rich system $\beta$ Pic this force do not affect bound grains (Kral et al. 2016b) but for more gaseous systems that are in transition to becoming debris discs and still contain a fair amount of primordial gas, it may well be that dust is affected by gas drag.

### 2.3 Collisions

In debris discs, mass flows from the biggest solid bodies ($\sim$ 100km) to the smallest grains (micron size) owing to collisions: this is called the collisional cascade and always replenishes the smallest grains that are blown out from the system as soon as they are small enough to be blown out by radiation pressure (i.e. $\beta \gtrsim 0.5$). Collisions happen at high-velocity in debris discs (a few km/s), which often lead to fragmentation of the colliding bodies. The biggest bodies from the mass reservoir can collisionally survive billions of years (Löhne et al. 2008) before being ground down to dust. An important quantity to work out the outcome of a collision is the critical specific

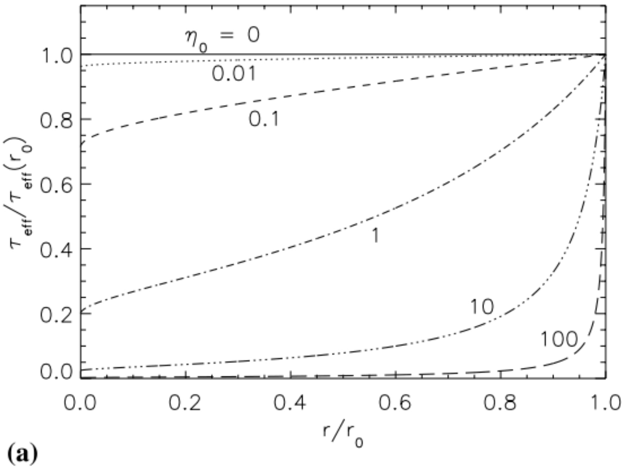


**Fig. 3.** Optical depth as a function of distance to star at steady-state for a narrow parent belt (located at $r_0$) evolving under PR-drag+collisions as a function of $\eta_0$ (which parameterises the dynamical excitation of the belt, see main text). From Wyatt (2005).

collisional energy

$$Q_D^* = Q_s \left(\frac{s}{1\text{m}}\right)^{-b_s} + Q_g \left(\frac{s}{1\text{km}}\right)^{-b_g}, \tag{2.5}$$

which is often characterised as two power laws and is the impact energy per unit mass of the target that results in a biggest fragment that has half the mass of the initial target. $Q_D^*$ varies with the impactor size. Indeed, lab experiments (with small grain collisions) and numerical simulations (for large body collisions) show that smallest grains become more coherent and thus harder to destroy and larger bodies can re-accrete fragments owing to their larger gravity (making them harder to destroy). Depending on the impact energy, a given collision can end up in a fragmentation, craterisation or even just a rebound (but this is rarely the case in debris discs). The physics of collisions is complex as it covers 12 orders of magnitude in size and can result in several outcomes depending on the respective sizes of the target and impactor and their relative velocity. Analytical solutions show that the resulting particle size distribution at steady-state scales as $s^{-3.5}$. More refined numerical models show that it is more complex and 4 different regimes exist: the small eccentric grain regime, the strength regime, the gravity regime and lastly the primordial regime (e.g. Thébault & Augereau 2007).

### *2.4 Other effects*

Some other effects can be at play in debris disc environments. For instance, the local flux of neutral atoms in the interstellar medium ($\sim 0.1$ cm$^{-3}$) can affect the dynamics of dust grains in debris discs that are not too collisionally active (i.e. when the optical depth $\lesssim 10^{-5}$, Marzari & Thébault 2011). This effect can create some potentially observable butterfly-like shapes (e.g. the debris disc around HD 61005 Olofsson et al. 2016). Recently, magnetic fields were proposed to be a potential mechanism to trap dust that would drift very close to the star (Rieke et al. 2016; Su et al. 2016). Sublimation can also affect the dynamics of grains when a particle drifts inwards by PR-drag. Indeed, grains when sufficiently heated sublimate and become smaller. This induces radiation pressure to be more effective to push grains, which can potentially be sent out again (e.g. Kobayashi et al. 2009). Also, planets in a debris disc system can influence the dynamics of solid bodies. Resonances can trap dust and create clumps (e.g. Wyatt 2003). Long term secular effects from an eccentric planet can induce an eccentricity to the disc and offset its centre compared to the star (the so-called pericentre glow, Wyatt et al. 1999). Also, a planet really close to the disc can truncate its inner edge and steepen its surface density profile because of the clearing of its chaotic zone (e.g. the narrow disc around HR 4796, Lagrange et al. 2012).

## 3 Dust modelling

We note that the whole field cannot be summarised in this brief proceeding and we will focus on the most state-of-the-art modelling methods that have been used recently.

### 3.1 Radiative transfer

Dust radiative transfer models were originally used to predict the best-fit dust distribution from a system's SED. However, this is a degenerate process as a bigger grain closer-in will produce the same flux as a smaller grain further out. These radiative transfer codes are now refined and fit at the same time the SED with resolved images and interferometric nulls, which break most of the degeneracies.

One recent example is the study of $\eta$ Corvi by Lebreton et al. (2016). They use the radiative transfer code GRaTeR (Augereau et al. 1999) to fit both the SED, Herschel images and KIN nulls against a large parameter space of different discs. Doing so, they were able to constrain the position of the outer belt and show marginal evidence for asymmetries, but also, they could determine the spatial distribution of the inner belt (exozodis) at a sub-au scale. They use Bayesian statistical analysis and integrate over each parameter of the model to work out a probability density for each disc and derive uncertainties. They were able to probe the best-fit compositions for both discs. The best-fit model can then be used to make predictions for observability with other instruments (ALMA, JWST, ...) and predict what more could be assessed through these new observations.

Another state-of-the-art study showing the capacity of radiative transfer modelling is Milli et al. (2016, recommended for publication). From SPHERE very high-angular resolution images of HR 4796A, they were able to derive the scattering phase function (SPF) of the dust up to very small angles (13.6°). It shows a peak of forward scattering for scattering angles below 30° and confirm the side of the disc inclined towards the Earth. Using the Mie theory assuming spherical dielectric grains, they computed SPFs for a large range of compositions, porosity, size distributions, ... Thanks to this modelling (and performing a Bayesian analysis), they predict that the dust population is dominated by large particles ($\sim 20\mu$m) well above the size that usually dominates the cross section, i.e. close to the blow-out size. The SPF also gives some constraints on the size distribution. One should then try to understand this prediction using one of the models described in the next subsections.

Kral et al. (2016a) used radiative transfer to check the impact of disc asymmetries on astrometric measurements. They find that new missions such as Theia (new name for NEAT, Malbet et al. 2012) that aim to detect small Earth-like planets with high precision astrometry could be affected by dust clouds (of cometary mass) that would create an astrometric signal of the same order of magnitude as an Earth-like planet. Moreover, current infrared missions could not detect IR-excesses of such small clouds that would create such a fictitious Earth-like astrometric signal. They find that there are ways to disentangle a dust cloud from a real planet (e.g. by observing at different wavelengths), and it also means that it will be a new way to discover asymmetric close-in discs that cannot be resolved or detected otherwise.

### 3.2 Collisional approach

Collisional modelling has been used in our community to understand the origin of the observed IR-excesses. Thanks to this approach, we could assess the mass reservoir needed as well as the planetesimal eccentricities required to create the right amount of dust and follow the time evolution of the planetesimal grinding process. These codes (using the particle-in-a-box approach) have now reached a high level of sophistication (e.g. Thébault & Augereau 2007) but still treat the dynamics poorly (e.g. no azimuthal dependence). We here give recent examples of what can be achieved with this approach.

Schüppler et al. (2015) studied the AU Mic (M-dwarf) debris disc with their sophisticated collisional code called ACE (Krivov et al. 2006; Löhne et al. 2008). They wanted to find the best disc model that would reproduce both the SED, the ALMA image (1.3mm) as well as scattered and polarised light data. Running their model they can find the best radial and size distributions of the particles in the whole disc and constrain the position of the outer edge of the belt as well as the preferred dynamical excitation in the belt ($e < 0.03$). They also find that the stellar mass loss rate should exceed the solar one by a factor $\sim$50 (which is expected around M stars) for the stellar wind to be able to drag enough material in.

Recently, Krijt & Kama (2014) pointed out that the minimum fragment size that can be produced after a collision is limited by the conservation of energy. Thebault (2016) implemented this new constraint in his code to study the observational effects it might have. It was thought that it could explain the mysterious fact that we observe grains that are much larger than the blow-out size (Pawellek & Krivov 2015). The use of this collisional code could prove that the minimum fragment size dependence has a weak effect on the predicted size distribution. Therefore, the intriguing result by Pawellek & Krivov (2015) has not yet been fully explained by debris disc models.

### 3.3 Purely dynamical approach

When one tries to reproduce complex structures observed in resolved images of debris discs, the N-body approach is widely used. It allows to take into account complex interactions with planets or a companion star but the collisions are totally neglected. It can still be useful to study purely dynamical effects on the biggest bodies and derive some general results that may be altered by collisions. We will now describe two new papers that used that type of approach recently, in conjunction with ALMA images.

The traditional thought that gaps in debris discs are created by a planet within the gap has been revisited recently. Pearce & Wyatt (2015) showed that a double ring system could be created from an eccentric planet of mass comparable to the disc mass that is located near the inner edge of the innermost disc and not between the two belts. Indeed, the initially eccentric planet is circularised by interactions with the disc and the secular effect of the planet can cause debris to apsidally antialign with the planet's orbit, clearing a larger region than a higher mass planet would and, therefore, creating a double belt shape. This scenario could potentially explain the shape of the disc around HD 107146 recently observed with ALMA.

The HR 8799 double belt star was recently imaged with ALMA (Booth et al. 2016). This system possesses 4 giant planets that are observed between the two belts. The inner edge of the outer belt could be resolved with ALMA for the first time, and is located at $\sim$ 145au. The outermost planet called HR 8799b has a semi-major axis $\sim$68au (Zurlo et al. 2016), which may be too small to sculpt the inner edge of the outer belt at 145au. Running N-body simulations or using analytical estimates, one can compute the chaotic zone of planet b (within which mean motion resonances overlap), which depends on the mass and eccentricity of the planet. Using this approach, they find that the planet b chaotic zone could clear objects up to 110au, which opens up for the possibility of having an additional, yet hidden, planet in the system. This potential planet would be located between 110 and 140au and would be lighter than $1.25M_J$. Goździewski & Migaszewski (2014) also ran simulations with the system of 4 (or 5) planets to test for the stability of the planetary system as a whole and see whether it is in a stable configuration. They find that the planets are most likely in a double Laplace resonance to explain the stability of this packed system over the age of the star ($\sim$160Myr).

### 3.4 Refined approach coupling dynamics and collisions

A big step forward has been made over the past few years, when the first codes coupling collisions and dynamics emerged. Amongst the most sophisticated debris disc models that have been developed to date are the DyCoSS and LIDT-DD codes (see also Levison et al. 2012; Nesvold et al. 2013). Both can follow the collisions at the same time as the dynamics. However, they are different in their principles and limitations. DyCoSS is restricted to steady-state situations under the influence of a single planet and collisions are fully destructive. LIDT-DD overcomes these limitations but the price to pay is a slower computational time.

DyCoSS can study very fine spatial structures and has been used to study debris discs around binaries (Thébault 2012) or discs with an embedded or exterior planet (Thebault et al. 2012; Lagrange et al. 2012). One such simulation with a planet embedded in a broad disc is shown in Fig. 4. Owing to the presence of the planet, resonant structures develop as well as a density gap at the planet position. According to previous N-body non-collisional simulations, the density gap, which is the chaotic zone of the planet should be totally devoid of dust. However, this new generation code is able to show that it is more complicated, as small grains produced in the inner disc that are on eccentric orbits, actually fill up the chaotic zone.

LIDT-DD (described in Kral et al. 2013) is able, for the first time, to treat collisions and dynamics in a self-consistent fashion and allows to follow the time evolution till steady-state of the many fragments that are produced during collisions. Kral et al. (2015) presents the first astrophysical application of the code, which follows the evolution of violent collisions between sub-planetary mass bodies that are expected to happen in the late stages of planetary formation. This new generation model is able to tackle such an arduous problem for the first time, and leads to some interesting results such as providing the brightness of such violent phenomena, their timescale, their detectability, as well as being able to predict an infallible signature of such events. These giant impacts create a strong brightness asymmetry at the collision point that could be observed with SPHERE (for the closest systems) or with MIRI/JWST in the mid-IR (see Fig. 5). Confirmed detections of this signature

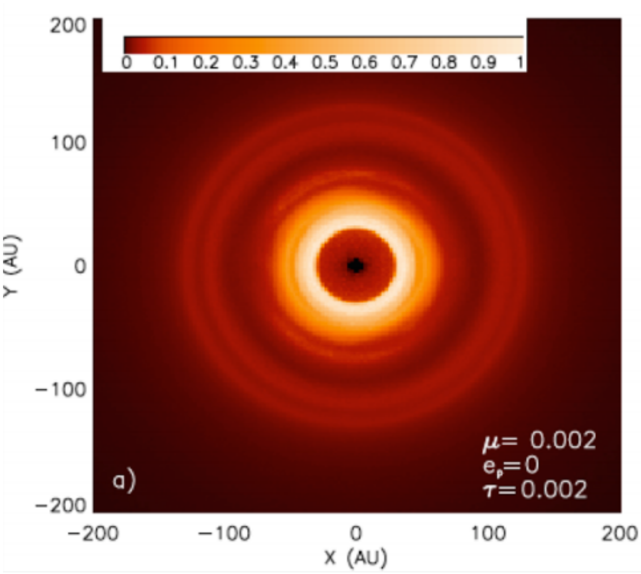


**Fig. 4.** The effects of a planet at 75au embedded within a broad disc (30-130au) modelled with the partial coupling code called DyCoSS.

would lead to actual observations of on-going planetary formation, which would be a major advance in our understanding of planetary formation.

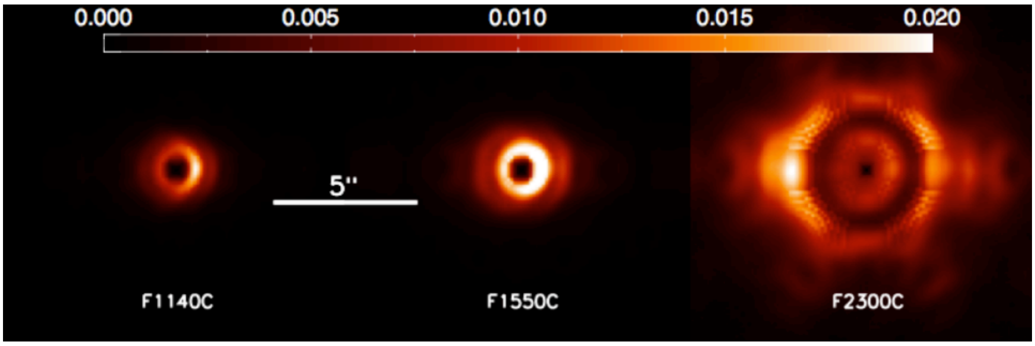


**Fig. 5.** MIRI/JWST synthetic observation of the aftermath of a massive collision between two asteroid-like objects. The asymmetry on the right side at 11 and 15 microns and on the left side at 23 microns is a typical signature of these events.

## 4 Gas modelling

The search for gas around main sequence stars is becoming a hot topic as it is a new way to probe volatiles in planetary systems, where planets have already formed. Molecular (CO) and atomic species (carbon, oxygen, metals) are now detected around more than 10 main sequence stars (e.g. Brandeker et al. 2004; Roberge et al. 2006; Dent et al. 2014; Brandeker et al. 2016). This was not expected as planetary systems were thought to be gas-free after the protoplanetary disc phase and subsequent dispersal of the primordial gas via accretion and photoevaporation (e.g. Pringle 1981; Clarke et al. 2001). The majority of the observed molecular gas in these $\sim$ 10 systems is presumably not primordial as the CO photodissociation timescale is on the order of 100 years and primordial CO would be long gone. We suppose that for most cases, the observed gas is secondary. Also, gas in these old systems is only observed around stars with a debris disc. We expect that the secondary gas is created from the volatile-rich solid bodies of debris discs, either by photodesorption (Grigorieva et al. 2007) or solid-body collisions (Czechowski & Mann 2007; Zuckerman & Song 2012).

A new model has recently been proposed by Kral et al. (2016b) to describe the thermodynamical evolution of such secondary gas in planetary systems. This model has been used on the famous $\beta$ Pic system, for which the largest number of species have been detected so far (see also Xie et al. 2013). The model is able to reproduce all $\beta$ Pic gas observations (and make predictions for future observations, see Fig. 6) and may, more generally, be used to explain the gas origin and dynamics around all debris discs. The model proposes that 1) CO is produced from volatile-rich solid bodies located in debris belts, 2) CO photodissociates in less than 120 years in C+O and, 3) the carbon and oxygen atoms evolve by viscous spreading (parameterised with an $\alpha$ prescription), resulting in an accretion disc inside the parent belt and a decretion disc outside. The thermodynamical model follows the dynamical evolution of atoms as well as their ionisation fractions, excitation and temperature. The viscosity may come from the magnetorotational instability that might be active in debris discs as proposed by Kral & Latter (2016).

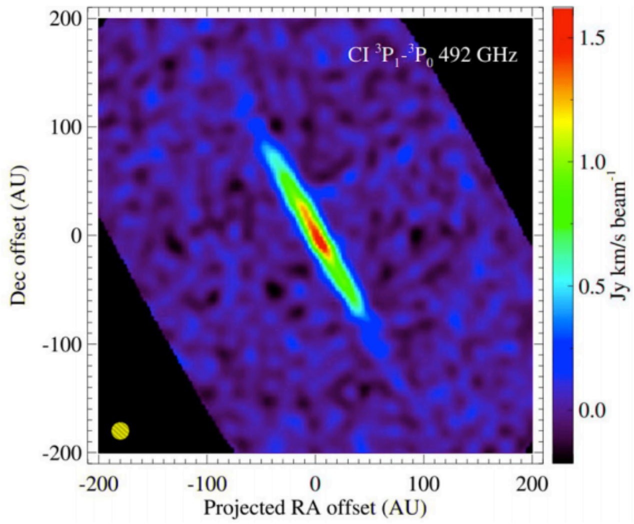


**Fig. 6.** Predicted ALMA CI map at 610 microns from Kral et al. (2016b) best-fit model.

This secondary gas model can be applied to a large sample of debris disc systems. Kral et al. (in prep) assume that the gas production rate depends on the debris disc properties. Indeed, the more collisional and massive is the disc, the more gas is expected to be released. They can then compare their secondary gas model predictions to existing observations and find that they can explain the bulk of the observations with this model. Therefore, they can use this model to assess the gas abundance in CO, carbon and oxygen around all debris disc stars. Fig. 7 shows their predictions for the detectability of neutral carbon with APEX and ALMA. They predict that CI around $\beta$ Pic should be detected with ALMA for the on-going observation (PI: Brandeker) and give predictions for the rest of the sample. They find that ALMA could revolutionise our understanding of gas around debris discs and predict detections of neutral carbon in at least 30 systems.

## 5 Conclusions

In this proceeding, the reader is given an understanding of the physics at work in debris discs as well as a state-of-the-art compilation of the different modelling methods that are used among the debris disc community. It is not our aim to review every single study but rather give an overview of the different modelling possibilities and the most recent works that have been published in our community.

The new codes coupling dynamics and collisions are a great step forward in terms of modelling debris discs and open a new era where these discs can be modelled self-consistently and taking into account their full complexity. We also emphasise that there is still room for new simpler approaches such as Lee & Chiang (2016), where they use a simple debris disc model with a planet and reproduce a wide variety of disc morphologies that are observed. Gas observations in debris disc systems could unveil a totally new independent picture of planetary systems compared to dust observations. This new field is emerging quickly and thanks to the high-resolution power of ALMA could lead to great results in the close future. For instance, atomic gas is expected to extend down to the central star whilst debris disc are located at tens of au. Observing these gas discs could be a way to probe, for the first time, the hidden inner parts of planetary systems and could potentially reveal some hidden planets through structures or asymmetries on the gas disc at a few au.

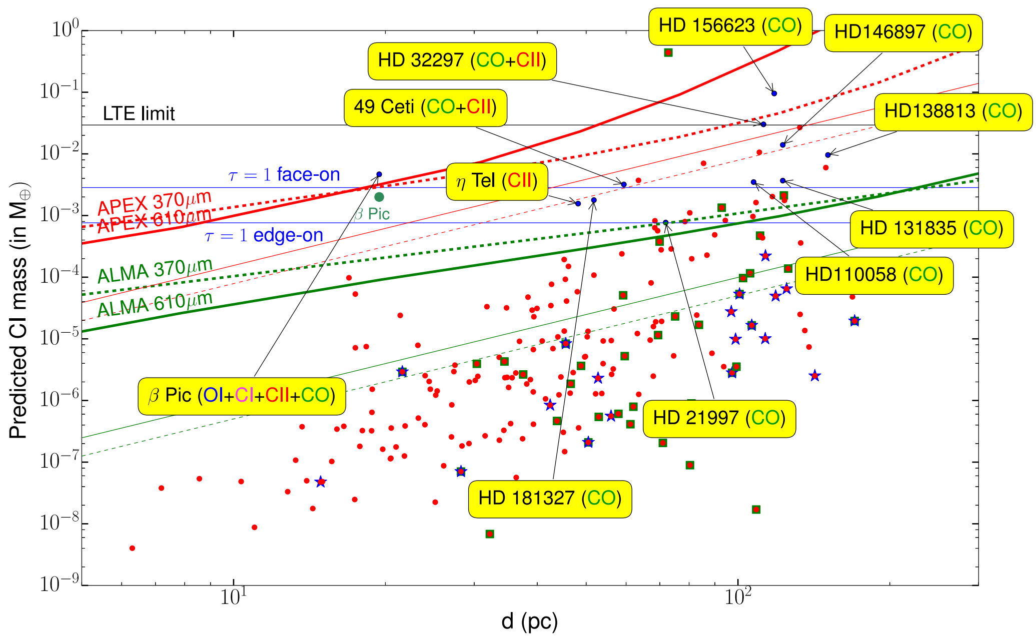


**Fig. 7.** Predicted CI mass (in $M_\oplus$) as a function of distance to Earth ($d$). Planetary systems with gas detections are annotated using yellow boxes and the elements detected within each system are written in between parenthesis. The CI mass for $\beta$ Pic, derived from Kral et al. (2016b) is shown as a green point. The red points are predictions for debris disc' systems without gas detected. Detection limits at $5\sigma$ in one hour are shown for APEX (in red) and ALMA (in green) at 370 (dotted) and 610 microns (solid). The thin lines are for LTE calculations and thick lines for more realistic NLTE calculations. The blue lines show the limit above which the CI line gets optically thick ($\tau > 1$) for both edge-on and face-on cases. The black line is the position under which LTE is not a good approximation anymore (assuming a belt located at 85au). The blue star and green square symbols show systems that are too warm to still retain gas or have a small photodissociation timescale, respectively.

QK acknowledges support from the European Union through ERC grant number 279973 and wishes to thank the PNP and the ASA for the invitation to give this talk. I also thank A. Bonsor and P. Thebault for interesting discussions.

## References


Augereau, J. C., Lagrange, A. M., Mouillet, D., Papaloizou, J. C. B., & Grorod, P. A. 1999, A&A, 348, 557

Boley, A. C., Payne, M. J., Corder, S., et al. 2012, ApJ, 750, L21

Booth, M., Jordán, A., Casassus, S., et al. 2016, MNRAS, 460, L10

Brandeker, A., Liseau, R., Olofsson, G., & Fridlund, M. 2004, A&A, 413, 681

Brandeker, A., Cataldi, G., Olofsson, G., et al. 2016, A&A, 591, A27

Burns, J. A., Lamy, P. L., & Soter, S. 1979, Icarus, 40, 1

Clarke, C. J., Gendrin, A., & Sotomayor, M. 2001, MNRAS, 328, 485

Czechowski, A., & Mann, I. 2007, ApJ, 660, 1541

Dent, W. R. F., Wyatt, M. C., Roberge, A., et al. 2014, Science, 343, 1490

Goździewski, K., & Migaszewski, C. 2014, MNRAS, 440, 3140

Grigorieva, A., Thébault, P., Artymowicz, P., & Brandeker, A. 2007, A&A, 475, 755

Kalas, P., Graham, J. R., Fitzgerald, M. P., & Clampin, M. 2013, ApJ, 775, 56

Kobayashi, H., Watanabe, S.-i., Kimura, H., & Yamamoto, T. 2009, Icarus, 201, 395

Konishi, M., Grady, C. A., Schneider, G., et al. 2016, ApJ, 818, L23

Kral, Q., Thébault, P., & Charnoz, S. 2013, A&A, 558, A121

Kral, Q., Thébault, P., Augereau, J.-C., Boccaletti, A., & Charnoz, S. 2015, A&A, 573, A39

Kral, Q., Schneider, J., Kennedy, G., & Souami, D. 2016, A&A, 592, A39
Kral, Q., Wyatt, M., Carswell, R. F., et al. 2016, MNRAS, 461, 845
Kral, Q., & Latter, H. 2016, MNRAS, 461, 1614
Krijt, S., & Kama, M. 2014, A&A, 566, L2
Krivov, A. V., Löhne, T., & Sremčević, M. 2006, A&A, 455, 509
Krivov, A. V. 2010, Research in Astronomy and Astrophysics, 10, 383
Lagrange, A.-M., Milli, J., Boccaletti, A., et al. 2012, A&A, 546, A38
Lebreton, J., Beichman, C., Bryden, G., et al. 2016, ApJ, 817, 165
Lee, E. J., & Chiang, E. 2016, ApJ, 827, 125
Levison, H. F., Duncan, M. J., & Thommes, E. 2012, AJ, 144, 119
Löhne, T., Krivov, A. V., & Rodmann, J. 2008, ApJ, 673, 1123-1137
MacGregor, M. A., Wilner, D. J., Andrews, S. M., & Hughes, A. M. 2015, ApJ, 801, 59
Malbet, F., Léger, A., Shao, M., et al. 2012, Experimental Astronomy, 34, 385
Marzari, F., & Thébault, P. 2011, MNRAS, 416, 1890
Matthews, B. C., Krivov, A. V., Wyatt, M. C., Bryden, G., & Eiroa, C. 2014, Protostars and Planets VI, 521
Nesvold, E. R., Kuchner, M. J., Rein, H., & Pan, M. 2013, ApJ, 777, 144
Olofsson, J., Samland, M., Avenhaus, H., et al. 2016, A&A, 591, A108
Pawellek, N., & Krivov, A. V. 2015, MNRAS, 454, 3207
Pearce, T. D., & Wyatt, M. C. 2015, MNRAS, 453, 3329
Pringle, J. E. 1981, ARA&A, 19, 137
Reidemeister, M., Krivov, A. V., Stark, C. C., et al. 2011, A&A, 527, A57
Rieke, G. H., Gáspár, A., & Ballering, N. P. 2016, ApJ, 816, 50
Roberge, A., Feldman, P. D., Weinberger, A. J., Deleuil, M., & Bouret, J.-C. 2006, Nature, 441, 724
Schüppler, C., Löhne, T., Krivov, A. V., et al. 2015, A&A, 581, A97
Su, K. Y. L., Rieke, G. H., Defrére, D., et al. 2016, ApJ, 818, 45
Takeuchi, T., & Artymowicz, P. 2001, ApJ, 557, 990
Thébault, P. 2012, A&A, 537, A65
Thébault, P., & Augereau, J.-C. 2007, A&A, 472, 169
Thebault, P., Kral, Q., & Ertel, S. 2012, A&A, 547, A92
Thebault, P. 2016, A&A, 587, A88
Wyatt, M. C., Dermott, S. F., Telesco, C. M., et al. 1999, ApJ, 527, 918
Wyatt, M. C. 2003, ApJ, 598, 1321
Wyatt, M. C. 2005, A&A, 433, 1007
Wyatt, M. C. 2008, ARA&A, 46, 339
Wyatt, M. C., Clarke, C. J., & Booth, M. 2011, Celestial Mechanics and Dynamical Astronomy, 111, 1
Xie, J.-W., Brandeker, A., & Wu, Y. 2013, ApJ, 762, 114
Zuckerman, B., & Song, I. 2012, ApJ, 758, 77
Zurlo, A., Vigan, A., Galicher, R., et al. 2016, A&A, 587, A57

*SF2A 2016*
*C. Reylé, J. Richard, L. Cambrésy, M. Deleuil, E. Pécontal, L. Tresse and I. Vauglin (eds)*

# MIGRATION OF ACCRETING GIANT PLANETS

A. Crida[1 2], B. Bitsch[3] and A. Raibaldi[1]

**Abstract.** We present the results of 2D hydro simulations of giant planets in proto-planetary discs, which accrete gas at a more or less high rate. First, starting from a solid core of 20 Earth masses, we show that as soon as the runaway accretion of gas turns on, the planet is saved from type I migration : the gap opening mass is reached before the planet is lost into its host star. Furthermore, gas accretion helps opening the gap in low mass discs. Consequently, if the accretion rate is limited to the disc supply, then the planet is already inside a gap and in type II migration.

We further show that the type II migration of a Jupiter mass planet actually depends on its accretion rate. Only when the accretion is high do we retrieve the classical picture where no gas crosses the gap and the planet follows the disc spreading.

These results impact our understanding of planet migration and planet population synthesis models.

The e-poster presenting these results in French can be found here :
*L'e-poster présentant ces résultats en français est disponible à cette adresse :*
`http://sf2a.eu/semaine-sf2a/2016/posterpdfs/156_179_49.pdf`.

Keywords: Planet-disk interactions, Accretion, Protoplanetary disks, Planets and satellites: formation

## 1 Introduction

In this e-poster, we present preliminary results relative to the problem of the migration of growing giant planets. Planetary migration is a phenomenon that changes the orbital radius of planets by gravitational interactions with the gaseous proto-planetary disc in which they form. Small planets are fully embedded in the disc, and subject to the *type I migration*. The typical speed of type I migration is inversely proportional to the mass of the planet, hence it can be extremely fast (few thousands of orbits) for planet of several tens of Earth masses. Giant planets (above typically $100 - 300$ Earth masses) in contrast open a gap in the disc profile, and are then driven by the disc, in so-called *type II migration*, generally slower. In the standard core-accretion model, a giant planet must grow from 0 to its final mass, and therefore experience type I migration as it grows, until it opens a gap. As a consequence, there is a significant risk that giant planets should be lost before having a chance of transitionning to the type II migration regime.

In section 2, we show that a giant planet should open a gap before being lost inside its host star by type I migration, provided it accretes gas in the runaway regime. In section 3, we study the subsequent type II migration of a giant planet, still in the runaway regime of accretion.

## 2 Type I – type II migration transition

Type I migration is directed inwards in standard isothermal discs (Ward 1997; Tanaka et al. 2002), but can be outwards when thermal effects are taken into account (e.g. Kley & Crida 2008; Kley et al. 2009). More precisely, this is due to the corotation torque, and requires specific conditions for the latter not to saturate, that is to vanish after a few libration periods in the horseshoe region. Paardekooper et al. (2011) provide a

[1] Université Côte d'Azur / Observatoire de la Côte d'Azur / CNRS, Laboratoire Lagrange, Boulevard de l'Observatoire, CS 34229, 06300 Nice, France
[2] Institut Universitaire de France, 103 Boulevard Saint-Michel, 75005 Paris, France
[3] Lund Observatory, Department of Astronomy and Theoretical Physics, Lund University, Box 43, 22100 Lund, Sweden

formula for the total torque felt by a planet which takes all these effects into account, and has been confirmed by 3D simulations Lega et al. (2014, 2015) (see Baruteau et al. 2014, for a complete review). From this, Bitsch et al. (2013, 2014a,b) have derived migration maps, in which the torque felt by a planet is shown as a function of the planetary mass and the distance to the star. These maps reveal the presence of an island of outward migration (at and beyond the snowline), which never goes above 30 Earth masses, and in most disks does not reach 20 Earth masses. Therefore, the too fast type I migration problem can be solved for giant planet cores, but remains open as soon as the mass exceeds $20-30M_\oplus$, where the corotation torque saturates.

Beyond this mass, there is a competition between accretion and migration to reach the gap opening mass (Crida et al. 2006) before having migrated inwards too much. We have performed 2D numerical simulations using the FARGO-2D1D code (Crida et al. 2007), with an isothermal equation of state (the thermal part of the corotation torque is therefore zero). The resolution is $dr/r = 0.01 = d\theta$. The aspect ratio of the disc is $h = H/r = 0.05$, uniform, and the viscosity is given by the Shakura & Sunyaev (1973) prescription: $\nu = \alpha H^2\Omega$ with $\alpha = 10^{-3}$. The planet starts at $r = 10$ with a mass of $20M_\oplus$, and is let free to migrate, while accreting gas. Gas accretion is performed using Kley (1999) recipe, caped by the accretion rate in runaway growth given by Machida et al. (2010, eq. (11)). The initial surface density of the gas disc is always of the form $\Sigma(r) = \Sigma_0 \times (L/r)^{-s}$ (where $L$ is the length unit), and we try various values of $\Sigma_0$ because the migration speed is proportional to the surface density of the disc. Here, we choose $s = 1$ because with this slope of the density profile, the viscous spreading of the disc, and hence the type II migration should be very slow (see next section).

The result is shown in figure 1. In type II migration's conditions, our planets follow an almost vertical line, because accretion become much faster than migration. Whatever $\Sigma_0$, that is whatever the type I migration speed, the planets always transit to type II migration when they reach the gap opening mass (marked by the grey line). In all our simulations, the planets avoid migrating too close to their central star. In the most massive disk, though, the positive feedback on the migration provided by the partial opening of the gap (Masset & Papaloizou 2003) drives the planet to a semi-major axis only 30% from where it started its runaway accretion. Nonetheless, we can conclude that in general, the migration and the runaway accretion timescales are comparable (they both scale with $\Sigma$). Passing from the mass above which the corotation torque saturates to the mass above which a gap is open by the planet can be done with type I migration only reducing the semi major axis by a factor 2 (more in massive discs, less in light discs).

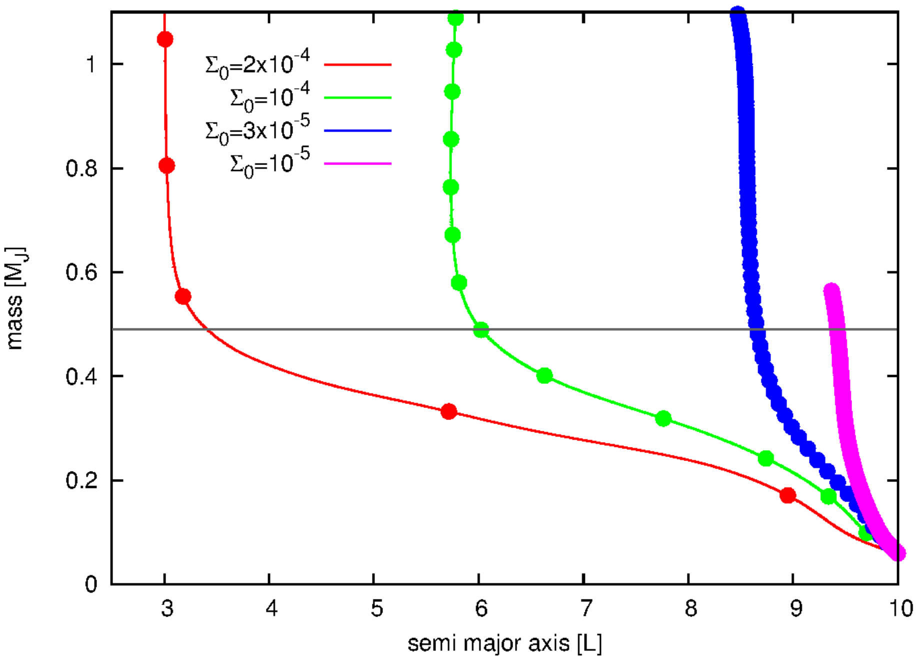


**Fig. 1.** Path of giant planets in the semi-major-axis versus mass plane, as they freely migrate while in runaway gas accretion. On each curve, a dot is placed every 1000 orbits at $r = 1$. Horizontal grey line: gap opening mass, which also marks the transition between the fast type I and the slow type II migration.

## 3 Type II migration of accreting giant planets

We now consider planets of Jupiter mass (that is a thousandth of the mass of the central star). In our simulations, they are first left on a fixed orbit for 200 orbits, to give them time to open a gap. They are then released free to migrate in type II migration. In standard type II migration the planets should be driven by the disc and follow its viscous evolution (Lin & Papaloizou 1986). However, it has been argued that some gas could pass through the gap, allowing the planet to decouple from the disc (e.g. Crida & Morbidelli 2007; Dürmann & Kley 2015). To test this, we change the slope of the power law of the gas profile $s$. Indeed, the viscous torque is $T_\nu = 3\pi\nu\Sigma r^2\Omega \propto r^{1-s}$. Hence, if $s < 1$, $T_\nu$ increases with $r$, and an elementary ring loses more angular momentum to its outer neighbour than it gains from its inner neighbour ; the gas drifts inwards. Conversely, if $s > 1$, the gas dirfts outwards. Therefore, one expects the type II migration to be directed inwards with $s = 0$, outwards with $s = 2$, and to be negligible with $s = 1$, as was the case in previous section.

The migration of the planets after release is shown in figure 2. Red curves correspond to the cases with $s = 0$, green to $s = 1$, and blue to $s = 2$. When the planets do not accrete (solid curves), they all end up migrating inwards. Thus, they must decouple from the disc, and gas is crossing the gap from the inner disc to the outer disc in the $s = 2$ case.

The dashed curves correspond to different accretion rates, using our smoothed version of Kley (1999) recipe, described hereafter. Within $0.8\,r_H$ of the planet (where $r_H$ is the Hill radius), gas is removed from the disc and added to the planet mass. More precisely, in a time step $dt$, a fraction $f(d) \times dt$ of the gas located at a distance $d$ from the planet is accreted, where $f(d)$ is given by :

$$f(d) = K \times \begin{cases} 1 & \text{if} \quad d < 0.3\,r_H \ , \\ \cos^2\left(\pi\left(\frac{d}{r_H} - 0.3\right)\right) & \text{if} \quad 0.3\,r_H < d \ . \end{cases} \tag{3.1}$$

The coefficient $K$ is 1 for the long dashed curves, and 10 for the dotted curves (and 0 for the solid curves). Convergence is reached in the $s = 0$ (red) case : the migration rate is the same whether $K = 1$ of $K = 10$. A natural interpretation of this is that no gas is passing through the gap, it is all accreted.

In the other two cases, the more the planet accretes, the less it migrates inwards (or the more it migrates outwards). In particular, in the $s = 2$ case (blue), outwards migration is only sustained with $K = 10$. We interpret this as $K = 10$ being sufficient for no gas from the inner disc to reach the outer disc and refill it. As the outer disc keeps spreading outwards, it empties and the planet feels a weaker negative torque from it. It's torque balance remains positive (thanks to the inner disc) and it migrates outwards, pushed by the spreading of the outer disc.

## 4 Conclusions

In summary, we have first shown that growing giant planet should open a gap and therefore transition from type I to type II migration, before being lost into their central star. This holds even if their type I migration changes their orbital radius by more than the width of the gap during this process, as illustrated by the 2 left curves of figure 1. This result is developed in a peer review article (Crida & Bitsch 2016, in press).

Then, we have found that the accretion of gas by a gap opening giant planet influences dramatically its type II migration. This desserves a further, more complete study, and will be the topic of a forthcoming paper.

## References

Baruteau, C., Crida, A., Paardekooper, S.-J., et al. 2014, Protostars and Planets VI, 667

Bitsch, B., Crida, A., Morbidelli, A., Kley, W., & Dobbs-Dixon, I. 2013, A&A, 549, A124

Bitsch, B., Morbidelli, A., Lega, E., & Crida, A. 2014a, A&A, 564, A135

Bitsch, B., Morbidelli, A., Lega, E., Kretke, K., & Crida, A. 2014b, A&A, 570, A75

Crida, A. & Bitsch, B. 2016, Icarus, accepted on Oct. 12

Crida, A. & Morbidelli, A. 2007, MNRAS, 377, 1324

Crida, A., Morbidelli, A., & Masset, F. 2006, Icarus, 181, 587

Crida, A., Morbidelli, A., & Masset, F. 2007, A&A, 461, 1173

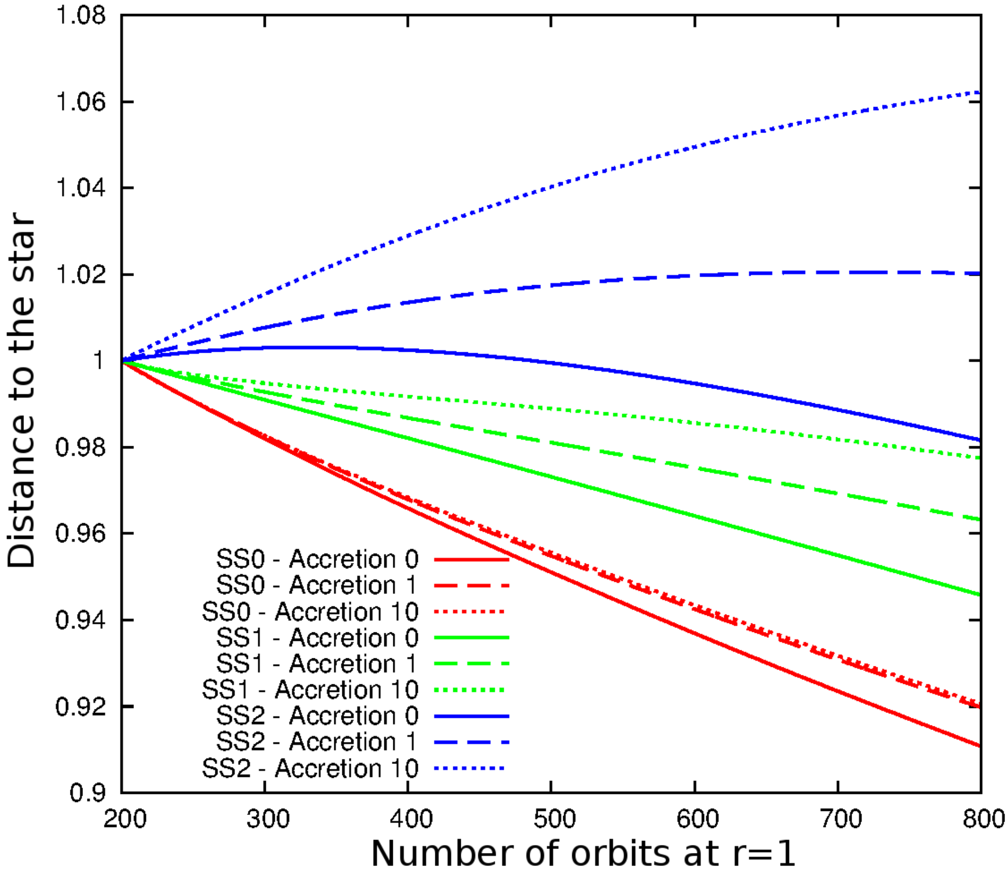


**Fig. 2.** Semi major axis as a function of time for Jupiter mass planets released after 200 orbits in a disc of initial profile of the density slope $s = 0, 1, 2$ (red, green, blue respectively). The planets accrete in an orbit the fraction of the gas located at a distance $d$ given by $f(d)$ with $K = 0$ (no accretion, solid curves), $K = 1$ (long dashed curves), or $K = 10$ (dotted curves).


Dürmann, C. & Kley, W. 2015, A&A, 574, A52

Kley, W. 1999, MNRAS, 303, 696

Kley, W., Bitsch, B., & Klahr, H. 2009, A&A, 506, 971

Kley, W. & Crida, A. 2008, A&A, 487, L9

Lega, E., Crida, A., Bitsch, B., & Morbidelli, A. 2014, MNRAS, 440, 683

Lega, E., Morbidelli, A., Bitsch, B., Crida, A., & Szulágyi, J. 2015, MNRAS, 452, 1717

Lin, D. N. C. & Papaloizou, J. 1986, ApJ, 309, 846

Machida, M. N., Kokubo, E., Inutsuka, S.-I., & Matsumoto, T. 2010, MNRAS, 405, 1227

Masset, F. S. & Papaloizou, J. C. B. 2003, ApJ, 588, 494

Paardekooper, S., Baruteau, C., & Kley, W. 2011, MNRAS, 410, 293

Shakura, N. I. & Sunyaev, R. A. 1973, A&A, 24, 337

Tanaka, H., Takeuchi, T., & Ward, W. R. 2002, ApJ, 565, 1257

Ward, W. R. 1997, Icarus, 126, 261

*SF2A 2016*
*C. Reylé, J. Richard, L. Cambrésy, M. Deleuil, E. Pécontal, L. Tresse and I. Vauglin (eds)*

# SPIRALS, GAPS, CAVITIES, GAPITIES: WHAT DO PLANETS DO IN DISCS?

A. Crida[1 2]

**Abstract.** In this presentation, part of the "Observations of discs" workshop, I address the theoretical point of view of planet-disc interactions. In section 2, I will review the physics of spirals, and explain why the inner and the outer wake created by a planet in a gaseous keplerian disc look very different, but their shape is independant of the mass of the planet and almost only depends on the aspect ratio of the disc. In the third section, I discuss the axisymmetric features (gaps and cavities), and how they differ in the gas or the dust component.

However, to start with, some clarification of the nomenclature seems to be required, as observers and theorists may have a different idea of what a gap is. The definition of a "gapity" may help to clarify the situation of pre-transitional discs.

Keywords: Planet-disk interactions, Protoplanetary disks, Planets and satellites: formation

## 1 Gaps, cavities and terminology

Let me first take this opportunity to write down clearly a few definitions. Our community generally agrees on these terms, but to avoid any misunderstanding between observers and theorists, and to help students discovering our field, here is a little glossary.

**Cavity :** A *cavity* in a disc is an empty region inside a given radius $r_{\rm cav}$. Cavities are observed in a few discs, called *transition discs*. For the sake of clairity, a cavity should be completely empty, that is there is nothing between the star and $r_{\rm cav} > 1AU$, which is then the radius of the inner edge of the disc.

**Gap :** In contrast to a cavity, a gap is an empty region separating an inner and an outer disc. A gap has the shape of an annulus, while the cavity has the shape of a full circle. Giant planets open gaps in the gas disc. Those gaps have roughly the width of the horseshoe region of the planet, that is in total $\sim 3r_{\rm Hill}$, where $r_{\rm Hill} = r_p(M_p/3M_*)^{1/3}$ is the Hill radius. Hence, in general, the radius of the outer edge of the inner disc (which is also the inner edge of the gap) $r_{\rm in}$ and the radius of the inner edge of the outer disc (or outer edge of the gap) $r_{\rm out}$ differ by less than a factor 2.

**Gapity :** In some discs (so called *pre-transitionnal discs*) a small inner disc is observed inside a cavity. Or in other words, very large gaps are seen, where $r_{\rm out}/r_{\rm in} > 3$. Such structure can not be caused by a single giant planet, in contrast with the gaps described above. To account for a possible different physical origin, a different word is needed. In-between a narrow gap and an empty cavity, I suggest a *gapity**.

**Migration versus drift :** Finaly, I would like to remind that the radial motion of planets and dust inside a protoplanetary disc are not the same phenomenon. Planets exchange orbital angular momentum with the gas via gratity, while dust does so via friction. Hence, it is important to keep using the word *migration* for planets and gravitationnal phenomenons, and *drift* for dust, pebbles, and friction phenomenons.

[1] Université Côte d'Azur / Observatoire de la Côte d'Azur / CNRS, Laboratoire Lagrange, Boulevard de l'Observatoire, CS 34229, 06300 Nice, France
[2] Institut Universitaire de France, 103 Boulevard Saint-Michel, 75005 Paris, France
*En français, ces structures intermédiaires entre sillons et cavités pourraient être appelées *cavillons.*

## 2 Spirals and wake

### 2.1 *Spirals : some reminders*

Consider a curve in polar coordinate $(r, \theta)$. The *pitch angle* is the angle between the curve and the azimuthal direction, so that :

$$\tan\alpha = \mathrm{d}r/r\,\mathrm{d}\theta \ . \tag{2.1}$$

The most famous spiral is *Archimede's spiral*, whose equation is simply $r = \lambda\theta$ with $\lambda$ any real constant. In this case, for every full rotation, $r$ increases by the same amount : $2\pi\lambda$. For this spiral, the pitch angle depends dramatically on $r$ : $\alpha = \arctan(\lambda/r)$. Hence, $\alpha = \pi/2$ at $r = 0$, where the spiral starts in the radial direction ; conversely $\alpha \to 0$ as $r \to \infty$, which means that the curve become more and more orthoradial and looks more and more like a circle when one goes far from the centre.

Imposing $\alpha$ constant, one gets $r = \exp(\lambda\theta)$ (with $\lambda = \tan(\alpha)$ ), that is the *logarithmic spiral.* This curves looks the same close to the centre and far from it, and crosses radii always with the same angle.

### 2.2 *Few prerequisites on disc physics*

We consider a protoplanetary disc made of perfect gas, with equation of state :

$$P = \left(\frac{c_s^2}{\gamma}\right)\rho \ ,$$

where $P$ is the pressure, $\rho$ the (volume) density, $c_s$ the sound speed, and $\gamma$ the adiabatic index, the ratio of specific heats. With this equation of state, one shows easily that the vertical hydrostatic equilibrium is fulfilled if the density follows (assuming $z \ll r$ and $c_s$ independent of $z$) :

$$\rho(r,z) = \rho_0(r) \times \exp\left(-\frac{z^2}{2\,H^2}\right) \tag{2.2}$$

where $H = c_s/(\Omega\sqrt{\gamma})$, with $\Omega = \sqrt{GM_* r^3}$ the Keplerian angular velocity ($G$ being the gravitational constant and $M_*$ the mass of the central star). This defines $H$, the scale height of the disc. We note $h = H/r$ the *aspect ratio* of the disc.

Last, using the perfect gases equation $P = (R/\mu)\rho T$ where $R$ is the constant of perfect gases, $\mu$ the molecular weight, and $T$ the temperature, one finds :

$$T = {c_s}^2\,\mu/(\gamma R) = h^2(GM_*/r)(\mu/R) \ . \tag{2.3}$$

With $h$ uniform, this leads to $c_s \propto r^{-1/2}$ and $T \propto 1/r$.

### 2.3 *Wake of a planet*

With these well-known prerequisites in mind, one can study the shape of the wake created by a planet in a protoplanetary disc. The wake is a pressure-supported wave, so it propagates radially away from the planetary orbit with a velocity $c_s$. The azimuthal velocity is the relative velocity between the planet and the gas, and is set by the Keplerian shear : $v_{\mathrm{rel}} = r(\Omega(r) - \Omega_p)$, where the index $p$ refers to the planet.

In the limit $r - r_p \ll r_p$, we can define $\Delta = (r - r_p)/r_p \ll 1$, and $v_{\mathrm{rel}} \approx \frac{3}{2} r\Omega_p\Delta$. Hence, the pitch angle of the wake follows :

$$\tan(\alpha) = c_s/v_{\mathrm{rel}} = \frac{3}{2}(c_s/\Omega_p r\Delta) = \frac{3}{2}\sqrt{\gamma}h_p/\Delta \ . \tag{2.4}$$

Close to the planet $\alpha \approx \pi/2$ and the wake is radial. The wake then bends as $\Delta$ increases.

In the inner disc, as $r \to 0$, $v_{\mathrm{rel}} \approx r\Omega(r) \sim r^{-1/2}$, and $\tan(\alpha) = \sqrt{\gamma}h$. With $h$ uniform, this is a logarithmic spiral. Taking $\gamma = 1.4$ and $h = 0.12$, one gets $\alpha = 8.5°$.

In the outer disc, as $r \to \infty$, $v_{\mathrm{rel}} \approx r\Omega_p \propto r$, and $\tan(\alpha) = c_s/v_{\mathrm{rel}}$ tends to 0 faster than in an Archimede's spiral. The outer wake bends a lot, and looks closer and closer to a ring.

As an illustration of how different the inner and outer wake look, the spiral structure observed by Benisty et al. (2015) in MWC758 could be satisfactorily reproduced by Dong et al. (2015a) only by placing a companion outside the disc, so that the spiral was the inner wake, not the outer one.

In all the above, the only paramater in the shape of the wake is $h$. The shape of the wake does not depend on the mass of the planet, nor on the viscosity of the gaseous disc. The larger $h$ (that is : the thicker the disc), the more open the wake is.

## 3 Gaps, cavities, gapities

It is well known that giant planets open gaps in a gaseous protoplanetary disc (Lin & Papaloizou 1986; Crida et al. 2006, 2016). If one puts a few giant planets in a proto-planetary disc, they may well have a convergent migration until they open a common gap and lock in a resonant chain. In this case, the large gap extends from inside the orbit of the innermost planet to outside the orbit of the outermost one, and could correspond to the definition of a gapity.

The edges of the gap open by a planet are pressure maxima in the gas component, therefore they behave as dust traps (dust always drifts towards the pressure maxima). Fouchet et al. (2010) "*show that the gap in the dust layer is more striking than in the gas phase and that it is deeper and wider for more massive planets as well as for larger grains*". In fact, Lambrechts et al. (2014) and Rosotti et al. (2016) found that even planets of mass $M_p > 20\, M_\oplus (h/0,05)^{1/3}$ are able to create a pressure maximum outside of their orbits, although they don't open a real gap, but barely carve a dip around their orbit.

Such planets can therefore create a gap in the dust component, which would not be detectable in the gas component. Rosotti et al. (2016) argue that measuring the distance between the pressure maximum (seen in sub-mm) and the middle of the gap (observed in scattered light) allows to derive the planet mass, as this distance should be 10 Hill radius.

Of course, dust grains of different sizes behave differently. More specifically, dust grains with a stopping time much shorter than the dynamical time (that is a Stokes number $St \ll 1$) are tightly coupled to the gas, and follow its distribution. As grains get larger and $St \to 1$, the pressure trap becomes more and more effective, and the dust gap becomes deep and sharp (e.g. Gonzalez et al. 2012; Dong et al. 2015b). Actually, when the pressure trap is so strong that no dust goes through, dust in the inner disc keeps drifting inwards whithout being replaced by drifting dust from the outer disc, and a gapity opens. Hence, a single massive planet can open a gapity in the dust component, but not in the gas component. Such gapities may transition to cavities once all the dust has drifted out of the inner disc.

Last, let us remind that if a giant planet is more massive than the disc, the latter can not push the former, and migration stalls (Crida & Morbidelli 2007). If the gap is so deep (or the planet accretes so fast) that the gas shall not pass from the outer to the inner disc, the inner disc will eventually spread into the host star and vanish, leading to the opening of a cavity in gas.

## 4 Conclusion

In this little review, I have discussed what planets can and can not do in discs. To interpret observations correctly, it is extremely important to be aware of these constains. Not all structures in discs can be due to planets, and structures like gaps, cavities or spirals could be created by other phenomenons, which are not the topic of this presentation. To date, there is no direct proof of a structure being created by a planet, but future observations will be extremely exciting. May this little contribution help bridging the gap between theory and observations of planet-disc interactions.

## References

Benisty, M., Juhasz, A., Boccaletti, A., et al. 2015, A&A, 578, L6

Crida, A., Bitsch, B., & Raibaldi, A. 2016, in SF2A-2016: Proceedings of the Annual meeting of the French Society of Astronomy and Astrophysics, ed. L. Cambrésy, M. Deleuil, E. Pécontal, C. Reylé, J. Richard, L. Tresse, & I. Vauglin

Crida, A. & Morbidelli, A. 2007, MNRAS, 377, 1324

Crida, A., Morbidelli, A., & Masset, F. 2006, Icarus, 181, 587

Dong, R., Zhu, Z., Rafikov, R. R., & Stone, J. M. 2015a, ApJ, 809, L5

Dong, R., Zhu, Z., & Whitney, B. 2015b, ApJ, 809, 93

Fouchet, L., Gonzalez, J.-F., & Maddison, S. T. 2010, A&A, 518, A16

Gonzalez, J.-F., Pinte, C., Maddison, S. T., Ménard, F., & Fouchet, L. 2012, A&A, 547, A58

Lambrechts, M., Johansen, A., & Morbidelli, A. 2014, A&A, 572, A35

Lin, D. N. C. & Papaloizou, J. 1986, ApJ, 309, 846

Rosotti, G. P., Juhasz, A., Booth, R. A., & Clarke, C. J. 2016, MNRAS, 459, 2790

# Author Index


Aboudarham, J., 293
Abrams, D. C., 267
Adam, R., 439
Ade, P., 439
Aguerri, A. L., 267
Akramov, T., 115
Albert, L., 243
Alecian, E., 199
Allard, F., 223
Alves, M. I. R., 353
Amari, T., 297
André, P., 439
Antoci, V., 217
Antoja, T., 281
Artigau, E., 243
Aubert, D., 399
Augereau, J.-C., 455
Aunai, N., 157
Aussel, H., 439
Author2, J.-P., 243
Author3, C. E., 243

Böttcher, M., 93
Bénilan, Y., 17
Béthune, W., 129
Babusiaux, C., 281
Bagchi, J., 367
Balança, C., 17
Baty, H., 115
Bauer, F. E., 411
Beck, P. G., 185, 203
Bedding, T. R., 217
Beelen, A., 439
Belkacem, K., 179
Benoît, A., 439
Bentum, M., 339, 343
Bergin, E., 321
Best, P. N., 271
Bideaud, A., 439
Billot, N., 439
Bina, D., 411
Biree, L., 293
Bitsch, B., 473
Blaizot, J., 407
Blanco-Cuaresma, S., 333
Blazère, A., 253
Blelly, P.-L., 297
Boisse, I., 243
Bolton, J. S., 259
Bonazzola, S., 45
Bonfils, X., 243
Bonifacio, P., 267
Bonnet-Bidaud, J.-M., 69
Bonoli, S., 259
Bottacini, E., 93
Bouchy, F., 243
Boulanger, F., 353
Bourdarie, S., 297
Bourrion, O., 439
Bouvier, J., 199, 203
Briand, C., 297, 339, 343
Britto, R. J., 93
Brouillet, N., 321
Brugger, B., 11
Brun, A. S., 297
Bucher, M., 339, 343
Buchlin, E., 297
Buckley, D. A. H., 93
Busca, N. G., 259
Bushouse, H., 39
Buson, S., 93
Busschaert, C., 69
Buysschaert, B., 229

Cabanac, R., 237
Calvo, M., 439
Carrasco, E., 267
Carvajal, M., 321
Catalano, A., 439
Ceccarelli, C., 321
Cecconi, B., 339, 343
Chadid, M., 207
Chadwick, P., 373
Chambodut, A., 297
Chamel, N., 51
Champion, D., 61
Chardin, J., 423
Chatterjee, D., 51
Chaves-Montero, J., 259
Chilingarian, I., 411
Ciardi, A., 69, 157
Clénet, Y., 57, 103
Claret, A., 297
Cochrane, R. K., 271
Cognard, I., 61
Coiffard, G., 439
Colom, P., 373
Combes, F., 153, 367, 373, 385, 429
Comis, B., 439
Coppin, K. E., 271
Corbard, T., 293, 297
Corsaro, E., 203
Cotton, W. D., 39
Crespeau, P.-J., 373

Crida, A., 473, 477
Crifo, F., 249
Crouzet, N., 243
Crussaire, D., 293

Désert, F.-X., 439
Dalton, G., 267
Dannerbauer, H., 271
Dargent, J., 157
Dassa-Terrier, J., 3
Davis, T. A., 271
Deguignet, J., 357
Deleuil, M., 11
Delfosse, X., 243
Deparis, N., 399
Despois, D., 321
Desvignes, G., 61
Di Matteo, P., 281
Donati, J.-F., 243
Dournaux, J.-L., 77
Doyle, S., 439
Doyon, R., 243
Drissen, L., 23
Drouin, M., 157
Dudok De Wit, T., 297
Duncan, K. J., 271

Eckart, A., 39
Edge, A., 367
Edge, A.-C., 385
El-Zant, A., 153
Ellis, R., 411

Falize, É., 69
Famaey, B., 281
Fantina, A. F., 51
Favre, C., 321
Ferrari, A., 357
Ferrari, C., 357
Ferreira, J., 129
Ferrière, K., 353
Figueras, F., 281
Folsom, C. P., 199
Font-Ribera, A., 259
Forveille, T., 243
Fragkoudi, F., 281
Freundlich, J., 153
Fuller, N., 293
Fumagalli, M., 259

Génot, V., 297
García, R. A., 185, 203
Garcia, A. J. L., 449
Garel, T., 393
Garzon-Lopez, F., 281
Geach, J. E., 271
Gebran, M., 209, 213
Gerin, M., 163, 309
Girard, J., 339, 343
Godard, B., 163, 309
Gonzalez, J.-F., 449
Gonzalez-Fernandez, C., 281
Goosmann, R., 57, 89, 103
Goupil, M. J., 179
Goupy, J., 439
Grandclement, P., 121
Gratadour, D., 57, 103
Griessmeier, J. M., 17
Grosset, L., 57, 103
Grosso, N., 39
Guépin, C., 83
Guennou, C., 297
Guiderdoni, B., 367, 373

Hébrard, G., 243
Haehnelt, M. G., 423
Hale, C. L., 271
Hamer, S., 429
Hamer, S.-L., 385
Hardcastle, M. J., 271
Hatch, N. A., 271
Hatfield, P. W., 271
Heald, G., 379
Hennebelle, P., 139, 163, 189, 203, 309
Hill, V., 281
Hoai, D. T., 433
Houghton, R. C. W., 271
Hussain, G., 199

Infante, L., 411
Intema, H., 379

Jørgensen, J., 321
Jacob, J., 367
Jarvis, M. J., 271
Jasniewicz, G., 249
Jelić, V., 353

Katz, D., 249
Keppens, R., 107
Kharb, P., 373
Kim, S., 411
Klein, K. L., 297
Kleiner, I., 321
Koechlin, L., 297
Kong, A. K. H., 73
Kotera, K., 83
Kral, Q., 463
Kramer, C., 439
Kundu, A., 65

Lagache, G., 439
Lagarde, N., 287

Lançon, A., 329
Laporte, N., 411
Laporte, P., 77
Laurens, A., 339, 343
Lavarra, M., 297
Lavraud, B., 157, 297
Lazarus, P., 61
Le Bertre, T., 433
Leblanc, F., 297
Lecavelier des Etangs, A., 243
Leclercq, S., 439
Lee, Y.-N., 139, 189, 203
Lefloch, B., 321
Lemorton, J., 297
Leroy, M. H. J., 107
Lesaffre, P., 163, 309
Lestrade, J.-F., 439
Lesur, G., 129
Lignières, F., 253
Lilensten, J., 297
Lopez-Ariste, A., 297
Lott, B., 93

Macías-Pérez, J. F., 439
Maddox, N., 271
Malherbe, J.-M., 293
Malo, L., 243
Marais, J. P., 93
Marchal, O., 249
Marchaudon, A., 297
Marcq, E., 17
Marin, F., 57, 89, 103
Martin, J.-M., 373
Martin, T. B., 23
Martinez-Valpuesta, I., 281
Mary, D., 357
Masson, S., 297
Mathis, S., 203
Mathur, S., 203
Maury, A., 439
Mauskopf, P., 439
Mayet, F., 439
McGee, S. L., 271
Meftah, M., 293
Meintjes, P. J., 93
Middleton, K., 267
Miralda-Escudé, J., 259
Monari, G., 281
Monfardini, A., 439
Monier, R., 209, 213
Montanet, F., 111
Mor-Crespo, R., 281
Morabito, L., 271
Morand, F., 293
Mossoux, E., 39
Mottez, F., 45, 83, 347
Mouchet, M., 69
Mousis, O., 11, 445
Moutou, C., 243
Murphy, S. J., 217

Narasimha, D., 367
Nasello, G., 287
Navarro, T., 17
Neiner, C., 229, 253
Nhung, P. T., 433
Nisbet, D., 271
Noterdaeme, P., 259
Novak, J., 51

Octau, F., 61
Ocvirk, P., 399
Oertel, M., 51
Ouazzani, R.-M., 217

Pérez-Fournon, I., 411
Pétri, J., 65
Pajot, F., 439
Pandey-Pommier, M., 271, 367, 373, 379
Panuzzo, P., 249
Pariat, E., 297
Pascale, E., 439
Peissker, F., 39
Pelat, D., 57, 103
Pelló, R., 411, 417
Perotto, L., 439
Peroux, C., 259
Petit, P., 253
Pieri, M. M., 259
Pignatale, F. C., 449
Pinçon, C., 179
Pinto, R. F., 297
Pisano, G., 439
Plambeck, R. L., 39
Pommier, M. P., 385
Ponthieu, N., 439
Porquet, D., 39
Powalka, M., 329
Prandoni, I., 271
Prugniel, P., 329
Puchwein, E., 423
Puy, D., 339, 343
Pâris, I., 259

Röttgering, H. J. A., 271
Rahmani, H., 259
Raibaldi, A., 473
Razzaque, S., 93
Renaud, C., 293
Renner, S., 17
Revéret, V., 439
Reverdy, V., 133

Reville, V., 297
Reylé, C., 287
Richard, J., 367, 373, 411
Ritacco, A., 439
Roberts, D. A., 39
Roberts-Borsani, G., 411
Robin, A. C., 287
Rodriguez, L., 439
Rojas Lobos, P. A., 57, 89, 103
Romero, C., 439
Romero-Gomez, M., 281
Ronnet, T., 445
Roques, F., 17
Rouan, D., 57, 103
Rouillard, A. P., 297
Roussel, H., 439
Royer, F., 209, 213
Ruppin, F., 439
Ruty, F., 293

Salabert, D., 185
Salmon, S. J. A. J., 217
Salomé, P., 429
Salomé, Q., 429
Santerne, A., 243
Sartoretti, P., 249
Saxena, A., 271
Sayède, F., 267
Schneider, J., 17
Schott, C., 17
Schuster, K., 439
Segret, B., 339, 343
Sezestre, É., 455
Shimabukuro, H., 403
Shimwell, T. W., 271
Siebert, A., 281
Sievers, A., 439
Simpson, C. J., 271
Sirothia, S., 373
Smets, R., 157
Smith, D., 61
Smith, D. J. B., 271
Sol, H., 31, 77, 315
Soler, J., 439
Sorce, J. G., 169
Soubiran, C., 249, 333
Stello, D., 203
Stiele, H., 73
Stott, J. P., 271
Streblyanska, A., 411

Tarr, M., 271
Theureau, G., 61
Trager, S., 267
Trager, S. C., 259
Trebitsch, M., 407
Triqueneaux, S., 439
Troncoso-Iribarren, P., 411
Tucker, C., 439
Turc, L., 297

Udry, S., 249

Valdivia, V., 163, 309
Valencia, M., 39
Vallenari, A., 267
van Bemmel, I., 271
Van Box Som, L., 69
van Driel, W., 373
van Soelen, B., 93
Vannier, M., 357
Vauglin, I., 329
Verma, A., 271
Vernazza, P., 445
Viel, M., 259
Villebrun, F., 199
Vilmer, N., 297
Voisin, G., 45, 83

White, G. J., 271
Williams, W. L., 271
Winters, J. M., 433

Yusef-Zadeh, F., 39

Zarka, P., 83, 347
Zheng, W., 411
Zucarello, F. P., 297
Zurbach, C., 249
Zylka, R., 439